Developments in Paleoenvironmental Research 17

Ian W. Croudace
R. Guy Rothwell *Editors*

# Micro-XRF Studies of Sediment Cores

## Applications of a non-destructive tool for the environmental sciences

Springer

# Developments in Paleoenvironmental Research

Volume 17

**Series Editor**
John P. Smol
Kingston, Ontario, Canada

Paleoenvironmental research continues to enjoy tremendous interest and progress in the scientific community. The overall aims and scope of the—*Developments in Paleoenvironmental Research*—book series is to capture this excitement and document these developments. Volumes related to any aspect of paleoenvironmental research, encompassing any time period, are within the scope of the series. For example, relevant topics include studies focused on terrestrial, peatland, lacustrine, riverine, estuarine, and marine systems, ice cores, cave deposits, palynology, isotopes, geochemistry, sedimentology, paleontology, etc. Methodological and taxonomic volumes relevant to paleoenvironmental research are also encouraged. The series will include edited volumes on a particular subject, geographic region, or time period, conference and workshop proceedings, as well as monographs.

Prospective authors and/or editors should consult the **Series Editor John P. Smol** for more details. Any comments or suggestions for future volumes are welcomed;

More information about this series at http://www.springer.com/series/5869

Ian W. Croudace • R. Guy Rothwell
Editors

# Micro-XRF Studies of Sediment Cores

## Applications of a non-destructive Tool for the Environmental Sciences

Springer

*Editors*
Ian W. Croudace
Ocean and Earth Science
National Oceanography Centre
University of Southampton
Waterfront Campus
Southampton
UK

R. Guy Rothwell
National Oceanography Centre
Southampton
UK

ISSN 1571-5299 ISSN 2215-1672 (electronic)
Developments in Paleoenvironmental Research
ISBN 978-94-017-9848-8 ISBN 978-94-017-9849-5 (eBook)
DOI 10.1007/978-94-017-9849-5

Library of Congress Control Number: 2015940319

Springer Dordrecht Heidelberg New York London


Printed on acid-free paper

Springer Science+Business Media B.V. Dordrecht is part of Springer Science+Business Media (www.springer.com)

BOSCORF core (CD166-19), recovered off northwest Africa. The core shows a sequence of pelagic nannofossil oozes (cream) and clays (light to medium brown) with interbedded turbidite sands (dark brown to black). Three logging parameters, magnetic susceptibility (dark blue), ITRAX measured Ca (green) and b* colour values (yellow) are overlaid and plotted downcore. These data were obtained using the BOSCORF ITRAX, MSCL-XYZ, core loggers and MSCL-S and displayed in CoreWall.

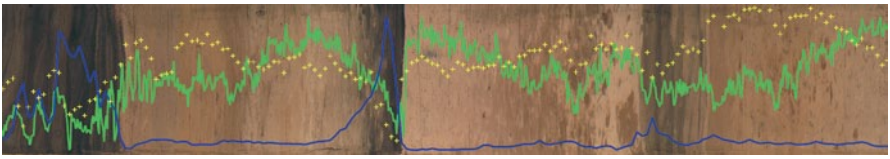

# Foreword

Over the last century, Earth sciences have evolved from disciplines mostly based on naked eye observations of rocks and sediments to a scientific field employing the most sophisticated tools developed in analytical physics and chemistry. The introduction of quantitative instrumentation has thus played a major role in enabling advances in our knowledge of Earth history and processes. Because geological archives are so unique and complex, the geoanalytical refinements have often been pushed to their ultimate limits of resolution, precision and detection limits in order to extract crucial information from objects found in nature.

High-resolution core scanners incorporating X-ray fluorescence (XRF) spectrometry are arguably one of the most useful tools that have become available to the research community. Their impact is based on their ability to rapidly, non-destructively and automatically scan sediment cores. Not only do they rapidly provide important proxy data without damaging samples, but they can obtain environmental data at decadal, annual and even sub-annual scales. Micro-XRF core scanners can indeed be used at the limit of the inherent heterogeneity of sediments linked to the presence of grains of different nature, chemical composition and mineralogy. In addition to producing geochemical profiles along the core length, these scanners also allow study of spatial heterogeneities within the sediment through optical images, X-radiography or micro-XRF 2D images of elemental composition.

In a little over a decade, micro-XRF core scanners have made a substantive contribution to paleoenvironmental research as evidenced by the exponential rise in the peer-reviewed scientific literature. For the field of paleoclimatology, the use of sediment cores from lakes and oceans had always been limited by the resolution of discrete sampling, but the introduction of XRF-scanners truly revolutionized the field allowing the study of similar details in sediments as in polar ice cores from Greenland and Antarctica. The versatility of XRF-scanners allows their application to other types of paleoclimate archives from diverse locations such as massive corals from tropical reefs, speleothems from caves and subfossil woods.

The key initial strength of XRF core scanners was their ability to scan a meter of sediment core at high resolution in about 24 hours. Ongoing instrumental developments are already leading to further enhancements in sensitivity and speed and

throughput. High-resolution XRF core scanners produce a high data output, with potentially several thousand spectra acquired per meter of core.

The increasing speed of analyses has allowed researchers to dare tackling projects based on large amounts of cored material, the XRF-scanner being often the first analytical tool used after opening and splitting the cores. The resulting elemental profiles, derived from the non-destructive analysis of cores and often involving several thousand XRF spectra, are thus used for reconnaissance studies and basic stratigraphic correlations. XRF core scanners can also be used for insightful geochemical studies, provided that proper calibration is performed by means of discrete geochemical measurements with accurate techniques such as conventional XRF or ICP. Whereas with these conventional techniques, data are acquired from dry homogenized fine-grained samples, wet natural sediment cores measured with scanners present very different sample conditions. Grain-size and water content variations, core surface imperfections, presence of organic matter and water pooling on the sample surface will all impact on data quality. Hence interpretation of core scanner data is not trivial and guidance is often needed to discriminate environmentally meaningful information from data artifacts.

As outlined above, the use of XRF core scanners is characterized by an inherent simplicity in acquiring useful elemental profiles, but making the best out of these sophisticated tools also requires experience and a deep knowledge in geochemistry and physical properties of sediments. XRF-scanner facilities are now used in about one hundred institutions spread throughout Europe, North America and Asia. This gave rise to a specific community of users with diverse technical expertise and scientific expectations.

As an illustration, I will say a few words about the specific example of the XRF-scanner installed in 2008 at CEREGE in Aix-en-Provence. We became interested in such analyses in the mid-2000s because of our tradition of working on deep-sea sediments, notably the basic quantification of major phases such as carbonates, detrital minerals and organic matter, but also several detailed studies of trace elements scavenged in the water column or trapped in the sediments because of specific redox conditions. These variables were quantified with various techniques of organic and inorganic geochemistry on discrete samples. Since then, micro-XRF scanner profiles have allowed us to better understand the relationships between these various profiles and integrate them into a coherent and high-resolution framework. This truly brought a new dimension to our research in paleoceanography.

The other main consequence of our XRF-scanner acquisition was that it fostered collaboration with specialists of other sedimentary archives, notably those taken from modern and ancient lakes. Our experience is obviously not unique and it can be stated with confidence that the rise of XRF core scanning contributed to bridging the gaps between scientific communities, which were working in parallel.

Scientists of this new community often have similar needs and expectations. By considering ratios of XRF profiles it has been possible to develop proxies for particle sizes, mineralogical composition and organic matter content of sediments. Hopefully, more direct evaluation of these parameters may come from future in-

novations in analytical core scanning based on other electromagnetic emissions and detecting systems.

This volume edited by Ian Croudace and Guy Rothwell, two pioneers and prominent contributors in the field, presents a broad ranging view of instrument capability and points to future developments that will combine higher precision elemental data coupled with faster core analysis. It also presents specific application papers reporting on the use of XRF core scanners in a variety of marine, lacustrine and pollution studies, together with papers examining practical aspects of core scanner usage and data calibration and interpretation. It is a welcome addition to the literature and the first volume of its kind to focus specifically on this important technology. Given the importance of XRF core scanning in modern paleoenvironmental research, this is a timely publication which environmental investigators will find useful. It contains essential reading for both experienced and new researchers using XRF core scanners.

**Specific Publications from CEREGE that used XRF core scanning (by date)**

Gasse F, Vidal L, Van Campo E, Demory F, Develle AL, Tachikawa K, Elias A, Bard E, Garcia M, Sonzogni C, Thouveny N. (2015) Hydroclimatic changes in northern Levant over the past 400,000 years. *Quaternary Science Reviews* 111, 1–8

Tachikawa K, Vidal L, Cornuault M, Garcia M, Pothin A, Sonzogni C, Bard E, Menot G, Revel M (2015) Eastern Mediterranean Sea circulation inferred from the conditions of S1 sapropel Deposition. *Climate of the Past* 11, 855–867

Cartapanis O, Tachikawa K, Romero OE, Bard E (2014) Persistent millennial-scale link between Greenland climate and northern Pacific Oxygen Minimum Zone under interglacial conditions. *Climate of the Past* 10, 405–418

Brisset E, Miramont C, Guiter F, Anthony EJ, Tachikawa K, Poulenard J, Arnaud F, Delhon C, Meunier J-D, Bard E, Suméra F (2013) Non-reversible geosystem destabilisation at 4200 cal. BP: Sedimentological, geochemical and botanical markers of soil erosion recorded in a Mediterranean alpine lake. *The Holocene* 23, 1863–1874

Simonneau A, Chapron E, Courp T, Tachikawa K, Le Roux G, Baron S, Galop D, Garcia M, Di Giovanni C, Motellica-Heino M, Mazier F, Foucher A, Houet T, Desmet M, Bard E (2013). Recent climatic and anthropogenic imprints on lacustrine systems in the Pyrenean Mountains inferred from minerogenic and organic clastic supply (Vicdessos valley, Pyrenees, France). *The Holocene* 23, 1764–1777

Jenny JP, Arnaud F, Dorioz JM, Giguet Covex C, Frossard V, Sabatier P, Millet L, Reyss JL, Tachikawa K, Bard E, Pignol C, P, Soufi F, Romeyer O, Perga ME (2013) A spatiotemporal sediment investigation highlights the dynamics of hypolimnetic hypoxia in a large hard-water lake over the last 150 years. *Limnology & Oceanography* 58, 1395–1408

Soulet G, Ménot G, Bayon G, Rostek F, Ponzevera, Toucanne S, Lericolais G, Bard E (2013) Abrupt drainage cycles of the Fennoscandian Ice Sheet. *Proceedings of the National Academy of Science* 110 (17), 6682–6687

Doyen E, Vannière B, Berger JF, Arnaud F, Tachikawa K, Bard E (2013) Land-use changes and environmental dynamics in the upper Rhone valley since Neolithic times inferred from sediments in Lac Moras. *The Holocene* 23, 961–973

Wilhelm B, Arnaud F, Sabatier P, Magand O, Chapron E, Courp T, Tachikawa K, Fanget B, Malet E, Pignol C, Bard E, Delannoy J-J. (2013) Paleoflood activity and climate change over the last 1400 years recorded by lake sediments in the North-West European Alps. *Journal of Quaternary Science* 28, 189–199

Simonneau A, Doyen E, Chapron E, Millet L, Vannière B, Di Giovanni C, Bossard N, Tachikawa K, Bard E, Albéric P, Desmet M, Roux G, Lajeunesse P, Berger J-F, Arnaud F (2013) Holocene land-use evolution and associated soil erosion in the French Prealps inferred from Lake Paladru sediments and archaeological evidences. *Journal of Archaeological Science* 40, 1636–1645

Cartapanis O, Tachikawa K, Bard E (2012) Latitudinal variations in intermediate depth ventilation and biological production over northeastern Pacific Oxygen Minimum Zones during the last glacial period. *Quaternary Science Reviews* 53, 24–38

Wilhelm B, Arnaud F, Sabatier P, Crouzet C, Brisset E, Chaumillon E, Disnar JR, Guiter F, Malet E, Reyss JL, Tachikawa K, Bard E, Delannoy J-J (2012) 1400yr of extreme precipitation patterns over the Mediterranean French Alps and possible forcing mechanisms. *Quaternary Research* 78, 1–12

Tachikawa K, Cartapanis O, Vidal L, Beaufort L, Bard E (2011) The precession phase of hydrological variability in the Western Pacific Warm Pool during the past 400 ka. *Quaternary Science Reviews* 30, 3716–3727

Cartapanis O, Tachikawa K, Bard E (2011) North-Eastern Pacific oxygen minimum zone variability over the past 70 kyr: Impact of primary production and oceanic circulation. *Paleoceanography* 26, PA4208, 1–17

Soulet G, Ménot G, Garreta V, Rostek F, Lericolais G, Zaragosi S, Bard E (2011) Black Sea "Lake" reservoir age evolution since the Late Glacial-hydrologic and climatic implications. *Earth and Planetary Science Letters* 308, 245–258

Böning P, Bard E, Rose E (2007) Towards direct micron-scale XRF elemental maps and quantitative profiles of wet marine sediments. *Geochemistry Geophysics Geosystems (G-cubed)* 8 (5), 1–14

**Edouard Bard**
Professor at the Collège de France
Vice-Director of CEREGE (Aix-en-Provence)

# Acknowledgements

Firstly we thank Edouard Bard (vice-Director of CEREGE, Aix-en-Provence) for his incisive Foreword to this DPER volume on micro-XRF core scanners. Edouard Bard is a Professor at the Collège de France and a Member of the French Academy of Sciences, the Academia Europaea and the US National Academy of Sciences and is a recipient of many international prizes including the Alfred Wegener Medal of the European Geosciences Union (2013).

We are also grateful to the following colleagues from Universities and research institutions who generously reviewed the papers submitted for this volume:

Belen Alonso (ICM-CSIC, Barcelona)
Fabien Arnaud (Université de Savoie)
Edouard Bard (CEREGE, Aix en Provence)
Vera Bender (MARUM, University of Bremen)
Sebastien Bertrand (Ghent University)
Simon Blockley (Royal Holloway University of London)
Erik Brown (Large Lakes Observatory, University of Minnesota Duluth)
Peter Brouwer (PANalytical B.V., Almelo, The Netherlands)
Ro Charlton (National University of Ireland Maynooth)
Andrew Cohen (University of Arizona)
Richard Chiverrell (University of Liverpool)
Andrew Cundy (University of Brighton)
Audrey Dallimore (Royal Roads University, British Columbia)
Piet Van Espen (University of Antwerp)
Pierre Francus (University of Quebec)
Aggeliki Georgiopoulou (University College Dublin)
Aline Govin (MARUM, University of Bremen)
Alex Hangsterfer (Scripps Institution of Oceanography)
Henk Heijnis (Australian Nuclear Science and Technology Organisation)
James Hunt (National Oceanography Centre, Southampton)
Carlos Jimenez (The Cyprus Institute, Nicosia)
Peter Langdon (University of Southampton)
Stephen Lewis (James Cook University, Queensland)
Suzanne Maclachlan (National Oceanography Centre, Southampton)

Jeff Peakall (University of Leeds)
Stephen Roberts (British Antarctic Survey, Cambridge)
Mike Rogerson (University of Hull)
John Smol (Queen's University, Ontario)
Kazuyo Tachikawa (CEREGE, Aix en Provence)
Kevin Taylor (University of Manchester)
Rik Tjallingii (GFZ—German Research Centre for Geosciences, Potsdam)
Jonathan Turner (University College Dublin)
Blas Valero Garces (Pyrenean Institute of Ecology, Zaragoza)
François De Vleeschouwer (CNRS EcoLab/CampusEnsat, Castanet-Tolosan)
Christoph Vogt (University of Bremen)
Phillip Warwick (University of Southampton)
Gert Weltje (University of Leuven, Belgium)
Volker Wennrich (University of Koeln)

We gratefully acknowledge a grant from the UK Office of Science and Technology that funded the development of the prototype Itrax in 2003.

Finally we thank Kate Davis of the University of Southampton (National Oceanography Centre) for her technical expertise in improving and drafting figures.

# Contents

# Contributors

**Fabien Arnaud** Pôle Montagne, EDYTEM, Université de Savoie/CNRS, Le Bourget du Lac, France

**P. Atahan** Institute for Environmental Research, Australian Nuclear Science and Technology Organisation (ANSTO), Lucas Heights, NSW, Australia

**Antonella Ausili** Istituto Superiore per la Protezione e Ricerca Ambientale (ISPRA), Roma, Italy

**Jostein Bakke** Department of Geography, University of Bergen, Bergen, Norway

**Nicholas L Balascio** Lamont-Doherty Earth Observatory of Columbia University, Palisades, NY, USA

Department of Geosciences, University of Massachusetts, Amherst, MA, USA

**Luisa Bergamin** Istituto Superiore per la Protezione e Ricerca Ambientale (ISPRA), Roma, Italy

**Sébastien Bertrand** Marine Chemistry and Geochemistry, Woods Hole Oceanographic Institution, Woods Hole, MA, USA

Renard Centre of Marine Geology, Ghent University, Ghent, Belgium

**Francis Bérubé** Institut National de la Recherche Scientifique Centre Eau, Terre et Environnement, Québec, QC, Canada

Aquartis, Technologie Aquartis, Montréal, QC, Canada

**M. R. Bloemsma** Department of Geoscience and Engineering, Delft University of Technology, Delft, The Netherlands

**John F. Boyle** Department of Geography and Planning, School of Environmental Sciences, University of Liverpool, Liverpool, UK

**Raymond S. Bradley** Department of Geosciences, University of Massachusetts, Amherst, MA, USA

**Achim Brauer** Section 5.2—Climate Dynamics and Landscape Evolution, GFZ German Research Centre for Geosciences, Potsdam, Germany

**Paul A. Brewer** Institute of Geography & Earth Sciences, Aberystwyth University, Aberystwyth, UK

**Erik T. Brown** Large Lakes Observatory and Department of Geological Sciences, University of Minnesota Duluth, Duluth, MN, USA

**Geert-Jan A Brummer** Department of Marine Geology, NIOZ Royal Netherlands Institute for Sea Research, Texel, The Netherlands

**Jonathan M. Bull** Ocean and Earth Science, National Oceanography Centre, University of Southampton, Waterfront Campus, Southampton, UK

**Maria Carmen Comas** Andalusian Institute of Earth Sciences, CSIC-University of Granada, Granada, Spain

**C. Chagué-Goff** Institute for Environmental Research, Australian Nuclear Science and Technology Organisation (ANSTO), Lucas Heights, NSW, Australia

School of Biological, Earth and Environmental Sciences, UNSW Australia, Sydney, NSW, Australia

**Richard C. Chiverrell** Department of Geography and Planning, School of Environmental Sciences, University of Liverpool, Liverpool, UK

**David R. Cohen** School of Biological Earth and Environmental Sciences, University of New South Wales, Sydney, NSW, Australia

**C. J. Cotterill** British Geological Survey, Edinburgh, UK

**Jean François Crémer** Université de Montréal, Montréal, QC, Canada

Institut National de la Recherche Scientifique Centre Eau, Terre et Environnement, Québec, QC, Canada

**Ian W. Croudace** Ocean and Earth Science, National Oceanography Centre, University of Southampton, Waterfront Campus, European Way, Southampton, UK

**Stéphanie Cuven** PalGeoSed, Bordeaux, France

Institut National de la Recherche Scientifique Centre Eau, Terre et Environnement, Québec, QC, Canada

**Sarah J. Davies** Department of Geography and Earth Sciences, Institute of Geography, History and Politics, Aberystwyth University, Aberystwyth, UK

**Justin K. Dix** Ocean and Earth Science, National Oceanography Centre, University of Southampton, Waterfront Campus, European Way, Southampton, UK

**Peter Dulski** Section 5.2—Climate Dynamics and Landscape Evolution, GFZ German Research Centre for Geosciences, Potsdam, Germany

**Dirk Enters** GEOPOLAR, Institute of Geography, University of Bremen, Bremen, Germany

**David Fortin** Institut National de la Recherche Scientifique, Centre Eau Terre Environnement, Québec, QC, Canada

**D. Fierro** Institute for Environmental Research, Australian Nuclear Science and Technology Organisation (ANSTO), Lucas Heights, NSW, Australia

**Pierre Francus** Institut National de la Recherche Scientifique, Centre Eau, Terre et Environnement, Québec, QC, Canada

GEOTOP Research Centre, Montréal, QC, Canada

**P. Gadd** Institute for Environmental Research, Australian Nuclear Science and Technology Organisation (ANSTO), Lucas Heights, NSW, Australia

**Liviu Giosan** Geology and Geophysics, Woods Hole Oceanographic Institution, Woods Hole, MA, USA

**J. Goralewski** Institute for Environmental Research, Australian Nuclear Science and Technology Organisation (ANSTO), Lucas Heights, NSW, Australia

**Craig A. Grove** Department of Marine Geology, NIOZ Royal Netherlands Institute for Sea Research, Texel, The Netherlands

**H. Heijnis** Institute for Environmental Research, Australian Nuclear Science and Technology Organisation (ANSTO), Lucas Heights, NSW, Australia

**D. Heslop** Research School of Earth Sciences, The Australian National University, Canberra, ACT, Australia

**Konrad Hughen** Marine Chemistry and Geochemistry, Woods Hole Oceanographic Institution, Woods Hole, MA, USA

**James E. Hunt** Marine Geoscience, National Oceanography Centre, European Way, Southampton, UK

**Stuart Jarvis** Ocean and Earth Science, National Oceanography Centre, University of Southampton, Waterfront Campus, European Way, Southampton, UK

**Anna F. Jones** School of Geography, Planning and Environmental Policy, University College Dublin, Dublin, Ireland

**Sarah J. Kelloway** Mark Wainwright Analytical Centre, University of New South Wales, Sydney, NSW, Australia

**Kinuyo Kanamaru** Department of Geosciences, University of Massachusetts, Amherst, Morrill Science Center, Amherst, MA, USA

**Bjørn C. Kvisvik** Department of Geography, University of Bergen, Bergen, Norway

**Henry F. Lamb** Department of Geography and Earth Sciences, Institute of Geography, History and Politics, Aberystwyth University, Aberystwyth, UK

**Carmen F. López-Rodríguez** Andalusian Institute of Earth Sciences, CSIC-University of Granada, Granada, Spain

**Adriano Macia** Departamento de Ciências Biológicas, Faculdade de Ciências, Universidade Eduardo Mondlane, Maputo, Moçambique

**Mark G. Macklin** Institute of Geography & Earth Sciences, Aberystwyth University, Aberystwyth, UK

**Suzanne E. MacLachlan** National Oceanography Centre, European Way, Southampton, UK

**Clara Mangili** Section of Earth and Environmental Sciences, University of Geneva, CH, Switzerland

**Christopher E. Marjo** Mark Wainwright Analytical Centre, University of New South Wales, Sydney, NSW, Australia

**Francisca Martínez-Ruiz** Andalusian Institute of Earth Sciences, CSIC-University of Granada, Granada, Spain

**Gila Merschel** Department of Marine Geology, NIOZ Royal Netherlands Institute for Sea Research, Texel, The Netherlands

Faculty of Earth and Life Sciences, Vrije Universiteit Amsterdam, Amsterdam, The Netherlands

School of Engineering and Science, Jacobs University Bremen, Bremen, Germany

**Gifford H. Miller** INSTAAR and Department of Geological Sciences, University of Colorado, Boulder, CO, USA

**Helen Miller** Ocean and Earth Science, National Oceanography Centre, University of Southampton, Waterfront Campus, European Way, Southampton, UK

**Christian Ohlendorf** GEOPOLAR, Institute of Geography, University of Bremen, Bremen, Germany

**Sara M. Rassner** Institute of Geography & Earth Sciences, Aberystwyth University, Aberystwyth, UK

**Sidonie Révillon** Pôle Montagne, EDYTEM, Université de Savoie/CNRS, Le Bourget du Lac, France

Laboratoire “Domaines Océaniques”, Université de Bretagne Occidentale/CNRS, IUEM, Plouzané, France

**Daniel Rey** Department of Marine Geosciences, University of Vigo, Vigo, Spain

**Stephen J. Roberts** British Antarctic Survey, Cambridge, UK

**Isabel Rodríguez-Germade** Department of Marine Geosciences, University of Vigo, Vigo, Spain

**Alberto Rodriguez-Ramirez** School of Earth Sciences, The University of Queensland, Brisbane, QLD, Australia

**U. Röhl** MARUM—Centre for Marine Environmental Sciences, University of Bremen, Bremen, Germany

**Elena Romano** Istituto Superiore per la Protezione e Ricerca Ambientale (ISPRA), Roma, Italy

**R. Guy Rothwell** National Oceanography Centre, Empress Dock, Southampton, UK

**Belén Rubio** Department of Marine Geosciences, University of Vigo, Vigo, Spain

**Daniel N. Schillereff** Department of Geography and Planning, School of Environmental Sciences, University of Liverpool, Liverpool, UK

**Benjamin B. Schupack** INSTAAR and Department of Geological Sciences, University of Colorado, Boulder, CO, USA

**Rex N. Taylor** Ocean and Earth Science, National Oceanography Centre, University of Southampton, Waterfront Campus, European Way, Southampton, UK

**Thorvaldur Thordarson** School of Geoscience, University of Edinburgh, Edinburgh, UK

**Rik Tjallingii** Section 5.2 Climate Dynamics and Landscape Evolution, GFZ, German Research Centre for Geosciences, Potsdam, Germany

Department of Marine Geology, NIOZ Royal Netherlands Institute for Sea Research, Den Burg, The Netherlands

**Jonathan N. Turner** School of Geography, Planning and Environmental Policy, University College Dublin, Dublin, Ireland

**Federico Vilas** Department of Marine Geosciences, University of Vigo, Vigo, Spain

**Irene E. Wainwright** Mark Wainwright Analytical Centre, University of New South Wales, Sydney, NSW, Australia

**Colin R. Ward** School of Biological Earth and Environmental Sciences, University of New South Wales, Sydney, NSW, Australia

**G. J. Weltje** Department of Earth and Environmental Sciences, University of Leuven, Leuven-Heverlee, Belgium

**Volker Wennrich** Institute for Geology and Mineralogy, University of Cologne, Cologne, Germany

**Russell B. Wynn** National Oceanography Centre, European Way, Southampton, UK

**A. Zawadzki** Institute for Environmental Research, Australian Nuclear Science and Technology Organisation (ANSTO), Lucas Heights, NSW, Australia

**Jens Zinke** School of Earth and Environment, The University of Western Australia and the UWA Oceans Institute, Crawley, WA, Australia

Australia and the Australian Institute of Marine Science, Nedlands, WA, Australia

# About the Editors

**Ian W. Croudace** is a geochemist with more than 40 years research experience, is a Professor at the University of Southampton (Ocean and Earth Science) and is Director of GAU-Radioanalytical. He is a specialist in several branches of analytical geochemistry including X-ray fluorescence spectrometry, gamma ray spectrometry and radioanalytical chemistry and has published more than 135 papers in the international geochemical and chemical literature. During his career he has supervised 28 PhD students on a variety of geochemical topics. He has also co-developed an industry standard instrument for extracting tritium and C-14 (and other volatile radionuclides) from nuclear and related materials. With NOC colleague Guy Rothwell in 2000 he conceived the fundamental design of what became the prototype Itrax X-ray core scanner. He jointly obtained development funding, identified and commissioned the analytical partner (Cox Analytical Systems) and contributed to the realisation of the first Itrax core scanner that emerged in 2003.

**R. Guy Rothwell** is a marine sedimentologist and Curator of the British Ocean Sediment Core Research Facility (BOSCORF), the UK's national deep-sea core repository, located at the National Oceanography Centre, Southampton. He has participated in over 25 research cruises including two legs of the Ocean Drilling Program. He and colleague Ian Croudace conceived of, and secured the funds, to realise the prototype Itrax core scanner and contributed to its design. He is author of *Minerals and Mineraloids in Marine Sediments* (Elsevier Applied Science, 1989) and editor of *New Techniques in Sediment Core Analysis* (Geological Society of London Special Publication, 2006).

# Explanation of Abbreviations and Acronyms

| | |
|---|---|
| AAS | Atomic absorption spectroscopy |
| AMO | Atlantic Multidecadal Oscillation |
| AMS | Accelerator mass spectrometry |
| ANSTO | Australian Nuclear Science and Technology Organisation |
| AO | Arctic Oscillation |
| ArcGIS | A geographic information system for working with maps and geographic data |
| ASTM | American Society for Testing and Materials |
| AVAATECH | Commercial XRF core scanner manufactured by Avaatech Analytical X-ray Technology, Alkmaar, The Netherlands |
| BGS | British Geological Survey |
| BOSCORF | British Ocean Sediment Core Research Facility, National Oceanography Centre, Southampton, United Kingdom |
| BRITPITS | British Pits (British Geological Survey mines and quarries database) |
| BSi | Biogenic silica |
| CANMET | Canada Centre for Mineral and Energy Technology |
| CATMHS | Cumbrian Amenity Trust Mining History Society |
| CAT-Scan | Computerized axial tomography scan |
| CBCI | Cumulative biogenic carbonate inventory |
| CCD | Charge-coupled device |
| CEREGE | Centre de Recherche et d'Enseignement de Géosciences de l'Environnement (based in Aix-en-Provence) |
| CF:CS | Constant flux—Constant sedimentation |
| CIC | Constant initial concentration |
| CLIMATCH | Climatic and anthropogenic change in seasonal river runoff and impacting cyclones resolved by novel spectral geochemistry of giant corals in Indian Ocean catchments (Netherlands Organisation for Scientific Research Earth and Life Sciences project 2010–2014) |
| CMOS | Complementary metal–oxide–semiconductor |
| CNRS | Centre Nationale de Recherche Scientifique (French National Scientific Research Agency) |

| | |
|---|---|
| COREWALL | A US-developed stratigraphic correlation, core description, and data visualization system used by the marine, terrestrial, and Antarctic science communities |
| CORSAIRES | Coring Stable and Instable Realms in European Seas, European Union Concerted Action research program 1996–1998 |
| CORTEX | Core Scanner Texel—forerunner of the AVAATECH core scanner |
| CPSD | Curved position sensitive detector |
| CRPG-ANRT | Centre de Recherches Pétrographiques et Géochimiques—Association Nationale de la Recherche Technique |
| CRS | Constant rate of supply |
| CSI | Cumulative sediment inventory |
| CSIC-UGR | Consejo Superior de Investigaciones Cientificas—Universidad de Granada, Spain |
| CSIRO | Commonwealth Scientific and Industrial Research Organisation, Australia |
| CSSD | Constant sample to detector distance |
| CT | Cryptotephra or numbers from the Hounsfield scale, a quantitative scale for describing radiodensity (in x-radiography) |
| CT-Scan | Computed tomography scan |
| DICOM | Digital Imaging and Communications in Medicine—a standard for handling, storing, printing, and transmitting data in medical imaging |
| DLC | Direct linear calibration |
| DOSSEC | Drilling, Observation and Sampling of the Earths Continental Crust not-for-profit corporation |
| EAGLE III | A micro-XRF elemental analyser manufactured by EDAX Inc., New Jersey, USA |
| ECD | Electron capture detection |
| EDS | Energy dispersive spectrometry |
| EDXRD | Energy dispersive X-ray diffraction |
| ED-XRF | Energy dispersive X-ray fluorescence |
| ENSO | El Niño Southern Oscillation |
| EPA | Environmental Protection Agency (USA) |
| EU | European Union |
| FT | Fourier transform |
| GAU | GAU-Radioanalytical Laboratories, University of Southampton, NOC, Southampton |
| G/B | Green/Blue colour ratio |
| G-BASE BGS | Geochemical Baseline Survey of the Environment, British Geological Survey |
| GC | Gas chromatography |
| GCR | Geological Conservation Review (Joint Nature Conservation Committee, U.K.) |
| GEOTEK | Commercial core logger manufacturer based in Daventry, U.K. |
| GICC05 | Greenland ice core chronology 2005 |

| | |
|---|---|
| GLAD800 | Global Lake Drilling Initiative |
| GMRT | Global multi-resolution topography |
| GRM | Geological reference material |
| GV | Gray-level values |
| HBSMR | National Trust Historic Buildings, Sites and Monuments Record, United Kingdom |
| HCB | Hexachlorobenzene |
| HDS | Hydrodesulfurization |
| HSI | Hyperspectral imaging |
| HPLC-FLD | High performance liquid chromatography with post-column fluorescence derivatization |
| HU | Hounsfield unit |
| IAEA | International Atomic Energy Agency |
| ICCD | Intensified charge-coupled device |
| ICDP | International Continental Scientific Drilling Program |
| ICP | Inductively coupled plasma |
| ICP-AES | Inductively coupled plasma atomic emission spectroscopy |
| ICP-MS | Inductively coupled plasma mass spectrometry |
| ICP-OES | Inductively coupled plasma optical emission spectroscopy |
| IFREMER | Institut Français de Recherche pour l'Exploitation de la Mer (French Research Institute for the Exploitation of the Sea), Brest, France |
| IfSAR | Interferometric synthetic aperture radar |
| IMAGES | International Marine Past Global Changes Study of the Past Global Changes Project of the International Geosphere-Biosphere Programme |
| INRS-ETE | Institut National de la Recherche Scientifique, Eau Terre Environnement Research Centre (Research Centre on Water, Earth, and the Environment), Université du Québec, Canada |
| IODP | International Ocean Discovery Program, successor to ODP |
| IR | Infrared |
| IRD | Ice-rafted debris |
| ISI | Institute for Scientific Information |
| ISPRA | Istituto Superiore per la Protezione e la Ricerca Ambientale (Institute for Environmental Protection and Research), Italy |
| ISQG | Interim sediment quality guidelines |
| ITRAX | Commercial XRF core scanner manufactured by Cox Analytical Systems, Mölndal, Sweden |
| ItraxPlot | Software for visualising ITRAX data initially developed at the National Oceanography Centre, United Kingdom |
| JAMSTEC | Japan Agency for Marine Earth Science and Technology |
| JEOL | Commercial manufacturer of scientific instruments, headquartered in Tokyo, Japan |
| JGS | Japanese Geotechnical Society |
| KDMRS | Kendal and District Mine Research Society |
| LA-ICP-MS | Laser ablation inductively coupled mass spectrometry |

| | |
|---|---|
| LDHER | Lake District Historic Environment Record |
| LE | Light element |
| LIBS | Laser-induced breakdown spectroscopy |
| LiDAR | Remote sensing technique that measures distance by using a laser to illuminate a target and analyzing the reflected light |
| LOI | Loss on ignition (test to estimate organic content of a sediment) |
| LWIR | Longwave infrared |
| MCCAP | Mercury cell chlor-alkali plant |
| MDA | Minimum detectable activity |
| MIS | Marine Isotope Stage |
| MLC | Multivariate log-ratio calibration |
| MOD | BGS BRITPITS Mineral Occurrence Database |
| MSCL | Multi-sensor core logger |
| MSCL-S | Multi-sensor core logger, standard type, for automated down-core analysis, manufactured by Geotek Ltd., Daventry, United Kingdom |
| MSCL-XYZ | Multi-sensor core logger for automated analysis of multiple core sections, manufactured by Geotek Ltd., Daventry, United Kingdom |
| MSCL-XZ | Multi-sensor core logger bench-top logging track manufactured by Geotek Ltd., Daventry, United Kingdom |
| MSE | Mean square error |
| MSPE | Mean squared prediction error |
| MTS | Moroccan turbidite system |
| MWIR | Mid-wave infrared |
| n | Number |
| NAO | North Atlantic Oscillation |
| Nd:YAG | Neodymium-doped yttrium aluminium garnet, a crystal used as a lasing medium in solid-state lasers |
| NEXTMap | Commercial terrain mapping product |
| NGRIP | North Greenland Ice Core Project |
| NIOZ | Nederlands Instituut voor Onderzoek der Zee (Netherlands Institute for Sea Research), Texel, The Netherlands |
| NIR | Near infrared |
| NOCS/NOC-S | National Oceanography Centre, Southampton, United Kingdom |
| NPL | National Physical Laboratory, Teddington, United Kingdom |
| ODP | Ocean Drilling Program |
| OxCal | Radiocarbon calibration program developed by the Oxford Radiocarbon Accelerator Unit, University of Oxford, United Kingdom |
| PAH | Polycyclic aromatic hydrocarbon |
| PASADO | Potrok Aike Maar Lake Sediment Archive Drilling Project |
| PCA | Principal component analysis |
| PCB | Polychlorinated biphenyl |
| PETM | Paleocene-Eocene Thermal Maximum |

| | |
|---|---|
| PLS | Partial least squares regression |
| POZ | Poznan Radiocarbon Laboratory, Poland |
| PSD | Position sensitive detector |
| QSpec | Spectral analysis software for the ITRAX core scanner developed by Cox Analytical Systems, Mölndal, Sweden |
| Q-switched | Production of a high-powered pulsed laser |
| $R^2$ | Coefficient of determination of a linear regression |
| REE | Rare earth element |
| RGB | Red, green and blue channels that constitute an image that broadly follows the colour receptors in the human eye |
| RRS | Radiographic reference sample |
| RX | X-radiography |
| SD | Standard deviation |
| SDD | Silicon drift detector |
| SDD-DPP | Silicon drift detector—digital pulse processing |
| SEM | Scanning electron microscope |
| SINDOCOM | Southern Indian Ocean/tropical Pacific teleconnections assessed by a coral—*in situ* ocean monitoring database (Netherlands Organisation for Scientific Research Earth and Life Sciences project 2007–2011) |
| SME | Small and medium-sized enterprise |
| SLS | Spectral luminescence scanning |
| STW | Sewage treatment works |
| SWIR | Shortwave infrared |
| T | Tephra |
| TATSCAN | Japanese-built XRF core scanner installed on the Japanese drilling vessel *D/V Chikyu* and at the Kochi/JAMSTEC/IODP Core Repository, Kochi, Shikoku, Japan |
| TOC | Total organic carbon |
| ULC | Univariate log-ratio calibration |
| UNEP | United Nations Environment Programme |
| UOS | University of Southampton |
| USGS | United States Geological Survey |
| UV | Ultraviolet |
| VAST | Volcanism in the Arctic System Project |
| VEI | Volcanic explosivity index |
| VIS | Visible spectrum |
| VNIR | Visible and near-infrared |
| WD-XRF | Wavelength dispersive X-ray fluorescence spectrometer |
| XRD | X-ray diffraction or X-ray diffractometer |
| XRF | X-ray fluorescence or X-ray fluorescence spectrometer |
| YTT | Younger Toba Tuff |
| Z | Symbol for atomic number |

# Chapter 1
# Micro-XRF Studies of Sediment Cores: A Perspective on Capability and Application in the Environmental Sciences

**R. Guy Rothwell and Ian W. Croudace**

**Abstract** XRF core scanners represent a major innovation in the analysis of cored sediment sequences and have revolutionised palaeoenvironmental research over the last decade. Such scanners provide capability to rapidly and non-destructively record element proxy variations at decadal, annual and even sub-annual scales. Their use, initially by the marine science community, was soon taken up by lake core researchers, particularly after the advent of high-resolution models incorporating x-radiography, particularly suited for analysis of varved sequences. Their impact on the environmental sciences is seen in the exponential rise in research papers published since 2005 involving their use. Although their main application has been in the study of Quaternary marine and lake cores, they have also been used in the analysis of terrestrial hard rock cores in mining applications, analysis of loess cores, speleothems, cores from peat bogs and river banks and cores collected for environmental forensics and pollution studies. Further, an important cohort of papers has addressed interpretation and calibration issues, increasing the robustness of acquired datasets. In this paper we review marine and lacustrine applications of XRF core scanning, together with environmental forensics applications and research into data optimisation and calibration presented in the current volume. We provide synopses of the principal findings and a concise summary of the current work.

**Keywords** XRF core scanners · Core scanner publications · Micro-XRF · Sediment cores · XRF core scanner data optimisation

R. G. Rothwell (✉)
National Oceanography Centre, Empress Dock, Southampton, SO14 3ZH, UK
e-mail: rgr@noc.ac.uk

I. W. Croudace
Ocean and Earth Science, National Oceanography Centre, University of Southampton, Waterfront Campus, European Way, Southampton SO14 3ZH, UK



I. W. Croudace, R. G. Rothwell (eds.), *Micro-XRF Studies of Sediment Cores,*
Developments in Paleoenvironmental Research 17, DOI 10.1007/978-94-017-9849-5_1

## Introduction

Non-destructive, high-resolution, sediment core scanners incorporating X-fluorescence (XRF) spectrometry and other sensors are now widely used in the earth and environmental sciences, and have radically improved our capacity to record environmental and process changes down to annual and even sub-annual scales. Such instruments measure down-core element variations, typically in the range Al ($Z=13$) to U ($Z=92$), with detection limits down to several ppm under favourable conditions depending on acquisition count time and X-ray tube excitation efficiency. Analysis is rapid (< 50 s per increment) with typically little user intervention and samples require little preparation prior to investigation.

Marine and lacustrine sediments have long been recognised as being excellent recorders of environmental change. Such sequences may contain long records of earth processes such as climate change, local and regional events (e.g. floods, tsunamis, earthquakes, volcanic eruptions, landslides, storms) and anthropogenic changes (e.g. changing land use, pollution). A large number of element proxies have been recognised as important indicators of climate, weathering and erosion, redox conditions, organic productivity and water mass changes. Although the value of many of these proxies were recognised prior to the advent of XRF core scanners, these instruments have revolutionised our capability to extract high-resolution environmental data from sediment records.

## The Development of XRF Core Scanners—A Boon to the Environmental Sciences

The recognition of climate change as a serious environmental and political concern from the 1980s onward and the growing collection of sediment cores for scientific research demanded fast, high-resolution instruments be developed to investigate environmental processes, particularly through element proxies. The origins of this new generation of instruments can be traced back to the CORTEX scanner developed by the Netherlands Institute for Sea Research (NIOZ) in the late 1980s (Jansen et al. 1998). This was commercialised as the AVAATECH core scanner by Avaatech Analytical X-ray Technology with installation at the University of Bremen and NIOZ in 2002. However, the down-core resolution of early instruments was 1 cm at best, meaning researchers could only realistically measure element proxies down to centennial to decadal timescales. Reconstruction of past environmental changes at annual or sub-annual scales, for example, through study of annual varves, needed millimetric or sub-millimetric resolution. This led to the development of high-resolution capability for the AVAATECH scanner (Richter et al. 2006). An independent enterprise headed by the Southampton Oceanography Centre (now National Oceanography Centre), United Kingdom, and Cox Analytical Systems, Gothenburg, Sweden, led to the innovative ITRAX prototype core scanner which was delivered in

early 2003. This instrument integrated high-resolution element analysis with optical and radiographic imaging (Croudace et al. 2006). Other XRF core scanners were independently developed. These include the Eagle III BKA scanner (Haschke 2006), the TATSCAN-F2 (Sakamoto et al. 2006) and more recently the Geotek system, which incorporates an Olympus Delta XRF spectrometer. The AVAATECH and ITRAX instruments are currently the most widely used and exist in over 65 institutions worldwide.

The number of scientific papers generated through XRF core scanner analysis of sediment cores rose rapidly in the first decade of the twenty-first century (Fig. 1.1). Rapid, almost exponential, growth in outputs is particularly evident after 2005, with the availability of high (sub-millimetric, termed μXRF) resolution models. Initially, use of XRF core scanners was mostly restricted to Quaternary marine sediments (Fig. 1.2). A smaller but significant number of studies related to pre-Quaternary sequences, largely recovered at Ocean Drilling Program (ODP) sites. However from 2005, an increasing literature appeared, based on lake core analysis that surpassed papers published on marine cores from 2011 (Fig. 1.2).

Literature searches show at least 496 refereed papers relating to XRF core scanner use were published to January 2013. Half of these relate to studies of marine cores, while just over a third relate to lake cores (35%; Fig. 1.3). Pre-Quaternary records accounted for 8% of publications, and technical papers describing instruments, methodology, data optimisation and calibration account for 4% of papers published. Papers relating to XRF core scanner analysis of terrestrial hard rock cores, mining applications, peat bog cores and cores analysed for environmental forensics and pollution studies account for 3% of the total (Fig. 1.3).

Of the refereed XRF core scanner papers published to January 2013, the AVAATECH/CORTEX and ITRAX instruments were used for around 95% of the studies (Fig. 1.4) with AVAATECH core scanners being used in 58% of the papers.

Examination of core scanner type used in published studies against science area suggests the AVAATECH instrument has been mainly used by marine scientists,

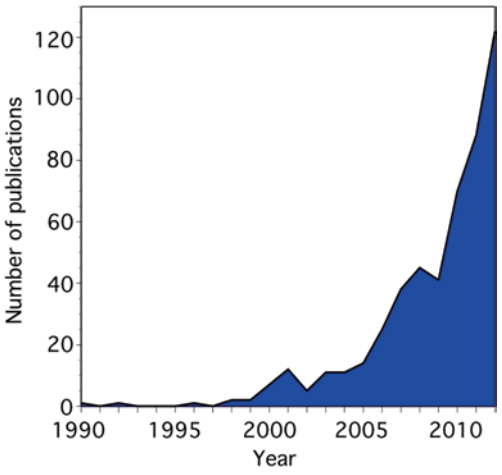


**Fig. 1.1** Publications resulting from XRF core scanning of sedimentary cores from 1990–2012 ($n$=496, source Google Scholar)

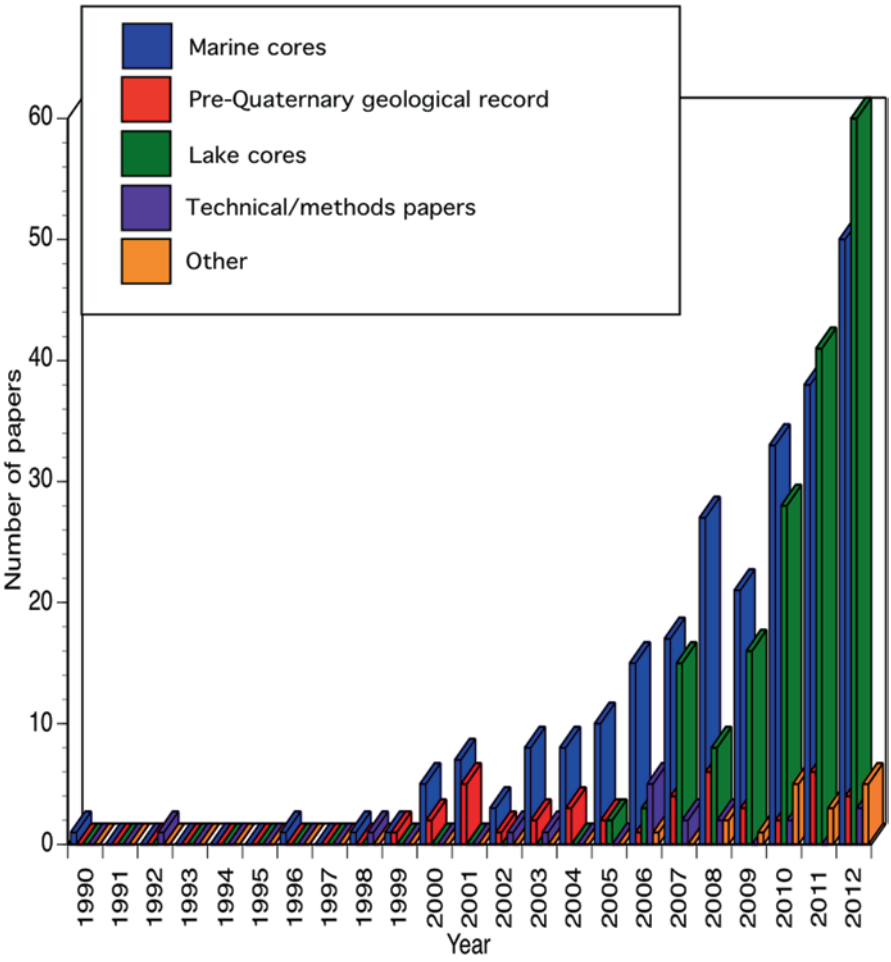


**Fig. 1.2** Breakdown of refereed XRF core scanner publications according to core type studied. Marine cores largely relate to the Quaternary record, those from the pre-Quaternary record are mainly ODP cores. Other category includes terrestrial hard rock cores, mining applications, loess cores, speleothems, cores from peat bogs and riverbanks, and cores studied in environmental forensics and pollution studies ($n = 496$, source Google Scholar)

whilst the ITRAX is predominantly used by the lake core community (Fig. 1.5). This probably reflects the early adoption of core scanners by active marine research groups in the early years of the new millennium prior to the advent of the ITRAX beyond the prototype instrument. Attraction of the ITRAX to lake core researchers may, in part, relate to the integral X-radiography, particularly useful in recording varved sediments, and providing information on past productivity and erosional input. In addition, the high-resolution capability of ITRAX from early models is particularly suited to decadal, annual and even sub-annual analysis, favoured by lacustrine and terrestrial studies. Core scanner studies of the pre-Quaternary

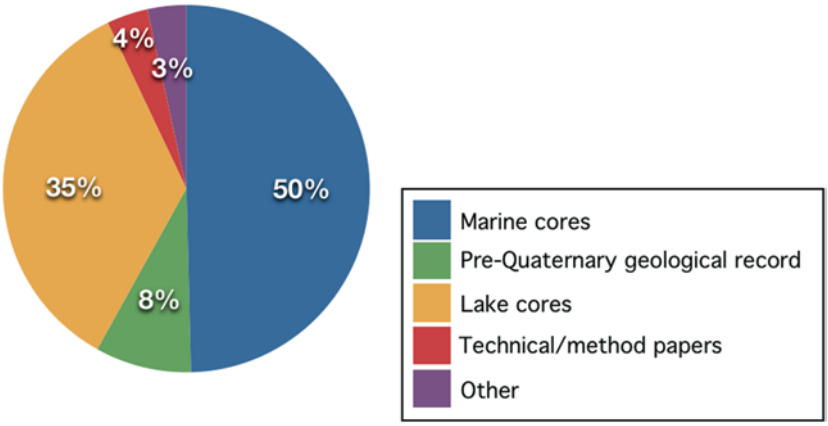


**Fig. 1.3** Breakdown of total refereed XRF core scanner publications up to January 2013 according to core type studied. Marine cores largely relate to the Quaternary record, those from the pre-Quaternary record are mainly ODP/IODP cores. Other category includes terrestrial hard rock cores, mining applications, cores from peat bogs and cores studied in environmental forensics and pollution studies ($n = 496$, source Google Scholar)

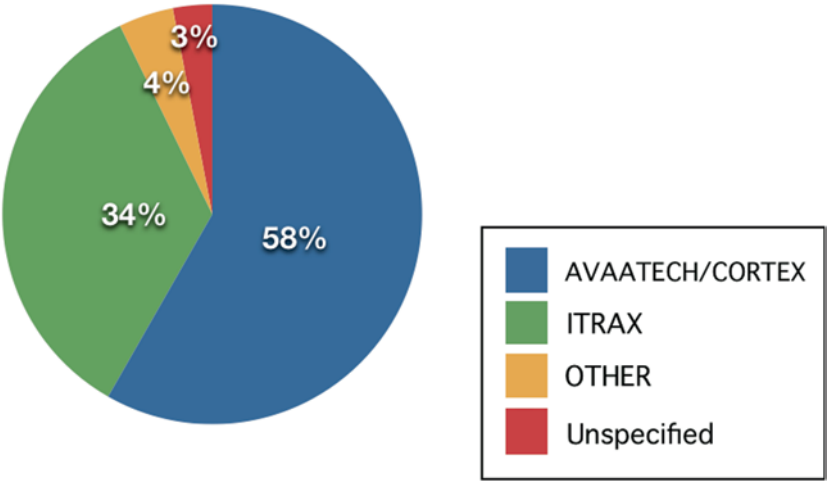


**Fig. 1.4** Breakdown of total refereed XRF core scanner publications to January 2013, according to type of core scanner used. The AVAATECH/CORTEX and ITRAX core scanners were used for ~95% of published studies. (Source Google Scholar)

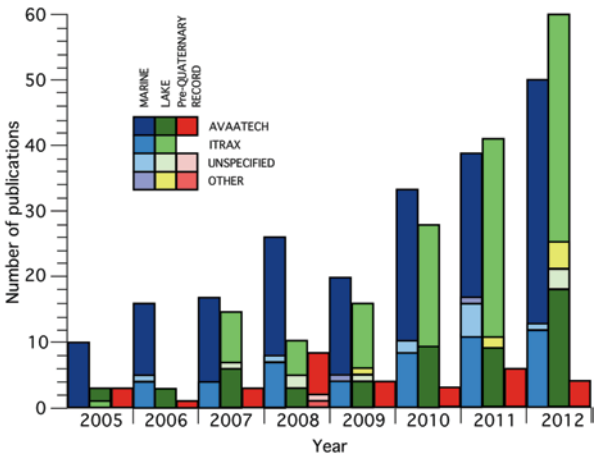


**Fig. 1.5** Breakdown of total refereed XRF core scanner publications from 2005 to 2012, according to type of core scanner used within studies of marine cores, lake cores and the pre-Quaternary geological record. The dominance of the AVAATECH instrument in marine core analysis and preeminence of the ITRAX in lake core studies is clear. (Source Google Scholar)

geological record, largely on Ocean Drilling Program (ODP) cores, has been almost exclusively the preserve of the AVAATECH instrument.

## The Core Scanner Community

XRF core scanner analysis is one of a range of tools in the environmental scientists toolbox. These include automated or semi-automated core logging techniques, which have evolved rapidly over the last two decades. In July 1997, the French Research Institute for the Exploitation of the Sea (IFREMER), Brest, organised a core logging workshop as part of the EU-funded CORSAIRES European Concerted Action (1996–1997), which reviewed developments in a wide range of logging methods (Auffret 1997). Shortly afterwards Ortiz and Rack (1999) reviewed current and future non-invasive tools for high-resolution climate studies in a benchmark paper. Since then, development of new and established technologies for core analysis and proxy identification has continued apace, leading to a community workshop on 'Advances in coring, drilling and non-invasive measurement technologies for paleoceanographic investigations: A community discussion on the state of the art' at the 7th International Conference on Paleoceanography (Sapporo, Japan, September 2001). This workshop, supported by Joint Oceanographic Institutions/Ocean Drilling Program and the IMAGES programme, was convened specifically to discuss calibration issues, data handling and how non-invasive measurements be best used to develop sedimentological and palaeoceanographic proxies. In September 2003, the community met again at the Southampton Oceanography Centre, United Kingdom, to review developments in core logging and imaging. This meeting was notable for the debut of the ITRAX core scanner and the proceedings were published as Rothwell (2006). Since 2003, the number of studies using core scanners have risen almost exponentially (Fig. 1.1) and the user base grown to include a substantial

cohort of lake core users (Fig. 1.2). Further, increased efficiency in digital XRF detectors has led to significantly reduced measurement times and increased signal-to-noise ratios, resulting in greater elemental sensitivity in modern instruments.

In April 2010, the ITRAX user community met in Lipari, Italy, to review applications of the ITRAX core scanner, while in September, the same year, AVAATECH users met at NIOZ, Texel, The Netherlands, to discuss technical aspects and application of XRF core scanning in palaeoceanography (Tjallingii et al. 2011). The present volume derives from papers presented at these workshops with significant additional contributions. It brings together papers by leading researchers that have used XRF core scanners in a broad range of scientific applications as well as considering technical aspects relating to core scanner use, such as data optimisation and calibration. With the rapid increase in use of non-destructive core scanners in palaeoenvironmental research during the last decade, we believe this volume will be a timely and useful addition to the literature, providing benchmark papers for current and potential users of such instruments.

## Scope of the Volume

XRF core scanners were first developed for use in the high-resolution analysis of marine sediments, although since 2005, they have been increasingly used to acquire high-resolution environmental records from lakes (Fig. 1.2). They have also proved very effective for recording heavy metal pollution, becoming an important diagnostic tool in the emerging field of environmental forensics. Concurrent with their use in determining environmental histories through elemental proxies, researchers have also considered technical aspects relating to core scanner use, such as data optimisation and calibration. This has led to greater understanding of what different proxies really mean, and developing better ways of expressing data to obtain geologically meaningful information, such as element log ratios (Weltje and Tjallingii 2008). These four research areas: marine cores, lake cores, environmental forensic applications, and data optimisation and calibration form natural sections for papers in the present work (Fig. 1.6).

### *Marine Sediment Applications*

The past two decades have seen a wide variety of marine science applications for XRF core scanners. Rothwell and Croudace (this volume) review the historical development of X-ray fluorescence and its application to marine sediments, and the development of XRF core scanners. Marine sediment applications of XRF core scanning are core characterisation, determination of climate changes through climatically driven cyclicities reflected in Ca or Fe variations, recognition of sedimentological events such as ash layers, turbidites, ice-rafted debris and aeo-

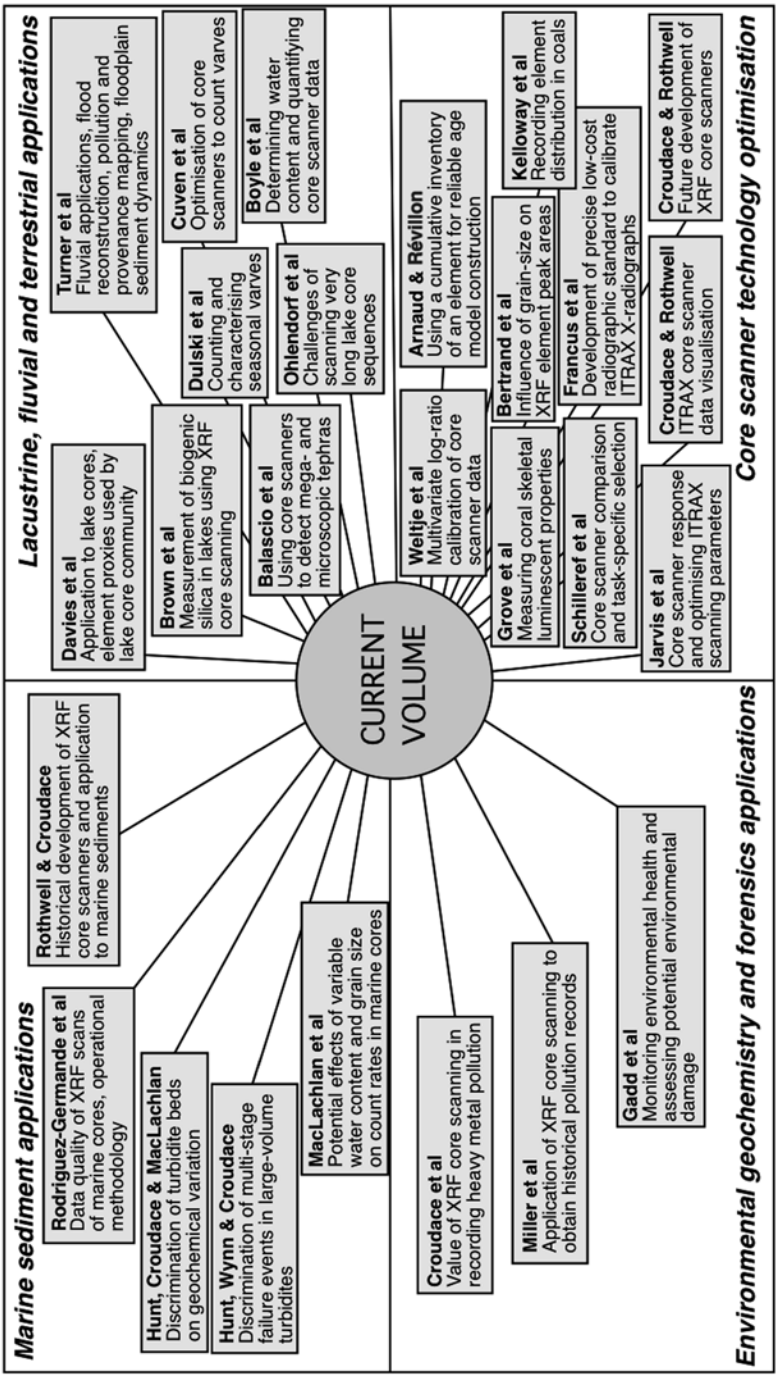


**Fig. 1.6** Scope of the current volume with summaries of main paper topics and categories

lian dust flux, provenance studies, facies interpretation, diagenetic studies and core correlation. Rothwell and Croudace reflect on the major marine science applications of the technique and identify 60 elements or ratios that have been used by researchers to document a wide range of environmental and process changes in the marine realm. In addition, elements have been ratioed with magnetic susceptibility to recognise authigenic and diagenetic processes. The authors summarise the origin, application and limitations of these proxies and provide a guide for element proxy selection and potential. They also associate elemental and supporting indicators to identify environmental conditions and quantify Earth System physical processes.

Although XRF core scanners provide rapid acquisition of high-resolution elemental datasets, lack of standardised protocols for parameter settings may reduce data quality compared to what might be achieved with optimal settings. Further, inherent uncertainties regarding exact volume and density of sediment excited inhibits quantification of core scanner data. Rodriguez-Germande et al. (this volume) examine a heterogeneous core from the Alboran Sea (Western Mediterranean Sea) to assess factors that affect data quality, such as x-ray tube type, exposure time and storage conditions. Although increase in exposure time provides more robust data particularly for light elements ($Z < 20$) and those present at low concentrations, high-resolution scanning of long cores is a lengthy process. For example, collection of major and minor element profiles (Si, S, Cl, K, Ca, Ti, Fe, As, Pb, Mn, Zn, Br, Rb, Sr and Zr) at 500 μm step-size for 1 m of core using an ITRAX may take 16 h, hence a 20 m long core may take 1 month of instrument time. So determination of optimal exposure time to provide adequate element recording but minimising runtime is desirable. The authors propose basic end-user guidelines for ITRAX studies to establish an operational methodology, particularly for effective acquisition of light element counts and data reproducibility after core storage.

Chemostratigraphy, or chemical stratigraphy, based on discriminating beds on geochemical variation has been long recognised as a powerful tool in core correlation and provenance studies, particularly for redeposited beds (e.g. Pearce and Jarvis 1995). Turbidites may show unique geochemical signatures and XRF core scanning potentially offers a rapid and efficient means of characterising turbidites and identifying source areas. Hunt et al. (Chap. 4) present a robust case study using calibrated ITRAX core scanner data to discriminate turbidite beds in Agadir Basin, off NW Africa. The turbidites studied are from an extensive turbidite mass flow distributory system that extends westwards from the NW African continental margin through the Agadir Basin and Seine Abyssal Plain to the deep-water Madeira Abyssal Plain in the west. This system has been extensively studied over the past 25 years and the turbidites identified as siliciclastic organic, volcaniclastic and calcareous in type (see Frenz et al. 2009 and references therein). Hunt et al. use calibrated ITRAX data to discriminate turbidites on their provenance characteristics within these broad categories. While volcaniclastic turbidites can be distinguished due to different magma chemistries in source areas, analysis of the siliciclastic turbidites shows that individual continental slope provenances can also be identified, as the composition of each turbidite lies on a subtly different array on element cross-plots. The authors demonstrate the importance of restricting analyses to turbidite

mud-caps as grain-size may affect geochemical composition. Further, analysis of fine-grained allochthonous material reduces effects of variable water content, as sediments with similar porosity-permeability characteristics are compared. Further homogenous fine-grained mudcap sediments better parallel the homogenous fine powders used in WD-XRF analysis.

Natural hazards are an important focus for geological research. In recent years there has been much attention to the potential tsunami threat posed by collapse of volcanic island flanks (e.g. Ward and Day 2001; Ward 2001; Løvholt et al. 2008). A slide's tsunamigenic potential will depend on volume of material displaced into the ocean, which may reflect whether the collapse is single or multistage. Multistage failure clearly mitigates tsunami risk and identification of failure type will inform debate on the likely tsunami hazard and threat to coastal populations. Collapse of volcanic island flanks will generate turbidity currents, the deposits of which accumulate in adjacent basins. Multiple fining-upwards sequences (subunits) within turbidite bases have been interpreted as reflecting multistage failure at source (Garcia 1996; Di Roberto et al. 2010). Hunt, et al. (Chap. 5) use ITRAX core scanning to aid correlation of such subunits in two extensive high-volume volcaniclastic megaturbidites within the Moroccan Turbidite System, off NW Africa. The ITRAX data is used to determine geochemical composition of the subunits, showing the composition of each is subtly different. This supports the interpretation that the turbidity currents were generated by multistage failures. Ca decreases upwards through the subunits suggesting early failures were submarine, but progressively becoming subaerial in origin. These interpretations from the ITRAX data are supported by determination of volcanic glass geochemistry using an Eagle III μXRF instrument that shows volcanic glasses from each subunit form discrete compositional fields, suggesting each subunit represents a separate failure.

Interpretation of core scanner data is not trivial as a variety of physical and operational factors may affect count rates, including changes in grain-size, water content and other sample heterogeneities. A number of authors assess accuracy and precision of XRF core scanners in the light of these factors (e.g. Tjallingii et al. 2007; Hennekam and de Lange 2012; Wilhelms-Dick et al. 2012), although to date, these studies have focused on the AVAATECH XRF core scanner. MacLachlan et al. (this volume) examine the potential effects of variable water content and grain-size on count rates using a marine core and an ITRAX core scanner. The authors' empirical study identifies specific thresholds above which water content and grain-size variability may significantly affect count rates, particularly for lighter elements. This is put at >25 wt% of sand-sized material and a water content of above 40%.

## *Lacustrine, Fluvial and Terrestrial Applications*

Lake sediments can be important archives of environmental change, recording catchment dynamics and regional climatic variability. In recent years, there has been increasing use of XRF core scanners by the lake core community (Fig. 1.2) with the

technique making a major contribution to results from large lake drilling projects. Davies et al. (this volume) comprehensively review the use of μXRF core scanning on lake sediments and examine element proxies used by lake core investigators. The authors show the wide application of μXRF core scanning in palaeolimnological research, which includes recording of flood histories, landslides, turbidites and lahars; detection of tephras, varve counting, acquisition of palaeoclimate records, and development of chronologies. It has also been used to determine anthropogenic changes such as agricultural expansion, deforestation, metal pollution from mining and/or industrial discharges and other catchment perturbations. Identification of specific event deposits (e.g. from floods, earthquakes, volcanic eruptions) and their episodicity provide valuable data for agencies involved in natural hazard mitigation. Lake sediments typically show greater variability, and have higher and more variable water and organic matter contents than marine sediments, thus necessitating normalisation of element integrals. The authors show that a wide range of elements are useful for recording detrital inputs, changes in weathering regimes, grain-size variability and choice of proxies depends on local basin context. As in the ocean, some elements are useful proxies for in-lake processes such as productivity, changing redox conditions and for correlation. Further, other scanning parameters can give important information on sediment properties. For example, incoherent/coherent scattering ratio (which approximates to average matrix composition atomic number) allows qualitative estimation of organic matter content, as organic carbon has a lower atomic number than measurable elements (e.g. Burnett et al. 2011) and can also be used to record water content variations. Davies et al. (this volume) conclude that interpretations of lake core scanner data should be informed by local catchment character and in-lake processes and supported by a multi-proxy approach.

Compared to marine and lake studies, there has been relatively little application of micro-XRF core scanning to fluvial sediments despite the sensitivity of river systems to environmental change and their proximity to human living space. Fluvial sequences are typically more fragmented and lack the continuity of marine and lacustrine records. They are also affected by pedogenesis and commonly human disturbance. However, they can have significant potential for palaeoenvironmental analysis. These sediments are examined by Turner et al. (this volume) who present applications of XRF core scanning in three key river management areas: flood reconstruction, pollution and provenance mapping, and floodplain sediment dynamics. They show how rapid geochemical investigation of fluvial deposits provided by XRF core scanning, can support floodplain reconstruction and contaminant dispersal studies (particularly in metal-mined catchments). As the authors point out, with growing population pressures and impending climatic change, there has never been a greater need to understand fluvial systems, their non-stationary behaviour, and associated flood risk. Micro-XRF core scanners with their potential ultra-high temporal resolution provide a new way of investigating millennial-length flood records from fine-grained alluvial sequences.

Biological productivity is an important parameter in palaeoenvironmental reconstructions and some elements like Ba and Si are long established production proxies. Biogenic Si is a commonly used indicator of past diatom production and

provides a record of biological response to environmental changes in both oceans and lakes. However, traditional wet chemical methods for determining biogenic silica are tedious, time-consuming and destructive. Reliance on discrete physical samples also means construction of high-resolution records is rarely possible. Brown (this volume) explores using XRF core scanners to rapidly acquire high-resolution records of biogenic silica concentrations, using Si/Ti as proxy. He tests the relationship between these elements, their efficiency in recording diatom productivity, and proposes optimum count times, using a calibrated 25-kyr sedimentation record in Lake Malawi, East Africa. As Brown demonstrates, caution is needed in selecting appropriate proxies for clastic input, as detrital elements may be affected by grain size (e.g. Ti), diagenesis (e.g. Fe) or volcanics (e.g. K, Zr). Hence depositional setting is an important control on proxy selection and development of site-specific calibration strategies. Temporal shifts in calibration fitting parameters may also be needed due to textural changes and increasing sediment consolidation downcore, and/or varying supply of detrital weathered material.

Another area where XRF core scanners can provide rapid automated analysis, far quicker and at higher resolution than traditional laboratory methods, is in varve counting to construct high-resolution chronologies. Cuven et al. (this volume) describe optimisation and use of the ITRAX core scanner to count varves in lacustrine sediment from the Canadian High Arctic, demonstrating the ITRAX's potential for texture-based investigations. The authors examine and validate tests for element presence, optimal exposure times, and result reproducibility, all vital factors for robust analysis of core scanner data. They also examine potential effects on high-resolution μXRF spectral acquisition of irregularities on the core surface. After consideration of the physical factors that may affect data acquisition for fine laminations, the authors propose a methodology for maximising ITRAX core scanner data quality for finely laminated sediments. The Canadian High Arctic case study demonstrates the ITRAX's ability to rapidly characterise finely laminated sediments at ultra-high resolution. Further the data allows estimation of grain size providing a new palaeohydrological proxy.

Tephrochronology is a major chronostratigraphic tool, providing a powerful method for correlating and dating sediment sequences. It is particularly useful for dating sequences devoid of other stratigraphic markers and has wide application in palaeoenvironmental research. The ability to detect distal cryptotephras not visible to the naked eye would be a significant advance, extending use of tephrochronology further from volcanic sources, and aid recording of eruptions whose proximal deposits are poorly preserved or masked by other events (Payne et al. 2008). XRF core scanning might seem a valuable potential tool for detecting cryptotephras. Balascio et al. (this volume) investigate core scanner detection of rhyolitic and basaltic tephras in both synthetic cores sown with megascopic and microscopic tephra layers and a lake core from northern Norway containing Icelandic cryptotephras. They demonstrate that detection of cryptotephra is problematic, particularly for rhyolitic glasses, which mirror upper continental crust minerogenic composition, and hence caution is needed in this application.

Although the AVAATECH and ITRAX core scanners are the main instruments in current use, the EAGLE III micro-XRF scanner (developed by Röntgenanalytik Messtechnik GmbH, Germany, and described by Haschke et al. 2002, and Haschke 2006) is an effective tool for high-resolution study of geochemical variability of small sub-samples (up to 15 × 15 cm). In contrast to the AVAATECH and ITRAX instruments, the EAGLE III holds the sample within a large vacuum-tight chamber to improve light element detection and uses a polycapillary lens to focus a small circular X-ray spot onto the sample surface. XRF spectra acquisitions are affected by a range of physical properties inherent to measuring a natural sample. These include porosity, textural variation and surface roughness, layer geometry and heterogeneity, matrix composition, and organic matter and water content (Löwemark et al. 2011; Böning et al. 2007). The effects of these parameters become progressively more important as XRF beam spot size decreases, for example, in study of finely-laminated sediments. Dulski et al. (this volume) use a well-preserved annually-laminated record from an Italian Quaternary palaeolake to explore application of high-resolution micro-XRF analysis in counting and characterising varves using the seasonal signature of specific elements. Detailed grid scanning using an EAGLE III XL scanner provide high-resolution 3D images of varves presenting for the first time elaborate insights into varve elemental structure. In addition the authors assess potential sources of error compared to varve counts determined through examination of thin-sections. The authors demonstrate the value of mico-XRF data in microfacies analyses and visualising internal valve structure, allowing even sub-millimetre-size features to be identified, such as micro-dropstones.

As environmental knowledge of the Holocene has become saturated (at least in Europe and North America) lake core researchers are turning to longer records and doing more work collectively with the development of international programs, such as the International Continental Scientific Drilling Program (ICDP). Deep lake drilling projects within such programs, may recover several 100 m of core spanning several million years. Core scanning of such long sequences presents challenges related to X-ray tube aging affecting count rates and issues related to sediment heterogeneity, such as downcore compaction, porosity changes, changes in organic matter content and textural variation. Ohlendorf et al. (this volume) compare results of scanning of two long lake core sequences—from Laguna Potrok Aike, southeastern Patagonia, Argentina, and from Lake El'gygytgyn in the far eastern Russian Arctic. At Laguna Potrok Aike, a total of 510 m of sediment was recovered extending back at least 51 ka. At Lake El'gygytgyn, 355 m of sediment was cored extending back c. 3.6 Ma. Interestingly, cores from the two lakes were analysed using a different methodology for each. Those from Laguna Potrok Aike were scanned using both a Mo- and Cr-tube at a constant voltage but the tube current adjusted for each section to maintain a constant count rate. Cores from Lake El'gygytgyn were also scanned with both Mo- and Cr-tubes but voltage and current was kept constant for all sections. The authors conclude that for relatively short sediment sequences (~10–30 m) constant voltage and current settings may be best, as tube ageing will be insignificant and profile shifts at section breaks due to different instrument settings are avoided. For long sequences, the constant count rate methodology appears

better as it ensures conformity in signal to noise ratio and detection limits for all sections. Further, abrupt increases in counts due to X-ray tube changes and changes in count intensity due to lithological changes are avoided. The authors stress the importance of normalisation to mitigate external influences (e.g. from tube ageing, physical property changes) whichever methodology is used.

As XRF core scanning becomes increasingly widely used, it is pertinent to examine whether core scanner data can be transformed into more quantitative composition data. The main difference between core scanning and conventional WD-XRF analysis is that core scanning acquires data from wet sediment whereas conventional analysis is based on dry mass concentrations. Thus in water saturated sediments wet mass concentrations may only be a fraction of dry mass concentrations for a particular element. Normalisation with a detrital element (e.g. Thomson et al. 2006; Rothwell et al. 2006) or to Compton scattered radiation (Kylander et al. 2012) helps mitigate variation due to factors such as changing water content. However, such measures do not entirely avoid water content-related data artefacts, as X-ray mass attenuation varies with photon energy (Hennekam and de Lange 2012). Further, direct comparison of core scanner results with other data may be difficult due to their semi-quantitative nature. In marine sediments Cl concentrations provide an indicator for water content (Hennekam and de Lange 2012) but for freshwater lakes another approach is needed, especially as water saturation can vary significantly in lacustrine sediments. Boyle et al. (this volume) examine methods for determining water content in cores and possible correction to transform core scanner results into more quantitative data. They note that all energy dispersive XRF spectra contain data related to water content, for instance, higher water content will lower mean atomic number, causing more scattering and the Compton scatter peak can be used to make a correction. The authors use an Olympus Delta XRF Analyser mounted on a Geotek MSCL-XZ logging track to acquire XRF scanner data from Swedish and Cumbrian lake cores, together with measurement from dried subsamples, to develop a method for estimating dry mass concentrations from wet cores. Two correction techniques are applied, simple regression, calibrated using dry samples, and a new technique that corrects for water content using x-ray scattering data acquired during scanning.

## *Environmental Geochemistry and Forensics Applications*

XRF core scanners are powerful tools in environmental geochemistry and the emerging field of environmental forensics. Environmental forensics is scientific investigation of contaminated air, water, land and biota, with the aim of determining the cause of pollution and providing evidence for legal redress. The discipline has it's own learned society (the International Society of Environmental Forensics, Amherst, Massachusetts) and journal (*Environmental Forensics Journal* published by Taylor and Francis). Croudace et al. (this volume) demonstrate the value of XRF core scanning in recording significant anthropogenic heavy metal pollution in

sediments from Augusta Bay, Sicily, using an ITRAX core scanner. The margins of the bay have been heavily industrialised since the 1950s becoming a major processing centre for chemical and petrochemical industries. This has resulted in serious contamination of near-shore sediments exacerbated by restricted water circulation. Discharges from a former chlor-alkali plant have posed a significant hazard through mercury pollution in parts of the bay. Using $^{137}$Cs dating to establish a reliable sediment chronology, the authors show that although Hg pollution declines due to introduction of mercury abatement measures in the late 1970s, later unexplained increases may relate to unauthorised discharges. The authors validate their ITRAX data against a conventional WD-XRF dataset, showing the ITRAX data accurately reflects element variations. The analytical speed and high-resolution capability of μXRF core scanner analysis clearly makes it an instrument of choice in environmental forensic investigations.

Miller et al. (this volume) progress this theme by using an ITRAX core scanner to record modern pollution signals in Lake Windermere, NW England, using $^{210}$Pb and $^{137}$Cs dating to establish a robust chronology. Within the Windermere catchment, historical heavy metal pollution from local mining, sewage discharge, heavy industry and burning of fossil fuels is significant (Millward et al. 2000). The ITRAX data shows pronounced lead enrichment in sediments from the 1930s and significant increases in zinc, copper and lead from around 1960 in the north of the lake. A similar record is recovered from the south, although Zn and Cu enrichment is recorded earlier. The authors investigate the source of the lead contamination by examining changes in lead isotope ratios ($^{206}$Pb/$^{207}$Pb) with depth. Although local lead mining is a likely long-standing source, the Pb isotope data suggest that early lead enrichments also originated from Carboniferous coal, most likely from local coal combustion including coal-fired steam ships that operated on the lake from 1845. Decreases in $^{206}$Pb/$^{207}$Pb ratios since the 1920s reflects the decline of steam ships and increasing contamination from leaded petrol. The Cu and Zn pollution measured are largely attributed to flood-induced metal inwash after cessation of mining and processed waste and human sewage inputs respectively. The authors demonstrate that XRF core scanner analysis (validated against WD-XRF) is an efficient method for obtaining robust contamination data, which when combined with radiochronologies and lead isotope data, can provide interpretable historical pollution records.

The effectiveness of XRF core-scanning in documenting human influence on natural systems is further demonstrated by Gadd et al. (this volume) who use an ITRAX core scanner to record environmental changes in a creek catchment near Sydney, Australia, over the past century. From a near pristine environment in the 1950s the creek catchment has seen extensive and continuing urbanisation with new housing, quarries, a rubbish tip and even a small nuclear waste burial ground. Significant increases in Pb seen in the ITRAX records (confirmed by WD-XRF) of the upper part of the core reflect increasing use of motor vehicles in the area. This interpretation is supported by a decline in Pb in the uppermost part of the core, reflecting phasing out of leaded petrol over the last 20 years. The authors find that although progressive urbanisation has led to direct input of detectable heavy metals, these

were not sufficient to pose ecological risk and there had been efficient containment of nuclear waste. The paper demonstrates the value of XRF core scanning in efficiently monitoring environmental health and assessing potential environmental damage.

## *Core Scanner Technology Optimisation*

Sedimentation rates in natural systems can vary significantly according to depositional mechanism, for instance in lakes and submarine basins, episodic influxes of terrigenous sediment can significantly increase sediment rates over short periods. This will complicate smooth age-depth relationship models based on radiometric spot dates, potentially leading to significant dating errors. Arnaud and Révillon (this volume) propose replacing use of depth with the cumulative inventory of an element whose flux is likely to change much less than total sediment flux. They test their method on an Alpine lake core using Ca as its flux is independent of detrital input, where it improves the previously established age-depth model. This technique generates objectively-established age models which recognise sedimentological and geochemical parameters. An advantage of their method is that any continuously-measured geological or biological component showing little temporal flux variation can be used as a stratigraphic reference for reliable age model construction.

XRF core scanner data will be affected by a range of sediment properties that vary down core such as grain-size, water content, bulk density and amount of organic matter. Investigation of the effects of these parameters, preferably with quantification, is essential if XRF counts are to be correctly interpreted in terms of element abundances. Bertrand et al. (this volume) investigate the influence of grain size on XRF element peak areas by comparing core scanner data to element data from ICP-AES measurement in two cores from Chilean Patagonian fjords that have variable grain-size. Their study suggests grain size has limited influence in cores where textural variation is within 10 μm; and that in cores with greater grain-size variation, correcting peak areas for water content significantly improves precision of XRF measurement.

The ITRAX core scanner besides having μXRF capability can also record high-quality, high-resolution X-radiographic images. Its X-ray camera lies directly below the shutter of the X-ray source so provides an ideal configuration to acquire undistorted x-radiographs of finely laminated sediments. However, different instrument settings, X-ray tube aging, and other factors can provide significant challenges to linking x-radiographs from successive core sections and comparing x-radiographs from different cores or acquired using different instruments. Francus et al. (this volume) develop a small, low cost, but precise radiographic standard that can be used to calibrate ITRAX x-radiographs and allows effective concatenation of x-radiographs and density curves from successive core sections; as well as objective comparison of x-radiographic data acquired using different instruments. They pres-

ent a standardisation protocol that will correct for core aging, different instrument settings and intrinsic core properties.

The great advantage of XRF core scanners over conventional laboratory WD-XRF in terms of speed, resolution, and the capacity to generate continuous downcore records, is offset by the semi-quantitative nature of the data, usually expressed as intensities. Hence, a universally applicable robust method for converting core scanner data to quantitative measures of sediment composition would be highly beneficial. There have been several approaches to calibration of core scanner data. The most widely used is direct linear calibration where WD-XRF analysis of discrete samples is plotted against counts on an element-by-element basis. However, core scanner data commonly shows considerable scatter due to sediment heterogeneities present in natural systems (e.g. changing water content, organic content and grain-size, together with bioturbation effects and due to pooling of water beneath anti-desiccation surface films used in some analyses) which can compromise calibration rigour. Weltje and Tjallingii (2008) demonstrate that robust quantitative calibration of XRF core scanner data is best made using log-ratios of intensities. Weltje et al. (this volume) develop the log-ratio calibration model and introduce multivariate log-ratio calibration which incorporates measurement uncertainties, accommodates absorption and enhancement effects on intensities and confirms covariance between intensities and element concentrations. The authors further introduce software that is available to the wider community for efficient quantitative calibration of core scanner output.

Core scanner users have a range of options to optimise data collection. Selection of the most appropriate X-ray tube (Mo, Cr, Cu and Rh anode tubes are the most commonly used in XRF core scanners), tube current, voltage, and whether to use plastic film to reduce sample desiccation during analysis will all affect analytical results. Further inherent properties of natural sediment (such as grain-size and water content variation) and factors associated with sample preservation and preparation (such as surface cracking and uneven sample surface) will also affect data quality. Jarvis et al. (this volume) review the range of parameters that affect ITRAX core scanner response and assess their effects on data integrity. They empirically test core scanner response to systematic variation in instrument settings (tube, current, voltage, count time), sedimentological parameters (grain-size and water content variation), and sample surface properties (presence and type of anti-desiccation film, surface slope variations). The authors further discuss uncertainty in core scanner data and empirically examine factors that affect scan reproducibility. They conclude with a series of recommendations for optimising ITRAX scanning parameters.

Core scanners provide effective logging tracks for which other scanning instruments can be fitted, besides XRF, for example, magnetic susceptibility sensors, as seen in some ITRAX models. Further, scanner sensors can be modified to provide additional data. Grove et al. (this volume) modify a CCD line-scan camera on an AVAATECH scanner to record downcore variability in coral skeletal luminescent properties, which they relate to temporal changes in river discharge, and hence precipitation, on Mozambique, Madagascar, and the Great Barrier Reef, Australia.

With several XRF core scanner instruments now currently in use (AVAATECH, ITRAX, Eagle III and more recently GEOTEK/Olympus Delta XRF), each using slightly different methods for data collection and output, inter-device comparison is timely for assessing the most suitable instrument for specific research tasks. Schillereff et al. (this volume) compare results from scanning a laminated Scottish lake core using their Geotek XZ MSCL carrying an Olympus Delta XRF analyser with data obtained using an ITRAX core scanner. They also compare results from two $5 \times 2$ cm dry rock samples; a finely laminated sandstone and a homogenous obsidian block. Both samples were scanned using ITRAX, GEOTEK and Eagle III instruments. The Itrax and Eagle scanned the samples at 200 μm resolution. Due to its higher resolution, ITRAX data appears more spikey or noisy in character than the Geotek/Olympic Delta XRF, but there is a strong correspondence between the two records, although the magnitude of peaks vary. The high-resolution instruments offer the user the possibility of examining fine scale chemical variations but also, through dynamic measurements, the ability to smooth out granular noise if it is an issue. The lower resolution Geotek is shown to provide data that are perfectly suitable for the studies carried out but might be less suitable for very fine scale variations. The authors reflect whether routine high-resolution μXRF scanning presents simply too much data, obscuring records with noise. Data from the Scottish core collected at lower analytical resolution gave a clearer record for some elements which longer count times would make more precise, making a good case for smoothing ITRAX data for long core records. Indeed, the authors suggest that for recording long-term environmental changes, the Geotek instrument with its lower resolution and rapid measurement is an effective approach for the cores examined. The data can also be readily calibrated using a method proposed by Boyle et al. (this volume), that is incidentally applicable to all micro-XRF methods. Comparison of data from the dry, laminated sandstone suggests the ITRAX is the most efficient at recording element variations across laminae, showing it to be the most appropriate tool for investigating annually-laminated sequences and recording thin event horizons, (e.g. ash layers).

Although most applications of μXRF core scanning have concentrated on marine and lake cores, the technique has been used on a wide range of other materials, including speleothems, peat and swamp cores and hard rock drill core. Kelloway et al. (this volume) explore application to drill cores acquired during coal prospecting. Although coal is primarily lithified plant material, it can contain a significant mineral component, which can be important in assessing suitability of coals for different industrial processes (e.g. Bryers 1996; Suárez-Ruiz and Crelling 2008). The potential of μXRF core scanning is clear as detailed records of inorganic elements downcore can be rapidly acquired. The authors use an ITRAX core scanner to investigate cores containing bituminous coal from the Bowen Basin, Queensland, Australia. Several dense mineral-rich areas were identified. Compton backscattering levels, inversely proportional to density and average atomic number, were interpreted as effectively representing relative amounts of organic matter. The data obtained provides a detailed understanding of mineral distribution through acquisition of major element profiles, calibrated by WD-XRF of powdered and

pressed reference coal standards. Combined with high-resolution optical core images and X-radiographs, the geochemical profiles helped identify clay bands and siderite nodules.

XRF core scanners generate large volumes of data that need to be readily and effectively visualised to allow evaluation, interpretation and presentation. Croudace and Rothwell (this volume) describe an independently developed, intuitive software program that efficiently aids visualization of ITRAX optical, x-radiographic imagery and element profiles. Its usefulness is evidenced by its use in many ITRAX-holding institutions. The program has many features that give good control to users. It correctly scales and displays core optical and x-radiograph images, up to ten elements as downcore profiles side-by-side, and provides smoothing and normalisation options. Further, data from up to seven separate core sections can be assembled as a sequence in a single image allowing data from whole cores or long core intervals to be visualised. The program has also been adapted to output data that can be opened using Corewall Corelyzer software, a widely used core data visualisation program that can integrate diverse and disparate datasets (www.corewall.org).

In the final chapter, Croudace and Rothwell (this volume) reflect on future developments for XRF core scanners that would be attractive to geoscientists. Core investigators (including workers examining stalagmites and tree rings) will always be interested in extending the capability of their non-destructive scanners through enhancements or innovations providing sensitive, high-resolution proxy records. Some newly available developments include improvements to X-ray silicon drift detectors (SDD) and associated pulse processing that lead to significant improvements in analytical speed. Other developments briefly discussed might involve adding already available, but less evaluated for core studies, technological sensors based on lasers (Laser-Induced Breakdown Spectroscopy (LIBS), Fourier Transform-Raman), light spectroscopy (hyperspectral imaging exploiting interactions in the visible and near-infrared (VNIR); shortwave infrared (SWIR); near-infrared (NIR) wavelength regions), X-ray (simultaneous X-ray diffraction (XRD) using position sensitive detector (PSD) and energy dispersive spectrometry (EDS) systems) and magnetic susceptibility.

## References

Auffret GA (ed) (1997) CORSAIRES-IFREMER core logging workshop, 24–26 July 1997, Plouzané, France, abstracts volume (unpublished)

Böning P, Bard E, Rose J (2007) Toward direct micron-scale XRF elemental map and quantitative profiles of wet marine sediments. Geochem Geophy Geosys 8. doi:10.1029/2006GC001480

Bryers RW (1996) Fireside slagging, fouling and high-temperature corrosion of heat transfer surface due to impurities in steam-raising coals. Prog Energy Combust Sci 22:29–210

Burnett A, Soreghan M, Scholz C, Brown E (2011) Tropical East African climate change and its relation to global climate: a record from Lake Tanganyika, Tropical East Africa, over the past 90+kyr. Palaeogeogr Palaeoclimatol Palaeoecol 303:155–167. doi:10.1016/j.palaeo.2010.02.011

Croudace IW, Rindby A, Rothwell RG (2006) ITRAX: description and evaluation of a new multi-function X-ray core scanner. In: Rothwell RG (ed) New techniques in sediment core analysis. Geol Soc Spec Publ 267:51–63

Di Roberto A, Rossi M, Bertagnini A, Marani MP, Gamberi F (2010) Distal turbidites and tsunamigenic landslides of Stromboli Volcano (Aeolian Islands, Italy). In: Mosher DC, Shipp C, Moscardelli L, Claytor J, Baxter C, Lee H, Urgeles R (eds) Submarine mass movements and their consequences, advances in natural and technological hazard research 28:719–732

Frenz M, Wynn RB, Georgiopoulou A, Bender VB, Hough G, Masson DG, Talling PJ, Cronin B (2009) Provenance and pathways of late Quaternary turbidites in the deep-water Agadir Basin, northwest African margin. Int J Earth Sci 98:721–733

Garcia MO (1996) Turbidites from slope failure of Hawaiian volcanoes. In: McGuire WJ, Jones AP, Neuberg J (eds) Volcano instability on the Earth and other planets. Geol Soc Spec Publ 110:281–294

Hascke M (2006) The Eagle III BKA system, a novel sediment core X-ray fluorescence analyser with very high spatial resolution. In: Rothwell RG (ed) New techniques in sediment core analysis. Geol Soc Spec Publ 267: 31–37. doi:10.1144/GSL.SP.2006.267.01.02

Haschke M, Scholz W, Theis U, Nicolosi J, Scruggs B, Herzceg L (2002) Description of a new micro-X-Ray spectrometer. J Phys IV France 12:83–95. doi:10.1051/jp4:20020216

Hennekam R, de Lange G (2012) X-ray fluorescence core scanning of wet marine sediments: methods to improve quality and reproducibility of high-resolution paleoenvironmental records. Limnol Oceanogr Methods 10:991–1003

Jansen JHF, Van der Gaast SJ, Koster B, Vaars A (1998) CORTEX, a shipboard XRF-scanner for element analyses in split sediment cores. Mar Geol 151:143–153

Kylander ME, Lind EM, Wastegård S, Löwemark L (2012) Recommendations for using XRF core scanning as a tool in tephrochronology. Holocene 22:371–375

Löwemark L, Chen HF, Yang TN, Kylander M, Yu EF, Hsu YW, Lee TQ, Song SR, Jarvis S (2011) Normalising XRF-scanner data: a cautionary note on the interpretation of high-resolution records from organic-rich lakes. J Asian Earth Sci 40:1250–1256. doi:10.1016/j.jseaes.2010.06.002

Løvholt F, Pedersen G, Gisler G (2008) Oceanic propagation of a potential tsunami from the La Palma Island. J Geophys Res 113:C9. doi:10.1029/2007JC004603

Millward D, Johnson EW, Beddoe-Stephens B, Young B, Kneller BC, Lee MK, Fortey NJ (2000) British Geological Survey: geology of the Ambleside district. Memoir for 1:50 000 Geological Sheet 38 (England and Wales). The Stationary Office, London

Ortiz JD, Rack FR (1999) Non-invasive sediment monitoring methods. In: Abrantes F, Mix A (eds) Reconstructing ocean history: a window into the future. Kluwer/Plenum Press, New York, pp 343–380

Payne R, Blackford J, van der Plicht J (2008) Using cryptotephras to extend regional tephrochronologies: an example from southeast Alaska and implications for hazard assessment. Quat Res 69:42–55

Pearce TJ, Jarvis I (1995) High-resolution chemostratigraphy of Quaternary distal turbidites: a case study of new methods for the analysis and correlation of barren sequences. In: Dunay RE, Hailwood EA (eds) Non-biostratigraphical methods of dating and correlation. Geol Soc Spec Publ 89:107–143

Richter TO, Van der Gaast S, Koster B, Vaars A, Gieles R, de Stigter HC, de Haas H, van Weering TCE (2006) The Avaatech XRF core scanner: technical description and applications to NE Atlantic sediments. In: Rothwell RG (ed) New techniques in sediment core analysis. Geol Soc Spec Publ 267:39–50

Rothwell RG (2006) New techniques in sediment core analysis, Geol Soc Spec Publ 267

Rothwell RG, Hoogakker B, Thomson J, Croudace IW, Frenz M (2006) Turbidite emplacement on the southern Balearic Abyssal Plain (western Mediterranean Sea) during Marine Isotope Stages 1–3: an application of ITRAX XRF scanning of sediment cores to lithostratigraphic analysis. In: Rothwell RG (ed) New techniques in sediment core analysis. Geol Soc Spec Publ 267:79–98. doi:10.1144/GSL.SP.2006.267.01.06

Sakamoto T, Kuroki K, Sugawara T, Aoike K, Iijima K, Sugisaki S (2006) Non-destructive X-Ray fluorescence (XRF) core-imaging scanner, TATSCAN-F2. Sci Drill 2:37–39

Suárez-Ruiz I, Crelling JC (eds) (2008) Applied coal petrology: application of petrology to coal utilization. Academic Press, Amsterdam 388 pp

Thomson J, Croudace IW, Rothwell RG (2006) A geochemical application of the ITRAX scanner to a sediment core containing eastern Mediterranean sapropel units. In: Rothwell RG (ed) New techniques in sediment core analysis. Geol Soc Spec Publ 267: 65–77. doi:10.1144/GSL.SP.2006.267.01.05

Tjallingii R, Röhl U, Kölling M, Bickert T (2007) Influence of the water content on X-ray fluorescence core-scanning measurements in soft marine sediments. Geochem Geophy Geosy 8:Q02004, doi:10.1029/2006GC001393

Tjallingii R, HaMann Y, Garbe-Schönberg D, Weltje GJ, Röhl U, Workshop participants (2011) 2010 International workshop on XRF core scanning. PAGES News 19:90–91

Ward SN (2001) Landslide tsunami. J Geophys Res 106:11201–11215. doi:10.1029/2000JB900450

Ward SN, Day SJ (2001) Cumbre Vieja Volcano-Potential collapse and tsunami at La Palma, Canary Islands. Geophys Res Lett 28:3397–3400. doi:10.1029/2001GL013110

Weltje GJ, Tjallingii R (2008) Calibration of XRF core scanners for quantitative geochemical logging of sediment cores: theory and application. Earth Planet Sci Lett 274:423–438. doi:10.1016/j.epsl.2008.07.054

Wilhelms-Dick D, Westerhold T, Röhl U (2012) A comparison of mm scale resolution techniques for element analysis in sediment cores. J Anal Atom Spectrom 27:1574–1584

# Part I
# Marine Studies

# Chapter 2
# Twenty Years of XRF Core Scanning Marine Sediments: What Do Geochemical Proxies Tell Us?

**R. Guy Rothwell and Ian W. Croudace**

**Abstract** XRF core scanners, with their rapid and non-destructive analytical capability, have now been used for two decades in the analysis of marine sediments. Initially they were used to record variations in fundamental parameters such as calcium carbonate stratigraphy and terrigenous sediment delivery, using major element integrals, such as Ca and Fe, to provide detailed insights into oceanographic and climatic processes. In recent years, proxy selection has progressed to routine normalisation and presentation as log-ratios to include 60 elements or ratios to document a wide range of environmental and process changes. We review the development and application of XRF core scanning of marine sediments and discuss the basis of particular proxies, their uses and limitations to assist users in their selection. To date, there has been no systematic overview of elemental proxies and their application in the analysis of marine sediment records.

**Keywords** XRF core scanning · AVAATECH core scanner · ITRAX core scanner · X-ray fluorescence · Geochemical proxies · Environmental analysis · Marine sediments

## Introduction

In a little over 20 years, XRF core scanners have developed from a single prototype instrument to commercially available high-resolution instruments routinely used in palaeoenvironmental research worldwide. Initially, use was restricted to marine sediments and the number of publications small, but use and resulting publications rapidly increased in the first decade of the twenty-first century with increasing application to lake cores and terrestrial records (Rothwell and Croudace, this volume).

R. G. Rothwell (✉)
National Oceanography Centre, Empress Dock, Southampton, SO14 3ZH, UK
e-mail: rgr@noc.ac.uk

I. W. Croudace
Ocean and Earth Science, National Oceanography Centre, University of Southampton, Waterfront Campus, European Way, Southampton SO14 3ZH, UK



I. W. Croudace, R. G. Rothwell (eds.), *Micro-XRF Studies of Sediment Cores*,
Developments in Paleoenvironmental Research 17, DOI 10.1007/978-94-017-9849-5_2

Modern core scanners can analyse sediments at sub-millimetric intervals (termed micro-XRF or μXRF), allowing insights at decadal, annual and even sub-annual scales.

Marine and lake sediments can provide detailed palaeoenvironmental archives accessible through element proxy data. These data commonly reflect past climate. On continents, precipitation, temperature and vegetation are the primary controls on chemical weathering and physical erosion. On geologic timescales, a measure of this is preserved in the chemistry and mineralogy of sediments transported by rivers and wind to the deep sea or lake. In the oceans, proxy elements can also provide valuable data on productivity, water movements and diagenesis.

Micro-XRF instruments have become increasingly powerful tools for studying high-resolution chemical variability linked to environmental change. High-resolution studies on continuous sedimentary archives are crucial for understanding climate change on seasonal to millennial scales. Ca, Fe, Sr, K and Ti, commonly occurring elements in marine sediments, are extensively used as tracers in environmental reconstructions (e.g. Gebhardt et al. 2008; Rooij van et al. 2007; Vidal et al. 2002; Grützner et al. 2003; Arz et al. 2001b, 2003; Kuhlmann et al. 2004b; Romero et al. 2008; Calvert and Pederson 2007; and others). In this paper we review the development and application of micro-XRF studies of marine sediments, discuss methods for robust data analysis and provide a catalogue of element integrals and ratios that have been used as proxies, discussing their origin, application and limitations. Finally we review proxy relationship to magnetic susceptibility, which together with spectrophotometry, may clearly correlate with element abundances.

This paper shows what proxies have been used by researchers investigating the marine record, it demonstrates what has been done and what can be done, with the aim of guiding core scanner users in proxy selection and potential. To date, there has been no systematic overview of element proxies and their application to marine sediments.

## History of XRF Core Scanning of Marine Sediments

### *Early Non-chemical Methods of Determining Climate Changes*

A major focus of marine geology since the 19th Century has been determination of environmental and process records from cored sediments. Initially temporal changes in microfossil distributions were used to record climate changes. Pioneering work includes Schott (1935) working on cores collected by the German *Meteor* expedition to the South Atlantic of 1925–1927; Cushman and Henbest (1940) using cores from a North Atlantic W-E transect by the American cable ship *Lord Kelvin*; Phleger (1947) using Tyrrhenian Sea cores collected by the Swedish vessel

*Skagerak* using the newly-developed piston corer (Kullenberg 1947); and Phleger et al. (1953) using cores collected by the *Albatross* during the Swedish deep-sea expedition of 1947–1948. Collectively, these works led to the founding of palaeoceanography as a distinct discipline within the earth sciences.

## *Discovery of X-ray Fluorescence*

The discovery of X-ray fluorescence (XRF) revolutionised the capability to efficiently extract detailed environmental records from the marine realm. The ability of materials to fluoresce when excited by incident X-rays, emitting secondary radiation of characteristic wavelength depending on atomic number, was recognised within two decades of the discovery of X-rays by Röntgen in 1895. This phenomenon, the basis of XRF analysis (XRFA), arises as electrons are ejected from inner atomic shells through X-ray excitation. The resulting vacancies are filled by electrons moving from the outer electron shells with the energy difference emitted as electromagnetic radiation, the wavelength of which is characteristic for each element (see Jenkins and De Vries 1970, for further discussion).

The potential of X-ray excitation, and secondary fluorescence, to determine material composition was quickly realised when Henry Moseley demonstrated a systematic mathematical relationship between fluorescent X-ray wavelength and atomic number of metals used as targets in X-ray tubes (Moseley 1913/1914). Initially electrons were used as the excitation source, but these were highly inefficient in creating X-rays, with almost 99% of the energy lost as heat. However, Hadding analysed mineral samples in 1922 using this technique. A much more efficient method is to use an X-ray source with a metal target to induce fluorescence. This technique was first used by Coster and Nishina in 1925, with Glocker and Schreiber performing the first quantitative analysis of materials using XRF in 1928.

It took another 20 years for detector technology to make XRF a practical method for routine geochemical analysis, with the first commercially-available X-ray spectrometers appearing in the 1950s. In 1970, the advent of the high resolution solid-state lithium-drifted silicon detector, Si(Li) (e.g. Jenkins 1988), set the basis for what is the most widely used technology today, the Silicon Drift Detector (Gatti and Rehak 1984). There are two main XRFA variants, wavelength dispersive (WD-XRF) and energy dispersive (ED-XRF). The former provides the highest analytical resolution in terms of elemental separation. In WD-XRF elemental determination is commonly made by scanning through the wavelength range—in practice an angular goniometer moves to a particular elemental position as determined by the Bragg Law $n\lambda = 2d.\mathrm{Sin}\theta$. In practice, analysis of materials is destructive and is normally carried out in a vacuum on a homogenized disc-like sub-sample. The WD-XRF instruments are often sequential scanning devices although simulatneous spectrometers also exist. The demanding design of a WD-XRF does not lend itself to the scanning of sediment cores but they are excellent instruments for quantitative analysis of sub-samples from cores. The advent of compact solid-state devices

(diodes) allowed the development of energy dispersive detectors that collect an energy spectrum simultaneously. The Silicon Drift Detector is the latest variant of EDS devices and their development has made a significant technical contribution to core scanners and other XRF instruments. Their very good energy resolution and count-rate tolerance and the fact that they do not need LN2 cooling makes them the detector of choice in micro-XRF analysis.

## *Early Geochemical Studies of Marine Sediments*

Geochemical analysis of marine sediments from the 1930s onward established the value of geochemical data in studying ocean properties and processes (e.g. Correns 1937; Bramlette and Bradley 1940; Arrhenius 1952; Goldberg 1954; Goldberg and Arrhenius 1958). Initially textural and mineralogical variations were used to document environmental processes and changes. For example, Radczewski (1939) used the presence of iron-coated *wüstenquartz* in cores collected by the *Meteor* in the Cape Verde Basin to demonstrate aeolian deposition in the deep sea. Rex and Goldberg (1958) showed variations of wind-blown quartz with depth in North Pacific sediments related to climate change. From this, recognition of elemental proxies for larger grain-size, such as Si/Al, Ti/Al and Zr/Al was a short step as Si, Ti and Zr typically reside in larger mineral grains (see Calvert and Pedersen 2007). Elemental proxies for palaeoproductivity were also recognised early with Goldberg and Arrhenius (1958) interpreting enhanced barium in Pacific sediments as reflecting enhanced surface productivity (see Dymond and Collier 1996; Klump et al. 2000) for further information on Ba as productivity proxy). Element analysis thus joined micropalaeontology as a major palaeoceanographic research tool.

## *The Development of XRF Core Scanners*

By the 1970s laboratory-based X-ray fluorescence analysis was an established routine technique for analysing marine sediments, which were long recognised as holding long-term archives of past environmental change. Prior to 1988, XRF analysis required taking of discrete samples, which are ground to fine powders and pressed into pellets or fused with a borate flux to produce glass beads that can be analysed to calculate element abundances. This process, though still used to produce data of excellent quality, is destructive to the core and takes significant preparation and analysis time, and limits the practical resolution that can be achieved.

Standard analytical methods for discrete sample analysis are thus discontinuous, time consuming, and expensive. Relatively fast non-destructive core logging methods yield continuous data at much finer scales (down to sub-millimetre) than are practical for individual sampling methods and their application to XRF measurements proved a remarkable boon to the environmental sciences.

The first non-destructive XRF scanner that could produce continuous element records from split sediment cores was CORTEX (CORe scanner TEXel) developed

by the Netherlands Institute for Sea Research (NIOZ), Texel, The Netherlands, in 1988. This instrument was the forerunner of the modern commercially-available AVAATECH XRF core scanner, and because of its head start it has been responsible for producing about two-thirds of all peer-reviewed publications citing XRF core scanning as a method. CORTEX is described by Jansen et al. (1992, 1998).

Although, semi-quantitative in that elemental variations are measured as 'counts' per second, absolute concentrations can be obtained following calibration using relatively few conventional WD-XRF analyses of discrete samples (see for example, papers by Hunt et al., this volume).

A major advantage of the CORTEX instrument was that it could be containerised for sea-going, allowing acquisition of proxy records within a few hours of coring. First results from the Angola Basin (Jansen et al. 1990, 1996, 1998) showed CORTEX produced reliable semi-quantitative data for the elements K to Sr. The continuous downcore XRF records could be related to carbonate stratigraphy, the $\delta^{18}O$ record, and identify redox transitions and variations in terrigenous input (Jansen et al. 1998).

The value of the new instrument in palaeoceanography was quickly recognised. An updated CORTEX instrument was installed at the University of Bremen in 1997 (Röhl and Abrams 2000) with the capacity to measure a broad suite of elements from K ($Z=19$) to Sr ($Z=38$). A second-generation scanner, now produced by AVAATECH Analytical X-Ray Technology of Alkmaar, The Netherlands (normally referred to as the AVAATECH scanner), was delivered to Bremen and NIOZ in 2002. The AVAATECH core scanner has been improved and modified, enabling higher measurement speed, better detection limits, increased number of detectable elements and higher spatial resolution. Prior to 2005 the scanner was used almost exclusively for research on marine cores, and cores from the pre-Quaternary geological record, such as those collected by the Ocean Drilling Program (ODP). Technical details for both CORTEX and AVAATECH scanners are provided by Richter et al. (2006).

A parallel development was the Eagle II and III BKA XRF core scanners, built by Röntgenanalytik Messtechnik GmbH, Germany (Haschke et al. 2002; Hascke 2006). These instruments, developed from the Eagle µprobe, had several innovations including use of capillary optics to focus the incident X-ray beam allowing very high spatial resolution, down to 30 µm spot size and 10 µm step size. Further, analysis within an environmentally-controlled chamber, reduced the need to protect cores from drying during analysis, thus removing potential data artefacts caused by protective film applied during AVAATECH analysis to prevent core dessication. In a seminal paper, Haug et al. (2003) used the Eagle II scanner to show that intense droughts, inferred from using Ti as a proxy for rainfall and run-off (Fig. 2.1) in cores from the Cariaco Basin, offshore Venezuela, may have contributed to Classic Mayan civilisation collapse in the ninth Century A.D. Titanium, a common component in Fe-Ti oxides and other minerals in rocks such as gneisses or schists, is supplied to the oceans by wind and river transport. Recent work, however, suggests rainfall reductions in Central America may have been modest, but enough to cause critical water shortages (Medina-Elizalde and Rohling 2012).

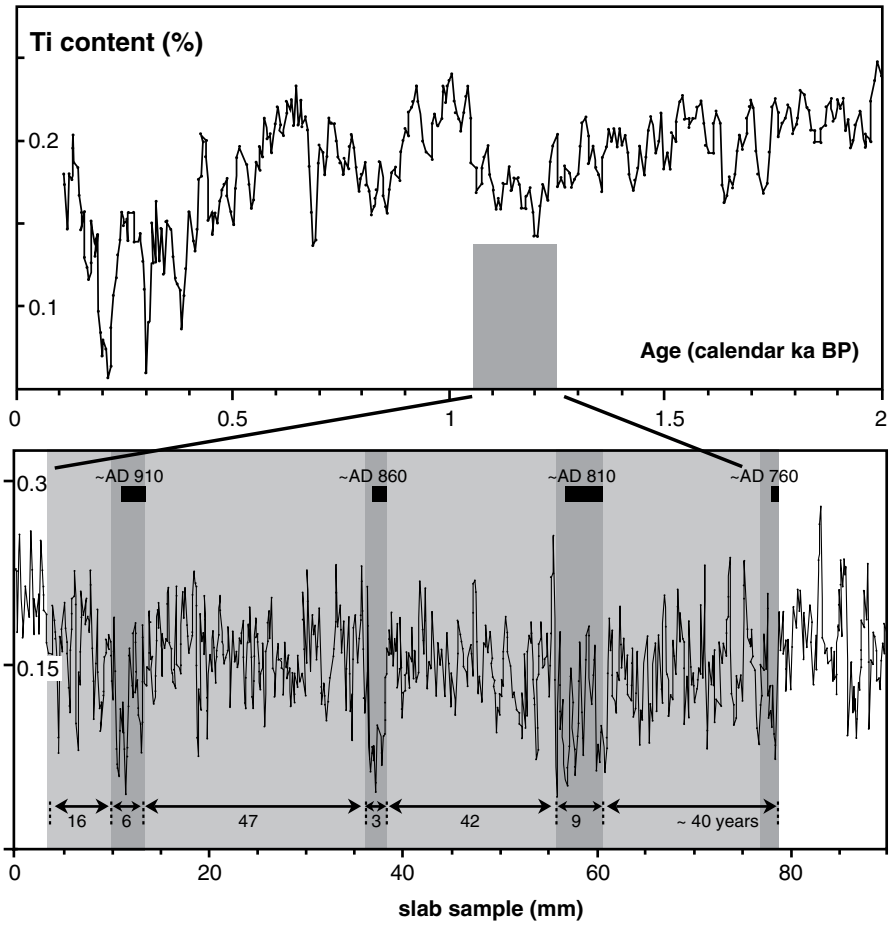


**Fig. 2.1** Ti content in two cores from the Cariaco Basin, offshore Venezuela, measured at different spatial resolution. Ti is used here as a proxy for terrigenous sediment delivery from surrounding watersheds and reflects rainfall changes. Episodes of low Ti (dated thick black bars) correlate with times of Mayan city abandonment dated from the archaeological record. (Reproduced with permission from Haschke 2006, and adapted from Haug et al. 2003, Figs. 2.2 and 2.3)

Another instrument, the ITRAX μXRF core scanner, was developed and funded by the Southampton Oceanography Centre (now National Oceanography Centre, UK) as a joint collaborative venture with Cox Analytical Systems, Gothenburg, Sweden. The first ITRAX instrument was delivered to SOC in 2003. Unique features of the ITRAX are its combination of a rectangular capilliary x-ray wave-guide and a digital micro-radiographic system, allowing acquisition of continuous digital x-radiographs as well as μXRF records. The radiographic image produced has a high dynamic range of $2^{16}$ grey-level values and a minimum pixel size of 20 μm (see Francus et al., this volume). The ITRAX is described by Croudace et al. (2006) and has become, with the AVAATECH scanner, the two most widely used in palaeoenvironmetal research.

XRF measurements usually show a significantly higher signal-to-noise ratio and more consistent core-to-core agreement than any other physical property measurement such as density, colour reflectance and magnetic susceptibility, thus providing comprehensive archives for time-series analysis of relatively complete sections (e.g. Pälike et al. 2001; Röhl et al. 2003; Jaccard et al. 2005; Tjallingii et al. 2007; and others).

## Review of Marine Science Applications

The past two decades have seen a wide variety of marine science applications for XRF core scanners but most fall into the following areas:

- core description and characterisation
- studies of climatically-driven cyclicities that are reflected, for instance, in $CaCO_3$ or Fe fluctuations over time
- sedimentological applications, where features or events such as ash layers, turbidites, ice-rafted debris, aeolian dust flux, or earliest stages of marine influences can be recognised through their exotic compositions or localised or organised character
- studies of sediment provenance based on chemical differences in source areas
- cluster analysis and facies interpretation of sedimentary environments
- diagenetic studies
- core correlation and orbitally-tuning high-resolution core log records
- environmental impact studies and environmental forensics.

### *Core Description and Characterisation*

XRF core scanning has been used, like many other techniques, as a core characterisation tool, allowing lithological units and textural/mineralogical variations to be identified and described. Arguably XRF core scanning provides the most detailed analytical results in the quickest possible time, particularly for identifying sediment layers worthy of more detailed investigation or dating.

Rothwell et al. (2006), for example, used a range of element integrals and ratios to characterise interbedded turbidites and pelagites from the Balearic Abyssal Plain, Western Mediterranean Sea. Compton scattering, which relates inversely to mass absorption coefficient and mean atomic number, decreased in silt and sand layers due to size/density-related mineral fractionation. Grading due to mineral variation could also be seen in this parameter, even when not visually obvious. Discrete pteropod layers were characterised by sharp decreases in Compton scattering, possibly due to current winnowing, as mean atomic number falls with looser sediment packing. As Al was then at the limit of ITRAX detection and counts low, Rothwell et al. (2006) considered other detrital elements for normalisation. Rb was preferred to Ti, as ratioed Rb showed better relation to grading and Compton scattering values in the sediments studied.

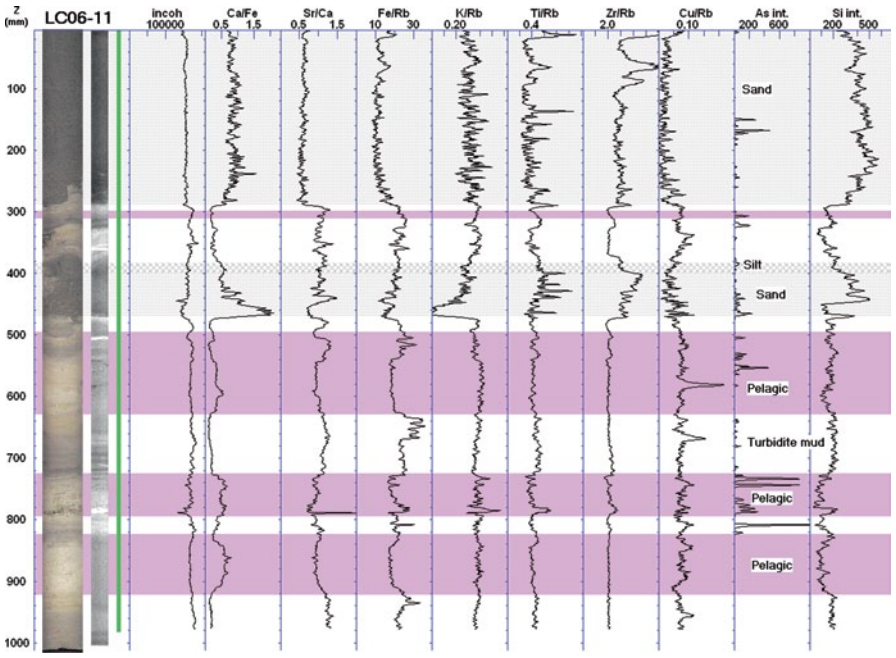


**Fig. 2.2** ITRAX-acquired XRF element profiles through interbedded turbidites (white or ornamented) and pelagites (mauve) from the Balearic Abyssal Plain, western Mediterranean Sea. Boundaries between turbidite and pelagic muds are difficult to distinguish visually but are clearly seen in the Ca/Fe profile, with Ca/Fe showing more variability in pelagic muds due to scattered foraminifers. Turbidites have more uniform profiles due to removal of foraminifers through gravitative settling. The Si profile shows the upper sand (between 0 and 300 mm) is massive and ungraded, while the sand between 400 and 480 mm is normally graded (from Rothwell et al. 2006). The image was generated using ItraxPlot™ (see Croudace and Rothwell, this volume)

Element ratios found useful as proxies by Rothwell et al. (2006) are:

- Ca/Fe (biogenic carbonate:detrital clay ratio, useful for turbidite/pelagite discrimination (Fig. 2.2), sediment grading, assessing textural character, and source distality-proximality relationships)
- Sr/Ca (indicating high-Sr aragonite requiring a shallow-water source)
- Fe/Rb (commonly showed grain-size-related fractionation effects within turbidites and elevated Fe in oxic, or formerly oxic, parts of turbidites)
- K/Rb (commonly enhanced in turbidite muds compared to silts, sands and pelagic mud, reflecting presence of K, like Rb, in clays)
- Zr/Rb and Ti/Rb (commonly enhanced in turbidite bases, possibly having value as provenance indicators)
- Cu/Rb (showing diagenetic mobilisation of Cu)
- As (indicating presence of pyrite).

Rothwell et al. (2006) demonstrate that XRF core scanning provides a quick efficient way of distinguishing pelagic from turbidite muds that may look visually

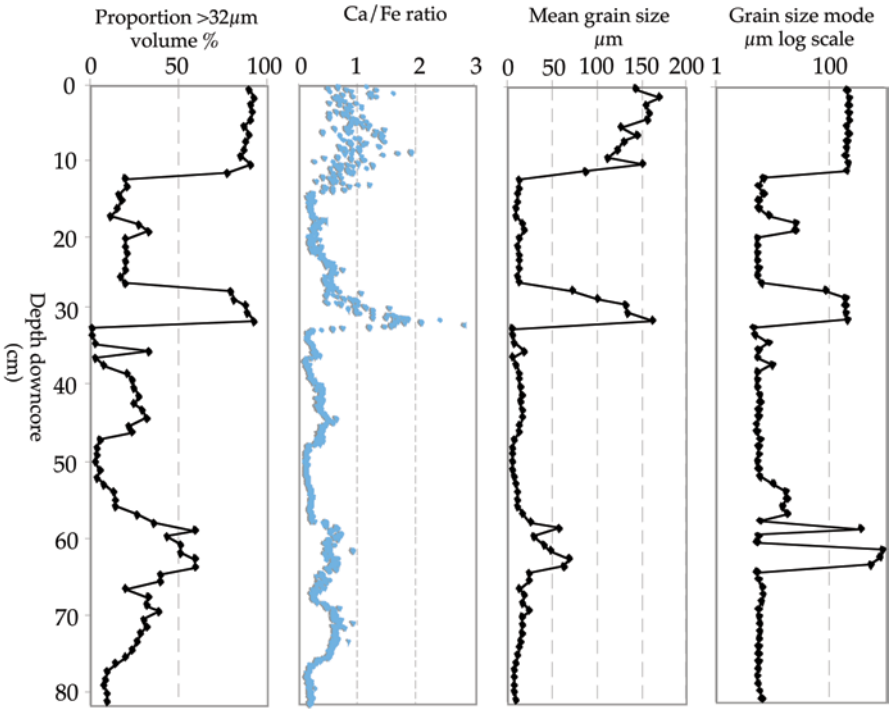


**Fig. 2.3** Grain-size profiles and Ca/Fe profile through core interval shown in Fig. 2.2. Note Ca/Fe provides a good proxy for textural variation, with a close correspondence to mean grain-size and proportion of grains > 32 μm suggesting Ca relates to presence of foraminifers (From Rothwell et al. 2006)

similar; can identify early arrivals of turbidite beds; and provide reliable indicators for grain-size variation and grading (Fig. 2.3).

Further examples of XRF core scanners used for core characterisation are shown in Table 2.1.

Core characterisation is a prerequisite for further core analysis and determining environmental history. Bed characterisation may reveal different sedimentary environments and facies changes downcore. For example, Wolters et al. (2010) used XRF core-scanning to document a ~1500 year record of early Holocene vegetation changes and mire development in a North Sea landscape now 33 m below sea-level (Fig. 2.4). Combined application of botanical and geochemical methods rapidly determined key horizons indicative of marine conditions and different environments showed specific element signatures—basal glacio-fluviatile sandy mud by high Si and relatively high Al, K and Ti, and peat development by increased S and decrease in Si, Al, K and Ti (Fig. 2.4). Mn and Fe peaks suggested fluctuating ground water levels in the early stages of mire development, which were not apparent in the vegetation record. Fluctuation of Ca and S suggested an oscillating coastline. The authors conclude that transgressive contacts are most precisely located by XRF core

**Table 2.1** Examples of studies where XRF core scanners have been used primarily to characterise marine sediment cores

| Reference(s) | Area | Notes |
|---|---|---|
| Bergh et al. (2003), Kaars van der and Bergh van der (2004) | Teluk Banten embayment, NW Java | Characterised the 1883 Krakatau tsunamiite, Ca record quickly defined the tsunamiite—a thin sandy layer of reworked bioclasts, pellets and volcanic ash |
| Franke et al. (2004) | SW Atlantic | Established combined palaeomagnetic and sedimentological dataset, including carbonate, opal and terrigenous content, grain-size distribution and clay mineral composition |
| Nørgaard-Pedersen et al. (2006) | Loch Etive, W Scotland | Core scanner Ca and Fe profiles quantified by discrete sample XRF spectrometry |
| Bergh et al. (2007) | Ba Lat prodelta (Red River Vietnam) | Downcore Ca and Fe measured, with relatively low Fe in sandy shelf deposits |
| Lebreiro et al. (2009) | Portuguese continental margin | Characterised element composition of deep-sea and land-derived sediments. K/Ca, Ti/Ca and Fe/Ca and magnetic susceptibility followed similar trends with prominent peaks matching Heinrich events |
| Ren et al. (2009) | Ameralik Fjord, SW Greenland | Measured Fe, Ti, K, Si, Ca and Br. Fe, Ti, K and Si common elements in hinterland bedrock, and intensities used as indicators of terrestrial influence, including melt-water discharge. Ca and Br interpreted as reflecting biogenic production |
| Land et al. (2010) | Carbonate mounds, SW Rockall Trough margin | Ca/Fe and magnetic susceptibility suggested regional control on sediment accumulation, rather than local, site-specific control |
| Pirlet et al. (2010) | Magellan carbonate mounds, Porcupine Seabight, NE Atlantic | Fe, Ca and Sr effective in distinguishing lithological boundaries |

scanning (through increase of K, Ti, Si), as visual interpretation of the lithostratigraphy can be uncertain and pollen analysis is mainly based on airborne particles.

## *Studies of Climatically-Driven Cycles in Sediment Deposition that are Reflected in Element (e.g. Ca or Fe) Fluctuations Over Time*

A major application of XRF scanning of marine cores has been to determine climatically-driven changes in sediment composition, largely relating to glacial-intergla-

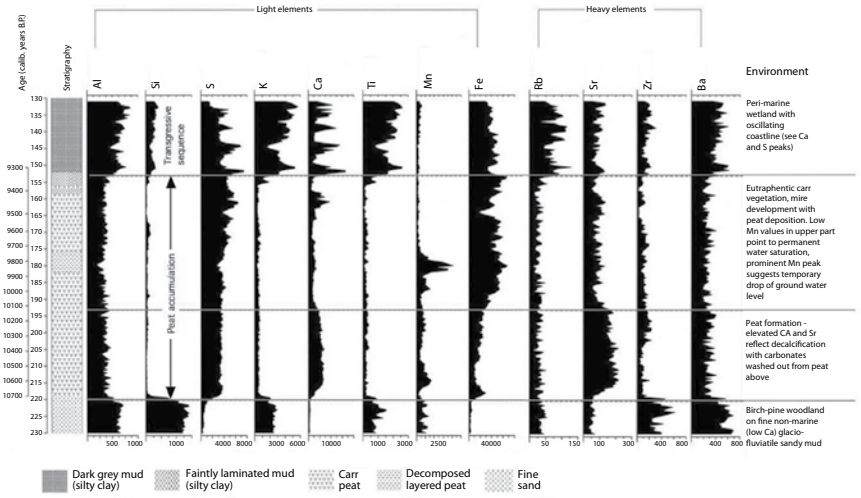


**Fig. 2.4** Element profiles through a core from the Heligoland Bight, Southern North Sea, documenting upcore transition from non-marine glacio-fluviatile sandy mud with birch-pine woodland (*bottom*), through carr and mire development with extensive peat formation to a marginal marine environment (*top*). Vegetation data derived from pollen analysis. The sequence is divided into four geochemical zones (bounded by *grey lines* in figure), characterised by differing element intensities, related to core lithology and useful for reconstruction of vegetation history. Mn profile within the peat shows level of water saturation. Ca and S peaks in the transgressive sequence (*top*) suggest an oscillating shoreline. (Adapted and reproduced with permission from Wolters et al. 2010)

cial cycles (e.g. Moreno et al. 2002; Lebreiro et al. 2009). The two main parameters measured are Fe as a proxy for terrigenous input (e.g. Vidal et al. 2002; Grützner et al. 2003, 2005) and Ca as a measure of biogenic production (e.g. Cheshire et al. 2005; Solignac et al. 2011). Ti has also been widely used as a terrigenous indicator (e.g. Peterson et al. 2000; Haug et al. 2001, 2003) and is preferable to Fe, being redox-insensitive. Variance of Ti and Fe, or use of the diagenetic proxy Fe/κ (where κ is magnetic susceptibility; Itambi et al. 2010), will show whether diagenetic alteration of Fe has been significant (Rincón-Martínez et al. 2010).

It is well-established that $CaCO_3$ records in the Atlantic Ocean are related to glacial-interglacial cycles, with higher carbonate concentrations during interglacials (e.g. Balsam and McCoy 1987). Hence, preliminary stratigraphic records can be based on downcore records of Ca and Fe, tracing fluctuations in the relative abundance of biogenic carbonate and terrigenous material respectively (Richter et al. 2006, Fig. 2.5).

XRF core scanner studies have involved cores containing records of the Quaternary glaciations and older cores recovered by the Ocean Drilling Program. Abrupt changes in Fe (and Ti) and Ca typically correlate well with glacial-interglacial

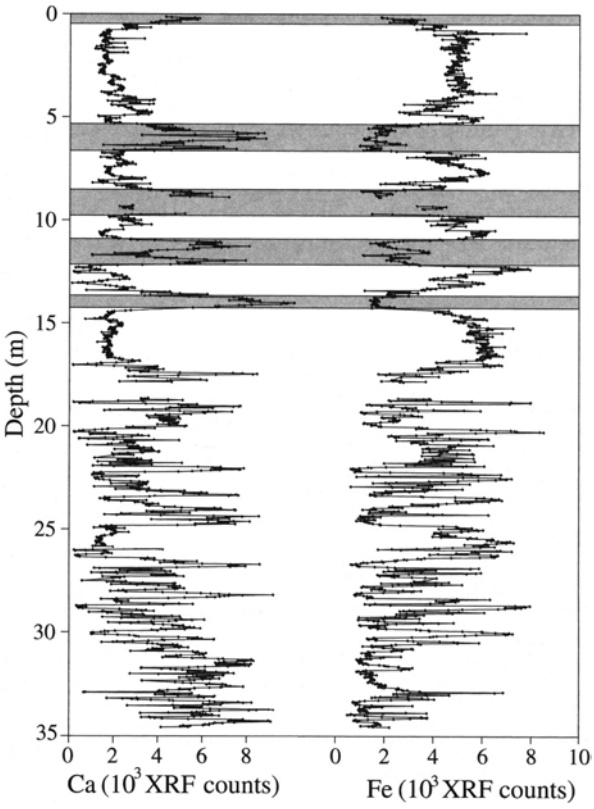


**Fig. 2.5** Ca and Fe count rates for a core from Rosemary Bank, NW of Scotland, showing glacial-interglacial variability in element flux. Interglacial intervals are shaded (high Ca, low Fe). (Reproduced with permission from Richter et al. 2006)

transitions (Fig. 2.5). Temporally-shorter episodes of iceberg rafting are commonly marked by Fe and Ti peaks. However, care is needed in interpretation as variability may relate to terrigenous dilution and/or variable calcite dissolution. As siliciclastic contents may be substantially affected by productivity changes and carbonate dissolution, Rincón-Martínez et al. (2010) proposed calculated siliciclastic mass accumulation rates (AR) as a more reliable proxy for terrigenous supply changes.

A fortuitous situation arises off West Africa where Fe and Ti represent fluvial and aeolian fluxes respectively, allowing Fe/Ti use as a discriminant (Itambi et al. 2010). Here, Fe is mostly transported by rivers (e.g. via Rivers Sanaga and Ougoue) and therefore varies with hydrological changes. Ti is a good Saharan dust proxy and has been used by several authors to trace aeolian input, as loess tends to concentrate heavy minerals, and hence is enriched in high field-strength elements, such as Ti (Balsam et al. 1995; Zabel et al. 2001; Itambi et al. 2009).

Further examples of XRF core scanner use to record climatically-driven cycles are given in Table 2.2.

**Table 2.2** Examples of studies where XRF core scanners have been used to record climatically-driven cycles in biogenic and terrigenous inputs

| Reference | Area | Age | Notes |
|---|---|---|---|
| Bahr et al. (2005) | Black Sea | Quaternary | Ti/Ca used to identify major episodes of Caspian water spilling into Black Sea during deglaciation |
| Hepp et al. (2006) | ODP Site 1095 (Antarctic Peninsula Pacific margin sediment drift) | Pliocene | Fe and Ti (terrigenous) and Ca (biogenic $CaCO_3$) correlated with glacial cyclicity with transitions as abrupt changes. Iceberg rafting at end of deglaciation seen as maximum Fe and K data amplitudes |
| Møller et al. (2006) | Ameralik Fjord, SW Greenland | Late Holocene | Fe used as terrigenous indicator and Ca to record marine productivity variations and biogenic Ca input relative to input of terrrestrial minerals |
| Blanchet et al. (2007) | Baja California | Quaternary | Si and K showed similar trend, inverse to TOC, suggesting Si carried mainly by silicate fraction. Fe, Ti, K and Si correlate with magnetic parameters suggesting variations in magnetic concentrations primarily reflect terrigenous input changes |
| Diekmann et al. (2008) | ODP Site 1202 (Okinawa Trough) | Quaternary | K/Ti used to emphasise differences in terrigenous material, and related to amount of mica and illite sheet silicates present. Variations in K/Ti reveal changes in sediment provenance, largely controlled by sea-level changes |
| Spofforth et al. (2008) | IODP Expedition 302 (ACEX) (Lomonosov Ridge, Central Arctic Ocean) | Middle Eocene | Input of terrigenous elements related to hinterland climate changes. XRF data provide additional information on sedimentation rate changes from cyclical changes matched to orbital forcing |
| Lippold et al. (2009) | ODP Site 1063 (Bermuda Rise) | Quaternary | Ratioed lithogenic elements to Ca during Heinrich events 1–3, showing peaked lithogenic elements during cold periods |
| Itambi et al. (2010) | Gulf of Guinea, eastern equatorial Atlantic | Quaternary | Fe/Ti used to distinguish fluvial and aeolian input. Fe represented mostly fluvial input and varied positively with hydrological changes. Ti established indicator for Saharan dust. Fe input higher during warm periods due to greater run-off, Ti higher during cold periods due to increased aeolian flux. Post-depositional modification of sediment composition checked using diagenetic proxy Fe/κ. Most of record unaffected and therefore recorded primary climate signals of adjacent continent |
| Rincón-Martínez et al. (2010) | ODP Site 1239 (~120 km off the Ecuadorian coast close to Guayas/Esmeraldas drainage systems) | Quaternary | Fe-Ti combined with mass accumulation rates of siliciclastics used to determine terrigenous supply. Log ratios of Fe and Ti over Ca used to record carbonate dilution. Terrigenous record showed consistent glacial-interglacial pattern. Sediments predominantly terrigenous during interglacials and siliciclastic contents substantially lower during glacials, related to hinterland run-off, indicating humid interglacial conditions and more arid hinterland during glacials |

## *Sedimentological Applications, Where Primary Features or Events May be Recognised by Their Exotic Composition or Localised and/or Organised Bed Characteristics*

A widely-used application of μXRF analysis is identifying and characterising primary sedimentological deposits reflecting discrete events on their exotic composition, localised nature, and/or organised bed characteristics. Tephra layers, for example, may show as discrete peaks in Si, Ti, Zr, or K, depending on whether acidic, basic or intermediate in composition, reflecting presence of volcanic glass and volcanic minerals. Tephras are particularly important as time-synchronous marker horizons. Detection of cryptotephras—dispersed distal volcanic ash not visible to the naked eye—might seem a promising application of μXRF analysis, although there have been few reported studies (but see Balascio et al., this volume). Detection of cryptotephras would allow identification of tephras further away from volcanic sources, and might record previously unidentified eruptions where proximal deposits are poorly preserved or masked by subsequent eruptions (Payne et al. 2008). Likewise, ice-rafted debris layers (IRD), also important time-synchronous markers, may show peaked terrigenous elements (Itambi et al. 2009; Jaeschke et al. 2007; Lebreiro et al. 2009). Both IRD and tephra layers normally also show as magnetic susceptibility peaks. Other short-lived but regionally-significant events such as extreme flooding may leave clear element signatures. For example, Kleiven et al. (2007) measured Ca, K and Si in a core from Erik Drift, south of Greenland, recording dilution of biogenic carbonate by terrigenous material, when Lake Agassiz freshwater flood outburst into the NE Atlantic.

Besides rapidly identifying ephemeral events such as ice-rafting, volcanic eruptions, and flooding, μXRF core scanning has been particularly effective in documenting longer-term histories of terrigenous flux such as aeolian dust supply, particularly offshore arid regions, such as North Africa (e.g. Hanebuth and Lantzsch 2008; Hanebuth and Heinrich 2009). Elements of terrigenous origin (Si, Fe, K, Ti, Al) will show comparable distribution patterns in logical opposition to carbonate/Ca content. Relative increase of representative terrigenous elements (Fe, Si, K) vs. carbonate (Ca) and Fe alone has been effectively used as aeolian dust proxies. Such data may allow inferences on wind strength and hinterland climate (i.e. humid versus arid) that may, together with IRD episodes, relate to Milankovitch-type orbital forcing (e.g. Sangiorgi et al. 2008).

## *Studies of Sediment Provenance Based on Chemical Differences in Source Areas*

Element ratios of samples from different catchments may provide information on fluvial sediment provenance (e.g. Amorosi et al. 2002; Moldenhauer et al. 2008). Several core scanner-based studies have used chemical differences in source areas to document long-term regional histories of sediment flux (Table 2.3).

**Table 2.3** Some examples of studies where XRF core scanners have been used in sediment provenance studies based on chemical differences in source areas

| Reference | Area | Notes |
|---|---|---|
| Stuut et al. (2007) | Chilean slope, SW Pacific | Measured K, Ca, Ti, Mn, Fe, Cu, and Sr in multi-cores. Element ratios showed distinct latitudinal trends identifying four areas with characteristic element mixtures. Terrigenous sediments deposited off arid N Chile likely predominantly wind blown, whereas further south under more humid conditions, terrigenous sediments probably river transported. Geochemical data documented southward shift in terrigenous input through aeolian and fluvial sources, and discriminated fluvial sediment provenance |
| Kujau et al. (2010) | DeSoto Canyon, Gulf of Mexico | Fe/Ti, K/Ti, and K/Fe used to characterize terrigenous sources. Correlation between Ti and Fe suggested shared common source. Ratios plot within known field of Mississippi River catchment and distinct from Alabama/Mobile catchment, showing Mississippi major sediment source. K important discriminant with high K concentrations in Mississippi catchment and low K in Alabama/Mobile area, so downcore K indicator for Mississippi River sediment flux changes. K/Ti thus differentiates Mississippi River and Alabama/Mobile sediment supply |
| Monien et al. (2010) | McMurdo Ice Shelf, W Ross Sea, Antarctica | K/Ti and Fe/Ti used to discriminate sediment sources in 1285-m long ANDRILL core AND-1B. Ratio differences showed three geochemical facies, representing three source areas: local McMurdo Volcanic Group (MVG),TransAntarctic Mountain rocks west of Ross Island, and more southerly TransAntarctic Mountain rocks.Downcore variations in geochemical facies interpreted as representing five major paleoclimate phases over past 14 Ma.Statistical analysis showed different sources during cored interval and identified material transport processes, such as ice flow patterns, meltwater influences and ice volume changes. Data showed sediment provenance within McMurdo Sound changed systematically over time |
| Montero-Serrano et al. (2010) | Pigmy Basin, Gulf of Mexico | Ti and K showed similar trends, consistent with clay mineral oscillations, interpreted as reflecting changes in terrigenous clay minerals. Mineralogical and geochemical data show Holocene detrital sediments have two sources. The first with high smectite content, the second enriched in illite and chlorite with high K and Ti.<br>Previous work suggests first end-member corresponds to NW Mississippi and Missouri watershed province and the second the NE Great Lakes province. Fluctuations of Mississippi River discharge reflects changes between two dominant terrigenous sources (smectite vs. illite+chlorite), interpreted as reflecting successive migrations of main rainfall belt over N America |

## *Cluster Analysis and Facies Interpretation of Sedimentary Environments*

Cluster analysis is an important method of exploring core scanner data and may be useful in facies interpretation, identifying sources for allochthonous sediments (e.g. Hunt et al., this volume), or for subdividing sediment into geochemical zones (e.g. in hydrothermal sediments, Müller et al. 2010). Groups with small distances between cluster members, dense areas of data space, or particular statistical distributions may distinguish geologically significant subsets. Principal component analysis (PCA) may be used to discriminate element data to identify different sedimentary facies. For example, Harff et al. (2011) used PCA for facies interpretation in a Baltic Sea core (Eastern Gotland Basin) identifying three factors each characterised by specific element character:

- One factor based on high negative loadings for Al, Si, K, Ti and Fe, interpreted as a proxy for detrital material.
- A second factor based on high loadings of Mn and Ca representing early diagenetic formation of a Ca-Mn-carbonate phase.
- A third factor (with dominant S) regarded as a proxy for oxygen depletion in bottom water.

Variation in K and Ti related to higher terrestrial discharge into the basin, either through higher precipitation and runoff or through more coastal erosion by storms or currents. Lower K and Ti were attributed to relative decrease in terrestrial discharge together with pelagic deposition, or interpreted as a function of aeolian dust input. High S concentrations suggested anoxic environments.

Itambi et al. (2009) used fuzzy cluster analysis of normalised element and magnetic data to discriminate fluvial and aeolian inputs offshore Senegal, NW Africa, interpreted as indicating humid and dry periods during the late Quaternary. Fuzzy cluster analysis showed four clusters:

- An aeolian dust signature characterised by high Ti and K. Ti-enrichment is regarded as a typical signature for Saharan dust due to presence of Ti-rich phase rutile (Schütz and Rahn 1982).
- A diagenetic cluster—marked by high concentrations in terrigenous elements Fe and Al coupled with very low magnetic parameter values. High Fe and low remanence was interpreted as reflecting reductive dissolution of magnetite, leaving behind less magnetic Fe phases (e.g. Karlin et al. 1987) probably due to increased influx of organic matter (Canfield and Berner 1987).
- A third cluster characterised by high Ca and low terrigenous signals, interpreted as representing marine productivity, and the dominant type during interglacials (Fig. 2.6).
- Cluster 4 dominated by high anhysteretic remanent magnetization (a measure of fine-grained ferrimagnetic mineral concentration) and intermediate-value terrigenous signals. Fe was relatively high (typical of fluvial sediments in the region) although high Ti indicated some aeolian input. This cluster was interpreted as fluvial in origin with significant aeolian contribution.

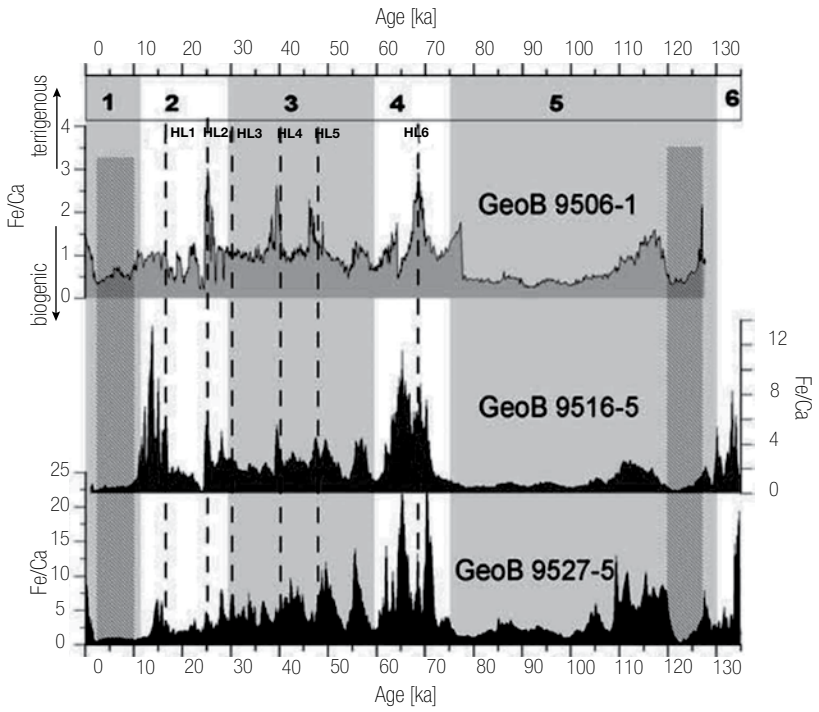


**Fig. 2.6** Terrigenous versus biogenic input shown by Fe/Ca in three cores on the lower continental margin off Senegal, NW Africa. Oxygen isotope stages indicated top and interglacials shaded. Fe/Ca shows increased terrigenous input during Heinrich-like events and glacial maxima. GeoB9506-1 is northernmost core and GeoB9527-5 the most southerly. Plots are on different y-axis scales due to southward increase in Fe and northward increase in Ca. This illustrates how core scanner-measured Fe/Ca can rapidly provide temporal records of terrigenous input and associated climatic forcing. (Reproduced with permission From Itambi et al. 2009)

Of the four clusters identified, three represent primary sediment sources, and one, sediments overprinted by post-depositional processes. Adkins et al. (2006) demonstrate that by normalizing terrigenous and carbonate fluxes, the terrigenous fraction dilutes the carbonate record and is a good indicator for climate change in this region (Fig. 2.6). Ti/Al and Si/Al indicate continental precipitation and wind strength respectively. High values point to pronounced aeolian flux and low values greater rainfall (Fig. 2.7). Terrigenous input increased significantly during glacial periods. Aeolian sediments, indicating continental aridity, are deposited at glacial maxima.

## *Studies of Diagenesis and Secondary Modification*

After deposition, geochemical and microbiological processes may modify original sediment composition. Early diagenetic processes affect primary signal preservation and their understanding is important for proxy interpretation. Breakdown of

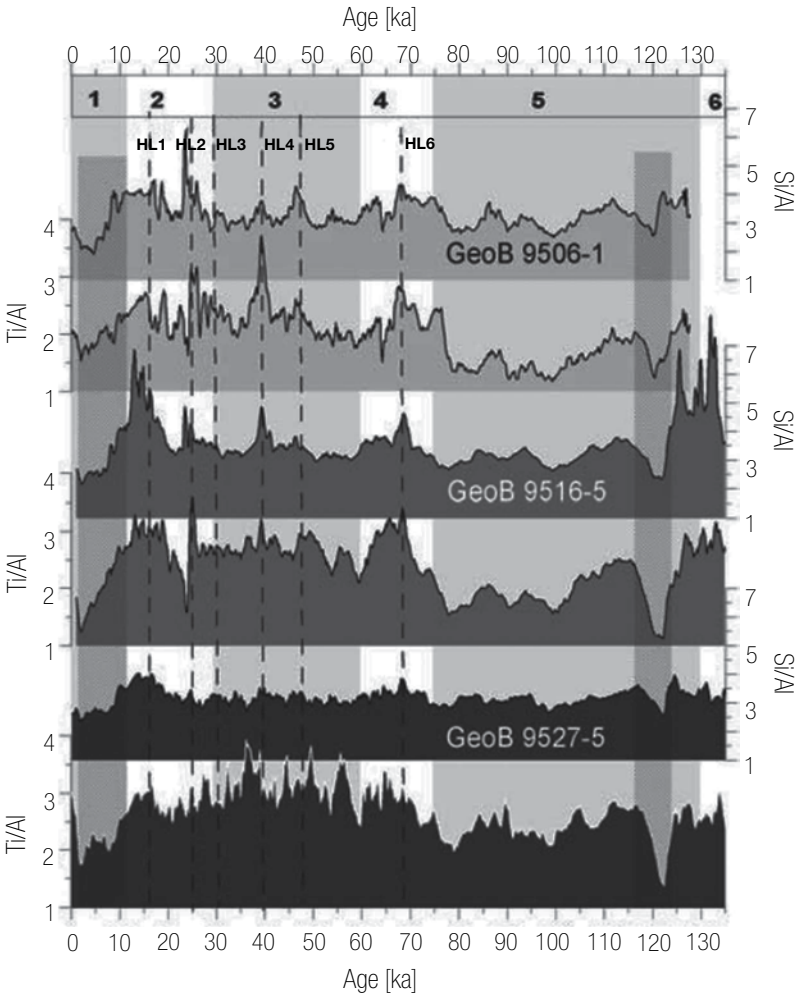


**Fig. 2.7** Ti/Al (proxy for continental rainfall and run-off) and Si/Al (proxy for wind intensity) used to discriminate aeolian versus fluvial sediment input on Senegalese continental margin. Si/Al positively correlates with aeolian input in the two northern cores (GeoB9506-1 and GeoB9516-5) but anti-correlate in the southernmost core (GeoB9527-5). High Si/Al values show high aeolian contribution and low values reflect enhanced continental rainfall. Terrigenous input increased significantly during glacial periods. Aeolian sediments, indicating continental aridity, were deposited at glacial maxima. Element proxies for hinterland precipitation and aridity provide detailed insight into hinterland climate and resultant sediment dynamics. (Reproduced with permission from Itambi et al. 2009)

organic matter within sediments typically leads to redox zonation with surface oxic sediments, underlain by post-oxic, sulphidic and methanic levels, determined by the overall energy yield of reactions (Froelich et al. 1979; Berner 1981). As marine sediments pass through this redox zone sequence during burial, secondary diagenetic signals affect primary sediment composition (e.g. Thomson et al. 1986, 1996; and others).

Although diagenetic processes may modify sedimentary records, they can reveal important paleoenvironmental changes. Diagenetic layers are often thin and typically require at least sub-centimetric sampling for adequate resolution. Hence only rapid scanning techniques, as provided by core scanners, permit high-resolution analysis of long and multiple sediment cores in reasonable time.

Funk et al. (2004a) present a novel method of studying diagenesis in two equatorial Atlantic cores. Fe represents a combined climatic and diagenetic signal, so the iron/susceptibility (Fe/κ) ratio can be used as proxy for magnetite dissolution. Combination of magnetic susceptibility and Fe core scanner derived logs revealed diagenetically affected intervals with unprecedented speed and precision. Fe/Ti was used to locate faint iron precipitation horizons associated with underlying layers of partial magnetite dissolution. Combining magnetic and geochemical logs was effective in detecting redox-related magnetic and nonmagnetic iron mineral diagenesis, and in distinguishing variations in primary input and diagenetic overprinting.

Fe is redox-sensitive and variance with inert Ti is a guide to diagenetic effects such as dissolution, migration and recrystallization. Sharp increases in Fe/Ti can also indicate diagenetic iron (Richter et al. 2006). Other Fe/element ratios may be used to detect Fe diagenesis. Blanchet et al. (2009) noted grey greigite layers in a core from the Santa Barbara Basin, California. Greigite ($Fe_3S_4$) can form as an intermediate species during conversion of FeS into pyrite ($FeS_2$) (Berner 1984). Slightly higher Fe/K ratios (as well as Fe/Ti and Fe/Al) just below the greigite-rich layers suggested Fe migration during early diagenesis.

Richter et al. (2006) used Fe, Mn and S to trace early diagenetic processes in a mud volcano on the Faroe-Shetland margin, noting changes in S marked redox boundaries. Sharp Fe and Mn peaks were interpreted as palaeo-oxidation fronts. Diagenetic Fe peaks were confirmed by sharp increases in Fe/Ti. Numerous abrupt S peaks within the reduced lower part of the mud volcano implied deposition of pyrite or some other Fe-sulphide phase. Pyritisation is a widespread process in marginal organic-rich sediments, leading to progressive dissolution of iron oxides and stepwise formation of pyrite ($FeS_2$).

Thomson et al. (2006) used various elements and ratios to study diagenesis within sapropel-bearing cores from the Eastern Mediterranean. These included:

- Ba/Ti (productivity indicator)
- Br/Cl (indicates increased organic matter, higher porosity)
- Mn/Ti (showed extent of post-depositional oxidation of sapropel)
- Cu/Ti (useful marker of post-depositional oxidation)
- Fe/Ti, S/Cl
- As (indicator of pyrite authigenesis)
- Sr/Ca (presence of aragonite, postulated to form as a consequence of the alkalinity produced by sulphate reduction diagenesis within sapropels).

Ba/Ti, Mn/Ti and Cu/Ti were especially useful in recording the inferred location of the active oxidation front in sapropels (Fig. 2.8). In this study, element/Ti ratios appeared a reasonable alternative to element/Al ratios normally used to define detrital aluminosilicate levels, and element/Cl ratios indicated where S and Br increased significantly over sea-salt values due to pyrite formation or association with organic

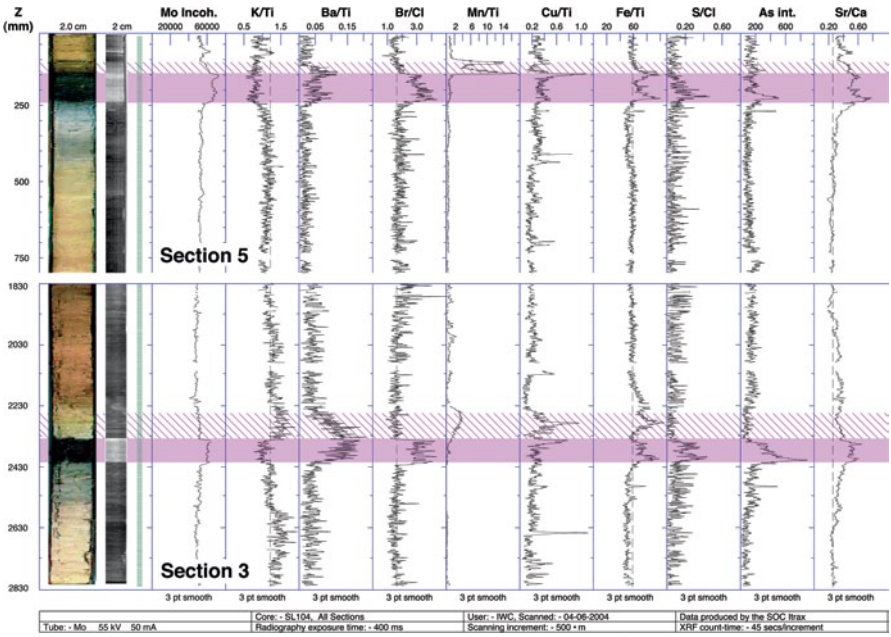


**Fig. 2.8** Selected element ratios, As and Mo Compton scatter peaks through two sapropel-containing cores from the Eastern Mediterranean (*sapropels black* in core photographs, *left*, and marked by *magenta bands*). Sapropels show high Ba, Br, Cu, Fe, S, As and Sr. Oxidised sapropel tops, although no longer visibly distinct, can be identified by elevated Ba, Mn, Cu and Fe (marked by magenta oblique hachure). The high water content in the unoxidised sapropels (*magenta bands*) causes local increases in Compton (incoherent) scattering, and the resultant changes in excitation efficiency probably affect the expected constancy of K/Ti (Reproduced with permission from Thomson et al. 2006). The image was generated using ItraxPlot

matter. Localised enrichments of redox-sensitive elements associated with organic carbon or sulphide formation could be readily identified through selected ratios, and profile trends provided evidence of post-depositional sapropel oxidation. Profile shapes showed direction of movement of some elements (e.g. Fe, As, Cu) during diagenesis. Narrow zones of high concentrations of particular elements, such as Cu, which may be missed by conventional analysis based on discrete samples, were effectively recorded.

## *Core Correlation and Orbitally-Tuning High-Resolution Core Log Records*

XRF core scanning is an efficient tool for core-to-core or hole-to-hole (e.g. at IODP and ODP drill-sites) correlation and confirming composite depth records (e.g. Jansen and Dupont 2001; Hofmann et al. 2005). Typically, XRF records are more consistent for correlation, and have a significantly higher signal-to-noise ratio than standard shipboard physical property measurements (Röhl and Abrams 2000). As

such, XRF data allow assembly of more accurate high-resolution composite depth scales. Elements ratios used include Ca, K, Ti/Ca (Bahr et al. 2008), Fe (Westerhold et al. 2005) and Ca/Fe (Dorschel et al. 2005).

Core scanning has proved valuable for dating cores through temporal correlation with nearby cores with established age models, with Ca and Fe especially useful in this regard (e.g. West et al. 2004), potentially providing very high-resolution time frameworks (e.g. Kwiecien et al. 2008). Additionally core scanning has been used effectively to correlate to climatic reference records. Brendryen et al. (2010) correlated a long piston core from the Norwegian Sea with the North Greenland NGRIP $\partial^{18}O$ record using Ca. Jumps in Ca related to climate transitions. In intervals where Ca showed less resemblance to NGRIP, Ti/K was used for correlation. Ti/K was very similar to the magnetic susceptibility record, a feature seen in other cores from Nordic Seas (Richter et al. 2006).

Frenz et al. (2009) used core scanner element data to tentatively correlate individual turbidites from adjacent abyssal plains in the NE Atlantic. Turbidites derived from the Moroccan margin showed high Si, while volcaniclastic turbidites sourced from Madeira and the Canary Islands were Fe-rich. One turbidite, linked to a large landslide on Tenerife, could be identified by its relatively high K content.

XRF core scanning has been used to orbitally-tune high-resolution ODP core log records. This has been particularly useful in studies of transient global warmings including the Paleocene–Eocene Thermal Maximum (PETM). For example, Zachos et al. (2010) orbitally-tuned the lower Eocene to upper Paleocene sequence (including the PETM) at ODP Site 1262 (Walvis Ridge, SE Atlantic) using high-resolution core log physical property and XRF core scanner records, resulting in the most stratigraphically complete upper Paleocene to lower Eocene sequence recovered to date. Other examples include Westerhold et al. (2009) who used high-resolution trace metal core scanner records to determine relative timing between PETM onset and two prominent tephra layers at ODP Site 550 (Goban Spur, NE Atlantic); and Sluijs et al. (2011) who used XRF core scanning and other techniques to reconstruct paleoenvironmental conditions across the PETM at ODP Site 1172 (East Tasman Plateau, off S Australia).

Strong cyclical element signals (e.g. Fe, K, Ti, Al, Si) compatible with Milankovitch-type orbital forcing are noted in several sequences including Middle Eocene (~46 Ma) sediments from Lomonosov Ridge, Arctic Ocean (Sangiorgi et al. 2008); Upper Miocene sediments (6.5–10.2 Ma) from ODP Sites 1085 and 1087 (SW African continental margin, SE Atlantic) (Westerhold et al. 2005) and from Quaternary Ca records in N Atlantic sediments (see Richter et al. 2006).

## *Environmental Impact Studies*

XRF scanners have proved useful in assessing extent and magnitude of anthropogenic pollution, for example in the emerging field of environmental forensics (see Croudace et al., this volume). However, a novel application has been in deep marine environmental impact studies. Cronan et al. (2010) used a XRF core scanner to assess chemical variability and hence substrate redox conditions along a core transect

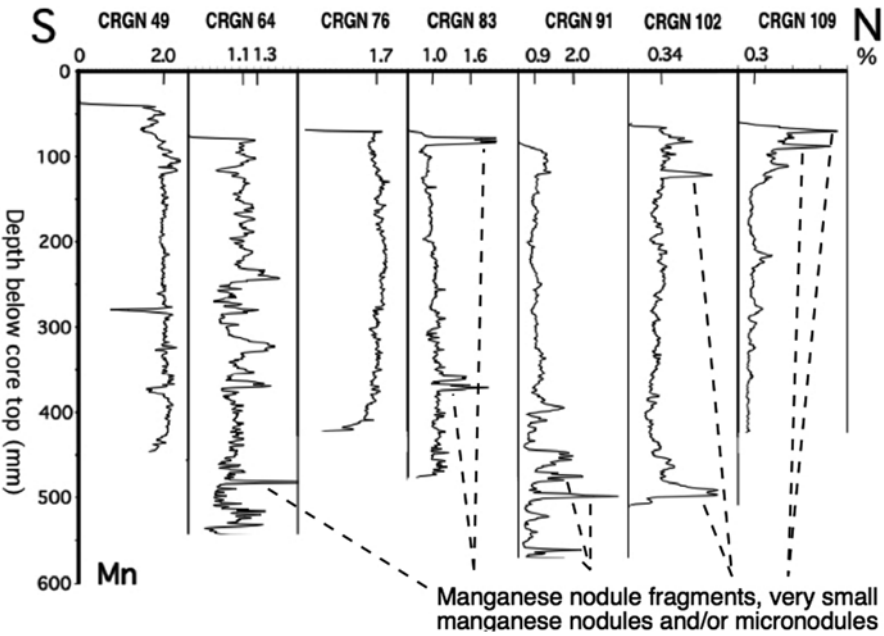


**Fig. 2.9** Core scanner Mn profiles through box cores from a N-S transect in the Penrhyn Basin, S Pacific Ocean. Mn peaks are not diagenetic features, but small Mn nodules or fragments and/or buried micronodules. Apparent lack of an oxidation/reduction front resulting from the oxidation of $Mn^{2+}$ to $Mn^{4+}$ in interstitial waters and its precipitation as $MnO_2$ shows there has been no sub-oxic diagenesis in these cores, suggesting Mn nodule mining will only resuspend oxic pelagic clay. (Adapted from Cronan et al. 2010)

in the Penrhyn Basin (Central Pacific Ocean). This aimed to determine potential environmental impacts of Mn nodule mining should this take place. In the Mn nodule rich area, the substrate is oxidised throughout down to approximately 50 cm below the seafloor, the depth likely to be disturbed by mining (Fig. 2.9). In contrast, parts of the Peru Basin (Eastern Pacific Ocean) have suboxic conditions below ~10 cm depth below seafloor. Hence, Mn nodule extraction is likely to resuspend oxic pelagic clay in the Penrhyn Basin, whereas sub-oxic sediments would be disturbed during mining in the Peru Basin.

## Methods of Data Analysis

XRF core scanners cannot deliver data of the same quantitative quality as WD-XRF or ICP-OES analysis, due to the small excitation volume used, the air path, and effects of mineralogy, texture, porosity and water content. The primary advantage of scanners is analytical rapidity and production of high-resolution continuous records. However a careful approach to data analysis is needed to ensure accurate data assessment. In many cases core scanner data correlates well with quantitative data and has the advantage that high-resolution compositional features can be dentified.

## *Factors Affecting Data Quality*

### Core Type

Modern core scanners can accommodate a variety of core diameters and lengths, including u-channels. However, caution is needed in interpreting records from giant piston cores due to stretching commonly seen in upper parts and compression in the lower part (Széréméta et al. 2004). Data from upper parts of cores may be affected by higher water contents (see MacLachlan et al., this volume), although Tjallingii et al. (2007) suggest most elements ($Z > Si$) are relatively unaffected by changing physical properties such as water content. As core scanner analysis is carried out on bulk sediment and not on carbonate-free fractions, element variations may be exaggerated due to dilution effects, a key factor in analysis.

Changes in XRF profiles may result from artificial factors unrelated to the sediment, such as section shifts, calibration errors, and water content differences from one section to another (Solignac et al. 2011).

### Sample Preparation

Although XRF scanning is non-destructive, care is needed to prevent core drying during analysis to avoid shrinkage and cracking. In contrast to the Eagle II BKA system (Haschke 2006), which cools the sample chamber to prevent drying, the ITRAX and AVAATECH scanners need application of thin high-purity polypropylene film (typically 1.5–6 μm-thick) over the sediment surface prior to analysis. Cohesive and adhesive properties of interstitial water may cause a thin water layer to form under the film. This artificially increases water content in the sample volume analyzed and will have a particularly strong absorption effect for lighter elements reducing element intensities. Attenuation is mainly significant only for Al and Si. Pooling of water directly under the film may also result in higher Cl values (Tjallingii et al. 2007). XRF intensities may also be affected by absorption in the air gap between the sample surface and the detector (Croudace et al. 2006). The ITRAX mitigates this by having a vacuum-pumped nozzle attached to the front of the detector, although a short air gap remains between the nozzle and sample surface. The optical system of the AVAATECH core scanner is He-flushed and makes contact with the sediment during measurement to enhance light element detection.

### Effects of Sample Heterogeneities

Hardware settings, sample geometry and small-scale sediment heterogeneities caused by variable porosity, water content, grain-size changes and matrix effects may theoretically, but not necessarily significantly, affect data quality (Röhl and Abrams 2000; Tjallingii et al. 2007; Weltje and Tjallingii 2008). Absorption/enhancement effects may occur when part of the emitted fluorescence of Fe and Ti is absorbed or scattered by increasing Ca content, and part of the fluorescence emitted by Ca may additionally excite K. Increasing Ca intensities may lead to absorption

effects that influence detection of Fe and Ti (Böning et al. 2007). Sandy sediments typically have greater surface roughness and mineral inhomogeneities resulting in enhanced radiation scatter (Jansen et al. 1998). Additionally, XRF core scanner data may be dependant on changes in density although this has been little quantified (Tjallingii et al. 2007). Source and detector instability, count statistics and the algorithms needed to convert X-ray emission spectra into relative element concentrations may also add data uncertainties (Funk et al. 2004b).

Water content cannot be measured directly by XRF core scanners, but is known to influence net intensities of low atomic weight elements such as Al and Si. Ge et al. (2005), Kido et al. (2006) and Tjallingii et al. (2007) show that correction of element intensities for water content improve prediction of element concentrations.

Tjallingii et al. (2007) compare XRF scanner measurements from a core off Cape Blanc, NW Africa, with dry powder samples from the same core and found that analysis from the wet core surface resulted in strongly reduced intensities for Al and Si. This related to the water content of the sample volume analysed. Cl intensity was used as a proxy for seawater to establish a function for Al and Si that corrected for radiation absorption by the water content. Heavier elements K, Ca, Ti and Fe were much less affected by physical property variations within the core.

### Response Depth

Secondary X-rays generated by excitation by the primary beam will lose intensity through scattering and/or photoelectic absorption as they pass through sediment and air to the detector. The degree of intensity loss depends on energy of the X-ray photons and composition of the sample matrix, according to the Beer-Lambert Law, which relates transmitted intensity to a function of the original intensity and energy, controlled by mass absorption coefficient, sample matrix density and path length. The mass absorption coefficient (μ) will be specific for a given X-ray wavelength for a defined sample matrix.

$$I_x = I_0 \exp^{-\mu\rho x}$$ (Jenkins 1988)

where

$I_x$ transmitted intensity
$I_0$ original intensity
$\mu$ mass absorption coefficient ($cm^2\ g^{-1}$)
$\rho$ sample matrix density ($g/cm^3$)
$x$ path length (cm)

However, this formula relates to analysis of homogenous samples with vacuum between sample and measuring device. The addition of a water and film layer over the surface of the sample in core scanning, and measurement in air, will particularly enhance light element attenuation, although effects on heavier elements may not be significant.

Response or critical depth in XRF core scanning is defined as the depth below the core surface at which 99 % of the X-ray photons emergent in the direction of the

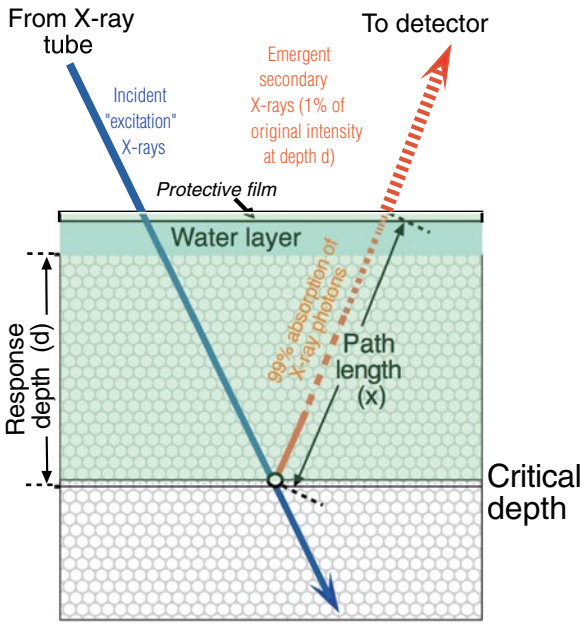


**Fig. 2.10** Definition of response or critical depth (*d*)—defined as the depth below the cut core surface from which emergent X-rays are attenuated to 1 % of their original intensity (at depth *d*), undergoing 99 % absorption over their path length *x* (modified after Seaman 2000). Protective XRF film placed over the core surface to prevent dessication during analysis typically leads to a thin water layer forming between the film and sediment through capillary action. This attenuates emergent fluorescent X-rays further with proportionately greater effect on lighter elements with relatively small response depths than for heavier elements with greater response depths. The green shaded area above the critical depth shows the volume from which the signal comes from

detector are absorbed along their path length (Fig. 2.10). Response depth will also depend on emergent beam angles and on instrument analysis geometry.

The incident X-ray beam penetrates the sediment, exciting elements to emit characteristic line energies that are recorded by the detector. Moseley's law dictates that elements with higher atomic numbers ('heavier') will emit X-rays with relatively high fluorescent energy that are less susceptible to absorption and scatter along their path lengths to the detector. Hence emergent fluorescent radiation intensity and response depth is closely linked to atomic number, with progressively deeper response depths for heavier elements. For example, typical response depths for Al ($Z=13$) has been calculated at ~8 µm, for Ca ($Z=20$) ~35 µm, and for Fe ($Z=26$), ~180 µm (Tjallingii 2006; Potts 1987). How sediment absorbs radiation along its path length depends on its composition and physical properties (Jenkins and De Vries 1970; Potts 1987) and is quantified by the mass attenuation coefficient. This value is calculated as the sum of the single contributions of all elements proportional to their elemental mass fraction (Potts 1987).

### *Plotting Core Scanner Data—the Importance of Normalisation and Log-Ratios*

Plotting ratios, rather than element integrals, to measure element variation is essential to avoid closed-sum effects (Rollinson 1993; Weijden 2002). For example, dilution by $CaCO_3$ may mask terrestrial element variability, hence, terrigenous elements (e.g. Fe, Ti and K) should be normalized to Ca, to account for temporal changes in $CaCO_3$ production. Closed-sum effects may be significant where elements beyond detection limits are significant sediment components. Organic matter and peat are probably the most common instances of this kind, but more typically affect lake cores.

Weltje and Tjallingii (2008) discuss normalisation to negate closed-sum effects and note ratios are flawed by asymmetry, i.e. conclusions based on ratio X/Y cannot directly translate into similar statements about Y/X. As there is no formal rule on which element is numerator or denominator, statistical analysis of ratios thus depends on chance decisions. They conclude that rigorous statistical modelling of compositional data requires compositions be expressed as logarithms of ratios of abundances, called log-ratios (Aitchison 1982, 1986). In contrast to ratios, log-ratios are mostly normally distributed and subject to multivariate statistics, thus more suited for solving core scanner calibration issues. Weltje and Tjallingii (2008) present a calibration equation for XRF core scanners based on intensity and concentration log-ratios. Compositional data analysis considers only relative quantities in the form of log-ratios of proportions, counts, and intensities. They recommend that raw core scanner data are reported as log-ratios of element intensities as these provide the most robust record of relative chemical changes and lessen interpretation risks.

Weltje and Tjallingii (2008) propose dropping reporting of "raw" intensities or peak integrals as XRF core scanner output as these lack a unique relation to sediment composition and are affected by statistical uncertainty (like normal ratios due to their asymmetry). Modelling the log-ratio calibration equation on a core from off Cape Blanc, NW Africa, derived by core-scanning wet core and dry powder sediment, calibrated by quantitative XRF analysis of discrete dry powder samples, showed excellent agreement between predicted and measured log-ratio concentrations. This suggests log-ratios of intensities relate to log-ratios of concentrations by a linear transformation. Plotting raw core scanner data as log-ratio intensities thus provides a more accurate picture of down-core geochemical variation and with calibration allows core scanning to develop into a more rigorous quantitative technology (see Weltje et al., this volume).

## The Geochemical Proxies

The geochemical composition of sediments depends on many factors, such as type and weathering of source rocks, transport, depositional conditions and diagenesis (Weltje and von Eynatten 2004). Statistical analyses of geochemical data help in identifying different sources of detrital material (Eynatten et al. 2003). Geochemi-

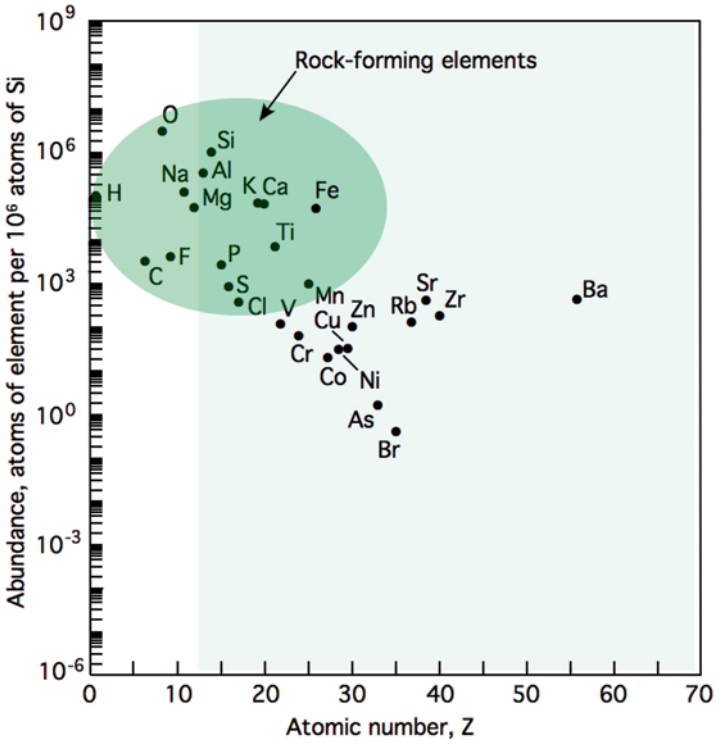


**Fig. 2.11** Abundance of chemical elements in the Earth's upper continental crust as a function of atomic number shown normalised to $10^6$ atoms of Si. Only elements likely to be seen in unpolluted marine sediments are shown. Elements detectable by current core scanners delineated within pale blue block ($Z > 12$). Note that a number of rock-forming elements (Mg, Na, F, C, O and H) fall outside the range of current core scanner detection because of significant X-ray absorption. (Data courtesy of the U.S. Geological Survey)

cal proxies have wide application and continuous and accurate measurements are a prerequisite for obtaining meaningful paleoclimate data.

Within typical core scanner measurement range (Al-U) only certain elements are commonly encountered in unpolluted marine sediments. These are in order of increasing atomic number—Al, Si, P, S, Cl (reflecting seawater content), K, Ca, Ti, V, Cr, Mn, Fe, Ni, Cu, Zn, As (if diagenetically-enriched), Br, Rb, Sr, Zr and Ba—reflecting elements commonly found in crustal rocks and sediments (Fig. 2.11).

Major elements appearing in significant amounts are K, Ca and Fe. Broadly, major elements can be considered to represent component inputs to the sediment. Fe, Ti, Si, K and Al occur mainly in terrigenous silicates and oxides, so form the detrital load, typically land-derived through erosion of continental rocks and indicative of sediment transport from land to the deep-sea (Fig. 2.12). Si and Ca may have a marine biogenic origin, often volumetrically substantial, while Fe and Mn may show diagenetic alteration. Potentially Al may be significantly affected by matrix effects, such as water content, resulting in statistically insignificant counts, although this may be mitigated

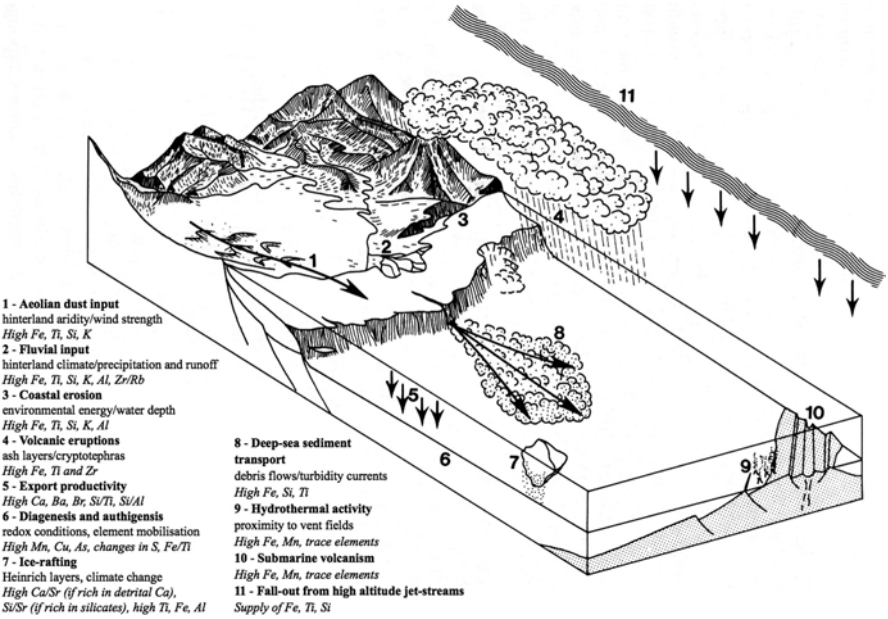


**Fig. 2.12** Element pathways to and within the marine environment, with environmental indicators. Terrigenous elements (Fe, Ti, Si, K and Al) are typically land-derived from erosion of continental rocks, and indicative of sediment transport from land to the deep-sea. Si and Ca may be supplied by surface water productivity and volumetrically substantial. Volcanic eruptions, ice rafting, hydrothermal activity and submarine volcanism are also important element sources. Diagenesis and authigenesis within sediments are important processes for element recycling. (Modified from Rothwell 1989)

by using a Cr tube that provides a significant improvement in excitation efficiency for lighter elements. Ti may be used to characteristise the detrital component. Fe is dissolved easily and can be integrated into authigenic iron sulfides or phosphates, hence Ti, which is redox-insensitive, may be a better indicator of detrital load.

Minor elements include various d-block transition metals. Accumulation of transition metals may reflect productivity at time of burial (Finney et al. 1988; Shaw et al. 1990). The relationship between productivity and transport of trace metals supports their use as tracers of detrital metal flux and has been subject of several studies. However, metal accumulation in sediments is not only dependent on detrital metal flux, but also on changes in sediment redox conditions that will affect metal accumulation and cycling (Shaw et al. 1990).

Survey of the literature on XRF core scanning of marine sediments (from 1998 to mid 2011) shows 60 element integrals or ratios have been used for palaeoenvironmental or process studies (Table 2.4). In addition two elements have been ratioed with magnetic susceptibility to recognise authigenic and diagenetic processes. Some element associations/trends are regarded as important environmental indicators (Table 2.5). Table 2.6 summarises the origin, application and limitations of these proxies and provides a guide for ITRAX users for element proxy selection and potential.

**Table 2.4** Elements and element ratios used as process and environmental proxies reported in the literature from 1998 to 2011

| Element or ratio | Interpretation/use/indicator | References |
|---|---|---|
| Ca | Carbonate stratigraphy, prediction of $\delta^{18}O$ record, carbonate content | Arz et al. (2001a, b); Bahr et al. (2005);Bozzano et al. (2002); Brendryen et al. (2010); Coolen et al. (2009); Dorschel et al. (2007); Foubert and Henriet (2009); Funk et al. (2004b); Gebhardt et al. (2008);Henrich et al. (2010); Helmke et al. (2005); Hepp et al. (2006); Hibbert et al. (2010); Hofmann et al. (2005); Jaccard et al. (2009); Jansen et al. (1998); Jorry et al. (2011); Kleiven et al. (2007); Krastel et al. (2006); Kwiecien et al. (2009); López-Martínez et al. (2006); MacLeod et al. (2001); Pälike et al. (2001); Peterson et al. (2000); Prins et al. (2000, 2001); Richter et al. (2001); Richter et al. (2006); Risebrobakken et al. (2006); Röhl and Abrams (2000); Sluijs et al. (2011); West et al. (2004) |
| | Aragonite preservation/bottom-water corrosiveness/alkalinity/thermohaline circulation changes/productivity | Bourget et al. (2011); Cheshire et al. (2005); Itambi et al. (2009, 2010); Kim et al. (2010); Møller et al. (2006); Rebolledo et al. (2008); Ren et al. (2009); Rooij van et al. (2007); Solignac et al. (2011); Soulet et al. (2011) |
| | Core correlation | Bahr et al. (2008); Kwiecien et al. (2008); Soulet et al. (2011) |
| | Marine transgression | Wolters et al. (2010) |
| Ca/Fe | Carbonate stratigraphy, timescale development, core correlation | Dorschel et al. (2005); Marsh et al. (2007); Pälike et al. (2001); Peck et al. (2007); Rothwell et al. (2006) |
| | Terrigenous turbidite mud discrimination, carbonate:detrital clay ratio | Hanebuth and Lantzsch (2008); Itambi et al. (2009); Rooij van et al. (2011); Rothwell et al. (2006) |
| | Textural character/grading in turbidites, sediment fabric character, productivity | Rothwell et al. (2006); Vare et al. (2009) |
| | Variation in terrigenous sediment delivery | Nizou et al. (2010) |
| Ca/Ca+Fe | Core correlation | Eisele et al. (2008) |
| Ca/Ti | Calcium carbonate content | Piva et al. (2008) |
| | Relative changes in biogenic verses lithogenic sedimentation | Ingram et al. (2010) |

**Table 2.4** (continued)

| Element or ratio | Interpretation/use/indicator | References |
|---|---|---|
| Ca/Al | Calcium carbonate stratigraphy/calcium carbonate preservation | Jaccard et al. (2005, 2010) |
| | Changes in biogenic/terrigenous contributions | Blanchet et al. (2009) |
| Ca/K | Biogenic carbonate/illite variation | Hebbeln et al. (2006) |
| Ca/Sr | High detrital carbonate, ice-rafted layers (Heinrich Events) | Hodell et al. (2008) |
| Sr | Pteropod abundance | Arz et al. (2001b) |
| | Distinguishing between foraminiferal calcite and coralline aragonite | Foubert and Henriet (2009); Richter et al. (2006) |
| | Marker of strictly biogenic origin | Zaragosi et al. (2006) |
| Sr/Ca | Presence of high-Sr aragonite (requires shallow-water source) | Grove et al. (2010); Rothwell et al. (2006); Thomson et al. (2006) |
| Fe | Often correlates well with magnetic susceptibility | Jansen et al. (1998); Kuhlmann et al. (2004a); Westerhold et al. (2008) |
| | Variations in terrigenous sediment delivery | Arz et al. (1998, 1999, 2001b, 2003); Carlson et al. (2008); Foubert and Henriet (2009); Gil et al. (2006); Grützner et al. (2003, 2005); Harff et al. (2011); Henrich et al. (2010); Hepp et al. (2006); Itambi et al. (2010); Jahn et al. (2005); Kaiser et al. (2007); Lamy et al. (2004); MacLeod et al. (2001); McGregor et al. (2009); Møller et al. (2006); Mohtadi et al. (2007); Peterson et al. (2000); Rebolledo et al. (2008); Richter et al. (2001); Rincón-Martínez et al. (2010); Röhl et al. (2004, 2007); Vidal et al. (2002); Westerhold et al. (2005, 2007) |
| | Aeolian dust input/hinterland aridity/variation in wind strength | Andres et al. (2003); Arz et al. (2001b); Bozzano et al. (2002); Hanebuth and Henrich (2009); Hanebuth and Lantzsch (2008); Helmke et al. (2008); Henrich et al. (2010); Jahn et al. (2003); Rohling et al. (2008) |
| | Changes in carbonate productivity, increased input from terrestrial sources, carbonate dissolution | Hofmann et al. (2005); Norris and Röhl (1999); Pälike et al. (2001); Röhl and Abrams (2000); Westerhold et al. (2008); Zachos et al. (2010) |
| | Carbonate dissolution caused by poor deep-water ventilation | Holbourn et al. (2005, 2007); Westerhold and Röhl (2009) |
| | Rainfall and run-off proxy | Haug et al. (2001); Kissel et al. (2010); Lamy et al. (2001); Revel et al. (2010) |

**Table 2.4** (continued)

| Element or ratio | Interpretation/use/indicator | References |
|---|---|---|
| | Climate—palaeoceanographic cycles | Röhl et al. (2001) |
| | Identification of pyrite layers | Seeberg-Elverfeldt et al. (2005) |
| | Identification of palaeo-oxidation fronts | Richter et al. (2006) |
| | Identification of hard grounds | Richter et al. (2006) |
| | Volcanic debris and tephra | Peck et al. (2007) |
| | Ice-rafted debris | Peck et al. (2007) |
| | Sediment density | Agnihotri et al. (2008) |
| | Turbidite provenance and correlation | Frenz et al. (2009) |
| | Reducing conditions on seafloor | Sluijs et al. (2009) |
| Fe/Ca | Variations in terrigenous sediment delivery, hinterland climate, detrital:carbonate ratio | Adgebie et al. (2003); Arz et al. (1998, 1999); Dickson et al. (2010); Hebbeln and Cortes (2001); Rogerson et al. (2006a, b) |
| | Aeolian dust input | Hanebuth and Henrich (2009) |
| | Changes in hinterland land use | McGregor et al. (2009) |
| Fe/Si | Terrigenous input to Antarctic sediments (Si = diatom frustules) | Konfirst et al. (2011) |
| Fe/Al | Anoxic bottom waters | Spofforth et al. (2008) |
| Fe/K | Basaltic material in IRD | Kuijpers et al. (2003) |
| | Changes in terrigenous mineralogy | Blanchet et al. (2009) |
| | Hinterland humidity and rainfall, aeolian dust provenance, enhanced fluvial transport | Zarriess and Mackensen (2010); Zarriess et al. (2011) |
| Fe/$\kappa^{a}$ | Intensity of magnetite dissolution, identification of diagenetically-affected layers, sub-oxic magnetite diagenesis, reductive diagenesis | Funk et al. (2004a, b); Hepp et al. (2009); Hofmann et al. (2005); Hofmann and Fabian (2007); Itambi et al. (2010); Land et al. (2011) |

**Table 2.4** (continued)

| Element or ratio | Interpretation/use/indicator | References |
|---|---|---|
| Fe/Ti | Detection of iron relocation | Blanchet et al. (2009); Funk et al. (2004a, b); Hepp et al. (2009); Kuhlmann et al. (2004a); Land et al. (2011); Richter et al. (2006) |
| | Pyrite authigenesis | Thomson et al. (2006) |
| | Changes in terrigenous mineralogy | Blanchet et al. (2009) |
| | Fluvial v. aeolian terrigenous input | Itambi et al. (2010) |
| | Sediment provenance | Monien et al. (2010) |
| Fe/Zr | Hinterland precipitation | Hanebuth and Lantzsch (2008) |
| Fe/Rb | Mobilisation of Fe during redox-related diagenesis | Rothwell et al. (2006) |
| Al/Si | Clay content | Hoang et al. (2010) |
| Al/Ca | Terrigenous input variability | Nizou et al. (2011) |
| Si | Terrigenous or productivity indicator | Rothwell et al. (2006) |
| | Variation in terrigenous sediment delivery | Blanchet et al. (2007); Kleiven et al. (2007) |
| | Turbidite provenance | Frenz et al. (2009) |
| Si/Ti | Proxy for biogenic silica content | Agnihotri et al. (2008); Marsh et al. (2007) |
| Si/Ca | Aeolian dust input | Hanebuth and Henrich (2009) |
| Si/Sr | Ice-rafted layers | Hodell et al. (2008) |
| Si/Al | Wind strength | Itambi et al. (2009) |
| | Changes in aluminosilicates | Tisserand et al. (2009) |
| | Biogenic production/export | Dickson et al. (2010) |

**Table 2.4** (continued)

| Element or ratio | Interpretation/use/indicator | References |
|---|---|---|
| Ti | Variations in terrigenous sediment delivery | Adgebie et al. (2003); Arz et al. (1998, 1999, 2001b, 2003); Berg et al. (2010); Blanchet et al. (2007); Carlson et al. (2008); Cheshire et al. (2005); Denis et al. (2006); Harff et al. (2011); Hepp et al. (2006); Itambi et al. (2010); Jaccard et al. (2009); Jansen et al. (1998); MacLeod et al. (2001); Marsh et al. (2007); Rebolledo et al. (2008); Rincón-Martínez et al. (2010); Teodoru et al. (2007) |
| | Rainfall and run-off proxy | Chiessi et al. (2009); Haug et al. (2001, 2003); Kissel et al. (2010); Petersen et al. (2000); Revel et al. (2010) |
| | Aeolian dust input/hinterland aridity | Arz et al. (2001b); Itambi et al. (2009); Rohling et al. (2008); Xu et al. (2008) |
| | Sediment density | Agnihotri et al. (2008) |
| | Tephra layers | Westerhold et al. (2009) |
| | Sediment provenance | Montero-Serrano et al. (2010) |
| | Melting sea ice | Solignac et al. (2011) |
| Ti/Ca | Variations in terrigenous sediment delivery, hinterland climate | Arz et al. (1998, 1999); Bahr et al. (2005, 2008); Berg et al. (2010); Bourget at al. (2008); Henrich et al. (2010); Hoang et al. (2010); Jaeschke et al. (2007); Kwiecien et al. (2009); Tjallingii et al. (2010) |
| | Wind strength, aeolian dust input | Pierau et al. (2010, 2011); Romero et al. (2008) |
| | Ice-rafted material (Heinrich events/melt-water discharges) | Lebreiro et al. (2009); Soulet et al. (2011) |
| Ti/Al | Variation in aeolian input, wind intensity | Jimenez-Espejo et al. (2007a); Jullien et al. (2007); Tisserand et al. (2009); Ziegler et al. (2009) |
| | Increase in particle size, environmental energy changes | Spofforth et al. (2008) |
| | Continental precipitation | Itambi et al. (2009) |

**Table 2.4** (continued)

| Element or ratio | Interpretation/use/indicator | References |
|---|---|---|
| Ti/K | Variations in sediment source or grain-size character, identification of ice-rafted sediment | Brendryen et al. (2010); Prins et al. (2001); Siani et al. (2010); Spofforth et al. (2008) |
| Ti/Fe | Aeolian dust transport and wind strength | Zarriess and Mackensen (2010) |
| | Sediment provenance | Konfirst et al. (2011) |
| Ti/Rb | Increased heavy resistate minerals | Rothwell et al. (2006) |
| Ti/Sr | Terrigenous versus biogenic supply | Zaragosi et al. (2006) |
| κ/Ti | Authigenesis | Land et al. (2011) |
| Zr | Tephra layers | Westerhold et al. (2009) |
| Zr/Ti | Presence of volcanic phases, tephra | Marsh et al. (2007) |
| Zr/Rb | Increased heavy resistate minerals | Rothwell et al. (2006) |
| | River floods | Wang et al. (2011) |
| Zr/Sr | Ice-rafted debris | Hodell et al. (2010) |
| Zr/Fe | Sediment provenance | Konfirst et al. (2011) |
| Mn | Identification of redox transitions | Hofmann et al. (2005); Jansen et al. (1998); Rey et al. (2008); Richter et al. (2006); Wolters et al. (2010) |
| | Variations in water column ventilation and riverine input | Löwemark et al. (2008); O'Regan et al. (2010) |
| Mn/Fe | Identification of redox transitions, sub-oxic diagenesis | Marsh et al. (2007) |
| Mn/Ti | Identification of redox transitions | Funk et al. (2004b); Hepp et al. (2009); Land et al. (2011); Rey et al. (2008); Thomson et al. (2006) |
| Mn/Al | Change in oxygenation levels | Spofforth et al. (2008) |
| | Identification of redox transitions | Jaccard et al. (2009) |
| K | Ash layers | Pälike et al. (2001) |
| | Indicator of terrigenous supply | Harff et al. (2011); Hepp et al. (2006); Holzwarth et al. (2010); Kleiven et al. (2007); Kuhlmann et al. (2004b); Kujau et al. (2010); Kwiecien et al. (2009) |

**Table 2.4** (continued)

| Element or ratio | Interpretation/use/indicator | References |
|---|---|---|
| | Land aridity/humidity | Romero et al. (2008) |
| | Turbidite provenance and correlation | Frenz et al. (2009) |
| | Sediment provenance | Montero-Serrano et al. (2010) |
| K/Ti | Changes in acidic/basaltic terrigenous sources | Hodell et al. (2010); Richter et al. (2006) |
| | Sediment provenance | Diekmann et al. (2008); Kujau et al. (2010); Monien et al. (2010) |
| | Intensity of weathering and erosion | Piva et al. (2008) |
| K/Ca | Aeolian dust input | Hanebuth and Henrich (2009) |
| | Ice-rafted layers (Heinrich events) | Lebreiro et al. (2009) |
| | Variations in terrigenous sediment delivery | McGregor et al. (2009) |
| K/Rb | May be enhanced in turbidite muds | Rothwell et al. (2006) |
| K/Al | Continental run-off/chemical weathering | Clift et al. (2008); Dickson et al. (2010) |
| | Provenance changes | Spofforth et al. (2008) |
| Zn | Source areas, anthropogenic pollution | Hebbeln et al. (2003); Cage and Austin (2010) |
| Ba | Export palaeoproductivity | Gebhardt et al. (2008); Jaccard et al. (2009); Röhl et al. (2007); Ziegler et al. (2009) |
| | Core correlation | Röhl et al. (2007) |
| | Oil-field discharges | Breier et al. (2010) |
| Ba/Ca | Aragonite in corals | Grove et al. (2010) |
| Ba/Al | Productivity | Hillenbrand et al. (2009); Jaccard et al. (2005, 2010) |
| | Correlation with ice core records for age modelling | Galbraith et al. (2008) |
| Ba/Ti | Productivity | Jaccard et al. (2005); Thomson et al. (2006) |
| Cu/Rb | Diagenetic mobilisation of copper | Rothwell et al. (2006) |
| Cu/Ti | Post-depositional oxidation of organic-rich layers | Thomson et al. (2006) |

**Table 2.4** (continued)

| Element or ratio | Interpretation/use/indicator | References |
|---|---|---|
| As | Presence of pyrite | Rothwell et al. (2006); Thomson et al. (2006) |
| S | Identification of redox transitions, precipitation of pyrite | Richter et al. (2006) |
| | Presence of pyrite | Blanchet et al. (2007) |
| | Reducing seafloor conditions/bottom-water anoxia | Harff et al. (2011); Sluijs et al. (2009) |
| S/Cl | Pyrite authigenesis, enrichment in organic matter | Thomson et al. (2006) |
| Rb | Increased clay contribution to sediments | Rothwell et al. (2006) |
| Br | Presence of organic matter, marine organic carbon content, productivity | Caley et al. (2011); McHugh et al. (2008); Ren et al. (2009); Ziegler et al. (2008, 2009) |
| Br/Cl | Presence of organic-rich layers, increased porosity | Rothwell et al. (2006); Thomson et al. (2006) |
| Br/Ti | Productivity | Agnihotri et al. (2008) |

[a] Iron/susceptibility ratio

**Table 2.5** Environmental interpretation using geochemical proxy data

| Environment indicators | Elemental indicators | Supporting indicators | References |
|---|---|---|---|
| Reducing conditions, anoxic or suboxic bottom waters | High Fe/Al, high S, high Fe/S, elevated trace element/Al ratios, high As | High TOC, framboidal pyrite, megascopic chemical laminae, reduction haloes | Harff et al. (2011); Sluijs et al. (2008); Spofforth et al. (2008) |
| Influx of terrigenous material | High Al, Si, Fe, K and Ti, low Ca/Fe, high Fe/Ca, high Ti/Ca | Textural changes, graded beds, increased magnetic susceptibility, low sediment colour reflectance | Arz et al. (2001b, 2003); Bahr et al. (2008); Bozzano et al. (2002); Carlson et al. (2008); Chiessi et al. (2009); Denis et al. (2006); Dickson et al. (2010); Hanebuth and Lantzsch (2008); Harff et al. (2011); Itambi et al. (2009, 2010); Kissel et al. (2010); Møller et al. (2006); Rebolledo et al. (2008); Rogerson et al. (2006a, b); Romero et al. (2008) |
| Aeolian dust input, hinterland aridity, wind strength | High Fe, high Ti, high Ti/Al, high Ca/Ti, high Si/Al, low Al/Ca, low Fe/K, high Ti/Fe, high Ti/Ca, high K, high Fe/Ca, high Si/Ca, high K/Ca | Coarser sediment particles, increased magnetic susceptibility, iron-coated *wüstenquartz* (offshore desert areas) | Andres et al. (2003); Arz et al. (2001b, 2003); Bozzano et al. (2002); Hanebuth and Henrich (2009); Hanebuth and Lantzsch (2008); Helmke et al. (2008); Itambi et al. (2009, 2010); Jahn et al. (2003); Jullien et al. (2007); Nizou et al. (2010, 2011); Pierau et al. (2010, 2011); Revel et al. (2010); Romero et al. (2008); Tisserand et al. (2009); Xu et al. (2008); Jiménez-Espejo et al. (2007a) |
| Humid hinterland | Low Fe, high Al/Ca, high Ti/Ca | Coarser sediment particles, increased magnetic susceptibility, higher amounts of land-derived organic matter evidenced by C/N ratios, freshwater and benthic diatoms, presence of continental-derived organisms, e.g. crysophycean cysts and phytoliths | Helmke et al. (2008); Jaeschke et al. (2007); Nizou et al. (2011) |
| Hinterland precipitation and river runoff | Fe/Al, high Fe, high Ti, Ti/Al, high Zr/Rb, K, high Fe/K, high K | | Haug et al. (2001); Holzwarth et al. (2010); Itambi et al. (2009); Jahn et al. (2005); Kissel et al. (2010); Kuhlmann et al. (2004b); Lamy et al. (2001); Petersen et al. (2000); Wang et al. (2011); Zarriess et al. (2011) |

**Table 2.5** (continued)

| Environment indicators | Elemental indicators | Supporting indicators | References |
|---|---|---|---|
| Ice-rafted debris | High Ca/Sr (if rich in detrital carbonate), high Si/Sr (if rich in silicates), high Ti, high Ti/Ca, high K/Ca, high Fe/Ca, high Al | Coarse angular poorly sorted siliciclastic or lithic grains with glacial origin microfeatures (e.g. linear step-like fractures, striations), increased magnetic susceptibility, megascopic dropstones with or without deformation structures, increases in bulk density | Hodell et al. (2008); Itambi et al. (2009); Jaeschke et al. (2007); Lebreiro et al. (2009) |
| Glacial-interglacial transitions | Abrupt anti-correlated changes in Ca, Fe and Ti | Changes in grey-scale reflectance, sediment lightness ($l^*$ values), changes from cold-water to warm-water foraminifer species, changes in lithology, changes in carbonate dissolution | Hepp et al. (2006) |
| Volcanic ash layers | High Ti and Zr (ash layers with low Ti and high Zr composition point to alkaline magma type) | Magnetic susceptibility peaks, mega- and microscopic volcanic glass shards, coarser grain-size, presence of accessory minerals | Westerhold et al. (2009) |
| Biogenic silica | High Si/Ti, high Si/Al | Siliceous microfossils (diatoms, radiolaria, silicoflagellates, and spicules), increased porosity and lower grain density and compressional velocity | Agnihotri et al. (2008); Dickson et al. (2010); Marsh et al. (2007) |
| Organic productivity | High Br/Ti, high Br, high Ba, high Ba/Al, high Ca, high Ba/Ti | Higher water contents and plasticity, lower wet bulk densities, higher undisturbed shear strength, redox-sensitive features such as oxidation fronts and haloes, presence of authigenic gypsum, dark colour, decreased lightness ($l^*$ values), rust-brown streaks or laminae | Agnihotri et al. (2008); Caley et al. (2011); Hillenbrand et al. (2009); Itambi et al. (2010); Ren et al. (2009); Thomson et al. (2006); Ziegler et al. (2009) |
| High salinity | High Sr | Aragonitic and evaporitic crusts, laminated or partially laminated sediments | Arz et al. (2001b, 2003) |

**Table 2.6** Origin, applications and limitations of elemental proxies found in marine sediments

***Calcium (Ca)***

*Origin:* May be biogenic or detrital, although biogenic sources are volumetrically of far greater importance. Ca as $CaCO_3$ is used as test material for ubiquitous groups of marine plankton, principally foraminifers and coccolithophorids

Integral Ca is a recognised proxy for oceanic productivity and Ca variation typically reflects $CaCO_3$ stratigraphy in pelagic cores. Detrital sources may be important in near-shore and estuarine waters, e.g. Rebolledo et al. (2008) found about half the Ca content in some Chilean Fjord sediment related to carbonates with rest derived from weathering of plagioclases in fjord watershed

*Use:* Ca typically anti-correlates with Fe and other terrigenous elements (e.g. MacLeod et al. 2001) as climatic modulation of productivity typically leads to low Ca during glacials and higher values during interglacials (e.g. Arz et al. 2001b, 2003; Gebhardt et al. 2008; Rooij van et al. 2007). Thus Ca is commonly an effective climatic indicator and efficient for establishing stratigraphic frameworks (e.g. Jorry et al. 2011; Kwiecien et al. 2008). Lower Ca may correlate with carbonate dissolution and/or dilution by terrigenous material. Ca dissolution can provide a proxy for bottom-water corrosiveness (especially if supported by foraminifer dissolution) and hence alkalinity (e.g. Gebhardt et al. 2008) and relate to oceanic water mass changes (e.g. Arz et al. 2001a). Detrital origin of Ca may be inferred by correlation with Fe (e.g. Röhl et al. 2004) to see if Ca mirrors terrigenous supply. Biogenic and detrital carbonate may be distinguished by Ca/Sr, as Sr fixed by calcifying organisms at same time as Ca and so can be used as marker of biogenic origin. Co-variation of Ca and Sr suggests Ca is mainly sourced from biogenic $CaCO_3$ (e.g. Carlson et al. 2008)

*Limitations:* Ca variation, particularly in marginal environments, may reflect dilution by terrigenous material rather than productivity changes

Revel et al. (2010) found low Ca during pluvial periods in a core from Nile margin, interpreted as mainly due to terrigenous dilution. A carbonate-rich facies, occurring systematically during glacial/arid periods was characterized by drastic decrease in accumulation rate, interpreted as reflecting significant reduction in Nile flood intensity

*Quantifying Ca counts:* Ca counts can be converted to $CaCO_3$ concentrations by analysis of discrete samples and regression analysis

López-Martínez et al. (2006) converted Ca intensities to $CaCO_3$ concentrations (wt.%) by applying regression equation derived from linear correlation ($r = 0.94$) of scanner measurements and 100 $CaCO_3$ LECO analyses on discrete samples in Late Pleistocene cores from ODP Site 1060 (Blake Outer Ridge, NE Atlantic). $CaCO_3$ content related to productivity. Changes in $CaCO_3$ at ODP Site 1060 showed Dansgaard/Oeschger pattern with higher values during Greenland interstadials

*Applications and literature*

- Calcium carbonate stratigraphy

  Coolen et al. (2009); Dorschel et al. (2007); Foubert and Henriet (2009); Henrich et al. (2010); Hibbert et al. (2010); Kwiecien et al. (2008); Risebrobakken et al. (2006); Rebolledo et al. (2008); Ziegler et al. (2009)

- Marine productivity

  Cheshire et al. (2005); Ren et al. (2009); Solignac et al. (2011)

- Climate studies

  Arz et al. (2001b, 2003); Gebhardt et al. (2008); Jorry et al. (2011); Kim et al. (2010); Rooij van et al. (2007); Rebolledo et al. (2008)

- Carbonate dissolution and dilution

**Table 2.6** (continued)

- Bottom-water corrosiveness/alkalinity
- Oceanic water mass changes

  Arz et al. (2001a); Gebhardt et al. (2008); Röhl et al. (2000)
- Detrital supply of Ca

  Abrantes et al. (2008); Carlson et al. (2008); Röhl et al. (2004)
- Pteropod preservation and hinterland climate

  Bourget et al. (2011); Klöcker and Henrich (2006); Pourmand et al. (2004); Prins et al. (2000); Sirocko et al. (1996)

***Ca/Fe***

*Use:* Ca/Fe reflects *biogenic carbonate*:*detrital clay* ratio and is widely used to determine carbonate stratigraphy and productivity in pelagic cores.Also used to distinguish pelagic and re-deposited muds and assess textural character in turbidite-containing sequences (Rothwell et al. 2006). These two elements reflect marine production and terrigenous input respectively. Primary use of Ca/Fe is as proxy for terrigenous sediment delivery (Fe) compared to marine-origin Ca (e.g. Nizou et al. 2010) although care is needed as Fe is redox-sensitive. Co-variance of Fe and other terrigenous indicators (e.g. Ti, K) will show relative importance of diagenetic effects. Correlation of Ca/Fe excursions with κ anomalies, superimposed on long-term climate signals, may be potentially useful provenance tool (e.g. Peck et al. 2007)

*Applications and literature*

- Variation in terrigenous sediment delivery

  McGregor et al. (2009); Nizou et al. (2010); Rogerson et al. (2006b)
- Identification of carbonate-rich layers
- Sediment provenance
- Detection of ice-rafted-debris and tephra

  Peck et al. (2007); Scourse and Furze (2001)
- Core correlation

  Hanebuth and Lantzsch (2008); Pälike et al. (2001)

***Ca/Ca+Fe***

*Use:* Ca/Ca+Fe used by Eisele et al. (2008) to characterise three cores from cold-water coral-covered mound (Galway mound), Porcupine Seabight, SW of Ireland. Ca and Fe amounted to >90% of all XRF counts, so Ca/Ca+Fe useful benchmark for Ca and Fe. Ca/Ca+Fe showed very similar patterns in all three cores allowing correlation and lithostratigraphic subdivision

*Applications and literature*

- Core characterisation
- Core correlation

  Eisele et al. (2008)

***Ca/Ti***

*Use:* Ca/Ti useful proxy for assessing relative changes in biogenic versus lithogenic sedimentation and recording carbonate content (e.g. Piva et al. 2008). Advantage over Ca/Fe in that Ti is inert

*Applications and literature*

- Variation in terrigenous sediment delivery

  Ingram et al. (2010); Piva et al. (2008)
- Calcium carbonate content

  Piva et al. (2008)

**Table 2.6** (continued)

***Ca/Al***

*Use*: Like Ca/Fe and Ca/Ti, Ca/Al represents the biogenic/detrital ratio so is a potential proxy for measuring changes in terrigenous sediment contribution, providing good Al data can be acquired. Al counts affected by tube type, attenuation in air gap between detector and core surface, water content and presence and thickness of any water layer below protective film covering core. Good Al counts using ITRAX are uncommon when using a Mo tube, but much better with a Cr tube, especially in current generation models. Al detection is good with AVAATECH instrument and may be sufficient for normalisation

*Applications and literature*

- Data normalisation
- Variation in terrigenous sediment delivery

  Blanchet et al. (2009)
- Ocean water mass changes

  Jaccard et al. (2010)

***Ca/K***

*Use:* Ca is proxy for biogenic content and K can be used as proxy for its main mineralogical carrier illite, hence for example, providing potential to map changes in K-rich clay minerals due to varying bottom current strength

*Applications and literature*

- Changes in K-rich minerals (illite)
- Current and water mass changes

  Hebbeln et al. (2006)

***Ca/Sr***

*Use*: Biogenic $CaCO_3$ precipitated by coccoliths and foraminifers has greater Sr than inorganic $CaCO_3$ or dolomite. Hence Ca/Sr may rapidly detect IRD layers rich in detrital carbonate, e.g. some Heinrich layers with larger Ca/Sr ratios when detrital carbonate content high and biogenic $CaCO_3$ is low (Hodell et al. 2008)

*Applications and literature*

- Detection of detrital carbonate

  Hodell et al. (2008)

***Strontium (Sr)***

*Use:* Sr is an alkaline earth metal fixed by calcifying organisms at same time as Ca. Hence Sr is a marker for biogenic origin. As Ca can be supplied from terrigenous sources (e.g. feldspars and clays) co-variation of Ca and Sr suggests Ca mainly sourced from biogenic $CaCO_3$. Sr is preferentially incorporated into aragonite, hence potentially useful in distinguishing foraminiferal calcite and coralline and/or pteropod aragonite, for example, in cold-water carbonate mounds (e.g. Richter et al. 2006). Sr is efficiently excited using Rh and Mo target tubes, so although frequently a trace element, it produces a good response

*Applications and literature*

- Discriminating types of carbonate rocks

  Foubert and Henriet (2009); Richter et al. (2006)
- Pteropod abundance
- Detection of inorganic aragonitic crusts

  Arz et al. (2001b, 2003)

**Table 2.6** (continued)

***Sr/Ca***

*Use:* Sr/Ca has been used as proxy for aragonite, e.g. in onshore massive corals in Madagascar (Grove et al. 2010).Thomson et al. (2006) used Sr/Ca as proxy for aragonite formed due to alkalinity from sulphate reduction within sapropels in E Mediterranean cores. Higher Sr/Ca values often interpreted as reflecting greater pteropod content (e.g. Krinsley and Bieri 1959). Rothwell et al. (2006) and Thomson et al. (2004) report Sr/Ca peaks in Mediterranean sediments as indicating high Sr aragonite requiring shallow-water source, and Rothwell et al. (2006) describe pelagic intervals containing abundant pteropods registering high Sr/Ca. This may be texturally-related artefact considering reports that pteropod shells in E Mediterranean are low-Sr aragonite (Krinsley and Bieri 1959; Kinsman 1969; Rutten et al. 2000)

*Applications and literature*

- Proxy for aragonite

  Grove et al. (2010); Thomson et al. (2006)
- Pteropod abundance

  Krinsley and Bieri (1959); Rothwell et al. (2006)

***Iron (Fe)***

*Origin:* Fe is the most common element (by mass) on Earth, forming much of outer and inner core and fourth most abundant element in the crust, after O, Si and Al. Most Fe in the crust is combined with O as Fe oxide minerals like haematite and magnetite. In marine sediments, Fe commonly mirrors changes in carbonate/clay ratios and its high abundance, relatively high signal relative to other elements, and high signal-to-noise ratio makes it a preferred proxy in environmental and process studies. Generally Fe variations relate to the sediment's terrigenous fraction and/or dilution of $CaCO_3$. Fe commonly correlates with other terrigenous markers like Ti but may be less reliable due to redox sensitivity. High Fe in intervals with very low κ suggests magnetite dissolution. Fe may correlate with a* CIELAB colour values as a* is a measure of sediment redness, largely reflecting concentration of Fe (oxides) bearing minerals (e.g. Westerhold et al. 2007)

*Use:* Fe, like Ti, has been widely used to document variations in terrigenous sediment delivery, informing on continental humidity/aridity and precipitation/river run-off changes; or aeolian dust flux/wind strength, all conditions/processes commonly related to climatic forcing (e.g. Vidal et al. 2002; Grützner et al. 2003 and others). As redox-sensitive, Fe can identify secondary diagenetic features or new mineral formation through authigenesis, such as framboid layers (e.g. Seeberg-Elverfeldt et al. 2005). High Fe and S may indicate reducing conditions (e.g. Sluijs et al. 2009). Fe slightly below average shale level, suggests a generally reducing suboxic environmental setting, particularly if with enhanced S, Mn values significantly below average shale level, and high trace element/Al ratios (Sluijs et al. 2008). Fe and Ti are closely related in terrigenous fractions, but Fe is partly prone to diagenetic remobilisation in pore waters. Ti is inert. Hence, good correlation of Fe to Ti suggests little diagenetic influence. Positive correlation of Fe with κ also suggests diagenetic processes are minimal. A smooth decreasing trend in Fe towards core tops has been attributed to dilution due to increasing water content (Mohtadi et al. 2007). Fe and Ti occur predominately in denser lithogenic fraction so may covary with density. Fe (and Ti) can thus be used as negative indices of surface productivity (e.g. Agnihotri et al. 2008)

*Applications and literature*

- Variation in terrigenous sediment delivery
- Hinterland climate
- Precipitation and runoff
- Aeolian dust flux/wind strength

**Table 2.6** (continued)

Andres et al. (2003); Arz et al. (1998, 1999, 2001b, 2003); Behling et al. (2000); Bozzano et al. (2002); Foubert and Henriet (2009); Gil et al. (2006); Grützner et al. (2003, 2005); Haug et al. (2001); Henrich et al. (2010); Helmke et al. (2008); Jahn et al. (2003, 2005); Kaiser et al. (2007); Lamy et al. (2001, 2004); Mohtadi et al. (2007); Petersen et al. (2000); Revel et al. (2010); Richter et al. (2001); Vidal et al. (2002); Westerhold (2003); Westerhold et al. (2007)

- Changes in carbonate productivity/dissolution
- Current and water mass changes

  Helmke et al. (2005); Holbourn et al. (2007); Norris and Röhl (1999); Röhl et al. (2000, 2001, 2007); Röhl and Abrams (2000); Westerhold and Röhl (2009); Zachos et al. (2001)
- Sediment provenance

  Kaiser et al. (2007); Lamy et al. (2001)
- Establishing stratigraphic frameworks

  Westerhold et al. (2007, 2008)
- Diagenetic studies
- Authigenesis
- Redox conditions

  Rothwell et al. (2006); Seeberg-Elverfeldt et al. (2005); Sluijs et al. (2008, 2009)

***Fe/Ca***

*Use:* Fe and Ca commonly anti-correlate and Fe/Ca quantifies relative proportions of terrigenous fluxes versus marine carbonate, often related to climatic forcing (e.g. Adegbie et al. 2003; Dickson et al. 2010; Rogerson et al. 2006a). Bond et al. (1993) and Bond and Lotti (1995) note close similarity in Fe/Ca in N Atlantic sediments to GRIP and GISP2 ice core records (Grootes et al. 1993; Johnsen et al. 1992) implying direct climatic correspondence of N hemisphere low and high latitudes

*Applications and literature*

- Variation in terrigenous sediment delivery
- Climatic variability
- Precipitation and runoff

  Adegbie et al. (2003); Dickson et al. (2010); Rogerson et al. (2006a)

***Fe/Si***

*Use:* A rarely used ratio, but used as proxy for terrigenous influx in Neogene sediments from Ross Sea, Antarctica (Konfirst et al. 2011). Low Fe/Si suggested open marine setting dominated by deposition of diatoms. Transient peaks in Fe/Si correlated with volcanic sands and iron-rich carbonate layers containing authigenic pyrite

*Applications and literature*

- Terrigenous flux to siliceous pelagic sediments

  Konfirst et al. (2011)

***Fe/Al***

*Use***:** Slightly elevated Fe/Al associated with low Si/Al and Ti/Al during PETM at IODP Site M0004 (Lomonosov Ridge) interpreted as possibly indicating more intense weathering (Sluijs et al. 2008). Elevated Fe/Al (with high S, TOC and framboidal pyrite) interpreted as indicating anoxic bottom waters by Spofforth et al. (2008)

*Applications and literature*

- Weathering intensity

**Table 2.6** (continued)

Sluijs et al. (2008)

- Bottom-water anoxia

  Spofforth et al. (2008)

***Fe/K***

*Use:* Fe and K are both terrigenous indicators and Fe/K has been used in provenance and climate studies (e.g. Kuijpers et al. 2003). Fe/K values in atmospheric Saharan dust samples increase towards the equator (Stuut et al. 2005). Hence increasing amounts of dust from deeply weathered terrains (Moreno et al. 2006) cause increased Fe/K values towards tropics, due to its relatively high Fe content compared to more mobile K (Mulitza et al. 2008)

Fluvial sediments in the region contain higher Fe/K values than wind-transported sediments (Gac and Kane 1986; Mulitza et al. 2008; Stuut et al. 2005). As highest water discharge and sedimentary load occurs during rainy seasons (Debenay et al. 1994; Kattan et al. 1987; Lesack et al. 1984) sharp decrease of Fe/K values indicated abrupt onset of arid conditions (Zarriess and Mackensen 2010). Fe/K thus considered indicative of continental rainfall

*Applications and literature*

- Sediment provenance
- Climate variability
- Precipitation and runoff
- Aeolian dust flux/wind strength

  Kuijpers et al. (2003); Zarriess et al. (2011); Zarriess and Mackensen (2010)

***Fe/κ***

*Use:* Fe/magnetic susceptibility (κ) is a sensitive proxy for magnetite diagenesis and Fe reduction (Funk et al. 2004b; Hepp et al. 2009; Hofmann and Fabian 2007; Land et al. 2011). Fe reduction may result in significant magnetic susceptibility signal loss, and zones of enhanced Fe/κ have been shown to correlate with presence of Fe- and Mn oxide/hydroxide coated grains in carbonate mounds (Land et al. 2011). Fe and $\kappa$ have also been used to identify distinct environmentally significant clusters in cores (Itambi et al. 2009)

*Applications and literature*

- Iron diagenesis

  Funk et al. (2004b); Hepp et al. (2009); Hofmann and Fabian (2007); Land et al. (2011)

- Sediment transport

  Itambi et al. (2009)

***Fe/Ti***

*Use:* Fe/Ti is used as a proxy for diagenetic iron enrichment (Blanchet et al. 2009; Funk et al. 2004a; Hepp et al. 2009; Land et al. 2011) and for excess Fe over basaltic lithogenic values, with high values suggesting additional sources of Fe-rich material (Marsh et al. 2007). Log ratios of Fe and Ti over Ca have been used to account for dilution by carbonate and non-linearities between XRF counts and elemental concentrations (Rincón-Martínez et al. 2010)

*Applications and literature*

- Iron diagenesis

  Blanchet et al. (2007); Funk et al. (2004b); Hepp et al. (2009); Land et al. (2011)

- Variation in terrigenous sediment delivery
- Carbonate dilution

  Marsh et al. (2007); Rincón-Martínez et al. (2010)

**Table 2.6** (continued)

***Fe/Zr***

*Use:* Fe/Zr has been used in cores off Mauritania as a proxy for rainfall in the Saharan hinterland (Hanebuth and Lantzsch 2008). Although Zr could not be linked to a specific climatic parameter, a mechanism related to sediment input or distribution was inferred, possibly a transport-and-sorting mechanism separating heavy Zr grains from lighter siliciclastic grains, probably through density-related separation in aeolian and surface water supply. Low Fe/Zr, representing relative enrichment of Zr, occurred at times of aridity, with high values during more humid conditions

*Applications and literature*

- Precipitation and runoff
- Aeolian dust flux/wind strength

Hanebuth and Lantzsch (2008)

***Fe/Rb***

*Use:* Fe/Rb has been used for Fe normalisation in absence of good Al data (Rothwell et al. 2006). Fe/Rb showed grain-size fractionation effects within turbidites and evidence for diagenetic Fe mobilisation within oxidised upper parts of turbidites. Increased Rb within turbidite muds reflected greater clay contribution to sediment

*Applications and literature*

- Textural character
- Iron diagenesis
- Clay content

Rothwell et al. (2006)

***Aluminium (Al)***

*Origin:* Al is the most abundant metal in the Earth's crust and third most abundant element, after O and Si, but too reactive to be found pure, and is instead found as oxides and silicates. Aluminosilicates are a major component of kaolin (one of the most common minerals), other clay minerals and zeolites. Other aluminosilicate minerals include andalusite, kyanite, sillimanite, beryl, garnet, spinel, and turquoise. Weathering of low Fe and $SiO_2$ bedrock in tropical climates results in high-alumina clays

*Use:* Al and Fe have been used as fluvial proxies (Nizou et al. 2011). In this study, Al was preferred for palaeoclimatic analysis due to potential Fe mobility

*Limitations:* Al is routinely used for normalisation of WD-XRF data, but its closeness to core scanner detection limits, rapid attenuation in air and through any sub-film water layer, low response depth, and dependence on tube type may constrain its use in core scanner data normalisation. Al is at the limit of early model ITRAX detection, although detection with current models using a Cr tube is usually good. Al is well detected by AVAATECH instruments with a detection limit of around 2000 ppm in current models

Diatoms actively uptake and accumulate Al, so it cannot be used to normalise Ti in diatomaceous sediments (Bennekom et al. 1989; Moran and Moore 1992)

*Applications and literature*

- Sediment transport
- Hinterland climate

Nizou et al. (2011)

***Al/Si***

*Use:* Al/Si has been used as a proxy for chemical weathering and as a measure of relative proportion of clays compared to quartz sand (Hoang et al. 2010). Clays are rich in Al and this proxy has the advantage of not being affected by large amounts of biogenic carbonate. Decreases in Al/Si signified less chemical weathering

**Table 2.6** (continued)

*Applications and literature*

- Weathering intensity
- Weathering processes
- Precipitation and runoff
- Clay content

  Hoang et al. (2010)

***Al/Ca***

*Use:* Al/Ca used to record terrigenous flux off NW Africa (Nizou et al. 2010, 2011) with low Al/Ca values interpreted as low river discharge indicating hinterland aridity and high Al/Ca values reflecting humid hinterland phases, use supported by palynological records. To avoid dilution effects, Al/Ca was plotted against time (Weltje and Tjallingii 2008). Water content may influence core scanner measurement for low-atomic-weight elements such as Al (Tjallingii et al. 2007) but Nizou et al. (2011) found little porosity variation downcore (~10%), hence water influence not considered significant. This analysis was supported by Fe/Ca (two high-atomic weight elements not influenced by water content) which showed same pattern as Al/Ca. When both Al/Ca and Fe/Ca are available, authors conclude Al/Ca is more suitable for recording river runoff as Al is non-mobile

*Applications and literature*

- Variation in terrigenous sediment delivery
- Precipitation and runoff
- Hinterland climate

  Nizou et al. (2010, 2011)

***Silicon (Si)***

*Origin:* Measured by mass, Si makes up 27.7% of Earth's crust and is the second most abundant element, only O having greater abundance. Si is usually found as complex silicate minerals and less often as quartz ($SiO_2$) a major component of sand and silt derived through physical weathering of continental crust. Silicate minerals comprise the largest and most important class of rock-forming minerals, constituting ~90% of crustal rocks. Si may be detrital, derived from mechanical weathering of crustal rocks, or biogenic, derived from siliceous phytoplankton (diatoms, silicoflagellates), protozoans and protists (radiolarians and ebridians), plant phytoliths, some scolecodonts (polychaete worm jaws) and sponge spicules. Normalisation using a detrital divisor can distinguish terrigenous or productivity origin

*Use:* Like Fe and Ti, Si used as a proxy for terrigenous sediment delivery (Blanchet et al. 2007; Kleiven et al. 2007) or in provenance studies, e.g. turbidite sources (Frenz et al. 2009). Si profile shape may give information on textural character of coarse-grained turbidites, e.g. distinguish massive and graded sands (Rothwell et al. 2006)

*Applications and literature*

- Variation in terrigenous sediment delivery

  Blanchet et al. (2007); Kleiven et al. (2007)
- Textural character

  Rothwell et al. (2006)
- Provenance studies

  Frenz et al. (2009)

**Table 2.6** (continued)

| |
|---|
| ***Si/Ti*** |
| *Use:* Si/Ti used as a proxy for siliceous productivity (Agnihotri et al. 2008; Marsh et al. 2007) |
| *Applications and literature* |
| • Siliceous productivity<br>Agnihotri et al. (2008); Marsh et al. (2007) |
| ***Si/Ca*** |
| *Use:* Si as a representative terrigenous element has been ratioed with Ca to record aeolian dust supply (Hanebuth and Henrich 2009) |
| *Applications and literature* |
| • Aeolian dust flux/wind strength<br>Hanebuth and Henrich (2009) |
| ***Si/Sr*** |
| *Use:* Si/Sr used to identify layers poor in biogenic carbonate and relatively rich in detrital silicates (quartz, feldspar etc.), such as ice-rafted debris layers (Hodell et al. 2008). In this study, Si/Sr peaks correlated with lows in bulk carbonate $\partial^{18}O$, probably representing lower biogenic carbonate productivity and/or increased delivery of IRD rich in silicate minerals |
| *Applications and literature* |
| • Detection of ice-rafted-debris<br>• Oceanic productivity<br>Hodell et al. (2008) |
| ***Si/Al*** |
| *Use:* Si/Al used as proxy for wind strength (Itambi et al. 2009; Revel et al. 2010) with high values indicating high aeolian flux, and as a proxy for biogenic production (Dickson et al. 2010). In one study used to infer weathering intensity (Sluijs et al. 2008). Si/Al considered a proxy for changes in aluminosilicate composition by Tisserand et al. (2009) |
| *Applications and literature* |
| • Aeolian dust flux/wind strength<br>Itambi et al. (2009); Revel et al. (2010)<br>• Oceanic productivity<br>Dickson et al. (2010)<br>• Weathering intensity<br>Sluijs et al. (2008)<br>• Aluminosilicate composition<br>Tisserand et al. (2009) |
| ***Titanium (Ti)*** |
| *Origin:* Ti is conservative element that generally varies directly with the coarse-grained terrigenous fraction. A common constituent of rocks, such as gneisses or schists, it primarily indicates a terrigenous continental source. Ti predominatly occurs as the sortable heavy mineral rutile ($TiO_2$). Other sources are anatase ($TiO_2$), brookite ($TiO_2$), ilmenite ($FeTiO_3$) sphene ($CaTiSiO_5$) and titanomagnetite ($Fe^{2+}(Fe^{3+}Ti)_2O_4$), all minerals commonly associated with sand and silt fractions. Ti may increase with biotite enrichment. It is enriched in tropical soils such as laterites and bauxites. Ti not affected by diagenetic overprinting or involved in biological processes and therefore represents allochthonous minerogenic input |

**Table 2.6** (continued)

*Use:* Ti is widely used to record terrigenous sediment delivery, particularly through runoff, and hence assess hinterland climate, particularly rainfall (e.g. Haug et al. 2001, 2003; Kissel et al. 2010; Peterson et al. 2000 and others). It commonly co-varies with Fe, but is arguably a better proxy for terrigenous sediment delivery than Fe as it is redox-insensitive (Calvert and Pedersen 2007; Yarincik et al. 2000). In any case, use of Fe as run-off proxy should be checked against Ti (e.g. Haug et al. 2001). Ti has also been widely used as a proxy for aeolian dust input (e.g. Xu et al. 2008), particularly throughout the Mediterranean/Middle East region (e.g. Ivanochko et al. 2005; Wehausen and Brumsack 2000)

Ti spikes may correlate with turbidites or ash layers (e.g. Westerhold et al. 2009). Turbidites commonly have coarser-grained bases, and if silty or sandy, typically show abrupt increases in element concentrations resulting in asymmetric Ti distributions. In contrast, tephra layers tend to show more symmetrical Ti peaks (Sluijs et al. 2008)

Ti has also been used to identify major sedimentary breaks and climatic precession and obliquity variations in IODP cores to produce a coherent age model (Backman et al. 2008) and recording sea-ice melting with release of terrigenous particles (Jaccard et al. 2009; Solignac et al. 2011)

Loess may concentrate heavy minerals, so be enriched in high field-strength elements like Ti (Itambi et al. 2010). Ti, like Fe, is commonly carried by wind as a clay coating/embedding coarse dust grains, as seen off NW Africa, where alluvial terraces with extensive ferruginous lateritic soils provide a Ti source (Nizou et al. 2011)

*Limitations:* Overall increase in Ti with depth has been attributed to compaction (e.g. Cheshire et al. 2005) and like other elements, values may decrease towards core tops, due to lower compaction and dilution by higher water content. Ti also likely to vary with grain size, as it is typically concentrated in coarser grain-sizes

*Applications and literature*

- Variation in terrigenous sediment delivery
- Precipitation and runoff
- Hinterland climate

  Carlson et al. (2008); Cheshire et al. (2005); Chiessi et al. (2009); Denis et al. (2006); Haug et al. (2001, 2003); Kissel et al. (2010); Marsh et al. (2007); Peterson et al. (2000); Teodoru et al. (2007)
- Aeolian dust flux/wind strength

  Ivanochko et al. (2005); Wehausen and Brumsack (2000); Xu et al. (2008)
- Turbidites and ash layers

  Sluijs et al. (2008); Westerhold et al. (2009)
- Production of coherent age models
- Recording ice melting

  Backman et al. (2008); Jaccard et al. (2009); Solignac et al. (2011)

***Ti/Ca***

*Use:* Ti/Ca records relative variation of terrigenous input and marine carbonate (e.g. Bahr et al. 2005, 2008; Hoang et al. 2010). It has been used to record changes from fluvial to marine deposits, for example, in incised-valley-fill sediments (Tjallingii et al. 2010). It has also been used as a proxy for dust supply (e.g. Henrich et al. 2010; Pierau et al. 2011; Romero et al. 2008) allowing assessment of continental aridity and relative wind strength. Ti/Ca also used to identify detrital-rich sands (high Ti) and foraminifer-rich turbidites (high Ca) (e.g. Bourget et al. 2008) and in varve counting and recording influx of IRD released by deglacial meltwater discharges (recorded as Ti/Ca spikes) (Soulet et al. 2011). Ti/Ca has also contributed to construction of regional chronologies (e.g. for the Black Sea, a sensitive recorder of past climate change) by tuning to climate reference records (Soulet et al. 2011)

**Table 2.6** (continued)

*Applications and literature*

- Variation in terrigenous sediment delivery
- Identification of freshwater/marine transitions

  Bahr et al. (2005, 2008); Hoang et al. (2010); Tjallingii et al. (2010)
- Aeolian dust flux/wind strength
- Hinterland climate
- Precipitation and runoff
- Sediment transport

  Romero et al. (2008); Henrich et al. (2010); Pierau et al. (2011); Jaeschke et al. (2007)
- Core characterisation
- Varve counting
- Recording ice melting
- Constructing chronology

  Bourget et al. (2008); Soulet et al. (2011)

***Ti/Al***

*Use:* Ti/Al used as proxy for aeolian dust flux/wind strength, hence hinterland aridity (Itambi et al. 2009; Jullien et al. 2007; Tisserand et al. 2009). Jiménez-Espejo et al. (2007a) used average concentration of Ti in Pleistocene cores from ODP Site 975 (Balearic Abyssal Plain, W Mediterranean Sea) to normalize Ti to Al. This normalized average, called $Ti_{mean}$/Al, related to aeolian terrigenous input to Balearic Basin, which, together with other data, provided information on Iberian hinterland climate during time of Neanderthal extinction around 25–30 ka. Higher Ti/Al values have been related to greater coarse-grained lithogenic flux, often climatically modulated (e.g. Ziegler et al. 2009). More intense weathering has also been inferred from low Ti/Al values (Sluijs et al. 2008)

*Applications and literature*

- Aeolian dust flux/wind strength
- Hinterland climate
- Precipitation and runoff

  Itambi et al. (2009); Jiménez-Espejo et al. (2007a); Jullien et al. (2007); Tisserand et al. (2009)
- Variation in terrigenous sediment delivery
- Climatic variability
- Weathering intensity

  Sluijs et al. (2008); Ziegler et al. (2009)

***Ti/K***

*Use:* Ti/K mainly used to infer variations in sediment source (Siani et al. 2010; Spofforth et al. 2008) and identify ice-rafted-debris (Prins et al. 2001). Ti/K also used for core correlation by Brendryen et al. (2010). In Nordic Seas, Ti/K shows a correlation with magnetic susceptibility and the Greenland NGRIP $\partial^{18}O$ temperature record (Brendryen et al. 2010; Richter et al. 2006), probably due to erosion and transport of magnetic and Ti-rich minerals from basaltic Iceland-Scotland Ridge by bottom currents dependant on inflow of Atlantic water to Nordic Seas

*Applications and literature*

- Sediment provenance

  Siani et al. (2010); Spofforth et al. (2008)

**Table 2.6** (continued)

- Detection of ice-rafted-debris

  Prins et al. (2001)
- Core correlation
- Sediment transport
- Current and water mass changes

  Brendryen et al. (2010)

***Ti/Fe***

*Use:* Ti/Fe used as proxy for wind strength/hinterland aridity (Zarriess and Mackensen 2010). As an element of heavy minerals (e.g. rutile), Ti is transported dominantly in Saharan dust, so its concentration reflects wind intensity off NW Africa (Schütz and Rahn 1982). Ti/Fe also used as a provenance indicator to discriminate material from local volcanic sources (Konfirst et al. 2011)

*Applications and literature*

- Aeolian dust flux/wind strength
- Hinterland climate

  Zarriess and Mackensen (2010)
- Sediment provenance

  Konfirst et al. (2011)

***Ti/Rb***

*Use:* Ti/Rb used to show enhanced heavy resistate minerals in turbidite bases (Rothwell et al. 2006)

*Applications and literature*

- Presence of heavy minerals

  Rothwell et al. (2006)

***Ti/Sr***

*Use:* Ti/Sr used to measure terrigenous versus biogenic sediment contribution and climatic modulation of supply (Zaragosi et al. 2006)

*Applications and literature*

- Variation in terrigenous sediment delivery
- Climate variability

  Zaragosi et al. (2006)

***κ/Ti***

*Use:* κ/Ti used as proxy for authigenesis in cores from summits of carbonate mounds in Rockall Trough, NE Atlantic (Land et al. 2011). A zone of Fe and Mn enrichments showed low κ/Ti and high Fe/κ, interpreted as resulting from dissolution of magnetic minerals

*Applications and literature*

- Iron and manganese diagenesis
- Authigenesis

  Land et al. (2011)

***Zirconium (Zr)***

*Origin:* Zr mainly occurs in zircon ($ZrSiO_4$), a dense resistant mineral, ubiquitous in the crust and occurring in igneous rocks as primary crystallisation products and in sediments as detrital grains. Zircons tend to maintain their original morphology during weathering and transport, and are usually enriched in coarse sediment fractions

**Table 2.6** (continued)

*Use:* Zr may be high in ash layers. Ash layers with low Ti and high Zr composition point to an alkaline magma type (Westerhold et al. 2009)

*Applications and literature*

- Identification of tephras

  Westerhold et al. (2009)

***Zr/Ti***

*Use:* Marsh et al. (2007) found Zr/Ti in cores around Crozet Plateau, S Indian Ocean, was provenance sensitive with high values indicating input of volcanic material from Crozet Island via sediment gravity flows

*Applications and literature*

- Sediment provenance

  Marsh et al. (2007)

***Zr/Rb***

*Use:* Zr/Rb provides a grain-size proxy as Zr resides mainly in coarser grains and Rb in clays. Has been used to reconstruct river flood histories, as floods carry greater coarse-grain sediment loads, hence Zr/Rb increases in flood events (e.g. Wang et al. 2011). The higher the Zr/Rb peaks, the greater number of coarse particles deposited by saltation processes. Zr/Rb has also been used as a winter monsoon proxy (Liu et al. 2002)

*Applications and literature*

- Precipitation and runoff

  Liu et al. (2002); Wang et al. (2011)

***Zr/Sr***

*Use:* Hodell et al. (2010) used Zr/Sr as IRD proxy in core from Garder Drift, Reykjanes Ridge, N Atlantic

*Applications and literature*

- Detection of ice-rafted-debris

  Hodell et al. (2010)

***Zr/Fe***

*Use:* Zr/Fe used to discriminate sediment supply from local volcanic sources (Konfirst et al. 2011)

*Applications and literature*

- Sediment provenance

  Konfirst et al. (2011)

***Manganese (Mn)***

*Origin:* Mn makes up ~1000 ppm of the Earth's crust, making it the 12th most abundant crustal element (Emsley 2001). Mn-bearing minerals not uncommon, occurring as oxides, silicates and carbonates, with pyrolusite ($MnO_2$) and rhodochrosite ($MnCO_3$) the most common. Most Mn in deep-sea sediments (~70–80%) has a hydrothermal origin and Mn-bearing minerals undergo substantial alteration during early diagenesis. Mn-rich crusts commonly cover rocky outcrops and Mn polymetallic nodules cover substantial areas of seafloor. Microscopic Mn micronodules are widely distributed in marine sediments

**Table 2.6** (continued)

*Use:* Highly redox-sensitive, Mn has been used in wide range of diagenetic and process studies. Covariance with other redox-sensitive or detrital elements may indicate potential Mn sources. Pervasive Mn enrichment occurs in central Arctic Ocean sediments during interglacials and interstadials (Löwemark et al. 2008; O'Regan et al. 2010). This is attributed to enhanced Mn flux to central Arctic during deglacial or interglacial periods, or from sluggish intermediate and deep-water circulation during glacials (Jakobsson et al. 2000). In the latter case, stagnant bottom and intermediate waters lead to dysoxia with Mn only precipitating during ventilated interglacial/interstadial periods. Downhole Mn was not strongly correlated with other redox-sensitive elements, suggesting it may record primary depositional signal (Löwemark et al. 2008). Mn enrichment in interglacials may reflect enhanced Mn flux from circum-Arctic rivers, or flooding of shelves, but the exact mechanism is unresolved. Arz et al. (2006) used Mn and other parameters to characterise pronounced dry event, dated 4.2 ka, recorded in sediments of Shaban Deep (Red Sea), previously linked to collapse of the Akkadian empire (Weiss et al. 1993)

*Applications and literature*

- Diagenesis
- Climate variability

Arz et al. (2006); Löwemark et al. (2008); O'Regan et al. (2010)

***Mn/Fe***

*Use:* Mn/Fe used to assess redox conditions as Mn is mobile under sub-oxic conditions and separates from Fe during diagenesis (Marsh et al. 2007). Constant Mn/Fe ratios indicate oxic conditions and no element fractionation. Mn/Fe peaks occur during suboxic diagenesis when Mn is mobilised and diffuses along concentration gradients to precipitate at new oxic/post-oxic boundary. Non-steady state diagenesis such as oxic burn-down through turbidites leads to Mn/Fe peak formation (Thomson et al. 1993)

*Applications and literature*

- Diagenesis
- Redox conditions

Marsh et al. (2007)

***Mn/Ti***

*Use:* Mn/Ti used to document diagenetic relocations and Mn enrichment (e.g. Land et al. 2011). Mn/Ti (and Fe/κ) used by Hepp et al. (2009) to document late Miocene-early Pliocene Antarctic deepwater record of repeated Fe reduction events, resulting in significant losses of magnetic susceptibility signal at ODP Site 1095 (Pacific continental rise, W Antarctic Peninsula). Mn/Ti also used to determine extent of post-depositional oxidation of Eastern Mediterranean sapropels (Thomson et al. 2006)

*Applications and literature*

- Diagenesis

Hepp et al. (2009); Land et al. (2011); Thomson et al. (2006)

***Mn/Al***

*Use:* Mn/Al interpreted as recording changes in oxygenation with high Mn/Al suggesting periodic oxygenation (Spofforth et al. 2008). Jaccard et al. (2009) used Mn/Al to map modern redoxcline and redox transitions in Quaternary cores from ODP Site 882 (subarctic NW Pacific)

*Applications and literature*

- Diagenesis

Jaccard et al. (2009); Spofforth et al. (2008)

**Table 2.6** (continued)

***Potassium (K)***

*Origin:* K generally associated with terrestrial siliciclastics, e.g. illite clays (potassium mica) and potassium feldspar (microcline, orthoclase, sanidine). Illite is K's main mineralogical carrier and in fine-grained sediments, high K suggests a high illitic component

*Limitations:* The K peak in the XRF intensity spectrum is attached to Ca peak, so is easily tampered by varying Ca signal. Normalisation of K in counts per second to total counts in order to receive independent K signal improves correlation (Kujau et al. 2010)

*Use:* An important terrigenous indicator, K has been used as a proxy for fluvial input allowing inferences on hinterland humidity/aridity and climatic modulation (e.g. Holzwarth et al. 2010; Kuhlmann et al. 2004b; Romero et al. 2008)

*Applications and literature*

- Variation in terrigenous sediment delivery
- Precipitation and runoff
- Hinterland climate

  Holzwarth et al. (2010); Kuhlmann et al. (2004b); Romero et al. (2008)

***K/Ti***

*Use:* K/Ti has been used to emphasize provenance differences of detrital material (Diekmann et al. 2008; Richter et al. 2006), with the proxy being useful with sediment supplied largely by weathering of schists and slates. Diekmann, et al. (2008) found K/Ti variations recorded provenance changes in Okinawa Trough sediments, off NE Taiwan. Ti is enriched above the mean of upper continental crust in the particulate load of Yangtze River, draining E China lowlands. Thus low K/Ti suggested sediment supply from E China, while high K/Ti marked influx of illite-rich material from Taiwan. K/Ti used by Hodell et al. (2010) to assess relative contribution of felsic and mafic sources of terrigenous sediments in a core from Garder Drift (Reykjanes Ridge, N Atlantic). These source changes reflected varying strength of Iceland-Scotland Overflow Water (ISOW) over time. These data showed ISOW was stronger during long warm interstadial periods. K/Ti has also been used as a proxy for weathering intensity and erosion with values related to sediment source and transport processes (Piva et al. 2008). At the PRADI-2 deep borehole on the Adriatic continental slope, K was mainly concentrated in K-feldspar and illite, while Ti was largely present in rutile and concentrated in the coarse fraction, probably predominantly brought in by aeolian dust. Both K/Ti and Ca/Ti allowed recognition of Dansgaard-Oeschger events in the Adriatic (Piva et al. 2008). Richter et al. (2006) used K/Ti to show Dansgaard-Oeschger cycles in Faeroe margin sediments accompanied by repetitive shifts in composition of terrigenous fraction. K and Ti were linked to acidic and basaltic sources respectively

*Applications and literature*

- Sediment provenance

  Diekmann et al. (2008)
- Current and water mass changes

  Hodell et al. (2010)
- Weathering intensity
- Climatic variability
- Sediment provenance

  Piva et al. (2008); Richter et al. (2006)

**Table 2.6** (continued)

***K/Ca***

*Use:* K/Ca used by McGregor et al. (2009) in cores from offshore S Morocco to demonstrate dramatic increase in terrigeneous sedimentation rate coincident with arrival of Islam around 650-850 A.D., probably related to population increase, expanded pastoralism, deforestation and agriculture

*Applications and literature*

- Variation in terrigenous sediment delivery
- Anthropogenic changes

  McGregor et al. (2009)

***K/Rb***

*Use:* Rothwell et al. (2006) record K/Rb enhanced in turbidite muds, presumably due to high illite. However, Croudace et al. (2006) regards K/Rb as potentially unreliable parameter as seawater Cl absorbs K X-rays, hence high K may reflect increased porosity

*Applications and literature*

- Clay content

  Rothwell et al. (2006)

***K/Al***

*Use:* K/Al used as a measure of mobile versus immobile elements by Clift et al. (2008) in a study investigating Monsoon inception. Most precipitation in India and China caused by seasonal storms of S and E Asian monsoons, which thus control runoff. K/Al and other weathering proxies revealed Monsoon activity history. K/Al also used a proxy for illite variation, and hence variation in hinterland rainfall where illite is abundant in continental soils, e.g. South Africa (Dickson et al. 2010)

*Applications and literature*

- Precipitation and runoff
- Weathering intensity

  Clift et al. (2008); Dickson et al. (2010)

***Zinc (Zn)***

*Origin:* Zn has low abundance in marine environment with concentrations typically < 150 ppm in argillaceous sediments. Zn enrichment, particularly in coastal sediments, normally points to anthropogenic sources, or extremely high terrigenous supply. Marginal environments such as fjords and lagoons near industrial areas may contain significant Zn due to high accumulation rates and tendency to act as natural sediment traps, providing potential for high-resolution anthropogenic impact studies

*Use:* Zn has been used to record anthropogenic pollution and identify different sediment sources (Hebbeln et al. 2003). Cage and Austin (2010) used Zn to test a decadal-scale reconstruction of UK coastal temperature anomalies over last millennium based on long core from Loch Sunart, NW Scotland. A rapid increase in Zn occurred post 1860 A.D., agreeing with reported increase in anthropogenic zinc attributed to atmospheric deposition from around 1850 A.D. in Scottish lake sediments from early industrial sources (e.g. Kreiser et al. 1990)

*Applications and literature*

- Anthropogenic pollution
- Sediment provenance

  Hebbeln et al. (2003)
- Chronology construction

  Cage and Austin (2010)

**Table 2.6** (continued)

***Barium (Ba)***

*Origin:* Ba is important proxy for export paleoproductivity and may be useful for core-to-core correlation where Ba signal-to-noise ratio is high. Its relationship to productivity is well-established. Relatively high concentrations of tiny Ba-rich particles (<2 μm in diameter) occur in near-surface waters (Dehairs et al. 1980 and others) especially in areas of high productivity (Dehairs et al. 1992; Cardinal et al. 2005). This Ba is commonly associated with biogenic aggregates, particularly siliceous debris (Bishop 1988) and constitutes most of the suspended Ba in water column. Particulate Ba occurs within skeletal and organic detritus, most likely precipitating in microenvironments containing concentrated dissolved Ba or sulphate, such as decaying organic matter (Chow and Goldberg 1960; Dehairs et al. 1980; Calvert and Pedersen 2007). Although Ba crystals form intracellularly in some marine protists, e.g. xenophyophores (Gooday and Nott 1982; Rieder et al. 1982), determination of a widespread Ba-secreting planktonic organism has proved elusive. There is evidence for tiny barite crystals forming during phytoplankton decay (Ganeshram et al. 1992, 2003). The insoluble nature of barite means a high degree of preservation in slowly-accumulating oxic sediments

Ba may have a lithogenic origin, occuring in K-feldspars and micas, where it substitutes isomorphically for K (Puchelt 1969–1978). Although compared to biogenic Ba this contribution is usually small. Normalization with Al commonly used to assess detrital Ba component, combined with estimates of Ba/Al ratio of average crustal rocks or of the aluminosilicate fraction in a specific sediment sample (Calvert and Pedersen 2007)

*Limitations:* Ba records may be compromised by post-depositional loss in suboxic (McManus et al. 1998; and others) and especially anoxic sediments affected by sulphate depletion (Os et al. 1991; Brumsack and Gieskes 1983; and others). Thus Ba records from many continental margins, where relatively high $C_{org}$ results in lower redox potentials at shallow depth, do not normally reflect productivity (Shimmield et al. 1994; Ganeshram et al. 1999). Sulphate reduction in microenvironments may result in Ba dissolution, even in oxic and suboxic settings, hence assessment of productivity needs multi-proxy approach, including measurement of $C_{org}$ and biogenic opal

*Use:* Ba has been effectively used as productivity proxy (e.g. Jaccard et al. 2009; Ziegler et al. 2009) and for core-to-core correlation (e.g. Röhl et al. 2007; Kelly et al. 2010). Westerhold et al. (2009) showed Ba intensity during Palaeocene-Eocene sequence at ODP Site 500 (Goban Spur, NE Atlantic) showed extremely well-developed cycles, related to precession cyclicity. Changes in Ba and barite fluxes during the Palaeocene-Eocene Thermal Maximum, if global, must largely be consequence of changes in Ba supply, either from rivers or methane hydrates, rather than due to productivity alone (Dickens et al. 2003). Some Ba is likely recycled during early diagenesis: adsorbed on mineral surfaces, co-precipitated with Fe-Mn oxyhydroxides or precipitated as barite (Paytan and Kastner 1996). In a novel application, Breier et al. (2010) used Ba in cores from semi-arid bays along south Texas coast to study dissolved radium isotopes, probably derived from relic sedimentary barite from discontinued practice of oil-field brine discharge

*Applications and literature*

- Export productivity

  Jaccard et al. (2009); Ziegler et al. (2009)
- Core correlation

  Kelly et al. (2010); Röhl et al. (2007)
- Climate variability
- Diagenesis

  Dickens et al. (2003); Westerhold et al. (2009)

**Table 2.6** (continued)

- Radium isotopes

  Breier et al. (2010)

***Ba/Ca***

*Use:* Grove et al. (2010) used Ba/Ca and Sr/Ca as a proxy for aragonite in onshore massive corals on Madagascar, relating this to spectral luminescence resulting from incorporation of soil-derived humic acids transported to reef during major flood events. These data were used to derive a proxy for runoff and hence hinterland rainfall

*Applications and literature*

- Proxy for aragonite
- Precipitation and runoff

  Grove et al. (2010)

***Ba/Al***

*Use:* Ba/Al used to determine export productivity, particularly in Pacific Ocean (e.g. Jaccard et al. 2005, 2010) and around Antarctica (Hillenbrand et al. 2009). Productivity often strongly modulated by climate. Jaccard et al. (2005) interpreted low biogenic Ba at glacial maxima at ODP Site 882 (N Pacific Ocean) as reflecting decreased nutrient supply, probably resulting from polar stratification during cold periods. Ba/Al used to construct age model for ODP Site 882 (E of Kamchatka, NW Pacific) (Galbraith et al. 2008)

*Applications and literature*

- Export productivity

  Hillenbrand et al. (2009); Jaccard et al. (2005, 2010)
- Climate variability

  Jaccard et al. (2005)
- Chronology construction

  Galbraith et al. (2008)

***Ba/Ti***

*Use:* Ba/Ti used as proxy for palaeoproductivity in sapropel-bearing cores from E Mediterranean (Thomson et al. 2006). Proxy especially useful in showing true sapropel thickness prior to bottom-water oxidation

*Applications and literature*

- Export productivity

  Thomson et al. (2006)

***Copper (Cu)***

*Origin:* Cu has low abundance in ocean sediments and little environmental significance. Elevated concentrations of hydrothermal origin recorded in crusts on the Mid Pacific Rise (Baturin et al. 1987) and Red Sea median valley sediments (Blossom 2006). Cu is redox-sensitive. Cu binds with organic matter, which generally occurs in greater amounts in freshwater sediments than in marine deposits, hence Cu typically has higher concentrations in freshwater sediments (Sparrenbom et al. 2006)

***Cu/Rb***

*Use:* Cu/Rb used to record diagenetic mobilisation of copper (Rothwell et al. 2006)

*Applications and literature*

- Diagenesis

  Rothwell et al. (2006)

**Table 2.6** (continued)

***Cu/Ti***

*Use:* Thomson et al. (2006) found Cu/Ti a useful marker of post-depositional oxidation in sapropel-bearing cores from E Mediterranean

*Applications and literature*

- Diagenesis

  Thomson et al. (2006)

***Arsenic (As)***

*Origin:* As is strongly incorporated into pyrite, substituting for S (Peterson and Carpenter 1986; Huerta-Diaz and Morse 1992). As has low concentration in detrital minerals and is generally close to the limit of detection in absence of pyrite. Its relative environmental rarity compared to ubiquitous Fe and efficient excitation using Mo tube makes As an efficient proxy for pyrite

*Use:* As used as proxy for pyrite authigenesis in sapropel-bearing cores from E Mediterranean by Thomson et al. (2006)

*Applications and literature*

- Pyrite authigenesis

  Thomson et al. (2006)

***Sulphur (S)***

*Origin:* S is closely linked to organic matter with S residing in biomass of marine plants and mineralised S in their dead remains. Within sediments organic S may be oxidised to sulphate and returned to seawater, or buried as organic S, sulphate or sulphide, through bacterial reduction (Ivanov 1981). S may be connected to a reduced iron sulphide phase, and bound in organic-rich laminated mud sequences (organic S) and hence serve as proxy for oxygen depletion in bottom water (Harff et al. 2011)

*Use:* High S contents, together with other suboxic indicators (e.g. increased pyritization, high Fe/S ratios, elevated trace element/Al ratios) indicate reducing conditions.For example, Sluijs et al. (2008) used S abundance in sediments from Upper Paleocene and Lower Early Eocene at IODP Site M0004 (Lomonosov Ridge, Arctic Ocean) to identify reducing suboxic conditions during Paleocene-Eocene Thermal Maximum

*Applications and literature*

- Redox conditions

  Sluijs et al. (2008)

***S/Cl***

*Use:* Thomson et al. (2006) used S/Cl in sapropel-bearing cores from E Mediterranean to detect enhanced S associated with pyrite or organic carbon (Passier et al. 1999) in excess of constant S/Cl sea-salt ratio

*Applications and literature*

- Pyrite authigenesis
- High organic carbon

  Thomson et al. (2006)

***Rubidium (Rb)***

*Origin:* Isomorphic Rb is a dispersed element in nature and widely distributed in rock-forming minerals, but seldom forms distinct mineral species. As Rb and K have similar particle radii, potential and other properties, Rb mainly occurs dispersed in minerals containing K, such as biotite, muscovite, feldspar and illite. During weathering, Rb is enriched in detrital clay minerals

**Table 2.6** (continued)

*Use:* In absence of precise Al data, Rb may be effective for normalisation (Rothwell et al. 2006)

*Applications and literature*

- Data normalisation

  Rothwell et al. (2006)

***Bromine (Br)***

*Origin:* Br does not occur naturally but occurs as bromide compounds in diffuse amounts in crustal rocks. Leaching results in seawater having a bromide salt content of 65 ppm (Tallmadge et al. 1964). Marine organisms in particular synthesize a variety of low molecular weight organic Br molecules (Dembitsky 2002; Gribble 2000; and others) and approximately 2000 natural Br compounds are known, the majority of marine origin (Gribble 2003).
Hence, bromine is concentrated in organic matter, showing marked enrichment in organic-rich layers, such as sapropels

*Use:* Br is widely used to quantify marine organic matter and related productivity (e.g. Caley et al. 2011; Ren et al. 2009; Ziegler et al. 2008, 2009). Terrestrial organic matter is comparatively poor in Br, making it a good discriminant of marine and freshwater conditions (Malcolm and Price 1984; Mayer et al. 2007). For example, McHugh et al. (2008) took Br contents of >200 cts/s as indicating marine rather than freshwater-derived organic matter in cores from Marmara Sea, Turkey. Such data taken together with other markers, such as foraminifer and molluscan faunal changes, were used to determine changes from marine to freshwater conditions during sea-level changes. The analysis allowed tracking of global sealevel as it breached the Bosphorus and Dardanelles sills

*Applications and literature*

- Marine organic matter
- Productivity

  Caley et al. (2011); Ren et al. (2009); Ziegler et al. (2008, 2009)
- Marine and freshwater conditions
- Sealevel changes

  McHugh et al. (2008)

***Br/Cl***

**Use:** Thomson et al. (2006) used Br/Cl as proxy for increased organic matter and higher porosity in sapropel-bearing cores from E Mediterranean

*Applications and literature*

- Marine organic matter
- Porosity changes

  Thomson et al. (2006)

***Br/Ti***

*Use:* Agnihotri et al. (2008) used Br/Ti as organic productivity indicator in core from Peru margin

*Applications and literature*

- Organic productivity

  Agnihotri et al. (2008)

## Fe, Ti and Magnetic Susceptibility

Of the physical properties routinely logged during core analysis, magnetic susceptibility, κ, has been most clearly shown to correlate with certain element abundances. Generally magnetic susceptibility reflects presence of iron mineral concentrations, with emphasis on ferromagnetic phases. Intensity values are reported in dimensionless units.

Magnetic susceptibility is the degree of magnetization in response to an applied magnetic field, and three categories of magnetisation are recognised:

- **Diamagnetism (not magnetic)**
  Diamagnetic minerals are slightly repelled by magnetic fields, do not retain magnetisation, show negative magnetic susceptibility and are considered non-magnetic. Examples are quartz, calcite, plagioclase, apatite.
- **Paramagnetism (weak but transient magnetism)**
  Paramagnetic minerals are weakly magnetised/attracted to magnetic fields, but do not retain magnetisation. This is because some elements like Fe, Ti, Mn, Cr, V, Co, Ni, and Cu can confer weak magnetism in a magnetic field. Minerals containing these elements may thus be weakly magnetic and separated from each other using a magnetic separator. However, paramagnetic minerals only show magnetism under an external magnetic field. When the field is removed, the minerals show no magnetism. Examples are pyroxenes, amphiboles, biotite, garnet.
- **Ferromagnetism/ferrimagnetism (permanent magnetism)**
  Ferromagnetic minerals are strongly attracted to magnetic fields and retain magnetisation after the field is removed, and show high positive magnetic susceptibility. The most important ferromagnetic minerals are Fe-Ti oxides (ulvospinel, ilmenite, pseudobrookite, magnetite, haematite), hence Ti and Fe, important terrigenous proxies, commonly closely correlate with susceptibility. Ferrimagnetic substances show similar behaviour to ferromagnets but have different magnetic ordering.

Magnetic susceptibility thus reflects Fe and Ti mineral concentrations, with emphasis on ferri/ferromagnetic species (Kent 1982; Doh et al. 1988; and others). Diagenetic reductive dissolution of Fe is mineral-selective and leads to gradual dissolution of magnetic primary ferric Fe minerals such as magnetite, maghemite and hematite. The resulting ferrous iron generally precipitates as paramagnetic $Fe^{3+}$oxyhydroxides, but can also form biogenic magnetite (Smirnov and Tarduno 2000). Variations in κ can therefore reflect variations in the primary input of ferromagnetic material or diagenetic alteration. XRF core scanning is largely unbiased by mineralogy and does not follow susceptibility variations due to alterations, or conversion, of strongly magnetic into weakly magnetic iron species. By combining κ with XRF-measured Fe, intervals where such conversions occur due to Fe reduction can be identified (Funk et al. 2004a). Normalising κ to Ti will highlight positive shifts in the κ signal due to biogenic magnetite precipitation. Absolute values of

these ratios will depend on local magnetic mineral source characteristics and sediment composition. Correlation of κ and Fe is presented by Abrantes et al. (2008), Kuhlmann et al. (2004a) and Hofmann et al. (2005).

Although, Fe counts generally correlate well with κ, in core-to-core correlation Fe is commonly more sensitive as, unlike κ, total Fe content is independent of redox state (e.g. Jansen and Dupont 2001; Westerhold et al. 2007). Magnetic susceptibility measurements are sensitive to oxidation state of Fe-bearing minerals as well as to the proportion of diamagnetic calcium carbonate—demonstrating that XRF Fe records may show a much clearer signal than susceptibility values. However, both parameters show similar features and same polarity (i.e. high Fe will correlate with high κ). Richter et al. (2001) show long-term parallel trends of κ and Fe, although profiles differed in detail. Fe and κ peaks may not have the same relative amplitude, or occur exactly at the same core depth. Richter et al. (2001) noted sharp κ peaks at bases of turbidites coincided with extremely low Fe count rates, and these Fe minima were interpreted as artefacts related to grain-size variability.

Magnetic susceptibility may record small changes in the amount of ferruginous coatings of clay minerals and quartz grains (Sarnthein et al. 1982), making down-core κ records of potential value as records of airborne dust input. However, use of κ as a proxy for aeolian dust needs confirmation by independent dust indicators. For example, Rohling et al. (2008) used Fe and Ti to validate the κ record of a Red Sea core as a proxy for aeolian dust input. Variability in Fe content was associated with haematite fluctuations, reflected by κ, which also strongly correlated with Ti, a widely used proxy for aeolian dust throughout the Mediterranean—Middle East region (e.g. Wehausen and Brumsack 2000; Ivanochko et al. 2005).

Magnetic susceptibility is not solely controlled by ferromagnetic mineral concentration but also affected by carbonate concentration, i.e. increased carbonate may reduce κ values (e.g. Andrews and Tedesco 1992; Hofmann et al. 2005), hence Ca records may be inverse to both Fe and κ. But this anti-correlation may not be unequivocal as other non-magnetic components may influence Ca and κ anti-correlation (Helmke et al. 2005). Small differences in signal variation between κ, Fe and Ca may be consistent between cores and thus useful for correlation purposes (Hofmann et al. 2005).

Diagenetic processes may significantly influence κ and Fe data, particularly fine-grained magnetite dissolution due to carbon oxidation (Kuhlmann et al. 2004a). Comparison with Ti (Fe/Ti) is necessary to confirm the Fe record, as Ti is diagenetically inert. Post-depositional reductive diagenesis can reduce ferrimagnetic Fe minerals to paramagnetic iron compounds diminishing κ. As diffusion rates are small, local Fe concentration changes little during this process. Consequently, reductive diagenesis increases Fe/κ above the constant value characteristic for the unaltered terrigenous phase (Hofmann et al. 2005).

## Concluding Remarks

The development of XRF core scanners has caused a revolution in environmental analysis over the last two decades due to their capability, speed and resolution. Indeed, XRF core scanners now rank as one of the most powerful tools in the environmental scientists' tool-box. Their application in marine geology has led to major advances in understanding past climates and climatic, meteorological, sedimentological and oceanographic processes in unprecedented detail.

A review of the marine science literature using core scanners shows 60 different element integrals or ratios have been used for palaeoenvironmental or process studies. Some of these (e.g. Ca, Ca/Fe, Fe, Ti) have been widely, almost routinely, used as proxies for carbonate content or terrigenous sediment delivery, others are important proxies for productivity (e.g. Ba, Ba/Al, Ba/Ti, Br/Ti), but some have had more restricted application. (e.g. in studies of diagenesis and authigenesis).

However, presentation and analysis of core scanner data is not trivial. Initial use of major element integrals (e.g. Ca and Fe) for recording calcium carbonate or terrigenous sediment delivery has been replaced by routine reporting as normalised ratios to negate closed sum effects. The statistical difficulty of ratios due to their asymmetry as there is no 'law' on how ratios should be ordered led Weltje and Tjallingii (2008) to propose log-ratio intensities as providing the most easily interpretable signals of relative changes in element composition, and the least likely to result in interpretation errors.

Core scanner-acquired element proxies have proved invaluable in providing robust data on environmental and process changes recorded in marine sediments, particularly changes in terrigenous input (and associated climatic inferences) and productivity, but caveats apply and some proxies are more reliable than others. In summary:

**Variation in terrigenous sediment delivery—High Fe, K or Ti, low Ca/Fe, high Fe/Ca, high Ti/Ca.** Although Fe has been widely used it is redox-sensitive and hence may be affected by diagenetic processes. Thus redox-insensitive Ti is a better choice for measuring terrigenous sediment fluxes, particularly as a rainfall and run-off proxy. However both elements may be affected by compaction and variation in water content, resulting in spurious lower values towards core tops.

**Productivity indicators—High Ba, Br, Ca, high Br/Ti, high Ba/Al, high Ba/Ti.** Ba is the most commonly used proxy for export productivity, although Ba may be affected by post-depositional loss especially in suboxic and anoxic environments affected by sulphate depletion as seen on many continental margins, where relatively high organic carbon contents result in lower redox potentials at shallow depth. Assessment of productivity needs a multi-proxy approach and if possible, measurement of organic carbon and biogenic opal. Variation in Ca may reflect terrigenous dilution rather than productivity changes, particularly in marginal environments.

This paper has reviewed the application of an extensive suite of proxies to marine sediments with the aim of providing core scanner users with a primer on their origin, use, and potential limitations, in order to guide proxy selection and aid interpretation of XRF core scanner records of marine sediments.

**Acknowledgements** We are very grateful to Mike Rogerson and James Hunt for their comments in review which helped improve the paper. We thank Michael Haschke, Steffen Wolters, Thomas Richter, Cletus Itambi, Alan Seaman, Springer, The Geological Society of London, John Wiley and Sons, and Taylor & Francis for permission to reproduce previously published figures. John Smol is thanked for his editorial handling of this paper. We also thank Kate Davis for help in drafting figures.

## References

Abrantes F, Alt-Epping U, Lebreiro S, Voelker A, Schneider R (2008) Sedimentological record of tsunamis on shallow-shelf areas: the case of the 1969 AD and 1755 AD tsunamis on the Portuguese Shelf off Lisbon. Mar Geol 249:283–293. doi:10.1016/j.margeo.2007.12.004

Adgebie AT, Schneider RR, Röhl U, Wefer G (2003) Glacial millennial-scale fluctuations in central African precipitation recorded in terrigenous sediment supply and freshwater signals offshore Cameroon. Palaeogeogr Palaeoclimatol Palaeoecol 197:323–333. doi:10.1016/S0031-0182(03)00474-7

Adkins J, de Menocal P, Eshel G (2006) The ''African humid period'' and the record of marine upwelling from excess $^{230}$Th in Ocean Drilling Program Hole 658C. Paleoceanography 21:PA4203. doi:10.1029/2005PA001200

Aitchison J (1982) The statistical analysis of compositional data (with discussion). J Roy Stat Soc B 44:139–177

Aitchison J (1986) The statistical analysis of compositional data. Chapman and Hall, London

Agnihotri R, Altabet MA, Herbert TD, Tierney JE (2008) Subdecadally resolved paleoceanography of the Peru margin during the last two millennia. Geochem Geophys Geosyst 9:Q05013. doi:10.1029/2007GC001744

Amorosi A, Centineo CM, Dinelli E, Lucchini F, Tateo F (2002) Geochemical and mineralogical variations as indicators of provenance changes in Late Quaternary deposits of SE Po Plain. Sediment Geol 151:273–292

Andres MS, Bernasconi SM, McKenzie JA, Röhl U (2003) Southern Ocean deglacial record supports global Younger Dryas. Earth Planet Sci Lett 216:515–525. doi:10.1016/S0012-821X(03)00556-9

Andrews JT, Tedesco K (1992) Detrital carbonate-rich sediments, northwestern Labrador Sea: implications for ice-sheet dynamics and iceberg rafting (Heinrich) events in the North Atlantic. Geology 20:1087–1090

Arrhenius G (1952) Sediment cores from the East Pacific. In: Pettersson H (ed) Reports of the Swedish Deep-Sea Expedition (1947–1948), Elanders Boktryckeri Aktiebolag, Göteborg

Arz HW, Pätzold J, Wefer G (1998) Correlated millennial-scale changes in surface hydrography and terrigenous sediment yield inferred from last-glacial marine deposits off Brazil. Quat Res 50:157–166

Arz HW, Pätzold J, Wefer G (1999) Climatic changes during the last deglaciation recorded in sediment cores from the northeastern Brazilian Continental Margin. Geo Mar Lett 19:209–218. doi:10.1007/s003670050111

Arz HW, Gerhardt S, Pätzold J, Röhl U (2001a) Millennial-scale changes of surface- and deep-water flow in the western tropical Atlantic linked to Northern Hemisphere high-latitude climate during the Holocene. Geology 29:239–242. doi:10.1130/0091-7613(2001)029<0239MSCOSA>20CO;2

Arz HW, Pätzold J, Moammar MO, Röhl U (2001b) Late Quaternary climate records from the Northern Red Sea: results on gravity cores retrieved during the R/V METEOR Cruise M44/3. J King Abdulaziz Univ Mar Sci 12:101–113

Arz HW, Pätzold J, Müller PJ, Moammar MO (2003) Influence of Northern Hemisphere climate and global sea level rise on the restricted Red Sea marine environment during termination I. Paleoceanography 18:1053. doi:10.1029/2002PA000864

Arz HW, Lamy F, Pätzold J (2006) A pronounced dry event recorded around 4.2 ka in brine sediments from the northern Red Sea. Quat Res 66:432–441. doi:10.1016/j.yqres.2006.05.006

Backman J, Jakobsson M, Frank M, Sangiorgi F, Brinkhuis H, Stickley C, O'Regan M, Løvlie R, Pälike H, Spofforth D, Gattacecca J, Moran K, King J, Heil C (2008) Age model and core-seismic integration for the Cenozoic Arctic Coring Expedition sediments from the Lomonosov Ridge. Paleoceanography 23:PA1S03. doi:10.1029/2007PA001476

Bahr A, Lamy F, Arz H, Kuhlmann H, Wefer G (2005) Late glacial to Holocene climate and sedimentation history in the NW Black Sea. Mar Geol 214:309–322. doi:10.1016/j.margeo.2004.11.013

Bahr A, Lamy F, Arz HW, Major C, Kwiecien O, Wefer G (2008) Abrupt changes of temperature and water chemistry in the late Pleistocene and early Holocene Black Sea. Geochem Geophys Geosyst 9:Q01004. doi:1029/2007GC001683

Balsalm WL, McCoy FW (1987) Atlantic sediments: glacial/interglacial comparisons. Paleoceanography 2:531–542

Balsam WL, Otto-Bliesner B, Deaton BC (1995) Modern and last glacial maximum eolian sedimentation patterns in the Atlantic Ocean interpreted from sediment iron oxide content. Paleoceanography 10:493–507

Baturin GN, Shevchenko Y, Zavadskaya NN (1987) On the structure and comparison of ore crusts from subsea mountains of the northern Pacific. Okeanologiya 27:624–629

Behling H, Arz HW, Pätzold J, Wefer G (2000) Late Quaternary vegetational and climate dynamics in northeastern Brazil inferences from marine core GEOB 3104-1. Quat Sci Rev 19:981–994. doi:10.1016/S0277-3791(99)00046-3

Bennekom van AJ, Jansen JHF, Van der Gaast SJ, Van Iperen JM, Pieters J (1989) Aluminium-rich opal: an intermediate in the preservation of biogenic silica in the Zaire (Congo) deep-sea fan. Deep Sea Res 36:173–190

Berg S, Wagner B, Cremer H, Leng MJ, Melles M (2010) Late Quaternary environmental and climate history of Rauer Group, East Antarctica. Palaeogeogr Palaeoclimatol Palaeoecol 297:201–213. doi:10.1016/j.palaeo.2010.08.002

Bergh van den GD, Boer W, de Haas H, van Weering TjCE, van Wijhe R (2003) Shallow marine tsunami deposits in Teluk Banten (NW Java, Indonesia), generated by the 1883 Krakatau eruption. Mar Geol 197:13–34. doi:10.1016/S0025-3227(03)00088-4

Bergh van den GD, Boer W, Schaapveld MAS, Duc DM, van Weering TjCE (2007) Recent sedimentation and sediment accumulation rates of the Ba Lat prodelta (Red River, Vietnam). J Asian Earth Sci 29:545–557. doi: 10.1016/j.jseaes.2006.03.006

Berner RA (1981) A new geochemical classification of sedimentary environments. J Sediment Res 51:359–365

Berner RA (1984) Sedimentary pyrite formation: an update. Geochim Cosmochim Acta 48:605–615

Bishop JKB (1988) The barite-opal-organic carbon association in oceanic particulate matter. Nature 332:341–343

Blanchet CL, Thouveny N, Vidal L, Leduc G, Tachikawa K, Bard E, Beaufort L (2007) Terrigenous input response to glacial/interglacial climatic variations over southern Baja California: a rock magnetic approach. Quat Sci Rev 26:3118–3133. doi:10.1016/j.quascirev.2007.07.008

Blanchet CL, Thouveny N, Vidal L (2009) Formation and preservation of greigite ($Fe_3S_4$) in sediments from the Santa Barbara Basin: implication for paleoenvironmental changes during the past 35 ka. Paleoceanography 24:PA2224. doi:10.1029/2008PA001719

Blossom N (2006) Copper in the ocean environment, American Chemet Corporation. http://www.chemet.com/file.asp?F=Copper+and+the+Ocean+Environment1%2EPDF&N=Copper+and+the+Ocean+Environment1%2EPDF&C=articles. Accessed 23 March 2012

Bond GC, Lotti R (1995) Iceberg discharges into the North Atlantic on millennial timescale during the Last Glaciation. Science 267:1005–1010

Bond G, Broecker W, Johnsen S, McManus J, Labeyrie L, Jouzel J, Bonani G (1993) Correlations between climate records from North Atlantic sediments and Greenland ice. Nature 365:143–147

Böning P, Bard E, Rose J (2007) Toward direct, micron-scale XRF elemental maps and quantative profiles of wet marine sediments. Geochem Geophys Geosyst 8:Q05004. doi:10.1029/2006GC001480

Bourget J, Zaragosi S, Garlan T, Gabelotaud I, Guyomard P, Dennielou B, Ellouz-Zimmermann N, Schneider JL, Fan Indien 2006 survey crew (2008) Discovery of a giant deep-sea valley in the Indian Ocean, off eastern Africa: the Tanzania channel. Mar Geol 255:197–185. doi:10.1016/j.margeo.2008.09.002

Bourget J, Zaragosi S, Ellouz-Zimmermann N, Mouchot N, Garlan T, Schneider J-L, Lanfumey V Lallemant S (2011) Turbidite system architecture and sedimentary processes along topographically complex slopes: the Makran convergent margin. Sedimentology 58:376–406. doi:10.1111/j.1365-3091.2010.01168.x)

Bozzano G, Kuhlmann H, Alonso B (2002) Storminess control over African dust input to the Moroccan Atlantic margin (NW Africa) at the time of maxima boreal summer insolation: a record of the last 220 kyr. Palaeogeogr Palaeoclimatol Palaeoecol 183:155–168. doi:10.1016/S0031-0182(01)00466-7

Bramlette MN, Bradley WH (1940) Geology and biology of North Atlantic deep-sea cores between Newfoundland and Ireland. Part 1. Lithology and geologic interpretations. US Geol Surv Prof Pap 196A:1–34

Breier JA, Breier CF, Edmonds HN (2010) Seasonal dynamics of dissolved Ra isotopes in the semi-arid bays of south Texas. Mar Chem 122:39–50. doi:10.1016/j.marchem.2010.08.008

Brendryen J, Haflidason H, Sejrup HP (2010) Norwegian Sea tephrostratigraphy of marine isotope stages 4 and 5: prospects and problems for tephrochronology in the North Atlantic region. Quat Sci Rev 29:847–864. doi:10.1016/j.quascirev.2009.12.004

Brunsack HJ, Gieskes JM (1983) Interstitial water trace-element chemistry of laminated sediments from the Gulf of California, Mexico. Mar Chem 14:89–106

Cage AG, Austin WEN (2010) Marine climate variability during the last millennium: the Loch Sunart record, Scotland, UK. Quat Sci Rev 29:1633–1647. doi:10.1016/j.quascirev.2010.01.014

Caley T, Malaizé B, Zaragosi S, Rossignol L, Bourget J, Eynaud F, Martinez P, Giraudeau J, Charlier K, Ellouz-Zimmerman N (2011) New Arabian Sea records help decipher orbital timing of Indo-Asian monsoon. Earth Planet Sci Lett 308:433–444. doi:10.1016/j.epsl.2011.06.019

Calvert SE, Pedersen TF (2007) Elemental proxies for palaeoclimatic and palaeoceanographic variability in marine sediments: interpretation and application. In: Hillaire-Marcel C, De Vernal A (eds) Proxies in Late Cenozoic Paleoceanography, Dev Mar Geol, Elsevier, pp 567–644

Canfield DE, Berner RA (1987) Dissolution and pyritization of magnetite in anoxic marine sediments. Geochim Cosmochim Acta 51:645–659. doi:10.1016/ 0016-7037(87)90076-7

Cardinal D, Savoye N, Trull TW, Andre L, Kopczynska EE, Dehairs F (2005) Variations of carbon remineralisation in the Southern Ocean illustrated by the Baxs proxy. Deep Sea Res 52:355–370

Carlson AE, Stoner JS, Donnelly JP, Hillaire-Marcel C (2008) Response of the southern Greenland Ice Sheet during the last two deglaciations. Geology 36:359–362. doi: 10.1130/G24519A.1

Cheshire H, Thurow J, Nederbragt AJ (2005) Late Quaternary climate change record from two long sediment cores from Guaymas Basin, Gulf of California. J Quat Sci 20:457–469. doi:10.1002/jqs.944

Chiessi CM, Mulitza S, Pätzold J, Wefer G, Marengo JA (2009) Possible impact of the Atlantic Multidecadal Oscillation on the South American summer monsoon. Geophys Res Lett 36:L21707. doi:10.1029/2009GL039914

Chow TJ, Goldberg ED (1960) On the marine geochemistry of barium. Geochim Cosmochim Acta 20:192–198

Clift PD, Hodges KV, Heslop D, Hannigan R, Van Long H, Calves G (2008) Correlation of Himalayan exhumation rates and Asian monsoon intensity. Nat Geosci 1:875–880. doi:10.1038/ngeo351

Coolen MJL, Saenz JP, Giosan L, Trowbridge NY, Dimitrov P (2009) DNA and lipid molecular stratigraphic records of haptophyte succession in the Black Sea during the Holocene. Earth Planet Sci Lett 284:610–621. doi:10.1016/j.epsl.2009.05.029

Correns CW (1937) Die sedimente des aquatorialen Atlantischen Ozeans II. Geochemie der Sedimente. Wiss Ergeb Dtsch Atl Exped Meteor 1925–1927 3:205–245

Cronan DS, Rothwell G, Croudace I (2010) An ITRAX geochemical study of ferromanganiferous sediments from the Penrhyn Basin, South Pacific Ocean. Mar Georesour Geotechnol 28:207–221. doi:10.1080/1064119X.2010.483001

Croudace IW, Rindby A, Rothwell RG (2006) ITRAX: description and evaluation of a new multifunction X-ray core scanner. In: Rothwell RG (ed) New techniques in sediment core analysis. Geological Society Special Publication 267, pp 51–63

Cushman JA, Henbest LG (1940) Geology and biology of North Atlantic deep-sea cores between Newfoundland and Ireland. Part 2. Foraminifera. US Geol Surv Prof Pap 196A:35–55

Debenay JP, Pages J, Guillou JJ (1994) Transformation of a subtropical river into a hyperhaline estuary: the Casamance River (Senegal)—paleogeographical implications. Palaeogeogr Palaeoclimatol Palaeoecol 107:103–119

Dehairs F, Chesselet R, Jedwab J (1980) Discrete suspended particles of barite and the barium cycle in the open ocean. Earth Planet Sci Lett 49:528–550

Dehairs F, Baeyens W, Goeyens L (1992) Accumulation of suspended baite at mesopelagic depths and export production in the Southern Ocean. Science 254:1332–1335

Dembitsky VM (2002) Bromo- and iodo-containing alkaloids from marine microorganisms and sponges. Russ J Bioorg Chem 28:170–182. doi:10.1023/A:1015748018820

Denis D, Crosta X, Zaragosi S, Romero O, Martin B, Mas V (2006) Seasonal and sub-seasonal climate changes recorded in laminated diatom ooze sediments, Adélie Land, East Antarctica. Holocene 16:1137–1147. doi: 10.1177/0959683606069414

Dickens GR, Fewless T, Thomas E, Bralower TJ (2003) Excess barite accumulation during the Paleocene-Eocene thermal maximum: massive input of dissolved barium from seafloor gas hydrate reservoirs. In: Wing SL et al (ed) Causes and consequences of globally warm climates in the early Paleogene. Special Paper Geological Society of America 369, pp 11–23 (Boulder, CO)

Dickson AJ, Leng MJ, Maslin MA, Röhl U (2010) Oceanic, atmospheric and ice-sheet forcing of South East Atlantic Ocean productivity and South African monsoon intensity during MIS-12 to 10. Quat Sci Rev 29:3936–3947. doi:10.1016/j.quascirev.2010.09.014

Diekmann B, Hofmann J, Henrich R, Fütterer DK, Röhl U, Wei K-Y (2008) Detrital sediment supply in the southern Okinawa Trough and its relation to sea level and Kurishio dynamics during the late Quaternary. Mar Geol 255:83–95. doi:10.1016/j.margeo.2008.08.001

Doh S, King JW, Leinen M (1988) A rock-magnetic study of giant piston core LL44-GPC3 from the central north Pacifc and its paleoceanographic implications. Paleoceanography 3:89–111

Dorschel B, Hebbeln D, Rüggeberg A, Dullo W-C (2007) Carbonate budget of a cold-water coral carbonate mound: propeller mound, porcupine seabight. Int J Earth Sci 96:73–83. doi: 10.1007/s00531-005-0493-0

Dorschel B, Hebbeln D, Rüggeberg A, Dullo W-C, Freiwald A (2005) Growth and erosion of a cold-water coral covered carbonate mound in the Northeast Atlantic during the Late Pleistocene and Holocene. Earth Planet Sci Lett 233:33–44. doi:10.1016/j.epsl.2005.01.035

Dymond J, Collier R (1996) Particulate barium fluxes and their relationships to biological productivity. Deep Sea Res Pt II(43):1283–1308

Eisele M, Hebbeln D, Wienberg C (2008) Growth history of a cold-water coral covered carbonate mound—Galway Mound, Porcupine Seabight, NE Atlantic. Mar Geol 253:160–169. doi:10.1016/j.margeo.2008.05.006

Emsley J (2001) Manganese. Nature's building blocks: an A-Z Guide to the elements. Oxford University Press, Oxford, pp 249–253

Eynatten von H, Barcelo-Vidal C, Pawlowsky-Glahn V (2003) Composition and discrimination of sandstones: a statistical evaluation of different analytical methods. J Sediment Res 73:47–57

Finney BP, Lyle MW, Heath GR (1988) Sedimentation at MANOP site H (Eastern Equatorial Pacific) over the past 400,000 years: climatically induced redox effects on transition metal cycling. Paleoceanography 3:169–189

Foubert A, Henriet J-P (2009) The top of the record: on-mound and off-mound. Lect Notes Earth Sci 126:167–191. doi:10.1007/978-3-642-00290-8_6

Foucault A, Stanley DJ (1989) Late Quaternary palaeoclimatic oscillations in East Africa recorded by heavy minerals in the Nile delta. Nature 339:44–46

Franke C, Hofmann D, Dobeneck von T (2004) Does lithology influence relative paleointensity records? A statistical analysis on South Atlantic pelagic sediments. Phys Earth Planet Inter 147:285–296. doi:10.1016/j.pepi.2004.07.004

Frenz M, Wynn RB, Georgiopoulou A, Bender VB, Hough G, Masson DG, Talling PJ, Cronin BT (2009) Provenance and pathways of late Quaternary turbidites in the deep-sea Agadir Basin, northwest African margin. Int J Earth Sci 98:721–733. doi:10.1007/s00531-008-0313-4

Froelich PN, Klinkhammer GP, Bender ML, Luedtke NA, Heath GR, Cullen D, Dauphin P, Hammond D, Hartman B, Maynard V (1979) Early oxidation of organic matter in pelagic sediments of the eastern equatorial Atlantic: suboxic diagenesis. Geochim Cosmochim Acta 43:1075–1090

Funk JA, von Dobeneck T, Reitz A (2004a) Integrated rock magnetic and geochemical quantification of redoxmorphic iron mineral diagenesis in Late Quaternary sediments from the equatorial Atlantic. In: Wefer G, Mulitza S, Ratmeyer V (eds) The South Atlantic in the Late Quaternary, Springer, pp 237–260

Funk JA, von Dobeneck T, Wagner T, Kasten S (2004b) Late Quaternary sedimentation and early diagenesis in the equatorial Atlantic Ocean: pattern, trends, and processes deduced from rock magnetic and geochemical records: In: Wefer G, Mulitza S, Ratmeyer V (eds) The South Atlantic in the Late Quaternary, Springer, pp 461–497

Gac JY, Kane A (1986) Le fleuve Sénégal: I. Bilan hydrologique et flux continentaux de matiéres particulaires á l'embouchure. Sci Géol Bull 39:99–130

Galbraith ED, Kienast M, Jaccard SL, Pedersen TF, Brunelle BG, Sigman DM, Kiefer T (2008) Consistent relationship between global climate and surface nitrate utilization in the western subarctic Pacific throughout the last 500 ka. Paleoceanography 23:PA2212. doi:10.1029/2007PA001518

Ganeshram RS, Pedersen TF, Murray JW (1992) The record of organic carbon burial in Holocene and LGM sediments in the oxygen minimum off northwestern Mexico. Trans Am Geophys Union 73:309

Ganeshram RS, Calvert SE, Pedersen TF, Cowie GL (1999) Factors controlling the burial of organic carbon in laminated and bioturbated sediments off NE Mexico: implications for hydrocarbon preservation. Geochim Cosmochim Acta 63:1723–1734

Ganeshram RS, François R, Commeau J, Brown-Leger SL (2003) An experimental investigation of barite formation in seawater. Geochim Cosmochim Acta 67:2599–2605

Gatti E, Rehak E (1984) Semiconductor drift chamber—An application of a novel charge transport scheme. Nucl Instr and Meth 225:608–614

Ge LQ, Lai WC, Lin YC (2005) Influence of and correction for moisture in rocks, soils and sediments on in situ XRF analysis. X-Ray Spectrom 34:28–34

Gebhardt H, Sarnthein M, Grootes PM, Kiefer T, Kühn H, Schmieder F, Röhl U (2008) Paleonutrient and productivity records from the subarctic North Pacific for Pleistocene glacial terminations I to V. Paleoceanography 23:PA4212. doi:10.1029/2007PA001513

Gil IM, Abrantes F, Hebbeln D (2006) The North Atlantic oscillation forcing through the last 2000 years: spatial variability as revealed by high-resolution marine diatom records from N and SW Europe. Mar Micropaleontol 60:113–129

Goldberg ED (1954) Marine geochemistry I. Chemical scavengers of the sea. J Geol 62:249–265

Goldberg ED, Arrhenius G (1958) Chemistry of Pacific pelagic sediments. Geochem Cosmochim Acta 13:153–212

Gooday AJ, Nott JA (1982) Intracellular barite crystals in two xenophyophores, *Aschemonella ramuliformis* and *Galatheammina* sp. (Protozoa, Rhizopoda) with comments on the taxonomy of *A. ramuliformis*. J Mar Biol Assoc UK 62:595–605

Gribble GW (2000) The natural production of organobromine compounds. Environ Sci Pollut Res Int 7:37–49. doi:10.1065/ espr199910.002

Gribble GW (2003) The diversity of naturally produced organohalogens. Chemosphere 52:289–297

Grootes PM, Stuiver M, Withe JWC, Johnsen S, Jouzel J (1993) Comparison of oxygen isotope records from the GISP2 and GRIP Greenland ice cores. Nature 366:552–554

Grove CA, Nagtegaal R, Zinke J, Scheufen T, Koster B, Kasper S, McCulloch MT, Van den Bergh G, Brummer GJA (2010) River runoff reconstructions from novel spectral luminescence scanning of massive coral skeletons. Coral Reefs 29:579–591. doi:10.1007/s00338-010-0629-y

Grützner J, Rebesco MA, Cooper AK, Forsberg CF, Kryc KA, Wefer G (2003) Evidence for orbitally controlled size variations of the East Antarctic Ice Sheet during the late Miocene. Geology 31:777–780. doi:10.1130/G19574.1

Grützner J, Hillenbrand C-D, Rebesco MA (2005) Terrigenous flux and biogenic silica deposition at the Antarctic continental rise during the late Miocene to early Pliocene: implications for ice sheet stability and sea ice coverage. Glob Planet Change 45:131–149. doi:10.1016/j.gloplacha.2004.09.004

Hanebuth TJJ, Henrich R (2009) Recurrent decadal-scale dust events over Holocene western Africa and their control on canyon turbidite activity (Mauritania). Quat Sci Rev 28:261–270. doi:10.1016/j.quascirev.2008.09.024

Hanebuth TJJ, Lantzsch H (2008) A Late Quaternary sedimentary shelf system under hyperarid conditions: unravelling climatic, oceanographic and sea-level controls (Golfe d'Arguin, Mauritania, NW Africa). Mar Geol 256:77–89. doi:10.1016/j.margeo.2008.10.001

Harff J, Endler R, Emelyanov E, Kotov S, Leipe T, Moros M, Olea R, Tomczak M, Witkowski A (2011) Late Quaternary climate variations reflected in Baltic Sea sediments. In: Harff J, Björck S, Hoth P (eds) The Baltic Sea Basin, vol. 3, pp 99–132. (Central and Eastern European Development Studies (CEEDES)). doi:10.1007/978-3-642–17220-5_5

Hascke M (2006) The Eagle III BKA system, a novel sediment core X-ray fluorescence analyser with very high spatial resolution. In: Rothwell RG (ed) New techniques in sediment core analysis, Geological Society Special Publication 267, pp 31–37. doi:10.1144/ GSL. SP.2006.267.01.02

Haschke M, Scholz W, Theis U, Nicolosi J, Scruggs B, Herzceg L (2002) Description of a new micro-X ray spectrometer. J Phys IV 12:6–83. doi:10.1051/jp 4:20020216

Haug GH, Hughen KA, Sigman DM, Peterson LC, Röhl U (2001) Southward migration of the intertropical convergence zone through the Holocene. Science 293:1304–1308

Haug GH, Günther D, Peterson LC, Sigman DM, Hughen KA, Aeschlimann B (2003) Climate and the collapse of Mayan civilisation. Science 299:1731–1735. doi:10.1126/science.1080444

Hebbeln D, Cortés J (2001) Sedimentation in a tropical fjord: Golfo Dulce, Costa Rica. Geo Mar Lett 20:142–148. doi:10.1007/s003670000047

Hebbeln D, Scheurle C, Lamy F (2003) Depositional history of the Helgoland Mud Area, German Bight, North Sea. Geo Mar Lett 23:81–90. doi: 10.1007/s00367-003-0127-0

Hebbeln D, Knudsen K-L, Gyllencreutz R, Kristensen P, Klitgaard-Kristensen D, Backman J, Scheurle C, Jiang H, Gil I, Smelror M, Jones PD, Sejrup HP (2006) Late Holocene coastal hydrographic and climate changes in the eastern North Sea. Holocene 16:987–1001. doi: 10.1177/0959683606hl989rp

Helmke JP, Bauch HA, Röhl U, Mazaud A (2005) Changes in sedimentation patterns of the Nordic Seas region across the mid-Pleistocene. Mar Geol 215:107–122. doi:10.1016/j.margeo.2004.12.006

Helmke JP, Bauch HA, Röhl U, Kandiano ES (2008) Uniform climate development between the subtropical and subpolar Northeast Atlantic across marine isotope stage 11. Clim Past Discuss 4:433–457 (www.clim-past-discuss.net/4/433/2008/)

Henrich R, Cherubini Y, Meggers H (2010) Climate and sea level induced turbidite activity in a canyon system offshore the hyperarid Western Sahara (Mauritania): the Timiris Canyon. Mar Geol 275:178–198. doi:10.1016/j.margeo.2010.05.011

Hepp DA, Mörz T, Grützner J (2006) Pliocene glacial cyclicity in deep-sea sediment drifts (Antarctic Peninsula Pacific Margin). Palaeogeogr Palaeoclimatol Palaeoecol 231:181–198. doi:10.1016/j.palaeo.2005.07.030

Hepp DA, Mörz T, Hensen C, Frederichs T, Kasten S, Riedinger N, Hay WW (2009) A late Miocene–early Pliocene Antarctic deepwater record of repeated iron reduction events. Mar Geol 266:198–211

Hibbert FD, Austin WEN, Leng MJ, Gatliff RW (2010) British Ice Sheet dynamics inferred from North Atlantic ice-rafted debris records spanning the last 175000 years. J Quat Sci 25:461–482. doi:10.1002/jqs.1331

Hillenbrand C-D, Kuhn G, Frederichs T (2009) Record of a Mid-Pleistocene depositional anomaly in West Antarctic continental margin sediments: an indicator for ice-sheet collapse? Quat Sci Rev 28:1147–1159. doi: 10.1016/j.quascirev.2008.12.010

Hoang van L, Clift PD, Schwab AM, Huuse M, Nguyen DA, Zhen S (2010) Large-scale erosional response of SE Asia to monsoon evolution reconstructed from sedimentary records of the Song Hong-Yinggehai and Qiongdongnan basins, South China Sea. Geol Soc Spec Publ 342:219–244. doi:10.1144/ SP342.13

Hodell DA, Channell JET, Curtis JH, Romero OE, Röhl U (2008) Onset of 'Hudson Strait' Heinrich events in the Eastern North Atlantic at the end of the Middle Pleistocene transition (~640 ka)? Paleoceanography 23:PA4218. doi:10.1029/2008PA001591

Hodell DA, Evans HF, Channell JET, Curtis JH (2010) Phase relationships of North Atlantic ice-rafted debris and surface-deep climate proxies during the last glacial period. Quat Sci Rev 29:3875–3886. doi:10.1016/j.quascirev.2010.09.006

Hofmann DI, Fabian K (2007) Rock magnetic properties and relative paleointensity stack for the last 300 ka based on a stratigraphic network from the subtropical and subantarctic South Atlantic. Earth Planet Sci Lett 260:297–312. doi:10.1016/j.epsl.2007.05.042

Hofmann DI, Fabian K, Schmieder F, Donner B, Bleil U (2005) A stratigraphic network across the Subtropical Front in the central South Atlantic: multi-parameter correlation of magnetic susceptibility, density, X-ray fluorescence and $\delta^{18}O$ records. Earth Planet Sci Lett 240:694–709. doi:10.1016/j.epsl.2005.09.048

Holbourn A, Kuhnt W, Schulz M, Erlenkeuser H (2005) Impacts of orbital forcing and atmospheric carbon dioxide on Miocene ice-sheet expansion. Nature 438:483–487. doi:10.1038/nature04123

Holbourn A, Kuhnt W, Schulz M, Flores J-A, Andersen N (2007) Orbitally-paced climate evolution during the middle Miocene "Monterey" carbon-isotope excursion. Earth Planet Sci Lett 261:534–550. doi:10.1016/j.epsl.2007.07.026

Holzwarth U, Meggers H, Esper O, Kuhlmann H, Freudenthal T, Hensen C, Zonneveld KAF (2010) NW African climate variations during the last 47,000 years: evidence from organic-walled dinoflagellate cysts. Palaeogeogr Palaeoclimatol Palaeoecol 291:443–455. doi:10.1016/j.palaeo.2010.03.013

Huerta-Diaz MA, Morse JW (1992) Pyritisation of trace metals in anoxic marine sediments. Geochim Cosmochim Acta 56:2681–2702

Ingram WC, Meyers SR, Brunner CA, Martens CS (2010) Late Pleistocene–Holocene sedimentation surrounding an active seafloor gas-hydrate and cold-seep field on the Northern Gulf of Mexico slope. Mar Geol 278:45–53. doi:10.1016/j.margeo.2010.09.002

Itambi AC, von Dobeneck T, Adegbie AT (2010) Millennial-scale precipitation changes over Central Africa during the late Quaternary and Holocene: evidence in sediments from the Gulf of Guinea. J Quat Sci 25:267–279. doi:10.1002/jqs.1306

Itambi AC, von Dobeneck T, Mulitza S, Bickert T, Heslop D (2009) Millennial-scale northwest African droughts related to Heinrich events and Dansgaard-Oeschger cycles: evidence in marine sediments from offshore Senegal. Paleoceanography 24:PA1205. doi:10.1029/2007PA001570

Ivanochko TS, Ganeshram RS, Brummer GJA, Ganssen G, Jung SJA, Moreton SG, Kroon D (2005) Variations in tropical convection as an amplifier of global climate change at the millennial scale. Earth Planet Sci Lett 235:302–314

Ivanov MV (1981) The global biogeochemical sulphur Cycle. In: Likens GE (ed) Some perspectives of the major biogeochemical cycles SCOPE, pp 61–78

Jaccard SL, Haug GH, Sigman DM, Pedersen TF, Thierstein HR, Röhl U (2005) Glacial/interglacial changes in Subarctic North Pacific stratification. Science 308:1003–1006. doi:10.1126/science.1108696

Jaccard SL, Galbraith ED, Sigman DM, Haug GH, Francois R, Pedersen TF, Dulski P, Thierstein HR (2009) Subarctic Pacific evidence for a glacial deepening of the oceanic respired carbon pool. Earth Planet Sci Lett 277:156–165. doi: 10.1016/j.epsl.2008.10.017

Jaccard SL, Galbraith ED, Sigman DM, Haug GH (2010) A pervasive link between Antarctic ice core and subarctic Pacific sediment records over the past 800 kyrs. Quat Sci Rev 29:206–212. doi:10.1016/j.quascirev.2009.10.007

Jaeschke A, Rühlemann C, Arz H, Heil G, Lohmann G (2007) Coupling of millennial-scale changes in sea surface temperature and precipitation off northeastern Brazil with high-latitude climate shifts during the last glacial period. Paleoceanography 22:PA4206. doi:10.1029/2006PA001391

Jahn B, Donner B, Müller PJ, Röhl U, Schneider R, Wefer G (2003) Pleistocene variations in dust input and marine productivity in the northern Benguela Current: evidence of evolution of global glacial-interglacial cycles. Palaeogeogr Palaeoclimatol Palaeoecol 193:515–533. doi:10.1016/S0031-0182(03)00264-5

Jahn B, Schneider RR, Mueller PJ, Donner B, Röhl U (2005) Response of tropical African and East Atlantic climates to orbital forcing over the last 1.7 Ma. In Head MJ, Gibbard PL (eds) Early-middle Pleistocene transitions: the land ocean evidence, Geological Society Special Publication 247, pp 65–84. doi:10.1144/GSL.SP.2005.247.01.04

Jakobsson M, Løvlie R, Al-Hanbali H, Arnold E, Backman J, Mörth M (2000) Manganese and color cycles in Arctic Ocean sediments constrain Pleistocene chronology. Geology 28:23–26

Jansen JHF, Dupont L (2001) Data report: a revised composite depth record for Site 1077 based on magnetic susceptibility and XRF (CORTEX) data. In: Wefer G, Berger WH, Richter C (eds) Proc Ocean Drill Program Part B Sci. Results 175:1–10. doi:10.2973/odp.proc.sr.175.236.2001

Jansen JHF, De Lange GJ, Van Bennekom AJ et al (1990) Paleoceanography and geochemistry of the Angola Basin (South Atlantic Ocean). Cruise Report, RV Tyro, 30 September-19 November 1989. Texel, Netherlands Institute for Sea Research

Jansen JHF, Van der Gaast SJ, Koster B, Vaars A (1992) CORTEX, an XRF scanner for chemical analyses of sediment cores. GEOMAR Rep/Ber Rep Geol-Paläontol Inst Univ Kiel 15/57:155

Jansen JHF, Ufkes E, Schneider RR (1996) Late Quaternary movements of the Angola-Benguela Front, SE Atlantic, and implications for advection in the equatorial ocean. In: Wefer G, Berger WH, Siedler G, Webb D (eds) The South Atlantic: present and past circulation. Springer, Berlin, pp 363–410

Jansen JHF, Van der Gaast SJ, Koster B, Vaars A (1998) CORTEX, a shipboard XRF-scanner for element analyses in split sediment cores. Mar Geol 151:143–153

Jenkins R (1988) X-ray fluorescence spectrometry. Wiley

Jenkins R, De Vries JL (1970) Practical X-ray spectrometry. Macmillan, London

Jiménez-Espejo FJ, Martínez-Ruiz F, Finlayson C, Paytan A, Sakamoto T, Ortega-Huertas M, Finlayson G, Iijima K, Gallego-Torres D, Fa D (2007a) Climate forcing and Neanderthal extinction in Southern Iberia: insights from a multiproxy marine record. Quat Sci Rev 26:836–852. doi:10.1016/j.quascirev.2006.12.013

Jimenez-Espejo FJ, Martinez-Ruiz F, Sakamoto T, Iijima K, Gallego-Torres D, Harada N (2007b) Paleoenvironmental changes in the western Mediterranean since the last glacial maximum: High resolution multiproxy record from the Algero–Balearic Basin. Palaeogeogr Palaeoclimatol Palaeoecol 246:292–306. doi:10.1016/j.palaeo.2006.10.005

Johnsen SJ, Clausen HB, Dansgaard W, Fuhrer K, Gundestrup N, Hammer CU, Iversen P, Jouzel J, Stauffer B, Steffensen JP (1992) Irregular glacial interstadials recorded in a new Greenland ice core. Nature 359:311–313

Jorry SJ, Jégou I, Emmanuel L, Jacinto RS, Savoye B (2011) Turbiditic levee deposition in response to climate changes: the Var Sedimentary Ridge (Ligurian Sea). Mar Geol 279:148–161. doi:10.1016/j.margeo.2010.10.021

Jullien E, Grousset F, Malaizé B, Duprat J, Sanchez-Goni MF, Eynaud F, Charlier K, Schneider R, Bory A, Bout V, Flores JA (2007) Low-latitude 'dusty events' vs. high-latitude 'icy Heinrich events'. Quat Res 68:379–386. doi:10.1016/j.yqres.2007.07.007

Kaars van der S, Bergh van den GD (2004) Anthropogenic changes in the landscape of west Java (Indonesia) during historic times, inferred from a sediment and pollen record from Teluk Banten. J Quat Sci 19:229–239. doi:10.1002/jqs.804

Kaiser J, Lamy F, Arz HW, Hebbeln D (2007) Dynamics of the millennial-scale sea surface temperature and Patagonian Ice Sheet fluctuations in southern Chile during the last 70 kyr (ODP Site 1233). Quat Int 161:77–89. doi:10.1016/j.quaint.2006.10.024

Karlin R, Lyle M, Heath GR (1987) Authigenic magnetite formation in sub-oxic marine sediments. Nature 326:490–493. doi:10.1038/326490a0

Kattan Z, Gac JY, Probst JL (1987) Suspended sediment load and mechanical erosion in the Senegal Basin—estimation of the surface runoff concentration and relative contributions of channel and slope erosion. J Hydrol 92:59–76

Kelly DC, Nielsen TMJ, McCarren HK, Zachos JC, Röhl U (2010) Spatiotemporal patterns of carbonate sedimentation in the South Atlantic: implications for carbon cycling during the Paleocene–Eocene thermal maximum. Palaeogeogr Palaeoclimatol Palaeoecol 293:30–40. doi:10.1016/j.palaeo.2010.04.027

Kent DV (1982) Apparent correlation of paleomagnetic intensity and climatic records in deep-sea sediments. Nature 299:538–539

Kido Y, Koshikawa T, Tada R (2006) Rapid and quantitative major element analysis method for wet fine-grained sediments using an XRF microscanner. Quat Res 229:209–225

Kim S-Y, Scourse J, Marret F, Lim D-I (2010) A 26,000-year integrated record of marine and terrestrial environmental change off Gabon, west equatorial Africa. Palaeogeogr Palaeoclimatol Palaeoecol 297:428–438. doi:10.1016/j.palaeo.2010.08.026

Kinsman DJJ (1969) Interpretation of $Sr^{2+}$ concentrations in carbonate minerals and rocks. J Sediment Petrol 39:486–507

Kissel C, Laj C, Kienast M, Bolliet T, Holbourn A, Hill P, Kuhnt W, Braconnot P (2010) Monsoon variability and deep oceanic circulation in the western equatorial Pacific over the last climatic cycle: insights from sedimentary magnetic properties and sortable silt. Paleoceanography 25:PA3215. doi:10.1029/2010PA001980

Kleiven HF, Kissel C, Laj C, Ninnemann US, Richter TO, Cortijo E (2007) Reduced North Atlantic Deep Water coeval with the Glacial Lake Agassiz fresh water outburst. Science 319:60–64. doi:10.1126/science.1148924

Klöcker R, Henrich R (2006) Recent and Late Quaternary pteropod preservation on the Pakistan shelf and continental slope. Mar Geol 231:103–111

Klump J, Hebbeln D, Wefer G (2000) The impact of sediment provenance on barium-based productivity estimates. Mar Geol 169:259–271

Konfirst MA, Kuhn G, Monien D, Scherer RP (2011) Correlation of Early Pliocene diatomite to low amplitude Milankovitch cycles in the ANDRILL AND-1B drill core. Mar Micropaleontol 80:114–124. doi:10.1016/j.marmicro.2011.06.005

Krastel S, Wynn RB, Hanebuth TJJ, Henrich R, Holz C, Meggers H, Kuhlmann H, Georgiopoulou A, Schulz HD (2006) Mapping of seabed morphology and shallow sediment structure of the Mauritania continental margin, Northwest Africa: some implications for geohazard potential. Norw J Geol 86:163–176

Kreiser AM, Appleby PG, Natkanski J, Rippey B, Battarbee RW (1990) Afforestation and Lake acidification—a comparison of 4 sites in Scotland. Philos Trans R Soc London Ser B 327:377–383

Krinsley D, Bieri R (1959) Changes in the chemical composition of pteropod shells after deposition on the sea floor. J Paleontol 33:682–684

Kuhlmann H, Freudenthal T, Helmke P, Meggers H (2004a) Reconstruction of paleoceanography off NW Africa for the last 40,000 years: influence of local and regional factors on sediment accumulation. Mar Geol 207:209–234. doi:10.1016/j.margeo.2004.03.017

Kuhlmann H, Meggers H, Freudenthal T, Wefer G (2004b) The transition of the monsoonal and the N Atlantic climate system off NW Africa during the Holocene. Geophys Res Lett 31:L22204. doi:10.1029/2004GL021267

Kuijpers A, Troelstra SR, Prins MA, Linthout K, Akhmetzhanov A, Bouryak S, Bachmann MF, Lassen S, Rasmussen S, Jensen JB (2003) Late Quaternary sedimentary processes and ocean circulation changes at the Southeast Greenland margin. Mar Geol 195:109–129. doi:10.1016/S0025-3227(02)00684-9

Kujau A, Nürnberg D, Zielhofer C, Bahr A, Röhl U (2010) Mississippi River discharge over the last ~560,000 years—indications from X-ray fluorescence core-scanning. Palaeogeogr Palaeoclimatol Palaeoecol 298:311–318. doi:10.1016/j.palaeo.2010.10.005

Kullenberg B (1947) The piston core sampler. Sven Hydrogr Biol Rommissionens Skr Tredje Ser Hydrogr 1(2):1–46

Kwiecien O, Arz HW, Lamy F, Wulf S, Bahr A, Röhl U, Haug GH (2008) Estimated reservoir ages of the Black Sea since the last Glacial. Radiocarbon 50:99–118

Kwiecien O, Arz HW, Lamy F, Plessen B, Bahr A, Haug GH (2009) North Atlantic control on precipitation pattern in the eastern Mediterranean/Black Sea region during the last glacial. Quat Res 71:375–384. doi:10.1016/j.yqres.2008.12.004

Lamy F, Hebbeln D, Röhl U, Wefer G (2001) Holocene rainfall variability in southern Chile: a marine record of latitudinal shifts of the Southern Westerlies. Earth Planet Sci Lett 185:369–382. doi:10.1016/S0012–821X(00)00381–2

Lamy F, Kaiser J, Ninnemann U, Hebbeln D, Arz HW, Stoner J (2004) Antarctic timing of surface water changes off Chile and Patagonian ice-sheet response. Science 304:1959–1962. doi:10.1126/science.1097863

Land van der C, Mienis F, Haas de H, Frank N, Swennen R, Van Weering TCE (2010) Diagenetic processes in carbonate mound sediments at the south-west Rockall Trough margin. Sedimentology 57:912–931. doi:10.1111/j.1365–3091.2009.01125.x

Land van der C, Mienis F, Haas de H, Stiger de HC, Swennen R, Reijmer JJG, van Weering TCE (2011) Paleo-redox fronts and their formation in carbonate mound sediments from the Rockall Trough. Mar Geol 284:86–95. doi:10.1016/j.margeo.2011.03.010

Lebreiro SM, Voelker AHL, Vizcaino A, Abrantes FG, Alt-Epping U, Jung S, Thouveny N, Gràcia E (2009) Sediment instability on the Portuguese continental margin under abrupt glacial climate changes (last 60 kyr). Quat Sci Rev 28:3211–3223. doi:10.1016/j.quascirev.2009.08.007

Lesack LFW, Hecky RE, Melack JM (1984) Transport of carbon, nitrogen, phosphorus and major solutes in the Gambia River, West Africa. Limnol Oceanogr 29:816–830

Leslie BW, Hammond DE, Berelson WM, Lund SP (1990) Diagenesis in anoxic sediments from the California borderland and its influence on iron, sulfur and magnetite behavior. J Geophys Res 95:4453–4470

Lippold J, Grützner J, Winter D, Lahaye Y, Mangini A, Christl M (2009) Does sedimentary $^{231}Pa/^{230}Th$ from the Bermuda Rise monitor past Atlantic Meridional Overturning Circulation? Geophys Res Lett 36:L12601. doi:10.1029/2009GL038068

Liu LW, Chen J, Chen Y et al (2002) Variation of Zr/Rb ratios on the Loess Plateau of central China during the last 130 ka and its implications for winter monsoon. Chin Sci Bull 47:1298–1302

López-Martínez C, Grimalt JO, Hoogakker B, Grützner J, Vautravers MJ, McCave IN (2006) Abrupt wind regime changes in the North Atlantic Ocean during the past 30000–60000 years. Paleoceanography 21:PA4215. doi:10.1029/2006PA001275

Löwemark L, Jakobsson M, Mörth M, Backman J (2008) Arctic Ocean manganese contents and sediment colour cycles. Polar Res 27:105–113. doi:10.1111/j.1751-8369.2008.00055.x

MacLeod KG, Huber BT, Pletsch T, Röhl U, Kucera M (2001) Maastrichtian foraminiferal and paleoceanographic changes on Milankovitch time scales. Paleoceanogr 16:133–154. doi:10.1029/2000PA000514

Malcolm SJ, Price NB (1984) The behaviour of iodine and bromine in estuarine surface sediments. Mar Chem 15:263–271

Marsh R, Mills RA, Green DRH, Salter I, Taylor S (2007) Controls on sediment geochemistry in the Crozet region. Deep Sea Res Part II 54:2260–2274. doi:10.1016/j.dsr2.2007.06.004

Mayer LM, Schick LL, Allison MA, Ruttenberg KC, Bentley SJ (2007) Marine vs. terrigenous matter in Louisiana coastal sediments: the uses of bromine:organic carbon ratios. Mar Chem 107:244–254. doi:10.1016/j.marchem.2007.07.007

McGregor HV, Dupont L, Stuut J-BW, Kuhlmann H (2009) Vegetation change, goats, and religion: a 2000-year history of land use in southern Morocco. Quat Sci Rev 28:1434–1448. doi:10.1016/j.quascirev.2009.02.012

McHugh CMG, Gurung D, Giosan L, Ryan WBF, Mart Y, Sancar U, Burckle L, Cagatay MN (2008) The last reconnection of the Marmara Sea (Turkey) to the World Ocean: A paleoceanographic and paleoclimatic perspective. Mar Geol 255:64–82. doi:10.1016/j.margeo.2008.07.005

McManus J, Berelson WM, Klinkhammer GP, Johnson KS, Coale KH, Anderson RF, Kumar N, Burdige DJ, Hammond DE, Brumsack HJ, McCorkle DC, Rushdi A (1998) Geochemistry of barium in marine sediments: implications for its use as a paleoproxy. Geochim et Cosmochim Acta 62:3453–3473

Medina-Elizalde M, Rohling EJ (2012) Collapse of Classic Maya civilization related to modest reduction in precipitation. Science 335:956–959

Mohtadi M, Romero OE, Kaiser J, Hebbeln D (2007) Cooling of the southern high latitudes during the medieval period and its effect on ENSO. Quat Sci Rev 26:1055–1066. doi:10.1016/j.quascirev.2006.12.008

Moldenhauer K-M, Zielhofer C, Faust D (2008) Heavy metals as indicators for Holocene sediment provenance in a semi-arid Mediterranean catchment in northern Tunisia. Quat Int 189:129–134

Møller HS, Jensen KG, Kuijpers A, Aagaard-Sørensen S, Seidenkrantz M-S, Prins M, Endler R, Mikkelsen N (2006) Late Holocene environment and climatic changes in Ameralik Fjord, southwest Greenland: evidence from the sedimentary record. Holocene 16:685–695. doi:10.1191/0959683606hl963rp

Monien D, Kuhn G, von Eynatten H, Talarico FM (2010) Geochemical provenance analysis of fine-grained sediment revealing Late Miocene to recent paleo environmental changes in the Western Ross Sea, Antarctica. Glob Planet Change. doi:10.1016/j.gloplacha.2010.05.001

Montero-Serrano JC, Bout-Roumazeilles V, Sionneau T, Tribovillard N, Bory A, Flower BP, Riboulleau A, Martinez P, Billy I (2010) Changes in precipitation regimes over North America during the Holocene as recorded by mineralogy and geochemistry of Gulf of Mexico sediments. Glob Planet Change 74:132–143. doi:10.1016/j.gloplacha.2010.09.004

Moran SB, Moore RM (1992) Kinetics of the removal of dissolved aluminium by diatoms in seawater: a comparison with thorium. Geochim Cosmochim Acta 56:3365–3374

Moreno A, Nave S, Kuhlmann H, Canals M, Targarona J, Freudenthal T, Abrantes F (2002) Productivity response in the North Canary Basin to climate changes during the last 250000 years: a multi-proxy approach. Earth Planet Sci Lett 196:147–159

Moreno T, Querol X, Castillo S, Alastuey A, Cuevas E, Herrmann L, Mounkaila M, Elvira J, Gibbons W (2006) Geochemical variations in aeolian mineral particles from the Sahara–Sahel dust corridor. Chemosphere 65:261–270

Moseley HGJ (1913/1914) High frequency spectra of the elements. Philos Mag 26:1024–1034 (27:703–713)

Mulitza S, Prange M, Stuut J-B, Zabel M, von Dobeneck T, Itambi AC, Nizou J, Schulz M, Wefer G (2008) Sahel megadroughts triggered by glacial slowdowns of Atlantic meridional overturning. Paleoceanography 23:PA4206. doi:10.1029/2008PA001637

Müller M, Handley KM, Lloyd J, Pancost RD, Mills RA (2010) Biogeochemical controls on microbial diversity in seafloor sulphidic sediments. Geobiology 8:309–326. doi:10.1111/j.1472-4669.2010.00242.x

Nizou J, Hanebuth TJJ, Heslop D, Schwenk T, Palamenghi L, Stuut J-B, Henrich R (2010) The Senegal River mud belt: A high-resolution archive of paleoclimatic change and coastal evolution. Mar Geol 278:150–164. doi:10.1016/j.margeo.2010.10.002

Nizou J, Hanebuth TJJ, Vogt C (2011) Deciphering signals of late Holocene fluvial and aeolian supply from a shelf sediment depocentre off Senegal (north-west Africa). J Quat Sci 26:411–421. doi:10.1002/jqs.1467

Nørgaard-Pedersen N, Austin WEN, Howe JA, Shimmield T (2006) The Holocene record of Loch Etive, western Scotland: influence of catchment and relative sea level changes. Mar Geol 228:55–71. doi:10.1016/j.margeo.2006.01.001

Norris RD, Röhl U (1999) Carbon cycling and chronology of climate warming during the Palaeocene/Eocene transition. Nature 401:775–778. doi:10.1038/44545

O'Regan M, John K St, Moran K, Backman J, King J, Haley BA, Jakobsson M, Frank M, Röhl U (2010) Plio-Pleistocene trends in ice rafted debris on the Lomonosov Ridge. Quat Int 219:168–176. doi:10.1016/j.quaint.2009.08.010

Os van BJH, Middelburg JJ, De Lange GJ (1991) Possible diagenetic mobilisation of barium in sapropelic sediment from the eastern Mediterranenan. Mar Geol 100:125–136.

Pälike H, Shackleton NJ, Röhl U (2001) Astronomical forcing in late Eocene sediments. Earth Planet Sci Lett 193:589–602. doi:10.1016/S0012–821X(01)00501–5

Passier HF, Middelburg JJ, De Lange GJ, Bottcher ME (1999) Modes of sapropel formation in the eastern Mediterranean: some constraints based on pyrite properties. Mar Geol 153:199–219

Payne R, Blackford J, van der Plicht J (2008) Using cryptotephras to extend regional tephrochronologies: an example from southeast Alaska and implications for hazard assessment. Quat Res 69:42–55

Paytan A, Kastner M (1996) Benthic Ba fluxes in the central equatorial Pacific: implications for the oceanic Ba cycle. Earth Planet Sci Lett 142:439–450

Peck VL, Hall IR, Zahn R, Grousset F, Hemming SR, Scourse JD (2007) The relationship of Heinrich events and their European precursors over the past 60 ka BP: a multi-proxy ice-rafted debris provenance study in the North East Atlantic. Quat Sci Rev 26:862–875. doi:10.1016/j.quascirev.2006.12.002

Peterson LC, Haug GH, Hughen KA, Röhl U (2000) Rapid changes in the hydrologic cycle of the tropical Atlantic during the last glacial. Science 290:1947–1951. doi:10.1126/science.290.5498.1947

Peterson ML, Carpenter R (1986) Arsenic distributions in pore waters and sediments of Puget Sound, Lake Washington, the Washington coast and Saanich Inlet, BC. Geochim Cosmochim Acta 50:353–369

Phleger FB (1947) Foraminifera of three submarine cores from the Tyrrhenian Sea. Oceanog Inst Göteborg Meddel 13:1–19

Phleger FB, Parker FL, Pierson JF (1953) North Atlantic foraminifera. Rep Swed Deep-Sea Exped 1947–1948 VIII Sediment cores from the North Atlantic Ocean 1. Elanders Boktryckeri Aktiebolag, Göteborg, pp 122

Pierau R, Hanebuth TJJ, Krastel S, Henrich R (2010) Late Quaternary climatic events and sea-level changes recorded by turbidite activity, Dakar Canyon, NW Africa. Quat Res 73:385–392. doi:10.1016/j.yqres.2009.07.010

Pierau R, Henrich R, Preiß-Daimler I, Krastel S, Geersen J (2011) Sediment transport and turbidite architecture in the submarine Dakar Canyon off Senegal, NW Africa. J Afr Earth Sci 60:196–208. doi:10.1016/j.jafrearsci.2011.02.010

Pirlet H, Wehrmann LM, Brunner B, Frank N, Dewanckele J, Rooij Van D, Foubert A, Swennen R, Naudts L, Boone M, Cnudde V, Henriet J-P (2010) Diagenetic formation of gypsum and dolomite in a cold-water coral mound in the Porcupine Seabight, off Ireland. Sedimentology 57:786–805. doi:10.1111/j.1365-3091.2009.01119.x

Piva A, Asioli A, Schneider RR, Trincardi F, Andersen N, Colmenero-Hidalgo E, Dennielou B, Flores J-A, Vigliotti L (2008) Climatic cycles as expressed in sediments of the PROMESS1 borehole PRAD1-2, central Adriatic, for the last 370 ka: 1. Integrated stratigraphy. Geochem Geophys Geosyst 9:Q01R01. doi:10.1029/2007GC001713

Pourmand A, Marcantonio F, Schulz H (2004) Variations in productivity and eolian fluxes in the northeastern Arabian Sea during the past 110 ka. Earth Planet Sci Lett 221:39–54.

Potts PJ (1987) A handbook of silicate rock analysis. Blackie, Glasgow

Prins MA, Postma G, Weltje GJ (2000) Controls on terrigenous sediment supply to the Arabian Sea during the late Quaternary: the Makran continental slope. Mar Geol 169:351–371. doi:10.1016/S0025-3227(00)00087-6

Prins MA, Troelstra SR, Kruk RW, Borg van der K, de Jong AFM, Weltje GJ (2001) The late Quaternary sedimentary record of Reykjanes Ridge, North Atlantic. Radiocarbon 43:939–947

Puchelt H (1969–1978) Barium: abundance in rock-forming minerals. In: Wedepohl KH, Correns CW, Shaw DM, Turekian KK, Zedmann J (eds) Handbook of Geochemistry. Springer, Berlin, pp D1–D18

Radczewski OE (1939) Eolian deposits in marine sediments. In: Trask PD (ed), Recent marine sediments. AAPG Tulsa Oklahoma, pp 496–502

Rebolledo L, Sepúlveda J, Lange CB, Pantoja S, Bertrand S, Hughen K, Figueroa D (2008) Late Holocene marine productivity changes in Northern Patagonia-Chile inferred from a multi-proxy analysis of Jacaf Channel sediments. Estuarine Coastal Shelf Sci 80:314–322. doi:10.1016/j.ecss.2008.08.016

Ren J, Jiang H, Seidenkrantz M-S, Kuijpers A (2009) A diatom-based reconstruction of Early Holocene hydrographic and climatic change in a southwest Greenland fjord. Mar Micropaleontol 70:166–176. doi:10.1016/j.marmicro.2008.12.003

Revel M, Ducassou E, Grousset FE, Bernasconi SM, Migeon S, Revillon S, Mascle J, Murat A, Zaragosi S, Bosch D (2010) 100,000 years of African monsoon variability recorded in sediments of the Nile margin. Quat Sci Rev 29:1342–1362. doi:10.1016/j.quascirev.2010.02.006

Rex RW, Goldberg ED (1958) Quartz content of pelagic sediments of the Pacific Ocean. Tellus 19:153–159

Rey D, Rubio B, Mohamed K, Vilas F, Alonso B, Ercilla G, Rivas T (2008) Detrital and early diagenetic processes in Late Pleistocene and Holocene sediments from the SW Galicia Bank inferred from high-resolution enviromagnetic and geochemical records. Mar Geol 249:64–92.

Richter TO, Lassen S, van Weering TCE, De Haas H (2001) Magnetic susceptibility patterns and provenance of ice-rafted material at Feni Drift, Rockall Trough: implications for the history of the British-Irish ice sheet. Mar Geol 173:37–54. doi:10.1016/S0025-3227(00)00165–1

Richter TO, Van der Gaast S, Koster B, Vaars A, Gieles R, de Stigter HC, de Haas H, van Weering TCE (2006) The Avaatech XRF Core Scanner: technical description and applications to NE Atlantic sediments. In: Rothwell RG (ed) New techniques in sediment core analysis, Geol Soc Spec Publ 267, pp 39–50. doi:10.1144/ GSL.SP.2006.267.01.03

Rieder N, Ott HA, Pfundstein P, Schoch R (1982) X-ray microanalysis of the mineral content of some protozoa. J Protozool 29:15–18

Rincón-Martínez D, Lamy F, Contreras S, Leduc G, Bard E, Saukel C, Blanz T, Mackensen A Tiedemann R (2010) More humid interglacials in Ecuador during the past 500 kyr linked to latitudinal shifts of the equatorial front and the Intertropical Convergence Zone in the eastern tropical Pacific. Paleoceanography 25:PA2210. doi:10.1029/2009PA001868

Risebrobakken B, Balbon E, Dokken T, Jansen E, Kissel C, Labeyrie L, Richter T, Senneset L (2006) The penultimate deglaciation: high-resolution paleoceanographic evidence from a north-south transect along the eastern Nordic Seas. Earth Planet Sci Lett 241:505–516. doi:10.1016/j.epsl.2005.11.032

Rogerson M, Rohling EJ, Weaver PPE (2006a) Promotion of meridional overturning by Mediterranean-derived salt during the last deglaciation. Paleoceanography 21:PA4101. doi:10.1029/2006PA001306

Rogerson M, Weaver PPE, Rohling EJ, Lourens LJ, Murray JW, Hayes A (2006b) Colour logging as a tool in high-resolution palaeoceanography. In: Rothwell RG (ed) New techniques in sediment core analysis. Geol Soc Spec Publ 267:99–112. doi:10.1144/ GSL.SP.2006.267.01.07

Röhl U, Abrams LJ (2000) High-resolution, downhole and non-destructive core measurements from Sites 999 and 1001 in the Caribbean Sea: application to the Late Paleocene Thermal Maximum. Proc Ocean Drill Program Part B Sci Results 165:191–203. doi:10.2973/odp.proc.sr.165.009.2000

Röhl U, Bralower TJ, Norris RD, Wefer G (2000) New chronology for the late Paleocene thermal maximum and its environmental implications. Geology 28:927–930. doi:10.1130/0091-7613(2000)28<927NCFTLP>2.0.CO;2

Röhl U, Ogg JG, Geib TL, Wefer G (2001) Astronomical calibration of the Danian time scale. In: Norris RD, Kroon D, Klaus A (eds) Western North Atlantic Paleogene and Cretaceous Paleoceanography. Geol Soc Spec Publ 183:163–183. doi: 10.1144/ GSL.SP.2001.183.01.09

Röhl U, Norris RD, Ogg JG (2003) Cyclostratigraphy of upper Paleocene and late Eocene sediments at Blake Nose Site 1051 (western North Atlantic). In: Gingerich P, Schmitz B, Thomas E, Wing S (eds) Causes and Consequences of Globally Warm Climates in the Early Paleogene, Geol Soc of Am (GSA) Spec Pap Ser 369:567–588. doi:10.1130/0–8137-2369-8.567

Röhl U, Brinkhuis H, Fuller M (2004) On the search for the Paleocene/Eocene boundary in the Southern Ocean: exploring ODP Leg 189 Holes 1171D and 1172D. In: Exon NF, Malone M, Kennett JP (eds) The Cenozoic Southern Ocean and Climate Change between Australia and Antarctica. Am Geophys Union Geophys Monogr Ser 151:113–126

Röhl U, Westerhold T, Bralower TJ, Zachos JC (2007) On the duration of the Paleocene-Eocene Thermal Maximum (PETM). Geochem Geophys Geosyst 8:Q12002. doi:10.1029/2007GC001784

Rohling EJ, Grant K, Hemleben C, Kucera M, Roberts AP, Schmeltzer I, Schulz H, Siccha M, Siddall M, Trommer G (2008) New constraints on the timing and amplitude of sea level fluctuations during early to middle Marine Isotope Stage 3. Paleoceanography 23:PA3219. doi:10.1029/2008PA001617

Rollinson HR (1993) Using geochemical data: evaluation, presentation, interpretation. Pearson Harlow Longman, NJ

Romero OE, Kim J-H, Donner B (2008) Submillennial-to-millennial variability of diatom production off Mauritania, NW Africa, during the last glacial cycle. Paleoceanography 23:PA3218. doi:10.1029/2008PA001601

Rooij van D, Blamart D, De Mol L, Mienis F, Pirlet H, Wehrmann LM, Barbieri R, Maignien L, Templer SP, Haas de H, Hebbeln D, Frank N, Larmagnat S, Stadnitskaia A, Stivaletta N, Weering van T, Zhang Y, Hamoumi N, Cnudde V, Duyck P, Henriet J-P, The MiCROSYSTEMS MD 169 shipboard party (2011) Cold-water coral mounds on the Penduick Escarpment, Gulf of Cadiz: the MiCROSYSTEMS project approach. Mar Geol 282:102–117. doi:10.1016/j.margeo.2010.08.012

Rooij van D, Blamart D, Richter T, Wheeler A, Kozachenko M, Henriet J-P (2007) Quaternary sediment dynamics in the Belgica mound province, Porcupine Seabight: ice-rafting events and contour current processes. Int J Earth Sci 96:121–140. doi:10.1007/s00531-006-0086-6

Rothwell RG (1989) Minerals and mineraloids in marine sediments: an optical identification guide. Elsevier Applied Science, London

Rothwell RG, Hoogakker B, Thomson J, Croudace IW, Frenz M (2006) Turbidite emplacement on the southern Balearic Abyssal Plain (western Mediterranean Sea) during Marine Isotope Stages 1–3: an application of ITRAX XRF scanning of sediment cores to lithostratigraphic analysis. In: Rothwell RG (ed) New Techniques in Sediment Core Analysis. Geol Soc Spec Publ 267:79–98. doi:10.1144/ GSL.SP.2006.267.01.06

Rutten A, De Lange GJ, Ziveri P, Thomson J, Van Santvoort PJM, Colley S, Corselli C (2000) Recent terrestrial and carbonate fluxes in the pelagic eastern Mediterranean: a comparison between sediment trap and surface sediment. Palaeogeogr Palaeoclimatol Palaeoecol 158:197–213

Sangiorgi F, van Soelen EE, Spofforth DJA, Pälike H, Stickley CE, John KS, Koç N, Schouten S, Sinninghe Damsté JS, Brinkhuis H (2008) Cyclicity in the middle Eocene central Arctic Ocean sediment record: orbital forcing and environmental response. Paleoceanography 23:PA1S08. doi:10.1029/2007PA001487

Sarnthein M, Thiede J, Pflaumann U, Erlenkeuser H, Futterer D, Koopmann B, Lange H, Seibold E (1982) Atmospheric and oceanic circulation patterns off Northwest Africa during the past 25 million years. In: von Rad U, Hinz K, Sarnthein M, Seibold E (eds) Geology of the Northwest African continental margin. Springer, Berlin, pp 584–604

Schott W (1935) Die Foraminiferen in dem äquatorialen Teil der Atlantischen Ozeans. Wiss Ergeb Dtsch Atl Exped "Meteor" 1925–27 3(3):43–134

Schütz L, Rahn KA (1982) Trace element concentrations in erodible soil. Atmos Environ 16:171–176. doi:10.1016/0004-6981(82)90324-9

Scourse JD, Furze MFA (2001) A critical review of the glaciomarine model for Irish Sea deglaciation: evidence from southern Britain, the Celtic shelf and adjacent continental slope. J Quat Sci 16:419–434

Seaman A (2000) Analysis depth for μ-EDXRF methods, EDAX Eagle μ-Probe Application Note

Seeberg-Elverfeldt I, Lange CB, Pätzold J, Kuhn G (2005) Laminae type and possible mechanisms for the formation of laminated sediments in the Shaban Deep, northern Red Sea. Ocean Sci 1:113–126

Shaw TJ, Gieskes JM, Jahnke RA (1990) Early diagenesis in differing depositional environments: the response of transition metals in pore water. Geochim Cosmochim Acta 54:1233–1246

Shimmield G, Derrick S, Mackensen A, Grobe H, Pudsey C (1994) The history of barium, biogenic silica and organic carbon accumulation in the Weddell Sea and Antarctic Ocean over the last 150,000 years. In: Zahn R, Pedersen TF, Kaminski MA, Labeyrie L (eds) Carbon cycling in the glacial ocean: constraints on the ocean's role in global chage, Springer, pp 555–574

Siani G, Colin C, Michel E, Carel M, Richter T, Kissel C, Dewilde F (2010) Late glacial to Holocene terrigenous sediment record in the Northern Patagonian margin: Paleoclimate implications. Palaeogeogr Palaeoclimatol Palaeoecol 297:26–36. doi:10.1016/j.palaeo.2010.07.011

Sirocko F, Garbe-Schonberg D, McIntyre A, Molɇno B (1996) Teleconnections between the subtropical monsoons and high-latitude climates during the last deglaciation. Science 272:526–529

Sluijs A, Bijl PK, Schouten S, Röhl U, Reichert G-J, Brinkhuis H (2011) Southern Ocean warming, sea level and hydrological change during the Paleocene-Eocene thermal maximum. Clim Past 7:47–61. (www.clim-past.net/7/47/2011/) doi:10.5194/cp-7-47-2011

Sluijs A, Röhl U, Schouten S, Brumsack H-J, Sangiorgi F, Sinninghe Damsté JS, Brinkhuis H (2008) Arctic late Paleocene-early Eocene paleoenvironments with special emphasis on the Paleocene-Eocene thermal maximum (Lomonosov Ridge, Integrated Ocean Drilling Program, Expedition 302). Paleoceanography 23:PA1S11. doi:10.1029/2007PA001495

Sluijs A, Schouten S, Donders TH, Schoon PL, Röhl U, Reichart G-J, Sangiorgi F, Kim J-H, Sinninghe Damsté JS, Brinkhuis H (2009) Warm and wet conditions in the Arctic region during Eocene Thermal Maximum 2. Nat Geosci 2:777–780. doi:10.1038/ngeo668

Smirnov AV, Tarduno JA (2000) Low-temperature magnetic properties of pelagic sediments (Ocean Drilling Program Site 805 C): tracers of maghemitization and magnetic mineral reduction. J Geophys Res Solid Earth 105:16457–16471

Solignac S, Seidenkrantz M-S, Jessen C, Kuijpers A, Gunvald AK, Olsen J (2011) Late-Holocene sea-surface conditions offshore Newfoundland based on dinoflagellate cysts. Holocene 21:539–552. doi:10.1177/0959683610385720

Soulet G, Ménot G, Garreta V, Rostek F, Zaragosi S, Lericolais G, Bard E (2011) Black Sea 'Lake' reservoir age evolution since the Last Glacial—Hydrologic and climatic implications. Earth Planet Sci Lett 308:245–258. doi:10.1016/j.epsl.2011.06.002

Sparrenbom CJ, Bennike O, Björck S, Lambeck K (2006) Holocene relative sea-level changes in the Qaqortoq area, southern Greenland. Boreas 35:171–187. doi:10.1111/j.1502-3885.2006.tb01148.x

Spofforth DJA, Pälike H, Green D (2008) Paleogene record of elemental concentrations in sediments from the Arctic Ocean obtained by XRF analyses. Paleoceanography 23:PA1S09. doi:10.1029/2007PA001489

Stuut J-B, Zabel M, Ratmeyer V, Helmke P, Schefuβ E, Lavik G, Schneider R (2005) Provenance of present-day eolian dust collected off NW Africa. J Geophys Res 110:D04202. doi:10.1029/2004jd005161

Stuut J-B, Kasten S, Lamy F, Hebbeln D (2007) Sources and modes of terrigenous sediment input to the Chilean continental slope. Quat Inter 161:67–76. doi:10.1016/j.quaint.2006.10.041

Széréméta N, Bassinot F, Balut Y, Labeyrie L, Pagel M (2004) Oversampling of sedimentary series collected by giant piston corer: evidence and corrections based on 3.5-kHz chirp profiles. Palaeoceanography 19:PA1005. doi:10.1029/2002PA000795

Tallmadge JA, Butt JB, Solomon HJ (1964) Minerals from sea salt. Ind Eng Chem 56:44–65

Teodoru CR, Friedl G, Friedrich J, Roehl U, Sturm M, Wehrli B (2007) Spatial distribution and recent changes in carbon, nitrogen and phosphorus accumulation in sediments of the Black Sea. Mar Chem 105:52–69. doi:10.1016/j.marchem.2006.12.013

Thomson J, Higgs NC, Jarvis I, Hydes DJ, Colley S, Wilson TRS (1986) The behaviour of manganese in Atlantic carbonate sediments. Geochim Cosmochim Acta 50:1807–1818

Thomson J, Higgs NC, Croudace IW, Colley S, Hydes DJ (1993) Redox zonation of elements at an oxic post-oxic boundary in deep-sea sediments. Geochim Cosmochim Acta 57:579–595

Thomson J, Higgs NC, Colley S (1996) Diagenetic redistributions of redox-sensitive elements in northeast Atlantic glacial/interglacial transition sediments. Earth Planet Sci Lett 139:365–377

Thomson J, Crudeli D, De Lange G, Slomp CP, Erba E, Corselli C, Calvert SE (2004) *Florisphaera profunda* and the origin and diagenesis of carbonate phases in eastern Mediterranean sapropel units. Paleoceanography 19:PA3003. doi:10.1029/2003PA000976

Thomson J, Croudace IW, Rothwell RG (2006) A geochemical application of the ITRAX scanner to a sediment core containing eastern Mediterranean sapropel units. In: Rothwell RG (ed) New Techniques in Sediment Core Analysis. Geol Soc Spec Publ 267:65–77. doi:10.1144/ GSL. SP.2006.267.01.05

Tisserand A, Malaizé B, Jullien E, Zaragosi S, Charlier K, Grousset F (2009) African monsoon enhancement during the penultimate glacial period (MIS 6.5–170 ka) and its atmospheric impact. Paleoceanography 24:PA2220. doi:10.1029/2008PA001630

Tjallingii R (2006) Application and quality of X-Ray fluorescence core scanning in reconstructing late Pleistocene NW African continental margin sedimentation patterns and paleoclimate variations. PhD Thesis Univ Bremen, pp 114

Tjallingii R, Röhl U, Kölling M, Bickert T (2007) Influence of the water content on X-ray fluorescence core scanning measurements in soft marine sediments. Geochem Geophys Geosyst 8:Q02004. doi:10.1029/2006GC001393

Tjallingii R, Stattegger K, Wetzel A, Van Phach P (2010) Infilling and flooding of the Mekong River incised valley during deglacial sea-level rise. Quat Sci Rev 29:1432–1444. doi:10.1016/j.quascirev.2010.02.022

Vare LL, Massé G, Gregory TR, Smart CW, Belt ST (2009) Sea ice variations in the central Canadian Arctic Archipelago during the Holocene. Quat Sci Rev 28:1354–1366. doi:10.1016/j.quascirev.2009.01.013

Vidal L, Bickert T, Wefer G, Röhl U (2002) Late Miocene stable isotope stratigraphy of SE Atlantic ODP Site 1085: relation to Messinian events. Mar Geol 180:71–85. doi:10.1016/S0025-3227(01)00206-7

Wang M, Zheng H, Xie X, Fan D, Yang S, Zhoa Q, Wang K (2011) A 600-year flood history in the Yangtze River drainage: comparison between a subaqueous delta and historical records. Chin Sci Bull 56:188–195. doi: 10.1007/s11434-010-4212-2

Wehausen R, Brumsack H-J (2000) Chemical cycles in Pliocene sapropel-bearing and sapropel-barren eastern Mediterranean sediments. Palaeogeogr Palaeoclimatol Palaeoecol 158:325–352

Weijden van der CH (2002) Pitfalls of normalisation of marine geochemical data using a common divisor. Mar Geol 184:167–187

Weiss H, Courty MA, Wetterstrom W, Guichard F, Senior L, Meadow R, Curnow A (1993) The genesis and collapse of third millennium North Mesopotamian civilization. Science 261:995–1004

Weltje GJ, Tjallingii R (2008) Calibration of XRF core scanners for quantitative geochemical logging of sediment cores: theory and application. Earth Planet Sci Lett 274:423–438. doi:10.1016/j.epsl.2008.07.054

Weltje GJ, von Eynatten H (2004) Quantitative provenance analysis of sediments: review and outlook. Sediment Geol 171:1–11

West S, Jansen JHF, Stuut J-B (2004) Surface water conditions in the Northern Benguela Region during the last 450 ky reconstructed from assemblages of planktonic foraminifera. Mar Micropaleontol 51:321–344. doi:10.1016/j.marmicro.2004.01.004

Westerhold T (2003) The Middle Miocene Carbonate Crash: relationship to Neogene Changes in Ocean Circulation and Global Climate. Dissertation, University of Bremen

Westerhold T, Bickert T, Röhl U (2005) Middle to late Miocene oxygen isotope stratigraphy of ODP Site 1085 (SE Atlantic): new constraints on Miocene climate variability and sea-level fluctuations. Palaeogeogr Palaeoclimatol Palaeoecol 217:205–222. doi:10.1016/j.palaeo.2004.12.001

Westerhold T, Röhl U, Laskar J, Raffi I, Bowles J, Lourens J, Zachos J (2007) On the duration of Magnetochrons C24r and C25n, and the timing of early Eocene global warming events: implications from the ODP Leg 208 Walvis Ridge depth transect. Paleoceanography 22:PA2201. doi:10.1029/2006PA001322

Westerhold T, Röhl U, Raffi I, Fornaciari E, Monechi S, Reale V, Bowles J, Evans HF (2008) Astronomical calibration of the Paleocene time. Palaeogeogr Palaeoclimatol Palaeoecol 257:377–403. doi:10.1016/j.palaeo.2007.09.016

Westerhold T, Röhl U (2009) High resolution cyclostratigraphy of the early Eocene—new insights into the origin of the Cenozoic cooling trend. Clim Past 5:309–327. (www.clim-past.net/5/309/2009/)

Westerhold T, Röhl U, McCarren HK, Zachos JC (2009) Latest on the absolute age of the Paleocene-Eocene Thermal Maximum (PETM): new insights from exact stratigraphic position of key ash layers + 19 and -17. Earth Planet Sci Lett 287:412–419. doi:10.1016/j.epsl.2009.08.027

Wolters S, Zeller M, Bungenstock F (2010) Early Holocene environmental history of sunken landscapes: pollen, plant macrofossil and geochemical analyses from the Borkum Riffgrund, southern North Sea. Int J Earth Sci 99:1707–1719. doi:10.1007/s00531-009-0477-6

Xu J, Holbourn A, Kuhnt W, Jian Z, Kawamura H (2008) Changes in the thermocline structure of the Indonesian outflow during Terminations I and II. Earth Planet Sci Lett 273:152–162

Yarincik KM, Murray RW, Peterson LC (2000) Climatically sensitive eolian and hemipelagic deposition in the Cariaco Basin, Venezuela, over the past 578,000 years: results from Al/Ti and K/Al. Paleoceanography 15:210–228

Zabel M, Schneider R, Wagner T, Adegbie AT, de Vries U, Kolonic S (2001) Late Quaternary climate changes in Central Africa as inferred from terrigenous input to the Niger Fan. Quat Res 56:207–217

Zachos J, Pagani M, Sloan L, Thomas E, Billups K (2001) Trends, rhythms, and aberrations in global climate 65 Ma to Present. Science 292:686–693

Zachos JC, McCarren H, Murphy B, Röhl U, Westerhold T (2010) Tempo and scale of late Paleocene and early Eocene carbon isotope cycles: implications for the origin of hyperthermals. Earth Planet Sci Lett 299:242–249. doi:10.1016/j.epsl.2010.09.004

Zaragosi S, Bourillet J-F, Eynaud F, Toucanne S, Denhard B, Van Toer A, Lanfumey V (2006) The impact of the last European deglaciation on the deep-sea turbidite systems of the Celtic-Armorican margin (Bay of Biscay). Geo Mar Lett 26:17–329. doi:10.1007/s00367-006-0048-9

Zarriess M, Johnstone H, Prange M, Steph S, Groeneveld J, Mulitza S, Mackensen A (2011) Bipolar seesaw in the northeastern tropical Atlantic during Heinrich stadials. Geophys Res Lett 38:L04706. doi:10.1029/2010GL046070

Zarriess M, Mackensen A (2010) The tropical rainbelt and productivity changes off northwest Africa: a 31,000-year high-resolution record. Mar Micropaleontol 76:76–91. doi:10.1016/j.marmicro.2010.06.001

Ziegler M, Jilbert T, De Lange GJ, Lourens LJ, Reichart G-J (2008) Bromine counts from XRF scanning as an estimate of the marine organic carbon content of sediment cores. Geochem Geophys Geosyst 9:Q05009. doi:10.1029/2007GC001932

Ziegler M, Lourens LJ, Tuenter E, Reichart GJ (2009) Anomalously high Arabian Sea productivity conditions during MIS 13. Clim Past Discuss 5:1989–2018. (www.clim-past-discuss.net/5/1989/2009/)

# Chapter 3
# Optimization of Itrax Core Scanner Measurement Conditions for Sediments from Submarine Mud Volcanoes

**Isabel Rodríguez-Germade, Belén Rubio, Daniel Rey, Federico Vilas, Carmen F. López-Rodríguez, Maria Carmen Comas and Francisca Martínez-Ruiz**

**Abstract** XRF scanners allow fast, high-resolution delivery of geochemical and physical property data from sediment cores. However, lack of standardized protocols for measuring parameter settings can lead to results of inferior quality to the instrument's real potential, particularly regarding light elements. In this study, a sediment core from a mud volcano in the Alboran Sea (off SE Spain) with very heterogeneous sedimentological character was analyzed using an Itrax™ Core Scanner (ITRAX). This study assesses some of the factors that influence measurements: type of anode used, X-ray exposure time, and effects resulting from the sample's exposure to room temperature during analysis as well as those caused by refrigerated storage. Quality and accuracy of the ITRAX data was evaluated by comparison with quantitative measurements obtained by conventional XRF and ICP-OES on discrete samples. The results obtained suggest 20 s is an optimal exposure time as this gives good quality results for the majority of elements analyzed, including light elements and trace elements (e.g. Al (1.9–6.6 %), Cr (84–161 μg $g^{-1}$), Ni (35–62.5 μg $g^{-1}$)). Additionally, this analysis time is not significantly detrimental to core condition. The ITRAX capacity to identify diagenetic and authigenic processes in this type of geochemical environment is also demonstrated.

**Keywords** Alborán Sea · Exposure time · ITRAX · Mud volcano

B. Rubio (✉) · I. Rodríguez-Germade · D. Rey · F. Vilas
Department of Marine Geosciences, University of Vigo, Campus Lagoas-Marcosende, 36310 Vigo, Spain
e-mail: brubio@uvigo.es

C. F. López-Rodríguez · Maria Carmen Comas · F. Martínez-Ruiz
Andalusian Institute of Earth Sciences, CSIC-University of Granada, Granada, Spain



I. W. Croudace, R. G. Rothwell (eds.), *Micro-XRF Studies of Sediment Cores*,
Developments in Paleoenvironmental Research 17, DOI 10.1007/978-94-017-9849-5_3

## Introduction

X-ray fluorescence (XRF) scanners like the Itrax™ Core Scanner (ITRAX) are valuable tools in geological and sedimentological research as they allow fast acquisition of high-resolution physical property and geochemical data from sediment cores. Numerous scientific studies in recent years have shown their value in different areas of the earth sciences like palaeoceanography (Peterson et al. 2000; Hodell et al. 2008; McHugh et al. 2008; Rebolledo et al. 2008; Hibbert et al. 2010; Hanslik et al. 2013), palaeoclimatology (Donnelly and Woodruff 2007; Löwemark et al. 2008; Metcalfe et al. 2010; Vasskog et al. 2011; Aarnes et al. 2012), dendrochronology (Helama et al. 2008, 2010), mining (Guyard et al. 2007) and forensic sciences (Smith et al. 2008). Currently they are widely used for facies characterisation in both marine and lacustrine sediments and subsequent interpretation of the geological evolution of oceans and lakes (Teodoru et al. 2007; Coolen et al. 2009; Kylander et al. 2011; Giguet-Covex et al. 2012). Some authors (e.g. Thomson et al. 2006; Rey et al. 2008; Mohamed et al. 2010) have also studied diagenetic processes in marine sediments with these XRF scanners. Due to their high spatial resolution (up to 100 μm), they have also been used to study varved sediments and tephras (Guyard et al. 2007; Lamb et al. 2007; Francus et al. 2009; Cuven et al. 2010; Langdon et al. 2011).

Despite their advantages, these instruments also have limitations in regard to determining concentration levels. An important factor in these limitations stems from uncertainties associated with determining the exact volume and density of the core segment probed. This hinders conversion of counts per second to absolute concentrations, and therefore results are not quantitative. Additionally, mineralogical, grain-size and density variations diminish data quality compared to conventional X-ray fluorescence analysis in which the referred parameters are known (Croudace et al. 2006). Tjallingii et al. (2007) in a study of the influence of water content on XRF measurement concluded that the intensity of light elements is significantly reduced with increasing wetness.

The ITRAX at the University of Vigo used in this study has run samples using Mo and Cr anode X-ray tubes (Mo-tube and Cr-tube). The Mo- tube is relatively inefficient in detecting light elements like Al or Si. The Cr- tube is better for detecting these elements, but does not produce consistent data for some of the heavy elements (e.g. Ni, Cu and rare earth elements (REE)) (Croudace et al. 2006). Hence the Mo-tube is generally used in the majority of studies. Only rarely has a direct comparison of the results obtained with both tubes been performed (Burnett et al. 2011; Giralt et al. 2011; Löwemark et al. 2011).

X-ray exposure time is a key parameter by which counts for the light elements can be improved; however, this has not been standardized to date. A survey of the literature suggests the most widely used exposure time is 10 s (e.g. Löwemark et al. 2008; Rolland et al. 2008, and others), although exposure times may vary as much as between 1 s (Guyard et al. 2007; St-Onge et al. 2008; Unkel et al. 2008) and 100 s (Croudace et al. 2006). Other authors (e.g. Cuven et al. 2007) choose X-ray exposure time on different data quality indicators, such as the fitting to a normal

distribution of an element's values obtained from an analyzed sediment core and the acquisition of a percentage of values equal to 0 to 30 %.

In this study we analyzed a sediment core from a mud volcano located in the Alboran Sea (offshore SE Iberian Peninsula). Mud volcanoes expel clastic and clayey material from deeper zones, resulting in mud breccia comprising a matrix of clay or silty clay containing heterogeneous clasts in regard to composition, form, and size (Sautkin et al. 2003). The geochemical interest of these deposits is that they provide important information about the underlying deeper sediments (Ivanov et al. 1996; Gardner 2001; Mazurenko et al. 2002; Somoza et al. 2003). However, XRF scanners have been rarely used for their chemical characterization (e.g. Richter et al. 2006).

This paper proposes some basic end-user guidelines for ITRAX studies in order to establish an operational methodology to facilitate selection of the most appropriate X-ray tube and optimal exposure time for any given case. We based our study on comparison of data obtained with Cr- and Mo-tubes from the same core and results obtained using different X-ray exposure times. In this way, we determined the exposure time required with Mo-tube, to get the same detection level for light elements as with the Cr-tube, keeping consistence of heavy elements and avoiding re-analysis of the core. At the same time, data quality was evaluated by correlating ITRAX results with quantitative measurements obtained by conventional XRF and ICP-OES analysis. Furthermore, we have also assessed effects of refrigerated storage time and analysis time spent at room temperature. All this information is key to choosing the best conditions for getting high quality results with good preservation of the core.

## Materials and Methods

For this study we analysed a 167 cm long gravity core (core designation 419G) collected by the Russian research vessel 'Professor Logachev' in June 2008 (SAGAS 08 cruise) from the upper part of the mud volcano 'Maya', at a water depth of 410 m. This mud volcano extends some 120 m in an E-W direction in the southern Alboran Sea (Fig. 3.1).

The core was cut into three sections (Fig. 3.2). A 2 cm diameter U-channel was extracted from each one. The top 105 cm consists of medium silt hemipelagic foraminifera-rich sediment with some shell fragments. Between 105 and 115 cm the core is composed of a mud breccia with cold-water coral debris and shell fragments. Between 115 and 167 cm, the core is composed of grey mud breccia containing soft but lithified clasts up to 3 cm across embedded in a coarse silt matrix. This section is slightly coarser and poorer in foraminifera than the former. Between 130 and 150 cm, there are bands of different colors, reflecting remobilized elements.

Core 419G was analyzed, after 7 months of storage at 3 °C, using the ITRAX at the University of Vigo. The core was covered with protective film transparent to X-rays to avoid desiccation. The first analyses were performed using Cr- and

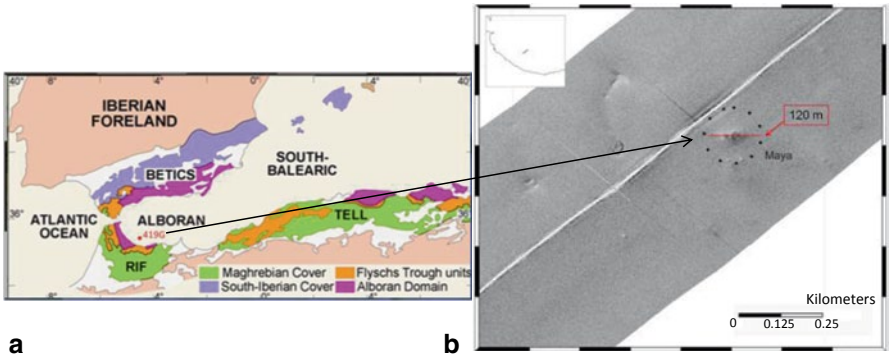


**Fig. 3.1** **a** Map of Alboran Sea showing location of core 419G taken from mud volcano Maya (35°27.11′N, 04°37.14′W). **b** The side-scan sonar image shows the mud volcano's morphology and scale

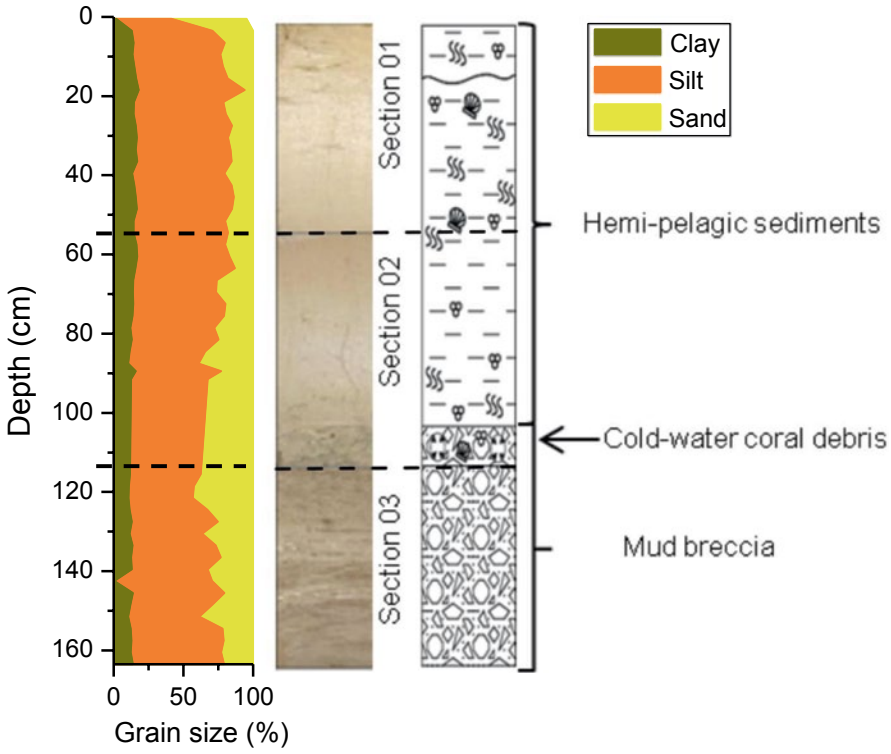


**Fig. 3.2** Grain-size percentage, photograph and sedimentary log of the split core 419G. The main sedimentary facies and boundaries of each core section are shown on *right*

**Table 3.1** X-ray fluorescence and radiographic parameters used with Mo- and Cr-tubes

| Radiographic parameters | | | | | XRF parameters | | |
|---|---|---|---|---|---|---|---|
| Tube | Exposure time (ms) | Voltage (kv) | Current (mA) | Resolution (μm) | Exposure time (s) | Voltage (kv) | Current (mA) |
| Mo | 200 | 45 | 55 | 300 | 10 | 30 | 45 |
| Cr | 275 | 50 | 38 | 300 | 10 | 30 | 50 |

Mo-tubes for comparison. The time of these first analyses is referred to as 'zero time' hereafter. In both cases a 10 s X-ray exposure time was used. Parameters used for this analysis are summarized in Table 3.1.

The core was then stored for 17 months at 3 °C and then analyzed with a Mo-tube using exposure times of 10, 20, 40 and 80 s. The rest of the radiographic and X-ray fluorescence parameters were unchanged. All results were re-evaluated using the Cox proprietary software Q-Spec 6.5.2. Reliability of the ITRAX data was evaluated by using some of Cuven et al. (2007) criteria such as the percentage of XRF values equal to zero and the fitting to a normal distribution of XRF values. At the same time, the confidence and accuracy of these criteria have been evaluated using quantitative data. Conventional XRF data were obtained from López-Rodríguez et al. (in prep.) for major elements. In this case, analyses were made every 2 cm in the first section, every 5 cm in the second section and every 10 cm in the third section. Samples were prepared as pressed pellets and were analyzed at the XRF laboratory in the Andalusian Institute of Earth Sciences (CSIC-UGR), using a Wavelength Dispersive X-Ray Fluorescence Spectrometry (WDXRF; Bruker AXS S4 Pioneer with an Rh anode X-ray tube), with an analytical detection limit of 0.1 % and an instrumental error < 1 %. In addition, trace element analysis was performed every 4 cm using an Inductively Coupled Plasma-Optic Emission Spectrometer (ICP-OES) Perkin Elmer Optima 4300 DV (with a relative standard deviation < 5 %), with previous $HNO_3$ and HF digestion at the University of Vigo.

The data were complemented with scanning electron microscope (SEM) imagery of selected samples at the University of Vigo using a JEOL JSM-6700F instrument. Samples were specifically selected from the mud breccia zone at significant peaks in the geochemical profiles. Moreover, grain-size distribution data were obtained every 3 cm using a LS 13 320 Laser Diffraction Particle Size Analyzer at the University of Vigo, but excluding cold-water coral debris and soft clasts of the mud breccia.

## Results and Discussion

### *Factors that Influence ITRAX™ Core Scanner Data Acquisition*

#### Comparison of Al and Si Results Obtained with Cr- and Mo-tubes

The importance of both Al and Si in marine sediment studies makes improvement in their detection very necessary. Al is one of the most important constituents in aluminosilicates, particularly clays, which means that it is often used as a grain size proxy in certain sediment types (Windom et al. 1989; Din 1992). Si indicates the presence of terrigenous material since it reaches marine sediments via similar inputs (rivers, wind transport, etc.), although individual peaks suggest the presence of biogenic opal (Schulz 2006). Moreover, tephra also contributes to Si favoring development of diatom populations (Cruces et al. 2006). Hence Si is a good indicator of marine sediment origin and productivity.

However, due to their low atomic number, the chemical elements most difficult to detect with the ITRAX are Al and Si, particularly in hemipelagic sediments. Figure 3.3 shows a comparison of the Al and Si geochemical profiles obtained with the Cr- and Mo-tubes for the core 419 G using an exposure time of 10 s and 80 s in the case of Al. In addition, the data variation coefficient, which gives a value of the difference between the peak areas averages obtained for these elements with both tubes using 10 s exposure time, is also shown. The peak area average increases for both elements by an order of magnitude using the Cr-tube. However, the percentage of the increase is slightly higher in the case of Al, exceeding 90 %. These data result in better resolution in the Al and Si profiles when the Cr-tube is used versus the Mo-tube, highlighting a significant decline in noise in the case of Al. Löwemark et al. (2011) also improved Al results in a similar way using a Cr-tube to analyze lacustrine sediments. However, the use of 80 s exposure time with Mo-tube results in a similar resolution and average peak area for Al as with the Cr-tube.

The Cr-tube primarily excites electrons in the light elements, making it more appropriate for measuring elements with an atomic number lower than K ($Z=19$) (Löwemark et al. 2011). This increased excitement of light elements is achieved to the detriment of heavy elements making it more difficult to obtain reliable data on the latter for subsequent quantification (Croudace et al. 2006). Hence re-analysis of the core with a Mo-tube may be required, duplicating measurement time and increasing the risk of sediment desiccation. Moreover, the difficulty inherent in precisely aligning both measurements provides further uncertainty. Another, more practical option for improving the detection of Al and Si is increasing Mo-tube count time, as demonstrated by Cuven et al. (2007) with lacustrine cores and marine cores from the North Pacific. According to Francus et al. (2009) an exposure time greater than 20 s is required to obtain good data for Al and Si, whereas Cuven et al. (2007) recommends exposure times of between 5 and 20 s depending on sediment type. The lack of agreement on selecting optimal exposure time, and the

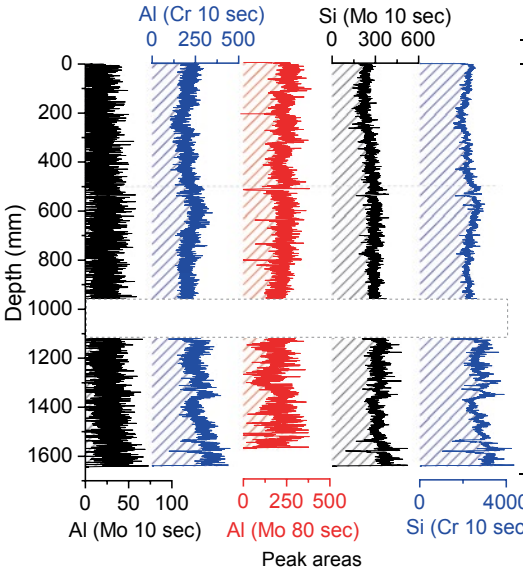


| | Al | Si |
|---|---|---|
| Peak area average (Mo 10 seconds) | 22.1 | 287.12 |
| Peak area average (Cr 10 seconds) | 229.73 | 2431.54 |
| Peak area average (Mo 80 seconds) | 216.62 | 2987.99 |
| % of Cr peak area increase | 90.38 | 88.19 |
| Variation coefficient (%) | 116.81 | 111.54 |

**Fig. 3.3** Geochemical profile comparison of Al and Si obtained with Cr- and Mo-tubes, with a 10 s X-ray exposure dwell time. In the case of Al, a profile obtained with a Mo-tube using 80 s shows the improvement obtained by increasing exposure time. ITRAX results are expressed as peak areas of each element obtained from all the measured spectra. The table (*right*) shows the averages of Al and Si peak areas obtained from the whole core using different X-ray tube and exposure time. The percentage of peak area increase obtained with the Cr-tube and the variation coefficient gives a measurement of the difference between peak areas averages obtained with both tubes for Al and Si using 10 s exposure time

improvement of the Al profile using 80 s (Fig. 3.3), lead us to make a comparative study using different exposure times. Our goal is to select a count time that provides quality data for light elements with Mo-tube without desiccating the sediment. In this way, re-analysis of the core with both x-ray tubes would be avoided.

### Comparative Study of Core 419G Using Different Exposure Times

Exposure time is a key factor in acquiring reliable data for light elements like Al and Si and it affects in the degree of detection of all elements. Table 3.2 shows the detectability evolution of the elements measured with Cr- and Mo-tubes using different X-ray exposure times, together with their concentration range obtained by quantitative measurements of discrete samples. XRF intensity expressed as peak surface area increases proportionally with increase in count time for all the elements analyzed but with different trends. Ca and Fe show the highest gradients, while this increase is lower for REE, Al and trace elements (e.g. Pb, Ni). To obtain a XRF intensity with the Mo-tube for Al and Si similar to that obtained with a Cr-tube, it is necessary to increase exposure time by up to 80 s for the Mo-tube. Taking

**Table 3.2** Detectability evolution expressed as peak area average based on tube and exposure time employed. Concentration range was obtained from conventional XRF and ICP-OES analysis and is expressed as percentage for major elements and as μg $g^{-1}$ for trace elements

| Elements | Peak area average with Mo-tube | | | | Peak area average with Cr-tube | Concentration range | |
|---|---|---|---|---|---|---|---|
| | 10 s | 20 s | 40 s | 80 s | 10 s | XRF | ICP-OES |
| *Al* | 28.54 | 54.51 | 104.59 | 216.62 | 229.73 | 11.59–18.49 | 1.93–6.63 |
| *Si* | 375.08 | 739.79 | 1423.30 | 2987.99 | 2431.54 | 38.21–44.88 | 0.02–0.15 |
| *K* | 1714.49 | 3341.35 | 6774.15 | 13,190 | 11,591.54 | 1.76–2.91 | 1.10–2.00 |
| *Ti* | 1579.82 | 3086.05 | 6303.69 | 12,061 | 9803.60 | 0.53–0.84 | 0.22–0.45 |
| *Fe* | 68,692.05 | 134,872.1 | 273,908.8 | 526,771 | – | 5.39–8.13 | 2.05–4.86 |
| *Mn* | 392.72 | 769.01 | 1545.86 | 2991.85 | – | 0.04–0.08 | 0.02–0.07 |
| *Ca* | 13,829.43 | 28,079.10 | 53,084.67 | 119,712 | 79,506.68 | 2.00–15.05 | 0.74–8.44 |
| *S* | 184.04 | 434.28 | 641.33 | 2479.89 | 399.01 | 0.12–1.20 | 0.14–2.17 |
| *Cl* | 283.00 | 534.87 | 1195.58 | 2123.97 | 2967.59 | 0.63–4.07 | – |
| *Br* | 416.02 | 769.97 | 1357.25 | 1814.67 | – | 30–136 | – |
| *Sr* | 2225.43 | 4380.17 | 8936.52 | 17,168.32 | – | 152–501 | 75.1–541.9 |
| *Ba* | 28.02 | 61.86 | 140.85 | 254.60 | 201.51 | 193–467 | 86.6–450.3 |
| *V* | 92.47 | 179.60 | 361.06 | 694.60 | – | <1–192 | 4.6–65 |
| *As* | 48.76 | 81.29 | 151.87 | 265.95 | – | – | <10–28.7 |
| *Co* | 785.42 | 1492.90 | 2988.06 | 5733.93 | – | – | 15.3–26.9 |
| *Cr* | 132.14 | 260.05 | 538.30 | 1011.26 | – | 115–260 | 84.5–161.2 |
| *Cu* | 60.27 | 93.18 | 143.52 | 366.29 | – | 46–70 | 10.3–43.9 |
| *Ni* | 56.12 | 103.30 | 203.54 | 430.55 | – | 54–89 | 35–62.5 |
| *Zn* | 407.37 | 798.17 | 1615.26 | 3133.13 | – | 85–120 | 59.9–114.5 |
| *Rb* | 549.12 | 1067.44 | 2182.07 | 4078.04 | – | 62–120 | <20–132.1 |
| *Y* | 114.87 | 216.36 | 428.94 | 766.70 | – | 10–19 | 0.78–12.94 |
| *Zr* | 811.25 | 1521.16 | 3147.54 | 5698.58 | – | 119–151 | 44.6–102.8 |
| *Pb* | 58.04 | 105.70 | 209.66 | 370.77 | – | <1–39 | 0.8–14.7 |
| *Pt* | 73.78 | 170.71 | 316.01 | 726.83 | – | – | <6–27.5 |
| *Ga* | 194.17 | 409.54 | 814.08 | 1670.90 | – | 12–27 | 187.4–254.6 |
| *La* | 19.84 | 31.23 | 57.64 | 101.60 | 117.01 | – | 2.1–23.8 |
| *Ce* | 38.29 | 60.41 | 128.40 | 219.03 | – | – | 13.6–15.6 |
| *Nd* | 12.54 | 21.30 | 49.11 | 65.66 | – | – | 12–20.1 |
| *Pr* | 22.46 | 35.35 | 84.67 | 121.06 | – | – | 4.2–11.2 |

into account facies, average of total counts per second is slightly higher in the mud breccia (2%) independent of the exposure time used. However, XRF intensity of S increases by 90% in the mud breccia, even though for most elements analyzed, this variation is less than 20% between facies, and is similarly independent of exposure time.

The increase in exposure time (Mo-tube) affects element variability by raising the standard deviation in all cases. To make comparisons between variability of

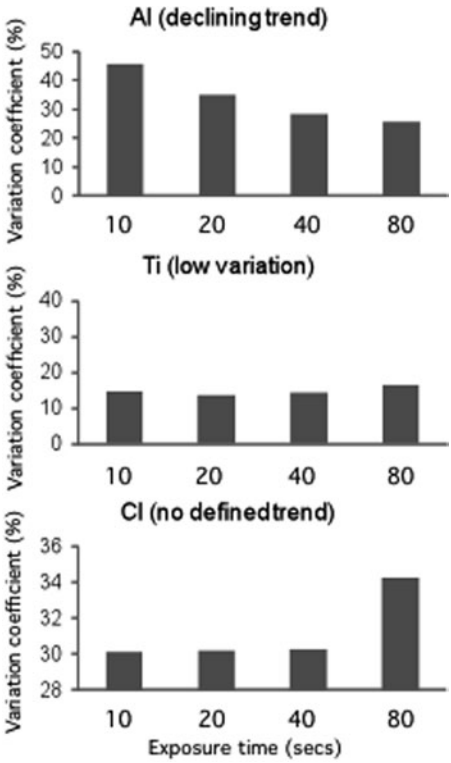


**Fig. 3.4** Examples of data variability evolution (expressed as variation coefficient) depending on exposure time

different elements it is necessary to calculate the variation coefficient given that magnitudes of each are significantly different depending on the element being analyzed and exposure time used. Figure 3.4 shows examples of variability behaviour depending on exposure time. For Al and elements present in low concentrations such as V or Pb, the variation coefficient decreases as exposure time increases (declining trend). This means that peak area average values become more representative and data dispersion diminishes. For elements that appear in high concentrations in the sample, like Fe, Ca and Ti and others like Zn, count time does not significantly affect the variation coefficient, which stays more or less constant (low variation). This reflects that reliable data is acquired with 10 s of exposure for these elements, and, as a consequence, their dispersion should not vary substantially with increase in exposure time. Some elements like Cl, Zr and Mn, do not present a clear pattern with count time. In the case of Cl, it stays more or less constant, but increases at 80 s exposure time (no defined trend). For Cl this may be due to inhomogeneities caused by salt precipitation on the plastic film covering.

To evaluate data quality obtained using the Mo-tube, percentages for peak surface values equal to zero were calculated for the different elements measured with a 10 s exposure time. Figure 3.5 shows the elements that present a percentage of zero values greater than 1% in their results, since smaller percentages were not

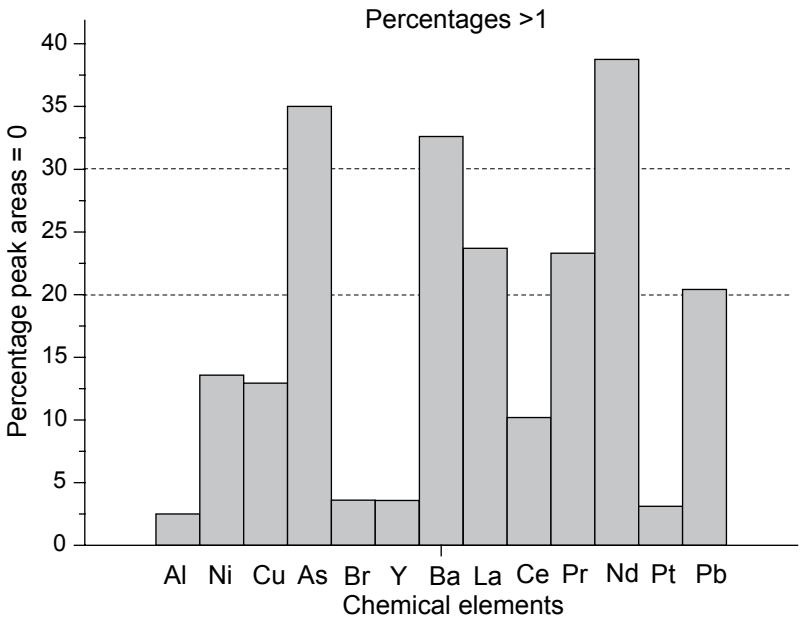


**Fig. 3.5** Elements that present a percentage of peak areas equal to 0 to 1% with a 10 s exposure time

considered important. According to Cuven et al. (2007), when the percentage of values equal to zero is greater than 30% of the total points analyzed for the same element, the results are not considered reliable. In such cases, that element should be eliminated, or exposure time increased. If that element exists in the sample, percentage of peak surface values equal to zero should decreases when count time increases. Considering a 30% limit, only As, Ba and Nd data would be unreliable with 10 s exposure time (Fig. 3.5). Based on these data, a 20% limit was set for detecting unreliable results, in order to assess validity of La, Pr and Pb and to acquire better quality data. In the case of Al peak surface results are reliable because the percentage of values equal to zero is 2.5%. However, the average peak surface values are very low as can be seen in Table 3.2, and better results are clearly achieved using a 40 s or greater exposure time. The proposal of Cuven et al. (2007) should consequently be considered under this regard before being accepted for a given set of measurements.

Table 3.3 shows the evolution of the peak area percentages equal to zero when increasing exposure time. Only those elements with a percentage greater than 1% at 10 s exposure time are considered. Values higher than 20% are highlighted in bold. On increasing count time just to 20 s, data for all elements improve, with the percentage of values equal to zero diminishing. Fifty-four percent of elements improve with up to 40 s of exposure, and 31% with up to 80 s. This reflects that concentration of these elements (except Al) in sediment is very low, and that longer exposure times are needed to obtain valid data. Consequently, the presence of

**Table 3.3** Percentage of peak area values equal to zero for different chemical elements displayed by exposure times. Values greater than 20% are highlighted in bold

| Elements | Percentage of peak areas equals zero | | | |
|---|---|---|---|---|
| | 10 s | 20 s | 40 s | 80 s |
| *Al* | 2.5 | 0.4 | 0.1 | 0.4 |
| *Ni* | 13.6 | 12.0 | 13.0 | 7.4 |
| *Cu* | 12.9 | 12.2 | 12.9 | 5.5 |
| *As* | ***35.0*** | ***29.9*** | ***21.8*** | 16.4 |
| *Br* | 3.6 | 2.7 | 0.8 | 2.6 |
| *Y* | 3.6 | 0.8 | 0.2 | 0.4 |
| *Ba* | ***32.6*** | 17.7 | 7.3 | 8.0 |
| *La* | ***23.7*** | 18.0 | 9.0 | 5.7 |
| *Pt* | 3.1 | 0.2 | 0.1 | 0.4 |
| *Pb* | **20.4** | 12.4 | 4.8 | 2.9 |
| *Ce* | 10.2 | 7.2 | 1.0 | 0.9 |
| *Pr* | ***23.3*** | 17.6 | 4.2 | 6.0 |
| *Nd* | ***38.8*** | ***29.8*** | 12.7 | 17.6 |

these elements in the sediment could be confirmed by this method, proving that the percentage of zero values progressively and significantly decreases with increase in exposure time. In this way, the quantitative confirmation made in this study by conventional XRF and ICP-OES analysis could be avoided. Another option of element confirmation is by examination in detail of spectra obtained with high exposure time. Figure 3.6 shows L and K lines of Pb in a spectrum obtained with 80 s count time. This spectrum supports the reliability of Pb results in spite of its low concentration. However, if data is considered reliable, an augmentation in exposure time may be counterproductive for a great variety of reasons. First because the longer the exposure time the higher the coherent and incoherent dispersion, resulting in an undesired decrease of the signal to noise ratio (SNR). Secondly is its potential interference with fluorescence peaks of other elements that did not appear with shorter exposure times. In this regard, we have to seriously consider that increasing the count rate by increasing exposure time may result in sum peaks artifacts. This effect is quite common when two intense photons arrive at the detector simultaneously and cannot be separated by signal processing. This generally affects major elements in the sample such as Fe (Robinson et al. 2005). Furthermore, if the radiation is very high, part of the radiation may escape the detector, depending on detector dimensions. In that case, the detected energy is lower than the energy of the characteristic X-ray photon (Aichinger et al. 2012). To solve both problems, ITRAX has an option, which allows the operator to add extra lines (like sum peaks, escape lines or diffraction lines) to the fitting process (Q-Spec 6.5.2. Manual). This option avoids confusion of those artifacts with elements peaks and minimizes problems associated with exposure time increase.

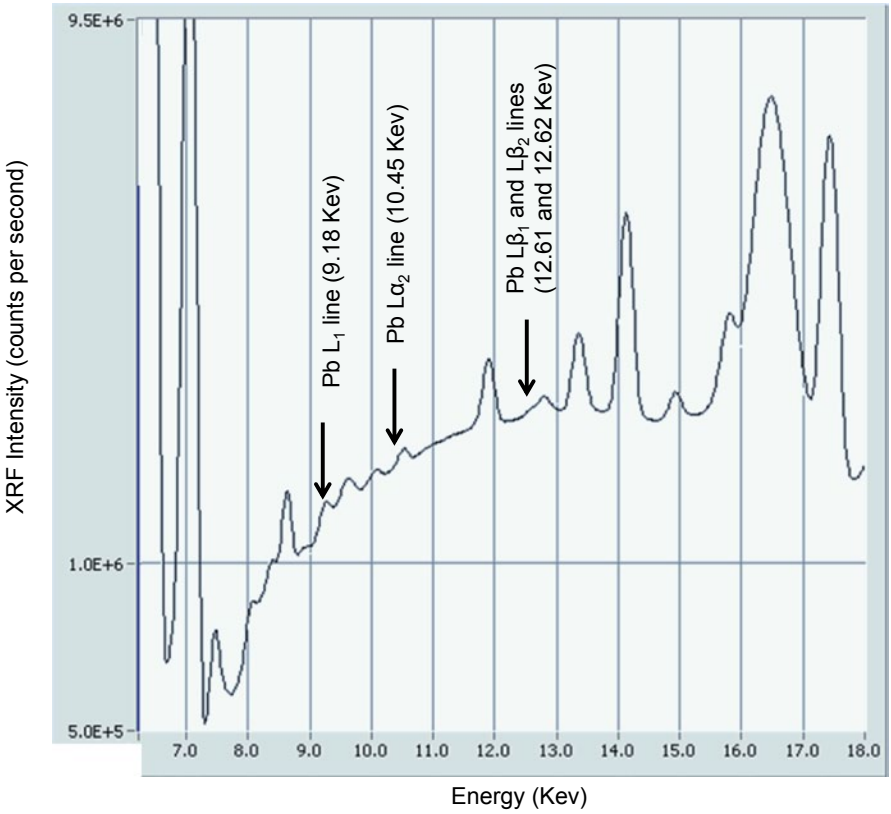


**Fig. 3.6** XRF spectrum obtained from hemipelagic sediments with the ITRAX using 80 s exposure time. In spite of the very low concentration of Pb (0.78–14.72 μg $g^{-1}$) L and K lines can be identified in the spectrum (marked with *arrows*)

According to Cuven et al. (2007), a useful method for selecting appropriate exposure times is through examining the fit to a normal distribution of element values present in the sediment analyzed. Figure 3.7 shows that 10 s of exposure time for the Mo-tube is sufficient to obtain acceptable data for Al, despite its low sensitivity to the ITRAX detector to this measurement (Q-Spec 6.5.2. Manual; Cuven et al. 2007). Detection increases notably for 20 s exposure time. Results for S do not present a normal distribution in spite of the fact that they belong to the group of elements with a moderate level of detectability (Q-Spec 6.5.2. Manual; Cuven et al. 2007) with this instrument and that its concentration range is relatively high (0.14–2.17%). However, Pb, which is a highly detectable element (Q-Spec 6.5.2. Manual; Cuven et al. 2007) with this instrument, is only present in low concentrations in the studied core (0.8–14.7 μg $g^{-1}$). When using 10 and 20 s exposure times, detection is good, but gets much better with 40 and 80 s exposures. To demonstrate the statistical significance of the changes produced in the data distribution, we have calculated the Kolmogorov-Smirnov Z statistic for Al, S, and Pb at 10, 20, 40, and 80 s

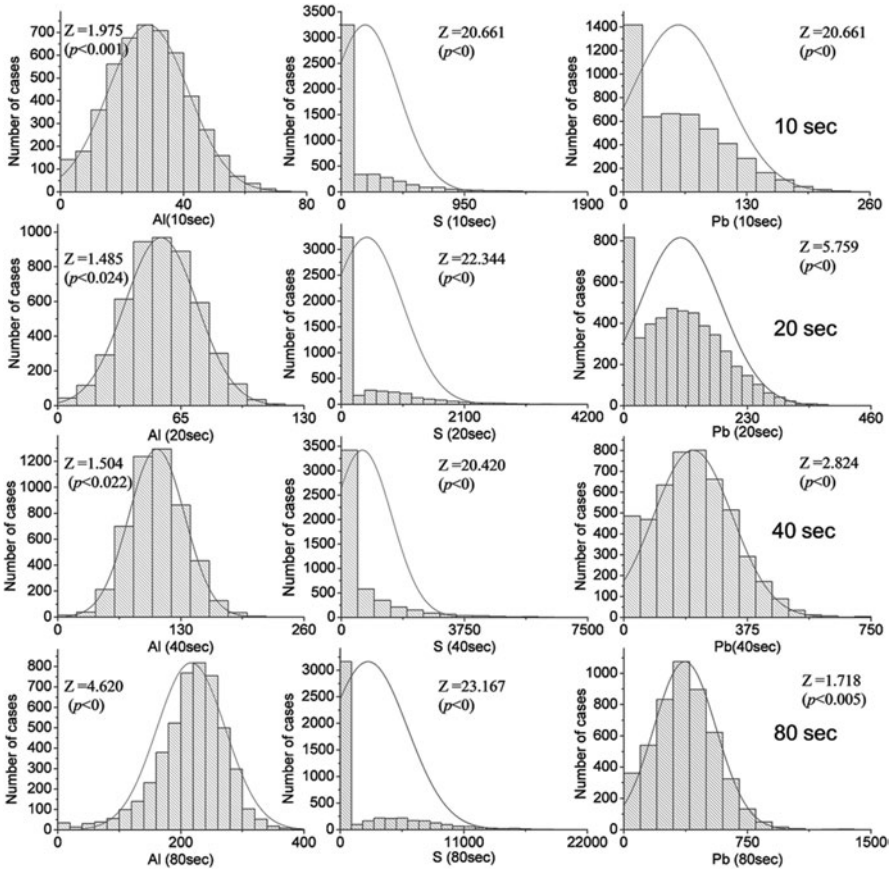


**Fig. 3.7** Normal distribution for Al, S and Pb at 10, 20, 40 and 80 s X-ray exposure times (Mo-tube). The Z statistic is shown in each plot

exposure times. This statistic is used to check if an empirical data set follows a normal distribution. The larger the value of Z (lower signification level) the more the data will move away from a normal distribution. Figure 3.7 shows how Pb shows a progressive decrease in the Z statistic with exposure time, more closely approaching the normal distribution. This corroborates our graphical observations. In contrast, only the Al data set obtained with 20 and 40 s of exposure time follow a normal distribution with a signification level of 0.01. Furthermore, S never approaches a normal distribution in any of the cases, and presents notably high Z values. Despite the above, we must consider the reliability of these measurements based on their good and significant correlation with conventional XRF analysis, even using 10 s exposure time for S (Table 3.4). The non-fitting to a normal distribution for S is attributed to textural reasons since this element is more concentrated in the mud breccia (average of 0.7 %± 0.24 %) than in hemipelagic sediments (average of 0.25 %± 0.1 %). Contrary to Cuven et al. (2007) findings, our data suggest that the

**Table 3.4** Pearson correlation coefficient ($r$) between ITRAX measurements and quantitative data obtained from conventional XRF and ICP-OES analysis of discrete samples

| Elements | $r$ values 10 s | $r$ values 20 s | $r$ values 40 s | $r$ values 80 s | |
|---|---|---|---|---|---|
| *Al* | **0.419**[a] | **0.487**[b] | 0.029 | **0.497**[b] | Conventional XRF analysis |
| *K* | **0.798**[b] | **0.792**[b] | **0.739**[b] | **0.904**[b] | |
| *Ti* | **0.651**[b] | **0.545**[b] | 0.193 | **0.695**[b] | |
| *Fe* | **0.634**[b] | **0.540**[b] | **0.463**[b] | **0.628**[b] | |
| *Mn* | **0.611**[b] | **0.395**[a] | **0.507**[b] | **0.431**[a] | |
| *Ca* | **0.841**[b] | **0.734**[b] | **0.623**[b] | **0.590**[b] | |
| *Sr* | **0.867**[b] | **0.795**[b] | **0.802**[b] | **0.803**[b] | |
| *Ba* | −0.197 | **0.471**[b] | **0.466**[b] | **0.489**[b] | |
| *S* | **0.761**[b] | **0.809**[b] | **0.666**[b] | **0.912**[b] | |
| *Cl* | 0.160 | 0.266 | 0.249 | 0.180 | |
| *Br* | −0.312 | **0.932**[b] | **0.952**[b] | **0.909**[b] | |
| *Rb* | **0.735**[b] | **0.834**[b] | **0.824**[b] | **0.894**[b] | |
| *Y* | **0.434**[a] | **0.381**[a] | 0.078 | **0.354**[a] | |
| *Zr* | 0.111 | **0.383**[a] | 0.270 | **0.523**[b] | |
| *Si* | 0.046 | −0.130 | −0.362[a] | **0.353**[a] | ICP-OES analysis |
| *As* | **0.357**[a] | **0.402**[a] | 0.179 | **0.557**[b] | |
| *V* | **0.861**[b] | **0.763**[b] | **0.669**[b] | −0.518[b] | |
| *Cu* | **0.447**[b] | −0.089 | −0.155 | −0.176 | |
| *Cr* | **0.716**[b] | **0.681**[b] | **0.589**[b] | **−0.704**[b] | |
| *Ni* | **0.784**[b] | **0.736**[b] | **0.756**[b] | **0.784**[b] | |
| *Co* | **0.625**[b] | **0.480**[b] | 0.314 | −0.010 | |
| *Zn* | **0.391**[a] | **0.372**[a] | 0.335 | **0.676**[b] | |
| *Pb* | 0.289 | 0.138 | **0.402**[a] | **0.437**[b] | |
| *Pt* | −0.466[b] | −0.286 | 0.152 | 0.011 | |
| *Ga* | **0.594**[b] | **0.588**[b] | **0.401**[a] | 0.123 | |
| *La* | −0.359[a] | −0.199 | −0.428[a] | 0.154 | |
| *Ce* | −0.077 | 0.296 | −0.039 | **0.381**[a] | |
| *Nd* | −0.041 | −0.187 | −0.095 | −0.259 | |
| *Pr* | −0.347[a] | −0.076 | 0.143 | 0.147 | |

ITRAX data were averaged every 1 cm. Significant positive correlations are highlighted in bold
[a] Correlation is significant at level 0.05
[b] Correlation is significant at level 0.01. $N = 33$

fit to a normal distribution is not a valid criterion for elements that are not uniformly distributed along the core, or for those that result from temporal contamination at particular horizons (showing isolated peaks at certain depths). Subsequently, some caution needs to be taken when employing this approach. Al and Pb have a similar concentration range along the core and in both cases the closeness to a normal distribution improves data quality. This has been confirmed by comparison of ITRAX

data with quantitative data (Table 3.4) obtained by conventional XRF and ICP-OES. Al shows a significant correlation with just 10 s exposure time, but it improves with 20 and 80 s. However, Pb needs 40 s exposure time to get a significant correlation and it improves with 80 s. In general, correlations are better between conventional XRF and ITRAX data for most of major elements because both techniques are similar. However, Si and most of the trace elements shows better correlations with ICP-OES data due to their low concentration in the sample. The largest number of positive significant correlations is obtained with 20 s exposure time. The 75.9% of these correlations get worse with 40 s but improve again with 80 s count time (62.1%). Some elements like, La, Nd, Pt and Pr did not show positive significant correlations with ITRAX measurements not even with 80 s exposure time, possibly due to their very low concentrations. Increasing exposure time may be considered an option to improve results for these elements.

### Effects of Aging on Core 419G

An important factor in reproducibility of results is the effects of core aging. During storage (including refrigeration at 3 °C) there will be a gradual contraction and shortening of cores due to sediment desiccation. However these effects are significantly greater during ITRAX analysis time as the core is at room temperature (up to

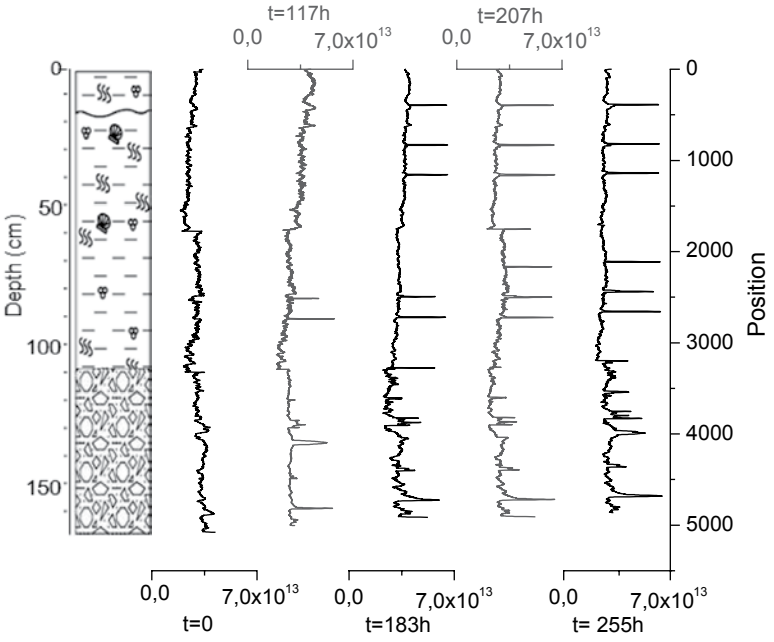


**Fig. 3.8** Core 419G grey levels according to time spent at room temperature. The peaks represent cracks caused by desiccation

**Table 3.5** Percentage increase or decrease and standard deviation for some elements analyzed under same conditions (Mo-tube and 10 s exposure time) after 17 months. Data points from the cracks were not considered

| Elements | % Increase or decrease ± standard deviation | Elements | % Increase or decrease ± standard deviation |
|---|---|---|---|
| Al | +18.07 ± 3.65 | Ni | −16.13 ± 7.63 |
| Si | +23.34 ± 61.91 | Zn | +1.64 ± 6.60 |
| K | +6.13 ± 74.37 | As | +34.23 ± 11.80 |
| Ti | +4.45 ± 68.10 | Cl | −27.97 ± 77.71 |
| Mn | +15.93 ± 44.24 | Br | +25.19 ± 74.11 |
| Fe | +2.52 ± 1225.38 | Rb | −11.81 ± 52.02 |
| Ca | +13.08 ± 1278.78 | Zr | −10.58 ± 67.84 |
| Sr | −8.56 ± 147.34 | La | −23.38 ± 4.28 |
| S | +66.60 ± 86.67 | Pt | −16.30 ± 10.16 |
| Ba | −57.45 ± 26.75 | Pb | −0.17 ± 0.07 |
| V | +5.71 ± 3.73 | Ce | −15.37 ± 4.92 |
| Cr | −11.17 ± 11.75 | Pr | −47.90 ± 14.60 |
| Co | +4.60 ± 25.57 | Nd | −57.62 ± 12.05 |
| Cu | +20.16 ± 8.59 | | |

20 °C) during analysis. The increase of analysis time results in a progressive desiccation of core surface and consequent generation of cracks. These cracks become deeper with analysis time. For this reason, re-analysis of the core will complicate matching of ITRAX results with other kind of scanner data (e.g. Geotek Multi Sensor Core Logger or 2G Cryogenic Magnetometer). For the core studied, desiccation did not affect the different facies in the same manner. The first 24 h of analysis at 20 °C did not result in changes to the length of the core and after 69 h only the mud breccia interval was affected. After 135 h of exposure the upper part of the hemipelagic sediments (the first 54 cm) was shortened, and by 183 h, all facies lengths were reduced. The cracks became more numerous and evident in the mud breccia, as it has a lower water content. Figure 3.8 shows the physical changes in the core as seen from study of grey levels of the X-rays, in which the appearance of cracks (peaks) and reduction in length of facies is clearly seen.

The effect of refrigerated storage time on the core was also examined. Table 3.5 shows the changes (expressed as an average percentage of increase or decrease in peak areas) in element distribution after 17 months of storage at 3 °C. The average peak area increases in 52 % of elements (Al, Si, K, Ti, Mn, Fe, Ca, S, V, Co, Cu, Zn, As and Br), while a decrease is seen in 48 % (Sr, Ba, Cr, Ni, Cl, Rb, Zr, La, Pt, Pb, Ce, Pr and Nd).

Sediment water content has a major influence on X-ray fluorescence values. Water absorption of X-rays in practical terms results in a general reduction in intensities, particularly for light elements. These are more sensitive to absorption effects than the heavy elements because characteristic fluorescence energy increases with

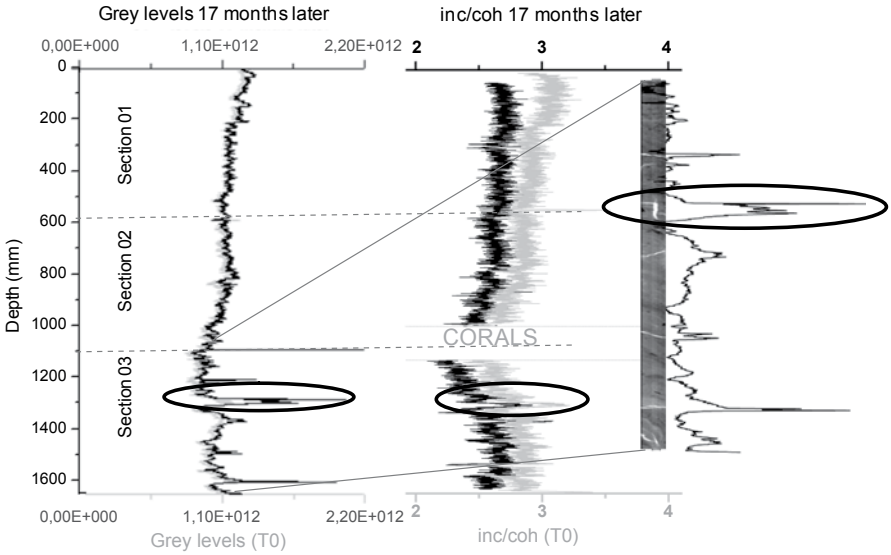


**Fig. 3.9** Grey levels for core 419G during the first analysis (*gray* profile), and second analysis made 17 months later (*black* profile). To the right profiles of the inc/coh ratio are shown, followed by a close up of the mud breccia X-radiographic image (section 03) with the grey level profile obtained at month 17 superimposed. The *circles* highlight correlation of maximum grey levels with maximum inc/coh ratio values when a significant crack appears

the square of atomic number (Moseley's Law), so when these energies are weaker, susceptibility to dispersion and absorption effects increases (Tjallingii et al. 2007). The increase in Al and Si peak area average might be due to water content diminishing with time and absorption effects are less. However, the element showing the largest increase in peak area is S, which shows intermediate detectability with the ITRAX (Q-Spec 6.5.2. Manual; Cuven et al. 2007). Of the majority of elements presenting a percentage increase in peak area less than 10 % are highly detectable and are found in significant concentrations in the sediment (e.g. Fe, Ti and K). Elements most affected by desiccation are Nd and Ba whose peak areas are reduced by 57 %.

The first 54 cm of hemipelagic sediments change less with time (i.e. show less aging) as their origin, texture and composition allow a higher water content. The interval length shows no changes and consequently is one of the more suitable zones to study correlations between zero time measurements and the 510 d time measurements. The best correlations are obtained for Ca with an $r$ of 0.861 ($p < 0.01$ and $n = 3292$) and Sr with an r of 0.671 ($p < 0.01$ and $n = 3292$). The worst correlations are found with light elements and REE. The other facies see their sediment length reduced by around one centimeter due to desiccation, and in this case the same measurement points cannot be compared.

X-radiographic images of hemipelagic sediments seem unaffected by time spent in refrigerated storage. Correlation between grey levels seen in the two measurements is very good for these facies, which are the muddiest and most uniform. In the

first 54 cm of hemipelagic sediment an $r$ of 0.950 ($p < 0.01$ and $n = 1774$) is acquired, and in the following centimeters until the change in facies, $r$ is 0.962 ($p < 0.01$ and $n = 1525$). For the mud breccia, $r$ is reduced to 0.806 ($p < 0.01$ and $n = 1747$), with the most significant changes in the X-radiographic images (Fig. 3.9). With time, the grey level peaks increase considerably in this facies due to the appearance of many desiccation cracks. In addition to the sediment's chemical composition, the ITRAX also measures a coherent (coh) and incoherent (inc) dispersion that is produced during the XRF scan. The grey levels for core 419G at time 0 and at time 510 d, followed by the inc/coh ratio and an amplification of the mud breccia X-ray can be seen in Fig. 3.9. The inc/coh ratio peaks coincide with the presence of significant cracks in the mud breccia. This ratio depends on the average atomic number of the sediment material. Generally it correlates with organic C content (Burnett et al. 2011) since this element has an average atomic weight smaller than carbonates, aluminosilicates or silica. However in this case, it is the absence of sediment that causes a fall in average atomic number. Therefore, in order to use the inc/coh ratio as an indicator of organic material and to get reliable geochemical data, it is important to remove artifacts caused by significant cracks in the core. Moreover, combination of this information with other indicators of organic matter variations, such as Br or Br/Cl ratio (Ziegler et al. 2008; Cartapanis et al. 2011), help avoid erroneous interpretations.

## *Geochemical Profiles from the Mud Volcano Maya*

Figure 3.10 shows some of the geochemical profiles taken with the Mo-tube with an X-ray exposure time of 10 s. The variability that occurs in some of the profiles is due to a low detection level with the Mo-tube (i.e. low SNR). Al is the element with the noisiest profile, due to its low detectability with a Mo-tube (Q-Spec 6.5.2. Manual; Cuven et al. 2007) Fe and Mn, both highly detectable (Q-Spec 6.5.2. Manual; Cuven et al. 2007), have maxima between 132 and 146 cm for Fe, and between 130 and 143 cm for Mn. This distribution by which Mn peaks are slightly shallower than Fe peaks, is generally attributed to diagenetic processes (Haese et al. 2000; Rey et al. 2008), given the greater sensibility of the first to changes in redox potential. Cu and Zn, also highly detectable (Q-Spec 6.5.2. Manual; Cuven et al. 2007), show maxima in the mud breccia zone. These maxima are interpreted as the consequence of sulfide precipitation under anoxic conditions (Calvert and Pedersen 1993). The profiles for Ca and Sr are quite similar to each other. From 20 cm downcore, Ca content increases due to presence of foraminifera in hemipelagic sediments. In the mud breccia Ca diminishes as the sediment is muddier and contains fewer foraminifera. However, some peaks appear in these facies and indicate presence of methane-related authigenic carbonates, considered a paleoproxy for ancient methane seepages. These carbonates may be aragonite, deduced from peaks present in the Sr/Ca and Mg/Ca ratios. According to Thomson et al. 2004, these peaks could indicate the presence of high magnesium calcite and/or aragonite. The increase in S associated

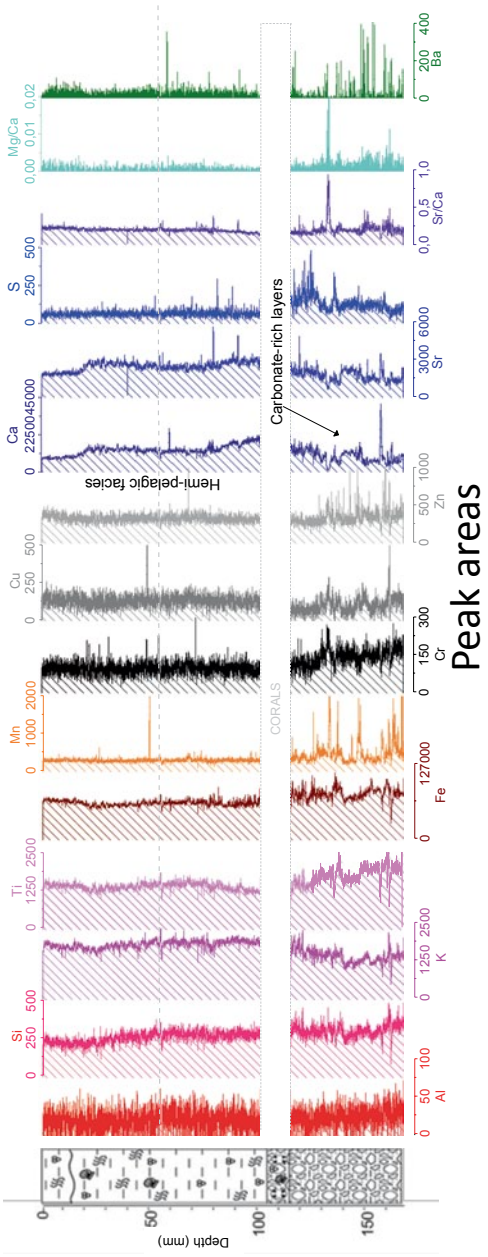


**Fig. 3.10** Geochemical profiles of some elements obtained with the Mo-tube where the intensity of the signal is expressed as a peak area for each element. The dotted bands represent a zone containing abundant coral debris, not analyzed with the ITRAX due to its rough and irregular surface

with these peaks suggests aragonite has been formed as a consequence of sulfate reduction during diagenesis, as demonstrated by Milliman and Müller (1973) and Calvert and Fontugne (2001) for Mg-rich calcites found in an equivalent geochemical environment in the eastern Mediterranean. Co-existence of anaerobic methane oxidation (inferred from presence of authigenic carbonates) and sulfate reduction in the mud breccia (also evidenced by S enrichment) indicates a significant accumulation of organic material and/or a relative decrease in oxygenation with depth.

Scanning electron microscopy (data not shown) confirmed the presence of pyrite and rhodochrosite, associated with Fe and Mn maxima, as well as barite coincident with Ba maxima in the mud breccia.

## Conclusions

Increase in X-ray exposure time principally favours elements that have low detectability (e.g. Al and Si), or those found in very low concentrations in sediment (e.g. Pb and REE), while it has less significant effect for elements found in higher concentrations or more readily detectable. However, exposure time does not influence XRF intensity variations of elements depending on sample lithology.

The fit to a normal distribution used by Cuven et al. (2007) to evaluate the reliability of ITRAX data is not valid for elements that are not uniformly distributed through the core. This is particularly relevant for pollution studies focused on assessing temporal contamination, or for those aiming to construct an event stratigraphy based on geochemical characterization of horizons such as tephras or ice rafted debris. However, it is a useful tool to evaluate data quality of homogeneously distributed elements.

Sediment desiccation increases detectability of Al and Si since loss of water content diminishes absorption effects on light elements. However, reduction in moisture results in crack formation and reduction in the length of the core, which causes significant changes in X-radiographic images and hinders comparison of different analytical results. Study of the effects that time has on core preservation shows that decrease in length may occur after ~ 70 h of analysis. Desiccation will be more acute the longer the core spends at room temperature, and the better preserved, the higher will be its water content.

The presence of sizeable cracks in the sediment due to desiccation causes significant increases in the inc/coh ratio. The use of this ratio as an indicator of organic material should be combined with detailed study of the sediment X- radiographic images and other indicators of organic matter variations such as Br or Br/Cl ratio.

Considering the quality of the results obtained for different elements using a Mo-tube and sediment preservation, the most appropriate exposure time for the analysis of a core with these characteristics at a resolution of 300 μm is considered to be 20 s. This recommendation is reinforced by the worsening correlations between quantitative data and ITRAX data obtained with 40 s exposure time and core desiccation after 80 s count time. However, 80 s or more exposure time is

recommended to get better results for Si when its concentration in the sample is lower than 0.15 %.

The previous conditions and considerations would be applicable to carbonate-rich sediments with low terrigenous content (even lake sediments) and for example, could be effective in studying varved sediments or distal Heinrich events. Moreover, the application of the ITRAX to the study of submarine mud volcanoes has proved its utility for identification of layers rich in methane-related authigenic carbonates. In addition, ITRAX core scanning provides valuable information for studying the significance of diagenetic reactions related to degradation of organic matter and its importance in global ocean cycles. This demonstrates the capacity of the instrument for the identification of these geochemical processes in this particular environment.

**Acknowledgments** FPU grant awarded to I. Rodríguez-Germade. This work was supported by the Spanish Ministry of Science and Innovation through projects CGL2008-03474-E, GCL2010-16688 and IPT-310000-2010-17; and by the Xunta de Galicia through project 10MMA312022PR.

## References

Aarnes I, Bjune AE, Birks HH, Balascio NL, Bakke J, Blaauw M (2012) Vegetation responses to rapid climatic changes during the last deglaciation 13,500–8,000 years ago on southwest Andøya, arctic Norway. Veget Hist Archaeobot 21:17–35

Aichinger H, Dieker J, Joite-Barfuß S, Säbel M (2012) Production and measurements of X-rays. In: Aichinger H, Dieker J, Joite-Barfuß S, Säbel M (eds) Radiation exposure and image quality in X-ray diagnostic radiology: physical principles and clinical applications, 2nd edn. Springer, New York

Burnett AP, Soreghan MJ, Scholz CA, Brown ET (2011) Tropical East African climate change and its relation to global climate: a record from Lake Tanganyika, Tropical East Africa, over the past 90 kyr. Palaeogeogr Palaeoclimatol Palaeoecol 303:155–167

Calvert SE, Fontugne MR (2001) On the late Pleistocene-Holocene sapropel record of climatic and oceanographic variability in the eastern Mediterranean. Paleoceanography 16:78–94

Calvert SE, Pedersen TF (1993) Geochemistry of recent oxic and anoxic marine sediments: implications for the geological record. Mar Geol 113:67–88

Cartapanis O, Tachikawa K, Bard E (2011) Northeastern Pacific oxygen minimum zone variability over the past 70 kyr: impact of biological production and oceanic ventilation. Paleoceanography 26:PA4208. doi:10.1029/2011PA002126

Coolen MJL, Saenz JP, Giosan L, Trowbridge NY, Dimitrov P, Dimitrov D, Eglinton TI (2009) DNA and lipid molecular stratigraphic records of haptophyte succession in the Black Sea during Holocene. Earth Planet Sci Lett 284:610–621

Cox Analytical System (2008) Itrax Core Scanner: Q-Spec 6.5.2. Software Manual. Mölndal, 13 pp

Croudace IW, Rindby A, Rothwell RG (2006) ITRAX: description and evaluation of a new multi-function X-ray core scanner. In: Rothwell RG (ed) New techniques in sediment core analysis. Geol Soc Spec Publ 267:51–63

Cruces F, Urrutia R, Parra O, Araneda A, Treutler H, Bertrand S, Fagel N, Torres L, Barra R, Chirinos L (2006) Changes in diatom assemblages in an Andean lake in response to a recent volcanic event. Arch Hydrobiol 165:23–35. doi:10.1127/0003-9136/2006/0165-0023

Cuven S, Francus P, Cremer JF (2007) Protocoles d'utilisation et essais de calibration du scanner de microfluorescence X de type "ITRAX Core Scanner". Rapport de recherché Nº 954. ISBN: 978-2-89146-552-6

Cuven S, Francus P, Lamoureux SF (2010) Estimation of grain-size variability with micro X-ray fluorescence in laminated lacustrine sediments, Cape Bounty, Canadian High Arctic. J Paleolimnol 44:803–817

Din TB (1992) Use of aluminium to normalize heavy-metal data from estuarine and coastal sediments of Straits of Melaka. Mar Pollut Bull 24:484–491

Donnelly JP, Woodruff JD (2007) Intense hurricane activity over the past 5,000 years controlled by El Niño and the West African monsoon. Nature 447:465–468 doi:10.1038/nature05834

Francus P, Lamb H, Nakagawa T, Marshall M, Brown E, Suigetsu 2006 Project members (2009) The potential of high-resolution X-ray fluorescence core scanning: applications in paleolimnology. Sci Highlights Paleolimnol 17:93–95. www.pages-igbp.org

Gardner JM (2001) Mud Volcanoes revealed and sampled on the Western Moroccan continental margin. Geophys Res Lett 28(2):339–342. doi:10.1029/2000GL012141

Giguet-Covex C, Arnaud F, Enters D, Poulenard J, Millet L, Francus P, David F, Rey P-J, Wilhelm B, Delannoy J-J (2012) Frequency and intensity of high-altitude floods over the last 3.5 ka in northwestern French Alps (Lake Anterne). Quat Res 77:12–22

Giralt S, Rico-Herrero MT, Vega JC, Valero-Garcés BL (2011) Quantitative climate reconstruction linking meteorological, limnological and XRF core scanner datasets: the Lake Sanabria case study, NW Spain. J Paleolimnol. doi:10.1007/s10933-011-9509-x

Guyard H, Chapron E, St-Onge G, Anselmetti FS, Arnaud F, Magand O, Francus P, Mélières MA (2007) High-altitude varve records of abrupt environmental changes and mining activity over the last 4000 years in the Western French Alps (Lake Bramant, Grandes Rousses Massif). Quaternary Sci Rev 26:2644–2660. doi:10.1016/j.quascirev.2007.07.007

Haese RR, Schramm J, Rutgers van der Loeff MM, Schulz HD (2000) A comparative study of iron and manganese diagenesis in continental slope and deep sea basin sediments of Uruguay (SW Atlantic). Int J Earth Sci 88:619–629

Hanslik D, Löwemark L, Jakobsson M (2013) Biogenic and detrital-rich intervals in central Arctic Ocean cores identified using x-ray fluorescence scanning. Polar Res 32:18386. http://dx.doi.org/10.3402/polar.v32i0.18386. Accessed 7 Feb 2013

Helama S, Vartiainen M, Kolstro T, Peltola H, Meriläinen J (2008) X-ray microdensitometry applied to subfossil tree-rings: growth characteristics of ancient pines from the southern boreal forest zone in Finland at intra-annual to centennial time-scales. Veget Hist Archaeobot 17:675–686. doi:10.1007/s00334-008-0147-9

Helama S, Vartiainen M, Kolström T, Meriläinen J (2010) Dendrochronological investigation of wood extractives. Wood Sci Technol 44:335–351. doi:10.1007/s00226-009-0293-y

Hibbert FD, Austin WEN, Leng MJ, Gatliff RW (2010) British ice sheet dynamics inferred from North Atlantic ice-rafted debris records spanning the last 175000 years. J Quat Sci 25:461–482

Hodell DA, Channell JET, Curtis JH, Romero OE, Röhl U (2008) Onset of "Hudson Strait" Heinrich events in the eastern North Atlantic at the end of the middle Pleistocene transition (~640 ka)? Paleoceanography. doi:10.1029/2008PA001591

Ivanov MK, Limonov AF, van Weering TjCE (1996) Comparative characteristics of the Black Sea and Mediterranean Ridge mud volcanoes. Mar Geol 132:253–571. doi:10.1016/0025-3227(96)00165-X

Kylander ME, Ampel L, Wohlfarth B, Veres D (2011) High-resolution X-ray fluorescence core scanning analysis of Les Echets (France) sedimentary sequence: new insights from chemical proxies. J Quat Sci 26:109–117. doi:10.1002/jqs.1438

Lamb HF, Leng MJ, Telford RJ (2007) Oxygen and carbon isotope composition of authigenic carbonate from an Ethiopian lake: a climate record of the last 2000 years. Holocene 17:517–526. doi:10.1177/0959683607076452

Langdon PG, Caseldine CJ, Croudace IW, Jarvis S, Wastegård S, Crowford TC (2011) A chironomid-based reconstruction of summer temperatures in NW Iceland since AD 1650. Quat Res 75:451–460

Löwemark L, Jakobsson M, Mörth M, Backman J (2008) Arctic Ocean manganese contents and sediment colour cycles. Polar Res 27:105–1013

Löwemark L, Chen HF, Yang TN, Kylander M, Yu EF, Hsu YW, Lee TQ, Song SR, Jarvis S (2011) Normalizing XRF-scanner data: a cautionary note on the interpretation of high-resolution records from organic-rich lakes. J Asian Earth Sci 40:1250–1256. doi:10.1016/j.jseaes.2010.06.002

Mazurenko LL, Soloviev VA, Belenkaya I, Ivanov MK, Pinheiro LM (2002) Mud volcano gas hydrates in the Gulf of Cadiz. Terra Nova 14:321–329. doi:10.1046/j.1365-3121.2002.00428.x

McHugh CMG, Gurung D, Giosan L, Ryan WBF, Mart Y, Sancar U, Burckle L, Çagatay MN (2008) The last reconnection of the Marmara Sea (Turkey) to the World Ocean: a paleoceanographic and paleoclimatic perspective. Mar Geol 255:64–82. doi:10.1016/j.margeo.2008.07.005

Metcalfe SE, Jones MD, Davies SJ, Noren A, Mackenzie A (2010) Climate variability over the last two millennia in the North American Monsoon region, recorded in laminated lake sediments from Laguna de Juanacatlán, Mexico. Holocene 20:1195–1206

Milliman JD, Müller J (1973) Precipitation and lithification of magnesium calcite in the deep-sea sediments of the eastern Mediterranean Sea. Sedimentology 20:29–45

Mohamed KJ, Rey D, Rubio B, Vilas F, Frederichs T (2010) Interplay between detrital and diagenetic processes since the last glacial maximum on the northwest Iberian continental shelf. Quat Res 73:507–520

Peterson LC, Haug GH, Hughen KA, Röhl U (2000) Rapid changes in the hydrologic cycle of the Tropical Atlantic during the Last Glacial. Science 290:1947–1950

Rebolledo L, Sepúlveda J, Lange CB, Pantoja S, Bertrand S, Hughen K, Figueroa D (2008) Late Holocene marine productivity changes in Northern Patagonia-Chile inferred from a multiproxy analysis of Jacaf channel sediments. Estuar Coast Shelf Sci 80:314–322. doi:10.1016/j.ecss.2008.08.016

Rey D, Rubio B, Mohamed K, Vilas F, Alonso B, Ercilla G, Rivas T (2008) Detrital and early diagenetic processes in Late Pleistocene and Holocene sediments from the SW Galicia Bank inferred from high-resolution enviromagnetic and geochemical records. Mar Geol 249:64–92

Richter TO, Van Der Gaast S, Vaars A, Gieles R, De Stigter HC, De Haas H, Van Weering TCE (2006) The Avaatech XRF Core Scanner: technical description and applications to NE Atlantic sediments. In: Rothwell RG (ed) New techniques in sediment core analysis. Geol Soc Spec Publ 267:39–50. doi:10.1144/GSL.SP.2006.267.01.03

Robinson JW, Frame EMS and Frame GM (2005) X Ray spectroscopy. In: Robinson JW, Frame EMS, Frame GM (eds) Undergraduate instrumental analysis, 6th edn. Marcel Dekker, New York

Rolland N, Larocque I, Francus P, Pienitz R, Laperrière L (2008) Holocene climate inferred from biological (Diptera: Chironomidae) analyses in a Southampton Island (Nunavut, Canada) lake. Holocene 18:229–241. doi:10.1177/0959683607086761

Sautkin A, Talukder AR, Comas MC, Soto JI, Alekseev A (2003) Mud volcanoes in the Alboran Sea: evidence from micropaleontological and geophysical data. Mar Geol 195:237–261. doi:10.1016/S0025-3227(02)00691-6

Schulz HD (2006) Quantification of early diagenesis: dissolved constituents in pore water and signals in the solid phase. In: Schulz HD, Zabel M (eds) Marine geochemistry, 2nd edn. Heidelberg, New York

Smith KT, Baloutet JC, Oudijk G (2008) Elemental line scanning of an increment core using EDXRF: from fundamental research to environmental forensics applications. Dendrochronologia 26:157–163. doi:10.1016/j.dendro.2008.06.001

Somoza L, Díaz-del-Río V, León R, Ivanov M, Fernández-Puga MC, Gardner JM, Hernández-Molina FJ, Pinheiro LM, Rodero J, Lobato A, Maestro A, Vázquez JT, Medialdea T, Fernández-Salas LM (2003) Seabed morphology and hydrocarbon seepage in the Gulf of Cádiz mud volcano area: acoustic imagery, multibeam and ultra-high resolution seismic data. Mar Geol 195:153–176. doi:10.1016/S0025-3227(02)00686-2

St-Onge G, Chapron E, Guyard H, Rochon A, Lajeunesse P, Locat J, Scott D, Stoner JS, Hillaire-Marcel C (2008) High-resolution physical and magnetic properties of rapidly deposited layers

associated with landslides, earthquakes and floods. In: Locat J, Perret D, Turmel D, Demers D, Leroueil S (eds) Comptes rendus de la 4e Conférence canadienne sur les géorisques: des causes à la gestion. Proceedings of the 4th Canadian conference on geohazards: from causes to management. Presse de l'Université Laval, Québec, 594 p

Teodoru CR, Friedl G, Friedrich J, Roehl U, Sturm M, Wehrli B (2007) Spatial distribution and recent changes in carbon, nitrogen and phosphorus accumulation in sediments of the Black Sea. Mar Chem 105:52–69

Thomson J, Crudeli D, de Lange GJ, Slomp CP, Erba E, Corselli C, Calvert E (2004) Florisphaera profunda and the origin and diagenesis of carbonate phases in eastern Mediterranean sapropel units. Paleoceanography 19:PA3003. doi:10.1029/2003PA000976

Thomson J, Croudace IW, Rothwell RG (2006) A geochemical application of the ITRAX scanner to a sediment core containing eastern Mediterranean sapropel units. In: Rothwell RG (ed) New techniques in sediment core analysis. Geol Soc Spec Publ 267:65–77. doi:10.1144/ GSL. SP.2006.267.01.05

Tjallingii R, Röhl U, Kölling M, Bickert T (2007) Influence of the water content on X-ray fluorescence core-scanning measurements in soft marine sediments. Geochem Geophys Geosyst. doi:10.1029/2006GC001393

Unkel I, Björck S, Wohlfarth B (2008) Deglacial environmental changes on Isla de los Estados (54.41S), southeastern Tierra del Fuego. Quat Sci Rev 27:1541–1554. doi:10.1016/j.quascirev.2008.05.004

Vasskog K, Nesje A, Støren EN, Waldmann N, Chapron E, Ariztegui D (2011) A Holocene record of snow-avalanche and flood activity reconstructed from a lacustrine sedimentary sequence in Oldevatnet, western Norway. Holocene. doi:10.1177/0959683610391316

Windom HL, Schropp SJ, Calder FD, Ryan DJ, Smith RG, Burney LC, Lewis FG, Rawlinson CH (1989) Natural trace metal concentrations in estuarine and coastal marine sediments of the southeastern United States. Environ Sci Technol 23:314–320

Ziegler M, Jilbert T, de Lange GJ, Lourens LJ, Reichart G-J (2008) Bromine counts from XRF scanning as an estimate of the marine organic carbon content of sediment cores. Geochem Geophys Geosyst 9:Q05009. doi:10.1029/2007GC001932

# Chapter 4
# Use of Calibrated ITRAX XRF Data in Determining Turbidite Geochemistry and Provenance in Agadir Basin, Northwest African Passive Margin

**James E. Hunt, Ian W. Croudace and Suzanne E. MacLachlan**

**Abstract** The Agadir Basin is a mixed siliciclastic-volcaniclastic deepwater turbidite system derived from several sedimentary sources. Estimating the influence of these sources requires detailed geochemical profiles of sediment cores. This is achieved using an ITRAX μXRF core scanner that normally produces elemental profiles in units of counts or count rate. Improved insights are achieved if the ITRAX data are calibrated to produce concentration data. Turbidite geochemistry can then be used to more reliably infer the sources of flows and identify primary sediment sources, which are the Moroccan slope for siliciclastic beds and the western Canary Islands for volcaniclastic turbidites. Cross-plots of the geochemical data discriminate variations between different siliciclastic and volcaniclastic beds. For example, differences between two distinctive volcaniclastic marker beds, named A2 and A14, reflect differences in their respective Canary Island sources and indicate a primitive basaltic source for bed A2 and an evolved source for bed A14. Compositional variations between siliciclastic deposits reflect potential variations in the sediment source that failed or the location of the failure on the Moroccan continental slope.

**Keywords** Turbidite · Sediment provenance · Agadir Basin · ITRAX · Submarine Landslides

## Introduction

The Moroccan Turbidite System is a multi-basin depositional province off the coast of NW Africa, comprising the Agadir Basin (proximal), Seine Abyssal Plain (northeast) and Madeira Abyssal Plain (west, distal) (Fig. 4.1). Previous studies of the

J. E. Hunt (✉) · S. E. MacLachlan
National Oceanography Centre, European Way, Southampton, SO14 3ZH, UK
e-mail: james.hunt@noc.ac.uk

I. W. Croudace
Ocean and Earth Science, National Oceanography Centre, University of Southampton, Waterfront Campus, European Way, Southampton SO14 3ZH, UK



I. W. Croudace, R. G. Rothwell (eds.), *Micro-XRF Studies of Sediment Cores*,
Developments in Paleoenvironmental Research 17, DOI 10.1007/978-94-017-9849-5_4

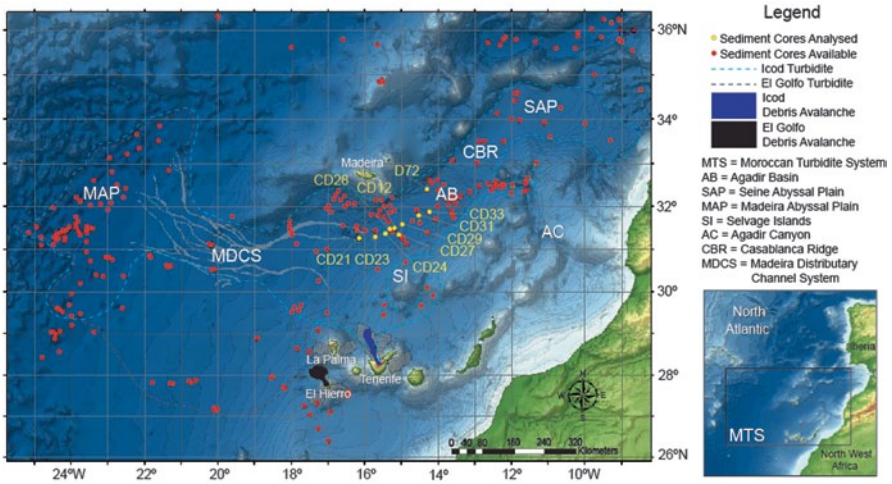


**Fig. 4.1** Bathymetric map of Agadir Basin, offshore Morocco. Map shows source of siliciclastic sediment gravity flows via Agadir Canyon, presence of two subtle sub-basins within Agadir Basin and the Madeira Distributary Channel System to the Madeira Abyssal Plain to the west. Core sites shown as *red squares*, numbered sites from cruise CD166 used in this study are shown as *yellow squares*

Madeira Abyssal Plain have shown that turbidite geochemistry can support turbidite correlation over hundreds of kilometres and identify their provenance (Weaver and Kuijpers 1983; de Lange et al. 1987; Weaver and Rothwell 1987; Pearce and Jarvis 1992, 1995; Weaver et al. 1992). Bulk geochemical studies of Madeira Abyssal Plain turbidites identified organic-rich siliciclastic, volcaniclastic and calcareous turbidite types (de Lange et al. 1987; Pearce and Jarvis 1992, 1995; Jarvis et al. 1998). Further, variations in major element compositions identified different volcanic and siliciclastic sources (de Lange et al. 1987; Pearce and Jarvis 1992, 1995; Jarvis et al. 1998).

Previous studies analysed bulk samples from each turbidite mudcap using inductively coupled plasma optical emission spectroscopy (ICP-OES) (de Lange et al. 1987; Pearce and Jarvis 1995; Jarvis et al. 1998). However, such methodologies requiring acid digests of numerous sub-samples are time-consuming, destructive and expensive. Non-destructive geochemical core scanners, such as the ITRAX micro-X-ray fluorescence (μXRF) core scanner (based at the British Ocean Sediment Core Research Facility, NOC, Southampton) can rapidly acquire geochemical profiles at resolutions of 200 μm or more (Croudace et al. 2006). Combining a continuous high-resolution record with a conversion to concentration using sub-samples analysed by ICP-OES provides a strong advantage over other methods by producing detailed geochemical profiles for the turbidites in Agadir Basin which allow assessment of bed provenance.

Core scanner XRF data have been previously used for turbidite correlations, sediment provenance and sediment diagenesis studies (Rothwell et al. 2006; Thomson et al. 2006; Giresse et al. 2009; Cronan et al. 2010). ITRAX μXRF data has been previously used to aid identification of volcaniclastic and siliciclastic turbidites from Agadir Basin (Frenz et al. 2009). That study directly compared ITRAX profiles that included variations in sand and mud. However, element variation is likely to be dependent on grain-size distribution. This study clarifies element variability by calibrating the ITRAX data from turbidite mud-caps.

## Geological Setting

Agadir Basin is a depocentre proximal to the Moroccan slope fed directly by Agadir Canyon (Fig. 4.1; Wynn et al. 2002a). It represents a mixed siliciclastic-volcaniclastic basin in 4000–4300 m water depth floored by allochthonous deposits that range from 1 to 250 $km^3$ in volume (Frenz et al. 2009). Siliciclastic turbidites are sourced from the Moroccan continental slope, while volcaniclastic turbidites are sourced from the western Canary Islands and calcareous turbidites from the Selvage Islands (Wynn et al. 2002a, b; Frenz et al. 2009). Turbidite Bed A2 has been previously linked with the El Golfo landslide from El Hierro, bed A8 from South Madeira, and bed A14 have been linked to the Icod landslide from Tenerife (see Hunt et al. 2011, 2013, and references therein).

## Methodology and Data

This study focuses on investigation of a single core (CD166/12) from Agadir Basin. This represents the 'type' sequence for the basin and has been the focus of several studies, including Frenz et al. (2009) (core location shown on Fig. 4.1). Core CD166/12 recovers the basin stratigraphy to bed A14 dated at 165 ka (Hunt et al. 2011, 2013). This core contains the distinctive turbidite bed A2 (linked to the El Golfo landslide from El Hierro), bed A8 from South Madeira, and bed A14 (linked to the Icod landslide from Tenerife).

### *Visual and Sedimentological Logging*

Sediment colour, grain size, sedimentary structures, diagenetic features and mineralogy were recorded to provide a framework for the study. Down core gamma-density, p-wave velocity and magnetic susceptibility data were collected using a standard *GEOTEK* multi-sensor core logger (MSCL-S), as presented in Hunt et al. (2013).

### *ITRAX µXRF Core Scanning*

Split sections of core CD166/12 were rescanned using the methodology of Frenz et al. (2009). Sections were progressively moved past a 3 kW Mo-tube X-ray source and XRF Si-drift chamber detector within an ITRAX core scanner (Croudace et al. 2006). The instrument was operated at 60 kV and 45 mA, with a count time of 30 s, and at 500 µm sample resolution. Monitoring the down-core profiles of element integrals, Compton scatter integral and detector-sediment distance supported data validity. The element normalised using the Mo incoherent integrals. These results were calibrated against a suite of 1 cm-wide samples taken from the core and analysed using inductively coupled plasma optical emission spectrometry (ICP-OES).

The ICP-OES analyses required acid digestions (Appendix Table 4.1 and 4.2). These samples were taken to provide quantified data for the geochemistry of the deposits, and to calibrate the raw ITRAX elemental counts. ITRAX intensities over the 1 cm sampled were averaged for calibration. Calibration coefficients for the ITRAX data produced $R^2$ values of 0.74–0.96 (Fig. 4.2).

An effective means of converting XRF core scanner outputs to elemental concentrations is to analyse a set of discrete sub-samples by WD-XRF or ICP-OES and to use these to calibrate the ITRAX data. Intensity-concentration cross-plots can show considerable scatter and potential biasing due to sample inhomogeneity, variable water content, inter-element matrix effects and physical imperfections caused by bad sample surfaces (e.g. Croudace et al. 2006; Weltje and Tjallingii 2008). Averaging intensities over the 1 cm sampled for ICP-OES analysis reduces the effects of small-scale inhomogeneities (e.g. mineral and grain-size effects) on the calibration. Issues with sample geometry and signal-to-noise are reduced by the ITRAX detector automatically adjusting its position relative to the split core surface according to core topography (Croudace et al. 2006).

Sediment within core CD166-12 varies in grain size according to lithological character. Hemipelagites average 10–30 µm, turbidite muds average 6–12 µm, and turbidite sands average 90–180 µm (d90 fraction at 350 µm) in particle size. The 500 µm ITRAX resolution is greater than the largest grains recovered from deposits in core CD166/12, hence issues regarding sample geometry are further reduced.

The plots of grain size and elemental variation show a small grain-size effect (Fig. 4.3). Therefore only turbidite mudcap geochemistry was compared to keep grain-size effects small; the average mud-cap grain-size is 6–12 µm (Fig. 4.4). Only comparing compositions of turbidite mudcaps also had another benefit by minimising any effects caused by variable water content due to their similar porosity-permeability-density characteristics.

The turbidite mudcaps contain high, but variable, proportions of carbonate and comparison between sections benefit from normalisation to suppress constant sum effects. As Al data was imprecise in the current dataset, Rb was used as an effective alternative as it is co-located in alumino-silicates (Croudace et al. 2006).

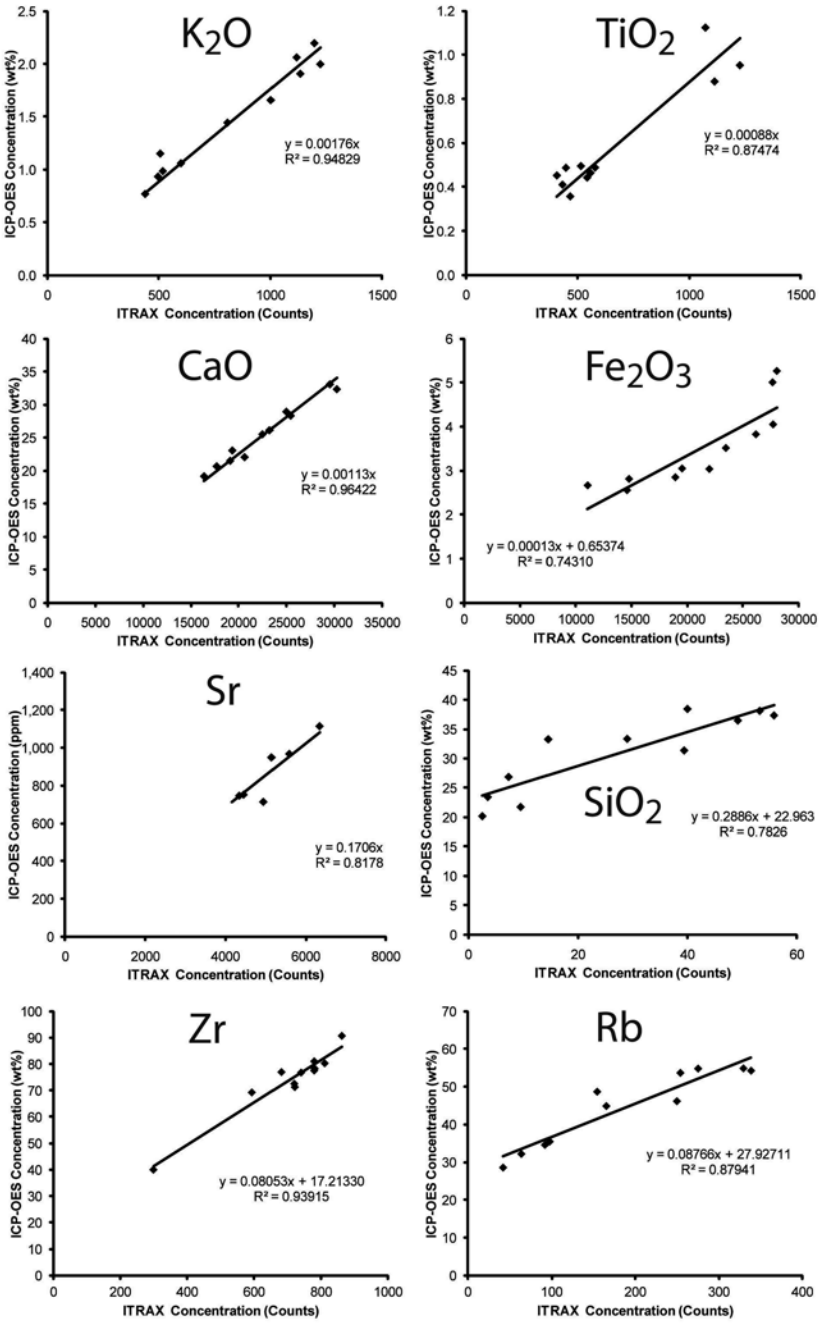


**Fig. 4.2** Calibration curves for major element oxides and trace elements between ITRAX counts and ICP-OES analyses for samples from core CD166/12

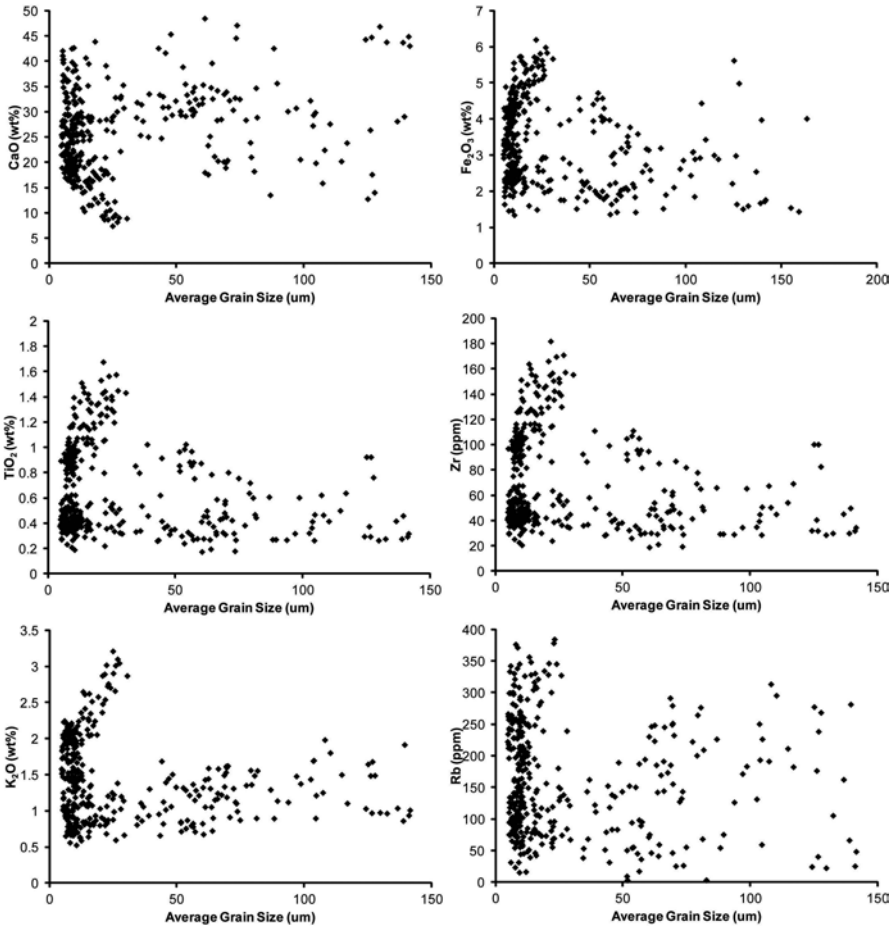


**Fig. 4.3** Plot of grain-size against calibrated ITRAX concentration of major element oxides and trace elements in core CD166/12

## *ICP-OES Analysis*

Bulk sediment analysis typically involves analysing discrete sub-samples by WD-XRF or ICP-OES with the former being more straightforward and rapid since dissolutions are not required. However, ICP-OES normally requires less than 0.5 g of sample compared with 3 g or more required for WD-XRF analysis of pressed powder pellets. Analysis of fusion beads by XRF typically use 0.5 g of sample but is mostly only used formajor element determinations. In this study, we used the ICP-OES methodology due to the smaller sample size required and is more compatible with on-going provenance studies. Bulk samples were taken from the turbidite mudcaps from the Agadir Basin cores analysed using ITRAX (Appendix 1).

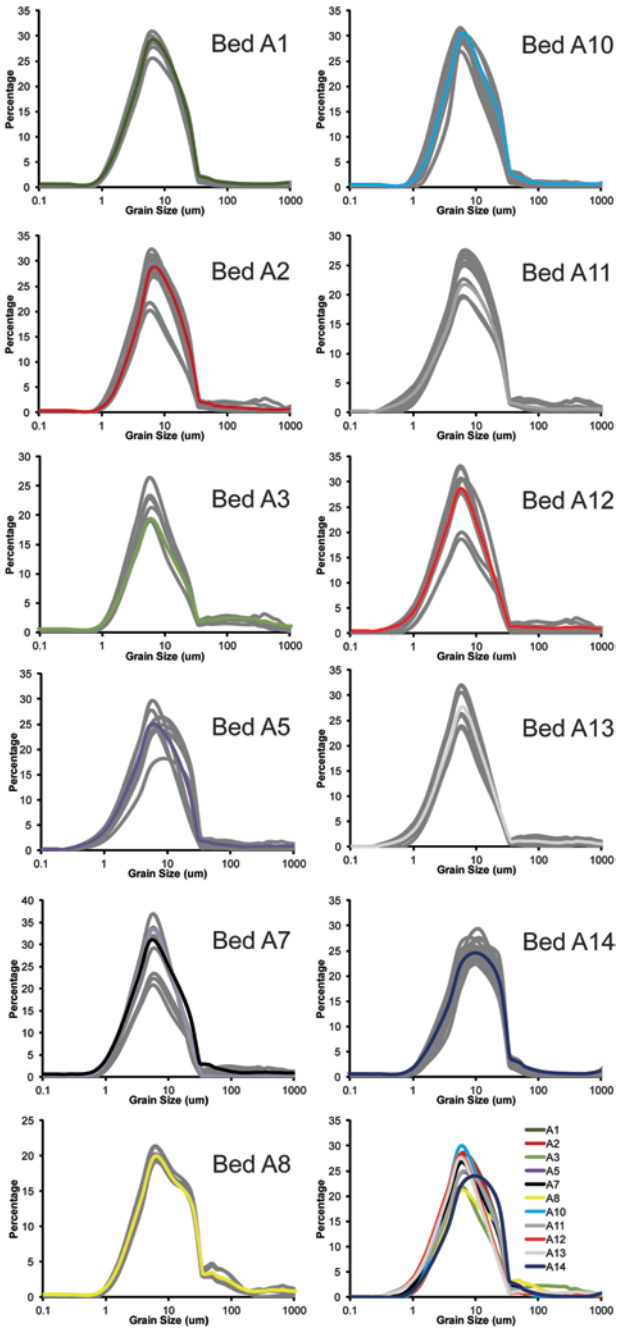


**Fig. 4.4** Grain-size distribution plots for mudcaps of turbidites in core CD166/12

The samples were dried and powdered using an agate pestle and mortar for acid digestion. Aliquots of 100 μg were first digested using 5 mL aqua regia (3:1 $HCl:HNO_3$), and then with 3 mL HF and 2.25 mL perchloric acid. The final silica-free residue was dissolved in 6 M HCl, from which 0.6 M HCl daughter solutions were made for analysis. A number of terrigenous (USGS MAG-1 and SCo-1) and volcanic (USGS BHVO-2 and BIR-1; JGS JB-1a, JB-2, JB-3 and JGB-1) geochemical reference materials (GRMs) were used to assess analytical accuracy and precision (Appendix 2). The ranges of concentrations used in the production of artificial standards were constrained by element concentrations from previous studies of Madeira Abyssal Plain turbidites (de Lange et al. 1987; Pearce and Jarvis 1995).

Analyses of standard reference materials demonstrate that major element analyses (Na, Mg, Al, K, Ca, Ti, and Fe) had average precisions of 2.1–3.1 % and average accuracies to the standard reference materials of 1.5–3.3 % (Appendix 2). With regards to trace elements, precision varied with Li, V, Co, Cr, Cu, Sr, Zr, Ba and La between 3.6 % and 9.7 %, and with accuracies ranging to within 2.2–8.9 % (Appendix 2). Trace elements Sc, Zn, Y, Ce, and to a lesser extent Zr had precisions of > 10 % and accuracies to standard reference materials to within 10 %.

### *Grain-Size Analysis*

Grain-size analyses were made on samples from hemipelagites, turbidite mudcaps and turbidite sands for sediment facies evaluation and to correlate with the geochemistry (Fig. 4.3). Turbidite mudcap grain-size distributions were used to identify any consistency in particle size distribution (Fig. 4.4). Samples of 1 mL volume were dispersed in 0.05 % sodium hexametaphosphate solution and analysed using a *Malvern Mastersizer 2000* particle sizer.

## Results

### *Turbidite Geochemistry*

#### Volcaniclastic Turbidites (Beds A2, A8 and A14)

Bed A2 has been previously linked with the El Golfo landslide from El Hierro (Masson et al. 2002; Frenz et al. 2009) and Pearce and Jarvis (1992, 1995) argue that the low $SiO_2$ and $K_2O$ contents of both the turbidite mud and sand indicate a primitive basaltic origin. Frenz et al. (2009) directly compared the composition of bed A2 with that of beds A8 and A14 (Icod turbidite—linked to Icod landslide from Tenerife, Hunt et al. 2011). Turbidite A8 is represented by a 0–30 cm-thick coarse basaltic sand, which was compared to the finer-grained A2 and A14 beds. Bed A8 has elevated $TiO_2$ compared to beds A2 and A14 (Fig. 4.5). However, this is primarily a function of grain size (see Frenz et al. 2009, Fig. 4.5). However, elevated $TiO_2$,

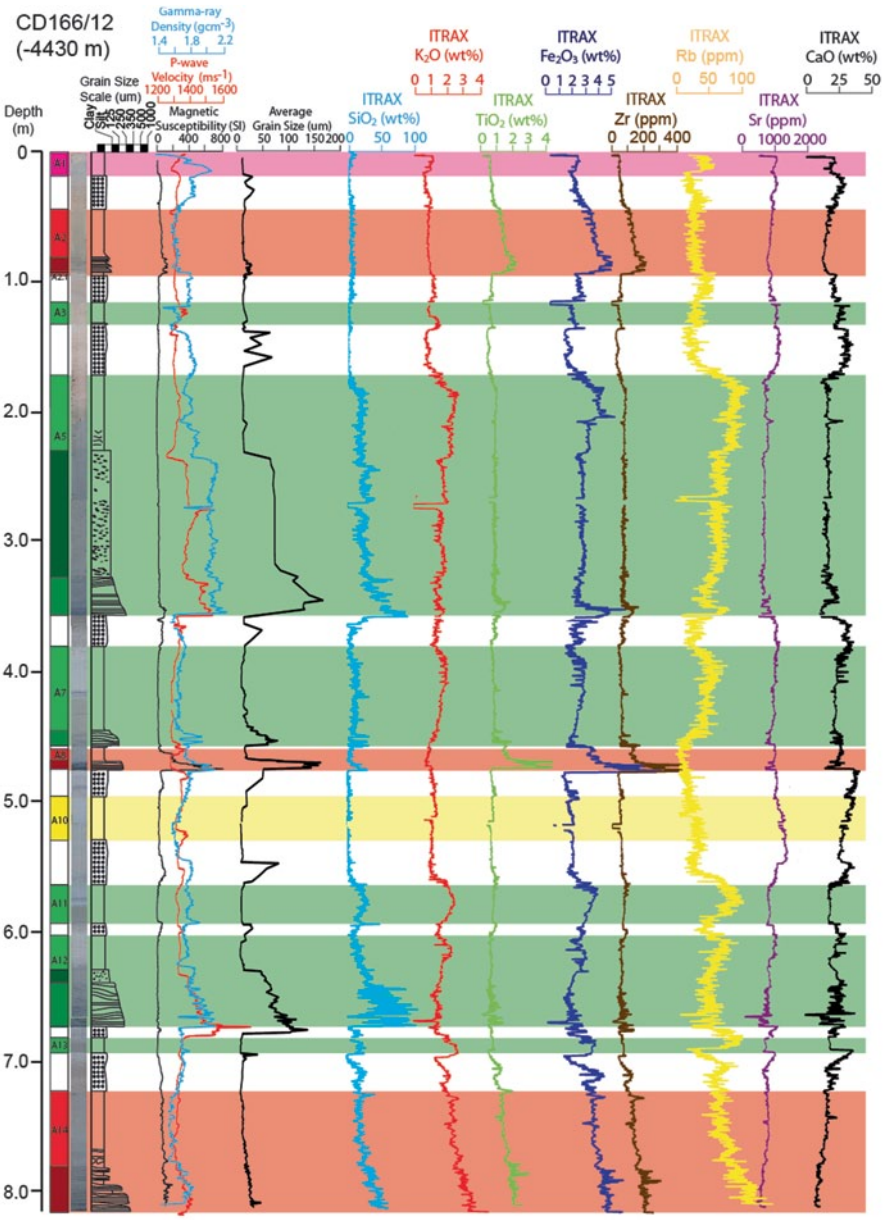


**Fig. 4.5** Down-core logs for CD166/12, showing sedimentary features, physical properties and calibrated ITRAX compositions. Turbidite colours are *green* (Organic-rich siliciclastic), *red* (volcanic) and *yellow* (carbonate). Bed names in left-hand column

Zr and $Fe_2O_3$ in the volcaniclastic turbidites allow them to be clearly discriminated from the siliciclastic and calcareous turbidites (Fig. 4.5).

Three volcaniclastic turbidites are recorded in Agadir Basin with volumes >5 $km^3$ (beds A2, A8 and A14). Study of the turbidite mud geochemistry allows the provenance of these volcaniclastic turbidites to be inferred. Geochemical variation plots show that beds A2, A8 and A14 fall into discrete compositional fields (Figs. 4.6 and 4.7).

The $Fe_2O_3$-$TiO_2$ cross-plot shows the Icod turbidite (A14) has a relatively higher range in $TiO_2$ and $Fe_2O_3$ concentration (Fig. 4.6). The El Golfo (A2) and A8 turbidites have subtly different compositions with different mixing lines (Fig. 4.6). Both show subtly different concentrations of $TiO_2$ and $Fe_2O_3$ (Fig. 4.6).

Further differences are shown by $K_2O$ content (Fig. 4.6). The Icod turbidite (A14) has relatively higher $K_2O$, whereas the El Golfo (A2) and A8 turbidites have lower $K_2O$ concentrations (Fig. 4.6). The A8 turbidite can be distinguished from the El Golfo turbidite (A2) by a slightly elevated $K_2O$ content. $SiO_2$ content can also discriminate between these volcaniclastic turbidites, with the Icod turbidite (A14) having higher $SiO_2$ compared to the El Golfo turbidite (A2) and the A8 turbidite (Fig. 4.6). The A8 turbidite can be best discriminated from the Icod (A14) and El Golfo (A2) turbidites by comparing the CaO concentrations in the mudcap. The A8 turbidite has a higher CaO concentration compared to the El Golfo (A2) and Icod (A14) turbidites (Fig. 4.7).

We normalise element ratios to Rb. Beds A2 and A14 have similar K/Rb ranges, but bed A8 has a higher K/Rb range. However, bed A14 has a lower range of Fe/Rb composition (Fig. 4.8). Beds A2 and A8 show a higher range of Fe/Rb, whereas bed A8 has distinctly higher Fe. Bed A14 also shows lower Zr/Rb values compared to beds A2 and A8, and bed A8 is again distinct in having a higher range of Zr/Rb values (Fig. 4.8).

### Organic-Rich Siliciclastic Turbidites (Beds A1, A3, A5, A7, A11, A12 and A13)

$SiO_2$ is naturally highest in the coarse fraction of siliciclastic turbidites (Figs. 4.5). However, due to the evolved phonolitic composition of the A14 Icod turbidite (Hunt et al. 2011), $SiO_2$ content cannot be reliably used to correlate these beds (Fig. 4.5). As an indicator of detrital clays, $K_2O$ is highest in siliciclastic turbidites (Fig. 4.5). However, its high content in the phonolitic A14 Icod turbidite precludes exclusive use of $K_2O$ to correlate siliciclastic beds (Fig. 4.6). The siliciclastic turbidites have higher CaO compared to volcaniclastic turbidites, although the calcareous turbidites (e.g. A10) also naturally show elevated CaO (Fig. 4.7). Therefore a combination of $SiO_2$, $K_2O$, $Fe_2O_3$ and Sr (instead of CaO) is most useful for identifying siliciclastic beds.

There are two primary sources for the siliciclastic turbidites: the Moroccan and Western Saharan continental slopes (Pearce and Jarvis 1992, 1995; Weaver et al. 1992; Rothwell et al. 1992; Wynn et al. 2002a; Frenz et al. 2009). Frenz et al. (2009) showed that the most recent bed A1 (1 ka) is a siliciclastic turbidite originating from reactivation of the Saharan Slide headwall on the Western Saharan slope, south of the Canary Islands. The chemistry of A1 shows variations in composition relative to other siliciclastic turbidites. Bed A1 has relatively lower concentrations of $TiO_2$

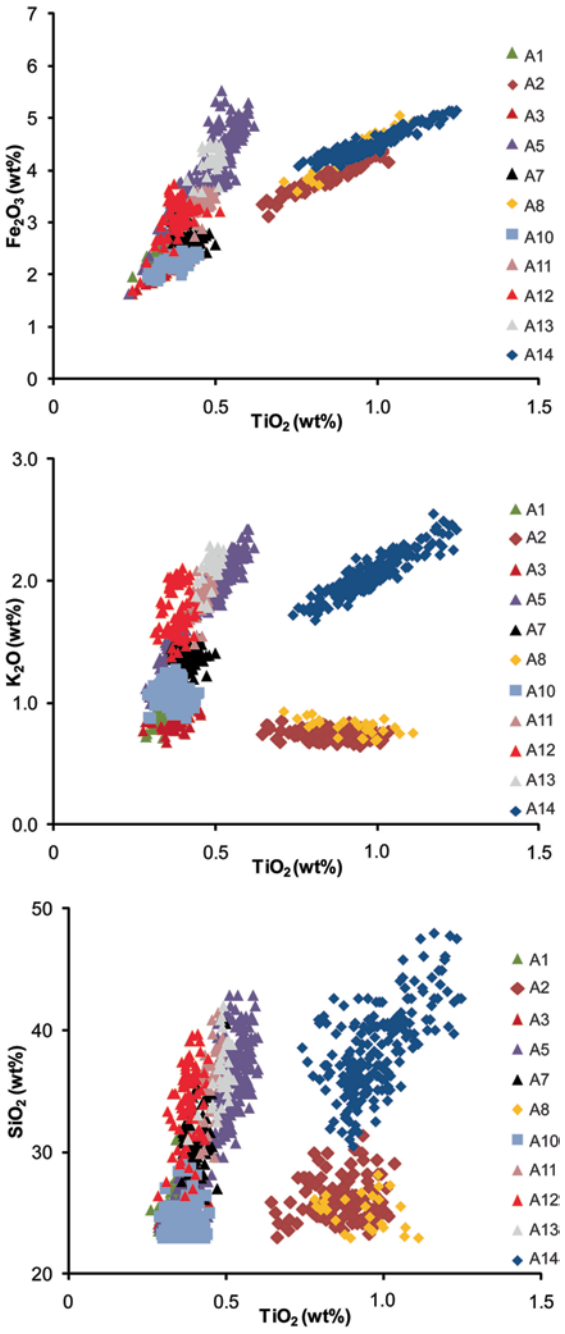


**Fig. 4.6** Calibrated element oxide concentrations for turbidite mudcaps in Agadir Basin, compared as a series of cross plots

and $K_2O$ (Fig. 4.6). It also has relatively low $Fe_2O_3$ and $SiO_2$. Bed A1 also has a relatively high composition of Sr (Table 4.1).

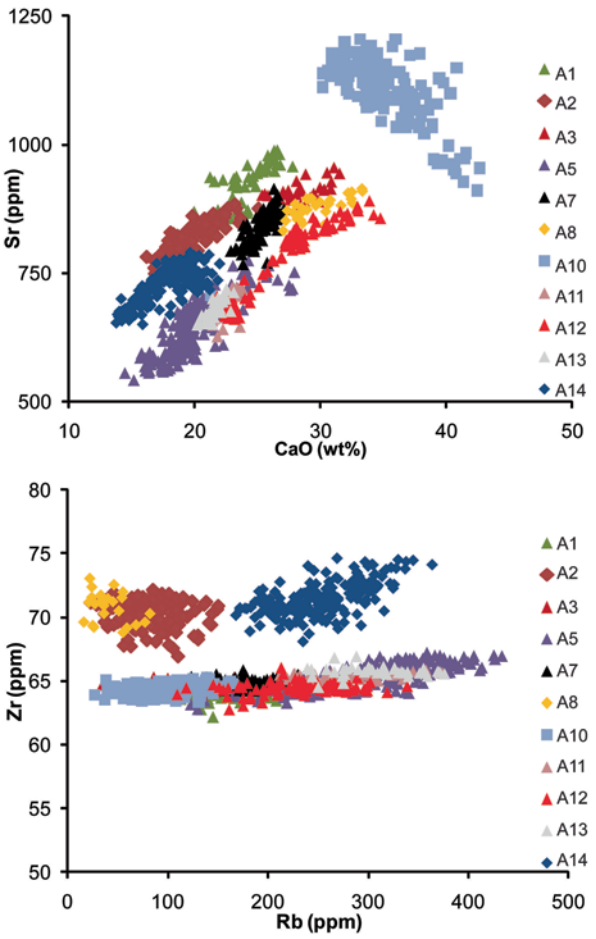


**Fig. 4.7** Calibrated element concentrations for turbidite mudcaps in Agadir Basin focusing on carbonate and terrigenous composition separately, compared as a series of cross plots

The other siliciclastic turbidites (beds A3, A5, A7, A11, A12 and A13) within Agadir Basin originate from the Moroccan slope via Agadir canyon. This is deduced from the depositional and sediment fining patterns shown by Frenz et al. (2009) and Hunt et al. (2013). However, the geochemistry of the turbidite muds (from ITRAX analysis) shows compositional variability between these organic-rich siliciclastic turbidites. Geochemical variation cross-plots of major elements show that a number of compositional fields define different siliciclastic turbidites along discrete compositional arrays (Figs. 4.6 and 4.7, Table 4.1).

Turbidite A3 has a composition with a similar range in $TiO_2$ to A1, but has a reduced $Fe_2O_3$ content. The $Fe_2O_3$ and $TiO_2$ content show additional trends (Fig. 4.6). For example, A5 has a very variable content compared to other turbidites. Turbidite A7 has a more restricted composition. The A11 and A12 turbidites also have restricted $Fe_2O_3$ content; although A11 has slightly higher $TiO_2$ compared to A12 (Fig. 4.6). Turbidite A13 has a higher $TiO_2$ and $Fe_2O_3$ content compared to A1, A3, A7, A11 and A12 (Fig. 4.6).

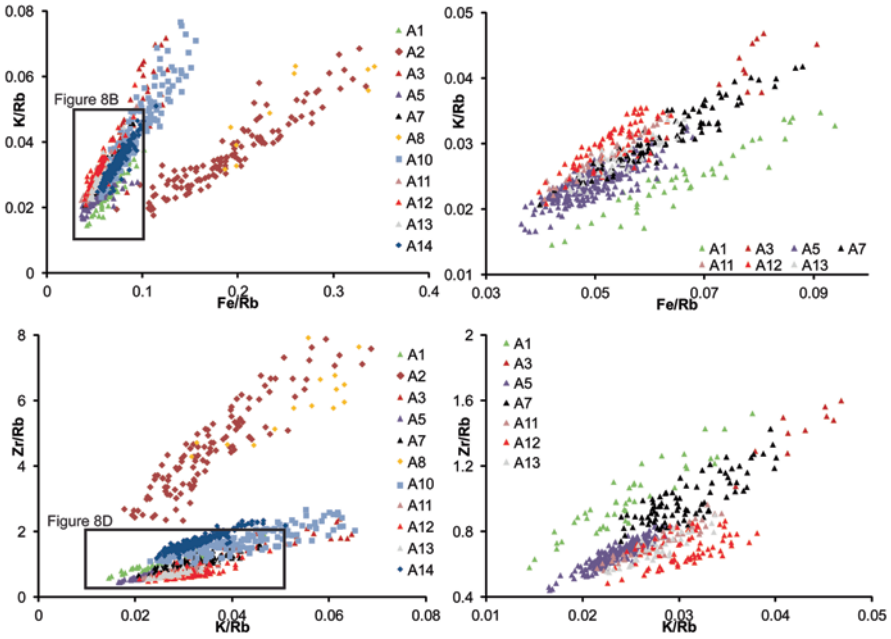


**Fig. 4.8** Element/Rb ratio discrimination plots for Agadir Basin turbidite mudcaps

Similar features can be seen when comparing other major elements in the turbidite muds. For example, with $K_2O$ similar trends are seen as with $Fe_2O_3$, whereby A3 has the lowest concentration (Fig. 4.6). $K_2O$ concentrations progressively increase in A1, A7, A11, A12, and A13. A5 however, shows a broad range of $K_2O$ (Fig. 4.6). Additional trends are seen in CaO and Sr defining discrete compositional fields for each of the organic-rich siliciclastic turbidites (Fig. 4.7).

The Rb normalised data also shows trends within the organic-rich siliciclastic turbidites. Bed A1 has a composition array of lower K/Rb for a given Fe/Rb composition. Likewise for a given value of K/Rb, A1 has a higher value for Zr/Rb (Fig. 4.8). In comparison to Moroccan slope-sourced turbidites, bed A3 has higher K/Rb and Zr/Rb. Bed A7 has higher Zr/Rb, and generally higher K/Rb and Fe/Rb ratios (Fig. 4.8). Bed A5 has a similar range of Zr/Rb and Fe/Rb to A11, A12 and A13, but has generally lower values of K/Rb (Fig. 4.8). Although beds A11, A12 and A13 have similar values of Zr/Rb and Fe/Rb, they can be segregated by K/Rb, as bed A12 has higher K/Rb compared to beds A11 and A13 (Fig. 4.8).

### Calcareous Turbidites (Bed A10)

Turbidite A10 has elevated CaO and Sr compared to siliciclastic and volcaniclastic turbidites. In addition, low $Fe_2O_3$ and $K_2O$ are characteristic of calcareous turbidites (Figs. 4.6 and 4.7).

## Discussion

### *Turbidite Correlation*

Previous studies have used geochemistry to determine turbidite provenance. However, these studies used a limited number of samples from turbidite mudcaps for analysis by ICP-AES (de Lange et al. 1987; Pearce and Jarvis 1995). The ITRAX μXRF core scanner allows direct and non-destructive measurement of sediment chemistry in-situ. Further, the ITRAX produces measurements with high levels of precision and accuracy (Croudace et al. 2006).

The present study has focused on the geochemical analysis of the turbidite mudcaps in Agadir Basin. The results show that siliciclastic turbidites have moderate $SiO_2$ compositions (23–45 wt%). However, it is lower $TiO_2$ content (0.2–0.6 wt%) that discriminates organic-rich siliciclastic turbidites from volcaniclastic turbidites (Fig. 4.6). Our analysis shows that higher $TiO_2$ and Zr concentrations are the dominant discriminating factors for volcaniclasic turbidite mudcaps (Figs. 4.6 and 4.7). This supports findings of previous studies in the distal Madeira Abyssal Plain (Pearce and Jarvis 1995; Jarvis et al. 1998). However, in contrast to previous studies $Fe_2O_3$ is not shown to be a reliable discriminating factor when comparing mudcaps.

However, when considering the coarser fraction in turbidite bases $Fe_2O_3$ becomes an excellent discriminator for the volcaniclastic turbidites providing they have sandy bases (Fig. 4.5). $Fe_2O_3$ can also be used to discriminate the two largest siliciclastic flows (A5 and A12), with minor spikes in $Fe_2O_3$ reflecting increased lithics and iron-stained quartz (aeolian-transported grains) in the basal sands (Fig. 4.5). Zr is also an important discriminator for volcanic turbidites within coarse fractions (Fig. 4.7). In siliciclastic turbidites Sr is an important diagnostic element within coarse-grained bases.

$SiO_2$ discriminates the coarser fraction of siliciclastic turbidites with values of 45–80 wt%, which support values reported by Pearce and Jarvis (1995) (Fig. 4.5). However, caution is needed when using $SiO_2$ as a correlative tool as the A14 volcaniclastic turbidite has an evolved igneous source from Tenerife. The phonolitic glasses in the A14 turbidite have $SiO_2$ contents of 57–64 wt% (Hunt et al. 2011) resulting in bulk sediment compositions of 42–62 wt%. In addition to the turbidite chemostratigraphy, correlation of the hemipelagite sequences (using CaO and $Fe_2O_3$) supports turbidite correlation within Agadir Basin (Hunt et al. 2013).

Raw activity counts generated by the ITRAX can be calibrated using results of bulk analyses of discrete core samples (Fig. 4.2). The accuracy and precision of the ITRAX core scanner is well documented (Croudace et al. 2006; Thomson et al. 2006; Rothwell et al. 2006). However, our calibration curves (Fig. 4.2) show scatter in the intensity-concentration cross-plots. Further, Fe, Si, Zr and Rb fail to plot through the origin. These features suggest that other factors, such as grain size and water content, may influence ITRAX results (Weltje and Tjallingii 2008). This study has been unable to resolve these issues, which has resulted in the present work using element ratios.

### *Turbidite Provenance*

Comparison of turbidite mud geochemistry using data from the ITRAX has defined discrete compositional fields for each turbidite (Figs. 4.6, 4.7 and 4.8). Mudcaps, representing deposition from suspension fallout, were chosen to make comparisons of similar (if not identical) grain-size distributions. Thus variations will primarily reflect geochemical differences, rather than effects due to different grain size and/or depositional processes.

Volcaniclastic turbidites can be clearly discriminated from siliciclastic or calcareous turbidites (Figs. 4.5, 4.6 and 4.7). Further, individual volcaniclastic turbidites can be discriminated from one another on their provenance character (Figs. 4.5, 4.6 and 4.7). The A14 turbidite (Madeira Abyssal Plain bed *g*) is linked to the ~165 ka Icod landslide from Tenerife (Hunt et al. 2011, and references therein). As a result the A14 turbidite has an evolved phonolitic composition represented by elevated $SiO_2$, $Fe_2O_3$, $K_2O$, $TiO_2$ and Zr, and lower values of CaO and Sr (Figs. 4.6 and 4.7). The basic igneous composition of turbidites A2 and A8 are defined by lower $SiO_2$, $TiO_2$, $K_2O$ and Zr, but have elevated Sr and CaO (Figs. 4.6 and 4.7).

The A2 turbidite has been linked to the El Golfo landslide from El Hierro (Masson et al. 2002; Frenz et al. 2009; Hunt et al. 2011, and references therein). The El Hierro source has a basic basaltic composition. The spatial distribution of the A8 turbidite indicates a Madeira provenance (Frenz et al. 2009), which suggests it has a basaltic character. Differences between the two basaltic El Hierro and Madeira sources can be seen by comparing major-element mudcap geochemistyt. The A2 turbidite (El Hierro source) has lower $Fe_2O_3$, $K_2O$ and CaO and elevated $SiO_2$ compared to turbidite A8 (Madeira source) (Figs. 4.6 and 4.7).

Analysis of the siliciclastic turbidites also shows that individual continental slope provenances can be identified. Although all siliciclastic turbidites (except A1 from Western Sahara slope) have broadly similar compositions, the composition of each turbidite mudcap lies on a subtly different array (Figs. 4.6 and 4.7). However, these differences as seen at basin sites (e.g. CD166/12) may reflect addition of material through erosion of the seafloor by the turbidity current at the mouth of Agadir Canyon, or within more proximal regions of the basin. Evidence for turbidity current erosion at the mouth of the Agadir Canyon is presented by Ercilla et al. (1998), Weaver et al. (2000), Wynn et al. (2002a), Talling et al. (2007), Wynn et al. (2010), and MacDonald et al. (2011). However, the disparities in turbidite composition may also result from the provenance and composition of the originally failed material (Figs. 4.5 and 4.6).

## Conclusions

Turbidites can be correlated according to bulk sand and mudcap geochemistry. Although grain size is shown to have only minimal control on composition, analysis of mudcaps has provided more consistent comparison of turbidite character. The

ITRAX data has provided detailed geochemical information for effective correlation of turbidites and better understanding their provenance.

The methodology used clearly distinguishes siliciclastic, volcaniclastic and carbonate turbidites, enabling detailed investigation of bed provenance and clearly demonstrating differences in volcanic and siliciclastic sources.

**Acknowledgements** The authors thank the crews and officers of the CD166 and JC27 research expeditions during which the cores studied were taken. JEH also acknowledges an NOCS PhD studentship hosted within the Marine Geoscience Group. The curators at BOSCORF are also thanked for access to their core archive and analytical instruments. Finally, JEH and co-authors thank the reviewers for their positive feedback and comments on improving the manuscript.

# Appendix 1

**Table 4.1** Major and trace element data (ICP-OES) for the turbidite mudcaps used to calibrate ITRAX data

| Code | CD166-12-01 | CD166-12-02 | CD166-12-03 | CD166-12-05 | CD166-12-07 | CD166-12-08 | CD166-12-10 | CD166-12-11 | CD166-12-12 | CD166-12-13 | CD166-12-14 |
|---|---|---|---|---|---|---|---|---|---|---|---|
| Turbidite | 1 | 2 | 3 | 5 | 7 | 8 | 10 | 11 | 12 | 13 | 14 |
| Provenance | Sahara | El Hierro | Morocco | Morocco | Morocco | Madeira | Selvage | Morocco | Morocco | Morocco | Tenerife |
| $TiO_2$ | 0.45 | 0.95 | 0.49 | 0.49 | 0.41 | 1.12 | 0.49 | 0.44 | 0.36 | 0.46 | 0.88 |
| $Al_2O_3$ | 5.97 | 6.59 | 4.76 | 9.14 | 6.45 | 7.05 | 5.17 | 8.55 | 7.24 | 9.57 | 9.79 |
| $Fe_2O_3$ | 2.81 | 5.01 | 2.67 | 3.52 | 2.85 | 5.27 | 2.56 | 3.04 | 3.05 | 3.83 | 4.05 |
| MnO | 0.05 | 0.15 | 0.08 | 0.04 | 0.04 | 0.11 | 0.07 | 0.04 | 0.07 | 0.05 | 0.11 |
| MgO | 1.70 | 2.52 | 1.57 | 2.57 | 1.91 | 2.33 | 1.64 | 2.49 | 1.88 | 2.43 | 1.70 |
| CaO | 28.97 | 23.10 | 33.12 | 20.71 | 25.55 | 28.37 | 32.38 | 22.09 | 26.16 | 21.54 | 19.20 |
| $Na_2O$ | 2.46 | 3.59 | 2.41 | 1.77 | 1.86 | 2.31 | 1.78 | 1.60 | 1.42 | 1.70 | 4.18 |
| $K_2O$ | 1.15 | 0.93 | 0.99 | 2.06 | 1.44 | 0.77 | 1.06 | 1.90 | 1.65 | 1.99 | 2.19 |
| $P_2O_5$ | 0.15 | 0.30 | 0.16 | 0.15 | 0.16 | 0.30 | 0.18 | 0.17 | 0.14 | 0.14 | 0.26 |
| $SiO_2$ Calc | 26.87 | 33.25 | 20.21 | 38.39 | 33.32 | 23.47 | 21.78 | 37.29 | 31.36 | 36.42 | 38.06 |
| V | 117.5 | 66.4 | 86.8 | 50.9 | 80.5 | 67.2 | 117.6 | 54.2 | 101.8 | 66.0 | 91.5 |
| Cr | 61.7 | 41.0 | 40.5 | 34.5 | 60.4 | 49.4 | 113.2 | 40.2 | 70.5 | 51.6 | 72.5 |
| Co | 13.4 | 9.3 | 17.7 | 8.7 | 8.9 | 8.2 | 18.3 | 8.9 | 10.0 | 7.2 | 15.7 |
| Ni | 30.1 | 29.7 | 38.2 | 20.6 | 32.1 | 27.9 | 54.0 | 26.1 | 33.5 | 22.5 | 36.7 |
| Cu | 14.6 | 47.3 | 50.4 | 41.7 | 28.7 | 51.4 | 41.6 | 26.8 | 64.2 | 15.6 | 58.0 |
| Zn | 140.9 | 73.2 | 72.6 | 52.6 | 78.8 | 64.2 | 70.0 | 54.6 | 71.7 | 74.2 | 78.7 |
| Sr | | | 968.5 | 1194.2 | 713.6 | 949.6 | 1115.3 | | 746.4 | 932.6 | 752.1 |
| Nb | 151.0 | 9.7 | 11.0 | 11.0 | 8.0 | 9.5 | 17.4 | 13.7 | 9.4 | 7.1 | 9.6 |
| Y | 35.5 | 16.7 | 16.6 | 16.8 | 17.0 | 16.1 | 17.6 | 16.7 | 16.4 | 15.6 | 18.5 |
| Zr | 90.7 | 69.2 | | 70.3 | 77.5 | 78.3 | | | 71.0 | 62.6 | 76.8 |
| Ba | | | 378.8 | | 385.0 | 405.0 | | | 414.7 | 409.4 | 459.0 |
| La | 0.0 | 22.2 | 29.9 | 20.9 | 24.0 | 21.7 | 23.4 | 22.5 | 22.3 | 21.3 | 26.2 |
| Ce | 78.4 | 40.9 | 61.5 | 38.7 | 47.5 | 41.2 | 48.2 | 42.6 | 43.2 | 40.7 | 50.0 |

# Appendix 2

**Table 4.2** Geochemical reference materials (GRMs) used to assess analytical accuracy and precision

| | BRR-1 g ($n$=18) | | JGb-1 ($n$=10) | | UMAT-1 ($n$=10) | | JB-3 ($n$=3) | | JB-1a ($n$=10) | | JB-2 ($n$=7) | BIR-1 g ($n$=7) | | | |
|---|---|---|---|---|---|---|---|---|---|---|---|---|---|---|---|
| | Mean | Ref | Mean | Ref | Mean | Ref | Mean | Ref | Mean | Ref | Mean | Ref | Mean | Ref | Nominal SD |
| $SiO_2$ | 50.57 | 49.82 | 44.43 | 43.66 | 54.04 | 53.57 | 50.56 | 50.96 | 52.47 | 52.41 | 53.02 | 53.25 | 47.77 | 47.75 | 0.24 |
| $TiO_2$ | 1.04 | 1.03 | 1.61 | 1.60 | 3.05 | 2.79 | 1.62 | 1.44 | 1.30 | 1.28 | 1.17 | 1.19 | 0.93 | 0.97 | 0.17 |
| $Al_2O_3$ | 15.13 | 14.37 | 20.07 | 17.45 | 13.52 | 13.48 | 17.60 | 17.20 | 15.22 | 14.45 | 15.21 | 14.64 | 15.58 | 15.44 | 0.10 |
| $Fe_2O_3$ | 10.93 | 11.88 | 14.05 | 15.06 | 13.59 | 12.54 | 12.06 | 11.82 | 8.91 | 9.05 | 13.96 | 14.25 | 11.20 | 11.22 | 0.18 |
| MnO | 0.21 | 0.18 | 0.24 | 0.19 | 0.20 | 0.21 | 0.23 | 0.18 | 0.11 | 0.15 | 0.23 | 0.22 | 0.16 | 0.17 | 0.03 |
| MgO | 7.61 | 8.57 | 6.66 | 7.85 | 2.31 | 2.87 | 4.43 | 5.19 | 6.94 | 7.83 | 3.77 | 4.62 | 9.22 | 9.70 | 0.07 |
| CaO | 10.92 | 11.95 | 11.14 | 11.90 | 6.07 | 6.39 | 9.13 | 9.79 | 8.98 | 9.31 | 9.04 | 9.82 | 12.58 | 13.32 | 0.07 |
| $Na_2O$ | 2.32 | 1.97 | 1.42 | 1.20 | 3.43 | 3.25 | 2.82 | 2.73 | 2.85 | 2.73 | 2.25 | 2.04 | 2.30 | 1.82 | 0.06 |
| $K_2O$ | 0.04 | 0.05 | 0.24 | 0.24 | 2.50 | 2.60 | 0.64 | 0.78 | 1.27 | 1.40 | 0.37 | 0.42 | 0.05 | 0.03 | 0.01 |
| $P_2O_5$ | 0.00 | 0.09 | 0.00 | 0.06 | 0.28 | 0.89 | 0.00 | 0.29 | 0.00 | 0.26 | 0.00 | 0.10 | 0.00 | 0.03 | 0.00 |
| Total | 98.78 | 99.91 | 99.85 | 99.21 | 99.00 | 98.59 | 99.07 | 100.38 | 98.05 | 98.87 | 99.01 | 100.55 | 99.79 | 100.45 | |

## References

Cronan DS, Rothwell G, Croudace I (2010) An ITRAX geochemical study of ferromanganiferous sediments from the Penryhn Basin, South Pacfic Ocean. Mar Georesour Geotechnol 28:207–221

Croudace IW, Rindby A, Rothwell RG (2006) ITRAX: description and evaluation of a new multifunction X-ray scanner. In: Rothwell RG (ed) New techniques in sediment core analysis, vol 267. Geological Society Special Publication, London, pp 51–63

de Lange GJ, Jarvis I, Kuijpers A (1987) Geochemical characteristics and provenance of late Quaternary sediment from the Madeira Abyssal Plain, N Atlantic. In: Weaver PPE, Thomson J (eds) Geology and geochemistry of Abyssal Plains, vol 31. Geological Society Special Publication, London, pp 147–165

Ercilla G, Alonso B, Perez-Belzuz F, Estrada F, Baraza J, Farran M, Canals M, Masson DG (1998) Origin, sedimentary processes and depositional evolution of the Agadir turbidite system, central eastern Atlantic. J Geol Soc 155:929–939

Frenz M, Wynn RB, Georgiopoulou A, Bender VB, Hough G, Masson DG, Talling PJ, Cronin B (2009) Provenance and pathways of late Quaternary turbidites in the deep-water Agadir Basin, northwest African margin. Int J Earth Sci 98:721–733

Giresse P, Pauc H, Déverchère J, Maradja Shipboard Scientific Party (2009) Sedimentary processes and origin of sediment gravity-flow deposits on the western Algerian margin during late Pleistocene and Holocene. Mar Petrol Geol 26:695–710. doi:10.1016/j.marpetgeo.2008.03.011

Hunt JE, Wynn RB, Masson DG, Talling PJ, Teagle DAH (2011) Sedimentological and geochemical evidence for multistage failure of volcanic island landslides: a case study from Icod landslide on north Tenerife. Geochem Geophys Geosyst 12:Q12007. doi:10.1029/2011GC003740

Hunt JE, Wynn RB, Talling PJ, Masson DG (2013) Frequency and timing of landslide-triggered turbidity currents within the Agadir Basin, offshore NW Africa: are there associations with climate change, sea level change and slope sedimentation rates? Mar Geol 346:274–291

Jarvis I, Moreton J, Gérard M (1998) Chemostratigraphy of the Madeira Abyssal Plain Miocene-Pleistocene turbidites, site 950. In: Weaver PPE, Schmincke H-U, Firth JV, Duffield W (eds) Proceedings of the ocean drilling program, scientific results, vol 157, pp 535–558

MacDonald HA, Wynn RB, Huvenne VAI, Peakall J, Masson DG, Weaver PPE, McPhail SD (2011) New insights into the morphology, fill and remarkable longevity (>0.2 m.y.) of modern deep-water erosional scours along the northeast Atlantic margin. Geosphere 7:845–867

Masson DG, Watts AB, Gee MRJ, Urgeles R, Mitchell NC, Le Bas TP, Canals M (2002) Slope failures on the flanks of the western Canary Islands. Earth Sci Rev 57:1–35

Pearce TJ, Jarvis I (1992) Composition and provenance of turbidite sands: late Quaternary, Madeira Abyssal Plain. Mar Geol 109:21–51

Pearce TJ, Jarvis I (1995) High-resolution chemostratigraphy of Quaternary distal turbidites: a case study of new methods for the analysis and correlation of barren sequences. In: Dunay RE, Hailwood EA (eds) Non-biostratigraphical methods of dating and correlation, vol 89. Geological Society Special Publication, London, pp 107–143

Rothwell RG, Pearce TJ, Weaver PPE (1992) Late Quaternary evolution of the Madeira Abyssal Plain, NE Atlantic. Basin Res 4:103–131

Rothwell RG, Hoogakker B, Thomson J, Croudace IW, Frenz M (2006) Turbidite emplacement on the southern Balearic Abyssal Plain (western Mediterranean Sea) during Marine Isotope Stages 1–3: an application of ITRAX XRF scanning of sediment cores to lithostratigraphic analysis. In: Rothwell RG (ed) New techniques in sediment core analysis, vol 267. Geological Society Special Publication, London, pp 79–98

Talling PJ, Wynn RB, Masson DG, Frenz M, Cronin BT, Schiebel R, Akhmetzhanov AM, Dallmeier-Tiessen S, Benetti S, Weaver PPE, Georgiopoulou A, Zühlsdorff C, Amy LA (2007) Onset of submarine debris flow deposition far from original giant landslide. Nature 450:541–544

Thomson J, Croudace IW, Rothwell RG (2006) A geochemical application of the ITRAX scanner to a sediment core containing eastern Mediterranean sapropel units. In: Rothwell RG (ed)

New techniques in sediment core analysis, vol 267. Geological Society Special Publication, London, pp 1–29

Weaver PPE, Kuijpers A (1983) Climatic control of turbidite deposition on the Madeira Abyssal Plain. Nature 306:360–363

Weaver PPE, Rothwell RG (1987) Sedimentation on the Madeira Abyssal Plain over the last 300,000 yrs. In: Weaver PPE, Thomson J (eds) Geology and geochemistry of Abyssal Plains, vol 31. Geological Society Special Publication, London, pp 71–86

Weaver PPE, Rothwell RG, Ebbing J, Gunn D, Hunter PM (1992) Correlation, frequency of emplacement and source directions of megaturbidites on the Madeira Abyssal Plain. Mar Geol 109:1–20

Weaver PPE, Wynn RB, Kenyon NH, Evans J (2000) Continental margin sedimentation, with special reference to the north-east Atlantic margin. Sedimentology 47:239–256

Weltje GJ, Tjallingii R (2008) Calibration of XRF core scanners for quantitative geochemical logging of sediment cores: theory and application. Earth Planet Sci Lett 274:423–438

Wynn RB, Weaver PPE, Stow DAV, Masson DG (2002a) Turbidite depositional architecture across three interconnected deep-water basins on the northwest African margin. Sedimentology 49:1441–1462.

Wynn, RB, Kenyon NH, Masson DG, Stow DAV, Weaver, PPE (2002b) Characterisation and recognition of deep-water channel-lobe transition zones. AAPG Bull 86:1441–1462

Wynn RB, Talling PJ, Masson DG, Stevenson CJ, Cronin BT, Le Bas TP (2010) Investigating the timing, processes and deposits of one of the world's largest submarine gravity flows: The 'Bed 5 Event' off northwest Africa. In: Mosher DC, Moscardelli L, Baxter CDP, Urgeles R, Shipp RC, Chaytor JD, Lee HJ (eds) Submarine mass movements and their consequences, Springer, Dordrecht (Adv Nat Technol Hazards Res, 28:463–474)

# Chapter 5
# Identification, Correlation and Origin of Multistage Landslide Events in Volcaniclastic Turbidites in the Moroccan Turbidite System

**James E. Hunt, Russell B. Wynn and Ian W. Croudace**

**Abstract** Generation of tsunamis from submarine landslides is sensitive to several parameters such as their volume, failure mechanism and location of failure relative to sea level. These conditions are often difficult to resolve for past events. However, previous studies of turbidites generated from landslides offer insight into the timing, total event volume and failure mechanism. This study confirms the ~165 ka Icod landslide originating from the northern flank of Tenerife as a retrogressive multistage landslide. It also shows that the latest volcanic flank collapse from the Canary Islands, the ~15 ka El Golfo landslide, is a retrogressive multistage failure. These inferences are developed using high resolution Itrax μXRF bulk geochemistry to better identify and correlate these subunits in a number of core examples of the Icod (seven subunits) and El Golfo (five subunits) event beds. Subunit variations identified through Itrax studies also allow examination of bulk intra-subunit geochemical heterogeneities. These heterogeneities reflect discrete landslides from a single source. A systematic decrease in calcium composition (proxy for carbonate) suggests initial submarine collapses that retrogressively fail the flank leading to an increasing component from subaerial collapses. However, both grain size and density sorting influence bulk geochemical compositions. The geochemistry of volcanic glasses (determined from Eagle III μXRF analyses) from the subunits of the Icod and El Golfo event beds from Agadir Basin demonstrate that these subunits represent discrete separate failures.

**Keywords** Itrax core scanner · Submarine landslide events · Volcaniclastic turbidites · Moroccan turbidite system · Geochemical correlation

J. E. Hunt (✉) · R. B. Wynn
National Oceanography Centre, European Way, Southampton, SO14 3ZH, UK
e-mail: james.hunt@noc.ac.uk

I. W. Croudace
Ocean and Earth Science, National Oceanography Centre, University of Southampton
Waterfront Campus, European Way, Southampton SO14 3ZH, UK



I. W. Croudace, R. G. Rothwell (eds.), *Micro-XRF Studies of Sediment Cores*,
Developments in Paleoenvironmental Research 17, DOI 10.1007/978-94-017-9849-5_5

## Introduction

Submarine landslides are a major mechanism for transporting up to several thousand cubic kilometres of sediment from shelf and slope environments to abyssal plains. Submarine landslide activity has been widely documented on modern passive and convergent continental margins (Hühnerbach et al. 2004; Barkan et al. 2009; Chaytor et al. 2009; Lee 2009). However, much work has focussed on submarine landslides on the flanks of volcanic islands, in particular the islands of the Hawaiian (Moore et al. 1989, 1994), Canarian (Watts and Masson 1995, 2001; Masson et al. 2002; Acosta et al. 2003) and Cape Verdean (Le Bas et al. 2007; Masson et al. 2008) archipelagos.

Both continental margin and volcanic island submarine landslides pose significant geohazards. Not only do they involve displacement of cubic kilometres of material, but have the potential to generate tsunamis (Ward and Day 2001). Historical events that have demonstrated the ability of landslides to generate tsunamis include 1888 Ritter Island, 1929 Grand Banks, 1946 Aleutian Islands, 1969 Lituya Bay, 1972 Nice Harbour, 1988 Vulcano Island, 1994 Skagway Harbour and 1998 Papua New Guinea (see Hunt et al. 2011, 2013a, b, c, and references therein)

Geological records of tsunami deposits on the Hawaiian and Canary Islands are further testament to the ability of volcanic island flank collapses to generate tsunamis (Pérez-Torrado et al. 2006; Giachetti et al. 2011). However, modelling of a postulated future La Palma flank collapse as a 500 $km^3$ single sliding-block has generated tsunami waves with differing properties, such as wave height and inundation (Ward and Day 2001; Mader 2001; Gisler et al. 2006; Abadie et al. 2012). To better determine tsunamigenic potential, it is imperative to resolve accurate measures of landslide characteristics such as total volume, failure mechanism (single or multistage and submarine or subaerial) and event recurrence.

This study uses turbidites to provide insight into original landslide character. In both continental margin and volcanic island settings, submarine landslides have been associated with generation of sediment gravity flows (Weaver and Rothwell 1987; Weaver et al. 1992; Rothwell et al. 1992; Wynn et al. 2002; Masson et al. 2006, and references therein; Hunt et al. 2011). These turbidity currents (typically $>1$ $km^3$) are either instigated by action of the landslide on the sea floor or from disaggregation of landslide materials into more dilute sediment suspensions. The sediment gravity flows include a spectrum of processes between laminar debris flows and dilute turbidity currents.

Deepwater basins are relatively quiescent environments with slow deposition (0.5–2.5 cm/1000 years) of pelagic and hemipelagic sediment interspersed with periodic influxes of sediment from turbidity currents (Hunt et al. 2013b). Turbidity currents deposited in the abyssal plains are often generated from submarine landslides, providing an excellent dateable record of landslide recurrence (Weaver and Kuijpers 1983; Weaver et al. 1992; Wynn et al. 2002; Hunt et al. 2013a, c). The geochemistry of the associated turbidites can provide insight into their provenance (Pearce and Jarvis 1992, 1995). In addition, studies have also shown that turbidite

depositional architectures can record the mechanism of failure of the original landslide (Wynn and Masson 2003; Hunt et al. 2011, 2013b).

Subunit facies is defined as a series of fining-upwards turbidite sands and muds within a single event bed. Wynn and Masson (2003) state that subunits present in the 15 ka El Golfo event bed (bed *b*) from El Hierro and ~165 ka Icod event bed (bed *g*) from Tenerife are evidence of multistage failures. In these cases, each staggered collapse phase generated a separate turbidity current. This is supported by physical and geochemical investigations of the subunits present in the Icod event bed (Hunt et al. 2011, 2013b).

This paper investigates the origin of the subunits in both the El Golfo and Icod event beds. We recorded the bulk geochemistry of cores using an ITRAX μXRF core scanner and investigated the chemistry of extracted volcanic glass fragments using an Eagle III μXRF scanner. The first objective was to demonstrate that high-resolution geochemical profiles through Agadir Basin volcaniclastic turbidites (El Golfo bed A2 and Icod bed A14) support identification and correlation of subunit intervals. Secondly, calibrated Itrax μXRF data from individual subunits were compared to investigate bulk geochemical heterogeneities between subunits in the El Golfo (A2) and Icod (A14) event beds. Finally, inferences of inter-subunit variability were established through analysis of individual tephra grains extracted from the subunits of both El Golfo and Icod event beds (using the Eagle III μXRF).

Recent studies of the Icod landslide by Hunt et al. (2011) show it to be multistage and retrogressive and the El Golfo turbidite may have originated from a similar multistage retrogressive failure, as suggested by Wynn and Masson (2003). This hypothesis was tested by high-resolution μXRF core scanning of turbidites associated with each landslide.

## Geological Setting

The Moroccan Turbidite System (MTS) occupies a deepwater region (>4000 m water depth) off the NW African passive margin (Fig. 5.1, Wynn et al. 2002). The MTS comprises three inter-connected basins: Agadir Basin proximal to the Agadir Canyon and Moroccan continental slope, the Seine Abyssal Plain to the north, and the Madeira Abyssal Plain to the west (Fig. 5.1, Weaver et al. 1992; Wynn et al. 2002). The Agadir Basin is the focus of the present study and represents a mixed siliciclastic-volcaniclastic turbidite system (Wynn et al. 2002). Siliciclastic turbidity currents sourced from the Moroccan slope are fed into the northwest of the basin via Agadir Canyon (Ercilla et al. 1998; Wynn et al. 2002). The Western Canary Islands are the source of the large-volume volcaniclastic turbidites in the MTS (Weaver and Rothwell 1987; Pearce and Jarvis 1992, 1995; Weaver et al. 1992; Rothwell et al. 1992; Wynn et al. 2002; Hunt et al. 2013c).

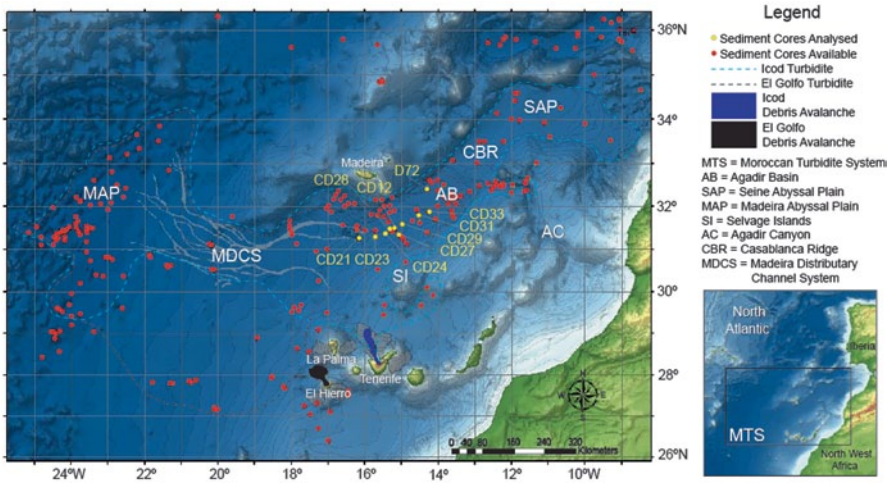


**Fig. 5.1** Map of the Moroccan Turbidite System showing location of the Canary Islands and Agadir Basin. Map shows key core locations for this study

## Methodology and Data

A turbidite is the deposit of a turbidity current, defined as a sediment gravity flow where the primary grain-support mechanism is fluid turbulence (Middleton 1993). A turbidite is characterised by an upwards-fining grain-size and associated upwards trend of tractional bedforms (e.g. structureless, parallel-laminated, ripple cross-laminated and convolute-laminated sands) associated with turbulent transport and deposition of coarse grains. Above these basal coarse deposits is commonly a sequence of laminated and structureless silts and muds representing deposition from low energy suspension fallout. Distally, coarse-grained bases may be lost, leaving homogenous muds. Subunit facies is defined as a multiple series of interbedded upwards-fining turbidite sand and mud units that represent a single deposit (event bed), where a subunit represents a single upwards-fining unit within that series.

The volcaniclastic El Golfo turbidite (bed *b* in the Madeira Abyssal Plain and bed A2 in the Agadir Basin from Weaver et al. 1992; Wynn et al. 2002; Hunt et al. 2013c) and the Icod turbidite (bed *g* in Madeira Abyssal Plain, bed A14 in Agadir Basin, and bed *Sm* in the Seine Abyssal Plain) are the primary focus of this paper. Both turbidites have been correlated through Agadir Basin using biostratigraphy and stratigraphic position (Wynn et al. 2002; Hunt et al. 2013c). Cores taken during CD166 and D225 cruises are used in the present study.

### *Visual Sediment Logging*

Cores were visually logged and grain size, lithology, bedforms, composition and colour recorded against depth to enable identification of subunits and associated turbidite facies.

### *WD-XRF Analyses*

Major and trace elements were determined on sub-samples using a Philips Magix-Pro WD-XRF instrument fitted with a 4 kW Rh end window X-ray tube (Croudace and Williams-Thorpe 1988; Croudace and Gilligan 1990). The instrument was calibrated using a broad set of international geochemical reference samples and accuracy was evaluated to be better than 5 % relative and precision better than 2 %. Glass beads were made by fusing a mixture (1:10) of 0.5 g of dried and ground sample with 5 g of di-lithium tetraborate flux at 1100°C in a platinum-gold crucible followed by pouring into a platinum-gold mould. The data obtained was used to calibrate the Itrax data (in normalised counts) to produce concentration data. The samples chosen were taken from the base of each subunit in CD166/27 (Icod bed) and CD166/23 (El Golfo bed); Appendix Table 5.1.

### *Itrax µXRF Core Scanning*

A set of cores from the Agadir Basin that contained the El Golfo (bed A2) and Icod (bed A14) event beds were analysed using an Itrax µXRF core scanner. The aim was to: a) determine subunit intervals, b) qualitatively correlate subunits between core sites, and c) examine quantitative intra-subunit bulk geochemical heterogeneities for a type example of each bed. Previous studies using single samples from subunit bases analysed using ICP-OES proved only partially effective in comparing bulk subunit compositions (Hunt et al. 2011).

Cores were scanned on the Itrax using a Mo target X-ray source to provide a radiographic image (settings 60 kV 45 mA at 200 µm resolution) and elemental profiles (50 kV 30 mA at 500 µm resolution). The Itrax system is described in Croudace et al. (2006). Element-element ratios were used to allow comparison between cores. Based on previous bulk geochemical studies of the Icod turbidite (Hunt et al. 2011) Fe, Zr and K provided best subunit discrimination.

Normalised Itrax data ($Mo_{inc}$) from CD166/27 (Icod bed) and CD166/21 (El Golfo bed) were calibrated using discrete subsamples analysed by WD-XRF. The two cores used for quantitative assessment were chosen as they provided the most proximal and most compelling sequences of subunits (Appendix Fig. 5.12).

### *Volcanic Glass Geochemistry*

Individual glass shards were extracted from cores containing subunits from the El Golfo bed (CD166/21) and Icod bed (CD166/27) and checked optically to ensure they were unaltered volcanic glasses, >63 µm in grain-size and carbonate-free. An Eagle III scanning µXRF instrument (EDAX Inc, USA; see also Dulski et al. 2015, this volume) was used to analyse the glass samples. The instrument has a 400 W Rh X-ray tube and a Si(Li) detector and is fitted with a Varispot polycapillary X-ray waveguide that allows irradiation with a 40 µm spot size. A set of individual glasses

was made using flux-less fusion of 20 μg of international geochemical reference samples (JGS-JB1a, JGS-JB3, JGS-JGb1 and USGS-BHVO2) to calibrate the instrument. Glass preparations were made by fusing portions of each reference material on an iridium strip heater at 1300°C in an argon atmosphere for 30 s. All analyses of samples and reference material glasses were made at 40 kV and 100 mA with a measurement time of 100 s. The Eagle III instrument was run in vacuum mode.

### *Grain-Size Analysis*

Grain-size data was collected to aid identification of subunits in the coarse-grained bases of individual turbidites and also evaluate influence of grain-size on the Itrax μXRF data. Throughout each cored example of the El Golfo and Icod turbidite studied a series of centimetre-sized samples were taken. These were disaggregated in 30 mL of 0.05% sodium hexametaphosphate dispersant and shaken for 12 hr. Three separate aliquots of each dispersed sediment sample were then analysed by laser diffraction using a *Malvern Mastersizer 2000* particle sizer. From the grain-size distribution profiles statistical measures of bulk grain-size properties for each sample (mean, mode and median grain size etc.) were established. Repeat samples and artificial standards were analysed to assess precision and accuracy, both found to be within 0.1–1.5%.

## Results

### *Visual Logging*

As in previous studies (Hunt et al. 2011), a series of seven subunits were identified within the Icod event bed (SBU1–7; Fig. 5.2). In the western Agadir Basin, being more proximal to source, the three basal subunits appear as a single amalgamated unit. However, these become separate units in the more distal eastern Agadir Basin (D13072; Fig. 5.2). The basal subunits (SBU1–3) each comprise a sequence of parallel-, ripple cross- and convolute-laminated intervals. Above an eroded base, the basal sands are dominated by mafic lithics and carbonate grains, followed by a vertical increase in volcanic glass content. The upper subunits (SBU4–7) of the Icod turbidite represent separate units interbedded with turbidite mud at each core site. Each is identified by a ripple- to parallel-laminated fine-sand to coarse silt base with laminated mud above (Fig. 5.2).

The El Golfo event bed has five subunits (SBU1–5) at proximal sites (CD166/21 and CD166/23) in the western Agadir Basin (Fig. 5.3). Eastwards there is loss of the uppermost subunit (absent in CD166/24 and CD166/28). Through the remainder of the western Agadir Basin (CD166/12, CD166/29 and CD166/31) only three subunits are seen (Fig. 5.3). More distally there is progressive cut-out to two and

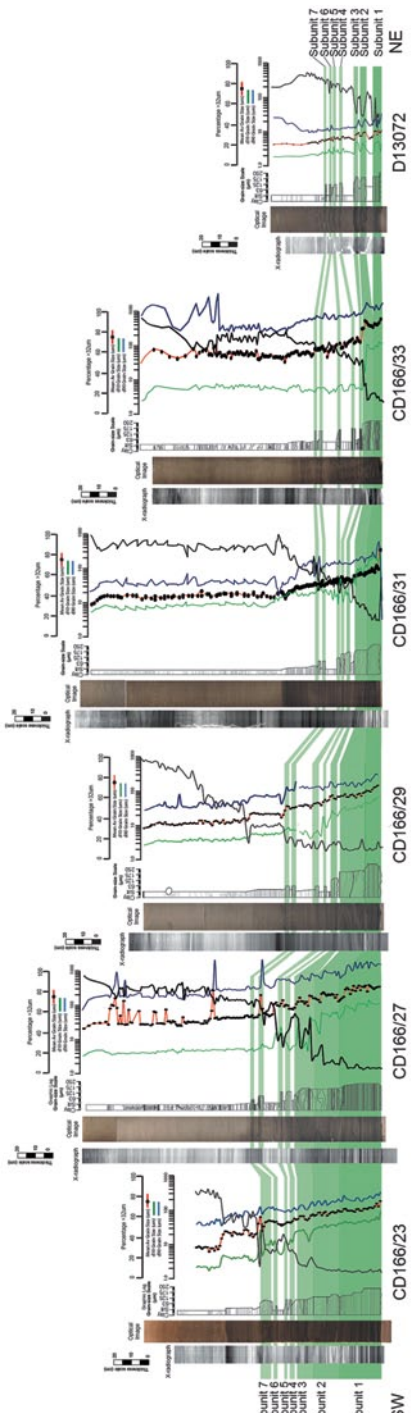


**Fig. 5.2** Core panels of Bed A14 (Icod turbidite) showing sedimentary logs and downcore grain-size data enabling identification and correlation of subunits. Profiles correspond by colour and symbol to the appropriate axes above. *Black lines* relate to Percentage > 32 μm scale

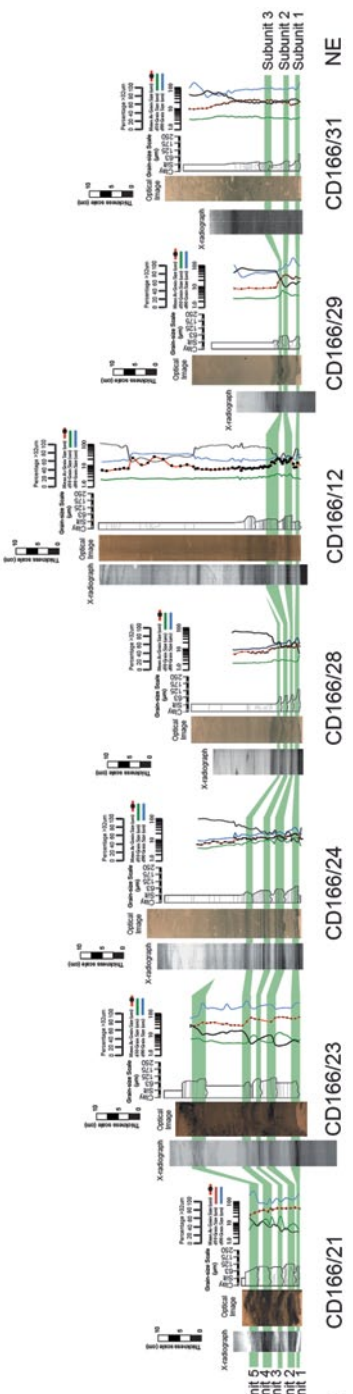


**Fig. 5.3** Core panels of Bed A2 (El Golfo turbidite) showing sedimentary logs and downcore grain-size data enabling identification and correlation of subunits. Profiles correspond by colour and symbol to the appropriate axes above. *Black lines* relate to Percentage >32 μm scale

ultimately one subunit. These subunits are characterised by a cm-thick sequence of basalt-rich laminations at the base, with a more carbonate-rich sequence of muddy silts above. These subunits rapidly fine towards the east and become fine silts and muds distally.

## *Grain-Size Profiles*

Grain-size profiles through the Icod bed confirm visual identification of subunits based on presence of coarse material. Repeated fining-upwards sequences in the Icod event bed (Fig. 5.2) can be distinguished in the basal amalgamated subunits (SBU1–3) and the upper subunits (SBU4–7). These subunits can be correlated using grain-size profiles, confirming visual interpretations. Further, the grain size of the basal subunits (SBU1–7) decreases vertically at each core site.

The fining-upwards trend above a coarse-grained base is also characteristic of the El Golfo subunits (Fig. 5.3), although the basal subunit (SBU1) appears to be finer-grained than the subsequent subunit (SBU2). This ‘Christmas-tree’ vertical profile through the deposits supports visual correlations of the subunits.

## *Correlation of Itrax XRF Profiles*

Icod event bed subunits are characterised by higher element concentrations (e.g. Ti, Zr and Fe) in their bases (Fig. 5.4). Basal subunits (SBU1–3) and upper subunits (SBU4–7) can be correlated on peaks in element intensities and troughs in the intervening muds between them. The base of each subunit shows enrichment in titanium that aids correlation of proximally amalgamated bases. Correlation of upper subunits is based on a subtle geochemical signature, aided by visual and grain-size criteria.

Correlation of the subunits in the El Golfo event bed is based on Itrax element profiles (Fig. 5.5) which, like the Icod sub-units bases, also show distinct enrichments in Ti, Zr, Fe, and to a lesser extent, increased K.

Itrax X-radiographs clearly show higher density layers at subunit bases and are useful for verifying identification of subunits (Figs. 5.4 and 5.5). This complements sedimentological and geochemical properties used to identify and correlate subunits. Using complementary data sets assists in identifying the presence of subunits within both the Icod and El Golfo event beds. Subunits discriminated by spikes in element concentrations coincide with spikes in p-wave velocity, bulk density, magnetic susceptibility and average grain-size (Figs. 5.6 and 5.7).

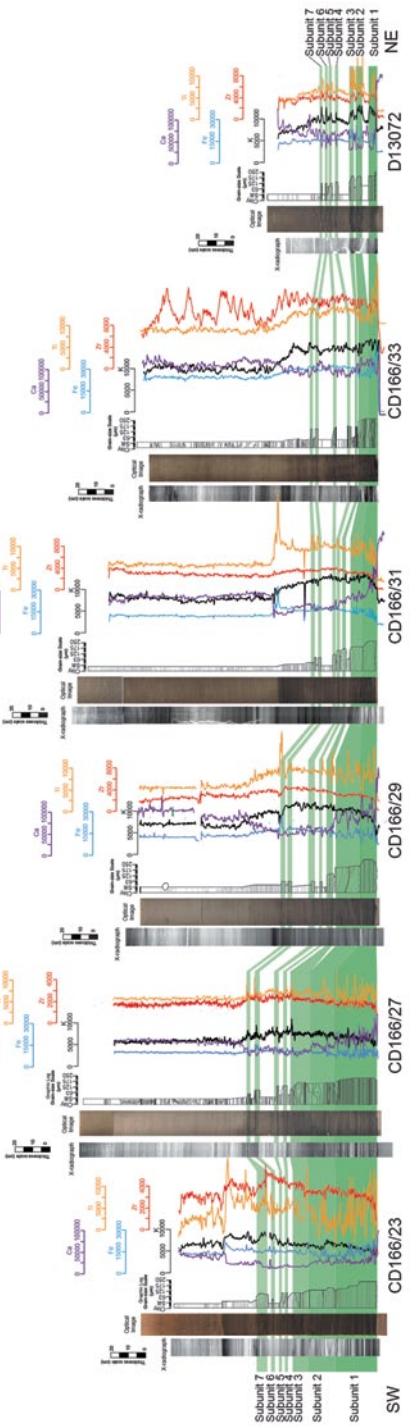


**Fig. 5.4** Core panels of Bed A14 (Icod turbidite) showing downcore Itrax micro-XRF data enabling identification and correlation of subunits

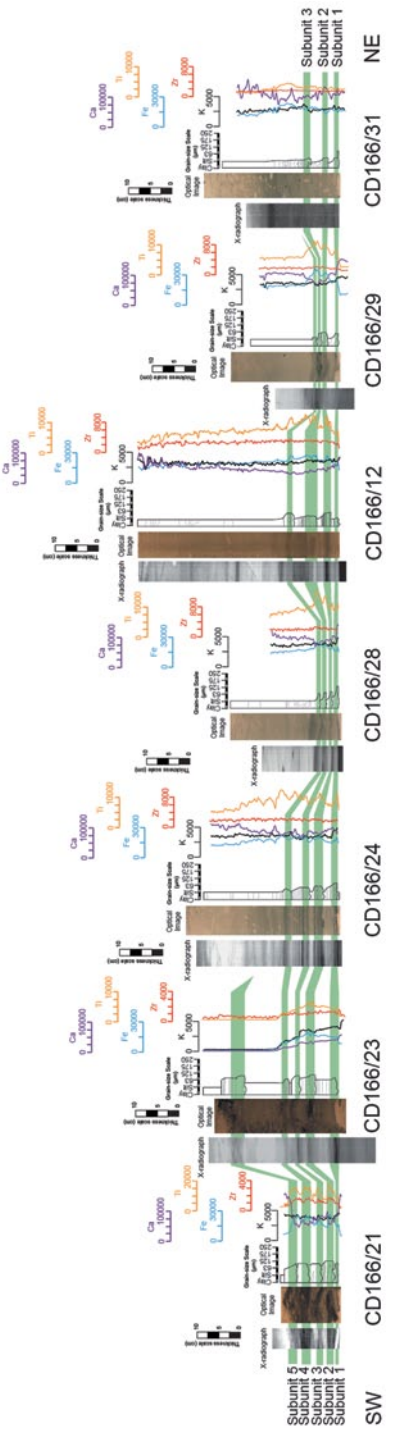


**Fig. 5.5** Core panels of Bed A2 (El Golfo turbidite) showing downcore Itrax micro-XRF data enabling identification and correlation of subunits

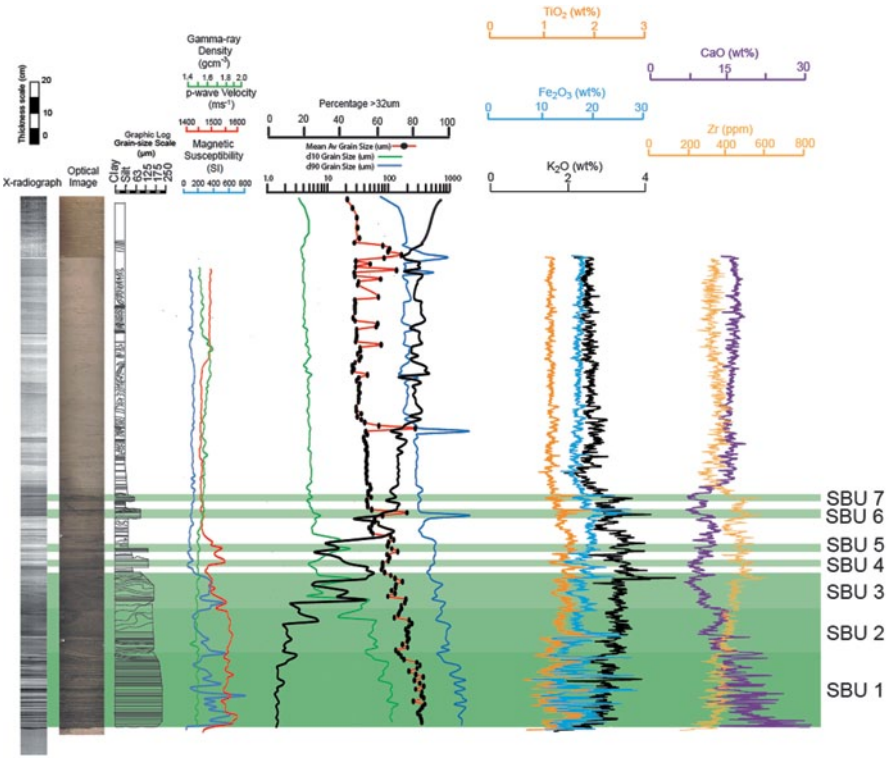


**Fig. 5.6** Bed A14 in CD166/27 showing down-core data used in identification of subunits. Profiles correspond by colour and symbol to the appropriate axes above. *Black line* relates to Percentage > 32 μm scale

## *Comparison of Bulk Subunit Compositions Using Calibrated Itrax μXRF Data*

Being able to compare compositional profiles between cores run at different times, and with cores run by other research groups, ideally requires Itrax data to be converted to concentration. The simplest way to do this is to obtain a regression equation of Itrax counts versus concentration for each element for identical samples. This was achieved by analysing a series of 1 mL sub-samples taken from a core using a well-established quantitative method such as WD-XRF and plotting against the corresponding Itrax count data, averaged over the same one cm region.

For the Icod event bed, the Itrax analysis was focused on a single core site (CD166/27; Fig. 5.6). Although data from additional core sites (CD166/12, CD166/29, CD166/31, CD166/33 and D13072) show similar trends in delineating compositional fields of the subunits, these require further processing and calibration to validate. The raw Itrax data was also calibrated for the coarsest deposit of the El Golfo turbidite in CD166/21 (Fig. 5.7). Calibration curves produced reliable results

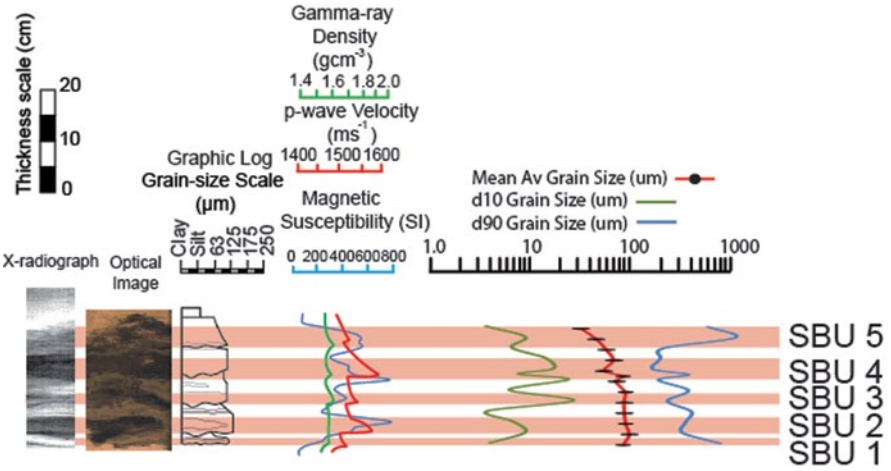


**Fig. 5.7** Bed A2 in CD166/24 showing down-core data used in identification of subunits. Profiles correspond by colour and symbol to the appropriate axes above

for $SiO_2$, $K_2O$, CaO, $Fe_2O_3$, $TiO_2$ MnO, Cu, Zn, Sr, and Zr and moderately reliable results for $Al_2O_3$, Cl, Rb and Ba. The relevant $R^2$ values of calibrations curve fit are: $SiO_2 = 0.804$, $K_2O = 0.926$, $CaO = 0.889$, $TiO_2 = 0.813$, $Sr = 0.823$ and $Zr = 0.975$. Major element analysis calibrations were obtained with calibration coefficients of $>0.8$, while trace elements either produced calibration coefficients of 0.5–0.8 or no useful calibration.

Measurement up-core allows discrimination of subunit sand intervals from the mud/silt interbedded intervals (Figs. 5.4, 5.5 , 5.6 and 5.7). However, the main application is to display geochemical variations within subunits, shown in a series of variation cross-plots with each subunit interval defining a separate field (Figs. 5.8 and 5.9).

**The Icod Event Bed** Results show that SBU1 has a large range of $SiO_2$ values (25–65 wt%) but a restricted $K_2O$ wt% range (2–3.2 wt%, Figs. 5.6 and 5.8). Distinctly different is SBU2 which defines a field of 2.9–3.5 wt% $K_2O$ and 38–60 wt% $SiO_2$. Also different is SBU3 which shows higher values of $K_2O$ wt% and more restricted ranges in $SiO_2$ wt% (3 −4 wt% and 42–63 wt% respectively). The SBU4–5 intervals define similar fields under this analysis, with a range of 44–54 wt% $SiO_2$ and 3.1–4.0 wt%. SBU6–7 defines compositional fields of lower $SiO_2$ (29–40 wt%) but maintain relatively high $K_2O$ (2.75–3.1 wt%).

Similar variation plots of Zr ppm vs. $TiO_2$ wt% allow better discrimination of the SBU1 and SBU2 intervals in the Icod event bed, with similar $TiO_2$ wt% ranges of 0.5–2.0 wt% and 0.75–1.65 wt%; the lower Zr values of 300–500 ppm in SBU1 are different from the higher 480–625 ppm range of SBU2 (Fig. 5.8). SBU3 was found to have a more restricted range in $TiO_2$ (0.95–1.40 wt%) and higher Zr values (540–770 ppm), overlapping the fields of SBU4–6. SBU2–3 have similar compositional fields of higher $TiO_2$ compared to SBU4–5, with a range of ~1.19–2.25 wt%, but a

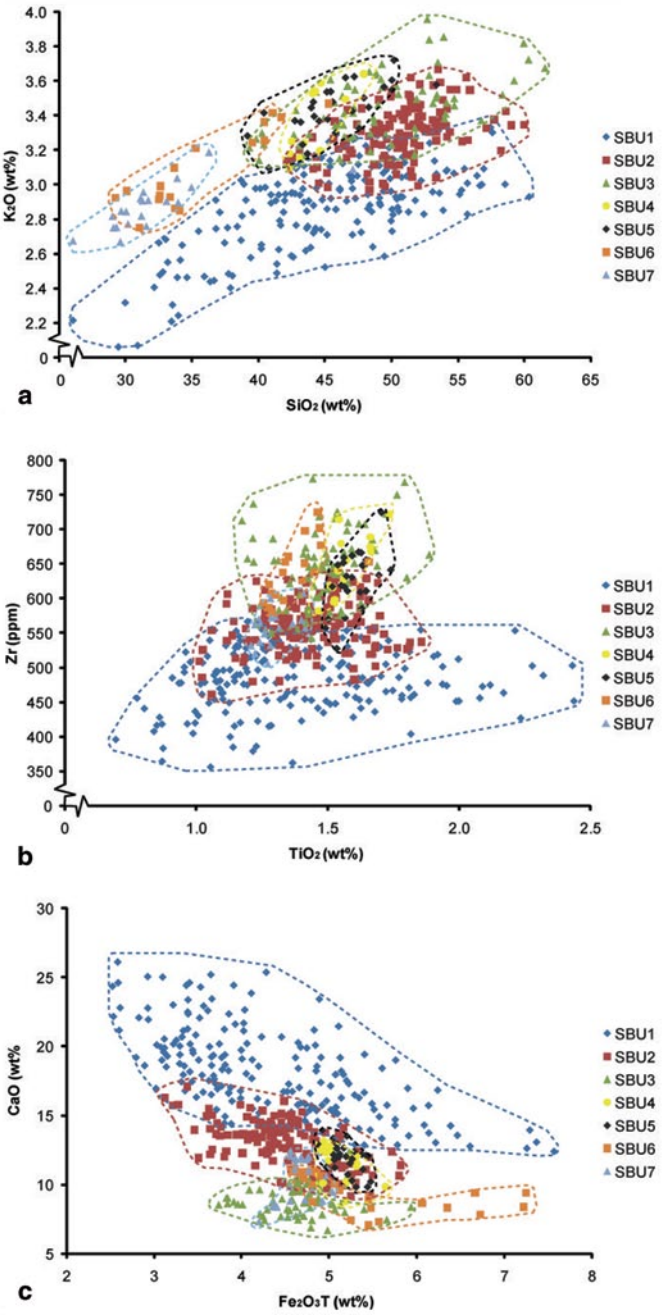


**Fig. 5.8** ITRAX micro-XRF compositions of individual subunits within Bed A14

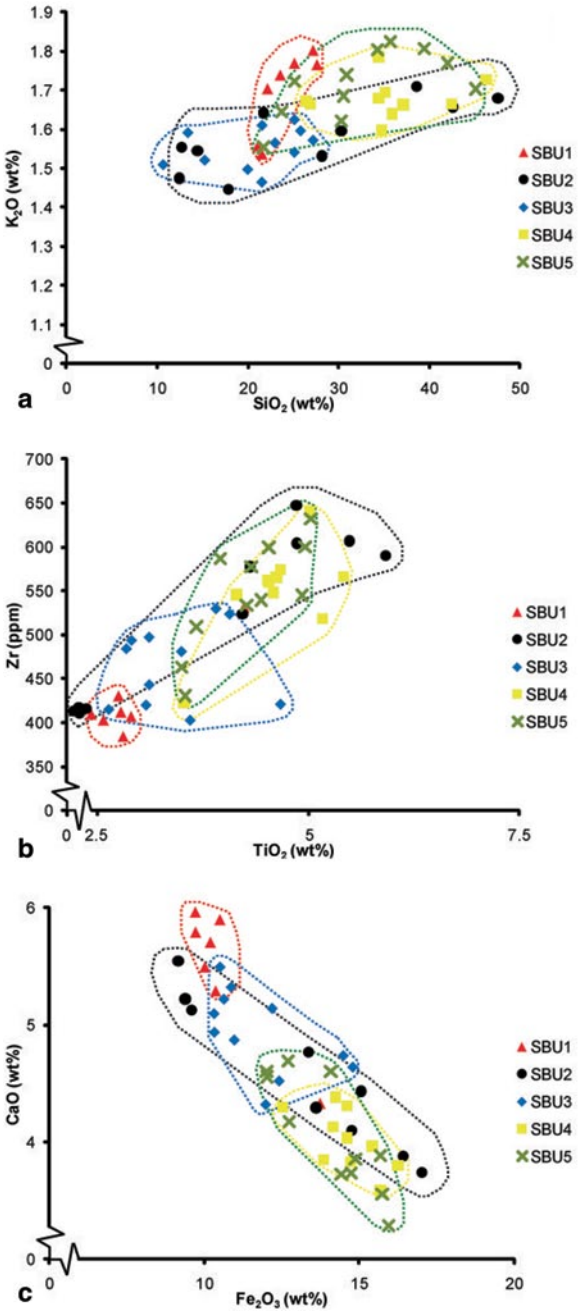


**Fig. 5.9** ITRAX micro-XRF compositions of individual subunits within Bed A2

similar range in Zr ppm compared to SBU6–7, with a range of 550–730 ppm. However, SBU4 can be segregated from SBU5 as at lower Zr concentrations, SBU5 has higher $TiO_2$ wt% values. SBU6–7 can be delineated in separate fields, where SBU6 has generally higher $TiO_2$ wt% and significantly higher Zr ppm (1.0–1.25 wt% and ~570–750 ppm), and SBU7 with lower $TiO_2$ wt% and lower Zr ppm (0.95–1.1 wt% and 505–600 ppm) (Fig. 5.8).

**The El Golfo Event Bed (in core CD166/21)** Data from the subunits here can be delineated into different geochemical and petrological fields (Fig. 5.9). The basal subunit (SBU1) has a restricted composition, with moderate $SiO_2$ and $K_2O$ concentrations ranging from 20–30 wt% and 1.5–1.8 wt% respectively and Zr (375–450 ppm), $TiO_2$ (2.5–2.75 wt%), CaO (5–6 wt%) and $Fe_2O_3$ (~10 wt%). The next subunit (SBU2) has a broader range, overlapping that of SBU1, with $K_2O$ 1.4–1.8 wt%, $SiO_2$ 10–50 wt%, Zr 400–650 ppm, $TiO_2$ 2.3–6.0 wt%, CaO 3.5–5.5 wt% and $Fe_2O_3$ 9–16 wt%. The third subunit (SBU3) has a more restricted range of composition, with similarities to SBU1 and SBU2 and contains low $K_2O$ (1.4–1.65 wt%), $SiO_2$ (10–30 wt%), Zr (400–550 ppm) and $TiO_2$ (2.5–5.0 wt%), but moderate CaO (4–5.5 wt%) and $Fe_2O_3$ (10–15 wt%). The upper subunits (SBU4 and SBU5) are geochemically similar to SBU2 but are distinct from SBU1 and SBU3. They have high values of $K_2O$ (1.5–1.8 wt%), $SiO_2$ (20–50 wt%), Zr (410–600 ppm), $TiO_2$ (3.5–5.5 wt%), and $Fe_2O_3$ (12–16.5 wt%), but low CaO (3–4.75 wt%). Overall however, these variations depend on the mineral assemblages present, which derive from density sorting. Furthermore the cores are analysed as non-carbonate free.

## *Grain Specific Geochemistry Within Subunits*

Unaltered volcanic glass grains were selected for analysis. Samples from subunit intervals of the Icod event bed were taken from CD166/27 to delineate geochemical fields for different subunit glass populations (Fig. 5.10). The Icod subunit glasses include phonolite and alkali trachyte compositions (Fig. 5.10). For the Icod event bed, SBU1–2 volcanic glasses were found to range from basalt-alkali trachyte-trachyandesite while SBU3 glasses varied from alkali trachyte-trachyandesite (Fig. 5.10). SBU4 glasses have a more evolved phonolitic character with a proportion of phonolite-trachyte. SBU5 and SBU6 glasses lie at the phonolite-alkali trachyte boundary (Fig. 5.10) while SBU7 glass geochemistry is tephriphonolite-phonolite type (Fig. 5.10). These results compare favourably to the SEM EDS volcanic glass analyses from the subunits of the Icod event bed of Hunt et al. (2011).

**El Golfo Volcanic Glass** These are geochemically distinct from the onshore El Hierro whole rock field (Fig. 5.11), although there are far fewer documented onshore samples to constrain the data. SBU1 for the El Golfo event has limited variation in volcanic glass geochemistry with alkalis < 10 wt% and silica < 50 wt%. The SBU1 volcanic glasses fall into highly basic picro-basalts and basanite-phonotephrite. SBU2 volcanic glasses cover a broad range from phonolites to basani-

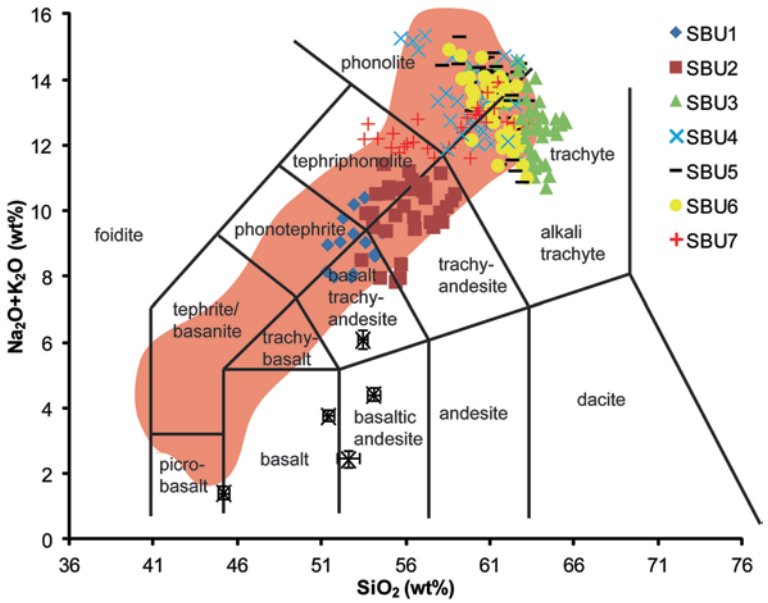


**Fig. 5.10** Total Alkali-Silica compositions of volcanic glasses from subunits of Bed A14 (Icod Turbidite) using Eagle III XRF measurement. The *crosses* represent standard reference material results with error bars

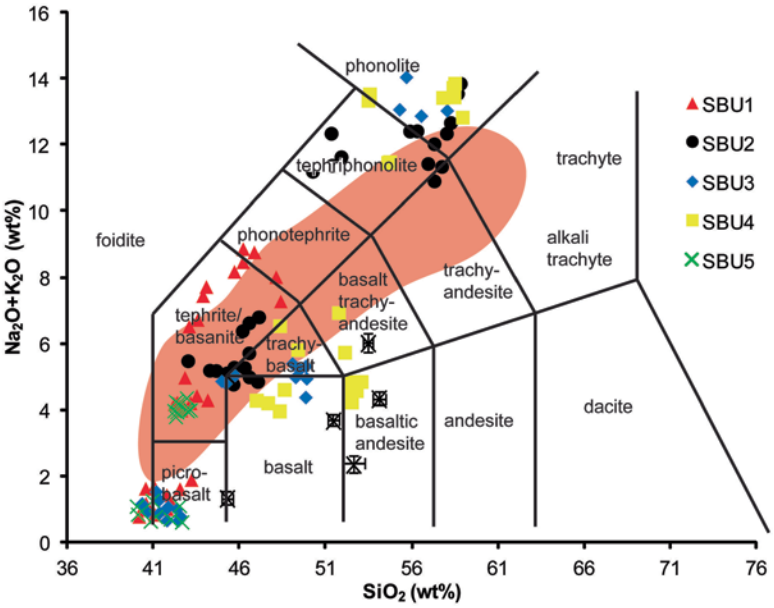


**Fig. 5.11** Total Alkali-Silica compositions of volcanic glasses from subunits of Bed A2 (El Golfo Turbidite) using Eagle III XRF measurement. The *crosses* represent standard reference material results with error bars

tes, but lack basalt-picrobasalt glasses. The volcanic glasses from SBU3 have the broadest geochemical range covering picrobasalt, basalt, basanite, phonotephrite and phonolite fields. The SBU4 volcanic glasses include an evolved group (>9 wt% alkalis and >52 wt% silica) and a basic group (<7 wt% alkalis). Lastly, the SBU5 volcanic glasses of the El Golfo event have highly restricted basic composition (40–45 wt% silica), with two groups of 3–4 wt% alkali basanites and 0.5–2 wt% alkali picrobasalts (Fig. 5.11).

Subunit glasses from the El Golfo event form discrete fields. Here SBU1 has a broad but relatively basic composition compared to SBU2–4, which have broad but relatively more evolved character whereas glasses in SBU3 are ultrabasic composition. The last subunit of the El Golfo Event (SBU5) has a restricted ultrabasic-basic character, where the ultrabasic glasses are comparable to SBU1 and SBU3 but also include distinct basanite glasses.

**Icod Event Volcanic Glasses** The glasses from each subunit form disparate geochemical fields. Within the Icod event bed, SBU1 and SBU2 are closely related to less evolved basic compositions with lower silica and alkali concentrations while SBU3, which contains more evolved glasses ranging compositionally from SBU1 and SBU2 to that SBU4–6. By contrast SBU7 contains relatively lower silica and higher alkalis.

## Discussion

### *Presence and Correlation of Subunits*

Previous work has recorded presence of subunits in the Icod event bed within Agadir Basin (Wynn and Masson 2003; Hunt et al. 2011, 2013b, ). The present study provides additional grain-size profiles through the Icod event bed to support previous visual and petrophysical identification of subunits (Fig. 5.6). Further, a series of high-resolution Itrax raw element intensity profiles support correlation of these subunits between core sites (Figs. 5.4 and 5.5). Both grain-size and geochemical profiles show the presence of three amalgamated subunits (SBU1–3) in the basal sands of proximal cores due to basal erosion (CD166/23, CD166/27, CD166/29 and CD166/31, Figs. 5.2, 5.4 and 5.5). However these form discrete layers interbedded with finer-grained silt and mud at the distal sites with minimal to no erosion at bases (CD166/33 and D13072). At all core sites in the present study the upper subunits (SBU4–7) form discrete layers (Figs. 5.2, 5.4 and 5.6).

The El Golfo event bed has been recorded as containing subunits within Agadir Basin (Wynn and Masson 2003). All subunits recorded in the El Golfo event bed form discrete layers with no evidence of amalgamation. Indeed, five subunits are recorded in the westernmost Agadir Basin (proximal) and these are found to thin and fine through the basin distally towards the east (Figs. 5.3, 5.5 and 5.7). Grain-size

profiles support visual identification and correlation of subunits (Fig. 5.3), which are also supported by Itrax elemental profiles.

In both the Icod and El Golfo deposits the subunits fine and thin upwards through the succession. This represents a progressive decrease in landslide volume during the multistage collapses, a characteristic of retrogressive failures (Masson et al. 2006; Hunt et al. 2011).

## *Itrax Comparison of Bulk Subunit Heterogeneities*

The geochemical variations of the Icod event bed subunits lie in different compositional fields on variation cross-plots (Fig. 5.8, Hunt et al. 2011). This is attributed to subtly different compositions of the failed material on the northern flank of Tenerife (Hunt et al. 2011). Detailed examination of the geochemistry of the whole subunit interval allows a more comprehensive comparison between subunits e.g. comparing the geochemistry of subunits (SBU1–7) within the Icod event bed at CD166/27. Patterns emerge in subunit character. The general increase in $K_2O$, $SiO_2$, Zr and $Fe_2O_3$ concentrations may represent an increase in the failure of evolved subaerial phonolitic rocks compared to earlier more basic submarine material.

There is a trend in decreasing CaO, resulting from decreasing amounts of biogenic carbonate incorporated in subunits upcore. CaO is highest in SBU1, followed by SBU2, then SBU3–5, and finally SBU6–7 (Fig. 5.8). Hunt et al. (2011) suggest retrogressive failure from submarine to subaerial conditions for the 165 ka Icod landslide, whereby initial subunits (SBU1–3) represent a major retrogressive shift from submarine flank to submarine and subaerial conditions, followed by subaerial failure of the upper subunits (SBU4–7). This is supported by the rapid decrease in CaO from SBU1 to SBU2 to SBU3 (Fig. 5.8). Although postulated as having a submarine, or at least partially submarine origin, SBU3 is more similar to the upper subunits (SBU4–7) than to SBU1 or SBU2. The bulk compositional fields can be grouped accordingly: Group 1 comprising SBU1 and SBU2, Group 2 comprising SBU3, SBU4 and SBU5, and Group 3 with SBU6 and SBU7. This compositional classification of subunits supports the grouping of Icod event bed subunits based on bulk geochemistry by Hunt et al. (2011).

The El Golfo turbidite also forms subunits with similar, but subtly different, bulk geochemistry (Fig. 5.9). SBU1 has the lowest Zr, $TiO_2$ and $K_2O$, and thus attributed to being the least evolved magma and most basic in character. SBU1 of the El Golfo turbidite also has the highest CaO (Fig. 5.9), which like the Icod turbidite, may relate to higher carbonate in the flow indicating a submarine origin. SBU2 has a broad composition covering both basic and evolved character, similar to SBU1 and the later SBU4 and SBU5. SBU2 also contains lower CaO compared to SBU1 (Fig. 5.9).

SBU3 has further decreased CaO and intermediate compositions of other major elements relative to SBU1–2 and SBU4–5 (Fig. 5.9). SBU4–5 both have the most evolved magma character with high $K_2O$, $TiO_2$, Zr and $Fe_2O_3$, and also have the

lowest CaO (Fig. 5.9). Decreasing CaO between SBU1 and SBU5 may represent decrease in the carbonate content of the subunits, which supports a retrogressive failure mechanism migrating from submarine to subaerial.

However, these bulk geochemical variations may result from density sorting within the flow. Successive flows may deposit grains under different hydrodynamic conditions, resulting in deposition of different mineral and grain assemblages. Also variable carbonate content may dilute the bulk composition of major elements. Ultimately, variations between the geochemistry of grains of similar size and density yield the most reliable results for discerning differences or similarities between subunits.

## *Variations in Glass (Grain-Scale) Geochemistry*

The results from Eagle III XRF analysis of volcanic glasses are comparable to those published by Hunt et al. (2011) using SEM EDS analyses obtained using a Hitachi *TM1000* scanning electron microscope. Analysis of the volcanic glass shows that glass in SBU1 of the Icod event bed were the most basic, followed by SBU2 (Fig. 5.10). Similarities exist between the SBU3 and SBU5 glasses and between glasses in SBU4 and SBU6. Although the glasses from SBU3–6 are broadly phonolitic-trachyte, there are variations between each population. Subunit SBU7 is petrologically distinct and has a less evolved phonolite-tephriphonolite composition.

Retrogressive collapse for the Icod landslide is likely to result in progressive failure to the most recent (to date of the slide) phonolitic rocks (Hunt et al. 2011). Indeed, there is a general petrological evolutionary trend from trachyandesite in SBU1 and SBU2 to phonolite-trachyte in SBU3–6, and finally to the SBU7 composition that resembles that of the El Abrigo ignimbrite of the Diego Hernandez formation. The El Abrigo ignimbrite represents the last volcanic event of the Cañadas III edifice on Tenerife prior to the Icod landslide (Bryan et al. 2002; Edgar et al. 2007; Hunt et al. 2011).

Although a proximal site, JC27/02, located on the continental rise north of Tenerife, is off axis from the bulk of the flow, while CD166/27 is located within Agadir Basin ahead of the main flow vector from Tenerife. Yet results in grain population trends are broadly similar at both sites. This implies that heterogeneities between subunits result from failure of different sections of the northern flank of Tenerife, rather than erosion by turbidity currents. These geochemical trends in volcanic glass from the Icod subunits at CD166/27 are similar to those found at the more proximal JC27/02 core site described by Hunt et al. (2011).

Analysis of El Golfo subunit volcanic glasses reveals heterogeneities that suggest each subunit represents an individual discrete failure (Fig. 5.11). The data show that SBU1 broadly comprises a basic basaltic glasses, while SBU2 glasses are more evolved and comparable to SBU4. SBU3 contains a broad range of volcanic glasses that span a range from ultrabasic to evolved phonolitic compositions. Lastly, contrary to bulk composition, the volcanic glasses of SBU5 of the El Golfo event bed have a restricted ultrabasic-basic character with glasses of picrobasalt to low-alkali

basanite. This shows that each subunit contains volcanic glasses from different geochemical fields. Compositional fields for SBU1–4 partially overlap, but although the picrobasalt glasses of SBU5 are similar to those of SBU1 and SBU3, the basanite volcanic glasses of SBU5 form a completely discrete field (Fig. 5.11).

## *Implications for Volcanic Island Landslides and Tsunamigenesis*

Previous work suggests that both the Icod and younger El Golfo landslides were multistage and retrogressive failures (Wynn and Masson 2003; Hunt et al. 2011). This interpretation is based on the occurrence of stacked subunits within the event beds in Agadir Basin and is corroborated by the detailed study of the Icod event bed by Hunt et al. (2011). The present investigation study builds on the Icod event bed study, but adds high-resolution geochemical profiling (from Itrax core scanning) to aid correlation and assessment of bulk subunit composition (Figs. 5.4, 5.6 and 5.8).

In addition to supporting the findings of Hunt et al. (2011) regarding the Icod event bed, the present study also better assesses identification, correlation and source of the subunits in the El Golfo turbidite in Agadir Basin. The bulk geochemical results from both beds suggest that the basal subunits are petrologically more basic and higher in carbonate content (shown by elevated CaO, Figs. 5.8 and 5.9). The trends in both bulk and grain-specific subunit geochemistry support retrogressive failure for both the Icod and El Golfo events.

Initial landslide character (i.e. water depth, volume, initial acceleration, maximum velocity) and whether the event is a single or multiple event have significant influence on its tsunamigenic potential (Harbitz et al. 2006; Ward 2001; Haugen et al. 2005; Masson et al. 2006). The implication for multistage failure is that the total volume involved in a landslide is divided between numerous smaller events. This reduces the volume entering the ocean at any one time, thereby reducing tsunami risk. Study of the proximal debris avalanche and resulting turbidite allow calculation of event volume. However, Hunt et al. (2011) demonstrated that at least two thirds of the Icod landslide mass was disaggregated and deposited in a series of associated turbidity currents. This demonstrates the importance of studying the turbidite history of a basin for resolving accurate total event volumes.

Previous studies claim that multiple fining-upwards sequences (subunits) in turbidites signify multistage failures at source (Wynn and Masson 2003; Hunt et al. 2011). Those studies and the current paper are significant as they demonstrate that the total volume of a landslide is divided between numerous smaller events. This reduces the volume of sediment entering the ocean at any one time, thus reducing tsunamigenic potential. This signals that caution is required in predicting ‘worst case’ scenarios for single large-volume failures when modelling past and future events (Ward and Day 2001; Mader 2001; Gisler et al. 2006). This view is supported by tsunami modelling of the Güímar landslide, where to produce the tsunami deposits onshore Gran Canaria, the failure event has to occur as smaller volumes distributed within a multistage collapse (Giachetti et al. 2011).

In summary, not only does the turbidite history of deepwater basins provide a dateable record of landslide events from neighbouring slopes, but turbidites can also provide insights into the properties of the landslide that generated them. These properties include: date, total event volume, area affected, multistage or single failure, and submarine/subaerial origin of landslide.

## Conclusions

High-resolution geochemical studies of volcaniclastic turbidites enable identification and correlation of subunits within the two most recent large-volume volcaniclastic event beds in Agadir Basin. Both the El Golfo and Icod event beds contain subunit events that show variations in compositions. Previous studies have qualified this, and demonstrated that the Icod landslide was also retrogressive and that the initial failure involved a submarine component while the upper subunit failures were subaerial.

Knowledge of submarine landslide occurrence and mechanics is furthered by the study of turbidites generated from them. Indeed, many of the defining characteristics that influence potential tsunamigenesis of past submarine landslide events can be determined from study of the resulting turbidites. In regard to methodology, the Itrax bulk geochemical analysis is best coupled with grain-specific geochemical investigations. The present study advocates a μXRF methodology for this; although traditional SEM EDS analysis generates more consistent results.

## *Acknowledgements*

The authors would like to thank the crews of the RRS Discovery and RSS Charles Darwin for their efforts during data collection. JEH gratefully acknowledges PhD funding for the present study provided by the Marine Geoscience Group at NOCS. JEH would also like to thank Suzanne MacLachlan for her help during the Itrax and SEM EDS data collection. The authors would also like to thank BOSCORF curator Guy Rothwell and the anonymous reviewers for their invaluable contributions in producing this work.

# Appendix

**Table 5.1** Geochemical data determined by WD-XRF

| Sample | | MC | SBU1 | SBU2 | SBU3 | SBU4 | SBU5 | SBU6 | SBU7 | LP |
|---|---|---|---|---|---|---|---|---|---|---|
| SiO2 | (%) | 33.38 | 33.96 | 38.48 | 40.06 | 44.05 | 40.20 | 40.35 | 40.70 | 17.47 |
| TiO2 | (%) | 1.19 | 1.45 | 1.33 | 1.29 | 1.37 | 1.33 | 1.26 | 1.19 | 0.64 |
| Al2O3 | (%) | 10.29 | 10.89 | 11.65 | 12.14 | 13.39 | 12.33 | 12.02 | 12.01 | 5.82 |
| Fe2O3 | (%) | 5.35 | 5.30 | 5.03 | 4.89 | 5.15 | 5.10 | 5.25 | 5.06 | 3.72 |
| MnO | (%) | 0.14 | 0.14 | 0.17 | 0.17 | 0.18 | 0.17 | 0.16 | 0.16 | 0.14 |
| MgO | (%) | 2.34 | 2.10 | 1.73 | 1.54 | 1.70 | 1.80 | 1.75 | 1.70 | 2.07 |
| CaO | (%) | 22.09 | 22.48 | 14.78 | 11.76 | 10.39 | 12.71 | 11.90 | 12.07 | 45.35 |
| K2O | (%) | 2.78 | 2.63 | 3.33 | 3.59 | 3.66 | 3.45 | 3.57 | 3.61 | 1.46 |
| Na2O | (%) | 4.08 | 4.74 | 5.40 | 5.70 | 5.68 | 5.01 | 5.42 | 5.57 | 1.51 |
| P2O5 | (%) | 0.20 | 0.21 | 0.19 | 0.18 | 0.20 | 0.20 | 0.18 | 0.17 | 0.11 |
| S | (%) | 0.05 | 0.05 | 0.05 | 0.05 | 0.04 | 0.04 | 0.04 | 0.04 | 0.05 |
| Cl | (%) | 0.64 | 0.40 | 0.42 | 0.41 | 0.37 | 0.39 | 0.45 | 0.48 | 0.48 |
| As | (ppm) | 3 | 6 | 4 | 4 | 5 | 5 | 4 | 3 | 3 |
| Ba | (ppm) | 408 | 487 | 376 | 408 | 435 | 433 | 367 | 344 | 346 |
| Br | (ppm) | 75 | 42 | 45 | 46 | 39 | 45 | 50 | 54 | 58 |
| Ce | (ppm) | 148 | 132 | 171 | 168 | 174 | 157 | 168 | 165 | 58 |
| Co | (ppm) | 12 | 18 | 15 | 12 | 15 | 17 | 9 | 11 | 16 |
| Cr | (ppm) | 54 | 93 | 70 | 55 | 59 | 56 | 53 | 47 | 66 |
| Cu | (ppm) | 32 | 27 | 22 | 22 | 22 | 26 | 33 | 30 | 73 |
| Ga | (ppm) | 17 | 17 | 19 | 20 | 21 | 21 | 20 | 22 | 9 |
| Hf | (ppm) | 8 | 8 | 9 | 9 | 10 | 9 | 8 | 10 | 5 |
| La | (ppm) | 77 | 63 | 83 | 92 | 87 | 90 | 92 | 88 | 35 |
| Nb | (ppm) | 101 | 99 | 128 | 144 | 145 | 142 | 146 | 145 | 15 |
| Ni | (ppm) | 29 | 38 | 31 | 28 | 30 | 32 | 23 | 22 | 37 |
| Pb | (ppm) | 8 | 6 | 8 | 9 | 12 | 9 | 9 | 9 | 10 |
| Rb | (ppm) | 64 | 55 | 73 | 83 | 83 | 79 | 86 | 86 | 41 |
| Sc | (ppm) | 13 | 11 | 11 | 9 | 6 | 8 | 10 | 8 | 13 |
| Sr | (ppm) | 820 | 773 | 599 | 546 | 548 | 600 | 579 | 553 | 1018 |
| U | (ppm) | 2 | 2 | 3 | 3 | 4 | 4 | 4 | 3 | 1 |
| V | (ppm) | 103 | 122 | 104 | 101 | 108 | 119 | 107 | 99 | 111 |
| Y | (ppm) | 30 | 24 | 31 | 35 | 33 | 34 | 34 | 33 | 19 |
| Zn | (ppm) | 86 | 82 | 95 | 103 | 106 | 105 | 100 | 99 | 47 |
| Zr | (ppm) | 447 | 405 | 527 | 601 | 608 | 602 | 619 | 620 | 93 |

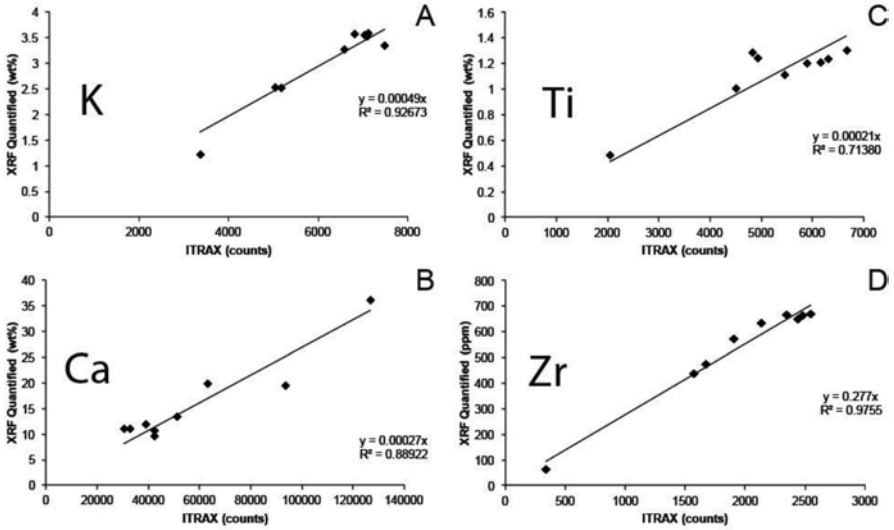


**Fig. 5.12** Correlation between Itrax (counts) and WD-XRF data

## References

Abadie SM, Harris JC, Grilli ST, Fabre R (2012) Numerical modeling of tsunami waves generated by the flank collapse of the Cumbre Vieja Volcano (La Palma, Canary Islands): tsunami source and near field effects. J Geophys Res Oceans 117(C5):1978–2012

Acosta J, Uchupi EA, Muñoz PH, Palomo C, Ballesteros M, ZEE Working Group (2003) Geologic evolution of the Canary Islands of Lanzarote, Fuerteventura, Gran Canaria and La Gomera and comparison of the landslides at these islands with those at Tenerife, La Palma and El Hierro. Mar Geophys Res 24:1–40

Barkan R, ten Brink US, Lin J (2009) Far field tsunami simulations of the 1755 Lisbon earthquake: implications for tsunami hazard to the U.S. East Coast. Mar Geol 264:109–122

Bryan SE, Marti J, Leosson M (2002) Petrology and geochemistry of the Bandas del Sur Formation, Las Cañadas Edifice, Tenerife (Canary Islands). J Petrol 43:1815–1856

Chaytor JD, ten Brink US, Solow AR, Andrews BD (2009) Size distribution of submarine landslides along the U.S. Atlantic margin. Mar Geol 264:16–27

Croudace IW, Gilligan J (1990) Versatile and accurate trace element determinations in iron-rich and other geological samples using X-ray fluorescence analysis. X-Ray Spectrom 19:117–123

Croudace IW, Williams-Thorpe O (1988) A low dilution, wavelength-dispersive X-ray fluorescence procedure for the analysis of archaeological rock artefacts. Archaeometry 30:227–236

Croudace IW, Rindby A, Rothwell RG (2006) ITRAX: description and evaluation of a new multi-function X-ray scanner. In: Rothwell RG (ed) New techniques in sediment core analysis. Geol Soc Spec Publ 267:51–63

Edgar CJ, Wolff JA, Olin PH, Nichols HJ, Pittari A, Cas RAF, Reiners PW, Spell TL, Marti J (2007) The late Quaternary Diego Hernandez Formation, Tenerife: volcanology of a complex cycle of voluminous explosive phonolitic eruptions. J Volcanol Geoth Res 160:59–85

Ercilla G, Alonso B, Perez-Belzuz F, Estrada F, Baraza J, Farran M, Canals M, Masson DG (1998) Origin, sedimentary processes and depositional evolution of the Agadir turbidite system, central eastern Atlantic. J Geol Soc 155:929–939

Giachetti T, Paris R, Kelfoun K, Pérez-Torrado FJ (2011) Numerical modelling of the tsunami triggered by the Güímar debris avalanche, Tenerife (Canary Islands): comparison with field-based data. Mar Geol 284:189–202

Gisler G, Weaver RP, Gittings ML (2006) SAGE calculations of the tsunami threat from La Palma. Sci Tsunami Hazards 24:288–301

Harbitz CB, Løvholt F, Pedersen G, Masson DG (2006) Mechanisms of tsunami generation by submarine landslides: a short review. Norw J Geol 86:255–264

Haugen KB, Lovholt F, Harbitz CB (2005) Fundamental mechanisms for tsunami generation by submarine flows in idealised geometries. Mar Pet Geol 22:209–217

Hühnerbach V, Masson DG, Partners of the COSTA-Project (2004) Landslides in the North Atlantic and its adjacent seas: an analysis of their morphology, setting and behaviour. Mar Geol 213:343–362

Hunt JE, Wynn RB, Masson DG, Talling PJ, Teagle DAH (2011) Sedimentological and geochemical evidence for multistage failure of volcanic island landslides: a case study from Icod landslide on north Tenerife. Geochem Geophys Geosyst 12 (Q12007):1–36

Hunt JE, Wynn RB, Talling PJ, Masson DG (2013a) Turbidite record of frequency and source of large volume (> 100 $km^3$) Canary Island landslides in the last 1.5 Ma: implications for landslide triggers and geohazards. Geochem Geophys Geosys 14:2100–2123

Hunt JE, Wynn RB, Talling PJ, Masson DG (2013b) Multistage collapse of eight western Canary Island landslides in the last 1.5 Ma: Sedimentological and geochemical evidence from subunits in submarine flow deposits. Geochem Geophys Geosys 14:2159–2181

Hunt JE, Wynn RB, Talling PJ, Masson DG (2013c) Frequency and timing of landslide-triggered turbidity currents within the Agadir Basin, offshore NW Africa: are there associations with climate change, sea level change and slope sedimentation rates? Mar Geol 346:274–291

Le Bas TP, Masson DG, Holtom RT (2007) Slope failures of the flanks of the southern Cape Verde Islands. In: Lykousis V, Sakellariou D, Locat J (eds) Submarine mass movements and their consequences, vol 3. Springer, Dordrecht, pp 337–346

Lee H (2009) Timing of occurrence of large submarine landslides on the Atlantic ocean margin. Mar Geol 264:53–64

Mader CL (2001) Modelling the La Palma landslide tsunami. Sci Tsunami Hazards 19:150–170

Masson DG, Watts AB, Gee MRJ, Urgeles R, Mitchell NC, Le Bas TP, Canals M (2002) Slope failures on the flanks of the western Canary Islands. Earth Sci Rev 57:1–35

Masson DG, Harbitz CB, Wynn RB, Pedersen G, Løvholt F (2006) Submarine landslides: processes, triggers and hazard prediction. Phil Trans R Soc A 364:2009–2039

Masson DG, Le Bas TP, Grevemeyer I, Weinrebe W (2008) Flank collapse and large-scale landsliding in the Cape Verde Islands, off West Africa. Geochem Geophys Geosyst 9:1–16

Middleton GV (1993) Sediment deposition from turbidity currents. Annu Rev Earth Planet Sci 21:89–114

Moore JG, Clague DA, Holcomb RT, Lipman PW, Normark WR, Torresan ME (1989) Prodigious submarine landslides on the Hawaiian Ridge. J Geophys Res 94:17,465–17,484

Moore JG, Normark WR, Holcomb RT (1994) Giant Hawaiian landslides. Annu Rev Earth Planet Sci 22:119–144. doi:10.1146/annurev.ea.22.050194.001003

Pearce TJ, Jarvis I (1992) Composition and provenance of turbidite sands: late Quaternary, Madeira Abyssal Plain. Mar Geol 109:21–51

Pearce TJ, Jarvis I (1995) High-resolution chemostratigraphy of Quaternary distal turbidites: a case study of new methods for the analysis and correlation of barren sequences: In Dunay RE, Hailwood EA (eds) Non-biostratigraphical methods of dating and correlation. Geol Soc Spec Publ 89:107–143

Pérez-Torrado FJ, Paris R, Cabrera MC, Schneider J-C, Wassmer P, Carracedo J-C, Rodríguez-Santana A, Santana F (2006) Tsunami deposits related to flank collapse in oceanic volcanoes: The Aegate Valley evidence, Gran Canaria, Canary Islands. Mar Geol 227:135–149

Rothwell RG, Pearce TJ, Weaver PPE (1992) Late Quaternary evolution of the Madeira Abyssal Plain, NE Atlantic. Basin Res 4:103–131

Ward SN (2001) Landslide tsunami. J Geophys Res 106:11201–11215
Ward SN, Day SJ (2001) Cumbre Vieja volcano: potential collapse and tsunami at La Palma, Canary islands. Geophys Res Lett 28:3397–3400
Watts AB, Masson DG (1995) A giant landslide on the north flank of Tenerife, Canary Islands. J Geophys Res 100:24487–24498. doi:10.1029/95JB02630
Watts AB, Masson DG (2001) New sonar evidence for recent catastrophic collapses of the north flank of Tenerife, Canary Islands. Bull Volcanol 63:8–19
Weaver PPE, Kuijpers A (1983) Climatic control of turbidite deposition on the Madeira Abyssal Plain. Nature 306:360–363
Weaver PPE, Rothwell RG (1987) Sedimentation on the Madeira Abyssal Plain over the last 300,000 years. In: Weaver PPE, Thomson J (eds) Geology and geochemistry of Abyssal Plains. Geol Soc Spec Publ 31:71–86
Weaver PPE, Rothwell RG, Ebbing J, Gunn D, Hunter PM (1992) Correlation, frequency of emplacement and source directions of megaturbidites on the Madeira Abyssal Plain. Mar Geol 109:1–20
Wynn RB, Masson DG (2003) Canary Island landslides and tsunami generation: can we use turbidite deposits to interpret landslide processes. In: Locat J, Mienert J (eds) Submarine mass movements and their consequences, vol 1. Kluwer Academic Publishers, Dordrecht, pp 325–332
Wynn RB, Weaver PPE, Stow DAV, Masson DG (2002) Turbidite depositional architecture across three interconnected deep-water basins on the Northwest African margin. Sedimentology 49:1441–1462

# Chapter 6
# An Empirical Assessment of Variable Water Content and Grain-Size on X-Ray Fluorescence Core-Scanning Measurements of Deep Sea Sediments

**Suzanne E. MacLachlan, James E. Hunt and Ian W. Croudace**

**Abstract** Deciphering the signal within X-ray fluorescence (XRF) core scanner data can be complex in comparison to conventional laboratory XRF analysis where samples are milled and pelleted or beaded. One complicating factor is that the down-core variability in water content and grain-size can affect element count rates thereby potentially leading to inaccurate interpretations. Experiences using an Itrax XRF core scanner data highlight some of the pitfalls that can occur when the sediment is inhomogeneous. We show that over a threshold of 25 wt.% coarse grained material (>63 μm) within the sediment there is a potential for causing significant variability in certain elements. It is also shown that water content variability has a major effect above 40 %.

**Keywords** X-ray fluorescence · XRF core scanner · Water content · Physical properties · Marine sediment

S. E. MacLachlan (✉)
National Oceanography Centre, European Way, Southampton SO14 3ZH, UK
e-mail: s.maclachlan@noc.ac.uk

J. E. Hunt
Marine Geoscience, National Oceanography Centre, European Way,
Southampton SO14 3ZH, UK

I. W. Croudace
Ocean and Earth Science, National Oceanography Centre, University of Southampton,
Waterfront Campus, European Way, Southampton SO14 3ZH, UK



I. W. Croudace, R. G. Rothwell (eds.), *Micro-XRF Studies of Sediment Cores*,
Developments in Paleoenvironmental Research 17, DOI 10.1007/978-94-017-9849-5_6

## Introduction

Micro X-ray fluorescence (XRF) core scanners are now widely used in sediment core research. These core scanners are employed as a rapid analytical tool in palaeoceanography (e.g. Ziegler et al. 2013), palaeoliminology (e.g. Guyard et al. 2007), geochemical investigations (e.g. Tian et al. 2011) and geochronological studies (e.g. Rothwell et al. 2006; Westerhold et al. 2007; Hunt et al. 2013). A major advantage of these core scanners, compared to conventional laboratory XRF analysis, is the rapid acquisition of high resolution continuous down-core elemental data without disturbance to the split sediment core. However, interpretation of XRF core scanner data can be more complex than conventional lab WD-XRF (wavelength dispersive x-ray fluorescence spectrometry) analysis, because of the range of variables that exist when analysing the surface of a split sediment core. For instance, even when carefully cut, split cores may have an uneven surface topography and grain-size variations will result in surface roughness (Rothwell and Rack 2006). Other data inaccuracies may occur due to variable interstitial water content, sediment surface mineral homogeneity, textural and porosity variability, and potential pooling of water between the sediment surface and x-ray film driven by capillary flow (Tjallingii et al. 2007).

Over the past decade efforts have been made to evaluate the accuracy and precision of XRF core scanners, addressing issues related to sediment surface heterogeneity (e.g. Richter et al. 2006; Tjallingii et al. 2007; Hennekam and de Lange 2012; Wilhelms-Dick et al. 2012). However, the majority of the published work relates to investigations using the Avaatech core scanner, and only limited consideration has been given to sediment cores run using the widely used Itrax core scanner.

The designs of the Itrax and Avaatech scanners are different, perhaps leading to slightly different data acquisition capabilities. The Avaatech scanner utilises a prism system that is lowered onto the sediment surface at each measurement point, and incoming radiation strikes the sample surface at 45°. The detector for outgoing fluorescent x-rays is likewise mounted at an angle of 45° (Richter et al. 2006). The Itrax core scanner has an incident radiation beam that is 90° to the sample surface. Samples are initially topographically scanned to generate a smoothed distance profile that is used to guide the position of a moveable XRF detector. The XRF detector therefore should remain at a constant distance to the sample surface as the sediment core is incrementally moved (Croudace et al. 2006).

Here, we review the effects of heterogeneity of the sediment surface, specifically examining variable water content and grain-size within a marine sediment core using an Itrax core scanner. The results are compared to published studies obtained with an Avaatech core scanner system. This contribution examines the impact of sediment surface heterogeneities on XRF elemental signals.

## Materials and Methods

### *Sediment Material*

Sediment core JC060-021-PC05 is a 667 cm-long core that was recovered from a water depth of 1054 m during the RRS James Cook cruise JC060 to the eastern mound field of the Darwin mounds area (59°50.882'N, 7°3.659'W) in the northern Rockall Trough, northwest of the UK (Fig. 6.1). The sediment input to the northern Rockall Trough has been minimal since the last glaciation. The Holocene sedimentary regime has been controlled by strong bottom currents redistributing older sediments (Kenyon 1986; Stoker et al. 1998; Masson et al. 2002, 2003). Regionally, the upper few metres of sediment on the lower slopes and basin floor of the northern Rockall Trough typically consist of a thin (<20 cm) surface layer of coarse, sandy Holocene sediment overlying thick glaciogenic mud containing sparse coarse-

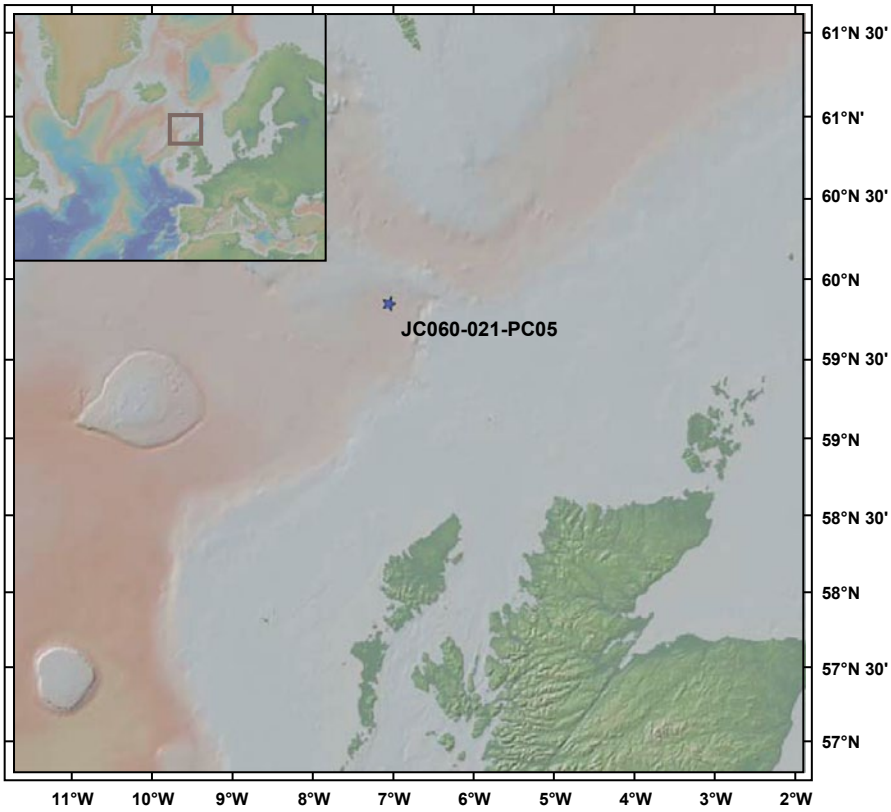


**Fig. 6.1** Location of core JC060-021-PC05 and the regional setting of the Darwin mounds area in the northern Rockall Trough, northwest Scotland. The base map is from the Global Multi-Resolution Topography (GMRT) synthesis. (Ryan et al. 2009)

grained horizons (Howe 1995, 1996). The core was selected for this study as it was not split at sea, thus allowing whole core logging of the physical properties and minimal loss of water content prior to analysis.

## *XRF-Core Scanning*

XRF measurements were obtained directly from the split core surface of the archive half with the Itrax XRF core scanner at the British Ocean Sediment Core Research Facility at National Oceanography Centre, Southampton (UK). XRF data were acquired using a molybdenum X-ray tube set at 30 kV and 50 mA with a dwell time of 30 s and a step size of 1 mm. The Itrax X-ray beam ($0.2 \times 20$ mm) is used to irradiate (excite) samples to generate a radiographic image and an energy-dispersive X-ray spectrum. This spectrum is derived from a somewhat smaller area than the full 20 mm beam width and is determined (especially so for lighter elements) by the 5 mm diameter vacuum nozzle connected to the SDD detector. The sample can remain statically in the beam for the chosen dwell time in which case the spectrum accumulated relates to an area of $0.2 \times \sim 5$ mm. Alternatively, the user can select a dynamic scan where the core moves through the Itrax beam according to the selected scan distance and dwell time.

The dataset from the Itrax core scanner is different from conventional laboratory XRF measurements where individual samples (typically 0.5 or 1 cm sub-samples cut out of the core) are measured in a vacuum as either homogeneous compact pellets or beads having a flat surface. The Itrax generates a single dispersive energy spectrum for each point down core, and each element intensity is calculated as a peak area (expressed in counts). The counts are not normally matrix corrected and several previous studies have shown that there is a good first approximation to concentration (e.g. Croudace et al. 2006, 2015, this volume). Users also commonly take small subsamples and analyse using a quantitative destructive method (ICP-OES or WD-XRF) to validate/calibrate Itrax data. In this study the Itrax data are directly compared with elemental concentrations derived using WD-XRF. The Itrax-scan data (1 mm resolution) have been averaged over 10 points to allow comparison with the WD-XRF data (1 cm resolution, the method used by Hunt et al. 2015, this volume).

## *Conventional WD-XRF*

Twenty-six 1 cm resolution subsamples were selected from a range of water contents (20.0–40.2 %; see Fig. 6.2 and Sect. 2.6) within the sediment core for conventional WD-XRF analysis. WD-XRF subsamples were selected to encompass the variability observed in the physical properties down-core. Subsamples were pressed into pellets and analyzed using a Philips Magix-Pro instrument fitted with a 4 kW Rh-target X-ray tube. The instrument was calibrated using a range of international geochemical reference samples with matrix correction applied using Compton correction and fundamental parameters models.

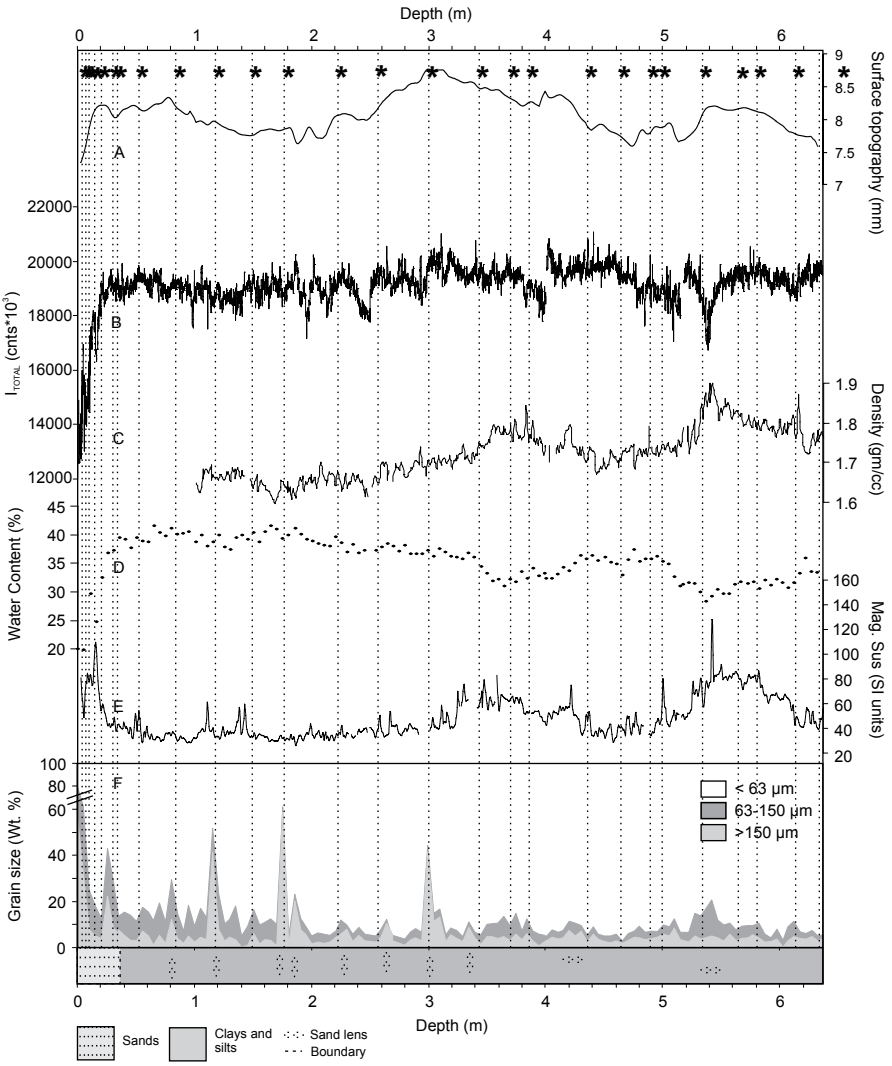


**Fig. 6.2** Compilation of parameters measured on sediment core: **a** surface topography from the Itrax; **b** total counts from the Itrax; **c** density from the MSCL-S; **d** percentage water content; **e** magnetic susceptibility measured on MSCL-XYZ; **f** variability of the grain-size fractions < 63 µm, 63–150 µm, and > 150 µm, in weight %. At the base of the compilation of parameters is the lithological log and key. The *asterisk* (*) and *dotted lines* indicate the locations of WD-XRF subsamples

## *Grain-Size*

Sediment core JC60-21 was sampled at 5 cm intervals for laser diffraction grain-size analysis. No pre-treatment was considered necessary due to previous studies indicating low total organic carbon values (typically 0.02 %, Serpetti et al.

2013). Subsamples were dispersed in 30 mL of RO water with 0.05% sodium hexametaphosphate dispersant and left on a shaking table for 12 h. The dispersed sediment solutions were analysed using a Malvern (model *Mastersizer 2000*) particle size analyser, which is able to measure grain-sizes in the range 0.02–2000 µm. Standard reference materials with mean diameters of 32 and 125 µm were used to monitor accuracy, while three repeat runs for each sample were used to monitor precision (reported at < 0.5% SD). The particle distribution output was then processed using the Gradistat software for sediment parameters (Blott and Pye 2001).

### *Multi-Sensor Core Logger Data*

Gamma density values for JC060-21 were measured using the *Geotek* MSCL-S (Standard Multi-Sensor Core Logger). The measurement interval was 1 cm. Magnetic susceptibility was measured using a Bartington Instruments point sensor fitted to a Geotek MSCL-XYZ logger at 0.5 cm down core resolution.

### *Water Content*

Samples were obtained at 5 cm intervals. To obtain volumetric sub-samples of 6.8 $cm^3$, cubes were pushed into the split sediment core surface. These fresh wet sediment samples of known volume were weighed. The same volumetric samples were then dried at 40 °C for 48 h to a constant weight. The water content wt.% was calculated as the difference between wet weight and dry weight relative to the original wet weight.

## Results

### *Correlation of Itrax-Scan Data with Conventional WD-XRF*

Measured concentration data values obtained from conventional WD-XRF and the Itrax-scan data for core JC060-021-PC05 are plotted in Fig. 6.3. The WD-XRF data were measured on 1 cm subsamples; the Itrax data presented are the mean values of scan data for the depth corresponding to the subsample. The elements show highly variable responses. For instance, K, Ti, Fe, Mn, V, Ni, Zn, Ba, Sr and Zr yield strong positive relationships, in a linear form. Ca showed a generally positive but highly scattered relationship that was not statistically significant. Si showed a highly scattered, non linear relationship.

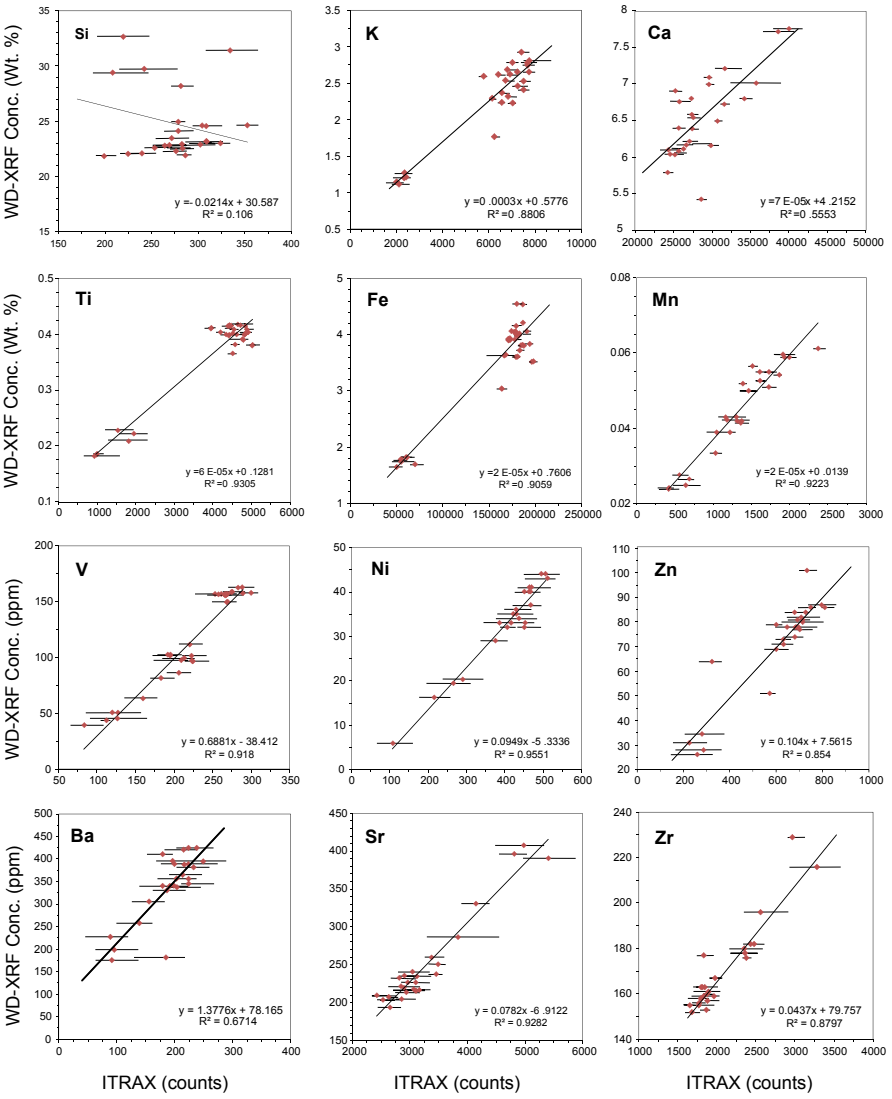


**Fig. 6.3** Correlations of Itrax element counts (counts per second) with conventional WD-XRF concentrations. Note: WD-XRF measurements were made on a 1 cm thick slice at each selected depth. The Itrax scan was undertaken at 1 mm step size; the *range bar* indicates the data spread across the 1 cm thickness that corresponds to the WD-XRF measurement. The *point* indicates the average value across the range

## *Correlation of Water Content Adjusted Itrax-Scan Data with Conventional WD-XRF*

To consider the potential effect of the variable water content on Itrax-scan data, we considered water content at each of the sample depths. Water corrected element

**Table 6.1** Correlation coefficients ($R^2$) for linear regression of XRF-scan to respective WD-XRF value and water content corrected XRF-scan to respective WD-XRF

| Element | $R^2$ value XRF-scan | $R^2$ value Water corrected XRF-scan |
|---|---|---|
| Si | 0.106 | 0.4663[a] |
| K | 0.8806 | 0.7576 |
| Ca | 0.5553 | 0.4785 |
| Ti | 0.9305 | 0.8194 |
| Fe | 0.9059 | 0.8047 |
| Mn | 0.9223 | 0.8465 |
| V | 0.918 | 0.7922 |
| Ni | 0.9551 | 0.823 |
| Zn | 0.854 | 0.8313 |
| Ba | 0.6714 | 0.5288 |
| Sr | 0.9282 | 0.9406[a] |
| Zr | 0.8797 | 0.9004[a] |

[a] Element $R^2$ improved by water correction

integrals ($I_{corr}$, based on the measured percentage water content, W, and Itrax wet integrals, $I_{wet}$, assuming a linear relationship, using Eq. 6.1) were calculated to investigate the potential water content effect.

$$I_{corr} = \frac{I_{wet}(100 - W)}{100}. \tag{6.1}$$

Table 6.1 indicates that the water correction only improves the relationship for Si, Zr and Sr. The Si still shows a highly scattered relationship that is not statistically significant. For all other elements (K, Ca, Ti, Fe, Mn, V, Ni, Zn, Ba) the relationship is weakened and statistically less robust.

## Discussion

The observed Itrax scan data deviations from the 'reference' data (WD-XRF) are attributed to the influence of physical properties during the scanning process. The deviations have a more significant effect on the relatively light elements (Si and Ca, see Fig. 6.3). It is likely that the deviations are primarily due to variability in water content, grain-size and sediment heterogeneity (Figs. 6.4 and 6.5).

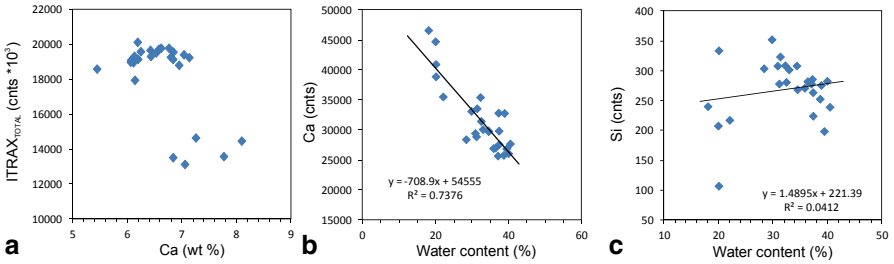


**Fig. 6.4** Effects observed in the Itrax Ca and Si intensity data: **a** correlation between total intensity and WD-XRF Ca (wt.%); **b** correlation between Itrax Ca intensity (counts) and water content (%); **c** correlation between Itrax Si intensity (counts) and water content

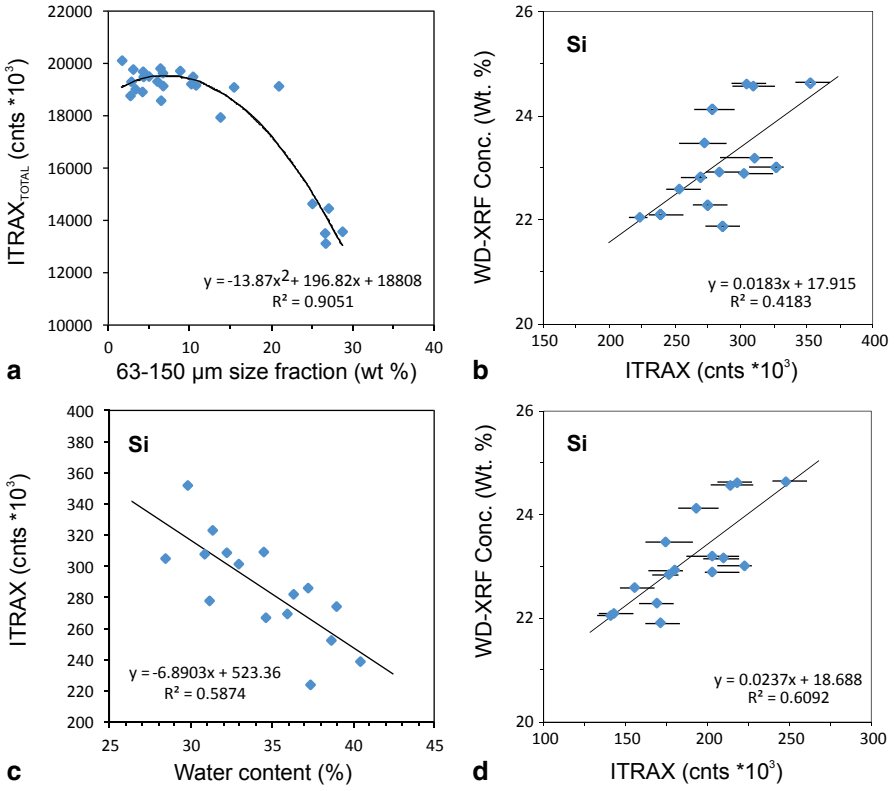


**Fig. 6.5** Effects observed due to grain-size variations down core: **a** correlation between total Itrax intensity and 63–150 µm grain-size fraction (wt.%); **b** correlation between WD-XRF Si (wt.%) and Itrax Si intensity (counts) with exclusion of the coarse grained samples (i.e. plotting only clay dominated samples; **c** correlation between Itrax Si intensity (counts) and water content (%) with exclusion of the coarse grained samples; **d** correlation between WD-XRF Si (wt.%) and water content corrected Itrax Si intensity (counts) with the exclusion of the coarse grained samples

## *Water Effects*

Tjallingii et al. (2007) showed that variability in calcium carbonate ($CaCO_3$) content down core may have a greater influence on the total intensity recorded by the Avaatech XRF scanner than changes in wet bulk density and grain-size. This was established for a marine sediment core with a range of $CaCO_3$ concentrations from ~30 to 60 wt.%. WD-XRF analysis for core JC060-021-PC05 indicates the Ca content to be much lower, typically around 6–7 wt.%. Figure 6.4a shows that at relatively low and stable Ca content that there is no effect on the total intensity recorded. The drop in total intensity that is observed for five data points is likely to be a result of sediment type, as these samples were from the coarse grained sections of the core. Figure 6.4b indicates that there is a correlation between Ca intensity and water content; clearly showing high Ca count rates for samples with low water content (~20–25 %) compared with 50–100 % lower count rate when the water content increases to 35–40 % range. This is not statistically robust although shows a similar trend to the relationship observed by Tjallingii et al. (2007). Other factors influencing the Ca intensity in core JC060-021-PC05 may be related to the dominant clay matrix. It is postulated that underestimation of Ca concentrations (by XRF scanners) where foraminifera are abundant is a result of the artificial burial of carbonate tests into the clay matrix during surface smoothing of the split core surface (Kido et al. 2006). Preparation of the split core surface for XRF scanning may decrease the volume of foraminifera in the upper several tenths/hundredths of a micron of the analysed sediment (Richter et al. 2006). However, Hunt et al. (2015, this volume) report that the Itrax data is robust for Ca concentrations above 15 wt.% (with a recorded $R^2$ value of 0.96). This suggests there may be a concentration threshold to achieve quality Ca data using the Itrax core scanner. We postulate that this threshold is between 8.5 and 15 wt.% Ca concentration, above 15 wt.% Ca the data quality is significantly improved.

The study by Tjallingii et al. (2007) similarly shows a relationship between Si intensity and water content. Figure 6.4c shows that the Si intensity/water content relationship is weak for core JC060-021-PC05. This demonstrates it is very difficult to isolate the dominant contributing factor influencing XRF core scanner elemental data, and it may be a combination of effects that produces poor data quality for the lighter elements such as Si.

## *Grain-Size and Surface Roughness*

Deep sea sediments are predominantly fine grained sediments consisting of clays and silts with little material coarser than >63 μm. Core JC060-021-PC05 predominantly consists of a glaciogenic mud sequence with sparse coarse-grained horizons, capped with a thin (<20 cm) surface layer of coarser, sandy sediment (Fig. 6.2). It therefore seems likely that grain-size is of minor influence across the majority of Itrax-scanned elemental data. However, the top section of the core JC060-021-PC05 contains up to 85 wt.% coarse grained material (>63 μm); consequently, some

grain-size effects are observed in the data (e.g. for total intensity, Figs. 6.2 and 6.5a). Surface roughness effects are more pronounced in sediments dominated by coarser sand-sized grains (Richter et al. 2006). For example, Fig. 6.5a shows that there may be a threshold to the amount of coarse grains within a sample before there is a significant effect on the total intensity. The data suggest that the threshold occurs between 20 and 25 wt.% of grains >63 µm size.

A minor grain-size effect is observed in the Si data, when the data for the clay-dominated samples are plotted the relationship between the conventional WD-XRF and the Itrax-scan counts is observed (Fig. 6.5b). The $R^2$ value was previously 0.106 (Fig. 6.3), but when the sand dominated data point is removed the $R^2$ value is 0.4183, suggesting that the Si data may be affected by grain-size and roughness, more evident when the sediment coarse fraction reaches a threshold of >25 wt.%. This finding is supported by Bertrand et al. (2015, this volume) who also confirm that Itrax data quality are influenced where sediment cores show large grain-size variations. Figure 6.5c indicates that the fine sediment Si samples (dominated by <63 µm fraction) shows a weak correlation with water content suggesting that there is both a water content and grain-size effect within the Si data. This demonstrated in Fig. 6.5d by plotting the water corrected Si data for only the fine grained samples. The $R^2$ value for the uncorrected data was 0.106 compared with the corrected value of 0.6092. It is noted that this is still a weak correlation, however, it demonstrates the complex relationship of the physical properties that can affect the data quality especially for the lighter elements.

## Conclusions

A review of previous investigations and the findings of this study suggest that the Itrax and Avaatech XRF core scanners are similarly affected by split core sediment heterogeneity. The Itrax-scan data from a marine sediment core illustrate how the data quality can be affected by physical and chemical properties at the split core surface. It is therefore, important to consider the impact of water content and grain size before making substantive palaeoenvironmental interpretations. For instance, increases in grain-size (>63 µm) and water content may substantially affect data quality in small sections of the core potentially; e.g. turbidite sands leading to misinterpretation of proxies.

## References

Bertrand S, Hughen K, Giosan L (2015) Limited influence of sediment grain size on elemental XRF core scanner measurements. This volume

Blott SJ, Pye K (2001) Gradistat: a grain-size distribution and statistics package for the analysis of unconsolidated sediments. Earth Surf Proc Land 26:1237–1248

Croudace IW, Rindby A, Rothwell RG (2006) ITRAX: description and evaluation of a new multi-function X-ray core scanner. In: Rothwell RG (ed) New techniques in sediment core analysis, vol 267. Geological Society Special Publication, London pp 51–63

Croudace IW, Romano E, Ausili A, Bergamin L, Rothwell RG (2015) X-ray core scanners as an environmental forensic tool: a case study of polluted harbour sediment (Augusta Bay, Sicily). This volume

Guyard H, Chapron E, St-Onge G, Anselmetti FS, Arnaud F, Magand O, Francus P, Mélières M-A (2007) High-altitude varve records of abrupt environmental changes and mining activities over the last 4000 years in the Western French Alps (Lake Bramant, Grandes Rousses Massif). Quat Sci Rev 26:2644–2660

Hennekam R, de Lange G (2012) X-ray fluorescence core scanning of wet marine sediments: methods to improve quality and reproducibility of high-resolution paleoenvironmental records. Limnol Oceanogr Meth 10:91–1003

Howe JA (1995) Sedimentary processes and variations in slope-current activity during the last glacial-interglacial episode on the Hebrides Slope, northern Rockall Trough, North Atlantic ocean. Sediment Geol 96:201–230

Howe JA (1996) Turbidite and contourite sediment waves in the Northern Rockall Trough, North Atlantic ocean. Sedimentology 43:219–234

Hunt JE, Wynn RB, Talling PJ, Masson DG (2013) Frequency and timing of landslide-triggered turbidity currents within the Agadir Basin, offshore NW Africa: are there associations with climate change and slope sedimentation rates? Mar Geol 346:274–291

Hunt JE, Croudace IW, MacLachlan SE (2015) Use of calibrated Itrax XRF data in examining turbidite composition and provenance in Agadir Basin, Northwest African Passive margin. This volume

Kenyon NH (1986) Evidence from bedforms for a strong poleward current along the upper continental slope of Northwest Europe. Mar Geol 72:187–198

Kido Y, Koshikawa T, Tada R (2006) Rapid and quantitative major element analysis method for wet fine-grained sediments using an XRF microscanner. Mar Geol 229: 209–225

Masson DG Howe JA, Stoker MS (2002) Bottom current sediment waves, sediment drift and contourites in the northern Rockall Trough. Mar Geol 192:215–237

Masson DG, Bett BJ, Billet DSM, Jacobs CL, Wheeler AJ, Wynn RB (2003) The origin of deep-water, coral-topped mounds in the northern Rockall Trough, Northeast Atlantic. Mar Geol 194:159–180

Richter RO, van der Gaast S, Koster R, Vaars A, Gieles R, de Stigter HC, de Haas H, van Weering TCE (2006) The Avaatech XRF Core Scanner: technical description and applications to NE Atlantic sediments. In: Rothwell RG (ed) New techniques in sediment core analysis, vol 267. Geological Society Special Publication, London pp 39–50

Rothwell RG, Rack FR (2006) New techniques in sediment core analysis: an introduction. In: Rothwell RG (ed) New techniques in sediment core analysis, vol 267. Geological Society Special Publication, London pp 1–29

Rothwell RG, Hoogakker B, Thomson J, Croudace IW, Frenz M (2006) Turbidite emplacement on the southern Baleraic Abyssal Plain (western Mediterranean Sea) during Marine Isotope Stages 1–3: an application of ITRAX XRF scanning of sediment cores to lithostratigraphic analysis. In: Rothwell RG (ed) New techniques in sediment core analysis, vol 267. Geological Society Special Publication, pp 79–98

Ryan WBF, Carbotte SM, Coplan JO, O'Hara S, Melkonian A, Arko R, Weissel RA, Ferrini V, Goodwillie A, Nitsche F, Bonczkowski J, Zemsky R (2009) Global multi-resolution topography synthesis. Geochem Geophys Geosyst 10:Q03014. doi:10.1029/2008GC002332

Serpetti N, Gontikaki E, Narayanaswamy BE, Witte U (2013) Macrofaunal community inside and outside of the Darwin Mounds special area of conservation, NE Atlantic. Biogeosciences 10:3705–3714

Stoker MS, Akhurst MC, Howe JA, Stow DAV (1998) Sediment drifts and contourites on the continental margin off northwest Britain. Sediment Geol 155:33–51

Tian J, Xie X, Ma W, Jin H, Wang P (2011) X-ray fluorescence core scanning records of chemical weathering and monsoon evolution over the past 5 Myr in the southern South China Sea. Paleoceanography:PA4202. doi:10.1029/PA002045

Tjallingii R, Röhl U, Kölling M, Bickert T (2007) Influence of the water content on X-ray fluorescence core-scanning measurements in soft marine sediments. Geochem Geophys Geosyst Geosy Geosyst 8:Q02004. doi:10.1029/2006GC001393

Westerhold T, Röhl U, Laskar, J, Raffi I, Bowles J, Lourens LJ, Zachos JC (2007) On the duration of magnetochrons C54r and C25n and the timing of early Eocene global warming events: implications from the Ocean Drilling Program Leg 208 Walvis Ridge depth transect. Paleoceanography:PA2201. doi:10.1029/2006PA001322

Wilhelms-Dick D, Westerhold T, Röhl U (2012) A comparison of mm scale resolution techniques for element analysis in sediment cores. J Anal At Spectrom 27:1574–1584

Ziegler M, Simon MH, Hall IR, Barker S, Stringer C, Zahn R (2013) Development of Middle Stone Age innovation linked to rapid climate change. Nature Commun 4:1905. doi:10.1038/ncomms2897

# Part II
# Lake and River Studies

# Chapter 7
# Micro-XRF Core Scanning in Palaeolimnology: Recent Developments

**Sarah J. Davies, Henry F. Lamb and Stephen J. Roberts**

**Abstract** Within the last ten years, micro-XRF (μXRF) core scanning has become an important addition to the suite of techniques for investigating lacustrine sediments. Most studies to date have focused on records of detrital material. These have typically used elements such as Si, K, Ca, Ti, Fe, Rb, Sr and Zr as single element profiles or ratios. Inferences are made about changing catchment dynamics such as glacier advance and retreat, variations in run-off and soil erosion, weathering rates and processes and grain-size fluctuations. These can be linked, depending on the context of the individual basin, to factors such as climatic variability, meteorological events, seismic activity, tephra deposition or anthropogenic disturbance such as agriculture or deforestation. Studies of in-lake dynamics focus on elements affected by redox changes (e.g., Fe, Mn) or those which can be produced authigenically either as a result of evaporative concentration or biological processes (e.g., Ca). Here, we review the use of μXRF core scanning on lake sediments and summarise the range of elements and ratios that have been applied as a reference point for users. We consider some of the challenges involved in interpreting elemental data, given the wide variety of internal and external factors that can affect lake sediment composition.

**Keywords** Lake sediments · Palaeolimnology · XRF core scanning · Environmental proxies · In-lake processes · Flood histories · Varves

## Introduction

The development of μXRF core scanning since the 1990s (see Rothwell and Croudace, this volume) has enabled rapid, non-destructive and high-resolution geochemical analysis of sediment cores. The first studies focused on marine sediments, building

S. J. Davies (✉) · H. F. Lamb
Department of Geography and Earth Sciences, Institute of Geography, History, Politics and Psychology, Aberystwyth University, Aberystwyth SY23 3DB, UK
e-mail: sjd@aber.ac.uk

S. J. Roberts
British Antarctic Survey, High Cross, Madingley Road, Cambridge CB3 0ET, UK



I. W. Croudace, R. G. Rothwell (eds.), *Micro-XRF Studies of Sediment Cores*,
Developments in Paleoenvironmental Research 17, DOI 10.1007/978-94-017-9849-5_7

upon the routine use of shipboard core scanning techniques for initial characterisation of physical properties. Since the arrival of a new generation of core scanners in the last decade (e.g., Croudace et al. 2006; Richter et al. 2006; for a recent overview, see Rothwell and Croudace, this volume), application of the technique to lake sediments has accelerated, with a notable rise in publications in the last five years.

Lake sediments are important terrestrial records of environmental change over a range of timescales, recording both catchment-scale dynamics and regional climatic variability (e.g., Cohen 2003). They can provide long, continuous and high-resolution archives comparable to those from oceans and ice cores. µXRF scanning has opened up new opportunities for the analysis of lake sediments, due to the range of elements that can be analysed, the high spatial resolution (up to 60 µm on some systems) and speed of analysis (Francus et al. 2009). This technological progress has occurred alongside efforts to standardise procedures for the curation, description and analysis of lake sediment cores (e.g., Schnurrenberger et al. 2001; Schnurrenberger et al. 2003). The impetus to develop more consistent protocols came from international collaborative initiatives such as the Global Lake Drilling Programme (GLAD) and the International Continental Scientific Drilling Programme (ICDP). µXRF scanning is now incorporated into the standard suite of initial palaeolimnological analyses applied to ICDP cores. With an increasing number of commercially available scanners in operation, access to facilities is also becoming more feasible for smaller scale projects.

In this paper, we examine how µXRF scanning of lake sediments has been used to interpret past environmental and climatic changes, often as part of broader multi-proxy investigations. The principal focus here is on the application of the technique. Issues relating to instrument configuration, sample preparation and data analysis are discussed in detail elsewhere by others (e.g., Tjallingii et al. 2007; Weltje and Tjallingii 2008; Boyle et al., this volume; Cuven et al., this volume; Jarvis et al., this volume; Rothwell and Croudace, this volume; Schillereff et al. 2014, although we do consider these issues where appropriate. First, we discuss the composition of lake sediments and consider the key elements and ratios in use and their environmental interpretation. We then discuss the use of µXRF core scanning in the characterisation of sediments and the development of core chronologies. We review the application of µXRF scanning across the spectrum of palaeolimnological research, including analysis of flood histories (e.g., Czymzik et al. 2013; Schillereff et al. 2014) and other 'event' deposits such as landslides, turbidites, seismites and lahars (e.g., Van Daele et al. 2014). We examine how µXRF scanning has contributed to the development of palaeoclimate records from lake sediments, such as long records of Quaternary climate variability (e.g., Scholz et al. 2007; Haberzettl et al. 2009; Melles et al. 2012), identification of rapid, abrupt climate shifts (e.g., Kylander et al. 2011; Lauterbach et al. 2011) and inter-annual climate variability (e.g., Metcalfe et al. 2010; Yancheva et al. 2007). We also discuss how µXRF can provide records of anthropogenic environmental changes such as catchment disturbance and metal pollution (e.g., Guyard et al. 2007; Niemann et al. 2013). Finally, we consider progress to date and discuss some potential future developments for µXRF scanning in palaeolimnological research.

## Interpretation of XRF Scanning Data from Lake Sediments

Lakes and their catchments vary enormously in their physical, chemical and biological characteristics. The complexity of responses to within-lake and catchment processes leads to a highly diverse range of sediment types (Schnurrenberger et al. 2003). Therefore, a multi-proxy approach is required to disentangle the various factors that influence sediment composition and thus environmental interpretation. Geochemical analysis has historically been an important component of multi-proxy palaeolimnological reconstructions (Boyle 2001). Comprehensive reviews of geochemical methods and interpretations by Engstrom and Wright (1984) and Boyle (2001) built on earlier work by Mackareth (1966) and are key reference texts for researchers. In both, it is argued that chemical analysis of lake sediments is best used as a supporting technique, as interpretation can be less certain when parallel biological methods are not applied (Boyle 2001).

With the development of μXRF core scanners, high-resolution, continuous, multi-element datasets (typically in the range of atomic numbers Al–U, but some scanners can detect Mg) have become straightforward and relatively rapid. The general capability and speed has revolutionised the possibilities for the analysis of long cores and finely laminated sediments, where previously, detailed investigation of complete sequences using conventional destructive methods would have taken many months, or even years. Continuous datasets are also suitable for the application of time series analysis (subject to appropriate chronological control to ensure equal time intervals). The degree of cyclicity in observed variations and changes in system behaviour over time can be identified. These factors have led to a distinct increase in the prominence of elemental analysis in palaeolimnology over the last 5–10 years.

### *Influence of Lake Sediment Composition on Element Detection and Interpretation*

Lake sediment composition is typically much more variable than that of marine sediments. The greater influence of catchment source area in most cases means that any changes on land are then transmitted to lake sediments. Abrupt boundaries between stratigraphic units are common, such as those at the Last Glacial-Interglacial Transition in deglaciated environments. Significant changes in water and organic content (higher and more variable than in marine sediments) require careful consideration when interpreting core scanning data (see Boyle et al., this volume). Detection of lighter elements is affected by the sediment water content (Tjallingii et al. 2007; Boyle et al. in Chap. 14), so downcore changes in the raw elemental counts may be caused by organic and water content variations, unrelated to sediment geochemistry. This was demonstrated by Elbert et al. (2012) in varved sediments from Lago Plomo in Argentina. Here, a decline in Si (from c. 8000 to 4–5000 counts per second

(cps)) and Ca (from c. 6500 to 5000 cps) in the top 25 cm of the core, is interpreted as an artefact of the increase in water content from c. 35 to 60%.

To counter these closed sum effects, and to avoid spurious patterns and relationships between elements, normalisation of raw data (peak area or cps) is increasingly commonplace. Weltje and Tjallingii (2008) proposed that data should be plotted as logarithmic ratios of element intensities, rather than as raw peak area cps data. Peak area element profiles are often normalised by the incoherent scatter (equivalent to Compton scattering) or total scatter (incoherent + coherent (Rayleigh) scatter) to minimise the effects of organic matter and water content (e.g., Guyard et al. 2007; Marshall et al. 2011; Kylander et al. 2011; Berntsson et al. 2014; Shala et al. 2014) or by the total counts at each depth interval (e.g., Cuven et al. 2011).

Löwemark et al. (2011) suggested normalising raw peak area data against Al to account for varying organic content, but noted that Al counts from core scanners can sometimes be too low to be effective. Nevertheless, normalisation by elements such as Al and Ti, both of which are abundant and stable, has been undertaken (e.g., Shala et al. 2014). For Al, comparatively poor detection limits require long dwell times to achieve reliable data, and in certain sediments, particularly organic-rich matrices, can be unachievable (Löwemark et al. 2011). Rubidium (Rb), being chemically similar to K, is often enriched in clay deposits. In minerogenic sediments where clay input remains relatively abundant and stable, Rb can be used as a normalising element in a similar manner to Al. Zr is more commonly abundant in some sediments and, advantageously, zirconium minerals (zircon) are resistant to weathering. However, Zr tends to be more concentrated in sand-size sediments and, therefore, is not suitable for use in normalisation, but is more useful as a proxy for variations in grain-size.

An alternative approach to removing the influence of water is by impregnating sediment blocks in resin before undertaking μXRF scanning. Although time-consuming, it is appropriate when high-resolution microfacies analysis of very finely-laminated sediments and/or varve counting are required (e.g., Van Daele et al. 2014).

An important consideration is whether quantitative data are required, which can then be compared with records from other sites. Most studies to date have presented data as peak area/counts per second or as ratios. To produce data equivalent to dry mass concentrations, calibration is required using conventional geochemical analysis of the sediments (see Boyle 2001). Boyle et al. (this volume) propose correcting for downcore variations in water content either using a regression based on a calibration dataset of elemental data from dry samples or x-ray scattering data produced during scanning. If the focus of the study is on those elements which are well detected by core scanning and the main interest is in relative changes downcore, or initial sediment characterisation, then quantification may not be necessary (Boyle et al., this volume).

Notwithstanding the issues relating to closed sum effects outlined above, the application of μXRF scanning in palaeolimnology has led to the use of a range of elements and elemental ratios for core characterisation and environmental proxies. We have identified 49 elements and ratios applied in palaeolimnological investigations, summarised in Table 7.1. The elements, ratios and associated interpretations

presented in Table 7.1 should not be taken as universally applicable, as several elements play multiple roles depending on their individual chemistry and on varying lake conditions (Kylander et al. 2011). Careful consideration is required of the climatic setting, local geology and key sediment sources, lake type and land use history. Investigation of modern catchment and lake processes (e.g., deployment of sediment traps) and elemental and mineralogical analysis of catchment material should, wherever possible, be used to ascertain the most appropriate elements and ratios to focus on and underpin the palaeoenvironmental interpretations for any given lake basin.

## *Catchment Erosion Proxies*

A key application of XRF core scanning is to identify changes in the relative amount and nature of material derived from the lake catchment. Indicators of detrital inputs include the lithogenic elements Al, Si, K, Ti, Fe, Rb and Zr, because they are geochemically stable, hosted by resistant minerals, and conservative in most geochemical environments (Boës et al. 2011). Ratios of K/Al, K/Ti and Rb/K can be used to investigate changes in weathering regimes (e.g., Brown 2011; Arnaud et al. 2012), because K, like all alkali elements, is relatively water-soluble, while Al and Rb are less mobile during mineral weathering (Clift et al. 2014). Changes in grain-size of allochthonous material found in lake sediments have been inferred from elemental ratios such as Fe/Ti (increase = smaller grain-size), Ti/K (increase = larger grain-size; Marshall et al. 2011). Higher values of Zr/Rb represent finer material because Rb adsorbs strongly to clay minerals, whereas Zr is more abundant in silts, containing heavy minerals such as zircon, but this ratio is less reliable in coarser silts and sands (Kylander et al. 2011). Al/Si may potentially be used as a proxy for grain-size, since clays are rich in Al and sands in Si (Clift et al. 2014), although issues relating to detection of lighter elements as described above need to be considered. The link between grain-size and geochemistry is catchment-specific and reconstructions should ideally be validated by either correlation with grain-size measurements on specific layers or through the analysis of sediment trap data (Schillereff et al. 2014).

The lithogenic element Titanium (Ti) is often used as a proxy for erosion and transport of silt and fine sand. It is commonly associated with silts, either as Fe–Ti-oxides or Ti-rich magnetites, occurring in Fe-rich clastic mineral particles (e.g., ilmenite, rutile, brookite, sphene). Downcore variation in Ti has arguably been the most widely used element in μXRF lake sediment studies. It is used both to produce single element profiles, but is also a valuable tool for normalisation as it is an unambiguous indicator of allochthonous inputs from the catchment (Cohen 2003). For example, the Ca/Ti ratio can be used to identify Ca derived from within-lake processes such as evaporative concentration or biogenic production, whilst Si/Ti is used as a proxy for biogenic silica productivity (Brown et al. 2007).

Ti often co-varies with Fe and magnetic susceptibility, but as Fe can be affected by redox conditions and diagenesis (Mackareth 1966; Engstrom and Wright 1984; Boyle 2001), Ti is regarded as a more reliable indicator of catchment inputs

**Table 7.1** Elements and elemental ratios from μXRF core scanning data applied in palaeolimnological studies as identified from published literature. For a number of elements and ratios, there are various interpretations based on the site-specific context

| Element or ratio | Environmental interpretation (higher values) | Example location | Example reference |
|---|---|---|---|
| Al | Flood/detrital layers | Lago Maggiore, Italy | Kämpf et al. 2012 |
| | Detrital siliclastics (Flysch Zone) | Lake Mondsee, Austria | Lauterbach et al. 2011 |
| Al/Si | Fine silt and clay layers | Lake Villarrica, Chile | Van Daele et al. 2014 |
| Br | Increased biological productivity/organic content | Lake Dalgan, Taimyr Peninsula, Siberia | Fedotov et al. 2012 |
| | Increased organic content | Shira Lake, Siberia | Kalugin et al. 2013 |
| | | Lake Teletskoye, Siberia | Kalugin et al. 2007 |
| | Sea spray/increased storminess | Isla de los Estados, Tierra del Fuego | Unkel et al. 2010 |
| ln (Br/Ti) | Increased salinity/ marine influence | Tatos Wetland, Mauritius | De Boer et al. 2014 |
| Ca | Increased calcite precipitation/evaporative concentration | Lake Malawi, eastern Africa | Scholz et al. 2007; Brown 2011 |
| | Endogenic calcite production + detrital carbonates | Chew Bahir, Ethiopia | Foerster et al. 2012 |
| | Increased primary productivity | Lake Mondsee, Austria | Lauterbach et al. 2011 |
| | Increased marine influence | East Lake, Cape Bounty, Canada | Cuven et al. 2011 |
| | Increased allochthonous lithoclastic material | Heimerdalsvatnet, Lofoten, Norway | Balascio et al. 2011 |
| | Tephra | Lago Castor/Laguna Escondida, Chile | Elbert et al. 2013 |
| | | Faroe Islands | Kylander et al. 2012 |
| Ca/Fe | Increased pedogenic input | Lago Castor/Laguna Escondida, Chile | Elbert et al. 2013 |
| Ca/Mg | Biochemical calcite precipitation | Lake Mondsee, Austria | Lauterbach et al. 2011 |
| Ca/Si | Water temperature change, either colder due to presence of calcite derived from ikaite or warmer due to association with green alga *Phacotus lenticularis* | Lake Potrok Aike, Argentina | Jouve et al. 2013 |

**Table 7.1** (continued)

| Element or ratio | Environmental interpretation (higher values) | Example location | Example reference |
|---|---|---|---|
| Ca/Ti | Increased evaporative concentration | Lake Potrok Aike, Argentina | Haberzettl et al. 2007; 2009; Jouve et al. 2013 |
| | In-lake carbonate precipitation | Les Echets | Kylander et al. 2011 |
| | Biologically mediated calcite production | Southwest Greenland | Olsen et al. 2013 |
| Ca/ΣTi, Fe, Al | Increased authigenic carbonate precipitation (drier conditions) | Lake Peten Itzá, Guatemala | Mueller et al. 2009 |
| Cu/Rb | Copper pollution from mining | Lake Bramant, French Alps | Guyard et al. 2007 |
| Fe | Clay rich layers in varved sediment | Cape Bounty, Canada | Cuven et al. 2010 |
| | Detrital inputs, redox conditions (non-stationarity) | Les Echets | Kylander et al. 2011 |
| | Fine silt, clay of volcanic origin | Lake Villarrica, Chile | Van Daele et al. 2014 |
| | Tephra | Faroe Islands | Kylander et al. 2012 |
| Fe/Mn | Reducing conditions | Lake Montcortès | Corella et al. 2012 |
| | | East Lake, Cape Bounty, Canada | Cuven et al. 2011 |
| | | Lake Potrok Aike | Haberzettl et al. 2007 |
| Fe/Si | Fine silt and clay, volcanic origin | Lake Villarrica, Chile | Van Daele et al. 2014 |
| Fe/Ti | Reducing conditions | Lake Prespa, Balkan Peninsula | Aufgebauer et al. 2012 |
| | Reduction in grain-size | Lake Tana | Marshall et al. 2011 |
| K | Increased detrital input | Lake Prespa, Balkan Peninsula | Aufgebauer et al. 2012 |
| | Increased detrital input | Lago Enol | Moreno et al. 2011 |
| | Flood layers | Lago Maggiore | Kämpf et al. 2012 |
| | Drier conditions (physical > chemical weathering) | Chew Bahir, Ethiopia | Foerster et al. 2012 |
| | Clay rich layers in varved sediments | Cape Bounty, Canada | Cuven et al. 2010 |
| | Fine-grained detrital inputs | Les Echets, France | Kylander et al. 2011 |
| | Tephra | Lake Ohrid, Balkans | Vogel et al. 2010 |
| | Tephra | Faroe Islands | Kylander et al. 2012 |

**Table 7.1** (continued)

| Element or ratio | Environmental interpretation (higher values) | Example location | Example reference |
|---|---|---|---|
| K/Al | Illite/kaolinite ratio (physical > chemical weathering) | Lake Tanganyika, eastern Africa | Burnett et al. 2011 |
| K/Ti | Increased physical relative to chemical weathering | Lake Bourget, France | Arnaud et al. 2012 |
| | Identification of upper varve boundary | Cape Bounty, Canada | Cuven et al. 2010 |
| Mg | Detrital dolomite | Lake Mondsee | Lauterbach et al. 2011 |
| Mg/Ca | Authigenic carbonate precipitation | Zoñar Lake, Spain | Martin-Puertas et al. 2011 |
| Mn | Detrital inputs | Lake Taravilla, Spain | Moreno et al. 2008 |
| | Mn-enriched siderite layers | Lake Suigetsu | Marshall et al. 2012 |
| | Oxygenation of bottom waters (lower lake level) | Les Echets, France | Kylander et al. 2011 |
| | Tephra | Faroe Islands | Kylander et al. 2012 |
| Mn/Fe | Oxygenation of water column | El-gygytgyn, Siberia | Melles et al. 2012 |
| | Oxic conditions | Albion Ponds, Jamaica | Burn and Palmer 2014 |
| | | Lago Galvarne Bog, Tierra del Fuego | Unkel et al. 2008 |
| Mn/Ti | Oxygenation of water column | Lake Chungara, Chile | Moreno et al. 2007 |
| | | Les Echets, France | Kylander et al. 2011 |
| Nb/Ti | Erosion of carbonate-rich magma intrusion | Lake Loitsana, Finland | Shala et al. 2014 |
| P | Nutrient enrichment | Lake Montcortès, Spain | Corella et al. 2012 |
| Pb | Pollution from mining | Lake Bramant, France | Guyard et al. 2007 |
| | | Lake Windermere, UK | Miller et al. 2014 |
| Rb | Detrital inputs | Shira Lake, Siberia | Kalugin et al. 2013 |
| | Fine-grained detrital inputs | Les Echets, France | Kylander et al. 2011 |
| | Tephra | Lake Bramant, France | Guyard et al. 2007 |
| | | Lake Prespa, Balkans | Damaschke et al. 2013 |
| Rb/K | Increased chemical weathering | Lake Malawi, eastern Africa | Brown 2011 |
| | | Lake Tanganyika, eastern Africa | Burnett et al. 2011 |
| Rb/Sr<br>log (Rb/Sr) | Increased chemical weathering | Laguna Cascada, Isla de los Estados, Tierra del Fuego | Unkel et al. 2010 |
| | | | Fernandez et al. 2013 |

**Table 7.1** (continued)

| Element or ratio | Environmental interpretation (higher values) | Example location | Example reference |
|---|---|---|---|
| S | Increased marine influence | Heimerdalsvatnet, Lofoten, Norway | Balascio et al. 2011 |
| | Gypsum precipitation (evaporative concentration) | Albion Ponds, Jamaica | Burn and Palmer 2014 |
| | Soil derived S from leaching | Lake Tanganyika, eastern Africa | Burnett et al. 2011 |
| | | Lake Petén Itzá, Guatemala | Hodell et al. 2012 |
| | | Southwest Greenland | Olsen et al. 2013 |
| S/Ti | Presence of pyrite, increased organic matter | Lake Chungara, Chile | Moreno et al. 2007 |
| Si | Coarse silt and sand | Cape Bounty, Canada | Cuven et al. 2010 |
| | Flood layers | Lago Maggiore, Italy | Kämpf et al. 2012 |
| | Increased detrital inputs | Zoñar Lake, Spain | Martin-Puertas et al. 2011 |
| | Increased detrital inputs | Lake Tana | Marshall et al. 2011 |
| | Increased clay and quartz content | Lago Enol, Spain | Moreno et al. 2011 |
| Si/Ti | Increased biogenic silica (principally diatoms) | Lake Malawi, eastern Africa | Brown et al. 2007; Brown 2011 |
| | | Lake Tanganyika, eastern Africa | Burnett et al. 2011 |
| | | Heimerdalsvatnet, Lofoten, Norway | Balascio et al. 2011 |
| | | Les Echets, France | Kylander et al. 2011 |
| | | Meerfelder Maar | Martin-Puertas et al. 2012 |
| | | El'gygytgyn, Siberia | Melles et al. 2012 |
| | | Laguna de Los Anteojos, Venezuela | Stansell et al. 2010 |
| | Grain-size (sand) | Lake Loitsana, Finland | Shala et al. 2014 |
| Si/Zr | High biogenic silica content relative to detrital material | East Lake, Cape Bounty, Canada | Cuven et al. 2011 |
| Sr | In-lake $SrCO_3$ precipitation | Albion Ponds, Jamaica | Burn and Palmer 2014 |
| | Erosion of granodiorite | Laguna Queshquecocha | Stansell et al. 2013 |
| | Tephra | Lake Ohrid, Balkans | Vogel et al. 2010 |
| Sr/Ca | Authigenic carbonate precipitation | Zoñar Lake, Spain | Martin-Puertas et al. 2011 |

**Table 7.1** (continued)

| Element or ratio | Environmental interpretation (higher values) | Example location | Example reference |
|---|---|---|---|
| Sr/Rb | Unweathered terrestrial fraction | Taimyr Peninsula, Siberia | Fedotov et al. 2012 |
| | | Teletskoye Lake, Siberia | Kalugin et al. 2007 |
| Sr/Ti | In-lake $SrCO_3$ precipitation | Les Echets, France | Kylander et al. 2011 |
| | In-lake $SrCO_3$ precipitation | Lake Chungara, Chile | Moreno et al. 2007 |
| | Silt influx | Lake Loitsana, Finland | Shala et al. 2014 |
| Th | Leaching of Th from soil during thawing of permafrost | Taimyr Peninsula, Siberia | Fedotov et al. 2012 |
| Ti | Increased run-off/ rainfall | Laguna de Juanacatlan, Mexico | Metcalfe et al. 2010 |
| | Increased run-off/ rainfall | Lake Montcortès, Spain | Corella et al. 2012 |
| | Increased detrital input | Heimerdalsvatnet, Lofoten, Norway | Balascio et al. 2011 |
| | Detrital input (glacier advance) | Laguna Lutacocha, Peru | Stansell et al. 2013 |
| | Fine grained detrital input | Meerfelder Maar, Germany | Martin-Puertas et al. 2012 |
| | Increased inwash of silt | Les Echets, France | Kylander et al. 2011 |
| | Identification of flood layers | Lake Vuoksjávrátje, Sweden | Berntsson et al. 2014 |
| | Increased glacial meltwater | Lake Ammersee, Switzerland | Czymzik et al. 2013 |
| | Increased aeolian deposition | Lake Kråkenes, Norway | Bakke et al. 2009 |
| | Silt-rich facies | Huguang Maar, China | Yancheva et al. 2007 |
| | Clay-rich sediment | Cape Bounty, Canada | Cuven et al. 2010 |
| | Tephra | Faroe Islands | Kylander et al. 2012 |
| Ti/Ca | Increased detrital input | Lake Van, Turkey | Litt et al. 2009 |
| Ti/K | Increased grain-size | Lake Tana | Marshall et al. 2011 |
| Zr | Coarse silt and sand | Cape Bounty, Canada | Cuven et al. 2010 |
| | Detrital inputs | Lake Tana | Marshall et al. 2011 |
| | Tephra | Lake Ohrid, Balkans | Vogel et al. 2010 |
| | Erosion of metasediments | Laguna Queshquecocha | Stansell et al. 2013 |
| Zr/Fe | Flood layers/grain-size | Lake Blanc, France | Wilhelm et al. 2013 |
| Zr/K | Coarser grain-size | East Lake, Cape Bounty, Canada | Cuven et al. 2011 |

**Table 7.1** (continued)

| Element or ratio | Environmental interpretation (higher values) | Example location | Example reference |
|---|---|---|---|
| Zr/Rb | Coarser grain-size | Lake Kumphawapi, Thailand | Chawchai et al. 2013 |
| | | Les Echets, France | Kylander et al. 2011 |
| Zr/Ti | Weathered volcanic ash (catchment inwash) | Lake Malawi, eastern Africa | Brown et al. 2007 |
| | Silt influx | Lake Loitsana, Finland | Shala et al. 2014 |
| Inc/Coh | Higher values = increased organic content | Lake Bramant, French Alps | Guyard et al. 2007 |
| | | Lake Tanganyika, eastern Africa | Burnett et al. 2011 |
| | | Lake Potrok Aike, Argentina | Jouve et al. 2013 |

(e.g., Metcalfe et al. 2010). There are two main environmental interpretations of Ti which represent contrasting inferences about climate change. Higher Ti values could result from catchment run-off, indicating wetter conditions (e.g., Haberzettl et al. 2005, 2007; Metcalfe et al. 2010), but in some settings it may also indicate enhanced aeolian deposition (e.g., Yancheva et al. 2007; Kienel et al. 2009). Where catchment characteristics have been dramatically altered through time by climate change, it is possible that the major transport mechanism for Ti has changed. This is a particular issue with longer records, such as those spanning glacial-interglacial cycles and in arid areas, where lakes more readily dry out. Establishing covariance across multiple elements and supporting evidence via multiple proxies can help to establish whether the hydrological regime has sufficiently altered to affect the nature of the Ti record. Other factors influencing Ti flux include agricultural activities in the catchment and short-lived peaks in Ti may be related to tephra deposition. The problem of equifinality is by no means confined to interpretation of Ti profiles, but illustrates the importance of a detailed understanding of local catchment processes affecting the lake, regional climatic context and supporting evidence from other proxies. The use of correlation matrices for individual stratigraphic units (e.g., Kylander et al. 2011) can help to identify downcore changes in proxy relationships.

Foerster et al. (2012) highlight the need to understand the local basin context in their investigation of a c. 45 ka record from Chew Bahir, Ethiopia. Of the six elements (K, Fe, Si, Ti, Ca, Sr) that demonstrate a clear palaeoenvironmental signal (Fig. 7.1), they argue that K is the most reliable indicator of moisture fluctuations. During arid phases with relatively low vegetation cover, K-rich gneisses in alluvial fans on the western slopes of the basin would be readily eroded in a more irregular but intense rainfall regime. When the terrain is stabilised by more extensive vegetation cover, K would be preferentially leached away through chemical weathering, resulting in lower K values. K values are lowest during the interval corresponding to the 'African Humid Period' (~15–5 cal ka BP) punctuated by higher K values representing drought conditions during the Younger Dryas chronozone (Foerster et al. 2012).

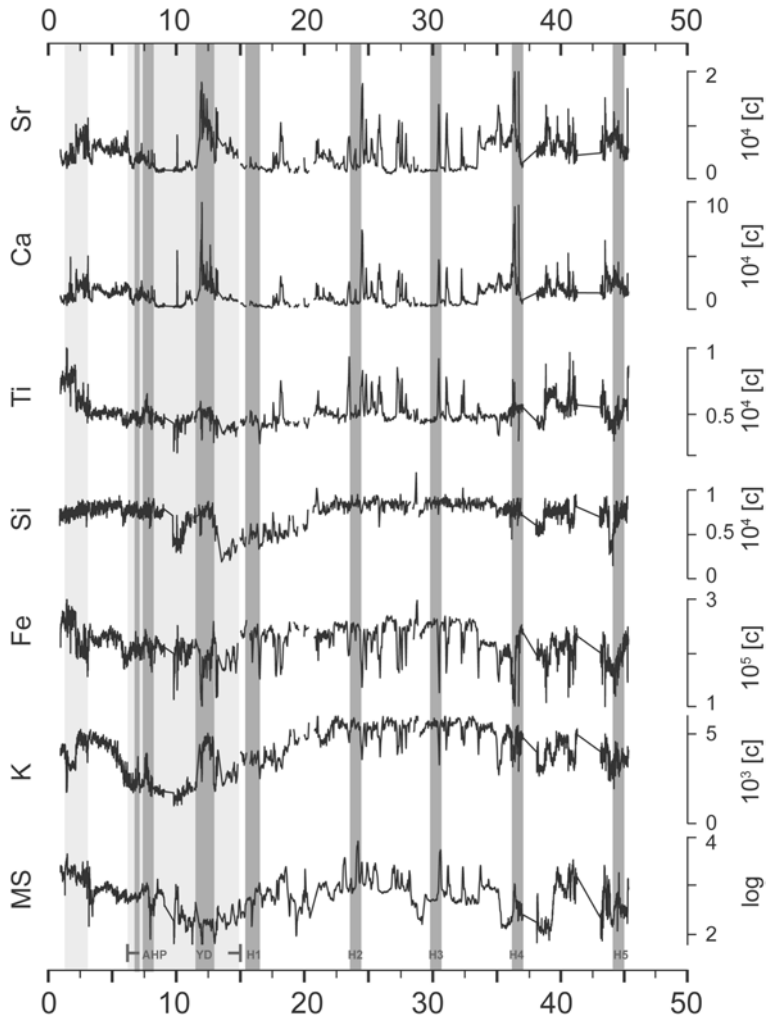


**Fig. 7.1** µXRF data (in counts per second) from Chew Bahir, Ethiopia against time (cal ka BP). The *light grey shading* represents the African Humid Period (AHP), interrupted by the Younger Dryas (*dark grey shading*). (Reprinted from Quaternary International 274, Foerster et al. (2012), with permission from Elsevier.)

## *Proxies for In-Lake Processes*

Within-lake responses to climatic and environmental change can also be identified using XRF scanning. During drier climatic episodes, lake levels decline, leading to the deposition of evaporative minerals. Eugster and Hardie (1978) described multiple pathways of brine evolution of lake waters which are dependent on the initial composition of fresh water, related to the underlying geology. Common evaporative minerals are $CaCO_3$ (calcium carbonate) and $CaSO_4$ (gypsum). XRF profiles of Ca (e.g., Scholz

et al. 2007; Mueller et al. 2009; Brown 2011) and S (Hodell et al. 2012) have been used to identify deposition of these minerals in lake sediment records (Table 7.1).

Iron (Fe) and manganese (Mn) profiles can provide information about changing redox conditions (Davison 1993). If lake waters are well-mixed, the water column remains oxygenated at depth. Anaerobic conditions at the sediment-water interface generally occur when lake waters are thermally and chemically stratified. Deeper lakes may remain stratified for extended periods, but generally, overturning of lake waters occurs on a seasonal/annual basis. Redox conditions can be affected by a range of factors, including changes in water depth, biological productivity, rapid sediment deposition as well as climatic drivers such as temperature, rainfall and wind regime. In a reducing environment, the solubility of Fe and Mn increases, but Mn is more readily affected (Boyle 2001), so an increase in Fe/Mn ratios can indicate the onset of anaerobic conditions. A shift to higher Fe/Mn may therefore point to a lowering of bottom-water oxygen content during enhanced stratification, or to de-oxygenation from organic decay following enhanced biological productivity linked to changing nutrient input. For example, at Lake Potrok Aike in Patagonia, low Fe/Mn ratios are interpreted to indicate increased lake mixing, either as a result of lower lake levels or increased wind speed (Haberzettl et al. 2007). At Lake Montcortes in northeast Spain, changes in aquatic productivity resulting from agricultural run-off is inferred from variations in Fe/Mn (Corella et al. 2012). As both Mn and Fe can also be derived from the surrounding catchment, normalising to Ti can help to establish the importance of redox processes relative to catchment inputs (e.g., Moreno et al. 2007; Kylander et al. 2011).

## Sediment Characterisation

Along with traditional methods of identifying key components of lake sediments and other scanning methods, such as multi-sensor core logging (which generates magnetic susceptibility, gamma-density and p-wave velocity data), μXRF scanning is particularly valuable for rapid identification and correlation of stratigraphic units within a single basin. Simple statistical analysis can reveal which elements are consistently present and constantly contribute to >95% or >99% of total elemental counts. Usually, a combination of elevated values of 'measureable' lithogenic elements (e.g., Al, Si, K, Ti, Fe, Rb, Zr) can be used to characterise clastic sediments, although Fe can be influenced by redox processes and Si can reflect biogenic deposition (Brown, this volume). The presence of Ca and Sr is commonly associated with authigenic carbonate minerals or biogenic calcium carbonates in arid and limestone/carbonate environments, but can be covariant with lithogenic elements in volcanic and/or glacial environments when derived from catchment inwash, aeolian activity, and/or soil development in the catchment (Sr). The use of ratios can help to clarify the key processes governing downcore variations. For example, Mueller et al. (2009) used the ratio of Ca/Σ (Al, Ti, Fe) to help identify a period of enhanced authigenic carbonate deposition in sediments from Lake Peten Itza, Guatemala between 4.5 and 3.5 cal ka BP. However, it is important to ascertain that as far as possible that the factors controlling observed geochemical changes remain consistent.

μXRF scanning can be used to make inferences about the biological component of lake sediments. Si/Ti has been used to estimate biogenic silica (Brown et al. 2007; Brown, this volume; Stansell et al. 2010), where high values represent enhanced productivity. Biogenic silica usually represents diatom productivity as the silica frustule of the algae is preserved in lake sediments, however there may also be contributions from chrysophytes and sponges. A potential allochthonous source of biogenic silica comes from grass phytoliths, which may be significant in some nearshore contexts. Ca values may also reflect biogenic calcium carbonate productivity, although this may be difficult to distinguish from calcite precipitation resulting from evaporative concentration without more detailed examination of the sediment.

XRF scanning data has also been used as a proxy for organic content of lake sediments. One of the most commonly used parameters is the incoherent/coherent (inc./coh.) scattering ratio (e.g., Guyard et al. 2007; Brown et al. 2007; Burnett et al. 2011). This ratio is an approximation of the atomic number of the average matrix composition. In wet sediments, most of the scatter is produced by X-ray interactions with elemental carbon and water (inc) and water (coh), whose elements (H, C, O) are not detectable by XRF. Since organic carbon has a lower average atomic number than silica, carbonates or any clastic material, increased organic content can be inferred qualitatively from higher inc/coh ratios (e.g., Burnett et al. 2011). This x-ray back scattering data (coh./inc. ratio) can also be used to account fluctuations in water content. Boyle et al., this volume demonstrate that the coh./inc. ratio can be used to convert wet concentration data to a dry mass basis, the method being particularly suited to cores with large variations in water content.

Moreno et al. (2007) suggested that S/Ti ratios may be a useful proxy for organic matter in Lake Chunagara, Chile, where higher S/Ti values corresponded to increased Total Organic Carbon (TOC). They proposed that this is due to increased pyrite formation in organic sediments, but caution that microscopic examination of sediments is also required, due to some very low values of S (Moreno et al. 2007). Bromine (Br) has also been proposed as a potential tool for identifying relative changes in organic content in lake sediments e.g., Kalugin et al. 2007) as Br forms strong covalent bonds with organic molecules (Gilfedder et al. 2011). In their study of an 800 year annually laminated record from Lake Teletskoye Lake, Siberia Kalugin et al. (2007) found that Br measured by μXRF core scanning covaries with % TOC measurements. Analysis of the Br flux in Lake Constance, where Br was found to be permanently removed to the lake sediment, supports the use of Br as a proxy for past biological productivity (Gilfedder et al. 2011). It has also been suggested that excess Br in cores from sites exposed to maritime influences, may also be the result of enhanced storminess (Unkel et al. 2010; Turner et al. 2014). In a recent Holocene record from Mauritius, De Boer et al. (2014) use increased (ln) Br/Ti ratios to infer infiltration of saline groundwater into a low-lying coastal wetland. As with other elements, there are a range of potential interpretations depending on local site characteristics. Further investigation of Br as a reliable proxy is needed and any potential geological sources should also be considered.

After determining which elements are present and most abundant (and useful), another important first step for lacustrine μXRF scanning studies is to establish

which elements are covariant, and which relate closely to scattering parameters. Simple correlation coefficient analysis can rapidly highlight which elements are most readily aligned with lithogenic elements (e.g., Al, Ti, Fe, Rb, Zr) or more likely to be closely aligned to organic variability (as measured by incoherent and coherent scatter and/or %LOI, %TOC subsample data). Multivariate approaches have been used to reveal associations between elements and deviations that can be environmentally significant (e.g., PCA; Balascio et al. 2011; Shala et al. 2014). Whichever statistical method used, it is important to be aware that that covariance can change between units, be related to sampling interval, and some elements, commonly Fe and Mn can change according to a combination of these factors.

## Applications of µXRF Scanning

### *Flood Histories*

A significant development in µXRF scanning has been the identification of flood layers and the reconstruction of flood histories (e.g., Moreno et al. 2008; Czymzik et al. 2013; Schillereff et al. 2014, this volume). This approach is complementary to that applied to fluvial sedimentary sequences (e.g., Jones et al. 2010; Turner et al., this volume). For example, in their study of two varved cores covering the last c. 5500 years from the pre-Alpine Lake Amersee, Czymzik et al. (2013) identified 1573 detrital layers in either one or both sequences using Ti data and layer thickness. Three principal depositional units were identified: from 5500 to 2800 varve years BP; from 2800 to 400 varve years BP and from 400 varve years BP to present. Between 2800 and 400 varve years BP, detrital layers were thicker and deposited more regularly. A further increase in flood intensity was observed during the last 400 years. Comparison with the record of human occupation of the basin does not indicate a strong link between human activity and flood intensity, a conclusion supported by other studies of pre-Alpine lakes (e.g., Arnauld et al. 2012). Czymzik et al. (2013) argue that the observed changes in flood intensity can be explained by a combination of reduced influence of orbital forcing in the late Holocene combined with solar activity minima.

Moreno et al. (2008) constructed a 2000 year flood chronology from Lake Taravilla in the central Iberian range of northeastern Spain using a combination of physical sediment properties and XRF data. Principal component analysis of the XRF data revealed that Axis 1 is linked to carbonate inputs (Ca), whilst Axis 2 is related to siliclastic deposition (Si, K, Ti, Fe, Mn). Centimetre to decimetre scale terrigenous layers were characterised by coincident peaks in carbonate and siliclastic indicators, particle fining upwards within a layer, and by relatively high organic content, particularly at the base of the sequences. Similar to Czymzik et al. (2013) findings, increased flood activity occurred during the last few hundred years. Comparison with pollen records revealed no evidence of anthropogenic influence and again centennial scale reduction in solar activity is postulated as a key driver of

flooding. Moreno et al. (2008) also argue that the North Atlantic Oscillation plays a role in influencing decadal scale variability in flooding.

In their comprehensive review of palaeoflood records from lake sediments, Schillereff et al. (2014) highlight the types of lake most suited for preserving an archive of historical floods. They stress the need for a detailed knowledge of the local geology, catchment characteristics (e.g., basin morphology) and in-lake processes (e.g., stratification), which may affect the nature of sediment transport and deposition. The framework provided by Schillereff et al. (2014) for this process-based approach is a valuable tool for this growing area of palaeolimnological research.

## *Identifying the Location of Tephra Layers*

There has been considerable interest in the potential of XRF scanning to assist in the location of tephra layers in sediment cores, including those which may not be easily found on visual inspection. For example, Vogel et al. (2010) examined the tephrostratigraphy of Lake Ohrid, on the Albania-Macedonia border, during the last glacial-interglacial cycle, using a combination of XRF scanning, magnetic susceptibility logging and visual inspection. Peaks in K, Zr and Sr relating to four visible tephras were used to help locate a further six tephra layers. Similarly, Damaschke et al. (2013) identified 11 tephra layers (including five 'cryptotephras') from nearby Lake Prespa in a record spanning at least the last c. 60,000 years, using in this case K, Rb and Sr. Moreno et al. (2007) found that peaks in Al, K, Ti and Fe were associated with tephra layers, along elements such as Zr, Sr, Sn and Ba. Tephras are not always easily distinguishable with XRF-scanning data. In their record from Laguna Cascada on Tierra del Fuego, Unkel et al. (2010) described two tephras in the core stratigraphy. One, at c. 8.5 cal ka BP, linked to Mt Hudson, is clearly marked by peaks in Ca, K, Ti, Zr and Sr, whilst the other at c. 4.5 cal ka BP, thought to originate from Mt Burney, visible in the sediments, does not exhibit a distinct geochemical signal. Wastegård et al. (2013) noted in a sequence from Potrok Aike, Patagonia, that tephra layers were often associated with a peak in K and a trough in Ti.

Kylander et al. (2012) examined the potential of XRF-scanning in tephrochronology. In their analysis of three sediment cores from the Faroe Islands, rhyolitic tephras in low shard concentrations ($<850/cm^3$) were not identified by μXRF scanning, whilst basaltic tephras present at more than 1000 shards per $cm^3$ were highlighted by peaks in Ti, Fe and Ca. Location of cryptotephras depends on whether sufficient shards are located near the core surface and can be detected. Kylander et al. (2012) concluded that whereas μXRF scanning can assist in highlighting areas for further detailed investigation and also in the identification of possible reworking, the elemental data cannot be a substitute for systematic microscopic examination and quantitative analysis of major and trace element geochemistry using conventional methods. In this volume, Balascio et al. take an experimental approach to characterising the signal from tephra layers. They also found that basaltic tephras had a distinctive geochemistry, different from the background matrix. It would be useful

to extend this type of study further by using tephras with a range of geochemical signatures set in a matrix of various sediment types.

## *Varved Sequences*

Given the high sampling resolution of µXRF scanning, it is particularly suitable for the examination of finely laminated sediments and varved sequences (e.g., Neugebauer et al. 2012; Schlolaut et al. 2014). µXRF scanning data can help to identify clay and tephra layers that are geochemically distinct from the regular varves (Francus et al. 2009). At Meerfelder Maar in Germany, varves are characterised by couplets of two main components: a spring/summer layer consisting almost entirely of biogenic silica from diatom blooms and an autumn/winter layer of minerogenic, detrital material (Martin-Puertas et al. 2012). Here, a seasonally resolved record was produced from µXRF data, with high Si/Ti values representing increased diatom productivity and Ti reflecting detrital inputs. Increased Si/Ti values between 2 and 5 cal ka BP were interpreted to reflect enhanced water circulation from increased wind stress. Martin-Puertas et al. (2012) note that Ti, when compared with a pollen-based precipitation reconstruction, did not exhibit a clear relationship with precipitation after 5 cal ka BP. This is attributed to changes in lake morphology as a result of rising lake levels. A reduction in the amount of detrital material reaching the deeper parts of the basin due to greater distance from the inflow would have led to sediment being trapped in the delta. This example highlights the importance of considering non-stationarity of processes in the local catchment as an explanation for observed variations in elemental data.

Van Daele et al. (2014) distinguished four different 'event' deposits (lacustrine turbidites, tephra-fall layers, 'runoff cryptotephras', and lahar deposits) in cores taken from Lago Villarrica and Lago Calafquén in the volcanically and seismically active Chilean Lake District. This multi-proxy investigation was underpinned by an ultra-high-resolution record of volcanic activity determined by XRF scanning of resin-embedded sediment blocks. Si, Al and Fe ratios were used to distinguish between the three sedimentary components: diatom frustules (high Si), terrestrial clays (Al enriched), and mafic volcanic ash (elevated Fe) (Fig. 7.2). The c. 600-yr-old eruption history for the Villarrica Volcano contained in varved lake-sediment sequences from Lago Villarrica demonstrates that the Villarrica volcano has had, on average, a 22 year dormancy period for eruptions with a Volcanic Explosivity Index (VEI) >2. Although Villarrica is constantly active, and a relatively minor Strombolian eruption started in on 3rd March 2015, the last VEI>2 eruption from Villarrica was in 1991, 24 years ago.

Cuven et al. (2010) examined clastic varved sequences from two high Arctic lakes to determine their composition and investigate links between grain-size and chemical characteristics. They found distinct geochemical signatures associated with different grain-sizes. Coarse layers dominated by sand were found to have high values of Si and Zr, Ti was characteristic of silt layers and clay layers were associated with Fe and K. Varve composition was split into four principal lithozones

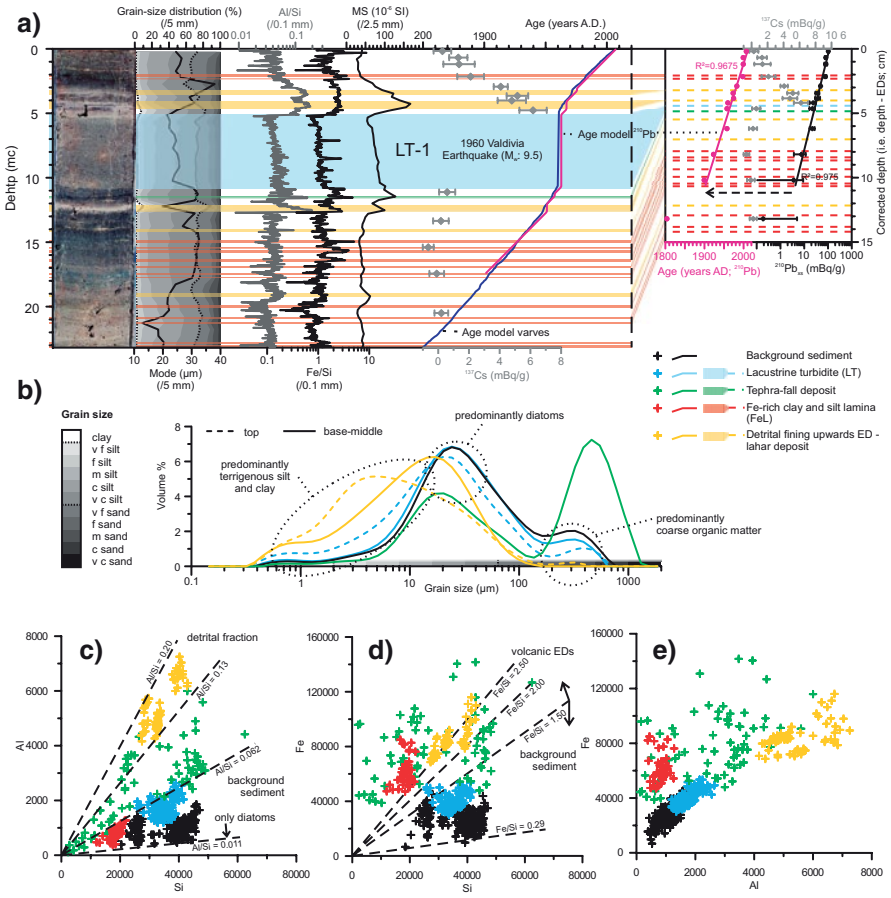


**Fig. 7.2** **a** Core CAGC02bis from Lake Calafquén with grain-size distribution and $^{137}$Cs (*grey diamonds*), $^{210}$Pb (*pink line*) and varve (*dark blue line*) age-depth models for the last 150 years distribution, µXRF ratios, and magnetic susceptibility (MS). The four different types of event deposits are shown by coloured symbols; **b** Grain-size distribution of background sediment (*black*), tephra-fall deposits (*green*), and both base/middle (*solid*) and top (*dashed*) of detrital fining -upward event deposits (*yellow*) and lacustrine turbidites (*blue*); **c–e** Micro-XRF elemental counts in core CAGC02bis of Al versus Si (**c**), Fe versus Si (**d**), and Fe versus Al (**e**). *Dashed lines* represent elemental ratios differentiating between background sediment and event deposits. (Adapted from van Daale et al. (2014))

reflecting different depositional processes. For example, the silt layer grading into clay (Lithozone A) was interpreted to derive from spring snowmelt, whilst the coarser sediments of Lithozones B and C were indicative of higher intensity run-off episodes (Cuven et al. 2010). It was also found that K/Ti was a reliable indicator of the upper boundary of varves. The two examples here highlight the role µXRF scanning can play in identifying links between elemental data, grain-size and depositional processes. In non-varved sequences, understanding these relationships can be more challenging.

A major contribution of µXRF scanning to the development of sediment chronologies came through the Lake Suigetsu 2006 Varved Sediments Project (Marshall et al. 2012; Nakagawa et al. 2012; Bronk-Ramsey et al. 2012). Laminated sediments of sub-annual resolution at Lake Suigetsu, Japan, extend back c. 70,000 years. In addition to seasonal layers represented by a spring diatom bloom, an organic summer layer, a siderite-rich autumn layer and a clastic winter layer, the sediments also contain well-preserved leaf macrofossils throughout. The Suigetsu sequence therefore presented an unparalleled opportunity to extend and refine the radiocarbon calibration curve. A key element of the study was accurate varve counting, which was undertaken using two independent methods: µXRF scanning (Marshall et al. 2012) and microscopic varve counting (Schlolaut et al. 2012). Specially-developed and freely-available, software, Peakcounter (http://dendro.naruto-u.ac.jp/~nakagawa/), was used to count varves from multiple element data generated by µXRF scanning. Mn, Fe and Ti were the key indicators used to identify layer boundaries along with greyscale values obtained from X-radiography using an Itrax core scanner (Fig. 7.3). Repeat analyses at different x-ray tube power settings and count times demonstrated that settings of 30 mA and 30 kV, with a relatively short count time of 4 s, produced an appropriate signal to noise ratio for the elements of interest without compromising the quality required for varve identification.

Figure 7.3 illustrates how quality-classified counts were produced, with Qlt-1 assigned to the clearest signals in multiple indicators through to Qlt-4, assigned to low and indistinct peaks, such as those produced by poorly preserved and indistinct siderite layers (Marshall et al. 2012). For each step, errors were identified and quantified. The µXRF data compared well with the counts derived from microscope analysis and the two methods were combined to produce a single, robust chronology. This sequence formed the cornerstone of a new terrestrial radiocarbon calibration curve from 11.2–52.8 cal ka BP, which for the first time allows atmospheric calibration of radiocarbon dates into the last glacial period and to the limits of the dating method (Bronk Ramsey et al. 2012), representing a major development in Quaternary science.

## Climate Variability Inferred from µXRF Scanning of Lake Sediments

In this section, we discuss the principal use of µXRF scanning to investigate past climate change. We examine records covering a range of timescales, from long records extending into the last glaciation and beyond, those which focus on the identification of rapid and abrupt changes and those which record high resolution variability over interannual timescales. The palaeoclimatic interpretation from geochemical profiles in lake sediments depends on the interplay between lake and catchment characteristics and the climatic regime and therefore may vary between sites and over time.

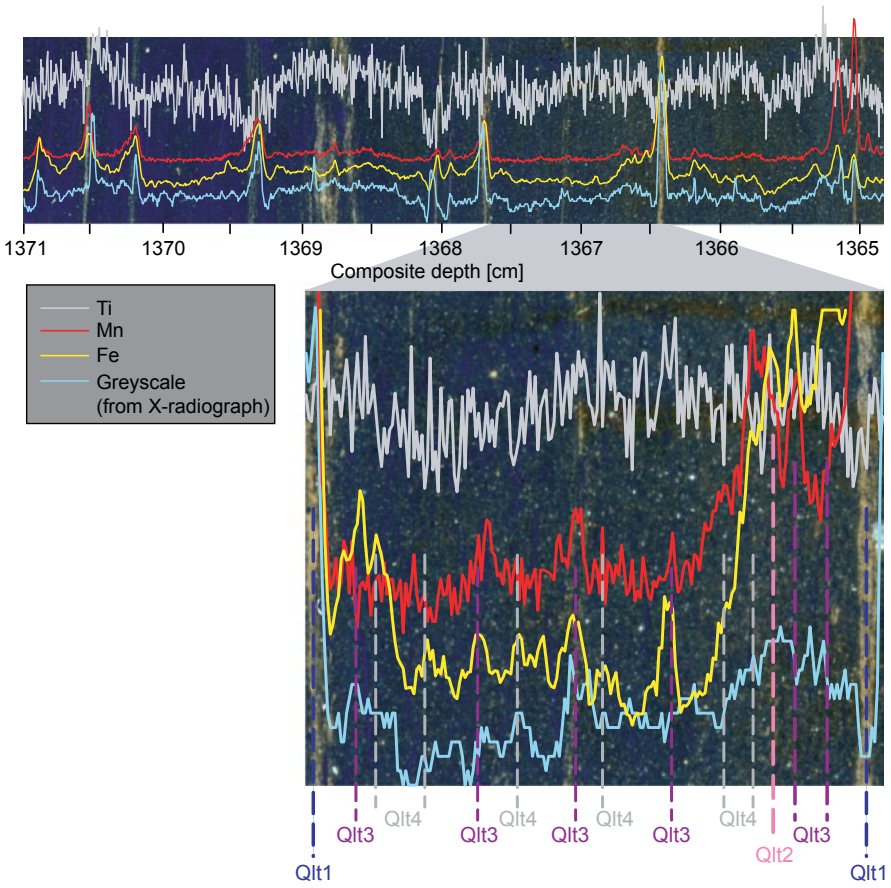


**Fig. 7.3** Thin section photograph overlain with µXRF indicator elements and X-radiograph greyscale data from core BN-07, Lake Suigetsu. The enlarged sub-section demonstrates how quality counts (Qlt to 4) were derived. (Reprinted from Marshall et al. (2012), with permission from Elsevier)

## *Long Records of Climate Change*

Some of the first published µXRF scanning data from lake sediments were obtained from Lake Malawi in eastern Africa (Brown et al. 2007; Scholz et al. 2007) and Laguna Potrok Aike in Patagonia (Haberzettl et al. 2005, 2007, 2009). Both projects were supported by the Global Lakes Drilling Program and the International Continental Scientific Drilling Program, with the aim of producing long palaeoclimatic sequences extending back through the last glacial cycle. Since these studies, µXRF scanning has been incorporated into the standard set of analyses for ICDP projects such as Lake Van in Turkey (Litt et al. 2009), Lake Ohrid in the Balkans (Vogel et al. 2010) and El'gygytgyn in Siberia (Melles et al. 2012).

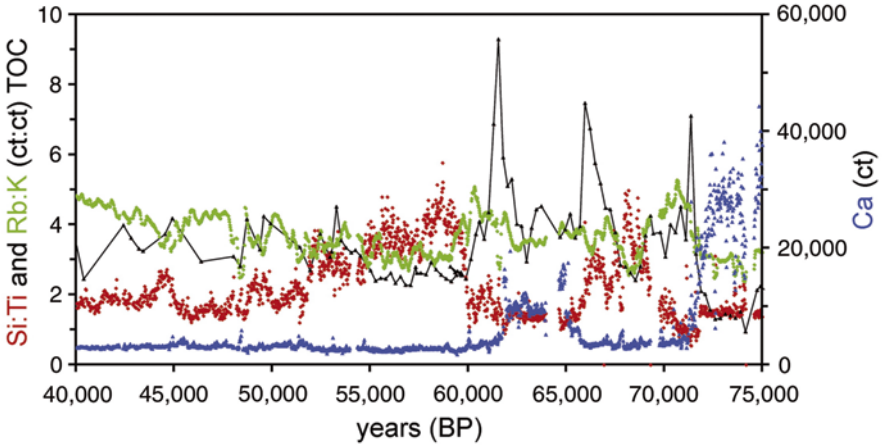


**Fig. 7.4** Profiles of Si/Ti (biogenic silica), Rb/K (chemical weathering), Ca (calcite precipitation) and % TOC for Lake Malawi from 40 to 75 ka BP. (Reprinted from Brown (2011), with permission from Elsevier)

The sediments of Lake Malawi are arguably the most comprehensively studied in Africa (see Scholz et al. 2011). Cores obtained by the Lake Malawi Scientific Drilling Project in 2005 have provided important insights into tropical climate dynamics during the last glacial-interglacial cycle. Scholz et al. (2007) identified evidence of a dramatic change in the hydrological regime of Lake Malawi c. 75,000 years ago. Between 135 and 75 ka BP, the lake was characterised by major fluctuations in lake level indicated by the downcore Ca profile. Higher values of Ca suggest generally drier conditions, with several major excursions indicative of a series of 'megadroughts.' This interpretation was supported by seismic profiles revealing evidence of unconformities and more recent μXRF data from Lake Tanganyika (Burnett et al. 2011). After c. 70 ka BP, Ca values were greatly reduced indicating more humid conditions. It was suggested that climate may have played a role in the dispersal of modern humans after 70 ka BP, with wetter conditions creating a more favourable environment for migration (Scholz et al. 2007). Detailed investigation of the megadroughts, using μXRF scanning data, suggests that a complex pattern of process is recorded in the μXRF data (Fig. 7.4; Brown 2011).

The termination of droughts at 72 and 62 ka BP was characterised by increased inwash of organic matter (%TOC), quickly followed by the deposition of chemically weathered material (Rb/K) which had been stored on the catchment slopes during the arid phase. Subsequent exposure of fresh material led to an increase in weathering of bioavailable silica which stimulated periods of enhanced diatom productivity when washed into the lake (Brown 2011). More recently, Lane et al. (2013) examined Malawi sediments to determine whether the eruption of Mount Toba, Sumatra c. 75,000 years ago, had an impact on climate in eastern Africa. A tephra layer in the sediments at 28.08–28.10 m below lake floor was identified as

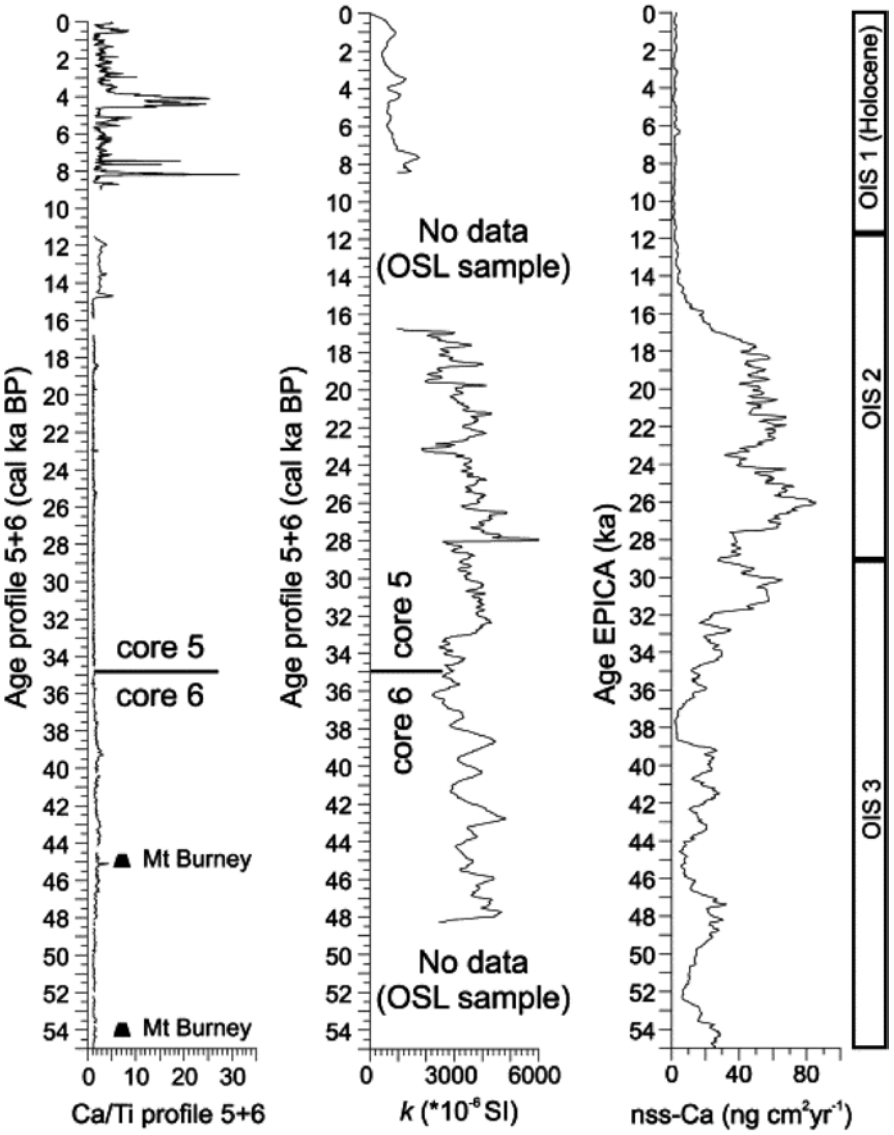


**Fig. 7.5** The Ca/Ti record from a 55 ka sequence at Potrok Aike, Argentina, compared with magnetic susceptibility (*k*) smoothed with an 11 point moving average and non sea salt calcium (nss-Ca) flux from Dome C. Cores 5 and 6 are correlated using the older Réclus tephra layer. (Reprinted from Haberzettl et al. (2009), with permission from Elsevier)

the Younger Toba Tuff (YTT) using electron microprobe analysis. μXRF scanning data (Si/Ti; inc/coh; Zr/Ti) showed no major change in the sediments immediately above the tephra layer. Lane et al. (2013) concluded that the eruption of the YTT did

not have a significant climatic impact in eastern Africa and therefore could not be the cause of a genetic bottleneck in human populations at that time.

At Laguna Potrok Aike, Ca/Ti is interpreted as a proxy for lake level fluctuations during the last c. 55 ka BP (Haberzettl et al. 2009). The Ca/Ti profile indicates a substantial shift in hydrological conditions after c. 8 cal ka BP, with higher values suggesting a negative water balance and significant drought events at c. 8, 4 and c. 0.5 cal ka BP (Fig. 7.5). Much lower values between c. 12 and 55 cal ka BP suggest high lake levels (possibly overflowing) which may be due to reduced evaporation during glacial conditions rather than increased precipitation (Haberzettl et al. 2009). With a consistently positive water balance through this period, minor lake level fluctuations may not have been sufficient to induce significant authigenic carbonate precipitation. Ca/Ti is slightly elevated during the Lateglacial, between c. 15.8 and 11 cal ka BP, with higher values corresponding to the Younger Dryas chronozone (Haberzettl et al. 2007, 2009). However, more recent analysis by Jouve et al. (2013) suggest that the presence of micropumice in sediments between 15.2 and 11.8 cal ka BP compromises the integrity of the Ca/Ti record during this period. Micropumice was found to have lower Ti values, thus having an impact on its use as a proxy for detrital inputs and in normalisation. Jouve et al. (2013) argue that Si is a more appropriate normalising tool in this context as analysis showed that Si values reflected detrital inputs rather than biogenic silica (Nuttin et al. 2013).

Due to the high sampling resolution, µXRF scanning is ideally suited to identify abrupt changes in climate such as Heinrich events during the last glaciation. Kylander et al. (2011) examined the geochemical record from the Les Echets sequence in northern France, where previous research had revealed evidence for a response to Heinrich events in the palaeoecological record (Wohlfarth et al. 2008). Correlation matrices established that the relationships between elements changed through the core, related to the substantial changes in lake status evident from the stratigraphy and other proxies (Kylander et al. 2011). A consistent relationship was, however, observed between Ti, K and Rb, reflecting inputs from the catchment and presence of clay minerals. Geochemical data were used to explore changes in detrital inputs (Ti, K, Rb, Zr, Si), grain-size (Zr/Rb) and lake levels and aquatic productivity (Ca, Sr, Mn, Si), summarised in Fig. 7.6. A key finding from the µXRF profiles was that Heinrich events previously identified in the diatom record (low productivity) corresponded with periods of lower lake level. For example, at 31.2 ka BP, an increase in Ti and decrease in Zr/Rb point to more detrital inputs from fine-grained sources, which coupled with lower lake levels based on Sr, Mn and Ca data, indicate a greater influence of aeolian transport of material (Kylander et al. 2011). The duration of H events as defined by µXRF scanning (Ti = detrital inputs and Zr/Rb = grain-size) was shorter than that inferred from the diatom record. This study demonstrates the need to consider changes in proxy relationships through time, particularly in relation to stratigraphic units.

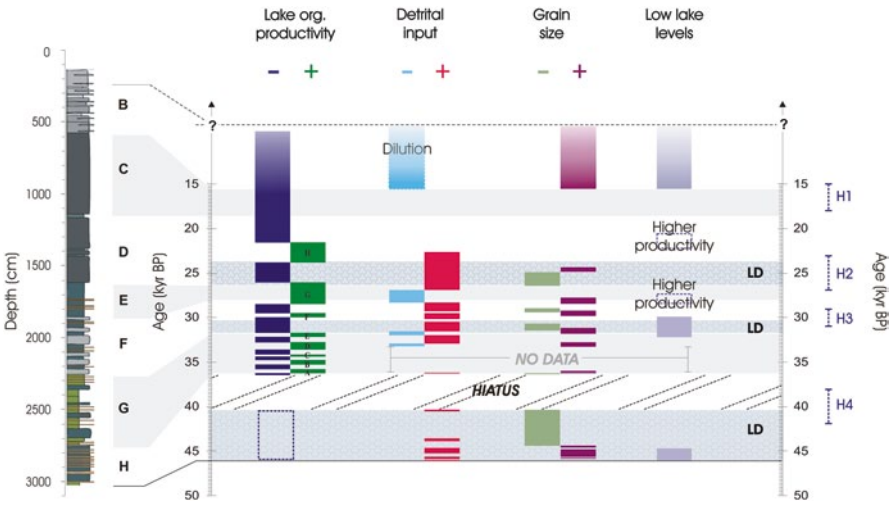


**Fig. 7.6** Summary of the palaeoenvironmental interpretation from the Les Echets sequence, France, from c. 40 to 16 cal ka BP. Lake productivity is from Wöhlfarth et al. (2008), detrital inputs based on Ti data, grain-size is inferred from Zr/Rb and lake levels based on Sr, Ca and Mn µXRF data. (Reprinted with permission from Kylander et al. (2011))

## *Last Glacial-Interglacial Transition and Holocene*

Rapid climate fluctuations during the last glacial-interglacial transition have been the subject of a number of studies involving µXRF scanning (e.g., Haberzettl et al. 2007; Bakke et al. 2009; Neugebauer et al. 2012). The resolution of the data enables comparison of the timing of responses of different locations to the major changes observed during deglaciation. For example, Stansell et al. (2010) using increased detrital inputs represented by Ti, identified a glacier advance at 12.85 cal ka BP at Laguna de los Anteojos, a cirque lake in the Venezuelan Andes. They established that maximum glacier extent occurred at 12.65 cal ka BP with deglaciation complete by 11.75 cal ka BP. The changes in the Ti profile are not as abrupt as those observed at higher latitudes, such as at Lake Kråkenes in Norway (Bakke et al. 2009; Stansell et al. 2010). It is argued that the early warming evident in Venezuela would have contributed to triggering warming in the northern high latitudes through the stimulation of a more vigorous hydrological cycle (Stansell et al. 2010).

Stansell et al. (2013) also used µXRF elemental profiles to investigate Holocene glacier fluctuations in the Peruvian Andes. They presented data from three sites, all of which show evidence of glacier advance between 8 and 4 cal ka BP through increased inputs from detrital material, bulk density and magnetic susceptibility. Here, knowledge of variations in the geochemical composition of catchment rocks was crucial to the interpretation of the XRF scanning data as the three catchments had slightly different downcore profiles. For example at Lake Queshquecocha, geochemical variations were observed at different elevations in the watershed as well

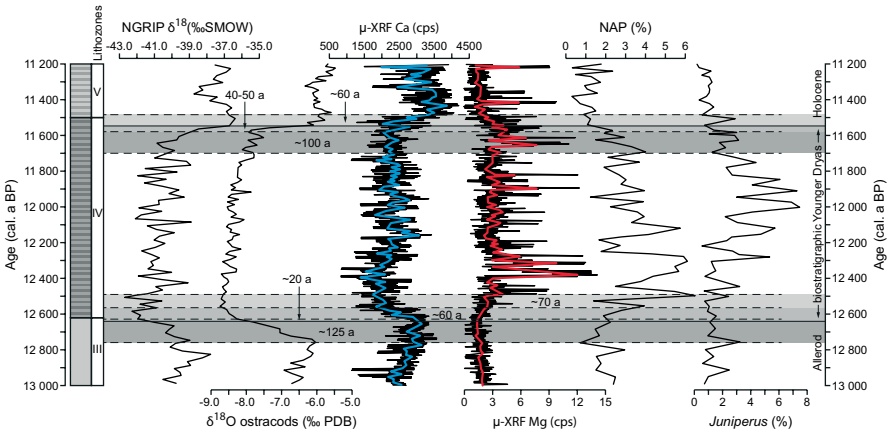


**Fig. 7.7** Selected proxy data from Mondsee spanning the Allerod-Younger Dryas and Younger Dryas-Holocene transitions. *Grey shaded* areas represent major proxy responses and their approximate durations. The *red line* on the Mg profile is a 25 pt running mean. (Redrawn from Lauterbach et al. (2011))

as distinct signatures from till and moraine samples. Bedrock at the headwall had higher concentrations of Zr, whilst at lower elevations Sr and Ca were present at higher levels in the surrounding granodiorites. Increased levels of Sr and Ca in down core profiles were therefore indicative of catchment erosion at lower elevations, whilst Zr inputs increased as the glacier retreated back towards the headwall (Stansell et al. 2013).

At individual sites, the rates of response of different proxies to rapid environmental change can be examined. At pre-Alpine Lake Mondsee in Austria, a range of proxies, including pollen, stable isotope geochemistry and elemental data from μXRF scanning, were used to establish the nature and timing of response to rapid environmental changes between 10 and 15 cal ka BP (Lauterbach et al. 2011). A combination of varve counting and the oxygen isotope record from ostracods was used to tie the Mondsee sequence to the GICC05 chronology from the NGRIP ice core (Rasmussen et al. 2006). XRF data clearly indicate the stratigraphic changes associated with the Younger Dryas, with increased values of Mg and reduced Ca (Fig. 7.7). However, detailed comparison of proxies indicates variability in the timing of the response to cooling at the onset of the Younger Dryas (Greenland Stadial-1). A shift in $\delta^{18}O$ values indicates declining temperature and is associated with an increase in non-arboreal pollen. The sedimentary response however, is somewhat slower. Ca (reflecting reduced authigenic precipitation of calcite in a colder lake) does not start to decline for another c. 125 years. Increased detrital inputs from surrounding dolomite, represented by the Mg profile, gradually increase at the same time as Ca declines, with a rapid influx occurring c. 12.4 cal ka BP. This record indicates a lag in the detrital response to Younger Dryas cooling of some 150–300 years. Lauterbach et al. (2011) also note a more rapid response of proxies to Holocene warming than to the increased temperatures at the onset of the Lateglacial Interstadial.

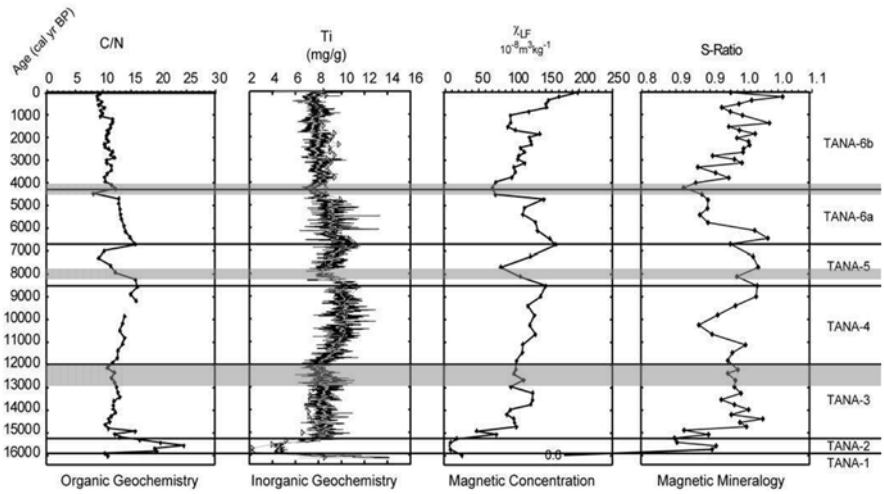


**Fig. 7.8** Comparison of XRF scanning data with magnetic properties and bulk organic geochemistry from Lake Tana, Ethiopia. XRF data were converted to mg/kg by regression of scanning data against conventional XRF analyses of dry sediment. *Grey bars* designate the timing of drought episodes identified in the record. (Adapted from Marshall et al. (2011))

Marshall et al. (2011) used a 17,000 year sequence from Lake Tana in northern Ethiopia, the source of the Blue Nile, to develop a record of hydrological variability. μXRF data confirmed previous palaeoecological investigations (Lamb et al. 2007) that low lake levels, characterised by high Ca, coincided with Heinrich Event 1. The lake became overflowing at 15.3 cal ka BP, with Ca and Sr declining rapidly and then maintaining low values throughout the remainder of the record. After this, the Ti record, supported by mineral magnetic data, is used to infer changing hydrological conditions, with reduced detrital inputs indicating drier episodes (Fig. 7.8). Reduced run-off is observed between 13.0 and 12.5 cal ka BP, possibly corresponding to the onset of the Younger Dryas. Lower values of Ti are recorded around 8 and 4.2 cal ka BP, accompanied by lower magnetic susceptibility values and a reduction in the S-ratio of the magnetic mineralogy. Marshall et al. (2011) argue that during dry phases, magnetic grain-size decreases and formation of anti-ferrimagnetic minerals (e.g., haematite) occurs, which is then washed into the lake at the culmination of the drought episode. The fluctuations in the Ti record are relatively subtle, but inferred droughts also coincide with seismic reflectors. It appears that the overflowing conditions of Lake Tana make it a less sensitive recorder of abrupt changes in moisture availability during the Holocene, but a combination of geochemical and mineral magnetic analysis provides evidence of drought events. The 4.2 ka event is thought to have contributed to the collapse of the Egyptian Old Kingdom (Bell 1971) and the geochemical and magnetic evidence from Lake Tana indicates that there were reduced flows from the source of the Nile at this time (Marshall et al. 2011).

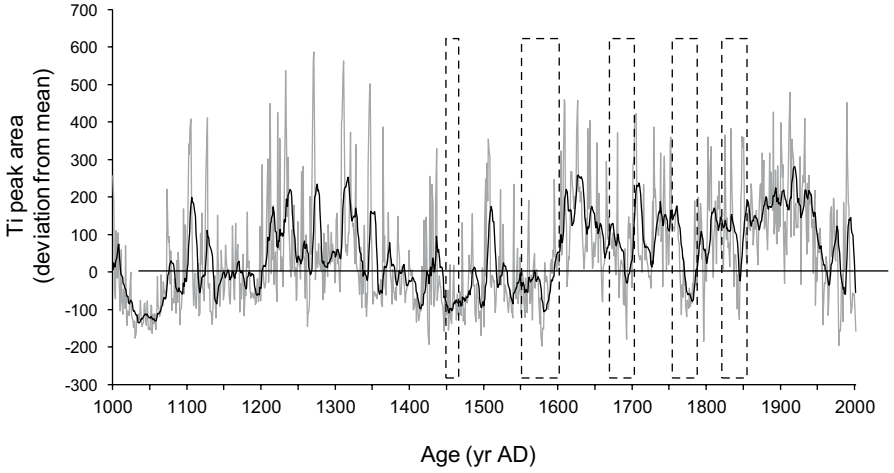


**Fig. 7.9** Ti record from Laguna de Juanacatlán, Mexico, presented as deviation from the mean, compared with known historical drought episodes in Mexico—AD. (Adapted from Metcalfe et al. (2010))

At Laguna de Juanacatlán in west-central Mexico, Metcalfe et al. (2010) established that the Ti record is a reliable record of catchment run-off over the last 2000 years in this basin. Laminated sediments are composed of diatom-rich organic layers and pink clay layers, the Ti profile closely tracking the pink layers. Ti values from μXRF scanning were compared with conventional XRF measurements through the core and confirmed the trends evident from the scanning data. Sediment trap data confirmed clay layers are deposited during the summer wet season. A robust age model developed from 26 radiocarbon dates on the full 7 m sequence spanning c. 6000 years enabled comparison of the recent sediments with historical droughts. Lower Ti values (expressed as deviation from the mean) occurred during several time periods within the last 500 years (Fig. 7.9), which have been identified as dry intervals from Spanish Colonial documentary sources. Nearby meteorological records only cover the period 1961–1991 and are incomplete during the 1980s, so the comparison with historical records is a useful alternative means of checking the validity of the Ti interpretation.

Varve chronologies from two crater lakes in the Valle de Santiago, central Mexico show a more complex relationship with Ti (Kienel et al. 2009), demonstrating the importance of understanding local catchment characteristics and how they are influenced by climate. The varved sediments are characterised by high Ca values in carbonate layers deposited during the winter, whereas Ti is deposited in the lakes from both run off in the wet season (summer) and aeolian sources during the dry season (winter). Kienel et al. (2009) propose that drought episodes could be identified when Ti and Ca are negatively correlated. This is interpreted as indicating that sub-laminae are more clearly separated, with enhanced winter evaporation and rainfall restricted to summer. Unfortunately, this hypothesis cannot be tested as

the lakes are now dry, but the periods of drought identified from the geochemical data correspond reasonably well to known historical droughts and suggest a link to ENSO.

## Records of Human Activity

Although most palaeolimnological studies using XRF scanning have focused on climatic reconstructions, the technique can also provide insights into past human activity. An increase in detrital elements may be the result of anthropogenic disturbance of catchment slopes. For example, Arnaud et al. (2012) presented evidence for soil destabilisation and changes in erosion patterns after 4.4 cal ka BP at Lake Bourget in the French Alps, although they argued that the dominant control throughout their record is climatic rather than anthropogenic. At Lake Paladru to the southwest of Lake Bourget, Simonneau et al. (2013) observed an increase in Ti from very low background levels at around 2.7 cal ka BP, which they interpreted as a response to more intense exploitation of the surrounding catchment during the Iron Age, with deeper ploughing of soils. Increased detrital inputs since then, particularly during the last 1600 years appear to have led to elevated nutrient levels and greater algal productivity, according to quantitative organic petrography (Simonneau et al. 2013).

In addition to evidence of catchment disturbance and soil erosion, XRF data can be used to identify pollution resulting from historic and pre-historic mining activity. Guyard et al. (2007) analysed sediment cores from Lake Bramant in the western Alps spanning the last c. 4 cal ka BP. A distinct peak in copper was identified (presented as Cu/Rb) and related to Bronze Age mining c. 3.87–3.77 cal ka BP (Fig. 7.10). Further up the core, another Cu peak is associated with a dramatic increase in Pb values, corresponding to the peak intensity of lead mining activity during the Roman period. It is, however, possible that the reduced levels for Rb between 430 and 455 cm and below 480 cm exaggerate the Cu/Rb peaks in the Bronze Age. In this case, it would have been beneficial to obtain some conventional XRF data based on dry mass concentrations, which could be used to calibrate the scanning data and provide a quantitative reconstruction of element concentrations. A more recent study of pollution in Lake Windermere, UK, combining μXRF scanning with WD-XRF data and stable Pb isotope measurements reveals a complex pattern of change over the last 500 years (Miller et al. 2014), with a notable increase in Pb, Zn and Cu since the 1930s. These elevated concentrations of Pb in the upper sediments are attributed to a combination of pollution from mining activity, coal burning and gasoline combustion along with a naturally derived component from the catchment. The lag between periods of mining and Pb entering the system is attributed to trapping of sediment in lakes upstream (Miller et al. 2014).

The first sedimentary record of Colonial copper smelting pollution in Mexico was obtained from Lago de Zirahuen, by Davies et al. (2004) where elevated levels of Cu and Pb were revealed using atomic absorption spectrometry. The period of

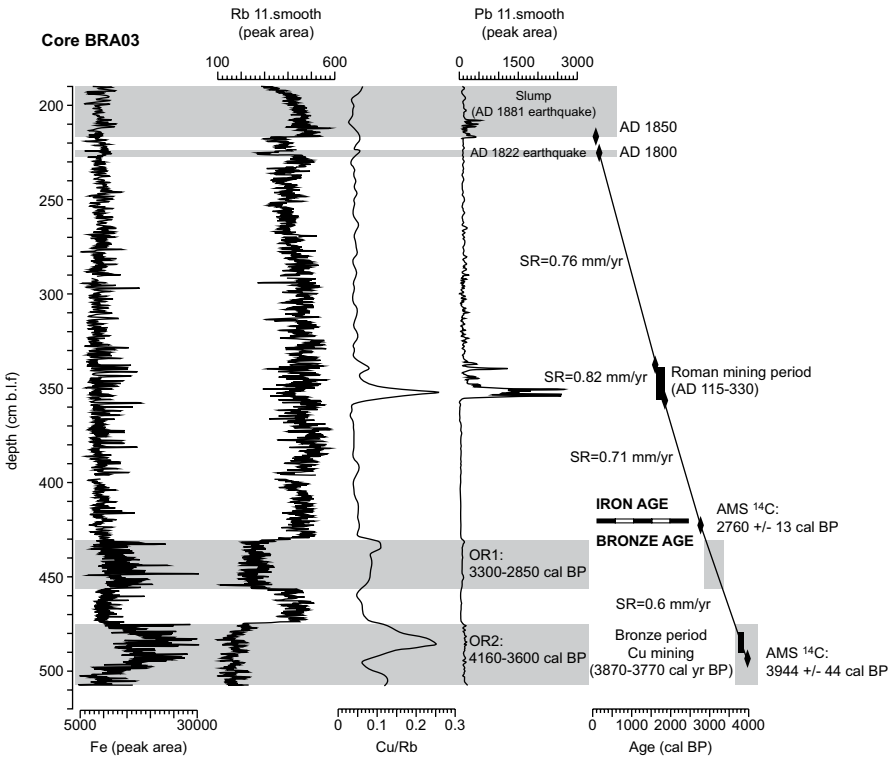


**Fig. 7.10** µXRF data from Lake Bramant, French Alps, reveal evidence of prehistoric mining activity in the catchment from Cu/Rb and Pb values. The age model is based on two radiocarbon dates and varve counting. (From Guyard et al. (2007), with permission from Elsevier)

smelting activity is bracketed between tephra layers from two historical volcanic eruptions—Jorullo (AD 1759–1764) and Paricutín (AD 1943–1952), with maximum values of Cu in the 10 cm above the Jorullo tephra. The site was re-cored and XRF scans reveal results consistent with the previous study (Fig. 7.11). In the new record from Lago de Zirahuen, Cu peak area values are low, with maximum values during the period of smelting of c. 100. This demonstrates that even at relatively low values, µXRF scanning can provide reliable signals. It is interesting to note that an increase in Pb values is not observed in the µXRF scanning data, but elevated values of c. 15 mg/kg (compared with background levels of c. 10 mg/kg) were observed in the original study.

To date, there have been relatively few palaeolimnological studies which have used XRF scanning to explore pollution records (Guyard et al. 2007; Miller et al. 2014). There is considerable potential, both as a tool for examining historical and pre-historic anthropogenic impacts, but also as a tool for identifying recent environmental disturbances.

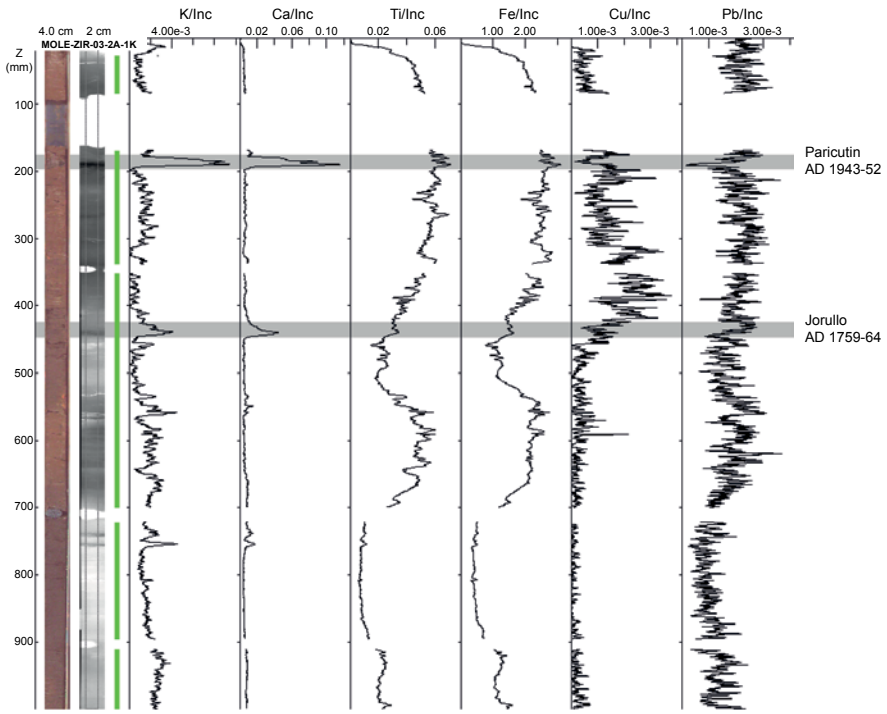


**Fig. 7.11** μXRF data from the Zirahuen Basin, Mexico spanning the last c. 1000 years. Fe and Ti represent detrital inputs, K and Ca highlight the tephra layers. Cu and Pb are potential indicators of pollution from Colonial copper smelting, which reached its peak in the basin during the late eighteenth century. The highest Cu values are bracketed by tephras from Volcan Jorullo (AD 1759–1764) and Volcan Paricutin (AD 1943) (Davies et al. unpubl. data)

## Summary and Conclusions

Within the last decade, micro-XRF scanning has become an increasingly powerful tool in palaeolimnology. As part of a suite of initial core analyses, elemental data provide rapid assessment of key stratigraphic changes creating a framework for a more targeted approach for the processing of more time-consuming proxy analyses. Rapid characterisation of sediments in unprecedented detail has also led to innovative developments, such as in varve counting. Significant advances have been made in the development of continuous, high-resolution palaeoclimatic records worldwide, with XRF scanning making a major contribution to the insights obtained from large lake drilling projects. Elemental data from XRF scanning have enabled the identification of rapid, abrupt climatic changes and thrown light on the relationships between proxies and the leads and lags in responses of different components of the lake-catchment system. A growing area is the use of μXRF scanning to identify event deposits (e.g., flooding, seismic events, volcanic eruptions). Rapid

assessment of the recurrence interval and magnitude of such events can contribute valuable data for agencies involved in planning for such hazards.

With a proliferation of data that is relatively easy to generate, some caution needs to be applied in order to ensure that results are robust. A key question at the start of any study should be—are fully quantitative data required? If so, then recommendations by Boyle et al., this volume should be followed in order to produce reliable concentration data for elements of interest. Checks should be made as to whether organic and/or water content are having an effect on downcore element profiles. It is important to ensure that environmental interpretations are grounded in knowledge about local catchment and in-lake processes as well as regional scale factors which may be the broader focus of the investigation. Interpretations from one lake basin should not be assumed to translate to another. We recommend that a clear relationship should be established between present day environmental processes and elemental concentrations in the sediment wherever possible. This can be achieved for example, through deployment of sediment traps, elemental and mineralogical analysis of the surrounding catchment soils and rocks and limnological monitoring. Where sampling the modern environment is not possible, or there is a 'no-analogue' situation, it is preferable that a multi-proxy approach is adopted to underpin interpretations from μXRF scanning data. These recommendations are standard for many aspects of palaeolimnology, but given the range of processes which may lead to elemental variations, they are of particular relevance for μXRF scanning studies.

A key theme arising from this review is the non-stationary behaviour of lake systems. This may manifest itself in various ways. The decoupling of the XRF data from climate reported by Arnaud et al. (2012) in their Holocene Alpine lake record occurred when lake level rose and altered basin morphology. Kylander et al. (2011) identified changes in the relationships between elements in different stratigraphic units over their 46 cal ka BP record from Les Echets. It is important to consider the possibility that the environmental interpretation of an element or ratio may not be constant through time as lake basins respond to environmental changes. Developing correlation matrices to identify changes in relationships between elements with lithology helps to highlight issues of non-stationarity.

To date, much of the focus of μXRF scanning in lake sediments has been on the environmental interpretation of detrital components (source, transport mechanism, rates of supply, extreme events, weathering processes). Forty-nine element integrals and ratios have been used in the palaeolimnological literature from core scanner data. Ti is the most widely used element and has been used both as an indicator of changing allochthonous inputs which may be linked to a variety of climatic drivers or sources and secondly as a normalising tool to allow determination of the role of within-lake processes such as redox conditions, lake stratification or authigenic carbonate precipitation. The use of Ca/Ti or Ca has also become an important tool for reconstructing hydrological variability, particular in closed basin lakes which are particularly sensitive to lake level change. The main focus of studies to date has been on the stratigraphic pattern of changing elemental abundances, so few authors have made the extra step to calibrating the XRF data to give absolute values equivalent to dry mass concentrations. Improving the quality of reconstructions through calibration should be a priority for future studies.

There is considerable potential for further development of the μXRF scanning in palaeolimnology, including:

- the examination of internal lake processes, such as changing redox conditions and nutrient status, through analysis of Fe, Mn, S and P profiles. To date, relatively few studies focus on these elements and interpretation can be complex.
- a detailed assessment of the potential for the use of Br in combination with possibly Cl and/or I (where measureable) as a proxy for coastal storm activity. Although Br is related to organic matter, in maritime settings, excess of these elements above background levels could indicate increased sea spray.
- the investigation of pollution histories and as a tool for rapid assessment of environmental impacts.
- further experimental work on the geochemical signatures of different types of tephra in a range of background sediment chemistries.

Due to the highly variable nature of lake sediments and the diverse range of internal and external mechanisms affecting their geochemical composition, interpretation of μXRF scanning data is not always straightforward. The potential for non-stationarity must be a key consideration for all studies. However, this review has demonstrated the valuable insights into environmental change and processes over a range of timescales, both natural and anthropogenic that can be obtained through the application of μXRF core scanning.

## References

Arnaud F, Révillon S, Debret M, Revel M, Chapron E, Jacob J, Giguet-Covex C, Poulenard J, Magny M (2012) Lake Bourget regional erosion patterns reconstruction reveals Holocene NW European Alps soil evolution and paleohydrology. Quat Sci Rev 51:81–92. doi:10.1016/j.quascirev.2012.07.025

Aufgebauer A, Panagiatopoulos K, Wagner B, Schaebitz F, Viehberg FA, Vogel H, Zanchetta G, Sulpizio R, Leng MJ, Damaschke M (2012) Climate and environmental change over the last 17 ka recorded in sediments from Lake Prespa (Albania/F.Y.R. of Macedonia/Greece). Quat Int 274:122–135. doi:10.1016/jquaint.2012.02.015

Bakke J, Lie Ø, Heegaard E, Dokken T, Haug G, Birks H, Dulski P, Nilsen T (2009) Rapid oceanic and atmospheric changes during the Younger Dryas cold period. Nat Geosci 2:202–205. doi:10.1038/ngeo439

Balascio N, Zhang Z, Bradley R, Perren B, Dahl S, Bakke J (2011) A multi-proxy approach to assessing isolation basin stratigraphy from the Lofoten Islands, Norway. Quat Res 75:288–300. doi:10.1016/j.yqres.2010.08.012

Bell B (1971) The dark ages in ancient history: the first dark age in Egypt. Am J Archaeol 75:1–25

Berntsson A, Rosqvist GC, Velle G (2014) Late-Holocene temperature and precipitation changes in Vindelfjällen, mid-western Swedish Lapland, inferred from chironomid and geochemical data. Holocene 24:78–92. doi:10.1177/0959683613512167

Boës X, Rydberg J, Martinez-Cortizas A, Bindler R, Renberg I (2011) Evaluation of conservative lithogenic elements (Ti, Zr, Al, and Rb) to study anthropogenic element enrichments in lake sediments. J Paleolimnol 46:75–87

Boyle JF (2001) Inorganic geochemical methods in palaeolimnology. In Last WM, Smol JP (eds) Tracking environmental change using lake sediments: physical and geochemical methods, vol 2. Kluwer, Dordrecht, pp 83–141

Bronk Ramsey C, Staff R, Bryant C, Brock F, Kitagawa H, Plicht J, Schlolaut G, Marshall M, Brauer A, Lamb H, Payne R, Tarasov P, Haraguchi T, Gotanda K, Yonenobu H, Yokoyama Y, Tada R, Nakagawa T (2012) A complete terrestrial radiocarbon record for 11.2–52.8 kyr B.P. Science 338:370–374. doi:10.1126/science.1226660

Brown E (2011) Lake Malawi's response to "megadrought" terminations: sedimentary records of flooding, weathering and erosion. Palaeogeogr Palaeoclimatol Palaeoecol 303:120–125. doi:10.1016/j.palaeo.2010.01.038

Brown E, Johnson T, Scholz C, Cohen A, King J (2007) Abrupt change in tropical African climate linked to the bipolar seesaw over the past 55,000 years. Geophys Res Lett doi:10.1029/2007GL031240

Burn M, Palmer S (2014) Solar forcing of Caribbean drought events during the last millennium. J Quat Sci 29:827–836. doi:10.1002/jqs.2660

Burnett A, Soreghan M, Scholz C, Brown E (2011) Tropical East African climate change and its relation to global climate: a record from Lake Tanganyika, tropical East Africa, over the past 90 + kyr. Palaeogeogr Palaeoclimatol Palaeoecol 303:155–167. doi:10.1016/j.palaeo.2010.02.011

Chawchai S, Chabangborn A, Kylander M, Löwemark L, Mörth C, Blaauw M, Klubseang W, Reimer P, Fritz S, Wohlfarth B (2013) Lake Kumphawapi—an archive of Holocene palaeoenvironmental and palaeoclimatic changes in northeast Thailand. Quat Sci Rev 68:59–75. doi:10.1016/j.quascirev.2013.01.030

Clift P, Wan S, Blusztajn J (2014) Reconstructing chemical weathering, physical erosion and monsoon intensity since 25 Ma in the northern South China Sea: a review of competing proxies. Earth Sci Rev 130:86–102. doi:10.1016/j.earscirev.2014.01.002

Cohen AS (2003) Paleolimnology: the history and evolution of lake systems. Oxford University Press, New York, p 528

Corella J, Brauer A, Mangili C, Rull V, Vegas-Vilarrúbia T, Morellón M, Valero-Garcés B (2012) The 1.5-ka varved record of Lake Montcortès (southern Pyrenees, NE Spain). Quat Res 78:323–332. doi:10.1016/j.yqres.2012.06.002

Croudace IW, Rindby A, Rothwell RG (2006) ITRAX: description and evaluation of a new multi-function X-ray core scanner. In: Rothwell RG (ed) New techniques in sediment core analysis, vol 267. Geological Society Special Publication, pp 51–63

Cuven S, Francus P, Lamoureux S (2010) Estimation of grain-size variability with micro X-ray fluorescence in laminated lacustrine sediments, cape bounty, Canadian High Arctic. J Paleolimnol 44:803–817. doi:10.1007/s10933-010-9453-1

Cuven S, Francus P, Lamoureux S (2011) Mid to Late Holocene hydroclimatic and geochemical records from the varved sediments of East lake, Cape Bounty, Canadian High Arctic. Quat Sci Rev 30:2651–2665. doi:10.1016/j.quascirev.2011.05.019

Czymzik M, Brauer A, Dulski P, Plessen B, Naumann R, Grafenstein U, Scheffler R (2013) Orbital and solar forcing of shifts in mid- to late Holocene flood intensity from varved sediments of pre-alpine Lake Ammersee (southern Germany). Quat Sci Rev 61:96–110. doi:10.1016/j.quascirev.2012.11.010

Damaschke M, Sulpizio R, Zanchetta G, Wagner B, Böhm A, Nowaczyk N, Rethemeyer J, Hilgers A (2013) Tephrostratigraphic studies on a sediment core from Lake Prespa in the Balkans. Clim Past 9:267–287. doi:10.5194/cp-9-267-2013

Davies SJ, Metcalfe SE, MacKenzie AB, Newton AJ, Endfield GH, Farmer JG (2004) Environmental changes in the Zirahuén basin, Michoacán, Mexico, during the last 1000 years. J Paleolimnol 31:77–98. doi:10.1023/B:JOPL.0000013284.21726.3d

Davies, SJ, Israde, I, Lozano, S, Ortega, B (unpubl.)

Davison W (1993) Iron and manganese in lakes. Earth Sci Rev 34:119–163

De Boer EJ, Tjallingii R, Velez MI, Rijsdijk KF, Vlug A, Reichart GJ, Prendergast AL, de Louw PGB, Florens FBV, Baider C, Hooghiemstra H (2014) Climate variability in the SW Indian ocean from an 8000-yr multi-proxy record in the Mauritian lowlands shows a middle

to late Holocene shift from negative IOD-state to ENSO-state. Quat Sci Rev 86:175–189. doi:10.1016/j.quascirev.2013.12.026

Elbert J, Grosjean M, Gunten L, Urrutia R, Fischer D, Wartenburger R, Ariztegui D, Fujak M, Hamann Y (2012) Quantitative high-resolution winter (JJA) precipitation reconstruction from varved sediments of Lago Plomo 47°S, Patagonian Andes, AD 1530–2002. Holocene 22:465–474. doi:10.1177/0959683611425547

Elbert E, Wartenburger R, von Gunten L, Urrutia R, Fischer D, Fujak M, Hamann Y, Greben ND, Grosjean M (2013) Late Holocene air temperature reconstructed from sediments of Laguna Escondida, Patagonia, Chile (45°S 30'W). Palaeogeogr Palaeoclimatol Palaeoecol 369:482–492. doi:10.1016/j.palaeo.2012.11.013

Engstrom DR, Wright HE Jr (1984) Chemical stratigraphy of lake sediments as a record of environmental change. In: Haworth EY, Lund JWG (eds) Lake sediments and environmental history. Leicester University Press, Leicester, pp 11–68

Eugster HP, Hardie LA (1978) Saline lakes. In: Lerman A (ed) Lakes: chemistry, geology, physics. Springer, New York, pp 237–289

Fedotov A, Phedorin M, Enushchenko I, Vershinin K, Melgunov M, Khodzher T (2012) A reconstruction of the thawing of the permafrost during the last 170 years on the Taimyr Peninsula (East Siberia, Russia). Glob Planet Change 98–99:139–152. doi:10.1016/j.gloplacha.2012.09.002

Fernandez M, Björck S, Wohlfarth B, Maidana N, Unkel I, Van der Putten N (2013) Diatom assemblage changes in lacustrine sediments from Isla de los Estados, southernmost South America, in response to shifts in the southwesterly wind belt during the last deglaciation. J Paleolimnol 50:433–446. doi:10.1007/s10933-013-9736-4

Foerster V, Junginger A, Langkamp O, Gebru T, Asrat A, Umer M, Lamb H, Wennrich V, Rethemeyer J, Nowaczyk N, Trauth M, Schaebitz F (2012) Climatic change recorded in the sediments of the Chew Bahir basin, southern Ethiopia, during the last 45,000 years. Quat Int 274:25–37. doi:10.1016/j.quaint.2012.06.028

Francus P, Lamb H, Nakagawa T, Marshall M, Brown E, Suigetsu 2006 project members (2009) The potential of high-resolution X-ray fluorescence core scanning: applications in paleolimnology. PAGES News 17:93–95

Gilfedder BS, Petri M, Wessels M, Biester H (2011) Bromine species fluxes from Lake Constance's catchment and a preliminary lake mass balance. Geochim et Cosmochim Acta 75:3385–3401. doi:10.1016/j.gca.2011.03.021

Guyard H, Chapron E, St-Onge G, Anselmetti F, Arnaud F, Magand O, Francus P, Mélières M-A (2007) High-altitude varve records of abrupt environmental changes and mining activity over the last 4000 years in the Western French Alps (Lake Bramant, Grandes Rousses Massif). Quat Sci Rev 26:2644–2660. doi:10.1016/j.quascirev.2007.07.007

Haberzettl T, Fey M, Lücke A, Maidana N, Mayr C, Ohlendorf C, Schäbitz F, Schleser G, Wille M, Zolitschka B (2005) Climatically induced lake level changes during the last two millennia as reflected in sediments of Laguna Potrok Aike, southern Patagonia (Santa Cruz, Argentina). J Paleolimnol 33:283–302. doi:10.1007/s10933-004-5331-z

Haberzettl T, Corbella H, Fey M, Janssen S, Lucke A, Mayr C, Ohlendorf C, Schabitz F, Schleser G, Wille M, Wulf S, Zolitschka B (2007) Lateglacial and Holocene wet–dry cycles in southern patagonia: chronology, sedimentology and geochemistry of a lacustrine record from Laguna Potrok Aike, Argentina. Holocene 17:297–310. doi:10.1177/0959683607076437

Haberzettl T, Anselmetti F, Bowen S, Fey M, Mayr C, Zolitschka B, Ariztegui D, Mauz B, Ohlendorf C, Kastner S, Lücke A, Schäbitz F, Wille M (2009) Late Pleistocene dust deposition in the Patagonian steppe—extending and refining the paleoenvironmental and tephrochronological record from Laguna Potrok Aike back to 55 ka. Quat Sci Rev 28:2927–2939. doi:10.1016/j.quascirev.2009.07.021

Hodell D, Turchyn A, Wiseman C, Escobar J, Curtis J, Brenner M, Gilli A, Mueller A, Anselmetti F, Ariztegui D, Brown E (2012) Late glacial temperature and precipitation changes in the lowland Neotropics by tandem measurement of $\delta^{18}O$ in biogenic carbonate and gypsum hydration water. Geochim et Cosmochim Acta 77:352–368. doi:10.1016/j.gca.2011.11.026

Jones A, Lewin J, Macklin M (2010) Flood series data for the later Holocene: available approaches, potential and limitations from UK alluvial sediments. Holocene 20:1123–1135. doi:10.1177/0959683610369501

Jouve G, Francus P, Lamoureux S, Provencher-Nolet L, Hahn A, Haberzettl T, Fortin D, Nuttin L, The PASADO Science Team (2013) Microsedimentological characterization using image analysis and μ-XRF as indicators of sedimentary processes and climate changes during Lateglacial at Laguna Potrok Aike, Santa Cruz, Argentina. Quat Sci Rev 71:191–204. doi:10.1016/j.quascirev.2012.06.003

Kalugin I, Daryin A, Smolyaninova L, Andreev A, Diekmann B, Khlystov O (2007) 800-yr-long records of annual air temperature and precipitation over southern Siberia inferred from Teletskoye Lake sediments. Quat Res 67:400–410. doi:10.1016/j.yqres.2007.01.007

Kalugin I, Darin A, Rogozin D, Tretyakov G (2013) Seasonal and centennial cycles of carbonate mineralisation during the past 2500 years from varved sediment in Lake Shira, South Siberia. Quat Int 290–291:245–252. doi:10.1016/j.quaint.2012.09.016

Kämpf L, Brauer A, Dulski P, Lami A, Marchetto A, Gerli S, Ambrosetti W, Guilizzoni P (2012) Detrital layers marking flood events in recent sediments of Lago Maggiore (N. Italy) and their comparison with instrumental data. Freshw Biol 57:2076–2090. doi:10.1111/j.1365-2427.2012.02796.x

Kienel U, Bowen S, Byrne R, Park J, Böhnel H, Dulski P, Luhr J, Siebert L, Haug G, Negendank J (2009) First lacustrine varve chronologies from Mexico: impact of droughts, ENSO and human activity since AD 1840 as recorded in maar sediments from Valle de Santiago. J Paleolimnol 42:587–609. doi:10.1007/s10933-009-9307-x

Kylander M, Ampel L, Wohlfarth B, Veres D (2011) High-resolution X-ray fluorescence core scanning analysis of Les Echets (France) sedimentary sequence: new insights from chemical proxies. J Quat Sci 26:109–117. doi:10.1002/jqs.1438

Kylander M, Lind E, Wastegard S, Lowemark L (2012) Recommendations for using XRF core scanning as a tool in tephrochronology. Holocene 22:371–375. doi:10.1177/0959683611423688

Lamb H, Bates C, Coombes P, Marshall M, Umer M, Davies S, Dejen E (2007) Late Pleistocene desiccation of Lake Tana, source of the Blue Nile. Quat Sci Rev 26:287–299. doi:10.1016/j.quascirev.2006.11.020

Lane C, Chorn B, Johnson T (2013) Ash from the Toba supereruption in Lake Malawi shows no volcanic winter in East Africa at 75 ka. Proc Natl Acad Sci U S A 110:8025–8029. doi:10.1073/pnas.1301474110

Lauterbach S, Brauer A, Andersen N, Danielopol D, Dulski P, Hüls M, Milecka K, Namiotko T, Obremska M, Grafenstein U, Participants D (2011) Environmental responses to Lateglacial climatic fluctuations recorded in the sediments of pre-alpine Lake Mondsee (northeastern Alps). J Quat Sci 26:253–267. doi:10.1002/jqs.1448

Litt T, Krastel S, Sturm M, Kipfer R, Örcen S, Heumann G, Franz S, Ülgen U, Niessen F (2009) "PALEOVAN", International continental scientific drilling program (ICDP): site survey results and perspectives. Quat Sci Rev 28:1555–1567. doi:10.1016/j.quascirev.2009.03.002

Löwemark L, Chen H, Yang T, Kylander M, Yu E, Hsu Y, Lee T, Song S, Jarvis S (2011) Normalizing XRF-scanner data: A cautionary note on the interpretation of high-resolution records from organic-rich lakes. J Asian Earth Sci 40:1250–1256. doi:10.1016/j.jseaes.2010.06.002

Mackareth FGH (1966) Some chemical observations on post-glacial lake sediments. Philos Trans R Soci Lond B 250:165–213

Marshall MH, Lamb HF, Huws D, Davies SJ, Bates CR, Bloemendahl J, Boyle JF, Leng MJ, Umer M, Bryant CL (2011). Late Pleistocene and Holocene drought events at Lake Tana, the source of the Blue Nile. Glob Planet Change 78:147–161. doi:10.1016/j.glopacha.2011.06.004

Marshall M, Schlolaut G, Nakagawa T, Lamb H, Brauer A, Staff R, Ramsey C, Tarasov P, Gotanda K, Haraguchi T, Yokoyama Y, Yonenobu H, Tada R (2012) A novel approach to varve counting using μXRF and X-radiography in combination with thin-section microscopy, applied to the Late Glacial chronology from Lake Suigetsu, Japan. Quat Geochronol 13:70–80. doi:10.1016/j.quageo.2012.06.002

Martin-Puertas C, Valero-Garcés B, Mata MP, Moreno A, Giralt S, Martinez-Ruiz F, Jimenéz-Espejo F (2011) Geochemical processes in a Mediterranean lake: a high-resolution study of the last 4,000 years in Zoñar Lake, southern Spain. J Paleolimnol 46:405–421. doi:10.1007/s10933-009-9373-0

Martin-Puertas C, Brauer A, Dulski P, Brademann B (2012) Testing climate–proxy stationarity throughout the Holocene: an example from the varved sediments of Lake Meerfelder Maar (Germany). Quat Sci Rev 58:56–65. doi:10.1016/j.quascirev.2012.10.023

Melles M, Brigham-Grette J, Minyuk PS, Nowaczyk NR, Wennrich V, Andreev AA, Coletti A, Cook TL, Haltia-Hovi E, Kukkonen M, Lohzkin AV, Rosén P, Tarasov P, Vogel H, Wagner B (2012) 2.8 million years of Arctic climate change from Lake El'gygytgyn, NE Russia. Science 337:315–320. doi:10.1126/science.1222135

Metcalfe SE, Jones MD, Davies SJ, Noren A, MacKenzie A (2010) Climate variability over the last two millennia in the North American Monsoon region, recorded in laminated lake sediments from Laguna de Juanacatlan, Mexico. Holocene 20:1195–1206. doi:10.1177/0959683610371994

Miller H, Croudace IW, Bull JM, Cotterill CJ, Dix JK, Taylor RN (2014) Sediment lake record of anthropogenic and natural inputs to Windermere (English Lake District) using double-spike lead isotopes, radiochronology, and sediment microanalysis. Environ Sci Technol 48:7254–7263. doi:10.1021/es5008998

Moreno A, Giralt S, Valero-Garcés B, Sáez A, Bao R, Prego R, Pueyo J, González-Sampériz P, Taberner C (2007) A 14kyr record of the tropical Andes: the Lago Chungará sequence (18°S, northern Chilean Altiplano). Quat Int 161:4–21. doi:10.1016/j.quaint.2006.10.020

Moreno A, Valero-Garcés B, González-Sampériz P, Rico M (2008) Flood response to rainfall variability during the last 2000 years inferred from the Taravilla lake record (Central Iberian Range, Spain). J Paleolimnol 40:943–961. doi:10.1007/s10933-008-9209-3

Moreno A, Lopéz-Merino L, Leira M, Marco-Barba M, González-Sampériz P, Valero-Garcés BL, Lopéz-Saez J, Santos L, Mata P, Ito E (2011) Revealing the last 13,500 years of environmental history from the multi-proxy record of a mountain lake (Lago Enol, northern Iberian Peninsula). J Paleolimnol 46:327–349. doi:10.1007/s10933-009-9387-7

Mueller A, Islebe G, Hillesheim M, Grzesik D, Anselmetti F, Ariztegui D, Brenner M, Curtis J, Hodell D, Venz K (2009) Climate drying and associated forest decline in the lowlands of northern Guatemala during the Late Holocene. Quat Res 71:133–141. doi:10.1016/j.yqres.2008.10.002

Nakagawa T, Gotanda K, Haraguchi T, Danhara T, Yonenobu H, Brauer A, Yokoyama Y, Tada R, Takemura K, Staff R, Payne R, Ramsey C, Bryant C, Brock F, Schlolaut G, Marshall M, Tarasov P, Lamb H (2012) SG06, a fully continuous and varved sediment core from Lake Suigetsu, Japan: stratigraphy and potential for improving the radiocarbon calibration model and understanding of late Quaternary climate changes. Quat Sci Rev 36:164–176. doi:10.1016/j.quascirev.2010.12.013

Neugebauer I, Brauer A, Dräger N, Dulski P, Wulf S, Plessen B, Mingram J, Herzschuh U, Brande A (2012) A younger dryas varve chronology from the Rehwiese palaeolake record in NE-Germany. Quat Sci Rev 36:91–102. doi:10.1016/j.quascirev.2011.12.010

Niemann H, Matthias I, Michalzik B, Behling H (2013) Late Holocene human impact and environmental change inferred from a multi-proxy lake sediment record in the Loja region, southeastern Ecuador. Quat Int 308/309:253–264. doi:10.1016/j.quaint.2013.03.017

Nuttin L, Francus P, Preda M, Ghaleb B, Hillaire-Marcel C, The PASADO Science Team (2013) Authigenic, detrital and diagenetic minerals in the Laguna Potrok Aike sediment sequence. Quat Sci Rev 71:109–118. doi:10.1016/j.quatscirev.2012.09.027

Olsen J, Anderson N, Leng M (2013) Limnological controls on stable isotope records of late-Holocene palaeoenvironment change in SW Greenland: a paired lake study. Quat Sci Rev 66:85–95. doi:10.1016/j.quascirev.2012.10.043

Rasmussen S, Andersen K, Svensson A, Steffensen J, Vinther B, Clausen H, Siggaard-Andersen M, Johnsen S, Larsen L, Dahl-Jensen D, Bigler M, Röthlisberger R, Fischer H, Goto-Azuma K, Hansson M, Ruth U (2006) A new Greenland ice core chronology for the last glacial termination. J Geophys Res. doi:10.1029/2005JD006079

Richter TO, Van der Gaast S, Koster B, Vaars A, Gieles R, de Stigter HC, de Haas H, van Weering TCE (2006) The Avaatech XRF core scanner: technical description and applications to NE Atlantic sediments. In: Rothwell RG (ed) New techniques in sediment core analysis, vol 267. Geological Society Special Publication, pp 39–50. doi:10.1144/GSL.SP.2006.267.01.03

Schillereff D, Chiverrell R, Macdonald N, Hooke J (2014) Flood stratigraphies in lake sediments: a review. Earth Sci Rev 135:17–37. doi:10.1016/j.earscirev.2014.03.011

Schlolaut G, Marshall M, Brauer A, Nakagawa T, Lamb H, Staff R, Ramsey C, Bryant C, Brock F, Kossler A, Tarasov P, Yokoyama Y, Tada R, Haraguchi T (2012) An automated method for varve interpolation and its application to the late glacial chronology from Lake Suigetsu, Japan. Quat Geochronol 13:52–69. doi:10.1016/j.quageo.2012.07.005

Schlolaut G, Brauer A, Marshall M, Nakagawa T, Staff R, Ramsey C, Lamb H, Bryant C, Naumann R, Dulski P, Brock F, Yokoyama Y, Tada R, Haraguchi T, Suigetsu 2006 project members (2014) Event layers in the Japanese Lake Suigetsu "SG06" sediment core: description, interpretation and climatic implications. Quat Sci Rev 83:157–170. doi:10.1016/j.quascirev.2013.10.026

Schnurrenberger D, Kelts K, Johnson T, Shane L, Ito E (2001) National lacustrine core repository (LacCore). J Paleolimnol 25:123–127. doi:10.1023/A:1008171027125

Schnurrenberger D, Russell J, Kelts K (2003) Classification of lake sediments based on sedimentary components. J Paleolimnol 29:141–154. doi:10.1023/A:1023270324800

Scholz CA, Johnson TC, Cohen AS, King JW, Peck JA, Overpeck JT, Talbot MR, Brown ET, Kalindekafe L, Gomez J, Pierson J (2007) East African megadroughts between 135 and 75 thousand years ago and bearing on early-modern human origins. Proc Natl Acad Sci U S A 104:16416–16421. doi:10.1073/pnas.0703874104

Scholz C, Cohen A, Johnson T, King J, Talbot M, Brown E (2011) Scientific drilling in the great rift valley: the 2005 Lake Malawi scientific drilling project—an overview of the past 145,000years of climate variability in Southern Hemisphere East Africa. Palaeogeogr Palaeoclimatol Palaeoecol 303:3–19. doi:10.1016/j.palaeo.2010.10.030

Shala S, Helmens K, Jansson K, Kylander M, Risberg J, Löwemark L (2014) Palaeoenvironmental record of glacial lake evolution during the early Holocene at Sokli, NE Finland. Boreas 43:362–376. doi:10.1111/bor.12043

Simonneau A, Doyen E, Chapron E, Millet L, Vannière B, Giovanni C, Bossard N, Tachikawa K, Bard E, Albéric P, Desmet M, Roux G, Lajeunesse P, Berger J, Arnaud F (2013) Holocene land-use evolution and associated soil erosion in the French Prealps inferred from Lake Paladru sediments and archaeological evidences. J Archaeol Sci 40:1636–1645. doi:10.1016/j.jas.2012.12.002

Stansell N, Abbott M, Rull V, Rodbell D, Bezada M, Montoya E (2010) Abrupt Younger Dryas cooling in the northern tropics recorded in lake sediments from the Venezuelan Andes. Earth Planet Sci Lett 293:154–163. doi:10.1016/j.epsl.2010.02.040

Stansell N, Rodbell D, Abbott M, Mark B (2013) Proglacial lake sediment records of Holocene climate change in the western Cordillera of Peru. Quat Sci Rev 70:1–14. doi:10.1016/j.quascirev.2013.03.003

Tjallingii R, Röhl U, Kölling M, Bickert T (2007) Influence of the water content on X-ray fluorescence core scanning measurements in soft marine sediments. Geochem Geophys Geosyst 8:Q02004. doi:10.1029/2006GC001393

Turner TE, Swindles G, Roucoux K (2014) Late Holocene ecohydrological and carbon dynamics of a UK raised bog: impact of human activity and climate change. Quat Sci Rev 84:65–85. doi:10.1016/j.quascirev.2013.10.030

Unkel I, Björck S, Wohlfarth B (2008) Deglacial environmental changes on Isla de los Estados (54.4°S), southeastern Tierra del Fuego. Quat Sci Rev 27:1541–1554. doi:10.1016/j.quascirev.2008.05.004

Unkel I, Fernandez M, Björck S, Ljung K, Wohlfarth B (2010) Records of environmental changes during the Holocene from Isla de los Estados (54.4°S), southeastern Tierra del Fuego. Glob Planet Change 74:99–113. doi:10.1016/j.gloplacha.2010.07.003

Van Daele M, Moernaut M, Silversmit G, Schmidt S, Fontjin K, Heirman K, Vandoorne W, De-Clercq M, Van Acker A, Woolf C, Pino M, Urrutia R, Roberts SJ, Vincze L, De Batiste M (2014) The 600 yr eruptive history of Villarrica Volcano (Chile) revealed by annually laminated sediments. Geol Soc Am Bull 126:481–498. doi:10.1130/B30798.1

Vogel H, Zanchetta G, Sulpizio R, Wagner B, Nowaczyk N (2010) A tephrostratigraphic record for the last glacial-interglacial cycle from Lake Ohrid, Albania and Macedonia. J Quat Sci 25:320–338. doi:10.1002/jqs.1311

Wastegård S, Veres D, Kliem P, Hahn A, Ohlendorf C, Zolitschka B (2013) Towards a late quaternary tephrochronological framework for the southernmost part of South America—the Laguna Potrok Aike tephra record. Quat Sci Rev 71:81–90. doi:10.1016/j.quascirev.2012.10.019

Weltje GJ, Tjallingii R (2008) Calibration of XRF core scanners for quantitative geochemical logging of sediment cores: theory and application. Earth Planet Sci Lett 274:423–438. doi:10.1016/j.epsl.2008.07.054

Wilhelm B, Arnaud F, Sabatier P, Magand O, Chapron E, Courp T, Tachikawa K, Fanget B, Malet E, Pignol C, Bard E, Delannoy J (2013) Palaeoflood activity and climate change over the last 1400 years recorded by lake sediments in the north-west European Alps. J Quat Sci 28:189–199. doi:10.1002/jqs.2609

Wohlfarth B, Veres D, Ampel L, Lacourse T, Blaauw M, Preusser F, Andrieu-Ponel V, Kéravis D, Lallier-Vergès E, Björck S, Davies S, Beaulieu J-L, Risberg J, Hormes A, Kasper H, Possnert G, Reille M, Thouveny N, Zander A (2008) Rapid ecosystem response to abrupt climate changes during the last glacial period in western Europe, 40–16 ka. Geology 36:407–410. doi:10.1130/G24600A.1

Yancheva G, Nowaczyk N, Mingram J, Dulski P, Schettler G, Negendank J, Liu J, Sigman D, Peterson L, Haug G (2007) Influence of the intertropical convergence zone on the East Asian monsoon. Nature 445:74–77. doi:10.1038/nature05431

# Chapter 8
# Micro-XRF Applications in Fluvial Sedimentary Environments of Britain and Ireland: Progress and Prospects

**Jonathan N. Turner, Anna F. Jones, Paul A. Brewer, Mark G. Macklin and Sara M. Rassner**

**Abstract** This chapter considers applications of micro-XRF scanning in fluvial depositional environments and presents case-studies from Britain and Ireland in three key river management areas: flood reconstruction; pollution and provenance mapping; and floodplain sediment dynamics. Although fluvial sediment archives are typically shorter and more fragmented than marine and lake sediment records, they do offer significant palaeoenvironmental potential, not least because of the sensitivity of river systems to environmental change. A major consideration in micro-XRF analysis, however, is the continuity and heterogeneity of alluvial sediments and the integrity of accretionary records once they have been subject to post-depositional processes, such as human disturbance and pedogenesis. Thus far, micro-XRF applications in fluvial environments have been limited. One research area currently being developed is the field of flood reconstruction, where elements and, in particular, element ratios (e.g. Zr/Rb, Zr/Ti) can be used as particle size proxies. Micro-XRF core scanning technologies allow for analysis at the event-scale, which hitherto has been unachievable in silt and clay sediments. The potential to build and significantly enhance our understanding of longer term flooding patterns and non-stationarity, offers considerable scope for augmenting instrumental records and providing new perspectives for contemporary river management. Rapid

J. N. Turner (✉) · A. F. Jones
School of Geography, Planning and Environmental Policy, University College Dublin, Newman Building, Belfield, Dublin 4, Ireland
e-mail: jonathan.turner@ucd.ie

A. F. Jones
e-mail: anna.jones@ucd.ie

P. A. Brewer · M. G. Macklin · S. M. Rassner
Institute of Geography & Earth Sciences, Aberystwyth University, Llandinam Building, Penglais Campus, Aberystwyth SY23 3DB, UK
e-mail: pqb@aber.ac.uk

M. G. Macklin
e-mail: mvm@aber.ac.uk

S. M. Rassner
e-mail: skr@aber.ac.uk



I. W. Croudace, R. G. Rothwell (eds.), *Micro-XRF Studies of Sediment Cores*,
Developments in Paleoenvironmental Research 17, DOI 10.1007/978-94-017-9849-5_8

geochemical assessment of fluvial sedimentary deposits can also be used to support floodplain reconstruction studies and pollution investigations, but greater scope will emerge from the calibration of raw XRF count data to elemental concentration. In this paper we demonstrate the potential for using micro-XRF data in sediment provenance investigations, but improvements in error quantification and propagation need to be explored. Given that river alluvium plays an integral role in the cycling and storage of contaminants, further applications in this field would be hugely beneficial for river managers. Although sediment heterogeneity places significant challenges to the quantification of micro-XRF core scanner results, there has been little attempt to establish what these limitations mean in practical terms.

**Keywords** Core scanning · Flood reconstruction · Fluvial sediment transport · Heavy metal pollution · Sediment provenance

## Introduction

Micro-XRF core scanners have been in operation for a decade or more and have become increasingly employed in palaeoenvironmental research. Thus far, however, there has been relatively little work carried out in fluvial environments, with only three papers investigating riverine alluvial deposits listed in the ISI Science Citation Index at the time of writing (Jones et al. 2010; Tjallingii et al. 2010; Wang et al. 2011). This may be related to the fact that during micro-XRF instrument development the initial research links and applications were established with the lacustrine and especially the marine scientific communities. Marine and lacustrine depositional environments act as very efficient sediment sinks and offer high palaeoenvironmental potential for the preservation of multi-millennial-scale records for climate change research (e.g. Moreno et al. 2007; Kujau et al. 2010). As conveyors of sediment and water, however, rivers play an instrumental role in landscape evolution and their catchments are home to a variety of depositional settings that can store sedimentological, stratigraphic and geochemical information about past and present sediment dynamics. Advances in radiometric dating, allied to the application of new palaeoenvironmental correlatives, also highlight the geomorphic sensitivity of fluvial systems and the role of alluvial sediments as archives of local and regional environmental change (Macklin and Lewin 2008; Macklin et al. 2010).

River channel and catchment management objectives and drivers are longstanding, reflecting societal and community associations with rivers that date back millennia (Downs and Gregory 2004). Given the unprecedented population pressures and projections faced by contemporary society, coupled with uncertain climate futures, there has probably never been a more pressing and urgent need to understand fluvial systems and their non-stationary behaviour. In Europe, key management considerations are reflected in new legislation that has come into force during

the last decade. The EU Floods Directive (2007/60/EC), for example, sets new benchmarks for the assessment and mitigation of flood risk. Information on former flooding regimes and dynamics will therefore become increasingly valuable, particularly where instrumental flood records are fragmented and short-lived. In terms of water resource management, the Water Framework Directive (2000/60/EC), which establishes an integrated approach to the protection and enhancement of waters and aquatic habitats across Europe, has placed renewed emphasis on the sustainable management of channel and riparian environments. Because fine-grained fluvial sediments frequently play a key role in the cycling of nutrients and contaminants (Miller 1997), patterns of contaminant dispersal and storage are often intimately linked to fluvial sediment conveyance, and alluvial sediment stores can become significant secondary (diffuse) sources of pollution (Macklin et al. 1994). Identifying and understanding the dynamics of sediment-borne contamination is therefore critical for effective river management, especially in catchments affected by metal mining (Macklin et al. 2006).

In the context of contemporary river management objectives, *flooding*, *pollution* and *channel dynamics* emerge as three key research areas. In this chapter we explore the application of micro-XRF to address these challenges using examples of research that is currently being carried out in Britain and Ireland. We assess how micro-XRF scanners may contribute to research in fluvial environments, by complementing existing approaches and methodologies, and through new and innovative techniques that utilise the unique characteristics of these facilities, such as the integration of multiple sensors, rapid and non-destructive analyses and ultra-high resolution precision. Much of the work reported in this chapter is previously unpublished and developmental, but by presenting a series of case-studies, across a range of environmental settings, we aim to provide a platform for discussion and stimulation of ideas in this relatively untapped research area.

## Attributes and Potential of Fluvial Sediment Archives for Micro-XRF Analysis

### *Attributes*

The sedimentological characteristics of sediments in fluvial environments depend on discharge, channel gradient, depositional energy environment, channel geometry, sediment supply and catchment characteristics. Coarse gravelly sediments are usually only mobile during flood flows and, unless the event is especially large, sediment is generally deposited on the channel bed or on bar surfaces. Fine-grained sediments (clays, silts and sands) are transported in suspension or as bedload under a much wider range of flow velocities, and during flood events these sediments will commonly be transported in overbank flows beyond the confines of the river

channel itself. Here, flow depths are shallower, boundary roughness is higher, and corresponding flow velocities and turbulence are significantly reduced. The result is the transport of predominantly fine-grained sediments to floodplain, floodbasin, palaeochannel and wetland environments, and modes of deposition that produce horizontal or sub-horizontal sedimentological structures more suitable for micro-XRF analysis (Table 8.1). These fine-grained deposits may be intercalated with coarser rippled and cross-bedded layers associated with crevasse splays and sand-gravel sheets formed during larger flood events. As well as catchment-scale drivers, autogenic lateral and vertical adjustments associated with channel migration and incision/aggradation, respectively, will influence sedimentological characteristics (Lewin 1978, 1996). In more dynamic fluvial settings and over extended timescales, fluvial sediment archives can therefore be highly heterogeneous and somewhat discontinuous in nature, owing to winnowing, reworking and erosion. Although similar influences can result from marine bottom and slope currents, and under hyperpycnal flows in lakes, transformative effects in fluvial environments are often encountered over relatively limited ($10^0$–$10^3$ m) spatial extents, leading to fragmentation of fluvial records. A critical consideration in interpreting fluvial archives is therefore relative channel position and in laterally active systems, the potential for preservation of extended palaeoenvironmental records may be significantly reduced (Lewin and Macklin 2003).

In low energy alluvial contexts (e.g. floodplains, floodbasins, palaeochannels and wetlands), sedimentation processes are invariably pulsed or episodic because they are linked to the frequency and magnitude of overbank flows. In humid temperate regions flood events may occur several times every year (Wolman and Miller 1960), but can be considerably less frequent in dryland zones (Tooth 2000). In most hydro-climatic settings the dynamics of overbank vertical sedimentation typically limit the potential for recovery of seasonal resolution, and in most instances annual sedimentation records. At the same time, sediment archives of flood events offer potential for flood reconstruction, including the tracking of extreme events (Baker et al. 1983), and in catchments with limited instrumented hydrographic records this may be the only means of establishing historical flooding patterns and trends (Benito et al. 2004). Because flood sediments are laid down by flowing water, they display both vertical and horizontal gradation in particle size that can provide valuable information on relative flood magnitudes. However, extracting information about flood magnitude-frequency relationships from alluvial archives has previously been hindered by a lack of suitable techniques. This is particularly the case in predominantly fine-grained (silt and clay-sized) sediments for two reasons. First, identification of the boundaries between the deposits of successive floods is frequently not possible. Second, the thickness of sediment deposited in many flood events may be of the order of a few millimetres or less, making destructive analysis of sediment grain-size impractical, even supposing that the deposits of individual events could be distinguished. Non-destructive micro-XRF analysis therefore provides the potential for reconstructing millennial-length palaeoflood histories from fine-grained alluvial sediments (Jones et al. 2010).

**Table 8.1** Depositional fluvial environments and their palaeoenvironmental potential

| | Structure | Texture | Preservation potential | Post-depositional modification | Palaeoenvironmental records | Micro-XRF potential |
|---|---|---|---|---|---|---|
| Within channel sedimentation | Variable—form and scale dependent on associated topographic feature(s)<br>Strongly influenced by river dimensions | Typically contains the coarsest clastic sediment<br>Spatially variable | Readily reworked<br>Preservation through burial | Winnowing of fines from interstices | May contain woody debris for dating | Difficult to core and unsuitable for scanning unless fine-grained<br>May provide basal dating control |
| Slackwater sedimentation | Planar horizontal/sub-horizontal, cross-bedded | Varies, usually fine – medium, but may contain coarse units/layers | Contingent on in-channel flow dynamics<br>Can be excellent with potential for stacked records | Physical erosion, possibly stripping<br>Leaching of labile elements | Individual or stacked records of high magnitude floods | Moderate to good, depending on texture and preservation of sedimentary record |
| Floodplain: lateral accretion | Variable—form and scale dependent<br>Planar horizontal/sub-horizontal, cross-bedded | Coarser, bed-type and channel marginal sediments. Typically fining upwards with fines contained in interstices of clast-supported matrix | Preservation through channel incision or burial<br>May be reworked regularly in laterally active channel belt | Migration of fines likely through fluctuating water table | Woody debris<br>Possibly contaminants<br>Floodplain development | Low suitability but may form integral part of composite floodplain records |
| Floodplain: vertical accretion | Planar horizontal, sub-horizontal and occasionally cross-bedded | Typically fines (<2 mm), comprising clay, silt and sand<br>Possibly coarser layers linked to large floods and/or splays | Good preservation through burial | Element mobility due to water table fluctuations and redox (Eh/pH) changes<br>Pedogenic processes and bioturbation could lead to blurring of record | Overbank flood events linked to magnitude<br>Pollution histories<br>Sedimentation dynamics | Moderate to high depending on continuity, preservation |

**Table 8.1** (continued)

| | Structure | Texture | Preservation potential | Post-depositional modification | Palaeoenvironmental records | Micro-XRF potential |
|---|---|---|---|---|---|---|
| Palaeochannel | Planar horizontal to cross-bedded | Typically fines (<2 mm), with basal coarse lag deposit<br>High organic content | Burial leads to good preservation | Water table fluctuations will alter redox state<br>Possibly winnowing of fines if intermittently active | Flood records<br>Pollution histories<br>Floodplain development Dateable organics | Moderate to high<br>Potentially influenced by high organic matter and water content |
| Floodbasin | Planar horizontal | Typically very fine silt and clay, with organics | Good preservation through burial | Water table influences and bioturbation could lead to blurring of record | Often longest records of flood frequency and magnitude<br>Sedimentation<br>Pollution histories | Moderate to high—influenced by high organic matter and mixing |
| Wetland | Planar horizontal | Typically very fine silt and clay, with organics | Good preservation through burial | Water table influences and bioturbation could lead to blurring of record | Sedimentation and pollution histories | Moderate to high but may be strongly influenced by organic matter |
| Alluvial fan | Planar horizontal/ sub-horizontal, cross-bedded | Typically coarse with fine layers | Good in an aggrading system | Reworking | Erosion histories and flooding | Low because of coarse texture |

## *Potential*

The potential and role of fluvial deposits as palaeoenvironmental archives is contingent on the preservation of primary depositional signatures. An understanding and interpretation of structural, sedimentological and chemostratigraphic information gleaned from micro-XRF scanning must, therefore, take into consideration post-depositional modifications and significant changes to sediment physico-chemical properties. Longstanding community and societal links to rivers mean that floodplain settings often have a history of human contact and disturbance (Downs and Gregory 2004). Tillage of floodplains, in particular, can lead to mixing and destruction of flood event layers in the upper 20–30 cm and will inevitably lead to the loss of high resolution records. Similarly, surface sediment degradation can arise from grazing through compaction, churning and poaching by livestock, especially when these activities occur in boggy, waterlogged settings. When considering palaeoenvironmental potential of fluvial sedimentary archives it is therefore essential not only to consider present land-use practices, but also past disturbance that may have occurred during phases of floodplain accretion and compromised sub-surface unit preservation.

In addition to anthropogenic influences, and arguably more important and widespread, are changes to original alluvial architecture and geochemistry resulting from soil-forming pedogenic processes. Soils will develop on land surfaces that are exposed to atmospheric and biological processes for a sufficient length of time, and the types of soil(s) found in alluvium will depend on parent material, the age and preservation of alluvial units and local rates of soil development (Gerard 1987). Young soils that retain fluviatile architecture such as horizontal banding (known as fluvents or fluvisols) (Fig. 8.1), can transform over extended periods of time into mature soils similar to those found on interfluves, often altering geochemical properties and losing primary depositional signatures in the process.

In terms of the dynamics of soil development in alluvial settings, a key driver is the balance between processes responsible for the addition of organic matter through biological activity (*melanization*) and the build-up of predominantly minerogenic sediment through aggradation (*cumulization*) (Carter et al. 2009). These influences are schematically illustrated in Fig. 8.2, showing the formation of distinctive sediment-soil assemblages related to time and rates of accretion. Although there are no definitive rates of change that might predetermine the patterns observed, Alexandrovskiy et al. (2004) found that well-developed surface A-horizons would not form where sedimentation rates exceeded 1 mm year$^{-1}$. In British and Irish catchments, sedimentation rates have typically exceeded this threshold for much of the Holocene, but especially from the eleventh century AD onwards when agriculturally-induced erosion led to a step change in sediment supply to rivers (Macklin et al. 2010; Turner et al. 2010). With similar sedimentation dynamics observed in continental Europe (Szmańda et al. 2004), many floodplain soils are cumulic in nature and the identification of well-preserved

**Fig. 8.1** Remnant flood layers in river bank alluvium can be seen in a cut bank section of the River Severn at Caesws, Powys, Wales. The bank sediment texture is predominantly fine silt and clay. (Source: AF Jones)

buried soils (palaeosols) is rare, particularly in late-Holocene alluvium. Micro-XRF technologies that could assist in the recognition of poorly-developed buried A-horizons, especially those that have been degraded by subsequent pedogenesis, would therefore be of value to scientists, not only to provide information on past

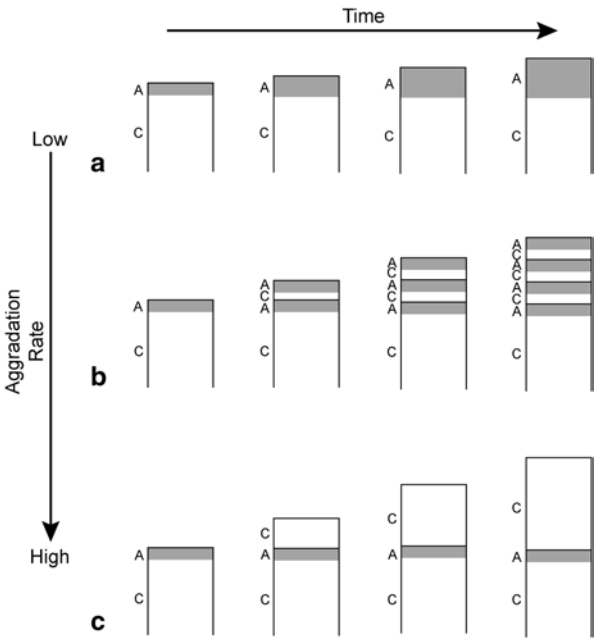


**Fig. 8.2** Schematic diagram of alluvial pedofacies models showing **a** cumulic soil profile, **b** multiple buried soils, **c** deposition exceeding the rate of pedogenic assimilation. (Reprinted from Daniels (2003), with permission from Elsevier)

fauna, flora and environmental conditions, but because $^{14}$C-dateable upper horizons of palaeosols mark critical junctures from vertical stability to increased sedimentation linked to the onset of flooding over Holocene timescales (Macklin and Lewin 2003).

## Materials and Methods

Coring of floodplain sediment sequences was undertaken at three sites in the UK and Ireland using a motorised percussion corer. Cased 50 mm cores were recovered in 1 m sections and sealed at each end immediately after extraction; they were subsequently transported and stored in a horizontal position. Cased cores were initially split in half lengthwise using a circular saw to cut through the plastic tubing and either a nylon wire or brass plates were used to split the sediment core into two halves. One half of the sample was designated as the archive half and was prepared for scanning using the Itrax core scanner and subsequently stored. The other half of the split core was sub-sampled for geochemical and particle size analysis and also used for the recovery of organic material for radiometric dating. Organic samples were dated by Beta Analytic Inc. and the results calibrated using OxCal version 4.1 (Ramsey 2009) and the IntCal09 calibration curve (Reimer et al. 2010); the 2 sigma ranges of the results are reported.

Micro-XRF analysis and optical/radiographic imaging was carried out using two Itrax core scanner instruments (c.f. Croudace et al. 2006) housed at Aberystwyth University, Wales, and University College Dublin, Ireland. Instrument settings were optimised using selected core sections to minimise the mean square error (MSE) values and step-lengths were based on sediment texture; 1 mm for sand-rich sediments and 0.5 mm for clay/silt-rich sediments. Count times for micro-XRF analysis ranged from 10 to 30 s.

## Case Studies

### *Flood Reconstruction Using Itrax XRF Profiles*

#### Introduction

The characteristics of fluvial sediments, in particular grain-size, are determined by the floods that deposited them. Analysis of these sediment sequences may therefore yield information about flood magnitude-frequency relationships during the period of deposition (Knox 1993, 2003; Macklin et al. 1992; Werritty et al. 2006). Such information is particularly desirable due to the short lengths of instrumental and historical records of flooding and the low frequency of the highest-magnitude, and therefore most destructive and costly, floods. Thus far, extracting information about flood magnitude-frequency relationships from the alluvial archive has been hindered by a lack of suitable techniques. This is particularly the case in silt- and clay-sized sediments because identification of the boundaries between the deposits of successive floods is frequently not possible and the thickness of sediment deposited in many flood events is of the order of a few millimetres, making destructive analysis of sediment grain-size at the event scale impractical. Non-destructive micro-XRF analysis therefore provides the potential for reconstructing millennial-length palaeoflood histories from fine-grained alluvial sediments.

#### Geochemical Grain-Size Proxies: Zr/Rb and Zr/Ti

A number of element ratios have previously been used as proxies for grain-size in the palaeo-environmental interpretation of sediment sequences, including Si/Al, Ti/Al, Zr/Al, Zr/Ti and Zr/Rb (e.g. Calvert et al. 1996, 2001; Dypvik and Harris 2001; Oldfield et al. 2003). However, detection limits of Si and particularly of Al are relatively poor in Itrax XRF analysis, rendering some of these element ratios unsuitable for use as grain-size proxies with this technique. For this reason, Zr/Rb and Zr/Ti were chosen for use in reconstruction of flood records. The Zr/Rb ratio has been used as a sediment grain-size proxy in marine (Dypvik and Harris 2001), lacustrine (Kylander et al. 2011), subaqueous deltaic sediments (Wang et al. 2011) and in loess (Chen et al. 2006). The Zr/Ti ratio has also been used as a grain-size proxy in lacus-

trine sediments (Oldfield et al. 2003). During transport by water or wind Zr, Rb and Ti tend to become concentrated in particular grain-size fractions due to the varying resistance of the minerals in which these elements principally occur. Zr tends to become concentrated in the fine sand and coarse silt fractions, Ti in somewhat finer fractions and Rb principally in the finest silt- and clay-sized fractions (Veldkamp and Kroonenberg 1993; Dypvik and Harris 2001; Oldfield et al. 2003). Zr/Rb or Zr/Ti ratios therefore increase as sediment grain-size increases. These three elements are relatively immobile in the surficial environment (Rose et al. 1979; Hardardóttir et al. 2001) and sediment Zr/Ti and Zr/Rb profiles should therefore retain the primary depositional signal. Micro-XRF profiles of Zr/Rb and Zr/Ti in floodplain sediments can hence be used to identify the deposits of the highest-magnitude floods which have occurred within the period of deposition and to provide a record of relative flood magnitudes through time. These data may be combined with sediment dating techniques and instrumental or historical flood records to constrain estimates of the frequencies and magnitudes of infrequent high-magnitude floods and of temporal variations in flood frequency during recent centuries and millennia.

## The Upper Severn Catchment

The upper Severn catchment is underlain principally by Lower Palaeozoic mudstones, greywackes and sandstones. Cores were obtained from three floodplain locations (Fig. 8.3 and Table 8.2). The Caersws Sports Ground and Red House-Dolhafren sites both fall within the upper Severn Geological Conservation Review (GCR) site, which has been described as "the epitome of a laterally unstable gravel-bed river in Wales" (Hey 1997, p. 152). Palaeochannels within this reach contain relatively thick (ca. 1–3 m) fine-grained fills overlying gravels of the former channel bed and six cores were recovered from this type of environment at Red House-Dolhafren. At Caersws Sports Ground two cores were recovered close to the present river channel bank. Overlying the basal gravels, the sediment sequence at this site consists of layered sands and silts which are further overlain by a unit of sandy clayey silt over 40 cm thick. Finally, the Roundabout site lies within the Roundabout GCR site (Higgs 1997). The thick (>5 m) floodplain sediment sequences in this low-gradient, highly sinuous stable reach consist predominantly of silt and clay. Cores were recovered from two palaeochannels. A record of historical flood levels beginning in 1672 is available for Shrewsbury ca. 50 km downstream of the Roundabout; the highest-magnitude floods in this record occurred in 1770 and 1795.

## Sediment Grain-Sizes and Geochemistry

Before micro-XRF profiles of Zr/Rb or Zr/Ti are used to produce a palaeoflood record, it is necessary to test whether these element ratios are suitable grain-size proxies at the study site. This is done by comparison with actual grain-size values, since factors other than grain-size may influence the distributions of these elements

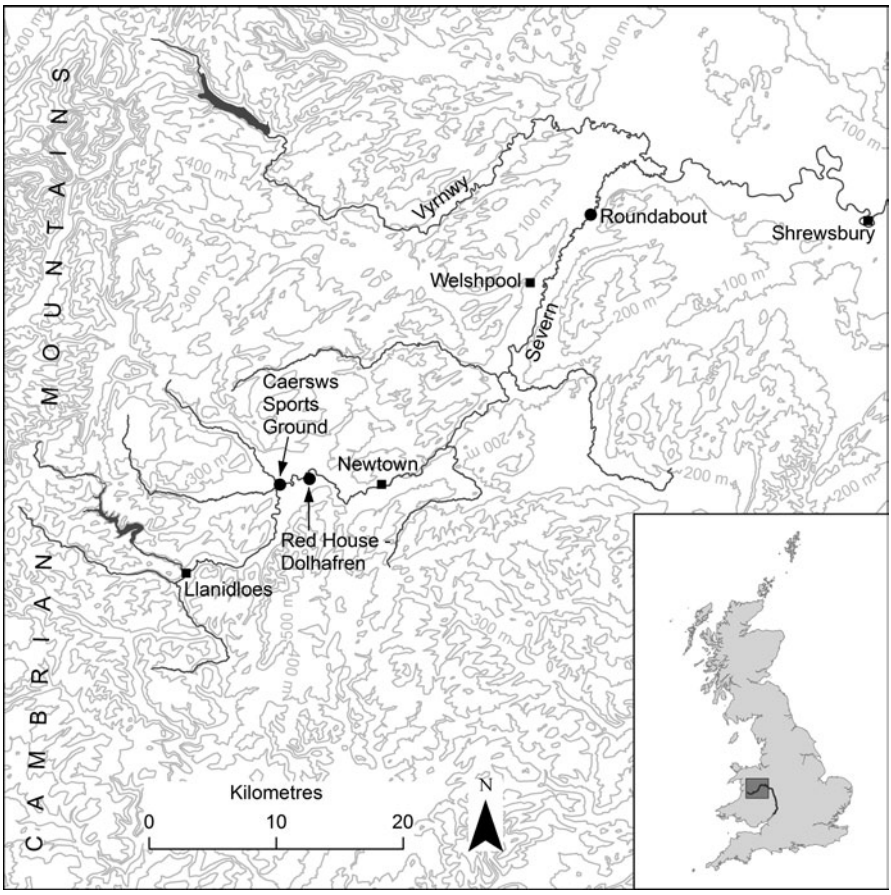


**Fig. 8.3** Location of the Caersws Sports Ground, Red House-Dolhafren and Roundabout sites in the upper Severn catchment

in sediment (Dypvik and Harris 2001). The grain-size proxies are presented as log-ratios of element intensities, following Weltje and Tjallingii (2008). The use of log-ratios with compositional data overcomes the constant sum constraint and transforms the data from the simplex into Euclidean real sample space, permitting rigorous statistical analysis (Aitchison 1982; Weltje and Tjallingii 2008). In addition, it has been shown that log-ratios of XRF intensities in which Itrax XRF results are produced are linearly related to log-ratios of absolute concentrations (Weltje and Tjallingii 2008). Correlation of the two grain-size proxies with actual grain-size data for samples between 5 and 10 mm thickness from the three sites in the upper Severn catchment illustrates the variations which may occur in their suitability within a single catchment (Fig. 8.4 and Table 8.2). Grain-size data are presented as log-ratios of the percentage of sediment in different size fractions. Log-ratios were calculated for each possible combination of 0.5 Φ size fractions, with the

**Table 8.2** Site characteristics, sediment type and suitability of the two grain-size proxies for application at the three sites on the upper Severn, mid-Wales

| Site | Grid reference | Site characteristics | Sediment characteristics | Correlation of proxies with actual grain-size |
|---|---|---|---|---|
| Caersws Sports Ground | SO 029917 | Cores recovered from close to channel bank. Sediment accumulated over gravel bar close to confluence of Severn with Carno. Channel highly laterally active. Channel gradient 0.0027 $mm^{-1}$ | Lower part of sequence consists of alternating sandy and silty layers overlying gravels. Sand layers contain occasional clasts. Upper part of sequence lacks obvious layering and consists of sandy silt. Overall grain-size is bimodally distributed. Modes: fine sand (21.5%) and fine silt (15.01%) | ln(Zr/Ti) is weakly correlated with grain-size—highest positive correlation coefficient = 0.28<br>ln(Zr/Rb) is negatively correlated with actual grain-size—strongest correlation = −0.84. This is the reverse of what is expected<br>Neither grain-size proxy is suitable for use in these sediments $N = 20$ |
| Red House-Dolhafren | SO 0592 | Palaeochannels on surfaces of three river terraces, all of which are at least partially inundated on a regular basis. Channel highly laterally active. Channel gradient c. 0.002 $mm^{-1}$ | Predominantly silts and clays although sands and gravels occur generally towards the base of palaeochannel fills. In some locations organic deposits are intercalated with minerogenic sediments. Unimodal grain-size distribution. Mode: fine silt | ln(Zr/Rb) weakly correlated with actual grain-size (coefficients between 0.25 and −0.38), strongest positive correlation not statistically significant—unsuitable as a grain-size proxy at this site<br>Sixty four significant positive correlations (coefficients up to 0.45) between grain-size log-ratios and ln(Zr/Ti), 22 of these significant at 1% level. ln(Zr/Ti) could be used as a grain-size proxy at this site but the strength of the relationship with actual grain-size is rather weak<br>$N = 38$ |
| Roundabout | SJ 2713 | Channel exhibits high degree of lateral and vertical stability. Low width-depth ratios. Low gradient (0.0004 $mm^{-1}$). Vertical accretion dominant on floodplain. Valley floor c. 2 km wide. Cores taken from palaeochannels and floodplain | Predominantly silts and clays. Occasional sandy or gravelly layers at base of palaeochannels or as a result of large floods. Wood and occasional peaty sediments exist in cores c. 1.5 km from channel. Close to modern channel sediments poor in organics. Unimodal grain-size distribution. Mode: fine silt | 101 significant positive correlations (coefficients up to 0.86) between grain-size log-ratios and ln(Zr/Rb), including 57 at the 0.01% level. Suitable for use as a grain-size proxy at this site<br>Thirteen significant positive correlations (coefficients up to 0.46) between grain-size and ln(Zr/Ti), including only two at 1% level. Strongest correlation between the log-ratio of the two very fine sand fractions (3.0–3.5 ϕ and 3.5–4.0 ϕ) and ln(Zr/Ti) not suitable for use as a grain-size proxy at this site<br>$N = 37$ |

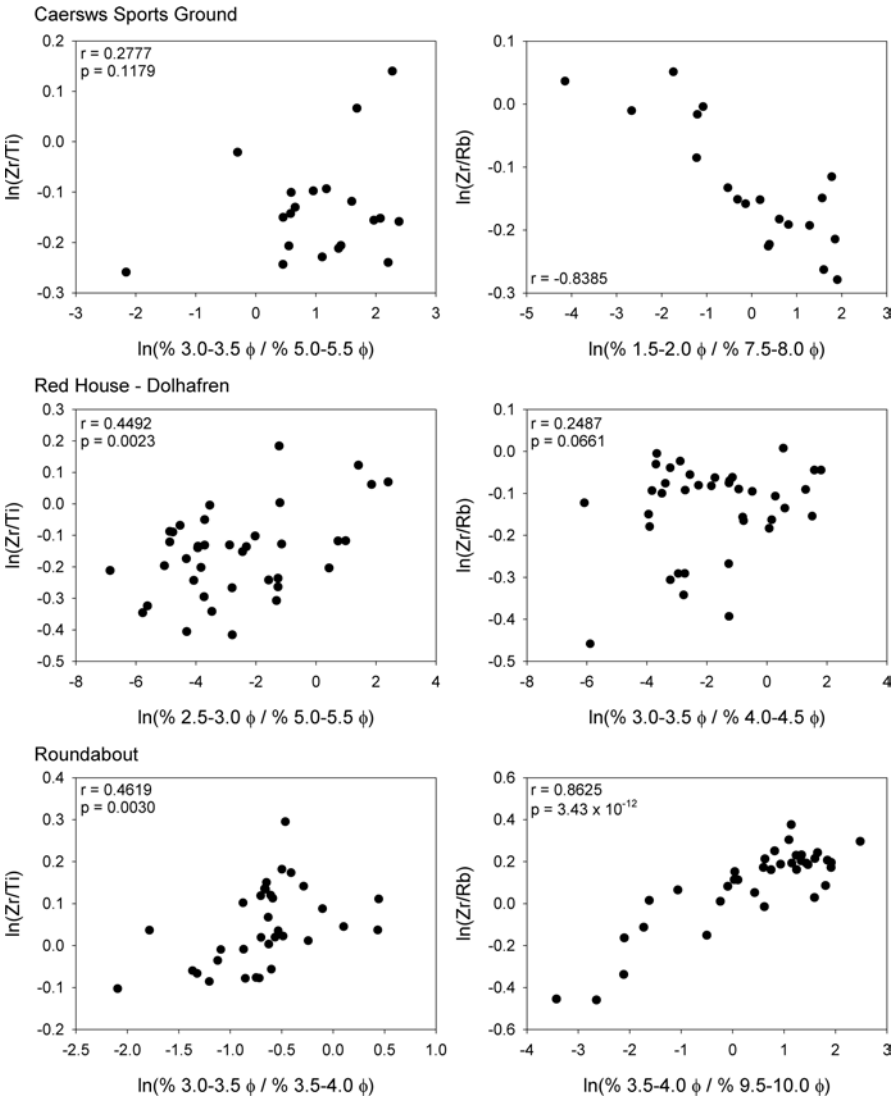


**Fig. 8.4** Comparison of ln(Zr/Ti) and ln(Zr/Rb) with grain-size log-ratios at the three sites in the upper Severn catchment. At Caersws Sports Ground correlations between ln(Zr/Ti) and grain-size are generally weak (strongest correlation shown *top left*), while those between ln(Zr/Rb) and grain-size are strongly negative (strongest negative correlation shown *top right*), contrary to what would be expected. Neither grain-size proxy is suitable for use at this site. At Red House-Dolhafren, correlations between ln(Zr/Rb) and grain-size log-ratios were weak (strongest correlation shown *middle right*) and not statistically significant. Sixty-four statistically significant positive correlations were found between ln(Zr/Ti) and grain-size log-ratios at this site, although the correlation coefficients are not high (most significant correlation shown *middle left*). At Red House-Dolhafren ln(Zr/Ti) may be suitable as a grain-size proxy but ln(Zr/Rb) is not. At the Roundabout only 13 statistically significant positive correlations were found between grain-size log-ratios and ln(Zr/Ti). As the most significant of these was with the log-ratio of the coarser to the finer of the fine sand fractions (*bottom left*) ln(Zr/Ti) is not considered to be a suitable grain-size proxy at this site. Between grain-size log-ratios and ln(Zr/Rb) 101 significant positive correlations were found. Correlation coefficients ranged up to 0.86 and *p*-values as low as $3.43 \times 10^{-12}$ (*bottom right*). ln(Zr/Rb) is a suitable grain-size proxy for sediment sequences at the Roundabout

larger grain-size fraction used as the dividend and the smaller as the divisor. Since increasing grain-size should result in increasing ln(Zr/Rb) and ln(Zr/Ti) if they are suitable grain-size proxies, a one-tailed test was used to evaluate the significance of the Pearson correlation coefficients. The results indicate that neither ln(Zr/Ti) nor ln(Zr/Rb) is a suitable grain-size proxy for the Caersws Sports Ground site (Fig. 8.4). At Red House-Dolhafren, ln(Zr/Ti) is significantly positively correlated with grain-size, although the correlations are not strong, but ln(Zr/Rb) is not a suitable grain-size proxy. At Roundabout ln(Zr/Ti) is not a suitable grain-size proxy, whereas the large number of highly significant strong positive correlations between ln(Zr/Rb) and grain-size indicate that it is a suitable grain-size proxy for reconstructing flood histories (Table 8.2 and Fig. 8.4).

Source area geochemistry as well as the distance and energy of sediment transport are factors previously identified as affecting the concentration of sediments into their characteristic size fractions during transport (Dypvik and Harris 2001). The negative correlation between grain-size and ln(Zr/Rb) at the Caersws Sports Ground site is probably due to a concentration of Rb-bearing minerals in the sand fraction (cf. Moalla 1997). The sediment at this site is coarser than at the Red House-Dolhafren and Roundabout sites and is also bimodal, with modes in the fine sand and fine silt fractions. The strong positive correlation between sediment grain-size and ln(Zr/Rb) at Roundabout suggests that Zr and Rb have been concentrated into their characteristic grain-size fractions during sediment transport to this downstream location. The scatter in the data for ln(Zr/Rb) from the Red House-Dolhafren site is the result of variability in the association between ln(Zr/Rb) and grain-size across the site. This non-systematic spatial variability also accounts for the unsuitability of ln(Zr/Ti) as a grain-size proxy at both the Red House-Dolhafren and Roundabout sites. The variability is probably caused by one or more of the following factors, *viz.* temporal variation in sediment provenance and in hydraulic sorting, and spatial variation in post-depositional alteration of the sediment sequence. Detailed investigations at the scale of individual cores may permit application of this method at sites such as Red House-Dolhafren.

### Flood Record Derived from Micro-XRF Analysis

The ln(Zr/Rb) profile of Roundabout Core 7 provides an example of a flood record obtained using this method (Fig. 8.5). A single flood may be represented by multiple peaks in ln(Zr/Rb), as a result of the occurrence of multi-peaked rainfall events or the arrival at the site of flood peaks from the various sub-catchments at different times. The highest-magnitude floods produce a series of peaks in ln(Zr/Rb), accompanied by an increase in mean ln(Zr/Rb) as a result of the increase in the percentage of coarse-grained sediment (e.g. at 2527 mm depth). Interpretation of the ln(Zr/Rb) profile requires an understanding of the degree of vertical and lateral river channel stability during the period of accretion and of the processes of floodplain development which have operated at the site (see Table 8.2). Historical maps and aerial photographs and ground-penetrating radar data from the Roundabout indicate that the channel has been highly stable, both laterally and vertically, during

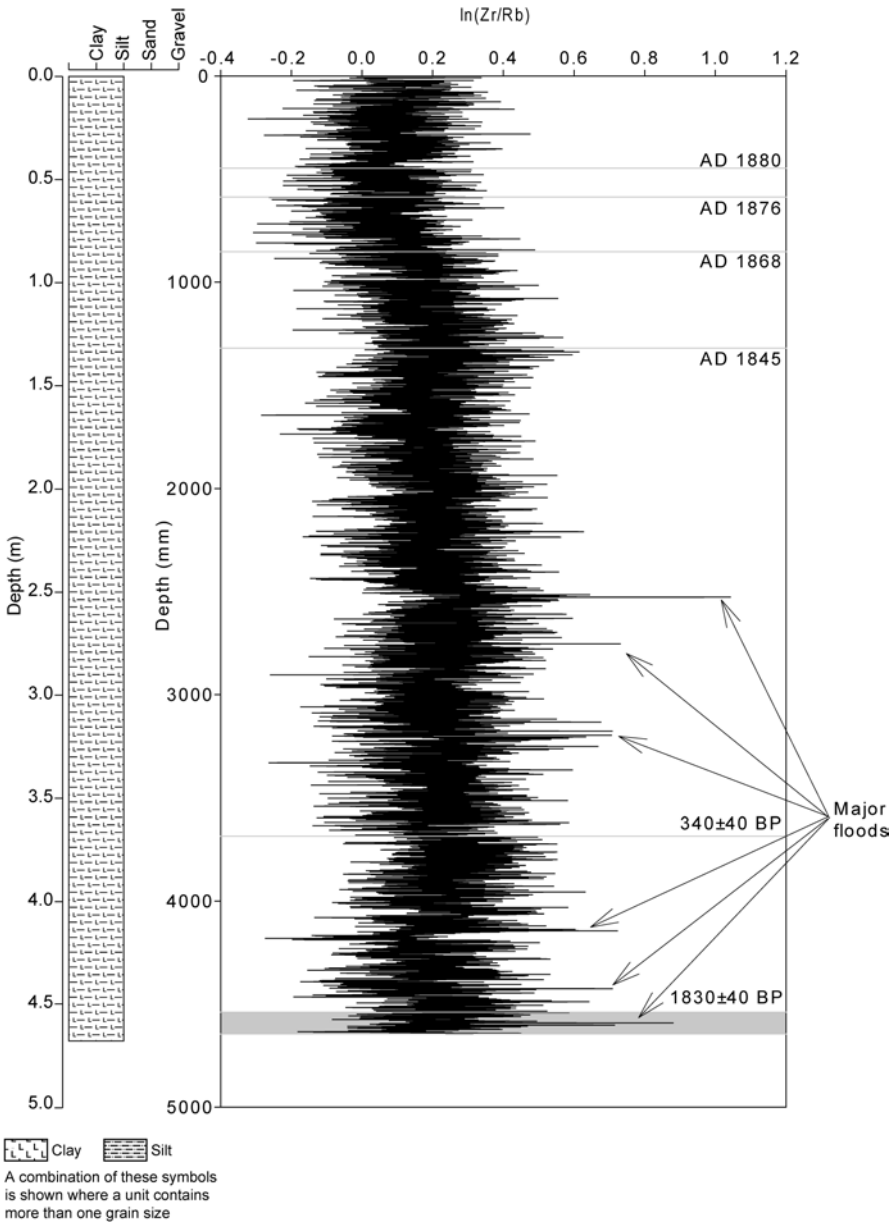


**Fig. 8.5** Profile of ln(Zr/Rb) in Roundabout Core 7. Four dates have been assigned to the upper part of the core based on comparison of the Pb profile with catchment mine production records. Two samples from the lower part of the core were radiocarbon dated

recent centuries and possibly for a much longer period of time. This, combined with frequent inundation due to a relatively small channel capacity, has resulted in the dominance of vertical accretion, which has been rapid during the past ca. four centuries (Fig. 8.5). The highest-magnitude floods identified in this ln(Zr/Rb) profile occurred prior to AD 1845 (date assigned using comparison of the Pb profile with catchment mine production records). The largest event in the profile occurred between deposition of the sample radiocarbon-dated to 340 ± 40 BP (490–300 cal. BP; cal. AD 1460–1650) and AD 1845. A record of a second major flood is found in the profile 227 mm below the highest-magnitude flood at 2754 mm depth. The location of these peaks in ln(Zr/Rb) indicates that they represent the two largest floods in the historical flood record at Shrewsbury which occurred in AD 1770 and AD 1795. Evidence for a number of major floods prior to the commencement of the record of historical flood levels at Shrewsbury is found in peaks in ln(Zr/Rb) in the lower part of the core (below the upper radiocarbon-dated sample). This includes the second largest peak in the ln(Zr/Rb) profile which lies within the depth range from which the lower radiocarbon-dated sample was recovered. The ln(Zr/Rb) profile may therefore provide information of use for flood risk assessment. For example, the data suggest that the flood recorded at 2527 mm depth, previously suggested to be one of the major floods of the late eighteenth century, may have been the largest which has occurred at the site during approximately the past 1800 years.

## *Contaminant Profiling and Provenance Using Itrax XRF*

### Introduction

The dispersal and storage of contaminant metals in fluvial systems has been intensively researched by geomorphologists, geochemists and soil scientists since the 1970s (see reviews by Macklin 1996; Macklin et al. 2006). A critical element of this research has been the recognition that more than 90 % of metal contaminants in rivers are transported in a particulate-associated form (Martin and Meybeck 1979; Miller 1997) and, therefore, follow the same transport pathways as the natural sediment load of a river (Miller 1997). An integrated understanding of geomorphology and geochemistry enables the detailed reconstruction of temporal and spatial river channel dynamics, such as contaminant dispersal. Additionally, the chemostratigraphy in floodplain sequences helps to constrain sedimentation rates/chronologies (Turner et al. 2008), investigate river system response to environmental change (Macklin 1996), reconstruct flood histories (see above), and model sediment provenance (Bird et al. 2010). The advent of micro-XRF core scanning now affords the opportunity to undertake these investigations at temporal resolutions hitherto unachievable.

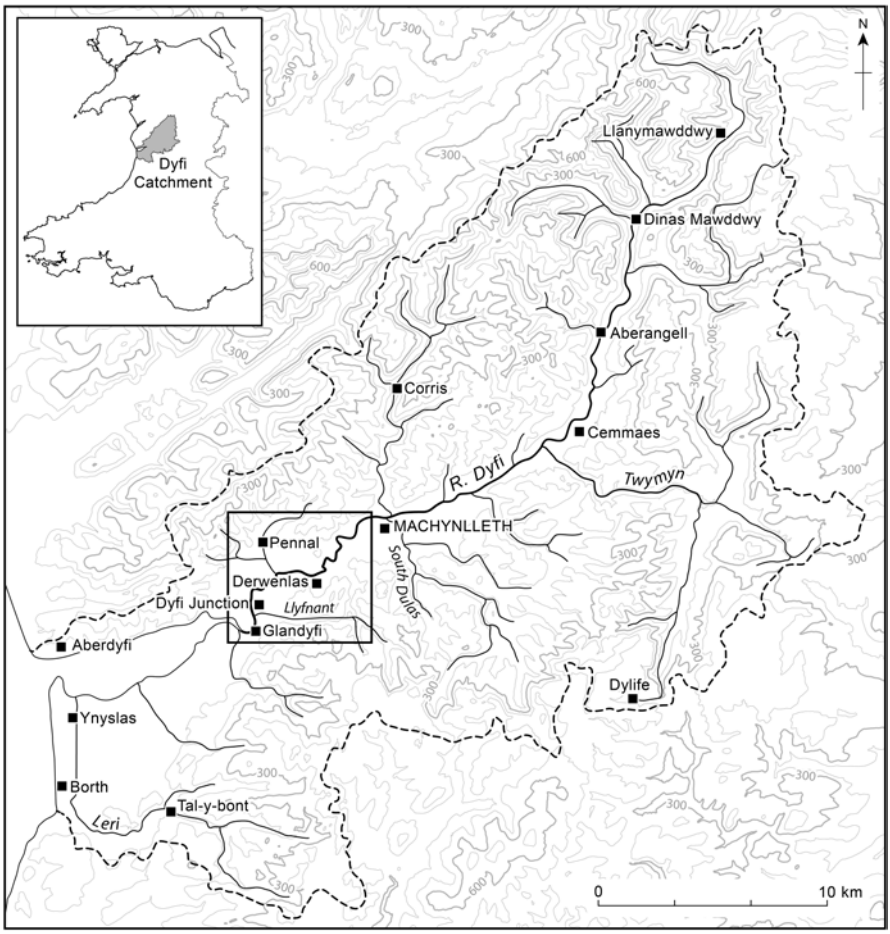


**Fig. 8.6** Location of the study site in the Dyfi Cathment, Wales, UK

## The Tidally Influenced Lower Dyfi

The Afon Dyfi rises at 655 m on the western flanks of the Cambrian Mountains and flows southwest for 47 km until it enters the Dyfi estuary on Cardigan Bay (Fig. 8.6). The underlying geology is Silurian turbiditic mudstones and grits of the Llandovery Series, but of geochemical significance is the presence of igneous rocks in the northern part of the catchment, and part of the Central Wales Orefield in the west and southwest. The main minerals worked in the orefield were galena (PbS), sphalerite (ZnS) and chalcopyrite ($CuFeS_2$) (Howells 2007). The largest and most productive mine was at Dylife in the Twymyn catchment that was probably first exploited in Roman times, but the main phase of mining activity was in the mid to late-nineteenth century.

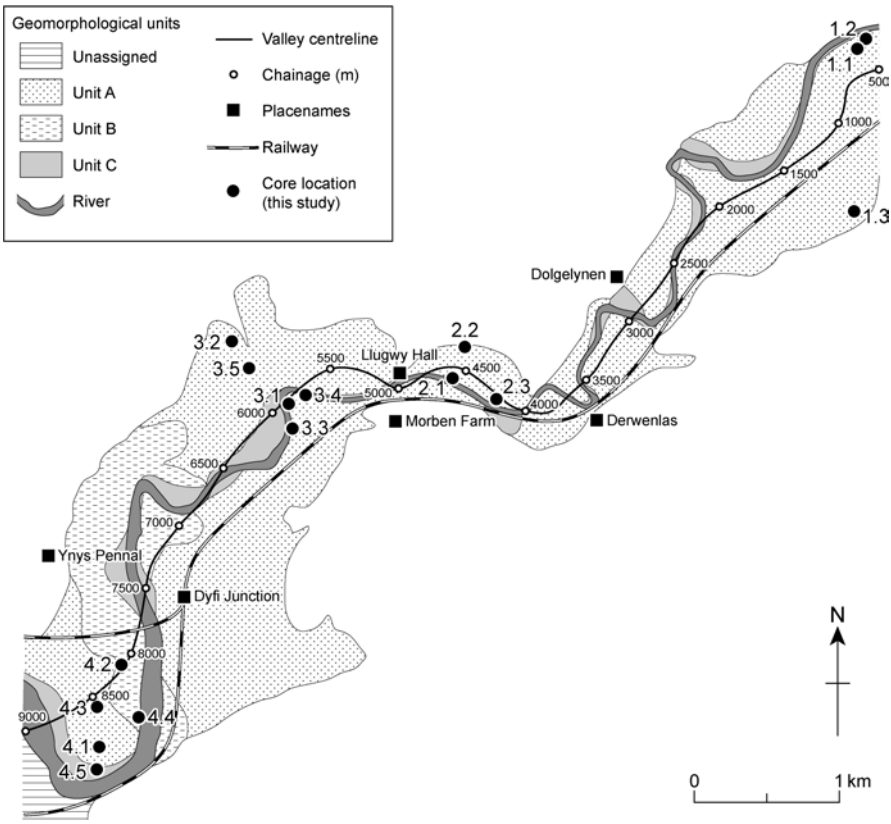


**Fig. 8.7** Geomorphological units and coring sites in the river-estuary transition zone of the Afon Dyfi. Unit A aggradation started c. 5400 years BP and was punctuated with a phase of incision between 1100 and 920 cal BP. Unit B aggradation was initiated between 920 and 730 cal BP. Unit C aggradation post-dates 1844

Morphodynamics in non-tidal rivers and estuaries have been widely researched and documented by fluvial geomorphologists and coastal scientists, respectively. However, relatively little geomorphological-geochemical research has been undertaken in tidally-influenced river reaches despite their obvious vulnerability to the effects of climate and sea-level change. Sediment cores, ranging from 2 to 5 m in length, were recovered from 18 sites in the downstream part of the Dyfi River that is still under tidal influence (Fig. 8.7). Organic material present in the cores was $^{14}C$ dated and the cores were Itrax-scanned at either 0.5 mm (silt and clay-rich sediments) or 1.0 mm (sand-rich sediments) resolution. Data are presented here for site 1 (cores 1.2 and 1.3) at Machynlleth upstream of the normal tidal limit and for site 4 (cores 4.1 and 4.3) at Dyfi Junction at the head of the Dyfi estuary.

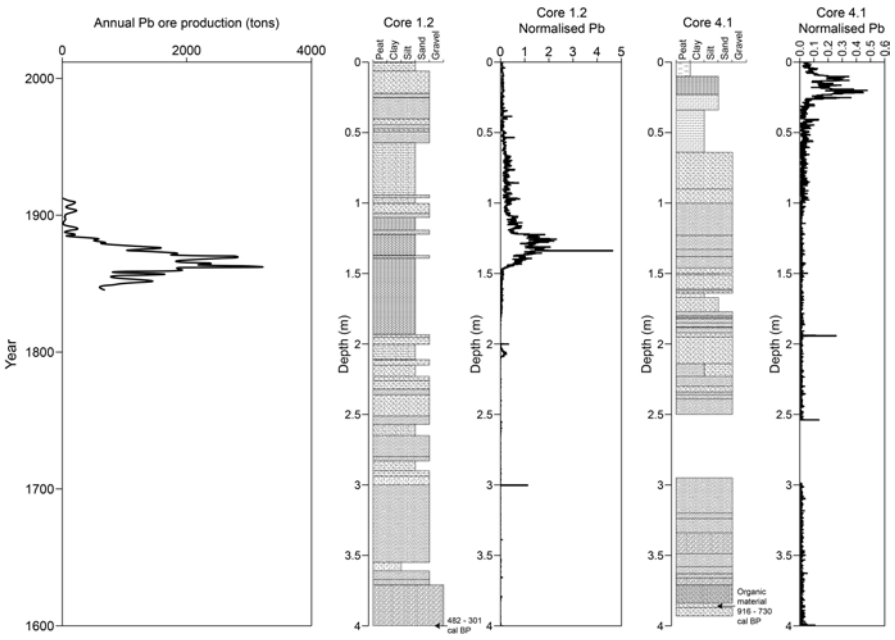


**Fig. 8.8** A comparison of annual lead (Pb) ore production rates in the Dyfi catchment (from Howells 2007) and micro-XRF Pb profiles in selected cores 1.2 and 4.1

## Geochemical Profiles

Figure 8.8 compares Pb ore production data from the Dylife mine and with the downcore Pb profiles at sites 1.2 (channel-proximal levée) and 4.1 (channel-proximal floodplain). The Pb profile from core 1.2 shows a striking similarity to the Pb production curve from Dylife mine suggesting that sedimentation on this part of the floodplain has preserved a near-continuous record of contaminant dispersal and floodplain deposition since the mid-nineteenth century. The Pb profile from the downstream core 4.1 differs from core 1.2 in a number of respects. First, even though elevated Pb values in both cores occur in sedimentologically similar silty units, the levels are lower in core 4.1. This is probably related to the more distal nature of core 4.1 with respect to the Dylife mine, the principal contaminant source in the catchment. Second, peak Pb values are at a shallower depth in core 4.1 (ca. 0.5 m compared to ca. 1.3 m). Since there is no evidence of a discontinuity in the core that might be indicative of erosion, this suggests that the difference in geochemical profile reflects lower sedimentation rates (confirmed by $^{14}C$ dating) on this part of the floodplain (1.4 mm year$^{-1}$ compared to 12.1 mm year$^{-1}$ at site 1.2). Finally, in core 4.1 the Pb curve is flatter, with a more complex profile suggesting that this distal core has received additional Pb-contaminated sediment from some of the mineralised catchments in the lower Dyfi catchment (e.g. Leri and Llyfnant).

**Sediment Provenance**

Although individual micro-XRF element profiles provide valuable information on down-core chemostratigraphy that can be used to reconstruct both the timing and magnitude of contaminant release, dispersal and sedimentation, they do not provide a complete picture of sediment sources within a catchment. To address this issue statistical techniques have been developed which enable geochemical 'fingerprinting', permitting sources of contaminated sediment to be distinguished and mapped (see Collins et al. 1997; Rowan et al. 2000). The fingerprinting procedure employs a two-step statistical selection procedure to create a composite fingerprint, containing the lowest number of diagnostic parameters capable of discriminating between different source groups (in this study a source group is defined as an area of the catchment with a distinct underlying geology) (Fig. 8.9a).

The geochemical character of each source group was established using a hand-held XRF analyzer (NITON XLt 792MZ). Stream and bank sediment samples were collected from 34 sites representative of the source group areas, giving a total of 149 individual samples. Analysis was carried out on the sieved silt and clay fraction (<63 μm) as this best represented the grain-size fraction of the estuarine core samples. XRF measurements were taken with the samples contained in zip-lock bags using the standard bulk mode and a 2 min exposure time. To compare the catchment and micro-XRF core scan data, count data were first converted into concentrations by correlating concentrations measured by hand-held XRF with the corresponding XRF core scan data (counts/Rayleigh scatter ratios), using 15 evenly distributed segments in core 1.3. Only those elements (Mn, Fe, Zn, Rb, Sr and Pb) that displayed a linear relationship between counts and concentrations ($R^2$ values ranged from 0.6 to 0.9) were included in the multivariate discriminant function analysis.

The mixing model (sensu Walling et al. 1999) provides the relative sediment contribution from each of the six geological source groups for five selected stratigraphic layers within cores 1.3 and 4.3 (Fig. 8.9b). The chronology in each core has been established using a combination of $^{14}$C-dated organic material and correlating the micro-XRF Pb profile with the Dylife mine production data (cf. Fig. 8.8). Core 1.3, located in the non-tidal reach of the river, shows that sediment supply from individual geological source groups has remained stable between 3660 BC and the onset of large-scale metal mining in AD 1845. During this period over 50 % of the sediment supplied to core 1.3 was sourced from the south (i.e. the South Dulas tributary) and the central geological source groups. At the peak of mining activity (AD 1860) the importance of the mining (Dylife Mine) source group increased from ca. 20 to 32 %, effectively swamping the sediment supply signal from both the east and north source groups. Following the cessation of mining, the relative proportion of sediments supplied from each geological source group largely reverted back to the pre-mining pattern, albeit with a slightly reduced importance from the east and north source groups.

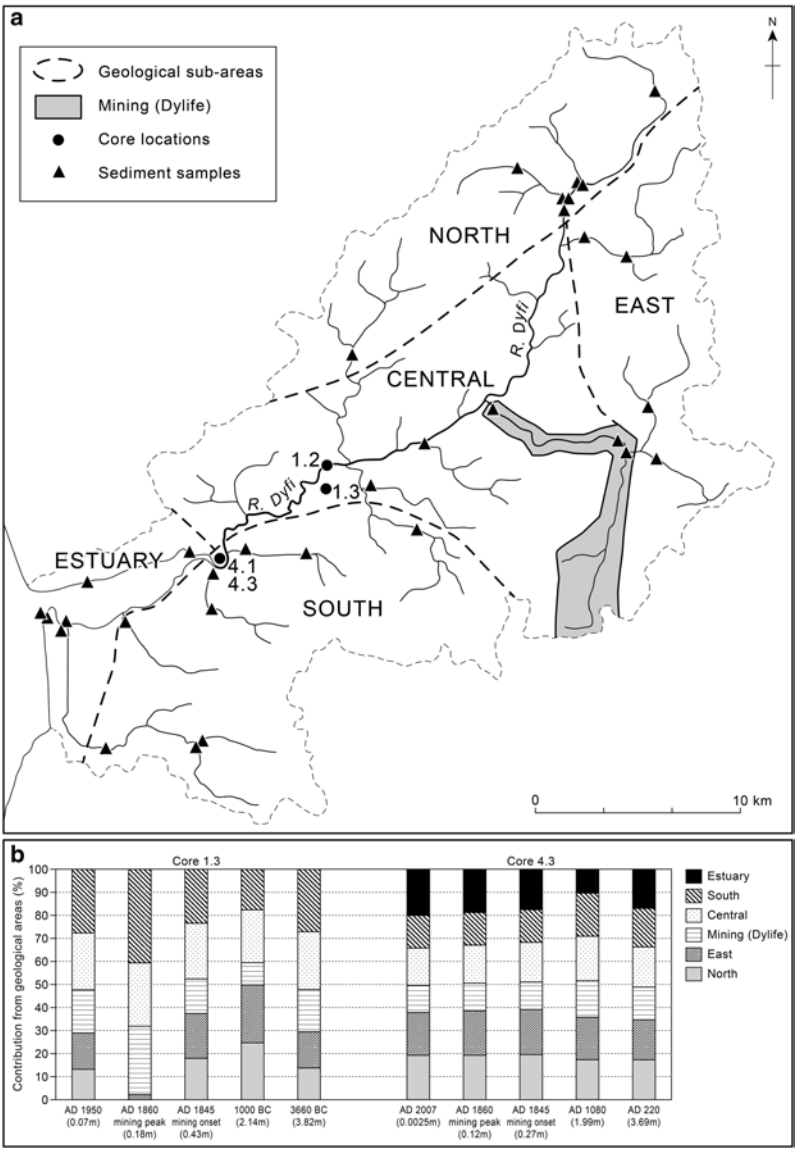


**Fig. 8.9** A division of the Dyfi catchment into geologically distinct areas (source groups) and the location of the two cores used for sediment provenance investigation. The percentage sediment contribution from each source group for selected stratigraphic layers within cores 1.3 and 4.3, based on a multivariate mixing model (bar chart)

Core 4.3, at the head of the Dyfi estuary shows an even greater degree of catchment supply stability over time, and there is no discernible increase in the proportion of sediment supplied from the mining-affected source group even during the mining period (AD 1845–AD 1860). Over the last 1800 years, the proportion

of estuary-derived sediment increased from ca. 11% (AD 1080) to ca. 20% (AD 2007), indicating the increasing influence of tidal sediment deposition in the tidally influenced reach over the last millennium. While these selected down-core results are preliminary and carry errors from the calibration process (discussed in Section "Prospects"), they demonstrate for the first time how micro-XRF analyses and sediment provenance modelling can be used in combination to establish millennial-scale fluvial sedimentation dynamics.

## *Itrax Inferred Patterns of Sand Floodplain Development*

### Introduction

River floodplains operate as sinks or stores in which fluvial sediment accumulates through lateral and vertical accretion (Lewin 1978). They can exhibit high rates of geomorphological modification because of lateral erosion and surface stripping, but where stability is dominant they can offer significant palaeoenvironmental and geoarchaeological potential (Howard and Macklin 1999). Reconstructing the evolution of floodplain deposits is important for a range of environmental research applications, but can be hampered by an absence of topographical surface expression associated with palaeochannels and river terraces due to surface infilling and disturbance. Rapid and non-destructive screening of floodplain sediment cores using micro-XRF analysis has the potential to make an important contribution to our understanding of preservation potential and depositional complexity in floodplain environments.

### Floodplain of the Lower Boyne Valley, Ireland

Cores were taken along a transect of the River Boyne floodplain, 14 km upstream of the World Heritage Site at Brú na Bóinne (Fig. 8.10), as part of a geoarchaeological project carried out for the Irish Heritage Council (Lewis et al. 2009). The Boyne is 112 km long and drains a catchment area of 2694 $km^2$ in the eastern part of the Midlands of Ireland. The catchment is underlain by Dinantian Limestone to the south and Lower Palaeozoic rocks, comprising Ordovician volcanic and meta-sediments to the north. For much of its length the low gradient channel cuts through glacial till and glaciofluvial gravels, which restrict lateral mobility. The coring site was situated at a meander bend where a ca. 80 m-wide Holocene floodplain is bounded by steep valley sides. Regular floods deliver fine-grained sediment (sand and silts) to the floodplain, together with organic detritus and reworked molluscan remains during large flooding events. Coring was informed by LiDAR-based evidence for minor (ca. $<0.1$ m) undulations in slope across the floodplain, believed to be related to former channel position and floodplain development. Itrax analysis was carried out to assist in the interpretation of sedimentation patterns and floodplain development for the purpose of exploring geoarchaeological potential.

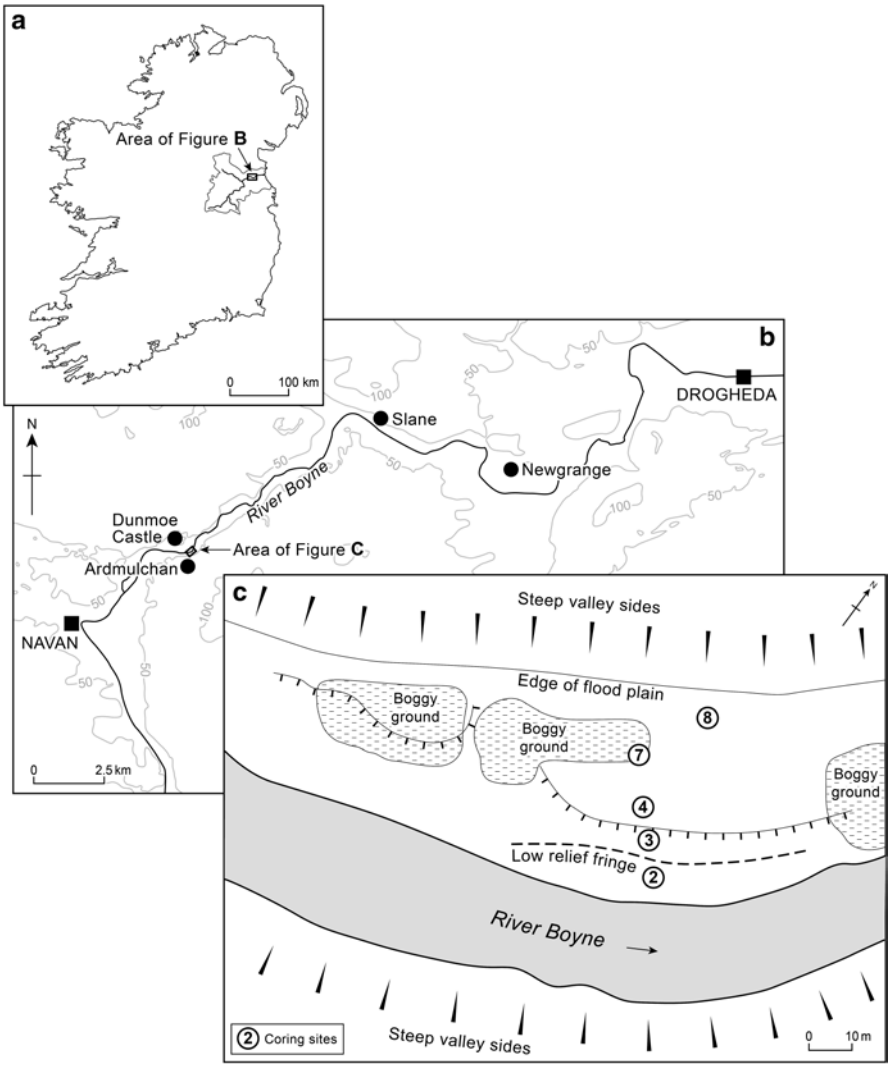


**Fig. 8.10** Location of coring sites along a transect of the River Boyne floodplain, at Dunmoe, Co. Meath, Ireland

## Floodplain Composition

A cross-section of the floodplain was covered by five sediment cores (Fig. 8.11a), although DMO-8 could not be retrieved along the transect line due to ground conditions. The sedimentological and chemostratigraphic variability of the floodplain cores at Dunmoe reveal three distinctive depositional units. DMO-2 comprises intercalated silts and flood sands, with occasional finer clay-rich layers, typical of channel-proximal overbank deposits. These sediments correspond to depositional

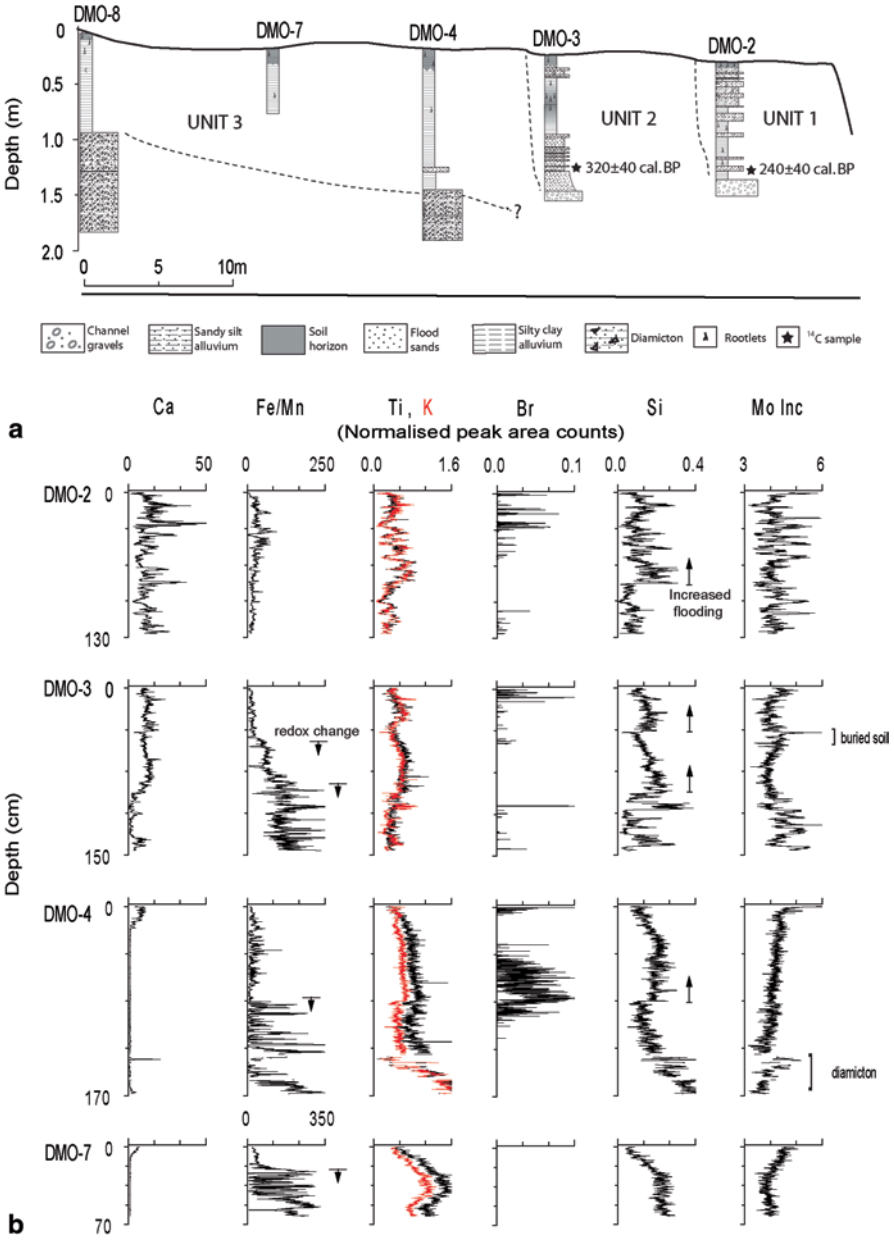


**Fig. 8.11** **a** Relative position and logs for the floodplain cores retrieved along the coring transect at Dunmoe on the River Boyne. The partitioning of alluvial units is based on sedimentological and chemostratigraphic variability. **b** Selected Itrax micro-XRF profiles in the Dunmoe cores (annotation relates to discussion in the text). Note the XRF results have been normalised using Raleigh scatter (Mo Coh) to account for variations in XRF intensity during analyses (Anders Rindby, Pers. Comm.)

unit 1 and were $^{14}C$ dated at the base to 240 ± 40 BP (intercept: 300 cal. BP; cal. AD 1650). DMO-3 is dominated by clayey sandy silt without fluviatile structure, but with evidence of orange-red and black mottling, and occasional distinct layers of sand. This core corresponds to unit 2 and was dated at the base to 320 ± 40 BP (intercept: 420–320 cal. BP; cal. AD 1520–1630). Both units 1 and 2 are underlain by fluvial gravels. Cores DMO-4, DMO-7 and DMO-8 correspond to unit 3, which is dominated by clayey silt with little or no evidence of coarser flood layers, but significant orange-red and black mottling. At the base of DMO-7 and DM0-8 are two diamict units of indistinguishable clast and matrix characteristics but contrasting physical properties, the lower being cohesive and the upper over-saturated. In DMO-8 the 'muddy' unit yielded archaeological materials.

**Role of XRF Data for Floodplain Partitioning**

Selected XRF profiles (Fig. 8.11b) reveal variation in geochemical composition that can be linked to depositional and post-depositional processes across the Dunmoe floodplain. A reduction in sub-surface Ca counts, particularly in DMO-4 and DMO-7, is indicative of floodplain age and the degree of Ca leaching that has occurred. Stepped decreases in Fe/Mn ratios in the cores from units 2 and 3 mark the onset of redoximorphic characteristics related to the aforementioned sediment colour changes. These characteristics are probably associated with high but variable water table levels at the site (Vepraskas 2002). Potassium (K) and Ti profiles help differentiate units 2 and 3 that are largely indistinguishable using colour and textural characteristics alone. In unit 3, K counts are clearly depleted relative to Ti values with depth. This may be linked to the greater age of the unit, whereby prolonged weathering has led to leaching of soluble $K^-$ (Sidhu et al. 1977). However, K vs. Ti trends in DMO-4 and DMO-7 could also be influenced by increased input of wash-borne sediments from differentially weathered adjacent slope soils depleted in K. Enhanced weathering of K-bearing silicates has been used to explain similar K/Ti trends in lake sediments (Mischke et al. 2010) and alluvium (Muhs et al. 2001). Elevated Br counts at depth in DMO-4 provide further evidence to support this hypothesis. Researchers have shown that terrestrial organic matter acts as a reservoir of Br (Oldfield et al. 2003; Leri and Myneni 2012), and all cores bar DMO-7 show elevated Br in organic rich surface and sub-surface layers. High Br counts in DMO-4 could therefore reflect a phase of accelerated erosion of the adjacent slope surface soils, concomitant with the accretion of this unit. Based on the reported radiocarbon dates, this erosion 'episode' could correspond with climatic deterioration during the Little Ice Age (ca. 16–18 centuries). Although the detection of Br using micro-XRF core scanning and its use as a proxy for soil organic matter needs further testing, this approach offers significant potential for the tracking of erosion episodes and for reconstructing phases of adjacent hillslope instability.

In terms of flood reconstruction, Zr/Rb and Zr/Ti ratios were ineffective at this site. The possibility of slope-derived sediments to parts of the floodplain has implications for the application of XRF ratios as proxies for flood magnitude at the

site. However, in DMO-2 elevated Si counts clearly correspond to distinct quartz-bearing sand-rich flood layers, often capped with Ca-rich detrital shells (Ca) and organics (Mo Inc). In units 2 and 3, a similar flood-related structure is undetectable geochemically, but systematic, broad variations in Si (marked in Fig. 8.11b) possibly reflect episodes of increased flood magnitude during the last 2–300 years. In DMO-3, a phase of vertical accretion appears to have buried an incipient A-horizon detected by an increase in the Compton scattering profile (Mo Inc) and a change in sediment density revealed by the radiograph (not shown). The poorly preserved fluvial architecture in units 2 and 3 is probably the result of mixing by post-Medieval land-use and pedogenesis, and appears to limit the veracity of high resolution flood records at this site.

## Discussion: Progress and Prospects

### *Progress*

One of the key drivers for present and future micro-XRF core scanning applications is the capacity for the rapid and non-destructive acquisition of continuous down-core chemostratigraphy to complement traditional approaches and methodologies. Coring requirements in fluvial environments are generally not subject to the same logistical and financial demands as marine and many lake coring programmes, which means that multiple, typically shorter, cores can be retrieved at relatively low cost. Our understanding of the complex and often composite nature of fluvial deposits, especially those that have undergone multiple phases of cut-and-fill, is therefore enhanced by the potential for rapid geochemical appraisal. XRF elemental records can furthermore provide guidance and frameworks for complementary and often destructive analyses, such as radiometric dating and particle-size analysis, as well as informing broader catchment-scale queries linked to sediment dynamics and provenance.

Micro-XRF core scanning technologies facilitate structural and geochemical data acquisition at process scales that were previously unachievable, enabling acquisition of fluvial sedimentary sequences on an event-by-event basis. This analytical precision opens up a new range of research opportunities linked to micro- to meso-scale floodplain formation and flood reconstruction. However, given the influence of human disturbance and, in particular, soil development in alluvial sediment, researchers working in the field would benefit from deterministic geochemical signatures in alluvial settings, particularly where there is a risk of over-interpreting high resolution XRF profiles. Most work on alluvial soils has traditionally focused on soil physico-chemical properties linked to agricultural potential (c.f. Gerard 1987). In practice, there are no definitive chemostratigraphic profiles to differentiate between primary vis-á-vis secondary signatures and the absence of stratification does not preclude the preservation of the original depositional environment (*Ibid.*). Much will depend on the character of allochthonous inputs that

are typically dominated by mineral sediment, eroded and transported from catchment sources, but may also include variable quantities of organics. In peatland catchments, for example, floodplains can be formed of distinctive flood couplets, comprising minerogenic sediment and an organic cap (Thorp and Gallagher 1999; Fig. 8.12), but where minerogenic material is very fine and lacks heterogeneity, horizontal structure may be absent. Autogenic accumulations and influences are primarily related to organic matter build-up and bioturbation, but may also involve the translocation and transformation of mineral material through mechanical and/or chemical transfer and weathering processes, respectively (Ellis and Mellor 1995; Brady and Weil 2008). Table 8.3 provides a summary of processes and characteristics indicative of soil forming mechanisms in temperate alluvial settings and considers some implications for the interpretation of micro-XRF profiles in alluvial environments. Many of the influences are linked to hydromorphic properties associated with gleysols (Fig. 8.13) and gleyic fluvisols, resulting from high and variable water tables. Gleying arises from prolonged waterlogged conditions which leads to the reduction of ferrous Fe and Mn oxides and either the removal or segregation of Fe/Mn bearing minerals into mottles or concretions (Fig. 8.13). These properties are strongly evident in the floodplain sediments at Dunmoe (Section "Itrax Inferred Patterns of Sedimentation and Floodplain Development") and are observed in many floodplains across northwest Europe. Cycles of oxidation and reduction fuelled by the bacterial decomposition of soil organic matter will eventually lead to the displacement of basic cations and the acid weathering of clay minerals (Brinkman 1970). Changes in pH and Eh associated with redox cycles and pedogenesis can also lead to the mobilization of labile elements, including heavy metals, which has implications for the interpretation of the fine-scale chemostratigraphy of metal XRF counts, concentrations and ratios (Hudson-Edwards et al. 1996, 1998). In arid zone environments subject to intense wetting *and* drying vertical decimetre-scale cracks have a tendency to form, resulting in the physical translocation of clay minerals. Over time this can lead to inverted upper soil profiles (vertisols) thereby confounding primary sedimentation patterns.

The utility of scanning fluvial deposits at sub-mm resolutions is therefore dependent on the modes of sediment accretion and, critically, the preservation of primary depositional signatures, which may be difficult to ascertain. In this chapter we demonstrate the application of micro-XRF element ratios for reconstructing millennial length flood histories (Section "Flood Reconstruction Using Itrax XRF Profiles"), but also the unsuitability of this approach where flood sediments may have been mixed or disturbed by slope deposits, human activity and/or pedogenesis (Section "Itrax Inferred Patterns of Sedimentation and Floodplain Development"). In this study and others (e.g. Wang et al. 2011), the veracity of micro-scale flood records is untested beyond the robust statistical relationships that can be established between aggregated XRF peak integral counts and particle size fractions obtained at relatively coarse cm to sub-cm intervals. The potential to build high resolution records also implicitly assumes that there is a positive relationship between particle size and flood magnitude in the fine to very fine (silt to clay) sediment fraction that can be modelled. The approach therefore revisits longstanding debates concerning effective

**Fig. 8.12** Minerogenic-organic flood couplets revealed in a bank exposure on the Kings River, Co. Wicklow, Ireland. The light sandier sediments, derived from weathered granites, are laid down during overbank flood events. These minerogenic sediments may be capped with a layer of dark, organic sediments, derived from weathered peat, that are deposited during flood recession. (Source: JN Turner)

**Table 8.3** Characteristics of physical and chemical properties associated with soil formation in river alluvium

| | Processes | Physical attributes | Chemical attributes | Micro-XRF attributes |
|---|---|---|---|---|
| Primary features | Vertical accretion with surface organic build-up | Preservation of horizontal laminations and banding, may be visible | Chemical variability primarily controlled by sediment heterogeneity, provenance and particle size | Elemental variability primarily controlled by primary deposition (and noise), potentially able to distinguish between flood layers |
| Secondary translocation | Dissolution and transfer of soluble products of chemical weathering<br>Redeposition of solutes driven by changes in moisture content, pH, temperature, exchange sites and $O_2$ availability<br>Water-borne transfer of particles in suspension, dominated by fine clays (e.g. smectite) and organic colloids. Occasionally involving coarser silt, sand and even gravel particles, where large macro-pores, vertical cracks and other open soil structures exist | Colour typically characterised by a washed-out, upper eluviated horizon and a darker, lower illuvial B-horizon<br>Infilling of soil pores through precipitation of dissolved materials. Sometimes associated with induration and panning (formation of iron pans requires prolonged drop in water level, unlikely in regularly inundated alluvium)<br>Elevated clay content in lower illuvial horizon, with deposition of 'clayskin' coatings ('illuviation cutons') on large particles | Leaching (loss) of free salts (e.g. Na, Ca) in upper horizons<br>Elements (Si, Zr) associated with resistant minerals (quartz, garnet, zircon) becoming elevated in the upper part of soil profile and conversely alkaline earth metals (Ca, K) increasing with depth if retained | Ratios to more stable elements Zr and Si decreasing with depth, where clay transfers dominant. Chemical trends may be superimposed on high resolution variability that reflects both primary and secondary chemostratigraphy, as well as instrument noise<br>Ratios to clay-associated elements (e.g. Rb) increasing with depth |

**Table 8.3** (continued)

| | Processes | Physical attributes | Chemical attributes | Micro-XRF attributes |
|---|---|---|---|---|
| Secondary transformation | Transformation of clays through ion exchange or removal of siloxane products<br>Neoformation of clays through hydrolysis chemical weathering<br>Ripening and homogenisation of soil structure through biological activity<br>Periodic or permanent saturation leading to reduction of Fe and Mn oxides and possible mobilisation/loss of soluble reduced species<br>Oxidation of Fe and Mn under aerobic conditions and in zones of localised aeration | Loss of primary horizontal structure with development of crumb structure, associated with particle size homogenisation, roots and macro-fauna burrows<br>Blue-grey colouration ('gleying') associated with permanent anaerobic soil conditions<br>Orange-brown micro-mottling around root and faunal casts under partial saturation<br>Black Mn staining<br>Formation of Fe and Mn nodules where localised concentrations occur under partial aerobic conditions | Vertically and horizontally localised and highly elevated Fe and Mn concentrations<br>Fe and Mn peaks possibly associated with adsorbed heavy metals (e.g Cd, Zn). Could indicated post-depositional mobilisation but may also be controlled by contaminant hydrological pathway | Rapid and significant changes in Fe and Mn in partially or temporarily saturated redox zone<br>Rapid drop-off in Fe and especially Mn in permanently saturated zone |


**Fig. 8.13** Profile of an alluvial gleysol from Co. Louth, Ireland, showing the typical *blue-gray* horizon (at the *bottom*) that results from Fe reduction under persistent waterlogged conditions. Evidence of oxidized Fe (*red*/*orange*) and Mn (*black*) mottling and concretions can also be observed below 40 cm. (Source: R Creamer, Irish Soils Information System Project)

particle size during transport and deposition; specifically the importance of flocculation processes that can increase particle size in the water column by several orders of magnitude (Philips and Walling 1995; Droppo 2001). Moreover, because controls on sediment calibre are not only driven by changes in climate, but are also governed

by human impacts such as land-use change, flow regulation and flood defences, as well as autogenic adjustments controlling channel-floodplain coupling and floodplain micromorphology, the interpretation of centennial to millennial length flood records necessitates an understanding of catchment history and macro- to micro-scale sediment dynamics (Werritty et al. 2006; Jones et al. 2010). In the Severn study, changes in sedimentation rate have been monitored by ensuring adequate dating control and having knowledge of the historical factors affecting sediment supply to the site. Where there are significant changes in mean Zr/Rb indicative of shifts in either the calibre of sediment supplied to the reach and/or changes in channel position or floodplain topography, selection of suitable statistical methods, along with theoretical or experimental work on the relationship between increases in flood magnitude and increases in maximum grain-size, are fundamental requirements.

In terms of directly testing and validating geochemical particle size proxies, fluvial geomorphologists can also look to recent developments in high resolution image analysis that have emerged in the last decade and have been applied to marine and lake core sediments (Francus 2004). The use of scanning electron microscopy, allied with strict sample preparation, enables comparison between particle size fractions and XRF data at the micrometer scale. For the most part, work to-date has focused on measuring and differentiating coarser clastic particles found in lake sediment varves (e.g. Cuven et al. 2010) and more research is required to explore similar applications for finer silt and clay-rich flood sediments. In the context of contemporary policy objectives and applications, the testing and validation of micro-XRF flood models in this manner will help build the confidence necessary for these innovative approaches to be instituted into the tool kit of engineers and river managers entrusted with flood risk management.

## *Prospects*

Micro-XRF core scanners typically report elemental composition based on peak area (integral) counts rather than absolute concentrations (Croudace et al. 2006). Owing to sub-mm XRF penetration depths, variable water and organic matter content and other sample surface and matrix considerations associated with heterogeneous fluvial sediments, any attempt to quantify core scanner XRF counts will prove difficult. For most palaeoenvironmental applications a measure of relative changes will provide sufficient information to discriminate environmental change, and the application of XRF element ratios can improve data quality by removing some of the artefacts associated with variable scattering intensities, X-ray attenuation and diffraction (Croudace et al. 2006). The challenges of quantifying core scanner XRF count data are illustrated in this chapter by the moderate R-squared values (0.6–0.9) reported for linear calibration models acquired using a hand-held XRF recorder (Section “Contaminant Profiling and Provenance Using Itrax XRF”). Given that the ultimate objective of the sediment mixing model approach is to develop full down-core models, at core scanner instrument resolution (e.g. individual flood units/laminations), greater resilience needs to be built into the calibration process, with quantification of analytical error at the precision of the instrument. For prov-

enance investigations improved accuracy and precision is likely to enable a wider range of elements to be used in the mixing model. A revised mixing model that calculates statistically-defined probability distributions for each sediment source group rather than a single percentage contribution would therefore be advantageous. Such models do exist, for example OpenBUGS (Lunn et al. 2009), but these are used for determining the relative contributions of various sources to a mixture based on stable isotope ratios (Phillips and Gregg 2003) and therefore need to be adapted for use with sediment transport, mixing and deposition.

Quantification of micro-XRF data would also have much wider benefits for environmental pollution studies concerned with the reconstruction of contaminant flux and loading rates in fluvial systems. Over limited ranges, the relationship between XRF counts and element concentrations is rectilinear for individual elements (Van Grieken and Markovicz 2001), making it possible to use counts rather than concentrations to look at anthropogenic loading above background count values at a core base. Similar 'enrichment' approaches are widely employed in conventional pollution investigations (e.g. Sutherland et al. 2000; Kaushik et al. 2009). However, where element concentrations range over several orders of magnitude these linear relationships may no longer apply. Further work is therefore required to explore the potential for effective calibration approaches to support policy objectives under the Priority Substances (2008/105/EC) and Water Framework (2000/60/EC) Directives. In the meantime micro-XRF core scanners will continue to be a valuable pollution screening tool that can inform conventional geochemical sampling strategies and analytical techniques.

## Conclusion

River alluvium exhibits characteristics of transport and deposition that reflect the geological and geomorphic nature of the drainage basin and conditions of alluviation, especially the energy environment. Fluvial sediment archives are typically shorter than marine and lake sediment records, but are nevertheless important because of the sensitivity of river systems to environmental change, as well as societies' longstanding and continuing association with fluvial environments. A major consideration in the micro-XRF analysis of fluvial sediments is the preservation, continuity and heterogeneity of alluvial sediments and the integrity of accretionary records, once they have been subject to post-depositional processes and modification. Thus, while fluvial sediment archives offer considerable palaeoenvironmental potential, they also present specific challenges in terms of the identification of optimal site conditions.

Thus far, micro-XRF applications in fluvial environments have been rather limited. A key area that can benefit from the high resolution core scanning is the field of flood reconstruction, where elements and element ratios can be used as particle size proxies to infer relative flood magnitudes over extended timescales, well beyond instrumental records. Micro-XRF core scanning technologies allow for analysis at the event-scale, which hitherto has been unachievable in floodplains composed of

silts and clays. This approach therefore has the potential to build and significantly enhance our understanding of longer term flooding patterns and non-stationarity. In so doing there is considerable scope for augmenting instrumental records and providing new perspectives for contemporary river management objectives; for example, under the EU Floods Directive (2007/60/EC).

The rapid geochemical assessment provided by core scanners can make a valuable contribution to investigations exploring the timing and character of floodplain dynamics, especially where cut-and-fill episodes have created complex sediment assemblages that may lack surface topographic expression. Similarly, pollution and provenance investigations, especially in metal-mined catchments, would benefit significantly from rapid and high resolution geochemical appraisal, especially where information on anthropogenic enrichment could be used to reduce costs of sampling and laboratory analysis. Given that river alluvium plays an integral role in the cycling and storage of contaminants, and therefore a critical secondary source of pollution, further applications in this field are anticipated. Although sediment heterogeneity places significant challenges to quantification of micro-XRF core scanner results, there has been little attempt to establish what these limitations mean in practical terms. A greater rolling out of pollution and provenance applications should therefore encourage renewed efforts to explore the potential for effective protocols for the conversion of XRF counts to absolute concentrations, where opportunities are presented.

**Acknowledgements** Funding was provided by the Welsh Assembly Government, Environment Agency Wales, Countryside Council for Wales, British Geological Survey, Aberystwyth University, and the Centre for Catchment and Coastal Research for the UK projects and by the Irish Heritage Council INSTAR Programme for the work in Ireland. The authors would like to thank E. Johnstone, G. Foster, I. Dennis and M. Rowberry for help with fieldwork and JNT would like to acknowledge the additional support provided by G. Foster for data processing and core logging on the Dunmoe project. We are grateful to W. Ebenezer for assistance with grain-size analyses and H. Lamb, S. Davies, and M. Marshall for assistance with XRF core scanning of the Welsh cores. We also thank C. Gallagher, volume editors I. Croudace and G. Rothwell and two anonymous referees for constructive comments that helped improve the manuscript.

## References

Aitchison J (1982) The statistical analysis of compositional data. J R Stat Soc Ser B (Methodol) 44:139–177

Alexandrovskiy AL, Glasko MP, Krenke NA, Chichagova OA (2004) Buried soils of floodplains and paleoenvironmental changes in the Holocene. Revista Mexicana de Ciencias Geológicas 21:9–17

Baker VR, Kochel RC, Patton PC, Pickup G (1983) Palaeohydrologic analysis of Holocene flood slack-water sediments. (Spec. Publ.) Int Assoc Sedimentol 6:229–239

Benito G, Lang M, Barriendos M, Llasat MC, Frances F, Ouarda T, Thorndycraft VR, Enzel Y, Bardossy A, Coeur D, Bobee, B (2004) Use of systematic, palaeoflood and historical data for the improvement of flood risk estimation. Review of scientific methods. Nat Hazards 31:623–643

Bird G, Brewer PA, Macklin MG, Nikolova M, Kotsev T, Mollov M, Swain C (2010) Quantifying sediment-associated metal dispersal using Pb isotopes: application of binary and multivariate mixing models at the catchment scale. Environ Pollut 158:2158–2169

Brady NC, Weil RR (2008) Nature and properties of soils, 14th edn. Prentice Hall, London
Brinkman R (1970) Ferrolysis, a hydromorphic soil forming process. Geoderma 3:199–206
Calvert SE, Bustin RM, Ingall ED (1996) Influence of water column anoxia and sediment supply on the burial and preservation of organic carbon in marine shales. Geochim Cosmochim Acta 60:1577–1593
Calvert SE, Pedersen TF, Karlin RE (2001) Geochemical and isotopic evidence for post-glacial palaeoceanographic changes in Saanich Inlet, British Columbia. Mar Geol 174:287–305
Carter BJ, Kelley JP, Sudbury JB, Splinter DK (2009) Key aspects of a horizon formation for selected buried soils in Late Holocene alluvium; Southern Prairies, USA. Soil Sci 174:408–416
Chen J, Chen Y, Liu L, Ji J, Balsam W, Sun Y, Lu H (2006) Zr/Rb ratio in Chinese loess sequences and its implications for changes in the East Asian winter monsoon strength. Geochim Cosmochim Acta 70:1471–1482
Collins AL, Walling DE, Leeks GJL (1997) Source type ascription for fluvial suspended sediment based on a quantitative composite fingerprinting technique. Catena 29:1–27
Croudace IW, Rindby A, Rothwell RG (2006) ITRAX: description and evaluation of a new multi-function X-ray core scanner. In: Rothwell RG (ed) New techniques in sediment core analysis, vol 267. Geological Society Special Publication, London, pp 51–63
Cuven S, Francus P, Lamoureux SF (2010) Estimation of grain-size variability with micro X-ray fluorescence in laminated lacustrine sediments, Cape Bounty, Canadian High Arctic. J Paleolimnol 44:803–817
Daniels JM (2003) Floodplain aggradation and pedogenesis in a semiarid environment. Geomorphology 56:225–242
Downs PW, Gregory KJ (2004) River channel management: towards sustainable catchment hydrosystems. Arnold, London
Droppo IG (2001) Rethinking what constitutes suspended sediment. Hydrol Proc 15:1551–1564
Dypvik H, Harris NB (2001) Geochemical facies analysis of fine-grained siliciclastics using Th/U, Zr/Rb and (Zr + Rb)/Sr ratios. Chem Geol 181:131–146
Ellis S, Mellor A (1995) Soils and environment. Routledge, London
Francus P (2004) Image analysis, sediments and paleoenvironments. Developments in paleoenvironmental research series, vol 7. Springer, Dordrecht
Gerard J (1987) Alluvial soils. Hutchinson Ross, New York
Hardardóttir J, Geirsdóttir Á, Sveinbjörnsdóttir ÁE (2001) Seismostratigraphy and sediment studies of Lake Hestvatn, southern Iceland: implications for the deglacial history of the region. J Quat Sci 16:167–179
Hey RD (1997) Upper River Severn between Dolwen and Penstrowed, Powys. In: Gregory KJ (ed) Fluvial geomorphology of Great Britain. Chapman & Hall, London
Higgs G (1997) River Severn between Welshpool and the confluence of the Vyrnwy and the Severn. In: Gregory KJ (ed) Fluvial geomorphology of Great Britain. Chapman & Hall, London, pp 157–159
Howard AJ, Macklin MG (1999) A generic geomorphological approach to archaeological interpretation and prospection in British river valleys: a guide for archaeologists investigating Holocene landscapes. Antiquity 73:527–541
Howells MF (2007) British regional geology: Wales. British Geological Survey, Keyworth
Hudson-Edwards KA, Macklin MG, Curtis CD, Vaughan DJ (1996) Processes of formation and distribution of Pb-, Zn-, Cd-, and Cu-bearing minerals in the Tyne Basin, northeast England: implications for metal-contaminated river systems. Environ Sci Technol 30:72–80
Hudson-Edwards KA, Macklin MG, Curtis CD, Vaughan DJ (1998) Chemical remobilisation of contaminated metals within floodplain sediments in an incising river system: implications for dating and chemostratigraphy. Earth Surf Process Landf 23:671–684
Jones AF, Lewin J, Macklin MG (2010) Flood series data for the later Holocene: available approaches, potential and limitations from UK alluvial sediments. Holocene 20:1123–1135

Kujau A, Nuernberg D, Zeilhofer LS, Bahr A, Rohl U (2010) Mississippi River discharge over the last ~560,000 years—indications from X-ray fluorescence core-scanning. Palaeogeogr Palaeoclimatol Palaeoecol 298:311–318

Kaushik A, Kansal A, Santosh M, Kumari S, Kaushik CP (2009) Heavy metal contamination of river Yamuna, Haryana, India: assessment by metal enrichment factor of the sediments. J Hazard Mater 164:265–270

Knox JC (1993) Large increases in flood magnitude in response to modest changes in climate. Nature 361:430–432

Knox JC (2003) North American paleofloods and future floods: responses to climatic change. In: Gregory KJ, Benito G (eds) Palaeohydrology: understanding global change. Wiley, Chichester, pp 143–164

Kylander ME, Ampel L, Wohlfarth B, Veres D (2011) High-resolution X-ray fluorescence core scanning analysis of Les Echets (France) sedimentary sequence: new insights from chemical proxies. J Quat Sci 26:109–117

Leri A, Myneni S (2012) Natural organobromine in terrestrial ecosystems. Geochim Cosmochim Acta 77:1–10

Lewin J (1978) Floodplain geomorphology. Prog Phys Geogr 2:408–437

Lewin J (1996) Floodplain construction and erosion. In: Petts G, Calow P (eds) River flows and channel forms. Blackwell Science, Oxford, pp 185–202

Lewin J, Macklin MG (2003) Preservation potential for late quaternary river alluvium. J Quat Sci 18:107–120

Lewis H, Gallagher C, Davis S, Turner JN, Foster GC et al (2009) An integrated, comprehensive GIS model of landscape evolution and land use history in the River Boyne valley: Phase II Report 2009. The Heritage Council, Ireland

Lunn D, Spiegelhalter D, Thomas A, Best N (2009) The BUGS project: evolution, critique and future directions. Stat Med 28:3049–3067

Macklin MG (1996) Fluxes and storage of sediment-associated heavy metals in floodplain systems: assessment and river basin management issues at a time of rapid environmental change. In: Anderson MG, Walling DE, Bates PD (eds) Floodplain processes. Wiley, Chichester, pp 441–460

Macklin MG, Lewin J (2003) River sediments, great floods and centennial-scale Holocene climate change. J Quat Sci 18:102–105

Macklin MG, Lewin J (2008) Alluvial responses to the changing Earth system. Earth Surf Process Landf 33:1374–1395

Macklin MG, Rumsby BT, Newson MD (1992) Historical floods and vertical accretion of fine-grained alluvium in the Lower Tyne Valley, Northeast England. In: Billi P, Hey RD, Thorne CR, Tacconi P (eds) Dynamics of gravel-bed rivers. Wiley, Chichester, pp 573–589

Macklin MG, Ridgway J, Passmore DG, Rumsby BT (1994) The use of overbank sediment for geochemical mapping and contamination assessment: results from selected English and Welsh floodplains. Appl Geochem 9:689–700

Macklin MG, Brewer PA, Hudson-Edwards KA, Bird G, Coulthard TJ, Dennis IA, Lechler PJ, Miller JR, Turner JN (2006) A geomorphological approach to the management of rivers contaminated by metal mining. Geomorphology 79:423–47

Macklin MG, Jones AF, Lewin J (2010) River response to rapid Holocene environmental change: evidence and explanation in British catchments. Quat Sci Rev 70:92–107

Martin JM, Meybeck M (1979) Elemental mass balance of material carried by world major rivers. Mar Chem 7:173–206

Miller JR (1997) The role of fluvial geomorphic processes in the dispersal of heavy metals from mine sites. J Geochem Explor 58:101–118

Mischke S, Rajabov I, Mustaeva N, Zhang C, Herzschuh U, Boomer I, Brown ET, Anderson N, Myrbo A, Ito E, Schudack ME (2010) Modern hydrology and late Holocene history of Lake Karakul, eastern Pamirs (Tajkistan): a reconnaissance study. Palaeogeogr Palaeoclimatol Palaeoecol 289:10–24

Moalla SMN (1997) Physical fractionation of trace and rare earth elements in the sediments of Lake Nasser. Talanta 45:213–221

Moreno A, Giralt A, Valero-Garces B, Saez A, Bao R, Prego R, Pueyo JJ, Gonzalez-Samperiz P, Taberner C (2007) A 14 kyr record of the tropical Andes: the Lago Chungara sequence (18 degrees S, northern Chilean Altiplano). Quat Int 161:4–21

Muhs DR, Bettis IEA, Been J, McGeehin JP (2001) Impact of climate and parent material on chemical weathering in loess-derived soils of the Mississippi River Valley. Soil Sci Soc Am J. 65:1761–1777

Oldfield F, Wake R, Boyle J, Jones R, Nolan S, Gibbs Z, Appleby P, Fisher E, Wolff G (2003) The late Holocene history of Gormire Lake (NE England) and its catchment: a multiproxy reconstruction of past human impact. Holocene 13:677–690

Phillips DL, Gregg JW (2003) Source partitioning using stable isotopes: coping with too many sources. Oecologia 136:261–269

Phillips JM, Walling DE (1995) An assessment of the effects of sample collection, storage and resuspension on the representativeness of measurements on the effective particle size distribution of fluvial suspended sediment. Water Res 29:2498–2508

Ramsey CB (2009) Bayesian analysis of radiocarbon dates. Radiocarbon 51:337–360

Reimer PJ, Baillie MGL, Bard E, Bayliss A, Beck JW, Blackwell PG, Bronk Ramsey C et al (2010) IntCal09 and Marine09 radiocarbon age calibration curves, 0–50,000 Years cal BP. Radiocarbon 51:1111–1150

Rose AW, Hawkes HE, Webb JS (1979) Geochemistry in mineral exploration, 2nd edn. Academic, New York

Rowan JS, Goodwill P, Franks SW (2000) Uncertainty estimation in fingerprinting suspended sediment sources. In: Foster IDL (ed) Tracers in geomorphology. Wiley, Chichester, pp 279–290

Sidhu PS, Sehgal JL, Randhawa NS (1977) Elemental distribution and associations in some alluvium-derived soils of the Indo-Gangetic Plain of Punjab (India). Pedology 27:225–235

Sutherland RA, Tolosa CA, Tack FMG, Verloo MG (2000) Characterization of selected element concentration and enrichment ratios in background and anthropogenically impacted roadside areas. Arch Environ Contam Toxicol 38:428–438

Szmańda JB, Oczkowski HL, Przegietka KR (2004) Age of the Vistula river overbank deposits in Toruń. Geochronometria 23:35–38

Thorp M, Gallagher C (1999) Dating recent alluvial sediments in the wicklow mountains. Ir Geogr 32:112–125

Tjallingii R, Stattegger K, Wetzel A, Phung VP (2010) Infilling and flooding of the Mekong river incised valley during deglacial sea-level rise. Quat Sci Rev 29:1432–1444

Tooth S (2000) Process, form and change in dryland rivers: a review of recent research. Earth Sci Rev 51:67–107

Turner JN, Brewer PA, Macklin MG (2008). Fluvial-controlled metal and as mobilisation, dispersal and storage in the Río Guadiamar, SW Spain and its implications for long-term contaminant fluxes to the Doñana wetlands. Sci Total Environ 18:221–239

Turner JN, Macklin MG, Jones AF, Lewis H (2010) New perspectives on holocene flooding in Ireland using meta-analysis of fluvial radiocarbon dates. Catena 82:183–190

Van Grieken R, Markowicz A (2001) Handbook of X-ray spectrometry, 2nd edn. Marcel Dekker, New York

Veldkamp A, Kroonenberg SB (1993) Application of bulk sand geochemistry in mineral exploration and quaternary research: a methodological study of the Allier and Dore terrace sands, Limagne rift valley, France. Appl Geochem 8:177–187

Vepraskas MJ (2002) Morphological features of seasonally reduced soils. In: Richardson JL, Vepraskas MJ (eds) Wetland soils: genesis, hydrology, landscapes and cultivation. CRC, London, pp 163–182

Walling DE, Owens PN, Leeks GJL (1999) Fingerprinting suspended sediment sources in the catchment of the River Ouse, Yorkshire, UK. Hydrol Process 13:955–975

Wang MJ, Zheng HB, Xie X, Fan DD, Yang SY, Zhao QH, Wang K (2011) A 600-year flood history in the Yangtze River drainage: comparison between a subaqueous delta and historical records. Chin Sci Bull 56:188–195

Weltje, GJ, Tjallingii, R (2008) Calibration of XRF core scanners for quantitative geochemical logging of sediment cores: theory and application. Earth Planet Sci Lett 274:423–438
Werritty A, Paine JL, Macdonald N, Rowan JS, McEwen LJ (2006) Use of multi-proxy flood records to improve estimates of flood risk: lower River Tay, Scotland. Catena 66:107–119
Wolman MG, Miller JP (1960) Magnitude and frequency of forces in geomorphic processes. J Geol 68:54–74

# Chapter 9
# Estimation of Biogenic Silica Concentrations Using Scanning XRF: Insights from Studies of Lake Malawi Sediments

**Erik T. Brown**

**Abstract** The use of XRF measurements of Si and Ti to estimate biogenic silica contents of lake sediment is evaluated by comparison of datasets from Lake Malawi sediment cores spanning 25 kyr of deposition under a range of environmental conditions. This approach is particularly attractive as it offers a several hundred-fold reduction in labor required for these analyses. Silicon can be present in both clastic and biogenic phases, and these phases dilute one another, so a simple relationship to calibrate XRF results to estimate percent biogenic silica was developed. This requires selection of an appropriate element (or elements) to use as a proxy for clastic sedimentary phases. Paired %BSi and XRF Si and Ti data from a short core (~35 cm) were used to develop a calibration scale. This calibration was applied to a 25,000-year record to estimate %BSi from XRF results. Comparison of this calculated BSi record with measured %BSi indicates that calibration parameters can vary with depth in sediment due to changes in chemical and physical characteristics. XRF scanning counting times for Si are evaluated; typically these should be set to allow >500 counts.

**Keywords** Biogenic silica · Lake Malawi · Scanning XRF · Detrital sediment · Dwell time · Calibration

## Introduction

Biogenic silica concentrations in sediments (%BSi) are commonly used as indicators of past diatom productivity and can be interpreted as records of biological responses to environmental changes in lakes (e.g Colman et al. 1995; Prokopenko et al. 2006; Johnson et al. 2002). Wet chemical measurement of BSi in sediment is laborious and requires destruction of ~0.05 g of dry sediment, making it difficult to produce high-resolution records. Even with timesaving modifications (e.g.

E. T. Brown (✉)
Large Lakes Observatory and Department of Earth and Environmental Sciences, University of Minnesota Duluth, Duluth, MN 55812, USA
e-mail: etbrown@d.umn.edu



I. W. Croudace, R. G. Rothwell (eds.), *Micro-XRF Studies of Sediment Cores*,
Developments in Paleoenvironmental Research 17, DOI 10.1007/978-94-017-9849-5_9

Johnson et al. 2002) a full time worker can probably process up to a maximum of ~40 samples in a week. ITRAX XRF core scanning has been shown to provide an efficient and non-destructive means of determining a range of elements (Croudace et al. 2006). This study examines the use of XRF measurements of Si:Ti to represent %BSi, establishing relationships between these parameters and evaluating optimal counting times by comparison of 25 kyr records preserved in Lake Malawi sediments, East Africa. These provide an opportunity for evaluation of the relationship between XRF and wet chemical results in sediments deposited under a range of climatic conditions.

## Methods

*Fieldwork* Piston cores (M98-1P and M98-2P) and a multicore (M98-10MC) were recovered from the north basin of Lake Malawi in 1998 as part of an expedition of the International Decade for the East African Lakes (Fig. 9.1; M98-1P and M98-10MC at 10° 0.2′ S, 34° 19.1′ E, 403 m depth; M98-2P, at 9° 58.6′ S, 34° 13.8′ E, 363 m). The piston cores, considered essentially as replicate cores, have been examined in numerous studies (e.g. Barry et al. 2002; Brown and Johnson 2005; Castañeda et al. 2007, 2009; Powers et al. 2005; Filippi and Talbot 2005) including 1 cm resolution determinations of %BSi over the 9-m length of the piston cores (Johnson et al. 2002). While it would have been desirable to undertake XRF scans of M98-1P or M98-2P these cores have been so heavily sampled that scanning is impossible. In their place, a more recently recovered drill core was used. Drill core MAL05-2A (10° 1.1′ S, 34° 11.2′E, 359 m) was taken during the Lake Malawi Drilling Project in March 2005 within a few km of the earlier coring sites; it has

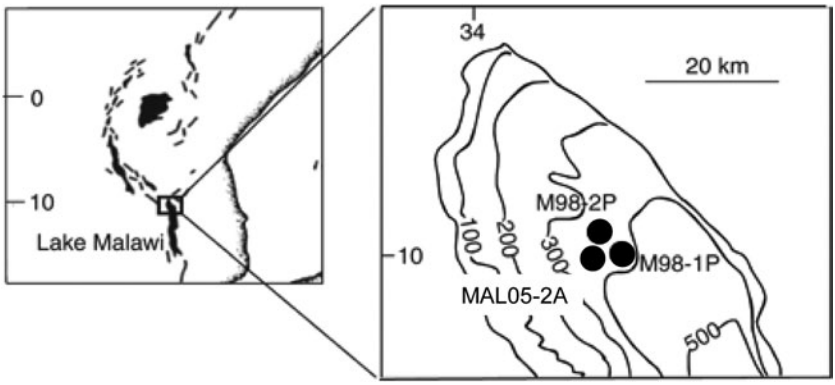


**Fig. 9.1** Site map showing coring locations in northern Lake Malawi. (modified from Johnson et al. (2002))

clear stratigraphic ties (e.g. homogenites, tephras, distinctive varve packages) to the earlier piston cores and a robust age-depth model.

*Laboratory Analyses* Biogenic silica was determined at 1-cm resolution in multicore M98-10MCB using a modification of the Mortlock et al. (1989) dissolution approach (Johnson et al. 2002); a replicate core from the same Multicorer deployment (M98-10MCA) underwent XRF scanning at 2.0 mm resolution with a 60 s counting time, using a Mo x-ray tube with a current of 15 mA and voltage of 30 kV. Piston cores M98-1P and M98-2P have had 1-cm resolution measurements of BSi using the same technique. For comparison, MAL05-2A was scanned at 1.0 cm resolution using the XRF settings noted above. To evaluate counting times and total counts necessary for precise elemental determinations, an additional experiment focused on the 5.0–7.0 cm depth interval of the uppermost section of MAL05-2A, corresponding to a decade of sediment deposition starting at ~1870 CE (Petrick 2009). This section of laminated sediment was repeatedly scanned at 0.2 mm resolution, with counting times of 15, 30, 60 and 120 s. All XRF raw data were reprocessed (using proprietary QSpec 8.6.0 software) to optimize peak fitting.

*Age and Depth Models* Analyses of the multicores were undertaken at different times and on different cores from the same multicorer deployment. The %BSi dataset is from core M98-10MCB, which had lost the uppermost ~1.5 cm in the field and has been heavily sampled, so M98-10MCA was analyzed with XRF scanning. To compare datasets a common depth scale was developed using depths of well-characterized marker beds (homogenites and tephras); this involved depth adjustments for core M98-10MCB that increased from 1.2 to 2.8 cm from top to bottom (Fig. 9.2).

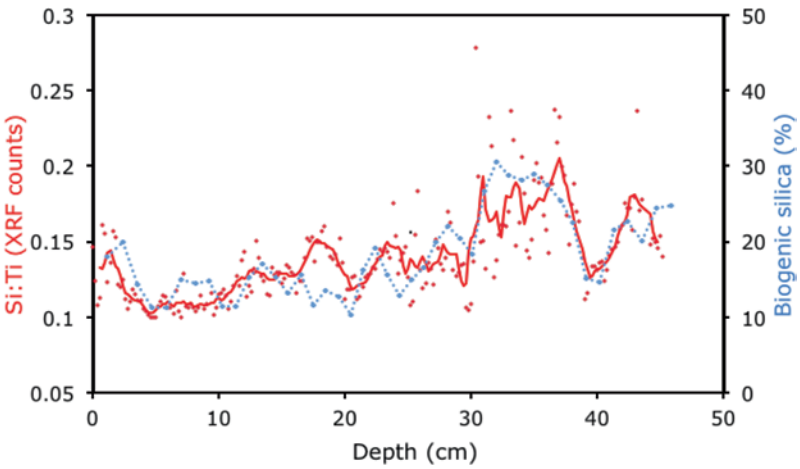


**Fig. 9.2** Comparison of Si:Ti measured by XRF (M98-10MCB) with percent biogenic silica (M98-10MCA) as functions of depth in near surface sediments, with 45 cm representing approximately 300 years of sedimentation. For comparison with the 1-cm resolution BSi data, the *solid red line* connects 5-point averages of the 2-mm resolution XRF results

The chronology of the uppermost 11 m of drill core MAL05-2A extends from 0 to 24 ka and is based on 15 bulk radiocarbon measurements evenly distributed through the sequence (Brown et al. 2007). The earlier piston cores (M98-1P and M98-2P) do not have this level of chronological control, particularly in the deeper sections; each piston core has only two radiocarbon dates older than 12 ka. Even with this imperfect chronological control, stratigraphic relations between the piston cores and the drill core are evident (Fig. 9.3). However, direct comparison requires a common age model, so peaks in %BSi from M98-1P and M98-2P were tuned to Si:Ti measurements (the only appropriate parameter available in both cores) in the better-dated core MAL05-2A, with further constraints set by stratigraphic markers such as volcanic ashes or distinctive lamination packets (Fig. 9.3a). Less tuning was required to match M98-1P to MAL05-2A, so it was selected for further analyses.

## Discussion

*Calibration of XRF Results* Use of XRF results to provide a measure of percent biogenic silica requires not only calibration, but also adjustments for dilution and for Si contained in clastic silicate minerals. This can be accomplished starting with statements that sediment is composed of biogenic silica, organic matter, carbonate and clastic materials (Eq. 9.1), and that silicon is present only in the biogenic silica and clastic phases (Eq. 9.2):

$$g\,sed = g\,clastic + g\,BSi + g\,carbonate + g\,org \tag{9.1}$$

$$\frac{BSi}{g\,sed} = \frac{Si_{tot}}{g\,sed} - \frac{Si_{clast}}{g\,sed}. \tag{9.2}$$

The assumption that carbonate and organic matter are negligible leads to:

$$\frac{BSi}{g\,sed} \approx \frac{\dfrac{Si_{tot}}{g\,clastic} - \dfrac{Si_{clast}}{g\,clastic}}{\dfrac{g\,clastic + g\,BSi}{g\,clastic}}. \tag{9.3}$$

If Ti has a constant concentration in clastic sediments, one can apply a calibration term linking XRF counts to total $SiO_2$ and clastic material:

$$\frac{BSi}{g\,sed} \approx \frac{\dfrac{Si_{tot}}{g\,clastic} - \dfrac{Si_{clast}}{g\,clastic}}{1 + \dfrac{Si_{tot}}{g\,clastic} - \dfrac{Si_{clast}}{g\,clastic}} \times \frac{\left[\dfrac{Si_{XRF}}{g\,SiO_2} \Big/ \dfrac{Ti_{XRF}}{g\,clastic}\right]}{\left[\dfrac{Si_{XRF}}{g\,SiO_2} \Big/ \dfrac{Ti_{XRF}}{g\,clastic}\right]} \tag{9.4}$$

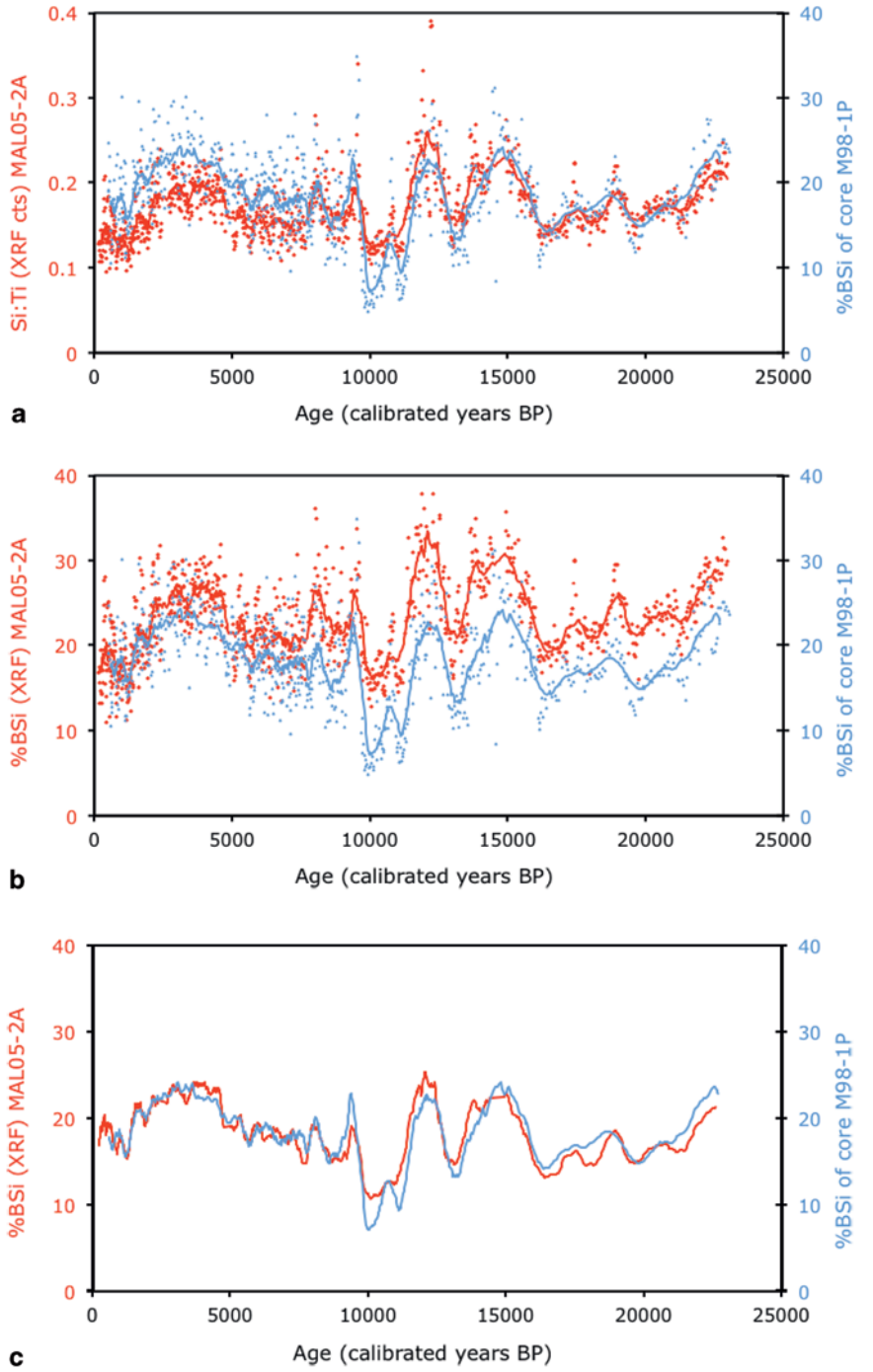


**Fig. 9.3** Comparison of Si:Ti measured by XRF with percent biogenic silica as functions of age (using the MAL05-2A chronology) in Lake Malawi sediments. **a** Uncalibrated $Si:Ti_{XRF}$ and measured %BSi. The lines represent 21-point running means of the raw data. The %BSi determinations

Or

$$\%BSi \approx \frac{100 \times \left( \frac{Si}{Ti}_{XRF\ measured} - \frac{Si}{Ti}_{XRF\ clastic} \right) \times \left[ \frac{\frac{g\ SiO_2}{Si_{XRF}}}{\frac{g\ clastic}{Ti_{XRF}}} \right]}{1 + \left( \frac{Si}{Ti}_{XRF\ measured} - \frac{Si}{Ti}_{XRF\ clastic} \right) \times \left[ \frac{\frac{g\ SiO_2}{Si_{XRF}}}{\frac{g\ clastic}{Ti_{XRF}}} \right]} \quad (9.5)$$

Equation 9.5 may be used to estimate %BSi in the sediments, accounting for Si in clastic minerals and for dilution of clastics by high levels of biogenic silica. The assumptions noted above (low or invariant Si:Ti in the clastic component of the sediments, implying low or invariant quartz contents; constant Ti in clastic sediment; low organic and carbonate contents) must be evaluated. Deep-water Malawi sediments have modest levels of organic matter (< 5 %), highly variable %BSi (5–40 %); the intervals studied here contain no carbonates.

Selection of the appropriate proxy for clastic sediment will depend upon the particular depositional setting. Although Ti is essentially immobile during chemical weathering and diagenesis, it is enriched in heavy minerals so its concentration often varies with grain size. While this is a potential concern, the Malawi coring site remained an offshore depositional environment for the period represented by these cores and thus displays modest grain-size variation. Other elements (e.g. Al, K, Fe, Rb, Zr) could be adopted as a proxy for clastic sediments, but are not appropriate in this setting. Aluminum and Rb are present in Lake Malawi sediments at low concentrations relative to XRF scanning detection limits, so their signals are more subject to random background noise than that of Ti. Diagenetic remobilization of redox-sensitive elements in Malawi sediments precludes the use of Fe as a proxy for silicate minerals (Brown et al. 2000). Sedimentary distributions of K and Zr are confounded by abundant tephras enriched in these elements from the nearby Rungwe volcanics (Brown et al. 2007).

This relationship expressed by Eq. 9.5 has two parameters that may be determined by fitting paired %BSi and $Si:Ti_{XRF}$ data: a background value for $Si:Ti_{clastics}$ (the ratio of count rates that a pure silicate clastic component would have) and a calibration term, in square brackets of Eq. 9.5, relating XRF counts of Si and Ti to the sedimentary $SiO_2$ and clastic mineral content, respectively. Direct comparison of

in the piston core required nearly 6 months of labor, while the XRF analyses were completed in less than 2 days. **b** Comparison of measured %BSi with %BSi estimated from $Si:Ti_{XRF}$ using fitting parameters empirically determined from analyses of multicore M98-10MC (see text). The calibration provides an excellent match with measured %BSi back to ~2.5 ka, but does not perform as well in older sediments. **c** Comparison of measured %BSi with %BSi estimated from $Si:Ti_{XRF}$ using empirical fitting parameters determined separately for three segments of the core (0–2.5 ka, 2.5–8.0 ka and 8.0–23 ka). Lines represent 21-point smoothed averages, as in Fig. 9.3a, b. The uppermost section used the parameters measured for surface sediments, while the parameters for the deeper sections were calculated by least squares optimization

%BSi and $Si:Ti_{XRF}$ in a short core of Lake Malawi sediments (M98-10MC) recovered at the site of M98-1P provides constraints on the fitting parameters (Fig. 9.2). Iterative least squares fitting yields values of 0.041 and 2.20 for the background and calibration terms, respectively. To evaluate the sensitivity of this calculation to the size of the dataset, the background and calibration terms were calculated for two-fold decimated datasets (yielding 2 datasets each with 22 calibration points). Values of these fitting parameters were within 5% of values for the full dataset, implying that ~20 wet chemical analyses of %BSi from representative samples would be sufficient for calibration of XRF results for the dynamic range observed in Malawi surface sediments.

Application of these surface values to the 25 kyr record of $Si:TI_{XRF}$ from Lake Malawi drill core and comparison to measured %BSi from the nearby piston core show calibration based on surface sediments works well for the past 2.5 kyr, but may not be appropriate for the entire record (Fig. 9.3b). It is clear that care must be taken when applying a calibration made for a given site and time period to other sedimentary sequences. Iterative least squares fitting of the dataset from the two older sections (2.5–8.0 ka and 8.0–23 ka) provides a better fit (Fig. 9.3c) and yields values of: 0.049 and 2.16; and 0.052 and 1.68 for the for the background and fitting terms, respectively. The background and fitting terms remained essentially unchanged (0.047 and 2.10; and 0.051 and 1.67) when calculated from a 30-fold decimated dataset (30 calibration points).

These temporal shifts in fitting parameters could be the result of variations in XRF response to changing sedimentary parameters such as water content, grain size and bulk density. Although sedimentation rates in Lake Malawi increased after the last Glacial Termination, bulk sedimentary characteristics did not undergo any systematic shifts that correspond with the changes in fitting parameters (Barry et al. 2002). The observed changes in fitting parameters are consistent with lower Si:Ti in more recently deposited clastic sediments; more humid conditions in Holocene relative to the late Glacial (Castañeda et al. 2007) could have led to increased riverine delivery of chemically weathered material depleted in Si.

*Evaluation of Counting Times* To determine counting times (and total counts) necessary to optimize precision of elemental determinations, a short section of laminated sediment was analyzed repeatedly at 0.2 mm resolution with differing counting times (15, 30, 60 and 120 s). Raw data were reprocessed (using QSpec 8.6.0) to optimize peak fitting. Summing peak areas measured for the various counting times provided elemental measurements with 225 s counting times.

Profiles of Si, K, Ti and Fe show improved precision, manifested by reduced scatter, with increasing counting times (Fig. 9.4a, b). To quantify these improvements, average relative standard deviations were calculated from the profiles of peak areas for each element normalized to the 225-s counting result. While there is clear improvement in precision with increased peak areas up to ~$10^4$ counts (Fig. 9.5), increasing counts beyond this level does not improve precision. The improvements in precision with counts are broadly consistent with simple "square root of N" counting statistics, but with instrumental instability apparently providing

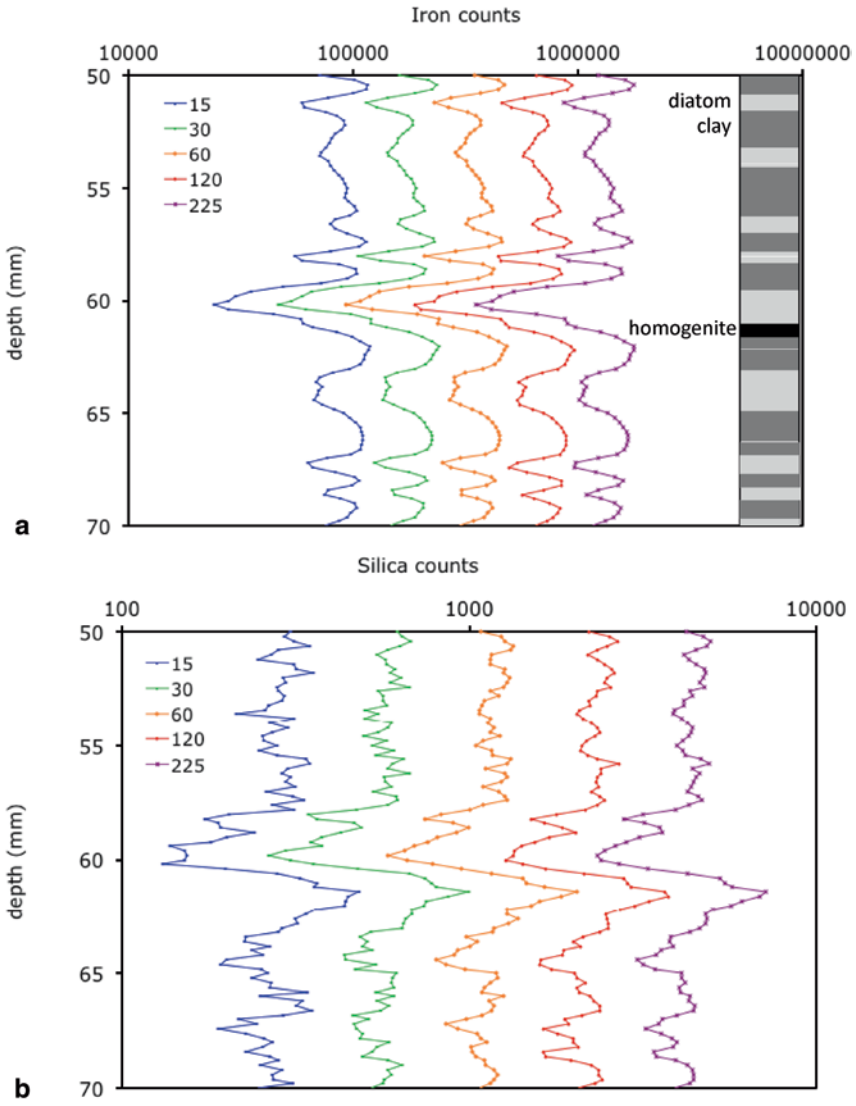


**Fig. 9.4 a and b** Profiles of Fe and Si for various counting times (from left to right in the figures: 15, 30, 60, 160 and 225 s) in a short section of core MAL05-2A-1H1. Depths are reported relative to the top of the core, which over-penetrated the lake floor by ~10 cm. This section has laminations, characterized by couplets linked to annual diatom blooms and clastic mineral layers. This section has an organic-rich diatomite, with lower concentrations of all elements, at 60 cm depth, which overlies a thin clastic homogenite

an additional uncertainty of 1–4 %. In addition, there is non-Gaussian behavior for small peak areas (< 100 counts), which are also susceptible systematic uncertainties due to minor changes in QSpec fitting parameters.

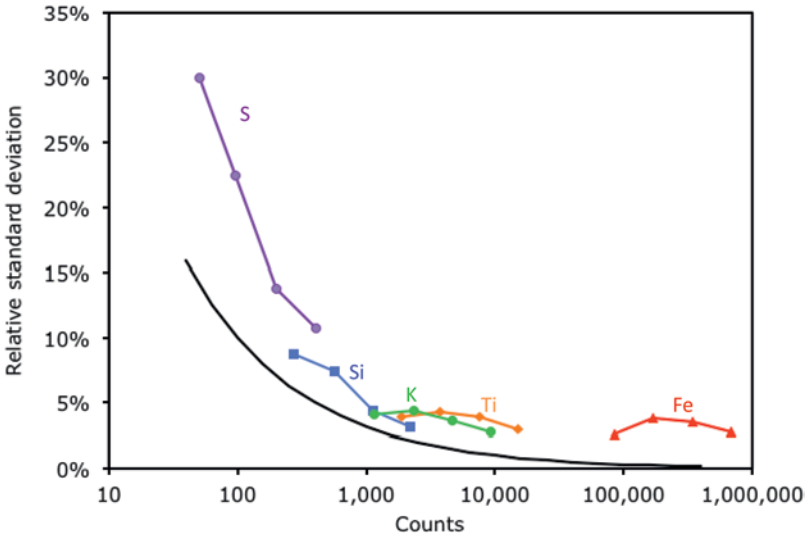


**Fig. 9.5** Relative deviations as a function of peak area. Data are shown for S, Si, K, Ti and Fe for counting times of 15, 30, 60 and 120 s (represented by points on each element's line). Average relative standard deviations were calculated from the profiles of peak areas for each element normalized to the 225-s counting result. The *black curve* shows relative deviations expected from simple counting statistics

Normalizing one element to another can often improve precision of XRF datasets because many elements respond similarly to fluctuations in the x-ray source and other instrumental variability. In such cases, instrumental errors in individual measurements of elements that fluoresce at similar energies (i.e. Fe and Ti or K and Ti) should covary. Indeed, the Malawi dataset shows that Fe:Ti and K:Ti have better precision than predicted from propagation of uncertainties from each elemental dataset (Fig. 9.6). In contrast, data for the ratio Si:Ti show only a modest improvement in precision relative to that expected from the results for individual elements. Light elements such as Si have relatively low energy fluorescence that is more readily attenuated, making results for such elements sensitive to variables (including physical properties of the irradiated material such as grain size, water content, and physical roughness) that do not have as significant effects on higher energy fluorescence from heavier elements (K, Ti, Fe).

## Summary and Conclusions

- XRF core scanning offers an attractive alternative to laborious wet chemical measurement of biogenic silica where %BSi is high (> 10 % and variable). Two days of XRF time and 3–4 h of labor produce a dataset comparable to results of 6 months of labor using traditional wet chemical techniques. Furthermore XRF scanning is essentially non-destructive.

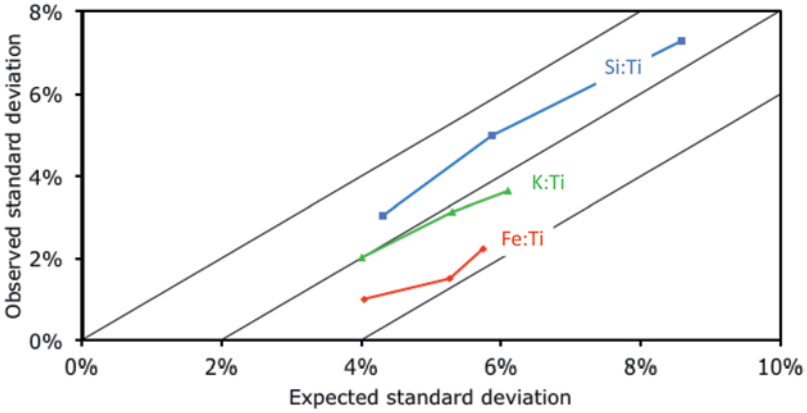


**Fig. 9.6** Observed average relative standard deviations of ratios of elements compared to values expected from propagation of average standard deviations of each dataset. Values are shown for Si:Ti, K:Ti and Fe:Ti (*blue*, *green* and *red*, respectively) for 30, 60 and 120 s counting times. The diagonal 1:1 line represents uncertainties expected if random errors (due to instrument instability, for example) were independent for each element. The lines to the right represent 2 % and 4 % reductions in observed standard deviations relative to those expected for datasets with uncorrelated errors

- Ti is an appropriate proxy for clastic sediments in Lake Malawi, but other elements (e.g. Al, K, Fe, Rb, Zr) should be considered in other environments.
- Paired XRF (Si:Ti in the case of Malawi) and %BSi data are needed for developing site-specific calibration schemes. Ten to 20 wet chemical analyses are likely to be sufficient for calibration. Calibration may vary with sediment characteristics (e.g. composition of clay minerals, water contents, grain size) so care must be taken in applying calibrations to sediments from other locations or time periods.
- It is desirable to set XRF scanner analytical parameters (current and dwell time) to assure a minimum peak area of ~500 counts to assure quality data.
- Whereas XRF analytical precision improves with increased count rates there is little improvement in XRF scanner precision for peak areas greater that ~$10^4$ counts, as there appears to be a instrumental variability of 1–4 %. Such uncertainties may be reduced through the use of ratios of XRF counts for elements with similar atomic numbers (e.g. Fe:Ti). Ratios including light elements (e.g. Si:Ti) do not show much improvement in precision relative to that expected from the individual elemental measurements because the weak fluorescence emitted by light elements is susceptible to additional experimental variables.

## References

Barry SL, Filippi ML, Talbot MR, Johnson TC (2002) Sedimentology and geochronology of Late Pleistocene and Holocene sediments from northern Lake Malawi. In: Odada EO, Olago DO (eds) The East African Great Lakes: limnology, palaeolimnology and biodiversity. Kluwer Academic Publishers, Dortrecht, pp 369–391

Brown ET, Johnson TC (2005) Coherence between tropical East African and South American records of the little ice age. Geochem Geophys Geosyst 6:Q12005. doi:10.1029/2005GC000959

Brown ET, Le Callonnec L, German CR (2000) Geochemical cycling of redox-sensitive metals in sediments from Lake Malawi: a diagnostic paleotracer for episodic changes in mixing depth. Geochim Cosmochim Acta 64:3515–3523

Brown ET, Johnson TC, Scholz CA, Cohen AS, King JW (2007) Abrupt change in tropical African climate linked to the bipolar seesaw over the past 55,000 years. Geophys Res Lett 34:L20702. doi:10.1029/2007GL031240

Castañeda IS, Werne JP, Johnson TC (2007) Wet and arid phases in the southeast African tropics since the Last Glacial Maximum. Geology 35:823–826

Castañeda IS, Werne JP, TC Johnson TC, Filley TR (2009) Late quaternary vegetation history of southeast Africa: the molecular isotopic record from Lake Malawi. Palaeogeogr Palaeoclimatol Palaeoecol 275:100–112

Colman SM, Peck JA, Karabanov EB, Carter SJ, Bradbury JP, King JW, Williams DF (1995) Continental climate response to orbital forcing from biogenic silica records in Lake Baikal. Nature 378:769–771

Croudace IW, Rindby A, Rothwell RG (2006) ITRAX: description and evaluation of a new multi-function X-ray core scanner. In: Rothwell RG (ed) New techniques in sediment core analysis, vol 267. Geological Society Special Publication, pp 51–63

Filippi ML, Talbot MR (2005) The palaeolimnology of northern Lake Malawi over the last 25 ka based upon the elemental and stable isotopic composition of sedimentary organic matter. Quat Sci Rev 24:1303–1328

Johnson TC, Brown ET, McManus J, Barry S, Barker P, Gasse F (2002) A high-resolution paleoclimate record spanning the past 25,000 years in Southern East Africa. Science 296:113–132

Mortlock RA, Froelich PN, Philip N (1989) A simple method for the rapid determination of biogenic opal in pelagic marine sediments. Deep Sea Res A 36:1415–1426

Petrick BF (2009) A 2000-year sub-annual record of climate change from Lake Malawi, MS Thesis, University of Minnesota Duluth

Powers LA, Johnson TC, Werne JP, Castañeda IS, Hopmans E, Sinninghe Damsté JS, Schouten S (2005) Large temperature variability in the southern African tropics since the Last Glacial Maximum. Geophys Res Lett 32:L08706

Prokopenko AA, Hinnov LA, Williams DF, Kuzmin MI (2006) Orbital forcing of continental climate during the Pleistocene: a complete astronomically tuned climatic record from Lake Baikal, SE Siberia. Quat Sci Rev 25:3431–3457

# Chapter 10
# Optimization of Itrax Core Scanner Protocols for the Micro X-Ray Fluorescence Analysis of Finely Laminated Sediment: A Case Study of Lacustrine Varved Sediment from the High Arctic

**Stéphanie Cuven, Pierre Francus, Jean François Crémer and Francis Bérubé**

**Abstract** Use of the highest resolution (0.1 mm) step-size of the Itrax core scanner on fine-scale structured sediment requires careful prior evaluation of the data. The first step for optimization is to select the best Itrax acquisition settings to obtain a robust geochemical record. μ-XRF results reproducibility can then be evaluated according to the abundance and the detectability of elements. Data are considered as 'good quality' when elements are highly or moderately detectable and highly abundant in the sediment. They are of 'medium quality' if elements are poorly detectable but highly abundant in the sediment. Data are described as 'low quality' when elements are highly and moderately detectable and moderately or weakly abundant. Further assessment of analytical errors shows that topographical anomalies on the core surface may decrease validity of μ-XRF results without consequences on the quality of the micro-radiography. Optimized protocols for μ-XRF acquisition are then applied to an Arctic lacustrine varved sediment sequence. This case study highlights the high potential of micro X-ray fluorescence for paleohydrological and -climatological interpretations at very high temporal resolution (i.e. annual and inter-annual scales).

S. Cuven (✉)
PalGeoSed and IODP-France, 14 Av. Edouard Belin, 31400 Toulouse, France
e-mail: phaniecuven@gmail.com

P. Francus · F. Bérubé · S. Cuven · J. F. Crémer
Institut National de la Recherche Scientifique Centre Eau, Terre et Environnement, 490 Rue de la Couronne, G1K 9A9, Québec, QC, Canada
e-mail: pierre.francus@ete.inrs.ca

P. Francus
GEOTOP Research Center, Montréal, QC H3C 3P8

F. Bérubé
Aquartis, Technologie Aquartis, 5472 rue Chabot, Montréal, QC H2H 1Z2, Canada
e-mail: francis@aquartis.ca

J. F. Crémer
Université de Montréal, CP 6128, Succ. Centre-Ville, Montréal, QC H3C 3J7, Canada
e-mail: jean-francois.cremer@umontreal.ca



I. W. Croudace, R. G. Rothwell (eds.), *Micro-XRF Studies of Sediment Cores*,
Developments in Paleoenvironmental Research 17, DOI 10.1007/978-94-017-9849-5_10

**Keywords** Laminated sediment · Varves · Micro X-ray fluorescence · Paleoenvironment · Climate reconstructions

## Introduction

Reconstruction of long- and short-term environmental variability from Arctic lacustrine sediment can be based on sedimentological or biological proxies. Sedimentological proxies are frequently provided by analysis of physical (Zolistschka 1998) and textural (Last 2001) sediment properties. Generally, conventional sedimentological analyses involve varve thickness as a paleohydrological indicator and varve counting as a robust dating method. Both data provide hydroclimatic reconstructions and are easily acquired from thin sections (Lamoureux 2001; Kaufman 2009) and X-radiographs (Lamoureux and Bollmann 2005; Ojala 2005). Textural analyses, based on grain size, -shape and -arrangement measurements from varves are typically made from discrete sub-samples (Ojala 2005) or thin sections. However, in both methods, the step-size of sub-sampling is generally 5 mm or greater, which does not permit reconstruction of variability at varve scale, especially in the case of Arctic lacustrine sediments with low sedimentation rates (≈1 mm year$^{-1}$). It has been shown that observational errors (e.g. missing or extra varves) with the rapid X-radiograph approach may introduce serious errors in the chronology (Lamoureux and Bradley 1996; Lamoureux 2001), while the more rigorous thin section technique is time-consuming and tedious. Thus, data acquisition at fine scale usually requires some additional degree of sub-sampling. For these reasons, and despite considerable advances in sedimentological analysis, it remains difficult to develop new methods that provide additional paleohydrological indicators and allow high-resolution investigations of Arctic fine-laminated deposits (MacDonald et al. 2000; Wolfe et al. 2006). Therefore, the capability of the Itrax core scanner in measuring the sediment's geochemical composition at an unprecedented resolution of 0.1 mm opens new opportunities for analysis of annually laminated sediment or varves. Apart from its very high resolution, the Itrax is a rapid and non-destructive method allowing the sediment to be re-used for multi-proxy analyses.

The first aim of this chapter is to present analytical attributes induced by the extremely high resolution (100–200 μm increments) of this kind of analysis (e.g. data noise, chemical abundance, data reproducibility, shift of sample position, detectability etc.). Secondly, we present a methodology developed for use of the Itrax to investigate fine-scale structured sediment. A first-generation Itrax core scanner hosted at INRS-ETE in Quebec City, Canada, was used for the following experiments and development. Here, the data reproducibility is evaluated according to the abundance and detectability of chemical elements as defined by the Itrax manufacturer. Finally, with the purpose of illustrating our methodological investigations, a case study on finely clastic varved sediments from the Canadian High Arctic is presented, testing the hypothesis that Itrax analyses can be used for textural investigations.

## Analytical Attributes

### *Spatial Resolution: Optical and Radiographic Image Acquisition*

The Itrax first generates RGB digital images of the sediment surface recorded in 10 lines/mm (high-resolution) or 2 lines/mm (low resolution) using an optical line camera with a light sensitive 2048 pixel CMOS (Croudace et al. 2006). It also generates a $20 \times 0.1$ mm rectangular incident X-ray beam that irradiates the core for both X-radiography and X-ray fluorescence analysis. X-ray radiographs are acquired by an X-ray digital camera consisting of a linear arrangement of 1024 X-ray sensitive diodes (Croudace et al. 2006).

Generally, the smallest step-size is recommended for optical images and/or radiograph acquisition because these data are quick to acquire. Furthermore, selecting the highest spatial resolution of 100 µm for optical image acquisition permits easy and direct comparison between the optical image pixels and radiographic pixels (Fig. 10.1), and also with the µ-XRF data points at the highest resolution (100 µm) as they are coming from the exact same place in the core. The most important outcome of using the highest possible resolution is that the resolution of data permits better characterization of finely laminated sediment (i.e. helping the varve delineation or measurements related to fine laminations).

### *Time Acquisition: Micro X-Ray Fluorescence Analysis*

A Si-drift chamber detector measures the X-ray fluorescence emitted by the sample. The X-ray beam is generated by a chromium or molybdenum tube. The geochemical data reported here are semi-quantitative. For each point, a dispersive energy spectrum is acquired and automatically interpreted by the instrument's software.

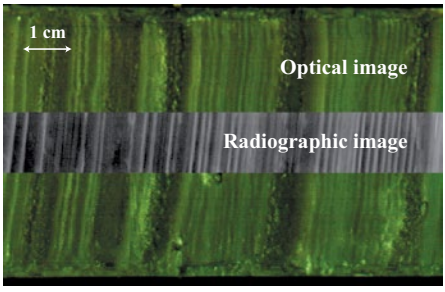


**Fig. 10.1** Comparison of a 100-microns resolution X-radiograph and optical image along a short section of clastic varved sediment from Cape Bounty, Canadian High Arctic. The 16-bit *grey* level X-ray radiograph produced is a 'radiographic positive': low-density areas appear *light* and higher density areas appear *darker*

This interpretation can be erroneous when the software attributes a peak of the spectrum to an element that is not present in the sediment. The 'real' presence of each chemical element should then be manually re-evaluated by considering one or several representative sections of the analyzed sediment core and inspection of the 'sum spectra'. The sum spectra corresponds to the sum of spectra obtained during the entire analysis. It is important to consider low peak areas in the sum spectra as they may be due to elements that are only present in a short interval of the total analyzed core. However, sometimes an element with a peak energy value close to another element is considered to be present by the software in the sum spectra even though this element is not present in the sediment. Even if the peak area integrals for each element are proportional to concentrations of major and minor elements within the sediment (Rothwell 2006), caution is needed because the peak area integrals are also influenced by sediment matrix characteristics. To determine the 'real' presence of an element, the first consideration was acquisition time considering its range of detectability by the Itrax (Fig. 10.2). For each sedimentary facies, increasing times

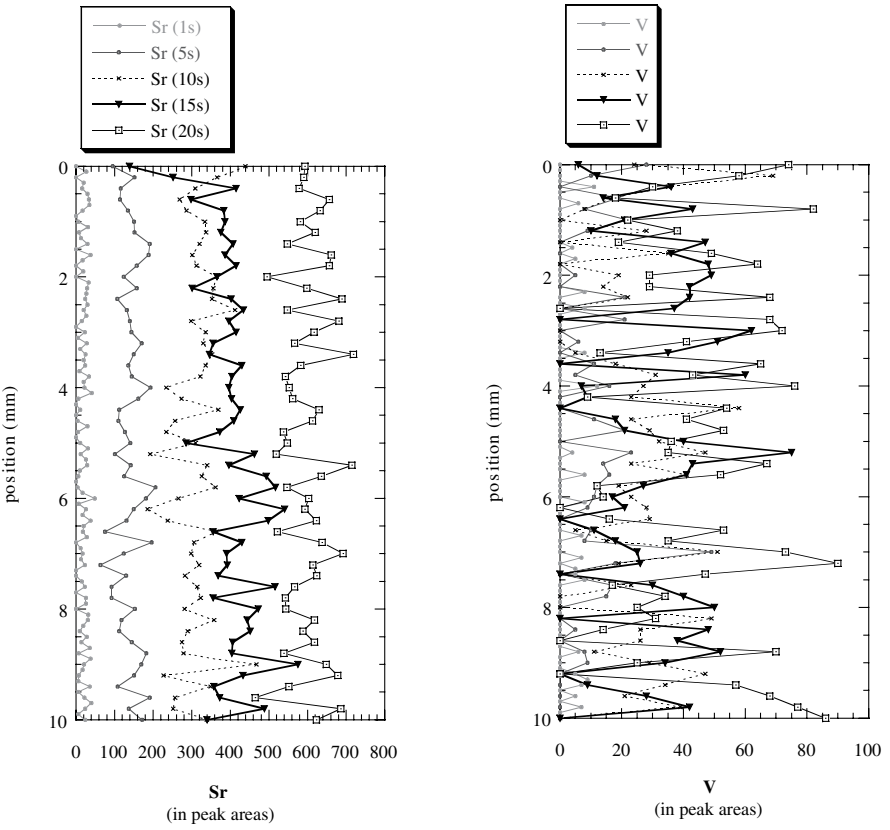


**Fig. 10.2** μ-XRF profiles for Sr and V on a varved core sample from the Canadian High Arctic (Cape Bounty) showing effects of increasing count-time (1, 5, 10, 15, 20 s)

of acquisition (t = 1, 5, 10, 15 and 20 s) were applied and the quality of the resulting re-evaluation curves evaluated. The 'real' presence of an element was determined by observing the minimum peak area value in the chemical profiles along the test sample, and to observe this minimum value when the acquisition time has been increased step by step. When the increase was negligible or random, the presence of the element was dismissed (e.g. V in Fig. 10.2).

In the Cape Bounty case study, a series of tests were performed to define the best settings for Cape Bounty sediment, which is characterized by low organic matter and low carbonate content (Figs. 10.2 and 10.3). The Cape Bounty sediment contained 25 detected elements (i.e. Al, Si, P, S, Cl, Ca, Ti, V, Cr, Mn, Fe, Ni, Cu, Zn, Ga, As, Br, Sr, Y, La, Ta, Bi), but most of these elements showed noisy profiles. To

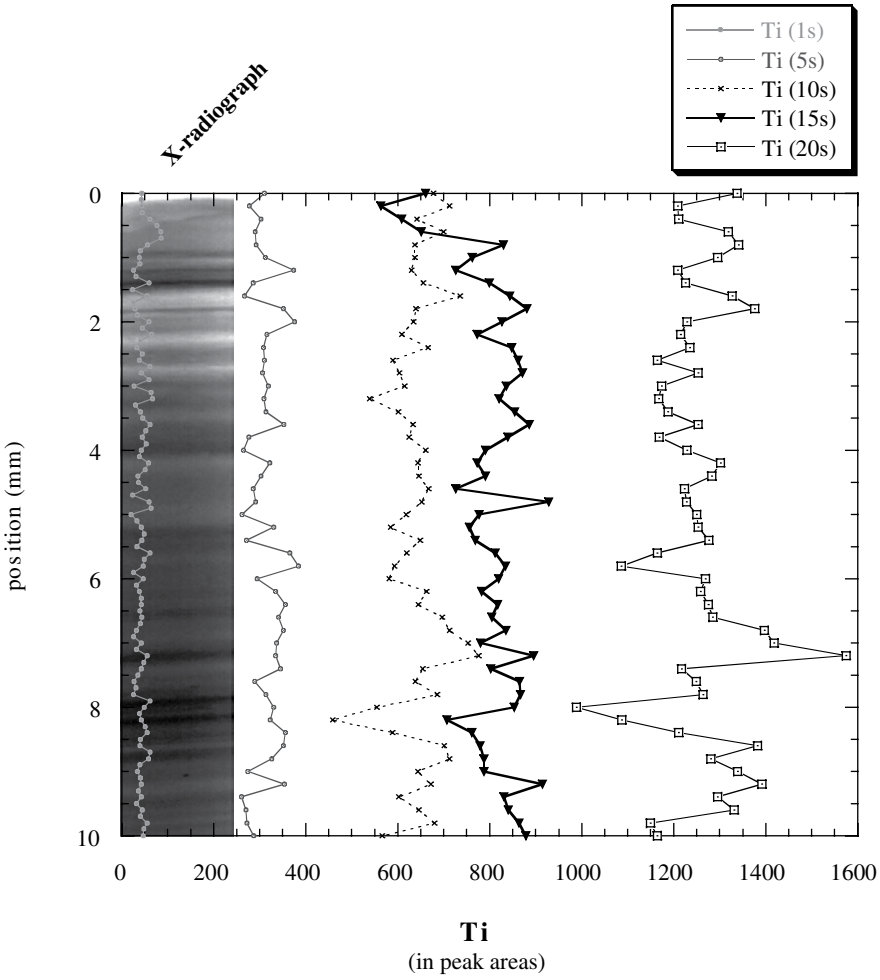


**Fig. 10.3** Variation of Ti across several laminations with acquisition times of 1–20 s

select the most representative and appropriate chemical profiles for this investigation, complementary chemical analyses were conducted for 16 major, minor, and trace elements by inductively coupled plasma-atomic emission spectrometry (ICP-AES) with a Varian instrument (Vista AX CCO Simultaneous ICP-AES, Palo Alto model).

Figure 10.2 shows that V is probably absent from the sediment because its peak area values do not increase significantly with exposure time. In this case, V was initially selected as an element potentially present in the sample forcing the Itrax reevaluation software to find vanadium. In some cases, it identifies a peak with energies characteristics to V (zero values), in others, it finds secondary peaks from other elements present in the sample that overlap with the main peaks of vanadium. In contrast, Sr is poorly represented in the sediment according to ICP-AES data, but the increase of its peak areas values with exposure time suggests that it is actually present. In this respect, the number of analysis points with zero values along the sample for an element is a practical indicator of the lack of robustness in its detection. When the number of zero values does not decrease significantly with exposure time, the element is probably not abundant in the sediment, especially for elements, which are highly detectable by Itrax measurement.

For the analysis of fine laminations it is sometimes necessary to increase exposure time further. Indeed, to detect these laminations, µ-XRF profiles need to contain sufficient amplitude in their variation. Figure 10.3 illustrates how the amplitude of Ti profile values starts to increase from 5 to 10 s of exposure to X-rays. In the Cape Bounty case study, tests showed that 10–15 s is an adequate acquisition time for each point of measurement (Cuven et al. 2007) for a source of radiation produced by a current of 40 kV and 45 mA resulting in count rates of 8,500–10,000 per second with a Mo anode (Figs. 10.2 and 10.3).

Based on these results, the best acquisition time for specific type of sediments are proposed as follows: (a) sediment rich in organic matter needs an acquisition time of 10–20 s (lacustrine sediments) or 5 s (marine sediments); (b) sediment poor in organic matter should have an acquisition time of 5–10 s (lacustrine sediments); (c) sediment rich in carbonate requires 5 s (lacustrine sediments) or 10 s (marine sediments) and (d) for sediment low in carbonate, suggested acquisition time is 10–15 s (lacustrine sediments) or 5 s (marine sediments) (Cuven et al. 2007).

## *Effects of Concentration and Detectability of Chemical Elements on the Reproducibility of µ-XRF Analyses*

Detection sensitivity generally increases with atomic number, but also depends on voltage and current settings (Croudace et al. 2006). Despite improvement in overall XRF elemental sensitivity, Al and Si remain poorly detected by first generation Mo detectors, whereas P, S, Cl and K have moderate detectability and elements from Ca to Zr are highly detectable. While the Cr-target x-ray tube permits better detection for chemical elements with low atomic number, e.g. Si (a major component

of geological material), the Mo-target tube generates an intense source of X-rays able to detect a wider range of elements (from Al to U) for concentrations down to 20 ppm for some elements (Croudace et al. 2006).

Good reproducibility of results is often a sign of high-quality data. In the case of the Itrax core scanner, there are three main factors that might simultaneously influence reproducibility of µ-XRF analyses at high resolution: (1) acquisition time (influencing amplitude variation of µ-XRF profiles as shown above), (2) element concentration in the sedimentary matrix and (3) element detectability.

Figure 10.4 illustrates the three factors and their inter-relationships. If all factors are 'high', the reproducibility will also be high; if all are 'low', reproducibility is likely to be low. Any other combination of high, low, medium for any factor falls into a grey area where reproducibility may vary.

To test this hypothesis, two consecutive analyses with exactly the same instrumental settings (40 kV; 45 mA; sample position; acquisition time: 10 s) were made. Prior to analysis, the range in the concentration (i.e. high, medium, low) of the chemical elements was determined using direct methods such as ICP-AES.

The Itrax user manual gives the µ-XRF detection limit for these elements, which generally increases with the atomic number (Croudace et al. 2006). Therefore, a range of detectability was assigned for each element. The elements tested in the sediments of Cape Bounty fall into six categories as shown in Fig. 10.5.

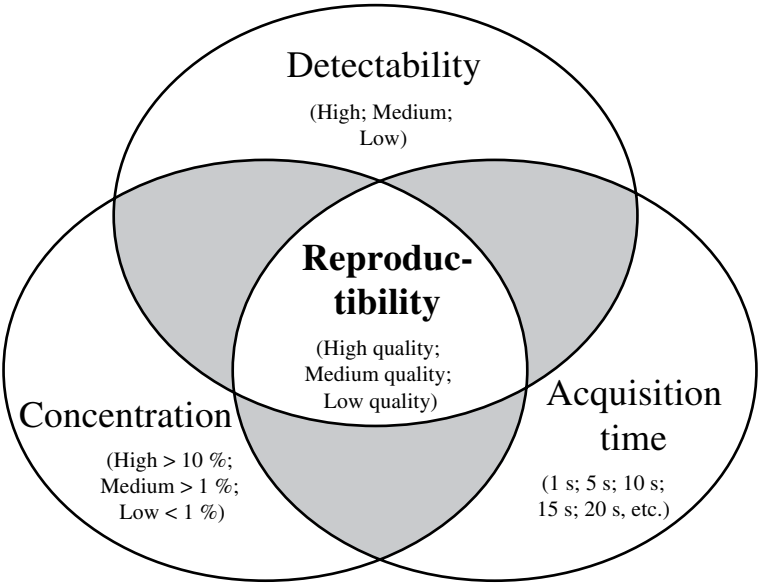


**Fig. 10.4** Factors influencing reproducibility of micro X-ray fluorescence analyses. The range of concentration was defined using ICP-AES analysis in this specific case study. For major elements the concentration is arbitrarily judged as 'high' for concentration > 10 %; as 'medium' for concentrations of 1–10 %; for minor (1–0.1 %) and trace elements (< 0.1 %) the concentration is arbitrarily judged as 'low'

### Visual Estimation of Reproducibility

The two consecutive µ-XRF analyses (described as Tests 1 and 2) were undertaken counting for 10 s every 200 microns along 150 mm of sediment, corresponding to 750 analysis points. First, we visually described the µ-XRF profiles variability, and then we examined statistical differences between the two tests.

| Detectability \ Concentration | High | Medium | Low |
|---|---|---|---|
| High | | Fe (3.84 %) | Ca (0.08 %), Ti (0.41 %), Sr (0.01 %), Zr (0.03 %) |
| Medium | | K (1.33 %) | Mg (0.61 %), P (0.59 %) |
| Low | Si (37.2 %) | Al (5.27 %) | |

Atomic number ↑

**Fig. 10.5** ICP-AES results of Cape Bounty sediments and level of element detectability depending on instrument settings (e.g. acquisition time, counts per second) defined by Itrax user manual. The range of chemical element concentration is categorized into three groups [high concentration (>10%); medium concentration (1–10%) and low concentration (<1%)]

Figure 10.6 highlights the degree of µ-XRF data reproducibility in the case of elements weakly detectable by the Itrax using a Mo-tube. Even if Si and Al have a similar level of detectability, the µ-XRF results from the two tests show little difference for Si in contrast to the clearly poor reproducibility for Al. This reflects their concentration in the sediment: Si has high concentration (37.2%) compared to Al that has moderate concentration (5.27%). In the case of Al, the poor reproducibility is also due to the substantial number of zero values analyses. These results suggest that 10 s is probably not sufficient to detect Al in that concentration (5%), and increasing acquisition time would decrease the number of intervals with zero values and bring the reproducibility of Al to level similar to Si.

Figure 10.7 illustrates the degree of µ-XRF data reproducibility for elements moderately detectable by the Itrax, but with slightly different concentrations (K=1.33%; P=0.59%). The two K profiles overlap quite well, with only a few differences (i.e. slight underestimation or over-estimation). In contrast, differences between the two P profiles are more apparent, even though analyses were undertaken in exactly the same position. Therefore, it is deduced that reproducibility for elements moderately detectable is acceptable for elements moderately present (K in this study case) in contrast to the poor quality of the reproducibility for elements weakly present (noisy P profiles in this case) (Fig 10.9).

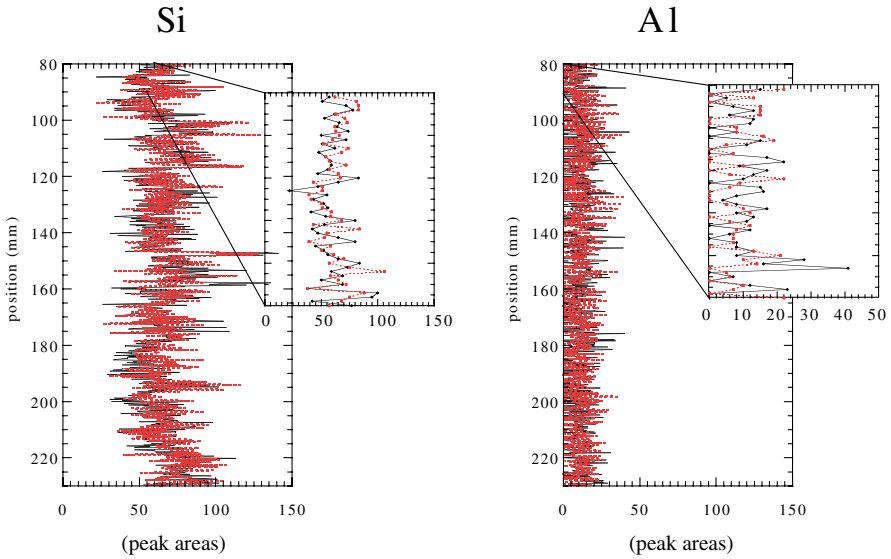


**Fig. 10.6** Comparison of Si and Al profiles, both elements having low detectability by Itrax measurement, but Si has high concentration (37.2%) while Al has moderate concentration (5.27%) in the sediment. *Red dotted* line represents Test 1 and *black solid line* Test 2

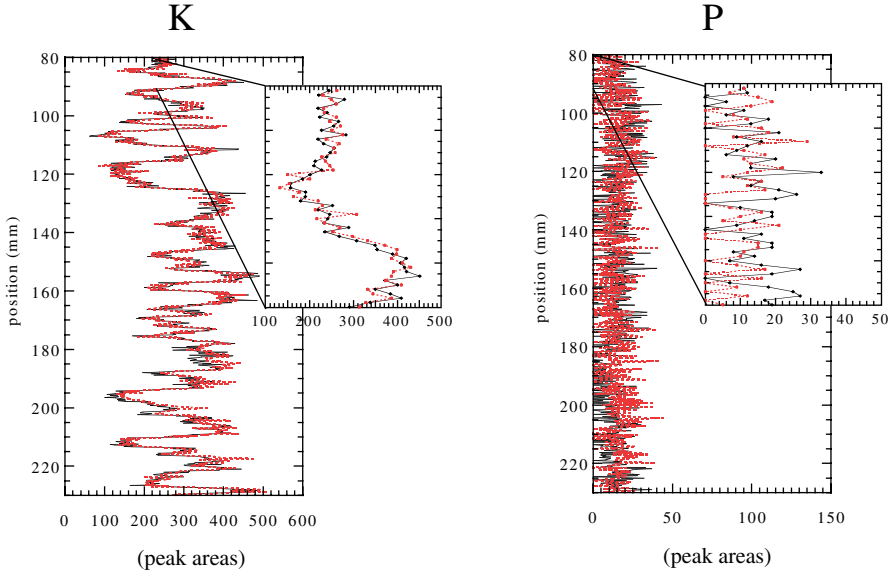


**Fig. 10.7** Comparison of K and P element profiles (in peak area), both elements having moderate detectability by Itrax measurement. K is moderately present in the sediment (1.33%) in contrast to P, which has low concentration (0.59%). *Red dotted line* is Test 1 and *black solid line* Test 2

Figure 10.8 shows profiles for chemical elements highly detectable by the Itrax. The Fe profile overlaps very well for both tests. Ca and Sr low frequency variations are similar for test 1 and 2, but the similarity declines in high frequency. The good Fe and Ti reproducibility could be explained by their combined high concentration in the sediment and high sensitivity to Itrax measurement compared to lower concentrations of Ca and Sr. These results suggest that the elements with the highest concentration are the most reproducible.

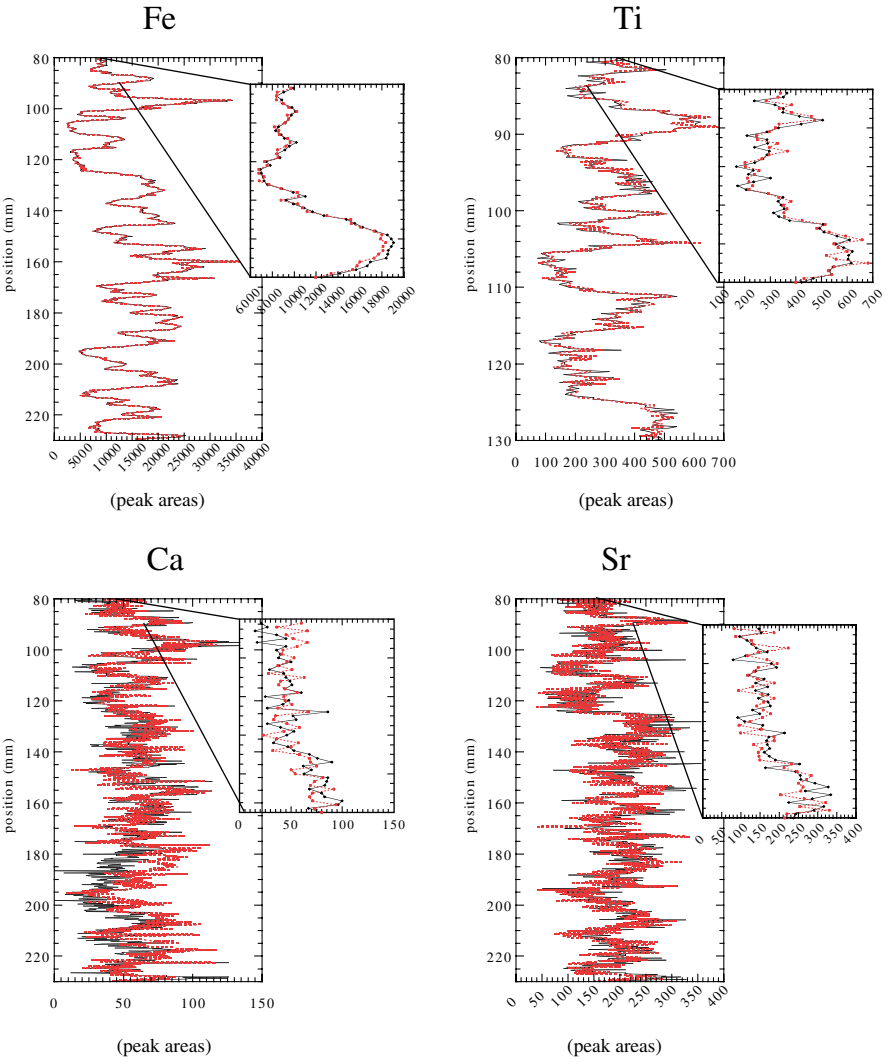


**Fig. 10.8** Comparison of chemical profiles for elements highly detectable by the Itrax. Fe is moderately present in the sediment (3.84 %) while Ti (0.41 %), Ca (0.008 %) and Sr (0.01 %) have low concentrations. *Red dotted line* represents Test 1 and *black solid line* is Test 2

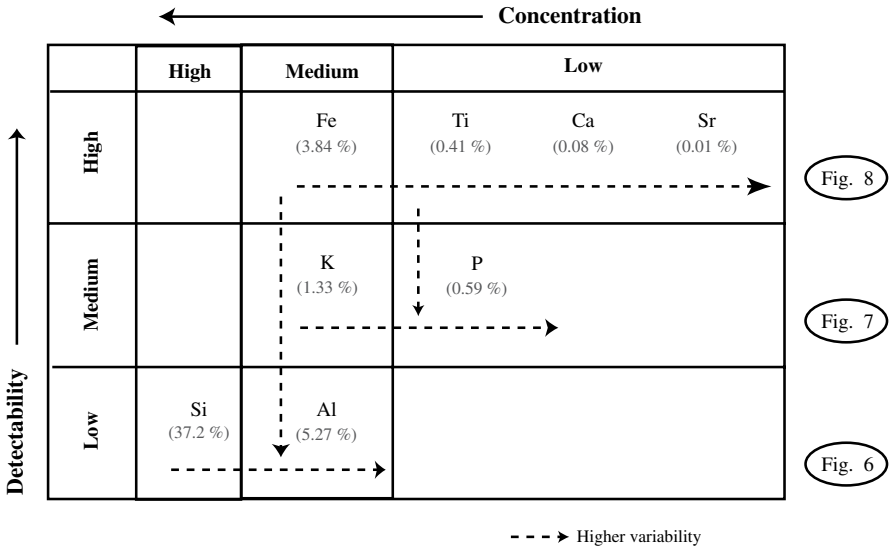


**Fig. 10.9** Summary of observations in Figs. 10.6, 10.7 and 10.8. The variability of the µ-XRF profiles increases with decrease in element concentration and with level of element detectability by Itrax measurement

In summary, comparison of two identical µ-XRF analyses illustrates that concentration greatly influences reproducibility for elements having similar detectability. Moreover, for elements having similar concentration but different detectability (Al, K and Fe profiles, Figs. 10.6, 10.7 and 10.8), the degree of detectability should also be considered as an important factor influencing the reproducibility. However, even though Si concentration (37.2 %) is much higher than Ti concentration (0.41 %), Si (weakly detectable) is less reproducible than Ti (highly detectable). Therefore, we infer that detectability plays a critical role in the reproducibility of µ-XRF analyses.

### Statistical Estimation of Reproducibility

To validate the qualitative observations and hypotheses described above, we calculated two statistical indices to measure the difference between the two identical runs. The first method consists of averaging all peak areas values for each element analyzed for each test, and then calculating an accuracy ratio value ("D/C" in Table 10.1) between the two tests. The second method consists of directly calculating the standard deviation ("E/C" in Table 10.1) of the peak area values of both tests. The coefficient of variation defined by the standard deviation of the average is then calculated and converted into a percentage for each chemical element.

Table 10.1 shows that the two methods give approximately the same values (lines 7 and 10). As was the case for graphical observations (see Figs. 10.6, 10.7 and 10.8), elements highly detectable and highly present in the sediment offer the

**Table 10.1** Statistical approach for estimating the reproducibility of μ-XRF results from two identical analyses. A and B represent the mean of peak area values for tests 1 and 2 respectively for the entire analysis. C represents the mean of the two tests. D represents the difference between the mean of the two tests. Lines 7 (accuracy ratio) and 10 (# coefficient of variation) correspond to the percentage errors estimated for the reproducibility of each chemical element, higher ratio values are considered more accurate. Presence of chemical element is arbitrary defined according the ICP-AES results. Dark gray cells represent better reproducibility (<2.5%) observed in this specific study

| | | | | *Increase of the atomic number* | | | | | | | | |
|---|---|---|---|---|---|---|---|---|---|---|---|---|
| | | | *Detectability* | ***Low*** | | ***Medium*** | | ***High*** | | | | |
| | | | *Elements* | **Al** | **Si** | **P** | **K** | **Ca** | **Ti** | **Fe** | **Sr** | **Zr** |
| **1** | (in peak areas) | A: | meaned Sum of the **test 1** | 10.62 | 65.59 | 13.93 | 291.39 | 54.76 | 364.82 | 14393.19 | 195.71 | 570.56 |
| **2** | | B: | meaned Sum of the **test 2** | 10.25 | 67.15 | 14.61 | 296.55 | 61.16 | 366.04 | 14215.98 | 185.68 | 559.32 |
| **3** | | C = Mean (A + B) | Mean | 10.44 | 66.37 | 14.27 | 293.97 | 57.96 | 365.43 | 14304.58 | 190.69 | 564.94 |
| **4** | | D = A - B | Difference (in absolute value) | 0.36 | 1.57 | 0.67 | 5.16 | 6.4 | 1.22 | 177.22 | 10.03 | 11.24 |
| **6** | | D / C: | Difference / Mean | 0.0345 | 0.0237 | 0.0470 | 0.0176 | 0.1104 | 0.0033 | 0.0124 | 0.0526 | 0.0199 |
| **7** | | D / C: | in % | 3.45% | 2.37% | 4.7% | 1.76% | 11.04% | 0.33% | 1.24% | 5.26% | 1.99% |
| **8** | | E (in peak areas): | Standard deviation | 0.26 | 1.11 | 0.48 | 3.65 | 4.53 | 0.86 | 125.31 | 7.09 | 7,95 |
| **9** | | E / C: | Coefficient of variation | 0.0250 | 0.0167 | 0.0340 | 0.0124 | 0.0780 | 0.0024 | 0.0088 | 0.0372 | 0,01 |
| **#** | | E / C: | in % | 2.5% | 1.67% | 3.4% | 1.24% | 7.8% | 0.24% | 0.88% | 3.72% | 1% |
| | | | *Concentration in the sediment* | **5.27%** | **37.2%** | **0.59%** | **1.33%** | **0.08%** | **0.41%** | **3.84%** | **0.01%** | **0.03%** |
| | | | *Presence* | **Medium** | **High** | Low | **Medium** | Low | **Low / Mid** | **Medium** | Low | Low |

→ High values of peak areas →

best reproducibility (Table 10.1). However, the quality of Al reproducibility appears overestimated by the statistical method compared to visual estimation. This might be explained by the large number of zero values. Therefore, in this case, the graphical representation of Al is more appropriate to estimate the quality of its reproducibility.

In summary, both graphical patterns of element abundance and statistical indices show the need to consider the presence and detectability of chemical elements as two important factors influencing quality of µ-XRF data reproducibility. Moreover, because detection limit depends on the element, the time of analysis and matrix composition (Croudace et al. 2006), it is crucial to increase the acquisition time in order to acquire valid data, especially for chemical elements with low atomic number (e.g. Si and Al, both weakly detectable with an Mo-tube).

## *Effects of Sample Topographical Irregularities on µ-XRF Results at High Resolution*

The standard Itrax analysis procedure starts by loading the split sediment core in a horizontal sample holder that incrementally moves the sample from left to right under XRF and RX detectors and under an incident X-ray beam that is oriented parallel to the stratigraphy (Croudace et al. 2006). Before analyzing the sediment core, an estimate of the error associated with the sediment type is needed. Caution in interpretation is needed as changes in grain-size, mineralogy, porosity and water content may affect data quality (Croudace et al. 2006). Increasing count rates is recommended to lessen the amount of invalid data. Nevertheless, risk of degradation of data quality remains specifically for high-resolution analyses, particularly for step-sizes under 200 µm. Topographic irregularities on the core surface present a potential bias in µ-XRF results and may result in invalid data. This might be important for sediments with rapid changes in lithology (such as laminated sediments) or during long time runs that could lead to sediment surface dehydration, desiccation and crack formation. To test whether such fine variability exists in samples, an experiment to verify the quality of the results following micro X-radiography (µ-RX) and X-ray fluorescence was undertaken at high resolution using copper wires placed on the fresh sediment surface. Cu wires have low X-radiographic intensity (corresponding to high density) and create zones with local high topographic relief clearly recognizable both visually (µ-RX image, Fig. 10.10) and graphically (through radiographic intensity and µ-XRF chemical profiles, Fig. 10.10).

Figure 10.10 shows an underestimation of µ-XRF compared to the radiograph, which occurs when the µ-XRF sensor encounters a relief feature. X-ray fluorescence radiation emitted by the sample is measured by a Si-drift chamber detector set at an angle of 45° to the incidental X-radiation, whereas the RX detector is located directly below the sample and hence perfectly aligned with the X-ray incident beam. Thus, the µ-XRF detector can produce a shading effect due to its geometry, as illustrated in Fig. 10.11a, where “S” represents its maximal area.

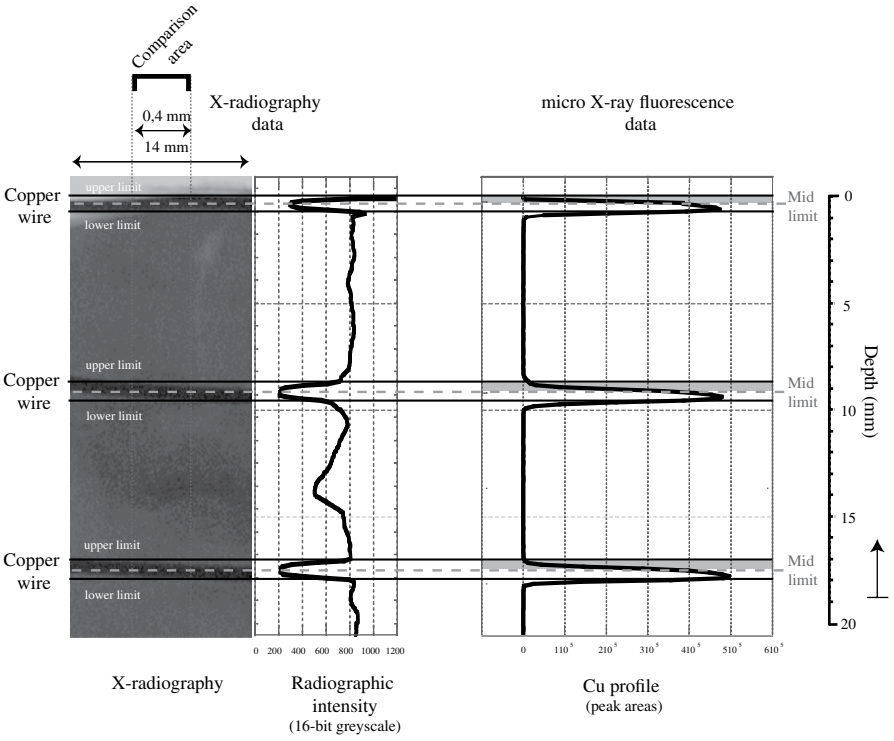


**Fig. 10.10** A 14-mm wide X-radiograph image with corresponding X-radiographic intensity and Cu profiles along a 20 mm long sediment core interval from Cape Bounty Lake, Canada, overlain by three copper wires. The radiographic profile was built using the 4 mm µ-XRF detection area to create a perfect match of µ-RX and µ-XRF profiles. Three *black lines* delimit the position of the Cu-wires, which correspond to irregularities on the surface sample and an offset between the µ-XRF geochemical data and the corresponding micro-radiography. Cu is not detected in the upper part of the Cu-wire interval corresponding to an underestimation of the µ-XRF results

Based on different patterns of topographic irregularities (i.e. hollow or relief), we define conditions that can produce erroneous µ-XRF data (Fig. 10.11). Figure 10.11b illustrates that the geometry of the system induces a length interval, d, with missed data that is proportional to the height, h, of the highest relief along a distance equivalent to d. In addition, slope of the relief is the key factor that controls the quality of results, with the presence of topographical relief on the sample surface disrupting the signal if $\alpha > \beta$ corresponding to $\alpha > 45°$ (Fig. 11a and b). The schematic illustrations of µ-XRF operations in Fig. 10.11b show that measurements are not considered valid for variation in height, h, between two points of analysis. µ-XRF measurements between points 1–1′ and 3–3′ are missing in the results. Therefore, the estimated error limits (shading effect area) of missed data interval will correspond to $d = h$ in cases of irregularities followed by relief where $\alpha \geq 45°$. This method could be used in the future to identify places where such biases are introduced. However, this idealised model is complicated by the deviation in the readjustment of the detector when it meets a topographical irregularity. The most important deviation between the detector and the sediment appears in the case of a relief compared to a hollow (Fig. 10.11c).

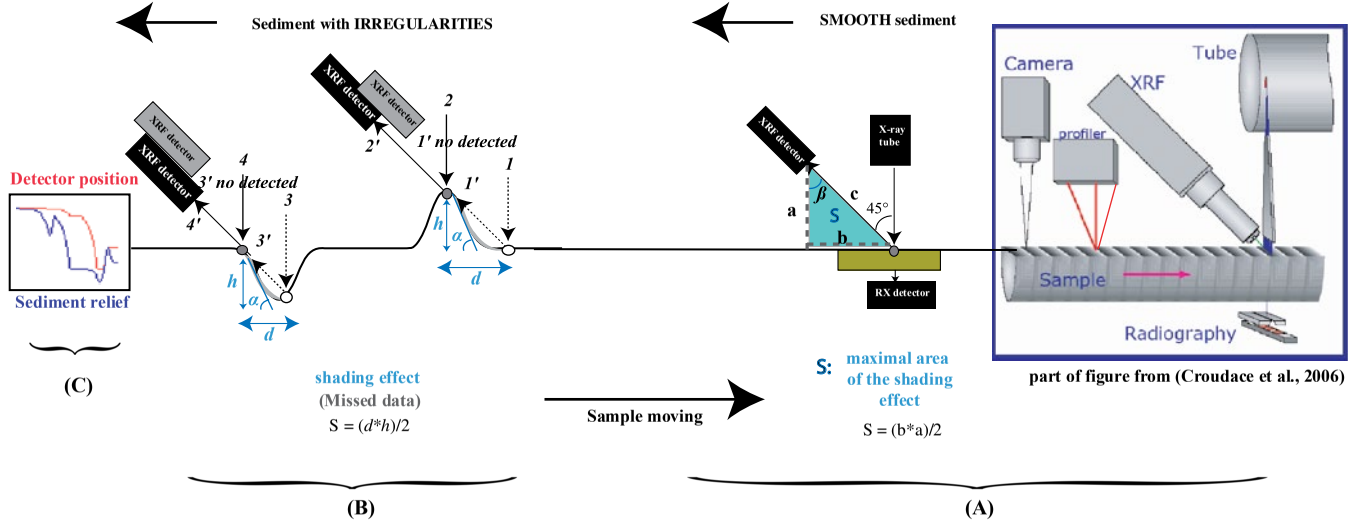


**Fig. 10.11** Comparison of operation patterns for data acquisition with an Itrax core scanner from topographical irregularities: **a** Geometrical schematization of the XRF system with smooth core surface. **b** Sediment with topographical irregularities. *Dotted arrows* represent erroneous data acquisition by the XRF detector and *solid arrows* represent correct data acquisition. The XRF detector does not record the points 1–1′ and 3–3′ because of a shading effect that causes an underestimation of the µ-XRF results sum. **c** Distance between the detector and the sample surface. The error consists of missed data along a distance, d, that is function of the maximum height of the relief, h, and its slope inclination, α. To acquire valid data, $\alpha < \beta$ ($\beta = 45°$); Tan $\beta = a/b$ (with $\beta = 45°$), thus $a = b$ and the surface area of the maximal shading effect, S, corresponds to $S = b^2/2$

Even if the XRF detector maintains a constant distance with respect to sample topography, a lack of µ-XRF measurements occurs if reliefs or hollows present an inclination slope $\alpha \geq 45°$ (Fig. 10.11a). To mitigate this problem the sample surface should be smoothed or sample holder moved laterally in order to minimize topographical irregularities as much as possible, if obtaining a perfectly smooth sediment surface proves difficult. When it is not possible to reduce surface irregularities, the inaccuracies caused should be taken into account in interpretation of results, especially when analyzing finely laminated sediments.

## Methodological Synthesis for Maximizing Data Robustness of the Itrax Core Scanner for Analysis of Thin Laminations

Based on the analytical attributes and the solution presented in Section "Case study: high-resolution µ-XRF analysis for estimation of grain-size variability and varve counts in fine clastic varved sediment from Cape Bounty Lake, Canadian High Arctic", the following method is proposed for using an Itrax core scanner for the analysis of thin laminations (Fig. 10.12). The first two steps are to select a higher

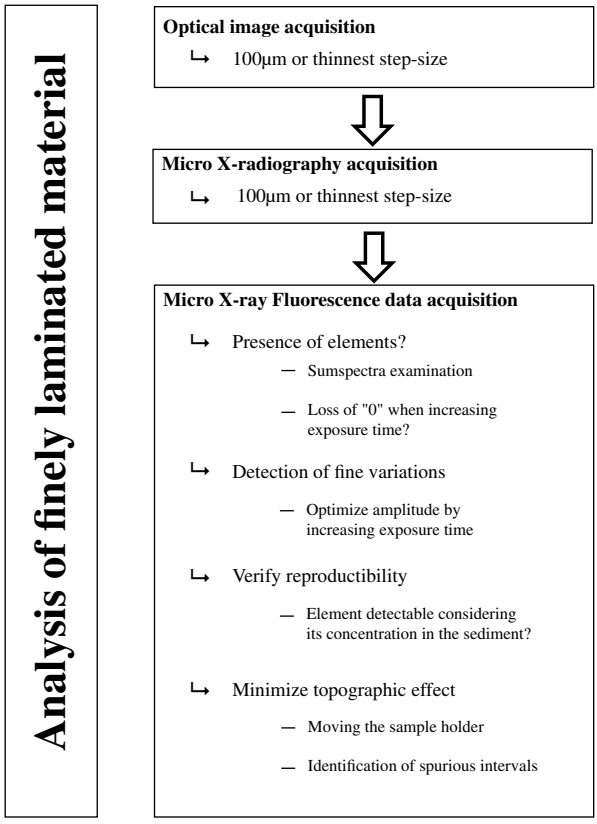


**Fig. 10.12** Operational flow chart for analysis of finely laminated sediment using an Itrax core scanner

step-size for optical image acquisition and micro X-radiography acquisition. For data assessment, the 'real' presence of chemical elements should be verified by examining the sum spectra, and increasing the exposure time on a test section. Then, a similar increase of exposure time should be used to check the amplitude of µ-XRF measurements across laminae. To maximize reproducibility, the combined values of detectability and the presence of each chemical element should be considered. Finally, careful examination of the smoothness of the topography should be made to determine where µ-XRF results might be affected by topographic irregularities.

## Case Study: High-Resolution µ-XRF Analysis for Estimation of Grain-Size Variability and Varve Counts in Fine Clastic Varved Sediment from Cape Bounty Lake, Canadian High Arctic

Investigations of high-resolution sedimentological archives that reflect annual or seasonal variability are fundamental for a better understanding of past changes in seasonal- to centennial-scale climatic and hydrological cycles. The Itrax core scanner provides µ-XRF measurements at high to ultra-high resolution (equal or greater than 100 µm), and is well adapted for characterization of finely laminated sediments. The analyses were performed on freshly split sediment cores and impregnated blocks used for preparation of thin sections presenting fine varves, commonly 1 mm thick (Cuven et al. 2010). Following the optimal analytical protocols described above and the validation of µ-XRF data by discrete sampling methods, we applied this technique to finely clastic varves from lake sediments in the Canadian High Arctic to develop new paleohydrological proxies and improve chronological constraints (Cuven et al. 2010). The sedimentary profile used in this case study was obtained at Cape Bounty, and represents a 4200-year long record of terrestrial sediment flux in the Western part of the Canadian High Arctic (Cuven et al. 2011). Since it is difficult to accurately date lacustrine paleoclimate records in the Arctic (due to the lack of terrestrial carbon and the remobilization of old carbon stored in watersheds limiting use of $^{14}C$ dating (Abbott and Stafford 1996)), we illustrate the potential of using µ-XRF data for varve counting.

### *Estimation of Grain-Size Variability: Development of Paleohydrological Indicators*

First, the different seasonal sedimentary deposits were characterized (Fig. 10.13). Sedimentary description of records from Cape Bounty lakes, Melville Island, Nunavut, Canada (74°53'N, 109°W) suggested the presence of, on average, 1-mm thick varves, composed of clay layers, produced under the ice-covered lake during winter, and silt layers produced by snow melt during the spring (Cuven et al. 2010;

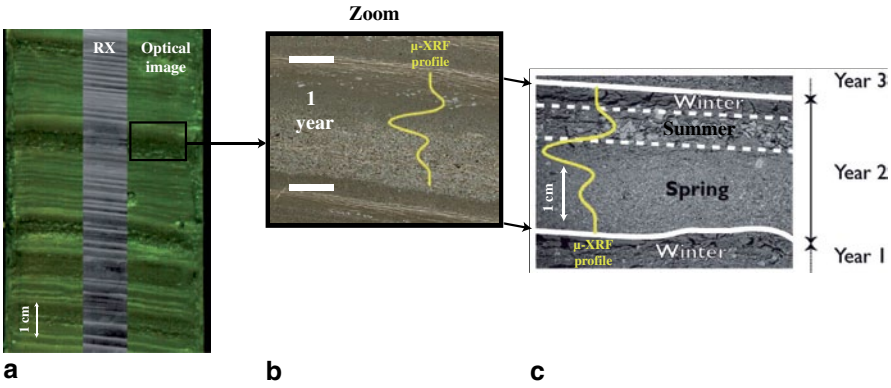


**Fig. 10.13** Sedimentary description and characterization of Cape Bounty varves: **a** optical image and X-radiograph (100 μm resolution); **b** thin-section image with overlapping μ-XRF profile (Si) showing element changes across an enlarged cross-section through one varve couplet composed of an upwards-fining graded bed deposit and an unsorted coarse grained deposit capped by a thin clay layer; **c** scanning electron microscope (SEM) image of cross-section b with seasons assigned to each sedimentary unit described

Cockburn and Lamoureux 2008). Sand layers were also frequently observed and represent summer rain events (Dugan et al. 2009).

Since the chemistry of sediments is known to be partly influenced by grain-size (Boyle 1983; Cuven et al. 2010), and because grain-size is used assess changes in the hydrological cycle, μ-XRF can be a powerful technique for paleohydrological studies (Cuven et al. 2010). Here, we use μ-XRF analysis to characterize fine-scale changes in sediment structure and grain-size, validating data obtained by comparison to conventional physical and geochemical methods.

Cuven et al. (2010) showed that, at centimeter scales, the relative abundance of some chemical elements present in the Cape Bounty sediment is related to the particle size distribution of discrete samples. Grain size is positively correlated with Zr, and negatively correlated with K and Fe (Fig. 10.14). On a macroscopic scale, μ-XRF results are validated by ICP-AES analyses performed on discrete samples sufficiently thick and homogeneous to avoid contamination from surrounding facies in subsamples.

At varve and microscopic intra-varve scales, chemical profiles of these elements (observed on digital images of thin-sections at 0.02 mm resolution) are also correlated with grain size. On the microscopic scale, sedimentary facies characterization was identified by grain-size analysis from SEM images from thin-sections and variation in μ-XRF profiles; trends in μ-XRF results are validated by Energy Dispersive Spectroscopy (EDS)-mapping analyses performed on thin-sections.

Cuven et al. (2010) concluded that clay layers are enriched in K and Fe, with variations in their abundance reflecting hydrological changes during winter. Similarly, silt layers are enriched in Ti and variation in its abundance reflects hydrological changes during spring, while sand layers are enriched in Zr and reflects hydrological changes during spring or summer (Cuven et al. 2010) (Fig. 10.15).

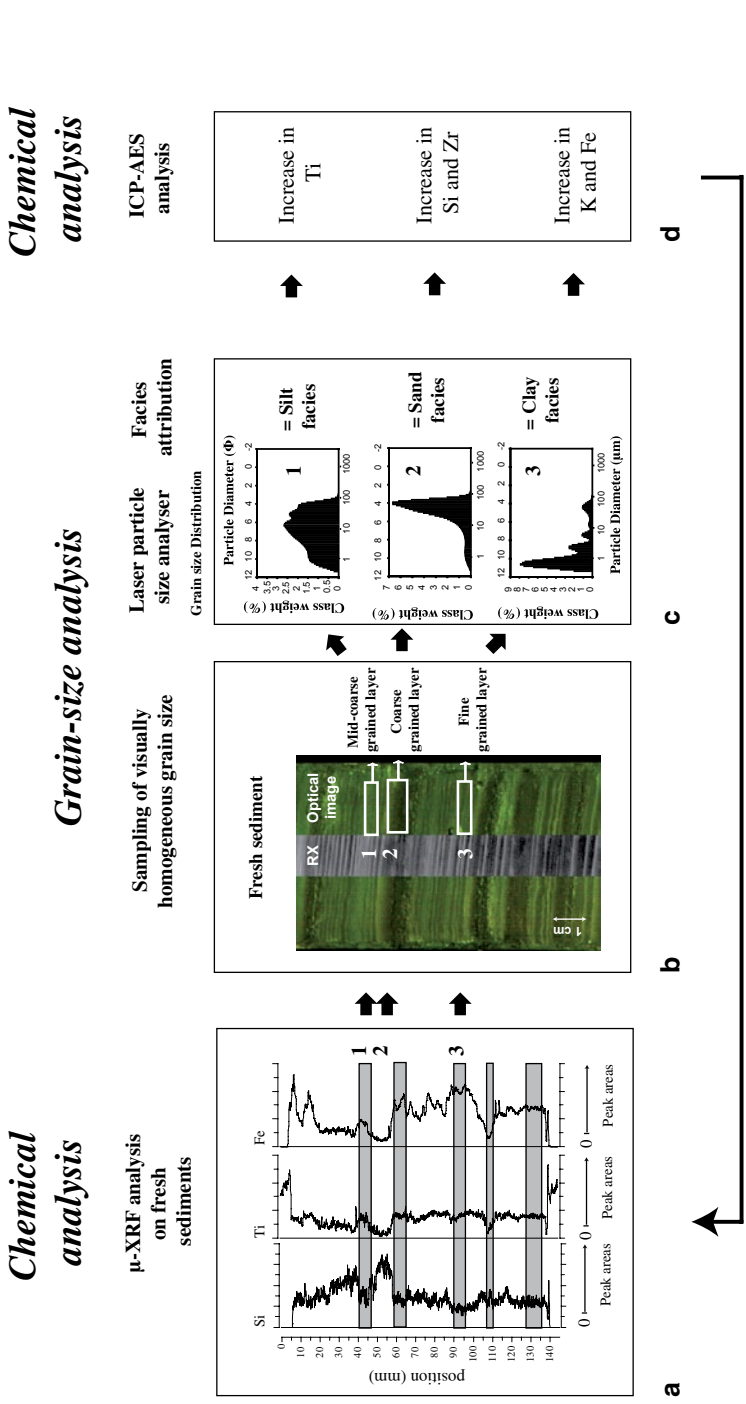


**Fig. 10.14** Grain-size and μ-XRF variability at centimetric scale from a clastic varved sediment (Cuven et al. 2010). **a** μ-XRF data variability along a core section from Cape Bounty presenting grain-size changes at centimeter scale. **b** Close-up of sampling areas with apparently homogeneous grain size. **c** Classical grain-size analyses using a laser particle analyser and the corresponding facies. **d** Chemical analysis outcome using ICP-AES analysis

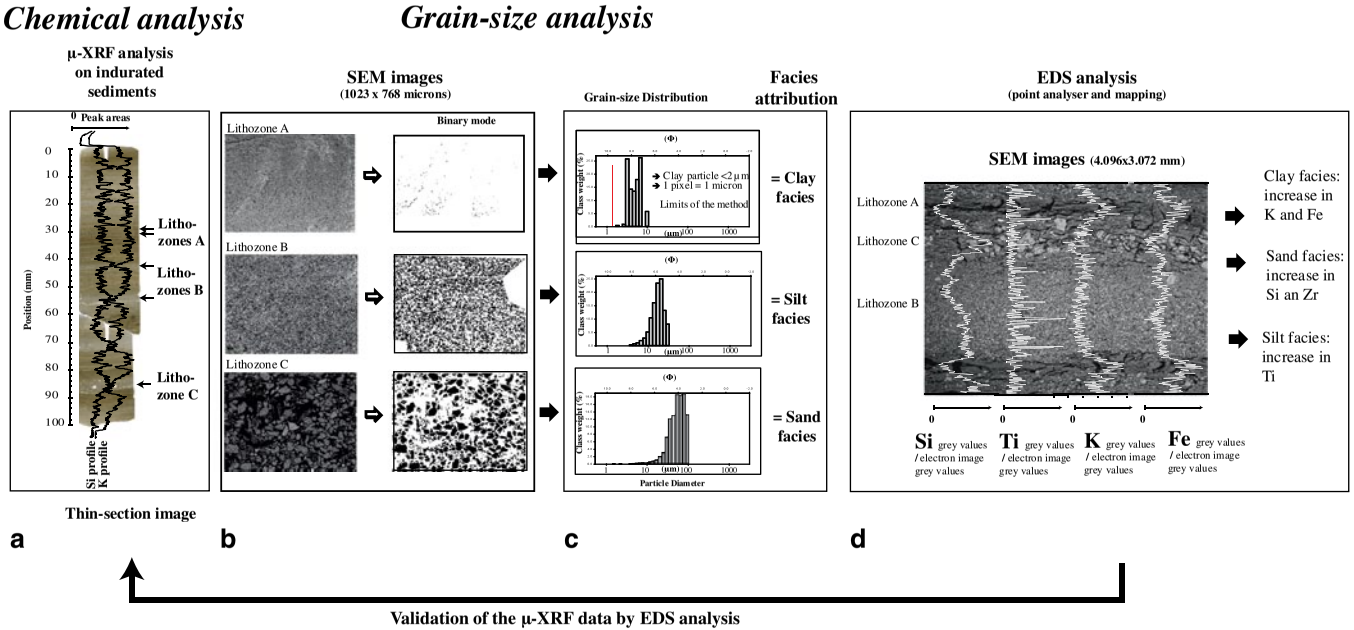


**Fig. 10.15** Grain-size and µ-XRF variability at microscopic scale using an example of clastic varved sediment (Cuven et al. 2010): **a** µ-XRF variability along a 7 cm long impregnated section with millimeter-scale grain-size variability; **b** BSE-SEM images of the different facies (or lithozones) present in the sediment and their corresponding black & white image after image analysis processing; **c** grain-size analyses obtained using image analysis and sedimentary facies characterization; **d** EDS chemical profiles across a varve

Further, changes in Si abundance are not related to grain size, probably because of the complex mixed origin of primary production and detrital deposition (Cuven et al. 2010). Work in progress highlights the potential of using high-resolution µ-XRF data for paleoclimatological studies in this environment.

Hence, sedimentary facies linked to snow melt, rain events and niveo-aeolian inputs can be partly identified based on µ-XRF profiles if the link between elemental chemistry and sedimentary facies is carefully established beforehand.

## *Recommendations and Steps to Estimate Grain Size from µ-XRF Data for use as Paleohydrological Indicators in Clastic Finely Laminated Sediments*

- Identify every sedimentary facies according to its apparent grain size.
- Attribute a paleohydrological signal for each sedimentary facies, for instance with help of hydrological monitoring data.
- Sample sediment with visually homogeneous grain size and analyze the grain size with standard techniques at low resolution (e.g. laser particle size analyzer on discrete samples) and at high resolution (e.g. image analysis on SEM images).
- Attribute a sedimentary facies for each grain-size class to a specific element provided by µ-XRF data.
- Perform additional chemical analyses in each sedimentary facies for comparison and validation of the chemical elements abundance given by the µ-XRF analysis. Comparison of chemistry results should be realized by standard techniques at low resolution (e.g. ICP-AES, Fig. 10.14), but also at high-resolution where fine laminated sediment exists (e.g. EDS, Fig. 10.15).
- Validate the chemical composition of sediment source in the watershed and verify its coherence to the observations above.
- Where changes in chemical element abundance or µ-XRF ratios are related to grain-size variations, define new paleohydrological indicators for each specific grain-size class by examining variation in µ-XRF data for each sedimentary facies (Figs. 10.14 and 10.15).

## *Estimate of Varve Counts*

Developing accurate chronologies are an important challenge for long-term paleoreconstruction, particularly for annually-resolved records. Varve counting is a time-consuming and labor-intensive task, especially when varves are thin and require counting from thin-sections. In this section, the potential use of µ-XRF profiles as a semi-automated varve counting method is highlighted. This method has been already tested and implemented for the development of a chronology for organic-rich Lake Suigetsu, Japan (Francus et al. 2009) and calcareous-rich lacustrine sediment from the Sahara (Kröpelin et al. 2008).

In the Cape Bounty case study, Fig. 10.16 shows that the K/Ti ratio is relatively concordant with upper limits of the clay-rich facies of the varves, because the clay caps are enriched with K and have a relatively low Ti content. Defining varve limits using this ratio is less accurate when sand-silt-clay couplets are present and further work is needed to count varves automatically using µ-XRF profiles. Indeed, the sediment fraction described in Fig. 10.16 presents 43 varves whose upper limits are marked by arrows, while only 38 peaks are clearly visible in K/Ti profile for the same interval. Nevertheless, rapid varve counting using µ-XRF profiles could help establish more robust chronologies in detrital sediment.

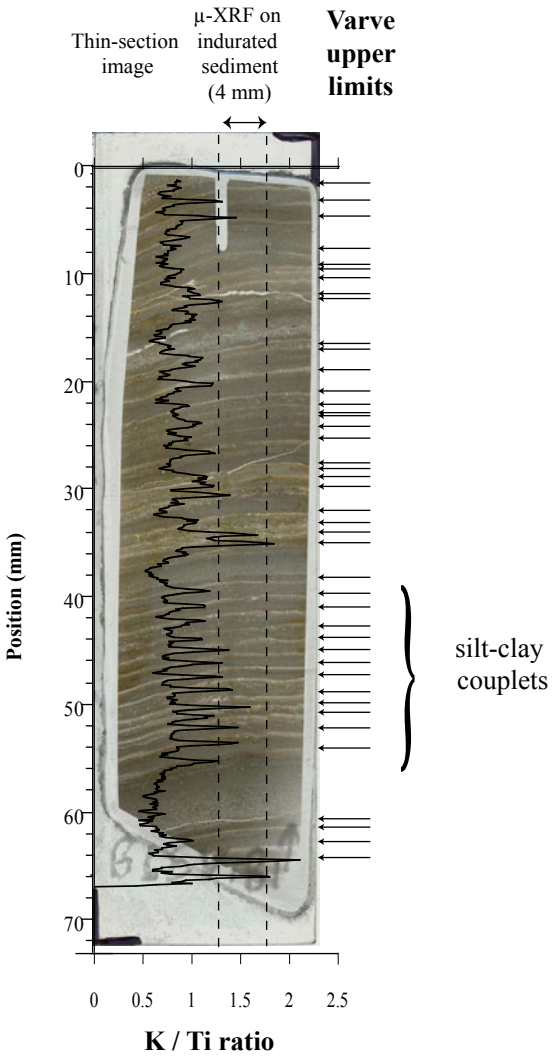


**Fig. 10.16** µ-XRF profile showing variation of K/Ti along a thin-section image used for varve counting. Delineation of varve upper limits by significant K/Ti peaks compared to manually marked upper limits of clay caps (*arrows*)

## Future Direction: Development of Climate Proxies

The use of micro X-ray fluorescence for sediment characterization can significantly enhance paleoclimatic and paleoenvironmental studies. Our cautious work on grain-size estimation using μ-XRF analysis of finely laminated sediment has provided information about seasonal changes in hydroclimatic conditions, and has shown that μ-XRF analysis is an effective tool for developing paleoclimate indicators from textural data. In the case study presented, coarser grained deposits (sandy layers) are attributed to rainfall events during summer (Dugan et al. 2009) or turbidity currents during snowmelt in spring (Cockburn and Lamoureux 2008). Significant increases in chemical elements, such as Zr, in these coarser deposits can be used as a paleoclimate proxy because they define, precisely, when the most extreme hydrological events in the Cape Bounty lake record occurred. Preliminary results show cyclic increases in relative Zr abundance, which most likely reflect increases in high frequency and high magnitude rain events during the last two centuries at Cape Bounty.

This study provides a better understanding of seasonal sediment deposition cycles, and also improves our understanding of sedimentological processes related to frequencies of cyclonic activity that effect precipitation and temperature at the study site. Changes in cyclonic activity in the Arctic over the last 2000 years have been linked to known modes of variability such as the North Atlantic Oscillation (NAO), Arctic Oscillation (AO) and Atlantic Multidecadal Oscillation (AMO) or to changes in external forcing mechanisms (e.g. solar irradiance, volcanism and/or increased greenhouse gas emissions).

## Summary

To obtain robust and valid μ-XRF measurements, caution is needed to ensure: (1) chemical elements are suitably representative; (2) the acquisition instrument's settings are controlled and maintained; (3) detected elements are environmentally meaningful.

Major factors that influence data quality when acquiring μ-XRF data at high resolution are: (1) acquisition time and element concentration, which both play a key role in data reproducibility; (2) underestimation of the μ-XRF data can be minimized by removing topographical irregularities on the sediment surface or by estimating affected lengths.

We use a clastic varved sediment sequence from Arctic Lake Cape Bounty as a case study to illustrate the high potential of μ-XRF data for paleoenvironmental studies. μ-XRF offers the possibility to quickly and non-destructively characterize fine-scale structures in sediment cores at an unprecedented resolution.Furthermore, estimation of grain size from μ-XRF profiles provides a new paleohydrological proxy, which has substantially improved our understanding of inter-annual variability of hydroclimatic and paleoclimate change in the Arctic over the last 2000 years.

**Acknowledgments** We thank the Polar Continental Shelf Project, Natural Resources Canada (PCSP) for logistical support. This work was supported by grants from the NSERC (Natural Sciences and Engineering Research Council of Canada) and the Canadian Federal Program for the International Polar Year (IPY) awarded to Pierre Francus and Scott Lamoureux. We thank Scott Lamoureux for the material, GEOTOP (Geochemistry and Geodynamics Research Center) for funding of experiments, and Cox Analytical Systems for their help in understanding instrument performance. We are especially grateful to David Fortin and Anna Pienkowski-Furze for their assistance in core processing and an anonymous reviewer, Guy Rothwell and Isabelle Larocque for translation assistance.

## References

Abbott MB, Stafford TW (1996) Radiocarbon geochemistry of modern and ancient Arctic lake systems, Baffin Island, Canada. Quat Res 45:300–311

Boyle EA (1983) Chemical accumulation variations under the Peru Current during the past 130,000 years. J Geophys Res 88:7667–7680

Cockburn JMH, Lamoureux SF (2008) Inflow and lake controls on short-term mass accumulation and sedimentary particle size in a High Arctic lake: implications for interpreting varved lacustrine sedimentary records. J Paleolimnol 40:923–942

Croudace IW, Rindby A, Rothwell RG (2006) ITRAX: description and evaluation of a new multi-function X-ray core scanner. In: Rothwell RG (ed) New techniques in sediment core analysis. Geol Soc Spec Publ 267:51–63

Cuven S, Francus P, Cremer J-F (2007) Protocoles d'utilisation et essais de calibration du scanner de microfluorescence X de type ITRAX™ Core Scanner. Quebec, INRS-ETE (Report 954) 108 pages

Cuven S, Francus P, Lamoureux SF (2010) Estimation of grain-size variability with micro X-ray fluorescence in laminated sediments, Cape Bounty, Canadian High Arctic. J Paleolimol 44:803–817

Cuven S, Francus P, Lamoureux SF (2011) Mid to Late Holocene hydroclimatic and geochemical records from the varved sediments of East Lake, Cape Bounty, Canadian High Arctic. Quat Sci Rev 30:2651–2665

Dugan HA, Lamoureux SF, Lafrenière ML, Lewis T (2009) Hydrological and sediment yield response to summer rainfall in a small high Arctic watershed. Hydrol Process 23:1514–1526

Francus P, Lamb H, Nakagawa T et al (2009) The potential of high-resolution X-ray fluorescence core scanning: applications in paleolimnology. Newsletter 17:93–95

Kaufman D (2009) An overview of late Holocene climate and environmental change inferred from Arctic lake sediment. J Paleolimnol 41:1–6

Kröpelin S, Verschuren D, Lézine A-M, Eggermont H, Cocquyt C, Francus P, Cazet J-P, Fagot M, Rumes B, Russell JM, Darius F, Conley DJ, Schuster M, von Suchodoletz H, Engstrom DR (2008) Climate-driven ecosystem succession in the Sahara: the past 6000 years. Science 320:765–768

Lamoureux SF (2001) Varve chronology techniques. In: Last WM, Smol JP (eds) Tracking environmental changes using lake sediments: physical and geochemical methods, vol 1. Kluwer, Dordrecht, pp 247–260 (Developments in Paleoenvironmental Research)

Lamoureux SF, Bollmann J (2005) Image acquisition. In: Francus P (ed) Image analysis, sediments and paleoenvironments, vol 7. Kluwer, Dordrecht, pp 11–34 (Developments in Paleoenvironmental Research)

Lamoureux SF, Bradley RS (1996) A late Holocene varved sediment record of environmental change from northern Ellesmere Island, Canada. J Paleolimnol 16:239–255

Last WM (2001) Textural analysis of lake sediments. In: Last WM, Smol JP (eds) Tracking environmental changes using lake sediments: physical and geochemical methods, vol 2. Kluwer, Dordrecht, pp 41–81 (Developments in Paleoenvironmental Research)

MacDonald GM, Felzer B, Finney BP, Forman SL (2000) Holocene lake sediment records of Arctic hydrology. J Paleolimnol 24:1–14

Ojala AEK (2005) Application of X-ray radiography and densitometry in varve analysis. In: Francus P (ed) Image analysis, sediments and paleoenvironments, vol 7. Kluwer, Dordrecht, pp 187–202 (Developments in Paleoenvironmental Research)

Rothwell RG (2006) (ed) New techniques in sediment core analysis. Geol Soc Spec Publ 267:253–259

Wolfe BB, Hall RI, Last WM, Edwards TWD, English MC, Karst-Riddoch TL, Paterson A, Palmini R (2006) Reconstruction of multi-century flood histories from oxbow lake sediments, Peace-Athabasca Delta, Canada. Hydrol Process 20:4131–4153

Zolistschka B (1998) A 14,000 year sediment yield record from western Germany based on annually laminated lake sediments. Geomorphology 22:1–17

# Chapter 11
# Investigating the Use of Scanning X-Ray Fluorescence to Locate Cryptotephra in Minerogenic Lacustrine Sediment: Experimental Results

**Nicholas L. Balascio, Pierre Francus, Raymond S. Bradley, Benjamin B. Schupack, Gifford H. Miller, Bjørn C. Kvisvik, Jostein Bakke and Thorvaldur Thordarson**

**Abstract** Methods to isolate and analyze low concentrations of tephra—*cryptotephra*—are destructive, time consuming, and can be prohibitive when sample size is limited, when looking for tephra over long stratigraphic intervals, or when sediments are minerogenic. Therefore, a more rapid, non-destructive approach to detecting cryptotephra would allow for wider application of tephrochronology and for more complete evaluation of tephra content within sedimentary profiles. In this experiment, we test the ability of scanning X-ray fluorescence to detect tephra glass shards with different composition, concentration, and grain-size in minerogenic lacustrine sediment. Synthetic sediment cores spiked with tephra were created in centrifuge tubes, which provided a simple means to introduce tephra

N. L. Balascio (✉)
Lamont-Doherty Earth Observatory of Columbia University, Palisades, NY 10964, USA

Department of Geosciences, University of Massachusetts, Amherst, MA 01003, USA
e-mail: balascio@ldeo.columbia.edu

R. S. Bradley
Department of Geosciences, University of Massachusetts, Amherst, MA 01003, USA

P. Francus
Institut National de la Recherche Scientifique, Centre Eau Terre Environnement, Québec, QC G1K 9A9, Canada

GEOTOP Research Center, Montréal, QC H3C 3P8, Canada

B. B. Schupack · G. H. Miller
INSTAAR and Department of Geological Sciences, University of Colorado, Boulder, CO 80303, USA

B. C. Kvisvik · J. Bakke
Department of Earth Science, University of Bergen, Fosswinckelsgate 6, N-5020 Bergen, Norway

T. Thordarson
School of Geoscience, University of Edinburgh, Edinburgh EH93JW, UK

Faculty of Earth Sciences, University of Iceland, Sturlugata 7, IS101, Iceland



I. W. Croudace, R. G. Rothwell (eds.), *Micro-XRF Studies of Sediment Cores*,
Developments in Paleoenvironmental Research 17, DOI 10.1007/978-94-017-9849-5_11

in known positions and to replicate the process of analyzing real sediment cores. Background sediment was added incrementally and spun in a centrifuge to create a series of 20 laminations in 4 synthetic cores. Rhyolitic and basaltic tephra were added between laminations with different concentrations and using two grain-size ranges (< 53 μm and 105–177 μm). The synthetic cores were split and analyzed on an XRF core scanner, which produced a signal of element composition every 100 μm. Ti, Mn, and Si produced the strongest response to the rhyolitic tephra, and Ti, Mn, Fe, and Cu were most diagnostic of the basaltic tephra. Element ratios were also used to accentuate the difference in composition between tephra and the background sediment. We were able to identify a distinct elemental response across a few cryptotephra horizons, but in general the signal of tephra attenuated quickly with decreasing concentration. Comparison of the signal between different tephra grain-size fractions showed that grain-size was inversely related to the strength of the elemental response. We also compared these experimental results to XRF scans of a lake sediment core where basaltic and rhyolitic cryptotephra layers had previously been identified using conventional methods. The rhyolitic tephra did not produce a distinct elemental response, but the basaltic tephra was identified in the XRF data. These experiments provide new perspectives on the application and limitations of scanning XRF for cryptotephra studies.

**Keywords** Tephra · Cryptotephra · Lake sediment · Micro-XRF · Itrax

## Introduction

Tephrochronology is a powerful geochronologic tool that can be used to correlate or determine precise ages of a variety of sedimentary archives, including: lake sediments, peat, soils, loess, marine sediments, and glacier ice. Tephra can provide age control in sediments void of material suitable for other dating techniques or supplement existing chronologies. Tephrochronology has a broad range of applications in paleoenvironmental research (Turney and Lowe 2001; Alloway et al. 2007; Lowe 2011). These encompass archaeology (Hall et al. 1994; Newnham et al. 1998; Dugmore et al. 2000; Lowe et al. 2000; Balascio et al. 2011), human evolution (de Menocal and Brown 1999; WoldeGabriel et al. 2005; Deino et al. 2010), the study of landscape change (Manville and Wilson 2004; Dugmore et al. 2009, Streeter et al. 2012), the impact of volcanic eruptions on climate (Zielinski et al. 1994; Zielinski 2000; Gao et al. 2008), and the recurrence interval and hazard assessment of volcanic activity (Newnham et al. 1999; Palumbo 1999; Shane and Hoverd 2002; Wulf et al. 2004; de Fontaine et al. 2007; Molloy et al. 2009).

Recent advances have expanded the potential for using tephrochronology in environments far from volcanic source regions. These regions receive fallout from volcanic eruptions, but in very low concentrations so tephra layers are not visible to the naked eye in sedimentary profiles and are defined as *crypto*tephra layers (Lowe and Hunt 2001; Alloway et al. 2007). It should be noted that c*ryptotephra* is an all encompassing term for tephra layers not visible in sedimentary profiles and can

refer to a large range of shard concentrations, from single grains to thousands of grains per $cm^3$, depending on the depositional environment and the distance from the source volcano. Improved techniques for extracting and geochemically analyzing tephra have made possible the use of cryptotephra horizons in paleoenvironmental research (Dugmore et al. 1995; Turney 1998; Hall and Pilcher 2002; Blockley et al. 2005). However, isolating cryptotephra from the background sediment requires detailed laboratory techniques. Generally, samples undergo ashing or acid digestion to remove organic matter. For organic-rich sediments such as peat, these steps are often enough to concentrate tephra. In more minerogenic sediments, fine sieving and multiple density separations are also performed. Samples are then mounted on slides and scanned using a polarized light microscope to identify tephra grains. These methods are destructive and time consuming, and can be prohibitive when sample size is limited, when looking for tephra over broad stratigraphic zones where little or no other age control is available, or when sediments are dominantly minerogenic. Therefore, a more rapid, non-destructive approach to detecting cryptotephra would allow tephrochronology to be applied in more investigations and allow for more complete evaluation of tephra content within sedimentary profiles in order to improve chronologies.

A range of alternative approaches have been attempted, all of which try to exploit unique properties of tephra that are distinguishable from the surrounding sediment. Gehrels et al. (2008) reviewed several non-destructive approaches for detecting tephra in peat cores including: spectrophotometry, x-radiography, magnetic susceptibility, and X-ray fluorescence (XRF). Others have tried to use magnetic properties (Peters et al. 2010), X-ray diffraction (Andrews et al. 2006), and instrumental neutron activation analysis (Lim et al. 2008). De Vleeschouwer et al. (2008) applied petrography, scanning electron microscopy, and scanning XRF to resin-impregnated peat columns. Kylander et al. (2012) examined XRF scans of highly organic-rich sediment cores.

As part of the *Volcanism in the Arctic System (VAST)* project, teams at the University of Massachusetts and the University of Colorado investigated the use of scanning XRF to locate cryptotephra within lacustrine sediment. Scanning XRF uses an intense micro-X-ray beam to analyze the surface of sediment profiles at sub-millimeter resolution and identifies a range of relative elemental components (Croudace et al. 2006). It has been applied in paleolimnology as a rapid and non-destructed approach to characterizing sediment cores. We designed a laboratory-based experiment to test if tephra-bearing sedimentary layers produce a detectable geochemical signature with scanning XRF. In particular, we examine the ability of scanning XRF to locate cryptotephra within minerogenic sediments. Minerogenic sediments are typical in lacustrine environments and are more challenging to date because they often lack enough material for radiocarbon dating, making them ideal targets for tephrochronology. In the laboratory, we created synthetic sediment cores, spiked them with tephra glass shards, and analyzed them on an XRF core scanner. We examined how different tephra concentrations, compositions, and grain-sizes are expressed in the scanning XRF elemental data. We also applied this approach to a sediment core from a lake in northern Norway, Sverigedalsvatn, where two

cryptotephra layers have been identified using conventional approaches, to test the applicability of our experimental results to an actual sediment profile.

## Methods

### *Experimental Design*

Synthetic sediment cores were made in 50 ml centrifuge tubes (Fig. 11.1). We used surface sediment from a glacially fed lake, Lake Tuborg, as the background material. Lake Tuborg is located on Ellesmere Island adjacent to the Agassiz Ice Cap (Smith et al. 2004; Lewis 2009). Sediment input is from snowmelt and glacially fed streams (Lewis et al. 2005, 2007, 2009). The upper sediments are generally in the silt size range (9–17 μm) with some lenses of fine sand (Lewis et al. 2009). We used sediment from this lake because it is almost entirely minerogenic. In addition, Ellesmere Island is located far from volcanic centers so it is unlikely that Lake Tuborg contains tephra in high concentrations.

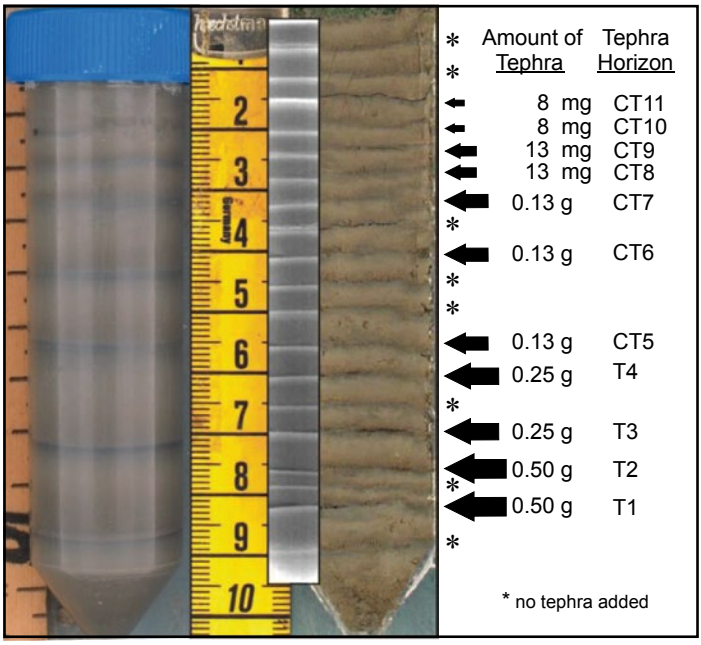


**Fig. 11.1** Synthetic sediment cores created in 50 ml centrifuge tubes (*left*). Sediment was added and spun in a horizontal-rotor centrifuge to create multiple fining upward laminations visible in the split cores and in the X-radiographs of the cores (*center*). Between some laminations, tephra was added in different concentrations to form 11 tephra layers, four as visible layers (T1–T4) and seven as cryptotephra layers (CT5–CT11) (*right*)

Sediment from a surface core was homogenized in deionized water, pipetted into centrifuge tubes, and spun in a horizontal-rotor centrifuge to create distinct, fining upward laminations (Fig. 11.1). We made four synthetic sediment cores (R1, R2, B1, B2) with 20, ~0.5 cm-thick laminations (Table 11.1). Tephra was added between some of the laminations and spun in the centrifuge to create discrete layers (Fig. 11.1).

We created 11 tephra layers, T1–T4 and CT5–CT11. Cores R1 and R2 were spiked with a rhyolitic tephra sample from the Icelandic eruption of Askja in 1875 (Sigvaldason 2002; Meara 2011) and cores B1 and B2 were spiked with a basaltic tephra sample from the Icelandic eruption of Grímsvötn in 2004 (Jude-Eton et al. 2012) (Tables 11.1 and 11.2). Both tephra samples were first sieved and cores R1 and B1 only contain tephra <53 µm and cores R2 and B2 only contain tephra between 105 and 177 µm (Table 11.1). All four cores were made simultaneously so the number of laminations, their approximate thickness, and the position where tephra was added are similar.

Tephra was added in successively smaller amounts from the bottom of each core to the top. We started by adding 0.5 g of tephra, which created a ~0.5 mm-thick visible tephra layer, and then progressively reduced the amount of tephra with the smallest amount being 8 mg (Fig. 11.1). By volume, tephra ranged from 100 % of the sediment per 0.5-mm section of the core down to 13 %. Tephra layers T1–T4 are visible in the split cores and tephra layers CT5–CT11 are cryptic. The visible tephra layers allowed us to identify the elements with the greatest response to tephra within each core. Between some laminations no tephra was added so we could define the background variations. This method of tephra dispersal allowed us to identify the precise locations of each layer and to focus on elemental data across these intervals. However, it does not exactly replicate how most cryptotephra layers are deposited in natural environments, where slower rates of deposition, bioturbation, and landscape reworking often occur causing tephra to be more uniformly incorporated into background sediment and to span broader depth intervals within sediment sequences. For this reason, the amount of tephra added to these synthetic cores may not be directly comparable to tephra concentrations from some cryptotephra studies.

Cores were split, photographed, and analyzed on an Itrax XRF core scanner at the University of Quebec's Institut National de la Recherche Scientifique, Centre Eau Terre Environnement with a first generation detector. The Itrax scans the surface of each core with a 22 mm × 100 µm beam. A range of elements from Al to Zr were detected and output as peak areas reflecting their relative concentration in the sediment. All of the split cores were scanned at 100-µm intervals using an exposure time of 20 s, voltage of 40 kV, and current of 45 mA. We focused our analysis on

**Table 11.1** Name of synthetic cores, the sample and grains size range of tephra glass shards added to each core

| Synthetic core | Tephra | Grain-size (µm) |
|---|---|---|
| R1 | Askja 1875 | <53 |
| R2 | Askja 1875 | 105–177 |
| B1 | Grímsvötn 2004 | <53 |
| B2 | Grímsvötn 2004 | 105–177 |

**Table 11.2** Major element compositions of the synthetic core sediment, tephra used in synthetic cores, and tephra isolated from Sverigedalsvatn

| Core | Tephra | | $SiO_2$ | $TiO_2$ | $Al_2O_3$ | FeO | MnO | MgO | CaO | $Na_2O$ | $K_2O$ | $P_2O_5$ | Total | *n* | Source |
|---|---|---|---|---|---|---|---|---|---|---|---|---|---|---|---|
| Synthetic core sediment | | | 53.63 | 0.68 | 13.82 | 5.14 | 0.05 | 5.69 | 16.71 | 0.65 | 3.50 | 0.14 | 100.0 | | This study |
| Synthetic core B1 & B2 | Grims-votn | *Mean* | 50.11 | 2.81 | 13.38 | 13.48 | 0.23 | 5.31 | 9.75 | 2.65 | 0.49 | 0.28 | 98.47 | | Jude-Eton et al. (2012) |
| | 2004 | 1 σ | 0.16 | 0.04 | 0.16 | 0.14 | 0.00 | 0.07 | 0.10 | 0.03 | 0.01 | 0.01 | 0.29 | | |
| Synthetic core R1 & R2 | Askja 1875 | *Mean* | 72.71 | 0.69 | 12.52 | 3.80 | 0.14 | 0.91 | 2.43 | 4.23 | 2.19 | 0.29 | 99.91 | 35 | Meara (2011) |
| | | 1 σ | 0.42 | 0.01 | 0.12 | 0.12 | 0.05 | 0.04 | 0.03 | 0.10 | 0.02 | 0.06 | 0.32 | | |
| Sverigedalsvatn | 246–247 cm | *Mean* | 49.68 | 2.97 | 13.14 | 13.91 | 0.25 | 5.58 | 10.06 | 2.56 | 0.42 | 0.37 | 98.93 | 25 | This study |
| | | 1 σ | 0.46 | 0.18 | 0.29 | 0.43 | 0.04 | 0.29 | 0.30 | 0.31 | 0.04 | 0.05 | 0.73 | | |
| Sverigedalsvatn | 283–284 cm | *Mean* | 70.61 | 0.31 | 13.70 | 3.84 | 0.16 | 0.21 | 1.39 | 4.15 | 3.31 | 0.08 | 97.76 | 21 | This study |
| | | 1 σ | 1.13 | 0.06 | 0.28 | 0.20 | 0.04 | 0.05 | 0.10 | 0.71 | 0.10 | 0.03 | 1.34 | | |

the following elements: Al, Si, Cl, K, Ca, Ti, V, Cr, Mn, Fe, Ni, Cu, Zn, Rb, Sr, and Zr. To avoid effects of the sediment matrix on the XRF signal, element peak areas were divided by the total counts per spectrum.

### *Application: Sverigedalsvatn Core SVP-207*

We compared the scanning XRF signal across tephra layers in the synthetic cores to XRF scans of a sediment core from Sverigedalsvatn (69°12.91′N; 16°02.60′E), a lake in northern Norway, where two Icelandic cryptotephra layers have been identified. A 4.5 m core was recovered from the lake, but we focus our analysis on a section of the core between 230 and 300 cm. The sediment composition is characterized by magnetic susceptibility that was measured every 0.2 cm using a Bartington MS2E meter and by organic matter content measured by loss-on-ignition every 0.5 cm.

Tephra samples were taken at 1-cm intervals from 245–247 cm and 283–287 cm, where tephra from specific Icelandic eruptions were suspected to be located based on a radiocarbon chronology. Samples were processed using conventional approaches to isolate volcanic glass shards (Turney 1998; Hall and Pilcher 2002). Samples were acidified, sieved to isolate grains between 20 and 63 μm, and then subject to heavy-liquid density separations with sodium polytungstate to isolate grains between 2.3 and 2.5 g $cm^{-1}$. Samples were mounted in epoxy resin and tephra particles were counted using a light microscope. Two significant peaks in tephra concentration were found at 246–247 cm and 283–284 cm where more than 500 shards were observed. Electron microprobe analysis of tephra grains from these samples shows that the lower horizon is a rhyolitic tephra and the upper horizon is a basaltic tephra (Table 11.2). Itrax core scans of the entire section were performed at the University of Bergen, Department of Earth Science. The core was scanned at a 200 μm interval using an exposure time of 10 s, voltage of 30 kV, and current of 55 mA.

## Results

### *Background Elemental Variations*

There are significant variations in the scanning XRF element profiles of all four synthetic cores that are driven by the physical characteristics of the background sediment and not associated with the presence of tephra (Fig. 11.2). These features are related to the repeated fining-upward sequences within each lamination that was formed during centrifuging. K, Rb, Fe, Ca, and Sr exhibit the strongest variations across each lamination (Fig. 11.2). K, Fe, and Rb increase in value from the base to the top of each lamination, while Ca and Sr decrease across each lamination

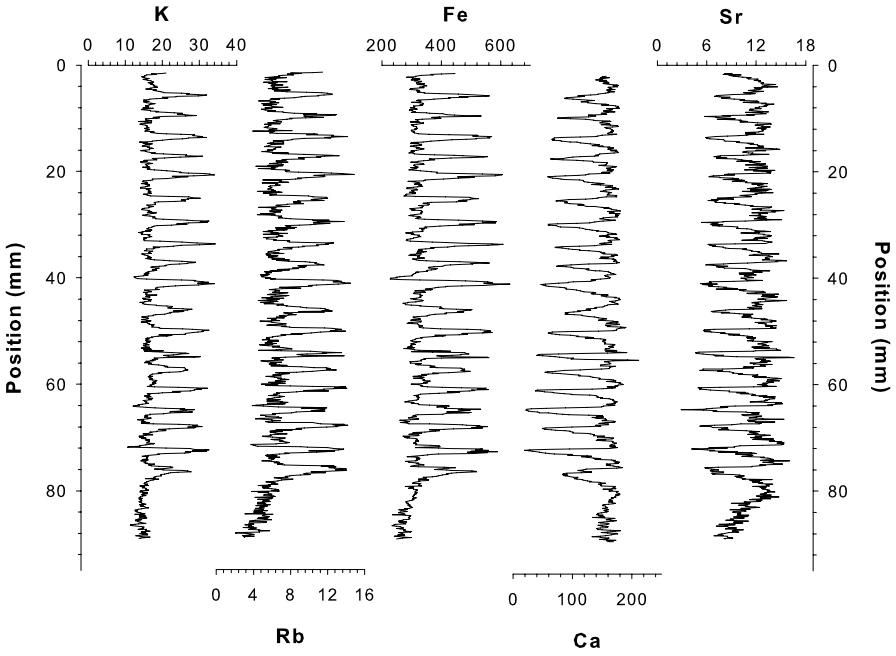


**Fig. 11.2** Example from core R1 of the background elemental response present in all of the synthetic cores from fining-upwards of grain-size within individual laminations. K, Rb, Fe, Ca, and Sr show the most significant variations across each lamination. Values for each element are presented as peak areas divided by the total counts per spectrum × $10^2$

(Fig. 11.2). Principal component analyses of the element matrix for each synthetic core demonstrate the strength of this signal (Table 11.3). The first principal components account for 37–40 % of the variation and are mainly controlled by K, Ca, Fe, Zn, and Rb, which all have factor loadings greater than 0.8 or less than −0.8. These data establish the background XRF signal and help guide how the elemental data are analyzed for the presence of tephra.

## *Synthetic Cores Spiked with Rhyolitic Tephra (R1 and R2)*

Eleven rhyolitic tephra layers were added between laminations within cores R1 and R2 with grain-size ranges of <53 μm and 105–177 μm, respectively (Figs. 11.3 and 11.4). In core R1, single element profiles of Ti, Mn, and Si show the strongest responses across the visible tephra layers (Fig. 11.3). Mn values have the most well defined peaks and clearly identify tephra layers T1, T2, T3, and T4 (Fig. 11.3). The peaks in Mn are larger across T1 and T2 than across T3 and T4. There is a small peak at cryptotephra layer CT6, but it is not as distinct and barely above background values. There is no clear signal in the Mn values of tephra layers with lower concentrations, CT7–CT11. Ti and Si also show slight increases at the positions of T1, T2, and T4.

**Table 11.3** Principal component analysis results for scanning XRF elemental data for each synthetic core. Data are from the first principle component. Factor loadings greater than 0.8 are in bold

| Synthetic core | R1 | R2 | B1 | B2 |
|---|---|---|---|---|
| Eigenvalue | 6.573 | 6.309 | 6.517 | 6.670 |
| % Variability | 41.084 | 39.430 | 40.733 | 41.689 |
| *Factor loadings* | | | | |
| Al | 0.229 | 0.281 | 0.374 | 0.375 |
| Si | –0.450 | –0.411 | –0.421 | –0.468 |
| Cl | 0.014 | 0.000 | –0.073 | –0.051 |
| K | ***0.930*** | ***0.936*** | 0.766 | ***0.927*** |
| Ca | ***–0.836*** | ***–0.820*** | ***–0.872*** | ***–0.833*** |
| Ti | 0.585 | 0.673 | 0.622 | 0.626 |
| V | 0.382 | 0.366 | 0.543 | 0.489 |
| Cr | 0.432 | 0.290 | 0.359 | 0.426 |
| Mn | 0.305 | 0.461 | 0.507 | 0.380 |
| Fe | ***0.965*** | ***0.958*** | ***0.918*** | ***0.956*** |
| Ni | 0.707 | 0.676 | 0.770 | 0.697 |
| Cu | 0.731 | 0.760 | ***0.814*** | 0.721 |
| Zn | ***0.859*** | ***0.856*** | ***0.879*** | ***0.840*** |
| Rb | ***0.858*** | 0.791 | 0.668 | ***0.831*** |
| Sr | –0.737 | –0.555 | –0.631 | –0.691 |
| Zr | –0.057 | 0.100 | –0.256 | –0.064 |

Profiles of Ti, Mn, and Si relative to Ca exhibit the most distinct peaks across these tephra layers as compared with the single element profiles (Fig. 11.3). Ca responds strongly to changes in grain-size associated with the artificial laminations.

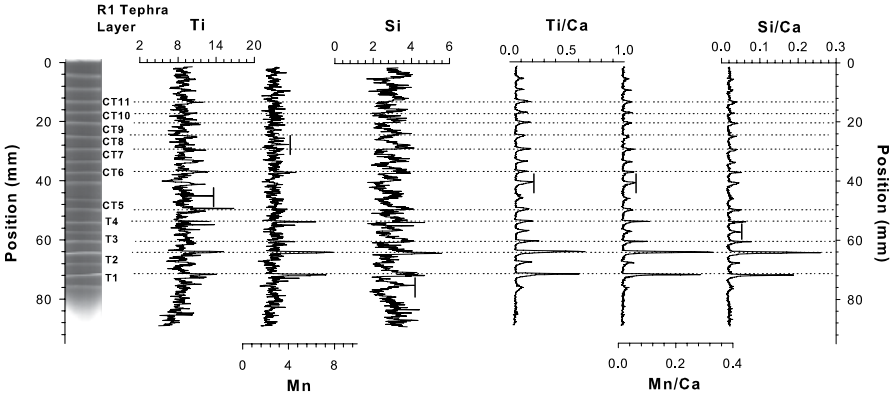


**Fig. 11.3** Scanning XRF data and X-radiograph for synthetic core R1, which was spiked with rhyolitic tephra less than 53 µm. Values for each element are presented as peak areas divided by the total counts per spectrum $\times 10^2$. The highest background value is marked on each plot with a vertical bar. Tephra (T) and cryptotephra (CT) layers interpreted to have element peaks above background variations that indicate their presence in the sediment are underlined

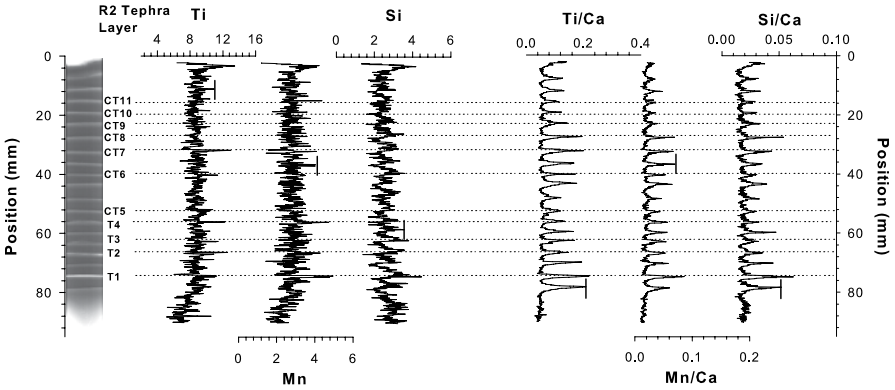


**Fig. 11.4** Scanning XRF data and X-radiograph for synthetic core R2, which was spiked with rhyolitic tephra from 105 to 177 μm. Values for each element are presented as peak areas divided by the total counts per spectrum × $10^2$. The highest background value is marked on each plot with a vertical bar. Tephra (T) and cryptotephra (CT) layers interpreted to have element peaks above background variations that indicate their presence in the sediment are underlined

Ca values decrease across the laminations while Ti, Mn, and Si values increase. These trends are expressed as the slight increases the element ratios that mark the top of each blank lamination. Peaks in these element ratios that are above these background variations occur at T1, T2, and T3 for Ti/Ca, Mn/Ca, and Si/Ca. Mn/Ca and Si/Ca values also show a response above background levels at T4, but none of the ratios indicate the presence of the cryptotephra layers (CT5–CT11).

In core R2, we also examined the response of Ti, Mn, and Si at each tephra layer (Fig. 11.4). Overall, the elemental response across the tephra layers is less pronounced. Si values show no clear signature of tephra at any position in the core. The Mn profile only shows a small peak above the background level at T1 and T4. Ti has peaks at T2, T4, and CT7 that are above the background, but show no variation in peak height that correspond with tephra concentration and do not seem to reliably represent the presence of tephra. Ratios of Ti, Mn, and Si to Ca only show a distinct response at T1 and the response across the other tephra layers are below the background variations.

## *Synthetic Cores Spiked with Basaltic Tephra (B1 and B2)*

Eleven basaltic tephra layers were added between laminations within cores B1 and B2 with grain-size ranges of < 53 μm and 105–177 μm, respectively (Figs. 11.5 and 11.6). In core B1, single element profiles of Ti, Mn, Fe and Cu show the strongest responses across the tephra layers and indicate the presence of three of the cryptotephra layers (Fig. 11.5). A sharp increase in values for Ti, Mn, and Fe is clearly distinguishable from background variations across tephra layers T1–T4 and CT5. Cu values show clear peaks at T1–T4. Peaks that exceed background values are also present in the profiles of Mn across CT6, and Ti across CT6 and CT8. In general, the peak heights generally decrease with decreasing concentration of tephra.

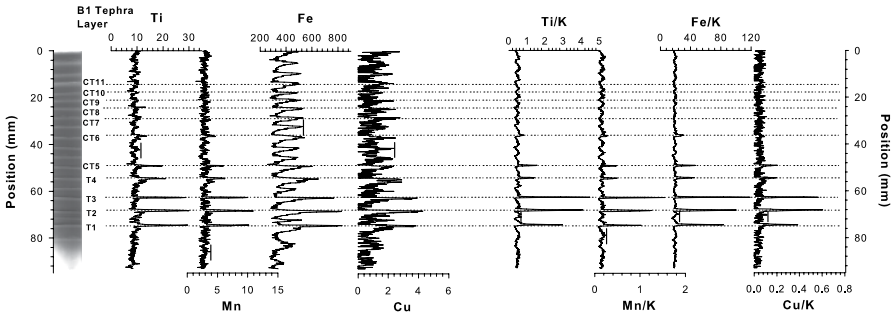


**Fig. 11.5** Scanning XRF data and X-radiograph for synthetic core B1, which was spiked with basaltic tephra less than 53 µm. Values for each element are presented as peak areas divided by the total counts per spectrum × $10^2$. The highest background value is marked on each plot with a vertical bar. Tephra (T) and cryptotephra (CT) layers interpreted to have element peaks above background variations that indicate their presence in the sediment are underlined

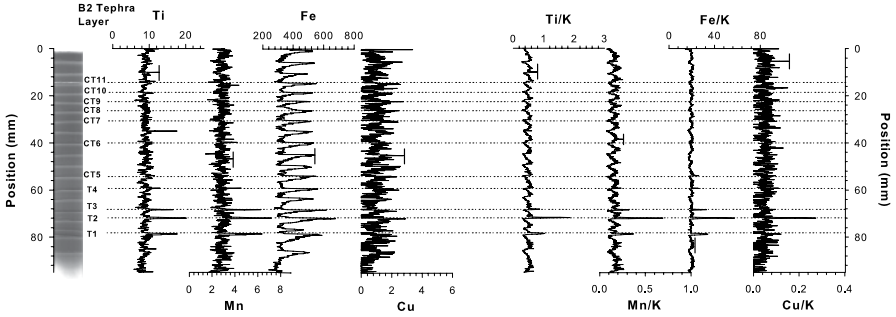


**Fig. 11.6** Scanning XRF data and X-radiograph for synthetic core B2, which was spiked with basaltic tephra from 105 to 177 µm. Values for each element are presented as peak areas divided by the total counts per spectrum × $10^2$. The highest background value is marked on each plot with a vertical bar. Tephra (T) and cryptotephra (CT) layers interpreted to have element peaks above background variations that indicate their presence in the sediment are underlined

The ratios of Ti, Mn, Fe, and Cu to K produce the most significant response across the basaltic tephra layers of core B1 (Fig. 11.5). K responds strongly to changes in grain-size associated with the artificial laminations. K values increase across the laminations relative to Ti, Mn, Fe, and Cu. These trends are expressed as the slight decreases in the element ratios that mark the top of each blank lamination. Profiles of Ti/K, Mn/K, Fe/K, and Cu/K have sharp peaks at the tephra layers that are much greater than the background values. All four profiles show strong responses across the first five tephra layers. Plots of Ti/K and Fe/K also show peaks above background values across CT6. The response across tephra layers T1–T3 is greater than across T4–CT6.

In core B2, we also examined the response of Ti, Mn, Fe, and Cu (Fig. 11.6). The single element profile of Mn has the most distinct peaks. Significant increases in Mn values occur across tephra layers T1–T3 and there are peaks just above the background values at T4 and CT6, but overall the response is not as strong as in

core B1. There are no peaks in Cu that indicate the presence of any of the tephra layers. The Ti and Fe profiles show slight increases at T1, T2, and T3, but lack clear evidence for the presence of any of the other tephra layers. Although Ti has peaks across T1–T3, there is a high background spike between CT6 and CT7 that is of similar height as at T1 and T3. This peak is only composed of a single data point and may be an aberrant value due to matrix effects or is possibly the signal of a small concentration of tephra that was introduced mistakenly during construction of the cores.

The ratio of Ti, Mn, Fe, and Cu to K in core B2 show distinct peaks and have low background variations (Fig. 11.6). Profiles of Ti/K, Mn/K, and Fe/K show distinct peaks at T1–T3 and Fe/K values also increase at T4 and CT5. These element ratio profiles more clearly define these tephra horizons compared to the single element plots. The Cu/K ratio only displays a significant peak at T2.

## *Sverigedalsvatn Core SVP-207*

Two cryptotephra horizons were identified in Sverigedalsvatn with peaks in concentration greater than 500 shards per $cm^3$ occurring at 246–247 cm and 283–284 cm (Fig. 11.7). The lower tephra horizon is rhyolitic and has a high $SiO_2$ (70.61 %) and low FeO (3.84 %) content and the upper tephra horizon is basaltic and has a lower

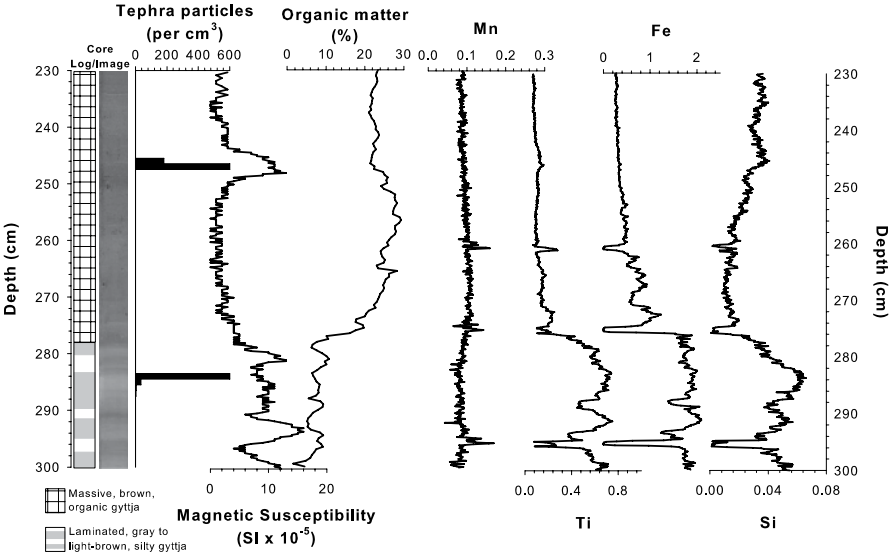


**Fig. 11.7** Section of the Sverigedalsvatn core where two cryptotephra layers were identified. The concentrations of tephra are compared to magnetic susceptibility and organic matter content profiles, which show significant changes in sediment composition, and scanning XRF profiles of Mn, Ti, Fe, and Si. Values for each element are presented as peak areas divided by the total counts per spectrum. Graphic log and core image are also shown

$SiO_2$ (49.68 %) and higher FeO (13.91 %) content, which are similar in composition to the two tephra used in making the synthetic cores (Table 11.2).

The section of the core from Sverigedalsvatn (230–300 cm), where the two cryptotephra horizons were found, contains significant compositional changes, reflected in organic matter content and magnetic susceptibility profiles (Fig. 11.7). The lower sediments, from 278 to 300 cm, are minerogenic with high magnetic susceptibility values and low organic content. There is a transition to more organic-rich sediment above 278 cm, where magnetic susceptibility decreases and organic matter values increase to an average of 24 %. There is an increase in magnetic susceptibility from 244 to –250 cm at the location where the upper tephra was identified.

Element profiles that were most diagnostic of tephra in the synthetic core experiment were examined in Sverigedalsvatn. Ti, Fe, and Si profiles across the entire core section show a response to the major compositional changes (Fig. 11.7). Values for these elements are highest from 278–300 cm, sharply decrease at 278 cm, and are low from 278 to 230 cm. These trends are similar to changes in magnetic susceptibility and are opposite the trend in organic content. Mn was also diagnostic of tephra in the synthetic core experiment, but varies independently with relatively constant high frequency, low amplitude fluctuations.

Across the rhyolitic tephra horizon, elemental values around 283–284 cm show no clear departures from the background (Fig. 11.8). There are slight increases in Si, Ti/Ca, and Si/Ca around this depth, but the changes in values are probably associated with other physical properties of the sediment. At the upper tephra horizon, elemental values immediately around 246–247 cm show a response that is likely related to the presence of tephra (Fig. 11.8). Ti values sharply increase and then slowly decline. Ti/K values exhibit a similar, but slightly more distinct trend. At both locations we also examined the response of other elements, but did not find any that showed a more significant response.

## Discussion

Scans of tephra-spiked synthetic cores provide a better perspective on the XRF response to tephra composition, concentration, and grain-size and how analysis of the data can be approached. There are a variety of background sediments and tephra that could have been used, but these experiments specifically target scenarios in lacustrine environments where sediments have variable grain-sizes and are dominantly minerogenic.

### *Elemental Signal of Tephra in Synthetic Cores*

For each core we used single element profiles to examine elements with the strongest response across the tephra layers as compared to background levels, which we defined as the range of values for a given element across the laminations where

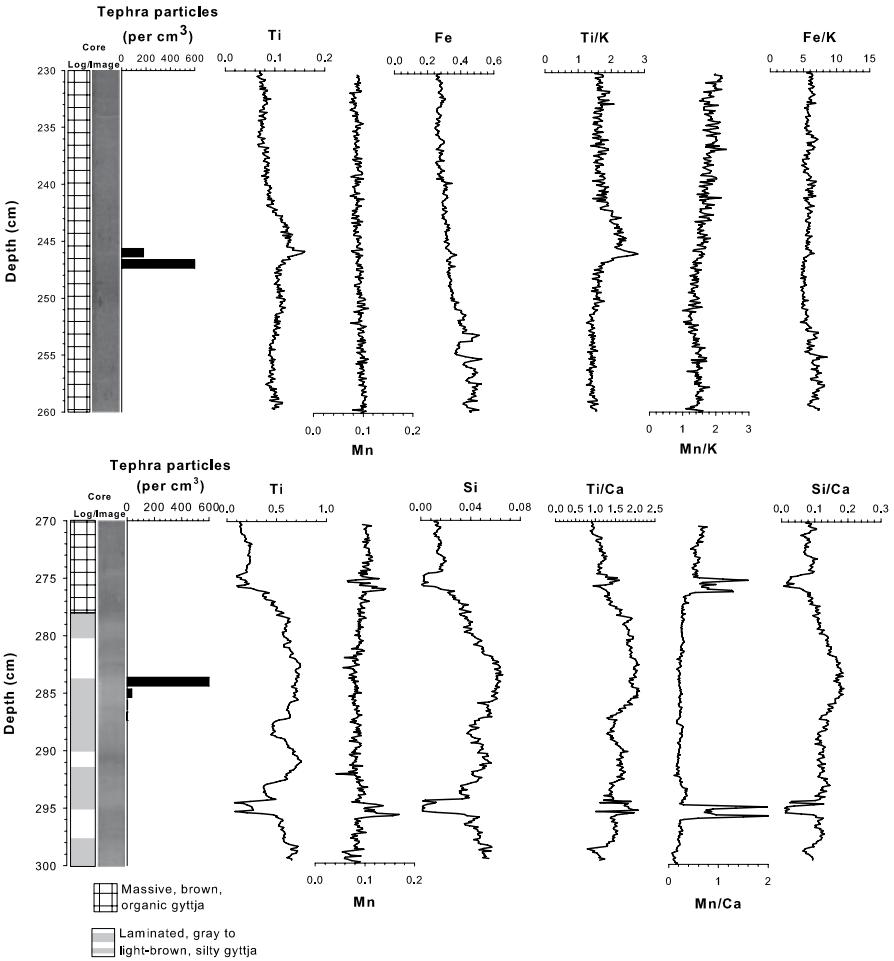


**Fig. 11.8** Expanded views of the sections of the Sverigedalsvatn core where the basaltic cryptotephra layer was identified (*upper panel*) and where the rhyolitic cryptotephra layer was identified (*lower panel*). The location of the basaltic tephra is compared to scanning XRF profiles of Ti, Mn, Fe, Ti/K, Mn/K, and Fe/K. The location of the rhyolitic tephra is compared to scanning XRF profiles of Ti, Mn, Si, Ti/Ca, Mn/Ca, and Si/Ca. Values for each element are presented as peak areas divided by the total counts per spectrum. Graphic log and core image are also shown

no tephra was added. Visible tephra layers, T1–T4, produce the strongest response and show which elements should be examined to try and locate cryptotephra layers, CT5–CT11. We also use element ratios, which show a greater response across tephra layers and more clearly define deviations from background elemental variations. We present the elements identified as most diagnostic of tephra relative to Ca and K for the cores spiked with rhyolitic and basaltic tephra, respectively, which are the element ratios that showed the greatest difference between tephra layers and the background variations. We were not able to detect all 11 tephra layers in any of the

four synthetic cores, but we were able to characterize conditions where the elemental response to tephra is greatest and we were able to identify a significant response to a few of the cryptotephra layers.

First, we consider the relative signature of the four visible tephra layers (T1–T4) to better understand how tephra grain-size and composition are detected by scanning XRF. The different tephra compositions (rhyolitic and basaltic) had slightly different diagnostic elements and relative responses. Synthetic sediment cores spiked with rhyolitic tephra show that Ti, Mn, and Si produced the strongest response to tephra, while Ti, Mn, Fe, and Cu are most diagnostic of the presence of the basaltic tephra. These results are a function of the compositional differences between rhyolitic and basaltic tephra (Table 11.1), as well as the relative difference between the composition of the tephra and the background sediment. Comparison between the relative response across tephra layers in the 'B' cores and the 'R' cores shows that the basaltic tephra layers in B1 and B2 produce the more distinct element peaks and at lower concentrations than the rhyolitic tephra layers in cores R1 and R2. Both of these properties reflect the greater compositional difference between the basaltic tephra and the background sediment as compared to the rhyolitic tephra. Similar results were found by Kylander et al. (2012) in their analysis of the response of basaltic and rhyolitic tephra in organic-rich sediment cores.

Tephra grain-size was found to affect the elemental response across both basaltic and rhyolitic tephra layers. Cores R1 and B1, spiked with tephra $<53$ μm, had greater elemental responses compared to cores R2 and B2, spiked with tephra 105–177 μm. There are no compositional variations of the tephra with grain-size that would cause this response and this trend is likely the result of difference in grain packing and density. The XRF response is greater across finer grained layers, which have a tighter packing and greater surface area per volume that interacts with the X-rays and causes a stronger response.

We found that the elemental response is directly related to tephra concentration. The visible tephra layers, T1 and T2 generally had a greater response than T3 and T4, where less tephra was added. However, most cryptotephra layers (CT5–CT11) were undistinguishable from the background sediment. The most cryptotephra layers were observed in core B1, where fine grained basaltic tephra, even in extremely low concentrations, was able to affect the bulk geochemical composition and produce an elemental peak above background values.

We analyzed both single element and element ratio profiles across the synthetic cores. Element ratios exhibited greater differences between tephra layers and the background sediment. For these tephra and background sediment compositions, elements relative to Ca provided optimum detection in cores R1 and R2, and elements relative to K in cores B1 and B2. This occurs because Ca and K are the elements with the greatest difference in concentration between the background sediment and the rhyolitic and basaltic tephra, respectively (Table 11.2). Ca and K do also respond differently to the fining-upwards of grain-size associated with each lamination, however the compositional difference of these two tephras had greater control on the element ratio than this background signal.

### *Elemental Signal of Tephra in Sverigedalsvatn Core SVP-207*

XRF scans of Sverigedalsvatn core SVP-207 provide a comparison of the elemental signal of cryptotephra in an actual sediment core to results from the synthetic core experiment. Scans of SVP-207 show a distinct signal of the basaltic tephra (Figs. 11.7, 11.8). This cryptotephra layer is associated with an increase in Ti and Ti/K values, but no other significant elemental response and no clear indication of the rhyolitic tephra was observed. The detection of the basaltic tephra shows a similar result as with the synthetic core experiment and is an expected trend since there is a greater difference between the composition of basaltic tephra and typical siliciclastic sediment.

This application also demonstrates the complicating factors that large changes in sedimentology have on detecting tephra with scanning XRF. In Sverigedalsvatn, there are significant changes in sedimentology and element values across this section of the core (Fig. 11.7). The elemental response to the basaltic cryptotephra layer is much less than the elemental response to changes in lithology associated with natural environmental conditions (minerogenic versus organic) and incidental events such as the unexplained Ti peak around 265 cm depth (Fig. 11.7). The core from Sverigedalsvatn was scanned using slightly different analytical conditions, including shorter counting times, which does complicate direct comparison.

### *Application and Limitations of Scanning XRF to Locate Cryptotephra in Sediment Profiles*

Here we present a systematic approach to exploring the use of scanning XRF to locate cryptotephra in sediment profiles, which allows us to assess the application and limitations of the method. We were able to identify a few cryptotephra horizons in this study. The elements and element ratios we found diagnostic of tephra can be applied in looking for tephra in natural sediment profiles, although these may vary depending on the specific tephra being targeted and the background sediment composition. The success of this method is also likely to be greater where the background element variations are minimal, where there are large differences in geochemistry between tephra and the background sediment, and where tephra is in a high enough concentration to affect the bulk geochemical composition of the sediment.

Despite these positive results, many of the cryptotephra layers in this study did not produce a distinct elemental response highlighting some of the difficulty in applying this method. Our laboratory experiment allowed for idealized sedimentary conditions. Specifically, the synthetic cores had a consistent background signal throughout, which is not the case in most sediment profiles where minor changes in sedimentology can result in large changes in the background XRF signal that can obscure a cryptotephra layer. In addition, we dispersed tephra as discrete layers between laminations, which allowed us to identify precise locations where tephra was located, but this is not representative of how tephra is naturally deposited. Another

complicating factor that may have affected this experiment is the XRF counting time (20 s) that we chose to use in analyzing all of the synthetic cores. By increasing the counting time we might have been able to show a more distinct response across some of the lower concentration tephra layers and may have increased detection of the lighter elements, specifically Al. $Al_2O_3$ is typically the second most abundant oxide in both basaltic and rhyolitic tephra and could be a diagnostic element, assuming there is a significant difference between its concentration and the background sediment.

These results provide a first step in establishing protocols for the analysis of cryptotephra by scanning XRF. Further work could include improvements to this experimental design, including: varying how tephra are dispersed within the sediment matrix, using a range of background sediment types without strong grain-size effects, using of a wider range of tephra compositions, and examining the effects of varying counting times. Moreover, the new generation of scanners come with detectors with lower detection limits, especially for light elements and would allow for the use of Al as a normalizer, hence an easier comparison with the results obtained by the tephra community with classical analysis techniques.

## Conclusions

Tephra-spiked synthetic cores were created and analyzed on an XRF core scanner to examine the elemental signal of tephra with different compositions, concentrations, and grain-size within a matrix of minerogenic lacustrine sediment. We were able to identify elements and element ratios diagnostic of basaltic and rhyolitic tephra. Synthetic sediment cores spiked with rhyolitic tephra showed that Ti, Mn, and Si produced the strongest response to tephra, while Ti, Mn, Fe, and Cu were most diagnostic of the presence of the basaltic tephra. The ratio of these diagnostic elements of tephra relative to Ca and K for the cores spiked with rhyolitic and basaltic tephra, respectively, showed the greatest difference between tephra layers and the background variations. We were not able to detect all of the tephra layers in any of the four synthetic cores, but we were able to characterize conditions where the elemental response to tephra is greatest and we were able to identify a significant response to a few of the cryptotephra layers. Our results also showed that finer grained tephra produced a larger elemental response. XRF scans of the synthetic cores were also compared to scans of an actual sediment profile, known to contain a basaltic and a rhyolitic cryptotephra to demonstrate how our controlled laboratory experiment might be applied. In addition to exploring the utility of scanning XRF to locating tephra in sedimentary sequences, the analytical approaches used in this experiment can be helpful for other studies examining discrete or exotic grains within a sedimentary matrix.

**Acknowledgements** This project was funded by National Science Foundation grant ARC-0714074, and by a NSERC discovery grant to PF. Support was also provided by a U.S. Fulbright Program Fellowship awarded to NLB, and analysis of the core from Lake Sverigedalsvatn was

part of the ARCTREC project supported by the Norwegian Research Council. We would like to thank members of the VAST project team for helpful discussions, Ted Lewis for providing us with surface sediment from Lake Tuborg, and two anonymous reviewers for their comments on an earlier draft.

## References

Alloway BV, Larsen G, Lowe DJ, Shane PAR, Westgate JA (2007) Tephrochronology. In: Elias SA (ed) Encyclopaedia of quaternary science. Elsevier, Oxford, pp 2869–2898

Andrews JT, Eberl DD, Kristjansdottir GB (2006) An exploratory method to detect tephras from quantitative XRD scans: examples from Iceland and East Greenland marine sediments. Holocene 16:1035–1042

Balascio NL, Wickler S, Narmo LE, Bradley RS (2011) Distal cryptotephra found in a Viking boathouse: the potential for tephrochronology in reconstructing the Iron Age in Norway. J Archaeol Sci 38:934–941

Blockley SPE, Pyne-O'Donnell SDF, Lowe JJ, Mathews IP, Stone A, Pollard AM, Turney CSM, Molyneux EG (2005) A new and less destructive laboratory procedure for the physical separation of distal glass tephra shards from sediments. Quat Sci Rev 24:1952–1960

Croudace IW, Rindby A, Rothwell RG (2006) ITRAX: description and evaluation of a new multi-function X-ray core scanner. In: Rothwell RG (ed) New techniques in sediment core analysis, vol 267. Geological Society Special Publication, London, pp 51–564

Deino AL, Scott GR, Saylor B, Alene M, Angelini JD, Haile-Selassie Y (2010) $^{40}Ar/^{39}Ar$ dating, paleomagnetism, and tephrochemistry of Pliocene strata of the hominid-bearing Woranso-Mille area, west-central Afar Rift, Ethiopia. J Hum Evol 58:111–126

de Menocal PB, Brown FH (1999) Pliocene tephra correlations between East African hominid localities, the Gulf of Aden, and the Arabian Sea. In: Agustí J, Rook L, Andrews P (eds) Hominoid evolution and climatic change in Europe, vol 1. Cambridge University Press, Cambridge, pp 23–54

De Vleeschouwer F, van Vliët-Lanoé B, Fagel N, Richter T, Boës X (2008) Development and application of high-resolution petrography on resin-impregnated Holocene peat columns to detect and analyse tephras, cryptotephras, and other materials. Quat Int 178:54–67

Dugmore AJ, Larsen G, Newton AJ (1995) Seven tephra isochrones in Scotland. Holocene 5:257–266

Dugmore AJ, Newton AJ, Larsen G, Cook GT (2000) Tephrochronology, environmental change, and the Norse settlement of Iceland. Environ Archaeol 5:21–34

Dugmore AJ, Gísladóttir G, Simpson IA, Newton A (2009) Conceptual models of 1200 years of Icelandic soil erosion reconstructed using tephrochronology. J North Atlantic 2:1–18

de Fontaine CS, Kaufman DS, Anderson RS, Werner A, Waythomas CF, Brown TA (2007) Late Quaternary distal tephra-fall deposits in lacustrine sediments, Kenai Peninsula, Alaska. Quat Res 68:64–78

Gao C, Robock A, Ammann C (2008) Volcanic forcing of climate over the past 1500 years: an improved ice core-based index for climate models. J Geophys Res 113:D23111

Gehrels MJ, Newnham RM, Lowe DJ, Wynne S, Hazell ZJ, Caseldine C (2008) Towards rapid assay of cryptotephra in peat cores: review and evaluation of various methods. Quat Int 178:68–84

Hall VA, Pilcher JR (2002) Late Quaternary Icelandic tephras in Ireland and Great Britain: detection, characterization and usefulness. Holocene 12:223–230

Hall VA, Pilcher JR, McVicker SJ (1994) Tephra-linked studies and environmental archaeology, with special reference to Ireland. Circaea 11:17–22

Jude-Eton T, Thordarson T, Gudmundsson MT, Oddsson B (2012) Dynamics, stratigraphy and proximal dispersal of supraglacial tephra during the ice-confined 2004 eruption at Grímsvötn Volcano, Iceland. Bull Volcanol 74:1057–1082

Kylander ME, Lind EM, Wastegård S, Löwemark L (2012) Recommendations for using XRF core scanning as a tool in tephrochronology. Holocene 22:371–375
Lewis T (2009) Normal and extreme sedimentation and physical processes in Lake Tuborg, Ellesmere Island, Nunavut. Ph. D. Thesis. University of Massachusetts Amherst, pp 199
Lewis T, Braun C, Hardy DR, Francus P, Bradley RS (2005) An extreme sediment transfer event in a Canadian high arctic stream. Arct Antarct Alp Res 37:477–482
Lewis T, Francus P, Bradley RS (2007) Limnology, sedimentology, and hydrology of a jökulhlaup into a meromictic high arctic lake. Can J Earth Sci 44:791–806
Lewis T, Francus P, Bradley RS (2009) Recent occurrence of large jökulhlaups at Lake Tuborg, Ellesmere Island, Nunavut. J Paleolimnol 41:491–506
Lim C, Ikehara K, Toyoda K (2008) Cryptotephra detection using high-resolution trace-element analysis of Holocene marine sediments, southwest Japan. Geochim Cosmochim Acta 72:5022–5036
Lowe DJ (2011) Tephrochronology and its application: a review. Quat Geochronol 6:107–153
Lowe DJ, Hunt JB (2001) A summary of terminology used in tephra-related studies. Les Dossiers de l'Archeo-Logis 1:17–22
Lowe DJ, Newnham, RM, McFadgen, BG, Higham, TFG (2000) Tephras and New Zealand archaeology. J Archaeol Sci 27:859–870
Manville V, Wilson CJN (2004) The 26.5 ka Oruanui eruption, New Zealand: a review of the roles of volcanism and climate in the post-eruptive sedimentary response. N Z J Geol Geophys 47:525–547
Meara R (2011) Climatic and environmental impact of Holocene silicic explosive eruptions in Iceland. Ph. D. Thesis. University of Edinburgh, p 324
Molloy C, Shane P, Augustinus P (2009) Eruption recurrence rates in a basaltic volcanic field based on tephra layers in maar sediments: Implications for hazards in the Auckland volcanic field. Geol Soc Am Bull 121:1666–1677
Newnham RM, Lowe D J, McGlone MS, Wilmshurst JM, Higham TFG (1998) The Kaharoa Tephra as a critical datum for earliest human impact in northern New Zealand. J Archaeol Sci 25:533–544
Newnham RM, Lowe DJ, Alloway BV (1999) Volcanic hazards in Auckland, New Zealand: a preliminary assessment of the threat posed by central North Island silicic volcanism based on the quaternary tephrostratigraphical record. In: Firth CR, McGuire WJ (eds) Volcanoes in the quaternary, vol 161. Geological Society of London Special Publications, London, pp 27–45
Palumbo A (1999) The activity of Vesuvius in the next millennium. J Volcanol Geotherm Res 88:125–129
Peters C, Austin WEN, Walden J, Hibbert FD (2010) Magnetic characterization and correlation of a Younger Dryas tephra in North Atlantic marine sediments. J Quat Sci 25:339–347
Shane P, Hoverd J (2002) Distal record of multi-sourced tephra in Onepoto Basin, Auckland, New Zealand: implications for volcanic chronology, frequency and hazards. Bull Volcanol 64:441–454
Sigvaldason GE (2002) Volcanic and tectonic processes coinciding with glaciation and crustal rebound: an early Holocene rhyolitic eruption in the Dyngjufjöll volcanic centre and the formation of the Askja caldera, north Iceland. Bull Volcanol 64:192–205
Smith SV, Bradley RS, Abbott MB (2004) A 300 year record of environmental change from Lake Tuborg, Ellesmere Island, Nunavut, Canada. J Paleolimnol 32:137–148
Streeter R, Dugmore AJ, Vésteinsson, O (2012) Plague and landscape resilience in premodern Iceland. Proc Natl Acad Sci U S A 109:3664–3669
Turney CSM (1998) Extraction of rhyolitic component of Vedde microtephra from minerogenic lake sediments. J Paleolimnol 19:199–206
Turney CSM, Lowe JJ (2001) Tephrochronology. In: Last WM, Smols JP (eds) Tracking environmental change using lake sediments, vol 1: basin analysis, coring, and chronological techniques. Kluwer, Dordrecht, pp 451–471
WoldeGabriel G, Hart W K, Katoh S, Beyene Y, Suwa G (2005) Correlation of Plio-Pleistocene tephra in Ethiopian and Kenyan rift basins: temporal calibration of geological features and hominid fossil records. J Volcanol Geotherm Res 147:81–108

Wulf S, Kraml M, Brauer A, Keller J, Negendank JFW (2004) Tephrochronology of the 100 ka lacustrine sediment record of Lago Grande di Monticchio (southern Italy). Quat Int 122:7–30

Zielinski GA (2000) Use of paleo-records in determining variability within the volcanism-climate system. Quat Sci Rev 19:417–438

Zielinski GA, Mayewski PA, Meeker LD, Whitlow S, Twickler MS, Morrison M, Meese DA, Gow AJ, Alley RB (1994) Record of volcanism since 7000 B.C. from the GISP2 Greenland ice core and implications for the volcano-climate system. Science 264:948–952

# Chapter 12
# Combined µ-XRF and Microfacies Techniques for Lake Sediment Analyses

**Peter Dulski, Achim Brauer and Clara Mangili**

**Abstract** This contribution presents an evaluation of still unexplored potentials, limitations and technical details of µ-XRF element scanning particularly for varved sediment analyses using the vacuum device EAGLE III XL. For this case study a 33 cm long interval of exceptionally well-preserved sub-millimetre scale calcite varves of the interglacial lake deposits from Piànico has been selected. In addition to the demonstration of the very good repeatability of XRF element scans, one focus of this paper is on discussing a suitable scanner resolution in terms of a compromise between short analyses times and a resolution that allows capturing the geochemical signature even of seasonal sub-layers. By combining scanner data with microscopic sediment inspection geochemical signatures of various micro-facies as, for example, varves, detrital layers and matrix-supported and clay layers are explored. The potential of counting varves using the seasonal signature of specific elements is discussed and potential error sources are disclosed by comparison with microscopic varve counts. Detailed grid- µXRF-scanning provides for the first time an insight into the internal structure of varves presented as high-resolution 3D-images. Finally, an approach of calibrating scanner data through comparison with ICP-MS analyses is introduced. Sensitivity factors for each element have been defined as ratios between mean count rates and bulk element concentrations.

**Keywords** Varves · EAGLE III XL spectrometer · VariSpot system · element mapping · Sediment microfacies · Lamination

P. Dulski (✉) · A. Brauer
Section 5.2—Climate Dynamics and Landscape Evolution GFZ German Research Centre for Geosciences, Telegrafenberg, D-14473 Potsdam, Germany
e-mail: dulski@gfz-potsdam.de

C. Mangili
Section of Earth and Environmental Sciences, University of Geneva, Rue des Maraichers 13, Switzerland



I. W. Croudace, R. G. Rothwell (eds.), *Micro-XRF Studies of Sediment Cores*, Developments in Paleoenvironmental Research 17, DOI 10.1007/978-94-017-9849-5_12

## Introduction

The increasing demand over recent decades for spatially resolved information from sediment cores has led to the development of several XRF scanning instruments for non-destructive and continuous analysis (Jansen et al. 1998; Koshikawa et al. 2003; Croudace et al. 2006; Haschke 2006; Richter et al. 2006), resulting in an increased number of publications presenting results of sediment core analyses from one per year in the 1990s to 41 in 2009 (Croudace and Rothwell 2010).

μ-XRF scanning allows the determination of the downcore element composition of sediments by continuous single line scanning along split cores of sediments and sediment blocks embedded in epoxy resin (e.g. Röhl and Abrams 2000; 2001; Brauer et al. 2008a). Latest generation core scanners provide spatial resolutions down to 100 μm but, depending on the focussing device of the μ-XRF instrument, the spot size can be narrowed down to as little as 50 μm (Haug et al. 2003; Haschke 2006; Brauer et al. 2007a, 2008a; Gennari et al. 2009). Typical spot sizes applied for sediment core analyses vary between 0.5 mm (Yancheva et al. 2007) and a few cm (Richter et al. 2001). For resin-embedded sediment blocks and dry samples spot sizes down to 20 μm have been reported (Shanahan et al. 2008).

Key parameters influencing the signal intensity are shown in Table 12.1. Apart from the scanner setup, such as X-ray tube type (e.g. Cr, Mo, Rh), tube voltage and

**Table 12.1** Selected key parameters influencing the generation and detection of X-ray fluorescence radiation

| Type of parameter | Parameter | Adjustment |
|---|---|---|
| Instrumental | Type of X-ray tube<br>XRF detector<br>Spectral analysis software<br>Focussing device<br>Device to reduce absorption of fluorescence (radiation path through air or He or vacuum) | Manufacturer setup |
| Experimental | Tube voltage<br>Tube current<br>Exposure time<br>Spot size<br>Step size<br>Use of cover foil to prevent desiccation | Operator setup |
| Sample related | Sample composition<br>Content of organic matter<br>Water content<br>Density<br>Porosity<br>Grain-size<br>Surface roughness | Fixed |

current, spot and step size and dwell time, numerous physical and chemical parameters significantly influence the generation and detection of the fluorescence radiation of the individual elements (Weltje and Tjallingii 2008; Francus et al. 2009). Key considerations include experimental characteristics like (i) use of a protective cover foil (Ge et al. 2005; Böning et al 2007; Tjallingii et al. 2007), (ii) X-ray beam focussing device based on a slit (Avaatech scanner), an X-ray capillary waveguide (Itrax) or by means of a polycapillary lens geometry (EAGLE III XL), (iii) measuring through air (SXAM, Katsuta et al. 2007), under vacuum (EAGLE III XL), through a hollow prism flushed with He (Avaatech scanner) or directly flushing the area between sample surface and detector window with He (EAGLE III BKA, Yancheva et al. 2007), (iv) software, data acquisition and peak processing techniques, background subtraction, sum-peak and escape-peak correction, deconvolution and peak integration and (v) sample characteristics like matrix composition, dilution effect by organic matter (Löwemark et al 2011), interstitial water content (Böning et al. 2007), porosity, grain-size, surface roughness, irregular geometric shape of layers and heterogeneity within individual layers. The importance of these parameters increases rapidly with decreasing spot sizes. Thus the conversion of core scanner output data (element intensities or count rates) into absolute element concentrations still remains a major problem of μ-XRF core scanning.

Several attempts have been made to convert element intensities or count rates into element concentrations by comparison with concentration data obtained by conventional chemical analyses of bulk samples, taken from the core at the same positions of the μ-XRF linescans (Jansen et al. 1998; Kido et al. 2006; Böning et al. 2007). However, resulting regression lines often reveal poor correlation and seldom pass the origin (Weltje and Tjallingii 2008). The log-ratio model of Weltje and Tjallingii (2008) seems to provide a more accurate and precise calibration method, although one has to keep in mind that calibration factors derived from one type of sediment are not readily applicable to other sediments (Weltje and Tjallingii 2008). This observation mandates that for reliable calibration purposes a reasonable large number of bulk samples of each core must be taken for conventional chemical analyses (e.g. ICP-AES, ICP-MS, AAS, XRF), which is not feasible for routine work. For high-resolution measurements (spot size $< 100$ μm) of finely laminated sediments (lamina width $<< 1$ mm) the preparation of discrete bulk samples for chemical analyses is extremely difficult or nearly impossible.

In spite of the obvious advantages of the μ-XRF method (i.e. resolution, continuity of the record, non-destructive character, marginal sample preparation), interpretation of μ-XRF data is not straightforward. This study aims to evaluate the capabilities and limitations of the μ-XRF technique at high-resolution. For this purpose, we have chosen as test material a varved lake sediment sequence from the Piànico palaeolake (Italy) which displays exceptionally well-preserved annual laminations (Brauer et al. 2008b), a relatively simple varve structure and well-defined event layers (Mangili et al. 2005). The detailed information obtained from microfacies analyses minimises complications resulting from more complex sedimentological settings and makes this sequence ideal for this feasibility study. Bulk sample analyses by inductively-coupled plasma mass spectrometry (ICP-MS) for selected sediment intervals, which have been analysed by μ-XRF scanning, is applied to estimate the relation between μ-XRF count rates and element concentrations.

## Study Site and Sediments

The sediments of the Piànico palaeolake (45° 48′ N, 10° 2′ E, Fig. 12.1a) are visible along outcrops in the Borlezza River valley (Southern Alps, Italy). The bedrock around the palaeolake consists mainly of Upper Triassic dolomitic rocks (Dolomia Principale) and limestones belonging to the Calcare di Zorzino Unit (Provincia di Bergamo 2000).

Within the palaeobasin the lacustrine Piànico Formation has been preserved (Moscariello et al. 2000). For this study only the unit named BVC ("Banco Varvato Carbonatoa" i.e. Carbonatic Varved Bed) is considered. This unit mainly consists of biogeochemically precipitated calcite varves (Fig. 12.1b) that formed under interglacial conditions. The age of these deposits has been determined by tephrochronology at ca 400 ka BP thus coinciding with Marine Isotope Stage (MIS) 11 (Brauer et al. 2007b). Although this age has been questioned (Pinti et al. 2007) it still appears to be the most realistic estimate (Brauer et al 2007c). Field varve counting of the entire unit yielded a minimum duration of ca. 15500 varve years for this period of peak interglacial conditions (Mangili et al. 2007).

The varves (Fig. 12.1c) are composed of two laminae: a light spring-summer lamina of biogeochemically precipitated calcite (Fig. 12.1d), and a dark autumn-winter lamina dominated by organic matter, diatom debris and scattered detrital grains (Brauer et al. 2008b). The mean varve thickness varies between 0.2 and 0.8 mm. Four detrital layer facies, intercalated in the varve succession, have been described: 0.03 mm–6 cm thick detrital layers composed of Triassic dolomite, ma-

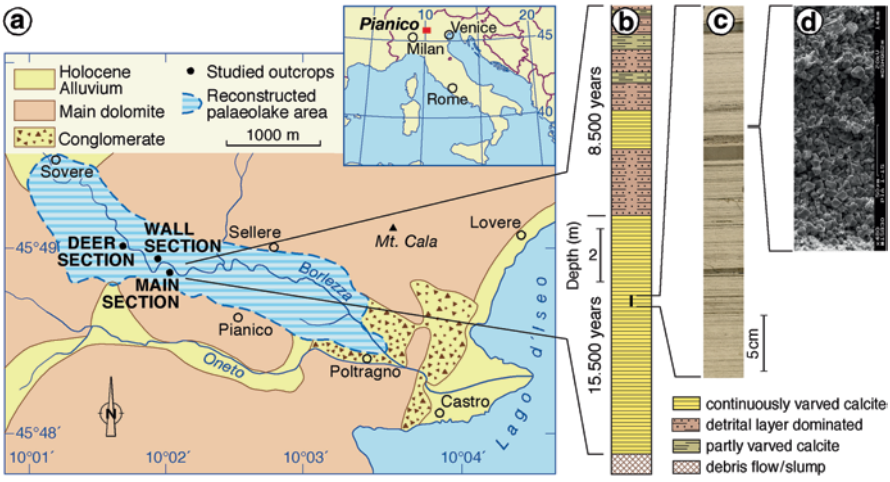


**Fig. 12.1** **a** Simplified geological map of the area of the Piànico palaeolake (modified after Casati 1968). The *dashed blue line* marks the reconstructed extension of the palaeolake. **b** Simplified stratigraphic column of the varved lacustrine interglacial unit (BVC; stands for the local stratigraphic term 'Banco Varvato Carbonaticoa' i.e. Carbonate Varved Bed) and of the upper unit (MLP; stands for the local stratigraphic term 'Membro di La Palazzina' i.e. La Palazzina Member) that is characterised by rapid alternation of detrital to endogenic calcite dominated intervals. **c** Optical image of the studied sample taken from the "main section" outcrop. **d** SEM image of a summer layer, showing the endogenic calcite crystals that form up to 98% of a single varve

trix supported layers (Mangili et al. 2005) consisting of medium to coarse silt-sized detrital grains embedded in a matrix of fine-grained isomorphic calcite, clay layers and a tephra layer rich in volcanic glass (Brauer et al. 2007b). Detrital layers are interpreted as triggered by extreme rainfall events (Mangili et al. 2005).

## Materials and Methods

### *Sample Collection and Preparation*

Sediment blocks were collected from the Main Section (Fig. 12.1), using 33 × 5 × 5 cm (L × W × H) special stainless steel boxes with removable side walls. In the laboratory the sample blocks were slowly dried at room temperature to avoid quick shrinkage and cracking, and then covered with Araldite® 2020 transparent epoxy resin. In this way, the resin impregnated the outer 1–2 mm of the sediments. Cutting the sample blocks along their length axis yielded corresponding plains for both thin section analyses and µ-XRF scanning. This is a crucial prerequisite for precise comparison of microscope and element scanning data. The surface of the sediment slice used for µ-XRF analyses was again slowly dried and dry-polished in order to obtain a smooth surface without further resin impregnation.

### *Micro X-ray Fluorescence (µ-XRF) Spectrometry*

For this study the high-resolution µ-XRF spectrometer EAGLE III XL (Röntgenanalytik Messtechnik GmbH, Germany) was used. The system specifications are summarized in Table 12.2. Major features of the instrument are described in more detail by Haschke et al. (2002) and Haschke (2006).

**Table 12.2** EAGLE III XL system specifications

| | |
|---|---|
| X-ray tube | Microfocus, Be-side window, air cooled |
| Anode material | Rhodium |
| X-ray optics | Polycapillary lens, spot size 50 µm<br>Variable between 50 and 250 µm (VariSpot™) |
| Detector | Si(Li), 80 mm$^2$, energy resolution 150 eV for MnKα, LN2 cooled |
| Sample chamber | 700 × 700 × 700 mm, vacuum tight |
| Vacuum system | Oil-free membrane pump, pressure < 1 mbar |
| Sample positioning | Stepper motor driven X-Y-Z-stage, step width 10 µm |
| max. stage move | 300 × 300 × 100 mm |
| Video system | Two colour video cameras, 10 and 100-fold magnification, visible area 16 × 12 and 1.6 × 1.2 mm |
| Software | EDAX vision software for instrument control, spectral data collection and data reduction<br>Sample stage control for single point, linescan and mapping |

Spectral data were processed (including background correction, escape-peak correction, peak deconvolution and peak area integration) using standard EDAX software (Vision). The resulting data represent element intensities expressed as count rates (counts per second, cps) for individual spots along the scanned line.

The EAGLE III XL spectrometer differs significantly from the worldwide leading X-ray -core scanners Itrax and Avaatech in four major respects.

a. The large vacuum chamber allows the measurement of dry samples under vacuum that improves the detection efficiency of low Z elements like Mg, Al and Si. For the Itrax core scanner Al is the lightest element which can be measured applying reasonable exposure times (Löwemark et al. 2011). This applies to the Avaatech core scanner, too (Tjallingii et al. 2007). For the Itrax core scanner the Cr tube is recommended for detection of lighter elements.
b. The polycapillary lens captures a large angle of the primary radiation beam and focuses it onto a small area on the sample surface, producing a nearly circular X-ray spot. The VariSpot-system of the EAGLE III XL spectrometer enables the variation of the spot size by moving tube and capillary-optic in direction of the axis of the optics without significant changes of the count rate (for a homogeneous sample) because the total number of the primary X-ray photons remains constant (Haschke et al. 2002) while the photon density (number of X-ray photons per $cm^2$) changes. A further increase of the "spot-size" may be achieved by raster-methods controlled by the software. The circular spot with down to 50 µm diameter or less is particularly suitable for mapping experiments. An additional advantage of the small circular spot becomes apparent for samples with inclined layer structure. Depending on the angle between the layers and the sedimentation direction the resulting resolution might be decreased when applying instruments using rectangular X-ray beams with lengths of ca. 1 cm or more. This is significantly less pronounced for the small circular spot.
c. A real-time video camera shows the sample image for each measured sample point for which an optical image can be stored for later examination. This enables the precise relocation of the X-ray beam on the sample, even after reloading a sample. The stored images allow inspection of sampling points of "outlier" values in element profiles in order to identify sample disturbances such as cracks or holes.
d. The computer controlled X-Y-Z-sample stage enables the operator to run predefined scanning lines in all three dimensions to avoid scanning across sample intervals which exhibit obvious disturbances. The autofocus function adjusts the z-position of the sample stage to maintain a constant distance between sample surface and detector.

µ-XRF measurements for this feasibility study were performed under vacuum on the fresh sediment surface of one 33 cm sediment block (sample PNC 17 of Piànico palaeolake, Italy). Figure 12.2 shows an optical scanning image of the sample with indications for two independent scanned lines (black lines), five mapped areas (black boxes), and references to the figures where data for these measurements are presented. For single line measurements instrument settings were 40 kV tube

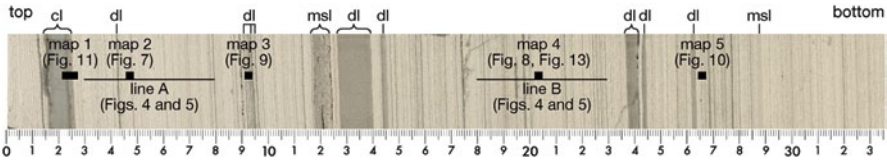


**Fig. 12.2** Optical image of the 33 cm long sediment block of sample PNC 17 taken from "main section" outcrop with indications for the different scanned lines (*black lines*), mapping areas (*black boxes*), and references to the figures where data are presented. *cl* clay layer, *dl* detrital layer, *msl* matrix supported layer

voltage, 200 µA tube current, ca. 54 µm spot size, 50 µm step size and an integration time of 60 s (livetime). Taking into account an average dead time of 35 % and time for sample movement and data storage, this results in a total measurement time of approximately 90 s for each sampling point.

Data for element mapping were collected at five characteristic intervals of the PNC 17 sediment block (Fig. 12.2). At each selected interval 61 parallel lines were scanned for either 3 mm (four sites) or 6 mm (one site) lengths. The distance between individual sampling points was 50 µm in x- and y-directions. These analyses were carried out using a tube voltage of 40 kV, a tube current of 250 µA, a spot size of ca. 54 µm and a step size of 50 µm, resulting in 3721 data points for a 3 × 3 mm matrix and 7381 data points for the 3 × 6 mm matrix. For an exposure time of 30 s (lifetime) the total analysis times were 46 h and 93 h for 3 × 3 mm and 3 × 6 mm scanned areas, respectively.

For calibration purposes two reference samples, limestone KH (Zentrales Geologisches Institut of the former GDR) and a 1:1 mixture (by mass) of KH and the basalt BM (CRPG-BRGM, France), were measured. The reference samples were prepared as pressed powder pellets from homogeneous sample powder (grain-size < 65 µm). A 1 × 1 cm raster was measured with a distance of 1 mm between each spot, resulting in 100 measuring points. To minimize a grain-size influence a 250 µm spot was used. Tube settings are the same as for linescans of the Piànico samples.

## *Inductively Coupled-Plasma Mass Spectrometry (ICP-MS)*

Eighteen "bulk" subsamples were analysed by inductively coupled plasma-mass spectrometry (ICP-MS) subsequently being scanned at 50 µm resolution using the EAGLE III XL. The ICP-MS procedure is described in detail by Dulski (2001). ICP-MS samples were obtained by scratching the fresh surface of sediment blocks with a razor blade. Each ICP-MS sample contains five varves. ICP-MS bulk concentration data has been used for comparison with the mean of the µ-XRF count rates (cps) of the corresponding scanning intervals of five varves whereby Mg, Al, Ca, Ti, Fe and Sr were determined using both techniques.

## Results

### *Repeatability of the µ-XRF Measurements*

To demonstrate the repeatability of the µ-XRF measurements with the EAGLE III system applying 50 µm spot size on a separate Piànico sample a single 30 cm scanning line was measured twice. For better viewing Fig. 12.3 shows results for a 0.5 cm section only. The consistency of replicate profiles of the same scanning line for Ca, Si and Mg demonstrates the good repeatability of the µ-XRF measurements. Even Mg, showing low count rates (< 10 cps) due to low sensitivity and concentration, can be clearly distinguished from instrumental noise.

### *Scanner Resolution*

Selecting the appropriate scanner resolution mainly depends on the sedimentological characteristics of the sediment. Higher resolution (smaller spot and shorter step sizes) results in more data points for individual layers and better statistical characterization of these layers. However, this clearly leads to a significant increase of measurement time for each sample. Applying 50 µm resolution and a dwell time of 60 s (life time), which are typical for analyses with our EAGLE III system, the duration for the measurement of 10 cm is about 50 h. Such duration is not practicable for routine measurements of long sediment sequences.

To optimize the discrimination between the various layers and to minimize measurement times we have determined the influence of the scanning resolution on the µ-XRF element profiles by scanning two 5-cm intervals using 50, 100, 200 and 500 µm spots and corresponding step sizes. One line (line A, Fig. 12.2) crosses an interval of thick varves while the other (line B, Fig. 12.2) intersects an interval of thinner varves. Results of the 5-cm long sequences for Ca (representing spring-summer layers, dominated by calcite) and Si (representing autumn-winter layers, dominated by diatom debris and detrital grains) are shown in Fig. 12.4 together with the corresponding thin section images. With increasing spot size the annual signatures in both profiles become progressively less distinct as indicated by a decreasing discrimination of individual peaks and a progressive lowering of the oscillation amplitude between minima and maxima of neighboured peaks. As expected, such signal degradations are less pronounced for the sample sequence with thicker varves (Fig. 12.4c, e, g) than for the sequence with thinner varves (Fig. 12.4d, f, h). According to the sedimentary features the 50 µm spot (centred on a thin dark autumn-winter layer, Fig. 12.4a and b) covers an area predominantly consisting of the Si-rich autumn-winter layer while for the 500 µm spot more than 90% of the spot area is represented by the Ca-rich spring-summer layer. This increase of the fraction of the thicker spring-summer layer within the spot area relative to the fraction of the autumn-winter layer leads to the reduction in the oscillation amplitudes for both elements (Fig. 12.4e–h). For both intervals (line A and B, Fig. 12.4) Ca profiles for

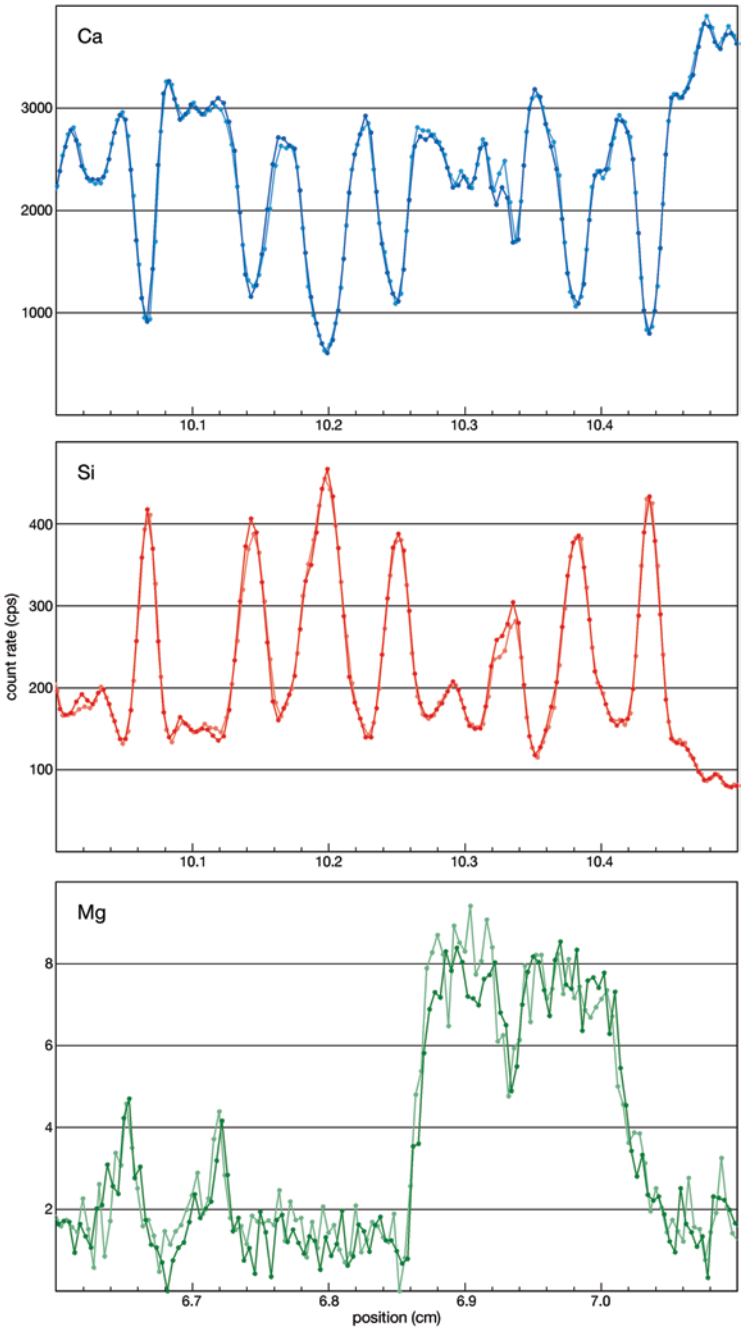


**Fig. 12.3** Ca, Si and Mg intensity profiles for a duplicate measurement of a single scanning line (50 µm spot- and step size) on Piànico sediment sample PNC W053. The consistence of both profiles for each element demonstrates the good repeatability of the µ-XRF measurements. Even Mg, showing low count rates (< 10 cps) due to low sensitivity, can be clearly distinguished from instrumental noise

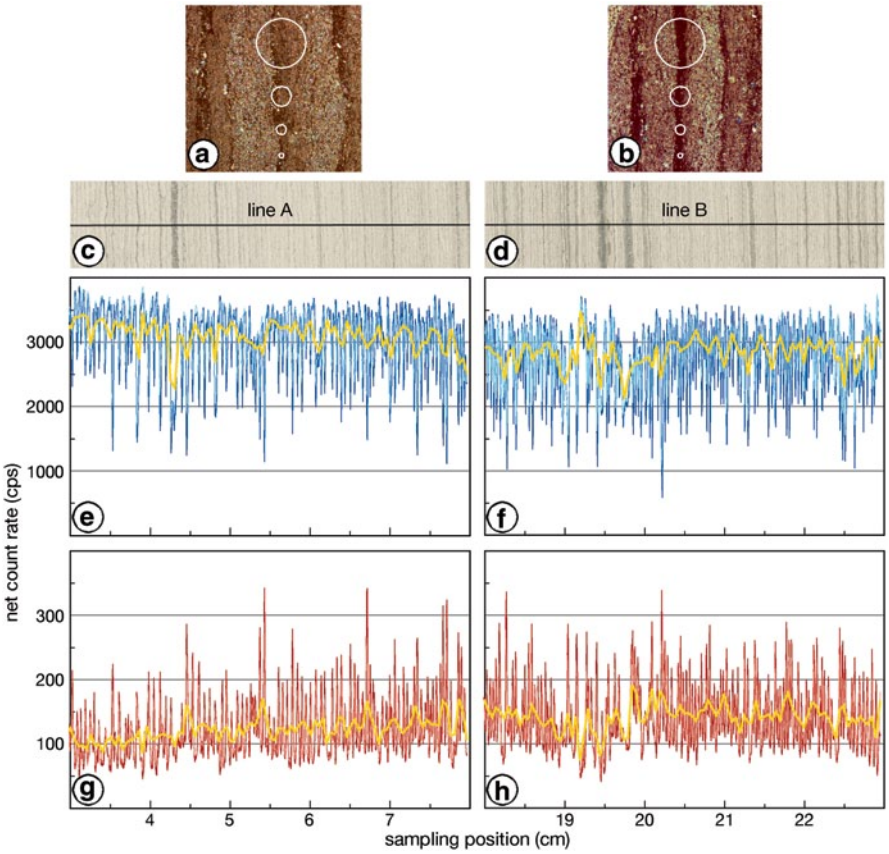


**Fig. 12.4** Thin section microscope image and various spot size areas (50, 100, 200, 500 µm diameter) compared to varve thickness (**a** and **b**), optical images of two five cm sequences of sample PNC 17 (**c** and **d**) with scanning line position (*black lines*) and Ca- (**e** and **f**) and Si- (**g** and **h**) intensity profiles using spot sizes of 50, 100, 200 and 500 µm (*dark blue* and *dark red lines* show 50 µm resolution). Ca profiles (**e** and **f**) are characterized by a relatively flat upper baseline and pronounced peaks dropping down to lower intensities while Si (**g** and **h**) shows the opposite behaviour with a relatively flat lower baseline and significant peaks to higher count rates. In profiles obtained with 500 µm spot- and step size (*yellow line* in **e** to **h**) the annual signature is partially masked because the spot area is dominated by nearly 90% of the Ca-rich spring-summer layers (**a** and **b**)

50 µm spots (blue lines in Fig. 12.4e and f) show a nearly flat upper base line of count rates between 3300 and 3700 cps and pronounced peaks dropping to lower count rates down to 600 cps. The opposite behaviour is observed for Si (red lines in Fig. 12.4g and h) with a relatively flat lower baseline between 60 and 100 cps and pronounced peaks rising up to 350 cps. Figure 12.5a, b, c, d, e, f, g, h shows a more detailed view of the profile structure for 0.5 cm intervals of both scanned sequences. The results clearly demonstrate that for both sequences spot sizes of 200 and 500 µm (Fig. 12.5c, d, g and h) are not suitable to resolve the Si-rich autumn winter layers from the Ca-rich spring-summer layers while using a 50 µ spot

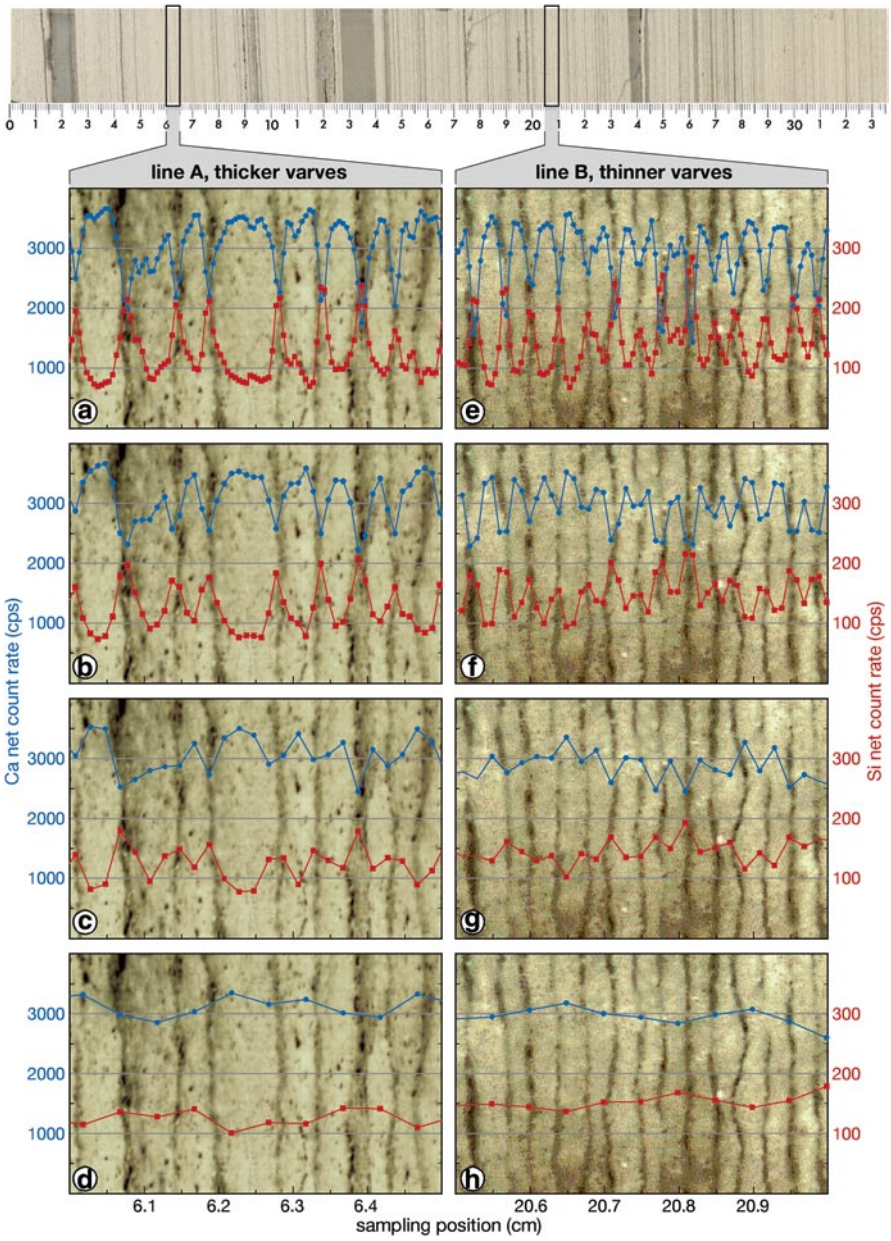


**Fig. 12.5** Ca- (*blue lines*) and Si- (*red lines*) intensity profiles for two 0.5 cm sequences of scanning line A (**a** to **d**) and B (**e** to **h**) using spot sizes of 50 (**a** and **e**), 100 (**b** and **f**), 200 (**c** and **g**) and 500 µm (**d** and **h**), respectively. Background images are thin section scans taken with a standard flatbed scanner and polarized light. With increasing spot size the annual signal of Ca and Si in profiles of line A (*thicker varves*) and line B (*thinner varves*) partially or totally disappears, indicated by worse discrimination of individual peaks and a progressive decrease of the oscillation amplitude between minima and maxima of neighboured peaks

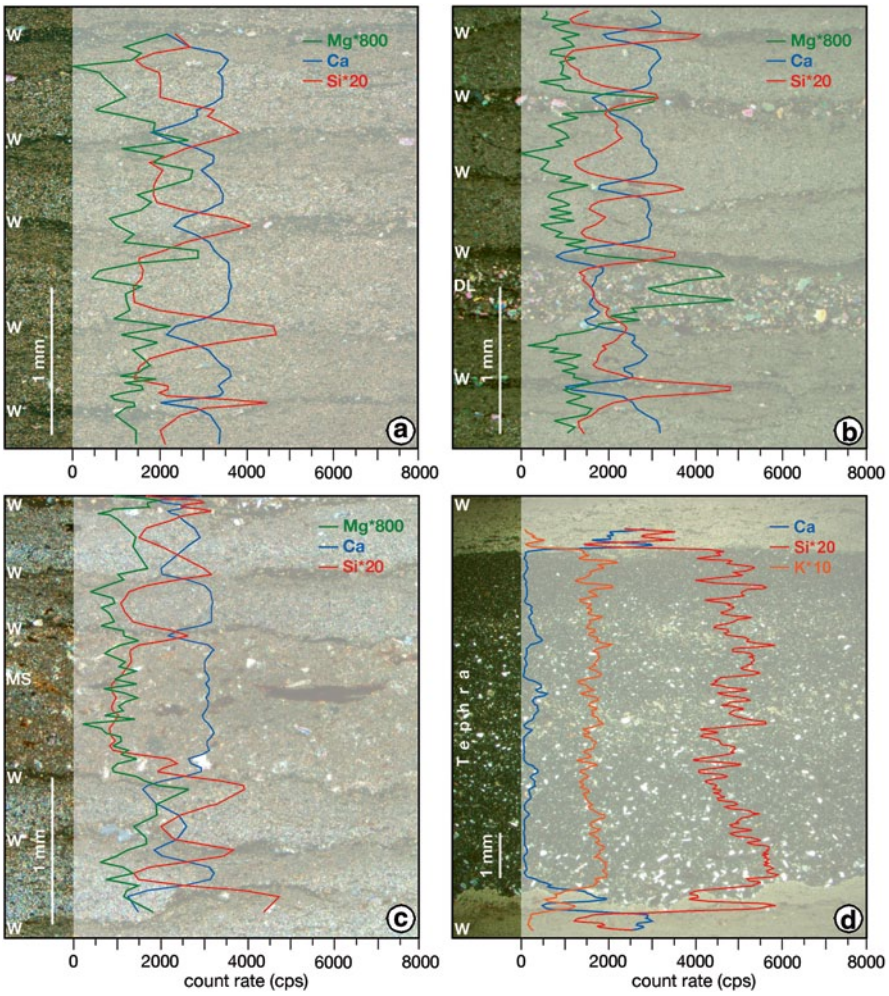


**Fig. 12.6** Thin section images of four different sediment sequences in PNC 17 and overlayed major element profiles. **a** Four varves (w = winter layer) and µ-XRF major element profiles (Mg*800, Ca, Si*20) for the same interval. Peaks in Ca coincide with the light summer layers, those of Si with the dark winter layers. **b** Thin section image of four varves and µ-XRF element profiles (Mg*800, Ca, Si*20). One varve includes a detrital layer (dl) which is indicated by the significant Mg peak just below the winter layer (peak for Si). **c** Thin section image of five varves and µ-XRF profiles (Mg*800, Ca, Si*20). One varve includes a matrix supported layer (ms) characterized by a constant and high Ca count rate across the whole layer. **d** Thin section image of the tephra layer included in the BVC unit and µ-XRF profiles (Ca, Si*20, K*10). The tephra layer is dominated by high and nearly constant Si and K signal intensities

(Fig. 12.5a and e) distinct peaks for the thin autumn winter layers of both sequences are seen which are characterized by 5 to 10 points per peak (line A, Fig 12.5a) and 3 to 5 points per peak (line B, Fig. 12.5e). A 100 µm spot appears to be sufficient for the interval with thicker varves (Fig. 12.5b) but not for the sequence with thinner varves (Fig. 12.5f).

## *Sediment Microfacies in µ-XRF Data*

The spatial element distributions within different types of microfacies are presented as 2D and 3D plots. We introduced 3D mapping to compare element intensities and microscope facies analyses of thin sections as a way to depict internal varve structure and as a tool to analyse lateral changes in µ-XRF scanning. For that purpose µ-XRF data have been gridded and plotted using the software Surfer, version 8.01.

Five major microfacies types were distinguished in the interglacial sediments of the Piànico palaeolake: (i) calcite varves, (ii) detrital layers, (iii) matrix supported layers, (iv) clay-rich layers, (v) and a tephra layer.

i. **Calcite varves:** In the 2D (Fig. 12.6a) and 3D plots (Figs. 12.7 and 12.8) Ca, as proxy for endogenic calcite precipitation in spring and summer, shows the highest count rates with significantly lower values for the thin autumn-winter layers. Peaks in Si indicate the detrital and diatom debris of the autumn-winter layers. The other elements (Mg, Fe, Al, K, Sr and Ti) show generally very low count rates. Sr generally follows the Ca pattern, indicating the presence of Sr in calcite crystals, Mg accounts for detrital Triassic dolomite from the catchment (Mangili et al. (2010) and Al, K, Fe and Ti reflect the sporadic presence of clay particles settling out from suspended detrital material which most likely has been

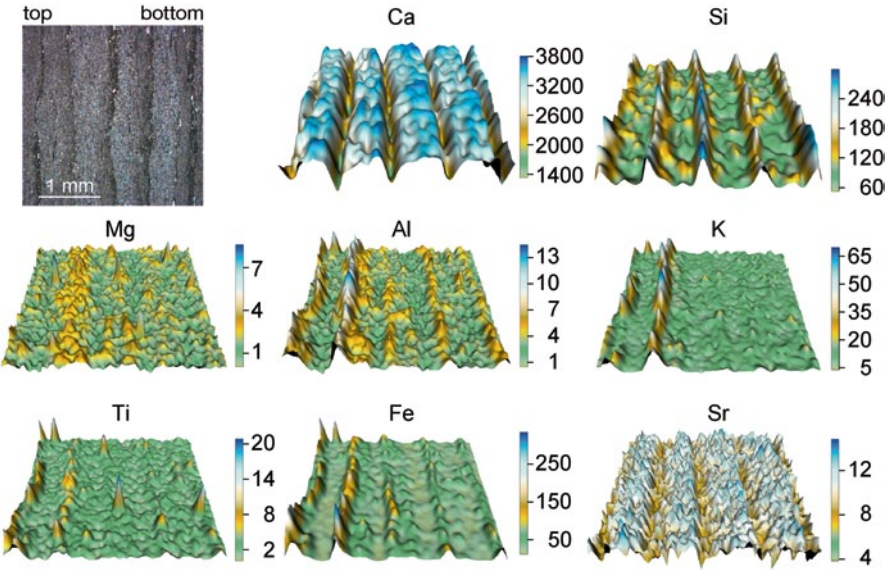


**Fig. 12.7** Thin section image and 3D µ-XRF element distribution maps (element intensities are expressed as counts per second) covering an area of 3 × 3 mm of thick varves. Ca and Sr peaks correspond to varve spring-summer layers composed mainly of endogenic calcite, Si peaks to autumn-winter layers dominated by diatom debris and scattered detrital grains. Al, K and Ti peaks are due to clay micro-fragments in the autumn-winter layers. Mg peaks reflect detrital dolomite grains of Triassic age washed into the lake from the catchment. These dolomite grains appear either scattered or enriched in winter and especially flood layers. (Mangili et al. 2005)

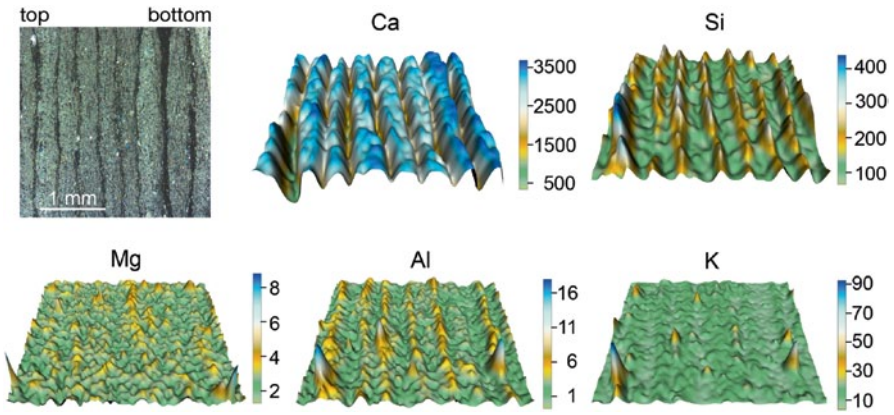


**Fig. 12.8** Thin section image and 3D μ-XRF element distribution maps (element intensities are expressed as counts per second) covering an area of 3 × 3 mm characterised by thin varves. Ca peaks correspond to varve spring-summer layers. Si peaks to autumn-winter layers. Al and K peaks are due to clay micro-fragments in the autumn-winter layers. Mg peaks reflect detrital dolomite grains of Triassic age washed into the lake from the catchment

transported into the lake by a stream coming from the inner Alps in the North (Moscariello et al. 2000).

ii. **Detrital layers:** In the 2D plot (Fig. 12.6b) the presence of the detrital layer (dl) is marked by the broad peak of Mg, representing the Triassic dolomite originating from the catchment area as main component of detrital layers. The 3D maps of a sequence containing detrital layers (Fig. 12.9) show a four varve interval, where each summer layer includes one to two detrital layers. Further components of detrital layers are clay fragments characterized by the Al and K peaks.

iii. **Matrix supported layers:** Matrix supported layers are indicated by elevated Ca values over the entire range of the layer. The 3D maps of a matrix supported layer (Fig. 12.10) clearly show an area of constant Ca values, interrupted only by a few isolated peaks in Si which result from isolated quartz grains. Mg, Al and K are generally low within the matrix supported layer.

iv. **Clay layers:** Clay layers exhibit a very different element composition. The 3D plots (Fig. 12.11) show high count rates for Al and K, intermediate count rates for Si and Mg and low count rates for Ca. Such millimetre to centimetre thick clay layers only rarely occur in the Piànico record. Sub-mm thick layers of clay are sometimes present within a varve, mostly associated to autumn-winter layers (e.g. peaks in Al and K in Figs. 12.7, 12.8).

v. **Tephra layer (Fig. 12.6d):** The presence of a tephra layer within the varved sequence (Brauer et al. 2007b) is detected by an abrupt increase of Si and K count rates and a sudden drop of Ca count rates at the beginning of the tephra. The high Si and K count rates characterise the entire tephra layer, but the semi-quantitative nature of μ-XRF scanner data limits any information about the volcanic source of the tephra. To discriminate between different volcanic sources and/or eruptions quantitative methods (e.g. microprobe analysis or laser ablation ICP-MS) must be applied.

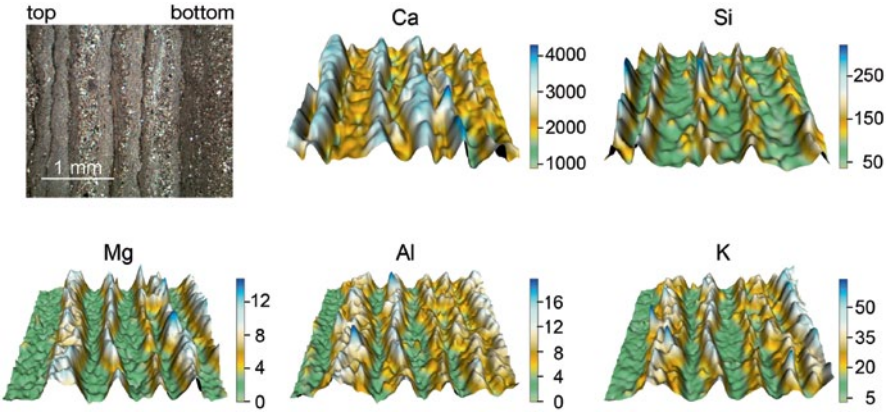


**Fig. 12.9** Thin section image and 3D µ-XRF element distribution maps (element intensities are expressed as counts per second) covering an area of 3 × 3 mm of varves including four detrital layers. Ca peaks correspond to varve spring-summer layers, Si peaks to autumn-winter layers. Al and K peaks are due to clay micro-fragments present in the autumn-winter layers. Mg peaks are due to the presence of Triassic dolomite forming the detrital layers

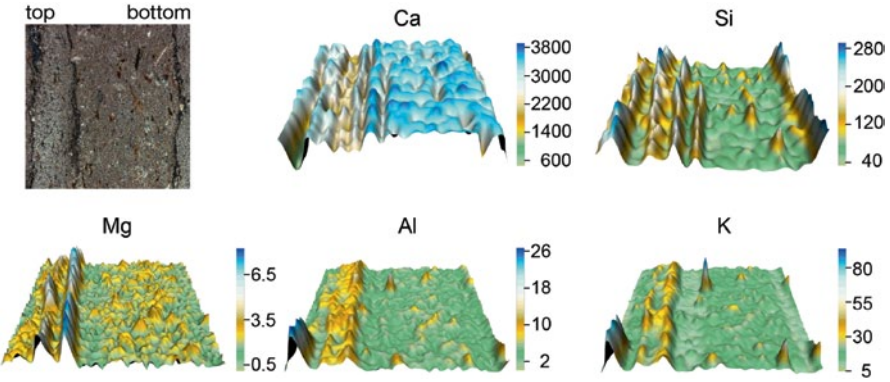


**Fig. 12.10** Thin section picture and 3D µ-XRF element distribution maps (element intensities are expressed as counts per second) covering an area of 3 × 3 mm for a matrix supported layer characterized by high and constant Ca values. Above the Matrix Supported layer, the varved pattern starts again, with Ca peaks alternated with Si peaks. The peaks in Mg mark the presence of a detrital layer within the varve succession

A particular advantage of high-resolution µ-XRF is that even sub-millimetre-size features can be identified. A micro-dropstone within the varve succession (Fig. 12.12) is identified by high Mg count rates while the deformation of the autumn-winter layers below the micro-dropstone is evident in the Si distribution. Within the area of the micro-dropstone, Ca, which is also constituent of dolomite, shows intermediate intensity values (lower than in the varve spring-summer layers).

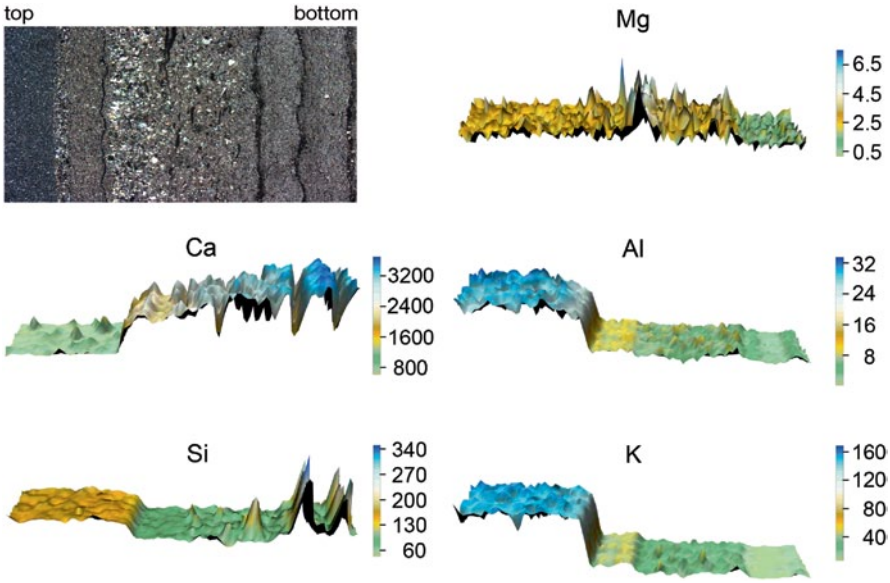


**Fig. 12.11** Thin section picture and 3D µ-XRF element distribution maps (element intensities are expressed as counts per second) covering an area of 6 × 3 mm of a sediment sequence containing two varves (Ca peaks on the *right*), a matrix supported layer (Mg rich, *middle*), and a thick clay layer (flat and high K and Al plateau on the *left*)

## *Intra-lamina Variability*

µ-XRF measurements were generally carried out on single lines (50 µm wide) along the stratigraphic sequence. Due to internal lamina heterogeneity, variations in layer thickness along individual lamina and skewing of layers, resulting µ-XRF intensity profiles vary depending on the lateral position of the scanning line. 3D µ-XRF element mapping show that µ-XRF count rates in the direction perpendicular to the sedimentation direction scatter significantly (e.g. Figs. 12.7–12.12) and can vary by more than one order of magnitude. Figure 12.13 shows the Ca- and Si intensity profiles of 61 parallel scanning lines crossing a 3 mm sequence of thin varves. For each line a spot size of ca. 54 µm and step size of 50 µm was applied. The distance between each of the parallel lines was 50 µm. Intra-varve variability causes variations of the signal intensities for the peak minima (Ca, 500–2500 cps) and maxima (Si, 150–450 cps) of the autumn-winter layers. The shift of the peak position up to 300 µm and the variation in peak width (a few tens µm) result from both the non-vertical layer geometry and the variable thickness along the layers. Despite the observed variations between the individual profiles seven significant thin autumn-winter layers (Ca low, Si high) are identified in all linescans.

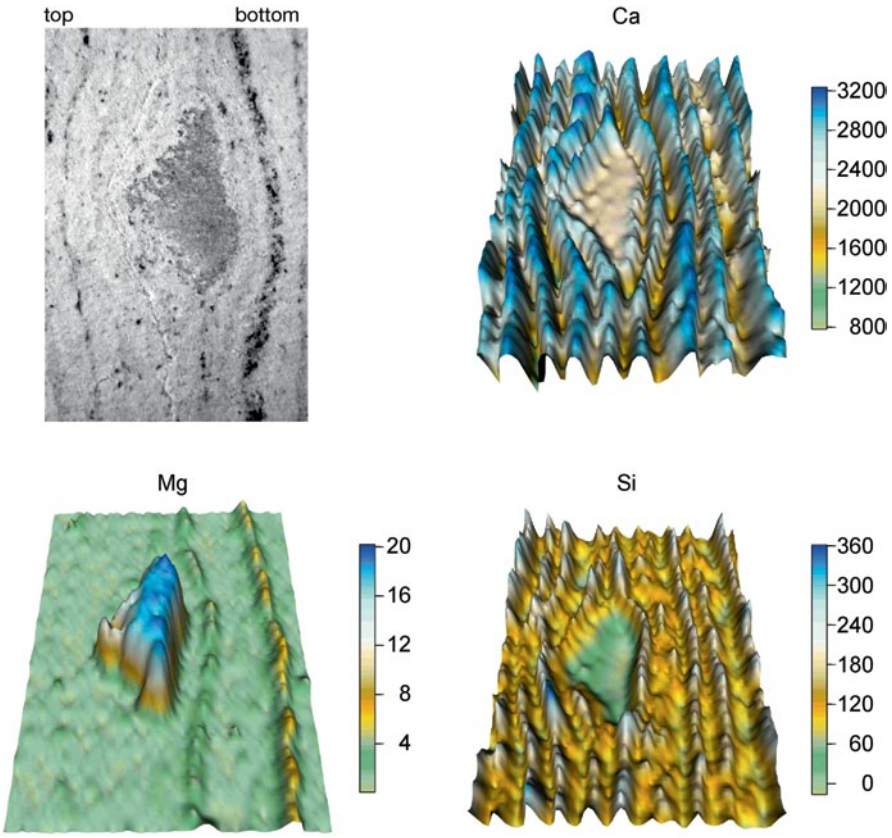


**Fig. 12.12** Optical image and 3D µ-XRF element distribution maps (element intensities are expressed as counts per second) for Ca, Mg and Si covering an area of a 3 × 5 mm sediment sequence containing a micro-dropstone inclusion. The varve succession has been deformed by the dolomite micro-dropstone. Ca peaks correspond to varve spring-summer layers, Si peaks to autumn-winter layers. Mg peak indicates the Triassic dolomite forming the dropstone

## *Varve Counting in µ-XRF Records*

Due to the good correspondence between µ-XRF and microscope data an attempt was made to varve count based solely on µ-XRF Ca profiles (Fig. 12.14). Control counts on thin section with a petrographic microscope reveal a total of 39 varves between two well-defined marker layers. It was not possible to obtain the same number of varves by counting the Ca minima (more pronounced than the maxima) in the µXRF data (Fig. 12.14a). The causes for this discrepancy in this specific case were the presence of a matrix supported layer, one varve that wedging out laterally (Fig. 12.14b) and by varves with very thin winter layers.

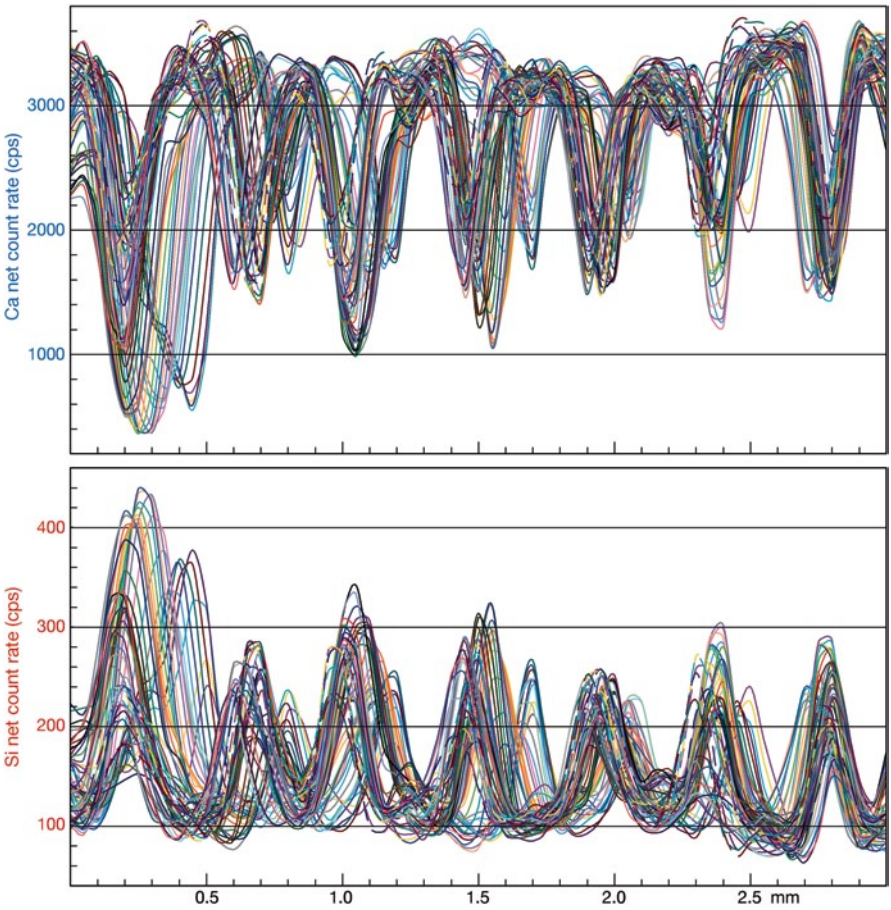


**Fig. 12.13** Ca- and Si intensity profiles of 61 parallel scanning lines crossing a 3 mm sequence of thin varves. Intra varve variability results in large variations of the signal intensity for the peak minima (Ca) and maxima (Si) of the autumn-winter layers. The observed shift of the peak position and the variation in peak width of the individual lamina are due to the skewed layer characteristic and the variable thickness along the layers, respectively. Despite the large variation of the individual profiles the seven significant thin autumn-winter layers (Ca low, Si high) within this sequence are identified by each scanning line

## *µ-XRF and ICP-MS Comparison*

The results of ICP-MS analyses for 18 bulk-samples of the Piànico sediment block, each averaging 5 varves, are shown in Table 12.3. They reveal that Ca is the most abundant metallic element in all subsamples, with concentrations between 29 and 35 wt%. Mg, Al and Fe are present in the lower percentage range (between 0.1 and 1.3 wt%) and Ti and Sr present only in trace amounts (60–500 µg/g). Si could not be determined because it is lost during the chemical decomposition procedure to

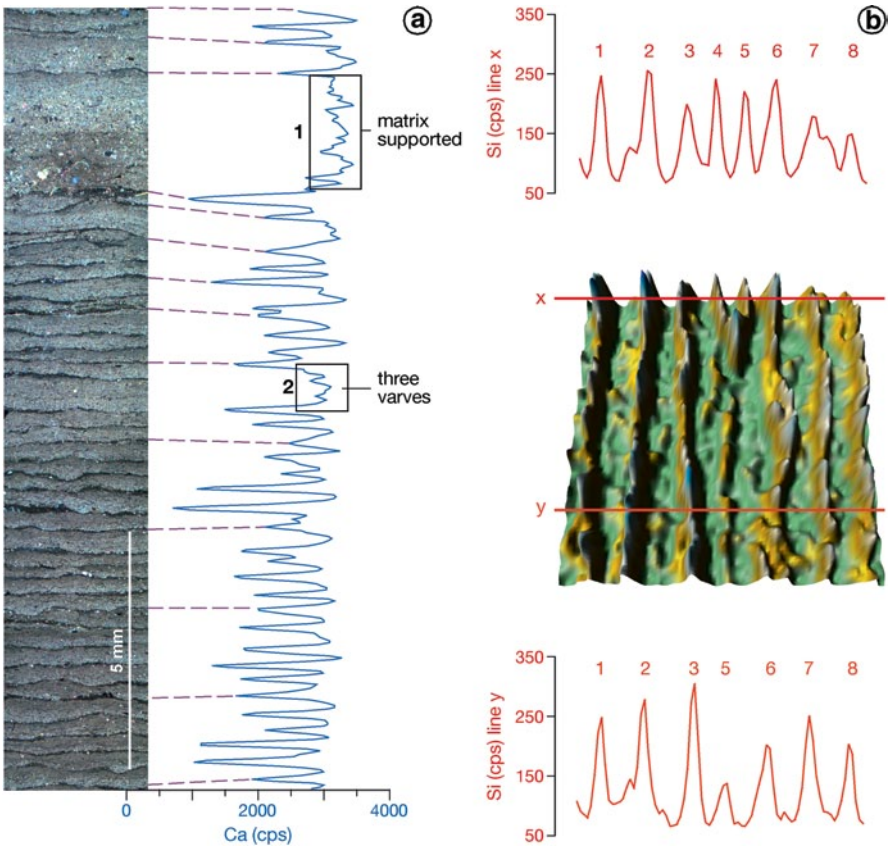


**Fig. 12.14** **a** Thin section image and Ca profile of a 15 cm long varved sediment sequence. The *dashed lines* mark the correspondences between the thin section image and the µ-XRF curve (dark autumn-winter layer represented by Ca minima). The boxes highlight parts of the Ca curve where varve counting based on µ-XRF peaks is difficult because of a lack of clear variations in the Ca signal for the matrix supported layer (*box 1*) and an interval of 3 varve years which are not well distinguishable (*box 2*). **b** 3D µ-XRF Si map for a particular varve interval, showing an additional winter layer along the line *x* compared to line *y*

dissolve the solid samples and K could not be analysed by ICP-MS due to the interference from the large Ar peak resulting from the plasma gas.

Sensitivity factors (cps/wt%), defined as the ratio between the mean count rates and the corresponding bulk concentrations determined by ICP-MS, were calculated for each element. For Si and K sensitivity factors were calculated using the net count rates obtained by the µ-XRF measurements of the pressed powder pellets of the two reference samples (limestone KH and 1:1 mixture of KH and basalt BM) and their reference concentration values (Govindaraju 1994). The results presented (Table 12.4 and Fig. 12.15) demonstrate that the obtained sensitivity factors increase with atomic mass of the elements. The sensitivity factors for the various ele-

**Table 12.3** Element concentration (wt%) for 18 bulk samples of PNC17 determined by ICP MS

| – | Mg | Al | Si | K | Ca | Ti | Fe | Sr |
|---|---|---|---|---|---|---|---|---|
| WC-01 | 0.79 | 0.34 | na | na | 31.5 | 0.025 | 0.32 | 0.053 |
| WC-02 | 1.26 | 0.46 | na | na | 29.3 | 0.028 | 0.37 | 0.046 |
| WC-03 | 1.03 | 0.37 | na | na | 30.4 | 0.026 | 0.32 | 0.050 |
| WC-04 | 0.78 | 0.34 | na | na | 30.4 | 0.023 | 0.31 | 0.049 |
| WC-05 | 1.56 | 0.68 | na | na | 29.2 | 0.039 | 0.50 | 0.046 |
| WC-06 | 0.98 | 0.46 | na | na | 30.9 | 0.028 | 0.36 | 0.049 |
| WC-07 | 0.94 | 0.40 | na | na | 31.0 | 0.026 | 0.31 | 0.050 |
| WC-08 | 0.99 | 0.49 | na | na | 29.3 | 0.030 | 0.39 | 0.047 |
| WC-09 | 9.93 | 0.84 | na | na | 22.5 | 0.044 | 0.60 | 0.018 |
| WC-10 | 10.1 | 0.90 | na | na | 22.5 | 0.052 | 0.65 | 0.021 |
| WC-11 | 9.03 | 0.90 | na | na | 25.2 | 0.047 | 0.64 | 0.026 |
| WC-12 | 2.04 | 9.44 | na | na | 8.4 | 0.351 | 2.92 | 0.028 |
| WC-14 | 0.62 | 0.19 | na | na | 34.7 | 0.016 | 0.26 | 0.052 |
| WC-15 | 1.62 | 0.81 | na | na | 31.0 | 0.045 | 0.48 | 0.046 |
| WC-16 | 0.59 | 0.15 | na | na | 34.4 | 0.014 | 0.19 | 0.053 |
| WC-17 | 0.71 | 0.23 | na | na | 34.0 | 0.018 | 0.24 | 0.052 |
| WC-20 | 0.71 | 0.23 | na | na | 34.0 | 0.018 | 0.24 | 0.052 |
| WC-21 | 0.58 | 0.14 | na | na | 33.5 | 0.015 | 0.19 | 0.050 |
| KH | 0.45 | 1.26 | 4.0 | 0.34 | 34.2 | 0.078 | 0.64 | 0.055 |
| KH/BM | 2.48 | 4.93 | 13.6 | 0.25 | 19.4 | 0.381 | 3.71 | 0.038 |

*na* not analysed by ICP-MS Reference values for Si and K for reference samples KH and KH/BM (1:1 mixture). Reference values KH and BM are taken from Govindaraju (1994)

**Table 12.4** Mean sensitivity factors (SF, cps/wt%), standard deviation (sd, cps/wt%) and relative standard deviation (rsd, %) obtained from analyses of 18 subsamples (covering five varves, each) by μ-XRF and ICP-MS

| – | Mg | Al | Si | K | Ca | Ti | Fe | Sr |
|---|---|---|---|---|---|---|---|---|
| SF (cps/w%) | 1.2 | 8.1 | 11 | 75 | 83 | 93 | 155 | 201 |
| sd (cps/w%) | 0.3 | 2.8 | – | – | 5 | 20 | 42 | 44 |
| rsd (%) | 26 | 34 | – | – | 6 | 21 | 27 | 22 |

Values for Si and K obtained from reference samples KH and 1:1 mixture of KH and BM only. Sensitivity factors are expressed as ratio of μ-XRF net count rates (cps) and element concentrations (wt%)

ments, established for the Piànico sediment, scatter considerably (relative standard deviation between 6 % for Ca and 34 % for Al) due to the low count rates and related low counting statistics for most of the elements. The calculated sensitivity factors obtained from the Piànico samples correlate reasonably well with those from the two reference samples KH and the 1:1 mixture of KH/BM.

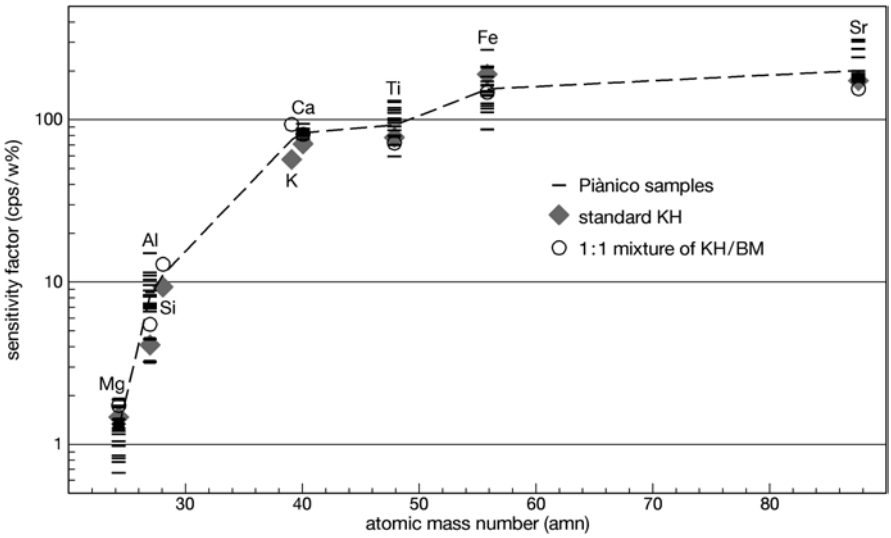


**Fig. 12.15** Sensitivity factors (cps/wt%) for selected elements versus atomic mass number. Horizontal bars indicate the Pànico samples, the squares the standard KH and the circles the 1:1 mixture of KH/BM. For the EAGLE III system, equipped with a Rh X-ray tube, the sensitivity factors systematically increase with atomic mass from Mg to Sr

## Discussion

The results of this study demonstrate that µ-XRF scanning is complementary to sediment micro-facies analyses because of the potential to provide geochemical data at seasonal resolution. In order to design optimal instrument setup it is crucial to make some fundamental considerations concerning measurement and data interpretation. Among those are repeatability, spatial resolution, time for measurement, sediment characteristics, homogeneity and continuity of lamina and calibration.

Duplicate measurements of the same scanning line on the Pànico sediment clearly prove that the observed uncertainties for our µ-XRF data are low and that they can be neglected for this study. Applying the 50 or 100 µm spot the observed relative variations of the count rates for each element between the different facies types of the Pànico sediments are significantly larger than the relative standard deviations of the measurement. This enables the discrimination of these facies types by the presented µ-XRF profiles.

The selected scanning resolution mainly depends on the sedimentation rate and the specific goals of the µ-XRF element scanning. Application of a larger spot size (lowering of the scanning resolution) results in a wider area over which the µ-XRF signal is integrated (Fig. 12.4a and b). Increasing spot sizes to values exceeding varve thickness prevents from resolving seasonal signals in annually laminated sediments. The reduction of µ-XRF count rate amplitudes (Figs. 12.4 and 12.5), measured at 500 µm resolution compared to 50 µm resolution results in smoothed

curves that lack any high-frequency signals. The smoothing of the µ-XRF records at lower resolution also affects intensity ratios of elements. For 50 µm resolution the Ca/Si intensity ratio for the spring-summer layers is ca. 40 while the ratio for the autumn-winter layer is around 10. At 500 µm resolution Ca/Si intensity ratios range between 20 and 30 for both layer types.

Obviously, the selected scanning resolution also affects the time required for µ-XRF analyses. Therefore sedimentation rate determination by micro-facies analyses prior to µ-XRF analyses is a suitable tool to define the ideal and effective scanning resolution in terms of minimum analytical times and precisely adjusted data resolution.

Reliable interpretation of µ-XRF data in terms of deciphering the environmental information necessitates a combination of different elements and element ratios (multi-proxy approach). Detrital and matrix supported layers in the Piànico sediment record show high and uniform Ca values that prevent a distinction based on micro-facies types and Ca data alone (Fig. 12.6). By contrast, Mg exhibits a clearly different pattern for these micro-facies types with high Mg count rates in detrital layers and low count rates in matrix supported layers. Microscopic observation enables us to explain this different pattern. While detrital layers predominantly consist of dolomite from the catchment (Fig. 12.6b) matrix supported layers mainly consist of reworked endogenic calcite (Fig. 12.6c). Ca profiles alone are not sufficient to distinguish between the two layer types and for correct interpretation of the µ-XRF signals.

Single line µ-XRF scanning is not representative of the geochemical composition of the analysed sediment because lateral heterogeneities are not detectable. In our case study we can demonstrate with 3D element maps (Figs. 12.7–12.12) and 61 parallel scanning lines (Fig. 12.13) lateral variations in the element distributions as a result of heterogeneity in the composition of single layers, varying thickness of single lamina caused by their undulating shape, as well as wedging out and oblique position of single lamina. The observed differences in count rates and position of the peaks for parallel scanning lines depict that high-resolution µ-XRF scanning data along only one single line increases the possibility of including local artefacts due to inhomogeneity or sample preparation. Consequently, only element variations exceeding the local differences related to the position of the measured line can be reliably interpreted in terms of environmental changes.

The comparison of ICP-MS and µ-XRF scanner data of the same sediment intervals confirms that a systematic relationship between sensitivity and atomic mass exist (Fig. 12.15). For our instrumental setup the element sensitivity continuously increase from lower mass (Mg) to higher mass (Sr) by a factor of approximately 100. Thus element X-ray intensity ratios do not directly correspond to element concentration ratios in the material being analyzed. The scattering in the sensitivity factors for certain elements may result from either the low count rates for some elements and/or from the large difference between the analysed volume by µ-XRF and ICP-MS. The analysed volume by µ-XRF is very low and results are therefore more strongly impacted by sample irregularities than those obtained by ICP-MS.

The set of sensitivity factors presented here are valid only for the Piànico sediments measured with the EAGLE III system under the described experimental conditions.

## Conclusions

Publications including data from the EAGLE III μ-XRF spectrometer are rare compared to those of the more commonly used Itrax and Avaatech core scanners. The results presented here demonstrate that this versatile instrument is a valuable tool for high-resolution studies of geochemical variability in sediment samples.

The use of small spot sizes (roughly between 50 and 100 μm) leads to good discrimination of thin layers present in sediments due to more sampling points across the peak and wider intensity amplitudes between maxima and minima of adjacent layers having distinct mineralogies. This results in higher count rates with better counting statistics for peak maxima. However, the use of a high spatial resolution leads to a large increase in the total measurement time. Small step sizes therefore should be applied only for selected intervals showing, for example, abrupt changes in sedimentary sequences or for element mapping.

Measurements employing small circular spots are more strongly affected by intra-varve variability compared to those applying rectangular X-ray beams with beam lengths up to 10 mm or more. Running several parallel lines would average these uncertainties but this is not practicable due to the large increase in measurement time.

The combination of μ-XRF element mapping and microfacies studies demonstrates the capability of the EAGLE III system. Additionally the multi-element character improves the interpretation of μ-XRF data by using multiple element profiles (multiproxy evaluation) to distinguish layers of different mineralogical composition.

The comparison between μ-XRF and ICP-MS analyses of subsamples from the same sediment intervals reveals that a systematic relationship between element concentration and μ-XRF exists. Sensitivity factors depend, amongst other parameters, on the atomic mass of the elements, the matrix composition of the sample and various instrument parameters. Such sensitivity factors cannot be regarded as universally valid for all instruments and measurement settings. Nonetheless, a general trend exists that μ-XRF is less sensitive for lighter elements (e.g. Al, Si) than for heavier elements (e.g. Fe, Sr). Consequentially this implies that element intensity ratios do not reflect corresponding absolute element concentration ratios in the sediment.

**Acknowledgments** The authors thank Brigitte Richert for assistance with the EAGLE μ-XRF measurements, Andreas Hendrich for graphical support and two anonymous reviewers for their comments which helped to improve the manuscript.

## References

Böning P, Bard E, Rose J (2007) Toward direct, micron-scale XRF elemental map and quantitative profiles of wet marine sediments. Geochem Geophys Geosyst 8. doi:10.1029/2006GC001480

Brauer A, Allen JRM, Mingram J, Dulski P, Wulf S, Huntley B (2007a) Evidence for last interglacial chronology and environmental change from Southern Europe. Proc Natl Acad Sci U S A 104:450–455. doi:10.1073/pnas.0603321104

Brauer A, Wulf S, Mangili C, Moscariello A (2007b) Tephrochronological dating of varved interglacial lake deposits from Piànico-Sèllere (Southern Alps, Italy) to around 400 ka. J Quat Sci 22:85–96. doi:10.1002/jqs.1014

Brauer A, Wulf S, Mangili C, Appelt O, Moscariello A (2007c) Reply: tephrochronological dating of varved interglacial lake deposits from Piànico-Sèllere (Southern Alps, Italy) to around 400 ka. J Quat Sci 22(4):415–418

Brauer A, Haug GH, Dulski P., Sigman DM., Negendank JFW (2008a) An abrupt wind shift in western Europe at the onset of the Younger Dryas cold period. Nat Geosci 1:520–523

Brauer A, Mangili C, Moscariello A (2008b) Palaeoclimatic implications from micro-facies data of a 5900 varve time series from the Piànico interglacial sediment record, Southern Alps. Palaeogeogr Palaeoclimatol Palaeoecol 259:121–135. doi:10.1016/palaeo.2007.10.003

Casati P (1968) Alcune osservazioni sul bacino lacustre pleistocenico di Pianico (Lombardia). Geologia-Istituto Lombardo (Rend. Sc.) A 102:575–595

Croudace IW, Rothwell RG (2010). Micro-XRF sediment core scanners: important tools for the environmental and earth sciences. Spectrosc Eur 22:6–13

Croudace IW, Rindby A, Rothwell RG. (2006) ITRAX: description and evaluation of a new multi-function X-ray core scanner. In: Rothwell RG (ed) New techniques in sediment core analysis. Geological Society of London Special Publication, London

Dulski P (2001) Reference materials for geochemical studies: new analytical data by ICP-MS and critical discussion of reference values. Geostand Newsl: J Geostand Geoanal 2:87–125

Francus P, Lamb H, Nakagawa T, Marshall M, Brown E, Suigetsu 2006 Project Members (2009) The potential of high-resolution X-ray fluorescence core scanning: applications in paleolimnology. PAGES News 17:93–95

Ge L, Lai W, Lin Y (2005) Influence of and correction for moisture in rocks, soils and sediments on in situ XRF analysis. X-Ray Spectrom 34:28–34. doi:10.1002/xrs.782

Gennari G, Tamburini F, Ariztegui D, Hajdas I, Spezzaferri S (2009) Geochemical evidence for high-resolution variations during deposition of the Holocene S1 sapropel on the Cretan Ridge, Eastern Mediterranean. Palaeogeogr Palaeoclimatol Palaeoecol 273:239–248. doi:10.1016/palaeo.2008.06.007

Govindaraju K (1994) Compilation of working values and sample description for 383 geostandards. Geostand Newsl 18:1–158

Haug GH, Günther D, Peterson LC, Sigman DM, Hughen KA, Aeschlimann B (2003) Climate and the collapse of Maya civilization. Science 299:1731–1735

Haschke M (2006) The EAGLE III BKA system, a novel sediment core X-ray fluorescence analyser with very high spatial resolution. In: Rothwell RG (ed) New techniques in sediment core analysis. Geological Society of London Special Publication, London

Haschke M, Scholz W, Theis U, Nicolosi J, Scruggs B, Herzceg L (2002) Description of a new Micro-X-Ray spectrometer. J Phys IV Fr 12(6):83–95. doi:10.1051/jp 4:20020216

Jansen JHF, Van der Gaast SJ, Koster B, Vaars AJ (1998) CORTEX, a shipboard XRF-scanner for element analyses in split sediment cores. Mar Geol 151:143–153

Katsuta N, Takano M, Kawakami S, Togami S, Fukusawa H, Kumazawa M, Yasuda Y (2007) Advanced micro-XRF method to separate sedimentary rhythms and event layers in sediments: its application to lacustrine sediment from Lake Suigetsu, Japan. J Paleolimnol 37:259–271. doi:10.1007/s10933–006-9028–3

Kido Y, Koshikawa T, Tada R (2006). Rapid and quantitative major element analysis method for wet fine-grained sediments using an XRF microscanner. Mar Geol 229:209–225

Koshikawa T, Kido Y, Tada R (2003) High-resolution rapid elemental analysis using an XRF microscanner. J Sediment Res 73:824–829

Löwemark L, Chen HF, Yang TN, Kylander M, Yu EF, Hsu YW, Lee TQ, Song SR, Jarvis S (2011) Normalizing XRF-scanner data: a cautionary note on the interpretation of high-resolution record from organic-rich lakes. J Asian Earth Sci 40:1250–1256. doi:10.1016/j.jseaes.2010.06.002

Mangili C, Brauer A, Moscariello A, Naumann R (2005) Microfacies of detrital event layers deposited in Quaternary varved lake sediments of the Piànico-Sèllere Basin (northern Italy). Sedimentology 52:927–943. doi:10.1111/j.1365–3091.2005.00717.x

Mangili C, Brauer A, Plessen B, Moscariello A (2007) Centennial-scale oscillations in oxygen and carbon isotopes of endogenic calcite from a 15,500 varve year record of the Piànico interglacial. Quat Sci Rev 26:1725–1735. doi:10.1016/j.quascirev.2007.04.012

Mangili C, Brauer A, Plessen B, Dulski P, Moscariello A, Naumann R (2010) Effects of detrital carbonate on stable oxygen and carbon isotope data from varved sediments of the interglacial Piànico palaeolake (Southern Alps, Italy). J Quat Sci 25(2):135–145

Moscariello A, Ravazzi C, Brauer A, Mangili C, Chiesa S, Rossi S, de Beaulieu J-L, Reille M (2000) A long lacustrine record from the Pianico-Sèllere Basin (Middle-Late Pleistocene, Nothern Italy). Quat Int 73/74:47–68

Pälike H, Shackleton NJ, Röhl U (2001) Astronomical forcing in Late Eocene marine sediments. Earth Planet Sci Lett 193:589–602

Pinti D, Rouchon V, Quidelleur X, Gillot P-Y, Chiesa S, Ravazzi C (2007) Comment: 'Tephrochronological dating of varved interglacial lake deposits from Piànico-Sèllere (Southern Alps, Italy) to around 400 ka' by Achim Brauer, Sabine Wulf, Clara Mangili, Andrea Moscariello. J Quat Sci 22(4):411–414

Provincia di Bergamo (2000) Carta Geologica della Provincia di Bergamo. Note illustrative. Provincia di Bergamo, Bergamo

Richter C, Blum P, Röhl U (2001) Data report: magnetic properties and XRF-scanner data of site 1075 (Lower Congo Basin). In: Wefer G, Berger WH, Richter C (eds) Proc Ocean Drill Prog Sci Results 175:1–31

Richter OT, van der Gaast S, Koster B, Vaars AJ, Gieles R, de Steigter HC, de Haas H, van Weering TCE (2006) The avaatech core scanner: technical description and applications to NE Atlantic sediments. In: Rothwell RG (ed) New techniques in sediment core analysis. Geological Society of London Special Publication, London

Röhl U, Abrams LJ (2000) High-resolution, downhole, and nondestructive core measurements from sites 999 and 1001 in the Caribbean Sea: application to the late paleocene thermal maximum. In: Leckie RM, Sigurdsson H, Acton GD, Draper G (eds) Proc Ocean Drill Prog Sci Results 165:191–203

Shanahan TM, Overpeck JT, Hubeny JB, King J, Hu FS, Hughen K, Miller G, Black J (2008) Scanning micro-X-ray fluorescence elemental mapping: a new tool for the study of laminated sediment records. Geochem Geophys Geosyst 9(2). doi:10.1029/2007GC001800

Tjallingii R, Röhl U, Kölling M, Bickert T (2007) Influence of the water content on X-ray fluorescence core-scanning measurements in soft marine sediments. Geochem Geophysics Geosyst 8(2). doi:10.1029/2006GC001393

Weltje GJ, Tjallingii R (2008) Calibration of XRF core scanners for quantitative geochemical logging of sediment cores: theory and application. Earth Planet Sci Lett 274:423–438

Yancheva G, Nowaczyk NR, Mingram J, Dulski P, Schettler G, Negendank JFW, Liu J, Sigman DM, Peterson LC, Haug GH (2007) Influence of the intertropical convergence zone on the East Asian monsoon. Nature 445:74–77. doi:10.1038/nature05431

# Chapter 13
# Experiences with XRF-Scanning of Long Sediment Records

**Christian Ohlendorf, Volker Wennrich and Dirk Enters**

**Abstract** Lacustrine sediment sequences of more than 100 m in length obtained in the framework of two deep drilling projects (PASADO and El'gygytgyn) were analysed with ITRAX XRF-core scanners. Core length and the long total scan time of 300–8000 h for these records made it necessary to consider downcore lithological changes and tube ageing. To account for these, two different approaches were realised for the acquisition of element data by XRF-scanning. Additionally, X-ray tube ageing was documented by regular measurements of a standard reference glass after each core run. The data obtained suggest that a normalisation of XRF raw-data is advisable for several reasons. (1) To level out effects of the observed long-term decrease in primary tube power that lead to lower count rates and thus lower element intensities. (2) To level out shifts in element profiles between sections that were measured with different X-ray tube current settings. From the tested normalisation procedures a division of element raw intensities by the intensity of coherent radiation (coh) yielded the best results for elements with mid to high atomic numbers. However, elements with low atomic numbers are less affected by a lowering of count rates related to tube ageing, and thus, the coh correction might over-compensate for this for these elements. Thus, for light elements it is advantageous to correct for the apparent energy loss by calculating ratios of elements with comparable atomic numbers (e.g. Si/Ti).

**Keywords** ITRAX · PASADO · El'gygytgyn · XRF-data correction · Coherent radiation

C. Ohlendorf (✉) · D. Enters
GEOPOLAR, Institute of Geography, University of Bremen, Celsiusstr. FVG-M, D-28359 Bremen, Germany
e-mail: ohlen@uni-bremen.de

V. Wennrich
Institute for Geology and Mineralogy, University of Cologne, Zuelpicher Str. 49a, D-50674 Cologne, Germany



I. W. Croudace, R. G. Rothwell (eds.), *Micro-XRF Studies of Sediment Cores*,
Developments in Paleoenvironmental Research 17, DOI 10.1007/978-94-017-9849-5_13

## Introduction

An increasing number of studies where sediment sequences with a total length of 100 m or more are examined continuously with XRF-scanning instruments is emerging (Monien et al. 2012). However, issues of down-core changes in the instrument settings or effects of X-ray tube ageing and strongly contrasting composition of the sediment matrix are only seldom addressed. It has been documented that the sediment matrix has a significant impact on the results of XRF-scanning (Löwemark et al. 2011; Tjallingii et al. 2007; Weltje and Tjallingii 2008). In particular the water and organic matter contents are well known for their diluting influence on element concentrations (Tjallingii et al. 2007) due to the closed-sum effect (Löwemark et al. 2011; Rollinson 1993). To account for this, in destructive geochemical analyses element concentrations are commonly normalized against aluminium (Al) as a conservative non-reactive element (Brumsack 2006). Although also possible for XRF-scanning (Löwemark et al. 2011), this method has only rarely been applied because of the relatively long counting times required due to the low fluorescence yield of Al (also contributing to the low yield is absorption of the Al K$\alpha$ by the air path). The organic matter content in some cases can be estimated by plotting the ratio of peaks that originate from the scattering of specific radiation, which is emitted by the X-ray tube anode and then scattered by the sample. In general, the ratio between inelastic Compton scattering (inc = incoherent scatter at a lower energy than the tube anode radiation) and elastic Rayleigh scattering (coh = coherent scatter at the same energy as the tube anode radiation), i.e. the inc/coh ratio, may show a good correlation with the organic matter content (Guyard et al. 2007). However, this relation is not applicable for all sediments since inc is inversely related to the mean atomic number of the sample (Rothwell et al. 2006), whereas coh is positively correlated to elements with high atomic numbers (Hoffmann 2006). Thus, both characteristics are not exclusively related to the organic matter content of the sample. In addition the intensities of inc and coh peaks in the XRF spectrum are related to the strength of the primary radiation, which apart from the chosen voltage and amperage is influenced by the age of the X-ray tube. Because inc and coh peak intensities integrate effects of both X-ray tube and sample-matrix changes we evaluate their usability as normalising parameters in long term studies of extensive continuous sediment sequences.

Two ICDP deep lake drilling projects were conducted in a short time interval in 2008/2009. Deep drilling in Laguna Potrok Aike (southern Argentina) was accomplished in the project PASADO (ICDP-Expedition No. 5022) during September to November 2008. Shortly after, deep drilling in Lake El'gygytgyn was completed in the framework of the Lake El'gygytgyn Drilling Project (ICDP-Expedition No. 5011) from February to May 2009. Protocols for coring, scanning and sampling were very similar in both projects (Ohlendorf et al. 2011; Wennrich et al. 2013). Both projects recovered several 100 m of lacustrine sediments reaching back in time to > 50 ka and 3.6 Ma, respectively. In both projects high resolution XRF-scanning of these long records was done with an ITRAX XRF core scanner (Croudace et al. 2006) and lasted several month. Concerning XRF-instrument settings two different strategies were pursued by the PASADO project on the one side and the

Lake El'gygytgyn Drilling Project on the other side. The PASADO strategy aimed at keeping constant count rates throughout the entire sediment sequence which involved an adjustment of X-ray tube settings for each core section. In contrast, the El'gygytgyn strategy relied on constant X-ray tube settings throughout the entire record regardless of the count rates that were achieved by these settings. Here we report our experiences with these two different strategies, describe advantages and disadvantages of both approaches, discuss the effects of X-ray tube ageing, and suggest a potential normalising procedure.

## Site Characterization

### *Laguna Potrok Aike*

Laguna Potrok Aike (51°57.789'S, 70°22.754'W; 113 m a.s.l.; Fig. 13.1) is a 100 m deep, nearly circular lake situated approx. 100 km west of the city of Río Gallegos, southeastern Patagonia, Argentina (Haberzettl et al. 2005; Zolitschka et al. 2006). The lake is located in the Pali Aike Volcanic Field and originates from a maar explosion (Zolitschka et al. 2006). The catchment rocks consist of young fluvial and lacustrine deposits, molasse-type sediments, basalts, phreatomagmatic deposits and glacial till. Due to its great water depth Laguna Potrok Aike is the only lake in this region that is currently unaffected by desiccation processes, which underlines its potential to hold a continuous sedimentary record. Nevertheless, as a terminal lake it reacts extremely sensitive to changes in the regional hydrological balance expressed as variations in the water level of the lake (Haberzettl et al. 2007; Ohlendorf et al. 2013).

### *Lake El'gygytgyn*

Lake El'gygytgyn (67°30' N, 172°050' E, 492 ma.s.l.; Fig. 13.1) is a 12 km wide impact crater lake located in central Chukotka/Far East Russian Arctic. Today, the roughly circular lake has a maximum water depth of 175 m (Melles et al. 2007; Nolan and Brigham-Grette 2007), filling the deepest part of the 18-km wide El'gygytgyn impact crater (Gurov et al. 2007). The bedrock in the vicinity of the lake predominantly consists of Upper Cretaceous ignimbrites, tuffs and andesite-basalts of the Okhotsk–Chukchi Volcanic Belt (OCVB) (Belyi and Raikevich 1994; Nowaczyk et al. 2002). Erosion and detrital sediment transport of bedrock material into the lake basin are mainly triggered by continuous permafrost in the catchment that presumably exists since the Late Pliocene (Glushkova and Smirnov 2007), as well as slope dynamics, and fluvial outwash in the lake surrounding (Fedorov et al. 2012; Schwamborn et al. 2008). Lake El'gygytgyn represents a unique site, because it holds the most long-lasting climate record of the terrestrial Arctic (Melles et al. 2011, 2012), reaching back to the time of meteorite impact event 3.58 ± 0.04 Ma ago (Layer 2000).

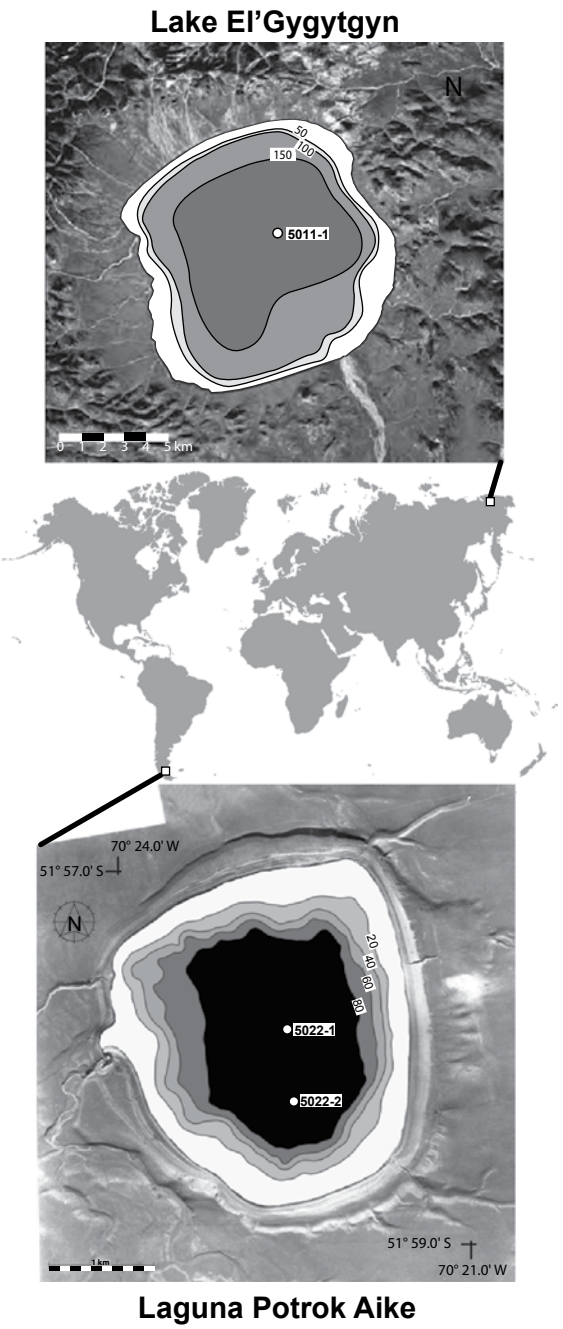


**Fig. 13.1** Locations of Lake El'gygytgyn and Laguna Potrok Aike are indicated by *white squares*. Bathymetric maps for both lakes are superimposed on aerial photographs. Locations of composite cores from site 5011–1 (Lake El'gygytgyn) and 5022–2 (Laguna Potrok Aike) are indicated by *white dots*

## Material

### *Sediment Cores*

Within the framework of the International Continental Drilling Program (ICDP)-project PASADO (Zolitschka et al. 2009) a total of 510 m of lacustrine sediments, down to a maximum depth of 101.5 m below lake floor (m blf), have been recovered from seven holes at two drill sites (Fig. 13.1). Coring was done with the GLAD800 platform equipped with a CS-1500 drill rig using wireline coring operated mainly with a hydraulic piston coring tool (Ohlendorf et al. 2011). Each hole consists of up to 36 core runs with a length of approx. 3 m, depending on sediment structure and gas expansion, that were cut into 1.5 m long sections on board of the platform. After core splitting and scanning a 106.08 m long composite profile was constructed for Site 2 (2CP). Cores were correlated mainly based on visual core correlation. The resulting 2CP consists of 99 core sections. Core scanning was performed with different techniques one of which was XRF scanning and X-radiography with the ITRAX (details are outlined below). After core scanning was completed, cores were sampled continuously in 2 cm intervals (Ohlendorf et al. 2011).

Coring at Lake El'gygytgyn took place in spring 2009 within the scope of the ICDP Lake El'gygytgyn Drilling Program (Melles et al. 2011, 2012; Brigham-Grette and Melles 2009). Drilling was performed from the lake ice cover using a DOSECC Russian GLAD 800 system equipped with a modified Christensen CS-14 coring rig especially developed for working under extreme cold conditions. In total 354.7 m of lacustrine sediments of Lake El'gygytgyn down to a maximum depth of 318 m blf have been recovered from three holes (1A, 1B, 1C) at the lake centre (Fig. 13.1; Melles et al. 2012).

The cores were opened and initially visually described in the laboratory following ICDP standard procedures (Wennrich et al. 2013), and subsequently logged for physical properties as well as for its geochemical composition by XRF-scanning using the ITRAX. Based on the visual core description and initial logging data, a core composite profile was compiled for subsequent sampling. Samples from the lacustrine sediments were taken in 2-cm resolution, whereas ash layers and mass movement deposits were excluded from sampling (Wennrich et al. 2013; Nowaczyk et al. 2013).

### *Lithology*

According to the preliminary age model, the sedimentary record from Laguna Potrok Aike reaches back in time to more than 51,000 years cal. BP (Kliem et al. 2013). Very contrasting lithologies are encountered especially in the Pleistocene part of the record. Fine-grained, organic-rich, carbonate bearing silts mainly occur in the uppermost 20 m of the record. In contrast, organic-poor, carbonate free silts

and sands are observed below 20 m. In the lowermost part even gravel lavers are encountered. Several intercalated rhyolithic and dacitic tephra layers of up to 1 m in thickness characterize the whole record. More than 50 % of the record consists of redeposited sediments e.g. partially with nodules of fine-grained, consolidated sediment embedded in a coarser grained matrix of poorly consolidated sediment.

The sedimentary record of Lake El'gygytgyn that covers the past ca. 3.6 Ma (Melles et al. 2012; Nowaczyk et al. 2013) is composed of an alternation of variable, mainly clastic sediments that can be classified into five different facies (Brigham-Grette et al. 2013). The majority of the Quaternary sediments consists of massive to faintly banded silts of facies B. Laminated sections of dark grey to black silt and clay of facies A as well as reddish brown silts of facies C are attributed to peak glacial and peak interglacial conditions, respectively. Furthermore, laminated sections of grey silt to clay of facies D and grey to reddish-brown clay, silt and fine sand of facies E with intermittent brecciated intervals exclusively occur in the Pliocene section of the core (Brigham-Grette et al. 2013). Mass movement deposits of different styles (turbidites, grain flow deposits, debrites, slumps and slides) account for 34.5 % of the sediment sequence (Sauerbrey et al. 2013), and eight distal tephra layers have been observed (Nowaczyk et al. 2013).

## Methods

For both projects, all core sections were scanned for their major and trace element composition with two different ITRAX XRF-core scanners (Croudace et al. 2006). Element data recorded by the ITRAX are semi-quantitative, and are expressed as total counts (cnts), i.e. integrated peak area. This denotes the number of total counts collected by the detector during the measurement time for each step. PASADO cores were scanned at the University of Bremen (CS-8) whereas El'gygytgyn cores were scanned at the University of Cologne (CS-9). Both scanners in a first step recorded a 250 dpi linescan image and accomplished a laser triangulation of the core surface. Subsequently, XRF-scanning was done using a molybdenum (Mo) X-ray tube for elements with high atomic numbers and a chromium (Cr) X-ray tube for elements with low atomic numbers. During the Mo X-ray tube run, an additional digital X-radiography was acquired.

For the PASADO-project the following XRF-scanning protocol was applied:

Considering only the three cores that were drilled at Site 2 (Fig. 13.1) in total 164 sections were scanned with both, a Mo-tube and a Cr-tube. For both tubes scanning was performed with a step size of 5 mm and a count time of 10 s. Tube voltage was kept constant at 30 kV. The tube current was adjusted for each section separately by recording a test XRF-spectrum for 30 s at positions in the section that represent the prevailing lithology of the respective core section. At these positions the tube current was adjusted to yield a count rate of 30,000 ± 2000 cps to avoid an overflow of the SDD (silicon drift detector) and to reach a spectral resolution of around 18 eV/channel. If small differences in the optimal tube current occurred

within the section, an average tube current for the scanning of the section was chosen. In rare cases with drastically different lithologies encountered in the same section, two separate scans with different tube current settings were performed. After scanning, the recorded individual XRF raw-spectra for each step were saved, and a sum-spectrum was automatically calculated for each section by adding up the counts of every single channel (in total 1024 channels) to one spectrum by the Cox Q-spec 6.5 XRF-processing software. This spectrum was subsequently used to fit the mathematical model to the measured data by adjusting sample matrix characteristics, element composition, tube, and detector parameters as well as matrix and tube effects in the model using the Q-spec software with the aim to minimize the mean square error (MSE). The optimized fit was then applied in a second step to re-evaluate all single spectra with a maximum of 100 iterations per spectrum in an automated batch procedure. The result of this batch evaluation is a table with counts above the background level per measurement time (cnts) for each element that was specified in the setting file.

In case of the ICDP El'gygytgyn Drilling Project, a more static approach has been applied, with the ITRAX for both the Cr and Mo tube permanently set to a voltage and current of 30 kV and 30 mA, (count time 10 s, step size 2 mm), respectively, regardless of the resulting signal strength and assuming only minor variation in the sediment composition. This static set-up yields very similar output signals for all elements on a core-to-core comparison, without major data shifts due to changes of the input X-radiation intensity. Nevertheless, tube ageing can result in a long-term loss of intensity in the primary radiation, which leads to a gradual decrease in the fluorescence radiation. To monitor this tube ageing effect, an internal reference glass of known composition was measured after each core run. To minimize the preparation and measuring time efforts, the standard glass was mounted to an epoxy block with the shape of a half cylinder with the same diameter as the sediment cores (Fig. 13.2). During the XRF scan, the block is routinely placed just at the lower edge of the core, and thus, also reduces possible edge-induced errors during the sediment scan. Additionally, the epoxy block is equipped with a centered slit to place commercially available lead letters used for medical X-radiography. This enables to label the radiographic images produced by the ITRAX, which are usually saved with the same default file name, with the appropriate core identity (Fig. 13.2). The simple construction of the epoxy block makes it easy to modify and adapt it to different user specific requirements (core diameter, multiple standards, etc.).

## Results and Discussion

### *Laguna Potrok Aike*

For the 164 Site 2 core sections form Laguna Potrok Aike tube current settings varied between 18 and 34 mA for the Mo-tube and between 26 and 50 mA for the

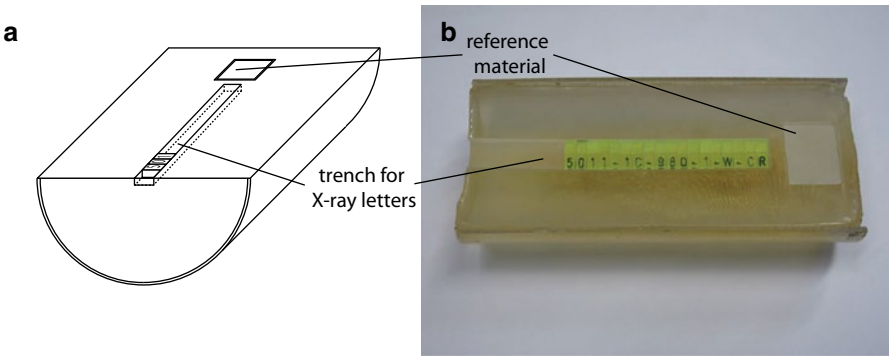


**Fig. 13.2** Photograph and sketch of the reference glass holder equipped with X-ray letters and a reference glass

Cr-tube (Fig. 13.3). In 2CP a down-core trend towards higher tube currents is detectable (Fig. 13.4). However, as intended, the count rates that were realized for all core sections remain at a relatively constant level of on average 30,022 ± 1903 kcps (Fig. 13.4). Very low count rates are observed in intervals with very coarse grained sediments or abundant small cracks. Such intervals are prone to edge effects that reduce count rates, and are thus visible as negative spikes in the raw-data shown in Fig. 13.4. Hence, the complete record should be checked for low count rates that

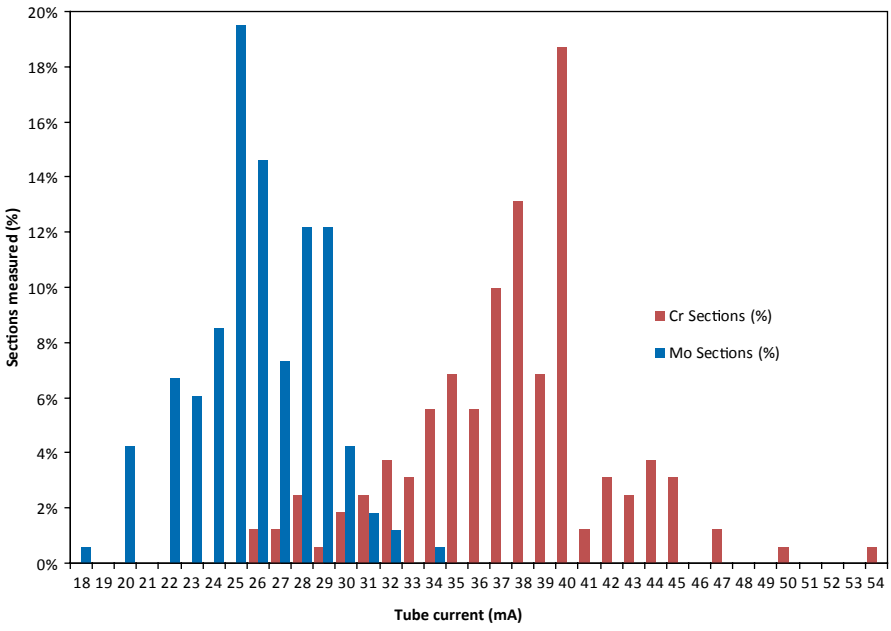


**Fig. 13.3** Histogram of XRF-tube current used for scanning of the 164 core sections drilled at PASADO Site 2

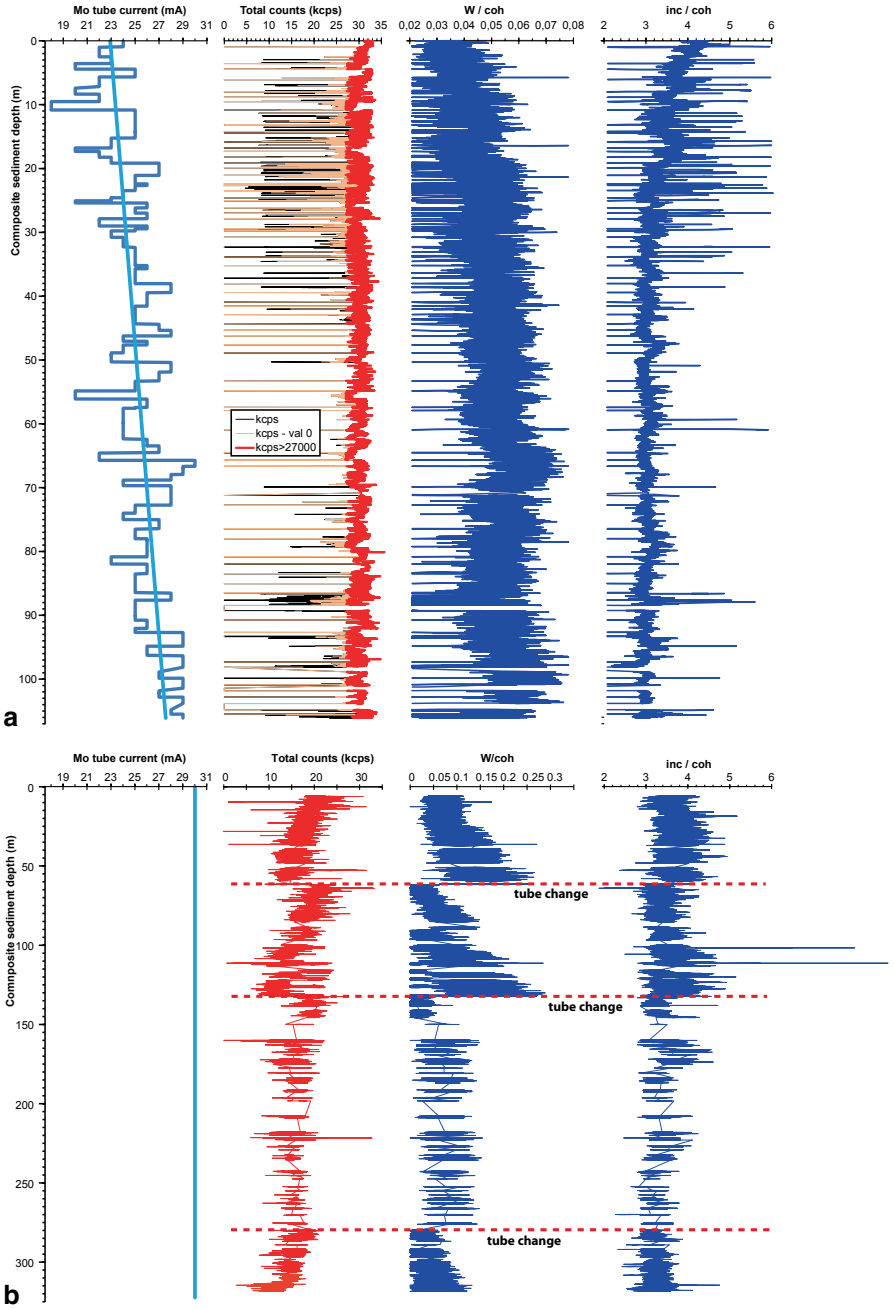


**Fig. 13.4** Tube currents, count rates, the W/coh and the inc/coh ratio for all core sections of the composite profile are shown for Laguna Potrok Aike (*upper panel*) and Lake El'gygytgyn (*lower panel*)

result from such effects, and these measurements should not be considered for further interpretation as has been done for the PASADO 2CP record (Hahn et al. 2014).

The trend towards higher tube currents with increasing sediment depth (Fig. 13.4) is an effect of both the ageing of the Mo-tube and a higher sediment compaction with increasing sediment depth. The first effect is documented by a parallel increase of the corrected tungsten (W) intensities (W/coh in Fig. 13.4) with increasing sediment depth. This feature is observed because W is released from the filament of the X-ray tube and is deposited on the interior surfaces of the tube in higher quantities as the tube age increases. This leads to an emission of W-radiation that is detectable in the X-ray spectra as characteristic peaks. For the PASADO core series (Fig. 13.4a), the observed W/coh increase from ca. 0.03 to ca. 0.06 represents a tube ageing of ca. 300 h, i.e. from 1200 to 1500 h of total tube lifetime, and thus, is rather small. This effect is more pronounced when XRF-scanning of a long sediment core series extends throughout the entire lifetime of a tube. In the case of the Lake El'gygytgyn core series, W/coh values increased from 0 (zero) for a new tube to values around 0.25 for a tube with 2000–3000 h of total tube lifetime (Fig. 13.4b). Since much longer life times of the Mo tube (up to 5000 h) are possible this value might also get significantly higher. The effect of sediment compaction is inferred from the Mo inc peak, as displayed by the inc/coh-ratio (Fig. 13.4a), that decreases with increasing sediment depth. Incoherent scattering is known to be inversely related to the mean atomic number of the sediment (Croudace et al. 2006). Higher intensities of inc scattering thus often reflect higher water and organic contents (Thomson et al. 2006) and/or lower compaction (higher porosity) in the sediments of the topmost parts of the profile.

Apart from overall down-core trends described above, in the PASADO 2CP record shifts in element profiles become obvious that occur at places were the composite profile changes from one section to another one. Here changes in the tube current occur at section breaks that are located (1) within one core run, (2) between two core runs or (3) when the composite profile switches from one hole to the parallel hole. For case (1) the change in tube current and thus the shift in element profiles should be minimal and in most cases negligible. Only when a drastic lithological change occurs within a core run, tube current settings were different for the sections of this run, and thus, had to be corrected. For cases (2) and (3) there are several possible reasons for a shift in the element profiles. Apart from lithological changes, differences in compaction caused by the coring operation may occur. Additionally changes in water content, grain-size, organic matter content, and also tube ageing may play an important role. Different tube current settings, and thus, the necessity for correction, are more likely in these cases. At the places of tube current change most elements show a shift of their total counts (cnts).

For the correction of inter-section shifts in element profiles that result from the usage of different tube currents we tested different methods. To cover the spectrum of sediments that occur in the PASADO 2CP, short test sections were selected from the middle part of the composite profile between 56.4 and 57.6 m composite depth (cd). Three different lithologies were chosen that are representative for major parts

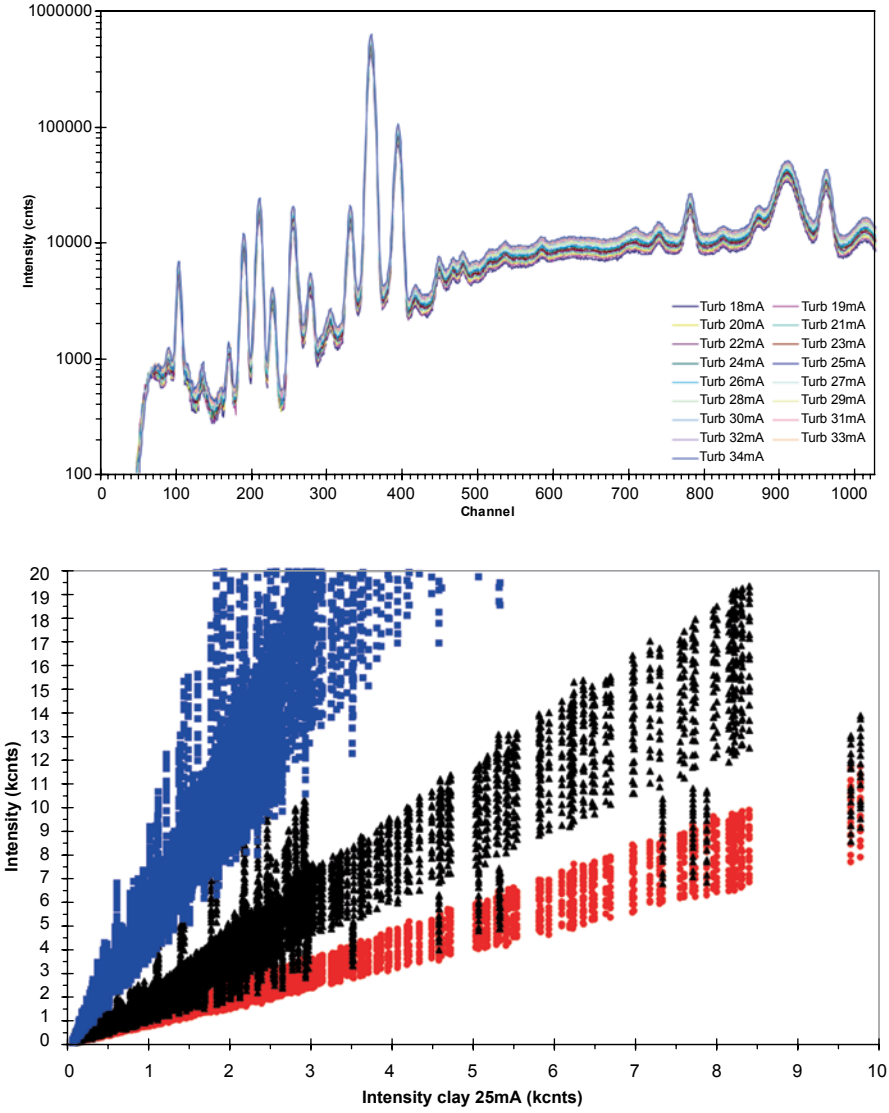


**Fig. 13.5** *Upper panel*: Raw spectra (1024 channels) of the turbidite lithology scanned with different tube currents (18-34 mA). *Lower panel*: Intensities for three representative lithologies (clay, tephra, turbidite) plotted vs. the intensities determined for clay at 25 mA. For clay and tephra linear relationships are comparable when high intensities are considered. For the turbidite layer and for low intensities, however, linear relationships differ significantly between the lithologies

of the sediment record: tephra (4 cm section), clay (2 cm section), and turbidite (30 cm section). Each of these selected sections was scanned with all different tube currents (18–34 mA) that were used for the other sections of the record (Fig. 13.5). Systematic offsets of the recorded spectra to higher intensities in all 1024 channels were observed (Fig. 13.5). Linear relationships between intensities at a fixed tube

current (25 mA) and XRF-intensities at varying tube currents were observed within the same lithology (Fig. 13.5). These linear relationships can be used to re-calculate raw spectra and normalize them to a common tube current if only minor lithological changes occur. However, for the PASADO cores, lithological changes, e.g. between clay, turbidite and tephra layers, are too extreme and hence result in linear relationships with different slopes depending on the scanned lithology (Fig. 13.5). Therefore, a correction of the raw spectra that relies on one of those determined linear relationships is not applicable for the entire sediment sequence. Hence, to correct for tube-current related changes several simple correction methods relying on features that are easily extractable from the energy dispersive X-ray spectra were tested for the PASADO 2CP test sections. Specifically, we normalized XRF-element counts to the tube current directly (mA), the total count rate (kcps), the intensity of the inc scatter peak (inc), and the intensity of the coh scatter peak (coh). The results are shown in Fig. 13.6 for Fe, but are similar for all other detected elements. The uncorrected raw data reveal the expected trend towards higher element intensities at higher tube currents. A simple normalisation with the tube current directly leads to an over-compensation of these high element intensities (Fig. 13.6). It turns out that a normalisation that uses the total count rate as a denominator produces better results but still leads to a slight overestimation of element counts especially concerning the tephra lithology. For the test sections a normalisation of element counts works equally well with both the inc and the coh peak (Fig. 13.6).

In general, the intensity of the sum of the scattered radiation is proportional to the average atomic number of the material that is being analysed (Kanngießer and Haschke 2006). Therefore, coherently and incoherently scattered X-rays are used both to characterise the sample matrix and to estimate instrumental errors (Rao et al. 1995). The inc scatter peak has previously been used to infer mass attenuation coefficients, and thus to characterize the matrix of a sample that is analysed by energy dispersive XRF-techniques (Nesbitt et al. 1976; Reynolds 1963, 1967). Inc scatter intensities for instance were related to a higher sediment porosity (Thomson et al. 2006) that often is related to the organic matter content of the sediments (Löwemark et al. 2011). To correct for matrix related effects, also the sum of both scatter peaks (inc + coh) has been used to normalize element counts (Kylander et al. 2011). As described above the PASADO 2CP shows a trend towards decreasing inc intensities with increasing sediment depth probably reflecting decreasing water and organic contents, and porosity (Thomson et al. 2006). In contrast, the intensity of the coh scatter peak does not show such a trend since it reflects the interaction of X-rays with tightly bound electrons, and thus, is correlated to elements with high atomic numbers (Hoffmann 2006). Because of this we expect that the coh peak intensity in the PASADO CP2 record is more related to instrument settings and probably to surface irregularities reflecting sediment grain-size (Potts et al. 1997). Therefore, in order to level out matrix differences (except organic content and porosity) and changes of the tube current simultaneously, we normalized element counts to the coh scatter peak (Fig. 13.6).

To demonstrate the effect of XRF-data normalisation, element profiles of Fe and Ca are shown in Fig. 13.7. Whereas there are cases when a steep gradient observed

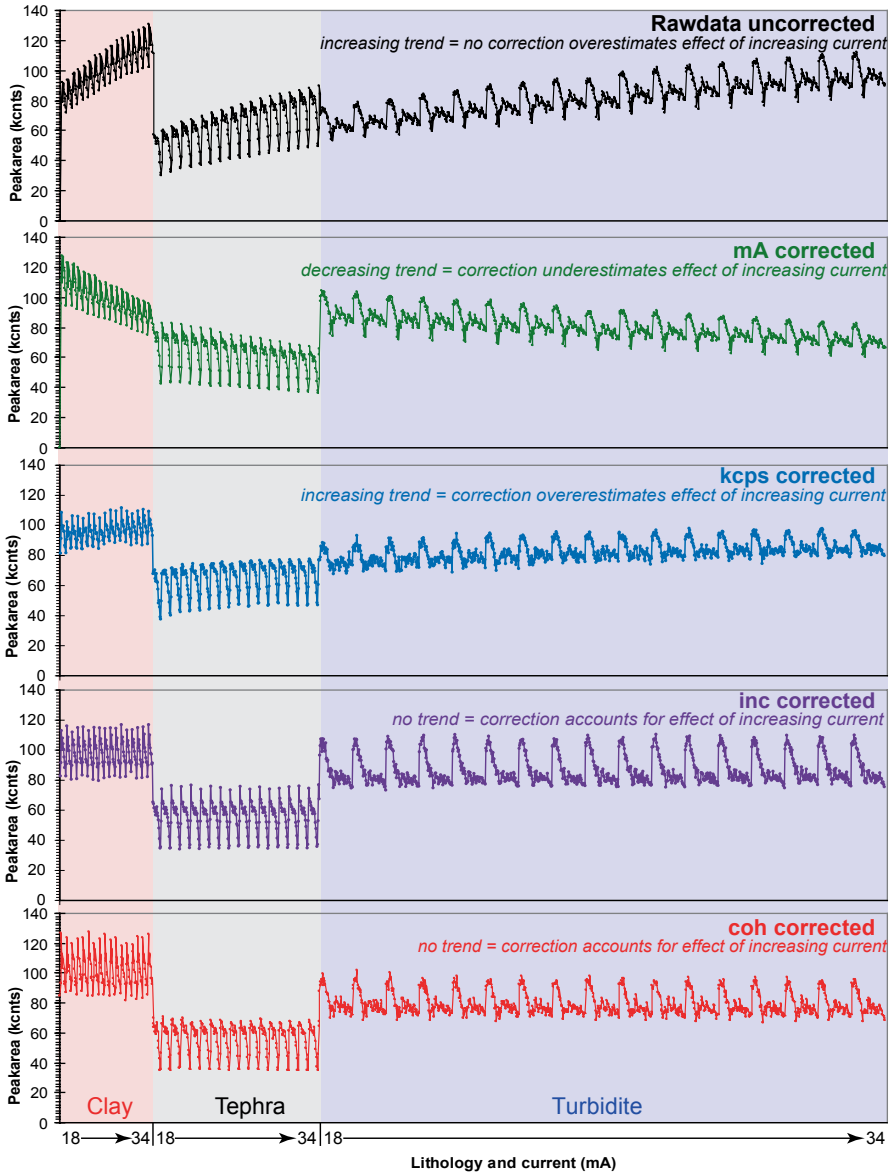


**Fig. 13.6** Raw data are compared to different correction methods (mA, kcps, inc, coh). Fe profiles of the three representative lithologies (sections with 2 cm of clay, 4 cm of tephra and a 30 cm thick turbidite) that were scanned with different tube currents are shown. Uncorrected raw data (*black*) show the expected linear increase with tube current. A correction by normalisation with the tube current directly over-compensates this linear increase (*green*). The trend is reliably levelled out by normalization with the Mo coherent radiation (*red*)

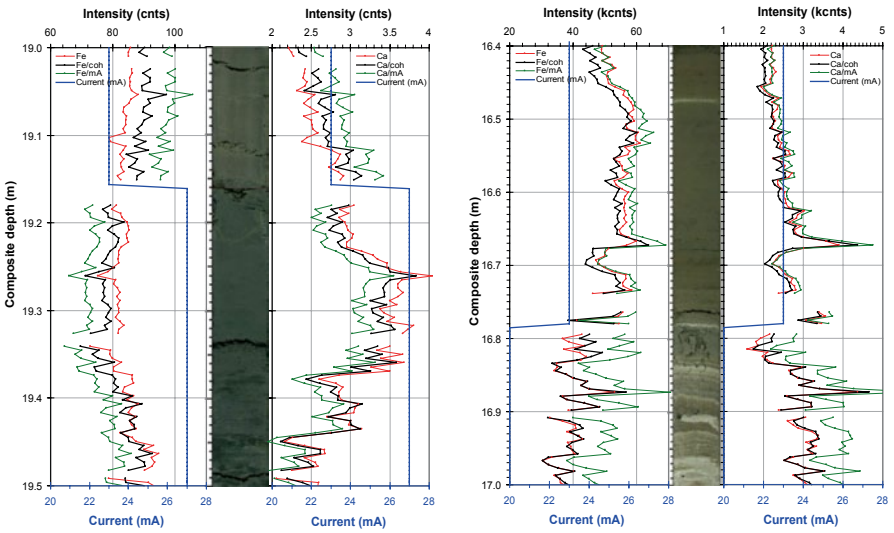


**Fig. 13.7** Example of a section break where a different tube current was used for adjacent sections of the PASADO 2CP profile. The effect of the different correction methods is visualized by the *coloured curves*

in the raw counts is alleviated by data normalisation with the coh peak there are also cases when a gradient is generated by the coh peak normalisation. This may even be different for Fe compared to Ca. Both phenomena become obvious, when data are compared in detail at section breaks where strong differences in the tube current occur (Fig. 13.7). At 16.78 m the tube current changed from 20 to 23 mA, which produced a step in the Fe and Ca XRF raw data that is attenuated by the coh correction (Fig. 13.7 right panel). In contrast at 19.16 m tube current changed from 23 to 27 mA, which did not result in a pronounced step in the Fe and Ca raw data. The coh correction at this level introduced a step in the Fe-profile which is not as pronounced in the Ca-profile. For both cases a normalisation with the tube current directly produced a much stronger change of the element profiles.

## *Lake El'gygytgyn*

For all sections of the composite profile from Lake El'gygytgyn current and voltage for both the Mo-tube and Cr-tube was set to 30 mA and 30 kV, respectively. Due to the constant current applied, inter-section shifts for light to heavy elements are negligible. This enables a rather easy splicing of the single core section data to a composite profile without higher correction efforts.

But on a long-term perspective, the loss in primary tube power due to tube ageing has a significant effect on the scanning data, whereas changes in the sediment compaction play only a minor role. The loss in the energy of the excitation source is clearly visible in a distinct count rate decrease with increasing tube age (Fig. 13.4b),

with values of around 25,000 kcps reached with a new tube, but a gradual drop to values around 12,000 kcps for a tube with more than 3000 h of operation. Simultaneously, the enhanced W release from the filament with increasing tube age, results in a sharply increasing W/coh ratio (Fig. 13.4b).

The fairly linear trend of the inc/coh ratio illustrates that on a broader scale compaction variations in the investigated section of the Lake El'gygytgyn sequence are rather negligible, and short-term fluctuation of the scatter ratio might rather be attributed to changes in the sediment matrix. A matrix correction approach using the inc/coh ratio is described in more detail elsewhere (Wennrich et al. 2013; Melles et al. 2012).

The intensity of power variations over the tube lifetime demonstrates the necessity to continuously monitor tube ageing. The use of the reference glass behind each scanned core section enables to monitor these intensity variations, and further allows investigation of element specific effects. Similar to the core results, the results of the standard glass measurements recorded with the Mo-tube ($n=337$) clearly illustrate a gradual drop in total count rate over time from 18–16,000 kcps for fresh tubes to approx. 7000 kcps after ca. 1500 h of tube lifetime (Fig. 13.8). Interestingly, the kcps values of the Mo tube plot in two clusters, with decreasing values from 0 to ca. 1200 h, and another cluster with a drop between ca. 1500 and 3000 h (Fig. 13.8; dashed lines). The first cluster mirrors the accelerated tube alteration of new X-ray sources during the continuous XRF scanning in combination with X-radiography. In contrast, the second cluster can be attributed to the beginning of the continuous measurements within the Lake El'gygytgyn project, when the measurements were started with a less intensely used Mo tube that already had a lifetime of ca. 1500 h. This parallel but delayed loss in the total count rate of the latter demonstrates the amplified ageing due to the enormous tube load during the long-term measurements.

In contrast to the rather quick signal loss of the Mo tube, the data of the Cr tube ($n=300$) show a much slower drop of the kcps values from ca. 20,000 to 14,000 (ca. 30 %) over a period of almost 7300 h. Since for the XRF scanning both tubes were run with the same current and voltage settings, the amplified ageing of the Mo tubes is most likely a result of the additional load due to the X-radiography. In the case of the Lake El'gygytgyn project, X-radiography was performed at 2750 W (55 kV and 50 mA), which is close to the maximum power of the Mo tube.

The long-term trends of specific element intensities of the used reference glass material show partly distinct variations, which are also dependent on the used X-ray source. For the Mo tube, the apparent loss in tube energy visible in the drop of the total count rate severely influences heavier (high atomic number, $Z$) elements (rel. signal loss Sr: 72.8 %, Zr: 72.8 %; Fig. 13.8e, f), whereas lighter elements are much less affected (rel. signal loss Si: 44.5 %, Ca: 43.2 %, Fe: 47.9 %; Fig. 13.8b, c, d). As both Compton and Rayleigh scatter are highly dependent on the energy of the excitation source (Potts et al. 1997; Tertian and Claisse 1982), the obvious intensity decrease of inc and coh of up to 78.6 and 77.8 %, respectively (Fig. 13.8e, f), is supposed to be caused by the reduction in tube power. Thereby, both the inc and coh scatter of the measurements with the Mo tube behave clearly linear to the total count

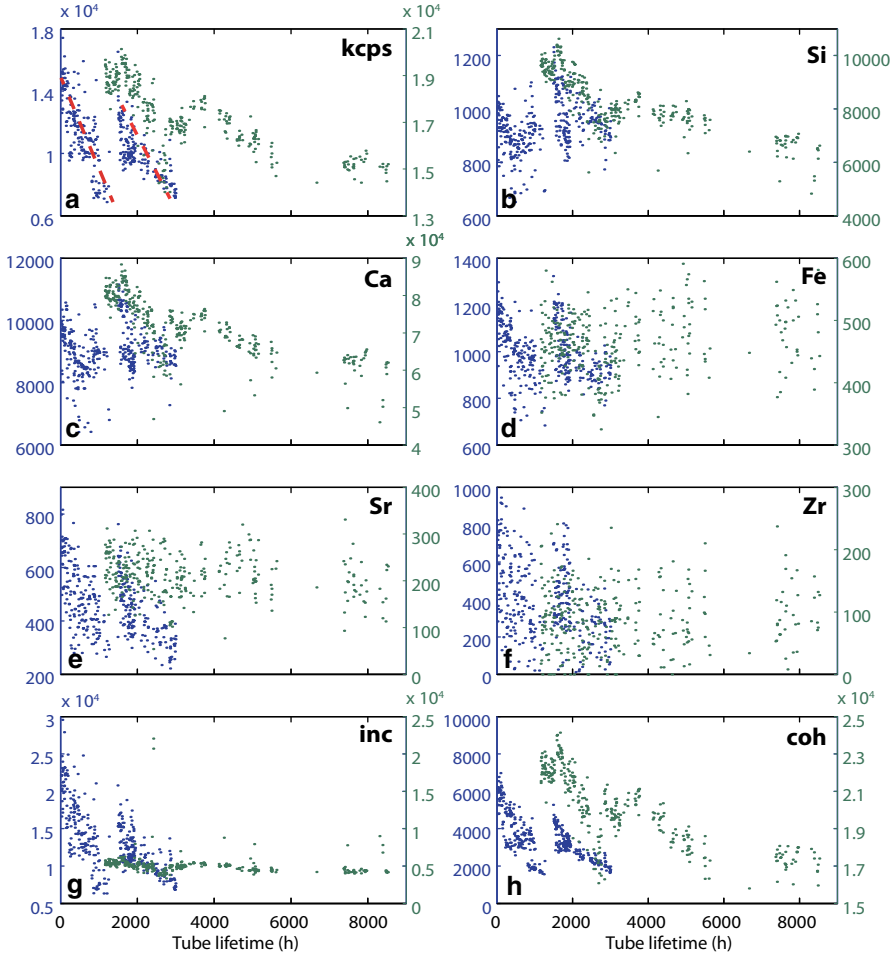


**Fig. 13.8** Intensities of **a** the kcps value, **b** silicon, **c** calcium, **d** iron, **e** strontium, **f** zirconium, and the **g** incoherent and **h** coherent scatter of an in-house glass reference material measured simultaneously with the Lake El'gygytgyn cores vs. tube lifetime (*blue dots* and axes refer to measurements with the Mo tube, *green dots* and axes refer to measurements with the Cr tube). *Dashed lines* in **a** illustrate two clusters with parallel decreasing kcps values of the Mo tube

rate (Fig. 13.9), with coefficients of determination ($r^2$) of 0.90 and 0.95, respectively. Thus, in general inc and coh scatter might be used to correct for the long-term tube ageing. In detail, such a correction is only applicable for mid to high-$Z$ and heavy elements ($z \geq 37$), whereas the correction would even over-compensate the effect on light elements. Thus, in case of lighter elements the apparent energy loss can be rather corrected by calculating ratios of elements with comparable atomic numbers (e.g., Si/Ti ratio, Mn/Fe ratio; Melles et al. 2012; Wennrich et al. 2013).

In contrast to the Mo tube data, the element intensities of the reference glass determined with the Cr tube indicate a much slower loss in signal intensity over the tube lifetime (> 8000 h), but with a surprisingly higher signal loss for lighter

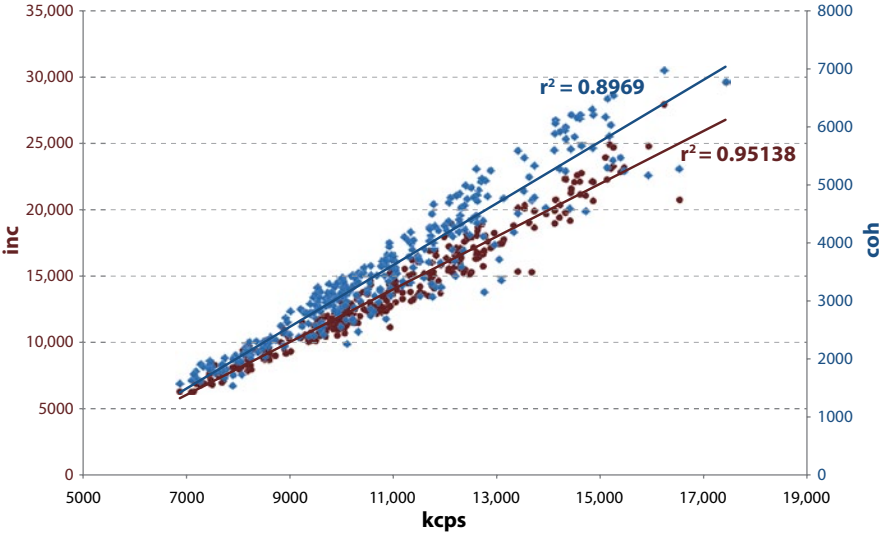


**Fig. 13.9** Intensities of the kcps value plotted against the intensities of the inc-scatter peak (*red*) and the coh-scatter peak (*blue*) of a Mo-tube both show a high correlation

elements (rel. signal loss Si: 54.6 %, Ca: 47.8 %; Fig. 13.8b, c). This direct correlation of light element intensities and the energy yield of the X-ray tube is also documented in a high correspondence of the Si intensity and kcps ($r^{2=}$0.77; Fig. 13.10). Although being fairly scattered, mid-Z elements, like Fe, Sr and Zr, in contrast,

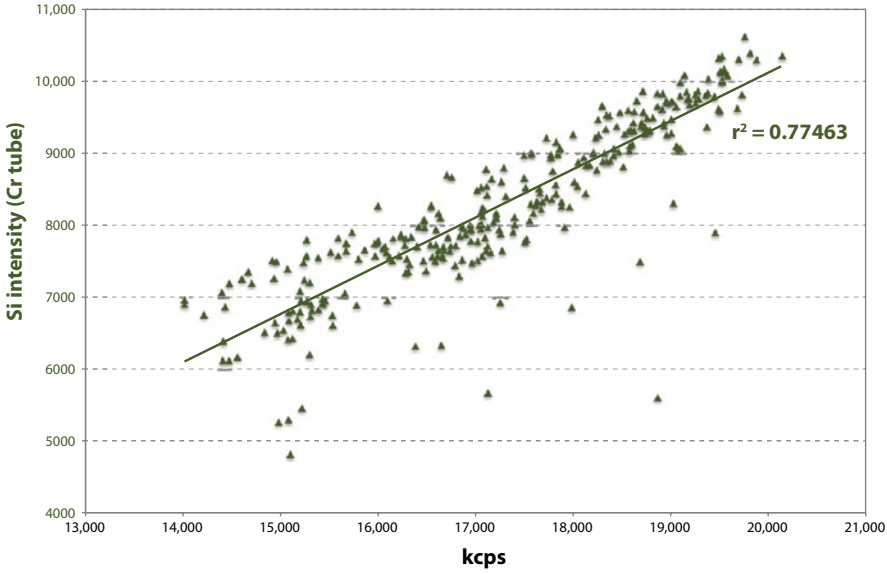


**Fig. 13.10** Intensities of the kcps value plotted against the intensities of the Si peak determined with a Cr-tube indicates a good correspondence

show rather constant values (Fig. 13.8e, f). The significant scatter of the heavier elements is presumably caused by the limited thickness of the used reference glass of only 1.1 mm. Thickness experiments of Zr, Sr, and Rb concentrations in obsidian, which is similar in its chemical composition to our reference glass, revealed a substantial distortion of the values below a thickness of 2 mm (Davis et al. 2011). Furthermore, the scattered Zr and Sr values might also be caused by the low concentrations of these elements in the reference glass. However, it cannot be excluded that a part of the scatter is also caused by measurements that partly included the plastic holder instead of the reference glass. In order to reduce scattering of the values shown in Fig. 13.8 related to the limited thickness of the reference glass and to achieve a better match between scanned cores and reference material in terms of grain-size, particle composition and porosity in future powdered certified reference material will be measured in addition to the reference glass.

The Rayleigh scatter of the Cr tube measurements strongly follows the total count rate ($r^{2=}0.94$) illustrating that the coherent scatter is rather linked to high-atomic-number elements (Hoffmann 2006), and thus, it's intensity is highly dependent on the energy yield of the tube. The Compton scatter of the Cr tube samples, in contrast, shows a weaker but still distinct correlation to the total count rate ($r^{2=}0.28$), presumably illustrating the higher proportion of the Compton scatter in lighter elements (Tertian and Claisse 1982)

## Conclusions

Two different strategies for XRF-scanning of long sediment records were evaluated. The constant count rate approach was compared to an approach with constant X-ray tube settings. The most striking differences arise from two main factors that influence the quality of XRF-scanning results. These are (1) the age of the X-ray tube and (2) the degree of heterogeneity encountered along the scanned sediment sequence. The first factor becomes relevant when the total scanning time for a sediment sequence approaches the life time of the X-ray tube. Depending on the applied X-ray tube voltage and current, the energy yield of the X-ray tube may decrease markedly after a total usage time of > 1000 h which will result in lower count rates and thus lower element intensities. The second factor is important in sediment sequences with drastic contrasts, namely in sediment porosity, organic content and grain size. These factors may significantly influence the count rate, and hence, the obtained element intensities, which may be critical if only raw element counts are considered. However, as long as element counts are normalized or element ratios are considered, both factors usually do not lead to detectable trends even in long data series.

For most short sediment core sequences, e.g. of 10–30 m, as typically obtained in many limnogeological studies the constant X-ray tube settings approach may be the most suitable, since it precludes shifts at section breaks due to different instrument settings, and thus, does not necessarily require corrections.

When extensive series of sediment core sections have to be measured, the constant count rate approach may be beneficial. A general advantage of adjusting the X-ray tube current to optimal values for each core section is that a constant count rate can be maintained along the entire analysed sediment profile (Fig. 13.4). This is advantageous because it ensures that the same detection limit and signal to noise ratio applies for all measured sections. This is not the case, when a constant current setting (e.g. 30 mA) is applied for all core sections of a large series (Fig. 13.4). In this case differences in lithology, porosity, grain-size, and in particular the effect of tube ageing will influence the count rate, and thus, raw element intensities. In extreme cases this can produce a disadvantageous signal to noise ratio for elements with low concentrations. In the worst case this could lead to misleading interpretations of element profiles. On the other side, inter-section shifts are negligible when a constant tube current is used. This is advantageous for the splicing of single core section data to a composite profile because no corrections are necessary. However, if tube current is changed along the profile most likely element shifts occur as artefacts at section breaks, and thus, have to be corrected. For these shifts our results show that the harmonisation of XRF-scanning data acquired with differing X-ray tube currents along a profile that is composed of a large number of lithologically different sediment sections is best achieved by normalisation of the processed data with the peak of Mo coherent radiation. In long sediment sections without strong lithological differences, however, a correction and reprocessing of the raw-data might yield better results.

For both approaches (constant count rate and constant instrument settings) a normalisation of the processed data with the peak of coh scattering or the usage of element ratios, e.g. as log-ratios (Weltje and Tjallingii 2008), is recommended in order to account for lithological differences and tube ageing.

**Acknowledgments** This research is supported by the International Continental Scientific Drilling Program (ICDP) in the frameworks of the "Potrok Aike Maar Lake Sediment Archive Drilling Project" (PASADO) and the Lake El'gygytgyn Drilling Project. Funding for PASADO drilling was provided by the ICDP, the German Science Foundation (DFG), the Swiss National Funds (SNF), the Natural Sciences and Engineering Research Council of Canada (NSERC), the Swedish Vetenskapsradet (VR) and the University of Bremen. Drilling operations at Lake El'gygytgyn were funded by the ICDP, the NSF, the German Federal Ministry of Education and Research (BMBF), Alfred Wegener Institute and Helmholtz Centre Potsdam (GFZ), the Russian Academy of Sciences Far East Branch, the Russian Foundation for Basic Research, and the Austrian Federal Ministry of Science and Research. Funding of Lake El'gygytgyn core analyses was provided by BMBF (grant 03G0642) and DFG (grants ME 1169/21 and ME 1169/24), The Russian Global Lake Drilling 800 drilling system was developed and operated by DOSECC. For their invaluable help in field logistics and drilling we thank the staff of INTA Santa Cruz and Río Dulce Catering as well as the Moreteau family and the DOSECC crew, and all participants of the Lake El'gygytgyn expedition for their engagement during recovery. Special thanks go to Anders Rindby and Per Engstrom from COX for their support concerning the spectra evaluation. We thank Sabine Stahl, Annette Hahn and Pierre Klie for operating the XRF-scanner and measuring the PASADO cores, and Armine Shahnazarian, Nicole Mantke, and numerous students (Univ. of Cologne) for the core processing and XRF scanning of Lake El'gygytgyn cores.

## References

Belyi V, Raikevich MI (1994) The El'gygytgyn lake basin (geological structure, morphostructure, impactites, problems of investigation and preservation of nature). NEISRI FEB RAS, Magadan

Brigham-Grette J, Melles M (2009) Complex drilling logistics for Lake El'gygytgyn, NE Russia. Sci Drill 7:38–39

Brigham-Grette J, Melles M, Minyuk P, Andreev A, Tarasov P, DeConto R, Koenig S, Nowaczyk N, Wennrich V, Rosén P, Haltia E, Cook T, Gebhardt C, Meyer-Jacob C, Snyder J, Herzschuh U (2013) Pliocene warmth, polar amplification, and stepped pleistocene cooling recorded in NE Arctic Russia. Science 340:1421–1427. doi:10.1126/science.1233137

Brumsack H-J (2006) The trace metal content of recent organic carbon-rich sediments: implications for Cretaceous black shale formation. Palaeogeogr Palaeoclimatol Palaeoecol 232(2–4):344–361. doi:10.1016/j.palaeo.2005.05.011

Croudace IW, Rindby A, Rothwell RG (2006) ITRAX: description and evaluation of a new multi-function X-ray core scanner. In: Rothwell RG (ed) New techniques in sediment core analysis, vol 267. Geological Society of London Special Publications, London, pp 51–63

Davis MK, Jackson T, Shackley MS, Teague T, Hampel J (2011) Factors affecting the energy-dispersive X-ray fluorescence (EDXRF) analysis of archaeological obsidian. In: Shackley MS (ed) X-ray fluorescence spectrometry (XRF) in geoarchaeology. Springer, New York, pp 45–63. doi:10.1007/978–1-4419–6886-9_3

Fedorov G, Nolan M, Brigham-Grette J, Bolshiyanov D, Schwamborn G, Juschus O (2012) Lake El'gygytgyn water and sediment balance components overview and its implications for the sedimentary record. Clim Past Discuss 8(4):3977–4001. doi:10.5194/cpd-8–3977-2012

Glushkova OY, Smirnov VN (2007) Pliocene to Holocene geomorphic evolution and paleogeography of the El'gygytgyn Lake region, NE Russia. J Paleolimnol 37(1):37–47. doi:10.1007/s10933–006-9021-x

Gurov EP, Koeberl C, Yamnichenko A (2007) El'gygytgyn impact crater, Russia: structure, tectonics, and morphology. Meteorit Planet Sci 42:307–319

Guyard H, Chapron E, St-Onge G, Anselmetti FS, Arnaud F, Magand O, Francus P, Mélières M-A (2007) High-altitude varve records of abrupt environmental changes and mining activity over the last 4000 years in the Western French Alps (Lake Bramant, Grandes Rousses Massif). Quat Sci Rev 26(19–21):2644–2660. doi:10.1016/j.quascirev.2007.07.007

Haberzettl T, Fey M, Lücke A, Maidana N, Mayr C, Ohlendorf C, Schäbitz F, Schleser GH, Wille M, Zolitschka B (2005) Climatically induced lake level changes during the last two millennia as reflected in sediments of Laguna Potrok Aike, southern Patagonia (Santa Cruz, Argentina). J Paleolimnol 33:283–302

Haberzettl T, Corbella H, Fey M, Janssen S, Lücke A, Mayr C, Ohlendorf C, Schäbitz F, Schleser G, Wille M, Wulf S, Zolitschka B (2007) Wet-dry cycles in southern Patagonia – Chronology, sedimentology and geochemistry of a lacustrine sediment record from Laguna Potrok Aike (Argentina). Holocene 17:297–311

Hahn A, Kliem P, Oehlerich M, Ohlendorf C, Zolitschka B, The PASADO Science Team (2014) Elemental composition of the Laguna Potrok Aike sediment sequence reveals paleoclimatic changes over the past 51 ka in southern Patagonia, Argentina. J Paleolimnol 52:349–366. doi:10.1007/s10933–014–9798–y

Hoffmann P (2006) Non-invasive identification of chemical compounds by EDXRS. In: Beckhoff B, Kanngießer B, Langhoff N, Wedell R, Wolff H (eds) Handbook of practical X-ray fluorescence analysis. Springer, Berlin, pp 769–783

Kanngießer B, Haschke M (2006) Micro X-ray fluorescence spectroscopy. In: Beckhoff B, Kanngießer B, Langhoff N, Wedell R, Wolff H (eds) Handbook of practical x-ray fluorescence analysis. Springer, Heidelberg, pp 433–474

Kliem P, Enters D, Hahn A, Ohlendorf C, Lisé-Pronovost A, St-Onge G, Wastegård S, Zolitschka B, The PASADO Science Team (2013) Lithology, radiocarbon chronology and sedimentological interpretation of the lacustrine record from Laguna Potrok Aike, southern Patagonia. Quat Sci Rev 71:54–69. http://dx.doi.org/10.1016/j.quascirev.2012.07.019

Kylander ME, Ampel L, Wohlfarth B, Veres D (2011) High-resolution X-ray fluorescence core scanning analysis of Les Echets (France) sedimentary sequence: new insights from chemical proxies. J Quat Sci 26(1):109–117. doi:10.1002/jqs.1438

Layer PW (2000) Argon-40/argon-39 age of the El'gygytgyn impact event, Chukotka, Russia. Meteorit Planet Sci 35(3):591–599

Löwemark L, Chen HF, Yang TN, Kylander M, Yu EF, Hsu YW, Lee TQ, Song SR, Jarvis S (2011) Normalizing XRF-scanner data: a cautionary note on the interpretation of high-resolution records from organic-rich lakes. J Asian Earth Sci 40(6):1250–1256. doi:10.1016/j.jseaes.2010.06.002

Melles M, Brigham-Grette J, Glushkova OY, Minyuk PS, Nowaczyk NR, Hubberten HW (2007) Sedimentary geochemistry of core PG1351 from Lake El'gygytgyn – a sensitive record of climate variability in the East Siberian Arctic during the past three glacial-interglacial cycles. J Paleolimnol 37(1):89–104. doi:10.1007/s10933–006-9025–6

Melles M, Brigham-Grette J, Minyuk P, Koeberl C, Andreev A, Cook T, Fedorov G, Gebhardt C, Haltia-Hovi E, Kukkonen M, Nowaczyk N, Schwamborn G, Wennrich V, and The El'gygytgyn Scientific Party (2011) The Lake El'gygytgyn Scientific Drilling Project – conquering Arctic challenges through continental drilling. Sci Drill 11:29–40

Melles M, Brigham-Grette J, Minyuk PS, Nowaczyk NR, Wennrich V, DeConto RM, Anderson PM, Andreev AA, Coletti A, Cook TL, Haltia-Hovi E, Kukkonen M, Lozhkin AV, Rosén P, Tarasov P, Vogel H, Wagner B (2012) 2.8 Million years of Arctic climate change from lake El'gygytgyn, NE Russia. Science 337(6092):315–320. doi:10.1126/science.1222135

Monien D, Kuhn G, von Eynatten H, Talarico FM (2012) Geochemical provenance analysis of fine-grained sediment revealing Late Miocene to recent Paleo-Environmental changes in the Western Ross Sea, Antarctica. Late Neogene chronostratigraphy and depositional environments on the Antarctic Margin: new results from the ANDRILL McMurdo Ice Shelf Project 96–97 (0), pp 41–58. doi:10.1016/j.gloplacha.2010.05.001

Nesbitt RW, Mastins H, Stolz GW, Bruce DR (1976) Matrix corrections in trace-element analysis by X-ray fluorescence: an extension of the Compton scattering technique to long wavelengths. Chem Geol 18(3):203–213. doi:10.1016/0009–2541(76)90004–8

Nolan M, Brigham-Grette J (2007) Basic hydrology, limnology, and meteorology of modern Lake El'gygytgyn, Siberia. J Paleolimnol 37(1):17–35. doi:10.1007/s10933–006-9020-y

Nowaczyk NR, Minyuk P, Melles M, Brigham-Grette J, Glushkova O, Nolan M, Lozhkin AV, Stetsenko TV, Andersen PM, Forman SL (2002) Magnetostratigraphic results from impact crater lake El'gygytgyn, northeastern Siberia: a possibly 300 kyr long terrestrial paleoclimate record from the Arctic. Geophys J Int 150(1):109–126. doi:10.1046/j.1365–246X.2002.01625.x

Nowaczyk NR, Haltia EM, Ulbricht D, Wennrich V, Sauerbrey MA, Rosén P, Vogel H, Francke A, Meyer-Jacob C, Andreev AA, Lozhkin AV (2013) Chronology of Lake El'gygytgyn sediments – a combined magnetostratigraphic, palaeoclimatic and orbital tuning study based on multi-parameter analyses. Clim Past 9:2413–2432. doi:10.5194/cp-9–2413-2013

Ohlendorf C, Gebhardt AC, Hahn A, Kliem P, Zolitschka B, The PASADO science team (2011) The PASADO core processing strategy–a proposed new protocol for sediment core treatment in multidisciplinary lake drilling projects projects. Sediment Geol 239:104–115. doi:10.1016/j.sedgeo.2011.06.007

Ohlendorf C, Fey M, Gebhardt C, Haberzettl T, Lücke A, Mayr C, Schäbitz F, Wille M, Zolitschka B (2013) Mechanisms of lake-level change at Laguna Potrok Aike (Argentina)-insights from hydrological balance calculations. Quat Sci Rev 71:27–45. http://dx.doi.org/10.1016/j.quascirev.2012.10.040

Potts PJ, Webb PC, Williams-Thorpe O (1997) Investigation of a correction procedure for surface irregularity effects based on scatter peak intensities in the field analysis of geological and archaeological rock samples by portable X-ray fluorescence spectrometry. J Anal Atomic Spectrom 12(7):769–776

Rao DV, Gigante GE, Cesareo R (1995) Coherent and incoherent scattering of 42.75 and 47.24 keV x-ray photons scattered from Al, Cu, Y, Mo, Au and Pb. X-Ray Spectrom 24(4):172–176. doi:10.1002/xrs.1300240406

Reynolds RC (1963) Matrix corrections in trace element analysis by X-ray fluorescence: estimation of the mass absorption coefficient by compton scattering. Am Mineral 48:1133–1143

Reynolds RC (1967) Estimation of mass absorption coefficients by compton scattering: improvements and extensions of the method. Am Mineral 52:1493–1502

Rollinson HR (1993) Using geochemical data: evaluation, presentation, interpretation. Longman Sci Tech, Singapore, p 352

Rothwell RG, Hoogakker B, Thomson J, Croudace IW, Frenz M (2006) Turbidite emplacement on the southern Balearic Abyssal Plain (western Mediterranean Sea) during Marine Isotope Stages 1–3: an application of ITRAX XRF scanning of sediment cores to lithostratigraphic analysis. In: Rothwell RG (ed) New techniques in sediment core analysis, vol 267. Geological Society of London, Special Publications, London, pp 79–98

Sauerbrey MA, Juschus O, Gebhardt AC, Wennrich V, Nowaczyk NR, Melles M (2013) Mass movement deposits in the 3.6 Ma sediment record of Lake El'gygytgyn, Far East Russian Arctic. Clim Past 9(1):1949–1967. doi:10.5194/cp-9–1949-2013

Schwamborn G, Förster A, Diekmann B, Schirrmeister L, Fedorov G (2008) Mid- to late-quaternary cryogenic weathering conditions at Elgygytgyn Crater, Northeastern Russia: inference from mineralogical and microtextural properties of the sediment record. In: Alaska U (ed) Ninth International Conference On Permafrost, Fairbanks, pp 1601–1606

Tertian R, Claisse F (1982) Principles of quantitative X-ray fluorescence analysis. Heyden, London, p 385

Thomson J, Croudace IW, Rothwell RG (2006) A geochemical application of the ITRAX scanner to a sediment core containing eastern Mediterranean sapropel units. In: Rothwell RG (ed) New techniques in sediment core analysis, vol 267. Geological Society of London, Special Publications, London, pp 65–77

Tjallingii R, Röhl U, Kölling M, Bickert T (2007) Influence of the water content on X-ray fluorescence core-scanning measurements in soft marine sediments. Geochem Geophys Geosyst 8(2):Q02004. doi:10.1029/2006gc001393

Weltje GJ, Tjallingii R (2008) Calibration of XRF core scanners for quantitative geochemical logging of sediment cores: theory and application. Earth Planet Sci Lett 274(3–4):423–438. doi:10.1016/j.epsl.2008.07.054

Wennrich V, Minyuk P, Borkhodoev V, Francke A, Ritter B, Nowaczyk N, Haltia-Hovi EM, Brigham-Grette J, Melles M, El'gygytgyn Scientific Party (2013) Pliocene and Pleistocene climate and environmental history of Lake El'gygytgyn/ NE Russia based on high-resolution inorganic geochemistry data. Clim Past Discuss 9:5899–5940. doi:10.5194/cpd-9–5899-2013

Zolitschka B, Schäbitz F, Lücke A, Corbella H, Ercolano B, Fey M, Haberzettl T, Janssen S, Maidana N, Mayr C, Ohlendorf C, Oliva G, Paez MM, Schleser G, Soto J, Tiberi P, Wille M (2006) Crater lakes of the Pali Aike Volcanic Field as key sites for paleoclimatic and paleoecological reconstructions in southern Patagonia, Argentina. J South Am Earth Sci 21(3):294–309. doi:10.1016/j.jsames.2006.04.001

Zolitschka B, Anselmetti F, Ariztegui D, Corbella H, Francus P, Ohlendorf C, Schäbitz F, The Pasado Scientific Drilling Team (2009) The Laguna Potrok Aike Scientific Drilling Project PASADO (ICDP Expedition 5022). Sci Drill 8:29–34. doi:10.2204/iodp.sd.8.04.2009

# Chapter 14
# Approaches to Water Content Correction and Calibration for µXRF Core Scanning: Comparing X-ray Scattering with Simple Regression of Elemental Concentrations

**John F. Boyle, Richard C. Chiverrell and Dan Schillereff**

**Abstract** Geochemical evaluation of sediment records traditionally exploits dry mass concentration data; the new generation of scanning XRF devices, however, are generally presented with wet sediment cores. Therefore, conversion of wet core measured XRF data to dry mass concentrations will aid the palaeoenvironmental interpretation, provided the method used is reliable and avoids loss of data quality. Here, using data from a GEOTEK/Olympus DELTA scanning µXRF device (approximately 5 mm resolution), we compare two methods: (1) correction by simple regression, calibrated using dry sediment elemental concentration data measured for a 'training set' of subsamples, and (2) a novel technique that corrects for water content estimated using X-ray scattering data obtained during scanning. We show that where sediment water contents are highly variable the regression method fails while water content correction methods can be highly effective. Where water sediment water contents are relatively constant, the elemental regression is as effective and introduces less noise.

**Keywords** Scanning XRF · Lake sediment · Chemical stratigraphy · Water content

## Introduction

The last decade has seen a proliferation in the use of high resolution or micro-scanning XRF data to discern stratigraphical changes in alluvial, lacustrine and marine sediment, work that exploits a growing family of µXRF equipment that includes the ITRAX core scanner (0.2 mm resolution) originally developed by Croudace, Rothwell and Cox Analytical (Croudace et al. 2006; http://coxsys.se/), the Avaatek XRF core scanner (0.1 mm resolution) (Richter et al. 2006; http://www.avaatech.com/),

J. F. Boyle (✉) · R. C. Chiverrell · D. Schillereff
Department of Geography and Planning, School of Environmental Sciences,
University of Liverpool, Liverpool L69 7ZT, UK
e-mail: jfb@liv.ac.uk



I. W. Croudace, R. G. Rothwell (eds.), *Micro-XRF Studies of Sediment Cores*,
Developments in Paleoenvironmental Research 17, DOI 10.1007/978-94-017-9849-5_14

developed over the last two decade for rapid analysis of marine sediment cores, and systems that automate (e.g. GEOTEK: http://www.geotek.co.uk/) the application of Handheld XRF Analysers such as the Olympus Delta XRF and Thermo-Niton XL3t (3–6 mm resolution). As μXRF scanning becomes an increasingly popular way of measuring element composition data in sediment cores over "conventional" XRF analysis (Boyle 2000), the question is raised of whether they generate sufficiently accurate quantitative compositional data. The answer to this is far from simple, depending as much on the application or purpose of the measurements as to other considerations. The palaeoecologist with cores of wet sediment who asks whether scanning μXRF is as good as conventional XRF methods must first specify the question and expectations of the data. If these involve assessing the meaning of relative variations in element concentration, and considering only elements that are well-measured by μXRF, then the answer may be a simple, yes. However, the device will clearly not produce precise and accurate dry mass concentration values, and if these quantitative data are required then the answer is, no.

**Micro-XRF Analysis Versus Conventional XRF Analysis**

As μXRF scanning becomes an increasingly popular way of measuring element composition data in sediment cores over "conventional" XRF or other analysis (Boyle 2000; Croudace et al. 2006), the question is raised of whether they generate sufficiently accurate quantitative composition data. The answer to this is far from simple, depending as much on the application or purpose of the measurements as to other considerations. The palaeoecologist with cores of wet sediment who asks whether scanning μXRF is as good as conventional XRF methods must first specify the question and their expectations of the data. If these involve assessing the meaning of relative variations in element concentration, and considering only elements that are effectively measured by μXRF, then the answer may be a simple, Yes. However, the device will clearly not produce precise and accurate dry mass concentration values, and if these quantitative data are required then the answer is, No.

These two end-member cases are unlikely to change in the near future, because the issues do not arise from technological limitations. Rather, the problem is that conventional methods in sediment geochemical evaluation (Boyle 2001) are based on dry mass concentrations, where the concentration of an element, X, is defined as the mass of X divided by the dry mass of sample in which it is measured (Note this remains true even if the mass of X is expressed in molar units). It is a convenient fact of XRF analysis that such dry mass concentration values are obtained without the need to know the sample mass, provided the sample is both dry and of "infinite" thickness (Tertian 1969) relative to X-ray penetration (generally a few millimetres of dry sediment will achieve this). μXRF scans of wet sediment do not meet this requirement. They still measure elements as concentrations (even where reported as

X-ray count per second as with the ITRAX system, this is proportional to, and thus a measure of, concentration), but this concentration is relative to the density of wet sediment. In the case of typical organic lake sediment, where water contents may exceed 95 %, the wet mass concentration may be only 5 % of the dry mass concentration for a particular element.

This diluting of the concentration by water presents a challenge when interpreting wet-core µXRF data. Consider the case of a sediment record which contains high frequency variations in the carbonate to silicate ratio, but which also has highly variable water content. The X-ray signal for Ca, for example, will vary both with the Ca concentration in the dry matter and with the water content of the sediment. As the geochemist is interested only in the dry mass concentration component, it is necessary to process the signal to reduce the contribution of other sources of variation. The most widely used approach is to normalise the element of interest to either another element (Löwemark et al. 2011; Richter et al. 2006) or to back-scatter peaks (Kylander et al. 2012). Working with element ratios has the advantage of eliminating several unknowns; the diluting water content and surface imperfections in particular. However, as X-ray mass attenuation by water varies with photon energy, element ratios do not wholly avoid water content artefacts (Hennekam and de Lange 2012). Furthermore, when working with element ratios it is easy to overlook associated variations in major components that alter the geochemical interpretation. Furthermore, direct comparison of results with other data is difficult or impossible unless the element composition data are expressed as absolute concentrations, and ideally in dry mass form. Thus, the element ratio solution to the water content problem is far from ideal.

It would be desirable, therefore, if wet sediment core scanning XRF signals could be reliably converted to a dry sediment basis. In relatively uniform and consistent stratigraphical sequences the absence of large changes in content of water or organic matter means this conversion to a dry sediment equivalent basis can be achieved by simple correlation as demonstrated by Croudace et al. (2006) and Weltje and Tjallingii (2008). This is because under such constraints the dry and wet mass concentrations are proportional. This simple approach can be used regardless of whether the XRF output is given in concentration units (as is typical for Handheld XRF devices) or as raw X-ray count data. However, if water content in the sediment varies systematically, then simple regression will lead to an invalid correction, potentially producing an apparent chemical stratigraphy that is highly misleading. Where water content varies strongly, such as at the sediment-water interface, or across the transition from inorganic to very organic sediments in lakes during the early Holocene (Shen et al. 2008), then wet and dry mass concentrations are not proportional, and an alternative approach must be taken which is capable first of estimating the water content of the wet sediment, and then correcting the XRF signal for this. In the special case of marine sediment, it may be assumed that the Cl concentration in the sediment is a useful measure of water content and may be used for correction (Hennekam and de Lange 2012), but in freshwater sites this cannot be done. Fortunately, all energy dispersive XRF spectra contain information that is strongly associated with the water content, offering the possibility that

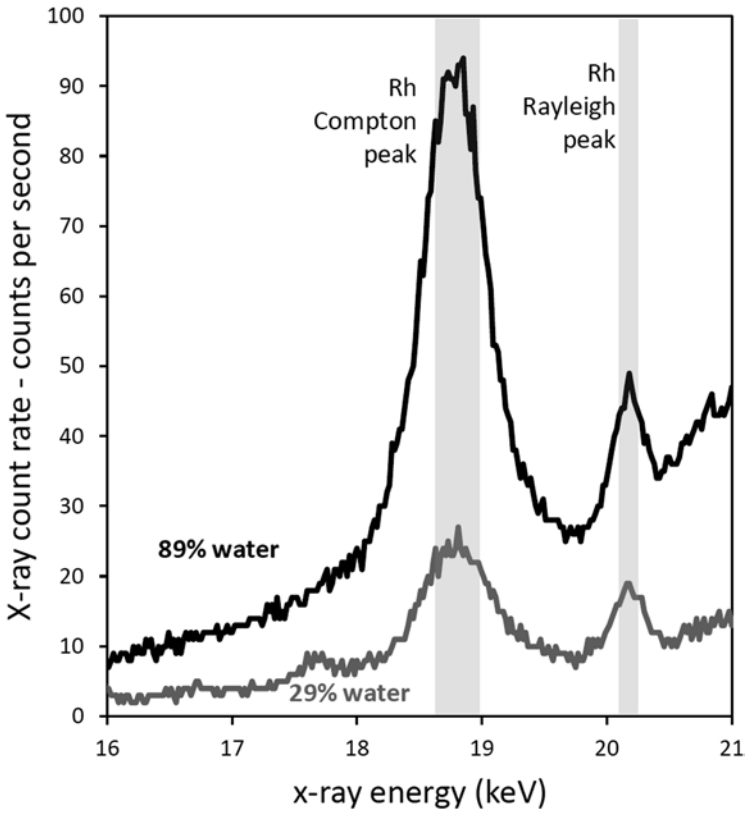


**Fig. 14.1** Scattering of primary rhodium x-rays as a function of sediment water content. The sediments are from the LOR3 core. The Rayleigh peak represents coherently (without loss of energy) scattered photons, while the Compton peaks represents incoherently (with partial energy loss) scattered photons. The wetter sample has a greater proportion of incoherent X-ray scattering

direct correction could be achieved. This information is contained in the part of the signal that arises from scattering of the primary x-rays rather than from fluorescence effects. Figure 14.1 shows the scattering of primary rhodium x-rays in two sediments with different water contents. Two different types of scattering can be seen. Rayleigh (or coherent) scattering leaves the photon energy unchanged, while Compton (or incoherent) scattering transfers some of the photon energy to electrons in the irradiated material, slightly lowering the energy of the photons. The amount and relative proportions of the different scattering mechanism varies with atomic number (Duvauchelle et al. 1999); high water content (thus low mean atomic number) causes more scattering and favours the Compton mechanism. If sediment water content is the primary control over mean atomic mass, then the sediment water content may be estimated using this scattering ratio.

Particle size also impacts the X-ray fluorescence signal (Finkelshtein and Brjansky 2009). We neglect this effect for two reasons. First, range of the particle size

variation in our lake sediment cores (as is typical for deep water cores) is sufficiently narrow that a large particle size effect of X-ray signal is not expected. At Lilla Öresjön particle size varies, in parallel with water content, between the late glacial sediment below 12.7 m (median size ca. 34 µm) and the overlying early Holocene sediment (median size ca. 10 µm). At Brotherswater, the median size varies through the core alternating between 17 and 27 µm in response to palaeo-floods. Second, while the substantial water content effect can be readily corrected using information already collected (X-ray scattering), no equivalent method is available for the particle size effect.

In this paper we present a procedure for estimating dry mass concentrations for wet core sediment developed for the GEOTEK MSCL-XZ system driving an Olympus Delta XRF Analyser as a scanning µXRF, and we assess the implications of this for the analysis of lake sediments by comparison with parallel analysis of the sediments by conventional dry loose-powder measurements.

## The Instruments

A Bruker S2 Ranger energy dispersive X-ray fluorescence analyser (EDXRF) was used to measure the dry mass composition of sediment subsamples (freeze dried) from the scanned cores. This instrument has a Pd-target X-ray tube and Peltier-cooled silicon drift detector. The instrument was run at three different measurement conditions (20, 40 and 50 kV, typically at 0.2, 0.4 and 1 mA respectively) on loose powder under helium. Powder cups were prepared with spectroscopic grade 6 µm polypropylene film (Chemplex Cat. No. 425). Calibration used a set of up to 18 certified reference materials (Table 14.1). Mass attenuation correction used theoretical alphas, with organic matter concentrations estimated by LOI.

The Geotek MSCL-XZ is a compact bench-top core-scanning system, located in the Central Teaching Laboratory of the University of Liverpool, that can conduct non-destructive measurements on split sediment core lengths (up to 1.55 m) obtaining multiple data sets simultaneously (XRF geochemistry, Colour photospectrometry, Magnetic Susceptibility and Line-scan high resolution imaging). The Olympus Delta is a handheld energy dispersive XRF Analyser fitted to the Geotek MSCL-XZ, which has a 4 W rhodium X-ray tube (8–40 kV 5–200 µA excitation) and a thermoelectrically cooled, large-area silicon drift detector. The detector window is covered with a Mylar film. The XRF was run in two modes; the first (Soil mode) uses three beam conditions: 40, 40 (filtered) and 15 kV each for 20 s to optimise beam conditions for materials where the elements of interest are relatively heavy, relatively dilute, and in a matrix of lighter elements. Elements are calibrated individually on a linear basis after spectra have been normalized to the Compton scattering peak to partially correct for mass attenuation effects. For the second mode, (Mining-Plus) the spectrometer performs two measurements in succession: 40 and 15 kV beam conditions each for 20 s, and in a configuration suited to measuring the overall composition of the rock or sediment. This mode uses a fundamental param-

**Table 14.1** Data for precision and accuracy of the S2 Ranger and Olympus DELTA XRF systems. The slope (certified/measured value) and root mean square difference (RMSD) indicate accuracy and precision. The number of certified reference materials used, *N*, and their mean and maximum concentrations are shown

| | | Bruker S2 Ranger | | | | | Olympus DELTA | | | | |
|---|---|---|---|---|---|---|---|---|---|---|---|
| | | Measured v. certified RMs[a] | | | | | Measured v. certified RMs[b] | | | | |
| | | Slope | RMSD | Mean | Max | *N* | Slope | RMSD | Mean | Max | *N* |
| Al | mg g$^{-1}$ | 1.004 | 2.17 | 42.9 | 85.0 | 16 | 0.984 | 4.29 | 49.8 | 88.7 | 6 |
| Si | mg g$^{-1}$ | 1.003 | 5.48 | 198.5 | 370.0 | 14 | 0.934 | 13.32 | 270.2 | 467.0 | 7 |
| P | mg g$^{-1}$ | 0.963 | 0.05 | 1.1 | 4.1 | 11 | *Non-significant correlation* | | | | |
| S | mg g$^{-1}$ | 0.970 | 0.11 | 0.8 | 2.5 | 12 | 1.326 | 0.04 | 4.8 | 12.6 | 3 |
| K | mg g$^{-1}$ | 1.049 | 0.91 | 20.1 | 43.0 | 12 | 1.128 | 0.98 | 15.6 | 33.8 | 7 |
| Ca | mg g$^{-1}$ | 0.997 | 1.85 | 51.4 | 300.0 | 16 | 1.160 | 0.68 | 10.6 | 26.0 | 6 |
| Ti | mg g$^{-1}$ | 0.994 | 0.16 | 2.9 | 5.6 | 17 | 1.002 | 0.16 | 3.1 | 7.0 | 6 |
| Mn | mg g$^{-1}$ | 0.993 | 0.03 | 0.7 | 2.5 | 16 | 1.049 | 0.02 | 0.4 | 1.0 | 7 |
| Fe | mg g$^{-1}$ | 0.961 | 1.26 | 21.5 | 93.8 | 14 | 0.925 | 0.59 | 25.0 | 39.4 | 7 |
| Cu | µg g$^{-1}$ | 0.997 | 5.42 | 108.3 | 247.0 | 18 | 0.891 | 6.87 | 82.1 | 237.0 | 7 |
| Zn | µg g$^{-1}$ | 0.988 | 3.43 | 72.8 | 373.0 | 15 | 0.861 | 3.54 | 88.3 | 251.0 | 6 |
| Rb | µg g$^{-1}$ | 0.999 | 2.23 | 101.1 | 466.0 | 18 | 1.066 | 3.96 | 81.9 | 175.0 | 7 |
| Sr | µg g$^{-1}$ | 0.993 | 10.30 | 275.7 | 790.0 | 17 | 1.022 | 11.27 | 151.0 | 239.0 | 6 |
| Y | µg g$^{-1}$ | 0.990 | 0.98 | 16.8 | 62.0 | 14 | 0.939 | 0.37 | 12.8 | 33.0 | 4 |
| Zr | µg g$^{-1}$ | 0.982 | 6.31 | 146.2 | 370.0 | 14 | 1.206 | 18.93 | 151.2 | 385.0 | 5 |
| Pb | µg g$^{-1}$ | 0.995 | 2.56 | 65.0 | 698.0 | 14 | 0.975 | 3.66 | 96.3 | 500.0 | 8 |

*Reference material used:* [a] CRM7002 Light sandy soil, GBW7309 Stream sediment, GBW7602 Bush, branches and leaves, GBW7603 Bush, branches and leaves, GBW7604 Poplar leaves, GBW7605 Tea, LGC6139 River clay sediment, NCSDC70302 Carbonate rock, NCSDC70309 Carbonate rock, NCSDC70314 Tibet sediment, NCSDC70317 Tibet sediment, NCSDC70319 Tibet sediment, NCSDC73301 Rock, NCSDC73302 Rock, NCSDC73303 Rock, NCSDC73309 Stream sediment, NCSDC73373 Stream sediment, NIST2709 San Joaquin Soil

[b] CCRM TILL-4 Till sample, MC CRM River sediment, NIES No. 2 Pond sediment, NIST 2780 Hard rock mine waste—elements, NIST2704 Buffalo River sediment, NIST2709a San Joaquin Soil, RCRA Soil standard, $SiO_2$ Specpure silica

eters approach to correct for matrix effects, where the software assumes that certain elements are present in the sample and iteratively fits a model to the spectra. This approach is better suited to samples with high concentrations of the target elements (rock, or mineral-rich soil/sediment). The Olympus Delta completes a daily calibration check against a known standard (Alloy 316 Stainless Steel), and will not measure unless within tolerance. For both modes of operation local consistency checks have been made using a set of up to eight certified reference materials (Table 14.1).

## The Experiment

Two sediment cores have been investigated from lakes sites (Fig. 14.2) that were selected to exemplify the two cases of (1) systematic variation in water content, and (2) relatively uniform water content (Fig. 14.3). The sediment at Lilla Öresjön, Sweden (In the boreal forest zone, Västra Götaland, core location 57.5514°N, 12.3166°E) is predominantly organic, but with an abrupt transition at the base of the Holocene from basal high-density glacial clays to low density wet organic gyttja (Fig. 14.3). The sediment core LOR3 (1.45 m total length) taken in August 2009 (Fig. 14.2)

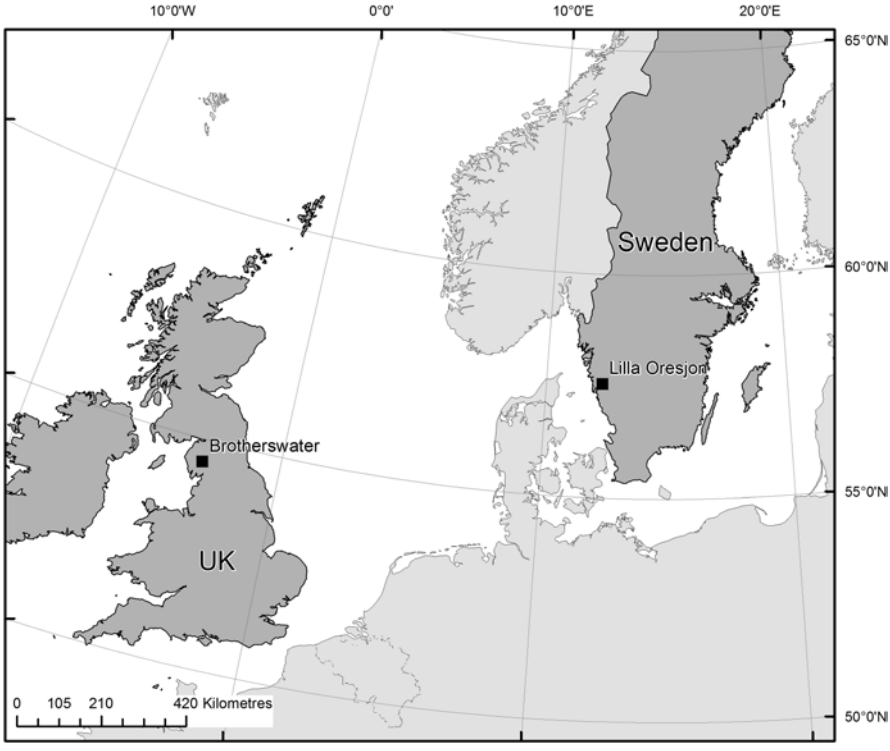


**Fig. 14.2** Geographical location of the study sites

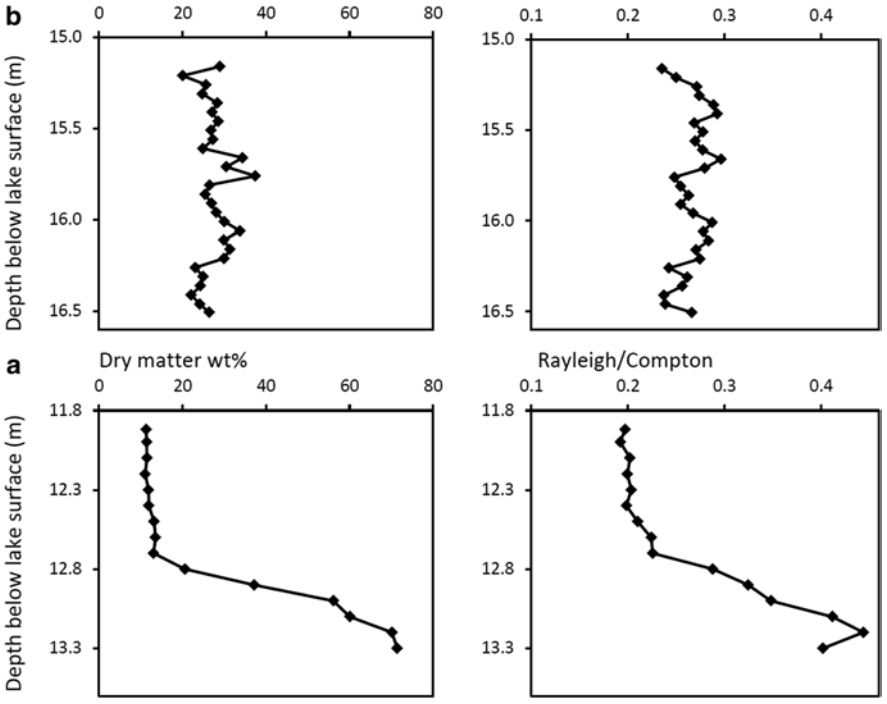


**Fig. 14.3** Dry matter content (wt %) for the subsamples, and coherent/incoherent backscatter ratio (Olympus DELTA scanning XRF) for the corresponding core interval for **a** Lilla Öresjön and **b** Brotherswater

samples the abyssal inflow-proximal sediments. A 1.5 m long, 70 mm diameter Russian corer was used. The core was tightly wrapped to prevent drying, and stored in darkness at 4 °C. The Brotherswater site (Cumbria, UK, 54.5066°N, −2.9249°E) was chosen for its more mineral-rich character and lack of systematic variation in water content (Fig. 14.3). The core drive BW12-9A (1.35 m total length) was extracted in October 2012 from the flat bottomed central basin using 1.5 m long, 70 mm diameter Russian corer.

The wet cores were scanned using the Olympus Delta instrument using the two measurement modes described above. The Mining-Plus mode was used for Al, Si, P, and Ca; the Soil mode was used for the other elements. For both modes the instrument automatically converts X-ray signals to elemental concentrations using factory-set calibrations. Split core lengths (up to 1.55 m length) were cleaned and covered with spectroscopic grade 6 μm polypropylene film (Chemplex Cat. No. 425) with measurements conducted at 5 mm intervals. Subsets of samples at intervals of 100 mm for Lilla Öresjön and 50 mm for Brotherswater were freeze dried, further oven dried at 50 °C to ensure constant dryness, and measured using the Bruker S2 Ranger under the conditions described above. Samples were weighed before and after drying to measure the water content of the sediment.

A series of tests were applied to the data collected.

1. Comparison of GEOTEK/Olympus DELTA XRF system wet core scanned concentrations with those measured on dried subsamples using the Bruker S2 Ranger XRF. The scanned data are compared both with (a) dry mass concentrations, and (b) calculated wet mass concentrations ($C_{wet}$, based on the measured percentage water content, $W$, of the sediment and S2 Ranger dry mass concentrations, $C_{dry}$, using Eq. 14.1.

$$C_{wet} = C_{dry} \times \frac{100}{(100 - W)} \tag{14.1}$$

These comparisons serve to test (a) whether µXRF scanning yields usually accurate wet concentration data, and (b) whether simple regression methods can be used to convert wet to dry mass concentrations.

2. Comparison of the ratio of coherent to incoherent X-ray scattering (coherent/incoherent) for the main tube line (Rh kα) of the Olympus DELTA XRF with (a) water content and (b) mean atomic mass.
3. Recalculation of the scanned XRF data on a dry mass basis by (a) direct simple regression using the coefficients from test 1, and (b) calculation using the water content estimate of test 2. This is achieved using Eq. 14.1 in reverse.
4. A brief assessment of the geochemical interpretation of (a) uncorrected wet sediment concentrations, (b) dry concentrations determined by simple regression, and (c) dry concentrations determined from back-scatter estimated water contents, for two different sediment cores.

## Results

### *Correlation of GEOTEK/Olympus DELTA Scanned XRF Data with Subsample Dry and Wet Mass Concentrations*

Figure 14.4 compares the measured concentration values obtained using the Olympus DELTA XRF and the Bruker S2 Ranger for the Lilla Öresjön LOR3 core. The S2 data were measured on subsamples; the Olympus DELTA XRF data used for the comparison is the mean value of scan data for the depth corresponding to the subsample. For each element there are two graphs. The left hand graph is based on the measured S2 Ranger value for the dried subsample. The right hand graphs uses the same measurements but recalculated to a wet composition basis, making the S2 data more comparable with the Olympus DELTA XRF data. The wet and dry basis-comparisons yield very different results.

In the dry mass comparison, elements displayed highly variable responses. Si, Al, Sr, Ca, K, Rb and Zr yield strong positive relationships, all exponential in form except for Sr which showed a linear relationship. P showed a weaker but statistically significant relationship. Fe, Mn, Cu, and Zn showed generally positive but highly scattered relationships that were not statistically significant. Y and Pb showed an

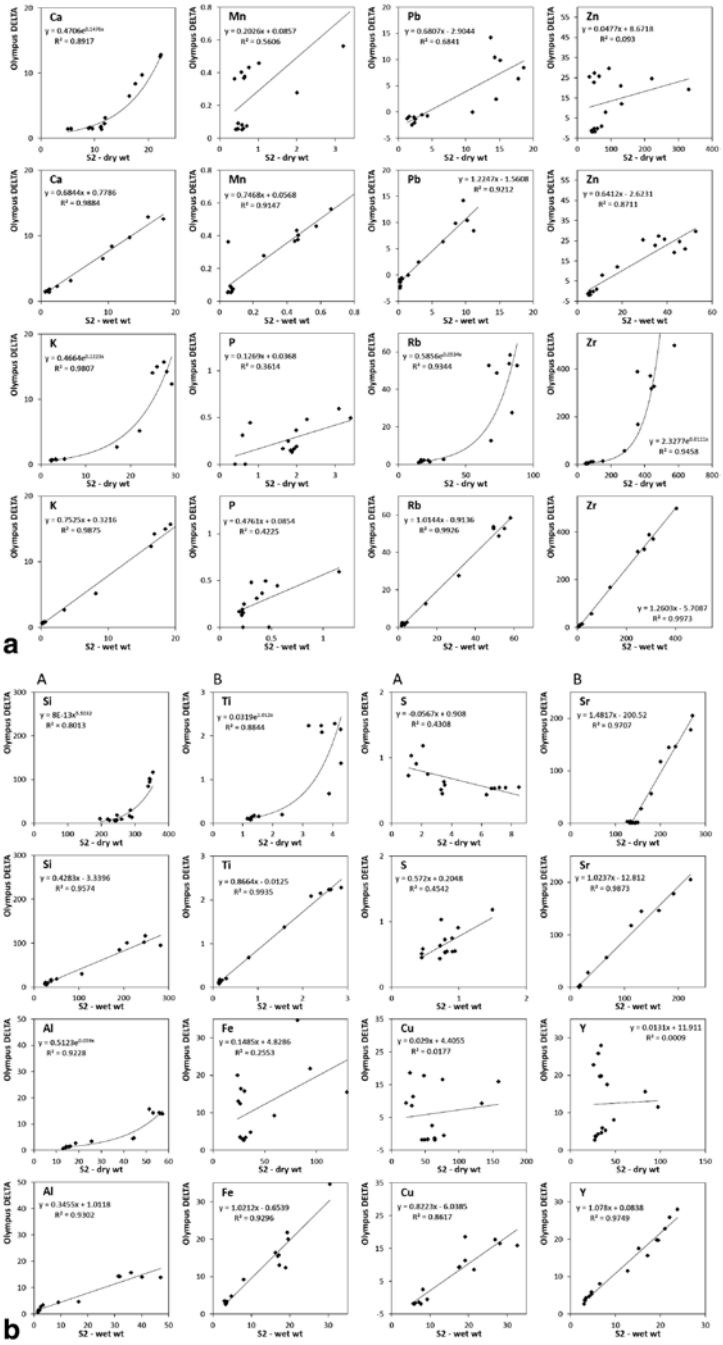


**Fig. 14.4** Correlations for the Lilla Öresjön core of element concentrations (ppm) measured by Olympus DELTA and by Bruker S2 Ranger. **a** Wet core Olympus DELTA v. dry sample Bruker S2, and **b** wet core Olympus DELTA v. wet concentration calculated from Bruker S2 dry sample measurements

organised but non-linear relationship. S showed a negative relationship. In the wet mass comparison all elements showed positive straight-line relationships. All are statistically significant, though for S and P this was weak. The lighter elements (Al, Si, P and S) all have low measured values by Olympus DELTA XRF relative to the S2 Ranger, with slopes ranging 0.3–0.5. Most other elements yield slopes between 0.8 and 1.25, and have coefficients of variation ($r^2$) greater than 0.9. The heavier elements (Rb, Sr, Y and Zr) have coefficients of variation close to 0.99.

The data for Brotherswater (Fig. 14.5) show some similarities with the results for LOR3, but with less striking differences between the wet and dry mass results. For most elements a stronger correlation is seen with the wet mass S2 data than for dry. However, none of the correlations are as good as for the LOR3 core. For Pb a similar degree of correlation was found for both, while for K the dry mass correlation was the better of the two.

The better fit between the scanned XRF data with the calculated wet concentrations is directly analogous to the finding of Tjallingii et al. (2007) who performed a similar experiment in reverse, comparing dry scanned data with conventional XRF data on dry material. This shows that better results are obtained when concentrations are expressed in terms of the same matrix type (wet or dry).

## *Sediment Core Water Content and X-ray Back-scattering*

The data in Fig. 14.3 show a clear positive association between the ratio of coherent to incoherent back-scattering and the sediment dry mass concentration (wt%). Figure 14.6 shows the correlation between the dry matter concentration and the back-scatter ratio, revealing a coefficient of variation is 0.89. A linear regression line generated for the combined data sets passes through the points for both cores showing a strong similarity in the dependence of X-ray scattering on water content for these two rather different sediments. The slightly better relationship seen with mean atomic mass, as conforms with theory, shows that variations in mineral matter composition and organic matter content (which are taken into account in calculating the mean atomic mass) only marginally improves prediction of scattering properties. This shows that variation in water content is the main factor driving variations in mean atomic mass. This in turn allows the measured X-ray back-scattering to be used to estimate the water content of the sediment core material.

## *Conversion of GEOTEK/Olympus DELTA XRF Scanned Data to Dry Mass Basis*

Figures 14.7 and 14.8 show, for the LOR3 and BW cores respectively, the dry mass concentration estimates for the two procedures, and compare these with both the uncorrected data and sub-sample dry mass concentration values.

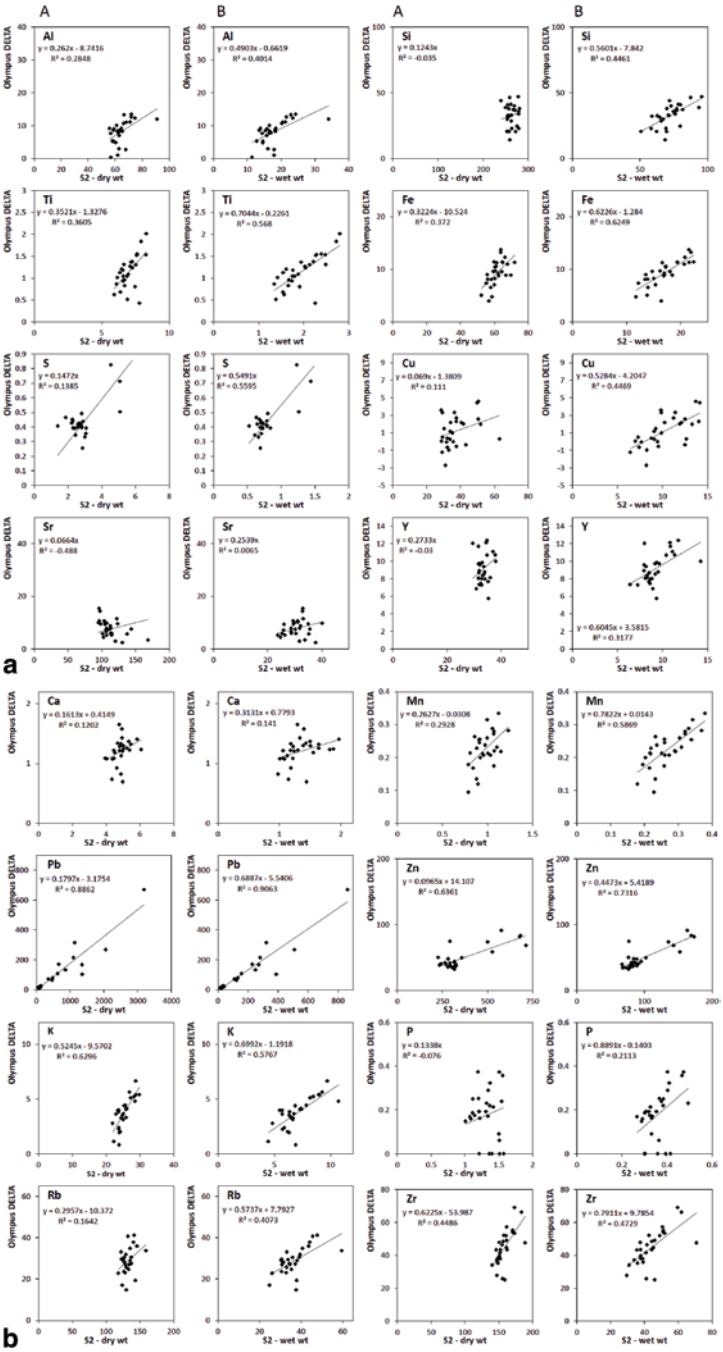


**Fig. 14.5** Correlations for the Brotherswater core of element concentrations (ppm) measured by Olympus DELTA and by Bruker S2 Ranger. **a** Wet core Olympus DELTA v. dry sample Bruker S2, and **b** wet core Olympus DELTA v. wet concentration calculated from Bruker S2 dry sample measurements

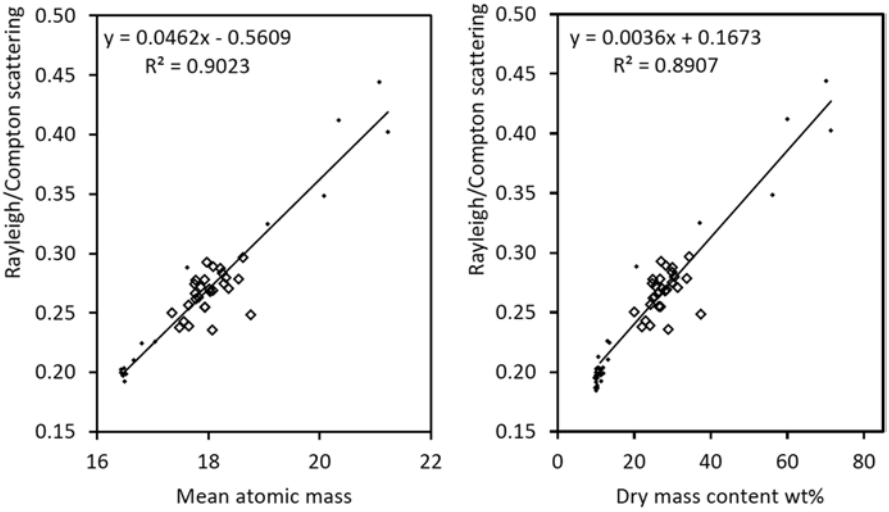


**Fig. 14.6** Relationship between measured subsample water content and the corresponding DELTA X-ray back scatter ratios for Lilla Öresjön (*points*) and Brotherswater (*diamonds*). The regression coefficients are used to generate high resolution water content estimates for the scanned cores using the measured X-ray back scatter peaks

The simple regression correction has been applied using the coefficients ($b_0$ and $b_1$) shown on Figs. 14.4 and 14.5 according to Eq. 14.2. $C$ is the elemental concentration measured by Olympus DELTA, the suffix indicating the sediment state (wet or dry).

$$C_{dry} = \frac{\left(C_{wet} - b_0\right)}{b_1} \tag{14.2}$$

The water content correction was applied by combining Eqs. 14.3, 14.4 and 14.5, where the regression coefficients ($b_0$ and $b_1$) were taken from the wet-wet comparison on Figs. 14.4 and 14.5. $W$ is the percentage water content of the sediment. "Coherent" and "incoherent" refer to measured source K-line back scatter peak heights (see Fig. 14.1), corresponding respectively to Rayleigh and Compton scattering.

$$C_{dry} = C_{wet,corrected}\frac{(100)}{(100 - W)} \tag{14.3}$$

$$C_{wet,\,corrected} = \frac{(C_{wet} - b_0)}{b_1} \tag{14.4}$$

$$W = \frac{\left(\left({}^{coherent}/_{incoherent}\right) - 0.167\right)}{0.0036} \tag{14.5}$$

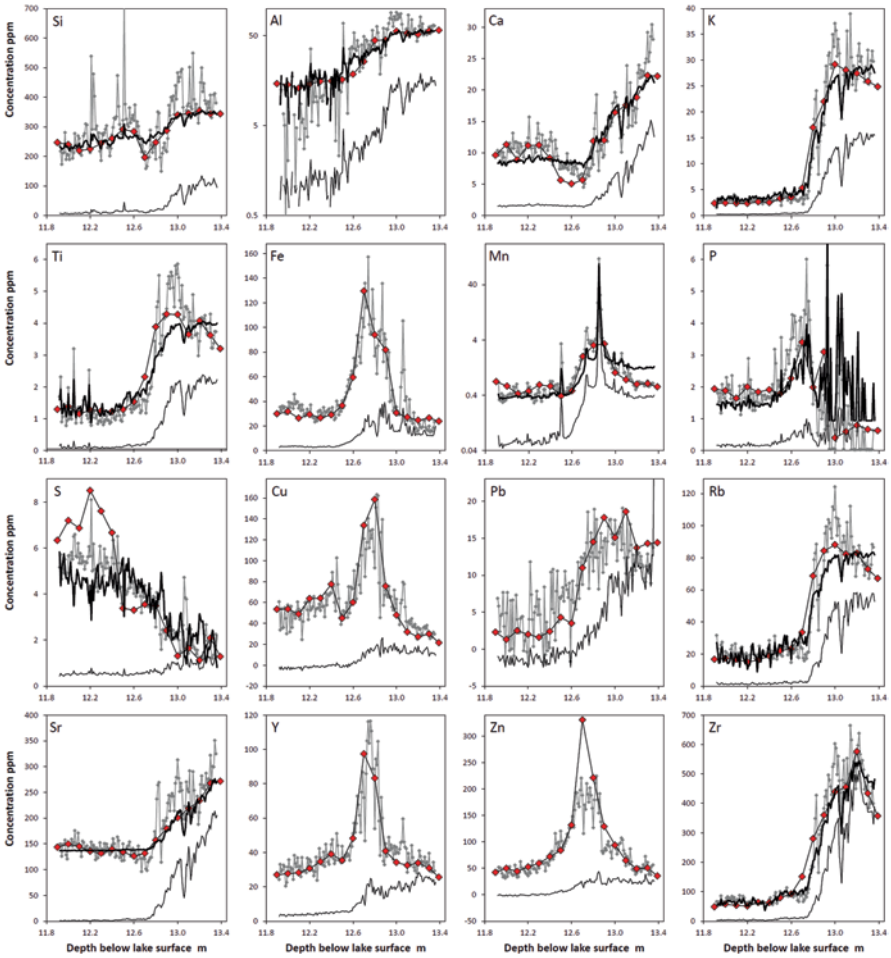


**Fig. 14.7** Lilla Öresjön element concentration data. *Red symbols* are S2 Ranger subsample data, accurate but low resolution dry mass concentration values. *Thin black line* represents Olympus DELTA uncorrected data. *Thick black line* reflects Olympus DELTA corrected by regression on dry S2 data (only shown for cases that showed statistically significant correlations). *Grey line* GEOTEK corrected using water contents inferred from back-scatter X-ray data

At Lilla Öresjön (Fig. 14.7) it can be seen that correction to dry mass basis brings the GEOTEK data in line with the subsample measurements, the uncorrected data having very much lower values. For the corrected values the elements may be divided into three classes. (1) Al and Zr show essentially identical patterns but with the simple regression (Eq. 14.2) yielding the best agreement with the subsample measurements, and very much the least noise. (2) For Si, Ca, K, Ti, Mn, P, S, Rb and Sr the two methods show similar degrees of agreement with the subsample data, though with clearly poorer capture of underlying trends for the simple regression method but rather lower noise. (3) For Fe, Cu, Pb, Y and Zn the simple regression

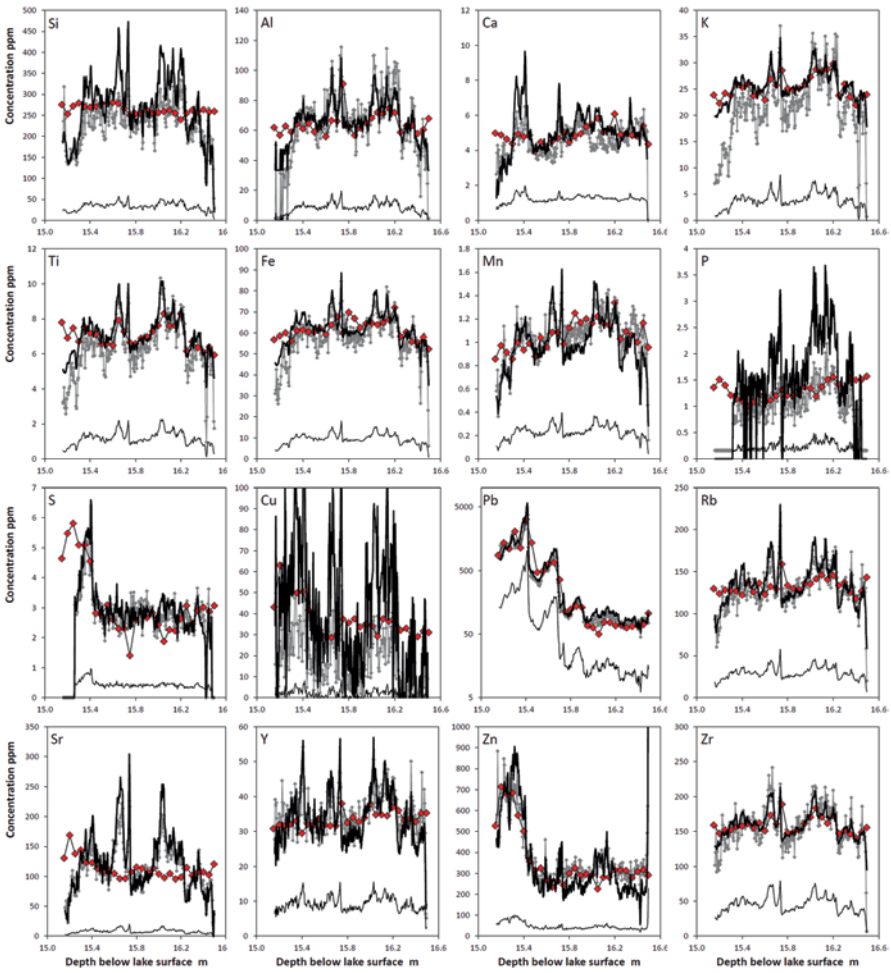


**Fig. 14.8** Brotherswater element concentration data. *Red symbols* are S2 Ranger subsample data, accurate but low resolution dry mass concentration values. *Thin black line* represents Olympus DELTA uncorrected data. *Thick black line* reflects Olympus DELTA corrected by regression on dry S2 data (only shown for cases that showed statistically significant correlations). *Grey line* GEOTEK corrected using water contents inferred from back-scatter X-ray data

method could not be used owing to lack of correlation, but the water content correction method works well. In this last case there is a very great difference between the uncorrected (wet) and corrected (dry) sediment concentrations.

Membership within these three classes is associated with the relationship between the element concentration profile and the water content (Fig. 14.3). Where an element correlates well with the sediment water content, positively or negatively (class 1), the simple regression method (Eq. 14.2) works well. Where these two are

uncorrelated (class 3), the relationship between wet and dry mass concentrations is weak or non-existent, and the simple regression method is inapplicable.

At Brotherswater (Fig. 14.8) the two methods yield a similar degree of fit with the subsample dry concentration values. They differ in the level of noise, which is far lower for the simple regression method.

For geochemical interpretation the two cores lead to different conclusions. At Brotherswater, the pattern of variation is similar for all three forms of the scanned data (uncorrected, and both corrected data sets). Except for considerations of magnitude (absolute dry mass concentration), the corrections have no impact on the geochemical interpretation. However, at Lilla Öresjön the situation is very different. The uncorrected and regression-corrected data both fail to show the trends of variation through the late glacial, and both fail to detect the enrichment in Fe, Cu, Zn, P and Y during the earliest Holocene, and thus fail to show a signal of substantial environmental significance (Boyle et al. 2013). Thus the successful dry mass correction obtained using the X-ray back-scatter water content estimate profoundly improves the geochemical interpretation.

## Discussion

The results from Lilla Öresjön (Fig. 14.7) show that where the correlation between wet core XRF and dry sediment XRF concentration is poor (illustrated on Fig. 14.4), then (a) failure to correct for water content will lead to highly distorted depth-concentration profiles, and (b) that water content estimation from X-ray back-scattering provides a useful degree of correction. A similar finding can be expected in any case where substantial systematic shifts in water contents are found through a core. We may also expect a comparable benefit from applying such a correction where large non-systematic shifts in water content are found; erratic signals resulting from erratic variation in water content will be reduced. However, this procedure comes at a price; the back-scatter signal is relatively noisy such that considerable noise is added to an element concentration profile through application of the method (Eqs. 14.3–14.5). Thus for any particular case, both methods should be applied. Where both reveal a similar underlying data structure, the lower noise of the direct simple regression gives it a distinct advantage. This case is well illustrated at Brotherswater (Fig. 14.8). There, it is apparent that both correction methods reveal patterns that are rather different from the subsampled dry mass data, which likely relates to imperfections in the core surface, but it is clear that the less noisy direct correction (Eq. 2) is better than the back-scatter approach (Eqs. 14.3–14.5).

The pros and cons of conversion to dry mass concentrations are also well illustrated by the two cores. The concentrations of Fe, Cu, Zn, P and Y in the mid-profile "spike" in LOR3 are exceptionally high by comparison with other lake sediments. Expressed as wet mass concentrations, element ratios or raw counts this phenomenon is much less clear. Of course, this alone could be achieved simply by measuring only the subsamples. However, it is also clear for LOR3 that considerable fine

scale compositional structure would be missed by coarse subsampling. It is similar at Brotherswater; the wet concentrations reveal very high Pb enrichment, but it is the dry mass values that can be compared with other cores and neighboring sites.

To apply dry mass correction with confidence it is necessary to analyse subsamples, ideally measured for both water content and element composition. This provides both a training set and a means of evaluating performance. There is some advantage to analyzing the subsample independently. However, our Olympus DELTA XRF produces sufficiently accurate dry mass concentration data that subsamples can be dried and presented loose-powder form (pressed into loose "pellets" in inverted XRF cups) for scanning, allowing it to be used to generate test or calibration data (Table 14.1).

The procedure we have developed for the GEOTEK system is equally applicable for other scanning XRF instruments. Even where these present results as X-ray count rather than concentration data, normalization to dry matter content estimated from X-ray scatter peaks (which can be readily extracted from the raw X-ray spectra files generated by each instrument) will correct for systematic variation in water content, and is an essential first step before recalculation of the X-ray count scans to dry mass concentration.

## Conclusions

Proliferation in the use of scanning μXRF has seen significant research gains in terms of resolution of analysis and examining fine structure within sediment profiles. However, reliance on elemental ratios in interpretation of count or concentration data loses important information on the dry mass concentration of elements, sometimes negating correlation between and within sites. Correction of scanned data to a 'quantitative' dry mass equivalent form offers potential benefits for the understanding of elemental concentrations and fluxes. Our analysis of the two cores reveals that X-ray back-scatter correction for water content can be usefully applied to convert Olympus DELTA XRF wet concentration data to a dry mass basis where large variations in water content are present. Although the correction procedure introduces noise at finer resolution, there is a very great improved accuracy in relation to the underlying trends. Where water contents are less variable, simple regression of wet and dry sediment element mass concentrations is likely the best approach.

## References

Boyle JF (2000) Rapid elemental analysis of sediment samples by isotope source XRF. J Paleolimnol 23:213–221

Boyle JF (2001) Inorganic geochemical methods in palaeolimnology. In: Last WM, Smol JP (eds) Tracking environmental change using lake sediments. Volume 2: physical and geochemical methods. Kluwer Academic Publishers, Dordrecht, pp 83–141

Boyle JF, Chiverrell RC, Norton SA, Plater AJ (2013) A leaky model of long-term soil phosphorus dynamics. Glob Biogeochem Cycle 27:516–525

Croudace IW, Rindby A, Rothwell RG (2006) ITRAX: description and evaluation of a new multi-function X-ray core scanner. In: Rothwell RG (ed) New techniques in sediment core analysis, vol 267. Geological Society of London, London, pp 51–63 (Special Publication)

Duvauchelle P, Peix G, Babot D (1999) Effective atomic number in the Rayleigh to Compton scattering ratio. Nucl Instrum Method B 155:221–228

Finkelshtein AL, Brjansky N (2009) Estimating particle size effects in X-ray fluorescence spectrometry. Nucl Instrum Method B 267:2437–2439

Hennekam R, de Lange G (2012) X-ray fluorescence core scanning of wet marine sediments: methods to improve quality and reproducibility of high- resolution paleoenvironmental records. Limnol Oceanogr Methods 10:991–1003

Kylander ME, Lind EM, Wastegård S, Löwemark L (2012) Recommendations for using XRF core scanning as a tool in tephrochronology. Holocene 22:371–375

Löwemark L, Chen HF, Yang TN, Kylander M, Yu EF, Hsu YW, Lee TQ, Song SR, Jarvis S (2011) Normalizing XRF-scanner data: a cautionary note on the interpretation of high-resolution records from organic-rich lakes. J Asian Earth Sci 40:1250–1256

Richter TO, van der Gaast S, Koster B, Vaars A, Gieles R, de Stigter HC, de Haas H, van Weering TCE (2006) The Avaatech XRF core scanner: technical description and applications to NE Atlantic sediments. Geol Soc Spec Publ 267:39–50

Shen ZX, Bloemendal J, Mauz B, Chiverrell RC, Dearing JA, Lang A, Liu QS (2008) Holocene environmental reconstruction of sediment-source linkages at Crummock Water, English Lake District, based on magnetic measurements. Holocene 18:129–140

Tertian R (1969) Quantitative chemical analysis with X-ray fluorescence spectrometry—an accurate and general mathematical correction method for interelement effects. Spectrochim Acta B 24:447

Tjallingii R, Röhl U, Kölling M, Bickert T (2007) Influence of the water content on X-ray fluorescence core-scanning measurements in soft marine sediments. Geochem Geophys Geosyst 8:1–12

Weltje GJ, Tjallingii R (2008) Calibration of XRF core scanners for quantitative geochemical logging of sediment cores: theory and application. Earth Planet Sci Lett 274:423–438

# Part III
# Environmental Geochemistry and Forensic Applications

# Chapter 15
# X-Ray Core Scanners as an Environmental Forensics Tool: A Case Study of Polluted Harbour Sediment (Augusta Bay, Sicily)

**Ian W. Croudace, Elena Romano, Antonella Ausili, Luisa Bergamin and R. Guy Rothwell**

**Abstract** Since the 1970s the highly industrialised and enclosed Augusta Bay (Sicily) has become internationally recognized as a polluted environment that could represent a hazard to human health. The pollutant of greatest concern, derived from a former chlor-alkali plant, is mercury that exists beyond Intervention Levels in parts of the harbour. The affected areas are also contaminated by other heavy metals and organic compounds (PAHs and PCBs) that were mainly discharged from co-located petrochemical industries. Several previous investigations established the magnitude of particular contaminants in sediments and evaluated the impact of the pollution on a range of biota. The current study, which represented part of a larger project managed by the Italian Environmental Research Institute ISPRA, was concerned with investigating a series of cores collected across the harbour area to establish reliable pollution chronologies based on elemental and radiochronological ($^{137}$Cs) profiles. The declared motivation for the main project was to acquire scientific evidence that could be used to support a legal investigation against the industries that caused the pollution and who could potentially be expected to contribute to remediation costs. Undisturbed cores were collected from the northern (mildly polluted), central (significantly polluted) and southern (strongly polluted) parts of the Bay using available bathymetric data to avoid areas affected by dredging. The study has demonstrated the value of using an automatic, X-ray sediment core scanner (Itrax) to acquire high-resolution geochemical data. The Itrax provided a non-destructive, sensitive and rapid capability to systematically analyse a broad range of major and trace elements. One of the collected cores of this study, taken from the most polluted site,

I. W. Croudace (✉)
Ocean and Earth Science, National Oceanography Centre, University of Southampton, Waterfront Campus, European Way, Southampton SO14 3ZH, UK
e-mail: iwc@noc.soton.ac.uk

E. Romano · A. Ausili · L. Bergamin
Istituto Superiore per la Protezione e Ricerca Ambientale (ISPRA), Via Vitaliano Brancati, 60, 00144 Roma, Italy

R. G. Rothwell
National Oceanography Centre, Empress Dock, Southampton, SO14 3ZH, UK



I. W. Croudace, R. G. Rothwell (eds.), *Micro-XRF Studies of Sediment Cores*, Developments in Paleoenvironmental Research 17, DOI 10.1007/978-94-017-9849-5_15

provided more than 20 continuous elemental profiles with depth (e.g. Ti, S, Ca, K, Mn, Fe, Cr, V, Ba, Cu, Zn, Br, Rb, Sr, Zr, Hg, Se, Mo). The Itrax data quality were validated against a dataset acquired using a conventional WD-XRF instrument and both sets of profiles are demonstrated to be consistent. This ability of the Itrax to automatically scan cores over a significantly shorter time compared to conventional laboratory methods (days compared to weeks) confirms its potential in contributing to environmental forensic studies. Its additional ability to simultaneously record a radiographic image (and radiographic digital profile) provides a link between sediment layering (density variations linked to mineralogy) and elemental composition.

**Keywords** Environmental forensics · Mercury pollution · Heavy metal pollution · Augusta Harbour · Mercury-cell chloralkali plant · Itrax core scanning

## Introduction

Significant environmental pollution arising from past industrial practices is a worldwide concern. In the European context, with relatively well-developed environmental guidelines and regulatory systems, the legacy of industrial contamination continues to be progressively targeted for evaluation and eventual remediation. The EU's Environmental Liability Directive 2004/35/EC applies the 'polluter pays' principle to prevent and remediate environmentally damaged land, water and natural habitats to ultimately ensure biosphere protection. Therefore, during early investigations of legacy contaminated sites specialist evidence needs to be established to contribute robust evidence to identify potential polluters. As investigations progress, regulatory agencies often employ internal scientific and other expertise but they may also employ independent external specialists. Where there is legal oversight and a potential criminal link the overall study approach has been termed *Environmental Forensics*. This recently emergent field has its own specialist society and a professional journal and it draws together relevant branches of chemistry (analytical, aquatic, atmospheric, geochemistry) and environmental science (ecology, transport and fate of contaminants) to address legal aspects of environmental contamination. The term has become more widely used to describe investigations where complex scientific evidence is used to apportion responsibility for instances of pollution to the satisfaction of a court (see for example Hester and Harrison 2008). A notable early reference to *Environmental Forensics* was associated with the legal investigation of the disastrous Exxon Valdez oil spill in 1989.

Given the complexities of how pollutants behave and impact on the environment multidisciplinary investigative approaches are invariably required. Establishing pollution histories in aqueous environments for example, normally involves the collection and investigation of sediment cores (e.g. Croudace and Cundy 1995;

Cearreta et al. 2002; Cundy et al. 2003). In this context, the introduction of high-resolution core scanners has provided a technical advance that allows rapid and non-destructive analysis. These new analytical tools, of which two proprietary instruments dominate the market (Croudace and Rothwell 2015), have stimulated research output in the environmental sciences (e.g. Croudace et al. 2006; Lepland et al. 2010; Croudace et al. 2012; Miller et al. 2014, 2015). A particular strength of the Itrax core scanner is its co-registration of radiographic and elemental profiles as well as an optical image.

**Augusta Bay** The highly industrialised Augusta Bay in eastern Sicily has been the focus of environmental investigations for over four decades as it became clear that the area was seriously polluted from multiple sources. Numerous studies have reported on the impact and scale of pollution in the area (e.g. Sciacca and Fallico 1978; Castagna et al. 1985; Ausili et al. 2008, 2012; Bellucci et al. 2012; Romano et al. 2009b, 2013; WHO 2012; **Text Box** 15.1**,** 15.2 **and** 15.3). This current Augusta Bay study arose from a project commissioned and managed by the Italian Institute for Environmental Protection and Research (ISPRA). The project was associated with a broader legal investigation by the Siracusa Prosecutor's Office into identifying, where possible, the companies that might have caused pollution in Augusta Harbour. The approach used was to acquire geochemical and chronological data from a set of sediment cores with the intention of establishing a pollution chronology. The cores were collected by ISPRA, in duplicate, from different parts of the Harbour with the purpose of investigating heavy metals, organic pollutants and selected radionuclides.

**Text Box 15.1 Industrial pollution history of Augusta Harbour**

Augusta Harbour sediments are significantly affected by past and present industrial activities having high concentrations, varying with depth, of mercury, barium sulphate, hydrocarbons, hexachlorobenzene (HCB), PCBs, dioxins and furans.

**1950** First construction of oil refineries.
**1958** Chlor-alkali plant begins operation.
**1960s** Closure of the Bay by an artificial wall to protect shipping and large industrial expansion
**1958-2003** The chlor-alkali plant and other industries are significantly operational and ~500 t of Hg was estimated to have been discharged to the Harbour.
**1980** Installation of a de-mercurisation plant.
**2005** Chlor-alkali plant closed and Hg cells removed.
**2011** Proposal to remediate Augusta Harbour (e.g. Guerriero et al. 2011).

**Text Box 15.2 The mercury cell chlor-alkali process**

The mercury cell industrial process has been in use for well over 100 years and involves the electrolysis of a NaCl brine to produce chlorine and sodium hydroxide both critical precursors in different aspects of industrial chemistry. In the process, also known as the Castner-Kellner process, a saturated brine solution floats on top of a thin layer of Hg (cathode). During electrolysis, chlorine was produced at the anode and sodium at the cathode forming a sodium-mercury amalgam that was continuously drawn out of the cell and reacted with water to produce sodium hydroxide. The Hg was recycled back into the electrolytic cell. It was very important to remove chemical impurities (Ca, Mg, sulphate, etc.) from the brine before electrolysis otherwise they adversely affected the efficiency of the process. Removing sulphate was typically achieved using barium chloride and the barium sulphate produced could also have become a waste product. If brine purification was inadequate then so-called 'mercury butter' formed that led to short circuits, poor mercury flow, increased power consumption and increased exposure to mercury vapour (Sedivy 2009). Over time, sludges formed that required extraction and disposal and at many poorly managed plants these may have been simply discharged to the environment.

Around 2005 it was estimated that European mercury cell chlor-alkali plants (MCCAPs) consumed 175–200 t/year of mercury, amounting to 40–50 % of the total EU mercury consumption. By contrast, modern chlor-alkali plants, that use ion-selective membranes (considered to be 'best-available-technology') use no mercury and are far more energy efficient.

**Global mercury elimination**: In 2009, UNEP Global Mercury Partnership Advisory Group reported that 44 countries still had 100 facilities with some industrial mercury cell chlorine capacity. The European chlor-alkali industry, represented by EuroChlor, declared they would phase out all mercury-cell chlor-alkali units by 2020 while the USA planned to close its four remaining mercury cell facilities by the end of 2018. In India, mercury-cell chlorine production was intended to cease by 2012 (Anirudh et al. 2009). Through international agreement coordinated by UNEP it is imminently expected that all 193 nations in the UN will have signed the ***Minimata Convention on Mercury*** which aims to reduce and ultimately eliminate mercury emissions in the environment (http://www.unep.org/hazardoussubstances/MinamataConvention; accessed Oct 2013).

**Text Box 15.3 Selected reports from a chemical industry news service**

**EniChem Priolo (Sicily) chloralkali plant shuts following pollution arrests—17 January 2003—Source: ICIS news LONDON (CNI)**

**(International Chemical Information Service—Chemical News and Intelligence)**

The Italian police confirmed Friday that they have arrested 18 people, including 17 EniChem executives, on charges of environmental pollution and criminal conspiracy in connection with the company's Priolo, southern Italy chemicals complex. The executives and a local government official are accused of breaking the Ronchi decree DL 22/1997 on industrial pollution, according to Ten. Col. Giovanni Monterosso, the head of the Siracusa, Sicily district financial police. Local reports suggest the charges relate to improper disposal of untreated, toxic mercury waste into the sewer system at Priolo, where EniChem and its subsidiary Polimeri Europa have extensive petrochemical installations, including caustic soda, chlorine and aromatics plants. Among those arrested are the former plant director and deputy plant director, who were responsible for the plant at the time of the alleged incident about a year ago; the current Priolo plant director and local government official in charge of pollution control. Other EniChem executives arrested are responsible for environment and safety, records, special waste disposal, chemical laboratory, chlor-alkali production and aromatics. They have all chosen to be represented by EniChem lawyers. Eight of the executives were held in jail and ten were placed under 'home arrest' following dawn raids on Thursday. In a statement, EniChem said it hopes the investigation throws light on the matter. It added: "EniChem and Polimeri Europa would like to point out that until this day the operative structure was run in respect of the law".

**21 January 2003—Source: ICIS news LONDON (CNI)**

Chloralkali production at EniChem's Priolo site in Sicily has been halted temporarily following the arrest of senior managers on pollution charges, a company spokeswoman confirmed to *CNI* on Tuesday. EniChem said that "the decision to halt production at the site was taken in order to guarantee safety at the plant and follows the absence of key personnel". The spokeswoman said the plant was closed last Friday (17 January), a day after 17 senior managers were arrested on charges of environmental pollution and criminal conspiracy. The 700 workers employed at the plant are now engaged in activities of "extraordinary maintenance", the spokeswoman added. She said she could not forecast a date for the resumption of operations at the site but said that no other units had been affected by the temporary closure.

**Industrialisation** Augusta Bay (Figs. 15.1 and 15.2) developed into a significant industrial Mediterranean harbour from the 1950s onward and became a major processing centre for petrochemicals and chemical industry precursors. The high concentration of these industries and their discharges imposed a pollution legacy on the Bay

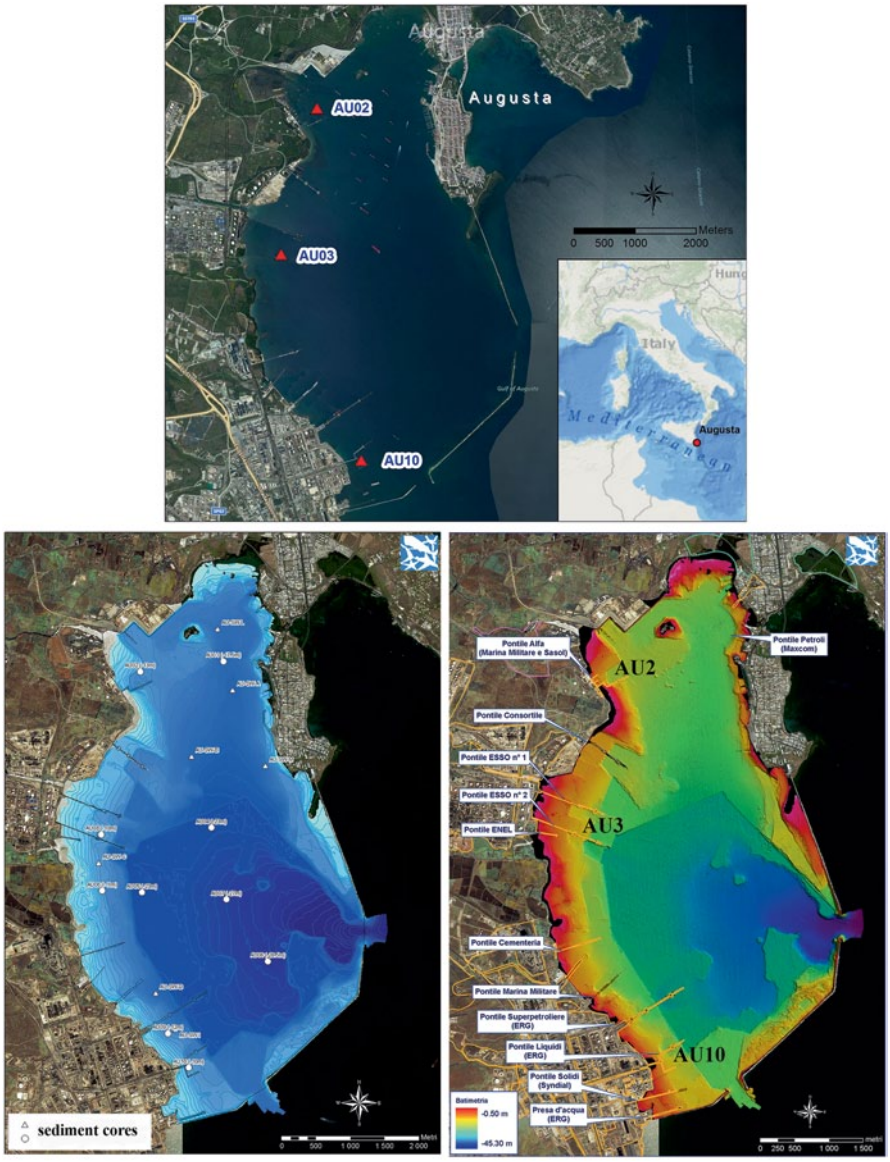


**Fig. 15.1** Location of sampling areas for AU2, AU3 and AU10 different cores, in the industrialised Augusta Harbour along with *bottom contours* indicating dredged areas

that has become a significant concern. Pressures to industrially develop the area after the Second World War and the lack of an appropriate environmental law led to many cases of poor ecological control. Further industrial development followed the construction of the breakwaters that closed the bay and also the dredging of the harbour in the early 1960s. The harbour area is 8 km long and 4 km wide with a mean water

**Fig. 15.2** Industrial views of parts of Augusta Harbour, Sicily. *(photos courtesy of E. Romano)*

depth of 14.9 m and is characterized by poor water circulation. Several industries such as chemical and petrochemical plants, oil refineries and electric power plants have impacted the area for several decades, but one of the most important contributors of hazardous waste to the Harbour was from a mercury cell chlor-alkali plant (MCCAP) that operated from 1958 to 2003.

It is estimated that over 500 t of untreated Hg waste entered the harbour from 1958 to 1979 along with by-products from the brine purification process linked to the MCCAP. Mercury mitigation measures were introduced at Augusta in the late 1970s and by 2005 the mercury cells were finally removed. From the 1970s it was clear that significant environmental degradation had occurred (Sciacca and Fallico 1978; Cernigliaro et al. 2008; Bellucci et al. 2012). Uncontrolled pollution had led to significant contamination of sediment by heavy metals, polychlorobiphenyls (PCBs), polycyclic aromatic hydrocarbons (PAHs) and hexachlorobenzene (HCB) most significantly in the southwestern part of the Harbour. Since the closure of the chloralkali plants there has been some recovery but sub-surface sediments remain adversely contaminated and mercury (Hg) contamination continues to be an environmental concern. Subsequent and regular monitoring programs were used to determine potential transfers of the Hg to the ecosystem and to establish the extent of contamination as a precursor to possible remediation (Guerriero et al. 2011).

Recent studies of the area have established the vertical and spatial distributions of some heavy metals (Hg and Ba), PAHs, HCB and PCBs in the Harbour and found the highest concentrations in the southern sector. Particularly, Hg was found up to 190 mg $kg^{-1}$ dwt in superficial sediments, and exceeding 500 mg $kg^{-1}$ dwt in the upper 50 cm sediment interval (ICRAM 2008; Romano et al. 2009b, 2013). Offshore sediments collected close to the Harbour showed considerable anthropogenic enrichment of Hg (EF > 40) and adverse response of benthic communities in terms of faunal density and incidence of morphological deformations (Di Leonardo et al. 2006, 2014). One study argued that the high Hg content in the Harbour sediments were important contributors for this element to the Mediterranean Sea, with an Hg output of 0.162 kmol/year to coastal and offshore waters (Sprovieri et al. 2011). Clear health concerns developed when it became clear that high Hg was accumulating in local sediment based on known serious impacts elsewhere (e.g. Minamata, Japan; Tomiyasu et al. 2006; Clarkson 1997). Bioavailable methyl mercury was expected to be present in the sediments as had been recorded around other Italian and European chlor-alkali plants (Covelli et al. 2001, 2009, 2010; Piani et al. 2005; Raldúa et al. 2007). Studies involving mercury in marine organisms from Augusta Harbour indicated a clear toxicological risk. Pregnant women were identified as an exposed group (Ausili et al. 2008) based on the incidence of neonatal malformations which were found to be more than three times higher than the Italian national average (Bianchi et al. 2004).

**Sediment Character** The character of sediment found in the Harbour reflects the local geology, soil composition and the hydrological catchment. The local geology consists of carbonate sequences (Cretaceous to Quaternary Age), with volcanoclas-

tic and volcanic interbedded horizons along with muddy sediments and calcarenites (Nigro and Renda 2000; Scicchitano et al. 2007). Three small streams flow into the western part of the harbour, but their freshwater and sediment flows are generally considered to be rather small (Celia Magno et al. 2012). In the southernmost part of the harbour patchy areas of emerging rocky substrate are present near the shore (Anonymous 1992, 1995). Weathering and fluvial transport of this mixed material into the harbour during periods of significant rainfall provides the main source of Harbour sediment.

## Methods

### *Sampling*

Seven sediment cores were collected from three stations (AU2, AU3 and AU10) in July 2008 located in the northern, central and southern part of the Harbour respectively (Fig. 15.1, Table 15.1). Two replicates were collected at stations AU2 and AU3, while three replicates were taken at AU10 station. Stations were carefully selected from areas identified from bathymetric survey data to be most likely to be unaffected by dredging. Two types of sediment corers were used, (a) an SW-104 gravity-corer (patented by the Italian Council of Research) specifically designed to minimize disturbance and preserve an optimal sediment/water interface and (b) a Rossfelder® vibrocorer. The latter was used to obtain longer cores when the gravity corer was unable to achieve significant penetration when encountering pebbly horizons/bedrock. Comparison of vertical chemical profiles obtained using the two corers offered a check on any possible disturbance of the sedimentary sequence

**Table 15.1** Summary of collected cores and analyses carried out for this study

| Core label | Coordinates | ISPRA analyses | GAU analyses |
|---|---|---|---|
| $AU2g_{iwc}$ | 4120496 N–517400 E | | Dating, WD-XRF |
| $AU2g_{er}$ | 4120498 N–514702 E | Grain size, Hg, PAHs, PCBs | Dating, WD-XRF |
| $AU3g_{iwc}$ | 4118104 N–516811 E | | Dating, WD-XRF |
| $AU3v_{er}$ | 4118106 N–516813 E | Grain size, Hg, PAHs, PCBs | Dating, WD-XRF |
| $AU10g_{iwc}$ | 4114716 N–518128 E | | Dating, WD-XRF |
| $AU10v_{iwc}$ | 4114715 N–518126 E | | Dating, WD-XRF, Itrax |
| $AU10v_{er}$ | 4114714 N–518126 E | Grain size, Hg, PAHs, PCBs | Dating, WD-XRF |

*v*—vibro corer sample, *g*—gravity corer sample

caused by sampling. All cores were immediately sub-sampled by ISPRA after collection with the exception of AU10$v_{iwc}$ which was sent directly to the Southampton GAU laboratories for Itrax analysis and radiochronological determinations. Gravity cores were sub-sampled by extrusion, while the vibrocores were sampled following longitudinal splitting. Samples for geochemical, grain size and radiochronological dating were carried out on 1-cm and 3-cm resolution samples. Sediments were stored/preserved in polyethylene bags in a freezer before analysis.

## *Grain Size, Trace Elements and Organic Compounds Analyses*

***Grain-size analysis*** was carried out treating sediment sample with a 30% $H_2O_2$ solution and separating it into coarse (>63 μm) and fine (<63 μm) fraction by wet sieving. Then, each fraction was dried and the coarse one was fractionated using ASTM series sieves, while the fine fraction was analyzed using a laser granulometer that determines silt and clay fractions separately (Romano et al. 2009a).

***Barium*** was analyzed using wavelength dispersive X-ray fluorescence analysis (WDXRF) by the Southampton Group (GAU).

***Mercury*** was analyzed at ISPRA on wet samples by means of a Direct Mercury Analyzer (DMA-80, FKV) through thermal desorption, gold amalgamation and atomic absorption without any chemical pre-treatment (EPA method 7473). Quantification limit was 0.0005 mg $kg^{-1}$ on a dry weight basis. Itrax and WD-XRF were also used to measure Hg and the data were found to correlate with the DMA-80 data (Maggi et al. 2009).

***Polycyclic Aromatic Hydrocarbons (PAHs)*** analyses were performed by a preliminary extraction and a successive purification on silica gel treatment. Successively, the determination was carried out using an Agilent 1100 HPLC-FLD system managed through the Chemstation software (Romano et al. 2009a). The quantification limit was 0.001 mg $kg^{-1}$.

***Polychlorobiphenyls (PCBs)*** were analysed as <2 mm homogenised, freeze dried ***s***amples and then extracted by pressurized fluid extraction using a Dionex model ASE 200 instrument. The determination was performed by high-resolution gas chromatography with electron capture detection (GC/ECD) in dual column-dual detector mode. The limit of quantification was 0.0001 mg $kg^{-1}$ on a dry weight basis. On each extraction batch a method blank, a spiked blank for recovery evaluation and sample replicates and CRMs were analysed to ensure quality control (Bergamin et al. 2009).

***Itrax non-destructive core scanning*** was carried out on a split core of AU10$v_{iwc}$ in Southampton. The key components of this instrument comprise a 3 kW Mo-target sharp, fine-focus X-ray tube coupled to a 0.2 × 20 mm rectangular capillary wave guide, a silicon-drift detector and an X-radiographic linear diode detector (Croudace et al. 2006). Along core profiles are presented as variation in counts (Fig. 15.3) that provide a reliable proxy for element concentration variations (see

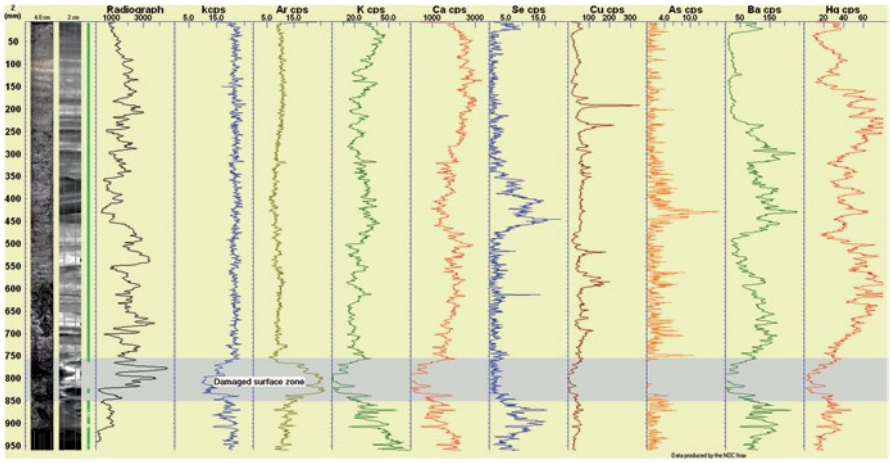


**Fig. 15.3** AU10v$_{iwc}$ (0–950 mm) elemental and radiographic data obtained using the Itrax core scanner. The figure was generated using ItraxPlot software (see Chap. 26). The small gap in the data at 750–850 mm is due to unreliable data caused by a poor sediment surface where hydrocarbon-rich, soft muddy sediment was slightly depressed. Poor surfaces result in erroneous detector counts

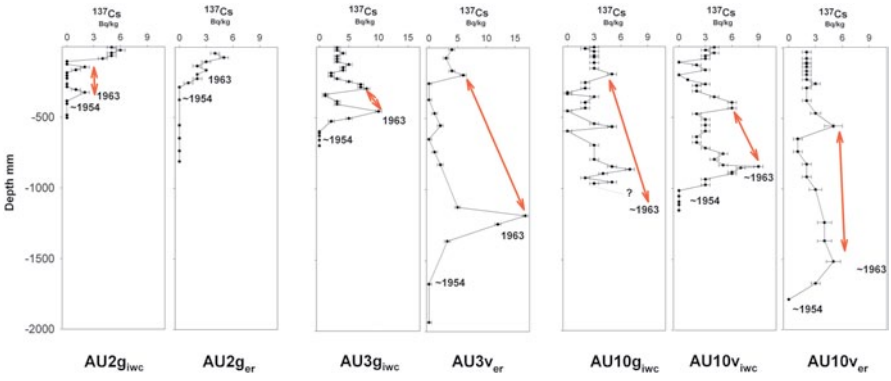


**Fig. 15.4** Cs-137 (Bq/kg) profiles for cores from locations AU2, AU3 and AU10. The red double-ended arrowed line marks out two recognizable features seen in most of the cores regardless of their accumulation rate (1963 'bomb' maximum and possible 1986 Chernobyl event). The recovery of core AU10g was too short to see the 1963 'bomb' maximum

Figs. 15.7 and 15.8). The Itrax collected X-ray fluorescence spectra at 200 µm intervals (approximately 5000 X-ray spectra are recorded per metre of core) leading to 20 element profiles (As, Ba, Br, Ca, Cl, Cr, Cu, Fe, Hg, K, Mn, Mo, Pb, Rb, S, Se, Sr, Ti, V, Zn).

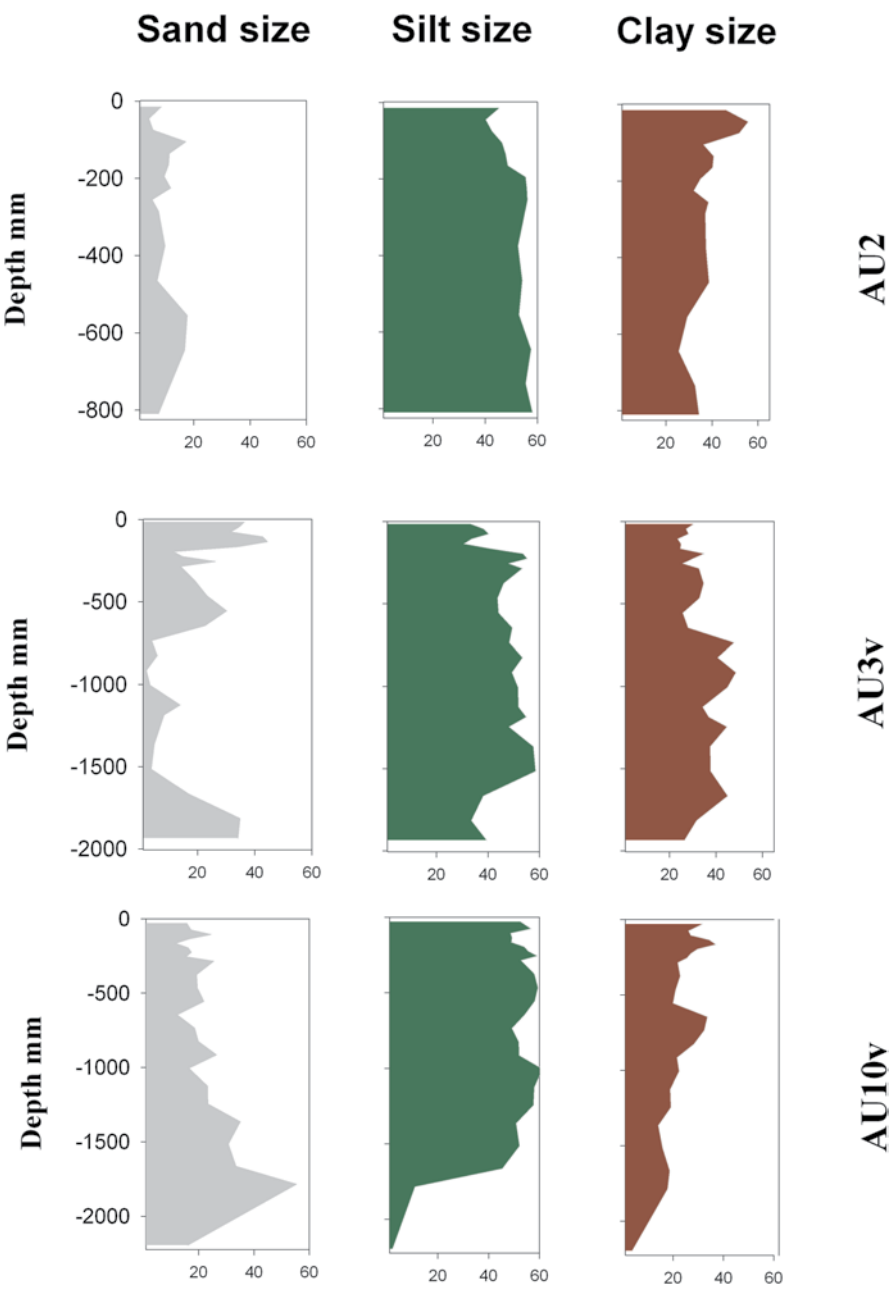


**Fig. 15.5** Grain-size variations with depth for cores from locations AU2, AU3 and AU10v

*WD-XRF Elemental Analysis* General elemental geochemistry (major elements and trace elements) on sediment core material was carried out using a Panalytical Magix-PRO WD-XRF spectrometer in Southampton. The instrument employed a 4 kW Rh end-window X-ray tube and the system quantitatively analysed sub-samples taken at 1-cm increments. All samples were ground and pelletised prior to analysis. The WD-XRF system had been previously calibrated using a suite of more than 20 international geochemical reference samples provided by CRPG-ANRT, USGS, JGS and CANMET. Accuracy was assessed by running the reference samples MESS-3, PACS-2 and MAG-1 and measured data were generally within 5–10 % of the consensus values. Detection limits for low-medium Z elements are 5–20 mg $kg^{-1}$ and for medium-high Z elements they are approximately 1–5 mg $kg^{-1}$.

*Radiochronological Determinations* Caesium-137 was measured using well-type ULB HPGe gamma spectrometry systems (Canberra Instruments, UK) in Southampton. All systems were calibrated using NPL certified mixed gamma solution. Samples were counted in scintillation vials for 100,000 s and analysed using Fitzpeaks gamma analysis software (JF Computing, Stanford in the Vale, UK).

## Results

A general impression of the variations in sediment geochemistry, derived from WD-XRF analysis, including anthropogenic elements (Ag, As, Ba, Ca, Co, Cr, Cu, I, Mo, S, Se, Sr, Zn) is provided in Table 15.2. For comparison, data for a typical uncontaminated marine muddy sediment (the well characterized USGS MAG-1 reference sample) allows the extent of pollution in the various cores to be evaluated. It is recognised that MAG-1 is a carbonate poor sediment but such a mineralogical composition is considered similar to one of the components of the Augusta sediment (Fig. 15.6). Mineralogically, uncontaminated Augusta sediment consists largely of two components, a calcium carbonate (Ca and Sr) and clays (Si, Al, K, Rb). Polluted sediment includes additional components (typically less than 6 wt%) such as barite, hydrocarbons and sulphides. Where there are significant down-core geochemical variations in major mineral components then elemental profiles will be influenced by the closed-sum effect (Rollinson 1993). With this effect, caused by analyses summing to 100 %, any variation in one major mineral component (e.g. Ca and Sr in carbonates) will affect the other mineral components (e.g. Si, K, Al, Rb, Si in clay). The use of element ratios (e.g. dividing elements associated with clays by $Al_2O_3$, $K_2O$, Rb etc) can compensate for the closed-sum effect and negate the effect of calcium carbonate variations. In this case $K_2O$ was used as the normalising element (Figs. 15.6 and 15.11).

Radiochronological dating inferred from $^{137}Cs$ measurements was performed on sub-samples from all cores (Fig. 15.8). Grain-size data from sub-samples taken from the cored sediment show variations (Fig. 15.5) that are reflected in the geochemistry to some extent.

**Table 15.2** Geochemical data for Augusta sites AU2 (mildly polluted), AU3 (significantly polluted) and AU10 (strongly polluted). (data from Govindaraju 1994)

| | | AU2 | | | | | AU3 | | | | | AU10 | | | | | USGS MAG-1 |
|---|---|---|---|---|---|---|---|---|---|---|---|---|---|---|---|---|---|
| | | Mean | SD | Min | Max | Median | Mean | SD | Min | Max | Median | Mean | SD | Min | Max | Median | |
| $SiO_2$ | % | 38.03 | 1.01 | 35.95 | 39.60 | 38.22 | 31.75 | 2.95 | 28.21 | 36.56 | 30.64 | 10.24 | 8.65 | 0.09 | 56.12 | 9.52 | 50.36 |
| $TiO_2$ | % | 1.59 | 0.06 | 1.44 | 1.69 | 1.59 | 1.56 | 0.11 | 1.32 | 1.73 | 1.58 | 0.49 | 0.10 | 0.26 | 0.78 | 0.51 | 0.75 |
| $Al_2O_3$ | % | 12.08 | 0.44 | 11.06 | 12.72 | 12.15 | 11.03 | 1.03 | 9.70 | 13.08 | 10.62 | 5.91 | 2.19 | 2.73 | 16.24 | 5.81 | 16.37 |
| $Fe_2O_3$ | % | 8.21 | 0.33 | 7.62 | 8.79 | 8.23 | 7.50 | 0.69 | 6.64 | 8.61 | 7.27 | 5.46 | 1.17 | 3.55 | 8.31 | 5.29 | 6.80 |
| MnO | % | 0.07 | 0.00 | 0.06 | 0.07 | 0.07 | 0.07 | 0.01 | 0.06 | 0.09 | 0.07 | 0.04 | 0.01 | 0.03 | 0.11 | 0.04 | 0.10 |
| MgO | % | 3.13 | 0.13 | 2.90 | 3.29 | 3.16 | 2.94 | 0.12 | 2.69 | 3.24 | 2.94 | 3.08 | 0.53 | 1.94 | 4.35 | 3.17 | 3.00 |
| CaO | % | 17.64 | 1.31 | 15.88 | 20.40 | 17.28 | 25.19 | 4.13 | 18.52 | 30.53 | 26.52 | 44.28 | 8.99 | 1.53 | 56.24 | 44.96 | 1.37 |
| $K_2O$ | % | 1.45 | 0.07 | 1.29 | 1.56 | 1.46 | 1.14 | 0.18 | 0.86 | 1.43 | 1.11 | 0.89 | 0.52 | 0.40 | 3.78 | 0.82 | 3.55 |
| $Na_2O$ | % | 3.40 | 0.68 | 2.77 | 5.51 | 3.14 | 3.30 | 0.28 | 2.84 | 3.92 | 3.23 | 2.00 | 0.45 | 1.23 | 3.11 | 1.89 | 3.83 |
| $P_2O_5$ | % | 0.25 | 0.01 | 0.23 | 0.28 | 0.25 | 0.27 | 0.02 | 0.24 | 0.32 | 0.27 | 0.56 | 0.22 | 0.11 | 0.91 | 0.62 | 0.16 |
| Cl | % | 2.87 | 0.91 | 2.12 | 5.99 | 2.57 | 2.62 | 0.17 | 2.29 | 3.04 | 2.64 | 2.73 | 0.88 | 0.94 | 4.27 | 2.81 | 3.10 |
| Ag | mg $kg^{-1}$ | <2 | <2 | <2 | <2 | <2 | <2 | <2 | <2 | <2 | <2 | 10 | 4 | 5 | 17 | 8 | 0.08 |
| As | mg $kg^{-1}$ | 19 | 2 | 17 | 26 | 19 | 14 | 2 | 11 | 20 | 14 | 20 | 4 | 11 | 31 | 19 | 9.2 |
| Ba | mg $kg^{-1}$ | 254 | 40 | 176 | 321 | 256 | 275 | 59 | 182 | 434 | 280 | 1.53% | 1.15% | 0.05% | 4.22% | 0.99% | 479 |
| Br | mg $kg^{-1}$ | 115 | 39 | 69 | 229 | 112 | 99 | 20 | 64 | 140 | 101 | 223 | 80 | 52 | 331 | 242 | 252 |
| Co | mg $kg^{-1}$ | 32 | 1 | 31 | 34 | 32 | 30 | 3 | 26 | 35 | 30 | 72 | 31 | 24 | 137 | 75 | 20 |
| Cr | mg $kg^{-1}$ | 133 | 7 | 121 | 147 | 133 | 164 | 37 | 129 | 269 | 151 | 192 | 88 | 88 | 428 | 148 | 97 |
| Cu | mg $kg^{-1}$ | 55 | 17 | 33 | 85 | 53 | 52 | 18 | 33 | 103 | 45 | 415 | 211 | 27 | 838 | 428 | 30 |
| Ga | mg $kg^{-1}$ | 16 | 1 | 12 | 17 | 16 | 14 | 1 | 12 | 16 | 14 | 10 | 3 | 6 | 23 | 10 | 20 |
| Hg | mg $kg^{-1}$ | 0.9 | 0.6 | 0.1 | 1.8 | 0.9 | 3 | 3.4 | 0.1 | 16.7 | 2.0 | 518 | 138 | 311 | 728 | 415 | 0.018 |
| I | mg $kg^{-1}$ | 85 | 23 | 52 | 140 | 85 | 76 | 33 | 49 | 164 | 62 | 79 | 61 | 22 | 409 | 72 | 380 |
| Mo | mg $kg^{-1}$ | <2 | <2 | <2 | <2 | <2 | 6 | 3 | 2 | 12 | 4 | 65 | 59 | 0 | 210 | 50 | 1.6 |
| Ni | mg $kg^{-1}$ | 48 | 3 | 43 | 53 | 49 | 51 | 10 | 37 | 67 | 51 | 19 | 7 | 7 | 35 | 19 | 53 |

**Table 15.2** (continued)

| | | AU2 | | | | | AU3 | | | | | AU10 | | | | | USGS MAG-1 |
|---|---|---|---|---|---|---|---|---|---|---|---|---|---|---|---|---|---|
| | | Mean | SD | Min | Max | Median | Mean | SD | Min | Max | Median | Mean | SD | Min | Max | Median | |
| Pb | mg kg$^{-1}$ | 24 | 8 | 10 | 35 | 25 | 42 | 47 | 10 | 208 | 23 | 50 | 16 | 14 | 75 | 56 | 24 |
| Rb | mg kg$^{-1}$ | 46 | 4 | 39 | 51 | 46 | 34 | 8 | 24 | 49 | 32 | 29 | 22 | 14 | 153 | 26 | 149 |
| S | mg kg$^{-1}$ | 18,013 | 4224 | 9937 | 22,470 | 19,297 | 16,815 | 2674 | 11,519 | 23,826 | 16,775 | 29,981 | 11,186 | 5136 | 49,585 | 31,755 | 3900 |
| Se | mg kg$^{-1}$ | <2 | <2 | <2 | <2 | <2 | <2 | <2 | <2 | <2 | <2 | 14 | 14 | 1 | 55 | 8 | 1.16 |
| Sr | mg kg$^{-1}$ | 481 | 56 | 381 | 562 | 490 | 581 | 129 | 370 | 905 | 582 | 1190 | 281 | 143 | 1616 | 1248 | 146 |
| V | mg kg$^{-1}$ | 151 | 10 | 128 | 169 | 149 | 154 | 14 | 134 | 199 | 151 | 137 | 25 | 89 | 192 | 142 | 140 |
| Y | mg kg$^{-1}$ | 31 | 1 | 30 | 33 | 32 | 31 | 1 | 28 | 33 | 31 | 51 | 16 | 19 | 81 | 55 | 28 |
| Zn | mg kg$^{-1}$ | 107 | 26 | 73 | 149 | 102 | 99 | 31 | 63 | 149 | 90 | 223 | 80 | 61 | 386 | 242 | 130 |
| Zr | mg kg$^{-1}$ | 196 | 7 | 177 | 206 | 197 | 173 | 19 | 137 | 203 | 175 | 51 | 21 | 17 | 137 | 51 | 130 |
| PCB | mg kg$^{-1}$ | 0.016 | 0.010 | 0.001 | 0.032 | 0.019 | 0.058 | 0.068 | 0.002 | 0.197 | 0.016 | 6.520 | 3.157 | 0.299 | 14.005 | 6.169 | n/a |
| PAH | mg kg$^{-1}$ | 0.38 | 0.09 | 0.16 | 0.49 | 0.38 | 0.89 | 1.07 | 0.14 | 4.19 | 0.37 | 25.61 | 11.96 | 6.90 | 47.70 | 25.90 | n/a |

USGS reference sample MAG-1 is used as an exemplar of a typical unpolluted (though non-calcareous) muddy sediment

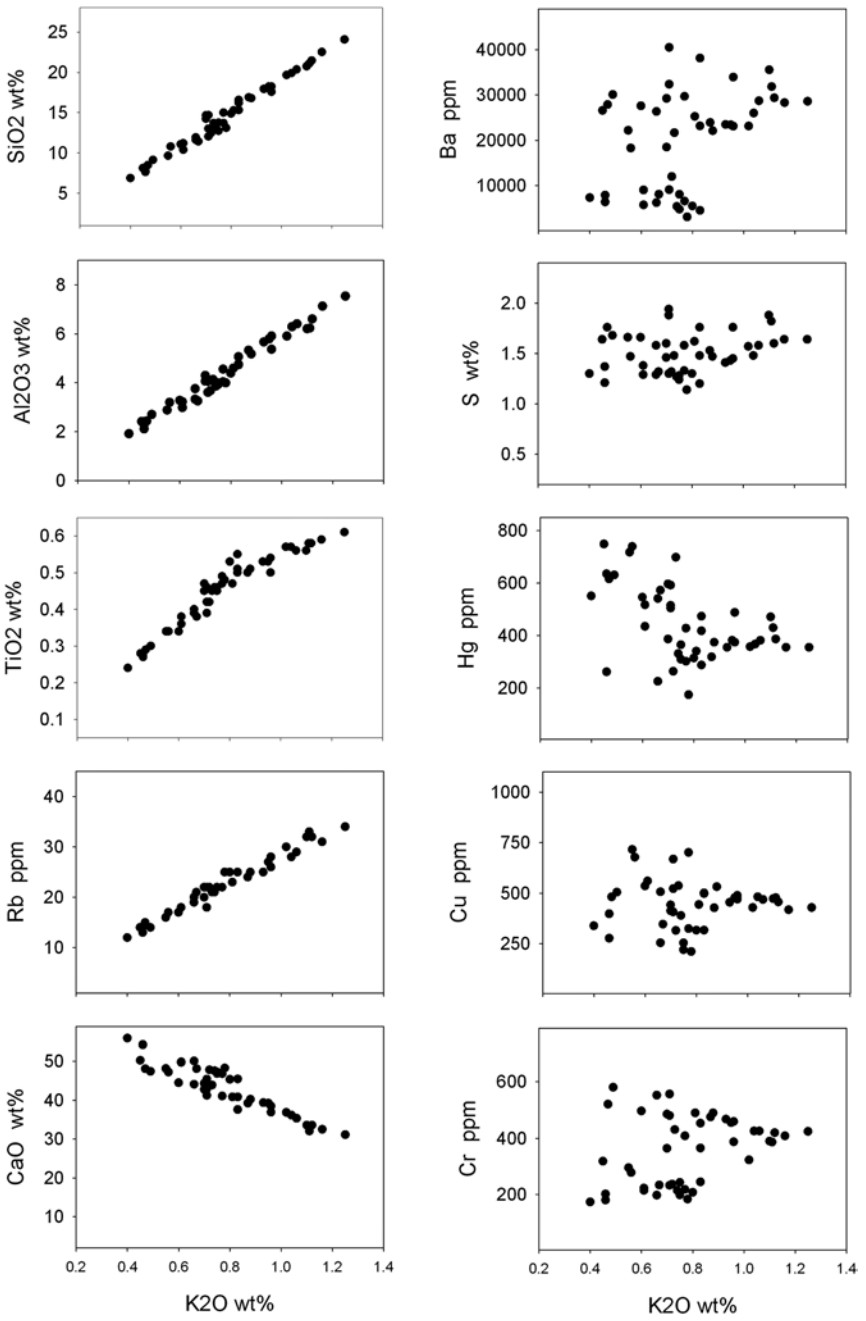


**Fig. 15.6** Elemental bi-plots for AU10$v_{iwc}$. The main components of dried sediment are clay and calcium carbonate minerals. Other components (< 5 wt% dry sediment) include sea salts and anthropogenic barium sulphate, calcium sulphate and hydrocarbons

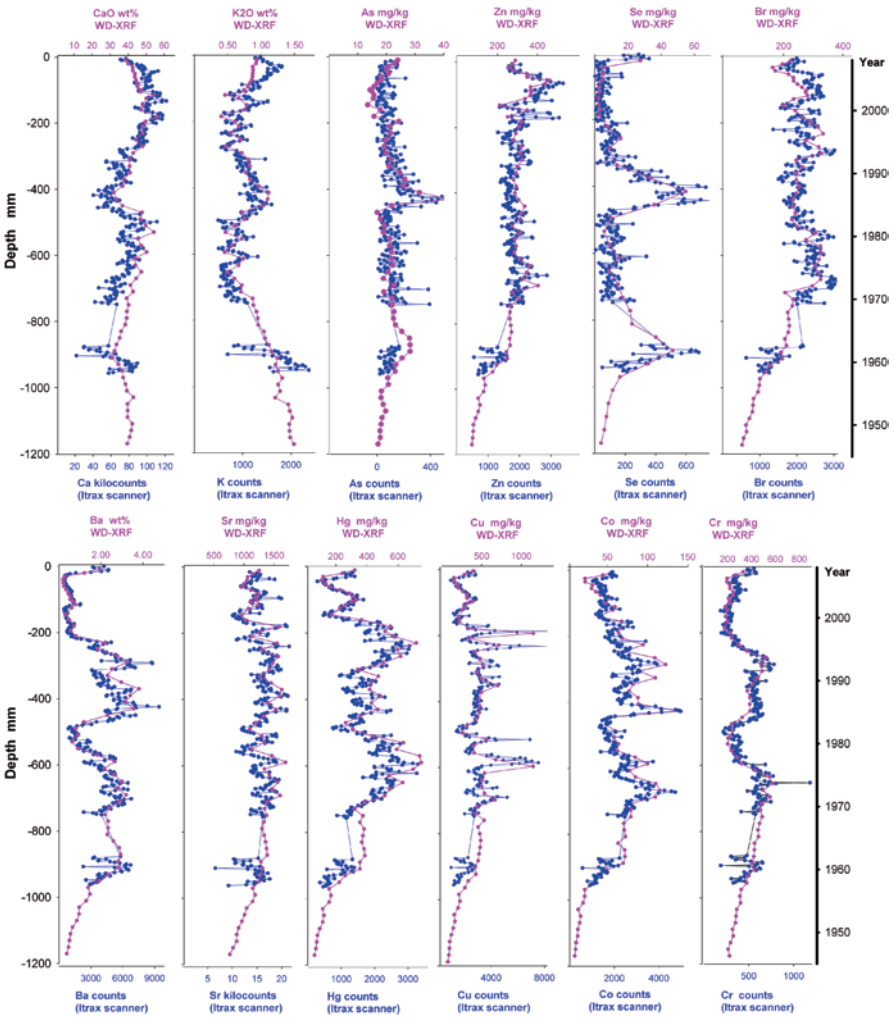


**Fig. 15.7** Comparison of Itrax (blue line, 200 µm scanning resolution) and WD-XRF data (*red line*, 1-cm sampling resolution) for AU10$v_{iw}$. The Itrax data are plotted as 5-point means. The right axis represents the Year based on the 137Cs chronology

**Site AU2** No significant variations in grain-size were recorded with depth and the sediment is mainly composed of silt with the highest content (58 %) at the core bottom (Fig. 15.5). The upper interval from 0 to 7.5 cm depth has clay >silt. Sand-sized material ranges from 4 to 18 % while gravel is absent. The two cores collected for sediment geochemistry analyses (AU2$g_{er}$ and AU2$g_{iwc}$) are generally similar and have a comparable accumulation rate. The uppermost 50 cm of sediment show only limited contamination of PCBs and Hg (Fig. 15.8).

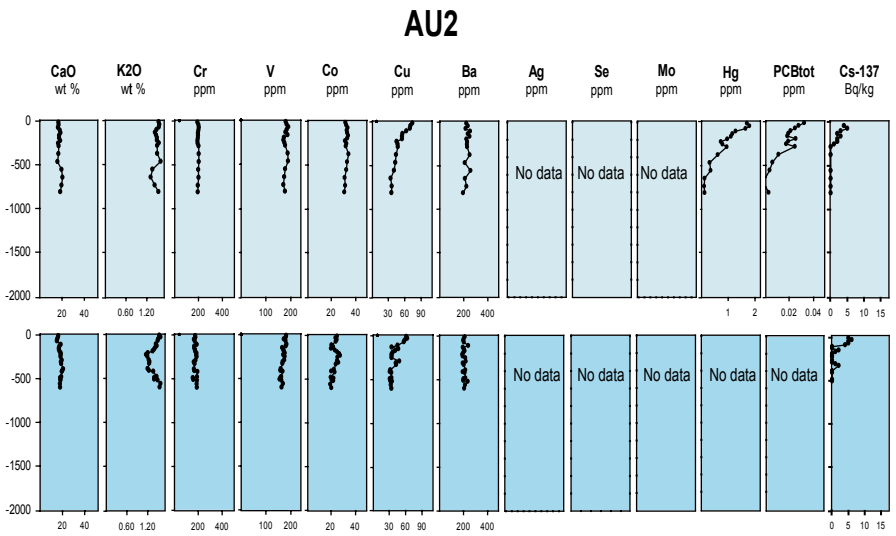


**Fig. 15.8** Elemental profiles for both AU2 cores determined by WD-XRF. Depth is shown on the y-axis in mm

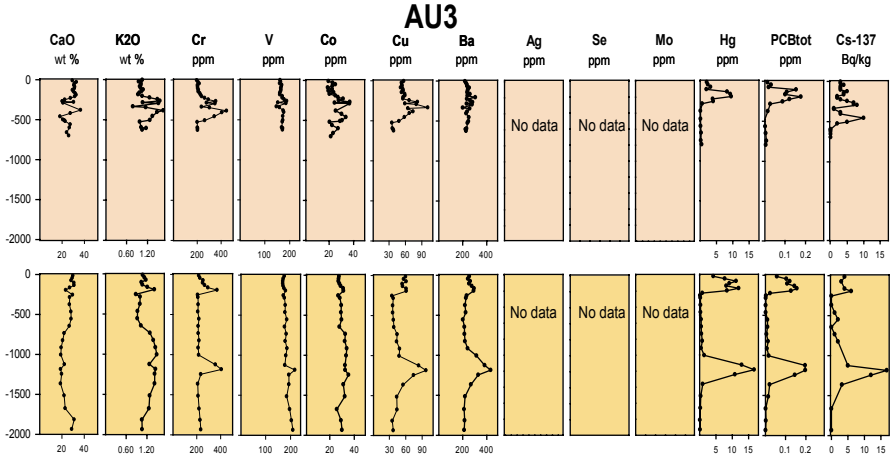


**Fig. 15.9** Elemental profiles for both AU3 cores determined by WD-XRF. Depth is shown on the y-axis in mm

**Site AU3** Grain-size shows the prevalence of fine fractions (clay and silt) throughout its length with the exception of the lower 12 cm and the upper 30 cm of the core, where sand attains values around 40 % (Fig. 15.5), while the highest clay content was recorded from −60 to −150 cm. The two cores studied for sediment geochemistry ($AU3g_{iwc}$ and $AU3v_{er}$) show quite different elemental and radionuclide profiles indicating significant variations in sediment accumulation rate (10–25 mm/year). At

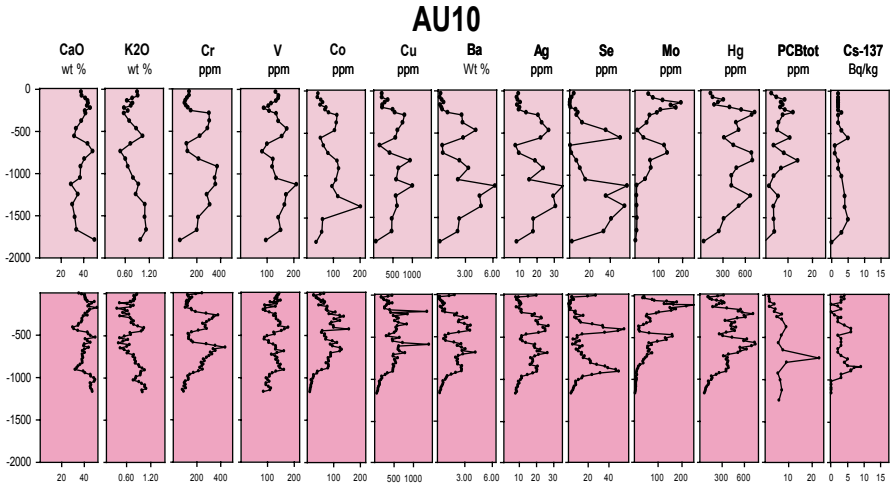


**Fig. 15.10** Elemental profiles for both AU10 cores (upper AU10v and lower AU10g) determined by WD-XRF. Depth is shown on the y-axis in mm

around −125 cm the profiles of Ba, Cr, Cu, V, Hg, PCB and $^{137}$Cs show a series of distinctive positive spikes (Fig. 15.9).

**Site AU10** As regards grain-size, with the exclusion of levels deeper than 180 cm where gravel is prevailing, silt-size material is the most abundant fraction throughout the investigated sediment depth, with values around 50%. All the collected cores from this location ($AU10g_{iwc}$, $AU10v_{iwc}$ and $AU10v_{er}$) show the highest concentrations of anthropogenic components (notably Ba, Hg and PCBs). Core $AU10v_{iwc}$ was examined both non-destructively (Figs. 15.3 and 15.7) and destructively (Figs. 15.6, 15.7, 15.10 and 15.11). The analysed cores show the highest amounts of anthropogenic contamination with PCBs (20 mg kg$^{-1}$), Ba (up to 5 wt%) and Hg (up to 600 mg kg$^{-1}$).

## Discussion

### *Sediment Accumulation Rates Based on $^{137}$Cs Distributions*

Caesium-137 dating was applied to all the seven cores of this study. Lead-210 dating was also carried out on three of the cores but the complex interplay between sediment composition and activity made its straightforward application somewhat difficult. The $^{137}$Cs dating method uses a set of indicator features viz: the first appearance of $^{137}$Cs (~1954) and the 1963 'bomb' maximum (Ritchie and McHenry 1990; Appleby and Oldfield 1994). The possible downward migration or mixing of

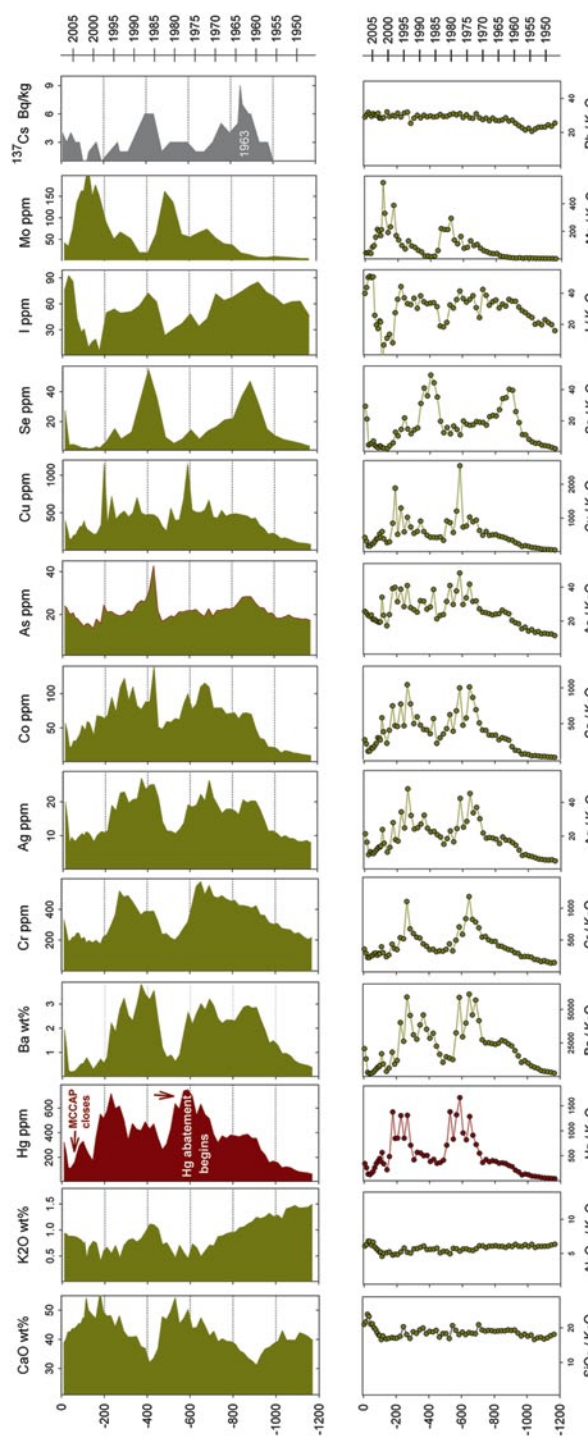


**Fig. 15.11** Elemental profiles for AU10vib at 1cm resolution determined by WD-XRF. The chronology is based on Cs-137 dating and is consistent with known historical events such as the MCCAP start-up, the introduction of mercury abatement (~ 1977–1979) and the Plant closure in 2005. Depth is shown in mm on the y-axis. Down-core elemental changes, normalised to K2O, are shown to enable clearer visualisation arising to the closed-sum effect caused by significant variations in carbonate (CaO)

**Table 15.3** Sediment accumulation rates estimated from $^{137}$Cs profiles (this study)

| Core | Coring date | 1954 (mm/year) | 1963 (mm/year) | 1986 (mm/year) |
|---|---|---|---|---|
| AU2g$_{iwc}$ | July 2008 | 7.1 | 7.2 | 6.6 |
| AU2g$_{er}$ | July 2008 | 4.2 | 4.9 | 7.0 |
| AU3g$_{iwc}$ | July 2008 | 9.7 | 10.1 | 13.4 |
| AU3v$_{er}$ | July 2008 | 25.9 | 26.3 | 25.5 |
| AU10g$_{iwc}$ | July 2008 | Core too short | ~24.4 | 25.6[a] |
| AU10v$_{iwc}$ | July 2008 | 33.1 | 33.7 | 25.2 |
| AU10v$_{er}$ | July 2008 | 18.1 | 19.2 | 19.8 |

The 1954, 1963 and 1986 dates represent key events in global and European $^{137}$Cs deposition
[a] This accumulation rate represents a reconsidered value from that quoted in the earlier report to ISPRA

$^{137}$Cs has a potential impact when using the first appearance criterion only. In some parts of Europe, an additional peak corresponding to the Chernobyl event (1986) is also seen (e.g. Miller et al. 2014, 2015) but the impact of Chernobyl is generally claimed to be low in Sicily, but is not necessarily absent (Cundy et al. 1998).

The Augusta sediment core profiles show that the different cores present widely varying sediment accumulation rates ranging from 4 to 33 mm/year based on first appearance of $^{137}$Cs and the location of the 1963 maximum. A peak at a higher level in the cores is potentially related to Chernobyl input but the observation that $^{137}$Cs also varies positively with sediment composition (K and Rb) means that the peak may simply corresponds to a co-incidental increase in a clay mineralogical control (see Figs. 15.4, 15.5, 15.8, 15.9, 15.10 and 15.11). This effect complicates the normal application of the method and care is needed in not simply equating maxima with features such as the 1963 bomb peak. Perhaps the most notable difference is the significantly higher accumulation rates found in cores collected around site AU10.

AU2: Both cores show low accumulation rates of 4–7 mm/year.

AU3: The two cores collected show quite different accumulation rates (~10 and ~26 mm/year) although the $^{137}$Cs profiles do show some similar features.

AU10: These three cores from this site show accumulation rates varying from 20, 25 to 33 mm/year. The only core run on the Itrax (AU10v$_{iwc}$), although similar to the other cores from the AU10 location, shows clear and persistent compositional layering (see the radiograph of Fig. 15.3). The layers correlate with variations in K and Ca (Fig. 15.3) which indicate variations in clay and carbonate components (Table 15.3).

## *Geochemical Variations: Itrax Vs WD-XRF*

There is a clear similarity in the geochemical profiles recorded using high-resolution Itrax scanning (data in counts) and those obtained using the quantitative WD-XRF (Ca, K, Fe, Ba, Sr, Hg, Zn, Cu, Cr, Se, Br, Cr, Fig. 15.7). This confirms the capability of X-ray core scanner to record reliable geochemical variations.

- The Itrax system scanning resolution is able to identify high frequency geochemical changes that can be missed with lower resolution (1-cm scale) conventional analysis.
- The speed and sensitivity of the Itrax analytical method provides broad range elemental variation data (Si–U) from normal levels through to anthropogenic enrichments.
- The simultaneously acquired high-resolution radiographic image(s) provides a powerful visual insight into sediment layering that corresponds to mineralogical and density changes. In some cores these may be inferred to have climatological significance (e.g. Miller et al. 2014, 2015).

## *Geochemical Variations with Location*

The geochemical data of the cores from the three areas show an increase in pollution going from north to south of the Harbour (AU2 to AU3 to AU10; Figs. 15.8, 15.9, 15.10 and 15.11). The main anthropogenic components (see Table 15.2) are Ag, Ba, Ca, Hg, Co, Cr, Cu, Mo, Zn, PAHs and PCBs. Heavy metal concentrations in cores collected from AU2 and AU3 are of the same order of magnitude while the concentrations in cores from the AU10 location are considerably elevated and reflect their close proximity to the main sources of contamination. A general feature of all cores is a covariation in the amount of anthropogenic contaminants. The major spikes could be explained in some cases through redox processes but the time required for such adjustments could be considerable in subtidal sediment (Thomson et al. 1993). The variations seen in Augusta Harbour are dominated by solid phase pollution inputs that became incorporated into the accumulating sediment but a case for some redox adjustment could be made for some elements (e.g. Mn, Se and Mo).

**Site AU2** The two cores collected from this site have a largely similar geochemistry and accumulation rates in the range 5–7 mm/year. Evidence of anthropogenic inputs (notably Hg and PCBs) first appear around −50 cm and generally increase to the surface (Fig. 15.8).

**Site AU3** These two cores are unusual in that for each core the pollution histories are contained in 50 cm and 150 cm respectively. A question arises as to why there is this difference? The core with the thicker sequence $AU3v_{er}$ is unusual in showing very low concentrations at depth until a maximum at about −125 cm that then falls off again to low values (Fig. 15.9). A similar pattern is seen for other anthropogenic elements and unusually also $^{137}Cs$. The covariation and the sharp rise and fall of Cr, Cu, Ba, Hg, PCB and $^{137}Cs$ could be explained if the sediment sequence included a significant thickness due to the dumping of old, mixed contaminated waste at this site.

**Site AU10** The concentration profiles of cores from AU10 site show different characters with respect to the other cores. Although the lowest concentrations are recorded at the core bottom, values both for trace elements and organic compounds at this level are already very high (Figs. 15.10 and 15.11). This indicates that bottom sediments were deposited after the onset of the petrochemical centre. Downcore

a clear trend is not distinguishable, although two main peaks around −80 cm and slightly below 20 cm depth are common to PCBs. All contaminants, with exception of Ba, show a decrease in the upper 20 cm, although concentrations at the top are still extremely high for all contaminants. The significant variations in CaO for Augusta cores lead to profiles that reveal the closed-sum effect. In other words since major element data sum to 100% where a component varies significantly there are corresponding variations seen in other components (Rollinson 2009). The use of ratios can suppress the closed-sum effect and typical divisors used are Al, K, Rb and Ti. In this study, based on observed elemental co-variations, $K_2O$ was used.

## *Anthropogenic Inputs*

**Barium and Calcium** Barium concentrations in all cores from AU10 are significantly higher than are found in typical marine sediments (Table 15.2). The close correlation with S, the high concentration and the observation of finely dispersed white grains in dried sediment shows that the high Ba is due to anthropogenic barite ($BaSO_4$). This is inferred to be a precipitate produced during brine purification linked to the MCCAP process. Chemical impurities in the brines (e.g. Ca, Mg and sulphate) were well known to have an adverse effect on the electrolytic process and were removed to avoid formation of so-called 'mercury butter'. This undesirable product would have led to short circuits, poor mercury flow, increased power consumption and increased exposure to mercury vapour (Text Box 15.2). The removal of sulphate was usually achieved by adding soluble $BaCl_2$ to create a barite precipitate.

The identification of significant barite in the AU10 core profiles shows that the brine purification wastes must have been discharged into the harbour. It might be anticipated that there would be a general correlation between Ba and Hg since their coexistence was linked to the MCCAP. However, the profile data show a slight mismatch suggesting a separate waste stream.

Calcium concentrations are significantly higher in the southernmost cores at site AU10 than in the other cores further north. Although carbonate is a significant natural component of the sediment it appears that the elevated Ca seen in Core AU10 (polluted) compared with ore AU2 (relatively unpolluted) could reflect an anthropogenic component. This might be due to $CaSO_4$ precipitates from the brine purification process.

**Mercury** Mercury is broadly recognized as a pernicious environmental pollutant and international agreements (co-ordinated through UNEP) have pledged to progressively eliminate it from virtually all industrial use (**Text Box 15.2**). In the past MCCAPs have been a significant source of mercury to the environment (Anirudh et al. 2009). The highest Hg concentration recorded in each core location are AU2 (1.8 mg $kg^{-1}$), AU3 (17 mg $kg^{-1}$) and AU10 (728 mg $kg^{-1}$).

The Hg profiles for the most contaminated cores (AU10; Figs. 15.3, 15.10 and 15.11) show a progressive rise from the early 1950s up to a maximum around 1977. This maximum corresponds closely to the introduction of mercury abatement around 1979. The decline in Hg persists until around 1984 whereupon there is an

increase to another maximum corresponding to around 1994. There is currently no evidence to explain this increase but a speculation could be that unauthorized discharges occurred. By 2005 the MCCAP had finally closed and the mercury cells removed. Overall, the variations in Hg concentrations, when linked to the $^{137}Cs$ chronology, accord with the main historical records (*viz*. inception of MCCAP, introduction of Hg abatement measures and final plant closure).

**Selenium** The geochemical profile for Augusta core AU10 shows two distinct peaks in Se reaching nearly 50 mg $kg^{-1}$. This selenium is likely to have an industrial origin since normal marine (carbonate or clay rich) sediments typically only contain up to 1 mg $kg^{-1}$. There are two plausible sources. One could be linked to materials derived from a mercury vapour capture technology that could have been used in the chlor-alkali plant (MCCAP). Selenium scrubbing is a wet media process for removal of fairly large quantities of mercury from flue gases. The gaseous mercury reacts with activated amorphous selenium, which is circulating in a scrubber with a 20–40% sulfuric acid. The mercury removal efficiency is claimed to be greater than 90% and the product is insoluble mercury selenide (Hagemann 2009). Another, more probable origin of the Se is from crude oil processed in the petrochemical industry as it is reported to contain relatively high concentrations (up to 2200 µg/L of Se; Lemly 2002).

**Chromium, Cobalt and Molybdenum** Co, Cr and Mo are elevated in Augusta sediment and are particularly evident in AU10. Chromium exists up to five times above muddy sediment concentrations (Table 15.2). The most likely explanation for this combination of elements in the harbour sediment is that they originate from discharges of waste catalyst used in petrochemical processes (desulphurization and cracking). Hydrodesulphurisation is commonly used in petrochemical refineries to remove sulphur for environmental and health reasons. The process involves passing crude oil and hydrogen over a catalyst at elevated T and P to convert any organic sulphur (commonly up to ~2.5%) to hydrogen sulphide. So-called CoMOX catalysts (typically 3–5% cobalt oxide and 14% $MoO_3$ immobilised on $Al_2O_3$) are used as they are resistant to poisoning and degradation and can be regenerated and reused for several years. Large quantities of spent hydrodesulfurization (HDS) catalysts are produced by the industry. Disposal of spent catalyst is a problem as it falls under the category of hazardous industrial waste. In recent times the value of these spent materials is recognized and recycling can be carried out (Rojas-Rodríguez et al. 2012) but in earlier, less environmentally sensitive times, it may have been considered more convenient to simply dispose of the spent catalyst into the Harbour.

**Copper** Cores from AU10 show sharp inflections in Cu, particularly in the core scanned by the Itrax and then sampled at high resolution. The sharp peaks approximately coincide with broader Hg and Cr peaks. It is unclear whether Cu had any role in the MCCAP. It is more likely that it was linked to refinery processes since it is known that copper chloride mixed with clay was widely used as a sweetening agent to remove malodorous mercaptans (organo-sulphur compounds) during oil refinery processing (Croudace and Cundy 1995).

**PCBs** Organic pollutants in the Harbour are derived from the longstanding petrochemical operations from the early 1950s to the current time. The main PCB

present is PC209 that is highly correlated with Hg concentration possibly indicating a link to the Chlor-alkali plant. Sediment from AU2 and AU3 has similar median values of 0.019 mg $kg^{-1}$ and 0.0016 mg $kg^{-1}$ respectively. Sediment from AU10 has concentrations several orders of magnitude higher with median values of 6.2 and 2.1 mg $kg^{-1}$ respectively. The concentration profiles of core AU10 show different characters with respect to the other cores. Although the lowest concentrations are recorded at the core bottom, values at this level are already very high (Fig. 15.11). This indicates that bottom sediments were deposited after the onset of the petrochemical centre. Along depth a clear trend is not distinguishable, although two main peaks around −80 cm and slightly below −20 cm depth are common to PCBs.

**Silver** Core AU10 shows measurable silver (WDXRF measurements). The co-variation with Ba may indicate a probable link to wastes discharges from the MCCAP.

### *Understanding the Geochemical Profiles*

Down-core elemental profiles for cores AU2 ($AU2g_{iwc}$ and $AU2v_{er}$) and $AU3g_{iwc}$ are generally similar and do not reveal high pollution showing that they are some distance from the main effluent input. The main characteristic features for the $^{137}Cs$ records are largely synchronous with the early industrial evolution of the area and they are all evident above −50 cm. Core $AU3v_{er}$ is more unusual in showing a set of peaks at approximately −125 cm for elements that are expected to be independent of each other (Cr, V, Cu, Ba, Hg, PCB, and $^{137}Cs$). The sharp rise followed by the rapid fall could be explained by relatively unpolluted dredge spoils being dumped near AU3 around 1965. The fact that geochemically unrelated components all have a peak at the same location might indicate the dumping of mixed material of early 1960s.

The cores from AU10 show similar geochemical variations to each other but are distributed over different sediment thicknesses. $AU10v_{iwc}$ has accumulated approximately 120 cm whereas $AU10v_{er}$ has accumulated 220 cm sediment. This variation could be explained by variations in bottom topography (Anonymous 1992, 1995). The geochemical profiles for $AU10v_{iwc}$ data show patterns clearly affected by variations in the calcium carbonate mineral component. After normalisation ($K_2O$) elemental pollutant profiles are simplified but essentially show similar features to the non-normalised profiles (Fig. 15.7).

## Conclusions

The considerable pollution legacy in Augusta Harbour has been a focus of interest for regulators and authorities interested in wholesale remediation to European standards. The current geochemical investigation has provided an excellent opportunity to evaluate the usefulness of the Itrax core scanner as an environmental forensic analytical tool. The Itrax data were validated against a conventional WD-XRF dataset and found to accurately reflect the elemental variations for a broad range of major, minor and trace elements.

Additional to the Itrax data, a range of other geochemical data were acquired including PCBs, PAHs, Hg, Ba, Cr, Cu and $^{137}$Cs and their variations were used to evaluate the timing of pollutant inputs. The Itrax radiographic image, when correlated with particle size data and XRF major elements (Ca and K) helped provide an insight into the composition of sediment layers.

Unusual enrichments of elements seen in the most polluted site (AU10) are interpreted as waste materials discharged into the Harbour during industrial operations.

- Ba (and Ca in part)—originate from the brine purification process linked to the MCCAP
- Hg—a waste element derived from inefficiencies in the MCCAP electrolytic process
- Cr, Co, Mo, (V)—derived from disposal of waste catalysts used in oil refineries
- Cu—linked to oil refinery operations (e.g. sweetening of gases)
- Se—ultimately derived from crude oil (Lemly 2002)
- Ag—likely to be related to the operations at the MCCAP based on co-variation with Ba

One of the key interests of the Italian Environmental Prosecutor was to reconcile variations in anthropogenic elements, particularly mercury, with specific polluting companies. This required a reliable sediment chronology and $^{137}$Cs dating was employed and found to provide a timescale consistent with known pollution events. In the most contaminated cores from site AU10 steep early changes in Hg, Ba and other anthropogenic components are linked to the known rapid expansion in the MCCAP and petroleum refining in the early 1950s. Around 1977 there is a decline in Hg that links to the known introduction of a mercury abatement process. From 1992 to 1997 Hg concentrations increase again to another maximum before they finally decline which links to the ultimate closure of the MCCAP in 2005. The increase seen from 1992 to 1997 could be associated with unauthorized discharges.

The ITRAX investigation of Augusta sediments has made a valuable contribution to this environmental forensic study. The geochemical variations seen in the most polluted core have been validated by comparing data obtained using conventional (quantitative) WD-XRF. The speed and resolution of ITRAX analysis are clear strengths of this method. As in all geochemical studies where significant variations in major components occur, consideration of the closed-sum effect should be taken into account to avoid misinterpretation of elemental profiles.

## References

Anirudh R, Rokade MA, Zingde MD, Borole DV (2009) Post-depositional memory record of mercury in sediment near the effluent disposal site of a chloralkali plant in Thane Creek–Mumbai Harbour, India. Environ Technol 30:765–783

Anonymous (1992) Sistema integrato per il monitoraggio automatico della rada di Augusta. I-Studi preliminari per il posizionamento di boe oceanografiche. Istituto Sperimentale Talassografico CNR Messina. Rapporti 6:1–120

Anonymous (1995) Studio sedimentologico e bionomico dei fondi mobili della Rada di Augusta. Istituto Sperimentale Talassografico CNR Messina. Rapporti 9:1–72

Appleby P, Oldfield F (1992) Application of lead-210 to sedimentation studies. In: Ivanovich M, Harmon RS (eds) Uranium-series disequilibrium: applications to earth, marine, and environmental science. Oxford University Press, pp 731–738

Ausili A, Gabellini M, Cammarata G, Fattorini D, Benedetti M, Pisanelli B, Gorbi S, Regoli F (2008) Ecotoxicological and human health risk in a petrochemical district of southern Italy. Mar Environ Res 66:215–217

Ausili A, Cappucci S, Gabellini M, Innocenti C, Maffucci M, Romano E, Rossi L, Taramelli A (2012) New approaches for multi source data sediment characterisation, thickness assessment and clean-up strategies. Chem Eng Trans 28:223–228

Bellucci LG, Giuliani S, Romano S, Albertazzi S, Mugnai C, Frignani M (2012) An integrated approach to the assessment of pollutant delivery chronologies to impacted areas: Hg in the Augusta Bay (Italy). Environ Sci Technol 46:2040–2046

Bergamin L, Romano E, Finoia MG, Venti F, Bianchi J, Colasanti A, Ausili A (2009) Benthic foraminifera from the coastal zone of Baia (Naples, Italy): assemblage distribution and modification as tools for environmental characterisation. Mar Pollut Bull 59:234–244

Bianchi F, Bianca S, Linzalone N, Madeddu A (2004) Sorveglianza delle malattie congenite in Italia: un approfondimento nella provincia di Siracusa. Epidemiol Prev 28:87–93

Bonsignore M, Salvagio D, Manta E, Oliveri M, Sprovieri M, Basilone G, Bonanno A, Falco F, Traina A, Mazzola S (2013) Mercury in fishes from Augusta Bay (southern Italy): risk assessment and health implication. Food Chem Toxicol 56:184–194

Castagna A, Sinatra F, Castagna G, Stoli A, Zafarana S (1985) Trace element evaluations in marine organisms. Mar Pollut Bull 16:416–419

Cearreta A, Ulibarra I, Irabien MJ, Yusta L, Leorri E, Croudace IW, Cundy AB (2002) Recent salt marsh development and natural regeneration of reclaimed areas in the Plentzia estuary, N. Spain. Estuar Coast Shelf Sci 54:863–886

Celia Magno M, Bergamin L, Finoia MG, Pierfranceschi G, Venti F, Romano E (2012) Correlation between textural characteristics of marine sediments and benthic foraminifera in highly anthropogenically-altered coastal areas. Mar Geol 315–318:143–161

Cernigliaro A, Addario SP, Nicolotti N (2008) Research on the health state of the Sicilian population living in areas at environmental or natural risk: the experience of the Regional Department of Epidemiology. Ital J Public Health 5:80–85

Clarkson T (1997) The toxicology of mercury. Crit Rev Clin Lab Sci 34:369–403

Covelli S, Faganeli J, Horvat M, Brambati A (2001) Mercury contamination of coastal sediments as the result of long-term cinnabar mining activity (Gulf of Trieste, northern Adriatic sea). Appl Geochem 16:541–558

Covelli S, Acquavita A, Piani R, Predonzani S, De Vittor C (2009) Recent contamination of mercury in an estuarine environment (Marano lagoon, Northern Adriatic, Italy). Estuar Coast Shelf Sci 82:273–284

Covelli S, Emili A, Acquavita A, Dinelli E, Koron N, Faganeli J (2010) Benthic fluxes measurement of mercury and methylmercury in Pialassa Baiona (Ravenna, Italy). Int J Environ Qual (EQA) 3:33–40

Croudace IW, Cundy AB (1995) A record of heavy metal pollution in recent sediments from Southampton Water, Southern England: a geochemical and isotopic study. Environ Sci Technol 29:1288–1296

Croudace IW, Rothwell RG (2015) Future developments and innovations in high-resolution core scanning in IW Croudace. In: Rothwell RG (ed) Micro-XRF studies of sediment cores. Springer, Netherlands

Croudace IW, Rindby A, Rothwell RG (2006) Itrax: description and evaluation of a new sediment core scanner. In: Rothwell RG (ed) New techniques in sediment core analysis. Geol Soc Spec Publ, London, 267:51–63

Croudace IW, Warwick PE, Morris JE (2012) Evidence for the preservation of technogenic tritiated organic compounds in an estuarine sedimentary environment. Environ Sci Technol 46:5704–5712

Cundy AB, Collins PEF, Turner SD, Croudace IWC, Horne D (1998) 100 years of environmental change in a coastal wetland. Augusta Bay, southeast Sicily: evidence from geochemical and palaeoecological studies. Geolog Soc Lond Spec Publ 139:243–254

Cundy AB, Croudace IW, Cearreta A, Irabien MJ (2003) Reconstructing historical trends in metal input in heavily-disturbed, contaminated estuaries: studies from Bilbao, Southampton Water and Sicily. Appl Geochem 18:311–32

Di Leonardo R, Bellanca A, Capotondi L, Cundy A, Neri R (2006) Possible impacts of Hg and PAH contamination on benthic foraminiferal assemblages: an example from the Sicilian coast, central Mediterranean. Sci Total Environ 388:168–183

Di Leonardo R, Adelfio G, Bellanca A, Chiodi M, Mazzola S (2014) Analysis and assessment of trace element contamination in offshore sediments of the Augusta Bay (SE Sicily): a multivariate statistical approach based on canonical correlation analysis and mixture density estimation approach. J Sea Res 85:428–442

Govindaraju K (1994) Compilation of working values and sample description for 383 geostandards. Geostand Newsl 18:1–158

Guerriero C, Bianchi F, Cairns J, Cori L (2011) Policies to clean-up toxic industrial contaminated sites of Gela and Priolo: a cost-benefit analysis. Environ Health 10:68 (Open Access)

Hagemann S (2009) GRS—252 Oktober 2009 Gesellschaft für Anlagen und Reaktor sicherheit (GRS), GmbH. GRS—252 ISBN 978-3-939355-27-4. http://ec.europa.eu/environment/air/pdf/pp_mercury7.pdf. Accessed Sept 2013

Hester RE, Harrison RM (eds) (2008) Environmental forensics. Issues in Environmental Science and Technology. RSC Publ, London, pp 190

ICRAM (2008) Progetto preliminare di bonifica della rada di Augusta inclusa nel sito di bonifica di interesse nazionale di Priolo Fase I e Fase II. Report. BoI-Pr-SI-PR-Rada di Augusta-03.22, Internal Report

Lemly AD (2002) Selenium assessment in aquatic ecosystems: a guide for hazard evaluation and water quality criteria. Springer, New York

Lepland A, Andersen TJ, Lepland A, Arp HP, Alve E, Breedveld GD, Rindby A (2010) Sedimentation and chronology of heavy metal pollution in Oslo harbour, Norway. Mar Pollut Bull 60:1512–1522

Maggi C, Berducci MT, Bianchi J, Giani M, Campanella L (2009) Methylmercury determination in marine sediment and organisms by direct mercury analyser. Anal Chim Acta 641:32–36

Miller H, Croudace IW, Bull JM, Cotterill JC, Dix JK, Taylor RN (2014) A 500 year sediment lake record of anthropogenic and natural inputs to Windermere (English Lake District) using double-spike lead isotopes, radiochronology, and sediment microanalysis. Environ Sci Technol 48:7254–7263

Miller H, Croudace IW, Bull JM, Cotterill CJ, Taylor RN (2015) Modern pollution signals in sediments from Windermere, NW England, determined by micro-XRF and lead isotope analysis, In: Croudace IW, Rothwell RG (eds) Micro-XRF studies of sediment cores. Springer, Netherlands

Nigro F, Renda P (2000) Un modello di evoluzione tettono-sedimentaria dell'avanfossa neogenica Siciliana. Boll Soc Geol Ital 119:667–686

Piani R, Covelli S, Biester H (2005) Mercury contamination in Marano Lagoon (Northern Adriatic Sea, Italy): source identification by analyses of Hg phases. Appl Geochem 20:546–1559

Raldúa D, Díez S, Bayona JM, Barceló D (2007) Mercury levels and liver pathology in feral fish living in the vicinity of a mercury cell chlor-alkali factory. Chemosphere 66:1217–1225

Ritchie JC, McHenry JR (1990) Application of radioactive fallout cesium-137 for measuring soil erosion and sediment accumulation rates and patterns: a review. J Environ Qual 19:215–233

Rojas-Rodríguez AD, Flores-Fajardo O, González FSA, Castillo NNL, Gómez MJC (2012) Chemical treatment to recover molybdenum and vanadium from spent heavy gasoil hydrodesulfurization catalyst. Adv Chem Eng Sci 2:408–412

Rollinson HR (1993) Using geochemical data: evaluation, presentation, interpretation. Pearson Harlow, Longman

Romano E, Bergamin L, Ausili A, Pierfranceschi G, Maggi C, Sesta G, Gabellini M (2009a) The impact of the Bagnoli industrial site (Naples, Italy) on sea-bottom environment. Chemical and textural features of sediments an the related response of benthic foraminifera. Mar Pollut Bull 59:244–255

Romano E, Bergamin L, Finoia MG, Celia Magno M, Ausili A, Gabellini M (2009b) The effects of human impact on benthic foraminifera in the Augusta harbour (Sicily, Italy), In: Dahl E, Moksness E, Støttrup, J (eds), Proceedings of the International Symposium on Integrated Coastal Zone Management. Wiley-Blackwell, Chichester, pp 97–115

Romano E, Bergamin L, Celia Magno M, Ausili A (2013) Sediment characterization of the highly impacted Augusta harbour (Sicily, Italy): modern benthic foraminifera in relation to grain-size and sediment geochemistry. Environ Sci Process Impacts 15:930–946

Sciacca S, Fallico R (1978) Presenza e concentrazione di sostanze inquinanti di origine industriale nella Rada di Augusta (Siracusa). Inquinamento 20(6):33–38

Scicchitano G, Monaco C, Tortorici L (2007) Large boulder deposits by tsunami waves along the Ionian coast of south-eastern Sicily (Italy). Mar Geol 238:75–91

Sedivy VM (2009) Environmental balance of salt production speaks in favour of solar saltworks. Glob NEST J 11:41–48

Sprovieri M, Oliveri E, Di Leonardo R, Romano E, Ausili A, Gabellini M, Barra M, Tranchida G, Bellanca A, Neri R, Budillon F, Saggiomo R, Mazzola S, Saggiomo V (2011) The key role played by the Augusta basin (southern Italy) in the mercury contamination of the Mediterranean Sea. J Environ Monit 13:1753–1760

Thomson J, Higgs NC, Croudace IW, Colley S, Hydes DJ (1993) Zonation of redox-sensitive elements at the oxic/post-oxic interface in deep-sea sediments. Geochim Cosmochim Acta 57:579–595

Tomiyasu T, Matsuyama A, Eguchi T, Fuchigami Y, Oki K, Horvat M (2006) Spatial variations of mercury in sediment of Minamata Bay, Japan. Sci Total Environ 368:283–290

WHO (2012) Biomonitoring-based indicators of exposure to chemical pollutants. Report of a meeting Catania, Italy, 19–20 April 2012, WHO Report (Europe), Regional Office for Europe, Copenhagen, Denmark

# Chapter 16
# Modern Pollution Signals in Sediments from Windermere, NW England, Determined by Micro-XRF and Lead Isotope Analysis

**Helen Miller, Ian W. Croudace, Jonathan M. Bull, Carol J. Cotterill, Justin K. Dix and Rex N. Taylor**

**Abstract** High resolution geochemical (Itrax micro-XRF and wavelength dispersive XRF) data, radiochronology ($^{210}$Pb and $^{137}$Cs analyses) and ultra-high precision double-spike lead isotope measurements from lacustrine sediment cores are used in combination with historical research of former mining landscapes to investigate modern pollution signals in sediments from Windermere, the largest lake in the English Lake District. The sediment record suggests that while most element concentrations have been stable, there has been a significant increase since the 1930s in lead, zinc and copper concentrations. Double-spike lead isotope measurements reveal a mixture of natural lead, and three major contributory sources of anthropogenic (industrial) lead, comprising gasoline lead, coal combustion lead (from coal-fired steam ships) and lead derived from Carboniferous Pb–Zn mineralisation (mining activities). A number of up-system sediment traps have limited the amount of mining related heavy metals entering Windermere, and as a result, periods of metal workings do not correlate with peaks in heavy metals. Increases could also be due to flood-induced metal inwash or weathering of bedrock in the catchment. Application of these non-destructive and high precision analytical techniques provides new insights into the pollutant depositional history of Windermere.

## Introduction

Lacustrine sediments provide an archive of environmental change and a high resolution record of catchment level anthropogenic activity, and can be used to examine temporal changes in natural and anthropogenic trace element input. Several

I. W. Croudace (✉) · H. Miller · J. M. Bull · J. K. Dix · R. N. Taylor
Ocean and Earth Science, National Oceanography Centre, University of Southampton, Waterfront Campus, European Way, Southampton SO14 3ZH, UK
e-mail: iwc@noc.soton.ac.uk

C. J. Cotterill
British Geological Survey, Murchison House, West Mains Road, Edinburgh EH9 3LA, UK



I. W. Croudace, R. G. Rothwell (eds.), *Micro-XRF Studies of Sediment Cores*,
Developments in Paleoenvironmental Research 17, DOI 10.1007/978-94-017-9849-5_16

studies attribute the enrichment of heavy metals in lacustrine sediments to human and industrial activity during the late nineteenth and early twentieth centuries, and more recent leaded gasoline usage (Williams 1991; Farmer et al. 1996; Yang et al. 2002; Yang and Rose 2005). In particular, lead isotope ratios have been increasingly used to establish the principal sources of lead pollution and yield information on geochemical origin (Gulson et al. 1994; Monna et al. 1997; Farmer et al. 1999; Hansmann and Köppel 2000; Shepherd et al. 2009). Development of the high precision double-spike lead isotope technique (e.g. Woodhead et al. 1995; Ishizuka et al. 2003) has also led to more sensitive environmental investigations.

Within the English Lake District, contamination of heavy metals as a result of direct human and industrial activity has been identified in several lacustrine settings. In particular, local point sources of heavy metals from mining activities have been identified within the sediments of Ullswater (Anderton et al. 1998; Kember 2001; Grayson and Plater 2009), Bassenthwaite (Hatfield et al. 2008; Chiverrell et al. 2012) and Brotherswater (Schillereff et al. 2013) (Fig. 16.1). In the Windermere catchment, the historical extent of heavy metal pollution is believed to be considerable (Millward et al. 2000). Concentrations of heavy metals in sediment cores (0.5–1 m long) from the South Basin have identified enriched levels of lead, zinc, copper and mercury related to anthropogenic inputs such as mining activities, denudation of land surfaces, sewage discharge, heavy industry and burning of fossil fuels (Aston et al. 1973; Hamilton-Taylor 1979; Hamilton-Taylor 1983).

This paper investigates modern pollution signals in sediments from Windermere and assesses the timing and scale of anthropogenic inputs using a combination of high precision analytical techniques. In particular, high-resolution Itrax micro-X-ray fluorescence and micro-radiographic analysis are used to identify fine scale compositional change, validated against conventional wavelength dispersive X-ray fluorescence (WD-XRF). High precision double spike lead isotopes measurements are used to examine multi-source inputs of lead. These interpretations are constrained by radiochronology ($^{210}$Pb and $^{137}$Cs) and extensive historical research of former mining landscapes. The results from the various analytical approaches are integrated to provide a robust assessment of various pollution signals in this special lacustrine environment.

## *Regional Setting*

Windermere is the largest natural lake in England and is divided into a North and South Basin, separated by an area of low islands and shallow water (Fig. 16.1). The lake occupies a radial pre-glacial river valley and is orientated NNW to SSW, measuring c. 17 km in length with a maximum width of c. 1.5 km and depth of 62 m in the north. The sedimentology of the lake bed is dominated by gyttja (fine to very coarse organic rich silt) and the geomorphology is characterised by several steps and ridges, interpreted as the surface expression of recessional moraines formed during ice retreat (Miller et al. 2013; Pinson et al. 2013). The bedrock of the catchment is predominantly comprised of the Borrowdale Volcanic Group (BVG)

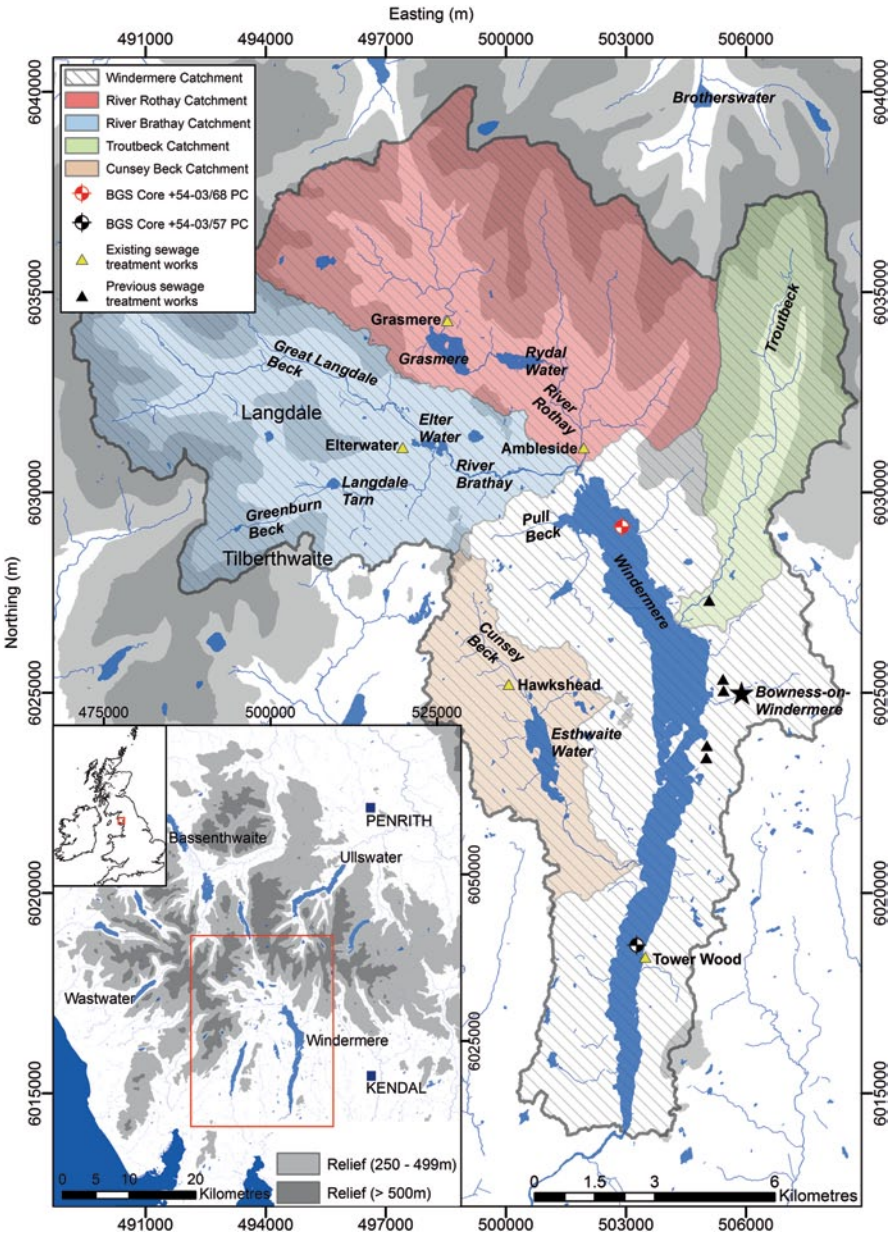


**Fig. 16.1** Location of study area, showing the Windermere catchment, rivers, lakes, valleys, Bowness-on-Windermere (*black star*) and the location of existing and previous sewage treatment works and BGS sediment cores. Onshore DEM and catchment areas calculated using 5 m resolution NEXTMap data. Inset shows location map of the study area in relation to the Lake District and the British Isles

in the north, and the Silurian (Windermere Supergroup) in the south (Mitchell 1956; Millward et al. 2000) (Fig. 16.2). There are two major fault systems in the region (orientated NNW-SSE and ENE-WSW) (Postlethwaite 1975; British Geological Survey 1996). These faults produce kilometre-scale map offsets within the oldest orientated Silurian formations, however large offsets are not seen to the north of Windermere (Woodcock and Soper 2006) (Fig. 16.2). The major fluvial inputs in the North Basin are the River Rothay, Brathay and Troutbeck, and in the South Basin the predominant inflow enters as flow from the North Basin and via Cunsey Beck (Fig. 16.1). The fluvial inputs drain several streams and small lakes, including Elterwater, Grasmere and Rydal Water in the north, and Esthwaite Water in the west. Land cover to the north is largely grassland on poor soils and acidified podsols, to the west is mixed woodland with improved grassland and to the east is more urban with the towns of Ambleside and Bowness-on-Windermere (Pickering 2001; Barlow et al. 2009a).

Within the Windermere catchment there are five existing sewage treatment works (STW) at Ambleside, Elterwater, Grasmere, Hawkshead and Tower Wood (Fig. 16.1). Wastewater entering Windermere was not treated until the opening of two STW, at Ambleside in 1886 and Beemire (near Bowness-in-Windermere) in 1888 (McGowan et al. 2012). Sewage from Beemire was subsequently diverted to a new STW at Tower Wood in 1924, which is currently the largest STW in the catchment, processing waste water from the Bowness/Windermere area. The level of nutrient enrichment and biological production in the water column has been assessed through regular monitoring since 1945, revealing a progressive change towards eutrophy (Reynolds and Irish 2000). Increases in nutrients to the lake are attributed to a growing human population in the catchment, changes in agricultural practice and increased sewage discharge (Talling 1999). In particular, an increase in the direct discharge of treated sewage effluents in the 1960s (due to centralisation of wastewater treatment) led to an increase in algal growth and phosphorus availability and a reduction in oxygen concentration in deep water (Reynolds and Irish 2000; Pickering 2001). In 1992, the introduction of a “phosphate stripping” treatment at Tower Wood and Ambleside STW led to a reduction in phosphate loading, particularly in the South Basin (Talling 1999; Parker and Maberly 2000). Similar findings were observed further north at Grasmere, where the onset of eutrophication is dated to 1855, analogous with the expansion of human settlement (Barker et al. 2005; Sabater and Haworth 1995).

The Lake District has a long history of metalliferous mining and quarrying dating back to the sixteenth century, with some evidence for earlier activity in the thirteenth, fourteenth and fifteenth centuries. In the Windermere catchment, the greatest period of mineral output (for lead, copper and iron) was in the latter half of the nineteenth century (Pickering 2001) and was followed by a rapid decline in the industry in 1870 due to foreign competition. There have been sporadic bursts of activity in the twentieth century, but all mining activity has now ceased (Adams 1988, 1995). Quarrying for slate, building stone and aggregates increased in the sixteenth century and developed into an important commercial industry, particularly during the nineteenth century. The industry declined during late Victorian times and

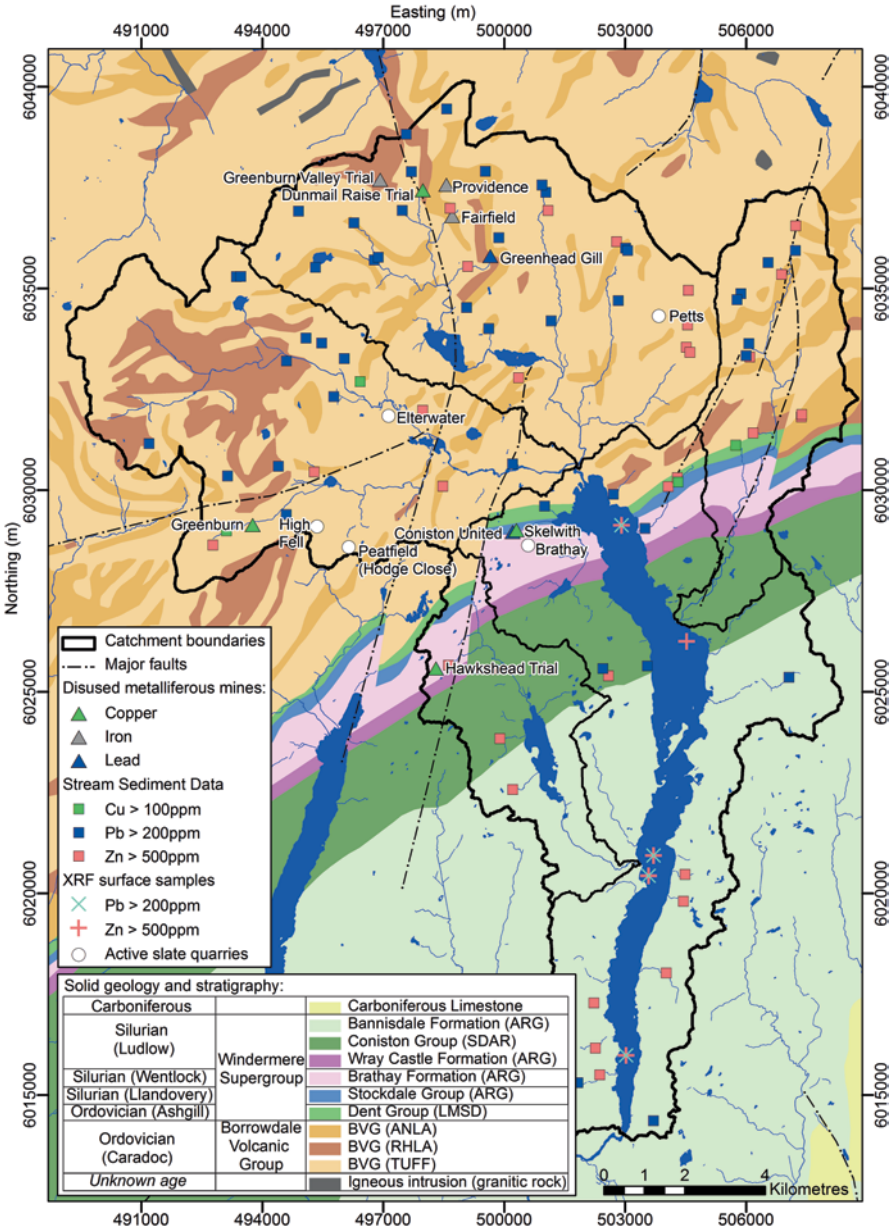


**Fig. 16.2** Location of disused metalliferous mines and currently active slate quarries. Stream sediment and WD-XRF samples with elevated concentrations of Pb, Zn and Cu are shown. Solid geology, stratigraphy and faults (British Geological Survey 1996). *BVG* Borrowdale Volcanic Group; *ARG* siliciclastic argillaceous rocks; *ANLA* andesitic, lava; *RHLA* rhyolitic, lava; *SDAR* sandstone and (subordinate) argillaceous rocks interbedded; *LMSD* limestone and (subordinate) sandstone interbedded. (Figure contains British Geological Survey materials © NERC (2013))

many small quarries closed during the early twentieth century, leaving only a few commercial operators active, at Elterwater, Peatfield, High Fell, Petts and Brathay (BGS BRITPITS database; British Geological Survey 2000; Millward et al. 2000; Cameron et al. 2010) (Fig. 16.2). In addition to slate quarrying, small scale open-pit or surface workings extracted igneous and metamorphic rocks (from the BVG), sandstone (from Silurian siltstones and mudstones within the Coniston Group and Bannisdale Formation) and sand and gravel. Quarrying in the catchment has led to increased fine sediment supply to Windermere, particularly evident in the North Basin (Pickering 2001; Barlow et al. 2009b).

## Methodology

### *Sediment Analysis*

Two piston cores from the North and South Basin were acquired in 2012 using a floating platform and piston corer designed by Uwitec[1] (Fig. 16.1). The North Basin core +54-03/68 PC (53.7 m water depth, UTM coordinates 502900, 6029136) and South Basin core +54-03/57 PC (37.3 m water depth, 503267, 6018702) were longitudinally split (core diameter 90 mm) and photographed at high resolution, with one half archived at the British Geological Survey Core Store (Keyworth, UK). U-channels were extracted from the working halves of each core and analysed using an Itrax micro-XRF core scanner at the British Ocean Sediment Core Research Facility (BOSCORF, National Oceanography Centre, UK) in accordance with the methodology detailed in Croudace et al. (2006). Itrax settings were as follows: step size 200 μm, counting time 30 s, molybdenum anode X-ray tube, XRF conditions 30 kV, 50 mA. The Itrax micro-XRF core scanner provides continuous, non-destructive, high-resolution elemental profile data, and is capable of identifying high frequency compositional changes. In addition, a number of studies (e.g. Croudace et al. 2012) have shown that Itrax elemental data (in counts) correlates well with quantitative analytical data (e.g. ICP-OES or WD-XRF). These combine to make the Itrax a unique high-resolution core scanner.

The cores were also sub-sectioned at 1 cm resolution and samples were freeze-dried. 35 samples from each core were analysed by WD-XRF using a Philips MagiX-Pro XRF spectrometer to measure concentrations of elements of atomic mass greater than or equal to sodium. Samples were homogenised by grinding and compressed into powder pellets in accordance with the standard methodology (Croudace and Williams-Thorpe 1988). A certified reference sample (BE-N, basalt, Centre de Recherches Pétrographiques et Géochimiques, France) was used as a control and calibrations previously established by analysis of 15 International Geochemical Reference samples were used. Further analysis of 16 representative lake bed sedi-

[1] http://www.uwitec.at

ment samples acquired in 2011 by a lightweight sediment sampler (Van Veen F42A grab) (Fig. 16.2) were also completed via WD-XRF analysis according to the same methodology.

Sediment accumulation rates were determined using $^{210}$Pb through the measurement of its granddaughter $^{210}$Po using alpha spectrometry (Flynn 1968). Each sample (1–3 g, 1 cm downcore) was spiked with $^{209}$Po (nominally 50 mBq), digested using double acid leaching and Po separated onto silver discs by auto-deposition before counting by alpha spectrometry (100,000 s). A Constant Flux—Constant Sedimentation (CF:CS) model of $^{210}$Pb dating (which assumes that both the flux of unsupported $^{210}$Pb to the sediment and the sedimentation rate are constant) was used (Robbins 1978). A Canberra well-type HPGe gamma-ray spectrometer (counting for 100,000 s) was used to determine the $^{137}$Cs activity of samples from 0 to 20, 29.5 and 39.5 cm (sampled at 1 cm resolution). The standard method of evaluating the 661 keV peaks of the spectra (Ritchie and McHenry 1990) was used, and each activity was corrected for sample mass and volume.

High precision lead isotopic abundances were also determined using a Thermo Scientific NEPTUNE Multi Collector (MC) inductively-coupled plasma mass spectrometer (ICPMS) to yield information on geochemical origin. Samples from both cores ranging from 0.5 to 55.5 cm depth (1 cm downcore sampling resolution) were digested using double acid leaching followed by the isolation of lead from the matrix using AG1-X8 200-400 mesh anion exchange resin. All samples were measured with a $^{208}$Pb ion beam intensity of $>1\times10^{-10}$ A as an integration of >20 measurements, each integrating 5 s. Instrumental mass bias was corrected using the SBL74 $^{207}$Pb–$^{204}$Pb double spike developed at the University of Southampton (Ishizuka et al. 2003; Taylor et al. 2015). Pb standard NBS 981 gave results, $16.9403\pm27$ (2SD) for $^{206}$Pb/$^{204}$Pb, $15.4973\pm21$ for $^{207}$Pb/$^{204}$Pb and $36.7169\pm66$ for $^{208}$Pb/$^{204}$Pb. Procedural blanks measured with the samples contained <80 pg Pb.

## *Historical Research*

Catchment boundaries were determined using 5 m resolution onshore terrain data from NEXTMap Britain (a national IfSAR digital elevation database, Dowman et al. 2003) and spatial analyst tools in ArcGIS. Information on the former mining landscapes and metalliferous mining sites, output and locations within the Windermere catchment was then compiled from multiple sources, including published books and reports (Eastwood 1921; Shaw 1970; Postlethwaite 1975; Adams 1988, 1995; Tyler 2005, 2006) and publications from local groups including the Cumbrian Amenity Trust Mining History Society (CATMHS) and the Kendal and District Mine Research Society (KDMRS). The BRITPITS Mineral Occurrence Database (MOD), the Lake District Historic Environment Record (LDHER)[2], the English Heritage Archive (PastScape Record)[3], the National Trust Historic Buildings, Sites

[2] http://www.heritagegateway.org.uk

[3] http://www.english-heritage.org.uk/professional/archives-and-collections/nmr

and Monuments Record (HBSMR) and two additional websites[4,5] were used to provide further information of mineral workings.

The BGS BRITPITS database and the LDHER were used to generate a complete list of disused quarries in the catchment. Active quarries were derived from these searches, and also the BGS BRITPITS Directory of Mines and Quarries 2010 (Cameron et al. 2010) and Millward et al. (2000). Stream sediment geochemical data were derived from BGS Geochemical Baseline Survey of the Environment (G-BASE)[6]. Small, first order streams were sampled from 1978 to 1980 and analysis was through direct current optical emission spectrometry (British Geological Survey 1992; Johnson et al. 2005).

## Results

### *Sediment Accumulation Rates*

The CF:CS model of $^{210}$Pb dating was used to determine accumulation rates. Supported $^{210}$Pb activity in the North Basin (core +54-03/68 PC) was estimated to be 0.019 Bq/g, based on average activities at depths in the core where $^{210}$Pb reduced to near-constant activities. A linear fit through a plot of the natural logarithm of the determined excess $^{210}$Pb activities for each sample suggests an average accumulation rate of 0.17 cm/year (2 S.E. 0.15–0.21 cm/year). In the Lake District, the impact of the Chernobyl disaster (1968) is significant, with the input of most Chernobyl-derived Cs through direct atmospheric deposition during a few hours of intense rainfall after the incident. $^{137}$Cs activity in core +54-03/68 PC was measured in order to validate the $^{210}$Pb accumulation rate over the last 49 years. At the top of the core, a peak in $^{137}$Cs activity is taken to correspond to the 1986 Chernobyl incident (Ritchie and McHenry 1990). An additional in peak in $^{137}$Cs activity at a depth of $4.5 \pm 0.5$ cm is taken to correspond to the 1963 atmospheric testing of nuclear weapons (bomb maximum) (Fig. 16.3). This suggests an average sediment accumulation rate of $0.17 \pm 0.02$ cm/year from 1963 to 1986, which is consistent with the $^{210}$Pb accumulation rate.

$^{137}$Cs activity was not observed in the South Basin (core +54-03/57 PC) and $^{210}$Pb results were more variable, with outlier values between 1–5 cm depth. Following removal of outliers, $^{210}$Pb activity was estimated to be 0.033 Bq/g (based on observing the activity in the deepest samples where the excess Pb activity tends towards a baseline of zero) giving an accumulation rate of 0.14 cm/year (2 S.E. 0.08–0.56 cm/year) (Fig. 16.3). The likely presence of erosion surfaces in core +54-03/68 PC and +54-03/57 PC will be discussed further in the discussion section.

[4] http://www.cumbria-industries.org.uk

[5] http://www.mine-explorer.co.uk

[6] http://www.bgs.ac.uk/gbase

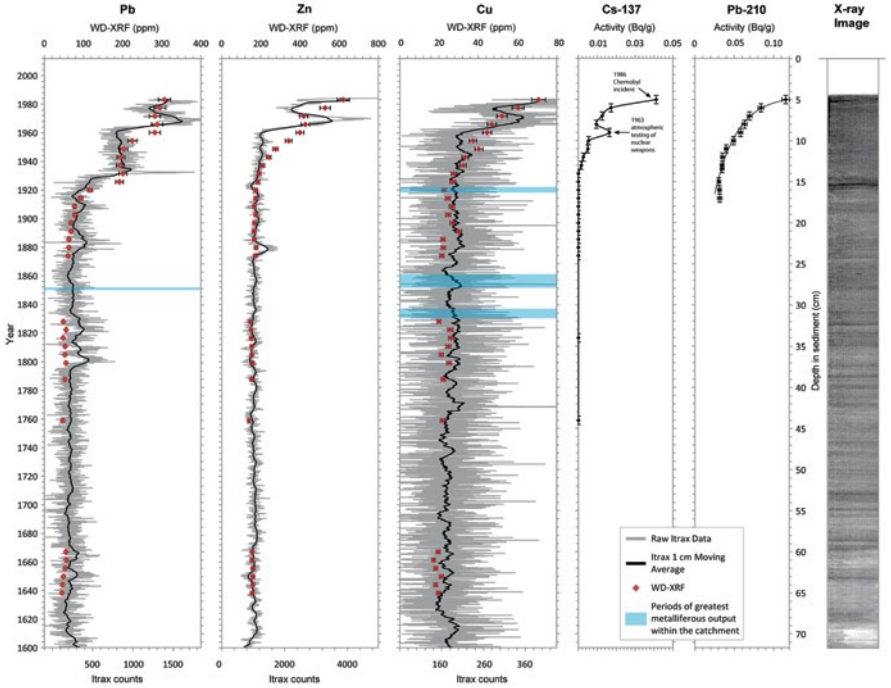


**Fig. 16.3** Elemental profiles, $^{137}Cs$ activity and total $^{210}Pb$ activity in core +54-03/68 PC (North Basin). Periods of metalliferous output are highlighted, continuous lines show Itrax peak areas, points show concentrations determined from sub-samples using WD-XRF and the X-ray image is from the Itrax core scanner. 4.52 cm is added to the sample depth to compensate for loss of sediment in the top of the core. (Reprinted (adapted) with permission from Miller et al. (2014), Copyright (2014) American Chemical Society)

## *Heavy Metal Profiles*

Itrax elemental profiles are presented as acquired but they have also been smoothed with a 1 cm moving average to aid comparison with the WD-XRF data, where the sample size was 1 cm. Itrax elemental profiles in the North Basin (core +54-03/68 PC) reflect conventional WD-XRF compositional variations and show a lake catchment that has been fairly stable over the period of sediment accumulation (Fig. 16.3). Within the top 12 cm of the recovered core (69 year period) there are significant deviations from this stability. The Itrax data show a stepwise increase in lead from 1935 to 1960, and increases in lead, zinc and copper are also observed from 1960 to 1968 and 1978 to 1984 (Fig. 16.3). This co-variation of elemental profiles indicates a common source for these contaminants.

In the South Basin (core +54-03/57 PC), Itrax and WD-XRF concentrations of lead and copper are relatively stable over the period of sediment accumulation; however, a marked increase is observed in lead from 1935 to 1950 and in copper from 1940 to 1950 (Fig. 16.4). Although zinc concentrations show a similar

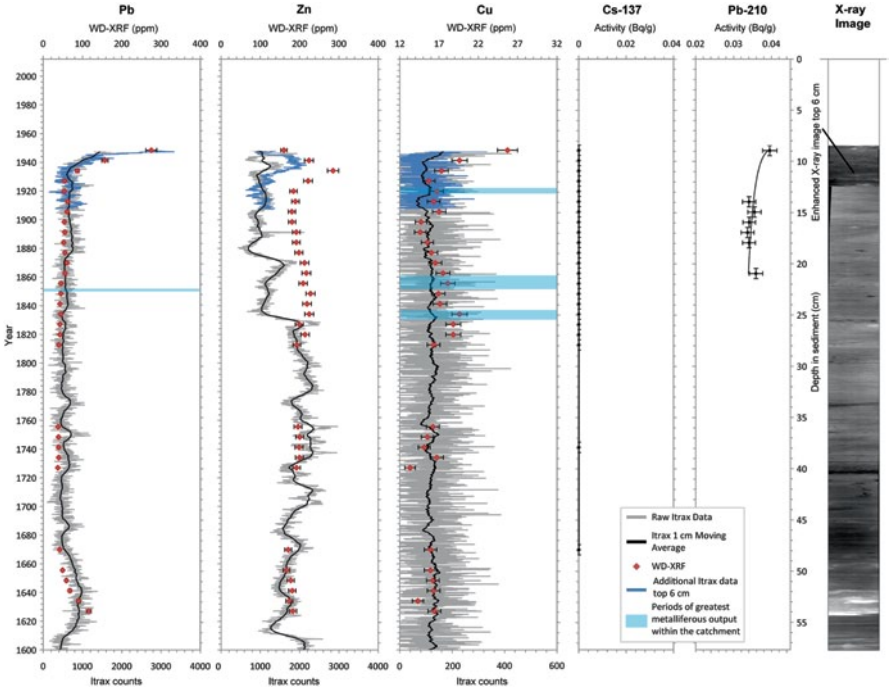


**Fig. 16.4** Elemental profiles, $^{137}$Cs activity and total $^{210}$Pb activity in core +54-03/57 PC (South Basin). Periods of metalliferous output are highlighted, continuous lines show Itrax peak areas, points show concentrations determined from sub-samples using WD-XRF and the X-ray image is from the Itrax core scanner. 8.4 cm is added to the sample depth to compensate for loss of sediment in the top of the core. (Reprinted (adapted) with permission from Miller et al. (2014), Copyright (2014) American Chemical Society)

increase, deeper in the core the Itrax zinc profile shows deviation whereas corresponding WD-XRF concentrations show a fairly regular profile (Fig. 16.4). This disagreement between Itrax and WD-XRF data is caused by an inter-element effect due to significant variations in iron content (there is a negative correlation between relatively high concentrations of iron and trace concentrations of zinc). WD-XRF fundamental parameter software corrects for inter-element effects, whereas this capability is not readily provided for in the Itrax software. It is also notable that smoothing the Itrax data can lead to a clearer comparison with the WD-XRF data. The latter data are in effect smoothed at the 1-cm scale and therefore smoothing the higher resolution Itrax data can be a useful part of the visualisation process (this is a feature of ItraxPlot software see Chap. 26).

## *Lead Isotopes*

$^{206}$Pb/$^{207}$Pb in the North and South Basin core shows a similar profile over time (based on the sediment accumulation rates derived from $^{210}$Pb dating). The data,

which has been depth shifted to compensate for loss of sediment in the top of the cores (see discussion section), reveal the oldest samples (from 1810 to 1620) have a relatively constant $^{206}Pb/^{207}Pb$ around 1.177. These samples trend towards end-member ratios for early-/pre industrial sediments (Hamilton and Clifton 1979; Croudace and Cundy 1995). Samples ranging in age from the 1920s to the 1840s are characterised by a $^{206}Pb/^{207}Pb$ around 1.179 and trend towards end-member ratios for Carboniferous coal (Shepherd et al. 2009). Samples characterised by a low $^{206}Pb/^{207}Pb$ (ranging in age from 1980 to the 1920s) trend towards the isotopically distinguishable UK gasoline end-member ratio (Monna et al. 1997) (Fig. 16.5, Table 16.1).

## Discussion

A number of studies have dated recent sediments in Windermere and other lakes in the catchment (Aston et al. 1973; Pennington et al. 1973; Pennington et al. 1976; Appleby et al. 1991; Appleby et al. 2003; Barker et al. 2005). In the North Basin, $^{210}Pb$ dates from a 1997 mini-core (located c. 600 m SW of core +54-03/68 PC) suggest a mean accumulation rate of approximately 0.18 cm/year (Appleby 2008). This is in agreement (within the estimated uncertainty) with the accumulation rate of 0.17 cm/year determined for core +54-03/68 PC. Appleby (2008) also identified two peaks in the $^{137}Cs$ record at 4.5 and 10.5 cm related to the 1986 Chernobyl incident and the 1963 bomb maximum. In core +54-03/68 PC, two peaks in $^{137}Cs$ activity are also identified: at the top of the core (related to the 1986 Chernobyl incident) and at $4.5 \pm 0.5$ cm. This suggests a loss of at least 4.52 cm (0.17 cm/yr over 26 years) of sediment from the top of the core (Fig. 16.3). In the South Basin, outlier $^{210}Pb$ values and the absence of $^{137}Cs$ suggests a loss of at least 60 years of accumulation (initial input of $^{137}Cs$ estimated to be 1952, related to atmospheric nuclear weapons testing). This suggests a loss of at least 8.4 cm (0.14 cm/yr over 60 years) of sediment from the top of the core (Fig. 16.4). The $^{210}Pb$ accumulation rates are valid in the surface sediments; however, it is important to note that the accumulation rate may not be representative at depth, and therefore the depth in the core and the extrapolated chronology are displayed for comparison (Figs. 16.3 and 16.4).

In the North Basin, Itrax elemental profiles and WD-XRF concentrations identify an increase in lead concentration from 1935 to 1960, and a significant increase from 1960 to 1968. A similar increase is observed in the South Basin from 1935 to 1950 (Figs. 16.3 and 16.4). These increases are most likely the result of increased industrialisation, urbanisation and road traffic following the introduction and use of ($^{206}Pb$-depleted) leaded gasoline post-1923. Within the UK, this led to a dramatic increase in atmospheric lead emissions, particularly during the 1960s and 1970s (Farmer et al. 1996; Komárek et al. 2008; Shepherd et al. 2009). High-precision lead isotopes (measured by double spike, errors $< \pm 0.002\,\%$) also reveal a significant decline in $^{206}Pb/^{207}Pb$ from the 1920s to 1980 (attributable to the use of alkyl-leaded fuel), demonstrating a significant anthropogenic input of lead in recent sediments (Fig. 16.5). In addition, $\Delta 7/4$ (calculated relative to the Northern Hemisphere Ref-

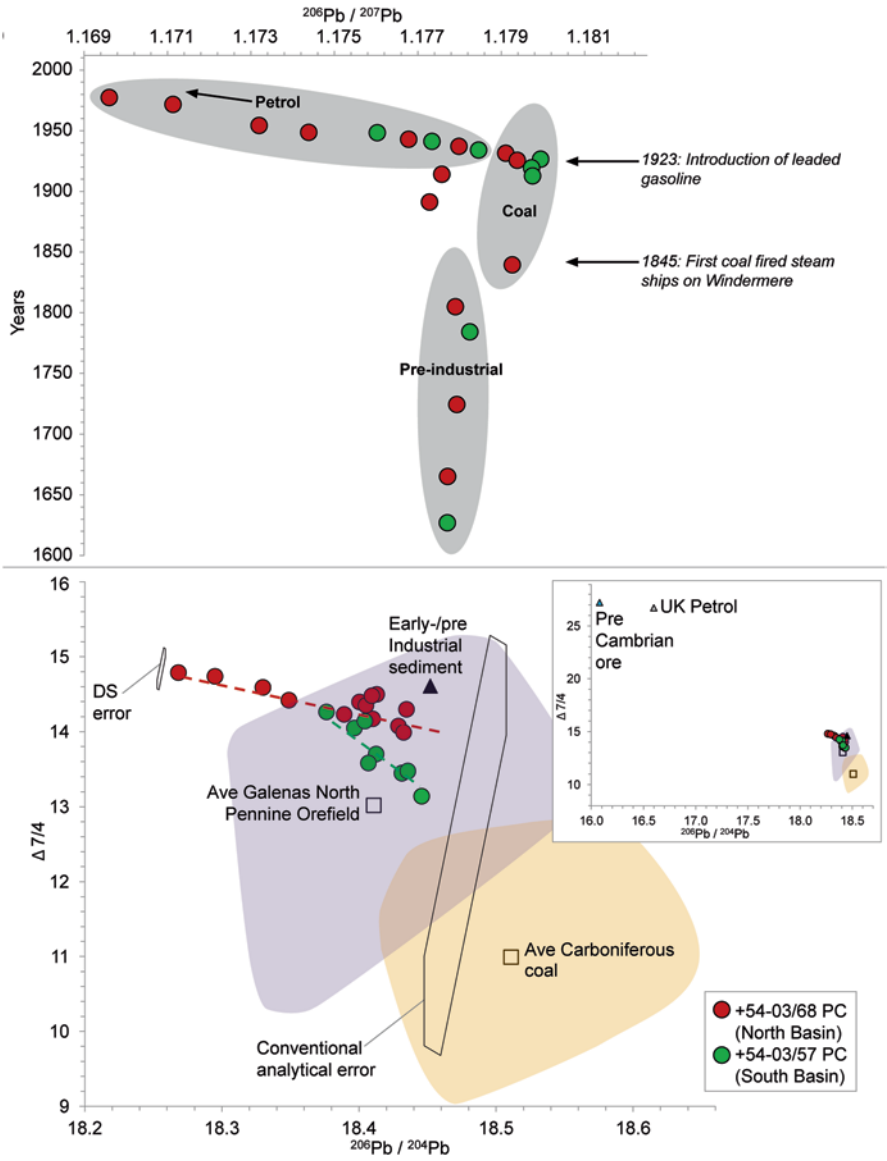


**Fig. 16.5** *Upper panel*: lead isotope ratios ($^{206}Pb/^{207}Pb$) over time. *Lower panel*: Δ7/4 versus $^{206}Pb/^{204}Pb$ with double-spike and conventional analytical errors for comparison, average (mean) end-member ratio for pre-/early industrial sediment and Carboniferous coal and galena ratios (derived by conventional lead isotope measurement techniques). Insert shows Pre-Cambrian ore ratios and UK gasoline end-member ratio. See Table 16.1 for details. Δ7/4 is $^{207}Pb/^{204}Pb$ expressed relative to the Northern Hemisphere Reference line (Hart 1984) and is calculated as $(^{207}Pb/^{204}Pb_{sample} - (0.1084 \times (^{206}Pb/^{204}Pb_{sample}) + 13.491)) \times 100$. This parameter enables subtle variations in Pb isotope composition to be visualised while retaining the linear nature of mixing trends in Pb–Pb isotope space. (Reprinted (adapted) with permission from Miller et al. (2014), Copyright (2014) American Chemical Society)

**Table 16.1** Lead isotope ratios in Windermere samples, major ore deposits and contemporary environmental materials. Errors are within measurement precision and represent 2 S.E. quoted as the last two d.p. of the isotope ratio. Details of the external standard reproducibility are given in the text. Windermere samples have been depth shifted to compensate for loss of sediment in the top of the cores (see discussion section). Ratios are displayed in Fig. 16.5. (Reprinted (adapted) with permission from Miller et al. (2014), Copyright (2014) American Chemical Society)

| Core | Depth in core (cm) | $^{206}Pb/^{204}Pb$ | ± | $^{207}Pb/^{204}Pb$ | ± | $^{208}Pb/^{204}Pb$ | ± |
|---|---|---|---|---|---|---|---|
| +54-03/68 PC North Basin | 6.02 | 18.2682 | 12 | 15.6192 | 11 | 38.2692 | 35 |
| | 7.02 | 18.2949 | 39 | 15.6216 | 38 | 38.3002 | 117 |
| | 10.02 | 18.3299 | 9 | 15.6239 | 9 | 38.3364 | 27 |
| | 11.02 | 18.3488 | 12 | 15.6242 | 12 | 38.3578 | 37 |
| | 12.02 | 18.3892 | 20 | 15.6267 | 19 | 38.4011 | 60 |
| | 13.02 | 18.4100 | 27 | 15.6283 | 25 | 38.4247 | 79 |
| | 14.02 | 18.4288 | 13 | 15.6294 | 13 | 38.4484 | 39 |
| | 15.02 | 18.4325 | 12 | 15.6290 | 12 | 38.4501 | 37 |
| | 17.02 | 18.4051 | 20 | 15.6296 | 19 | 38.4174 | 61 |
| | 21.02 | 18.4004 | 11 | 15.6296 | 11 | 38.4097 | 33 |
| | 30.02 | 18.4346 | 11 | 15.6323 | 10 | 38.4747 | 32 |
| | 36.02 | 18.4129 | 10 | 15.6319 | 10 | 38.4303 | 30 |
| | 60.02 | 18.4094 | 19 | 15.6314 | 18 | 38.4289 | 57 |
| +54-03/57 PC South Basin | 8.9 | 18.3762 | 12 | 15.6256 | 11 | 38.3754 | 35 |
| | 9.9 | 18.3968 | 9 | 15.6257 | 8 | 38.3906 | 25 |
| | 10.9 | 18.4121 | 18 | 15.6239 | 17 | 38.4089 | 54 |
| | 11.9 | 18.4356 | 22 | 15.6242 | 21 | 38.4394 | 66 |
| | 12.9 | 18.4453 | 42 | 15.6218 | 14 | 38.4388 | 42 |
| | 13.9 | 18.4313 | 37 | 15.6234 | 35 | 38.4311 | 109 |
| | 31.9 | 18.4067 | 15 | 15.6221 | 15 | 38.4125 | 45 |
| | 53.9 | 18.4042 | 29 | 15.6274 | 28 | 38.4025 | 87 |

**Table 16.1** (continued)

| Core | Depth in core (cm) | $^{206}Pb/^{204}Pb$ | ± | $^{207}Pb/^{204}Pb$ | ± | $^{208}Pb/^{204}Pb$ | ± |
|---|---|---|---|---|---|---|---|
| *End member* | *Source* | | *Isotopic composition of lead* | | | *Reference* | |
| | | | *$^{206}Pb/^{204}Pb$* | *$^{207}Pb/^{204}Pb$* | | | |
| Carboniferous coal | Durham Northumberland coalfield ($n=11$) | | 18.51 | 15.60 | | Shepherd et al. (2009) | |
| Galenas (Pb–Zn mineralisation) | North Pennine Orefield ($n=26$) | | 18.41 | 15.61 | | Shepherd et al. (2009) | |
| Pre Cambrian (ores in UK lead-alkyls) | Australia: Mt Isla | | 16.08 | 15.50 | | Chow et al. (1975) | |
| Pre-/early industrial sediments | Swansea Bay | | 18.45 | 15.63 | | Hamilton and Clifton (1979) | |
| | Southampton Water | | 18.45 | 15.63 | | Croudace and Cundy (1995) | |
| Gasoline | Southampton 1994–1995 ($n=7$) | | 16.60 | 15.55 | | Monna et al. (1997) | |

erence Line; Hart 1984) trends towards the UK gasoline end-member ratio which suggests leaded gasoline is a common source of lead in recent sediments (Fig. 16.5, lower panel). The lead derived from gasoline would be deposited generally over a broad area but would be expected to be higher near busy roads where road vehicles (seasonal heavy tourist traffic) would deposit exhaust residues. Later, this deposited material would be transported into the lake along with other particulates.

The isotopic character of lead changes with depth, and samples ranging in age from the 1840s to the 1920s trend towards the end-member ratio for Carboniferous coal (Shepherd et al. 2009) (Fig. 16.5). In Windermere, the most likely source of Carboniferous coal is coal-fired steam ships, which operated on the lake from 1845 onwards (Pattinson 1981; Pickering 2001; McGowan et al. 2012). Expansion in the use of these boats took place following arrival of the railway in Windermere in 1847 and Lakeside in 1869, and also the introduction of a steam cargo service in 1872 (Pattinson 1981). From the 1920s onwards, motor vehicles were common and the age of steam on Windermere gradually came to a close. The decline observed in $^{206}Pb/^{207}Pb$ from the 1920s to 1980 is most likely due to the end of coal-fired steamer operation on the lake and the introduction and use of leaded gasoline. Coal combustion (associated with the Industrial Revolution) also represents another possible source of Carboniferous coal.

Analysis of Δ7/4 also identifies components of natural lead and galena ore from mineral veins, most likely derived from the discharge of lead-rich waste from abandoned mines (Carboniferous Pb–Zn mineralisation) (Fig. 16.5, lower panel). To the north of the Windermere catchment, metalliferous mining exploited mineral (copper, haematite and lead-zinc) veins within Ordovician (BVG) rocks, particularly during the latter half of the nineteenth century (Fig. 16.2, Table 16.2). In particular, lead mines in the catchment worked mineral veins within the fault system at Greenhead Gill and Coniston United. The lead mine high up Greenhead Gill to the north of Grasmere was worked for lead and silver and although zinc was present in higher quantities it was not mined because it had no commercial value (Shaw 1939). Stream sediment geochemical data in this region identifies elevated levels of lead (>200 ppm). Natural lead is derived from surface weathering (particularly in headwater regions not influenced by mining activities), soil erosion and Pb–Zn mineralisation. The elevated levels of lead in Windermere are therefore considered to be a mixture of natural lead, and three major components of anthropogenic lead (gasoline lead, coal combustion lead and lead derived from Carboniferous Pb–Zn mineralisation).

Copper concentrations also show an increase from 1960 to 1968 and 1978 to 1984 in the North Basin and from 1940 to 1950 in the South Basin (Figs. 16.3 and 16.4). Lead and zinc concentrations (particularly in the North Basin) show similar variations, suggesting a co-variance of these contaminants and a common source. To the north of Windermere, a number of up-system sediment traps (e.g. Grasmere, Elterwater and Langdale Tarn) (Fig. 16.2) have limited the amount of mining related heavy metals entering Windermere. As a result, periods of metal workings do not correlate with peaks in mining related heavy metals due to the trapping efficiency of these up-system lakes. For example, the largest copper mine in the catchment

**Table 16.2** Disused copper, lead and iron mines in the Windermere catchment. (Reprinted (adapted) with permission from Miller et al. (2014), Copyright (2014) American Chemical Society)

| Mine | Mineral | Coordinates (UTM) | Period of operation | Greatest period mineral output | Details |
|---|---|---|---|---|---|
| Greenburn (Great Coniston Mine/New Coniston | Copper | 493746, 6029173 | 1845, evidence for 1690; closed 1942 (Adams 1988, 1995; Blundell 1994) | 1854–1861 (mid nineteenth century) (Millward and Robinson 1974) | Suspension in late nineteenth century, re-opened in early twentieth century |
| Hawkshead trial | Copper | 498289, 6025614 | c. 1830 (Tyler 2006) | – | Small copper trial |
| Skelwith | Copper | 500290, 6029024 | Opened 1540 (English Heritage Archive), closed 1901 | 1850s | Post medieval copper mine |
| Dunmail raise trial | Copper | 499665, 6035813 | c. 1920 (Adams 1988, 1995; Tyler 2005, 2006) | – | Good quality copper ore, not in commercial quantities |
| Providence (Tongue Gill Iron Mines) | Iron | 4986619, 6037515 | Providence and Fairfield: start unknown, although mine supplied ore to the smelter in Langdale around 1700; re-opened in 1873, closed in 1877 (Tyler 2005). Re-opened in 1930s (Postlethwaite 1975) | Providence and Fairfield: early seventeenth century, revival 1874–1876 (Shaw 1970) | Providence and Fairfield: ancient iron ore mines |
| Fairfield | Iron | 498659, 6036880 | | | |
| Greenburn valley trial | Iron | 496900, 6037679 | 1880s | – | Small trial (Tyler 2006) |
| Greenhead Gill (Grasmere lead mine) | Lead | 499665, 6035813 | Opened 1564, closed 1573 (Shaw 1970; Tyler 2005). Re-worked in 1870s but soon abandoned (KDMRS newsletter, 1983, Tyler 2005, 2006) | – | Extensive account, including production data (Tyler 2005) |
| Coniston United | Lead | 500196, 6028966 | c. 1853 (Adams 1988, 1995) | – | Group of trials, two levels, little mineralisation |

was at Greenburn to the west of Windermere, where five named E-W copper veins (through coarse ashes and breccias of the BVG) yielding copper pyrites and a large quantity of oxide of copper were worked to varying degrees (Postlethwaite 1975) (Table 16.2). Stream sediment geochemical data (BGS G-BASE) identifies elevated levels of copper (above the background level of 10–25 ppm) near the mine, most likely derived from spoil heaps and workings (Fig. 16.2). At Elterwater (downstream from Greenburn Mine), copper contamination is recorded in sediments (Pickering 2001), demonstrating the effectiveness of up-system sediment traps. Copper increases in the 1940s and 1960s could also be due to flood-induced metal inwash after the cessation of mining (similar to findings in other upland regions of Britain; Kelly 1991), or weathering of bedrock in the catchment. It is likely that the presence of mineral veins acts as conduits for heavy metals in some headwater regions which are not influenced by mining activities. Increases in zinc could also be due to anthropogenic activity within the catchment, in the form of processed waste and human sewage inputs. In particular, an increase in direct discharge of treated sewage effluents in the 1960s corresponds with an increase in zinc at this time.

## Conclusions

This study has investigated two sediment cores collected from Windermere, the largest lake in England, using a range of high resolution and high sensitivity geochemical methods. The variation of Cu, Zn and Pb in particular are investigated using high-resolution Itrax analysis (validated against WD-XRF), radiochronology ($^{210}$Pb and $^{137}$Cs) and double spike lead isotopes (offering ten times the precision of the conventional single spike method). An evaluation of the data provides an insight into the deposition and sources of pollutants that have entered the lake from the surrounding catchment. By integrating data derived from these geochemical methods the timing, scale and origin of anthropogenic inputs into a lacustrine environment are powerfully presented.

## References

Adams J (1988) Mines of the Lake District fells. Dalesman Books, Clapham

Adams J (1995) Mines of the Lake District fells, 2nd edn. Dalesman Publishing Company, Clapham

Anderton J, Haworth EY, Horne DJ, Wray DS (1998) Environmental impacts of lead mining in the Ullswater catchment (English Lake District): dam failures and flooding. In: Bennett MR, Doyle P (eds) Issues in environmental geology: a British perspective. The Geological Society, London, pp 226–242

Appleby P (2008) Three decades of dating recent sediments by fallout radionuclides: a review. Holocene 18:83–93

Appleby P, Richardson N, Nolan P (1991) $^{241}$Am dating of lake sediments. Hydrobiologia 214:35–42

Appleby PG, Haworth EY, Michel H, Short DB, Laptev G, Piliposian, GT (2003) The transport and mass balance of fallout radionuclides in Blelham Tarn, Cumbria (UK). J Paleolimnol 29:459–473

Aston SR, Bruty D, Chester R, Padgham RC (1973) Mercury in lake sediments: a possible indicator of technological growth. Nature 241:450–451

Barker PA, Pates JM, Payne RJ, Healey R. M (2005) Changing nutrient levels in Grasmere, English Lake District, during recent centuries. Freshw Biol 50:1971–1981

Barlow D, Harris E, McFarlane A (2009a) Windermere fluvial audit. Report A: catchment scale geomorphology—technical report. Report to Environment Agency North West Region prepared by JACOBS Engineering UK Ltd. Technical Report

Barlow D, Harris E, McFarlane A (2009b) Windermere fluvial audit. Report B: catchment action plan. Report to Environment Agency North West Region prepared by JACOBS Engineering UK Ltd. Technical Report

Blundell DJ (1994) Greenburn or great Coniston copper mine Little Langdale. A collected history. In: Borthwick D (ed) The mine explorer, vol 4. Cumbria Amenity Trust Mining History Society, pp 76–80. www.catmhs.org.uk

British Geological Survey (1992) Regional geochemistry of the Lake District and adjacent areas

British Geological Survey (1996) Ambleside. England and Wales Sheet 38. Solid geology, vol 1. Keyworth, Nottingham, pp 50000

British Geological Survey (2000) Geology of the Ambleside district. The Stationary Office, London

Cameron DG, Idoin NE, Brown TJ, Patton MAG, McGinn C, Mankelow JM (2010) Directory of mines and quarries. British geological survey, 9th edn. Keyworth, Nottingham

Chiverrell RC, Sear D, Dearing J, Warburton J, Schillereff D, Croudace IW (2012) Farming, mining and extreme floods: impacts of accelerated sediment flux to Bassenthwaite Lake, International Palaeolimnology Conference (IPS2012), August 21–24th, Glasgow SECC.

Chow TJ, Snyder CB, Earl JL (1975) Isotope ratios of lead as pollutant source indicators. In: Isotope ratios as pollutant source and behaviour indicators. IAEA, Vienna, pp 95–108

Croudace IW, Cundy AB (1995) Heavy metal and hydrocarbon pollution in recent sediments from Southampton water, Southern England: a geochemical and isotopic study. Environ Sci Technol 29:1288–1296

Croudace IW, Williams-Thorpe O (1988) A low dilution, wavelength-dispersive x-ray fluorescence procedure for the analysis of archaeological rock artefacts. Archaeometry 30:227–236

Croudace IW, Rindby A, Rothwell RG (2006) ITRAX: description and evaluation of a new multifunction X-ray core scanner. Rothwell R (ed) New techniques in sediment core analysis, vol 267. Geological Society Special Publication, pp 51–63

Croudace IW, Warwick PE, Morris JE (2012) Evidence for the preservation of technogenic tritiated organic compounds in an estuarine sedimentary environment. Environ Sci Technol 46:5704–5712

Dowman I, Balan P, Renner K, Fischer P (2003) An evaluation of Nextmap terrain data in the context of UK national datasets. Technical Report

Eastwood T (1921) Memoirs of the geological survey. Special reports on the mineral resources of Great Britain: the lead and zinc ores of the Lake District, vol 22

Farmer JG, Eades LJ, Mackenzie AB, Kirika A, Bailey-Watts TE (1996) Stable lead isotope record of lead pollution in Loch Lomond sediments since 1630 A.D. Environ Sci Technol 30:3080–3083

Farmer JG, Eades LJ, Graham MC (1999) The lead content and isotopic composition of British coals and their implications for past and present releases of lead to the UK environment. Environ Geochem Health 21:257–272

Flynn WW (1968) Determination of low levels of polonium-210 in environmental materials. Anal Chim Acta 43:221–227

Grayson RP, Plater AJ (2009) A lake sediment record of Pb mining from Ullswater, English Lake District, UK. J Paleolimnol 42:183–197

Gulson BL, Mizon KJ, Law AJ, Korsch MJ, Davis JJ, Howarth D (1994) Source and pathways of lead in humans from the broken hill mining community; an alternative use of exploration methods. Econ Geol 89:889–908

Hamilton-Taylor J (1979) Enrichments of zinc, lead, and copper in recent sediments of Windermere, England. Environ Sci Technol 13:693–697

Hamilton-Taylor J (1983) Heavy metal enrichments in the recent sediments of six lakes in northwest England. Environ Technol Lett 4:115–122

Hamilton EI, Clifton RJ (1979) Isotopic abundances of lead in estuarine sediments, Swansea Bay, Bristol Channel. Estuar Coast Mar Sci 8:271–278

Hansmann W, Köppel V (2000) Lead-isotopes as tracers of pollutants in soils. Chem Geol 171:123–144

Hart SR (1984) A large-scale isotope anomaly in the Southern Hemisphere mantle. Nature 309:753–757

Hatfield RG, Maher BA, Pates JM, Barker PA (2008) Sediment dynamics in an upland temperate catchment: changing sediment sources, rates and deposition. J Paleolimnol 40:1143–1158

Ishizuka O, Taylor RN, Milton JA, Nesbitt RW (2003) Fluid-mantle interaction in an intra-oceanic arc: constraints from high-precision Pb isotopes. Earth Planet Sci Lett 211:221–236

Johnson CC, Breward N, Ander EL, Ault L (2005) G-BASE: baseline geochemical mapping of Great Britain and Northern Ireland. Geochem Explor Environ Anal 5:347–357

Kelly M (1991) Mining and the freshwater environment. Elsevier Applied Science, London

Kember HM (2001) A study of metal contamination of sediments within Lake Ullswater and the Glenridding Beck catchment. Undergraduate Dissertation, Department of Environmental Science, University of Lancaster

Komárek M, Ettler V, Chrastný V, Mihaljevic M (2008) Lead isotopes in environmental sciences: a review. Environ Int 34:562–577

McGowan S, Barker P, Haworth EY, Leavitt PR, Maberly SC, Pates J (2012) Humans and climate as drivers of algal community change in Windermere since 1850. Freshw Biol 57:260–277

Miller H, Bull JM, Cotterill JC, Dix JK, Winfield IJ, Kemp AES, Pearce RB (2013) Lake bed geomorphology and sedimentary processes in glacial lake Windermere, UK. J Maps 9:299–312

Miller H, Croudace IW, Bull JM, Cotterill JC, Dix JK, Taylor RN (2014) A 500 year sediment lake record of anthropogenic and natural inputs to Windermere (English Lake District) using double-spike lead isotopes, radiochronology, and sediment microanalysis. Environ Sci Technol 48:7254–7263

Millward R, Robinson A (1974) The regions of Britain. Eyre Methuen, The Lake District

Millward D, Johnson EW, Beddoe-Stephens B, Young B, Kneller BC, Lee MK, Fortey NJ (2000) British geological survey: geology of the Ambleside district. Memoir for 1:50,000 Geological Sheet 38 (England and Wales). The Stationary Office, London

Mitchell GH (1956) The geological history of the Lake District. Proc Yorks Geol Soc 30:407–463

Monna F, Lancelot J, Croudace IW, Cundy AB, Lewis JT (1997) Pb isotopic composition of airborne particulate material from France and the southern United Kingdom: implications for Pb pollution sources in urban areas. Environ Sci Technol 31:2277–2286

Parker JE, Maberly SC (2000) Biological response to lake remediation by phosphate stripping: control of Cladophora. Freshw Biol 44:303–309

Pattinson GH (1981) The great age of steam on Windermere. The Windermere Nautical Trust

Pennington W, Cambray RS, Fisher EM (1973) Observations on lake sediments using fallout $^{137}Cs$ as a tracer. Nature 242:324–326

Pennington W, Cambray RS, Eakins JD, Harkness DD (1976) Radionuclide dating of the recent sediments of Blelham Tarn. Freshw Biol 6:317–331

Pickering AD (2001) Windermere: restoring the health of England's largest lake. Freshwater Biological Association, Ambleside Special Publication No. 11

Pinson LJW, Vardy ME, Dix JK, Henstock TJ, Bull JM, Maclachlan SE (2013) Deglacial history of glacial lake Windermere, UK: implications for the central British and Irish Ice Sheet. J Quat Sci 28:83–94

Postlethwaite J (1975) Postlethwaite's mines and mining in the English Lake District. Michael Moon, Beckermet
Reynolds CS, Irish AE (2000) The phytoplankton of Windermere (English Lake District). Freshwater Biological Association, Ambleside
Ritchie JC, McHenry JR (1990) Application of radioactive fallout cesium-137 for measuring soil erosion and sediment accumulation rates and patterns: a review. J Environ Qual 19:215–233
Robbins JA (1978) Geochemical and geophysical applications of radioactive lead isotopes. In: Nriagu JO (ed) Biochemistry of lead. Elsevier, Amsterdam, pp 285–393
Sabater S, Haworth EY (1995) An assessment of recent trophic changes in Windermere South Basin (England) based on diatom remains and fossil pigments. J Paleolimnol 14:151–163
Schillereff D, Chiverrell R, Macdonald N, Hooke J (2013) A multi-proxy lake sediment record of recent anthropogenic influence on catchment processes from Brotherswater, northwest England. Oral presentation at European Geosciences Union General Assembly 2013, 7–12 April 2013, Vienna, Austria. Session: landscape in the Anthropocene: state of the art and future directions
Shaw WT (1939) Elizabethan Mining: an account of a visit paid to an old lead mine near Grasmere, Lake District
Shaw WT (1970) Mining in the Lake Counties. Dalesman, Clapham
Shepherd TJ, Chenery SR, Pashley V, Lord RA, Ander LE, Breward N, Hobbs SF, Horstwood M, Klinck BA, Worrall F (2009) Regional lead isotope study of a polluted river catchment: River Wear, Northern England, UK. Sci Total Environ 407:4882–4893
Talling JF (1999) Some English lakes as diverse and active ecosystems: a factual summary and source book. Freshwater Biological Association, Far Sawrey
Taylor RN, Ishizuka O, Michalik A, Milton JA, Croudace IW (2015) Evaluating the precision of Pb isotope measurement by mass spectrometry. J Anal Atomic Spectrom 30(1):198–213
Tyler I (2005) Thirlmere mines and the drowning of the valley. Blue Rock Publications, Cumbria
Tyler I (2006) The lakes and Cumbria mines guide. Blue Rock Publications, Cumbria
Yang HD, Rose N (2005) Trace element pollution records in some UK lake sediments, their history, influence factors and regional differences. Environ Int 31:63–75
Yang HD, Rose NL, Battarbee RW, Boyle JF (2002) Mercury and lead budgets for Lochnagar, a Scottish mountain lake and its catchment. Environ Sci Technol 36(7–8):1383–1388
Williams T (1991) A sedimentary record of the deposition of heavy metals and magnetic oxides in the Loch Dee basin, Galloway, Scotland, since c. AD 1500. Holocene 1:142–150
Woodcock NH, Soper NJ (2006) The Acadian orogeny: the mid-Devonian phase of deformation that formed slate belts in England and Wales. In: Benchley PJ, Rawson F (eds) The geology of England and Wales, 2nd edn. The Geological Society, London
Woodhead JD, Volker F, McCulloch MT (1995) Routine lead-isotope determinations using a Pb-207 Pb-204 double spike—a long-term assessment of analytical precision and accuracy. Analyst 120:35–39

# Chapter 17
# ITRAX Core Scanner Capabilities Combined with Other Geochemical and Radiochemical Techniques to Evaluate Environmental Changes in a Local Catchment, South Sydney, NSW, Australia

**P. Gadd, H. Heijnis, C. Chagué-Goff, A. Zawadzki, D. Fierro, P. Atahan, Ian W. Croudace and J. Goralewski**

**Abstract** In this study, geochemical and radioanalytical techniques are used together with the ITRAX core scanner to reconstruct the environmental history of Mill Creek catchment, located on the south-western fringes of Sydney. This ITRAX capability study was undertaken to investigate environmental changes in a local catchment which incorporates a nuclear research reactor, a small legacy nuclear waste burial ground, extensive new housing developments, a large rubbish tip, as well as quarries. This catchment changed from being near pristine in the 1950's to an extensively developed catchment with wide ranging land uses. This rapid development has led to silting up near the mouth of the creek, and there is also evidence of periodic siltation triggered by catchment disturbance from local bushfires, associated with peaks in magnetic susceptibility. The sedimentary environment changed from a creek system to a mangrove swamp and saltmarsh. Changes in Cu, Zn and Pb distributions over the last 60 years suggest an anthropogenically-driven input, although concentrations measured by WD-XRF indicate that the level of urbanisation is lower in the study area than in many of the more industrialised and urbanised neighbouring catchments of Sydney estuary and Botany Bay. The activities of $^{239+240}$Pu and $^{241}$Am in the sediment are below detection limit, which strongly suggests that the legacy nuclear waste has not entered the creek system.

P. Gadd (✉) · H. Heijnis · C. Chagué-Goff · A. Zawadzki · D. Fierro · P. Atahan · J. Goralewski
Institute for Environmental Research, Australian Nuclear Science and Technology Organisation (ANSTO), Lucas Heights, NSW 2234, Australia
e-mail: psp@ansto.gov.au

C. Chagué-Goff
School of Biological, Earth and Environmental Sciences, UNSW Australia, Sydney, NSW 2052, Australia

I. W. Croudace
Ocean and Earth Science, National Oceanography Centre, University of Southampton, Waterfront Campus, European Way, Southampton SO14 3ZH, UK



I. W. Croudace, R. G. Rothwell (eds.), *Micro-XRF Studies of Sediment Cores*, Developments in Paleoenvironmental Research 17, DOI 10.1007/978-94-017-9849-5_17

**Keywords** ITRAX · μXRF · Alpha and gamma spectrometry · Sediment quality · Laser Diffraction Particle Size Analysis · Magnetic Susceptibility · $^{210}$Pb Dating

## Introduction

In the last decade, the use of sediment core scanners has become extensive across the world; however, the first Cox Analytical ITRAX micro-X-Ray Fluorescence (μXRF) core scanner in Australia has only been operational since early 2012. In this study we examine a sediment core from Mill Creek catchment to demonstrate the capabilities of the ITRAX core scanner based at the Australian Nuclear Science and Technology Organisation (ANSTO). This core scanner provides high resolution optical and X-radiograph images, elemental and magnetic susceptibility data. The latter are generated via a Bartington Magnetic Susceptibility meter that records the response to ferromagnetic minerals.

Mill Creek catchment is a local catchment which incorporates a nuclear research site, with two research reactors (one operational and one decommissioned), a small legacy nuclear waste site which was used from 1960 and abandoned in 1968, extensive new housing developments from the 1970s onwards, a large rubbish tip which developed from a small municipal tip to a large waste disposal site from 1990 onwards, as well as quarries. It has evolved from being a near pristine catchment with development covering about 5 % of its area in the 1950s, to having developed areas covering approximately 40 % at present.

The aim of this study was to reconstruct the environmental changes and contamination history in Mill Creek catchment, based on the analysis of a sediment core taken in its lower reaches (Fig. 17.1). The multi-proxy approach included ITRAX XRF elemental data and radiograph, magnetic susceptibility, grain-size characteristics, actinide activities, elemental concentrations obtained by conventional wavelength dispersive x-ray fluorescence analysis (WD-XRF) and radiometric dating. Actinide ($^{239+240}$Pu and $^{241}$Am) activities were determined as they are known to be present at the legacy waste site (Payne et al. 2013).

## Methods

### *Sampling*

A 40 cm sediment core was taken in 2012 from the Mill Creek saltmarsh, near the confluence with the Georges River, southwest of Sydney, New South Wales, Australia (Fig. 17.1). The core was transported vertically to prevent disturbance of the sediment-water interface and was later split in half with one half of the core being immediately scanned on the ITRAX. The second half of the core was visually inspected and described, before being subsampled in 1cm intervals that were placed in resealable plastic bags, then stored at 4 °C until further analysis.

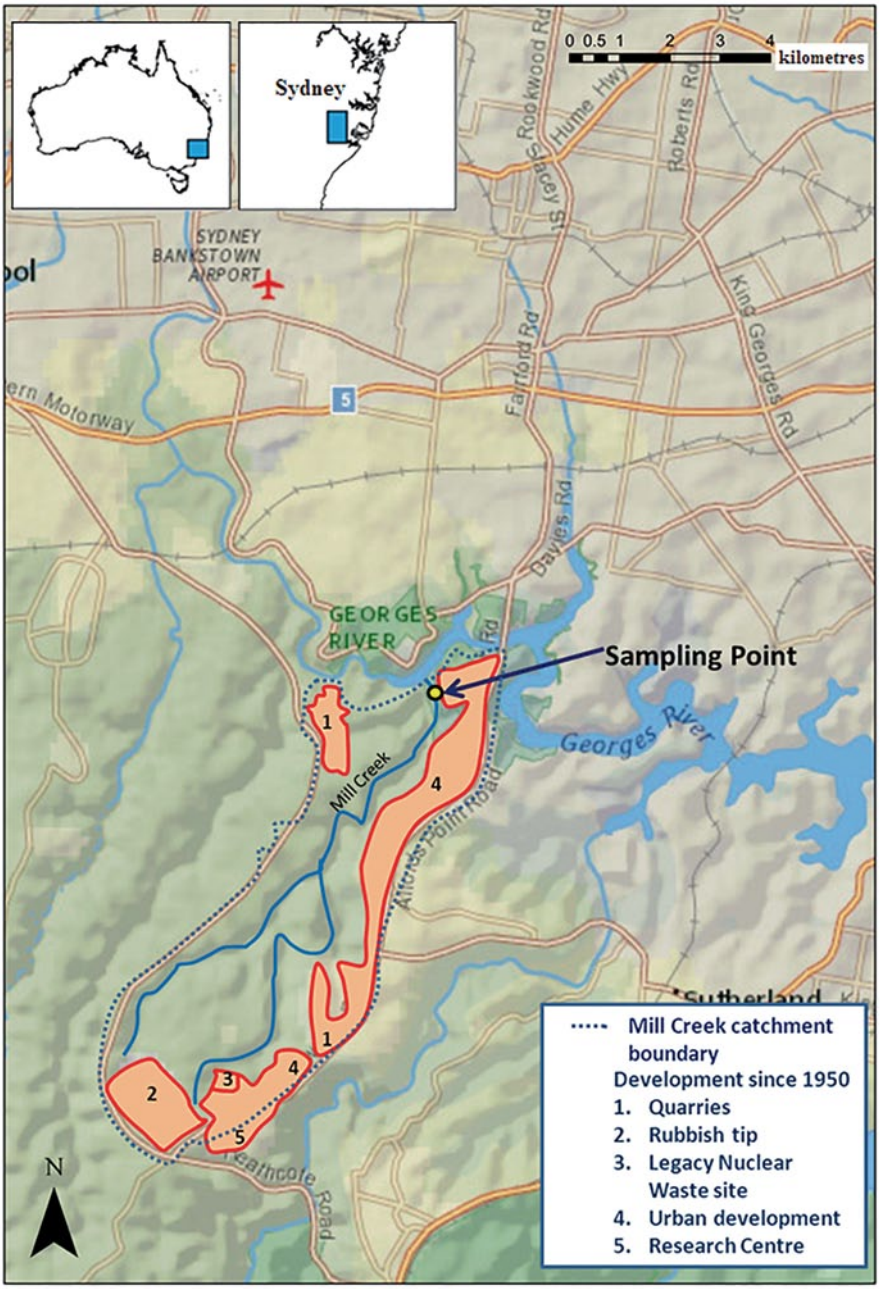


**Fig. 17.1** Sampling location map

## *Lithostratigraphy and Sedimentology*

Selected samples were ashed at 550 °C, and the organic matter content (LOI, loss on ignition) determined on a dry weight basis. Particle size analysis was performed on a Malvern Mastersizer 2000 following methods outlined in Sperazza et al. (2004), after removal of the organic matter with hydrogen peroxide.

## *ITRAX and WD-XRF*

An optical high resolution image and radiographic image of the core were taken at 200 µm resolution. The XRF scans were performed using a molybdenum tube set at 55 kV and 30 mA with a dwell time of 10 s. A step size of 200 µm was selected to capture elemental variations occurring in laminations observed in the radiographic image. Ratios of incoherent and coherent scattering measurements (Mo Inc/Coh) produced by the core scanner were also used as a proxy for the organic matter content, as described in Burnett et al. (2011). Magnetic susceptibility measurements were taken at 5 mm intervals.

Twenty-nine subsamples (1 cm intervals) within the sediment core were selected for conventional WD-XRF analysis (Croudace and Gilligan 1990; Croudace and Williams-Thorpe 1988). They were pelleted by pressing to 25 t into Al cups and analysed using a Philips Magix-Pro instrument fitted with a 4 kW Rh-target X-ray tube. The instrument had been previously calibrated using a wide range of international geochemical reference samples with matrix corrections being applied using Compton scatter or fundamental parameters, FP models, all applied within SuperQ 3.0k software.

The qualitative ITRAX-XRF data were compared to the quantified data obtained by WD-XRF. The ITRAX-XRF results were presented as 5 point averages to make the resolution scales more comparable. This allowed assessment of the data with respect to the Australian and New Zealand interim sediment guidelines (ANZECC/ARMCANZ 2000) and studies carried out in neighbouring catchments.

## *Chronology*

The sediment core chronology was determined by the $^{210}$Pb dating method and independently verified based on the $^{137}$Cs fallout peak (Appleby 2001). $^{210}$Pb (half-life 22.2 years) is a member of the uranium decay series that accumulates in sediment as a result of fall-out from the atmosphere and in-situ production. $^{210}$Pb activity derived from atmospheric fall-out is referred to as unsupported, whereas activity derived from in-situ production is referred to as supported $^{210}$Pb. The unsupported $^{210}$Pb activity, which is the fraction used in the dating models, is calculated by subtracting the supported $^{210}$Pb activity from the total $^{210}$Pb activity. Total $^{210}$Pb activity was determined from its daughter product polonium-210 ($^{210}$Po), while supported $^{210}$Pb

activity was determined from its grandparent radium-226 ($^{226}$Ra). Samples were dried at 60ºC, ground and processed following the method described in Harrison et al. (2003), with both $^{210}$Po and $^{226}$Ra activities measured by alpha spectrometry.

The $^{210}$Pb chronology was independently verified by measuring the activity of $^{137}$Cs using a Canberra Compton suppressed gamma spectrometry system. $^{137}$Cs in sediments is derived from atmospheric atomic weapon testing, with the fall-out reaching a maximum after the Nuclear Test Ban Treaty in 1963 (Carter and Moghissi 1977). Dried and ground samples were sealed in 55 mm petri dishes, and activities determined using the 661.7 keV photo peak. The detector efficiency was determined using IAEA reference material IAEA-300 (Baltic Sea Sediment).

### *Actinide analysis*

Selected samples between 0 and 25 cm depth were analysed for $^{239+240}$Pu and $^{241}$Am activities by alpha spectrometry, following methods outlined in Harrison et al. (2011). Samples were dried, ashed and digested in a combination of nitric, hydrochloric and hydrofluoric acid on a hot plate, and then further processed to isolate plutonium and americium using TEVA™ and TRU™ Eichrom resins.

## Results and Discussion

Based on visual inspection of the core, colour change, organic matter content (based on Mo Inc/Coh and LOI data) (Fig. 17.2), particle size distribution (Fig. 17.3), and the X-radiograph, four distinct facies could be identified in the sedimentary sequence (Fig. 17.2). The lowest, Unit 4 (31–34 cm depth), was composed of "compacted" grey/brown silty sand. It appeared dark on the radiograph, suggesting that the material was dense, and thus this unit was interpreted as compacted creek sediment. The next unit (3) (9–31 cm depth), with a sharp lower boundary, was an organic sandy silt and silty sand layer with vertical rootlets present. Clear laminations were visible on the radiograph, and grain-size data also revealed repeated silt layers (Fig. 17.3). This unit was interpreted as mangrove swamp. It gradually changed into Unit 2 (3–9 cm depth) which was an organic-rich sandy silt layer characterised by an upward increase in silt, but also lower organic content in the upper half of that unit. Unit 2 exhibited laminations but with fewer rootlets than in Unit 3, and represents the transition from mangrove swamp to salt marsh. The top unit (1) (top 3 cm) had a sharp lower boundary and was dominated by organic-rich silt with a low sand content. It appeared white on the X-radiograph implying that the sediment was highly organic. This reflects recent accumulation of plant material (sedges) in the existing salt marsh, associated with high silt content (90 %; Fig. 17.3). Although limited, the quantitative LOI data also confirmed that Mo Inc/Coh provided a good estimate of the organic matter content in the investigated sedimentary sequence (Fig. 17.2).

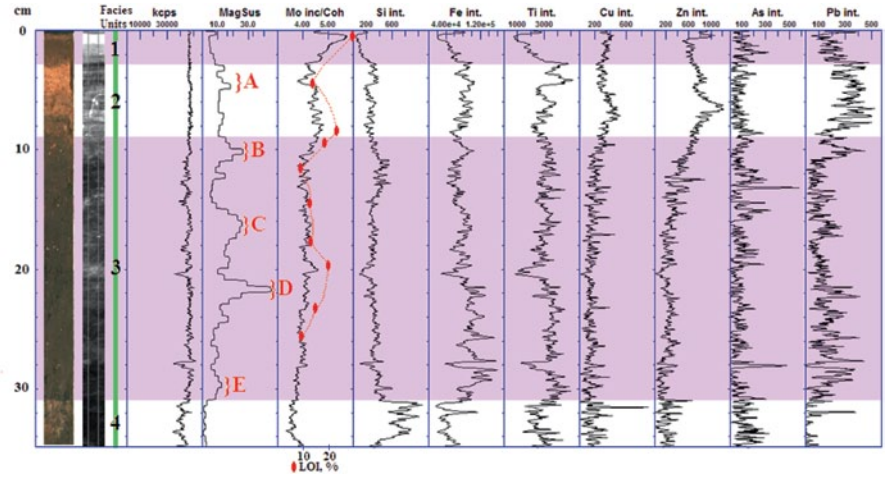


**Fig. 17.2** Optical image, X-radiograph, magnetic susceptibility, Mo Inc/Coh (as a measure of organic matter content), selected LOI (loss on ignition) results, and selected ITRAX-XRF results

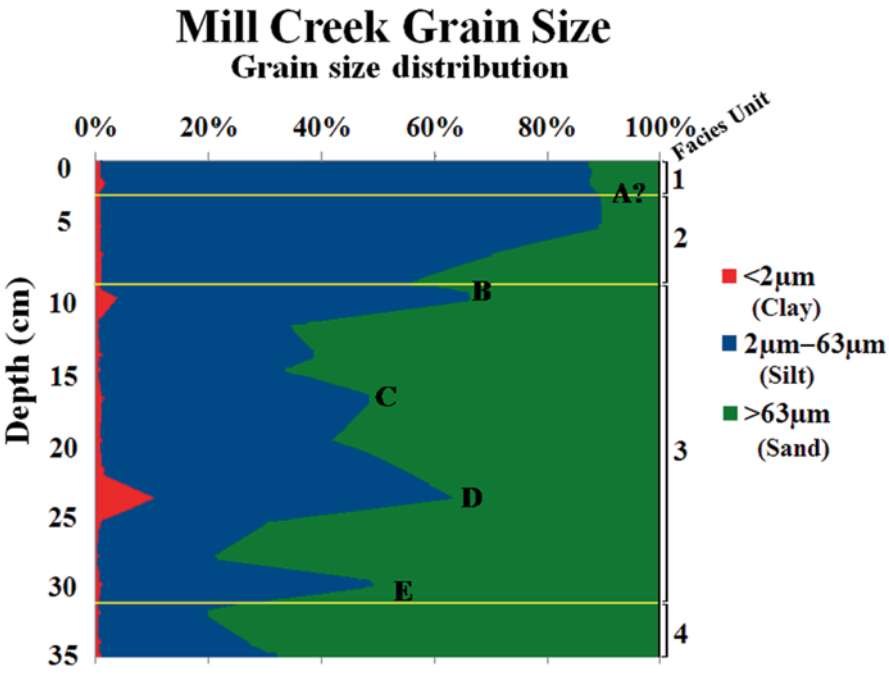


**Fig. 17.3** Grain-size distribution, with silt peaks correlated with peaks in magnetic susceptibility (A–E) from Fig. 17.2

**Table 17.1** Mill Creek core, depths, core cumulative dry masses and $^{210}$Pb activities

| Sample ID | Depth | Cumulative Dry Mass | Total $^{210}$Pb activity | Supported $^{210}$Pb activity | Unsupported $^{210}$Pb activity |
|---|---|---|---|---|---|
| | (cm) | (g/cm$^2$) | (Bq/kg) | (Bq/kg) | (Bq/kg) |
| N889 | 0–1 | 0.2±0.2 | 112±5 | 8.6±0.7 | 108±5 |
| N890 | 1–2 | 0.6±0.2 | 145±6 | 6.3±0.5 | 145±6 |
| N891 | 2–3 | 1.0±0.2 | 87±3 | 7.3±0.6 | 84±4 |
| N893 | 4–5 | 2.1±0.2 | 64±3 | 9.0±0.7 | 57±3 |
| N895 | 6–7 | 3.3±0.3 | 54±2 | 8.9±0.7 | 47±2 |
| N898 | 9–10 | 5.2±0.3 | 40±2 | 6.9±0.6 | 35±2 |
| N903 | 14–15 | 8.9±0.3 | 6.9±0.4 | 5.4±0.4 | 2±1 |
| N908 | 19–20 | 13.3±0.3 | 7.5±0.5 | 6.0±0.5 | 2±1 |
| N914 | 25–26 | 18.4±0.4 | 8.0±0.5 | 6.2±0.5 | 2±1 |
| N919 | 30–31 | 23.4±0.4 | 7.3±0.5 | 5.0±0.4 | 2±1 |
| N923 | 34–35 | 28.1±0.4 | 7.2±0.5 | 3.9±1.5 | 4±2 |
| N928 | 39–40 | 33.9±0.4 | 6.0±0.4 | 4.8±0.4 | 1±1 |

Total, supported and unsupported $^{210}$Pb activities in 12 samples from the Mill Creek core are shown in Table 17.1. The CIC (Constant Initial Concentration) and CRS (Constant Rate of Supply) $^{210}$Pb dating models were used to calculate the sediment ages and mass accumulation rates (Table 17.2). Due to the limited number of unsupported $^{210}$Pb data from this core, the calculated uncertainty for each sediment age was relatively high, particularly for the CIC model. Despite the limited number of data, the $^{210}$Pb dating results suggest that the sediment at 6–10 cm depth was probably deposited between 1967-1957 based on the CIC model and 1977–

**Table 17.2** Mill Creek core: calculated mass accumulation rates, sediment ages and calendar years, based on CIC and CRS models. No data below 10 cm depth, as unsupported $^{210}$Pb activities near background levels

| Sample ID | Depth (cm) | Calculated CIC Ages (years) | CIC mass accumulation rates (g/cm$^2$/year) | CIC Calendar year | Calculated CRS Ages (years) | CRS mass accumulation rates (g/cm$^2$/years) | CRS Calendar year |
|---|---|---|---|---|---|---|---|
| N889 | 0–1 | 4±4 | 0.05±0.02 | 2008 | 2±1 | 0.10±0.01 | 2010 |
| N890 | 1–2 | 11±6 | | 2001 | 7±3 | 0.07±0.01 | 2005 |
| N891 | 2–3 | 19±8 | | 1993 | 12±3 | 0.10±0.01 | 2000 |
| N893 | 4–5 | 39±15 | 0.19±0.01 | 1973 | 22±5 | 0.10±0.01 | 1990 |
| N895 | 6–7 | 45±15 | | 1967 | 35±6 | 0.08±0.01 | 1977 |
| N898 | 9–10 | 55±15 | | 1957 | 64±8 | 0.05±0.01 | 1948 |
| N903 | 14–15 | | | | | | |
| N908 | 19–20 | | | | | | |

**Table 17.3** Mill Creek core, depths and $^{137}$Cs activities

| Sample ID | Depth (cm) | $^{137}$Cs activity (Bq/kg) |
|---|---|---|
| N889–N891 | 0–3 | 3.4 ± 0.7 |
| N892–N894 | 3–6 | 3.9 ± 0.4 |
| N895–N897 | 6–9 | 13.1 ± 1.2 |
| N898–N900 | 9–12 | 0.4 ± 0.5 |
| N901–N903 | 12–15 | 0.3 ± 0.2 |
| N904–N906 | 15–18 | 0.3 ± 0.2 |

1948 based on the CRS model (Table 17.2). Therefore, the peak of $^{137}$Cs activity at 6–9 cm depth (Table 17.3), which represents 1963-1964, following the Nuclear Test Ban Treaty in 1963 (Carter and Moghissi 1977), can be used to validate the $^{210}$Pb CIC and CRS models (Appleby 2001). This is presented in Fig. 17.4 using the CIC model results as an example.

While ITRAX elemental data are qualitative, they can be used in combination with magnetic susceptibility and other parameters, such as grain-size, to reveal environmental changes, source of sediment and anthropogenic influences (Figs. 17.2 and 17.3).

Unit 4 (31–34 cm depth) is characterised by high Si counts and a low magnetic susceptibility, reflecting the mineralogy of the creek sediments, which is probably

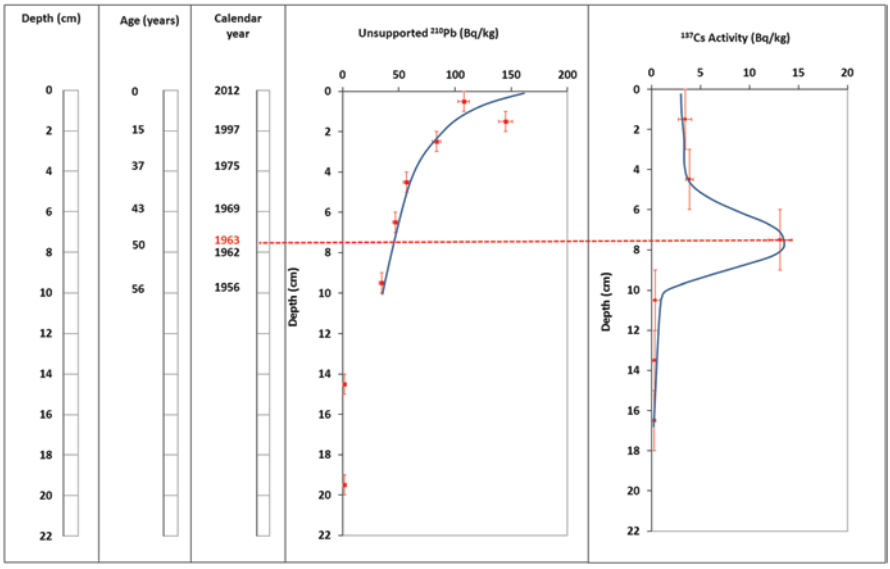


**Fig. 17.4** Unsupported $^{210}$Pb and $^{137}$Cs activities plotted against depths, CIC model sediment ages and calendar years, showing the $^{137}$Cs peak approximately corresponding to the year 1963 on the CIC model $^{210}$Pb calendar year

dominated by sand with low magnetic minerals, such as quartz and feldspars. The small Si maxima between 3 and 5 cm depth in Unit 2 on the other hand coincide with peaks in Ti and Fe, a peak in magnetic susceptibility (peak A; Fig. 17.2), lower Mo Inc/Coh and an increase in the silt fraction (Fig. 17.3). This most probably reflects an increase in runoff, with might be attributed to erosion following a bushfire in the late 1990s or early 2000s (Sutherland Shire, Bush Fire Risk Management Plan 2009). Indeed, previous studies (e.g. Smith et al. 2011) have shown that hill slope erosion increases following bushfires, and that it can result in mobilisation and transport of fine sediment to the catchment outlet. Other magnetic susceptibility peaks in the sedimentary profile, which are often associated with small increases in Fe and/or Ti (Fig. 17.2) and peaks in silt (Fig. 17.3) are likely to represent runoff episodes related to bushfires, which are known to have occurred repeatedly in the area since the late 1930s (Sutherland Shire, Bush Fire Risk Management Plan 2009). However, the lack of robust dating control below 10 cm depth does not allow us to positively identify these bushfire events, and further research would be required.

Copper (Cu), Zinc (Zn) and Lead (Pb) profiles generally exhibit low counts in the lower part of the core and upward increases from about 12 cm depth, in particular in Unit 2, and then decreases towards the surface. These suggest that the data below 12 cm is probably representative of background concentrations, before the changes in land use from the 1950s, thus corroborating $^{210}$Pb data, that indicates that the sediment at about 10 cm depth was deposited in the 1950s. While data are qualitative and are likely to be affected by moisture, organic content and grain-size distribution (Croudace et al. 2006), their vertical distribution is comparable to that reported by Birch et al. (2013), who investigated temporal changes in metal contamination in Sydney estuary, a neighbouring catchment. These authors also reported increases in Cu, Zn and Pb above background, which they attributed to a number of sources, including stormwater from roads and residential properties, that were followed by a decline from the 1990s, at least in the upper estuary (Birch et al. 2013). Similar development and urbanisation in the catchment are also likely to have contributed to the increase in contamination recorded in the sedimentary profile in Mill Creek. The As profile did not display any upward increase, suggesting that there might not be any particular source of As contamination in Mill Creek catchment, such as treated timber. Urban development also appears to have resulted in an increase in the fine sediment load, as shown by a general upward increase in silt content from about 10–11 cm depth (Fig. 17.3).

To quantify the ITRAX-XRF data and determine whether the concentrations are below or exceed the ANZECC/ARMCANZ (2000) sediment quality guidelines and are comparable to those in other areas within the Sydney region (e.g. Birch et al. 1996; Hayes et al. 1998; Birch and McCready 2009; Birch et al. 2013), samples were analysed by conventional WD-XRF. As shown in Fig. 17.5, data obtained by WD-XRF generally show a good correlation with ITRAX data, although there are some variations, which might be attributed to spatial differences, such as moisture content, grain-size, or organic content.

WD-XRF data for Cu and Zn in the core are all below the ANZECC/ARMCANZ (2000) low interim sediment quality guidelines (ISQG-low) of 65 and 200 mg/kg, respectively (Table 17.4) thus suggesting that these metal concentrations are un-

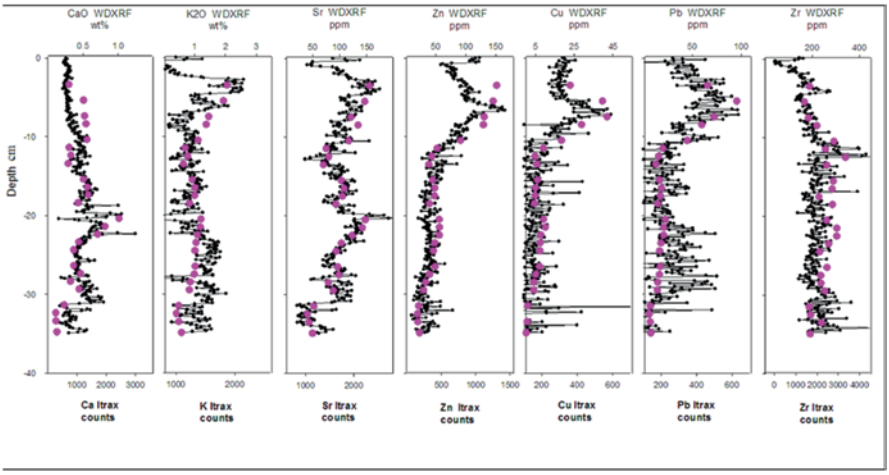


**Fig. 17.5** Comparison of ITRAX and Conventional WD-XRF Results

likely to result in any adverse effect to biota. Pb concentrations are below the ISQG-low of 50 mg/kg in the lower part of the core below 12 cm depth. However, they are above the ISQG-low trigger value in the top part, at least between 3 and 10 cm depth (no WD-XRF data in top 3 cm), although remaining far below the ISQG high trigger value of 220 mg/kg (Table 17.4). The ISQG trigger values, which are based on total concentrations, represent a statistical probability of adverse effect (low: 10%; high: 50%) on biological species, and correspond to the effect range and guidelines developed by Long et al. (1995). Thus, our results indicate that there is a 10% probability that Pb concentrations in the sediment might have an adverse effect on biota (ANZECC/ARMCANZ, 2000), in particular if these sediment layers were disturbed. The upward increase in Pb concentrations from about 12 cm depth, and subsequent decline, which were also recorded in the ITRAX data, are probably linked to urbanisation and leaded petrol in stormwater, followed by a decrease due to the phasing out of leaded petrol in Australia from 1985 (e.g. Taylor et al. 2004), although Pb is still released due to vehicle and tyre wear.

The background concentrations (below 12 cm depth) of Cu, Pb and Zn in our study (Fig. 17.5) are within the background levels reported for the neighbouring Sydney Harbour (mean of 10, 33 and 47 mg/kg, respectively; Irvine 1980). The maximum concentrations recorded for Cu, Pb and Zn in Unit 2 reach 42, 96

**Table 17.4** Interim sediment quality guidelines for selected heavy metals and arsenic

| Contaminant Metals (mg/kg dry weight) | ISQG low | ISQG high |
|---|---|---|
| Copper | 65 | 270 |
| Lead | 50 | 220 |
| Nickel | 21 | 52 |
| Zinc | 200 | 410 |
| *Metalloid* | | |
| Arsenic | 20 | 70 |

and 152 mg/kg, respectively (Fig. 17.5). The data for this study were obtained by WD-XRF analysis of the bulk sediment, while results in neighbouring catchments (e.g. Birch et al. 1996; Hayes et al. 1998; Birch et al. 2013) are mostly based on the < 63 µm fraction followed by analysis by AAS, or ICP-OES. Thus, it is not always possible to exactly compare our data with those of other studies. Nevertheless, the highest Cu, Pb and Zn concentrations reported in the core taken at Mill Creek are well below the range of concentrations recorded in studies carried out in neighbouring heavily industrialised catchments, such as Botany Bay (e.g. Birch et al. 1996; Hayes et al. 1998) and Sydney estuary (e.g. Birch et al. 2013). Mean Cu, Pb and Zn concentrations reported for total sediment in Sydney estuary by Birch et al. (2013) range from 124–353, 177 to 554, and 374 to 1178 mg/kg, respectively. While these results are associated with a wide range in concentrations, depending on the location in Sydney estuary, they are well above the maximum concentrations measured in Mill Creek sediments, reflecting the higher rate of industrialisation and urbanisation. Hayes et al. (1998), who investigated trace metal distributions in sediments and oysters of Botany Bay, measured Cu, Pb and Zn concentrations in sediments ranging from 190–1113, 600–4080, and 227–1472 mg/kg, respectively, indicating high levels of contamination.

It is however interesting to note that the maximum concentrations measured in Mill Creek core are at the lower range of the metal distributions occurring in surface sediments of Georges River (Birch et al. 1996). These authors reported 40–80 mg/kg Cu, 90–110 mg/kg Pb and 260–340 mg/kg Zn in the upstream section of Georges River, which includes Mill Creek, although much higher metal levels occurred in Salt Pan creek, a tributary of the Georges River NW of Mill Creek, due to early uncontrolled metal dumping (Birch et al. 1996). Napoli (1996) also measured similar metal concentrations in creeks close to Mill Creek. However, metal concentrations exceeded the ISQG-High levels for most of the 20th century on the northern side of the Georges River, in creeks draining highly industrial and densely populated areas of the Southern Sydney area of Liverpool, Cabramatta and Bankstown as part of the larger Georges River catchment (Napoli 1996).

The distribution and levels of metals in Mill Creek sediments reflect the changes in land use since the 1950s, with the development of housing estates and road surfaces, and the expansion of a large waste management centre. The decline in the top part of the sedimentary sequence might be attributed to better waste and stormwater management practices, although it appears to be associated with an increase in sediment load.

The legacy nuclear waste site (Fig. 17.1—area 3) is a possible source of anthropogenic isotopes in the sediments. The activities of $^{239+240}$Pu and $^{241}$Am in all the analysed samples were below the calculated Minimum Detectable Activity (MDA) of 1 mBq/g. Besides $^{137}$Cs, no other possible isotopes from the legacy waste site were detected at the sampling site. The sub-surface maximum in activity of $^{137}$Cs (Fig. 17.4), strongly suggests that it can be solely contributed to global fallout from atmospheric testing (1945–1963). If there had been a constant supply of $^{137}$Cs from the legacy waste site, the sub-surface maximum would not be observed. Therefore, our data suggest that the legacy waste site is not a contributing source of $^{137}$Cs at the sampling site.

## Conclusions

The ITRAX core scanner provides a rapid method for obtaining high resolution qualitative data to study the effects of urbanisation on fragile environments. In this study, an increase in key metal indicators (Cu, Pb and Zn) from background levels is reported, which are attributed to an increase in urbanisation from the 1950s, as indicated by $^{210}Pb/^{137}Cs$ dating. The supplementary quantitative data obtained by conventional WD-XRF showed that the direct input of pollutants was detectable but that the metal concentrations mostly remained below those likely to cause any ecological impact, according to the interim sediment quality guidelines for heavy metals, and were lower than in neighbouring more industrialised catchments. Subsurface Pb concentrations however exceeded the low trigger guideline values, however were well below the high trigger values. This study also suggests that the legacy waste site is well contained and not contributing any actinide nor $^{137}Cs$. Periodic pulses in siltation associated with increases in magnetic susceptibility and Fe and Ti are attributed to bushfires leading to increased erosion in the catchment. The findings here show that urban development has resulted in an increase in metal concentrations and sediment load from the 1950s, however the legacy nuclear waste has not entered the creek system. This study thus provides a baseline for the sediment quality in Mill Creek catchment, which can be used in any new management and/or development plans for the area.

**Acknowledgements** The authors would like to thank Ms Patricia Smith of Gloucester, UK for editorial assistance and to the two anonymous reviewers for their constructive comments which improved the manuscript.

## References

ANZECC/ARMCANZ (2000) Australian and New Zealand guidelines for fresh and marine water quality. Australian and New Zealand Environment and Conservation council and Agricultural and Resource Management Council of Australia and New Zealand, National Water Quality Management Strategy 2000

Appleby PG (2001) Chronostratigraphic techniques in recent sediments. In: Last WM, Smol JP (eds) Tracking environmental change using lake sediments, volume 1: basin analysis, coring and chronological techniques. Kluwer, Dordrecht, pp 171–203

Birch GF, McCready S (2009) Catchment condition as a major control on the quality of receiving basin sediments (Sydney Harbour, Australia). Sci Total Environ 407:2820–2835

Birch GF, Evenden D, Teutsch ME (1996) Dominance of point source in heavy metal distributions in sediments of a major Sydney estuary (Australia). Environ Geol 28:169–174

Birch GF, Chang CH, Lee JH, Churchill LJ (2013) The use of vintage surficial sediment data and sedimentary cores to determine past and future trends in estuarine metal contamination (Sydney estuary, Australia). Sci Total Environ 454–455:542–561

Burnett AP, Soreghan MJ, Scholz CA, Brown ET (2011) Tropical East African climate change and its relation to global climate: a record from Lake Tanganyika, tropical East Africa, over the past 90+ kyr. Palaeogeogr Palaeoclimatol Palaeoecol 303:155–167

Carter M, Moghissi A (1977) Three decades of nuclear testing. Health Phys 33:55–71

Croudace IW, Gilligan J (1990) Versatile and accurate trace element determinations in iron-rich and other geological samples using X-ray fluorescence analysis. X-ray Spectrom 19:117–123
Croudace IW, Rindby A, Rothwell RG (2006) ITRAX: description and evaluation of a new multi-functional X-ray core scanner. In: Rothwell R (ed) New techniques in sediment core analysis. Special Publications, The Geological Society of London, London, pp 51–63
Croudace IW, Williams-Thorpe O (1988) A low dilution, wavelength-dispersive X-ray fluorescence procedure for the analysis of archaeological rock artefacts. Archaeometry 30:227–236
Harrison J, Heijnis H, Caprarelli G (2003) Historical pollution variability from abandoned mine sites, Greater Blue Mountains World Heritage Area, New South Wales, Australia. Environ Geol 43:680–687
Harrison J, Zawadzki A, Chisari R, Wong HKY (2011) Separation and measurement of thorium, plutonium, americium, uranium and strontium in environmental matrices. J Environ Radioact 102:896–900
Hayes WJ, Anderson IJ, Gaffoor MZ, Hurtado J (1998) Trace metals in oysters and sediments of Botany Bay, Sydney. Sci Total Environ 212:39–47
Irvine I (1980) Sydney Harbour: sediments and heavy metal pollution. PhD thesis. University of Sydney, Sydney, 260 p
Long E, Macdonald D, Smith S, Calder F (1995) Incidence of adverse biological effects within ranges of chemical concentrations in marine and estuarine sediments. Environ Manage 19:81–97
Napoli M (1996) The contaminant chronologies of Prospect Creek and Salt Pan Creek as recorded in their sediments. Bachelor of Science Honours thesis, University of Sydney
Payne TE, Harrison JJ, Hughes CE, Johansen MP, Thiruvoth S, Wilsher K, Cendon DI, Hankin SI, Rowling B, Zawadzki A (2013) Trench 'bath-tubbing' and surface plutonium contamination at a legacy radioactive waste site. Environ Sci Technol 47:13284–13293
Smith HG, Sheridan GJ, Lane PNJ, Noske PJ, Heijnis H (2011) Changes to sediment sources following wildfire in a forested upland catchment, southeastern Australia. Hydrol Process 25:2878–2889
Sperazza M, Moore JN, Hendrix MS (2004) High-resolution particle size analysis of naturally occurring very fine-grained sediment through laser diffractometry. J Sediment Res 74:736–743
Sutherland Shire, Bush Fire Management Committee (2009) Bush Fire Risk Management Plan
Taylor SE, Birch GF, Links F (2004) Historical catchment changes and temporal impact on sediment of the receiving basin, Port Jackson, New South Wales. Aust J Earth Sci 51:233–246

# Part IV
# Technological Aspects

# Chapter 18
# A Geochemical Approach to Improve Radiocarbon-Based Age-Depth Models in Non-laminated Sediment Series

**Fabien Arnaud and Sidonie Révillon**

**Abstract** The recent development of Holocene paleoenvironmental studies has led to the emergence of an abundant scientific literature that improves use of $^{14}C$ ages in constructing age-depth models. Most of these attempts are based on the multiplication of $^{14}C$ measurements and/or the use of sophisticated mathematical models. However, most of them disregard detailed sedimentological study that may help establishing realistic age-depth relationships. We propose a simple procedure to introduce sedimentological and geochemical data into such models. We change the stratigraphic reference, replacing the classic notion of depth by the cumulative inventory of an element whose flux is likely to vary much less than total sediment flux. We apply the method to a sediment core from Lake Bourget (Savoie, France) in which the biogenic carbonate flux likely varies less than the terrigenous flux. Our results both confirm this assumption and lead to an improved, objectively-established, reproducible age-depth model taking into account geological data (*i.e.* the evolution of terrigenous input). Our method can be transposed to any sediment system comprising a mixture of components, providing that the accumulation rate of one of them varies much less than the other one.

**Keywords** Radiocarbon · Age-model · Sedimentation rate · Terrigenous input · Biogenic carbonate · Sediment · Major element

## Introduction

Holocene paleoenvironmental studies have significantly increased in recent years. Consequently, use of radiocarbon dating has increased and how to use radiocarbon dates to transform depth into age has become a key scientific question (*e.g.* Pearson

F. Arnaud (✉) · S. Révillon
EDYTEM, Université Grenoble-Alpes, Université Savoie Mont-Blanc, CNRS,
F-73000 Chambéry, France
e-mail: fabien.arnaud@usmb.fr

S. Révillon
Laboratoire "Domaines Océaniques", Université de Bretagne Occidentale/CNRS, IUEM,
Place N. Copernic, 29280 Plouzané, France
e-mail: sidonie.revillon@univ-brest.fr



I. W. Croudace, R. G. Rothwell (eds.), *Micro-XRF Studies of Sediment Cores*,
Developments in Paleoenvironmental Research 17, DOI 10.1007/978-94-017-9849-5_18

1986; van Geel and Mook 1989; Bennett 1994; Kilian et al. 2000; Blaauw et al. 2003; Telford et al. 2004; Goslar et al. 2005; Heegard et al. 2005; Blockley et al. 2007; Goslar et al. 2009).

Recently, common practise has been to perform more and more $^{14}C$ dates on the same series and mathematical models to determine age-depth relationships. Multiplication of radiocarbon dates on the same series can greatly improve age-model reliability. However, the so-called wiggle-matching method (Pearson 1986; van Geel and Mook 1989) implies, in addition to a substantial financial cost, that enough appropriate material is available, which is not always the case, especially in deep lakes and oceanic sediment series. Nonetheless, age-modelling allows estimation of the probability field of the age-depth relationship, *i.e.* determining how "uncertain" the model output is and finally mathematical wiggle-matching models often provide smooth age-depth relationships models. This may however lead to significant errors, as natural systems do not always evolve in a smooth way (*e.g.* Arnaud et al. 2005; Goslar et al. 2009). This is particularly true in sediment systems affected by substantial terrigenous input which can vary by one to several orders of magnitude, over very short time intervals. This is why it has been proposed to cross-check age-models using other proxies assumed to have a constant flux such as pollen data (Goslar et al. 2009). However pollen data are not systematically acquired in paleoenvironmental studies and the assumption constant flux is hard to be verified. Detailed sedimentological studies, describing changes in allochthonous inputs, should provide the required data. We propose in this paper a procedure aiming at introducing this information into an age-depth model using high resolution geochemical logging.

The emergence of new fast, non-destructive, high resolution methods allowing semi-quantitative geochemical measurement along sediment cores using XRF core scanners has revolutionised palaeoenvironmental analysis (Haug et al. 2001; Arz et al. 2001, Zolitschka et al. 2001). Such methods can be used to study the continuous evolution of sediment geochemical composition and hence to determine the cumulative inventory of various elements.

The method described here is to calculate an age-inventory relationship using an element that is less subject to changes in accumulation rate than the total sediment fraction. This inventory will represent the cumulative weight of this specific element per surface area unit above a given stratigraphic position. Once this new stratigraphic scale has been established, chronological information—*e.g.* $^{14}C$ ages—may be added and used to determine an age-inventory relationship. An age-depth model can then be established, back calculating the inventory-depth relationship. One difficulty however is to choose a chemical element that is both almost invariant and independent of the amount of allochthonous terrigenous material. In hard water lakes, calcium carbonate provides a good candidate. Although the $CaCO_3$ fraction here is partly supplied by rivers, most is bio-precipitated calcite (Kelts and Hsu 1978) whose flux is independent of detrital inputs. These fractions can be distinguished using high resolution geochemical data.

In our example, two basic assumptions are (1) we are able to compute the inventory of biogenic carbonate at any depth and (2) biogenic carbonate flux varies

far less than terrigenous fraction flux. It is noteworthy that our approach does not assume a constant biogenic $CaCO_3$ flux as its variability is finally assessed by the model.

## Material and Methods

### *Lake Bourget Sediment Series*

Lake Bourget is a fjord-type hard-water lake located at the footstep of the French northern Alps (Savoie, France; Fig. 18.1). We showed previously that, since at least

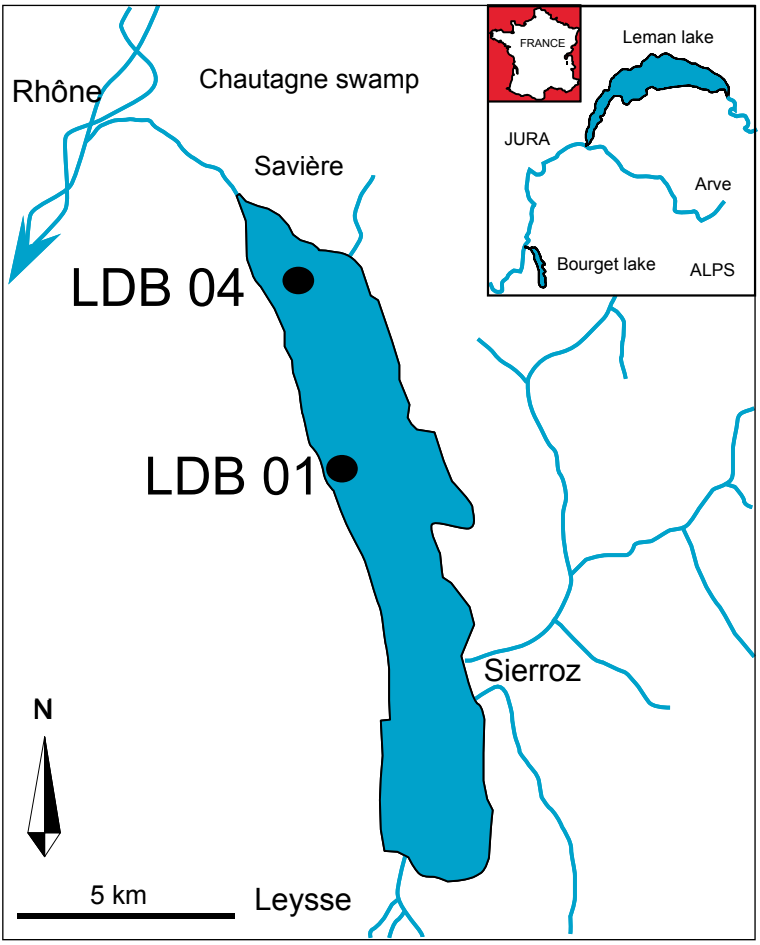


**Fig. 18.1** Location of Lake Bourget in France and location of studied sediment cores in the northern basin of the lake. More details on the sediment sequences can be found in (Arnaud 2012, #2993)

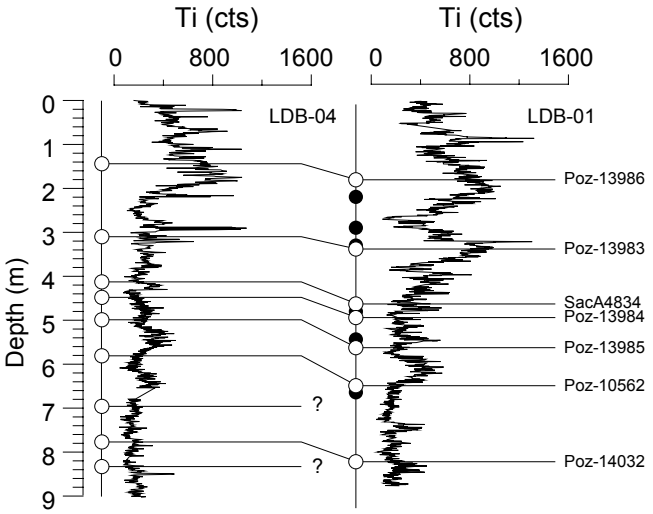


**Fig. 18.2** Ti content (cts) measured by XRF core scanner versus depths for sediment cores LDB-01 and LDB-04 used to correlated to two cores. *Open circles* represent $^{14}C$ dates in LDB-04 and *black circles* represent $^{14}C$ dates in LDB-01. *Lines* are drawn to highlight tie points used in the correlation. (see also Table 18.1 and Arnaud 2012, #2993)

9000 years B.P., the lake has been sporadically fed by the River Rhône during its major floods (Chapron et al. 2002; Arnaud et al. 2005; Arnaud et al. 2012). During such events, biogenic carbonates, which constitute the main sediment fraction under normal conditions, are diluted by a silicate-rich detrital fraction. It is also noticed that the carbonate fraction grain-size did not substantially change since the onset of biogenic carbonate production in the Early Holocene, suggesting a relative stability of this process through time (Arnaud 2005).

Our study is based on two long sediment cores LDB01-I and LDB04-I that were retrieved in the Northern basin of Lake Bourget about 5 km apart (Fig. 18.1). Details on both sediment sequences can be found in (Arnaud 2012, #2993). Both cores were correlated using XRF core scanning data (Fig. 18.2; Arnaud 2012, #2993).

## *Physical and Geochemical Measurement*

Dry bulk densities were measured on 100 discrete samples, with a sampling interval of about 10 cm along core LDB01-I (Fig. 18.3a). Known volumes of sediment were taken, weighted, dried at 60°C for 72 h and finally weighted again. The dry bulk density was calculated by dividing the dry weight by the initial sample volume. Errors on dry bulk densities are related to weighting errors and can be estimated to 5 %. XRF major element analyses were performed on the same samples at the University of Lyon (France).

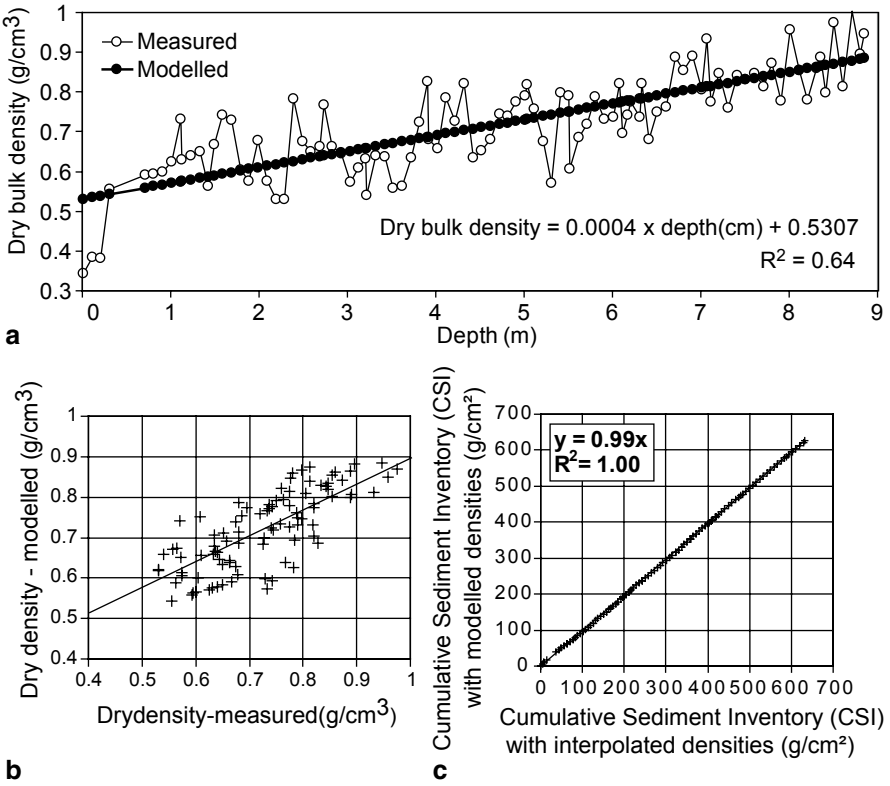


**Fig. 18.3** **a** Dry bulk densities measured in core LDB-01 and linear density model used in the calculations as a function of depth. **b** Measured dry bulk densities as a function of modelled dry bulk densities. **c** Cumulative sediment inventory (*CSI*) obtained using modelled or interpolated densities

XRF core scanning was performed with a 5 mm step at Bremen University using an Avaatech core scanner (Arz et al. 2001; Haug et al. 2001; Zolitschka et al. 2001).

The consistency between elemental concentrations, analysed by XRF on discrete samples, and semi quantitatively measured by XRF core scanner is particularly good (Fig. 18.4). It was therefore possible to calibrate the XRF core scanner data and calculate CaO wt% and $TiO_2$ wt% contents at each depth within the core. The calibration procedure and detailed equations are presented in (Arnaud 2012, #2993).

## *Radiocarbon Measurements and Calibration*

AMS radiocarbon measurements were all performed on AMS either at the Saclay $^{14}C$ measurement laboratory (LMC14) or at Poznan radiocarbon laboratory (POZ)

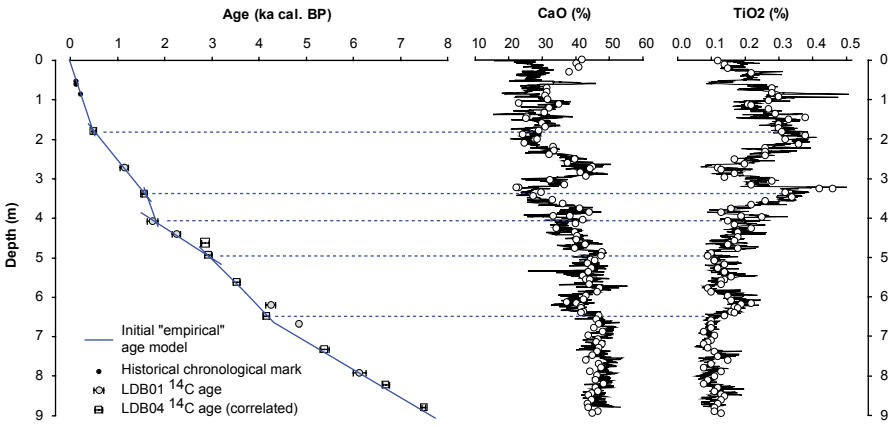


**Fig. 18.4** Stratigraphic position of age markers, compared to the evolution of calcium and titanium contents presented as a function of depth. The location of breaks in the age-depth line was drawn manually and delineates intervals of constant sedimentation. *Black circles* represent historical makers, *grey circles* are $^{14}$C dates measured on core LDB-01 and *grey squares* are $^{14}$C dates measured on core LDB-02 (see also Table 18.1). Error bars represent 2σ error. In CaO and $TiO_2$ contents versus depth, *black lines* represent calibrated XRF core scanner intensities and *open circles* represent quantitative XRF analyses on punctual samples. *Dotted lines* are drawn at each change in the sedimentation rate as determined from the classical initial age model. However, these changes do not always correspond to a change in the sediment composition as would be expected from a change in the sedimentation dynamics of the system. Nonetheless, there is general agreement with the high resolution geochemical measurements: the greater the terrigenous content in the sediment then the greater the sedimentation rates determined

(Table 18.1). A routine age-modelling approach was applied by running the "CLAM" program (Blaauw 2010, #2994) under the mathematics software "R" version 2.12.2 (R Development Core Team 2011). The used calibration curve was Intcal09 (Reimer et al. 2009, #2995). All ages were acquired on vegetal terrestrial macroremains to avoid reservoir effect. The age-model was generated based on 15 AMS-radiocarbon ages and three historical markers (recent eutrophication and floods) (Arnaud 2005, #2716, 2012, #2993) (Fig. 18.4).

## Constructing an Inventory Based Age-Depth Model: Results and Discussion

The model obtained from available $^{14}$C dates, when placed into an age-depth plot; result in a non-linear broken line where changes of slope are supposed to reflect changes in sediment accumulation rates (Fig. 18.4). It is however very difficult to determine where to place changes in sedimentation rates and these breaks are often positioned in the model at the specific depths where a date is available. This issue was previously addressed and we chose to "manually" adjust straight lines, defining

**Table 18.1** Chronostratigraphic information used to generate age-depth models

| Stratigraphic mark or $^{14}C$ lab. code | Sampled in core | Depth in LDB01 (cm) | Depth in LDB04 (cm) | Age (cal. BP) | $^{14}C$ age (BP) | Thickness (cm) | Cal. min. (cal. BP) | Cal. max. (cal. BP) |
|---|---|---|---|---|---|---|---|---|
| Top Eut. Unit[c] | LDB-04 | | 3 | 7 | | 1 | | |
| Flood (1905)[b] | LDB-04 | | 19 | 45 | | 5 | | |
| Flood (1733)[a] | Both | 85.5 | 64 | 217 | | 1 | | |
| Poz-710[d] | LDB-01 | 271 | 250.5 | | 1200±30 | 1 | 1055 | 1180 |
| Poz-718[d] | LDB-01 | 407 | 335 | | 1800±45 | 1 | 1610 | 1830 |
| Poz-716[d] | LDB-01 | 4405 | 381 | | 2250±30 | 1 | 2160 | 2340 |
| Poz-717[d] | LDB-01 | 619 | 548 | | 3820±30 | 1 | 4090 | 4300 |
| Poz-715[d] | LDB-01 | 6675 | 614 | | 4280±40 | 1 | 4815 | 4965 |
| Poz-721[d] | LDB-01 | 791 | 750 | | 5310±40 | 1 | 5990 | 6205 |
| Poz-13986[b] | LDB-04 | 180.5 | 144 | | 435±30 | 1 | 460 | 530 |
| Poz-13983[b] | LDB-04 | 338 | 310 | | 1665±30 | 1 | 1515 | 1630 |
| SAcA4834[b] | LDB-04 | 463 | 412.8 | | 2770±30 | 1 | 2790 | 2930 |
| Poz-13984[b] | LDB-04 | 494 | 448 | | 2815±30 | 1 | 2850 | 3000 |
| Poz-13985[b] | LDB-04 | 562.5 | 499 | | 3300±30 | 1 | 3450 | 3590 |
| Poz-10562[b] | LDB-04 | 649 | 581 | | 4160±35 | 1 | 4580 | 4830 |
| Poz-14033[b] | LDB-04 | | 696 | | 4640±35 | 1 | 5305 | 5465 |
| Poz-14032[b] | LDB-04 | 822 | 777 | | 5870±40 | 1 | 6620 | 6790 |
| Poz-10563[b] | LDB-04 | | 840 | | 6610±40 | 1 | 7435 | 7565 |

All data were previously published in the following
[a] (Chapron et al. 1999, #2991)
[b] (Debret et al. 2010, #2840)
[c] (Giguet-Covex et al. 2011, #2992)
[d] (Arnaud 2005, #2716) and compiled in (Arnaud 2012, #2993)

fields with constant sedimentation rates (Fig. 18.4) (Arnaud 2005, #2716). Whatever the option taken, between manual adjustments or sophisticated mathematical models, changes in sedimentation rates must originate in the sediment system dynamics and is very likely recorded in the sediment composition.

This is the case here where changes in sedimentation rates appear concomitant with changes in CaO and $TiO_2$ contents, reflecting variations in terrigenous input (Fig. 18.4). It seems therefore that the age-depth model needs to take into account these compositional changes. We therefore developed a new method that will ultimately exploit depths of geochemical changes to place changes in sedimentation rates in the age model. It consists in a geochemical inventory approach where the accumulation of biogenic carbonate (in $g/cm^2$) is used instead of stratigraphic depth (cm).

## *Computing the "Cumulative Sediment Inventory" (CSI)*

Firstly, the evolution of dry bulk was assessed to compute the "cumulative sediment inventory" (CSI), *i.e.* the weight of sediment above a given depth per surface unit. This has been done, by establishing a density model (Fig. 18.3a). In this system the only change in dry bulk density is driven by compaction. Indeed, mineral changes are only due to changes in the carbonate/silicate ratio (Arnaud 2005, #2716), both of them showing similar densities (2.7–2.9 and 2.5–3.4, respectively) and grain-size is fairly constant through the core (Arnaud 2005, #2716). As a result, we interpret the variations in the dry bulk density curve as noise due to uncertainty in measurement (usually in the order of 5 %). We hence established a continuous linear function describing the dry bulk density vs. depth relationship (Fig. 18.3a). This was preferred to an interpolation-based relationship in order to be able to determine the dry bulk density at any depth and to determine the CSI at any chosen sample interval. It can also be noticed that both calculations results in the same final CSI at any depth (Fig. 18.3c).

The CSI is then calculated by integrating the density function over the considered depth interval.

## *Computing the Cumulative Biogenic $CaCO_3$ Inventory (CBCI)*

$CaCO_3$ % content was calculated assuming that all Ca is associated with carbonates. The next step consists in distinguishing which proportion of carbonate is of terrigenous origin ($CaCO_{3terr}$) compared to carbonates of biogenic origin ($CaCO_{3bio}$). The two starting assumptions are (a) The sample which displays the lowest concentration in Ca is assumed to have no biogenic carbonates (Arnaud 2005, #2716; Wessels 1998, #2996) and (b) the ratio between Ca and any

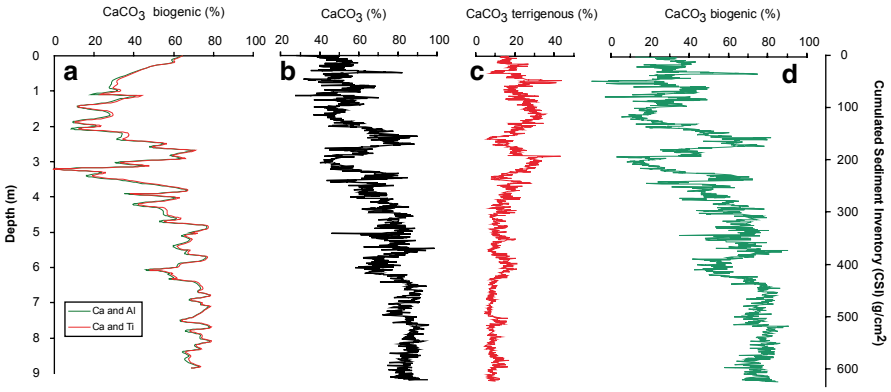


**Fig. 18.5** $CaCO_{3bio}$ as a function of depth calculated using Ca and Al (*green line*) and Ca and Ti (*red line*) concentrations. Calculated $CaCO_3$, $CaCO_{3terrigeneous}$ and $CaCO_{3biogenic}$ as a function of cumulated sediment inventory (*CSI*). See also text for details

lithogenic element is constant in the terrigenous fraction (Arnaud 2005, #2716; Wessels 1998, #2996). Following previous assumptions, $CaCO_{3bio}$ depends only on CaO % and the concentration of a lithogenic element. We led two experiments using Ti and Al as lithogenic elements (Fig. 18.5a). $CaCO_3$ total is calculated from CaO content and $CaCO_{3terr}$ is calculated from lithogenic (Ti or Al) element concentration and Ca/Ti or Ca/Al ratios from the sample in which we assume there is no biogenic carbonates ($CaCO_{3bio} = 0$).

$$CaCO_3 = CaO \times MCaCO_3/MCaO$$

*Where $MCaCO_3$ and $MCaO$ are molecular weights of $CaCO_3$ and CaO, respectively*

$$CaCO_{3ter} = litho \times (CaOref/lithoref) \times MCaCO_3/MCaO$$

*Where $CaCO_{3ter}$ is the $CaCO_3$ concentration in the terrigenous fraction, litho is the concentration of the chosen lithogenic element concentration expressed in oxide weight % ($TiO_2$ or $Al2O_3$), CaOref is CaO content of the reference sample in which $CaCO_{3bio} = 0$, Lithoref is lithogenic element concentration in reference sample, expressed in oxide weight %, $MCaCO_3$ and $MCaO$ are molecular weights of $CaCO_3$ and CaO, respectively.*

$CaCO_{3bio}$ is then obtained by subtracting $CaCO_3$ total and $CaCO_{3terr}$ (Fig. 18.5a).

Then, for each depth, the cumulative biogenic carbonate inventory (CBCI) is obtained by multiplying the CSI by the biogenic carbonate content.

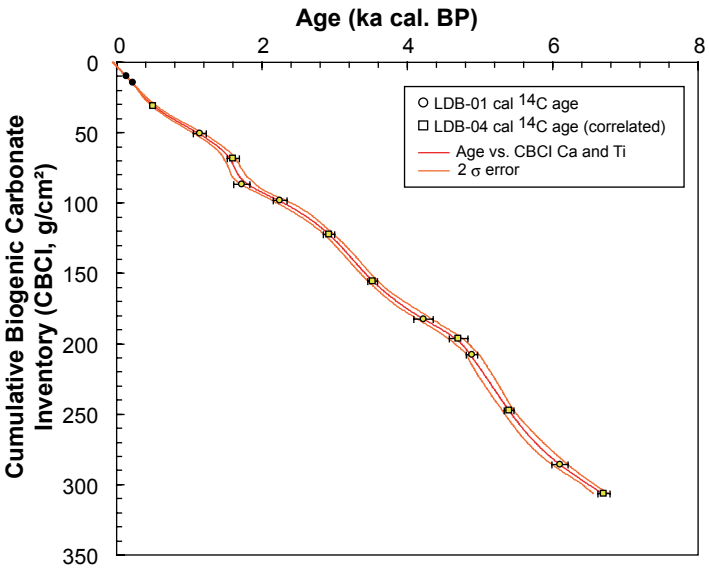


**Fig. 18.6** Age markers plotted as a function of cumulative biogenic carbonate inventory (CBCI). *Thick grey line* represents the age-CBCI relationship computed following Heegard et al. (2005), *thin black line* are the associated uncertainty (+/−2σ)

## *Establishing a New Age-Depth Model*

Available chronological data are reported as a function of CBCI in Fig. 18.6. A classic age-modelling procedure was then applied, following Heegard et al. (2005). It can be noticed that both type of calculations (Ti only or Ca and Ti) result in smooth relationships.

A new age-depth model can now be constructed by back calculating CBCI into depth (Fig. 18.7). This may be done using any mathematical computing tool, such as Matlab. Final models obtained with the two different ways of calculating $CaCO_{3bio}$ are identical, showing they do not depend on the chosen lithogenic element. Although the new model is only slightly different from the initial classical one, it presents no more a disrupted shape due to arbitrary assumption of instantaneous changes in sedimentation rate (Fig. 18.7). The main advantage of this approach is that it takes objectively into account the geochemically assessed fluctuations in terrigenous sediment supply for each time interval. As a consequence it allows the calculation of instantaneous sedimentation rates and elemental fluxes.

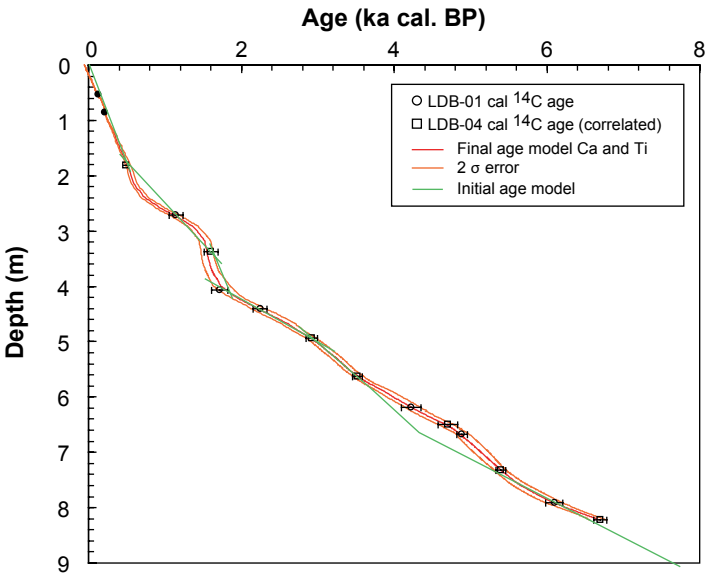


**Fig. 18.7** Comparison between initial "empirical" model and the new age-model. Initial (*green line*) and new age models for core LDB-01. The *thick red line* is the final age model generated with our new method. The *thin red lines* are the associated uncertainty (+/−2σ)

## *Flux Calculation*

Our method allows calculation of instantaneous fluxes. Hence, total sediment flux (accumulation rate), can be calculated at each depth (Fig. 18.3), using the equation:

$$\Phi = d / (\delta_{Age} . \delta_{Depth})$$

Where Φ is the total sediment flux (g cm$^{-2}$ a$^{-1}$); d is dry bulk density (g cm$^{-3}$); $\delta_{Age}$ is the duration of the considered interval (a) and $\delta_{Depth}$ is the thickness of the considered interval (cm).

Subsequently, the flux of any component of known proportion may be simply calculated using the equation:

$$\Phi x = \Phi . [x]$$

Where $\Phi_x$ is the flux of component x (g cm$^{-2}$ a$^{-1}$), Φ is the total sediment flux (g cm$^{-2}$ a$^{-1}$) and [x] is the proportion of component x (without dimension).

In Fig. 18.8 we reported the flux calculations of biogenic carbonates and terrigenous fractions. We hence show that the terrigenous flux is much more variable than the biogenic carbonate flux. This explains why the sedimentation rate is highly variable and mainly dependant on detrital flux.

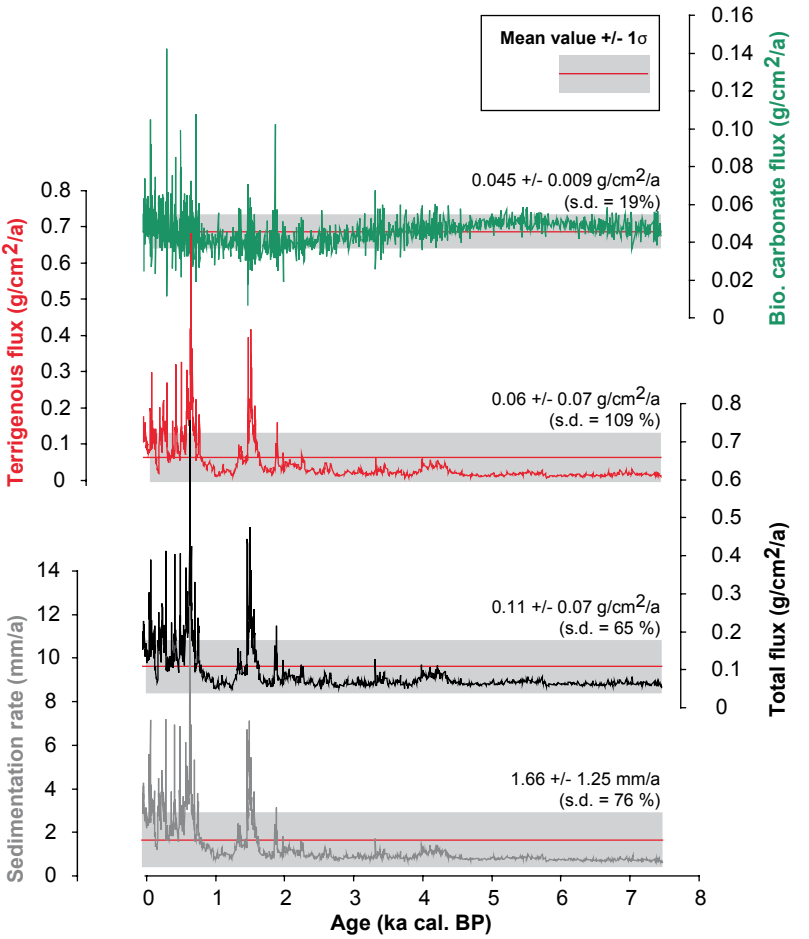


**Fig. 18.8** Time series of sedimentation rates as well as flux calculations of total, terrigenous and biogenic carbonate fractions. All were computed according to the final age-depth model

## Conclusion

Our method is simple and may be applied to various continental or marine sedimentary system where sediment is made of two fractions, providing that the accumulation rate of one of them varies far less than the other one. In the case of Lake Bourget, our results improved the previously established age-depth relationship. The main novelty of our approach is the possibility of establishing an automatically-generated age-depth model in a case where it would have given incorrect results without a change of stratigraphic reference. Such a model presents the two benefits of being objectively-established and taking into account sedimentological and geochemical parameters.

Nevertheless, it is clear that the mathematics applied here is rather simple and could be improved. In particular, error propagation could be better refined, especially in the assessment of biogenic carbonate inventory. This would in particular allow determination of whether the fluctuations in biogenic carbonate fluxes are significant enough to be interpreted. More effort is therefore needed to improve our model by further collaborations between geoscientists and modellers in order to integrate geological knowledge into age-modelling procedures.

Finally, any geological or biological element can be used as a relevant stratigraphic reference, providing that it can be measured continuously and it presents low flux variations through time.

**Acknowledgements** This work was supported by an "ECLIPSE" grant from CNRS and the research program "Pygmalion" funded by the French National Research Agency (ANR BLANC07–2_204489). Some of the $^{14}C$ ages were acquired thanks to the national program ARTEMIS at Saclay $^{14}C$ measurement laboratory (LMC14). Other $^{14}C$ dates were acquired at Poznan radiocarbon laboratory, the authors warmly thank Dr. Tomasz Goslar for many years of fruitful collaboration. Fabien Arnaud is grateful to Dr. Eric Lewin for the fruitful discussion from which the ideas developed in this paper are inspired. The authors wish to thank Paul Capiez who made the major element analyses. XRF core scanner measurements were performed at the University of Bremen as part of the EU-Project "Paleostudies" (contract-no.: HPRI-2001–00124). Drs. Frank Lamy and Holger Kuhlmann are acknowledged for having managed this project. The author also wishes to thank Heike Pfletschinger (University Bremen—ODP Core Repository) for her help in using the core scanner. Dr. Yves Perrette helped with Matlab computing tasks and is here friendly thanked.

## References

Arnaud F, Revel M, Chapron E, Desmet M, Tribovillard N (2005) 7200 years of Rhône river flooding activity in Lake Le Bourget, France: a high-resolution sediment record of NW Alps hydrology. Holocene 15:420–428

Arnaud F, Révillon S, Debret M, Revel M, Chapron E, Jacob J, Giguet-Covex C, Poulenard J, Magny M (2012) Lake Bourget regional erosion patterns reconstruction reveals Holocene NW European Alps soil evolution and paleohydrology. Quat Sci Rev 51:81–92

Arz HW, Gerhardt S, Pätzold J, Röhl U (2001) Millennial-scale changes of surface- and deep-water flow in the western tropical Atlantic linked to Northern Hemisphere high-latitude climate during the Holocene. Geology 29:239–242

Bennett KD (1994) Confidence intervals for age estimates and deposition times in late-Quaternary sediment sequences. Holocene 4:337–348

Blaauw M (2010) Methods and code for "classical" age-modelling of radiocarbon sequences. Quat Geochronol 5:512–518

Blaauw M, Heuvelink GBM, Mauquoy D, van der Plicht J, van Geel B (2003) A numerical approach to $^{14}C$ wiggle-match dating of organic deposits: best fits and confidence intervals. Quat Sci Rev 22:1485–1500

Blockley SPE, Blaauw M, Bronk Ramsey C, van der Plicht J (2007) Building and testing age models for radiocarbon dates in Lateglacial and Early Holocene sediments. Quat Sci Rev 26:1915–1926

Chapron E, Beck C, Pourchet M, Deconinck J-F (1999) 1822 earthquake-triggered homogenite in Lake Bourget (NW Alps). Terra Nova 11:86–92

Chapron E, desmet M, De Putter T, Loutre M-F, Beck C, Deconinck J-F (2002) Climatic variability in the northwestern Alps, France, as evidenced by 600 years of terrigenous sedimentation in Lake Le Bourget. Holocene 12:59–68

Debret M, Chapron E, Desmet M, Rolland-Revel M, Magand O, Trenteseaux A, Bout-Roumazeille V, Nomade J, Arnaud F (2010) North western Alps Holocene paleohydrology recorded by flooding activity in Lake Le Bourget, France. Quat Sci Rev 29:2185–2200

Giguet-Covex C, Arnaud F, Poulenard J, enters D, Reyss J-L, Millet L, Lazzaroto J, Vidal O (2010) Sedimentological and geochemical records of past trophic state and hypolimnetic anoxia in large, hard-water Lake Bourget, French Alps. J Paleolimnol 43:171–190

Goslar T, van der Knaap WO, Hicks S, Andric M, Czernik J, Goslar E, Räsänen S, Hyötylä H (2005) Radiocarbon dating of modern peat profiles: pre- and post-bomb $^{14}C$ variations in the construction of age-depth models. Radiocarbon 47:115–134

Goslar T, van der Knaap WO, Kamenik C, van Leeuwen JFN (2009) Free-shape $^{14}C$ age-depth modelling of an intensively dated modern peat profile. J Quat Sci 24:481–499

Haug GH, Hughen KA, Sigman DM, Peterson LC, Röhl U (2001) Southward migration of the intertropical convergence zone through the Holocene. Science 293:1304–1308

Heegard E, Birks HJB, Telford RJ (2005) Relationships between calibrated ages and depth in stratigraphical sequences: an estimation procedure by mixed-effect regression. Holocene 15:612–618

Kelts K, Hsu KJ (1978) Freshwater carbonate sedimentation. In: Lerman A (ed) Lakes chemistry, geology, physics. Springer, New York

Kilian MR, van Geel, van der Plicht J (2000) $^{14}C$ AMS wiggle matching of raised bog deposits and models of peat accumulation. Quat Sci Rev 19:1011–1033

Pearson GW (1986) Precise calendrical dating of known growth-period samples using a "curve fitting" technique. Radiocarbon 28:292–299

Reimer PJ, Baillie MGL, Bard E, Bayliss A, Beck JW, Blackwell PG, Bronk Ramsey C, Buck CE, Burr GS, Edwards RL, Friedrich M, Grootes PM, Guilderson TP, Hajdas I, Heaton TJ, Hogg AG, Hughen KA, Kaiser KF, Kromer B, Mccormac FG, Manning SW, Reimer RW, Richards DA, Southon JR, Talamo S, Turney CSM, Van Der Plicht J, Weyhenmeyer CE (2009) IntCal09 and Marine09 radiocarbon age calibration curves, 0–50,000 years cal BP. Radiocarbon 51:1111–1150

Telford RJ, Heegard E, Birks HJB (2004) All age-depth models are wrong: but how badly? Quat Sci Rev 23:1–5

Van Geel B, Mook WG (1989) High-resolution $^{14}C$ dating of organic deposits using natural atmospheric $^{14}C$ variations. Radiocarbon 31:151–155

Wessels M (1998) Natural environmental changes indicated by Late Glacial and Holocene sediments from Lake Constance, Germany. Palaeogeogr, Palaeoclimatol, Palaeoecol 140:421–432

Zolitschka B, Mingram J, Van Der Gaast S, Jansen F, Naumann R (2001) Sediment logging techniques. In: Last WM, Smoll JP (eds) Tracking environmental change using lake sediments. Springer, Netherlands

# Chapter 19
# Limited Influence of Sediment Grain Size on Elemental XRF Core Scanner Measurements

**Sébastien Bertrand, Konrad Hughen and Liviu Giosan**

**Abstract** X-ray fluorescence (XRF) scanning of sediment cores allows the rapid acquisition of bulk geochemical data at high resolution. The XRF core scanner data, which are expressed as elemental counts or peak areas, are mainly related to elemental concentrations, but they are also influenced by a series of sediment physical properties that vary with depth, such as bulk density, water content, organic matter content, and grain size. Here, we investigate the influence of grain size on elemental XRF peak areas by comparing ITRAX XRF core scanner measurements to ICP-AES elemental concentrations for two sediment cores with variable grain size. Results provide evidence for a limited influence of sediment grain size on XRF peak areas. This influence is negligible for sediment cores with grain-size variations of 10 μm or less. Our data also demonstrate that for cores with large grain-size variations, correcting the peak areas for water content improves the precision of the XRF measurements by a factor of three. This study therefore demonstrates that, for most sediment cores, the precision of data obtained by XRF core scanning is not significantly altered by grain-size variations.

**Keywords** Calibration · Grain size · Inorganic geochemistry · Sediment cores · Water content · ITRAX XRF core scanner

S. Bertrand (✉) · K. Hughen
Marine Chemistry and Geochemistry, Woods Hole Oceanographic Institution, Woods Hole, MA, USA
e-mail: sebastien.bertrand@ugent.be

S. Bertrand
Renard Centre of Marine Geology, Ghent University, Ghent, Belgium

L. Giosan
Geology and Geophysics, Woods Hole Oceanographic Institution, Woods Hole, MA, USA



I. W. Croudace, R. G. Rothwell (eds.), *Micro-XRF Studies of Sediment Cores*,
Developments in Paleoenvironmental Research 17, DOI 10.1007/978-94-017-9849-5_19

## Introduction

XRF core scanning is increasingly used to generate geochemical records of sediment cores at high resolution. This non-destructive technique provides bulk sediment chemical data, expressed as elemental counts or peak areas. Although XRF measurements are mostly a function of elemental concentrations, they are also influenced by the characteristics of the X-ray source (energy level, nature of the tube) and detector (counting time), by core surface topography, and by a series of sediment physical properties such as bulk density, water content, organic matter content, and grain-size. Since these physical parameters frequently vary with depth in sediment cores, it is crucial to understand their effect on XRF geochemical data to better constrain the potential and limits of the method and avoid over-interpretation of the data.

Among those physical parameters, grain-size is thought to exert a strong influence on XRF peak areas (Croudace et al. 2006). In traditional WD-XRF analysis, the grain-size effect is reduced by grinding the sediment samples to homogenous sizes, generally below 60 μm (Injuk et al. 2006). Since XRF core scanners analyze raw sediment cores, downcore changes in grain-size distributions may significantly affect the results, especially for cores containing sand-size particles. In this study, we therefore investigated the influence of grain-size on elemental XRF peak areas by comparing ITRAX XRF measurements to ICP-AES concentrations obtained on two sediment cores with variable grain-size. We deliberately selected two cores from the same region, but with clearly distinct grain-size variations.

## Material and Methods

### *Sediment Cores*

The two sediment cores used in this study were collected in the fjords of Chilean Patagonia (Fig. 19.1; Bertrand et al. 2012b). Core JPC14 (46.449°S–73.798°W) is a 15 m long jumbo piston core collected at a depth of 129 m during cruise NBP05-05 on board RVIB Nathaniel B. Palmer. It is composed of a 3 m thick sand unit, surrounded by fine-grained sediment (Fig. 19.2). It covers the last 5400 years and essentially contains sediment delivered by a proglacial river system (Bertrand et al. 2012a). Accumulation rates vary between ~1 and ~10 mm/year (Bertrand et al. 2012a). In 2008, a complete core half was shipped from the Antarctic Marine Geology Research Facility of Florida State University, USA, to the Woods Hole Oceanographic Institution, MA, USA, for XRF core scanning and sub-sampling. Samples (3 $cm^3$) were taken every 10 cm with a plastic syringe (diameter 15 mm) for geochemical and water content analysis. Additional small (~0.1 $cm^3$) samples were taken every 2–4 cm for grain-size analysis, and kept wet in microcentrifuge tubes.

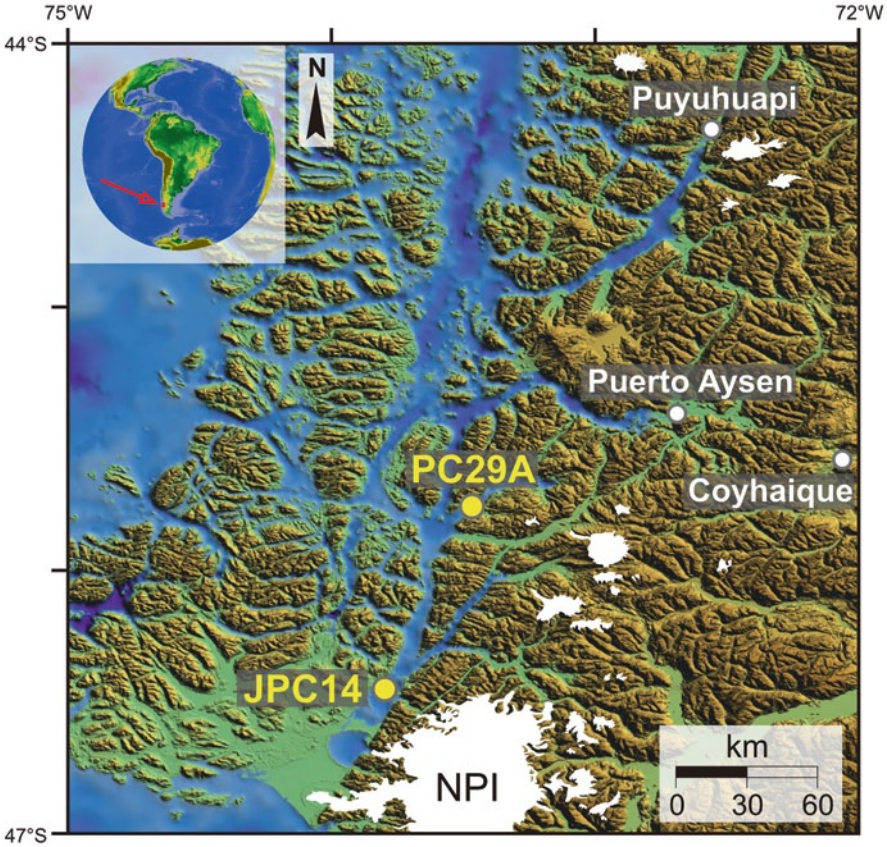


**Fig. 19.1** Location of sediment cores JPC14 and PC29A in the fjords of Northern Chilean Patagonia. The location of the Northern Patagonian Icefield (NPI) and other ice masses is from Glasser et al. (2011)

Core PC29A (45.756°S–73.467°W) is a 208 cm long piston sediment core collected at a depth of 112 m during cruise Cimar Fiordo 7 (Fig. 19.1). It is entirely composed of fine-grained (silt) sediment and it represents the last 1400 years (Fig. 19.2; Bertrand et al. 2014). Accumulation rate is ~1–1.5 mm/year. One core half was sub-sampled in 1 cm thick slices for geochemical and water content analysis. Additional small (~0.1 $cm^3$) samples were taken every 4 cm in the second half for grain-size measurements.

The samples from both cores were freeze-dried and the wet and dry sample weights were recorded for water content calculation. Both cores are carbonate-free and contain low amounts of organic matter (TOC < 2 %) and biogenic opal (< 15 %).

## *XRF Core Scanning*

The inorganic geochemistry of sediment cores JPC14 and PC29A was measured with an ITRAX XRF core scanner (Cox Analytical Instruments) at a resolution of 2 and 1 mm, respectively. The sediment surface was smoothed and covered with a 4 μm thin Chemplex 416 Prolene foil to avoid contamination of the XRF detector, prevent cross-contamination, and limit drying of the sediment during analysis. The scanner was operated with 20 s scan times using a Mo X-Ray tube set to 30 kV and 45 mA, which produces good excitation for a large range of elements of interest in geochemistry (Croudace et al. 2006; Cuven et al. 2007). The XRF spectra were interpreted and the peak areas quantified using software Q-Spec 6.5. For comparison with ICP-AES measurements, the XRF peak areas corresponding to the size of the sub-samples (10 or 15 mm) were averaged. In addition, pressed pellets of 102 non-ground freeze-dried samples of sediment core PC29A were scanned to assess the influence of grain-size on XRF peak areas without influence of bulk density and water content. The pellets were pressed at 20 t and they were scanned on the ITRAX XRF core scanner using the same configuration as for the wet sediment cores.

## *Wet Chemistry*

A subset of 44 samples from core JPC14 and 102 samples from core PC29A was analyzed for inorganic geochemistry by ICP-AES. Samples were prepared using the Li-metaborate fusion technique of Murray et al. (2000), which is preferred over HF digestion because it is the only technique that allows the complete dissolution of sediment samples containing refractory minerals such as zircon (Sholkovitz 1990; Huang et al. 2007). Sample preparation consisted in mixing 200 ± 1.0 mg of ultrapure Li-metaborate (SCP Science) in 3 ml Pt:Au (95:5) crucibles, with 50 ± 0.5 mg of sediment. Ten microliter of 25 % LiBr were then added to the mixture and the crucibles were placed in a muffle furnace for 12 min at 1050 °C. The newly formed glass bead was then allowed to cool down for 2–3 min, detached from the crucible, and poured into a Teflon beaker containing a swirling 25 ml solution of 5 % $HNO_3$. Complete dissolution occurred within ~45 min. The solution was then filtered through a 0.45 μm PVDF Millipore filter and diluted in 5 % $HNO_3$ to obtain a 4000 x final dilution of the sample. The exact dilution factor was calculated from the precise weight of sediment used for fusion. Thirteen elements were measured on a JY Ultima C ICP-AES. Analytical details are given in Bertrand et al. (2012b).

## *Grain-Size*

Grain-size was measured on the terrigenous fraction of the sediment using a Coulter LS200 laser particle size analyzer. To isolate the terrigenous fraction, samples were

treated with boiling $H_2O_2$, HCl, and NaOH to remove organic matter, eventual carbonates, and biogenic silica respectively. No diatoms were observed in core JPC14, so the alkaline treatment was only applied to core PC29A. Prior to analysis, samples were boiled with 300 mg of sodium pyrophosphate ($Na_4P_2O_7 \cdot 10H_2O$) to ensure complete disaggregation of the particles. The grain-size distribution of the samples was measured during 90 s intervals and the arithmetic mean was calculated from the 92 size classes.

## Results and Discussion

### *Lithology, Grain-Size, Water Content and Elemental Concentrations*

Core JPC14 is essentially composed of three lithological units separated by relatively abrupt transitions (Fig. 19.2a). It is composed of fluvio-glacial silts (~20 μm) at 0–740 cm and 1109–1500 cm, and of poorly sorted sand (80–120 μm) at 800–1086 cm (Bertrand et al. 2012a). The water content of the sediment is negatively correlated to grain-size, with high water content (45–50 %) in fine-grained samples and low water content (20–30 %) in the sand unit (Figs. 19.2 and 19.3). The few exceptions are the low water content silt layers in the upper 2 m of the sediment core. The lower water content of the sand unit is due to the combination of low porosity in poorly sorted sands (e.g., Syvitski 2007) and faster dewatering of coarse deposits.

The grain-size of core PC29A gradually evolves from medium to fine silt (16–31 μm; Fig. 19.2b). The water content is rather constant (47–53 %) and it shows no relation to grain-size (Fig. 19.3). By comparison, the range of grain-size variations in core JPC14 is 12 times higher than for core PC29A (Table 19.1 in Appendix; Fig. 19.3).

Both cores are essentially composed of alumino-silicates that originate from the mixing of slightly weathered granodiorites and North Patagonian andosols (Bertrand et al. 2012b). The chemical composition of the two sediment cores is roughly similar, albeit much more variable for core JPC14 (Table 19.1 in Appendix). Some elements such as Sr and Zr are clearly enriched in the coarse unit of core JPC14, while K and Fe are concentrated in fine-grained sediments (Figs. 19.2 and 19.4; Bertrand et al. 2012b), in agreement with the observations of Cuven et al. (2010). For core PC29A, Ti and Fe concentrations are ~25 and ~15 % higher in fine silts than in coarse silts, respectively (Fig. 19.5).

### *Relation Between XRF Peak Areas and Elemental Concentrations*

XRF peak areas and elemental concentrations, as measured by ICP-AES, show significant positive correlations for most elements (Figs. 19.4 and 19.5). Correla-

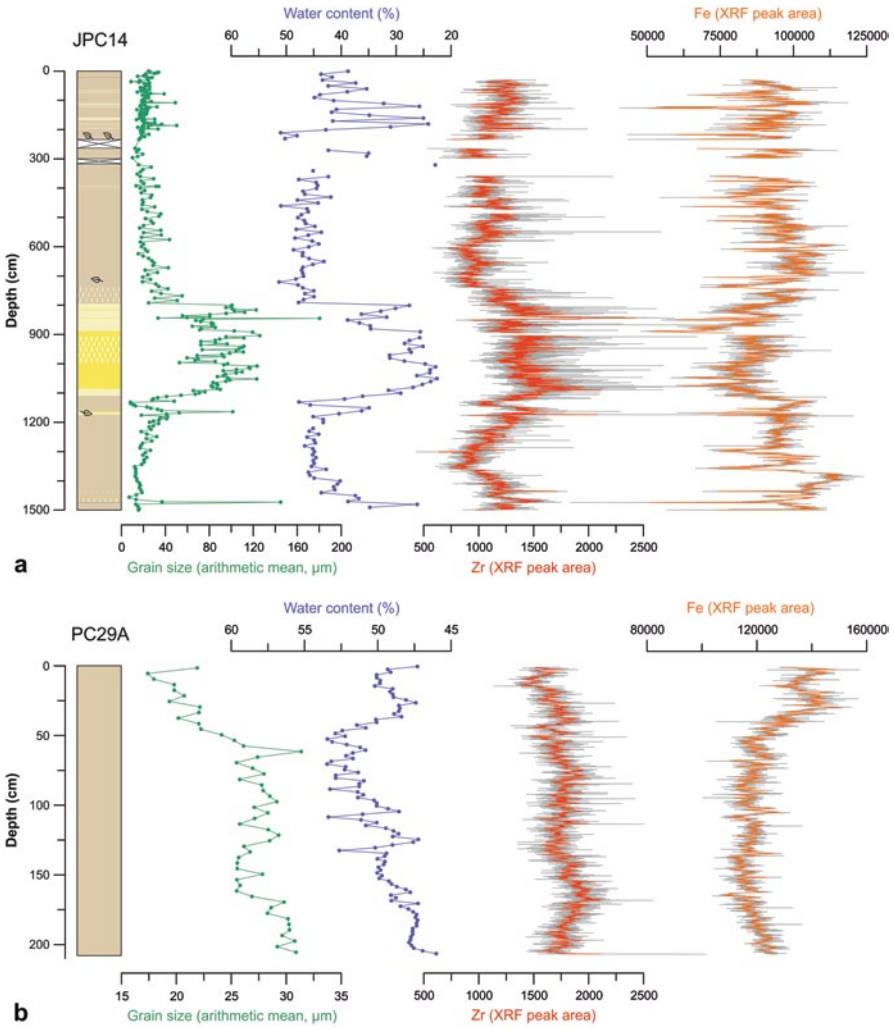


**Fig. 19.2** Lithology of sediment cores JPC14 and PC29A, and downcore variations in grain-size, water content, and selected geochemical elements. (From Bertrand et al. 2012a, 2014)

tions are better for heavy and abundant elements such as Ca and Fe (Table 19.2 in Appendix), as previously observed (Croudace et al. 2006; Richter et al. 2006; Tjallingii et al. 2007). The light elements Al and Si show no significant correlation, even though these elements are well above their theoretical detection limit (~10,000 ppm, Cox Analytical Systems, technical documentation). One of the reasons is that the XRF radiation for these elements is heavily absorbed by the variable water film that forms between the sediment surface and the covering plastic foil (Kido et al. 2006; Tjallingii et al. 2007). Since fjord sediments are deposited in environments of highly variable salinity, using chlorine to correct the XRF peak areas for absorption by the interstitial water layer, as proposed by Tjallingii et al.

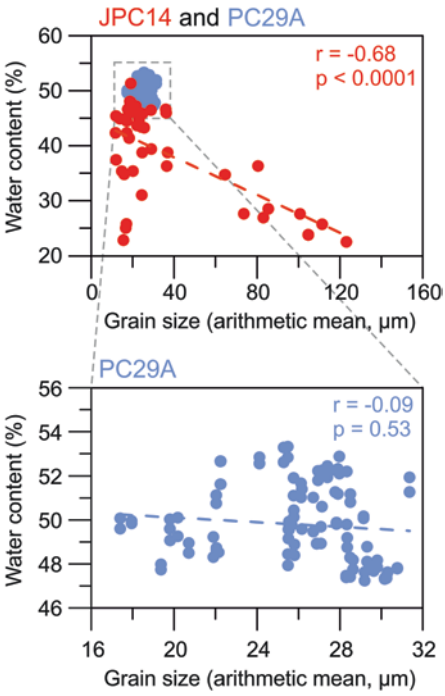


**Fig. 19.3** Correlation plots between water content and grain-size. Note the significant negative correlation for core JPC14 (*red dots*) and the absence of correlation for core PC29A (*blue*). The four JPC14 data points corresponding to low grain-size and low water content values represent unusual silt layers in the upper part of the sediment core. (see Fig. 19.2)

(2007), does not improve the correlations for Al and Si. For the XRF data obtained on pressed pellets, the correlation coefficients between XRF peak areas and ICP-AES elemental concentrations are better for all elements except Sr (Table 19.2 in Appendix; Fig. 19.5). This is in contrast with Tjallingii et al. (2007), who found that the improvement of the correlation coefficients mainly concerned light elements (Al and Si).

## *Assessing the Influence of Grain-Size Variations on XRF Peak Areas*

To assess the influence of sediment grain-size on XRF core scanner peak areas, we compared the normalized ratio between XRF peak area and ICP-AES concentration (hereafter XRF/ICP) to sediment grain-size for both cores. Normalization consisted in dividing the XRF peak area to ICP-AES concentration ratio by the average value of this ratio for each core. If grain-size has an influence on XRF intensities, the XRF/ICP values should be significantly correlated to grain size.

### Core JPC14

For core JPC14, which presents high variations in grain-size, the XRF/ICP ratio of most elements shows a weak positive correlation with grain-size (Fig. 19.6a). This

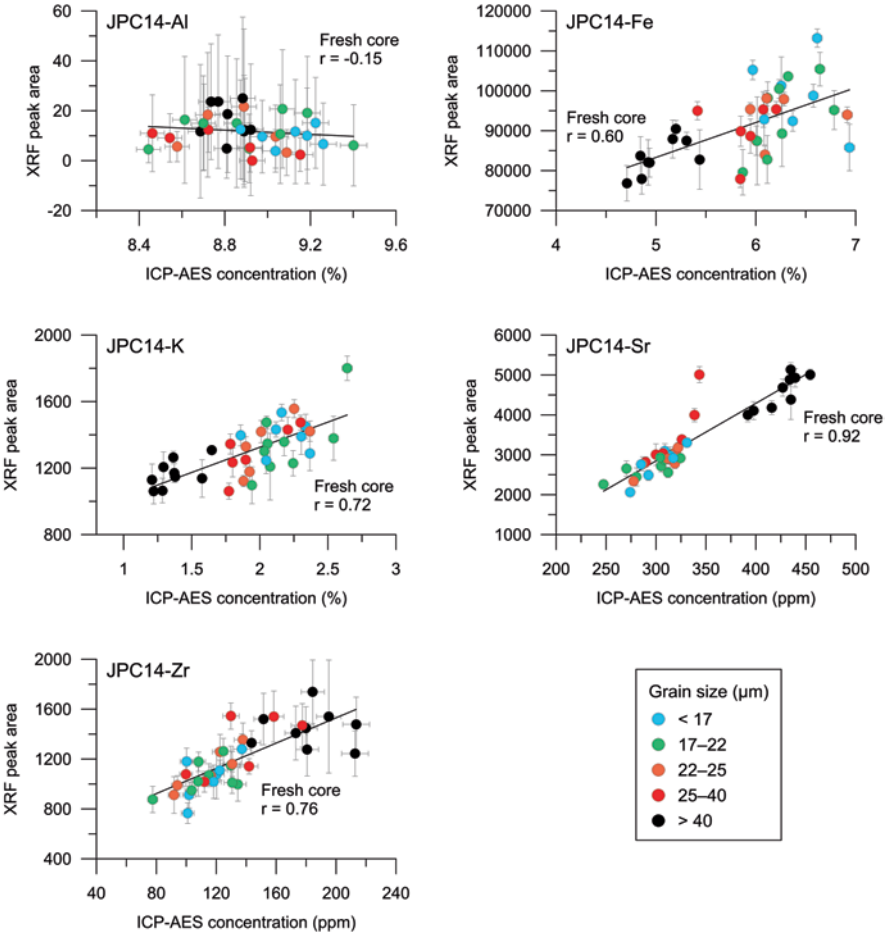


**Fig. 19.4** Correlations between ITRAX XRF core scanner peak areas and ICP-AES concentrations for selected elements measured on sediment core JPC14 ($n = 37$). The *error bars* represent 1 sigma

relation is significant for K, Ti, Fe, and Sr (Table 19.3a in Appendix). Only Zr shows a statistically significant negative correlation. The absolute values of the slopes of the significant correlations reach $1.2–4.3 \times 10^{-3}$, i.e., an increase of the XRF peak areas of 0.1% per micron for Ti and Fe, of 0.2% per micron for Sr, of 0.4% per micron for K, and a decrease of 0.2% per micron for Zr (Table 19.3 in Appendix).

Since the water content of core JPC14 is tightly linked to grain-size ($r = -0.68$, $p < 0.0001$, see Fig. 19.3), a significant negative correlation is also observed between XRF/ICP and water content for most elements (Fig. 19.6b, Table 19.3b in Appendix). This reflects a general decrease of the XRF peak areas with increasing water content. Except for Ti, the significant correlations concern the same elements as for the correlations between XRF/ICP and grain-size (Table 19.3 in Ap-

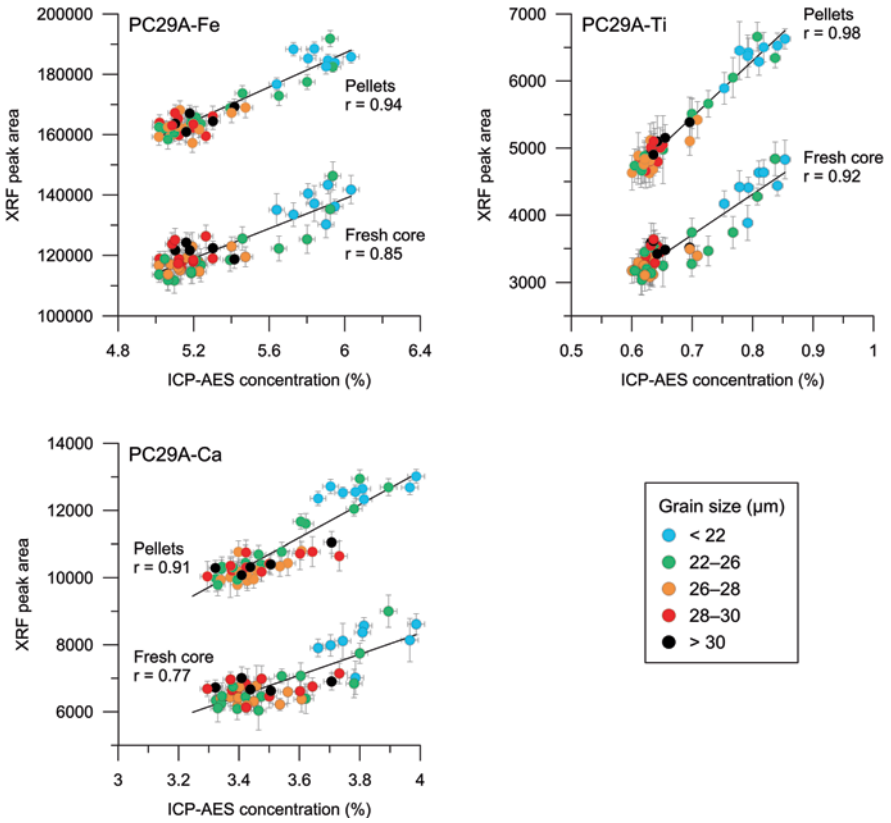


**Fig. 19.5** Correlations between ITRAX XRF core scanner peak areas and ICP-AES concentrations for selected elements measured on sediment core PC29A ($n = 51$). The plots show results obtained on wet sediment and on pressed pellets (see Core PC29A for details). The *error bars* represent 1 sigma

pendix). This demonstrates that changes in water content are responsible for part of the observed variability in XRF peak areas. This observation also highlights the potential of water content data to correct XRF peak areas obtained on sediments of highly variable grain-size.

For core JPC14, correcting the XRF peak areas for water content (using the linear regressions displayed in Fig. 19.6b) reduces the slopes of the XRF/ICP versus grain-size relations by 60–85 % (Table 19.3c and d in Appendix; Fig. 19.7). After water content correction, the XRF/ICP ratios of all elements but K lose their significant correlation to grain-size (Table 19.3c in Appendix), which means that after water content correction, the relations between XRF peak areas and elemental concentrations are mostly independent of grain-size variations. For sediments of highly variable grain-size, such as those of core JPC14, correcting XRF peak areas for water content therefore significantly reduces the apparent influence of grain-size on XRF peak areas.

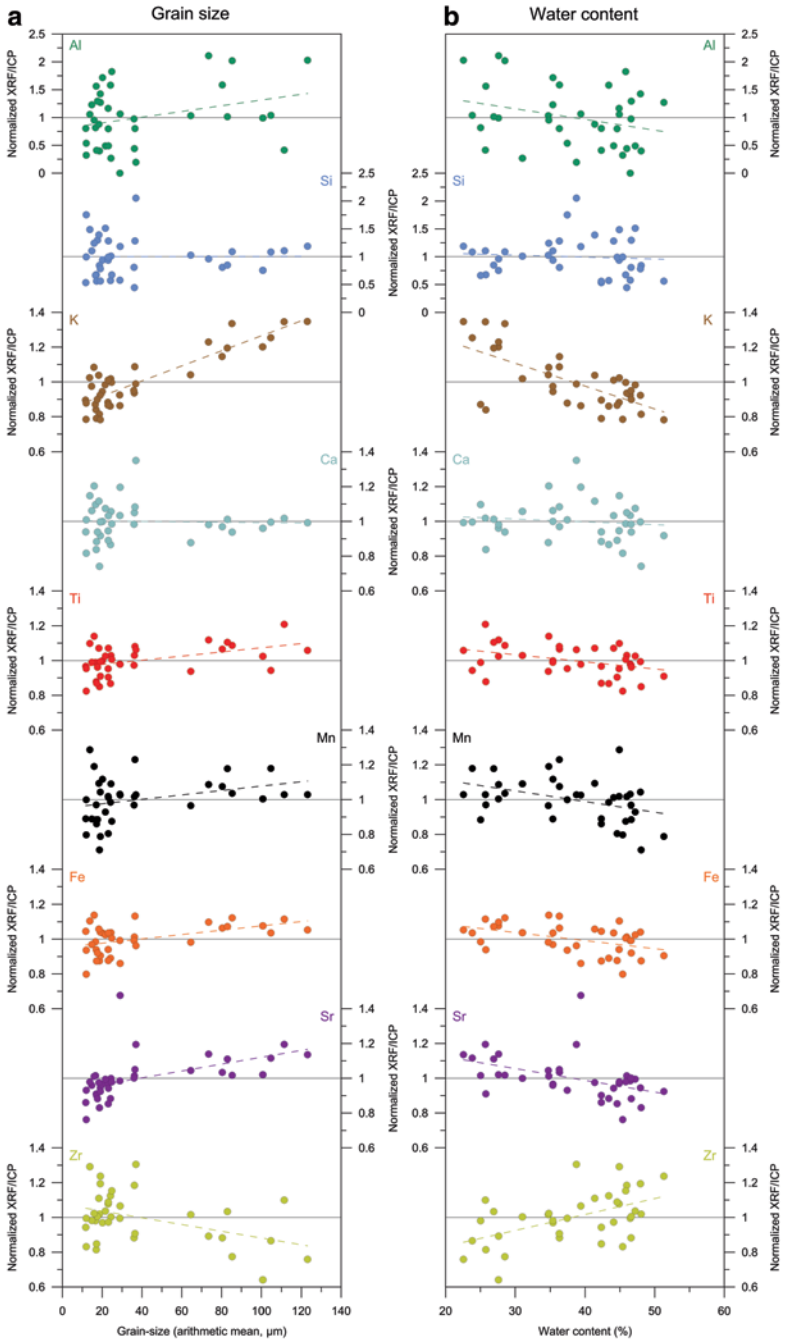


**Fig. 19.6** Correlations between normalized XRF peak areas/ICP-AES concentrations and (**a**) grain-size, or (**b**) water content for geochemical elements measured on sediment core JPC14. Note the vertical scale difference between Si–Al and the other elements. (0–2.5 for Si and Al and 0.6–1.4 for the other elements)

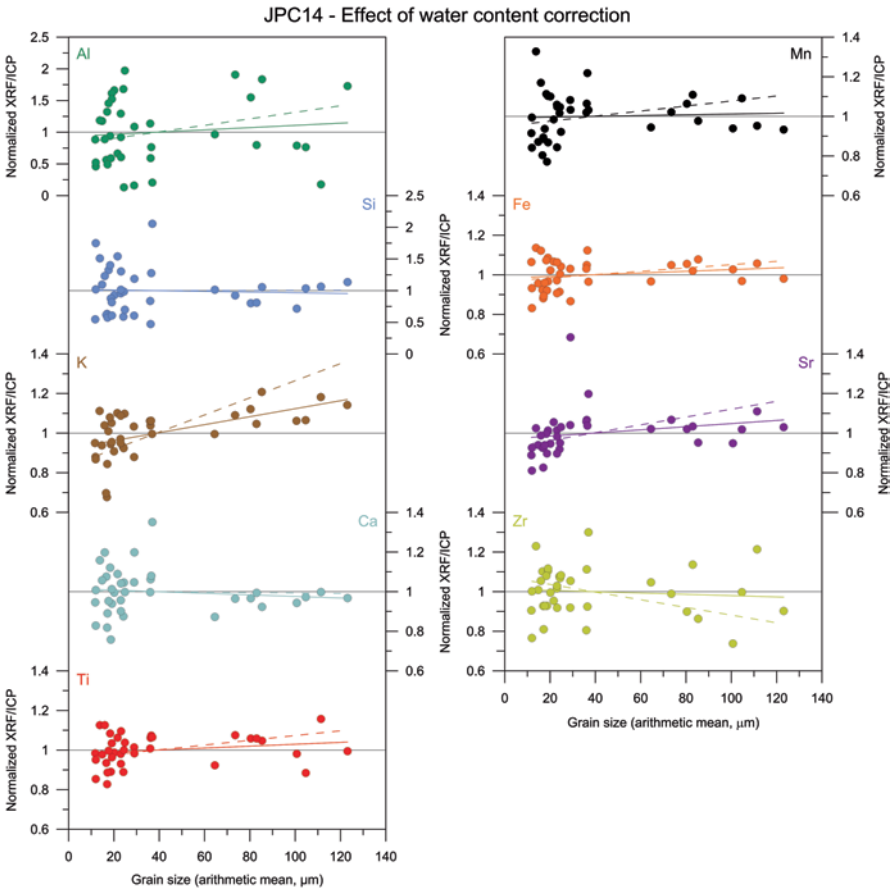


**Fig. 19.7** Correlations between normalized XRF peak areas corrected for water content/ICP-AES concentrations and grain-size for geochemical elements measured on sediment core JPC14. The correlations corresponding to water content-corrected measurements are represented by *continuous lines*, while those corresponding to raw measurements are shown as *dashed lines*, as in Fig. 19.6a. The water content correction is derived from the linear regressions presented in Fig. 19.6b. Geometrically, correcting the JPC14 data for water content corresponds to flattening the trends shown in Fig. 19.6b. Note the general decrease in the slope of the correlation lines after water content correction, except for Si and Ca

Overall, correcting the XRF peak areas for either water content or grain-size slightly improves the correlation between XRF peak areas and ICP concentrations (Table 19.4 in Appendix). This improvement is however relatively minor, and the difference between the correlation coefficients is never significant at $p < 0.05$ (Fisher's transformation test). We particularly note that the correlations between XRF peak areas and elemental concentrations for Al and Si remain insignificant after correction.

**Core PC29A**

For core PC29A, which shows minor grain-size variations compared to core JPC14, the relations between XRF/ICP and grain-size are insignificant for most elements, and the sign of the relation varies inconsistently among elements (Fig. 19.8a; Table 19.5a in Appendix). The relation is only significant for Ca, Mn and Sr (Table 19.5a in Appendix). The absolute values of the slopes vary between 0.53 and 8.98 (Table 19.5a in Appendix), which represent fluctuations of the XRF peak areas of 0.05–0.9 % per micron.

Since the water content of core PC29A is rather stable and that it is not significantly correlated to grain-size, the Pearson correlation coefficients between the XRF/ICP ratios and water content are also weak and the significant correlations relate to different elements (Fig. 19.8b, Table 19.5b in Appendix). Therefore, correcting the XRF peak areas obtained for core PC29A for water content does not decrease the number of significant correlations with grain-size or the slope of the correlations (Table 19.5c in Appendix). Correcting the PC29A XRF peak areas for water content therefore does not render the data less dependent on grain-size.

To focus on the influence of grain-size and avoid the influence of other physical properties such as bulk density, correlations between XRF/ICP and grain-size were also calculated for the XRF data obtained on dry pellets. These pressed pellets have a constant bulk density and they contain no water. It is therefore expected that grain-size is the main physical parameter influencing the XRF peak areas. The results are rather similar to what was obtained for the wet sediment core (Table 19.5d in Appendix). The influence of grain-size on XRF peak areas is only significant for elements Ca, Fe, and Sr, which demonstrates that the effect of grain-size on the XRF peak areas of core PC29A is limited, and insignificant for most elements. The absolute values of the slopes reach values of 0.3–10.9, which are of the same order of magnitude than for the measurements obtained on wet sediment cores.

In summary, the PC29A dataset shows that grain-size variations significantly affect the XRF peak areas of a few elements only, and that these variations are on the order of 0–1 % per micron. There is however no consistency in the level of imprecision caused by grain-size variations. Since the correlations between XRF peak areas and ICP-AES concentrations are significantly improved when using pressed pellets (Table 19.2 in Appendix), other physical properties such as bulk density must play an important role in the relatively high imprecision of XRF measurements obtained on wet sediment cores. Changes in bulk density are generally related to sediment packing, i.e., porosity, rather than grain density, and could be estimated using core logging of gamma-ray (e.g., Zolitschka et al. 2001) or x-ray (Francus et al., this volume) attenuation.

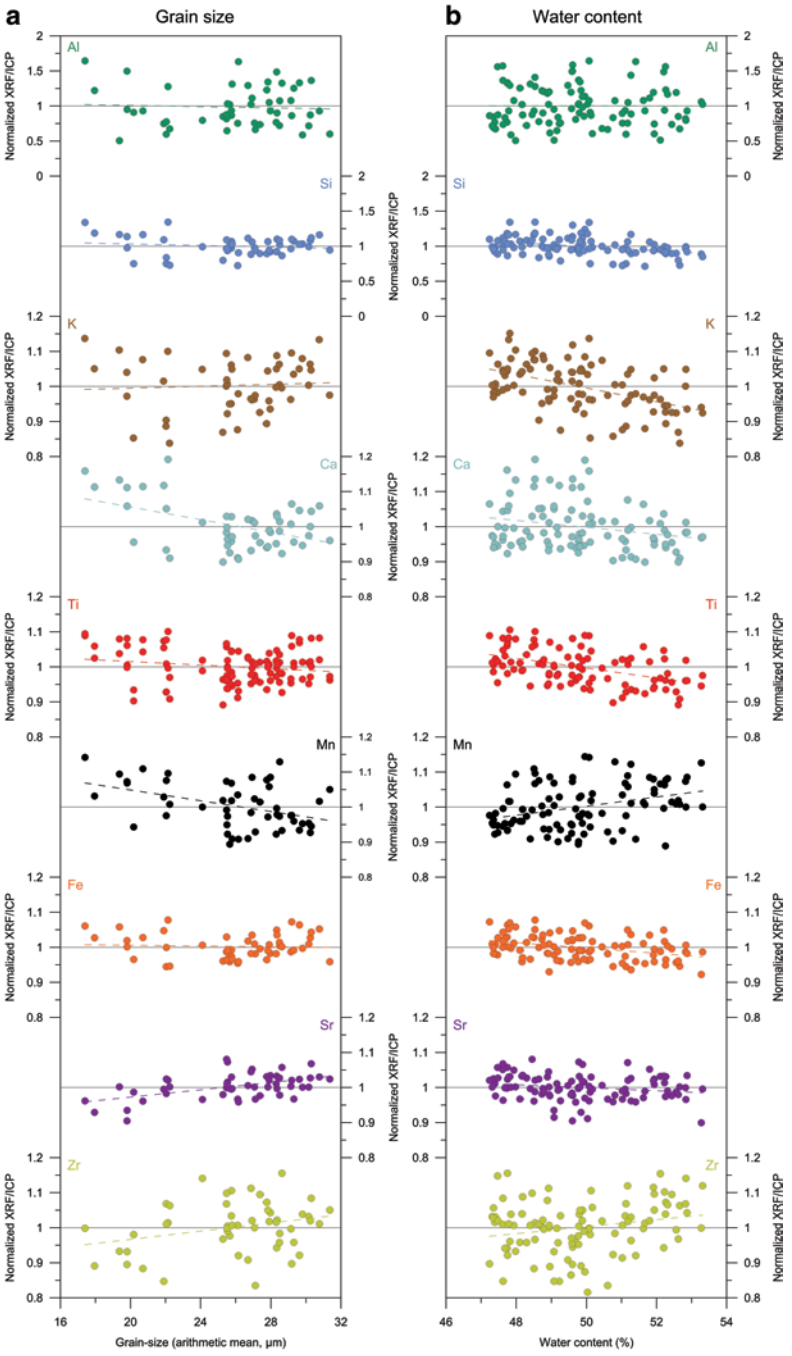


**Fig. 19.8** Correlations between normalized XRF peak areas/ICP-AES concentrations and (**a**) grain-size, or (**b**) water content for geochemical elements measured on sediment core PC29A. Note the vertical scale difference between Si–Al and the other elements. (0–2 for Si and Al and 0.8–1.2 for the other elements)

### *Quantifying the Influence of Grain-Size Variations on XRF Peak Areas*

In Table 19.6 (in Appendix), the slopes of the correlations between the XRF/ICP ratio and grain-size are used to quantify the effect of grain-size variations on XRF peak areas. The strongest significant imprecisions caused by changes in sediment grain-size are for elements K, Sr and Zr, on sediment core JPC14, and for elements Ca and Mn on sediment core PC29A. These imprecisions on peak areas caused by grain-size are always lower than 1 % per micron.

If we consider that imprecisions of 5 % are satisfactory, which is acceptable in elemental geochemistry (e.g., De Vivo et al. 2008), the results obtained on core JPC14 show that XRF peak areas obtained on sediment cores with grain-size variations of up to 20–40 μm. do not need to be corrected for grain-size. This value is however lower when considering the results obtained on core PC29A, for which an imprecision of 5 % corresponds to grain-size variations of as little as 6 μm for some elements.

For Fe and Ti, which are among the most frequently used elements in XRF studies of sediment cores, grain-size variations of up to 40 μm do not affect the XRF peak areas for more than 5 %. For cores that present large grain-size variations, such as JPC14, correcting the XRF peak areas for water content significantly improves the precision, and therefore increases the grain-size range for which good XRF data can be obtained, by a factor of three.

## Conclusions

The comparison between XRF core scanner peak areas and ICP-AES elemental concentrations obtained on sediment cores JPC14 and PC29A provides evidence for a limited influence of sediment grain-size variations on XRF peak areas. Grain-size variations only affect a limited but inconsistent number of elements. For the elements that are affected, the effect of grain-size is negligible for grain-size ranges of 10–20 μm. For cores that show large variations in grain-size, correcting the peak areas for water content variations improves the precision of the XRF core scanner data by a factor of three. This study therefore demonstrates that grain-size variations are not a major issue in XRF core scanning of sediment cores. Further studies should focus on assessing the influence of other sediment physical properties, e.g., bulk density, on XRF peak areas.

**Acknowledgments** This research was supported by an EU FP6 Marie Curie Outgoing Fellowship to S.B. Cruise NBP0505 was funded by the US National Science Foundation, Office of Polar Programs grant number NSF/OPP 03-38137 to J. Anderson (Rice University) and J. Smith Wellner (University of Houston). The Cimar-7 Program was supported by the Chilean National Oceanographic Committee (CONA, Grant C7F 01-10 to S. Pantoja). We thank the curators of the Florida State University Antarctic Marine Geology Research Facility (Simon Nielsen and Lindsey Geary) for their assistance with shipping core JPC14 to WHOI. We are grateful to Jess Tierney (WHOI) for her help with the XRF core scanner measurements, and to Jan-Berend Stuut and Inka Meyer (MARUM, Bremen, Germany) for providing access to the Coulter particle size analyzer. S.B. is currently a postdoctoral fellow of the Flemish Research Foundation (FWO, Belgium).

# Appendix

**Table 19.1** Descriptive statistics (arithmetic mean, minimum and maximum) of grain-size, water content and ICP-AES elemental concentrations for cores JPC14 (n geochemistry = 44) and PC29A (n geochemistry = 102). The relative range (r.r., or range percent variation, i.e., range divided by mean) is indicated in parentheses

| | JPC14 | | PC29A | |
|---|---|---|---|---|
| | Mean | Min-max | Mean | Min-max |
| Grain-size (μm) | 40.1 | 7.1–180.4 *(n = 319)* | 26.0 | 17.4–31.4 (*n* = 51) |
| Water content (%) | 39.9 | 22.6–51.3 *(n = 141)* | 49.7 | 47.2–53.3 *(n = 102)* |
| Al (wt.%) | 8.87 | 8.44–9.40 *(r.r. = 10.8%)* | 7.80 | 7.59–8.21 *(r.r. = 8.0%)* |
| Si (wt.%) | 26.4 | 24.4–29.4 *(r.r. = 19.1%)* | 25.0 | 23.8–25.9 *(r.r. = 8.5%)* |
| K (wt.%) | 1.93 | 1.21–2.64 *(r.r. = 74.3%)* | 1.32 | 1.20–1.42 *(r.r. = 16.7%)* |
| Ca (wt.%) | 3.47 | 2.60–4.41 *(r.r. = 52.2%)* | 3.53 | 3.20–4.02 *(r.r. = 23.4%)* |
| Ti (wt.%) | 0.62 | 0.55–0.66 *(r.r. = 18.1%)* | 0.68 | 0.60–0.85 *(r.r. = 37.4%)* |
| Mn (wt.%) | 0.108 | 0.089–0.130 *(r.r = 38.5%)* | 0.093 | 0.086–0.103 *(r.r = 18.2%)* |
| Fe (wt.%) | 5.93 | 4.71–6.94 *(r.r. = 37.6%)* | 5.35 | 4.94–6.14 *(r.r. = 22.6%)* |
| Sr (ppm) | 332 | 247–454 *(r.r. = 62.3%)* | 385 | 350–430 *(r.r. = 20.6%)* |
| Zr (ppm) | 135 | 78–213 *(r.r. = 101.0%)* | 183 | 159–210 *(r.r. = 28.1%)* |

**Table 19.2** Pearson correlation coefficients (*r*) between elemental XRF core scanner peak areas and ICP-AES concentrations. The XRF measurements were obtained on fresh sediment cores for (a) and (b) and on dry pressed pellets for (c). Values in bold indicate correlations that are significant at $p < 0.01$. The elements are ranked by atomic number. Correlation plots for selected elements are represented in Figs. 19.4 and 19.5. The low values of r for Ti in JPC14, and for K and Zr in PC29A are due to the low range of concentrations of these elements in these specific cores (see Table 19.1). Because not all variables are normally distributed, especially for core PC29A (Shapiro-Wilk test), Spearman correlation coefficients were also calculated. The results show no change in the significance of the correlations at $p < 0.01$

| Element | Atomic number | (a) JPC14 | (b) PC29A | (c) Pellets PC29A |
|---|---|---|---|---|
| Al | 13 | −0.15 | −0.03 | 0.22 |
| Si | 14 | 0.34 | −0.10 | **0.33** |
| K | 19 | **0.72** | −0.03 | **0.49** |
| Ca | 20 | **0.77** | **0.77** | **0.91** |
| Ti | 22 | 0.26 | **0.92** | **0.98** |
| Mn | 25 | 0.37 | **0.72** | **0.81** |
| Fe | 26 | **0.60** | **0.85** | **0.94** |
| Sr | 38 | **0.92** | **0.71** | **0.57** |
| Zr | 40 | **0.76** | 0.21 | **0.37** |
| *n* | – | *37* | *102* | *102* |

**Table 19.3** Pearson correlation coefficients ($r$) and slopes of the linear regressions ($\times 10^3$) between normalized XRF peak areas/ICP concentrations and (a) grain-size, or (b) water content, for sediment core JPC14 ($n = 37$). See graphical representation in Fig. 19.6. Values in bold indicate correlations that are significant at $p < 0.01$. The slope values in gray indicate the elements for which correlations are not significant at $p < 0.01$. Note the opposite signs of the regressions between (a) and (b) for most elements. Higher absolute values of the slopes indicate a higher influence of (a) grain-size or (b) water content variations on XRF core scanner peak areas. Correcting the XRF peak areas for water content (c) decreases the significance and the absolute values of the slopes of the correlations between XRF peak areas/ICP concentrations and grain-size. The relative decrease in the slope is indicated in (d). The water content correction consisted in back-calculating the XRF peak area/ICP concentration values using the regressions shown in Fig. 19.6b. See illustration in Fig. 19.7

| JPC14 | (a) Grain size | | (b) Water content | | (c) Grain size after water content correction | | (d) Relative decrease in slope after water content correction (%) |
|---|---|---|---|---|---|---|---|
| Element | $r$ | slope | $r$ | slope | $r$ | slope | |
| Al | 0.30 | 5.14 | –0.29 | –19.2 | 0.11 | 1.76 | 66 |
| Si | 0.01 | 0.06 | –0.08 | –3.44 | –0.05 | –0.54 | – |
| K | ***0.87*** | 4.32 | ***–0.69*** | –13.1 | ***0.56*** | 2.02 | 53 |
| Ca | –0.03 | –0.01 | –0.12 | –1.61 | –0.11 | –0.40 | – |
| Ti | ***0.45*** | 1.2 | –0.40 | –4.10 | 0.19 | 0.48 | 60 |
| Mn | 0.32 | 1.27 | –0.40 | –3.06 | 0.05 | 0.19 | 85 |
| Fe | ***0.47*** | 1.24 | ***–0.46*** | –4.65 | 0.18 | 0.43 | 65 |
| Sr | ***0.51*** | 1.98 | ***–0.45*** | –6.77 | 0.23 | 0.79 | 60 |
| Zr | ***–0.43*** | –1.94 | **0.52** | 9.17 | –0.08 | –0.33 | 83 |
| | | | | | | | mean = 69 |

**Table 19.4** Pearson correlation coefficients ($r$) between elemental XRF core scanner peak areas and ICP-AES concentrations before any correction (a), after water content correction only (b), and after grain-size correction only (c), for sediment core JPC14 ($n = 37$). Values in bold indicate correlations that are significant at $p < 0.01$. The low values of $r$ for Ti are due to the low range of Ti concentrations in core JPC14 (relative range of 18.1%, see Table 19.1). Correcting the XRF peak areas for water content or grain-size, using the regressions shown in Fig. 19.6, does not significantly increase the correlation coefficients between elemental XRF core scanner peak areas and ICP-AES concentrations. (Fisher r-to-z transformation, two-tailed test, $p < 0.05$)

| JPC14 | Correction | | |
|---|---|---|---|
| Element | (a) None | (b) Water content | (c) Grain-size |
| Al | −0.15 | −0.21 | −0.08 |
| Si | 0.34 | 0.27 | 0.25 |
| K | *0.72* | *0.81* | *0.81* |
| Ca | *0.77* | *0.74* | *0.78* |
| Ti | 0.26 | 0.30 | 0.19 |
| Mn | 0.37 | *0.50* | *0.56* |
| Fe | *0.60* | *0.73* | *0.72* |
| Sr | *0.92* | *0.87* | *0.85* |
| Zr | *0.76* | *0.86* | *0.85* |

**Table 19.5** Pearson correlation coefficients ($r$) and slopes of the linear regressions ($\times 10^3$) between normalized XRF peak areas/ICP concentrations and (a) grain-size, or (b) water content, for sediment core PC29A [$n = 51$ for (a) and 102 for (b)]. See graphical representation in Fig. 19.8. Values in bold indicate correlations that are significant at $p < 0.01$. The slope values in gray indicate the elements for which correlations are not significant at $p < 0.01$. Higher absolute values of the slopes indicate a higher influence of (a) grain-size or (b) water content variations on XRF core scanner peak areas. Correcting the XRF peak areas for water content (c) does not systematically decrease the slope of the regressions. Column (**d**) represents the Pearson correlation coefficients ($r$) and slopes of the linear regressions ($\times 10^3$) between normalized XRF peak areas obtained on pressed pellets/ICP concentrations and grain-size ($n = 51$). The relative change in the slope of the linear regressions between data obtained on dry pellets (d) and fresh sediment cores (a) is indicated in (e). The results show that, for core PC29A, XRF data obtained on pressed pellets are not more or less dependent on grain-size than data obtained on fresh sediment cores

| PC29A | (a) Grain size | | (b) Water content | | (c) Grain size after water content correction | | (d) Grain size - pressed pellets | | (e) Relative change in slope after correction (%) |
|---|---|---|---|---|---|---|---|---|---|
| Element | $r$ | slope | $r$ | slope | $r$ | slope | $r$ | slope | |
| Al | –0.05 | –4.36 | –0.07 | –0.02 | –0.01 | –1.06 | –0.30 | –8.51 | –95 |
| Si | –0.14 | –5.39 | ***–0.34*** | –2.82 | ***–0.27*** | –9.43 | –0.24 | –2.20 | 59 |
| K | 0.06 | 1.33 | ***–0.48*** | –19.5 | ***–0.05*** | –0.80 | 0.11 | 1.19 | 11 |
| Ca | ***–0.46*** | –8.98 | –0.24 | –9.88 | –0.56 | –10.67 | ***–0.78*** | –10.88 | –21 |
| Ti | –0.13 | –1.95 | ***–0.49*** | –14.0 | ***–0.25*** | –3.06 | –0.33 | –2.46 | –26 |
| Mn | ***–0.42*** | –7.68 | ***0.35*** | 13.0 | ***–0.25*** | –4.24 | –0.10 | –0.58 | 92 |
| Fe | –0.05 | –0.53 | ***–0.39*** | –7.59 | ***–0.07*** | –0.66 | ***0.37*** | 0.32 | 40 |
| Sr | ***0.52*** | 5.20 | –0.21 | –4.31 | 0.46 | 4.64 | ***0.51*** | 5.65 | –9 |
| Zr | 0.29 | 5.84 | 0.22 | 9.97 | 0.49 | 10.57 | 0.35 | 7.44 | –27 |
| | | | | | | | | | mean = 3 |

**Table 19.6** Decrease in the relative precision of XRF core scanner measurements due to grain-size variations, for data obtained on sediment core JPC14 before (a), and after (b) water content correction, and for data obtained on sediment core PC29A (c). These values are derived from the slope of the linear regressions presented in Figs. 19.6a, 19.7 and 19.8a. Columns (d) to (f) present the range of grain-sizes that corresponds to a relative precision of XRF core scanner measurements of 5 %. (see Tables 19.3a, 19.3c and 19.5a)

| Element | Decrease in relative precision per micron (%) | | | Range of grain-sizes corresponding to 5 % precision (μm) | | |
|---|---|---|---|---|---|---|
| | (a) JPC14 | (b) JPC14-corrected for water content | (c) PC29A | (d) JPC14 | (e) JPC14-corrected for water content | (f) PC29A |
| Al | – | – | – | – | – | – |
| Si | – | – | – | – | – | – |
| K | 0.43 | 0.20 | – | 12 | 25 | – |
| Ca | – | – | 0.90 | – | – | 6 |
| Ti | 0.12 | – | – | 42 | – | – |
| Mn | – | – | 0.77 | – | – | 7 |
| Fe | 0.12 | – | – | 40 | – | – |
| Sr | 0.20 | – | 0.52 | 25 | – | 10 |
| Zr | 0.19 | – | – | 26 | – | – |

"–" indicates elements for which the influence of grain-size on XRF peak areas is insignificant at $p < 0.01$

## References

Bertrand S, Hughen KA, Lamy F, Stuut JBW, Torréjon F, Lange CB (2012a) Precipitation as the main driver of Neoglacial fluctuations of Gualas glacier, Northern Patagonian Icefield. Clim Past 8:519–534

Bertrand S, Hughen K, Sepúlveda J, Pantoja S (2012b) Geochemistry of surface sediments from the fjords of Northern Chilean Patagonia (44–47°S): spatial variability and implications for paleoclimate reconstructions. Geochim Cosmochim Acta 76(1):125–146

Bertrand S, Hughen KA, Sepúlveda J, Pantoja S (2014) Late Holocene covariability of the southern westerlies and sea surface temperature in northern Chilean Patagonia. Quat Sci Rev 105, 195–208

Croudace IW, Rindby A, Rothwell RG (2006) ITRAX: description and evaluation of a new multi-function X-ray core scanner. In: Rothwell RG (ed) New techniques in sediment core analysis. Geol Soc Spec Publ 267:51–63

Cuven S, Francus P, Cremer J-F (2007) Protocoles d'utilisation et essais de calibration du scanner de microfluorescence X de type "ITRAX core scanner". INRS-ETE, Québec, rapport de recherche no 954, p 108

Cuven S, Francus P, Lamoureux SF (2010) Estimation of grain-size variability with micro X-ray fluorescence in laminated lacustrine sediments, cape bounty, Canadian high arctic. J Paleolimnol 44(3):803–817

De Vivo B, Belkin HE, Lima A (2008) Environmental geochemistry: site characterization, data analysis and case histories. Elsevier, Amsterdam, p 429

Glasser NF, Harrison S, Jansson KN, Anderson K, Cowley A (2011) Global sea-level contribution from the Patagonian icefields since the little ice age maximum. Nat Geosci 4:303–307

Huang S, Sholkovitz E, Conte M (2007) Application of high-temperature fusion for analysis of major and trace elements in marine sediment trap samples. Limnol Oceanogr Methods 5:13–22

Injuk J, Van Grieken R, Blank A, Eksperiandova L, Buhrke V (2006) Specimen preparation. In: Beckhoff et al (eds) Handbook of practical X-ray fluorescence analysis. Heidelberg, Springer, pp 411–429

Kido Y, Koshikawa T, Tada R (2006) Rapid and quantitative major element analysis method for wet fine-grained sediments using an XRF microscanner. Mar Geol 229:209–225

Murray R, Miller D, Kryc K (2000) Analysis of major and trace elements in rocks, sediments, and interstitial waters by inductively coupled plasma atomic emission spectrometry (ICP-AES). ODP Technical Note 29

Richter TO, van der Gaast S, Koster B, Vaars A, Giele R, de Stigte HC, De Haas H, van Weering TCE (2006) The avaatech XRF core scanner: technical description and applications to NE Atlantic sediments. In: Rothwell RG (ed) New techniques in sediment core analysis, vol 267. Geological Society Special Publication, London, pp 39–50

Sholkovitz E (1990) Rare-earth elements in marine sediments and geochemical standards. Chem Geol 88(3–4):333–347

Syvitski JPM (2007) Principles, methods and applications of particle size analysis, 3rd edn. Cambridge University Press, New York, p 388

Tjallingii R, Röhl U, Kölling M, Bickert T (2007). Influence of the water content on X-ray fluorescence core scanning measurements in soft marine sediments. Geochem Geophys Geosystems 8(2). doi:10.1029/2006GC001393

Zolitschka B, Mingram J, van der Gaast S, Jansen JHF, Naumann R (2001) Sediment logging techniques. In: Last WM, Smol JP (eds) Tracking environmental change using lake sediments, vol 1. Kluwer Academic, Dordrecht, pp 137–153

# Chapter 20
# Standardization and Calibration of X-Radiographs Acquired with the ITRAX Core Scanner

**Pierre Francus, Kinuyo Kanamaru and David Fortin**

**Abstract** A calibration procedure that uses a radiographic reference sample (RRS) to compensate for instrumental, time- and sample-related variations encountered with Itrax X-radiographs is introduced. This RRS is always included whenever a core section is run on the Itrax and it allows radiographs to be standardized. This allows different cores to be compared ultimately leading to increased efficiency, cost saving and scientific value. A standardization protocol is presented that corrects for X-ray tube output (ageing), different acquisition settings and sediment core properties (diameter and material). This allows for the direct comparison and accurate concatenation of radiographic images from long sequences. Other Itrax laboratories using an identical RRS can also share radiographic data. The standardized X-ray attenuation profiles from the Itrax compare very well with attenuation profiles obtained by CT-scan, a technology providing attenuation values very close to density and not influenced by sample thickness.

**Keywords** X-radiographs · Radiographic reference sample · CT-Scan · Laminated and varved sediments

P. Francus (✉)
Institut National de la Recherche Scientifique, Centre Eau Terre Environnement, Québec, QC G1K 9A9, Canada

GEOTOP Research Centre, Montréal, QC H3C 3P8, Canada
e-mail: pfrancus@ete.inrs.ca

K. Kanamaru
Department of Geosciences, University of Massachusetts, Amherst, Morrill Science Center, 611 North Pleasant Street, Amherst, MA 01003–9297, USA
e-mail: kinuyok@geo.umass.edu

D. Fortin
Institut National de la Recherche Scientifique, Centre Eau Terre Environnement, Québec, QC G1K 9A9, Canada
e-mail: david.fortin@ete.inrs.ca



I. W. Croudace, R. G. Rothwell (eds.), *Micro-XRF Studies of Sediment Cores*, Developments in Paleoenvironmental Research 17, DOI 10.1007/978-94-017-9849-5_20

## Introduction

The Itrax core scanner technology that emerged in 2003 was mainly developed for the non-destructive and high-resolution geochemical analysis of sediment cores (Croudace et al. 2006; Jansen et al. 1998). The main focus for most Itrax users has been the micro-XRF feature. However, the instrument also has the routine ability to provide excellent quality X-radiographs and less attention has been given to this valuable aspect of the instrument. These Itrax digital radiographic images have a very high dynamic range (16-bits or $2^{16}$ grey-level values) and offer a very high resolution (a pixel size down to 20 μm) and are produced with an optimum optical geometry. This optimal geometry results from the detector being right below the X-ray source and prevents image distortions caused by the parallax effect (e.g. Ojala 2004). These characteristics are ideal for the analysis of very finely laminated sediments (e.g. Ojala et al. 2012) and encompass a wide range of densities usually encountered in very long sedimentary sequences (e.g. St-Onge et al. 2007).

X-radiography is a mature technology routinely used in Earth Science (e.g. Hamblin 1962; Bouma 1964; Jackson et al. 1996; Migeon et al. 1999) and many other different fields (e.g. Rockley 1964; Fosbinder and Kelsey 2002; Chhem and Brothwell 2007). In sedimentology, X-radiographs are useful for comparing lithostratigraphy among multiple cores, examining sedimentary facies variations, detecting and measuring Ice Rafted Debris (IRD) (Principato 2004), as well as sedimentary discontinuities (Besonen 2006) or coring disturbances (Stow and Townsend 1990). They also have been used to estimate and quantify bioturbation (Cremer et al. 2002), counting and measuring laminations (Kanamaru et al. 2013), and determine sediment density (Fortin et al. 2013). Incident X-rays are attenuated by a wide range of phenomena including attenuation and scattering. Hence, grey-level values in Itrax X-radiographs are a measure of X-rays attenuation. The dominant control on beam attenuation is sediment thickness and bulk sediment density. The latter is influenced by various factors such as sediment porosity, water content, composition (organic matter, biogenic silica content, terrigenous fraction mineralogy), and texture (grain size) (St-Onge et al. 2007).

Despite the comprehensive theoretical knowledge of X-radiography and the high quality of Itrax radiographs and their potential in sedimentological studies, surprisingly few Itrax studies report radiographic results. Practical issues may be responsible for this. For instance, some researchers may have faced difficulty when concatenating long X-radiographic attenuation curves. This is possibly worsened when using data from different core sections, different instrumental settings, different core barrels (size and composition) and acquired with X-ray tubes with different excitation outputs (caused through ageing). It also remained quite difficult to compare and assemble Itrax measurements obtained from two different laboratories. To overcome these difficulties effectively is relatively straightforward if a radiographic reference sample customized for the Itrax core scanner is used.

This paper first illustrates the practical issues related to the construction of an X-ray attenuation curve using an example from a 40-m long laminated sequence. It then introduces a radiographic reference sample (RRS) customized for the Itrax core scanner and a protocol to perform a calibration. The overall procedure serves to concatenate long attenuation curves acquired from several core sections or different laboratories with an example from a u-channel of lacustrine sediments. Finally, it explores the possibility to anchor standardized attenuation Itrax curves with CT-scan images because (1) CT-scan images are easily linked to actual density, and (2) it validates our approach with an independent measurement.

## Instruments Used

High-resolution digital X-radiographs were acquired with an Itrax of the first generation at the Institut National de la Recherche Scientifique (INRS), Quebec city, Canada. This instrument has a 100 µm-thick incident beam and all analyses were conducted using a Mo tube. Longitudinal X-radiographs are 16-bit positive images, i.e. light pixels represent low-density material. Images are 14 mm wide sections of the sample with a pixel size of 100 µm. Additional technical details about the instrument can be found in Croudace et al. (2006).

Computerized axial tomography (CT-scan) images were obtained using a third generation Siemens Somatom Volume Access sliding gantry medical CT-Scanner, also located at INRS.

## Example of Radiographs Obtained from u-Channels

The quality of X-radiographs from full or half sediment cores is limited by two main issues: (1) the uneven sediment thickness resulting from the cylindrical shape of the core tubes induces varying attenuation coefficients at similar core depth; (2) the thickness of the sediment sample may obscure fine sediment structures when those structures are not perfectly parallel to the X-ray beam. One way to circumvent those problems is to use thin sediment samples with a constant thickness such as impregnated sediment blocks (Ojala 2004), sediment slabs (Migeon et al. 1999) or u-channels (Nagy and Valet 1993). U-channels are routinely sampled for palaeomagnetic analysis but can also be analysed effectively by the Itrax-core scanner. Hence, µ-XRF and palaeomagnetic analysis can be conducted on the exact same sample, which is an advantage for the study of long sedimentary sequences (Ohlendorf et al. 2011). However, the use of multiple u-channels scanned under different conditions is associated with some issues that are illustrated and discussed below.

### *Using Different Sample Containers (or With and Without u-Channel Cover)*

X-radiographs were acquired from u-channels of core MD02–2490, a 51.07-m long giant piston core recovered by the French research ship, *RV Marion Dufresne,* from the central basin of Saanich Inlet, British Columbia, Canada, at water depth 224 m. Seven out of 18 scanned u-channels were processed with u-channel covers in place, while the 11 other u-channels were scanned with the covers removed. Although this particular situation was due to a laboratory malpractice, it does mimic the situation when some cores are taken with plastic liners of different thicknesses or when different coring equipment is used at a single site. Grey-level values were measured using *ImageJ*, image analysis software that is freely available on the Web (Rasband 1997–2012), along a 10-pixel-wide line equivalent to a sediment section having a width of 1 mm. The line is drawn perpendicular to the long-axis of the image and averages of the Grey-level values (GVs) are plotted against the image (Nederbragt and Thurow 2001). When plotting the entire record (Fig. 20.1), it was clear that sections with covers had lower GV compared to the ones measured without covers.

In order to correct for this bias, one section (S18) was re-scanned with and without its cover. Figure 20.2a shows that the cover increases the GV of the sample by attenuating part of the X-ray signal, but the variability and the amplitude of the GV variations remain the same. A strong linear correlation between the two sets of GVs demonstrates that a linear regression is a reliable transfer equation for all X-radiographs scanned with u-channel covers (Fig. 20.2b). Figure 20.1 shows the entire sequence with GVs of the uncovered u-channel sections adjusted with the regression established on S18 to be equivalent to the values obtained with covers. This correction significantly changes the initial density record, demonstrating that

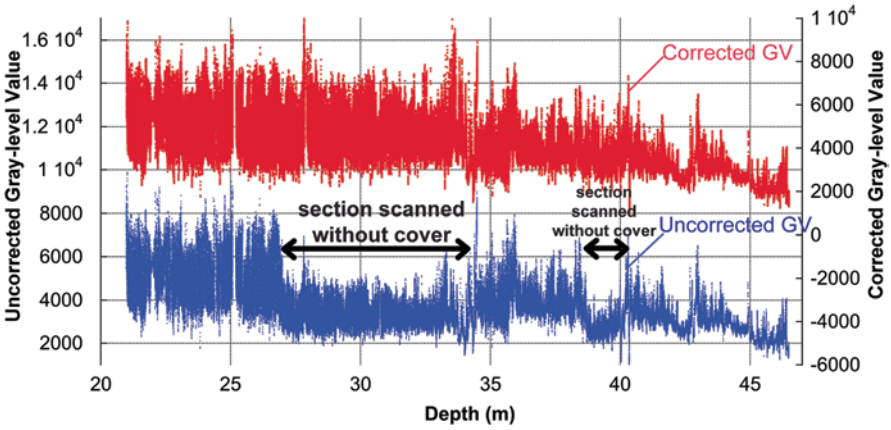


**Fig. 20.1** Corrected and uncorrected grey-level values of core MD02-2490. The intervals scanned without u-channel covers are indicated by the *arrows*

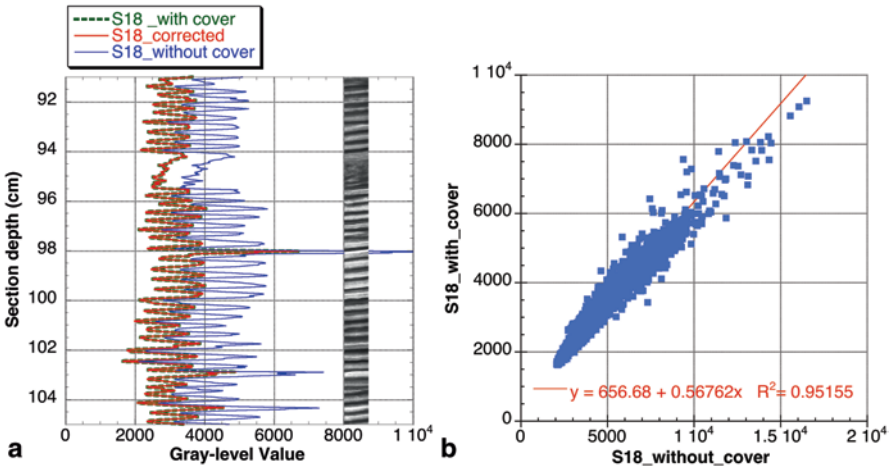


**Fig. 20.2** **a** Grey-level values (*GV*) and corresponding X-radiographic image of core MD02-2490 section 18 from 105 to 90 cm section depth. Higher GVs correspond to less dense biogenic varve segments, seen as light-colours on X-radiographic image, and lower GVs coincide with dark-coloured terrigeneous varve segments. GVs of a covered u-channel have lower values (*green*) than uncovered u-channel (*blue*). Corrected GVs using linear regression shown in (**b**) is plotted in *red*. **b**. Scatter plot between GVs acquired with and without cover along the section of panel (**a**), the regression equation and the correlation coefficient

the correction was necessary. In this example, we were able to perform a correction because the samples were still available and intact. Otherwise, another solution, i.e. an internal standard, would have been necessary, and in this case, the u-channels should have been scanned with and without the cover.

## *Using Different Acquisition Settings*

Figure 20.3 displays an example of a single u-channel radiographed with different acquisition settings. Grey-level values of the first run yielded grey-level values between 1176 and 1877 (standard deviation = 211), while the second run measured grey-level values between 581 and 917 (standard deviation = 110) (Fig. 20.3b). From this example, it is clear that one need to maintain acquisition settings strictly similar if there is a need to assemble several core sections into a long composite sequence as is usually the case for large drilling projects. However, this cannot always be achieved for practical reasons. Moreover, X-ray tubes are aging and identical settings of the same sample taken at different time will not provide exactly identical grey-level values. The issue is more serious when analyses from two separate Itrax instruments need to be compared: the X-ray sources are different, and the incident beams can be 100 or 200 µm thick (Croudace et al. 2006). A reference sample in each run can circumvent this issue.

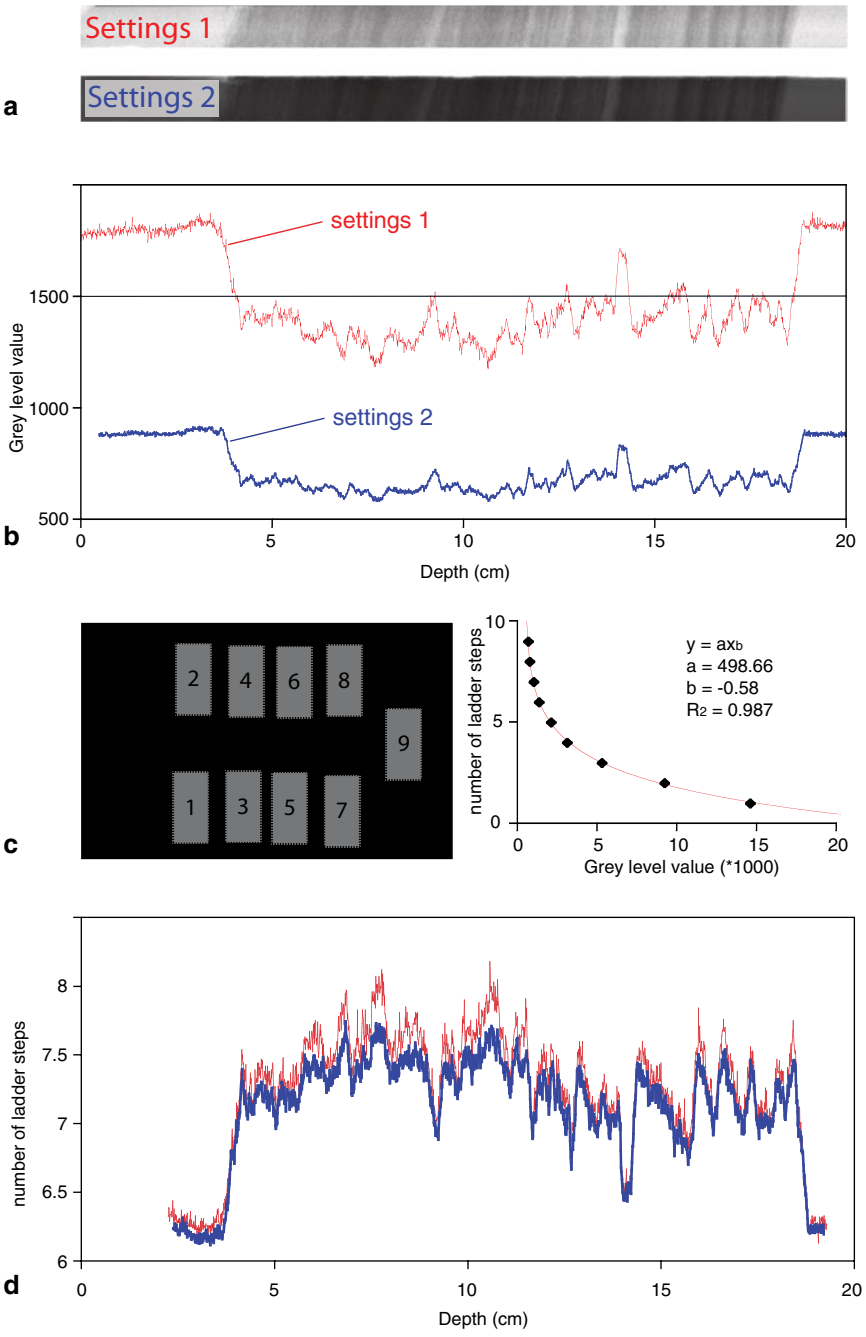


**Fig. 20.3.** **a** Two u-channels sections from Laguna Potrok Aike acquired with 50 kV, 48 mA during 300 ms (settings 1) and 40 kV, 40 mA during 600 ms (settings 2). **b** Plot of the grey-level values along the two sections outlined in (a). **c** (*Left*) X-radiograph of the radiographic reference sample and the nine regions of interest used to measured average grey-values for each ladder step; (*right*) scatter plot of the grey-level values against the number of ladder steps and the fitted relationship between the two variables. **d** Grey-level profiles of panel (a) transformed in number of ladder steps

## The Radiographic Reference Sample (RRS)

The RRS was designed to meet several requirements (Fig. 20.4). It needed to be small-sized in order to be included in all X-radiography runs without adding significant scanning time, and hence keeping the operating costs as low as possible. The RRS produced is only 20 mm thick, the acquisition time being of 80 s (settings: 100 µm resolution and 400 ms).

The RRS is made of an aluminium block with nine ladder steps of equal thickness (2 mm) designed to encompass a wide range of densities and sediment thickness (sediment cores and u-channels). It is intended to be clamped in the lower part of the Itrax sample carrier, at the beginning or at the end of a sample. Butterfly nuts ensure an easy and quick installation and removal (Fig. 20.4).

A raw X-radiograph of the RRS acquired by the Itrax core scanner is shown in Fig. 20.5a (settings: 45 kV; 45 mA; 500 ms; Mo tube). Contrast enhancement of image is necessary to visualize all ladder steps (Fig. 20.5b). Each step is large enough to be covered by a 20 by 40 pixels region of interest from which the average grey-level value can be measured by any common image analysis software. In our example, grey-level values are comprised between 482 and 16,137 (Fig. 20.5c, d) and the relationship between the number of ladder steps and attenuation is logically exponential according to the attenuation expression

$$I = I_0^{\left[-\left(\frac{\mu}{\rho}\right)(\rho t)\right]} \tag{20.1}$$

where $I$ is the measured intensity, $I_0$ the incident intensity, µ the sample attenuation coefficient, ρ its density and $t$ its thickness (e.g. Goldstein et al. 2003).

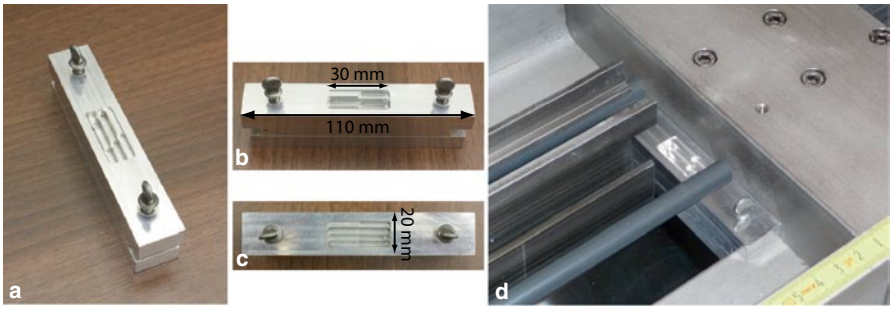


**Fig. 20.4** Pictures of the radiographic reference sample. It is made of two pieces of aluminium that are held together by butterfly nuts. **a** Overall view. **b** Side view and dimensions. Note the notch used to clamp the RSS onto the Itrax sample carrier. **c** Top view and width. **d** RSS in position within the Itrax

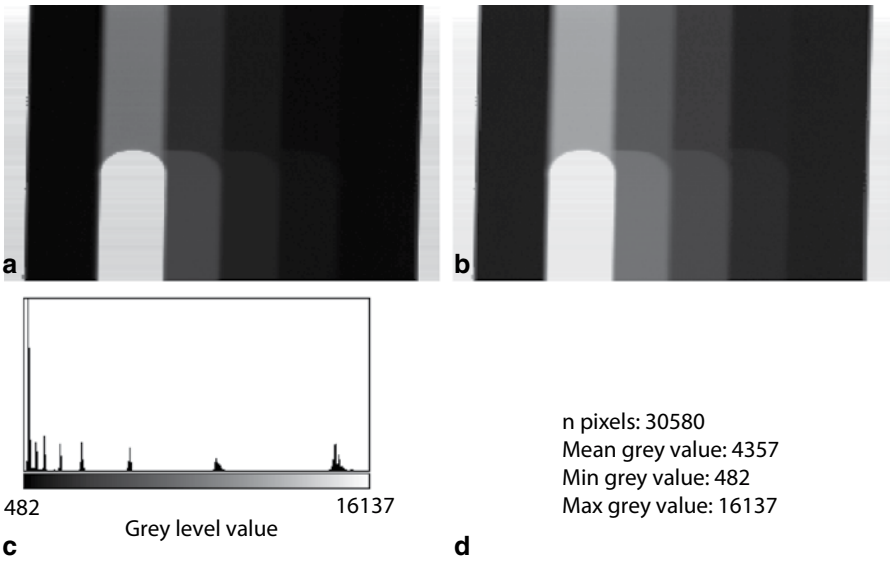


**Fig. 20.5** Radiograph of the reference sample by the Itrax. **a** Raw image. **b** Image (**a**) enhanced to optimize contrast (for better view only). **c** Grey-level value histogram of (a). **d** Descriptive statistical parameters of image (**a**) grey-level values

## Standardization Protocol

The suggested standardization protocol is rather straightforward. The example below is provided with *ImageJ* but can be performed by any common image analysis software that supports 16-bits images. Measurement needs to be performed on the raw tiff files provided by the Itrax, i.e., without having the images enhanced for contrast. First, the average grey-level value of each RSS step of the RRS is measured within a fixed-sized region of interest using the *Analyze/Measure* function (Fig. 20.3c). We recommend using a minimum $20 \times 40$ pixels-sized surface area to perform such measurements in order to yield a result that is an average of 800 pixels, hence providing an efficient noise reduction. Once all nine measurements are performed, the *Analyze/Calibrate* function displays a table with the average grey-level values measurements. The number of ladder steps is entered besides the measured grey-level value, and the *Power* function in the dropout menu is selected (Fig. 20.3c). Once this operation is performed, all pixels values of the X-radiograph are now converted into "RRS ladder step" values. This operation needs to be repeated for all X-radiographs separately, but if the RRS is located at the same place in each image, a macro can be programmed to automate the whole process. Now both runs of Fig. 20.3d are converted into "RRS ladder step" units and, when superposed, show a near perfect fit, the correlation between the two profiles being $R^2 = 0.97$.

For laboratory intercomparison purpose, the RRS used in each laboratory needs to have the exact same characteristics in terms of size and material. Of course this standardization protocol for X-radiographs only works for samples having the exact same thickness. Indeed, Eq. 20.1 outlines that sample thickness has a strong influence on X-ray attenuation. Hence, the analysis of u-channels seems to be more appropriate for such intercomparison. Regardless, it is likely that, given the limited time available for analysis, sediment scanning is generally conducted on split cores. In this situation, X-ray attenuation will be affected by longitudinal changes in sediment thickness (topography). However, if the core halves to be measured are evenly filled in and the core liners are carefully cut at the exact centre of the tube, then it should be possible to measure consistent attenuations profiles despite minor lateral changes in thickness due to the curved nature of the liner.

Even if the standardization protocol eases the construction of long X-ray attenuation profiles, it yields results expressed in "RRS ladder step" units. This unconventional unit[1] will be meaningless for most scientists. Therefore, the next section investigates the possibility of anchoring this unit into meaningful physical units as it is provided by X-ray tomodensitometry.

## CT-Scan

3D tomodensitometric images of CAT-scanners are the result of the same physical interactions of X-rays; X-rays are aimed at a sample and their attenuation is measured at the other side. Therefore the same physical sample properties are influencing the attenuation. The main difference is that CT-scan has the advantage to yield 3D X-ray attenuation images that are not affected by sample thickness. Indeed, CT-scans have an array of X-ray sources that rotate around the sample while the attenuation is measured on the opposite side. Tomographic reconstruction is computed to generate 3-D images from a series of 2-D X-radiographs (Hsieh 2003). CT-scan yields two types of images: tomograms are 2-D transverse images (perpendicular to the length of the core or u-channel), and topograms are 2-D longitudinal cross-sections (St-Onge et al. 2007). The maximum spatial resolution is obtained in tomograms where the size of each voxel, i.e. volumetric pixel, can be as small as 600 $\mu m^3$ with the instrument used in this study.

Moreover, each voxel is characterized by an attenuation value that is expressed in a standard Hounsfield unit (HU) (Hounsfield 1973) defined as

$$CT = \left(\mu / \mu_w - 1\right) \text{ x } 1000 \tag{20.2}$$

[1] Note that grey-level values are somewhat arbitrary like "RSS ladder steps" as both are instrument dependent.

Where μ is the attenuation coefficient of the voxel and $\mu_w$ is the one of water. Practically, images are 12 bit negatives in DICOM format where CT = −1024 for air, CT = 0 for water and CT = 2500 for calcite (de Montety et al. 2003). Still, attenuation coefficients in computerized axial tomography are similarly affected by bulk sediment density, mineralogy and porosity (e.g., Boespflug et al. 1995). Nevertheless, CT units are directly related to sediment bulk density, because this scale is linked to elements found in sediment cores (e.g. water, calcite), and is not influenced by the sample thickness nor affected by the potentially varying properties of the sediment core's container. Therefore, we compared our standardized Itrax attenuation data with CT-scan output in order to check if both technologies provide similar results.

## *Production of a Longitudinal Profile with HU Numbers*

In the example presented here (Fig. 20.6), tomograms were obtained with the CT-Scanner at INRS-Québec on a 1.5 m-long u-channel of lacustrine sediments from the PASADO composite profile (Ohlendorf et al. 2011). Tomograms were acquired continuously at every 0.4 mm, along a 0.6 mm-thick slice with an overlap from a tomogram to another of 0.2 mm, totalling 3750 images for a 1.5 m-long u-channel section. The u-channels were scanned with X-ray peak energy of 140 kV with 250-mA current, in captured images of the size of 512 × 512 pixels. Once acquired, tomograms were transformed into topograms using a custom Matlab routine. This Matlab routine averages HU pixel values along a specified zone of interest on each tomogram and recalculates a longitudinal 2-D image of the u-channel according to these averaged values. The topogram presented here was obtained by averaging a 2 mm cross-section of every tomogram centred on the middle of the u-channels. The result (Fig. 20.7) consists in a 2-D attenuation map with a pixel size of 0.4 mm. Several other softwares can be used to reconstruct topograms from tomograms, including the open source *ImageJ* package. HU values from these topograms were then extracted by averaging the HU value (pixel value) at every depth using *ImageJ*.

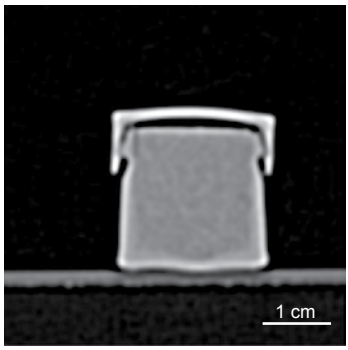


**Fig. 20.6** A tomogram from a 2 × 2 cm (width and depth) u-channel. The image represents a 0.6 mm thick slice of a u-channel. The image is 512 × 512 pixels. The image is in DICOM format; grey-level values correspond to Hounsfield Units

**Fig. 20.7** Topogram (1.5 m long) reconstructed from 3750 overlapping tomograms. The image is in DICOM format; grey-level values correspond to hounsfield units

## *Comparison of CT-Scans and ITRAX Radiographs*

The use of computed axial tomography offers the advantage of producing 3D attenuation maps of the sediment, which allows quantifying the presence of voids, cracks and other discontinuities within a given sample, and to remove them from attenuation profiles. X-radiographs are, on the other hand, very sensitive to all changes in sediment thickness and discontinuities since the 2D grey-level value map they result in integrates the entire thickness of a given sample. However, when using a sample of constant volume, with minimal discontinuities such as is typical of u-channels, direct comparison of HU number and Itrax X-radiographs becomes possible.

Figure 20.8 compares HU values obtained on the topogram presented in Fig. 20.7 with the grey level values from an Itrax X-radiography obtained on the same u-channel at a resolution of 100 μ (kV = 40; mA = 40, exposure = 600 ms). Grey-level values were averaged along every depth in order to obtain an average attenuation curve of the u-channel. Figure 20.8 shows both HU and grey-level value variability along the 1.5 m, after resampling the X-radiograph at the resolution of the CT-scan, i.e. 0.4 mm per pixel or 3750 data points. The anti-correlation results from the fact that the Itrax X-radiographs are positive images. Good agreement between the two data sets is confirmed by the scatter plot ($R^2 = 0.80$), demonstrating that when using sediment samples of even thickness, the calibration of grey-level values, or step-ladder values, into HU is possible (Fig. 20.9). When dealing with long sedimentary sequences, the best approach is to calibrate the radiographs of sediments of contrasting densities against CT-Scans of the same sections. One limitation of such an approach is the homogeneity of the sediment matrix; highly heterogeneous sediments within a same depth would result in erroneous or weak calibrations.

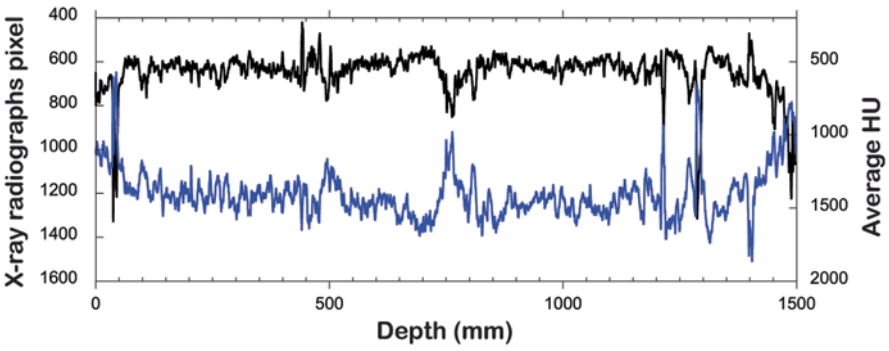


**Fig. 20.8** *Black curve*: X-radiographs average pixel value at every depth (resampled at 0.4 resolution). *Blue curve*: average HU at every depth from the topogram presented in Fig. 20.8

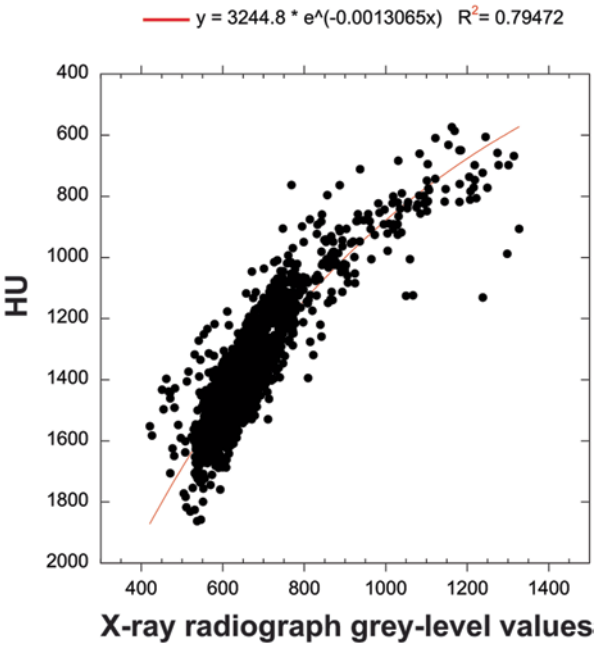


**Fig. 20.9** Regression of HU against X-radiograph grey-level values

## *Future Direction: Calibration of X-Radiographs Grey-level Values into Densities*

The example above makes use of a sample that has a fixed thickness to minimize the problem of uneven thickness. However, most Itrax users will find it cumbersome to extract u-channels only to get good X-radiographs. The thickness of the sample is however, precisely measured by the topographic laser that is used to position the XRF detector at a constant distance of the sample. In a future development, it should therefore be possible to use this set of data to have a precise estimation of the sample thickness and hence to correct for the attenuation variations due to the uneven sediment thickness within the core liners.

Density is an important parameter for the analysis of sediment cores. Indeed, provided that an accurate age model is available, it is possible to calculate the flux of any component *c* of the sediment in kg $a^{-1}$ $m^{-2}$ or in mol $a^{-1}$ $m^{-2}$. These component fluxes can then be used for comparisons with monitoring data (e.g. sediment traps), for process modelling or for calculating mass balance or budget, which are the ultimate goal of any quantitative environmental reconstruction. However, the flux calculation is not a common practice in sedimentary analyses because it is practically difficult to perform. The first main complication arises from the fact that age models are frequently resolved in low time resolution. Nevertheless, annually laminated (varved) sediments yield annually resolved time constrains (Ojala et al. 2012), and yet several protocols have been suggested to provide results expressed

in fluxes (e.g. Petterson et al. 1999; Besonen et al. 2008). The second complication arises from the density measurement itself. Accurate density measurements from discrete samples require volumetric sampling that are often imprecise due to incomplete filling of the sampling tool (Fortin et al. 2013), while density measurements from gamma ray attenuation are allowing a centimetric down-core spatial resolution (Zolitschka et al. 2001; St-Onge et al. 2007).

When considering Eq. 20.1, the measurements provided by the Itrax core scanner provide all the information necessary to calculate density $\rho$ at resolution down to 100 µm. As already mentioned above, sediment thickness ($t$) is precisely measured by the Itrax. Attenuation $I$ is the grey-level in the X-radiography, and $I_0$ the incoming radiation controlled by the X-ray source. The attenuation coefficients $\mu$ are unknown, but the fluorescence detector provides information about the chemical composition of the sample. Hence, knowing the mineralogy of the sediment, and using attenuation coefficients from the existing tables (Duchesnes et al. 2009), it should be possible, through a series of mathematical iterations, to calculate densities of each pixel of the X-radiograph provided that µ-XRF analysis was performed at the same resolution. Of course this achievement requires further developments, but this would bring substantial benefits for all scientists working on sediment cores.

## Conclusion

We introduced a small size and versatile radiographic reference sample (RRS) that can be included in each run of the Itrax core scanner at a low cost. In order to make the best use of this RRS, the following practical recommendations should be followed:

- The RRS should be placed at the end or the beginning of each run.
- Scanning U-channels or sediment cores with constant thickness is necessary until a protocol is developed to correct for the sediment core topographic variations.
- Scanning resolution should be no less than 500 µm in order to obtain enough measurements points of the RSS itself.
- Voltage, current (A) and dwell time can be optimized independently for each run and afterwards brought on a common scale by the protocol presented here, but it is always good practice to try optimizing the Itrax settings in order to accommodate all sections/runs from the different parts of a sedimentary sequence that can have different densities (organic/terrigenous, surface sediment/compacted).

We also introduced a protocol to standardize grey-level values into a number of ladder steps that resolve practical issues related to the construction of an X-ray attenuation curve. This RSS and its related protocol can be used to combine multiple core sections into a single composite radiographic image. Its use is very pertinent for inter-laboratory comparison purposes and for building long sequences in the frame of large international projects such as the ICDP and IODP. Importantly, it shows

that CT-scan images are comparable to X-radiographic images of constant thickness sample. Four laboratories currently have and use such a RSS, which is available upon request to the first author. Finally, we suggest that Itrax output could be used to calculate sediment density at high resolution in the near future.

**Acknowledgments** We thank Jean-François Crémer, Arnaud De Coninck and Philippe Nobert for technical assistance. We also thank Ian Croudace, Guy Rothwell and Cox analytical system for organizing the workshop that initiated this work. We thank the IMAGES VIII (International Marine Past Global Changes Study) program and Dr. Carlo Laj of the Laboratoire des Sciences du Climat et de l'environnement who provided access to the Saanich Inlet sediment core. U-channels from lacustrine sediments were provided by the PASADO (Potrok Aike Maar Lake Sediment Archive Drilling Project) supported by the International Continental Scientific Drilling Program (ICDP), the German Science Foundation (DFG), the Swiss National Funds (SNF), the Natural Sciences and Engineering Research Council of Canada (NSERC), the Swedish Vetenskapsradet (VR) and the University of Bremen. The Itrax core scanner was funded by a grant to Pierre Francus and Isabelle Larocque from the Canadian Foundation of Innovation. This research was supported by several grants of the Natural Sciences and Engineering Research Council of Canada to PF. We thank Guillaume St-Onge and Jacques Labrie for providing the Matlab routine used to produce the high-resolution topograms.

## References

Besonen MR (2006) A 1,000 year high-resolution hurricane history for the Boston area based on the varved sedimentary record from the Lower Mystic Lake (Medford/Arlington, MA). Ph.D. thesis

Besonen MR, Patridge W, Bradley RS, Francus P, Stoner JS, Abbott MB (2008) A record of climate over the last millennium based on varved lake sediments from the Canadian High Arctic. Holocene 18(1):169–180. doi:10.1177/0959683607085607

Boespflug X, Long BFN, Occhietti S (1995) Cat-scan in marine stratigraphy—a quantitative approach. Mar Geol 122(4):281–301

Bouma AH (1964) Notes on X-ray interpretation of marine sediments. Mar Geol 2:278–309

Chhem RK, Brothwell DR (2007) Paleoradiology: imaging mummies and fossils. Springer, Berlin

Cremer JF, Long B, Desrosiers G, de Montety L, Locat J (2002) Application of scanography to sediment density analysis and sediment structure characterization: case of sediments deposited in the Saguenay River (Quebec, Canada) after the July 1996 flood. Can Geotech J 39(2):440–450

Croudace IW, Rindby A, Rothwell RG (2006) ITRAX: description and evaluation of a new multi-function X-ray core scanner. In: Rothwell RG (ed) New Techniques in Sediment Core Analysis, vol 267. Geological Society of London Special Publication. pp 51–63

de Montety L, Long B, Desrosiers G, Crémer J-F, Locat J, Stora G (2003) Utilisation de la scanographie pour l'étude des sédiments: influence des paramètres physiques, chimiques et biologiques sur la mesure des intensités tomo- graphiques. Can Geotech J 40:937–948

Duchesne MJ, Moore F, Long BF, Labrie J (2009) A rapid method for converting medical computed tomography scanner topogram attenuation scale to hounsfield unit scale and to obtain relative density values. Eng Geol 103(3–4):100–105

Fortin D, Francus P, Gebhardt AC, Hahn A, Kliem P, Lisé-Pronovost A, Roychowdhury R, Labrie J, St-Onge G, Team PS (2013) Destructive and non-destructive density determination: method comparison and evaluation from the Laguna Potrok Aike sedimentary record. Quat Sci Rev 71:147–153

Fosbinder R, Kelsey C (2002) Essentials of radiologic science. McGraw-Hill, New York
Golstein J, Newbury D, Joy D, Lyman C, Echlin P, Lifshin E, Sawyer L, Michael J (2003) Scanning electron microscopy and X-Ray Microanalysis. Springer, New York
Hamblin WMK (1962) X-ray radiography in the study of structures in homogeneous sediments. J Sed Petrol 32:201–210
Hounsfield GN (1973) Computerized transverse axial scanning (tomography). Br J Radiol 46:1016
Hsieh J (2003) Computed tomography: principles, design, artifacts, and recent advances. Collections: SPIE Press monograph PM114. SPIE Press, Bellingham
Jackson PD, Briggs KB, Flint RC (1996) Evaluation of sediment heterogeneity using microresistivity imaging and X-radiography. Geo-Mar Lett 16:219–225
Jansen JHF, Van der Gaast SJ, Koster B, Vaars AJ (1998) CORTEX, a shipboard XRF-scanner for element analyses in split sediment cores. Mar Geol 151:143–153
Kanamaru K, Francus P, François R, Besonen M, Laj C (2013) New insight into Saanich Inlet varved sediments (British Columbia, Canada) from micro-scale analysis of sedimentary facies and micro-XRF core scanning analyses. J Geol Soc Swed (Geologiska Foreningen, GFF) 135(3–4):316–339
Migeon S, Weber O, Faugeres JC, Saint-Paul J (1999) SCOPIX: a new X-ray imaging system for core analysis. Geo-Mar Lett 18:251–255
Nagy EA, Valet J-P (1993) New advances for paleomagnetic studies of sediment cores using U-channels. Geophys Res Lett 20:671–674
Nederbragt AJ, Thurow JW (2001) A 6000 year varve record of holocene climate in saanich Inlet, British Columbia, from digital sediment colour analysis of ODP Leg 169S cores. Mar Geol 174:95–110
Ohlendorf C, Gebhardt C, Hahn A, Kliem P, Zolitschka B (2011) The PASADO core processing strategy—A proposed new protocol for sediment core treatment in multidisciplinary lake drilling projects. Sediment Geol 239:104–115
Ojala AEK (2004) Application of X-Ray radiography and densitometry in varve analysis. In: Francus P (ed) Image analysis, sediments and paleoenvironments. Developments in paleoenvironmental research, vol 7. Kluwer Academic, Dordrecht, pp 187–202
Ojala AEK, Francus P, Zolitschka B, Besonen M, Lamoureux SF (2012) Characteristics of sedimentary varve chronologies—A review. Quat Sci Rev 43:45–60
Petterson G, Odgaard BV, Renberg I (1999) Image analysis as a method to quantify sediment components. J Paleolimn 22:443–455
Principato S (2004) X-Ray radiographs of sedimenr cores: a guide to analysing diamicton. In: Francus P (ed) Image analysis, sediments and paleoenvironments, developments in paleoenvironmental research. Kluwer Academic, Dordrecht
Rasband WS (1997–2012) ImageJ. U. S. National Institutes of Health. http://imagej.nih.gov/ij/. Accessed 19 Aug 2013
Rockley J (1964) An introduction to industrial radiology. Butterworths, London
St-Onge G, Mulder T, Francus P, Long B (2007) Continuous physical properties of cored marine sediments. In: Hillaire-Marcel C, De Vernal A (eds) Developments in marine geology, vol 1. Elsevier, Amsterdam pp 63–98
Stow DAV, Townsend MR (1990) X-ray techniques and observations on distal Bengal Fan sediments cored during Leg 116. Proc, scientific results, ODP, Leg 116, distal Bengal Fan: 5–14
Zolitschka B, Mingram J, van der Gaast S, Jansen JHF, Naumann R (2001) Sediment logging techniques. In: Last WM, Smol JP (eds) Tracking environmental change using lake sediments: physical and chemical techniques. Kluwer Academic, Dordrecht, pp 137–153

# Chapter 21
# Prediction of Geochemical Composition from XRF Core Scanner Data: A New Multivariate Approach Including Automatic Selection of Calibration Samples and Quantification of Uncertainties

**G. J. Weltje, M. R. Bloemsma, R. Tjallingii, D. Heslop, U. Röhl and Ian W. Croudace**

**Abstract** A multivariate log-ratio calibration (MLC) model for XRF-core-scanning devices is presented, based on a combination of basic XRF-spectrometry theory and principles of compositional data analysis. The performance of the MLC model is evaluated in comparison with other empirical calibration procedures for XRF core scanner data using two data sets acquired with two different XRF core scanners. The quality of calibration models is assessed by calculating the uncertainties associated with predicted concentrations using cross-validation techniques. Results show that

G. J. Weltje (✉)
Department of Earth and Environmental Sciences, University of Leuven, Celestijnenlaan 200E, 3001 Leuven-Heverlee, Belgium
e-mail: gertjan.weltje@ees.kuleuven.be

M. R. Bloemsma
Department of Geoscience and Engineering, Delft University of Technology, Stevinweg 1, 2628CN Delft, The Netherlands

R. Tjallingii
Section 5.2 Climate Dynamics and Landscape Evolution, GFZ, German Research Centre for Geosciences, Telegrafenberg, 14473 Potsdam, Germany

Department of Marine Geology, NIOZ Royal Netherlands Institute for Sea Research, Den Burg, P.O. Box 59, 1790 AB Texel, The Netherlands

D. Heslop
Research School of Earth Sciences, The Australian National University, Canberra, ACT 0200, Australia

U. Röhl
MARUM—Centre for Marine Environmental Sciences, University of Bremen, Leobener Strasse, 28359 Bremen, Germany

I. W. Croudace
Ocean and Earth Science, National Oceanography Centre, University of Southampton, Waterfront Campus, European WaySouthampton SO14 3ZH, UK



I. W. Croudace, R. G. Rothwell (eds.), *Micro-XRF Studies of Sediment Cores*, Developments in Paleoenvironmental Research 17, DOI 10.1007/978-94-017-9849-5_21

(1) the commonly used direct linear calibration (DLC) methods, which are based on the questionable assumption of a unique linear relation between intensities and concentrations and do not acknowledge the compositional nature of the calibration problem, give poor results; (2) the univariate log-ratio calibration (ULC) model, which is consistent with the compositional nature of the calibration problem but does not fully incorporate absorption and enhancement effects on intensities, and permits estimation of "relative" concentrations only, is markedly better, and (3) the MLC algorithm introduced in this contribution, which incorporates measurement uncertainties, accommodates absorption and enhancement effects on intensities, and exploits the covariance between and among intensities and concentrations, is the best by far. The predictive power of the MLC model may be further increased by employing automatic sample selection based on the multivariate geometry of intensity measurements in log-ratio space. The precision attained by MLC in conjunction with automatic sample selection is comparable to that attained by conventional XRF analysis of heterogenous materials under laboratory conditions. A solution to the long-standing problem of XRF core scanner calibration implies that high-resolution records of sediment composition with associated uncertainties can now be routinely established, which should increase the range of quantitative applications of XRF-core-scanning devices and strengthen inferences based on analysis of geochemical proxies.

**Keywords** Log-ratio transformation · Partial least squares regression · Compositional data · Chemometrics · Palaeoceanography · Micro-XRF core analysis

## Introduction

X-ray fluorescence analysis (XRF) is a well-established technique for determining the composition of rocks and sediments (Ramsey et al. 1995; Jenkins 1999; De Vries and Vrebos 2002). Progress in XRF instrumentation has opened the way to on-line measurement of (soft) sediment cores aboard ship by means of XRF-core-scanning devices (Jansen et al. 1998; Wien et al. 2005; Ge et al. 2005; Rothwell and Rack 2006). Technical descriptions of the various XRF core scanners in current use are given by Jansen et al. (1998), Croudace et al. (2006), Haschke et al. (2002), Haschke (2006), and Richter et al. (2006) and summarised in this volume by Jarvis et al. The major advantage of XRF core scanning over conventional geochemical analysis of discrete specimens is that element intensities are obtained directly at the surface of a split sediment core, which implies up to two orders of magnitude increase in analytical speed. In addition, the spatial resolution of XRF core-scanning devices is much higher than that of conventional destructive methods, and allows the extraction of near-continuous records of element intensities from sediment cores. XRF core scanning is therefore recognised as a technique with great potential for palaeoenvironmental research (Calvert and Pedersen 2007; Weltje and Tjallingii 2008).

In order to realize the full potential of high-resolution XRF core scanning, a universally applicable, robust procedure must be developed for converting core scanner output to quantitative measures of sediment composition with associated

measures of uncertainty. Previous attempts to convert XRF core scanner output to element or oxide concentrations by means of linear regression on an element-by-element basis (referred to as direct linear calibration; DLC) have been only moderately successful (Jansen et al. 1998; Jaccard et al. 2005; Croudace et al. 2006; Kido et al. 2006; Böning et al. 2007; Tjallingii et al. 2007).

Direct linear calibration (DLC) models take the following form:

$$W_{ij} = a_j I_{ij} + b_j \tag{21.1}$$

where $W_{ij}$ represents the concentration (weight proportion) of element $j$ in specimen $i$. $I_{ij}$ represents the net intensity of element $j$ in specimen $i$, obtained by preprocessing of the raw spectrum by background subtraction, sum-peak and escape-peak correction, deconvolution and peak integration. Coefficients $a_j$ and $b_j$ are empirical constants specific to the data set and element under consideration.

The simplest DLC model is one in which direct proportionality is assumed, i.e. $b_j = 0$. In this model, referred to as DLC-1, concentrations and intensities are both constrained to be non-negative. A more flexible model, referred to as DLC-2, is obtained by allowing non-zero values of $b_j$ in Eq 21.1. The DLC-2 model implies that the relation between $W$ and $I$ cannot be linear over their full range, because negative concentrations or intensities would occur. Therefore, the conventional interpretation of the DLC-2 model is that it represents the approximately linear relation between $W$ and $I$ over the limited range of intensities and concentrations covered by the data.

Practical problems associated with DLC models are apparent from considerable scatter and bias in cross-plots of intensity and concentration, which are attributable to inhomogeneity of the specimens (e.g. variable water content and grain-size distribution), irregularities of the split core surface, and in some setups, spatial variations in thickness of an adhesive pore-water film which forms directly below a protective foil covering the core surface. The conceptual problems of DLC are apparent from the fact that the seemingly straightforward (linear) calibration of intensities to concentrations is inconsistent with the parametric model used in XRF spectrometry (Weltje and Tjallingii 2008). The absence of a viable underlying physical model manifests itself in a number of ways: (1) None of the published regression equations passes through the origin, or alternatively, through the point representing the detection limits corresponding to the two measurements being compared; (2) Calibration on an element-by-element basis provides no guarantee that predicted concentrations are positive and sum to unity, which is a violation of fundamental physical constraints on compositional data.

In view of the problems associated with quantification of XRF core scanner output by DLC, the general view has been that such data should be regarded as semi-quantitative only (Croudace et al. 2006; Richter et al. 2006; Rothwell and Rack 2006). In a recent paper however, Weltje and Tjallingii (2008) showed that rigorous quantitative calibration of XRF core scanner output is possible. The key to this breakthrough was provided by a new mathematical formulation of the calibration equation in terms of log-ratios of intensities and concentrations, which is consistent with basic XRF-spectrometry theory, as well as the statistical theory of

compositional data analysis (Aitchison 1982, 1986). The present contribution documents the progress made since publication of the log-ratio calibration model of Weltje and Tjallingii (2008), and introduces a software package designed for efficient quantitative calibration of XRF core scanner output.

## Calibration in Conventional XRF Spectrometry

In conventional (destructive) quantitative XRF analysis under well-constrained laboratory conditions, conversion of the net intensity of an element to a weight proportion is provided by the following general equation (Jenkins 1999; De Vries and Vrebos 2002):

$$W_{ij} = K_j I_{ij} M_{ij} S_i \tag{21.2}$$

Where $W_{ij}$ and $I_{ij}$ are defined as above, $K_j$ represents a device-specific calibration constant for element $j$ (the sensitivity or detection efficiency of the measurement device), and $M_{ij}$ is the matrix effect which corrects for scattering, absorption and enhancement effects on $I_{ij}$ caused by the presence of other elements in the specimen.

Note that for a series of specimens covering a range of compositions, the matrix effect is a non-linear function of the concentrations (or intensities) of the full range of elements present. $S_i$ is the specimen effect which captures the measurement geometry and specimen homogeneity relative to the standard configuration.

Under laboratory conditions, $K_j$ and $S_i$ are fixed, and $W_{ij}$ is estimated from $I_{ij}$ with a correction factor given by $M_{ij}$. The matrix effect is commonly expressed as a function of the concentrations or intensities of the other elements present in the specimen under consideration. Various methods for estimating $M_{ij}$ have been proposed, most of which are based on a combination of theory and empirical evidence (calibration specimens). Under ideal conditions, entirely theoretical methods for estimating $M_{ij}$ (so-called fundamental parameter methods) may be utilized to predict net intensities based on known specimen compositions. Fundamental parameter methods are commonly implemented in the form of non-linear optimisation techniques, in which intensities calculated from an initial guess of a specimen's composition are compared to measured intensities, and the estimated composition of the sample is iteratively adjusted so as to minimise some measure of discrepancy between predicted and measured intensities (Jenkins 1999; De Vries and Vrebos 2002).

## Log-Ratio Calibration

The fundamental problem in on-line XRF core scanning is that $S_i$ is unconstrained, owing to inhomogeneity of the specimens (e.g. variable water, organic content, grain-size distribution of sediments, the presence of burrows, etc) and the irregular

surface of a split core. In some setups, spatial variations in thickness of an adhesive pore-water film which forms directly below a protective foil covering the split core surface also have to be considered (Kido et al. 2006; Tjallingii et al. 2007). Down-core variability of these factors implies that the measurement geometry $S_i$ is not constant, contrary to XRF analysis under laboratory conditions, and Eq. 21.2 cannot be solved within reasonable limits of uncertainty, because every single measurement requires the solution of a set of calibration equations associated with a location-specific value of $S_i$. In other words, there is no unique relation between $I$ and $W$, which implies that every core scanner measurement must be calibrated by means of destructive analysis, which would render the whole measurement strategy meaningless. This seemingly insurmountable problem may be solved by considering the problem in terms of log-ratios of element intensities and concentrations (Weltje and Tjallingii 2008).

Although log-ratio transformations (Aitchison 1982, 1986) have not been widely applied to geochemical compositions and XRF core scanner output, several authors have pointed to the advantage of using ratios of element intensities (or concentrations) instead of intensities (or concentrations) of single elements (Croudace et al. 2006; Richter et al. 2006; Rothwell et al. 2006; Calvert and Pedersen 2007; Löwemark et al. 2011). Down-core patterns of element-intensity ratios have proved extremely useful for correlation (e.g. Pälike et al. 2001; Vlag et al. 2004; Bahr et al. 2005), because they are unaffected by variations in the concentrations of other elements in a specimen (so-called dilution effects), which is especially relevant considering the fact that XRF core scanners do not measure the full range of elements.

Despite their usefulness, ratios do not permit rigorous statistical modelling of compositional data. Ratios have the undesirable property of asymmetry, i.e., conclusions based on evaluation of the ratio of two elements, say A/B, cannot be directly translated into equivalent statements about B/A. This implies that the results of statistical analysis of ratios depend on arbitrary decisions, since there is no Law of Nature to suggest which element should act as numerator or denominator. Fortunately, this problem was solved by Aitchison (1982), who discovered that rigorous statistical modelling of compositional data merely requires that compositions are expressed in terms of logarithms of ratios of component abundances (so-called log-ratios), in order to achieve the desired symmetry, and allow compositional data to be described with a unique set of statistics. Concepts and applications of compositional data analysis by means of log-ratios are covered by Aitchison (1986), Aitchison and Egozcue (2005), and in the monograph edited by Buccianti et al. (2006).

Weltje and Tjallingii (2008) derived a univariate log-ratio calibration (ULC) equation by combining two conventional calibration equations (Eq. 21.2) in the form of a ratio. They assumed that all values of $W$ and $I$ are positive (i.e., greater than or equal to the detection limits of the measurement devices used). Elements are indicated by subscripts $j$ and $D$, whereas subscript $i$ denotes the measurement location and the corresponding specimen:

$$\frac{W_{ij}}{W_{iD}} = \frac{K_j I_{ij} M_{ij} S_i}{K_D I_{iD} M_{iD} S_i} = \frac{K_j I_{ij} M_{ij}}{K_D I_{iD} M_{iD}}$$

Calibration in terms of ratios removes the measurement geometry from the problem to be solved, because $S_i$ drops out of the equation. For each pair of elements, the ratio of detection efficiencies is a constant, the so-called relative detection efficiency:

$$\frac{K_j}{K_D} = B_{jD} \tag{21.3}$$

Further simplification is achieved by assuming that the ratio of matrix effects is a non-linear function of the ratio of measured element intensities:

$$\frac{M_{ij}}{M_{iD}} = C_{jD}\left(\frac{I_{ij}}{I_{iD}}\right)^{A_{jD}} \tag{21.4}$$

In the above expression, $A_{jD}$ and $C_{jD}$ are empirical coefficients specific to the pair of elements in the data set under consideration. Substitution of Eqs. 21.3 and 21.4 into Eq. 21.2 gives:

$$\frac{W_{ij}}{W_{iD}} = B_{jD}C_{jD}\left(\frac{I_{ij}}{I_{iD}}\right)^{A_{jD}+1} \tag{21.5}$$

Equation (21.5) may be rewritten by defining the empirical coefficients:

$$\alpha_{jD} = A_{jD} + 1 \tag{21.6a}$$

$$\beta_{jD} = \ln(B_{jD}C_{jD}) \tag{21.6b}$$

If we substitute Eqs. 21.6a and 21.6b into Eq. 21.5 and take logarithms, we obtain the ULC equation:

$$\ln\left(\frac{W_{ij}}{W_{iD}}\right) = \alpha_{jD}\ln\left(\frac{I_{ij}}{I_{iD}}\right) + \beta_{jD} \tag{21.7}$$

Equation 21.7 is a non-dimensional unconstrained linear equation expressed in terms of log-ratios of element intensities and concentrations. The coefficients $\alpha$ and $\beta$ are the log-ratio equivalents of the matrix effect and detection efficiency in single-element XRF-spectrometry (Eq. 21.2), respectively. Although the variability of the specimen effect has been eliminated, the average values of variables such as grain-size, water content, and any matrix effects attributable to the presence of elements which have not been measured, will be reflected in the empirical model parameters $\alpha$ and $\beta$. The ULC equation is largely insensitive to down-core variability of these

quantities, which implies that the scatter of *I*-*W* log-ratio plots will be much smaller than the scatter observed in conventional ("raw") *I*–*W* plots under conditions of variable measurement geometry. An additional advantage of the above approach is that the relation between log-ratios of *I* and *W* is expected to be linear, unlike the relation between raw *I* and *W* data (cf. Eq. 21.1).

Solution of the log-ratio calibration equation for $\alpha$ and $\beta$ yields positive concentration estimates $\tilde{W}_{ij}$ which sum to unity. This is easily shown by letting the log-ratios of concentrations predicted from log-ratios of measured intensities be:

$$x_{ij} = \ln\left(\frac{\tilde{W}_{ij}}{\tilde{W}_{iD}}\right) \tag{21.8a}$$

The above expression accounts for all elements but one: the element acting as common denominator, whose log-ratio value is by definition equal to zero: $x_{iD} = 0$. The predicted concentrations $\tilde{W}_{ij}$ of all elements, including the one used as common denominator ($j = 1, D$) are obtained by applying the inverse log-ratio transformation:

$$\tilde{W}_{ij} = \frac{e^{x_{ij}}}{\sum_{j=1}^{D} e^{x_{ij}}} \tag{21.8b}$$

The above method was used by Weltje and Tjallingii (2008) to obtain unbiased predictions of "relative" concentrations of elements which were measured by the XRF core scanner ("relative" means that the sum of all elements measured is automatically constrained to unity). Although ULC presents a major step forward compared to DLC, it does not allow "absolute" concentrations to be determined.

## MLC Workflow

Ongoing research into the underlying mathematical form of the log-ratio calibration equation has resulted in a further generalisation of the estimation procedure proposed by Weltje and Tjallingii (2008). The second-generation multivariate calibration algorithm introduced in this contribution (MLC) makes effective use of the covariance between and among measured element intensities and concentrations, which reflect absorption and enhancement of intensities, as well as the fact that several elements may reside in the same mineral. The MLC model allows us to further minimize the uncertainty of predicted log-ratio quantities and extend predictions to elements which have not been measured by the XRF core scanner, so as to generate "absolute" concentrations. The MLC workflow also includes more rigorous estimation of prediction uncertainties and automatic selection of calibration samples. The automated MLC workflow is schematically shown in Fig. 21.1.

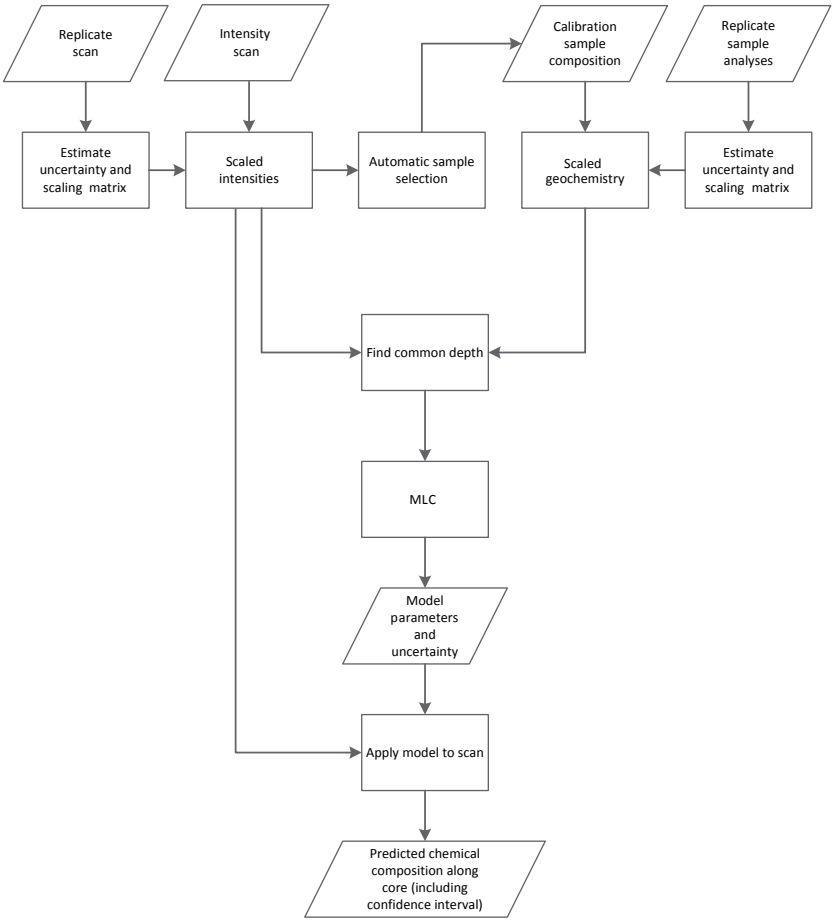


**Fig. 21.1** MLC workflow; see text for discussion

## Prediction of "Absolute" Element Concentrations

XRF core scanners measure a limited range of elements only. Hence, the sum of all detectable elements is equal to a proportion, $p$, of the total mass. In order to express log-ratio-calibrated quantities in terms of actual concentrations (and not just as mass fractions of the total number of elements actually measured), we must account for the total mass of the material analysed. We therefore introduce one additional unknown to be calibrated, which is simply the mass fraction of the material which cannot be assigned to specific elements:

$$\text{Undef} = W_{i,D+1} = 1 - \sum_{j=1}^{D} W_{ij} \tag{21.9}$$

In practice, "Undef" represents the union of all elements which have not been detected by the core scanner and by the chemical technique used to provide the reference concentrations for calibration. Prediction of "Undef" requires that calibration is formulated as a multivariate problem. The MLC workflow is therefore based on a slightly different log-ratio representation of compositional data relative to the ULC model of Weltje and Tjallingii (2008). Instead of using additive log-ratios to perform pairwise element calibration, we have adopted centred log-ratios which enable calibration of all elements at the same time (including "Undef"). The centred log-ratio transformation of a composition vector **x** comprising *D* parts is defined as:

$$\mathrm{clr}(\mathbf{x}) = [\ln x_1 - \ln g, \ldots, \ln x_j - \ln g, \ldots, \ln x_D - \ln g] \tag{21.10a}$$

Where:

$$\ln g = \frac{1}{D}\sum_{j=1}^{D} \ln x_j \tag{21.10b}$$

Centred log-ratio-transformed compositional data may be analysed with standard multivariate statistical methods, which implies that model parameters may be determined with unconstrained least-squares methods. Therefore, we will implicitly assume throughout the remainder of this text that all data have been clr-transformed. It is important to note that clr-transformed variables can always be retransformed to concentrations by using Eq. 21.8b.

## Automatic Selection of Calibration Samples

Effective calibration requires that the compositional trends in the data are adequately sampled. Improvements to the workflow proposed by Weltje and Tjallingii (2008) have been achieved by introducing two processing steps in the MLC workflow: (1) an algorithm which estimates the level of noise based on the measured spread among replicate intensities and scales the data accordingly, and (2) an algorithm for automatic selection of calibration samples, based on the multivariate geometry of the scaled intensities.

The MLC workflow (Fig. 21.1) relies on replicate intensity measurements for empirical uncertainty quantification. In the absence of prior knowledge we may collect replicate intensity measurements according to a systematic sampling scheme, e.g. collect at least three measurements at every tenth location down-core. We estimate the level of noise from the average spread within each set of replicates for each element separately.

For the purpose of automatic sample selection, the clr-transformed intensities are scaled with the inverse of their empirically determined uncertainties in order to meet the requirements for rigorous application of least-squares estimation techniques. The average uncertainty is now identical for all intensities, which implies that Euclidian dis-

tances between intensity vectors may be directly interpreted in terms of compositional variability. This provides a solid basis for automatic selection of calibration samples.

In order to automatically select the locations at which calibration samples should be collected, the desired number of unique calibration sites ($N_c$) must be specified by the analyst. The most suitable locations are selected by means of hierarchical cluster analysis of the scaled clr-transformed intensities. We use Ward's method (Ward 1963) in conjunction with a Euclidian distance measure to subdivide the clr-transformed scaled intensities into $N_c$ clusters, and select one data point from each cluster (the one closest to the cluster centroid). The set of $N_c$ intensities thus selected is subjected to another round of cluster analysis with the objective to further subdivide the set of calibration locations into the desired number of replicate sets, $N_{W,s}$. From each of these $N_{W,s}$ clusters, one data point is selected to be sampled and analysed in replicate (three times or more). This two-step sampling strategy ensures that calibration and uncertainty estimation make use of the full range of variation in the intensity data. Because this procedure does not rely on stratigraphic information, additional sampling may be deemed desirable if one wishes to achieve a more uniform stratigraphic/spatial coverage of the core.

The chemical composition of the set of calibration samples should be determined by conventional destructive methods such as XRF and ICP-AES. The compositional data are subjected to the same treatment as the intensities, i.e. clr-transformation and scaling with the inverse of the estimated uncertainties. The resulting data sets provide the optimal starting point for multivariate calibration with the MLC algorithm (Fig. 21.1).

## MLC Algorithm

Parameter estimation for the purpose of predicting element concentrations with the MLC model is carried out by means of Partial Least Squares (PLS) regression, a generalized multivariate linear regression model which maps one data set onto another by making use of a common covariance matrix (De Jong 1993). One of the properties of PLS, which it shares with all other regression models, is that the regression error is inversely proportional to the number of model coefficients (model complexity). When the number of model parameters equals the size of the data set, each data point can be reproduced exactly. Because our data are not noise-free and we should allow for the possibility that the model may not be fully correct, we use a more objective and robust measure of model performance than the regression error: leaving-out-one cross validation (Geisser 1975). The idea behind cross validation is to estimate the parameters of the calibration equation by leaving one measurement out of the data set, and predict the value of this missing data point from the equation fitted to the other data points. By repeating this procedure for all data points, the discrepancies between predicted and measured values may be used to estimate the actual prediction uncertainty. This approach works well if the calibration data set is sufficiently large (the bare minimum would be ~30 specimens).

A straightforward goodness-of-fit measure of logratio-transformed compositional data is the mean squared Euclidian distance between $\hat{\mathbf{x}}$ and $\mathbf{x}$ (predicted and measured composition, respectively):

$$\mathrm{MSE} = \frac{1}{nD}\sum_{i=1}^{n}\sum_{j=1}^{D}\left\{\mathrm{clr}(x_j) - \mathrm{clr}(\hat{x}_j)\right\}^2 \tag{21.11}$$

In the ULC workflow, the set of $D$ models with different common denominators is evaluated to find the one which corresponds to the minimum MSE (cf. Weltje and Tjallingii 2008). Model selection in the MLC workflow is more advanced, because use is made of cross validation to estimate prediction uncertainties. In cases where cross validation has been used, the value of MSE as defined by Eq. 21.11 will be referred to as the mean squared prediction error (MSPE). A similar approach is used to construct error bars around predicted log-ratios of concentrations of specific element pairs. In cases where log-ratio calibration is not required, error bars around log-ratios of measured intensities may be derived from the spread among replicate intensity measurements (Weltje and Tjallingii 2008).

The misfit between the reference and predicted concentrations varies among the different elements and the different calibration models. This misfit is quantified by calculating the residual variance (MSPE), which is a statistically meaningful measure that can be used to construct confidence intervals. However, the MSPE does not tell us anything about the nature of the misfit. We therefore introduce two pseudo-statistical quantities which serve as a measure of the bias and the scatter of estimated concentrations, respectively. Although these measures provide insight into model-data discrepancies, it should be kept in mind that concentrations cannot be rigorously evaluated owing to compositional constraints (Aitchison 1986; Weltje and Tjallingii 2008).

The bias-indicator $B$ is defined as the angle between the major axis of the point-cloud and the line $y = x$. When the two are exactly equal, the bias-indicator $B$ equals zero. If, however, the major axis is perpendicular to the line $y = x$, $B$ will have a value of 100 (it does not matter how the major axis is oriented with respect to the line $y = x$). $B$ is calculated by subtracting the mean from the point cloud and then estimating the major axis by means of a Singular Value Decomposition (Press et al. 1994). Given that $u = \begin{bmatrix}1 & 1\end{bmatrix}$ (i.e. the line $y = x$ in vector form) and $v_1$ is the major axis vector:

$$B_j = 100 \times \frac{\left|0.5\pi - \cos^{-1}(u \cdot v_1)\right|}{0.5\pi} \tag{21.12}$$

The scatter-indicator $S$, which also ranges from zero to 100, is based on the percentage of variance along the minor axis, i.e., the axis perpendicular to the earlier calculated major axis. Given that $\lambda_1$ is the eigenvalue of the major axis and $\lambda_2$ the eigenvalue of the minor axis:

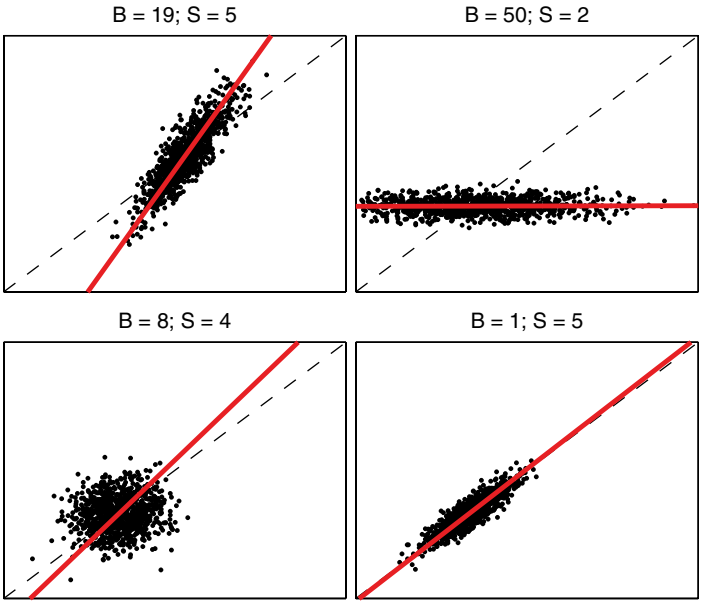


**Fig. 21.2** Definition of scatter and bias in compositional space

$$S_j = 100 \times \frac{\lambda_2}{\lambda_1 + \lambda_2} \tag{21.13}$$

Hence, $S$ and $B$ are in principle independent and can therefore also be interpreted as such. Figure 21.2 gives an impression of $S$ and $B$ in a number of different situations. For the purpose of comparing calibration models, we derive their median values across all elements, which we refer to as $\overline{S}$ and $\overline{B}$.

## Comparative Calibration Exercise

We will compare the performance of four different calibration models (DLC-1, DLC-2, ULC, and MLC), using two data sets: Core GeoB7920 acquired with an Avaatech scanner, and Core AU10v acquired with an Itrax scanner. Each of these instruments is equipped with a software package which extracts intensities of a range of chemical elements from the spectra recorded by the detector. For the purpose of the comparative calibration exercise, we will simply assume that these intensities are correct. Moreover, no attempts will be made to evaluate the results of our calibrations in the light of geological knowledge.

### *Data Set 1: GeoB7920*

This legacy data set of core GeoB7920, taken offshore West Africa, consists of 168 intensity measurements at 2-cm resolution measured at the University of Bremen with a second-generation Avaatech core scanner (ca. 2004) using 10 kV (250 μA) and 50 kV (1 mA) tube settings, at 30 s per measurement. Automatic processing of the XRF spectra provided intensities of 13 elements. Five replicate sets of intensity measurements (measured five or six times) are available for estimation of uncertainties. A set of 168 table-top ED-XRF measurements (Wien et al. 2005) of samples taken at each down-core location measured with the core scanner is used for calibration. No replicate ED-XRF measurements are available. Detailed information about the sample preparation and the geological setting of the core may be found in Weltje and Tjallingii (2008), Tjallingii et al. (2008), and Bloemsma et al. (2012).

### *Data Set 2: AU10v*

Core AU10v was collected in July 2008 from Augusta Harbour, Sicily (see also Croudace et al., this volume). The core was split and the top 9.6 cm was scanned at 500 μm resolution using a high-resolution Itrax instrument (Croudace et al. 2006) at the University of Southampton. Tube settings used were 30 kV (30 mA) at 30 s per measurement. The XRF spectra were automatically processed and provided intensities of 20 elements. After Itrax scanning, the core was incrementally sub-sampled, pelleted and analysed to obtain quantitative element data using conventional WD-XRF analysis. A total of 51 calibration samples was collected (no replicates). Intensity replicates (126 repeat measurements each) were acquired on two homogenised and powdered pellets taken from the core for the purpose of calibration.

## Results

Calibration of the intensities to concentrations of chemical elements involved a selection step, in which elements which could not be predicted (because their residual variance was almost equal to their total variance) were removed from the data sets. This category also included elements whose concentrations were below detection limits in more than half of the calibration samples. Elements which could not be calibrated were added to “Undef” (except in the case of the ULC model, which predicts “relative” concentrations only). The final models contain 12 elements for GeoB7920 (Al, Ba, Br, Ca, Cl, Fe, K, Mn, Rb, Si, Sr, Ti) and 16 elements for AU10v (Ba, Br, Ca, Cl, Cr, Cu, Fe, K, Mn, Pb, S, Si, Sr, Ti, V, Zn), respectively. Table 21.1 gives the goodness-of-fit statistics of the four calibration models, whereas Figs. 21.3, 21.4, 21.5, 21.6, 21.7 and 21.8 permit a visual appraisal of their predictive power. The

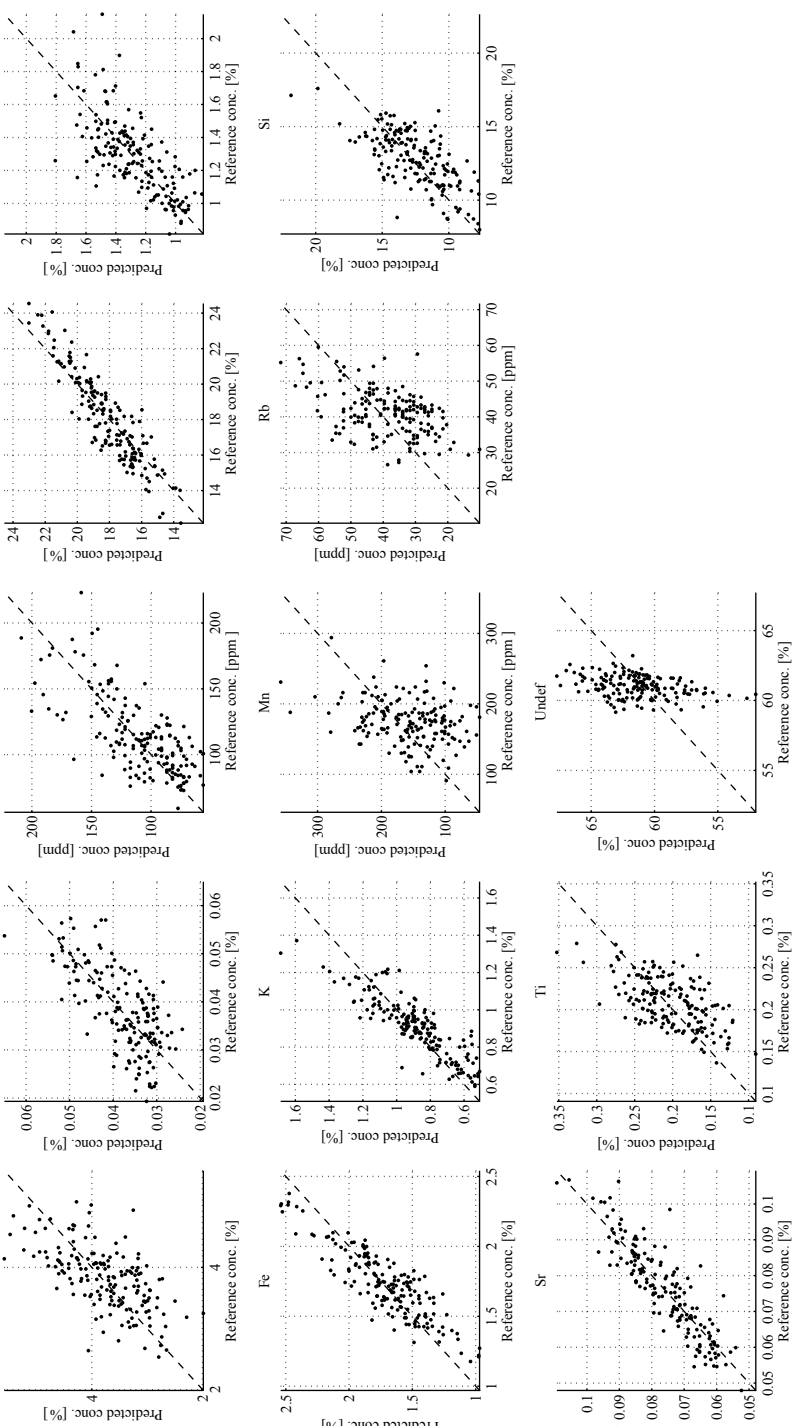


**Fig. 21.3** Measured versus predicted concentrations for DLC-1 model of GeoB7920

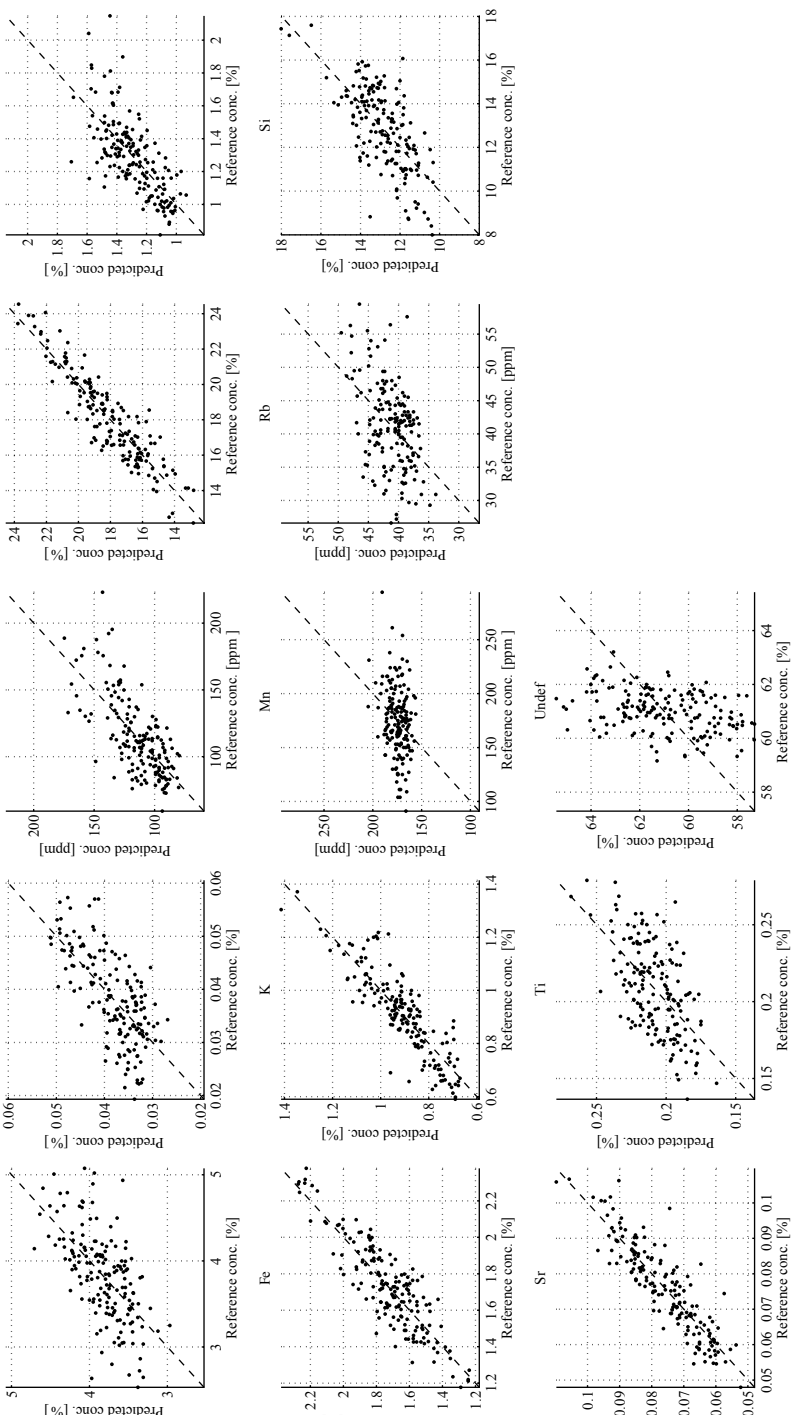


**Fig. 21.4** Measured versus predicted concentrations for DLC-2 model of GeoB7920

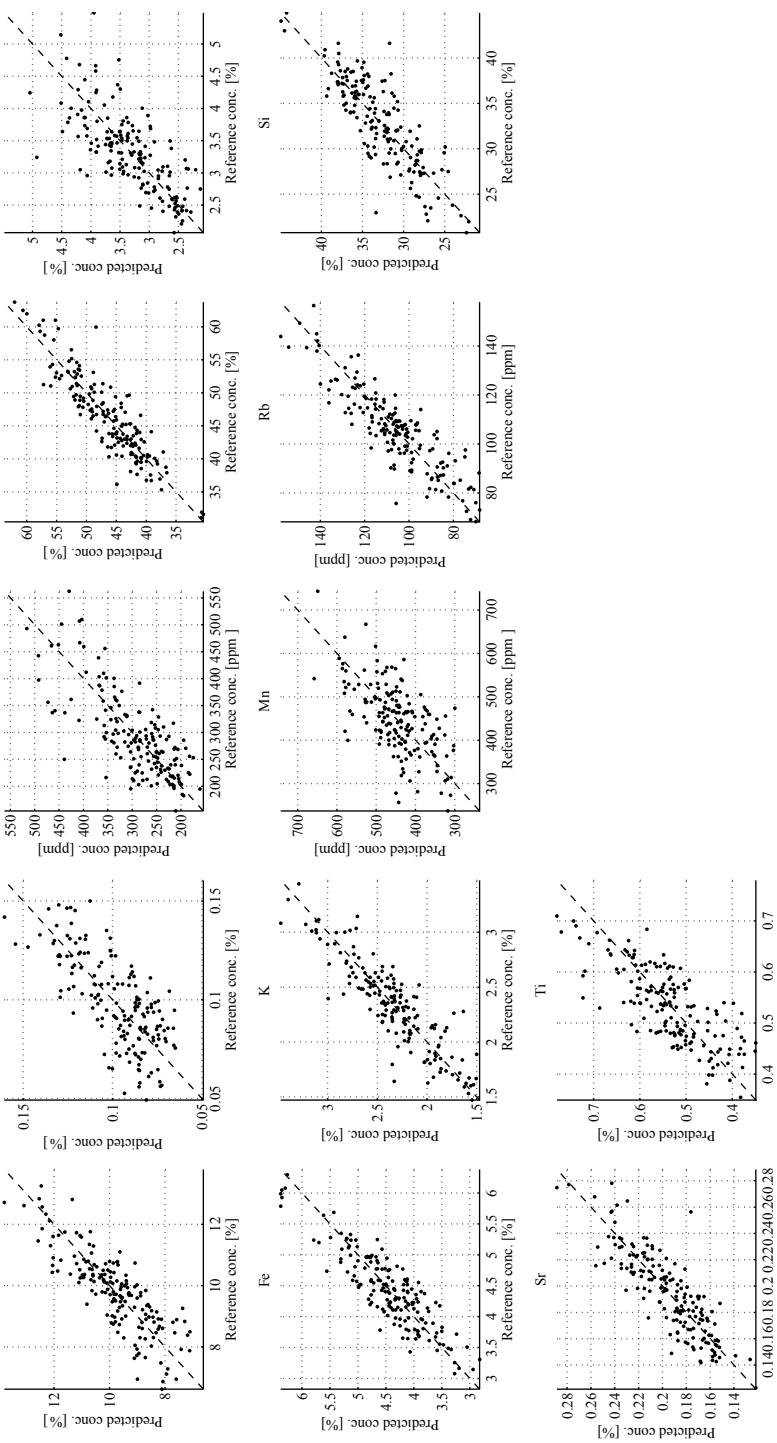


**Fig. 21.5** Measured versus predicted concentrations for ULC model of GeoB7920

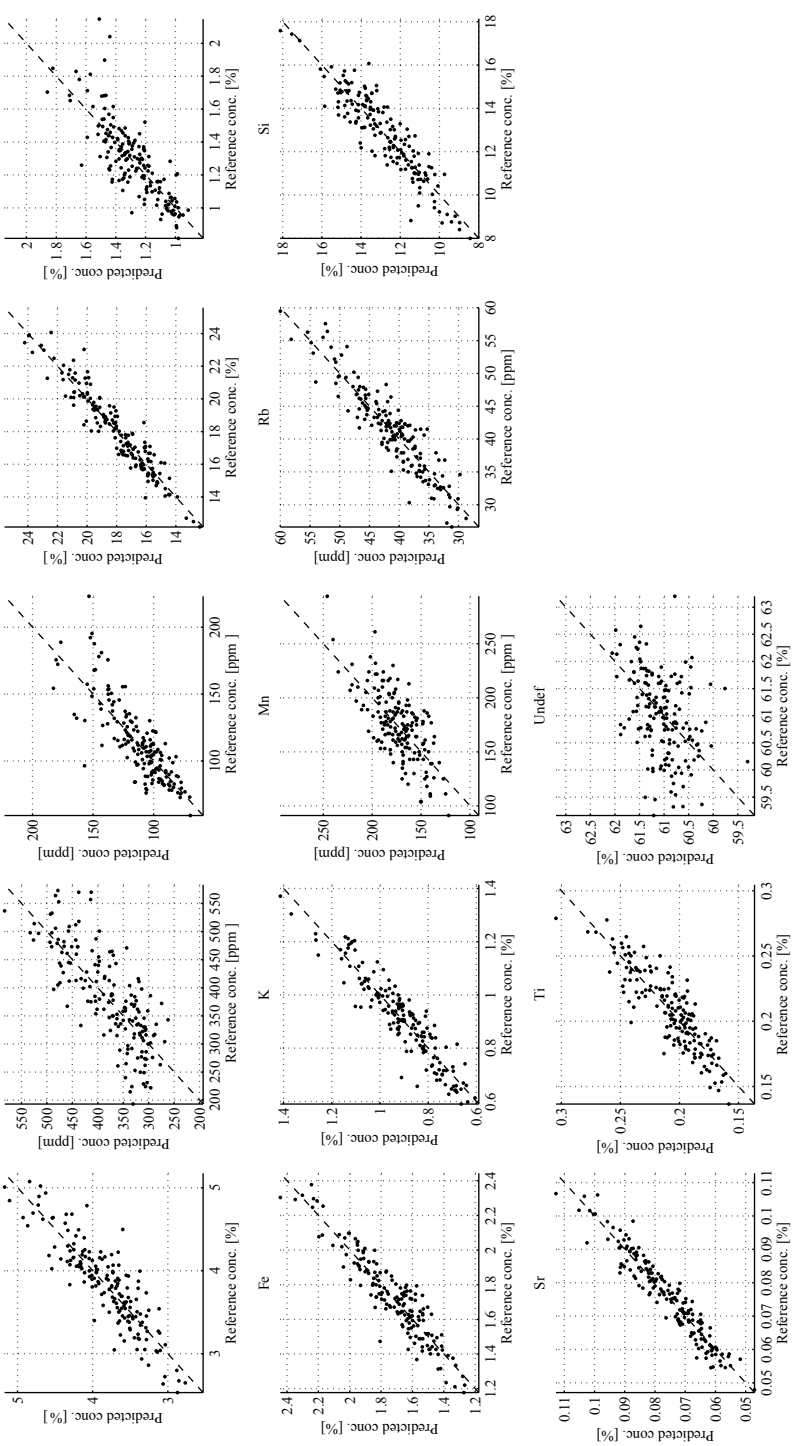


**Fig. 21.6** Measured versus predicted concentrations for MLC model of GeoB7920

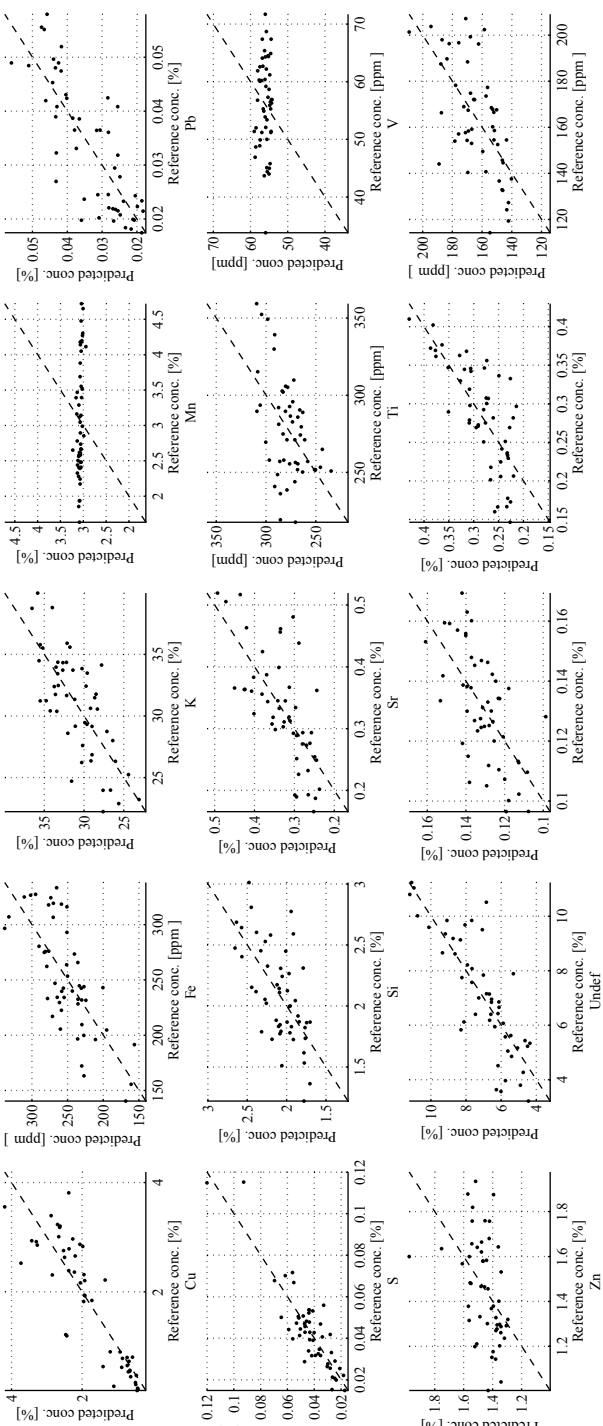


**Fig. 21.7** Measured versus predicted concentrations for DLC-2 model of AU10v

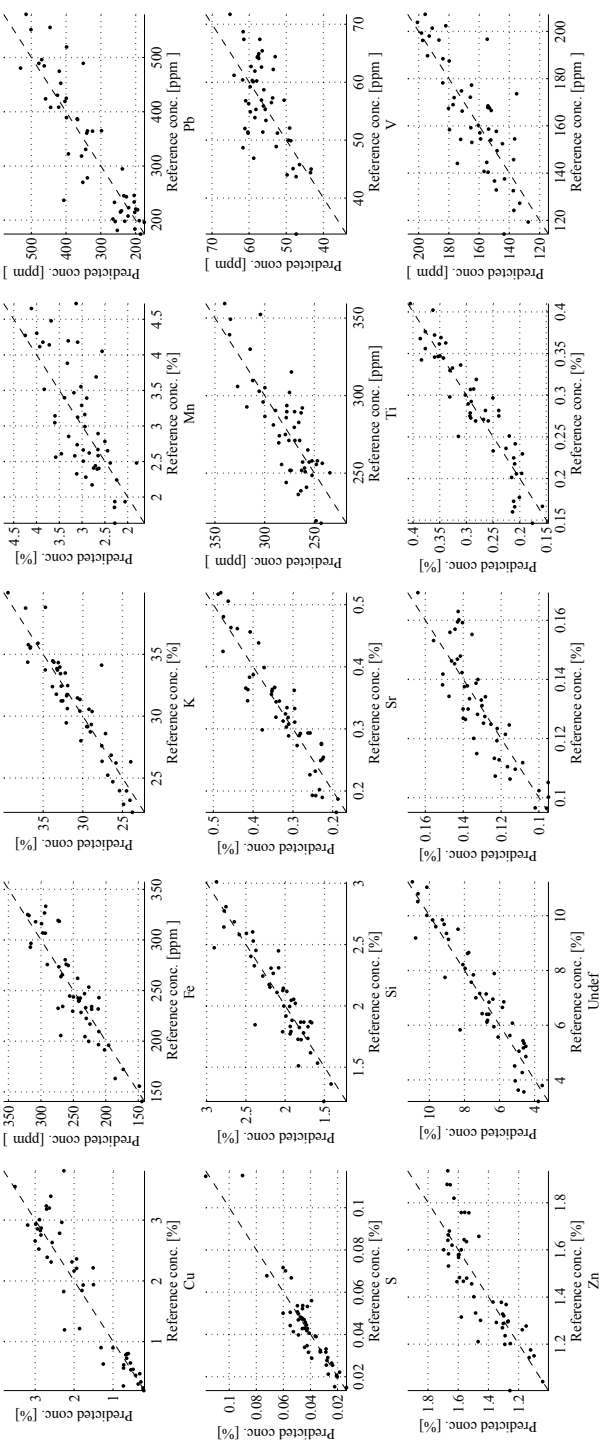


**Fig. 21.8** Measured versus predicted concentrations for MLC model of AU10v

**Table 21.1** Comparative performance of calibration techniques based on cross validation

| Data set | Model | B (%) | S (%) | MSPE |
|---|---|---|---|---|
| GeoB7920 | DLC1 | 11.69 | 14.31 | 0.0319 |
| GeoB7920 | DLC2 | 15.66 | 13.02 | 0.0131 |
| GeoB7920 | ULC | 3.46 | 8.59 | 0.0124 |
| GeoB7920 | MLC | 3.80 | 6.90 | 0.008 |
| AU10v | DLC1 | 14.88 | 9.48 | 0.0530 |
| AU10v | DLC2 | 13.86 | 12.09 | 0.0239 |
| AU10v | ULC | 7.40 | 8.80 | 0.0218 |
| AU10v | MLC | 5.43 | 7.90 | 0.0163 |

MSPE values of both data sets show that the MLC model performs better than the ULC model, the ULC model performs better than the DLC-2 model, and the DLC-1 model is the least satisfactory (Table 21.1). The median values of scatter and bias for each model confirm this ranking, and draw attention to the fact that the least advanced log-ratio-based model (ULC) performs much better than the most advanced direct linear calibration model (DLC-2).

Figure 21.9 provides a visual impression of core GeoB7920. In the upper half of this figure, the high-resolution RGB image (Fig. 21.9a) is shown alongside the records of ln(Ca/Ti) intensities (Fig. 21.9b) and predicted concentrations (Fig. 21.9c, d). The gray bands in these four graphs represent the 95% confidence interval of measured intensities and predicted concentrations. Comparison of the raw (Fig. 21.9b) and calibrated (Fig. 21.9c, d) intensities highlights their close similarity. Furthermore, the MLC estimate (Fig. 21.9d) has a smaller confidence interval than the ULC estimate (Fig. 21.9c). The lower half of the image (Fig. 21.9e, f, g) illustrate the chemical composition predicted by the MLC model. Note the strong correlations between element concentrations arising from the compositional constraints. In this particular case, "Undef" is nearly constant down-core and does not contribute much to the variability of "absolute" concentrations.

Figure 21.10 shows the relation between the number of randomly selected calibration samples and the median values of the MSPE for MLC models of core GeoB7920 using different methods of sample selection. The performance of random sampling is represented by the median value of MSPE over a series of 1000 simulations. The performance of systematic sampling (using a fixed sampling interval) is represented by the median MSPE over a series of 83 simulations, and is therefore more "spiky." Our automatic sampling strategy produced only one MSPE for every number of calibration samples, and is therefore even more "spiky". For small numbers of calibration samples (less than 40), the automatic selection method yields the lowest MSPE and thus provides better results than the other methods.

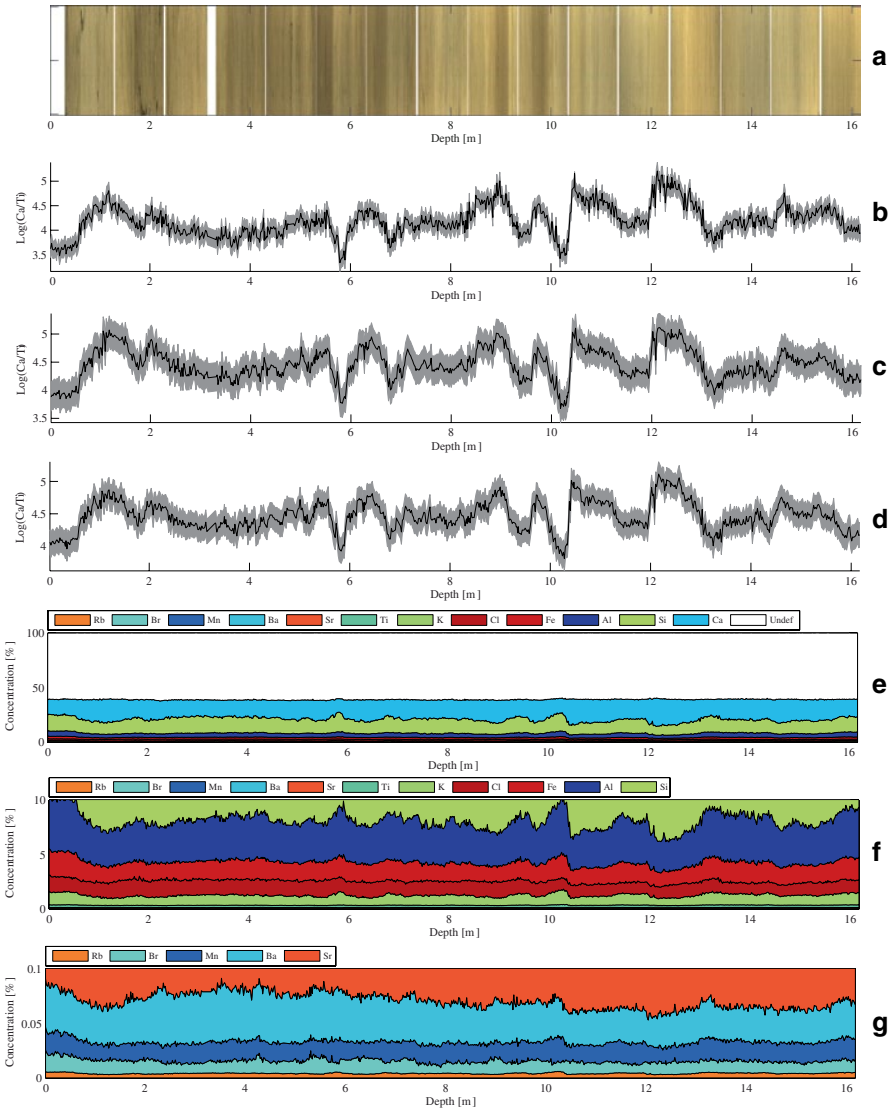


**Fig. 21.9** Overview of core GeoB7920. **a** High-resolution RGB image; **b** raw ln(Ca/Ti) intensities with 95 % confidence interval; **c** ULC prediction of ln(Ca/Ti) concentrations with 95 % confidence interval; **d** MLC prediction of ln(Ca/Ti) concentrations with 95 % confidence interval; **e** concentrations from 0 to 100 %; **f** concentrations from 0 to 5 %; **g** concentrations from 0 to 0.5 %. Elements are sorted in descending order of average concentration

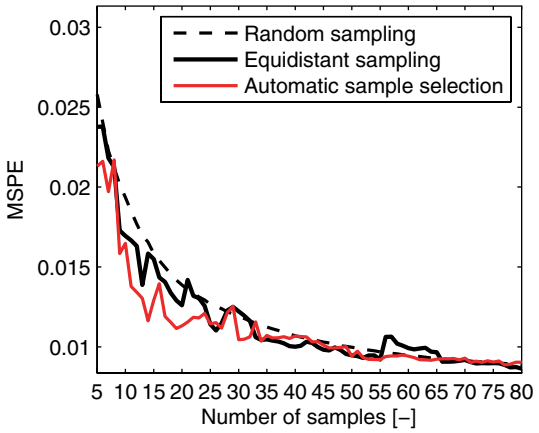


**Fig. 21.10** Comparative performance of sampling strategies in the MLC model for core GeoB7920

## Discussion

### *Comparative Performance of Calibration Models*

Because all statistics in Table 21.1 are based on cross validation, they tell us something about the actual predictive power of the four calibration models. The comparative evaluation clearly brings out the lack of fit of the DLC models, which stems from a combination of deficiencies: (1) the parametric form of the DLC model (Eq. 21.1) bears no relation to the calibration equation used in XRF spectrometry (Eq. 21.2); (2) there is no unique relation between intensities and concentrations if the measurement geometry is unconstrained; (3) the "single element" calibration does not take into account that concentrations are compositional data. It should be noted that the third deficiency is also present in the "single element" calibration equation used in XRF spectroscopy (Eq. 21.2), but its implications are far less severe, because prediction uncertainties are very small owing to standardization of measurement geometry, which implies that ignoring this fundamental problem will not usually lead to unrealistic results (although these are by no means precluded). It follows directly from the parametric form of the DLC-2 model that its predictive power outside the range of concentrations with which it has been calibrated is extremely small. Hence, extrapolation of DLC-2 models may lead to erroneous results even under laboratory conditions.

Comparison of the ULC and MLC models indicates that the latter provides a more comprehensive description of the calibration problem at hand. The ULC approach is based on the simplifying assumption that the problem to be solved can be reduced to estimation of relative concentrations of two elements simultaneously. This is clearly an oversimplification, because the quality of ULC predictions depends on which element is selected as the common log-ratio denominator. The

MLC approach takes the covariances of all log-ratios into account and allows for direct fitting of matrix effects (absorption and enhancement), which cannot be adequately represented in the ULC model.

The ULC model (Eq. 21.7) implies that log-ratios of concentrations are linear functions of log-ratios of intensities. Hence, if the interest of a researcher lies with down-core changes in a specific proxy, such as the ratio of calcium to iron—commonly taken as a robust marine-to-terrestrial flux ratio indicator—there is no need to perform calibration. In cases where researchers are merely interested in the relative fluxes of marine and terrestrial material, converting intensities to concentrations does not provide any additional information, and XRF-core scanning may be carried out in fully non-destructive mode (compare for instance Fig. 21.9b, c). Moreover, the linear transformation embodied in Eq. 21.7 implies that the correlation matrix of log-ratio intensities is an excellent predictor of the correlation matrix of log-ratio concentrations. This fact may be exploited by researchers who are interested in studying the correlation between log-ratios of element intensities on the one hand, and other properties measured on the same core (or time series obtained from other locations) on the other hand. Hence, multi-proxy analysis may be formalised using exploratory statistical analyses for the purpose of identifying specific geochemical log-ratios as proxies of palaeo-environmental conditions in a specific basin. The usefulness of this empirical approach was demonstrated by Bloemsma et al. (2012), who showed that log-ratios of element intensities or concentrations obtained from bulk measurements do not provide universal shortcuts to palaeo-environmental interpretation, but are site-specific and should thus be validated before they may be applied with some confidence. Calibration of XRF output to obtain estimates of element concentrations is only required if the objective of the research is to carry out quantitative analyses of fluxes or mass-balance calculations.

The ULC model implies that log-ratios of concentrations are linear functions of log-ratios of intensities. Hence, if the interest of a researcher lies with down-core changes in a specific proxy, such as the ratio of calcium to iron—commonly taken as a robust marine-to-terrestrial flux ratio indicator—there is no need to perform calibration.

Calibration of XRF output to obtain estimates of element concentrations is only required if the objective of the research is to carry out quantitative analyses of fluxes or mass-balance calculations.

## *Recommended Measurement and Sampling Strategies*

Automatic selection of calibration samples appears to be a promising method for minimizing the damage to sediment cores in cases where calibration to

concentrations is required. Stochastic simulation experiments carried out with core GeoB7920 (Fig. 21.10) suggest that the prediction error of the MLC model stabilizes at ~60 calibration samples. Although such knowledge is useful if we intend to measure many more cores from the same basin, it is not possible to make broad generalizations about the number of calibration samples in relation to the quality of the calibration model, because this depends on many different factors, such as the type of material analysed, the performance of the core scanner and the device used to measure the compositions of calibration samples, and the practical limitations of time and money.

A generic (i.e., hardware-independent) approach to calibration of XRF core scanner data requires that data-model discrepancies are interpreted in the light of the measurement errors associated with the input data (intensities and concentrations). Hence, replicate measurements of intensities and concentrations are required. Empirical estimates of measurement errors may be derived from the variability of repeated intensity measurements at the same spot and from replicate geochemical analyses. The latter should be obtained by splitting samples into subsamples and analysing them separately. Although the two data sets used for the comparative analysis of calibration models fulfil some of these requirements, they are by no means ideal for effective use of the MLC model. Below we list some guidelines for compiling high-quality core scanner data which are to be converted to quantitative estimates of bulk composition.

As a rule of thumb, adequate coverage of replicate intensities along a core requires the following measurement strategy:

$$N_{I,s} \geq ceil(n^{1/2}) \tag{21.14a}$$

$$\Delta N_{I,s} \leq floor(n / N_{I,s}) \tag{21.14b}$$

$$N_{I,r} \geq 3 \tag{21.14c}$$

$$N_{I,tot} = n + N_{I,s}(N_{I,r} - 1) \tag{21.14d}$$

The number of replicate intensity measurements is coupled to the length of the record, which is defined by the number of locations at which unique intensity measurements are collected, $n$. For example, scanning of a 1-m long segment of core at 1-cm resolution gives $n = 100$. $N_{I,s}$ represents the number of replicate sets, i.e. the number of locations at which replicate intensity measurements are to be collected. The spacing between these locations is defined as $\Delta N_{I,s}$, and the number of replicate measurements collected at every location as $N_{I,r}$. The total number of intensity measurements on the core segment is given by $N_{I,tot}$. The terms *ceil* and *floor* refer

to the method of rounding to adjacent integer values (up and down, respectively). In the above case where $n=100$, we obtain $N_{I,s}=10$, $\Delta N_{I,s}=10$, $N_{I,r}=3$. The measurement strategy is complete if we specify where the first set of replicates is to be collected, for instance at location 5. The other sets of replicates are then collected at locations 15, 25, …, 95. The total number of measurements needed, $N_{I,tot}=120$, indicates that the overhead associated with this strategy equals 20%. The use of inequalities in Eqs. 21.11a–c implies that the above guidelines should be regarded as reasonable minimum values. Collecting more replicates may contribute to improving the uncertainty estimation of measured intensities, but it will also increase the overhead.

Based on our current experience, we recommend the following strategy for acquisition of calibration samples:

$$N_c \geq 3D \tag{21.15a}$$

$$N_{W,s} \geq ceil(D^{1/2}) \tag{21.15b}$$

$$N_{W,r} \geq 3 \tag{21.15c}$$

$$N_{W,tot} = N_c + N_{W,s}(N_{W,r} - 1) \tag{21.15d}$$

The number of unique sites at which calibration samples should be taken, $N_c$, is coupled to the number of elements to be calibrated, $D$. Replicates of some of the calibration samples are needed for the purpose of uncertainty quantification. $N_{W,s}$ represents the number of replicate sets, and $N_{W,r}$ the number of replicates in each set. The total number of calibration samples to be analysed thus equals $N_{W,tot}$. For example, if the number of elements to be calibrated equals 10, $N_c=30$, $N_{W,s}=4$, $N_{W,r}=3$, and $N_{W,tot}=38$. The overhead associated with this strategy equals 27%. Again, more samples may be analysed if deemed necessary.

**ASCAR: Advanced Sediment and Core Analysis Research www.ascar.nl**

To boost developments in XRF core scanning technology and interpretation, a software package was developed. On this website one finds a version of this software package XELERATE, which is a software package to evaluate, process and visualize XRF core scanning data. A download of this software package is available when you are logged in, at the section ‘downloads’

## Conclusions

The second-generation multivariate log-ratio calibration (MLC) algorithm illustrated in this contribution allows unbiased prediction of geochemical compositions from XRF core scanner output with a degree of precision that is comparable to conventional XRF analysis of heterogeneous materials under laboratory conditions. It represents a vast improvement over previous attempts at direct calibration of intensities using concentrations, and is significantly better than the univariate ULC model proposed by Weltje and Tjallingii (2008). The main advantages of multivariate log-ratio calibration (MLC) over univariate log-ratio calibration (ULC) are (1) elimination of the need to select the best model from the set of $D$ alternative models; (2) effective use of the covariances of intensity and concentration measurements, which reflect absorption and enhancement of intensities, as well as the fact that certain elements reside in the same minerals, and (3) the possibility to estimate the mass fractions of samples which could not be attributed to specific elements ("Undef"), allowing prediction of "absolute" concentrations. Solution of the long-standing problem of XRF core scanner calibration implies that high-resolution records of quantitative sediment composition with associated uncertainties can now be routinely established, which should increase the usefulness of XRF-core-scanning devices and pave the way for quantitative evaluation of geochemical proxies (Weltje and Tjallingii 2008; Bloemsma et al. 2012).

**Acknowledgments** GJW and MRB wish to thank Wintershall Noordzee BV, TNO, Avaatech, and Panterra for their support of the research project "Advanced Sediment Characterisation, Analysis and Research." RT was supported by the Netherlands Organisation for Scientific Research (NWO) as part of INATEX-B (grant number 839.08.430) and the SCAN2 program on advanced instrumentation. The data set of cores GeoB7920 and Augusta Harbour core AU10v (see Croudace et al., this volume), as well as executables of the program and a user guide may be downloaded from web site "www.ascar.nl" Please note that the current version of the program has been designed to read output of the Avaatech and Itrax core scanners only. As this is research code and not a commercial product, we do not provide support.

## References

Aitchison J (1982) The statistical analysis of compositional data (with discussion). J R Stat Soc Ser B 44:139–177

Aitchison J (1986) The statistical analysis of compositional data. Chapman and Hall, London, p 416

Aitchison J, Egozcue JJ (2005) Compositional data analysis: where are we and where should we be heading? Math Geol 37:829–850

Bahr A, Lamy F, Arz H, Kuhlmann H, Wefer G (2005) Late glacial to Holocene climate and sedimentation history in the NW Black Sea. Mar Geol 214:309–322

Bloemsma MR, Zabel M, Stuut JBW, Tjallingii R, Collins JA, Weltje GJ (2012) Modelling the joint variability of grain-size and chemical composition in sediments. Sediment Geol 280: 135–148 (+ Erratum: 284–285, 214)

Böning P, Bard E, Rose J (2007) Toward direct, micron-scale XRF elemental maps and quantitative profiles of wet marine sediments. Geochem Geophys Geosyst 8

Buccianti A, Mateu-Figueiras G, Pawlowsky-Glahn V (eds) (2006) Compositional data analysis in the geosciences (Special Publication). Geological Society, London, p 264

Calvert SE, Pedersen TF (2007) Elemental proxies for palaeoclimatic and palaeoceanographic variability in marine sediments: interpretation and application. In: Hillaire C, de Vernal A (eds) Proxies in Late Cenozoic paleoceanography. Developments in marine geology, vol 1. Elsevier Science, Amsterdam, pp 567–644

Croudace IW, Rindby A, Rothwell RG (2006) ITRAX: description and evaluation of a new multi-function X-ray core scanner. In: Rothwell RG (ed) New techniques in sediment core analysis, vol 267 (Special Publication). Geological Society, London, pp 51–63

De Jong S (1993) SIMPLS: an alternative approach to partial least squares regression. Chemom Intell Lab Syst 18:251–263

De Vries JL, Vrebos BAR (2002) Quantification of infinitely thick specimens by XRF analysis. In: van Grieken RE, Markovicz AA (eds) Handbook of X-ray spectrometry, 2nd edn. Marcel Dekker, New York, pp 341–405

Ge LQ, Lai WC, Lin YC (2005) Influence of and correction for moisture in rocks, soils and sediments on in situ XRF analysis. X-Ray Spectrom 34:28–34

Geisser S (1975) The predictive sample reuse method with applications. J Am Stat Assoc 70:320–328

Haschke M (2006) The Eagle III BKA system, a novel sediment core X-ray fluorescence analyzer with very high spatial resolution. In: Rothwell RG (ed) New techniques in sediment core analysis, vol 267 (Special Publication). Geological Society, London, pp 31–37

Haschke M, Scholz W, Theis U, Nicolosi J, Scruggs B, Herzceg L (2002) Description of a new micro-X-ray spectrometer. J Phys IV Fr 12:6–83

Jaccard SL, Haug GH, Sigman DM, Pedersen TF, Thierstein HR, Röhl U (2005) Glacial/interglacial changes in subarctic North Pacific stratification. Science 308:1003–1006

Jansen JHF, Van der Gaast SJ, Koster B, Vaars AJ (1998) CORTEX, a shipboard XRF-scanner for element analyses in split sediment cores. Mar Geol 151:143–153

Jenkins R (1999) X-ray fluorescence spectroscopy, 2nd edn. Wiley, New York, 207 pp

Kido Y, Koshikawa T, Tada R (2006) Rapid and quantitative major element analysis method for wet fine-grained sediments using an XRF microscanner. Mar Geol 229:209–225

Löwemark L, Chen HF, Yang TN, Kylander M, Yu EF, Hsu YW, Lee TQ, Song SR, Jarvis S (2011) Normalizing XRF-scanner data: a cautionary note on the interpretation of high-resolution records from organic-rich lakes. J Asian Earth Sci 40:1250–1256

Pälike H, Shackleton NJ, Röhl U (2001) Astronomical forcing on late Eocene marine sediments. Earth Planet Sci Lett 193:589–602

Press WH, Teukolsky SA, Vetterling WT, Flannery BP (1994) Numerical recipes in FORTRAN: the art of scientific computing, 2nd edn. University Press, Cambridge, 963 p

Ramsey MH, Potts PJ, Webb PC, Watkins P, Watson JS, Coles BJ (1995) An objective assessment of analytical method precision: comparison of ICP-AES and XRF for the analysis of silicate rocks. Chem Geol 124:1–19

Richter TO, Van der Gaast SJ, Koster B, Vaars A, Gieles R, De Stigter H, De Haas H, van Weering TCE (2006) The Avaatech XRF core scanner: technical description and applications to NE Atlantic sediments. In: Rothwell RG (ed) New techniques in sediment core analysis, vol 267 (Special Publication). Geological Society, London, pp 39–50

Rothwell RG, Rack FR (2006) New techniques in sediment core analysis: an introduction. In: Rothwell RG (ed) New techniques in sediment core analysis, vol 267 (Special Publication). Geological Society, London, pp 1–29

Rothwell RG, Hoogakker B, Thomson J, Croudace IW, Frenz M (2006) Turbidite emplacement on the southern Balearic Abyssal Plain (western Mediterranean Sea) during Marine Isotope Stages 1–3: an application of ITRAX XRF scanning of sediment cores to lithostratigraphic analysis. In: Rothwell RG (ed) New techniques in sediment core analysis, vol 267 (Special Publication). Geological Society, London, pp 79–98

Tjallingii R, Röhl U, Kölling M, Bickert T (2007) Influence of the water content on X-ray fluorescence core-scanning measurements in soft marine sediments. Geochem Geophys Geosyst 8

Tjallingii R, Claussen M, Stuut JB, Fohlmeister J, Jahn A, Bickert T, Lamy F, Röhl U (2008) Coherent high- and low-latitude control of the northwest African hydrological balance. Nat Geosci 1:670–675

Vlag PA, Kruiver PP, Dekkers MJ (2004) Evaluating climate change by multivariate statistical techniques on magnetic and chemical properties of marine sediments (Azores region). Palaeogeogr Palaeoclimatol Palaeoecol 212:23–44

Ward JH (1963) Hierarchical grouping to optimize an objective function. J Am Stat Assoc 58:236–244

Weltje GJ, Tjallingii R (2008) Calibration of XRF core scanners for quantitative geochemical logging of sediment cores: theory and application. Earth Planet Sci Lett 274:423–438

Wien K, Wissmann D, Kölling M, Schulz HD (2005) Fast application of X-ray fluorescence spectrometry aboard ship: how good is the new portable Spectro Xepos analyzer? Geo-Mar Lett 25:248–264

# Chapter 22
# Parameter Optimisation for the ITRAX Core Scanner

**Stuart Jarvis, Ian W. Croudace and R. Guy Rothwell**

**Abstract** A range of parameters affects Itrax core scanner response. These include operational instrument factors such as anode tube type, current and voltage settings, the effect of protective films applied to prevent sample desiccation and also physical factors related to the sample itself such as surface topography, textural variation and water content. This paper examines the significance of these factors on recorded counts and hence allows an assessment of their impact on data integrity.

**Keywords** ITRAX core scanner · Data optimisation · Data reproducibility · Data artefacts · Core scanner parameters

## Introduction

The Itrax core scanner provides a range of options to optimise scanning conditions for the sample. The user has a number of key choices:

- X-ray tube type (tubes with Mo, Rh and Cr anodes are the most commonly used and Cu was used in the past)
- High voltage adjustment of tube power supply
- Current adjustment for the tube power supply
- Use of plastic film to reduce sample desiccation during analysis

This study examines a range of choices to determine optimal settings for a range of sediment types. Irrespective of the instrumental settings used, results may be affected by various sample characteristics such as surface topography, cracks and other surface defects, grain-size and water content. These are examined and possible strategies are presented that can overcome or limit their impact. Finally, some of the factors affecting the reproducibility of Itrax scan data are considered and proposals given on optimal XRF counting times.

I. W. Croudace (✉) · S. Jarvis
Ocean and Earth Science, National Oceanography Centre, University of Southampton, Waterfront Campus, European Way, Southampton, SO14 3ZH, UK
e-mail: iwc@noc.soton.ac.uk

R. G. Rothwell
National Oceanography Centre, Empress Dock, Southampton, SO14 3ZH, UK



I. W. Croudace, R. G. Rothwell (eds.), *Micro-XRF Studies of Sediment Cores*,
Developments in Paleoenvironmental Research 17, DOI 10.1007/978-94-017-9849-5_22

## *Optimisation Choices*

**X-ray Tube Type** The ITRAX core scanner uses standard glass X-ray diffraction tubes with a sharp fine focus and these are sourced from suppliers such as PANalytical (Cambridge UK). Although chromium anode tubes are considered optimal for recording light elements (i.e. $Z \leq Fe$), molybdenum (and rhodium) anode tubes enable excitation of the full range of detectable elements, with better response from heavier elements (i.e. $Z \geq Fe$; Croudace et al. 2006).

**X-ray Tube Voltage** The voltage of the tube power supply sets the potential through which electrons are accelerated and therefore the energy with which they arrive at the anode target. Variation in tube voltage changes the shape of the bremsstrahlung (Tavora et al. 2001; Gupta et al. 2010). Tube voltage can thus be adjusted to optimise excitation of particular elements.

**X-ray Tube Current** A higher current to the tube cathode provides more electrons for acceleration through the potential in the tube and therefore increases the intensity of fluorescent X-rays produced. A balance must be found between using a current that is high enough to generate sufficient fluorescence to minimise XRF count times, but not high enough to generate significant sum peaks (these occur when the fluorescent photon flux is so high that individual photons cannot be resolved at the detector).

**Plastic Films Used to Prevent Sample Desiccation** It is common practice to cover the sample with a thin plastic film to prevent desiccation during core scanning (Croudace et al. 2006; Richter et al. 2006). However, these films reduce transmission of fluorescent X-rays from the sample to the detector (Davies 1997). They can also trap a layer of water on the sediment surface (Kido et al. 2006; Tjallingii et al. 2007; Weltje and Tjallingii 2008). Typical film materials used are polypropylene, Mylar (stretched polyethylene terephthalate) and Ultralene, in thicknesses ranging from 1.5 to 6.0 μm.

## *Sample Properties that May Affect XRF Counts*

**Surface Topography** Even apparently flat cut core surfaces may show a microtopography and textural variation that could affect core scanner response. Additionally samples may contain cracks, voids, clasts and other features that may influence recorded data (Voglis and Rindby 1995).

**Bulk Grain-Size** Clastic sediment components can vary in grain-size due to sediment source and depositional mechanism (Slattery and Burt 1997). In conventional WD-XRF using discrete sub-samples, grain-size variation is reduced by grinding or eliminated by fusing the sample to produce a glass bead. In Itrax scanning, textural variation may be a significant feature affecting data quality. Small grains packing around larger ones may absorb fluorescence from the larger grains (Finkelshtein and Brjansky 2009) and larger grains on the core surface may provide a shadowing effect, blocking fluorescence from smaller particles (Criss 1976).

**Water Content** Water content can reduce element peak areas (Ge et al. 2005; Kido et al. 2006; Tjallingii et al. 2007). Kido et al. (2006) assert that the thickness of a water film between the sediment surface and the plastic film applied to prevent sample desiccation is proportional to the bulk water content and that element peak areas depend on this.

### *Reproducibility and XRF Counting Time*

Each interaction between an X-ray photon and electrons in an atom can be considered a random, independent event. It is therefore expected, as suggested by Croudace et al. (2006), that uncertainty in Itrax reported peak areas obeys Poisson statistics and is equivalent to the square root of the peak area; in the equation below $\sigma P$ is the standard deviation in recorded peak area, $P$.

$$\sigma P = \sqrt{P} \tag{22.1}$$

As the recorded peak area should be proportional to the counting time, a longer counting time should reduce the relative uncertainty (standard deviation as a percentage of the peak area).

## Materials and Methods

*Geochemical Reference Samples* A range of pelletised geochemical reference samples were used in the scans that have well characterized elemental compositions. The powdered samples were compressed at 12 t into rectangular tiles and stacked together in a custom-made Perspex holder for Itrax scanning. The use of these materials enabled factors such as water content, sample heterogeneity, grain-size variation and surface slope to be eliminated while investigating other effects. The geochemical reference samples used were:

- BE-N—alkali basalt, CRPG, France
- JCh-1—chert, Geological Survey of Japan
- JLs-1—limestone, Geological Survey of Japan
- MAG-1—muddy marine sediment with low carbonate content, US Geological Survey
- NIM-G—granite, South African Bureau of Standards
- NIM-S—syenite, South African Bureau of Standards
- SGR-1—petroleum and carbonate-rich shale, US Geological Survey

An engineered aluminium block (from Cox Analytical) and a 2 × 1 cm shaped block of obsidian (Icelandic volcanic glass) were also used during testing.

*Other Sample Types Used—Lake and Marine Test Sediments* Lake and marine sediments were used to provide samples typical of those commonly scanned on the Itrax

core scanner. One sample was sourced from a carbonate lake in the Chacabuco Valley, Chilean Patagonia. It was the bottom 30 cm section of a 4.5 m long core. The bulk of the section is calcareous micrite with shell inclusions, but it also contains some clastic layers of glacial origin. The second lake sediment came from Lake Igelsjön, Uppsala, Sweden. This sample was highly homogenous with a high organic content. The marine samples used were core CD166–19 section 2 and core CD166–27 section 5 (NW African continental margin close to the Canary Islands, and containing a sequence of volcaniclastic turbidites and pelagic ooze (Wynn and Cronin 2005). Both cores had water contents in the range 35–45 wt%.

## *Choice of X-ray Tube*

Three Itrax X-ray tubes (Mo, Cr and Cu anode targets) were used to scan the geochemical reference samples. Excitation efficiency for each element was defined as the number of counts per second per percentage of sample that the element makes up by mass. Counts per second were determined by taking the peak area for the element determined by the Itrax spectral analysis software, QSpec (Cox Analytical, Gothenburg), and dividing by XRF count time. The X-ray tubes were energised using 30 mA current at 30 kV accelerating potential with a count time of 30 s. A sample step size of 200 μm was used to ensure that at least ten measurements were made on each reference material, from which mean values were determined for each material.

## *X-ray Tube Voltage*

The reference samples were scanned at nine different voltages to assess the effect of tube voltage on element detection. The first scan was performed at 10 kV and 30 mA using a Cr tube. The voltage was then increased in increments of 5 kV for each subsequent scan, up to a maximum of 50 kV. The current was maintained at 30 mA throughout. The process was repeated using the Mo anode tube.

## *X-ray Tube Current*

To assess the effect of tube current, the reference samples were scanned with the Cr and Mo anode tubes, with voltage fixed at 30 kV and current varied from 10 mA to 50 mA in 5 mA intervals.

## *Plastic Films Used to Prevent Desiccation*

An Al sample was covered with five strips of different commercially available XRF film types and scanned using the Mo anode tube (settings 30 kV, 30 mA, with 100 s

count time). A region of the sample was left uncovered to record the Al peak area when film was not used. The films used in this test were: polypropylene (a robust and chemically-resistant thermoplastic polymer) in 1.5 μm, 5 μm and 6 μm thicknesses, 3 μm thick Mylar (economical, very strong, chemically resistant stretched polyester film) and 4 μm thick Ultralene (high strength, high purity polymeric film with excellent X-ray transmission). The geochemical reference samples were also scanned, first without film, then with 6 μm polypropylene and then 3 μm thick Mylar. The scans used the Mo anode tube with 30 mA current at 30 kV and a 30 s count time.

## *Surface Slope Variations*

A homogeneous modelling clay was used to test effects of surface slope. Half was pressed into a u-channel and smoothed to give a flat surface and allowed to dry before scanning using the Mo anode tube at 30 kV and 30 mA. The other half was pressed into a u-channel and the surface moulded to introduce height variations of approximately 5 mm between the highest and lowest points. It too was allowed to dry before scanning. Peak areas were compared between the flat and sloping surfaces for elements with a range of atomic numbers and fluorescent X-ray energies (elements Al, Si, Ca, Fe, Sr and Ba; $Z = 13 - 56$; detectable emission energies 1.48 – 15.84 keV) found in the clay. The gradient of the surface (rate of change in surface height with distance along surface, determined from the Itrax core scanner laser profiler) varied from 0 (flat) to approximately ± 0.25 (ascending and descending slopes).

## *Grain-size Variations*

Silicon carbide grains in four sizes with nominal diameters 29, 62, 190 and 850 μm were mixed with fine-grained clay to simulate sandy sediment. One sample was prepared for each grain-size, each consisting of 33 % silicon carbide by mass. A fifth sample had no silicon carbide added. The samples were smoothed into a u-channel to present a flat surface and scanned. Peak areas were compared for Al (only present in the clay) and Si (present both in the clay and silicon carbide).

## *Water Content*

The effects of water content were measured using three sediment samples.

1. **Igelsjön lake sediment sample:** This was homogenised and did not crack during drying. For this reason, it was the primary sample used for assessing the effect of water content on peak areas. However, it had low concentrations of Al and Si, so CD166–27 Section 5 was used to study the effects of water content on those two elements. The Cr anode tube was used to scan CD166–27 Section 5 to maximise

peak areas for Al and Si; for the Igelsjön and CD166–19 Section 2 samples the Mo anode tube was used to excite the widest range of elements. The Igelsjön sample contained initially 69 % water and was allowed to dry over a period of 1 week. It was scanned (Mo anode tube; 30 mA; 30 kV) multiple times during this period and its mass recorded before each scan to determine changes in water content. A sub-sample was freeze dried after the final scan to determine residual water content.

2. **Marine sample CD166–19 Section 2** was not dried. It was scanned (Mo anode tube; 30 mA; 30 kV) once and then sub-samples were taken to determine element concentration and water content at points along the scan line. Elemental peak areas, normalised to element concentration, were then compared to water content along the sample.
3. **Marine core CD166–27 Section 5** (U-channel) was progressively dried by heating at 50 °C and 100 °C. It was scanned (Cr anode tube; 30 mA; 30 kV) before any drying and after drying at 50 °C and 100 °C. Its mass was recorded before each scan to determine changes in water content. A sub-sample was freeze dried after drying at 100 °C to determine residual water content.

### *Reproducibility and XRF Count Time*

Reproducibility was evaluated by running ten consecutive scans of the same sample with constant tube (Mo anode) voltage (30 kV) and current (30 mA) with a count time of 30 s. First, the Chilean lake sediment sample was scanned, then the set of geochemical reference samples. To test reproducibility with a larger sample size, the obsidian sample was repeatedly scanned to provide a set of 260 spectra representing the same chemical composition. The geochemical reference samples were scanned ten times for seven different count times (1, 2, 5, 10, 30, 60 and 150 s) to compare variation between scans with the count time used to obtain data.

## Results

### *Choice of X-ray Tube*

For elements lighter than Cr, use of a Cr anode tube gives best excitation efficiency (Fig. 22.1). A Cu anode tube provides maximum efficiency for Mn and Fe while both Cr and Mo tubes provide good excitation for elements heavier than Fe.

### *X-ray Tube Voltage*

Excitation can vary greatly with tube voltage (Fig. 22.2). Sr, Zr and Mo have low relative excitation (<0.5) for Cr anode tube voltages lower than 25 kV and then enhanced relative excitation for tube voltages from 30 to 50 kV.

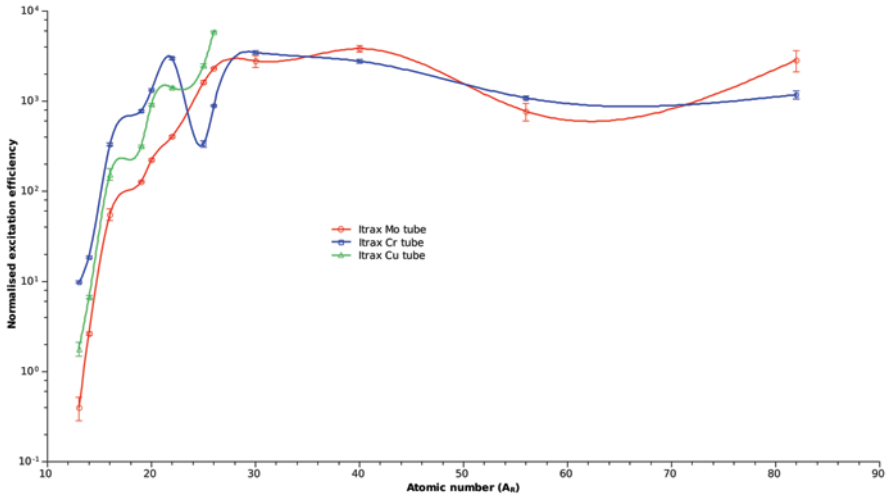


**Fig. 22.1** Comparison of excitation efficiency for X-ray tubes with different anode targets. Normalised excitation efficiency is the mean net peak area recorded for an element across a range of reference samples, normalised to the count time and elemental concentration in each reference sample. A log scale is used to better differentiate between the responses of lighter elements ($Z \leq Fe$)

For the Mo anode tube, there is little variation between most elements above 20 kV tube voltage. The exceptions are elements from Br to Zr, which have relative excitation at 50 kV tube voltage more than five times that at 20 kV.

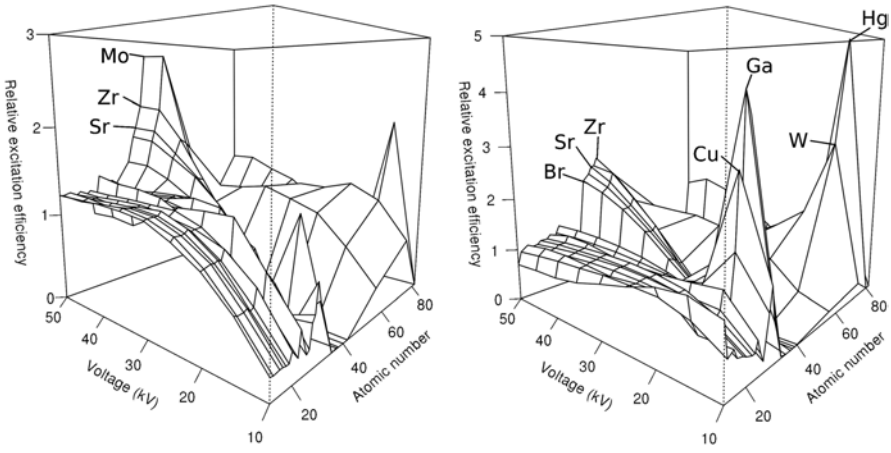


**Fig. 22.2** Relative counts recorded per element in a set of geochemical reference samples with differing tube voltages for Cr anode tube (*left*) and Mo anode tube (*right*). Relative excitation efficiency is the element counts normalised so that the mean value across all voltages for a given element is 1. A constant current of 30 mA was used for both tubes

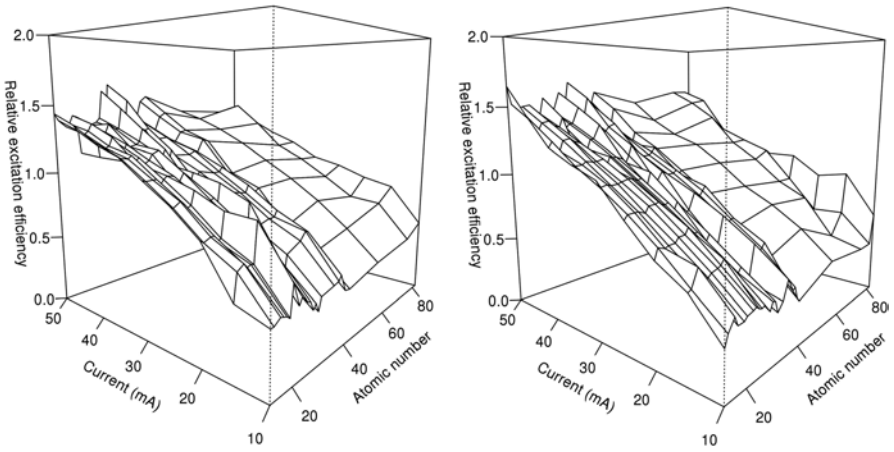


**Fig. 22.3** Relative counts recorded per element in a set of geochemical reference samples with differing tube currents for a Cr anode tube (*left*) and Mo anode tube (*right*). Relative excitation efficiency is the element counts normalised so that the mean value across all currents for a given element is 1. A constant voltage of 30 kV was used for both tubes

## *X-ray Tube Current*

For most elements, excitation is approximately linear with tube current (Fig. 22.3). However, normalising excitation against the tube current shows some non-linearity (Figs. 22.4 and 22.5). Despite the nonlinearity, a linear regression provides a good approximation over the range of tube voltages normally used (Fig. 22.5).

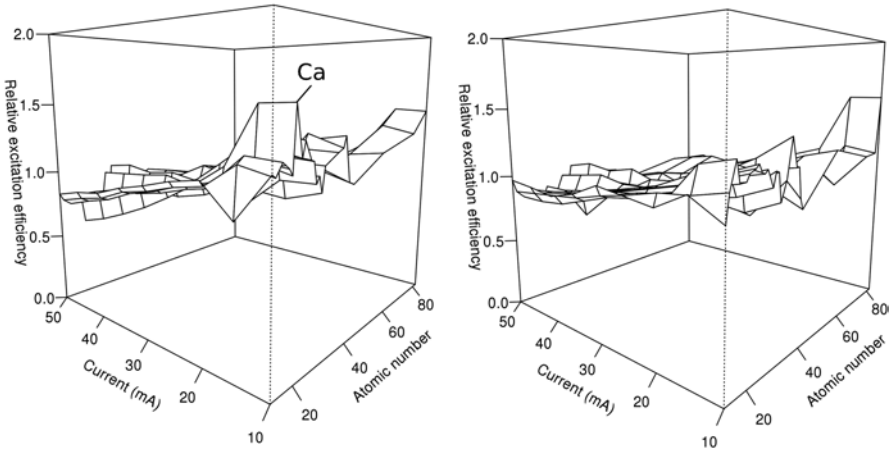


**Fig. 22.4** Relative counts normalised to current for elements in a set of geochemical reference samples with differing tube currents for a Cr anode tube (*left*) and Mo anode tube (*right*). Relative excitation efficiency is element counts divided by the tube current and normalised so that the mean value across all currents for a given element is 1. A constant voltage of 30 kV was used for both tubes

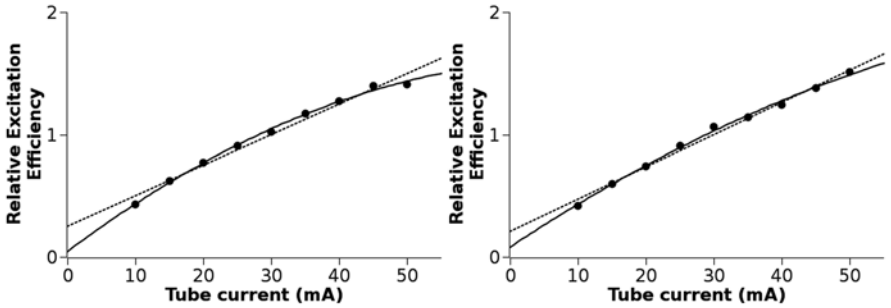


**Fig. 22.5** Linear and polynomial regression lines for the relationship of relative excitation efficiency (a measure of the relative counts of all elements) with tube current. *Left*: geochemical reference samples excited using a Cr anode tube, *right*: the same samples excited using a Mo anode tube

If excitation is instead normalised to the coherent scatter energy of the tube anode characteristic radiation, dependence on current is mostly eliminated for the Cr anode tube and reduced for the Mo anode tube (Fig. 22.6). Exceptions for the Cr anode tube are Ca (elevated normalised relative efficiency at low voltages) and Co and Cu (elevated normalised relative efficiency at high voltages).

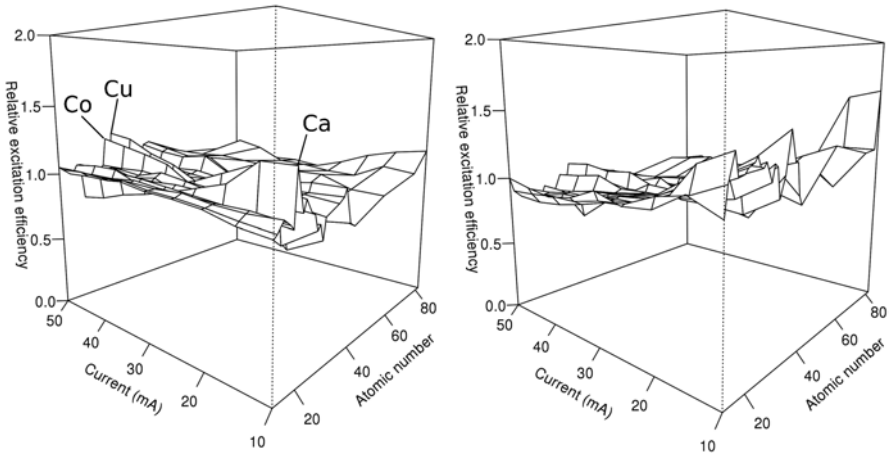


**Fig. 22.6** Relative counts normalised to coherent scatter peak for elements in a set of geochemical reference samples with differing tube currents for a Cr anode tube (*left*) and Mo anode tube (*right*). Relative excitation efficiency is element counts divided by the size of the coherent scattering peak and normalised so that the mean value across all currents for a given element is 1. A constant voltage of 30 kV was used for both tubes

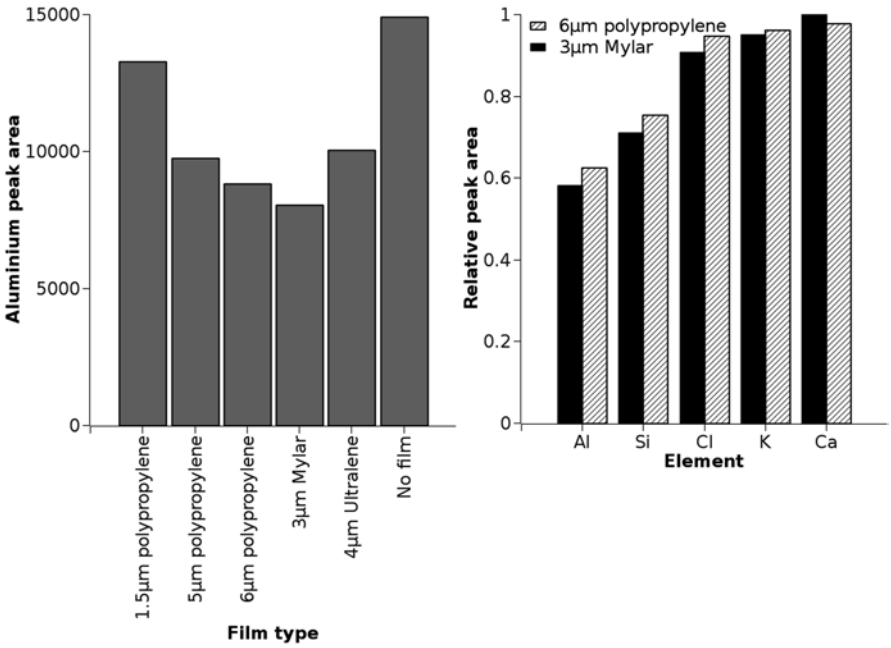


**Fig. 22.7** Effect of plastic film composition on XRF peak areas. *Left*: a comparison of recorded Al peak areas using a range of available XRF films and no film (scanned with Mo anode tube at 30 kV and 30 mA, with 100 s count time). *Right*: a comparison by element for two popular XRF films, showing relative peak areas (peak area with film divided by peak area with no film; Mo anode tube with 30 mA current at 30 kV and a 30 s count time). For elements heavier than Ca the use of films has little effect on peak areas

## *Effect of Plastic Films Used to Prevent Desiccation During Scanning*

Absorption of fluorescent X-rays from Al varies according to the film used (Fig. 22.7). Use of thinner film does not necessarily result in increased transmission of fluorescent X-rays as the film composition is important—for example, 3 µm thick Mylar film reduces Al counts more than 6 µm thick polypropylene. For Ca and heavier elements ($Z \geq 20$), the use of films has a lesser effect.

## *Surface Slope*

There is consistent dependence of elemental peak areas on surface slope across a range of elements, with areas of negative gradient having elevated counts compared to areas of positive gradient (Fig. 22.8). Gradients are defined in relation to whether surface height passing the detector increases or decreases. Therefore, surfaces that fall towards the left (as viewed from the front of the Itrax measurement chamber)

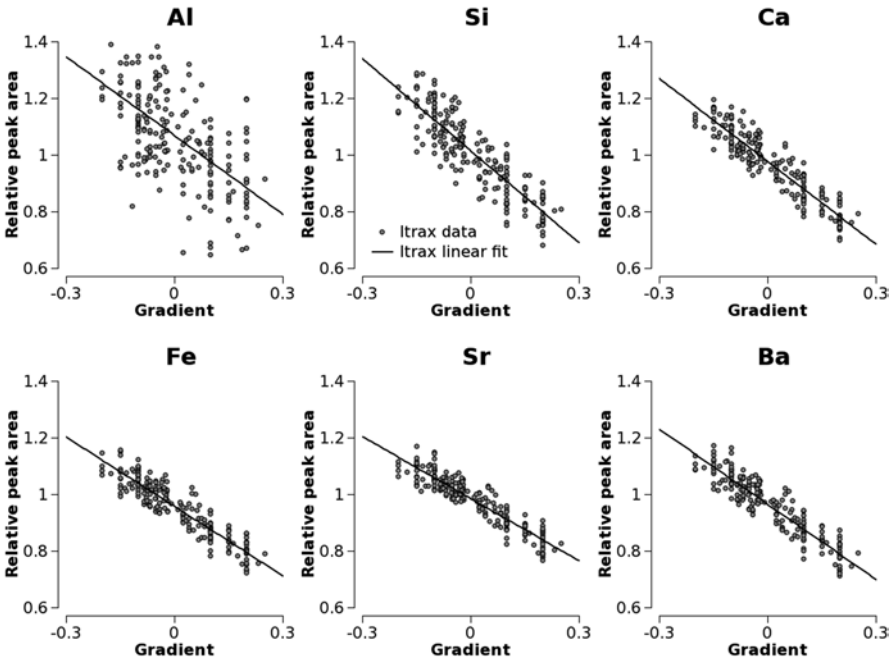


**Fig. 22.8** Variation of Itrax peak areas with gradient of the sample surface, showing recorded Itrax data and linear regression lines for those data. The relative peak area is the peak area at a point on the sloping surface divided by the peak area at the equivalent point on the flat surface

are deemed to have negative gradient; those that rise towards the left are deemed to have positive gradient.

## *Bulk Grain-Size*

For the sediment samples containing one-third silicon carbide, Si peak areas are dependent on silicon carbide grain-size (Fig. 22.9). For the largest (850 μm diameter) silicon carbide grains, Si and Al peak areas are the same—within the uncertainty in Itrax data—as for a sample containing no silicon carbide. Al peak areas, reflecting detection of clay, decrease as silicon carbide grain-sizes decrease.

## *Water Content*

Plotting element peak areas against water content for the lake sediment case study suggests a correlation (Fig. 22.10). However, if peak areas are "corrected" to take into account the diluting effect of water (so that peak areas for a sample with 50 % water are doubled) then the apparent correlation disappears

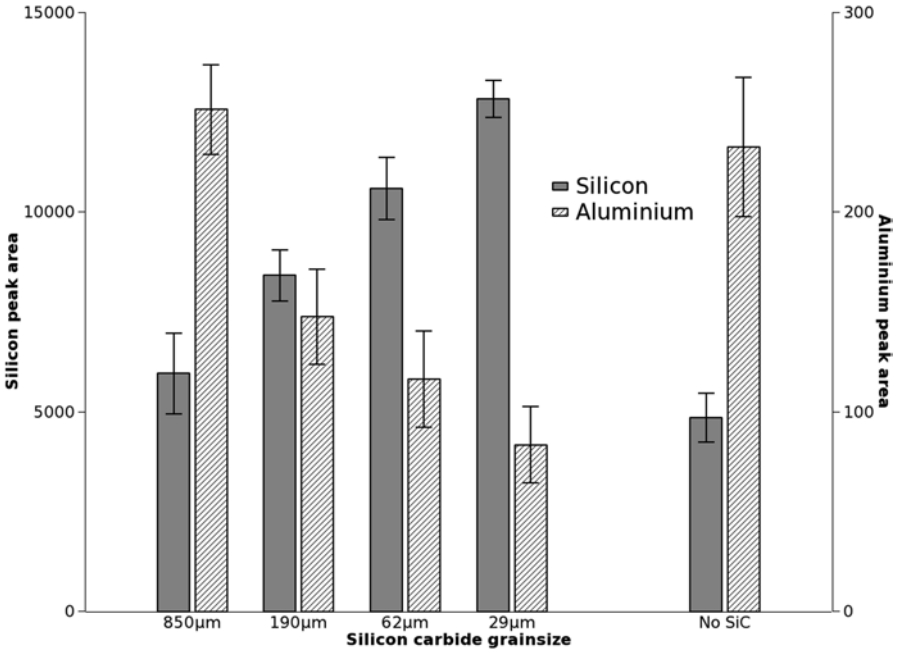


**Fig. 22.9** Al and Si peak areas for four clay samples with one-third silicon carbide by mass (first four column pairs) and a clay sample without silicon carbide (*right column*). Detection of Si is dependent on silicon carbide grain-size

Water content is also compared to the scattering ratio of the tube anode characteristic radiation (incoherent to coherent scatter). In scans carried out at different times with different samples (marine core CD166–19 Section 2 and a high organic content lake sediment from Igelsjön Sweden) there is a correlation ($R^2 = 0.996$) between the ratio of incoherent to coherent scatter and water content (Fig. 22.11). A regression line based on the data from the marine core intersects the data from the lake sediment.

## *Reproducibility and XRF Counting Time*

There is an apparent correlation between the square root of recorded element counts and the standard deviation in those counts for many elements in the lake sediment sample (Fig. 22.12). Those that do not show strong correlation (Mn, Sr and Zr) have a smaller range in recorded counts than those that do show a strong correlation. However, most recorded standard deviations are much higher than the square root of counts predicted by Poisson statistics (typically 2–3 times higher and in some cases an order of magnitude greater).

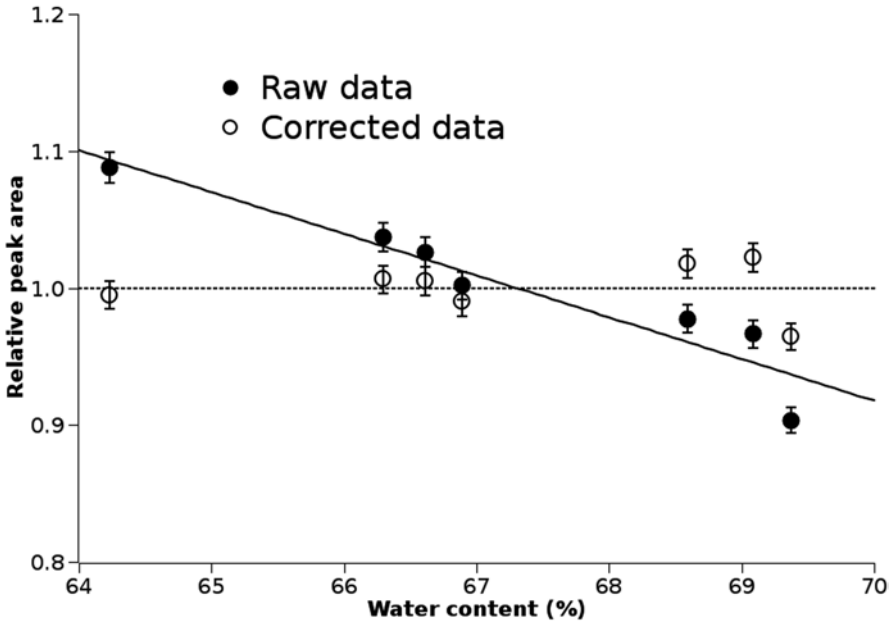


**Fig. 22.10** Effect of water content on mean peak areas (for all elements with peak area > 100) for the Igelsjön lake-sample. Raw peak areas ("Raw data") decrease with increased water content. However, when peak areas are normalised against element concentrations in the wet sample ("Corrected data") there is no apparent dependence on water content

For the obsidian sample, there is good correlation between standard deviation in peak areas and the square root of peak areas ($R2 = 0.88$). However, the standard deviation is higher than expected (Fig. 22.13). The standard deviation for Fe is excluded from this plot, as it is more than six times higher than the square root of the mean Fe counts and hence does not fit the general trend shown by other elements.

The uncertainty in Itrax data (and other XRF data) varies inversely with the square root of the count time—i.e. if the counting time is quadrupled, then uncertainty is halved.

## Discussion

### *Differences Between X-ray Tubes*

A Cr anode tube provides best excitation for elements lighter than Cr (Z = 24), while Mo and Cr anode tubes provide good excitation for those heavier than Fe (Z = 26) (Fig. 22.1). A Cu tube provides best excitation for Mn and Fe, but detection of these

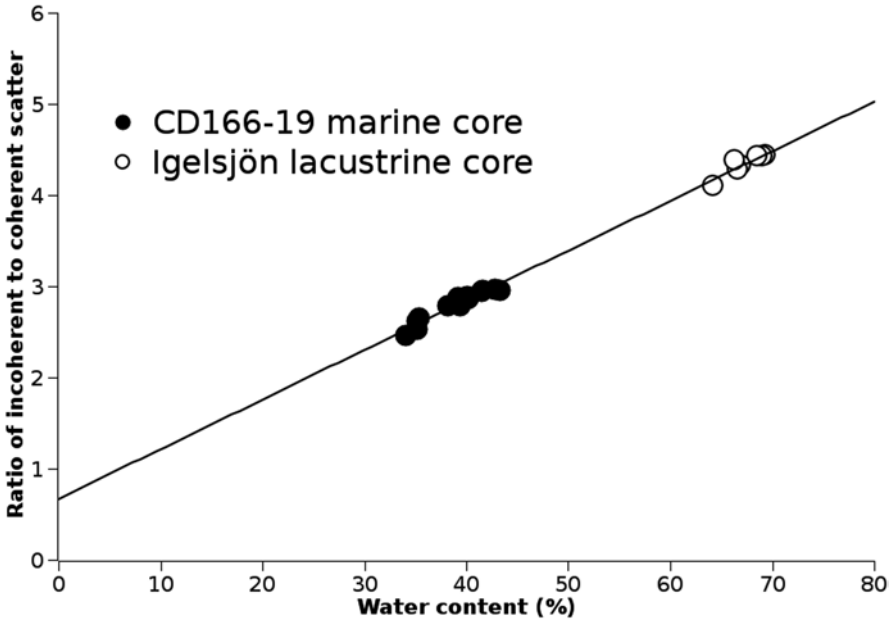


**Fig. 22.11** Water content compared to the ratio of incoherent to coherent scatter of X-ray tube characteristic radiation, for a marine sediment (CD166-19 Section 2) and lake sediment (Igelsjön). A linear regression based on the marine core data intersects the lake sediment data. Error bars (not shown) are of similar dimension to the point markers

using Cr and Mo tubes is generally satisfactory. Indeed, there are few circumstances when use of a Cu tube would bring specific benefit.

There are other reasons to consider particular tubes besides for best excitation of particular elements. The coherently scattered Cr peak present in spectra collected using the Cr tube partially overlaps with the Mn Kα peak. This may causes difficulty in determining Mn peak area when using a Cr anode tube. With Mo tubes, there is overlap between the incoherently scattered Mo peak, the Sr Kβ peak and Zr Kα peaks, confusing determination of the peak area for these.

## *Effect of Tube Voltage*

In order to efficiently excite elements across the full detectable range (of approximately 0–18.6 keV) a tube voltage of at least 20 kV is required (Fig. 22.14). Lower voltages will not provide bremsstrahlung to excite fluorescence across the full detectable range.

The lowest voltage used, 10 kV, accelerates electrons sufficiently to give them the required energy of 5.99 keV (Bearden and Burr 1967) to displace core electrons in the Cr target and produce Cr K-line radiation at 5.41–5.95 keV. The variations in X-rays produced by operating the Cr tube at differing voltages therefore depend

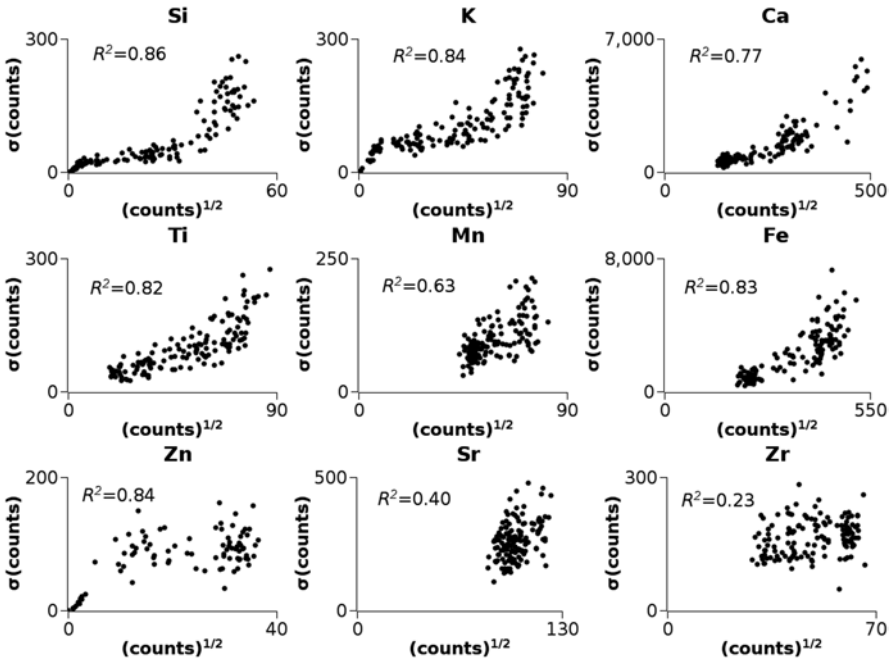


**Fig. 22.12** Comparison of the standard deviation, σ, in element counts at each point over ten scans of a lake sediment (micrite with clastic layers of glacial origin) with the square root of the mean value of the element counts. Poisson statistics suggest that the two quantities should be equal. $R^2$ gives the correlation coefficient between the two quantities

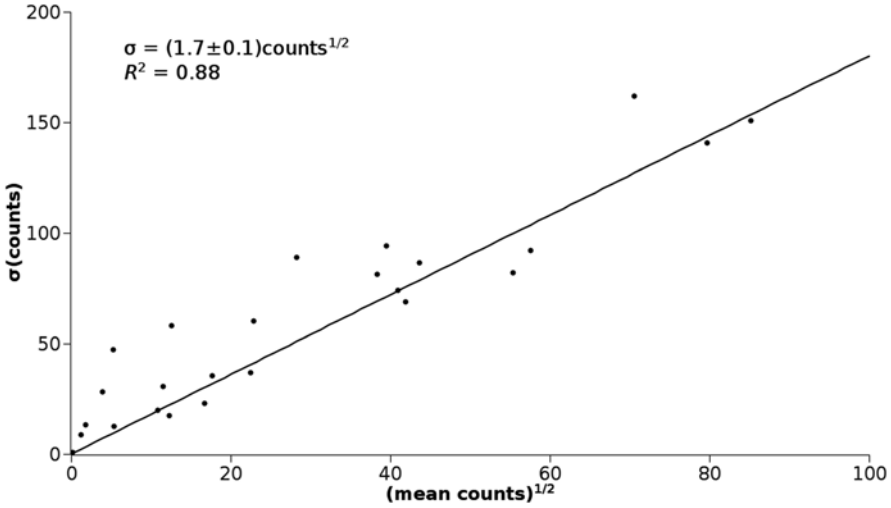


**Fig. 22.13** Variation of standard deviation, σ, in processed counts with the square root of the mean counts recorded for 260 processed spectra collected from an obsidian sample. Each point represents a different element. Fe, excluded from plot, does not fit on the observed trend line and has σ > 6 times greater than the square root of its mean counts

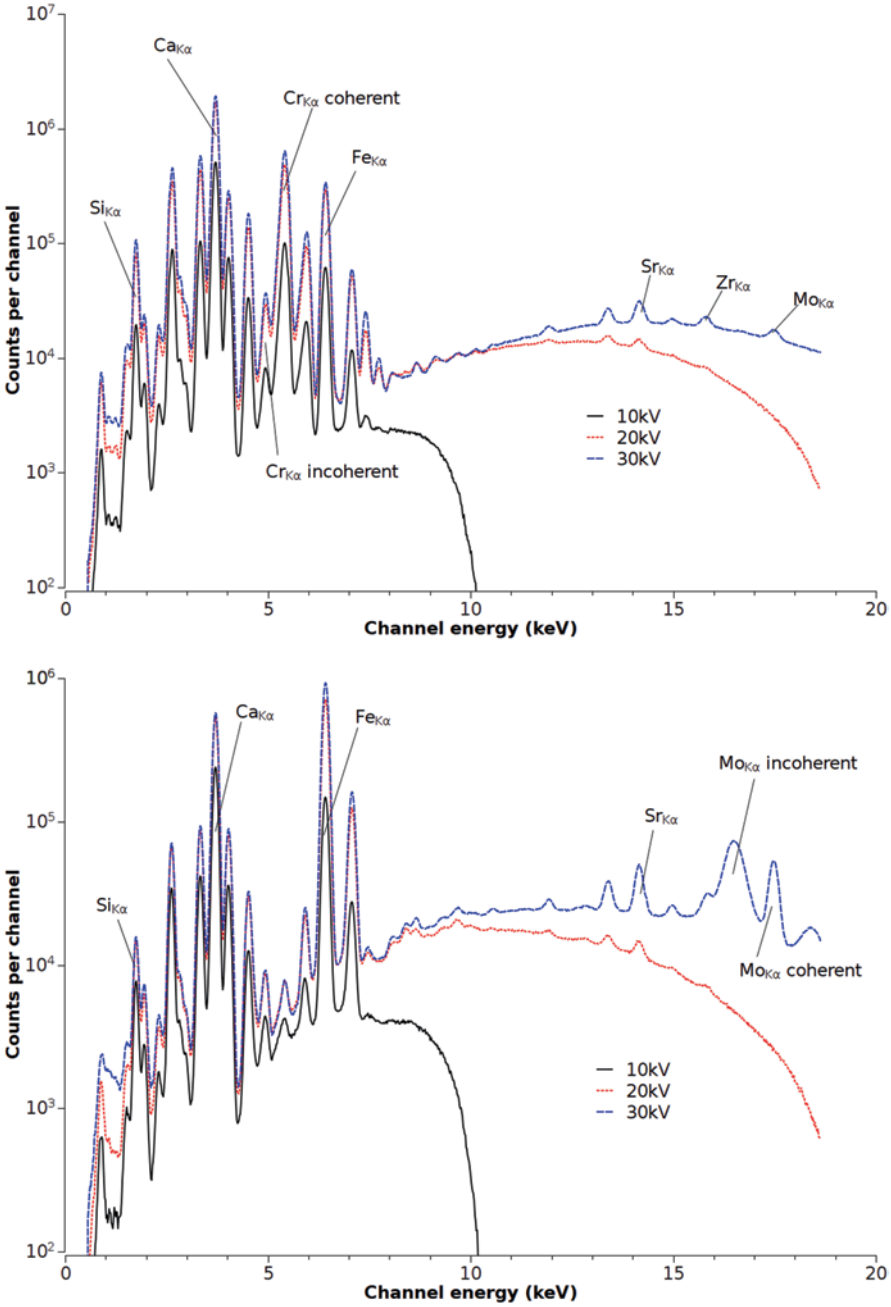


**Fig. 22.14** Spectra from scans of a geochemical reference sample (MAG-1) using a Cr (*top*) and Mo (*bottom*) anode X-ray tube for different tube voltages. For clarity only 10, 20 and 30 kV scans are shown as differences between scans at 30−50 kV are smaller. The tube voltage sets the limit on the bremsstrahlung.

mainly on the bremsstrahlung. Zr, with K-lines at 15.69 keV and above, requires a tube supply of at least 30 kV for efficient excitation using a Cr anode tube—excitation comes only from the bremsstrahlung. Zr reaches a peak excitation at 45 – 50 kV tube potential. Similar trends are seen for Sr and Mo (K-lines from 14.10 keV and 17.37 keV, respectively) when using a Cr anode tube.

A Cr tube voltage of 30 kV provides efficient excitation across the broadest range of elements (relative excitation efficiencies in the range 0.87 – 1.31—Fig. 22.2). At a voltage of 30 kV for the Cr tube the excitation efficiency of the lightest (and often least well detected) elements no longer increases with voltage.

For Mo tubes, the response to tube voltage is more complex. Mo K-line radiation is present at 17.37 keV, 17.48 keV and 19.61 keV. However, this characteristic radiation from the tube anode is only present when electrons accelerated towards the target have sufficient energy to displace a core electron, i.e. energy > 20 keV (Bearden and Burr 1967). At voltages below 20 kV the radiation incident on the sample contains only bremsstrahlung. The lightest elements ($Z \leq 24$, Al–Cr) can be excited by the bremsstrahlung using tube voltages of > 10 kV (relative excitation efficiency of > 0.4). Above 30 kV tube voltage, they show decreases or minimal increases in excitation as voltage increases (Fig. 22.2).

There is enhanced excitation of some heavier elements using the Mo anode tube at 15 kV (e.g. Cu, Ga, As, W and Hg all show relative efficiencies > 2.5). Here, the bremsstrahlung extends to energies at which electrons are ejected from the K energy levels of Cu (9.0 keV), Ga (10.4 keV) and As (11.9 keV) and the L levels of W at 10.2 – 12.1 keV and Hg at 12.3 – 14.8 keV (all energies from Bearden and Burr 1967).

There is little variation in relative excitation efficiency of elements for Mo anode tube voltages above 20 kV, except for elements from Br to Zr. Each of these shows increased excitation as voltages are increased to 50 kV. Higher voltages shift the bremsstrahlung towards higher energies, increasing the radiation available with sufficient energy to eject K level electrons from heavier elements. For Br to Zr the photon energy required is 13.5 – 18.0 keV (Bearden and Burr 1967). Elements heavier than Zr are detected using their L lines, the result of electron ejection from lower energy L shells, the efficiency of which is not enhanced by higher tube voltage. A tube voltage of > 30 kV provides the best overall element excitation across the full detectable range when using Mo tubes.

## *Tube Current*

Although element peak areas are not truly linearly related to tube current, they can be approximated to a linear relationship (Fig. 22.5).

An alternative approach is to divide by a detected quantity not sensitive to variations in individual elements, such as the coherent scatter of the anode characteristic fluorescence lines. This is effective for the Cr anode tube: relative excitation efficiencies after normalisation are close to unity across the current range (Fig. 22.6). The exception is Ca, for which relative excitation is elevated at low current settings

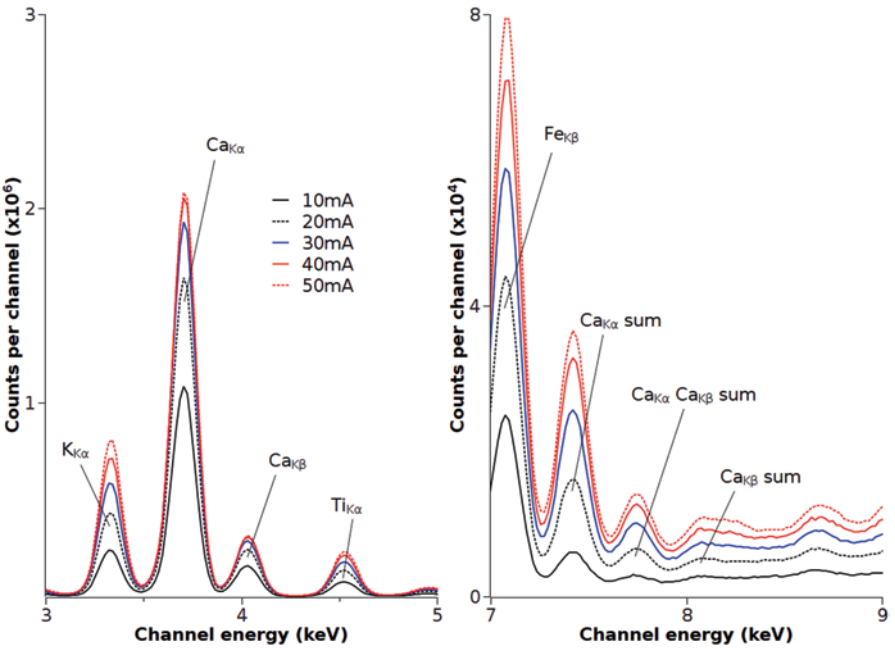


**Fig. 22.15** Sections of the same spectrum from a geochemical reference sample (MAG-1), collected using the Cr anode tube. *Left*: the part of the energy spectrum containing the Ca Kα and Kβ peaks; *Right*: part of the spectrum containing sums of these peaks. As tube current is increased, the size of Ca sum peaks increases but the main calcium peaks show smaller increases with higher currents—for the Ca Kα and Kβ peaks there is little distinguishable difference in peak size between scans using 40 and 50 mA tube current

(10 mA) and reduced at higher current settings (50 mA). Spectra from scans using a Cr anode tube show that Ca sum peaks are visible and increase in magnitude with increasing current (Fig. 22.15). For scans with current settings > 30 mA the main Ca K peaks (used to determine calcium peak areas) show smaller increases with current. As reported Ca peak area increases more slowly than current, the relative excitation efficiency is lower for higher currents. This also explains the elevated counts for Co and Cu seen at 50 mA. The Ca sum peaks at 7.69 keV and 8.02 keV are adjacent to the Co (Kβ at 7.65 keV) and Cu (Kα at 8.03 – 8.05 keV) peaks and hence may be falsely attributed to these elements. Similar effects are not seen when using the Mo tube, as Ca is less efficiently excited.

Normalising against the Mo coherent scatter peak when using a Mo anode tube does not effectively eliminate variations due to differing current settings (Fig. 22.6). The result resembles normalisation against current (Fig. 22.4). Whilst the Cr coherent scatter peaks, centred on 5.41 keV and 5.95 keV, occur entirely within the range of energies (approximately 0 – 18.6 keV) detected by the Itrax core scanner, the Mo coherent scatter peaks locate at 17.48 keV, 17.37 keV and 19.61 keV. The highest energy of these (the Kβ peak at 19.61 keV), is outside the range of energies detected and so coherent scatter is measured using only the Kα peaks. These are adjacent to

the often larger incoherent scatter peak and so lead to difficulties determining the extent of the peaks and background levels.

## *Use of Protective XRF Films*

XRF films reduce X-ray transmission, but are normally considered essential to reduce water loss and so maintain a core in good condition. X-ray attentuation is material dependent, so a film of one type of material may cause less attenuation than a thinner film of different composition.

While thinner films are generally preferred for minimising attenuation, thinner films may be more liable to folding and more difficult to satisfactorily apply to the cut core surface. Folds may increase transmission paths through the film and hence further increase attenuation of fluorescent X-rays. Thicker films are likely to be easier to handle and apply smoothly.

## *Surface Slope Effects*

To understand the effects of surface slope, it is necessary to consider the geometry of the Itrax core scanner. Starting from the approximation that all fluorescence comes from the surface, or very near the surface (Fig. 22.16a), the effective width

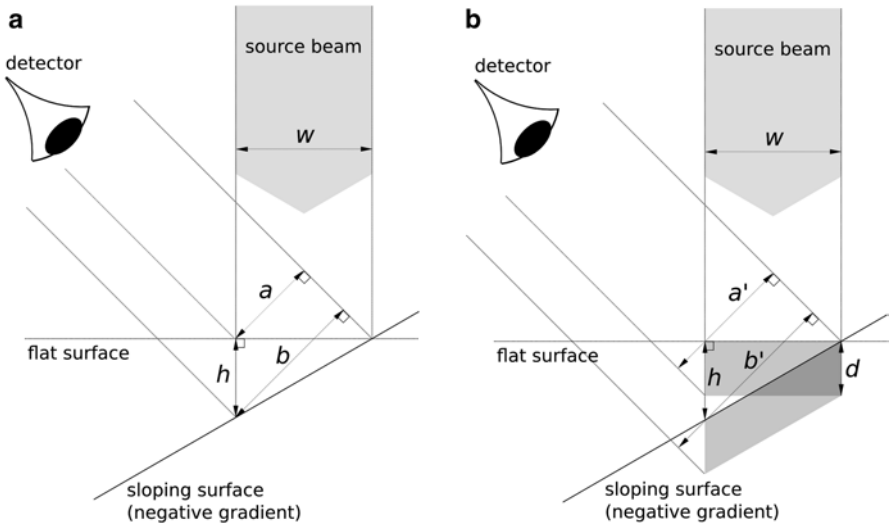


**Fig. 22.16** Schematic view of ITRAX XRF path geometry. The incoming beam is vertical of width w. **a** The effective width of the irradiated area, viewed from the detector at an angle of 45°, depends on the gradient of the sediment surface (compare dimensions **a** and **b**). **b** The relative sizes of effective irradiated surface, *a* and *b*, change with penetration depth, *d*

of the irradiated area on the sample surface, as seen by the detector, is given by $b$, which depends on the sample gradient, $\gamma = h/W$.

The length $b$ for a sloping surface is given by:

$$b = \frac{\sin\left(\frac{\pi}{4} + \gamma\right)}{\cos(\gamma)} W \tag{22.2}$$

Whereas, for a flat surface, $a$ is given by:

$$a = \sin\left(\frac{\pi}{4}\right) W \tag{22.3}$$

If $P_{slope}$, the peak area from a sloping surface of gradient $\gamma$ is related to the peak area, $P_{flat}$, by $P_{slope}/P_{flat} = b/a$, it follows that:

$$P_{slope} = \frac{\sin\left(\frac{\pi}{4} + \gamma\right)}{\cos(\gamma)\sin\left(\frac{\pi}{4}\right)} (P_{flat}) \tag{22.4}$$

Applying this relationship to data from Fig. 22.8 shows a good fit between the experimental data and the model, except the model overestimates the effect of surface slope, particularly for heavier elements (Fig. 22.17).

This disagreement may be explained by considering the effect of X-ray penetration into the sample (Fig. 22.16b). If fluorescent X-rays are detected from a depth $d$, then the difference $(b - a)$ between the effective width of irradiated areas seen from the detector remains constant while both $a$ and $b$ become larger as $d$ increases. Therefore the effect of surface slope becomes less significant.

Despite its limitations, the simple model presented above in Eq. 22.4 can eliminate most of the effects of surface slope when scanning samples with an uneven surface. Refining the model requires $d$ to be known for each element, which is dependent on an estimate of the sample matrix.

## *Effects of Bulk Grain-Size*

The dependence of Itrax element counts on bulk grain-size is significant in samples showing textural variation. A sample containing one third silicon carbide grains of diameter ~1 mm was indistinguishable, within the uncertainty in the data, from a sample containing no silicon carbide grains. The dependence may be due to fine grains smeared across coarser grains, burying them below the surface and prevent-

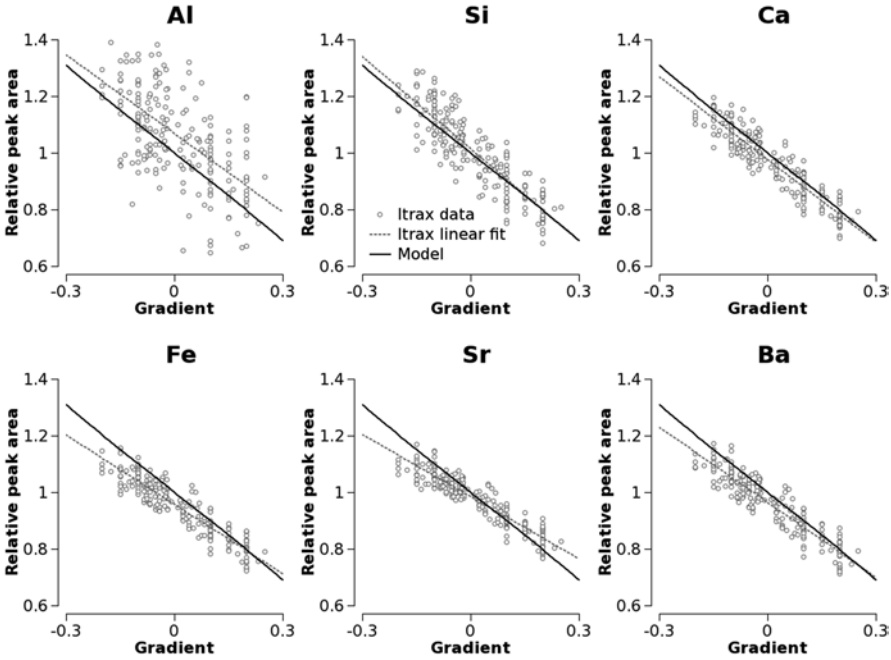


**Fig. 22.17** Variation of Itrax peak areas with gradient of the sample surface, showing recorded Itrax data, linear regression lines for those data and lines representing the modelled variation from Eq. 22.4

ing their detection. The scan was repeated with the samples cut to expose larger grains, but no changes in results were observed.

Awareness of this effect is necessary when dealing with poorly sorted samples. For well-sorted sediments, or those composed entirely of coarser grains, the grain-size effects are likely to be much less. Isolating effects of grain-size on XRF peak areas in sediment samples is complicated by the relationship between grain-size and mineralogy. Grain-size mixtures will depend on sediment sources and depositional mechanisms and grains of differing size may have differing elemental composition.

## *Effects of Water*

The effect of water content on Itrax peak areas reflects dilution; hence Itrax peak areas are proportional to wet rather than dry element concentrations. Such effects may be removed from data either by taking multiple subsamples and drying to determine water content, or by using the ratio of incoherently scattered to coherently scattered tube anode characteristic radiation (the two are related—see Fig. 22.11). As other factors (such as mean atomic number of the sample) can also have an effect on this ratio, a few subsamples should be taken and their water content checked by drying.

## *Reproducibility and Scanning Time*

That variation between peak areas for multiple scans of the same sample is greater than expected may necessitate users to more carefully consider the significance of apparent deviations in peak areas along a sample and perform replicate scans to obtain uncertainty estimates. In some cases, there is an apparent correlation between the square root of recorded element counts and standard deviation in those counts. However, even in these cases, recorded standard deviations are much higher than the square root of counts predicted by Poisson statistics (typically 2–3 times higher and in some cases an order of magnitude greater). While the lake sediment may desiccate between scans, introducing variability, the geochemical reference samples and obsidian are stable so unexpectedly high levels of variation between scans cannot be attributed to changes in sample condition.

### Subtraction of Background Counts

Counts reported by the Itrax operating software are not the full sum of counts in the detector channels, but have a background count level subtracted. However, the background is much smaller than the peak for most of the elements, so uncertainty in reported peaks would still be of the same order of magnitude as uncertainty in full peaks.

### Reproducibility of Raw Spectra

Raw spectra collected from the same position over ten scans of the geochemical reference samples appear to show that the square root of the mean counts provides a reasonable approximation of the standard deviation in counts, when considered over the whole spectrum (Fig. 22.18). However, the standard deviation, at $1.07 \pm 0.01$ times the square root of the mean counts, is slightly higher than expected.

Variation between peaks in individual spectra is caused not only by random variation in channel values (Fig. 22.19). Here the Fe Kα peak narrows and shifts towards lower channels in one spectrum compared to the other (apparent on the higher channel side of the peak, Fig. 22.19). This shift may introduce significant count changes in a single channel. The Itrax spectral analysis software does not report raw counts per channel, but fits a modelled spectrum to the raw spectrum by adjusting the background, channel energy width, spectrum energy offset and peak shapes. This enables differences in detector response and shifts of peaks to higher or lower channels to be partly compensated for, but means that results are no longer directly dependent on counting of photons.

Considering the spectrum channel by channel, if channel counts obeyed Poisson statistics then dividing the standard deviation of counts in each channel by the square root of mean counts for that channel ($\sigma/\text{counts}^{1/2}$) should result in values consistently close to unity. However there are distinct peaks in $\sigma/\text{counts}^{1/2}$ that align with peaks

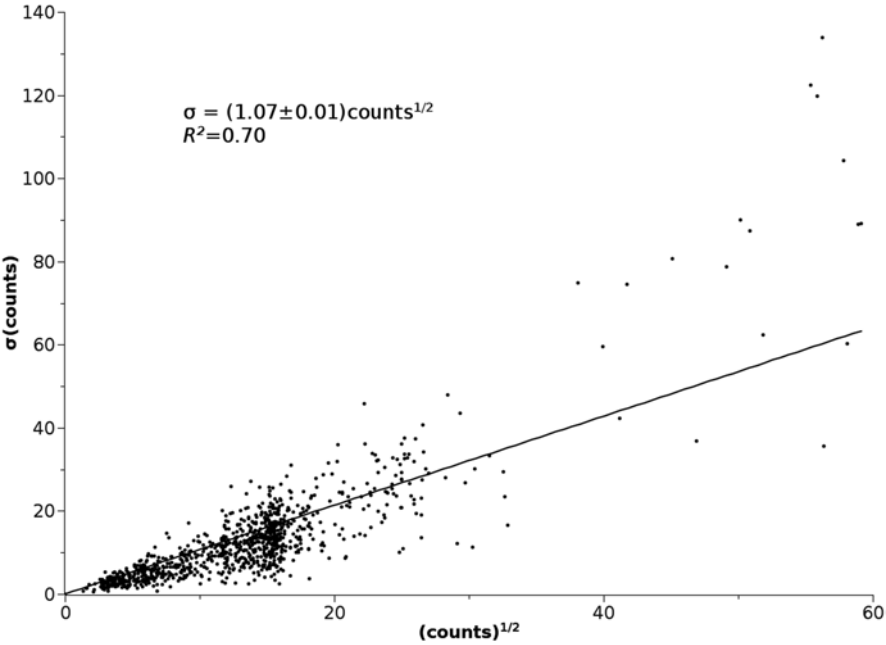


**Fig. 22.18** Comparison of standard deviation, $\sigma$, in channel counts for each detector channel over ten scans of a set of geochemical reference samples with the square root of the mean value of the channel counts over ten scans. Poisson statistics suggest the two quantities should be equal. $R^2$ gives the correlation coefficient between the two quantities

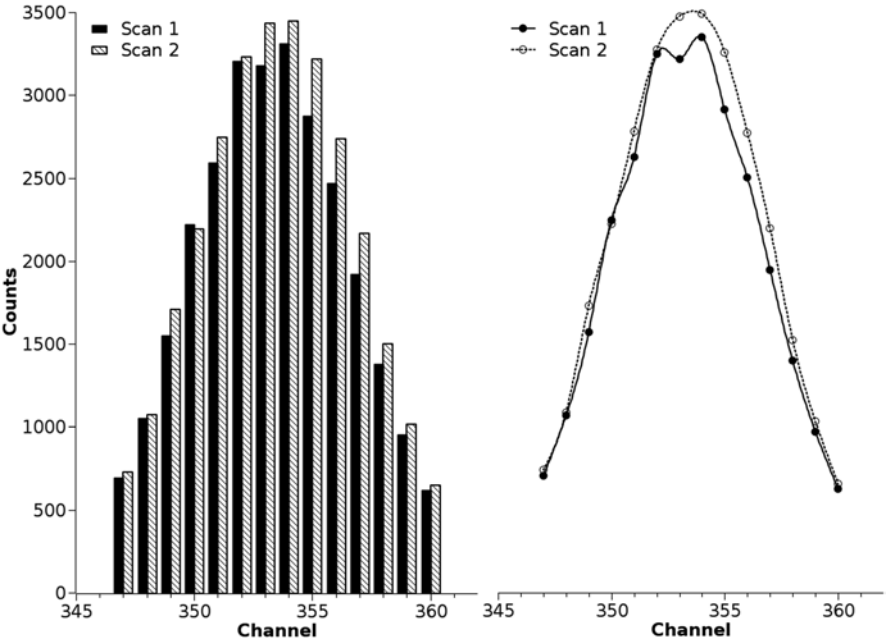


**Fig. 22.19** Comparison of channel counts within the main Fe Kα peak for two spectra (from geochemical reference material JCh-1). *Left*: counts per channel; *right*: the same discrete data, joined with lines to illustrate the difference in position and width of peaks

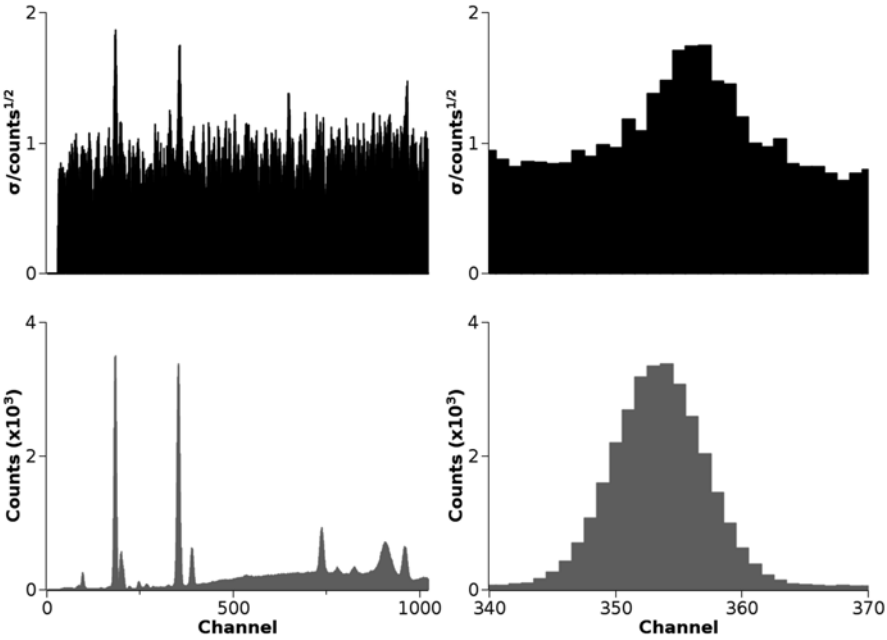


**Fig. 22.20** *Left*: comparison of (*bottom*) mean channel counts with (*top*) standard deviation, σ, divided by mean counts for geochemical reference material JCh-1. Maxima in σ/counts1/2 are found adjacent to peaks in the spectra. *Right*: an extract from the same data showing the Fe Kα peak (*bottom*) and the corresponding peak in σ/counts$^{1/2}$ (*top*)

in the raw channel spectrum (Fig. 22.20). Focusing on the Fe Kα peak shows the peak in σ/counts$^{1/2}$ is offset slightly from the Fe Kα channel peak, towards the high-channel side. This corresponds to the apparent shift in the Fe Kα peak illustrated in Fig. 22.19. If there is a shift in peak position and width then there will be larger variations between channel counts at the edge of the peak where the shift occurs.

## Count Times

While data precision from a given Itrax scan is unpredictable, the effect of varying count time is not. A longer count time enables more accurate recording of fluorescent photons and channel counts rise linearly with counting. Therefore, uncertainty varies inversely with the square root of the count time—i.e. if count time is quadrupled, uncertainty is halved. A count time of 30 s gives an overall uncertainty (one standard deviation) for all elements of 7 % for the geochemical reference samples. The uncertainty for many better-detected elements such as Fe is much lower (see Table 22.1 for values for a selection of elements). A count time of 30 s will often be satisfactory if uncertainty (one standard deviation) of 5 % or better is acceptable. For low element concentrations or for acquisition of valid data for poorly detected elements, such as Al, a longer counting time of up to 100 s or more may be desirable.

**Table 22.1** Standard deviation, σ in reported element peak areas over ten scans of marine sediment sample CD166-19 Section 2. A Mo anode tube and a 30 s count time were used and values reported as a percentage of the mean peak area over the ten scans and quoted to two significant figures

| Element | Si | S | K | Ca | Ti | Mn | Fe | Zn | Br | Sr | Zr | Pb |
|---|---|---|---|---|---|---|---|---|---|---|---|---|
| $\sigma$/mean counts (%) | 13 | 50 | 3.7 | 2.3 | 2.6 | 4.4 | 1.0 | 21 | 8.5 | 1.4 | 11 | 37 |

## Conclusions and Recommendations

### *Optimisation of Itrax Scanning Parameters*

#### Tube, Voltage and Current

- For accurate comparison between data sets, the same tube voltage and current settings should be used. If samples are run at different times then changes in tube output could have a potentially significant impact on counts. Using count-rate may suppress this effect to some degree but not entirely as the tube spectral shape will vary with age to some degree. A sequence of cores should be run at the same time ideally to avoid tube output effects.
- A Cr anode tube is preferred when elements lighter than Cr ($Z < 24$) are of primary interest. The Mo or Cr anode tubes are best for elements heavier than Fe ($Z > 26$) and for most studies provides data on a good range of elements at normal operating currents and voltages.
- If Mn ($Z = 25$) is of interest, then a Cr anode tube should not be used as there will be difficulties in resolving the Cr scatter peak and Mn peaks in the spectrum.
- A tube voltage of 30 kV is suitable for exciting a wide range of elements with both the Cr and Mo anode tubes. Higher voltages may be needed where the heaviest elements detected using K line emissions are of interest.
- If it is necessary to use different currents in different scans, the effect of current changes can be minimised by normalising peak areas against coherent scatter of the tube anode characteristic radiation (this is particularly effective for scans using the Cr anode tube).

#### Protective XRF Films

- XRF films reduce the quantity of fluorescent photons detected, particularly for elements lighter than Ca ($Z < 20$) (for heavier elements, films have little effect).
- Both film thickness and material affect fluorescent X-ray attenuation. For example, 6 μm thick polypropylene film reduces peak areas less than 3μm thick Mylar film. For the range of films tested, 1.5 μm polypropylene caused the lowest attenuation in element counts.

**Surface Slopes**

- Surface slopes have a clear effect on detected counts, but are not likely to be significant for most core samples.
- The effect of slope can be modelled, and mostly eliminated.

**Bulk Grain-Size**

- Grain-size is commonly associated with mineralogy and so may show a close relation to elemental composition. The presence of a mixture of grain-sizes within a sample, such as quartz-rich sandy inclusions within a clay interval can significantly change peak areas.
- Smoothing of fine grains over larger ones may effectively mask them from detection, leading to erroneously low peak areas recorded for elements present in the large grains (and conversely high peak areas for materials in the small grains)

**Water Content**

- Water has a diluting effect on recorded element counts.
- Correction of Itrax data for these effects is straight-forward if water content is known.
- Water content may be determined from the ratio of incoherent to coherent scatter of the tube anode characteristic radiation (but this relationship should be verified for each sample).

**Reproducibility and XRF Count Time**

- Uncertainties in Itrax data are not easily quantified, except by repetition of scans to determine count standard deviations.
- There is greater uncertainty in the data than suggested by the conventional view that standard deviation is equal to the square root of recorded counts.
- Depending on element concentrations, a typical spectrum with a counting time of 30 s can still provide data in which the uncertainty (one standard deviation) is 5 % or less for many elements.

## *Issues to Consider for Particular Sample Types*

The following observations and recommendations can be made on the effects on particular sample types:

- Fresh peat cores will generally have highly porous, irregular surfaces and a high water and organic content. Elements detectable by the Itrax core scanner are likely to be highly diluted and therefore good data will require long count times and normalisation is essential. Uneven core surfaces will cause reduced peak areas in lower parts of the surface that are not easily tracked by the Itrax detector and there may be effects due to variations in slope. Similarly, dried peat cores are equally challenging to measure because of the high scattered background caused by the low mean atomic number.
- Well-sorted terrigenous sediments should have lower water content and a relatively flat surface. Intervals of coarser grain sizes may show increased count variability and a drop in peak areas if some parts of the surface are not closely tracked by the detector.
- Pelagic oozes may have high water content and present a rough or porous surface, increasing the variability in scan results and potentially reducing peak areas. Surface slopes may influence recorded peak areas.
- Clays should usually present a smooth surface and need little special consideration. However clay-rich intervals may be especially prone to desiccation and cracking which may degrade the data obtained.
- Turbidites may show coarser-grained graded bases. The elements present in the coarser grains may have smaller than expected peak areas. Where turbidite layers are well graded, the surface presented to the Itrax core scanner at any point should have a locally close to uniform grain-size.
- Soft, gassy lake sediments may have high water content and a puckered surface due to bubbles and voids. Surface slope effects may be important and longer counting times may be needed as detectable elements are diluted by water content and have a high scattered background caused by the low mean atomic number.

## References

Bearden JA, Burr AF (1967) Reevaluation of X-ray atomic energy levels. Rev Mod Phys 39:125–142

Criss JW (1976) Particle size and composition effects in X-ray fluorescence analysis of pollution samples. Anal Chem 48:179–186

Croudace I, Rindby A, Rothwell R (2006) ITRAX: description and evaluation of a new multi-function X-ray core scanner. In: Rothwell R (ed) New techniques in sediment core analysis. Special Publications, The Geological Society of London, pp 51–63

Davies S (1997) Survey of sample support films and their effect on light element radiation. X-ray Spectrom 26:111–114

Finkelshtein A, Brjansky N (2009) Estimating particle size effects in X-ray fluorescence spectrometry. Nucl Instrum Methods Phys Res Sect B: Beam Interact Mater Atoms 267:2437–2439

Ge L, Lai W, Lin Y (2005) Influence of and correction for moisture in rocks soils and sediments on in situ XRF analysis. X-ray Spectrom 34:28–34

Gupta S, Deep K, Jain L, Ansari M, Mittal V K, Mittal R (2010) X-ray fluorescence (XRF) set-up with a low power X-ray tube. Appl Radiat Isot 68:1922–1927

Jarvis S (2012) Optimising, understanding and quantifying Itrax XRF data. Unpublished PhD thesis University of Southanpton, UK 237 pp

Kido Y, Koshikawa T, Tada R (2006) Rapid and quantitative major element analysis method for wet fine-grained sediments using an XRF microscanner. Mar Geol 229:209–225

Löwemark L, Chen H-F, Yang T-N, Kylander M, Yu E-F, Hsu Y-W, Lee T-Q, Song S-R, Jarvis S (2011) Normalizing XRF-scanner data: a cautionary note on the interpretation of high-resolution records from organic-rich lakes. J Asian Earth Sci 40:1250–1256

Richter T, Van der Gaast S, Koster B, Vaars A, Gieles R, De Stigter H, De Haas H, Van Weering T (2006) The Avaatech XRF core scanner: technical description and applications to NE Atlantic sediments. In: Rothwell R (ed) New techniques in sediment core analysis. Special Publications, The Geological Society of London, pp 39–50

Slattery M, Burt T (1997) Particle size characteristics of suspended sediment in hillslope runoff and stream flow. Earth Surf Process Landf 22:705–719

Tavora L, Morton E, Gilboy, W (2001) Enhancing the ratio of fluorescence to bremsstrahlung radiation in X-ray tube spectra. Appl Radiat Isot 54:59–72

Tjallingii R, Röhl U, Kölling M, Bickert T (2007) Influence of the water content on X-ray fluorescence core- scanning measurements in soft marine sediments. Geochem Geophy Geosyst 8:1–12

Voglis P, Rindby A (1995) Quantitative methods for the application of the scanning X-ray analytical microprobe (SXRAM). J Trace Microprobe Tech 13:177–193

Weltje G, Tjallingii R (2008) Calibration of XRF core scanners for quantitative geochemical logging of sediment cores: theory and application. Earth Planet Sci Lett 274:423–438

Wynn R, Cronin B (2005) RRS "Charles Darwin" Cruise CD166, 29 Oct–22 Nov (2004) Sedimentary processes and deposits in the Agadir Basin and Gulf of Cadiz. Southampton Oceanography Centre Cruise Report, 59, 13

Ziegler M, Jilbert T, de Lange G, Lourens L, Reichart G (2008) Bromine counts from XRF scanning as an estimate of the marine organic carbon content of sediment cores. Geochem Geophys Geosyst 9:6

# Chapter 23
# UV-Spectral Luminescence Scanning: Technical Updates and Calibration Developments

**Craig A. Grove, Alberto Rodriguez-Ramirez, Gila Merschel, Rik Tjallingii, Jens Zinke, Adriano Macia and Geert-Jan A. Brummer**

**Abstract** Spectral luminescence scanning (SLS) is a novel technique that uses a UV light source and line-scan camera to generate photoluminescence images of carbonate materials, such as corals. The camera in the Avaatech XRF core scanner records luminescence signals in three spectral domains of visual light, providing Red, Green and Blue (RGB) luminescence intensity data. Spectral luminescence Green/Blue ratios (G/B) of coral skeletons have previously been employed as a proxy to reconstruct river runoff. Prior G/B reconstructions have been formulated based on indirect G/B-runoff relationships (e.g. modelled discharge), as coral cores were drilled from regions where reliable long-term instrumental data were lacking,

C. A. Grove (✉) · G. Merschel · G.-J. A. Brummer
Department of Marine Geology, NIOZ Royal Netherlands Institute for Sea Research, Den Burg, P.O. Box 59, 1790 AB Texel, The Netherlands
e-mail: c.a.grove@umcg.nl

A. Rodriguez-Ramirez
School of Earth Sciences, The University of Queensland, Steele Building (#3), Staff House Road, St. Lucia, Brisbane, QLD 4072, Australia

G. Merschel
Faculty of Earth and Life Sciences, Vrije Universiteit Amsterdam, De Boelelaan 1105, 1081 HV Amsterdam, The Netherlands

School of Engineering and Science, Jacobs University Bremen, Campus Ring 1, 28759 Bremen, Germany

R. Tjallingii
Section 5.2 Climate Dynamics and Landscape Evolution, GFZ-German Research Centre for Geosciences, Telegrafenberg, 14473 Potsdam, Germany

J. Zinke
School of Earth and Environment, The University of Western Australia and the UWA Oceans Institute, 35 Stirling Highway, Crawley, WA 6009, Australia

Australia and the Australian Institute of Marine Science, 39 Fairway, Nedlands, WA 6009, Australia

A. Macia
Departamento de Ciências Biológicas, Faculdade de Ciências, Universidade Eduardo Mondlane, C.P. 257, Maputo, Moçambique



I. W. Croudace, R. G. Rothwell (eds.), *Micro-XRF Studies of Sediment Cores*,
Developments in Paleoenvironmental Research 17, DOI 10.1007/978-94-017-9849-5_23

i.e. Madagascar. Here, we provide additional evidence that G/B is directly related to runoff by comparing instrumental data with four coral cores from the Keppel Islands, Australia; a region where instrumental data are both reliable and plentiful. A four coral core G/B-composite record was found to correlate significantly with precipitation, stream height level and stream discharge rate over a 53 year period. The strongest G/B relationship observed was with stream discharge rate, which explained 37 % of the total interannual variance of G/B.

Modifications to the Avaatech XRF core scanner are ongoing. Here, we describe the use of a new commercially available light cut off filter (Schott GG 455 nm long pass filter) to block reflected Blue light from the UV light source, and compare it with the previously employed 450 nm filter. Conversion of the 450 nm filtered data to 455 nm filtered data was carried out by a linear correction function based on major axis regression, providing statistically similar G/B data for monthly resolved coral records, as well as offering greater insights into the nature and cause of skeletal luminescence. In addition to modifications to the scanner, developments in the sample preparation are described here. We show that when treating coral cores with NaOCl to remove organic contaminants, soaking once or twice for 24 h can have different effects on absolute G/B values. Corals must therefore be treated consistently to ensure accurate cross core comparisons. A single 24 h treatment is sufficient in most cases; however, when resistant contaminants remain a second 24 h treatment improves the signal. Absolute values can therefore not be compared when cores are cleaned using different treatment methods.

**Keywords** Cleaning · Coral · Great Barrier Reef · Luminescence · Skeleton · SLS · UV-light

## Introduction

Spectral Luminescence Scanning (SLS) utilises a high-resolution line-scan camera to separate the intensity of carbonate luminescence emissions into three spectral domains: Red, Green, and Blue (RGB) (Grove et al. 2010). The Avaatech XRF core scanner is equipped with a CCD line-scan camera and two long-wave UV-A tubes centred in the 350–450 nm range for SLS (Grove et al. 2010). High quality normalised photoluminescence images are generated, which are composed of multiple RGB pixels. Quantitative photoluminescence data are produced with a linear resolution of 71.4 µm (pixel length); compatible for coupling with other high resolution generated data, such as XRF and LA-ICP-MS (Grove et al. 2010, 2012, 2013; Maina et al. 2012). The most significant application of the SLS technique thus far has involved the down-core analysis of tropical coral cores (Grove et al. 2010, 2012, 2013; Maina et al. 2012).

## *Luminescence in Coral Skeletons*

The down-core variability in coral skeletal luminescent properties is related to temporal changes in river discharge (Isdale 1984; Boto and Isdale 1985; Lough et al. 2002; Grove et al. 2010, 2012, 2013; Lough 2011a; Maina et al. 2012). Changing luminescence intensities were originally thought to be caused by the skeletal incorporation of soil-derived luminescent organic compounds ("humic acids") introduced by seasonal changes in river runoff (Isdale 1984; Susic and Boto 1989; Matthews et al. 1996; Isdale et al. 1998; Wild et al. 2000). Later, changing coral skeletal density and architecture were proposed as the cause since massive coral skeletons are composed of luminescent aragonite (MacRae and Wilson 2008), and banded luminescence was also observed in corals far from terrestrial inputs (Barnes and Taylor 2001, 2005). Grove et al. (2010) found that both humic acids and skeletal density/architecture were likely responsible for the changing luminescent intensities observed in corals, and that deconvolution of the two fractions was required to reconstruct river runoff. This was achieved through the SLS technique (Grove et al. 2010).

As the luminescent emission wave lengths of humic acids (G) are slightly longer than aragonite (B), taking the Green/Blue (G/B) ratio identifies the amount of humic acids locked within the coral relative to the skeletal density (Grove et al. 2010). SLS resolves many density/architectural effects associated with luminescence intensities, such as declining trends in intensity with coral age (Jones et al. 2009; Lough 2011a, b). The resulting spectral luminescence ratio (Green/Blue; G/B) is therefore a far more robust climate proxy than the previously employed luminescence intensities, of which values have likely been affected by other skeletal properties (Grove et al. 2010; Lough 2011b).

## *The UV Cut-off Filter*

Measuring luminescence in carbonates involves replacing the standard visual light bulbs of the Avaatech XRF core scanner with two long-wave UV-A tubes centred in the 350–450 nm range (Grove et al. 2010). In order to achieve quantitative RGB luminescence intensities, the camera and electronic settings are adjusted to maximise light intensity without saturating the recorded signal. A 450 nm light cut-off filter has previously been employed beneath the camera lens using a fixing bracket, which eliminates the direct reflections from the UV light source itself. Therefore, only carbonate associated luminescence intensities in the blue domain are recorded by the camera (Grove et al. 2010, 2012, 2013; Maina et al. 2012). In this study, we provide details of a new commercially available filter (Schott GG 455 nm long pass filter) that can be screwed directly onto the camera lens, avoiding the use of any metal bracket holding the filter in place. We compare G/B values, using both filters, of three coral cores from different environments to convert previously generated data for inter-coral core comparison. A full description of the technical setup of the SLS technique can be found in Grove et al. (2010).

## *Preparation of Coral Cores Before SLS*

As SLS provides high quality photoluminescence images, establishing a number of physical properties by visual assessment can be highly beneficial when deciding on an optimal sampling track. As well as identifying the growth axis and physical discrepancies, down-core changes in skeletal composition unrelated to humic acids or aragonite can also be observed (Grove et al. 2010; Nagtegaal et al. 2012). Primarily, organic contaminants appear responsible for quenching the luminescence signal of coral cores, which are easily visually identified as dark stains or patches when placed under UV light,. Such (organic) contaminants can have a detrimental effect on both luminescence and geochemical data (Nagtegaal et al. 2012).

Using SLS generated photoluminescence images, Nagtegaal et al. (2012) addressed the dark patchy areas associated with (organic) contaminants, and assessed their removal through NaOCl oxidation. In some cases, contaminants within the coral skeleton still remained after exposure to NaOCl for 24 h (Nagtegaal et al. 2012). Such persistent interferences can often be avoided by drawing transects on the image that do not overlap with the affected skeletal areas as SLS generated photoluminescence images essentially act as an optical map. When this is not possible and contaminants are too many, a more vigorous oxidative treatment is required to remove these interferences (Nagtegaal et al. 2012). For this study we investigate the effects on G/B when treating corals containing persistent interferences with an additional cleaning step, exposing a long coral core to NaOCl for a further 24 h ($2 \times 24$ h).

## *Interpretation of Spectral Luminescence G/B Ratios*

Much progress in river runoff reconstructions has undoubtedly been made through the application of SLS (Grove et al. 2010, 2012, 2013; Maina et al. 2012; Nagtegaal et al. 2012). However, until now there has been no thorough calibration of the G/B spectral luminescence ratio, as the corals tested thus far were sampled in remote locations where weather station data are scarce, i.e. Madagascar (Dewar and Wallis 1999; Dewar and Richard 2007), and satellite derived rainfall data are often unreliable (Quartly et al. 2007). Relationships of G/B with runoff have therefore been formulated on comparisons with other runoff proxies (Grove et al. 2010, 2012), modelled river discharge (Grove et al. 2012; Maina et al. 2012), gridded data (Grove et al. 2013) and/or weather station data located hundreds of kilometres from the study site (Grove et al. 2010, 2013). All evidence suggests that G/B is linked to runoff and in turn precipitation. Nevertheless, a full assessment of the G/B spectral luminescence ratio with instrumental data would serve a purpose to increase confidence in the proxy as links thus far have been qualitative only.

In this study, we assess whether coral skeletal G/B variability is linked to precipitation, river discharge and river water level changes. We test this by analysing four coral cores drilled from the Keppel Islands, Great Barrier Reef. As instrumental

data in this region are plentiful, it is possible to assess long-term relationships on annual time-scales. Further, we will also assess the relationship of each of the instrumental datasets (i.e. precipitation, river discharge and river level data) with G/B and suggest which parameter is primarily responsible for the observed variability in coral skeletal G/B. The results presented here are a part of a wider study which fully documents climatic controls of Great Barrier Reef runoff using a number of coral cores, including the four cores described here (Rodriguez-Ramirez et al. 2014).

## Materials and Methods

Using a number of different coral cores from separate locations we (1) test the recorded spectral luminescence signal using a new 455 nm cut-off light filter, (2) assess the impact of a secondary cleaning step on luminescence and (3) provide an assessment of G/B with instrumental data. For each of the three tests, different corals from different locations are used and the sample preparation and/or the scanning setup vary depending on the test. These are highlighted within the text when necessary. Specific coral cores were chosen for individual tests because of (1) the availability of material from different environments, (2) comparisons to previously published core data and (3) proximity with instrumental data, respectively.

### *Sample Locations*

#### UV-Filter Test

The performance of two UV-filters was tested on three corals from Mozambique taken as part of the CLIMATCH program. In October 2011, three coral cores were drilled from *Porites* sp. colonies along the coastline of Mozambique (Fig. 23.1). Coral core BV4 (S 26°01,410; E 032°53,931) dates back to 1966 and was sampled in Maputo Bay (Barreira Vermelha at Inhaca Island) (Fig. 23.1). This location is directly influenced by the Maputo River, which drainage area covers approximately 30,000 km$^2$ and discharges into the bay approximately 25 km south of the coral (Table 23.1). Coral core PEM1 (S 12°58,118; E 040°32,591) was drilled 3 km from the Pemba Bay inlet and covers the time period 1887–2011 (Fig. 23.1; Table 23.1). A number of small rivers discharge into the bay within a distance of 15 km from the sampling location. It is expected that coral PEM1 experiences seasonal runoff conditions, yet not to the same scale as coral BV4 (Maputo River). Coral core QUI6 (S 10°44,112; E 040°32,646) was sampled in the bay 'Baia de Tunge' (Quirimbas Archipelago) and covers the time period 1967–2011 (Fig. 23.1). This location experiences primarily oceanic conditions, however, during periods of high rainfall during the wet season the coral may be influenced by the Rovuma River and/or some smaller rivers draining into the Baia de Tunge. The Rovuma River watershed is

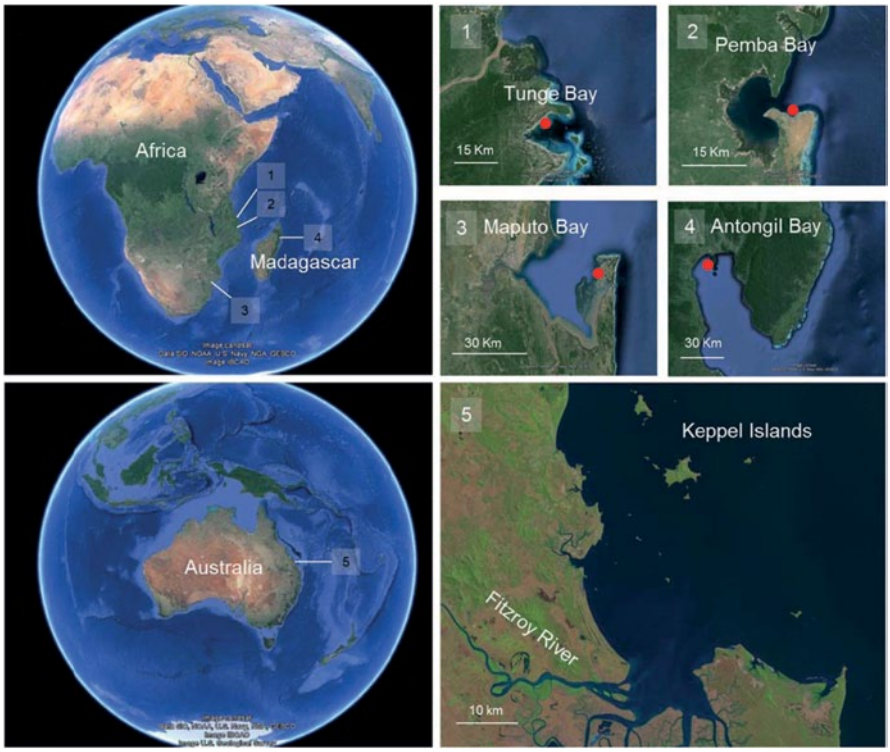


**Fig. 23.1** Map of the sites where coral cores used in this study were drilled. Sites 1–3 represent (1) Tunge Bay, (2) Pemba Bay and (3) Maputo Bay, where corals QUI6, PEM1 and BV4 were drilled, respectively. These corals were used for the filter test. Site 4 represents Antongil Bay, where coral MASB was drilled, and used for the cleaning test. Coral locations are represented by a *red circle* (*filled*). Site 5 represents the Keppel Islands, where corals A–D were drilled and assessed for their G/B relationship with instrumental data from the Fitzroy River catchment area. Additional information about coral core locations can be found in Table 23.1. (Images 1–4 were obtained from Google Earth, and image 5 (satellite image) obtained from http://glovis.usgs.gov/)

approximately 155,000 km$^2$ and disembogues into the Indian Ocean approximately 32 km north of the sampling site. For this study the time period 1990–2011 only was considered (Table 23.1).

## Cleaning Test

The effects of sample cleaning prior to SLS were performed on a coral from Madagascar (Nagtegaal et al. 2012; Grove et al. 2013). Coral core MASB (S 15°30,566; E 49°45,437) was drilled from a *Porites* sp. colony as part of the SINDOCOM program in October 2008 from Antongil Bay, Madagascar, dating back to 1708 (Grove et al. 2013) (Fig. 23.1; Table 23.1). The coral is directly influenced by the

**Table 23.1** Coral core names with GPS co-ordinates, distance to the closest river source and the years used for this study. Coral cores were applied to test the spectral signal using a new 455 nm light cut-off filter (Filter), assess the impact of a secondary cleaning step on luminescence (Cleaning) and provide a assessment of G/B with instrumental data (Instrumental)

| Core name | Location | Distance to river mouth (km) | Coral years (used for this study) | Test |
|---|---|---|---|---|
| PEM1 (Mozambique) | S 12°58.118 E 40°32.591 | 15 | 1990–2011 | Filter |
| QUI6 (Mozambique) | S 10°44.112 E 40°32.646 | 32 | 1990–2011 | Filter |
| BV4 (Mozambique) | S 26°01.410 E 32°53.931 | 25 | 1990–2011 | Filter |
| MASB (Madagascar) | S 15°30.566 E 49°45.437 | 5 | 1709–2007 | Cleaning |
| A (Australia) | S 23°09.027 E 150°58.436 | 42 | 1957–2009 | Instrumental |
| B (Australia) | E 23°05.981 S 150°53.163 | 47 | 1957–2009 | Instrumental |
| C (Australia) | S 23°05.980 E 150°53.169 | 47 | 1957–2009 | Instrumental |
| D (Australia) | S 23°09.300 E 150°54.209 | 41 | 1957–2009 | Instrumental |

Antainambalana River draining into the bay, which is the major river in the region (Grove et al. 2012). The source of the river lies 1450 m above sea level and its watershed covers an estimated 4000 km$^2$. In Antongil Bay, the driest month of the year is October.

### G/B Relationship with Instrumental Data

The relationship between G/B ratios of coral cores, obtained by SLS, and instrumental data was established for four coral records from the Keppel Islands, located in the southern Great Barrier Reef. The four coral cores, A, B, C, and D, were collected from massive *Porites* spp. colonies in July, 2010, from three different locations of the Keppel Islands in the inshore Great Barrier Reef, Australia (S 23°05′-04′ and E 150°54′-53′). All sampling sites were located within 50 km from the mouth of the Fitzroy River, which has a catchment area of 143,000 km$^2$. The Fitzroy River is the major supplier of terrestrial suspended material to this part of the Great Barrier Reef and directly influences all four corals (Furnas 2003; Bostock et al. 2007). Coral cores A, B, C and D date back to 1944, 1921, 1949 and 1956, respectively, of which we only assess the shared period 1957–2009 (Table 23.1). The climate of the Great Barrier Reef is characterised by a winter dry season and a summer wet season (Lough et al. 2002). While the driest month of the year for the region is September, the lowest discharge rate of the Fitzroy occurs in August.

## *Coral Drilling and Preparation*

All coral cores were drilled from massive colonies of *Porites* spp. at depths between 2 and 6 m from different locations. A commercially available pneumatic drill was used to extract 4 cm diameter cores along the central growth axis of the colony. Cores were sectioned lengthwise into 7 mm thick slabs, rinsed several times with demineralised water, blown with compressed air to remove any surficial particles and dried for more than 24 h in a laminar flow hood. All coral slabs were then cleaned with a 1:1 mix of reagent grade sodium hypochlorite (NaOCl, 10–13 % reactive chlorine; Sigma-Aldrich Company) and Milli-Q water for 24 h to remove residual organics that might quench luminescence (Nagtegaal et al. 2012). Coral MASB was cleaned for a further 24 h with a fresh batch of NaOCl to test the effects of a secondary cleaning step. Annual density bands were visualised by X-radiograph-positive prints, and together with photoluminescence imagery, the growth axis of the coral slab was defined as the line perpendicular to the growth bands (Hendy et al. 2003; Grove et al. 2010).

## *Spectral Luminescence Scanning*

SLS was performed on bleached coral slabs using a JAI CV-L105 3 CCD RGB line-scan camera fitted with a Dichroic beam splitter prism (Grove et al. 2010). The camera separates light emission intensities into three spectral ranges; Blue (B), Green (G) and Red (R) (Fig. 23.2). Digital core images were analysed with the Line Scan Software Version 1.6 (Avaatech), providing RGB intensity values for each individual image pixel (pixel resolution is 71 μm). Since the spectral emissions of humic acids are slightly longer than aragonite, spectral G/B ratios reflect the changing humic acid/aragonite ratios within the coral skeleton (Grove et al. 2010).

All corals were scanned using the original 450 nm light cut-off filter fixed below the camera lens (Grove et al. 2010). Corals PEM1, QUI6 and BV4 were scanned again with the new Schott GG 455 nm long pass filter (2 inch square) that was placed directly onto a square threaded filter holder and screwed directly onto the camera lens (Fig. 23.2).

## *Coral Age Models*

Coral chronologies were based on the seasonal cycle of G/B ratios (Hendy et al. 2003; Grove et al. 2010). G/B minima values were assigned the driest month of the year, which varied depending on the region. This created consistent climate-based age models between cores. All years were then interpolated linearly between the driest month anchor points using AnalySeries 2.0 (Paillard et al. 1996). This resulted in a monthly time scale resolution of 12 equidistant data points. Annual averages were calculated by averaging all monthly values starting from the driest month for any given year.

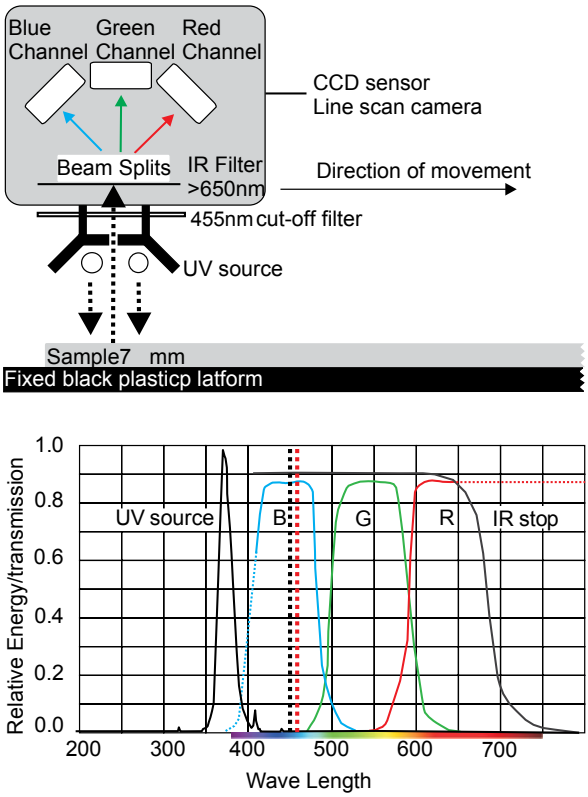


**Fig. 23.2** Schematic diagram of the modified Avaatech core scanner used for spectral luminescence imaging (*upper panel*), and the spectral distribution and sensitivity of the light source and camera sensors (*lower panel*). The UV light source efficiently emits in the range of 315–450 nm. The 450 and 455 nm cut-off filters are marked as *black* and *red dashed lines* on the *left* and *right*, respectively (*lower panel*). The filters remove UV source emissions (reflected light) before splitting into *Red*, *Green* and *Blue* fractions by a dichroic RGB beam splitter. A 650 nm infrared cut-off filter prevents light of greater wavelengths from entering the three separate CCD sensors

For the instrumental-based assessment of G/B, a composite record was constructed using the four cores drilled from the Keppel Islands (Table 23.1). Each of individual 53 year records were first standardised by subtracting the long-term G/B average from the monthly values and then divided by the respective long-term standard deviation. The four cores were then averaged to create one single 53 year composite record. A composite record reduced the intrinsic variation of individual cores (Pfeiffer et al. 2009). The annual values of the composite record were calculated by averaging all monthly G/B values from August to July.

## *Instrumental Data*

River flow data (Megaliters/day) and stream water level (m) were obtained from the Queensland Department of Environment and Resource Management gauging station on the Fitzroy River at The Gap (Station number 13005A) for 1957–2009 (http://watermonitoring.derm.qld.gov.au/host.htm). Monthly values were calculated by taking the sum of daily recorded values, yet, are expressed as daily data. Rainfall (mm) data were obtained from the Queensland Government Bureau of

Meteorology at Pacific Heights (Station number 033077) for 1965–2009 (http://www.bom.gov.au/climate/data). Annual averages of the data were calculated in the same way described for the coral cores (Coral Age Models).

## Results

### *Filter Test*

Three corals from Mozambique were scanned using a 450 nm and a 455 nm light cut-off filter to investigate the effects of different filters on coral G/B values. The resulting G/B monthly time series, covering the period 1990–2011, were subsequently compared and the offset between data determined. Monthly resolved time series were chosen for analyses instead of annual averages, as conversion factors should be applied to monthly data, not annual, to convert data.

The measured G/B ratio using the 450 nm cut-off filter ($G/B_{450\ nm}$) was consistently lower than the measured G/B ratio using the 455 nm cut-off filter ($G/B_{455\ nm}$) (Fig. 23.3). The higher $G/B_{455\ nm}$ values were related to a greater decline in the Blue (B) domain relative to the Green (G). Highly significant correlations were found between the $G/B_{450\ nm}$ and $G/B_{455\ nm}$ records for BV4 ($R^2$=0.896) and Pem1 ($R^2$=0.778), yet were slightly lower for the Qui6 record ($R^2$=0. 652) (Table 23.2). Converting the $G/B_{450\ nm}$ into the $G/B_{455\ nm}$ time series was achieved by application of the linear major axis equation (Fig. 23.3). Each individual record showed different amounts of scatter and offset around the regression line (Fig. 23.3), however, the predicted $G/B^*_{455\ nm}$ values still matched well with the $G/B_{455\ nm}$ results (Fig. 23.4). $G/B^*_{455\ nm}$ values therefore corrected for different filters used, yet not for differences between $G/B_{450\ nm}$ and $G/B_{455\ nm}$ (Fig. 23.4).

### *Cleaning Test*

The annual average G/B values for MASB were calculated for 298 years ($n$ = 298) by averaging the months October to September. Assigning the individual years to MASB after a single 24 h NaOCl treatment was problematic as persistent interferences could not be fully removed, which obscured the seasonal luminescence signal. Once the coral was cleaned once more for 24 h, the individual years appeared more clearly defined, resulting in a more accurate age model. There was a statistically significant relationship observed between annual average G/B values for the singular 24 h NaOCl treatment and the double 24 h NaOCl treatment ($R^2$=0.39; $P$ <0.001; $n$ = 298) (Fig. 23.5). The mean annual average G/B signal increased by 14.3 % relative to the singular 24 h NaOCl treatment after MASB was treated twice for 24 h, (Fig. 23.5). Further, the average standard deviation increased by 26.4 % after the coral was treated twice (Fig. 23.5).

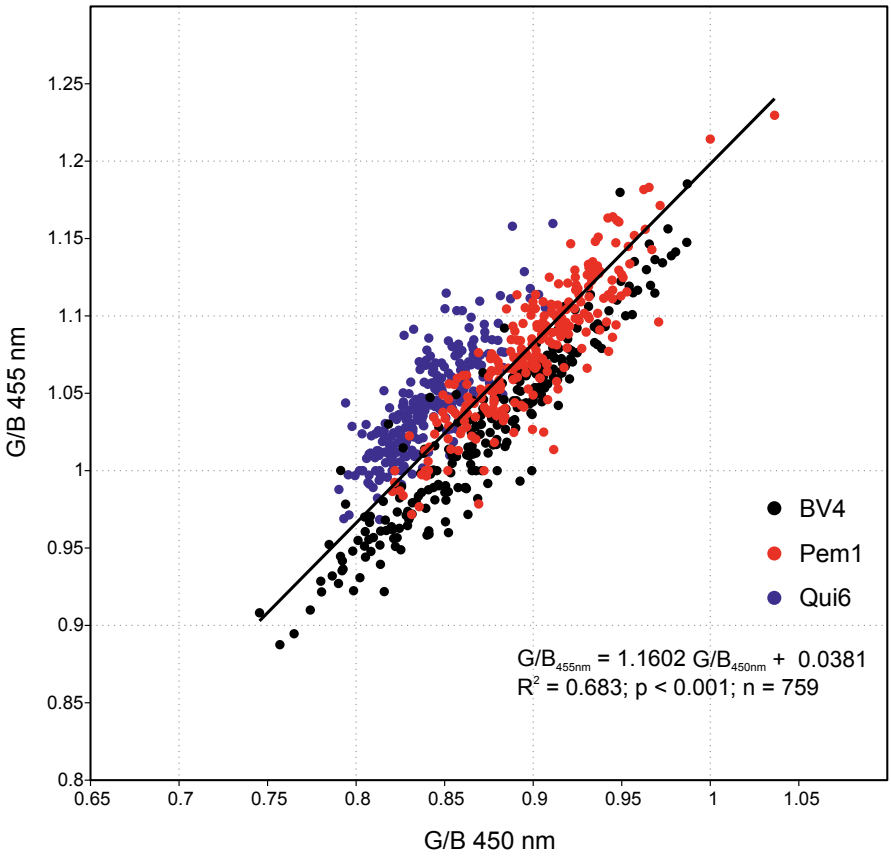


**Fig. 23.3** Linear major axis regression of $G/B_{450\ nm}$ and $G/B_{455\ nm}$ data for BV4 (*black*), PEM1 (*red*) and QUI6 (*blue*). The regression equation (*bottom right corner*) allows for the conversion of $G/B_{450\ nm}$ into $G/B_{455\ nm}$ values

## *G/B Relationship with Instrumental Data*

All four coral cores A, B, C and D, drilled from the Keppel Islands, showed significant inter-colony relationships in G/B over the common 53 year period on annual average time-scales (Table 23.3). As all corals shared significant variance, a coral composite record was created to reduce localised variability associated with each

**Table 23.2** Correlation coefficients ($R^2$ value) of measured G/B ratios using a 450 nm cut-off filter (upper row) and the predicted G/B*values (lower row) with the G/B ratios using a 455 nm cut-off filter

| | BV4 | Pem1 | Qui6 |
|---|---|---|---|
| $G/B_{450\ nm}$–$G/B_{455\ nm}$ | 0.8959 | 0.7788 | 0.6518 |
| G/B*–$G/B_{455\ nm}$ | 0.8959 | 0.7788 | 0.6518 |

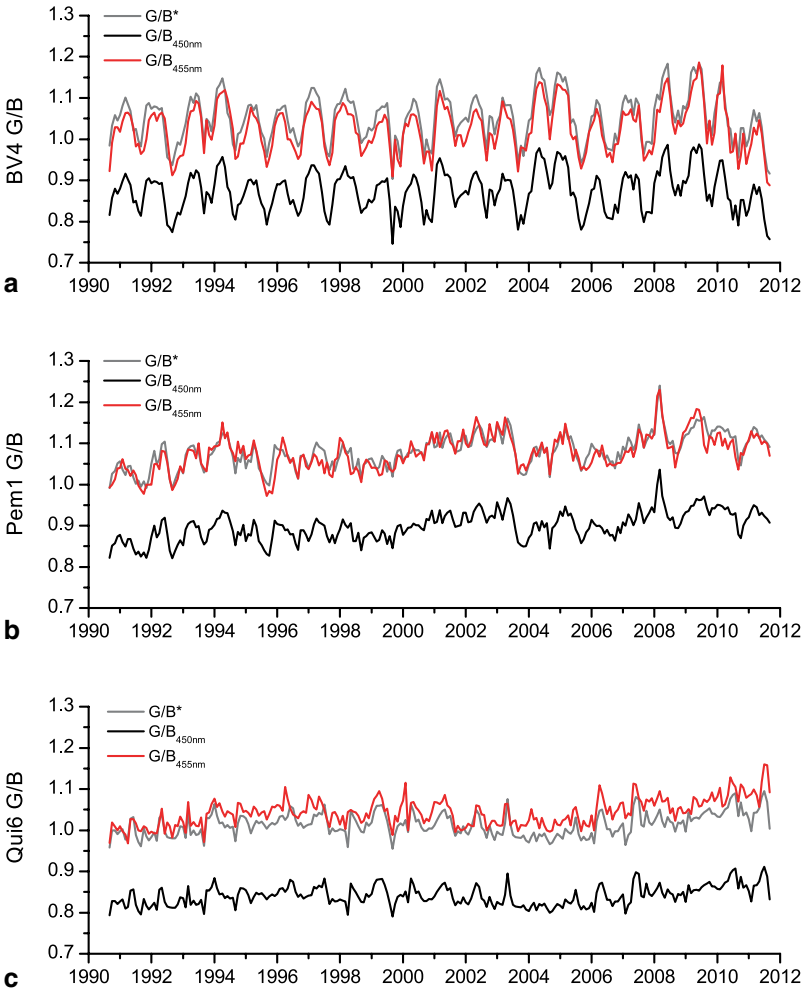


**Fig. 23.4** Comparison of the monthly resolved $G/B_{450\ nm}$ (*red*), $G/B_{455\ nm}$ (*black*), and $G/B_{455nm}$* (*grey*) time series of the Mozambique coral cores **a** BV4, **b** PEM1 and **c** QUI6. For all three corals, the two time series were significantly related (Table 23.2)

single record. The composite record therefore represented the regional G/B signal between 1957 and 2009.

The annual average G/B coral composite record showed a significant positive correlation with all three instrumental datasets (Fig. 23.6). The strongest G/B composite relationship was observed with the stream discharge rate, which explained 37% of the variance ($R^2 = 0.37$; $P < 0.001$; $n = 53$) (Fig. 23.6). Although significant, the weakest relationship of the G/B composite was observed with rainfall, which explained 10% of the recorded variance ($R^2 = 0.10$; $P < 0.05$; $n = 53$) (Fig. 23.6). Stream water level explained 25% of the variance in the G/B composite record, which was again statistically significant ($R^2 = 0.25$; $P < 0.01$; $n = 53$) (Fig. 23.6).

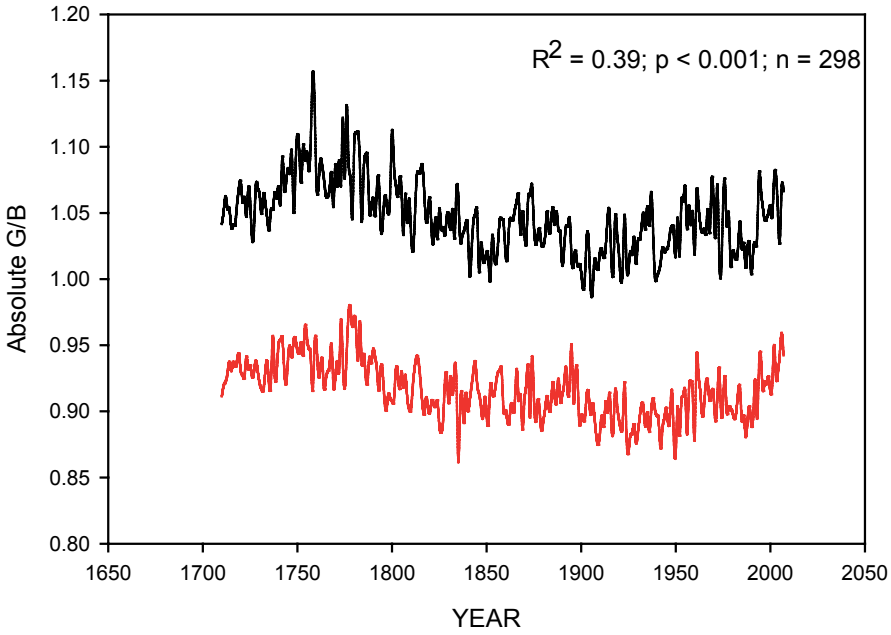


**Fig. 23.5** Comparison of MASB annual average G/B values after a single (*red*) and double (*black*) 24 h treatment with NaOCl. The double NaOCl treatment caused average G/B values to increase by 14.3 % and standard deviations to increase by 26.4 %, compared to the single treatment. The significant relationship between the two treatments is highlighted in the *top right* hand corner

**Table 23.3** Pearson correlation coefficients (*R* value) of annual G/B anomalies between coral cores sharing the common period 1957–2009. Significance levels are given in parentheses

| | Core B | | Core C | | Core D | |
|---|---|---|---|---|---|---|
| Core A | 0.36 | ($P = 0.009$) | 0.53 | ($P < 0.001$) | 0.74 | ($P < 0.001$) |
| Core B | | | 0.28 | ($P = 0.046$) | 0.66 | ($P < 0.001$) |
| Core C | | | | | 0.50 | ($P < 0.001$) |

## Discussion

### *Filter Test*

The SLS camera is highly sensitive in the Blue (B) domain to changes in the 450–455 nm spectral range (Fig. 23.2). Within the same 450–455 nm spectral range, the Green (G) domain is less sensitive, as there is only a slight overlap between the filter range and camera (G) sensitivity (Fig. 23.2) (Grove et al. 2010). When applying the commercially available 455 nm filter (Schott GG 455 nm long pass filter) to the line scan camera, there was a consistent increase in the G/B ratio between the three corals sampled from Mozambique. The $G/B_{455\ nm}$ ratio increase as a result of

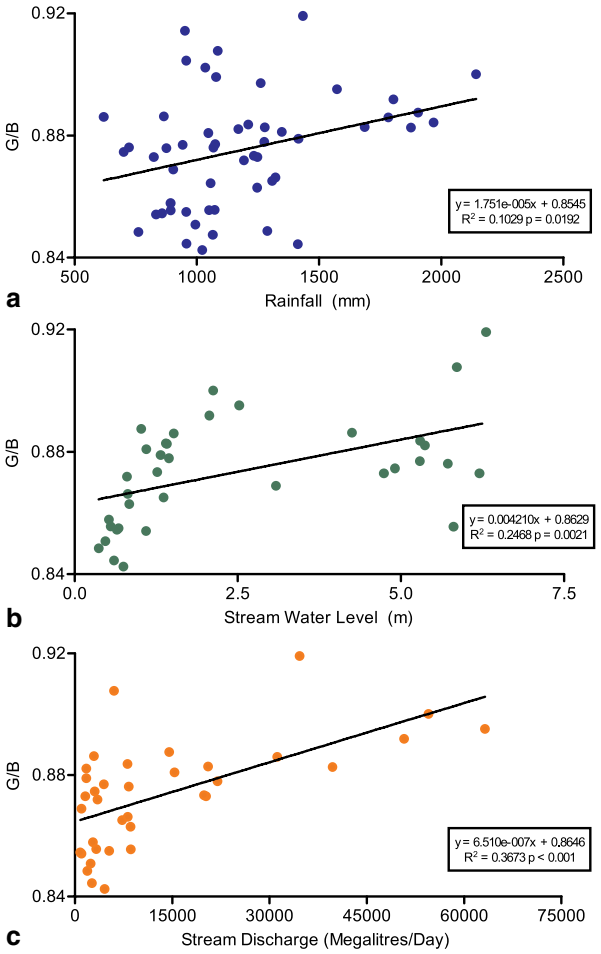


**Fig. 23.6** Linear regressions of the annual average G/B composite record with **a** annual average rainfall data (*blue*), **b** annual average stream water level (*green*) and **c** annul average stream discharge rate (*orange*). The regression equations are given in the *bottom left* hand corner together with correlations ($R^2$) and confidence levels ($P$ values). Note that precipitation data are from a single rainfall station in a total catchment area of 143,000 km$^2$

additional filtering of the blue domain between 450 and 455 nm and consequently causing a stronger reduction of Blue (B) relative to the Green (G).

The predicted $G/B^*_{455\,nm}$ values linearly compensated for the differences between the two filters used, resulting in similar values between $G/B^*_{455\,nm}$ and $G/B_{455\,nm}$, yet not identical (Fig. 23.4). These differences may have resulted from minor offsets in the selected transect areas between $G/B_{450\,nm}$ and $G/B_{455\,nm}$ (Fig. 23.4). However, more likely, differences are related to the combined effects of wavelength-selective scatter of the luminescence radiation and the relative concentration of two luminophores within the coral, aragonite and humic acids.

The $G/B_{450\,nm}$ and $G/B_{455\,nm}$ data of BV4, Pem1, and Qui6 revealed varying amounts of scatter and offset from the regression line (Fig. 23.3).The location of coral BV4 is directly influenced by a large river, whereas PEM1 is influenced by a series of smaller rivers and QUI6 is exposed to runoff periodically (Fig. 23.4). Corals devoid of terrestrial organic material (humic acids) are predominantly composed

of the aragonite luminophore. Down core G/B variations in such corals commonly reflect density related changes of coral growth bands that respond differently to internal light reflections within the complex coral skeleton (Barnes and Taylor 2001; Grove et al. 2010). In such coral records, wavelength-selective scatter appears to be stronger for shorter wavelengths, such as in the 450–455 nm domain. Consequently, short wavelengths (B) are more susceptible to internal scattering and cause larger differences between $G/B_{450\ nm}$ and $G/B_{455\ nm}$ for coral skeletons containing little or no humic acids (Barnes and Taylor 2001; Grove et al. 2010).

Corals influenced by humic acids possess two luminophores that are normalised against one another by applying the G/B spectral luminescence ratio. In such corals, skeletal internal reflections cause both the B signal related to humic acids and B of aragonite to shift in proportion to one another, therefore masking the scatter effects of porosity and density. Moreover, the more humic acids locked within the coral skeleton the less background noise related to the skeletal structure. Differences in coral composition therefore likely explain the different correlation coefficients observed between the three Mozambique coral $G/B_{450\ nm}$ and $G/B_{455\ nm}$ values (Table 23.2). Coral QUI6 was likely least influenced by river runoff and therefore showed the lowest correlation coefficient.

The linear regression function used for converting $G/B_{450\ nm}$ into $G/B_{455\ nm}$ data provides acceptable results for all three corals (Fig. 23.3). Any potential correction factor should be applied to the monthly interpolated data only before calculating annual averages. When required, the regression function can potentially convert $G/B_{450\ nm}$ data acquired from other coral records into $G/B_{455\ nm}$ values allowing for cross core comparisons of absolute G/B values. Nevertheless, re-measuring a small part of the coral core with the 455 nm filter will provide more fundamental correction results. When applying absolute G/B values to accurately assess relative runoff rates of different rivers, using coral runoff proxy data requires information beyond what corals can generally offer (Grove et al. 2012). Coral G/B is not only a function of runoff from a particular river; it is also affected by the distance between the river and the coral, current direction, coral depth and composition of the river watershed in terms of humic acids (Grove et al. 2012).

## *Cleaning Test*

Nagtegaal et al. (2012) observed a 6% increase in monthly G/B values for the MASB top core after 24 h treatment with NaOCl. Cleaning the coral MASB a second time following the same procedure, further increased the absolute G/B values and the variability relative to the single treatment. In agreement with Nagtegaal et al. (2012), the green intensity increased relative to the blue with the removal of resistant organic material, causing the absolute G/B to further increase. Although the two coral records were significantly correlated, the $R^2$ value (0.39; $n = 298$) was relatively low. This is likely a result of residual contaminants quenching/obscuring the luminescence signal related to humic acids after single NaOCl treatment and a poorly defined age model as a consequence.

As there is a significant difference between the absolute G/B values using single and double treatments, we would suggest only using repeated NaOCl cleaning if absolutely necessary, i.e. organic contaminants unavoidable when drawing a transect. If a repeated NaOCl treatment is required, it is no longer possible to compare absolute G/B values with other coral cores that were treated only once. Comparisons between cores can therefore only be achieved when corals are treated using exactly the same cleaning protocol. For the majority of corals analysed, a single treatment removed most organic contaminants, which allowed for clear photoluminescence imagery (Grove et al. 2010, 2012; Maina et al. 2012; Nagtegaal et al. 2012).

## *G/B Relationship with Instrumental Data*

Until now relationships of G/B with runoff have been formulated on comparisons with other runoff proxies (Grove et al. 2010, 2012), modelled river discharge (Grove et al. 2012; Maina et al. 2012), gridded data (Grove et al. 2013) and/or weather station data located hundreds of kilometres from the study site (Grove et al. 2010, 2013). Here, coral records from the Keppel Islands provide evidence that G/B is tightly coupled to parameters associated with runoff. Significant positive relationships of the G/B composite record are observed with precipitation, stream water level and stream discharge, based on a four coral core G/B-composite record spanning 53 years (Fig. 23.6). Increasing coral luminescence (G/B) with precipitation, runoff and discharge is related to the skeletal incorporation of terrestrial humic acids (Isdale 1984; Susic and Boto 1989; Matthews et al. 1996; Isdale et al. 1998; Wild et al. 2000). As runoff increases, so does the concentration of humic acids in the water column, and the amount incorporated into the coral skeleton as it grows/precipitates.

Precipitation and discharge are not always linearly related due to factors including land cover, elevation, temperature, and soil water storage capacity (Agarwal et al. 2005; Hofmann et al. 2005; Maina et al. 2012). The strongest observed relationship with G/B was with stream discharge, rather than precipitation or stream water level. As humic acids are associated with terrestrial matter/erosion, rather than freshwater, this likely explains the tight G/B-discharge relationship. Also, for this study only one rainfall station was analysed in a 143,000 $km^2$ catchment area, which may offer one explanation as to why correlations with G/B were lowest. However, given local precipitation drives runoff, the G/B-precipitation relationship was still significant. As stream water level is closely related to stream discharge, this likely explains the high significant relationship observed with G/B. All instrumental data comparisons with G/B therefore augment the ability of corals to record a runoff signature within their skeleton (Lough et al. 2002; Grove et al. 2010, 2012; Lough 2011a).

## Conclusions

It is important that this type of study is carried out to ensure methods can be easily replicated as well as increasing the confidence in data produced. This especially holds in the field of (coral) paleoclimatology where replication and reproducibility is lacking in many cases or impossible. Fitting a commercially available light cut off filter directly to the camera lens of the Avaatech XRF core scanner allows for improved replication in spectral luminescence scanning of coral cores. Previous measurements using a uniquely manufactured 450 nm filter can now be converted by applying a linear correction function based on major axis regression. Similarly, cleaning protocols must be identical, as there are large differences in absolute G/B values resulting from the specific treatment method applied. A single 24 h treatment with NaOCl is recommended to remove organic contaminants before spectral luminescence scanning. However, when resistant organic contaminants remain, the same treatment should be repeated, although cross core comparisons of absolute G/B values may be compromised. Here, four similarly treated corals from the Keppel Islands, Australia, showed statistically similar variability in G/B on annual time scales, allowing for a single coral composite record to be constructed. Comparing the composite G/B record with instrumental data provides more solid evidence that coral G/B is directly related to runoff related parameters. Significant relationships were observed with precipitation, stream water height and stream discharge over a 53 year period. The strongest relationship of G/B was with stream discharge rate, explaining 37 % of the total interannual variance.

**Acknowledgements** This work was supported by the Netherlands Organisation for Scientific Research (NWO) as part of CLIMATCH (grant number 820.01.009), the SINDOCOM program on 'Climate Variability' as well as the SCAN2 program on advanced instrumentation. We thank Bob Koster and Rineke Gieles for continuous development and maintenance of the UV-Core Scanner. We thank the Wildlife Conservation Society (WCS) Madagascar, and the WCS/ANGAP team in Maroantsetra, for their support in fieldwork logistics and in the organisation of the research permits, CAF/CORE Madagascar for granting the CITES permit and ANGAP Madagascar for support of our research activities in the vicinity of the marine and forest nature parks. We also thank the Eduardo Mondlane University team, especially Santos Luis Mucave and Sergio Mapanga, for their support with fieldwork and logistics, Tecomaji Lodge for supporting our field campaign in the Quirimbas islands and Isabel Marques da Silva of WWF Mozambique. ARR thanks Sander Scheffers for assistance with collecting cores from the Great Barrier Reef. The laboratory work of the Great Barrier Reef cores was supported by a Graduate School International Travel Award (GSITA) from the University of Queensland and the PADI foundation. JZ was supported by a joint UWA/AIMS/CSIRO postdoctoral fellowship.

## References

Agarwal DK, Silander JA, Gelfand AE, Dewar RE, Mickelson JG (2005) Tropical deforestation in Madagascar: analysis using hierarchical spatially explicit, Bayesian regression models. Ecol Model 185(1):105–131

Barnes DJ, Taylor RB (2001) On the nature and causes of luminescent lines and bands in coral skeletons. Coral Reefs 19:221–230

Barnes DJ, Taylor RB (2005) On the nature and causes of luminescent lines and bands in coral skeletons: II. Contribution of skeletal crystals. J Exp Mar Biol Ecol 322:135–142

Bostock H, Brooke B, Ryan D, Hancock G, Pietsch T, Packett R, Harle K (2007) Holocene and modern sediment storage in the subtropical macrotidal Fitzroy River estuary, Southeast Queensland, Australia. Sediment Geol 201:321–340

Boto K, Isdale P (1985) Fluorescent bands in massive corals result from terrestrial fulvic-acid inputs to nearshore zone. Nature 315:396–397

Dewar RE, Richard AF (2007) Evolution in the hypervariable environment of Madagascar. Proc Natl Acad Sci U S A 104:13723–13727

Dewar RE, Wallis JR (1999) Geographical patterning of interannual rainfall variability in the tropics and near tropics: an L-moments approach. J Clim 12:3457–3466

Furnas MJ (2003) Catchments and corals: terrestrial runoff to the Great Barrier Reef. Australian Institute of Marine Science and CRC Reef Research Centre, Townsville, p 334

Grove CA, Nagtegaal R, Zinke J, Scheufen T, Koster B, Kasper S, McCulloch MT, van den Bergh G, Brummer G-JA (2010) River runoff reconstructions from novel spectral luminescence scanning of massive coral skeletons. Coral Reefs 29(3):579–591

Grove CA, Zinke J, Scheufen T, Maina J, Epping E, Boer W, Randriamanantsoa B, Brummer G-JA (2012) Spatial linkages between coral proxies of terrestrial runoff across a large embayment in Madagascar. Biogeosciences 9:3063–3081. doi:10.5194/bg-9-3063-2012

Grove CA, Zinke J, Peeters F, Park W, Scheufen T, Kasper S, Randriamanantsoa B, McCulloch M, Brummer G-JA (2013) Madagascar corals reveal a multidecadal signature of rainfall and river runoff since 1708. Clim Past 9:641–656. doi:10.5194/cp-9-641-2013

Hendy EJ, Gagan MK, Lough JM (2003) Chronological control of coral records using luminescent lines and evidence for non-stationary ENSO teleconnections in northeast Australia. The Holocene 13:187–199

Hofmann J, Behrendt H, Gilbert A, Janssen R, Kannen A, Kappenberg J, Lenhart H, Lise W, Nunneri C, Windhorst W (2005) Catchment-coastal zone interaction based upon scenario and model analysis: Elbe and the German Bight case study. Reg Environ Chan 5:54–81

Isdale PJ (1984) Fluorescent bands in massive corals record centuries of coastal rainfall. Nature 310:578–579

Isdale PJ, Stewart BJ, Tickle KS, Lough JM (1998) Palaeohydrological variations in a tropical river catchment: a reconstruction using fluorescent bands in corals of the Great Barrier Reef, Australia. The Holocene 8:1–8

Jones PD, Briffa KR, Osborn TJ, Lough JM, van Ommen TD, Vinther BM, Luterbacher J, Wahl ER, Zwiers FW, Mann ME, Schmidt GA, Ammann CM, Buckley BM, Cobb KM, Esper J, Goose H, Graham N, Jansen E, Kiefer T, Kull C, Kuttel M, Mosley-Thompson E, Overpeck JT, Riedwyl N, Schulz M, Tudhope AW, Villalba R, Wanner H, Wolff E, Xoplaki E (2009) High-resolution paleoclimatology of the last millennium: a review of current status and future prospects. The Holocene 19:3–49

Lough JM (2011a) Great Barrier Reef coral luminescence reveals rainfall variability over northeastern Australia since the 17th century. Paleoceanography 26:PA2201. doi:10.1029/2010PA002050

Lough JM (2011b) Measured coral luminescence as a freshwater proxy: comparison with visual indices and a potential age artefact. Coral Reefs 30:169–182

Lough JM, Barnes DJ, Mcallister FA (2002) Luminescent lines in corals from the Great Barrier Reef provide spatial and temporal records of reefs affected by land runoff. Coral Reefs 21:333–343

MacRae CM, Wilson NC (2008) Luminescence database I-Minerals and materials. Microsc Microanal 14:184–204

Maina J, de Moel H, Vermaat JE, Bruggemann H, Guillaume MMM, Grove CA, Madin JS, Mertz-Kraus R, Zinke J (2012) Linking coral river runoff proxies with climate variability, hydrology and land-use in Madagascar catchments. Mar Pollut Bull. doi:10.1016/j.marpolbul.2012.06.027

Matthews BJH, Jones AC, Theodorou NK, Tudhope AW (1996) Excitation-emission-matrix fluorescence spectroscopy applied to humic acid bands in coral reefs. Mar Chem 55:317–332

Nagtegaal R, Grove CA, Kasper S, Zinke J, Boer W, Brummer G-JA (2012) Spectral luminescence and geochemistry of coral aragonite: effects of whole-core treatment. Chem Geol 318–319:6–15

Paillard D, Labeyrie L, Yiou P (1996) Macintosh program performs time series analysis. Eos Trans Am Geophys Union 77:379–379

Pfeiffer M, W-C Dullo, Zinke J, Garbe-Schönberg D (2009) Three monthly coral Sr/Ca records from the Chagos Archipelago covering the period of 1950–1995 A.D.: reproducibility and implications for quantitative reconstructions of sea surface temperature variations. Int J Earth Sci 98:53–66. doi:10.007/s00531-008-0326-z

Rodrigues-Ramirez A, Grove CA, Zinke J, Pandolfi JM, Zhao JX (2014) Coral luminescence identifies the Pacific Decadal Oscillation as a primary driver of river runoff variability impacting the southern Great Barrier Reef. PLOS One

Quartly GD, Kyte EA, Srokosz MA, Tsimplis MN (2007) An intercomparison of global oceanic precipitation climatologies. J Geophys Res 112:D10121. doi:10.1029/2006JD007810

Susic M, Boto KG (1989) High-performance liquid-chromatographic determination of humic-acid in environmental-samples at the nanogram level using fluorescence detection. J Chromatogr 482:175–187

Wild FJ, Jones AC, Tudhope AW (2000) Investigation of luminescence banding in solid coral: the contribution of phosphorescence. Coral Reefs 19:132–140

# Chapter 24
# An Inter-comparison of μXRF Scanning Analytical Methods for Lake Sediments

**Daniel N. Schillereff, Richard C. Chiverrell, Ian W. Croudace and John F. Boyle**

**Abstract** The acquisition of high-resolution geochemical data from wet sediment cores through μXRF scanning is an increasingly important analytical tool. A number of μXRF core scanners are in use today that measure elemental concentrations using slightly different methods and several correction methods have been proposed in order to generate more precise quantitative geochemical data. However, only few inter-device comparisons have been undertaken to date and this contribution addresses this deficiency. The main focus is based on a sediment core 1.44 m in length extracted from Loch of the Lowes, Southern Uplands of Scotland, and analysed using a Geotek XZ MSCL carrying an Olympus Delta XRF (University of Liverpool) and an ITRAX core scanner housed at the National Oceanography Centre—Southampton (NOCS). The core is strongly laminated but layers are not consistent in terms of thickness or frequency, thus it provides a good test of the comparative analytical resolution of the devices. The cores were measured at 5 and 1 mm intervals using the Geotek scanner and steps of 0.3 mm on the ITRAX instrument. Seven elements were selected for this inter-comparison: the Geotek 5 mm measurements of Ti, Zr, K and Rb concentration picked up all phases of enhanced mineral supply to the lake as characterised by light-coloured sediments. The finer detail (mm-scale laminations) was more effectively captured by the Geotek 1 mm and ITRAX scans, however Zr, Sr and Rb measured on the ITRAX were significantly more spikey or noisy in character; in particular, peaks and troughs in ITRAX count rate of similar amplitude to the light/dark layers also appeared across intervals with no visible stratigraphic variability. The Geotek less effectively discriminated thin layers within a sediment matrix of geochemically-different lithology. The decision as to which scanning resolution to choose depends on the research question being asked. If abrupt sedimentological or climatic transitions are not under investigation, then lower resolution scans, which are well within the capability of the 5 mm Geotek runs, may be sufficient to capture palaeoenvironmental change. The

D. N. Schillereff (✉) · R. C. Chiverrell · J. F. Boyle
Department of Geography and Planning, School of Environmental Sciences, University of Liverpool, Liverpool L69 7ZT, UK
e-mail: dns@liv.ac.uk

I. W. Croudace
Ocean and Earth Science, National Oceanography Centre, University of Southampton, Waterfront Campus, European Way, Southampton SO14 3ZH, UK



I. W. Croudace, R. G. Rothwell (eds.), *Micro-XRF Studies of Sediment Cores*,
Developments in Paleoenvironmental Research 17, DOI 10.1007/978-94-017-9849-5_24

Itrax can also be operated to run in such a low-resolution mode but on this occasion this was not selected. Another approach investigated was to externally calibrate the Geotek data using a regression correction method (proposed by Boyle et al. 2015, this volume) was tested and consistent dry-mass equivalent concentrations were found for both techniques despite variable statistical relationships. We thus recommend that future research presents μXRF data in terms of dry-mass concentration to facilitate more effective method and field site intercomparison. A final instrument comparability test was performed by measuring a short laminated sandstone section and a homogenous, parallel faced obsidian piece on the ITRAX (NOCS), the Geotek and an Eagle III μXRF system (NOCS). As an example, the Ti profiles through the laminated sandstone output from the three instruments showed some differences: clear peaks and troughs in the ITRAX measurements effectively tracked the alternating light and dark layers while the Geotek returned a more smoothed signal. Interestingly, the Eagle III data exhibit several Ti peaks that do not fully correspond to layer thickness. For the obsidian piece, the signal-to-noise ratio was good in all cases but the relative major element composition varied between devices, possibly due to different instrument configurations' keeping this firmly in mind when comparing geochemical data thus seems critical.

**Keywords** Micro-XRF scanning · Geotex XRF scanner · Itrax scanner · Eagle III scanner · Analytical intercomparision

## Introduction

X-ray fluorescence (XRF) is a well-established geoanalytical technique (Boyle 2001) used to characterise the chemical composition of rocks or soft sediments traditionally measuring dried sub-samples as powders, pressed pellets or glass beads. The proliferation of μXRF core scanning devices has seen the approach become the optimal preliminary and in many cases the primary tool for analysing wet sediment cores extracted from fluvial, lacustrine or marine settings. The ability to non-destructively examine the chemical composition of sediments rapidly (at sub-millimetre resolutions, e.g., Croudace et al. 2006) are the main reasons for the increasing use of core scanners. Until recently, the common use of uncalibrated data has been a potential weakness of core scanners but increasingly users have quantified their data using a variety of external methods. For example, Boyle et al. (2015, this Volume) have used a previously calibrated, bench-top EDXRF to analyse dried subsamples. Since the development of the first core scanner in 1998 (Jansen et al. 1998), several different manufacturers have established commercial core scanners, and these include the Avaatech (Richter et al. 2006; http://www.avaatech.com/), the ITRAX from Cox Analytical (Croudace et al. 2006; http://coxsys.se/), the Eagle III BKA (Haschke 2006) and the Geotek Multi-sensor core logger (http://www.geotek.co.uk/). To date, the first two manufacturers have overwhelmingly dominated the market.

The speed of data acquisition offers an effective means for conducting exploratory analysis to rapidly obtain stratigraphic information from long cores. In the case of lake sediments, this could inform later field sampling and enable rapid stratigraphical correlation between cores across a basin. The μXRF resolution is of value, for example, analysing annually-laminated sequences consisting of sub-laminations too thin to manually sub-sample (Ojala et al. 2012). μXRF also enables event-scale stratigraphic investigations to be undertaken, discriminating historical flood layers from the background sediment matrix at Lake Ammersee (Czymzik et al. 2013) or Lake Suigetsu (Marshall et al. 2012; Schlolaut et al. 2014). μXRF data have also proved valuable for supporting sedimentological analysis of turbidite layers, such as deposits linked with the 1755 Lisbon earthquake (Cuven et al. 2013). Longer term patterns of change in sediments are also revealed in μXRF data, such as Sr/Ca ratios reflecting increased salinity and the progressive drying of the Sahara through the Holocene in Lake Yoa (Chad) sediments (Francus et al. 2013).

It is clear that the rapid acquisition of geochemical data using μXRF core scanning techniques is a major strength compared with laborious traditional methods. However, this is only of value if data quality are maintained when compared to sub-samples measured individually on a dry-mass basis via conventional XRF. However, there are several potential impediments that may introduce artefacts into core scanning datasets, including surface irregularities along the core surface or gaps in the sediment sequence (Weltje and Tjallingii 2008), non-homogenous mineral and grain-size composition (Hennekam and de Lange 2012) and variable down-core water and organic content (Boyle et al., this volume). The μXRF platforms differ themselves in the mechanics of data acquisition and the format of data output. For example, hand-held XRF analysers such as the Olympus Delta XRF and Thermo-Niton XL3t output concentrations of various elements based on internal calibrations from raw X-ray spectra whereas raw data obtained using the ITRAX device are commonly based on total counts per second. Itrax and other core scanner data can often be quantified using instrument-supplied software or using external methods. Where data are output in count form then the different instruments, with their different excitation functions, have the potential to introduce confusion and erroneous interpretation. Conversion of the counts to dry mass equivalent concentration data effectively removes or reduces the problems discussed.

Here we present an assessment of the performance of two different core scanning platforms, the Geotek Multi-Sensor Core Logger (MSCL) carrying an Olympus Delta XRF and the ITRAX, with a calibration dataset obtained by conventional energy dispersive XRF (Bruker S2 Ranger), through analysis of a sediment core extracted from Loch of the Lowes, Southern Uplands of Scotland. We consider the analytical resolution of the devices, the trade-off that exists between higher-resolution but more time-consuming and costly scans, the similarities and differences that emerge across multiple elements and the impact of these issues in palaeoenvironmental research. We also assess the effectiveness of employing established dry-mass equivalent conversion techniques for both devices and, finally, to assess μXRF intercomparision on a dry, whole-rock basis we ran two further samples, a heterogeneous laminated sandstone and a highly homogenous sample of obsidian glass on the three instruments: Geotek, the ITRAX as well as an Eagle III μXRF scanner.

## The Study Site

Loch of the Lowes (Fig. 24.1) lies in the headwaters of the River Tweed catchment in the Southern Uplands of Scotland. The lake (0.47 km$^2$) has a large upland catchment (area 27 km$^2$; maximum elevation 610 m; lake elevation 243 m; catchment to lake area ratio 57:1). The lake is oligotrophic and comprises a simple bathymetry dominated by a flat central plain at water depths 12–15 m (Murray and Pullar 1910). Drainage enters the lake from five sub-catchments, three at the south shore (Little Yarrow, Chapelhope, Riskinhope) and two at the north (Crosscleugh, Oxcleugh) (Fig. 24.1) (Foster et al. 2008). Loch of the Lowes drains north into the adjacent St Mary's Loch via a small stream outflow. Catchment bedrock geology is dominated by Lower Palaeozoic greywacke sand/silt/mud-stones, which have been sculpted by Quaternary glacial erosion into an upland terrain comprising U-shaped valleys and more rounded summits. Previous lake sediment investigations at the site (Foster et al. 2008) using 1 m Mackereth mini-cores identified flood-related indications in environmental magnetic and geochemical data that suggested an association with the North Atlantic Oscillation (NAO). Parallel investigations in the catchment (Foster et al. 2008) show phases of extensive region-wide slope instability AD 700–900, 1100–1300 and after AD 1450–1550 and gully stabilization over the last 150 years. Loch of the Lowes thus meets many of the traits conducive to the effective record-

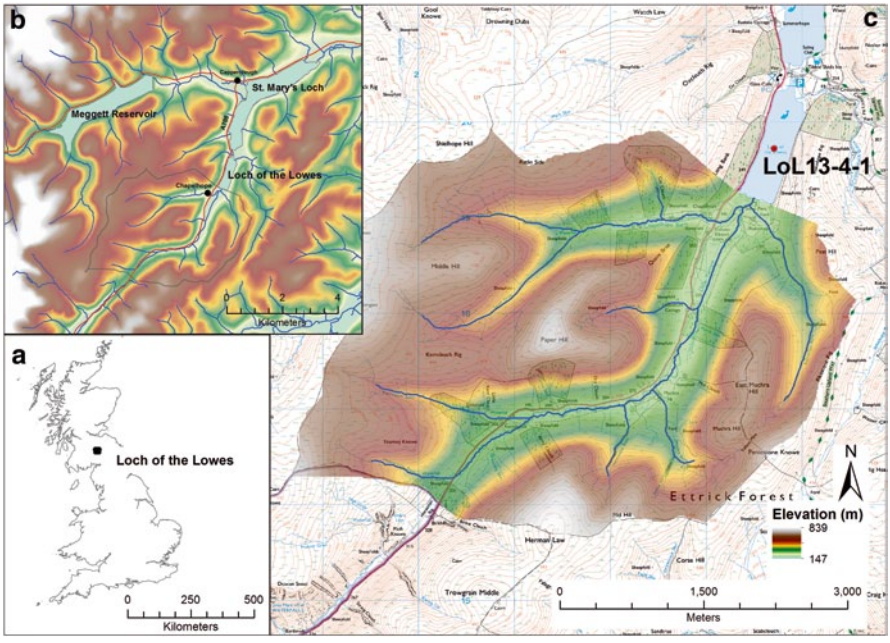


**Fig. 24.1** Location of the study site within the UK (**a**) and the adjacent St. Mary's Loch and Meggett Reservoir (**b**). Loch of the Lowes catchment elevation, the fluvial system and position of the lake core (**c**)

ing of changes in catchment sediment flux in the profundal sediments, and flood stratigraphies in particular (Schillereff et al. 2014), and thus offers a good test case for reconstructing high-resolution environmental change including flood laminations using μXRF scanning techniques.

## Field and Laboratory Methods

The core data were obtained using the University of Liverpool Geotek Multi-Sensor Core Scanner (MSCL-XZ), a bench-top instrument capable of line-scan high-resolution imagery as well as simultaneous acquisition of XRF geochemistry, point magnetic susceptibility and visual light diffuse reflectance spectrometry (DRS) on split sediments cores (max length 1.53 m). The XRF measurements were undertaken using an Olympus Delta Energy-Dispersive XRF (ED-XRF) analyser fitted to a robotic arm. The XRF has a 4 W rhodium x-ray tube (8–40 keV; 5–200 μA excitement) and a thermo-electrically cooled large-area silicon drift detector and the detector window is covered with a thin (6 μm) polypropylene film to avoid contamination of the internal measurement sensors. The Olympus Delta in 'Soil' mode applies three successive x-ray intensities (15, 40 and 40 (filtered) keV beam condition) and for 'Mining plus' two successive x-ray intensities (15 and 40 keV beam condition).

μXRF measurements on the same split core were carried out on the ITRAX system housed in the National Oceanography Centre (Southampton) using a step size of 300 μm and a measurement dwell time of 30 s. The ITRAX has a rectangular beam footprint of $20 \times 0.2$ mm focused through a flat-beam optical device (not a collimator) with the long axis perpendicular to the sample main axis thus 0.2 mm sampling resolutions are possible (Croudace et al. 2006). ITRAX uses a 3 kW X-ray generator, with the current system using a 3 kW molybdenum target tube that operated at 30 kV and 30 mA for XRF analysis and 60 kV and 50 mA for radiographic scanning. The XRF detector fitted to the ITRAX is a silicon drift detector (Peltier cooled SDD).

To calibrate these μXRF scanning data to mass specific values a calibration training-set was subsampled from the core. Elemental analyses were performed on a dry-mass basis using the University of Liverpool Bruker S2 Ranger Energy-Dispersive XRF. This instrument has a palladium x-ray tube with a maximum current of 2000 μA, a Peltier-cooled silicon drift detector and it applies three successive x-ray intensities (20, 40 and 50 keV tube excitement) under a helium atmosphere to each sample. Samples were homogenised using a mortar and pestle and the powdered pellets were compressed into cups sealed with polypropylene film. A certified set of 18 calibration samples were measured (see Table 24.1, Boyle et al., this volume) and concentrations were adjusted for organic matter content measured using thermogravimetry (Perkin Elmer STA6000), using the mass loss between 150° and 530°C in a nitrogen atmosphere.

**Table 24.1** Major element composition for the 52 mm length piece of Obsidian glass measured non-destructively on three different µXRF scanners as well as via WD-XRF. The Geotek/Olympus values were obtained using the MiningPlus mode and converted from parts per million for display purposes. The final column are the converted concentrations of each element less the LE content of the sample (mean = 57.73 %)

| Element | WD-XRF (%) | ITRAX (counts) | Eagle III (%) | Geotek/ Olympus (%) | Geotek/Olympus (% of non-LE composition) |
|---|---|---|---|---|---|
| $SiO_2$ | 73.58 | 31,734 | 70.38 | 30.14 | 71.30 |
| $Al_2O_3$ | 11.61 | 1834 | 9.34 | 4.75 | 11.24 |
| $Fe_2O_3$ | 3.57 | 1,704,780 | 7.76 | 2.63 | 6.22 |
| $K_2O$ | 2.66 | 79,283 | 5.97 | 2.51 | 5.94 |
| CaO | 1.64 | 72,640 | 3.38 | 1.43 | 3.38 |
| $TiO_2$ | 0.23 | 23,761 | 0.46 | 0.17 | 0.40 |

A sediment core 1.38 m in length was extracted in April 2013 from the central basin of the lake in water depths of 13 m (core plots are expressed in metres below lake surface) using a Russian-type device with a diameter of 70 mm. The core was tightly wrapped to prevent drying, and stored in darkness at 4°C at the University of Liverpool. The core were cleaned and photographed at 100 µm resolution after calibration to grey and white plates using the Line-scan camera fitted to the Geotek instrument. The core was covered with 5 µm polypropylene film and measured at 5 mm intervals using the Olympus Delta device using factory defined Soil and MiningPlus modes as described above. The Mining Plus mode was used for Al, Si, P, and Ca; the Soil mode was used for the other elements. The core was then measured on the ITRAX core scanner (December 2013) at the National Oceanography Centre, Southampton. Finally, the core was re-measured on the Geotek/Olympus at 1 mm resolution (April 2014), increasing the time span between machine standardisation to 24 h compared with 12 h standardisation for the 5 mm interval runs. The calibration dataset was developed from sub-samples taken at 50 mm intervals from the core. These were weighed, freeze-dried and reweighed after drying to calculate moisture content and dry mass, and then measured as hand-pressed powders using the Bruker S2 Ranger. Dry masses were calculated assuming a mineral density of 2.65 g $cm^{-3}$.

## Whole Core Data from µXRF Scanning Methods

The sediments largely comprise gyttja-type material, essentially a lightish-brown silty matrix that is heavily laminated throughout (Fig. 24.2). The uppermost 65 cm in particular are characterised by very fine (often ≤ 1 mm thick) light (very light brown to grey) and dark (very dark brown to black) laminations, occasionally interspersed with thicker layers (≥ 5 mm thick). Light, thicker bands are more common through the lower portion of the core, although the black band at 14.34–14.36 cm

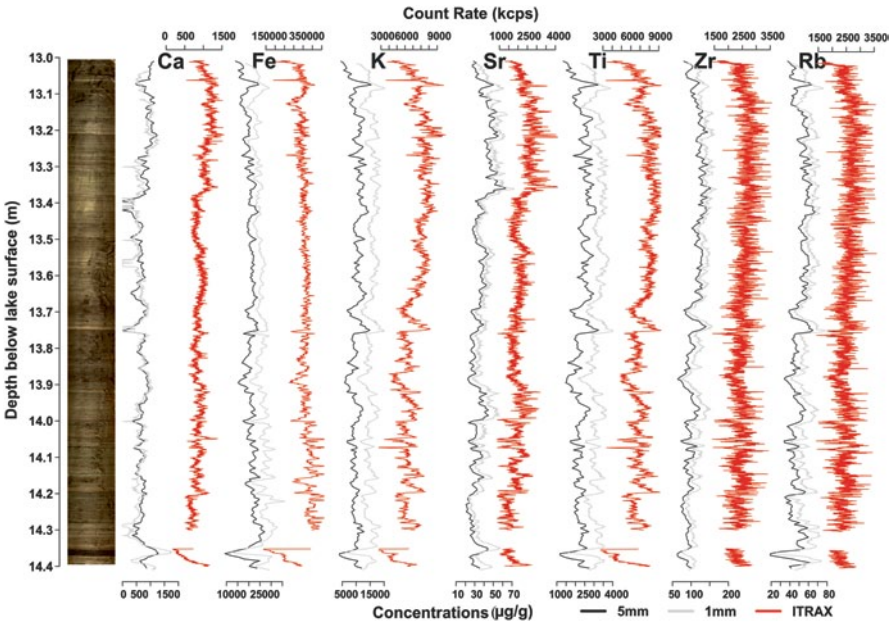


**Fig. 24.2** High-resolution photograph of core LoL13-4-1 obtained using the line-scan camera mounted on the Geotek platform and concentrations/ counts for seven elements measured at 5 and 1 mm intervals on Geotek and the ITRAX

is especially prominent. Organic matter concentrations are modest throughout (< 10 %). The mean grain-sizes lie predominantly in the fine to medium silt fraction (~ 8–20 µm) but display some variation in grain-size between the lighter, finer-grained (~ 8–12 µm) layers and the coarser (~ 15–25 µm) dark units. For this whole core comparison, seven elements were selected: Ca, Fe, K, Rb, Sr, Ti and Zr. Their profiles (Fig. 24.2) appear to divide into two groupings; Fe, K, Rb, Ti and Zr largely co-vary throughout and reflect variations of catchment-derived mineral in-wash. While the ITRAX data range for Fe and noise present in the Zr and Rb ITRAX datasets means the co-variance is somewhat less apparent for these elements, the major stratigraphic structures are identified in each of the ITRAX 0.3 mm and Geotek/ Olympus 1 mm and 5 mm µXRF scans. In particular, well defined in all three scanning datasets are the elevated Ca and Sr concentrations above 13.40 m, a distinct band at 14.36 cm which corresponds with a thick black organic layer and a thick lighter sediment layer at 13.70 m that shows peaks in terrigenous elements (K, Sr, Ti and Zr).

In Fig. 24.2, there are similar trends for all seven elements in both the 1 and 5 mm runs on the Geotek/Olympus. The 1 mm scans returned higher concentrations for Fe, K and Ti and slightly lower concentrations of Sr and Zr, in part this reflects the drying and reduced water content of the core over the 9 month gap in measurement. These issues notwithstanding, most of the finer detail is captured at both resolutions. For example, five small peaks in Fe between 14.05 and 14.20 m are

visible and the relative magnitude of the peaks is similar at both scanning resolutions. The Sr measurements at 1 mm resolution exhibit the most marked differences from the 5 mm scans. For example, sub-cm scale fluctuations between 13.5 and 14 m are only visible in the 1 mm run superimposed on larger scale variations in Sr concentration. Zr exhibits similar characteristics in comparing 5 mm and 1 mm scans across this interval. Measurements made at 1 mm resolution return values that are averaged across the beam area (10 mm diameter), thus 5 mm intervals requires a 50 % measurement overlap and 1 mm a 90 % measurement overlap. Fine resolution detail is captured with greater clarity for the heavier atomic mass elements e.g. Sr and Zr. For other elements the detail is smoothed within the measurement overlap. The Olympus Delta XRF range includes models with a beam collimator that focuses to a 3 mm diameter footprint, but signal is attenuated requiring longer count times. In summary, comparison of the full-core results shows benefits of operating the Geotek/Olympus at fine resolution, with ~ 1 mm runs for cores recovering finer detail evidence for environmental change, but it offers improved results for many elements (e.g. Zr, Sr, Ti, Rb).

Given the 300 μm resolution of the ITRAX scanning (Fig. 24.2) it is not surprising that the geochemical profiles have an appearance that is more spikey or noisy in character. Initially (Fig. 24.2) we have applied no smoothing to the whole core data which were collected as counts per second for defined element peaks, and broadly there is a strong correspondence with the Geotek/Olympus measurements. Sub-cm scale oscillations in Fe between 14.05 and 14.2 m are clearly defined in the ITRAX data (Fig. 24.2) and mirrored in the Geotek/Olympus 1 mm output, but the relative magnitudes of the peaks vary between techniques. Perhaps this reflects the different machine configurations, particularly the 2 × 0.3 mm (ITRAX) and 10 mm diameter (Geotek/Olympus) beam footprints and the ITRAX output as x-ray count rather than ppm on the Olympus Delta XRF. In summary for the selected elements there is a strong correspondence between the ITRAX and Geotek/Olympus, but at a whole core scale there appears greater clarity in the Ti, K and Fe compared to Ca, Rb, Sr and Zr in the ITRAX data. However, it is not clear whether this reflects greater between-sample variability, a phenomenon not detected in the Geotek/Olympus 1 mm scans, or simply greater analytical noise. Whether these issues persist when examined at fine resolution is explored in the following section using subsections of the core.

A further consideration is that with the more routine use of μXRF as a first stage to the analysis of core materials, researchers face an unfamiliar question as to whether they are presented with too much data. For fine resolution patterns across short core lengths this concern does not apply, but interpreting longer duration patterns of geochemistry for the Loch of the Lowes (Fig. 24.2) data collected at lower analytical resolutions gives a clearer story (e.g. Zr and Sr) and given longer XRF count times is potentially more precise. Smoothing or aggregating the ITRAX data to 2–3 measurement intervals (600–900 μm) would increase the count times to 60–90 s and may enhance the signal.

## *Micro-Structures Revealed by µXRF of Laminated Lake Sediments*

The real strength and original motivation for µXRF lies in discerning detail of geochemistry at very fine resolutions. Here we have selected two short 10–26 cm length sections of the Loch of the Lowes core to exemplify this. The stratigraphy (Fig. 24.3) between 13.2 and 13.46 m shows detrital flood laminations in the profundal sediments of the lake with numerous sub-cm laminations with lighter beige layers punctuating the accumulation of darker mineral and organic (<20%) gyttja. The 13.7–13.8 m section (Fig. 24.4) shows ~5 cm of dark brown organic sediment with weak laminations giving way to 4.5 cm containing four sub-cm light laminations overlain by a further 2.5 cm of dark brown organic gyttja. The laminations mentioned occur throughout the core but not consistently and are unlikely to represent annual-laminations; more likely they reflect high magnitude river flows (floods) driven by either synoptic rainfall or snow-melt in this upland catchment.

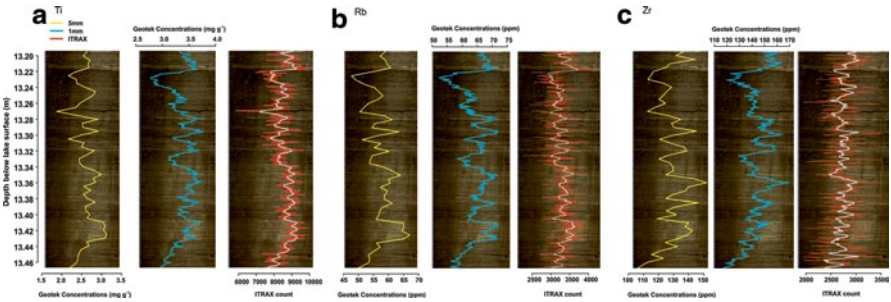


**Fig. 24.3** High-resolution line-scan image of a core section from 13.20 to 13.46 m depth overlain by **a** Ti; **b** Rb and **c** Zr concentrations for the 5 mm (*yellow*) and 1 mm (*blue*) Geotek scans and the ITRAX count (*red*). The 15-point moving average is superimposed (*light grey*) on the ITRAX data

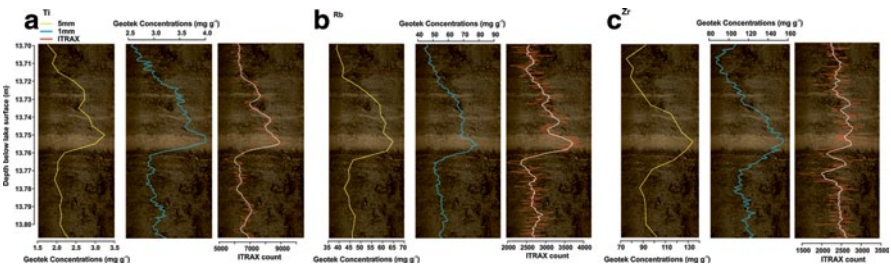


**Fig. 24.4** High-resolution line-scan image of a core section from 13.70 to 13.80 m depth overlain by **a** Ti; **b** Rb and **c** Zr concentrations for the 5 mm (*yellow*) and 1 mm (*blue*) Geotek scans and ITRAX count (*red*). The 15-point moving average is superimposed (*light grey*) on the ITRAX data

Figures 24.3 and 24.4 show high resolution photographs taken with the Geotek MSCL Linescan Camera (pixel resolution 100 μm) overlain by Zr, Ti and Rb concentrations (Olympus/Geotek) or counts (ITRAX). The elements selected are often used as proxies for the delivery of fine-grained soil derived materials (Rb and Ti) and coarser grained materials (Zr) in this region and type of lake (Boyle et al., this volume; Schillereff et al. 2014).

For the finely-laminated sediments 13.2–13.46 m there is a strong correspondence between the visible stratigraphy and variations in Ti detected in all three scans. Geotek/Olympus 5 mm scan has identified all phases with light-coloured laminations and these are also characterised by higher Ti concentrations. The data resolution cannot discern the structure within intervals containing multiple discrete sub-laminations (e.g. 13.41–13.43 m), but the light layers at 13.22, 13.28, 13.31, 13.35, 13.385, 13.40 and 13.41–13.43 m correspond with positive spikes in Ti concentration. This affirms the value of using low resolution scans, e.g. the 5 mm Geotek/Olympus data shown here, to rapidly (3–4 h per 1.5 m) characterise sequences and in circumstances where the research objectives or chronological control do not require mm resolution, this level of analysis might be all that is required.

The ITRAX and 1 mm Geotek/Olympus scans both appear particularly powerful techniques for analysing heavily laminated sediments, with the Ti data exhibiting numerous peaks that correspond to the lighter layers. Our interpretation is that the Ti is being eroded as finer grained materials in catchment soils. The 1 mm Geotek/Olympus scans appear to have captured the majority of the light bands, although in the heavily-laminated section at 13.41–13.43 m depth, the ITRAX scan picks out four discrete laminations based on maximum Ti count rates while the 1 mm Geotek/Olympus curve only has three peaks. The ITRAX scan data appear more spiky or noisy when contrasted with the 1 mm Geotek/Olympus scans. These differences most likely reflect the configuration of the respective beams. The 1 mm Geotek/Olympus scans were collected by moving a circular 10 mm diameter beam window at 1 mm increments across the micro-laminated sediments. It is very encouraging the level of detail collected notwithstanding the inherent smoothing in this scanning process. The beam passed up the centre of the shown photograph and so the location of the beam matters, for example the peak in Ti at 13.40m corresponds with a lighter layer that is less clearly represented towards the edge of the core. Conversely a second lighter lamination ~4–5 mm below is clear towards the edge of the core but less so in the centre; the Geotek/Olympus scans fail to discern the second lamination probably lost in the smoothing. The ITRAX data were sampled from a $2 \times 0.3$ mm window that also moved across the centre of the core. It samples every aspect of the sediment structure and benefits from a lack of overlap in using a contiguous moving sampling window but is susceptible to discontinuous structure across the core segment. In addition a crack in the core at 13.27 m plots as a trough in Ti reflecting low count rate across the gap, whereas the Geotek/Olympus integrates data from a larger window and is less affected. Both datasets need careful checking for data integrity in the form of discontinuous layers and gaps or blemishes in the core surface.

Rb is also sourced from fine grained materials, probably clay minerals in soils, and shows a very strong correspondence between the photograph and the 1 mm

Geotek/Olympus scan data. All lighter layers correspond with peaks in Rb and dark layers troughs in Rb concentration. The resolution of the scan discerns almost all light coloured units, with the exception at 13.40 m where discontinuous laminations are not sampled or smoothed from the moving 10 mm diameter window. The ITRAX Rb data are intriguing, with the data smoothed to 1 mm showing a strong correspondence to the Geotek/Olympus 1 mm scans. The raw ITRAX data show a very spiky profile that resembles noise. The improved agreement with the Geotek scans resulting from aggregating counts by smoothing suggests that there is structure within the noise of the ITRAX output. Zr reflects the flux of coarser grained materials to the lake, displays some similarities to the other elements (Rb and Ti), though some of the light layers, e.g. 13.33–13.35 m, do not correspond with peaks in Zr, most layers do. Comparison of the 1 mm Geotek/Olympus and ITRAX Zr profiles shows again a noisy raw ITRAX Zr profile that on smoothing better resembles the Geotek/Olympus. There are some notable discrepancies with pronounced shifts from dark to light sediment at 13.22, 13.32 and 13.39 m showing a less clear response in the ITRAX Zr profile.

The sub-section 13.70–13.80 m depth contains two thin, light bands as well as a major stratigraphic feature in the form of a 1.5 cm-thick light-brown unit overlying a 0.5 cm dark black unit (Fig. 24.4). All methods show low values at the bottom of this sub-section, a sharp rise across the black band to maximum concentrations or counts in the light unit and then steadily declining upwards through the core. The slope of the steep rise is similar across all three datasets despite the different data acquisition resolutions. The most prominent feature in the ITRAX data not present in the Geotek/Olympus scans is the internal structure of the light unit. While peak values occurs in the middle of the unit in all plots, the ITRAX data shows a steep rise to the peak and a steadier decline, perhaps reflecting changes in grain-size, Ti is often associated geochemically with the fine-grained fraction (Taboada et al. 2006). The absence of a clear signal in the Geotek/Olympus data reflecting the two thin bands likely relates to the beam diameter not discriminating finer structure. The noisy character to the Rb and Zr ITRAX curves identified in Fig. 24.3 repeats in Fig. 24.4; smoothing the ITRAX data (in essence, extending the count time) produces a stronger match to the Geotek/Olympus data. There is also comparatively lower amplitude noise in the Ti data, visible in particular a dark brown unit below 13.76 m that lacks for laminated structures. Regular fluctuations in count rates for all elements have amplitudes in some cases equivalent to that characterising the thin laminations at 13.726 and 13.738 m. Fluctuations in the 5 mm and 1 mm Geotek/Olympus data are much more muted across this interval. These results suggest caution should be used when interpreting μXRF data from an ITRAX where supporting high-resolution stratigraphic data (photography, radiography or computerised tomography) are not available.

Published deep core records utilising ITRAX data often plot a running mean (e.g., white line: Figs. 24.3 and 24.4) through the dataset to aid visual presentation of long-term datasets (e.g., Kylander et al. 2013). Figure 24.5 compares the 5 mm Geotek data for Rb, Ti and Zr with the corresponding ITRAX counts smoothed using a 15-point running average to generate a dataset of equivalent analytical reso-

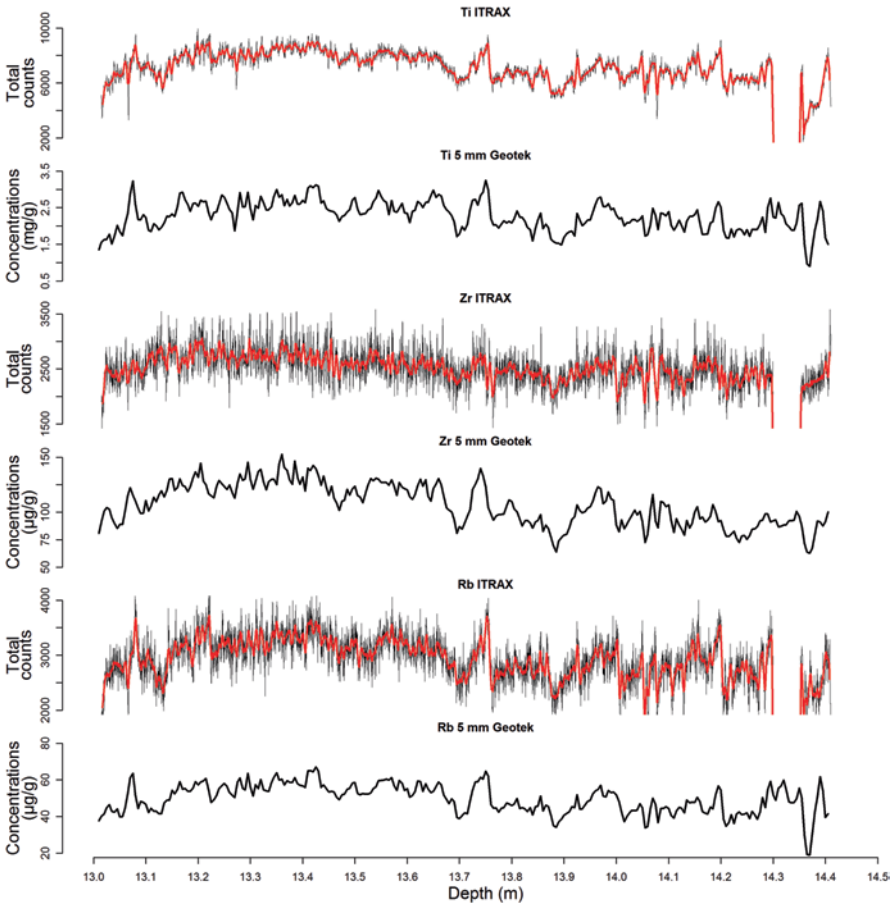


**Fig. 24.5** Count rate and concentrations (*black lines*) for core LoL13-4-1 measured on the ITRAX (*top*) at 0.3 mm and the Geotek (*bottom*) at 5 mm intervals for Ti, Zr and Rb. A 15-point running average has been applied to the ITRAX data (*red line*), plotting the data at a 5 mm equivalent analytical resolution

lution. The 5 mm Geotek and smoothed ITRAX data show highly comparable patterning, most prominent stratigraphic features are identified and fluctuations are predominantly of a similar magnitude between all techniques. Four major troughs in Rb between 14.05 and 14.15 m featured in the ITRAX profile are not as prominent in the Geotek data. Thus we propose that where longer-term palaeoenvironmental changes are the primary research objective, lower resolution but substantially more rapid Geotek scans may be a more appropriate data acquisition approach.

## Correcting µXRF Scan Data to Mass Specific Values

The XRF geochemical data presented here could be for a variety of purposes, but for the most part interest lies in dry mass concentrations for a range of elements, with all expressed as the element concentration divided by the dry mass of sample. µXRF scanning of wet sediment does not operate in this manner, however, with elements typically (semi-)quantified as concentrations (including the ITRAX X-ray count per second), but these values are relative to the density of wet sediment. Boyle et al. (this volume) proposed two correction methods, one of which is novel employing the relative intensities of x-ray backscatter emitted from the XRF instrument mounted on a Geotek/Olympus platform to estimate sediment water content the full-length of a scanned core. This procedure assumes the ratio between Rayleigh (or coherent) and Compton (incoherent) scattering processes varies primarily in response to water content. The ITRAX instrument also collects coherent and incoherent backscatter data. Here we have assessed the relationship between the Geotek/Olympus (1 and 5 mm) and ITRAX backscatter intensities for each of the scans and the general pattern of coherent/incoherent appears repeatable between the ITRAX and Geotek/Olympus. The actual water contents, estimated before and after freeze drying, are low (50–60 %) and vary minimally; as the correction procedure works well for sediment sequences characterised by significant changes in water content (Boyle et al., this volume), the second approach to correcting µXRF data advocated by the authors appears therefore more appropriate. This uses regression equations derived from µXRF element concentrations and equivalent dry mass geochemical data collected for subsamples on a Bruker S2 Ranger ED-XRF (Fig. 24.6).

Overall, six elements yield moderately positive relationships, although the responses are variable between element and instrument, and a relationship is absent for Rb. Overall, the Geotek/Olympus scans produce stronger correlations than the ITRAX device, except for Ca ($R^2$=0.53). K ($R^2$=0.757 for the Geotek/Olympus 5 mm) and Zr ($R^2$>0.6 for 1 mm and 5 mm Geotek/Olympus) generally return the strongest correlations while the 5 mm Geotek/Olympus $R^2$ value for Ti significantly exceeds the other measurements. The fluctuating geochemical profiles visible in the ITRAX dataset throughout the core, not simply characterising the light and dark laminations, likely account for the observed weaker statistical relationships. Nevertheless, Fig. 24.7 illustrates that the regression equations derived from these relationships are sufficiently strong to generate consistent dry-mass corrected concentrations for Ti and Zr. The variable ITRAX Zr curve is derived from the more noisy raw data (Fig. 24.2). This is an encouraging finding as these calibrated concentrations are much more appropriate for comparison to other published µXRF data than attempting to infer similarities and differences between two datasets presented in counts per second, for example.

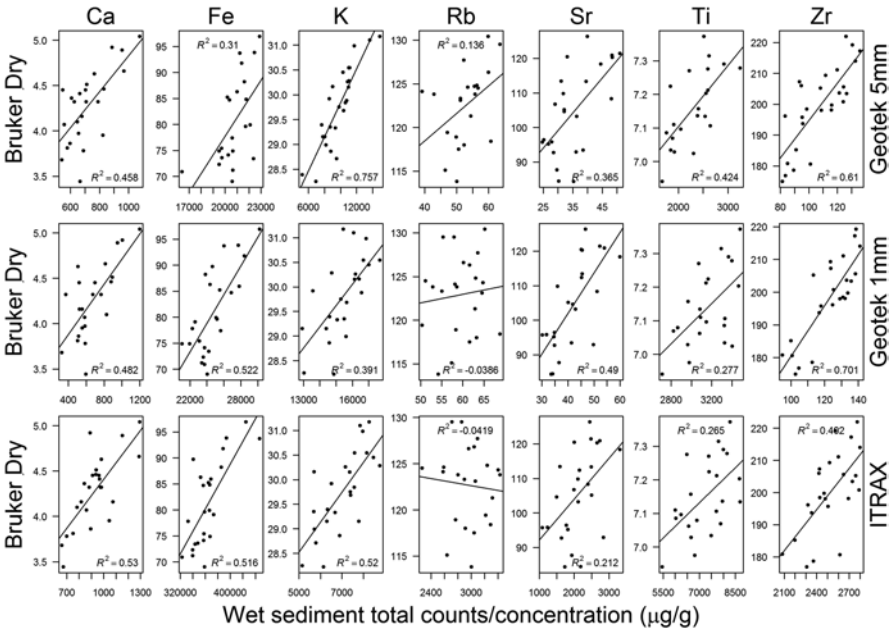


**Fig. 24.6** Scatter plots illustrating the linear relationships and regression coefficients between wet sediment concentrations measured by the Geotek scanner at 5 and 1 mm intervals, count rates emitted by the ITRAX instrument and dry-mass concentrations for 5 cm intervals measured on the Bruker S2 Ranger

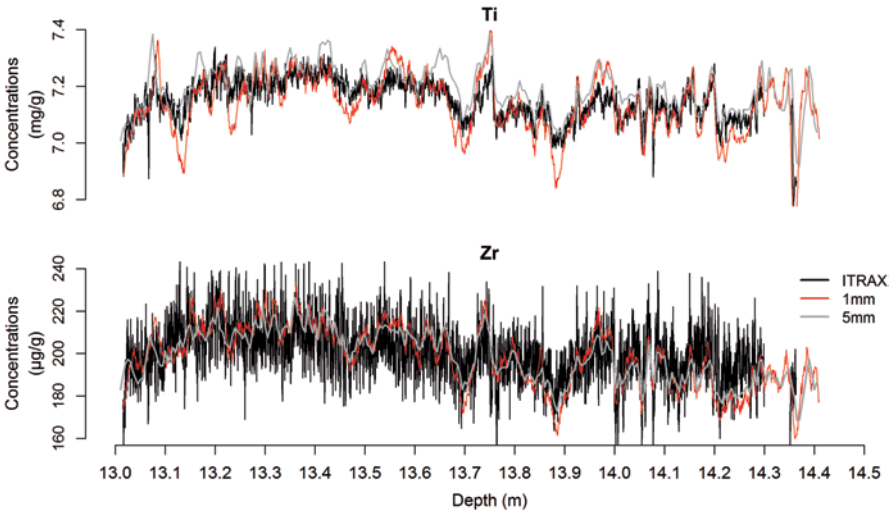


**Fig. 24.7** Profiles of Ti and Zr for core LoL13-4-1 using the three analytical methods and displaying concentrations (mg $g^{-1}$ and μg $g^{-1}$) that have been calibrated to dry-mass equivalent values using the regression correction method. The more variable Zr ITRAX values are derived from the noiser raw dataset

## µXRF Intercomparison for Rock Samples (Laminated Sandstone and Obsidian)

To assess the comparative performance of the three µXRF instruments without the complication of variable water and organic content we ran a short section of intensely laminated North Sea sandstone (57 mm length) and a piece of obsidian glass (52 mm length) on the ITRAX held at NOC-S, the Geotek/Olympus at Liverpool and an Eagle III core scanner (Haschke 2006).

The laminations visible within the sandstone (Fig. 24.8) are generally 2–4 mm thick (occasionally < 1 mm). The dark layers are picked out well by peaks in Ti concentrations measured on the ITRAX and Eagle III, a function of their narrow step size (200 and 180 µm, respectively, compared to the 1 mm interval measurements on the Geotek/Olympus). As a result, the pattern of laminations is difficult to decipher from the Geotek/Olympus data, although the three thicker black layers at 12.4, 12.7 and 13.0 cm depth are represented by subtle peaks. Interestingly, the magnitude between the peaks and troughs is markedly different between the Eagle and ITRAX data and the Eagle III measurements do not appear to fully capture the variable thickness of the dark laminations, for example at 13.7 cm.

A similar background trend in Ti content is observed between the ITRAX and Geotek/Olympus data, with lower values at 12–12.5 and 14–14.5 cm. However, while the majority of the dark laminations are represented by a Ti peak, lower resolution variability is absent in the Eagle III dataset. Instead, the discrete peaks rise from background values that rarely exceed 100 counts throughout the section. Whilst this is useful for recognizing the discrete laminations, any longer-term variability in sediment supply or changes in sediment provenance may be missed.

The obsidian is a useful and robust quality control sample due to its largely homogenous composition and high Si content, as well as moderate values of other major elements (Table 24.1). The obsidian was also measured using WD-XRF enabling a quantitative comparison of the geochemical composition. While the Eagle

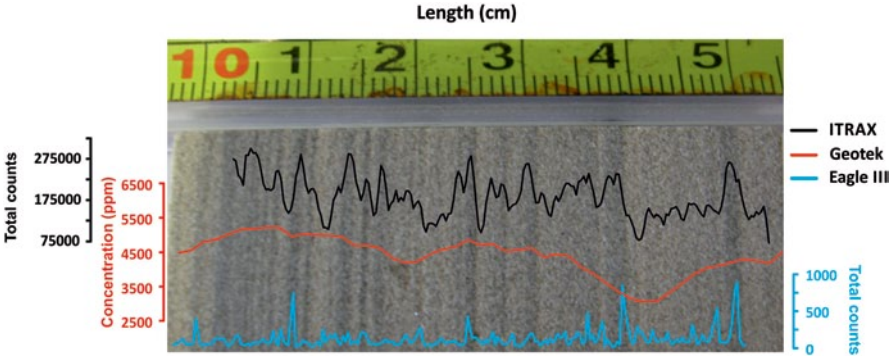


**Fig. 24.8** Photo of the laminated North Sea sandstone section overlain by Ti measurements from the ITRAX (200 µm), Geotek (1 mm) and Eagle III (200 µm) core scanners

III, ITRAX and Geotek/Olympus geochemical profiles are clearly analogous with minimal variability, differences emerge when the measurements are compared to the WD-XRF composition data. For example, mean Si content of the obsidian measured on the Eagle is 70.38 %, close to the WD-XRF value (73.58 %), and 71.3 % on the Geotek/Olympus under MiningPlus mode (expressed as % with average light element, LE content removed). Raw data from the Geotek/Olympus under Mining Plus mode are in ppm but include a substantial contribution from LE (mean 57.73 %; note SOIL mode does not help in this instance as neither Si nor Al are measured). Expressing each element as a percentage of the total non-LE composition (Table 24.1) produces values very similar to the Eagle III and a very close match to the WD-XRF measurements. The relative major element composition measured on the Eagle III and Geotek/Olympus data is equivalent to the WD-XRF data while the ITRAX counts do not follow a similar pattern. It is important to keep in mind that the number of elements chosen to be measured by the operator can influence the data output. The signal-to-noise ratios assessed by comparing the standard deviations of the three scans are impressive, with comparative poorer performance from the Getek/Olympus probably a function of fewer data points and lower scan resolution. For Si, the Geotek/Olympus σ was 1.93 %, 0.6 % on the Eagle and 0.99 % on the ITRAX. For Fe, the Geotek/Olympus σ was 1.08 %, 0.005 % on the Eagle and 0.41 % on the ITRAX.

## Conclusions

The results from Loch of the Lowes show that, at this site, the geochemical composition of a wet sediment core is well estimated using both a Geotek/Olympus and an ITRAX core scanner. Most importantly, we show for the first time that μXRF data acquired using different instruments exhibit similar patterning, overall. One useful result is that the 5 mm scans performed using the Geotek/Olympus platform captured the vast majority of prominent stratigraphic features, despite its comparatively low analytical resolution, as all phases of lighter, more mineral-rich laminations were characterised by higher concentrations of Ti, Rb and Zr (Figs. 24.3 and 24.4). A key question we sought to address in this chapter is whether the finer resolution geochemical data offered insight into environmental changes missed by other techniques. Our results suggest the answer will depend on the research objectives of individual projects: 5 mm runs are sufficient to geochemically characterise most sedimentological shifts instead of plotting smoothed ITRAX data. Analysing annually-laminated sequences or identifying geochemical shifts across event layers will require finer resolution data acquisition, however, and the associated increased time and costs.

The diameter of the Geotek/Olympus laser aperture means some overlap between samples is inevitable. As a result, some fine laminations were not captured by the 1 mm runs, especially where they are located within a matrix of geochemically-different material. The ITRAX measurements (undertaken at 200 μm intervals)

were able to distinguish these mm-/sub-mm scale light and dark bands, confirming its value when annually-laminated sequences, event deposits or tephra layers are being analysed. However, the ITRAX data also showed peaks and troughs with similar amplitudes to the laminated sections across intervals where no stratigraphic changes were visible (Fig. 24.4). This may be a particular issue for long cores with no visible stratigraphic boundaries but highly fluctuating geochemical profiles. Our data also show that μXRF core scanning devices are sensitive to non-continuous laminations; operators should pay particular attention where discrete layers do not extend across the full core width.

The geochemical characterisation of sediments is often most effective when dry material is being measured. Our results are encouraging, indicating that despite the statistical relationships between the Geotek/Olympus or ITRAX measurements and the calibration dataset varying in strength (Fig. 24.6), the dry-mass corrected values were very similar. We thus advocate that future published μXRF data is presented as concentrations calibrated to the dry sediment equivalent to facilitate more robust inter-comparison regardless of the method employed.

Finally, the μXRF scanning for whole rock samples (sandstone and obsidian) show a strong inter-comparability, but reinforce the need for careful assessment of μXRF data quality and indicate that directly comparing published geochemical data from sedimentary sequences without fully considering differences in instrument configuration and sample characteristics should be avoided. There is clearly scope to conduct more detailed inter-comparisons of the different μXRF core scanners currently used by palaeoenvironmental scientists.

**Acknowledgements** D. Schillereff is the recipient of a PhD Graduate Teaching Assistantship from the School of Environmental Sciences at the University of Liverpool. D. Schillereff also gratefully acknowledges financial support from The British Society of Geomorphology to conduct the ITRAX scans at the National Oceanography Centre Southampton under the guidance of Professor Ian Croudace. We also appreciate the thoughtful and constructive comments of Professor Andy Cundy and Professor Phil Warwick that improved the final manuscript.

## References

Boyle JF (2001) Inorganic geochemical methods in palaeolimnology. In: Last WM, Smol JP (eds) Tracking environmental change using lake sediments. Volume 2: physical and geochemical methods. Kluwer, Dordrecht, pp 83–142

Croudace IW, Rindby A, Rothwell RG (2006) ITRAX: description and evalutation of a new multi-function X-ray core scanner. In: Rothwell RG (ed) New techniques in sediment core analysis. Geological Society of London Special Publications pp 51–63

Cuven S, Paris R, Falvard S, Miot-Noirault E, Benbakkar M, Schneider J-L, Billy I (2013) High-resolution analysis of a tsunami deposit: case-study from the 1755 Lisbon tsunami in south-western Spain. Mar Geol 337:98–111

Czymzik M, Brauer A, Dulski P, Plessen B, Naumann R, von Grafenstein U, Scheffler R (2013) Orbital and solar forcing of shifts in Mid- to Late Holocene flood intensity from varved sediments of pre-alpine Lake Ammersee (southern Germany). Quat Sci Rev 61:96–110

Foster GC, Chiverrell RC, Harvey AM, Dearing JA, Dunsford H (2008) Catchment hydro-geomorphological responses to environmental change in the Southern Uplands of Scotland. The Holocene 18:935–950

Francus P, von Suchodoletz H, Dietze M, Donner RV, Bouchard F, Roy A-J, Fagot M, Verschuren D, Kröpelin S (2013) Varved sediments of Lake Yoa (Ounianga Kebir, Chad) reveal progressive drying of the Sahara during the last 6100 years. Sedimentology 60:911–934

Haschke M (2006) The Eagle III BKA system, a novel sediment core X-ray fluorescence analyser with very high spatial resolution. In: Rothwell RG (ed) New techniques in sediment core analysis, vol 267. Geological Society of London Special Publications, London, pp 21–37

Hennekam R, de Lange G (2012) X-ray fluorescence core scanning of wet marine sediments: methods to improve quality and reproducibility of high-resolution paleoenvironmental records. Limnol Oceanogr Methods 10:991–1003

Jansen J, Van der Gaast S, Koster B, Vaars A (1998) CORTEX, a shipboard XRF-scanner for element analyses in split sediment cores. Mar Geol 151:143–153

Kylander ME, Klaminder J, Wohlfarth B, Löwemark L (2013) Geochemical responses to paleoclimatic changes in southern Sweden since the late glacial: the Hässeldala Port lake sediment record. J Paleolimnol 50:57–70

Marshall M, Schlolaut G, Nakagawa T, Lamb H, Brauer A, Staff R, Ramsey CB, Tarasov P, Gotanda K, Haraguchi T, Yokoyama Y, Yonenobu H, Tada R (2012) A novel approach to varve counting using μXRF and X-radiography in combination with thin-section microscopy, applied to the Late Glacial chronology from Lake Suigetsu, Japan. Quat Geochronol 13:70–80

Murray J, Pullar L (1910) Bathymetrical survey of the fresh-water lochs of Scotland

Ojala AEK, Francus P, Zolitschka B, Besonen M, Lamoureux SF (2012) Characteristics of sedimentary varve chronologies—a review. Quat Sci Rev 43:45–60

Richter TO, van der Gaast S, Koster B, Vaars A, Gieles R, de Stigter HC, De Haas H, van Weering TCE (2006) The Avaatech XRF core scanner: technical description and applications to NE Atlantic sediments. Geolog Soc Lond Spec Publ 267:39–50

Schillereff DN, Chiverrell RC, Macdonald N, Hooke JM (2014) Flood stratigraphies in lake sediments: a review. Earth-Sci Rev 135:17–37

Schlolaut G, Brauer A, Marshall MH, Nakagawa T, Staff RA, Bronk Ramsey C, Lamb HF, Bryant CL, Naumann R, Dulski P, Brock F, Yokoyama Y, Tada R, Haraguchi T (2014) Event layers in the Japanese Lake Suigetsu "SG06" sediment core: description, interpretation and climatic implications. Quat Sci Rev 83:157–170

Taboada T, Cortizas AM, García C, García-Rodeja E (2006) Particle-size fractionation of titanium and zirconium during weathering and pedogenesis of granitic rocks in NW Spain. Geoderma 131:218–236

Weltje GJ, Tjallingii R (2008) Calibration of XRF core scanners for quantitative geochemical logging of sediment cores: theory and application. Earth Planet Sci Lett 274:423–438

# Chapter 25
# Analysis of Coal Cores Using Micro-XRF Scanning Techniques

**Sarah J. Kelloway, Colin R. Ward, Christopher E. Marjo, Irene E. Wainwright and David R. Cohen**

**Abstract** This chapter explores the application of micro-XRF scanning to the inorganic geochemical analysis of drill cores obtained from coal exploration programs. It describes the development and use of a calibration to obtain detailed quantitative profiles of major inorganic elements through cores of bituminous coal seams, and hence allow rapid evaluation of mineral matter variations at a much greater detail than traditional bulk sampling techniques. The calibration was applied to core segments from an Australian coal seam, to quantify micro-XRF data obtained at 200 µm intervals using an Itrax core scanner system. In combination with high resolution optical imaging and X-radiography, also obtained from the scanning process, this enabled a detailed understanding of the variations in inorganic element characteristics through each coal segment, which could then be related to the distribution of particular mineral matter components. Such an approach can be used to provide a better understanding of the factors responsible for variations in coal quality, including the distribution of elements within the seam having particular economic or environmental significance.

**Keywords** Coal analysis · Itrax core scanner · Mineral matter · X-radiography · XRF spectrometry

## Introduction

Coal is an organic sedimentary rock, composed essentially of lithified plant debris (Thomas 2001; Ward 1984, 2013). While the organic matter is the main component for most considerations, the admixed mineral and inorganic material, collectively referred to as mineral matter (Ward 2002), is also significant in understanding the

C. R. Ward (✉) · D. R. Cohen
School of Biological Earth and Environmental Sciences, University of New South Wales, Sydney, NSW 2052, Australia
e-mail: c.ward@unsw.edu.au

S. J. Kelloway · C. E. Marjo · I. E. Wainwright
Mark Wainwright Analytical Centre, University of New South Wales, Sydney, NSW 2052, Australia



I. W. Croudace, R. G. Rothwell (eds.), *Micro-XRF Studies of Sediment Cores*, Developments in Paleoenvironmental Research 17, DOI 10.1007/978-94-017-9849-5_25

processes of coal formation, and in assessing the suitability of individual coal deposits for different industrial purposes (e.g. Bryers 1996; Suárez-Ruiz and Crelling 2008).

The different components of the mineral matter are unevenly distributed within coal seams, due to a combination of the coal's depositional and post-depositional history. Bulk sampling techniques have traditionally been used to determine the inorganic chemistry of coal seam cores (Standards Australia 1993); length-based portions of the core are sampled and ashed, and the resultant ash is analysed using inductively coupled plasma (ICP) or wavelength-dispersive X-ray fluorescence (WD-XRF) spectrometry techniques. This approach can be used to accurately characterise large amounts of coal from individual seams or deposits, and provide data of great value to resource assessment and mine planning operations. However, the selection of intervals for such sampling inherently involves a trade-off between the length of core sampled and the spatial resolution required to assess the mineral matter distribution. Sampling of shorter lengths for more detailed assessment may significantly increase the total cost of the analysis program.

The advent of micro-XRF core scanner technology has meant that drill cores of coal seams can be analysed relatively rapidly at millimetre to sub-millimetre scales with energy-dispersive X-ray fluorescence (ED-XRF) spectrometry. Such technology allows all the major inorganic elements of interest in coal to be analysed, with the exception of Na and Mg, which are light elements that usually occur only in low concentrations (Dai et al. 2012). The amount of data obtained from such scanning is much larger than that gained from traditional bulk sampling and analysis; for example up to 10,000 separate analyses may be obtained per metre of coal using core scanner techniques. When evaluated in combination with high-resolution optical imaging and X-radiography, also obtained in the core scanning process, a detailed understanding of the variations in inorganic element characteristics along the core can readily be achieved.

This chapter provides an overview of recent experience in using the Itrax core scanner to provide detailed quantitative profiles of major inorganic elements in different segments of coal seam drill core (Kelloway et al. 2014b). The results of the chemical profiling are also assessed in conjunction with optical images and X-radiographs, as well as other chemical, mineralogical and lithological features of the coals concerned.

## Coal Samples Studied

### *Coal Core Segments*

A series of core segments to evaluate the application of the Itrax scanner to coal seams were taken from a core of the Goonyella Middle seam, a Permian age bituminous coal in the Moranbah Coal Measures, northern Bowen Basin, Australia (Mallett et al. 1995). Previous X-ray diffraction studies by Henwood (2004) indicate that the coals of this seam typically contain 13–23 % mineral matter, consisting

mainly of quartz (15–60 %), kaolinite (20–50 %) and interstratified illite/smectite (15–30 %), with minor amounts of siderite (3–6 %) and traces of ankerite in some parts of the seam.

A significant part of the core had been crushed for other studies and was unsuitable for scanning, but a number of intact core intervals, located between sampled sections, were still available to test the capability of the scanning system. Nine segments of coal were selected, 100–150 mm in length, and analysed using the Itrax core scanner. The segments were made up of interbedded dull (inertinite-rich) to bright (vitrinite-rich) coal lithotypes with admixed mineral matter. The cores, approximately 60 mm in diameter, were analysed without further preparation, except for one segment (segment 9, see below) which was used to cross-check the scanner results.

### *Calibration Standards*

Powdered and pressed reference coals from other sources were used to provide a basis for calibration, following a process more fully described by Kelloway et al. (2014a). These calibration standards included an international reference material from South Africa (SARM-18, Ring and Hansen 1984); a range of reference coals prepared and extensively analysed by CSIRO Energy Technology, Australia; and coals from several other sources analysed for different purposes at the University of New South Wales. The latter included four coal samples taken from the same seam as the core segments described above.

## Analysis Techniques

### *Chemical Analysis of Calibration Samples*

Subsamples (~11 g) of the reference coals for calibration, and also the coal of segment 9 (after scanning), were ashed at 815 °C for a minimum of 8 h, except SARM-18, for which published concentration values are available. The ashes were fused into 40 mm diameter glass beads at 1050 °C for 15 min (Norrish and Hutton 1969) using 12:22 lithium borate flux (1:10 sample:flux ratio), and the glass beads analysed using a Philips PW2400 XRF spectrometer to determine the element oxide concentrations (weight percent) in each ash. These were then back-calculated and expressed as percentages of the respective elements (or oxides) in the original whole-coal samples. Sulphur concentrations were determined by analysing approximately 0.1 g of each powdered whole coal using a LECO TruSpec Sulfur Module, with a reference coal supplied by Standards Australia (ASCRM-009) used to check the (total) sulphur percentages obtained.

Powdered subsamples of each reference coal were pressed into 40 mm diameter aluminium caps at a pressure of 20 t, with Ceridust (wax) as a binder using a sample

to wax ratio of 10:1; one coal (SARM-18), however, had previously been pressed into a pellet using a sample to wax ratio of 9:1 under the same pressure conditions. The pressed pellets were analysed using the Itrax, and calibration curves for the different elements were developed as described more fully by Kelloway et al. (2014a).

One of the core segments (segment 9) had been split by a natural fracture along the core axis. The natural surface of this fracture was smoothed to create a hemicylindrical core segment using 1200-grade wet abrasive paper, and both the flat and curved surfaces of this segment were scanned to provide a basis for comparison. After scanning the core was powdered, ashed and analysed in the same way as the other calibration standards. The results were used to provide a cross-check of the scanner results against independent WD-XRF data (Kelloway et al. 2014b).

## *Analysis of Cores and Standards using the Core Scanner*

The coal core segments and calibration standards were analysed using the Itrax core scanner housed at the Mark Wainwright Analytical Centre, University of New South Wales. The core segments were placed in a 100 mm diameter acrylic tube half, 5 mm thick. A high-resolution optical image of each core segment was obtained, along with an X-radiographic image. The segments were then analysed by ED-XRF using a Cr-anode X-ray tube at steps of 200 µm. The radiograph for each segment was collected using 60 kV and 30 mA with a 1600 ms exposure time; the XRF conditions for profiling were 30 kV and 30 mA with an exposure time of 15 s. The area of the radiograph at each step was 16 mm by 100 µm, and 8 mm by 100 µm for each step for XRF analysis.

The curved surface of each segment was analysed, except for segment 9, for which both the flat and curved surfaces were analysed. Kelloway et al. (2014a) found that core scanner analysis of curved and flat sample surfaces produce very similar chemical data. Scratched and pitted surfaces on coal cores, however, may have some impact on the chemical profiles obtained. If the drill cores are analysed without being split, as in the present study, the coal core can still be subjected, after scanning, to a conventional analysis program. The flat surfaces of the calibration standard pellets were analysed by the scanner under the same conditions as the core segments (Kelloway et al. 2014a).

Cox *Core Scanner* software (v8.6.3) was used to operate the instrument; *Q-spec* software (v8.6.0) was used to carry out spectra fitting and deconvolution, as well as to determine peak areas. The concentration data for each standard and the respective peak areas obtained from processing the ED-XRF data from the Itrax analysis of each standard were used to develop a calibration, including a Compton ratio correction (Kelloway et al. 2014a). The resultant calibration curves (Fig. 25.1) were then used to obtain concentration data for each element in the ED-XRF profile for each core segment. *Matlab* was used to create false colour X-radiographs from the monochrome data produced by the core scanner, *Adobe Photoshop* was used to adjust optical images, and *Microsoft Excel 2007* and *ItraxPLOT (Raddec Ltd, Southampton UK)* were used to display the data.

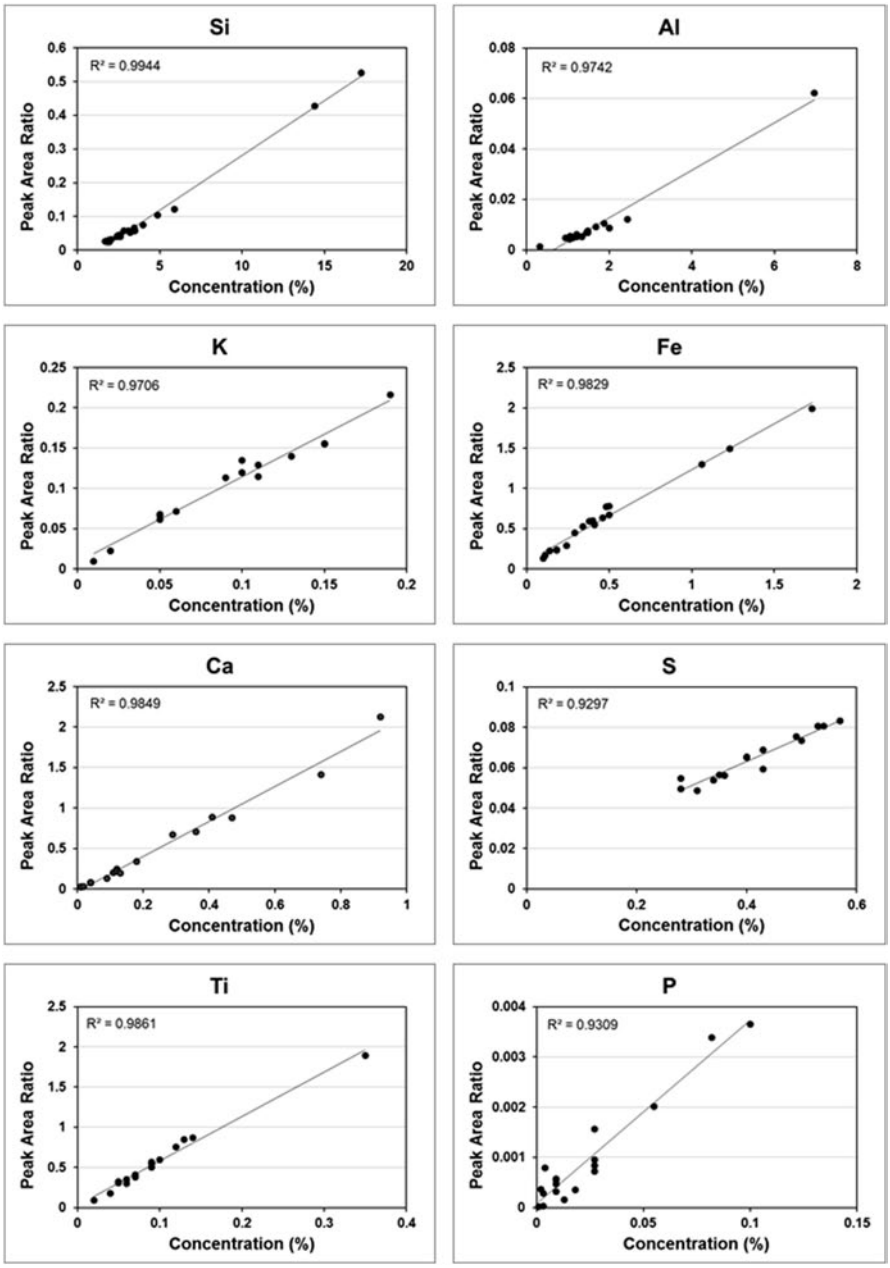


**Fig. 25.1** Calibration curves for elements studied, showing peak area ratio plotted against the concentration of each element in the calibration samples (after Kelloway et al. 2014a). The linear correlation coefficients ($R^2$) in each case are also shown

## Qualitative Element Profiles

The peak area data for the elements of interest were compiled for each segment using *Microsoft Excel* and plotted against their respective positions (depth) to create a set of qualitative elemental profiles for each core segment. Figure 25.2 provides an example of such a profile. The Z values in Fig. 25.2 represent the distance in mm from the top of the carriage on which the core segments were placed. The optical image and X-radiograph of the core segment are also displayed, both of which were copied from the scanner system, processed using *Adobe Photoshop*, and scaled and positioned to match the intensity profiles.

The element profile in Fig. 25.2 shows fluctuations in peak intensity for the elements at a millimetre to sub-millimetre scale. The element profile and X-radiograph also show that the intensity fluctuations for each element are related to features in the coal core. Although the XRF data are drawn from the near-surface of the core (ranging from microns to centimetres depending on the critical depth for each element) and the X-radiographs represent X-ray scattering through the entire segment, the comparison still provides a basis for interpreting the links between the various elements and the macroscopic features of the coals' mineral matter.

The peak intensity profiles for Si, Al and K in Fig. 25.2 each show a similar pattern of fluctuation, suggesting that they represent variations in the abundance of a K-bearing aluminosilicate assemblage within the core segment. Highest intensities for all three elements are developed opposite the dark (mineral-rich) horizon in the X-radiograph at around Z = 200 mm, consistent with more stony coal in that part of the section. Since the main minerals in the coal are quartz, kaolinite and interstratified illite/smectite (Henwood 2004), the intensity fluctuations in Si, Al and K shown in Fig. 25.2 are consistent with variations in the proportions of quartz and clay relative to the proportion of organic matter. The intensity profile for Ti shows a similar pattern of fluctuation, suggesting an association of Ti with this admixed clay-rich material. Ti and P also show a sharp spike just above Z = 200 mm, consistent with similar spikes in the Al and K profiles.

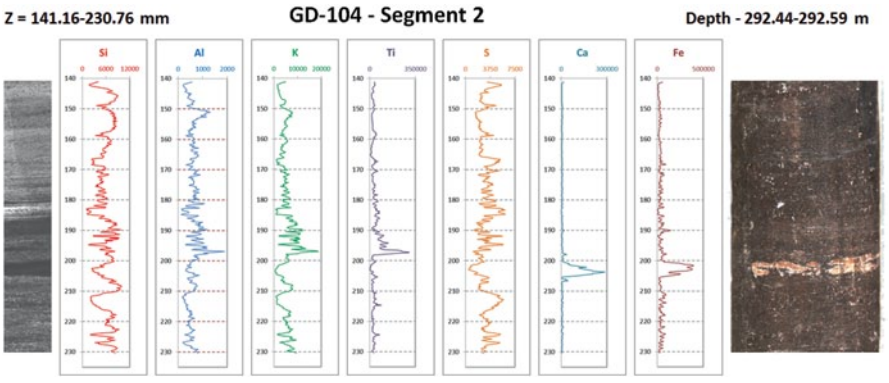


**Fig. 25.2** Qualitative chemical profile of Grosvenor coal segment 2, showing element peak area profiles together with corresponding optical image and radiograph

The profiles for Fe and Ca, although different to the Si-Al-K series, are broadly similar to each other, with each having a broad peak at around Z = 205 mm and low values throughout the rest of the interval. This increase in Fe and Ca intensity corresponds to a prominent non-coal band in the optical image, which from other studies (e.g. Patterson et al. 1994; Henwood 2004) probably represents a layer of Ca-bearing siderite nodules. Smaller fluctuations also occur in the rest of the profile for Fe, especially below Z = 170 mm. Comparison to the X-radiograph, where dark spots are visible within the lighter-coloured organic matter, suggests that these fluctuations may represent smaller siderite nodules within the coal bed.

The profile for S fluctuates to some extent throughout this core segment, but indicates particularly low intensities in the interval where the highest intensities for Fe are developed. This suggests that the sulphur in the coal is mainly associated with the organic matter; the lack of correlation between Fe and S suggests that pyrite is not a significant part of the mineral matter in this coal.

## Quantitative Element Profiles

Qualitative profiles such as that in Fig. 25.2 may provide general information on the distribution of elements within the core, as well as the correlations of individual elements to each other and to the macroscopic features of the coal. However, the peak area values in these profiles are not directly related to the overall abundance of the respective elements in the coal itself. To provide a more quantitative set of profiles, with concentration data for each element, the peak area data were calibrated using the procedure indicated above, and more fully described by Kelloway et al. (2014a). Comparative tests on a control coal sample indicate that the percentages derived from the calibration (Fig. 25.1) are semi-quantitative rather than quantitative (Kelloway et al. 2014a), although the concentrations obtained were mostly very close to the published values for the control sample.

The concentration data for the segments were displayed using ItraXPlot (v2.61). The element concentrations were also calculated to provide the element oxide concentrations (e.g. $SiO_2$, $Al_2O_3$, CaO, $Fe_2O_3$) of the whole-coal for each analysed step (Fig. 25.3). Representing the elements as oxides provides a better basis for comparison to conventional ash analysis data, and broadens the potential application of core scanner data to resource evaluation and utilisation studies. Sulphur and phosphorus were presented as element percentages, in accordance with the common reporting formats in coal quality evaluations. False colour X-radiographs were used to facilitate the evaluation of mineral matter distributions, allowing a better differentiation of various features than the monochrome X-radiographs. Cool colours, such as deep blue, represent the organic-rich areas whereas warm colours, such as bright red, represent the dense, mineral-rich areas.

The total of the element oxide percentages ($\sum Ox = SiO_2 + Al_2O_3 + K_2O + TiO_2 + CaO + Fe_2O_3 + P_2O_5$) was also plotted for each core segment. Although the $Na_2O$ and MgO concentrations were not included, the total approximates the expected percentage of inorganic residue/ash at each increment. The level of Compton backscattering (Cr

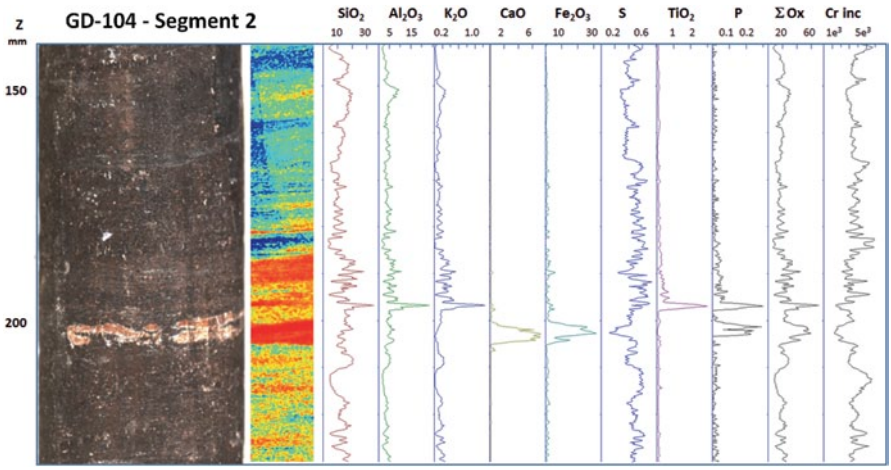


**Fig. 25.3** Quantitative profile for segment 2, showing optical image (*left*), false-colour X-radiograph and percentages of elements or element oxides as fractions of the coal. The sum of the element oxides (∑Ox) and the level of Compton backscattering (as peak area) is also plotted

inc), expressed as the relevant peak area, is also given in these plots. This value is inversely proportional to the density and average atomic number of the material, and effectively represents the relative amount of organic matter in each part of the coal core.

Figure 25.3 provides the quantitative profiles, false-colour X-radiograph and optical image for segment 2; similar images for other segments are provided by Kelloway et al. (2014b). As might be expected, the individual profiles are similar in form to the corresponding profiles in Fig. 25.2; however, the calibration step also allows the actual percentages of each oxide or element associated with the various fluctuations to be evaluated. Some of the indicated percentages are outside the range covered by the calibration curves in Fig. 25.1, but still provide a useful indication of the concentrations involved.

The percentage of $SiO_2$ ranges from around 5 % to around 20 % within this cored interval, with a thin band having more than 30 % near Z = 200 mm. Alumina ($Al_2O_3$) ranges from approximately 3–10 % with a peak near Z = 200 mm of more than 20 %, and $K_2O$ ranges up to around 0.4 % with a peak of over 1 %. Lowest values for all three oxides occur at Z = 150, 160, 185 and 215 mm, corresponding to horizons with lower proportions of mineral matter in the X-radiograph. The proportion of $TiO_2$ is generally low, but increases to around 0.5 % and peaks at more than 2 % in the interval with high $SiO_2$, $Al_2O_3$ and $K_2O$ near Z = 200 mm.

The proportion of $Fe_2O_3$ is mostly around 1 %, but increases to more than 30 % in the probable sideritic horizon just below Z = 200 mm. The proportion of CaO increases to around 6 % at this same horizon, closely but not precisely following the $Fe_2O_3$ profile. Although electron microprobe studies by Patterson et al. (1994) indicate that siderite nodules in some Australian coals may also contain significant proportions of Ca, the presence of white coloured edges around the nodular bodies of this horizon in Fig. 25.3 suggest that a separate Ca-rich carbonate (calcite or possibly dolomite) may also contribute to the high CaO concentrations. Sharp spikes in

the profile for P (up to around 0.3 %) occur both in association with the high $TiO_2$ percentage above Z = 200 mm and the high proportion of $Fe_2O_3$ just below that level.

Sulphur typically makes up around 0.6 % of the coal over most of the core segment, but decreases to as low as 0.2 % in some of the mineral-rich intervals. Coals from other deposits in the Moranbah Coal Measures typically have total sulphur contents of around 0.6 % (dry ash-free), with the sulphur being almost entirely occurring in organic form (ACARP 2010). The lower percentages of S in the mineral-rich intervals of segment 2 are consistent with dilution of such organic sulphur by higher proportions of mineral matter.

## Total Oxides and Compton Backscatter

Also included in Fig. 25.3 is a profile representing the sum of the major-element oxides (∑Ox), except sulphur, for each increment in the segment. Although the percentages of $Na_2O$ and MgO are not included, this value provides a close approximation to the expected ash yield for each step analysed. The Compton backscatter profile measured by the scanner (Cr inc) is also plotted. This profile appears to be inversely related to that of the ∑Ox values. As discussed by Ward (1984) and Thomas (2001), the level of Compton backscattering in coal depends on the proportion of light elements, especially the carbon making up the bulk of the organic matter. As such it would be expected to be highest in those parts of the segment with less dilution of the organic matter by mineral components, and to decrease as the proportion of mineral matter increases.

Figure 25.4 shows the relationship between ∑Ox and the reciprocal of the Cr inc values for segment 2. Such a relationship also forms the basis for interpreting coal quality from down-hole density (gamma-gamma) logs in coal exploration programs.

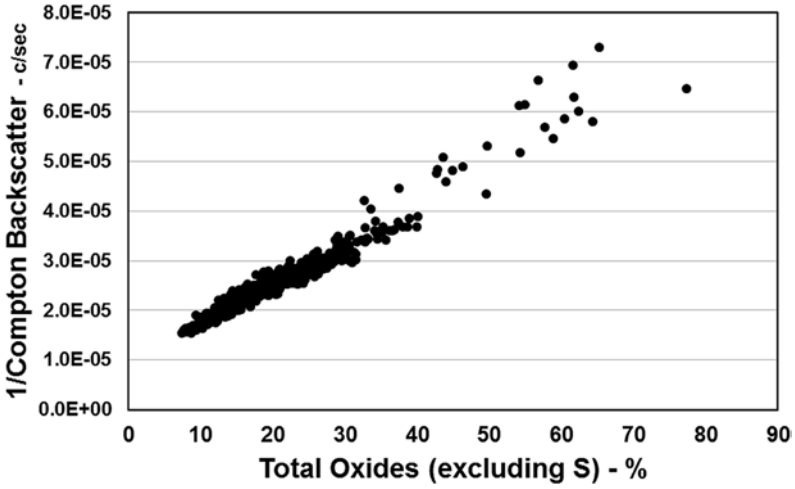


**Fig. 25.4** Inverse relationship between total Compton backscatter peak area (Cr inc) and total percentage of inorganic oxides (∑Ox) for core segment 2

## Comparison to Bulk Coal Chemistry

As discussed further by Kelloway et al. (2014b), a core scanner profile was also obtained through a short segment of coal core (segment 9), 25 mm in length, which had been naturally split by a planar joint fracture parallel to the core axis. This segment was scanned on both its curved and flat surfaces; although differences were observed for some elements (e.g. $TiO_2$, $Fe_2O_3$), reflecting the fact that different 8 mm strips along the core surface were measured in each case, the overall pattern for most elements in the two profiles was found to be broadly similar.

The average chemical composition of segment 9 was calculated for each scan from the individual element or oxide percentages measured at each step. Although a simple numerical average could have been used, a weighted average calculation was applied (Kelloway et al. 2014b), to allow for the higher density expected from the more mineral-rich parts of the scanned interval. The density-weighted composite percentages for the various components, calculated from the scans of both the curved and the flat core surfaces, are shown in Table 25.1.

The coal from the entire core segment was crushed after scanning. A representative sample of the crushed coal was then ashed at 815 °C, and the chemical composition of the ash determined using WD-XRF techniques. The total sulphur content of the crushed coal was also determined using a LECO TruSpec Sulfur Module. Table 25.1 shows the percentage of ash determined for the crushed coal sample, as well as the total sulphur and each the percentages of each inorganic component in the coal as measured by direct chemical analysis of the ash material. Although the core scanner data are regarded as being semi-quantitative from the calibration process (Kelloway et al. 2014a), the percentages calculated from the scan profiles for this segment are very close to the respective percentages measured on the same coal by direct chemical techniques.

**Table 25.1** Element or oxide concentrations for segment 9 (after Kelloway et al. 2014b), based on density-weighted averages of Itrax data for scans on flat and rounded core surfaces, compared to equivalent concentrations determined by WD-XRF analysis of coal ash and expressed on a whole-coal basis

| | $SiO_2$ | $Al_2O_3$ | $K_2O$ | $Na_2O$ | MgO | CaO | $Fe_2O_3$ | $TiO_2$ | $P_2O_5$ | Ash | S |
|---|---|---|---|---|---|---|---|---|---|---|---|
| Curved | 12.22 | 3.03 | 0.11 | ND | BLD | 0.10 | 0.05 | 0.07 | 0.02 | 15.60 | 0.65 |
| Flat | 12.52 | 2.54 | 0.09 | ND | BLD | 0.05 | 0.00 | 0.05 | 0.00 | 15.25 | 0.66 |
| Analysed | 11.72 | 2.34 | 0.09 | 0.09 | 0.08 | 0.02 | 0.07 | 0.06 | 0.01 | 14.86 | 0.54 |

*BLD* below detection limit, *ND* not determined, *Ash* ∑Ox for Itrax data; otherwise ash at 815 °C

## Conclusions

Analysis of coal drill cores using the Itrax core scanner enables a detailed understanding of the distribution of mineral matter, based on significantly smaller increments than traditional bulk sampling techniques. Concentration profiles of the major elements of interest can be determined, except Na and Mg; when combined with high resolution optical imaging and X-radiography, these profiles can aid in relating the results to features in the coal core, such as nodules and clay bands.The sum of the available elemental concentrations can be used to calculate the total percentage of inorganic elements measured by the scanner ($\sum$Ox). This value is similar to the percentage of ash expected from proximate analysis. It is also inversely related to the Compton backscatter profile measured by the scanner, potentially enabling core scanner profile data to be related to down-hole density (gamma-gamma) logs, widely used in coal exploration and mine geology studies.

**Acknowledgements** The assistance of CSIRO Energy Technology, especially Dr David French, for provision of coal samples to assist the calibration process is gratefully acknowledged. Thanks are also expressed to Professor Ian Croudace of the National Oceanography Centre, Southampton, for assistance in developing the chapter.

## References

Australian Coal Association Research Program (ACARP) (2010) Quality of Australian black coals: physical and chemical properties. Report on Project C17053, Australian Coal Research Limited, Brisbane, 72 pp

Bryers RW (1996) Fireside slagging, fouling and high-temperature corrosion of heat transfer surface due to impurities in steam-raising coals. Prog Energy Combust Sci 22:29–210

Dai S, Ren D, Chou CL, Finkelman RB, Seredin VV, Zhou Y (2012) Geochemistry of trace elements in Chinese coals: a review of abundances, genetic types, impacts on human health, and industrial utilization. Int J Coal Geol 94:3–21

Henwood RE (2004) Mineral matter variations in the Goonyella Middle seam, Grosvenor Downs: a comparison with CSIRO's HyLogger™. BSc. thesis, School of Biological, Earth and Environmental Sciences, University of New South Wales, Australia

Kelloway SJ, Ward CR, Marjo CE, Wainwright IE, Cohen DR (2014a) Calibration for ED-XRF profiling of coal core using the Itrax core scanner. Powder Diffr 29(S1):S28–S34

Kelloway SJ, Ward CR, Marjo CE, Wainwright IE, Cohen DR (2014b) Quantitative chemical profiling of coal using core-scanning X-ray fluorescence techniques. Int J Coal Geol 128–129:55–67

Mallett CW, Pattison P, McLennan C, Balfe P, Sullivan D (1995) Bowen Basin. In: Ward CR, Harrington HJ, Mallett CW, Beeston JW (eds) Geology of Australian coal basins, vol 1. Geological Society of Australia Coal Geology Group Special Publication, pp 299–339

Norrish K, Hutton JT (1969) An accurate X-ray spectrographic method for the analysis of a wide range of geological samples. Geochim Cosmochim Acta 33:431–453

Patterson JH, Corcoran JF, Kinealy KM (1994) Chemistry and mineralogy of carbonates in Australian bituminous and sub-bituminous coals. Fuel 73:1735–1745

Ring EJ, Hansen RG (1984) The preparation of three South African coals for use as reference materials. Report M169, Council for Mineral Technology, 130 pp

Standards Australia (1993) Guide to the technical evaluation of hard coal deposits. Australian Standard 2519. 60 pp
Suárez-Ruiz I, Crelling JC (eds) (2008) Applied coal petrology: application of petrology to coal utilization. Academic, Amsterdam, 388 pp
Thomas L (2001) Coal geology. Wiley, London, 338 pp
Ward CR (ed) (1984) Coal geology and coal technology. Blackwell Scientific Publications, Melbourne, 345 pp
Ward CR (2002) Analysis and significance of mineral matter in coal seams. Int J Coal Geol 50:135–168
Ward CR (2013) Coal geology. In: Elias S (ed) Reference modules in earth systems and environmental sciences. 30 pp. http://www.sciencedirect.com/science/referenceworks/9780124095489

# Chapter 26
# ItraxPlot: An Intuitive Flexible Program for Rapidly Visualising Itrax Data

**Ian W. Croudace and R. Guy Rothwell**

**Abstract** ItraxPlot is data visualization software specifically designed to rapidly and efficiently display Itrax micro-XRF core scanner data to aid effective scientific interpretation. Data from sediment cores or slabbed material such as rock, concrete, speleothems, wood etc. can be efficiently displayed. The program does not modify any original data but incorporates a wide range of features to customise visual representation of Itrax datasets. The program was written for a Windows environment and allows users to rapidly display, optimize, organize, adjust and analyse their data following the completion of their scans or at any time after. A variety of final output options allow data to be produced for spreadsheets, presentations and publications.

**Keywords** ItraxPlot · Itrax core scanner · Data visualization software · Corelyzer-ready

## Introduction

The Itrax high-resolution X-ray core scanner (manufactured by Cox Analytical Systems, Gothenburg, Sweden), in common with similar scanners, generates large volumes of data from scanned cores that ultimately need to be displayed efficiently to enable users to evaluate, analyse, interpret and present or publish data. Cox Analytical Systems produced the RediCore program around 2003 that provides some visualization capability. It includes image optimization, the facility to overlay up to two element profiles over optical and radiographic profiles and determines correlation coefficients for any pair of variables selected. ItraxPlot (Fig. 26.1) was independently developed in 2004 with a key objective being to ensure it was simple and intuitive to use and could display a broad range of elements alongside optical and radiographic images. RediCore is undoubtedly complementary to ItraxPlot but lacks some of the latter's diverse features which were seen as fundamental to allow

I. W. Croudace (✉)
Ocean and Earth Science, National Oceanography Centre, University of Southampton, Waterfront Campus, European Way, Southampton SO14 3ZH, UK

R. G. Rothwell
National Oceanography Centre, Empress Dock, Southampton, SO14 3ZH, UK



I. W. Croudace, R. G. Rothwell (eds.), *Micro-XRF Studies of Sediment Cores*, Developments in Paleoenvironmental Research 17, DOI 10.1007/978-94-017-9849-5_26

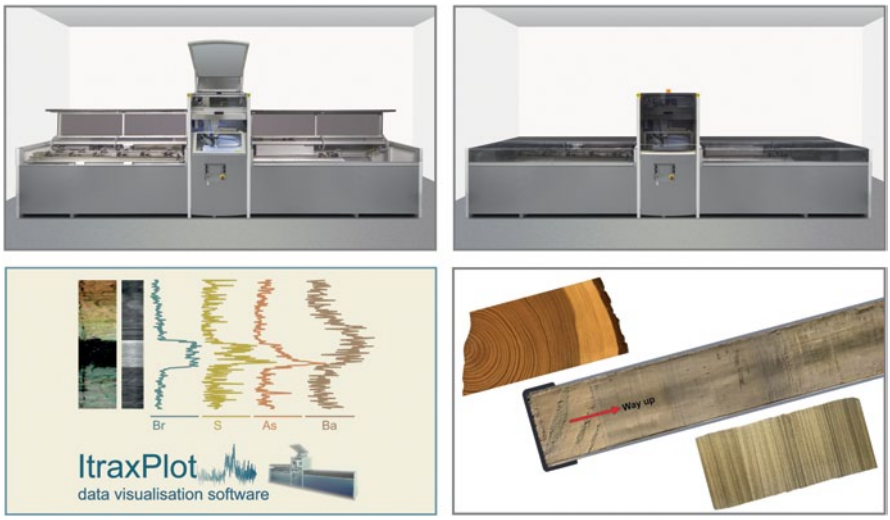


**Fig. 26.1** The Itrax core scanner, ItraxPlot and examples of sample types commonly run (wood, sediment, rock)

users to simultaneously evaluate optical, radiographic and multiple elements. Since its first appearance it has been regularly enhanced, updated and modified according to user requests and is now widely used in many Itrax laboratories around the world (Table 26.1).

## Components of Itrax Data

High-resolution core scanners produce copious amounts of data. For example, scanning a 1-m sediment core on an Itrax, at 200 μm increments, will create 5000 XRF spectral data files. At the same time graphical image files (optical.tif and radiograph.tif) and a results summary file (result.txt) are also created and saved. XRF spectra are analysed during the scanning process and the selected elemental peak areas are appended into the result.txt file as the run progresses. During the Itrax run any data visualization is limited and most users evaluate data at the end of a scan session. Following the completion of a run all spectra can, if considered necessary, be re-analysed (re-evaluated) and further optimized using Cox's Q-Spec spectral analysis software.

## Features of ItraxPlot

Data visualization needs to be a simple and efficient process that provides a comprehensive range of options that facilitate scientific interpretation. ItraxPlot allows users to efficiently and automatically open a set of Itrax-generated data and graphic

**Table 26.1** Summary of features provided by ItraxPlot

| |
|---|
| Displays up to ten elemental profiles alongside optical and radiographic images in a single window |
| Allows optimisation of optical and radiographic images by simply double clicking on an image to set levels |
| Allows control of colour and contrast |
| Allows coarse and fine size adjustment for optical image |
| Optical and radiograph images can be turned off or on |
| Multiple core sections can be stacked to view longer core sequences |
| Bartington sensor and radiograph 'grey-scale/density' data can be plotted along with element data |
| Allows normalisation of elements to another element or division by the incoherent or coherent scatter lines |
| Elemental data scaling and intercepts can adjusted |
| Modification of text labels and font size |
| Selection of smoothing for elemental plots |
| Zoom function to aid study of fine detail |
| Addition of horizontal and vertical shading or colour to define regions of interest |
| Addition of vertical and horizontal reference lines |
| Control of colours on graphics (background, text, data, lines etc) |
| Saving and printing of complete ItraxPlot graphic as a .pdf, .bmp or .tif files |
| Smoothed data can be saved as a .csv file |
| Three mathematical filtering functions are available to extract time series data (e.g. sediment laminae or tree ring counting) |
| Produces XRF data files formatted for reading by NSF CoreWall (Corelyser) software |
| Users can run multiple copies of the program on the same computer to enable visualization of all elemental data |

files by pointing at the main data folder for a particular file set. Alternatively, it is also possible to manually select specific data or graphic files by pointing at each file if distributed over more than one folder. After display parameters are manually selected a display window opens to reveal the plotted data. This consists of optical and radiographic images with up to ten columns of elements profiles all in the same coordinate framework (Fig. 26.2). The user has complete control of the number of elements, their ordering and the number of images displayed (Table 26.2 and Fig. 26.3).

The user can select many features from dropdown menus to zoom into the assembled data, adjust the optical image, change scaling limits, add horizontal or vertical reference lines, define regions-of-interest by shading or colour (Fig. 26.3, Table 26.1). Colour schemes for text, axes, data and background can be readily adjusted (Figs. 26.4 and 26.5). Data may be smoothed, normalized, temporarily deleted, re-scaled etc. Where multiple related core sections have been scanned the user can open each section in sequence and add together to produce a single stacked image, showing the whole core. Up to seven separate core sections can be displayed

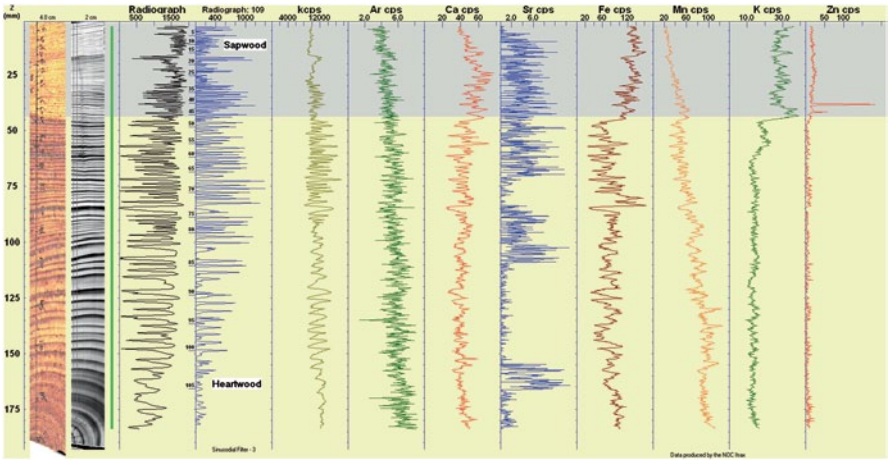


**Fig. 26.2** Example of ItraxPlot output for Itrax data acquired (*highlighted area*) from a 120 year old oak section collected in north Hampshire, UK (cut in Jan 2001)

(Fig. 26.6). The software provides flexible image and data saving options to facilitate presentational output. There are no practical limits to the number of copies of the program that can be run during an ItraxPlot session so many displays can be created to complete visualization.

## *Inspection and Interpretation of Itrax Data Using ItraxPlot*

Efficient visualizing of Itrax data, where optical, radiographic and elemental variations are aligned side-by-side, presents core data in an optimal way to make interpretations and correlations. For example, dense sediment layers may identify coarser-grained layers caused by storms or sediment movement, or linking frequency of radiographic greyscale variations with elemental fluctuations may identify seasonal controls in sedimentation. Elemental co-variations can be used to infer sediment mineralogy, redox processes, pollution inputs and sediment accumulation rates (Croudace et al. 2006; 2015). Chemical and mineralogical changes may relate to changing environmental conditions such as climate-related controls on sediment sources (Thomson et al. 2006; Rothwell et al. 2006; Rothwell and Croudace 2015; Maclachlan et al. 2015; Weltje et al. 2015). The study of tree rings (Fig. 26.2) may provide important information on climate and Itrax core scanner (or Itrax Multiscanner) data are increasingly used to extract environmental data from dendrochemical records (e.g. Balouet et al. 2007; McCarroll et al. 2011; Smith et al. 2014).

**Table 26.2** Expanded view of ItraxPlot user-selectable options. Selected program elements will open dialogue boxes requesting further information

| File | Zoom | Expand core region | Optical image | Radiograph image | Element data | Define region | Section | Edit | Colour & data setup | Help |
|---|---|---|---|---|---|---|---|---|---|---|
| Read core section | 100 % | Define region for expanded display | Contrast | Contrast | Select | Define horizontal region | Selection of added sections | Edit info | Background | Contents |
| Add core section | 200 % | Top depth | Size/ Position | Image size | Delete points | Define vertical region | | Set main title | Axis | Search |
| Insert core section | 400 % | Bottom depth | | Overlay over optical image OR | | Define horizontal line | | Set section title | Text | About |
| Read complete core | 800 % | Expanded/ Normal view | | Overlay over optical image AND | | Define vertical line | | Set text | Shaded H/L region | |
| Read optical image | | | | Define data region | | | | | Highlighted region | |
| Read radiograph image | | | | | | | | | Horizontal lines | |
| Add radiograph image | | | | | | | | | Vertical lines | |
| Read element data | | | | | | | | | kcps data | |
| Read previous element data | | | | | | | | | Al data | |
| Read bartington data | | | | | | | | | Si data | |

**Table 26.2** (continued)

| File | Zoom | Expand core region | Optical image | Radiograph image | Element data | Define region | Section | Edit | Colour & data setup | Help |
|---|---|---|---|---|---|---|---|---|---|---|
| Copy to clipboard | | | | | | | | | etc | |
| Save image | | | | | | | | | | |
| Save data | | | | | | | | | | |
| Save csv Data file | | | | | | | | | | |
| Save csv data for CoreWall | | | | | | | | | | |
| Print | | | | | | | | | | |
| New | | | | | | | | | | |
| Exit | | | | | | | | | | |

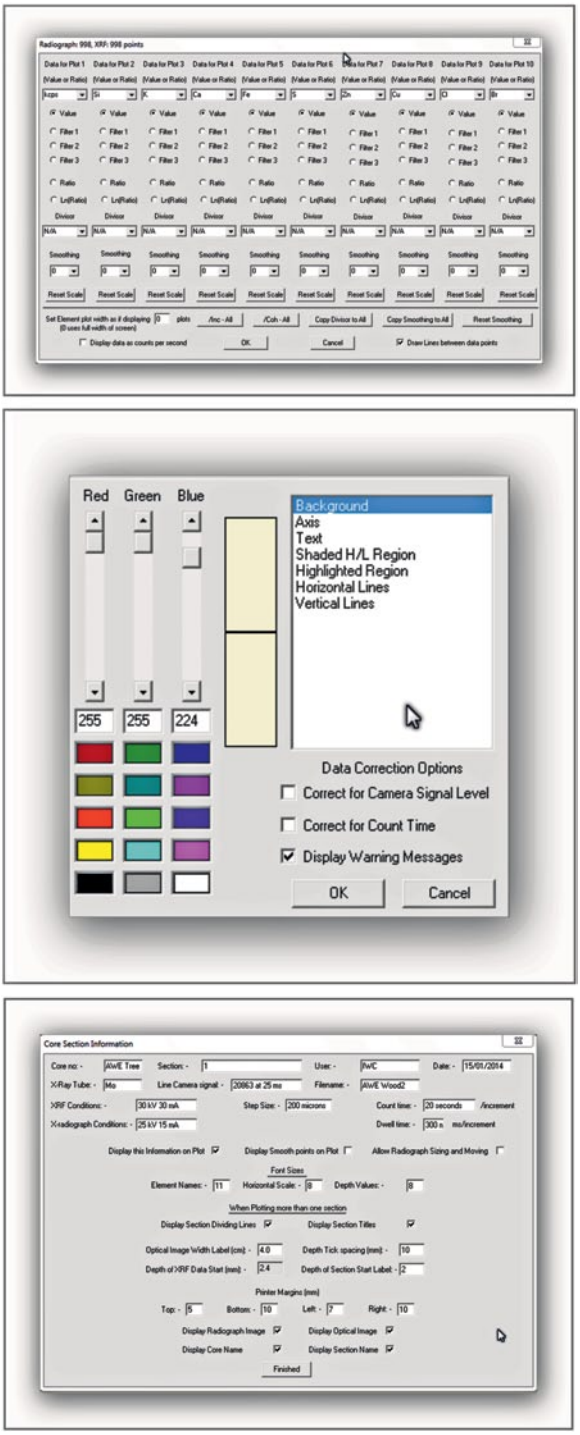


**Fig. 26.3** ItraxPlot user-input forms that allow users to choose element display options (*top*), editable graphic features such as titles, axis tick marks etc (*middle*) and colour scheme options (*bottom*)

## *Changes in the Sample-Detector Distance During Scans: kcps and Ar Profiles*

Sediment cores are generally split prior to Itrax scanning and imperfections and irregularities in the split sample surface can affect the elemental responses and may lead to misinterpretation of geochemical profiles (Figs. 26.4, 26.5 and 26.6). Sample surfaces may be affected by cracking, slumping, damage during splitting such as dragging of material (e.g. shells, roots, drop stones), changes of grain-size, desiccation, etc. Effective Itrax XRF scanning depends on a constant sample to detector distance (CSDD). XRF signals will depend on both elemental abundance and sample to detector distance. The Itrax system is designed to maintain a CSDD by determining a topographic profile along the sample surface prior to XRF scanning. These profile data are then used to control the position of the XRF detector holder via a z-axis motor drive to maintain a constant distance between sample and detector. An effective means of monitoring the effectiveness of the Itrax CSDD system is to examine the kcps and Ar profiles. If the topographic profile feedback tells the detector to move away from the sample surface then the X-ray flux to the detector will decrease, leading to a reduction in kcps. However, any increase in distance between the detector and the sample will be associated with an increase in the air gap and therefore the Ar counts will increase. The Ar signal is derived not from the sample (unless the sample is porous) but from excitation of argon in the air gap.

The ability of ItraxPlot to display so many features in a single window means that sample artefacts can be readily identified (Figs. 26.5 and 26.6). Where anoma-

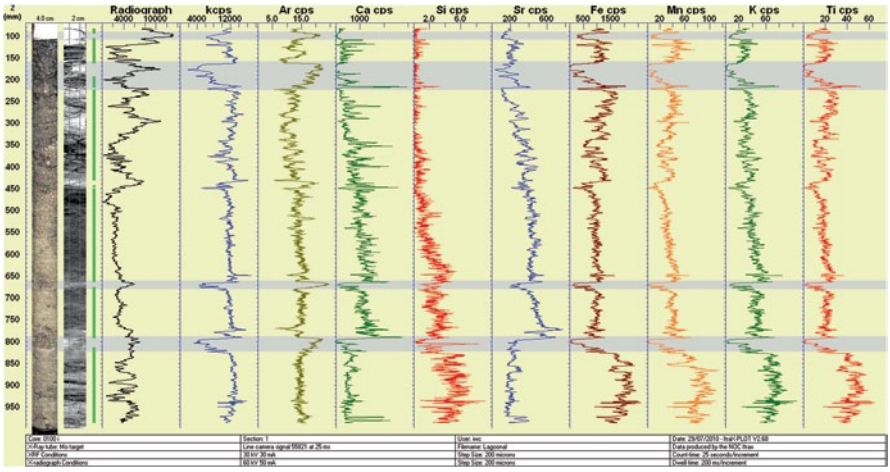


**Fig. 26.4** ItraxPlot image showing the impact of damaged/irregular core surfaces. Such effects are recognised from a negative correlation between total count-rate (kcps) and Ar (from irradiation of air). ItraxPlot readily allows such data regions to be highlighted or 'deleted' for display purposes (Core courtesy of Elena Romano, ISPRA)

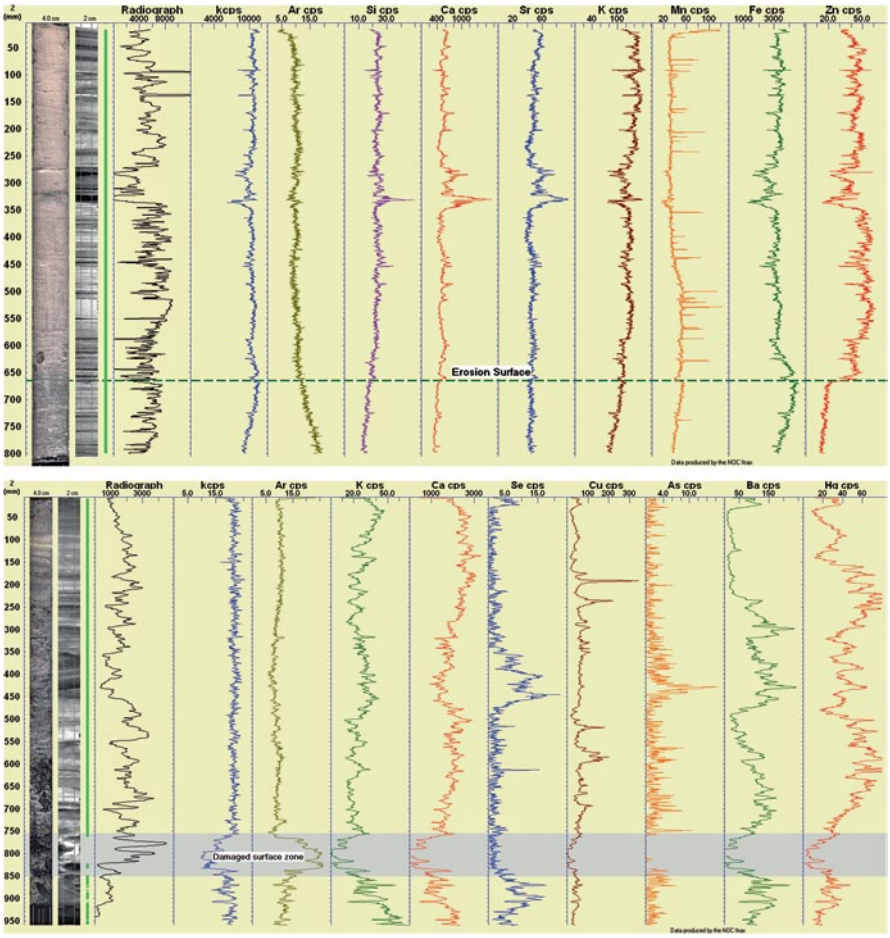


**Fig. 26.5** Example ItraxPlot output for two core sections. (*upper figure*: estuarine sediment, Bridgwater Bay, UK; *lower figure*: harbour sediment from Augusta Bay, Sicily Croudace et al. (2015))

lous regions are identified it is straightforward to either delete the 'bad data' (although original data files are not altered) or mark the data regions as suspect on the plot. Multiple copies of the program can be run in different windows so all elemental data can be displayed.

## *Surface Cracks*

Distinctive abrupt short-lived deflections are seen in Itrax element profiles where cracks and surface defects occur (Fig 26.4 and 26.5). The amplitude of these fea-

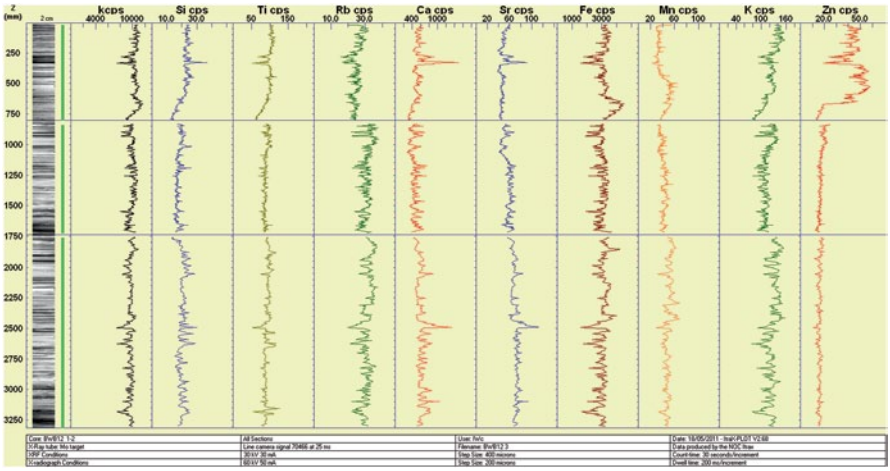


**Fig. 26.6** ItraxPlot display of a 3.2 m-long continuous sediment sequence based on three separate core sections of estuarine sediment. (Bridgwater Bay, UK)

tures depends on the size of the crack. These artefacts can mar the appearance of outputs but ItraxPlot allows users to delete data linked to cracks or other defects from displays and outputs.

## *Mathematical Functions*

ItraxPlot incorporates several mathematical functions. General data smoothing can also be used to suppress 'noise' in plotted data but caution is advised against over-smoothing. An 'event' counting features for counting elemental regularities (peaks and troughs in data) or radiograph grey-scales. This approach can help, for example, in determining numbers of sedimentary layers, seasonal couplets or tree rings (Fig. 26.2). If this option is selected the user chooses one of three mathematical functions (first differential, smoothed first differential or sine function) to identify and count variations.

The data used in the filtering functions are either the selected element data or the sum of the radiograph pixel strip values corresponding to each element data point. When the radiograph is selected, the user has control over the region of interest. For all types of filtering, an 'event' is registered when a local maximum value greater than 1 % of the overall maximum data value occurs. The location and number of events is displayed on the profile(s) chosen.

1. First differential filtering—this is based on the differential of the data.
2. Smoothed first differential—based on the weighted smoothed data.
3. Sinusoidal function—this uses a period of 'n' where 'n' is selectable.

## CoreWall and ItraxPlot

CoreWall is a US-developed stratigraphic correlation, core description, and data visualization system widely used by the marine, terrestrial, and Antarctic science communities (www.corewall.org). The CoreWall software suite was developed at the University of Illinois at Chicago's Electronic Visualisation Laboratory through collaboration between the US National Lacustrine Core Repository at the University of Minnesota and the International Ocean Discovery Program (IODP). CoreWall has revolutionalised core logger data display by integrating diverse and disparate core datasets and allowing them to be visualised as an integrated whole. It uses standard computer interfaces; provides for displaying of large core datasets; supports data capture and safe-keeping; provides a scalable and portable visualisation tool (through Corelyzer part of the CoreWall software suite); is able to handle high resolution photo- and radiographic images and XRF core scanner data. ItraxPlot has been adapted to produce an XRF data output file data in a format that is suitable for opening by CoreWall's Corelyzer program, allowing ITRAX-generated downcore elemental data to be integrated with other core datasets.

## Conclusion

Highly efficient analytical instruments producing large volumes of measurement data require equally effective data visualization software. ItraxPlot is designed to rapidly display elemental profiles and images produced by the Itrax core scanner for sediment and rock cores, wood slabs and other samples. The simultaneous display of Itrax data (optical and radiographic images with up to ten co-registered elemental profiles) in a single window makes it straightforward to distinguish real from anomalous signals caused by sample artefacts and makes correlation and interpretation easier The program provides several options to analyse the data (e.g. through smoothing and normalization) and event counting (using up to three mathematical functions). An option also exists to output Itrax data in a format suitable for reading by Corelyzer (CoreWall).

**Acknowledgement** ItraxPlot software was largely developed by Ian Croudace with some initial contribution from Guy Rothwell and programmed in C+. Interested parties should contact Ian Croudace if they wish to acquire an evaluation copy of the software.

## References

Balouet JC, Oudijk G, Smith KT, Petrisor I, Grudd H, Stocklassa B (2007) Applied dendroecology and environmental forensics. Characterization and age dating environmental release: fundamentals and case studies. Environ Forensics 8:1–17

Croudace IW, Rindby A, Rothwell RG (2006) Itrax: description and evaluation of a new sediment core scanner. In: Rothwell RG (ed) New techniques in sediment core analysis, vol 267. Geological Society Special Publication, pp 51–63

Croudace IW, Romano E, Ausili A, Bergamin L, Rothwell RG (2015) X-ray core scanners as an environmental forensics tool: a case study of polluted harbour sediment (Augusta Bay, Sicily). In: Croudace IW, Rothwell RG (eds) Micro-XRF studies of sediment cores: a non-destructive tool for the environmental sciences. Springer, The Netherlands

MacLachlan SE, Hunt JE, Croudace IW (2015) An empirical assessment of variable watercontent and grain-size on X-Ray fluorescence core-scanning measurements of deep sea sediments. In: Croudace IW, Rothwell RG (eds) Micro-XRF studies of sediment cores. Springer, Nederlands

McCarroll D, Tuovinen M, Campbell R, Gagen M, Grudd H, Jalkanen R, Loader NJ, Robertson IA (2011) Critical evaluation of multi-proxy dendroclimatology in northern Finland. J Quaternary Sci 26:7–14

Rothwell RG, Croudace IW (2015) Twenty years of XRF core scanning marine sediments: what do geochemical proxies tell us? In: Croudace IW, Rothwell RG (eds) Micro-XRF studies of sediment cores: a non-destructive tool for the environmental sciences. Springer, The Netherlands

Rothwell RG, Hoogakker B, Thomson J, Croudace IW (2006) Turbidite emplacement on the southern Balearic Abyssal Plain (W. Mediterranean Sea) during marine isotope stages 1–3; an application of XRF scanning of sediment cores in lithostratigraphic analysis. In Rothwell RG (ed) New techniques in sediment core analysis, vol 267. Geological Society Special Publication, London, pp 51–63

Smith KT, Balouet JC, Shortle WC, Chalot M, Beaujard F, Grudd H, Vroblesky DA, Burken JG (2014) Dendrochemical patterns of calcium, zinc, and potassium related to internal factors detected by energy dispersive X-ray fluorescence (EDXRF). Chemosphere 5:58–62

Thomson J, Croudace IW, Rothwell RG (2006) A geochemical application of the ITRAX scanner to a sediment core containing eastern Mediterranean sapropel units. In: Rothwell RG (ed) New techniques in sediment core analysis, vol 267. Geological Society Special Publication, London, pp 51–63

Weltje GJ, Bloemsma MR, Tjallingii R, Heslop D, Röhl U, Croudace IW (2015) Prediction of geochemical composition from XRF core scanner data: a new multivariate approach including automatic selection of calibration samples and quantification of uncertainties. In: Croudace IW, Rothwell RG (eds) Micro-XRF studies of sediment cores. Springer, Nederlands

# Part V
# The Future of Non-destructive Core Scanning

# Chapter 27
# Future Developments and Innovations in High-Resolution Core Scanning

**Ian W. Croudace and R. Guy Rothwell**

**Abstract** The rapid expansion of palaeoclimate research from the late 1990s onward stimulated the introduction and subsequent use of non-destructive XRF core-scanning systems worldwide. As a result these scanners now exist in approximately 90 international institutions and they must rank as one of the most useful analytical screening tools in the geosciences. Their development has contributed to an analytical revolution in palaeoclimate and environmental research due to their overall capability, speed and spatial resolution. From the 1990s to the present time five separate commercial XRF core scanners have been available with two being dominant in the academic research sector. Up to the current time the two market leaders have been Avaatech Analytical X-Ray Technology (Netherlands) and Cox Analytical Systems (Sweden; manufacturers of the ITRAX). Other manufacturers include Geotek (United Kingdom) who are developing a growing international presence while Jeol Ltd. (Japan; manufacturers of the Tatscan) is largely limited to Japan. The Avaatech core scanner, which evolved from the Dutch CORTEX instrument, firmly established itself in the marine research sector but has also served the lake and Pre-Quaternary research community. The Itrax core scanner (Cox Analytical Systems) has been widely used by both the marine and lake sediment community. Its integration of a high power X-ray tube, X-ray capillary wave-guide, advanced silicon-drift detectors and radiographic imaging proved of great interest to users (particularly the lakes community) requiring high-resolution elemental analysis and radiographic imaging of fine sediment layers. In the last few years Geotek have expanded their core logging instrument expertise to include XRF analysis. With their user base they are likely to become a significant competitor in the XRF core scanning sector. Looking to the next decade geoscientists are likely to see extended capability arising from the addition of new or enhanced sensors to existing systems or to the appearance of new dedicated systems carrying out specific scans. Some system developments that are just becoming available involve the enhancement of existing components that allow greater analytical speed with no loss of spectral

I. W. Croudace (✉)
Ocean & Earth Science, University of Southampton Waterfront Campus,
National Oceanography Centre, European Way, Southampton SO14 3ZH, UK
e-mail: iwc@noc.soton.ac.uk

R. G. Rothwell
National Oceanography Centre, Empress Dock, Southampton, SO14 3ZH, UK



I. W. Croudace, R. G. Rothwell (eds.), *Micro-XRF Studies of Sediment Cores*,
Developments in Paleoenvironmental Research 17, DOI 10.1007/978-94-017-9849-5_27

data quality. Future development will likely involve addition of other non-contact technological sensors perhaps exploiting investments made in the *in-situ* extra-terrestrial sector. Fertile areas for development could be based on lasers (LIBS, dispersive Raman), hyperspectral imaging (reflectance spectrometry in the VNIR, SWIR and NIR wavelength regions), X-rays (simultaneous XRD) and magnetic susceptibility. Overall, future non-destructive scanning instrument are likely to provide improved sensitivity and additional high-resolution proxy records from natural materials including sediment and rock cores, speleothems and tree rings.

**Keywords** Itrax core scanner · Hyperspectral imaging · Laser-induced breakdown spectrometry · Simultaneous X-ray diffraction

## Introduction

The papers presented in this volume demonstrate the impressive breadth and depth of applications involving high-resolution X-ray core scanners that have arisen in a little over a decade. With their ability to simultaneously and non-destructively measure thirty or more elements (and other co-registered properties such as magnetic susceptibility and a radiographic image), X-ray core scanners have made a significant contribution to the study of marine, estuarine and lacustrine sedimentary sections as well as rocks, coal, speleothems and tree rings (e.g. Croudace et al. 2006; Rothwell et al. 2006; Thomson et al. 2006; Croudace and Rothwell 2010; Rothwell and Croudace 2015; Croudace et al. 2015; Kelloway et al. 2015). Many of the existing XRF core scanners originated as concepts or prototypes in marine science establishments (universities and research institutions in Holland, UK and Japan) from the 1990s through to the early 2000s. Following from these early initiatives, the leading prototypes became commercialized by specialist instrument companies who responded to institutional demand created by the international expansion in paleoclimate research. The clear success of core scanner technology is an exemplar for how funding streams from research institution, combined with scientific demand, stimulated opportunities for specialist SMEs. The success of the instruments is graphically demonstrated by the exponential rise in publications over the last decade (see review by Rothwell and Croudace (2015)) and shows that they have become one of the most powerful analytical screening tools available to geo- and environmental scientists.

There are currently around 90 XRF core scanners worldwide that up to now are dominated by Avaatech and Itrax instruments (Table 27.1). The early development and success of these two main core scanners represents a kind of technological Darwinism where they became the dominant market leaders. Going forward, however, as new companies compete within the XRF core scanner market, positions may change with institutions choosing instruments on the basis of reputation, capability, suitability-for-purpose and cost. For example, Geotek Ltd, an established leader in traditional core logging technology is now competing in the XRF core scanning market. All available core scanners have a robust core-handling platform with asso-

**Table 27.1** General locations of known XRF core scanners (italicized text indicates known instruments installed on ships)

| Avaatech | ITRAX | Geotek XRF | Tatscan |
|---|---|---|---|
| MARUM, Bremen, Germany | National Oceanography Centre, Southampton, UK (2003) | 14 Olympus—based units | ***DV Chikyu, Japan*** |
| NIOZ—Netherlands | Woods Hole Oceanographic Institution, USA (2004) | 4 new-type Units | Kochi Repository, Japan |
| Alfred-Wegener Institute, Germany | Université de Quebec INRS, Canada (2004) | – | Mie University, Japan |
| IFREMER, Brest, France | University of Wales, Aberystwyth, UK (2005) | – | – |
| Kiel University, Germany | Istanbul Technical University, Turkey (2006) | – | – |
| University of Tromsø, Norway | University of Minnesota LLO, USA (2006) | – | – |
| EDYTEM-CNRS, Université de Savoie, France | University of Stockholm, Sweden (2007) | – | – |
| EPOC-CNRS, Université Bordeaux 1, France | University of Bremen, Germany (2007) | – | – |
| University of Cambridge, U.K. | University of Vigo, Spain (2007/2008) | – | – |
| University College, London, U.K. | Universität zu Köln, (2007) | – | – |
| Universitat de Barcelona, Spain | University of Bergen, Norway (2008) | – | – |
| E.T.H Zurich, Switzerland | CEREGE, Aix-en-Provence, France (2008) | – | – |
| BGR, Hannover, Germany, 2012 | University College Dublin, Geology (2008) | – | – |
| Texas A&M University, College Station, USA | Second Institute of Oceanography, Hangzhou, China (2009) | – | – |
| Scripps Institution of Oceanography, USA | First Institute of Oceanography, Qingdao, China (2009) | – | – |
| University of North Carolina, USA | National Taiwan University, Taipei, Taiwan (2009) | – | – |
| Rosenstiel School, Miami, USA | KIGAM, Daejeon, S. Korea | – | – |
| University of Wisconsin, Madison, USA | China University of Geology, Beijing, China. (2010) | – | – |
| KIGAM, Daejeon, S. Korea | University of Rostock, Germany (2010) | – | – |
| State Key Lab of Marine Geol, Tongji Uni, China | Helmholtz-Centre, Potsdam. (2011) | – | – |
| Nanjing University, China | ***Korea Polar Research Institute, RV Araon (2011)*** | – | – |

**Table 27.1** (continued)

| Avaatech | ITRAX | Geotek XRF | Tatscan |
|---|---|---|---|
| University of the Philippines, Philippines | University of Massachusetts, Amherst, USA (2011) | – | – |
| University Lanzhou, China | ANSTO, Lucas Heights, Sydney, Australia (2011) | – | – |
| Yunnan Normal University, China | Institute of Mineral Resources, Beijing, China (2012) | – | – |
| Xiamen University, China, 2012 | Institute of Tibetan Plateau Research, Beijing, China (2012) | – | – |
| Nanyang Technological University, Singapore | University of Aarhus, Denmark (2012) | – | – |
| The Australian National University, Canberra | State Key Laboratory of Geol. Proc. & Mineral, Wuhan, China | – | – |
| – | Kuwait Petroleum Institute, Kuwait Inst. Scientific Research | – | – |
| – | University of New South Wales, Australia | – | – |
| – | State Key Laboratory of Continental Dynamics, Chengdu, China | – | – |
| – | ***GSI RV Samudra Ratnakar, Mumbai, India*** | – | – |
| – | University of Bern, Switzerland | – | – |
| – | Korean Institute of Ocean Science & Technology, S. Korea | – | – |
| – | Guangzhou Marine Geological Survey, China | – | – |
| – | University of Copenhagen, Natural History Museum of Denmark | – | – |
| – | McMaster University, Hamilton Canada (2014) | – | – |
| – | KCC Kochi University, Japan (2014) | – | – |
| – | University of Köln, Itrax core scanner No. 2 (2014) | – | – |
| – | Oregon State University (2014) | – | – |

ciated precision motor drives. Onto this basic platform have been added a range of specialized components developed by (external) original equipment manufacturers (OEMs producing X-ray tubes, X-ray detectors, CCD cameras, optical spectrometers etc). Several of these XRF corescanning systems have been successfully deployed on research vessels but so far the best analytical data are acquired in a stable terrestrial laboratory environment.

Software developments are crucial in strengthening the capability of core scanners. The manufacturers have generally provided most core scanner instrument control software. Spectral analysis software has either been developed by the manufacturer (e.g. QSpec for the ITRAX) or has used proprietary software from other providers (Canberra WinAxil for Avaatech and Geotek). Future developments in core scanning technology may arise when other high-resolution sensors are integrated into existing XRF core scanners or when new companies enter the market stimulating competition and innovation. The co-registration of core data on a single instrument (e.g. Itrax's elemental, magnetic susceptibility, radiography) is always likely to be attractive to users subject to affordability. Possible additional technical developments that may eventually be incorporated into current non-destructive core scanners are likely to be based on lasers excitation (LIBS—laser-induced breakdown spectroscopy and Dispersive Raman Spectroscopy), optical illumination (hyperspectral imaging), X-ray excitation (X-ray diffraction, XRD) and magnetics (Fig. 27.1).

In this paper we review a range of possible hardware and software developments that could become incorporated into future core scanners. The ultimate value of any of these technologies, beyond those currently available, needs to be established through systematic investigation using previously studied, well-understood cores. Relatively new sensors could emerge from other areas of investigation. For example, there may be spin-offs from the significant investment made in planetary research programmes where non-contact (standoff) sensors are being evaluated.

## Hardware Developments

### *X-ray Based Techniques*

**Improved SDD Detectors and MCAs** The continued improvement of silicon drift detector technology and associated digital pulse processing (SDD-DPP) with multichannel analysers (MCAs) is already leading to significant performance enhancements for X-ray core scanners. Over the last ten years detector count-rate capability has increased by a factor of 10–30 based entirely on developments in SDD-DPP technology. It is now possible to achieve up to 1 Mcps input count rates, with virtually no degradation of peak resolution. Fifteen years ago count-rates needed to be kept below 0.01 Mcps to ensure X-ray energy resolutions were not adversely affected. The clear benefit of these SDD-DPP improvements is the provision of shorter analysis times and improved precision, especially important for less efficiently excited elements (such as Al and Si).

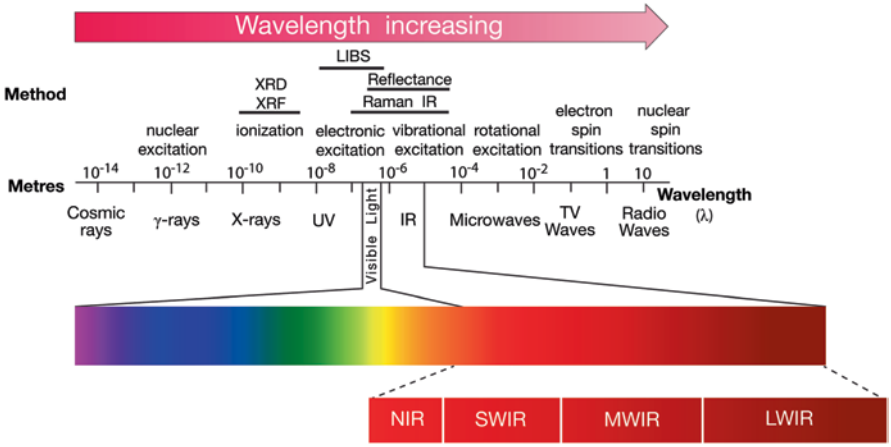


**Fig. 27.1** The electromagnetic spectrum showing the spectral regions and methods used by current core scanning technologies

**Twin X-Ray Detector Systems** The Itrax uses a medium power (2–3 kW) X-ray generator and allows users to select a range of X-ray tubes (Cr, Mo, Rh) to optimize their analysis. The choice of tube determines elements that can be effectively measured (based on the varying excitation efficiencies) and for the broadest range of elements it is necessary to use more than one tube, currently involving a sequential scan. Changing of X-ray tubes is time consuming and inconvenient. To improve efficiency it might be possible to use two X-ray tubes on a single scanning system. In the case of the Itrax a low power X-ray tube (with a different anode from the main system) and associated detection system could be integrated. The incorporation of an additional close-coupled, low power X-ray tube with its own SDD could reduce the analytical overhead by acquiring data simultaneously using two separate, co-mounted XRF systems. Such a technical development seems feasible but would require research funding or company investment.

**X-Ray Diffraction** Sediment layers may comprise mixtures of minerals derived from a wide variety of sources such as local re-working, biogenic materials, terrigenous material derived from terrestrial erosion etc. The mineralogical composition can provide valuable insights into environmental processes and may be inferred from the geochemistry measured by the XRF core scanner, or it may be determined directly using a method such as X-ray diffraction analysis (XRD). Mineralogical analysis at high speed using X-ray diffraction would require the use of simultaneous acquisition systems such as curved position sensitive detector (CPSD) technology. These XRDs can simultaneously measure a 110° 2θ diffraction angle pattern (Fig. 27.2, Table 27.2), are capable of resolving 0.04 degrees-2θ FWHM (full width at half maximum) and can analyze sample areas as small as ten microns. These CPSD replace older mechanical scanning goniometers used by traditional XRD manufacturers. Instruments using CPSDs are now well established although currently promoted by only a small number of companies (e.g. www.inel.fr). Modern CPSDs use a robust "knife edge" alloy blade anode in place of the older, more

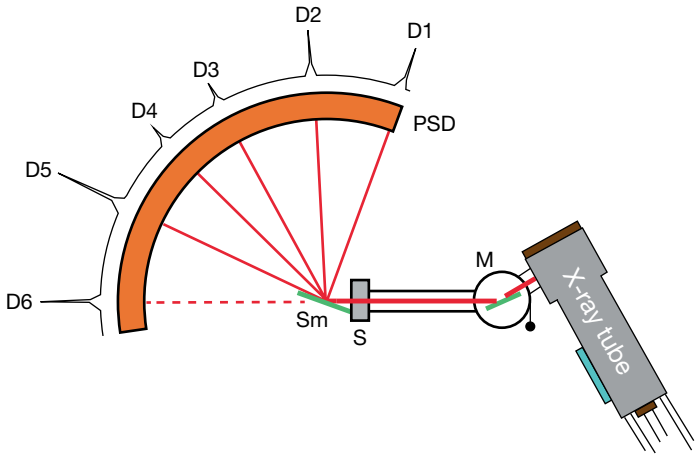


**Fig. 27.2** Schematic of Inel™ Curved Position-sensitive detector (PSD) for simultaneous XRD. These systems have no moving parts and eliminate the need for mechanical scanning devices such as complex scanning goniometers used in conventional scanning XRD Systems using goniometers. *M* monochromator, *S* Slit, *Sm* sample, *PSD* Position sensitive detector, D1–D6 are possible diffraction lines produced when Sample Sm is irradiated with CuKa

fragile wire anode detectors. Curved Position-sensitive XRDs allows dynamic (simultaneous) measurement of diffraction data in real-time at very high resolution.

**Energy-Dispersive-XRD** An alternative non-destructive XRD technology offering some potential is EDXRD (Feng et al. 2004; Escarate et al. 2009; Beck et al. 2014; O'Dwyer and Tickner 2008) where simultaneous mineralogical information is obtained following on-line development for the minerals industry (Fig. 27.3). This technology has some technical challenges that need to be overcome but there is some application potential. The prototype EDXRD technique of O'Dwyer and Tickner (2008) used much higher X-ray energies (up to 120 keV) and is a transmission method compared with conventional reflection XRD that uses 10–30 keV.

EDXRD is also capable of measuring material tens of millimetres in thickness due to the use of higher energy X-rays whereas a conventional reflection mode XRD analyser measures a small amount of material on the surface of the sample. Important factors in EDXRD use are:

- Sample preparation is less critical in EDXRDs that use higher-energy X-rays because micro-absorption effects are reduced.
- EDXRD analysers have no moving parts
- EDXRD data acquisition times can be short as the complete diffractogram is collected simultaneously
- Mathematical techniques are needed to deconvolve complex diffractograms
- The main disadvantage of EDXRD is its relatively low d-spacing resolution compared to conventional XRD. This resolution stems almost entirely from the relatively wide collimator openings required to achieve sufficient counting statistics in an acceptable measurement time.

**Table 27.2** Summary of existing and future possible non-destructive methods for investigating sediment cores

| Method | Property measured | Principle | Sensitivity | Non-destructive capability, data type | Analysis time scale per increment | Typical sample spatial resolution | Potential for non-destructive core scanning |
|---|---|---|---|---|---|---|---|
| *XRF* | Elements Mg-U | X-ray fluorescence following orbital transitions An x-ray source generates fluorescent x rays in the sample that are detected by an energy discriminating detector | Low ppm for selective elements | Yes Semi-quantitative to quantitative | 1 s for major elements 10 s for trace elements | >50 µm | Established, but detection enhancements regularly occurring |
| *XRD* Simultaneous XRD using position sensitive detector | Mineralogy identified via X-ray diffraction | X rays are directed through the sample and a diffraction pattern is collected using an energy discriminating detector | >1 wt% of mineral | Yes Semi-quantitative | >100 s likely | 1000 µm | Offers potential |
| *XRD* Simultaneous XRD via EDXRD | Mineralogy identified via X-ray diffraction | Monochromatic X rays are directed through the sample and a diffraction pattern is collected | >1 wt% of mineral | Yes Semi-quantitative | >1000 s likely | 1000 µm | Offers potential |
| *X-radiography* | Density variations; textural features | X-ray absorption, radiography | Sensitive to small changes | Yes Semi-quantitative | Seconds | >50 µm | Established |

**Table 27.2** (continued)

| Method | Property measured | Principle | Sensitivity | Non-destructive capability, data type | Analysis time scale per increment | Typical sample spatial resolution | Potential for non-destructive core scanning |
|---|---|---|---|---|---|---|---|
| *FT Raman Dispersive Raman* | Mineralogy, organic compounds | Vibrational spectroscopy—Laser light scattered from the surface is detected. The wavelength of the Raman scattered peaks are mineral-specific | High | Yes Semi-quantitative | Seconds | >50 µm | Offers potential |
| *LIBS* | Elements | Atomic emission spectrometry—a short pulse from a high power laser initiates a high T plasma. As the plasma cools optical emission spectra from excited atomic states are recorded | ppm for selective elements | Laser ablation, micro-pitting Use on soft sediment may be problematic Semi-quantitative | Seconds | >500 0.5 mm | Potentially good for some elements |
| *Hyperspectral imaging* | Mineralogy, organic compounds | Optical reflectance spectroscopy | Highly variable | Yes Semi-quantitative | Seconds | >50 µm | Established |
| *Magnetic susceptibility* | Ferromagnetic minerals | Magnetic susceptibility using Bartington sensor | Ferromagnetism 50 µg | Yes | Seconds | >1000 µm | Proven at ~5 mm resolution |

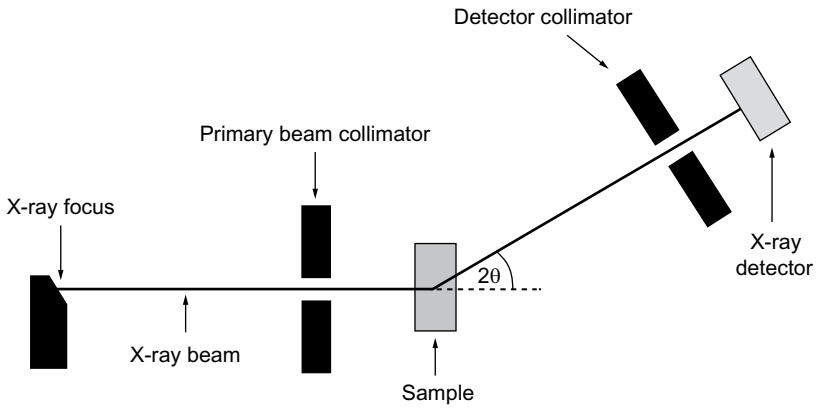


**Fig. 27.3** Schematic representation of an EDXRD spectrometer. (From O'Dwyer and Tickner 2008)

Both of the XRD techniques discussed above could be added to a scanning platform with few technical obstacles, and either could become incorporated into a core scanning system if there was a sufficiently strong user driver.

## *Optical Methods*

**Hyperspectral Imaging (HSI)** Hyperspectral imaging is a passive, non-destructive, surface analytical technique that only requires illumination of the sample and detection of the reflected light spectrum. Measurements can be made *in-situ* with virtually no sample preparation, except where high magnification imaging is the focus of attention. Hyperspectral imaging collects and processes information from across the electromagnetic spectrum (typically near the red part of the visible light spectrum) and its purpose is to obtain a spectrum for each pixel in the image of a scene, with the purpose of identifying compositional variations in materials. Whereas the human eye sees visible light in three colour bands (RGB), hyperspectral imaging divides the spectrum into many more bands and the recorded high-resolution spectra extend over a wide range of wavelengths. The key measuring component of a hyperspectral scanning system is the spectroscopic camera (incorporating a CCD, ICCD or CMOS) that acquires reflected light intensity for a large number of spectral bands.

Reflectance spectrometry, the basis of the HSI technique, relies on the property that when molecules are exposed to energy they vibrate with stretching and rotating of their chemical bonds. Changes at the molecular and atomic level result in selective absorption of incident and reflected light at specific and unique wavelengths.

**Table 27.3** Main regions of the visible spectrum

| Range | Abbreviation | Range (nm) | Minerals showing a reflection spectral response |
|---|---|---|---|
| Ultraviolet | UV | 200–400 | – |
| Visible-near infrared | VIS | 500–700 | – |
| | VNIR | 400–1000 | Iron oxides and hydroxides manganese oxides |
| Short-wave infrared | SWIR | 1000–2500 | Hydroxyls, carbonates, sulphates micas |
| Mid-wave infrared | MWIR | 3000–6000 | – |
| Long-wave infrared | LWIR | 6000–12000 | Carbonates, silicates, quartz, feldspar |

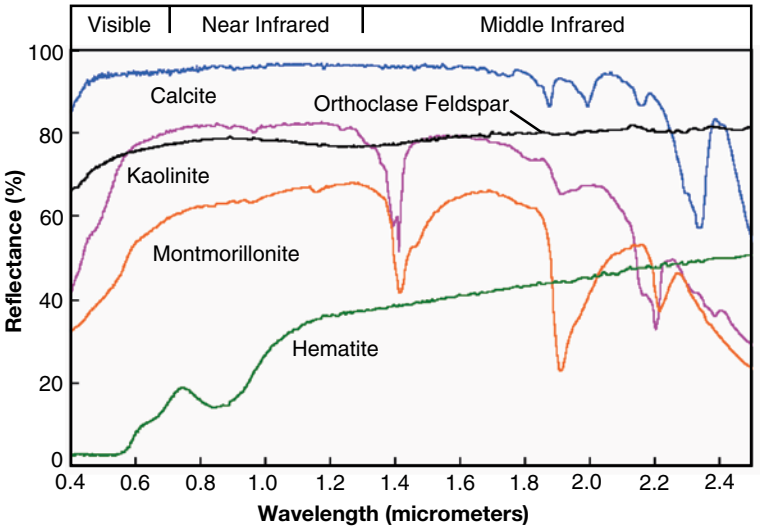


**Fig. 27.4** Reflectance spectra of some representative minerals (adapted from Smith 2012). In the spectrum of hematite, the strong absorption in the visible light range is caused by ferric iron (Fe3+). In calcite, the major component of limestone, the carbonate ion (CO3-2) is responsible for the series of absorption bands between 1.8 and 2.4 micrometers (μm). The clay minerals, kaolinite and montmorillonite, have a strong absorption band near 1.4 μm (hydroxide ions, OH-1) and a weaker band at 1.9 μm (bound water molecules)

The infrared region is effective for mineral detection as many minerals provide spectral responses across different IR wavelengths (Table 27.3 and Fig. 27.4). For example, iron oxides and pyroxenes can be detected in the VNIR spectral range (400–1000 nm; so requiring a VNIR spectral camera), while micas, clays and many other minerals produce responses in the SWIR region (1000–2500 nm; so requiring a VNIR spectral camera).

Hyperspectral imaging is already established in some geoscience sectors (e.g. as portable or laboratory-based scanning devices in mineral exploration; CSIRO 2014; Huntingdon et al. 2004; Huntingdon 2007; Roache et al. 2011) and is used to derive compositional information (minerals or other components) or it can be used to present compositional maps derived by combining digital imaging and spectroscopy (Specim, Finland; see Fig. 27.5 and Table 27.4).

**Hyperspectral Imaging**

Covalent bonds in chemical components can absorb particular wavelengths of the visible and near visible light spectrum and can be measured using one or more specialist cameras that combine imaging and spectroscopy (see www.specim.fi). Hydroxyl and carbonate bond-related vibrations are typically measured in the shortwave infrared (SWIR). Phyllosilicate and carbonate minerals are commonly identified across the SWIR region. Clay minerals, micas, chlorites and different carbonate species are detectable. Longer wavelength ranges are necessary to detect the fundamental vibrations related to aluminosilicate minerals, e.g. in the long-wave (thermal) infrared (LWIR) region quartz, feldspar and other silicate minerals can be detected and identified.

With a standard digital camera, the lens system projects the image onto the focal plane array. In a hyperspectral imaging system a high quality imaging spectrograph is installed between the camera lenses and the focal plane array. The lens images the object at the entrance slit of the spectrograph which produces a spectrum on the focal plane array, preserving the location of respective points on the slit. Consequently, each line of the focal plane array is an image of the slit, containing one wavelength. One frame produced with the hyperspectral imager contains full spectral information of a single line of the image.The entire image (called the data cube) is produced line by line, each frame representing a consecutive line. Capturing the full image takes just seconds. Standard spectroscopic analytical methods are applied to analyze the image.

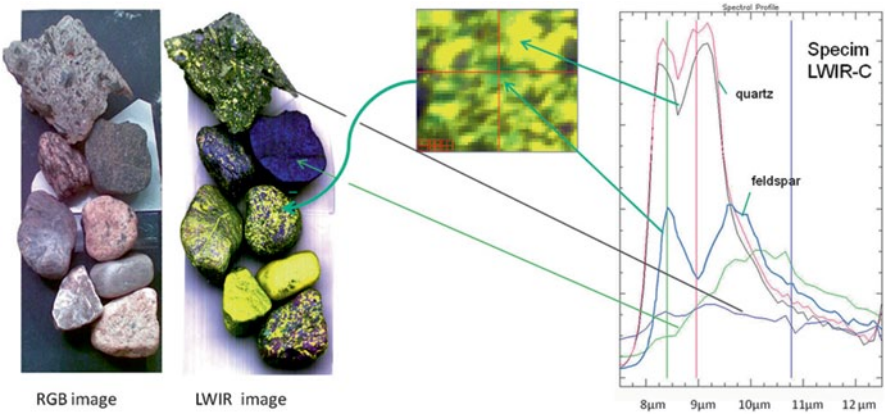


**Fig. 27.5** Example of a hyperspectral mineral map a set of rock pebbles produced using a Specim LWIR-C imager. Every pixel of the LWIR image encompasses a full infrared spectrum range from 7.7 to 12.4 um. Based on the different characteristics, minerals such as quartz and feldspar spectra are clearly recognizable

**Table 27.4** Single core hyperspectral scanner, SisuSCS (Specim, Finland)

| – | VNIR | SWIR* |
|---|---|---|
| Spectral range | 400–1000 nm | 1000–2500 nm |
| Number of spectral bands | 96–768 (adjustable by binning) | 288 |
| Spectral sampling | 0.78–6.27 nm/pixel | 5.6 nm/pixel |
| The number of spatial pixels | up to 1312 | 384 |
| Pixel size on target | 0.04–0.09 mm (1312 pixels) | 0.130–0.312 mm (384 pixels) |
| Sample scanning | Single scan | |
| Scan speed (50 mm FOV) | ~2.5 mm/s<br>up to 6.7 mm/s with binning) | 13 mm/s (at 100 Hz frame rate, up to 400 Hz possible) |
| Scan speed (120 mm FOV) | ~6 mm/s(up to 16 mm/s with binning) | 31 mm/s (at 100 Hz frame rate, up to 400 Hz possible) |
| Scan time for 1.5 m long sample | ~4 min (90 s with binning) | ~ 50s |
| Field of view (FOV) | 50–120 mm | 50–120 mm |
| Imagery | High resolution hyperspectral images | |
| Principle | Spectral reflectance spectrometry provides molecular compositional information | |
| Typical applications | Minerals in sediment or rocks | Organic compounds in sediment |
| Max sample size | 130 × 1 500 × 75 mm (L × W × H) | |
| System dimensions | 3 210 × 522 × 1 000 mm (L × W × H) | |
| Operating conditions | Laboratory environment | |
| Camera output format | Digital 12 bit | Digital 16 bit |
| Instrument calibration | Spectral calibration. Normalization using internal referencing | |

*These are the characteristics of the new generation SWIR spectral camera introduced in the middle of 2014

| Class | Mineral | VNIR Response | SWIR Response | LWIR Response |
|---|---|---|---|---|
| **Wavelength** | | **400-1000 nm** | **1000-2500 nm** | **8000-12000 nm** |
| Silicates | Amphibole | Poor | Good | Moderate |
| Silicates | Pyroxene | Good | Moderate | Good |
| Silicates | Tourmaline | Poor | Good | Moderate |
| Silicates | Garnet | Moderate | Poor | Good |
| Silicates | Olivine | Good | Poor | Good |
| Silicates | Epidote | Poor | Good | Moderate |
| Silicates | Mica | Poor | Good | Moderate |
| Silicates | Chlorite | Poor | Good | Moderate |
| Silicates | Illite | Poor | Good | Moderate |
| | Kaolinite | Poor | Good | Moderate |
| Silicates | Orthoclase | Poor | Poor | Good |
| | Albite | Poor | Poor | Good |
| Silicates | Silica | Poor | Poor | Good |
| Carbonates | Calcite | Poor | Moderate | Good |
| Carbonates | Dolomite | Poor | Moderate | Good |
| Hydroxide | Gibbsite | Poor | Good | Moderate |
| Sulphate | Alunite | Moderate | Good | Moderate |
| Sulphate | Gypsum | Poor | Good | Good |
| Borate | Borax | Poor | Moderate | Uncertain |
| Chloride | Halite | Poor | Uncertain | Uncertain |
| Phosphate | Apatite | Moderate | Poor | Good |
| Hydrocarbons | Bitumen | Uncertain | Moderate | Uncertain |
| Oxide | Haematite | Good | Poor | Poor |
| Oxide | Chromite | Poor | Poor | Poor |
| Sulphide | Pyrite | Poor | Poor | Poor |

Good – Minerals that produce a good response in the infrared region.
Moderate – Minerals that can be identified in the IR region. These minerals may not have high contrast responses or are not easily distinguished from some minerals if the system resolution is low.
Poor – Non-diagnostic responses observed for these minerals across the specific infrared regions.
Uncertain – Uncertain response for these minerals across these regions of the infrared.

Adapted from Geospectral imaging (Johannesburg, SA; www.geospectral.co.za) and Specim (Oulu, Finland; www.specim.fi)

Specialised HSI camera systems acquire reflectance spectra from rock or sediment surfaces over a spectral range determined by the camera. As an example, the currently available SisuSCS sediment/rock core scanner (Specim Ltd, Finland) uses one of two demountable cameras that are sensitive over the range 400–1000 nm or 1000–2500 nm (Table 27.4). The choice depends on the intended application such as investigation of rock or wet sediment. Wet sediment investigations can be challenging because water in the samples will cause interference effects in the SWIR, which is the preferred region for mineralogical detection. For wet sediment a VNIR sensitive camera has been used (Grosjean et al. 2014). In some cases it may be possible to temporarily dry the sample surface to acquire useful mineralogical data in the SWIR. Trachsel et al. (2010), Butz et al. (2013) and Grosjean et al. (2014) examined lake sediments and identified useful variations at a sub-varve scale using a SisuSCS (Fig. 27.6).

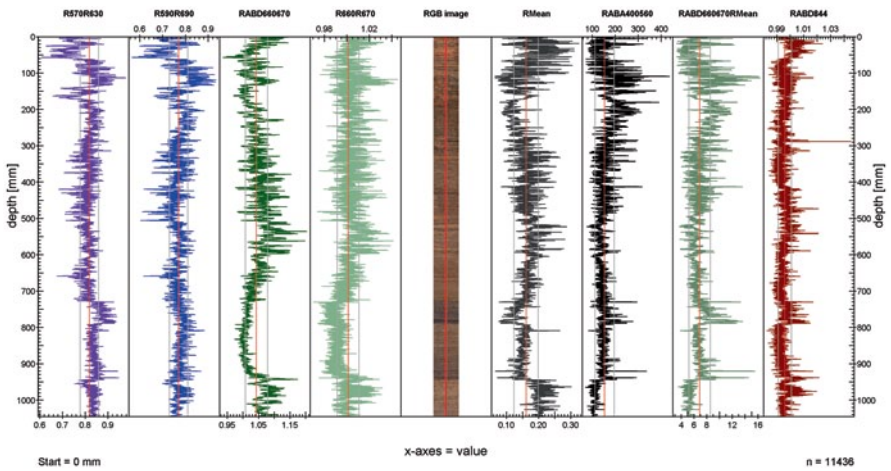


**Fig. 27.6** Spectral indices derived from a hyperspectral scan of a 1 m long lake sediment core from Lake Jaczno (Poland) using a Specim SiSuSCS system. Butz et al. 2013, 2014 (Image courtesy of C. Butz and M. Grosjean)

R570/630 and R590/690 (band ratios) are used in minerogenic sediments to evaluate the amount of clay minerals (e.g. chlorite, illite) against the amount of organic material present.
RABD660670 (Relative absorption band depth) is a relative measure for concentrations of chlorophylls and derivative products in marine sediments and freshwater lakes.
R660/R670 (band ratio) is an index showing the degree of chlorophyll diagenesis.
RMean is the mean of all spectral bands and indicates the total brightness of the sediment.
RABA400560 (Relative Absorption Band Area) is the area of absorption in the blue spectrum indicative of total organic carbon content in marine sediments.
RABD660670/RMean reflects red absorption of pigments.

## *Laser-Based Methods*

**Molecular Spectroscopy** Raman spectroscopy is a type of vibrational spectroscopy that uses a monochromatic laser light source to irradiate a sample and is non-destructive, does not normally require sample preparation and provides information-rich data. Raman is a light scattering technique, and normally all that is required for spectrum collection is to place the sample in the excitation beam and analyse the scattered light. There are several varieties of the technique, termed Dispersive Raman (Smith and Clark 2004; Izake 2010), FT-Raman (Fourier Transform Raman; Cangemi et al. 2010; Kristova et al. 2013) and Time-resolved Raman spectroscopy (Fig. 27.7) (Blacksberg and Rossman 2010). Raman and FT-Raman are complementary techniques resulting in acquisition of very similar spectral information. Generally, dispersive Raman provides more information from microscopic applications due to its higher sensitivity, but FT-Raman is more suitable for bulk material analyses due to their lack of fluorescence.

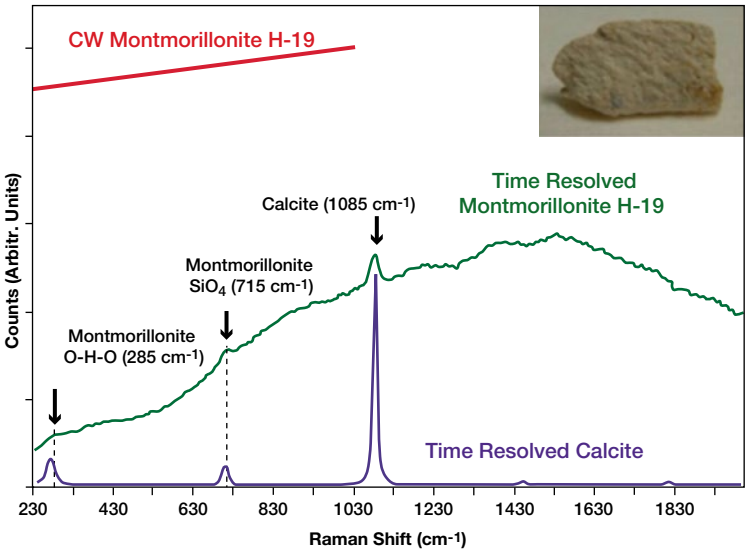


**Fig. 27.7** Example of a time-resolved Raman spectrum showing the benefits of fluorescence removal (Blacksberg et al. 2014). Raman spectra of montmorillonite obtained using pulsed and CW Raman. Under CW illumination, the fluorescence saturates the CCD detector. A pulsed Raman spectrum of calcite is shown revealing that a minor phase of calcite is likely present. (Reproduced with permission from the Optical Society)

**Raman Spectroscopy**

1. Raman spectroscopy acts as a molecular fingerprint containing unique, reproducible, detailed features and provides the possibility of highly selective determinations.
2. The Raman fingerprint is independent of the excitation wavelength. This allows the use of any laser excitation wavelength.
3. Raman spectroscopy can be applied to virtually any sample, of any size that is capable of absorbing the laser excitation beam and where the scattered photons can be detected.
4. Solid, liquid and gaseous samples can be measured as well as transparent or non-transparent samples. Wet samples present no special technical problems.
5. No special pre-scanning preparations of the sample are necessary.
6. Scanning is non-destructive, non-invasive and response is rapid.
7. Raman spectroscopy instruments can be highly compact and portable and their overall characteristics make them suitable as an instrument for extreme environments (e.g. in-situ planetary studies).

**Minerals** are often Raman sensitive, but most have a native color (i.e. are not white or transparent) and often display high fluorescence when excited by visible lasers. Thus, it can be difficult to measure them using conventional Raman measurements. With one proprietary system (Bayspec, San Jose, CA, USA) using a 1064 nm laser, IR sensitive detector and volume-phase-grating, Raman spectra can be measured with high signal:noise without fluorescence interference.

**Dispersive Raman**—usually employs visible laser radiation with typical laser wavelengths of 780 nm, 633 nm, 532 nm, and 473 nm although others are common (1064 nm). One advantage of using shorter wavelength lasers is the enhancement in the Raman signal that occurs at shorter wavelengths. The efficiency of Raman scatter is proportional to $1/\lambda^4$, so there is a strong enhancement as the excitation laser wavelength becomes shorter. However, sample fluorescence becomes a problem at shorter excitation wavelengths and in some cases even minor fluorescence can overwhelm the desired Raman measurement.

**FT-Raman**—An FT-Raman spectrometer uses a laser in the near infrared (1064 nm) and at this wavelength fluorescence is almost completely absent, however because of the $1/\lambda 4$ relationship between Raman scattering intensity and wavelength, the Raman signal is weak. In addition, silicon CCD detectors cannot be used in this region of the spectrum. FT-Raman spectroscopy is particularly well-suited for bulk sample analysis.

**Time-resolved Raman Spectroscopy—**Raman scattering occurs instantaneously in time, while fluorescence occurs on longer time scales. Minerals can contain as many as 25 luminescence centers, each with different decay times from nsec to msec. The distinct timing differences of Raman and fluorescence can be used to separate them.This allows fluorescence-free Raman spectra to be acquired using traditional visible laser excitation (532 nm) and simultaneously measure time-resolved fluorescence spectra for the detection of trace ionic components. Through the combined use of these techniques, the probability of successful mineral identification is greatly increased. Time-resolved pulsed Raman spectroscopy is ideal for fluorescence rejection, since the Raman signal is collected simultaneously with the laser pulse, and photons emitted after the laser pulse can be rejected. Laser pulse widths of the order of 10 ns are typically combined with an intensified charge-coupled device (ICCD) based gated detection system. Most of the fluorescence signal can be rejected by electronic gating so as to detect only photons emitted during the laser pulse.

Adapted from Thermo-Nicolet; BaySpec (San Jose, USA); Smith and Clark (2004); Izake (2010); Blacksberg et al. (2014)

Blacksberg et al. (2014) note that the Raman technique offers clear advantages for non-destructive analysis but there are challenges when investigating complex multi-mineralic systems like soils and rocks. The presence of organic matter also causes difficulties in that fluorescence can overwhelm Raman signals when using 532 nm laser excitation. The use of time resolved Raman helps to reduce the high background signal caused by fluorescence because Raman scattering is an instantaneous process while fluorescence processes are associated with decay times that vary from picosecond to millisecond. In geological materials there can be several fluorescent phases, leading to both long lifetime (mineral) and short lifetime (organic) fluorescence.

**Atomic Spectroscopy** An analytical technology that shows some potential for rapid core scanning is Laser-Induced Breakdown Spectroscopy (LIBS), described as an emerging technology for more than ten years. This is a type of atomic emission spectroscopy in which a single, dual or triple pulse of laser energy is used as the excitation source. It is a high-speed non-contact and virtually non-destructive method of elemental analysis and provides data of semi-quantitative quality. However, generating quantitative data from a complex wet sediment matrix remains a major challenge at present. The output of a pulsed laser, such as a Q-switched Nd:YAG type, is focussed onto the surface of the sample. For the duration of the laser pulse (typically 10 ns) the power density at the surface of the sample can exceed 1 GW per $cm^2$ using a compact laser device and simple focusing lenses. At such high power densities, several micrograms of material may be vapourised from the sample surface through laser ablation after a laser shot (or multiple shot) that generates a short-lived but luminous plasma having a temperature up to 10,000 K. A wide range of volatilised elements in the plasma from the sample will initially exist as excited ionic and atomic species that upon cooling emit characteristic optical radiation as they return to lower energy states. The emitted light can be readily measured using a sensitive CCD device, often via the same fibre optic bundle that delivered the excitation laser. LIBS therefore provides potential to qualitatively, and possibly quantitatively, identify elements in a sediment sample with high sensitivity (Barbinia et al. 2002; Cremers and Radziemsk 2013). However, in soft sediments, the laser excitation pulses used during a LIBS single point analysis may produce an ever-deepening pit that can limit the light collected by the CCD.

## *Magnetic Methods*

**High-Resolution Magnetic Devices** Bartington magnetic susceptibility sensors are already included on some core scanners as options and have long been used on Geotek MSCL systems (Geotek, Daventry, UK). The current resolution is typically 5 mm but it may be possible to increase resolution to 1 mm. Such measurements require flat samples and close coupling. It remains to be seen whether further developments take place leading to higher resolution measurements.

## Numerical and Software Developments

Efficient quantification of core scanner data will continue to develop and is a key requirement in the evolution of core scanner technology. Many researchers continue to use either count or count-rate data as supplied by the instrument's software or they may adopt a semi-empirical approach by analyzing a small number of sub-samples using WD-XRF, ED-XRF or ICP-OES to calibrate their data (e.g. Boyle et al. 2015; Croudace et al. 2015). A more advanced approach based on the use of multi-variate statistics is described by Weltje et al. (2015) and represents a significant advance that could become increasingly used. Further developments in data quantification are likely. Instrument manufacturers are tending to move toward more integrated and comprehensive quantification software (e.g. Cox Analytical Systems have recently developed a package called Q-quant which offers improved peak fitting, calibration and calculation procedures for ITRAX data). Data Analysis and data visualization is already quite well developed (e.g. ItraxPlot, RediCore software etc.) but there is scope for further enhancements depending on application. At least one core scanner manufacturer is working on a software solution to infer mineralogy and mineralogical distribution from elemental data (e. g. Cox RockCore, Cox Analytical Systems, Gothenburg) using multivariate statistical analysis.

## Conclusion

The commercial development of non-destructive, high-resolution core scanners from the year 2000 to the present has contributed to a rapid expansion of palaeoclimate and environmental research. Recent application of these scanners to mineral exploration has expanded the market and led to innovation and competition among instrument manufacturers. The international scale of these research enterprises has been marked by an exponential rise in published output from 1995–2015. Other areas benefitting from the high-resolution capability of these scanners include dendrochemistry, environmental forensics, environmental geochemistry and more recently mineral exploration. The impact of these instruments could grow if new sensors and data processing options are added to existing platforms. Some of these sensors may emerge from R&D associated with studies of extreme environments. The significant investment made in planetary research programmes (such as the Mars Science Lab Rover), where there has been a focus on producing non-contact (standoff) sensors, could also be adapted for core scanners. Inclusion of some of these developments on current core scanner models will depend on their analytical value, user interest and company investment. Alternatively, specialist instrument manufacturers may develop specific sediment/rock scanning instruments (several already exist) that would complement existing XRF core scanners.

**Acknowledgments** The authors are grateful to the owners of various proprietary information sources (Inel, France; Specim, Finland; Geospectral Imaging, South Africa) that have facilitated this forward look. We are also grateful to Rainer Bars and Hanna Junttila of Specim for their helpful comments. Finally, we thank Kate Davis (OES-NOC) for adapting and re-drawing several of the figures.

## References

Barbinia R, Colaoa F, Lazica V, Fantonia R, Paluccia A, Angelone M (2002) On board LIBS analysis of marine sediments collected during the XVI Italian campaign in Antarctica. Spectrochimica Acta B 57:1203–1218

Beck L, Rousselière H, Castaing J, Duran A, Lebon M, Moignard B, Plassard F (2014) First use of portable system coupling X-ray diffraction and X-ray fluorescence for in-situ analysis of prehistoric rock art. Talanta 129:459–464

Blacksberg J, Rossman GR, Gleckler A (2010) Time-resolved Raman spectroscopy for in situ planetary mineralogy. Appl Opt 49:4951–4962

Blacksberg J, Alerstam E, Maruyama Y, Cochrane C, Rossman GR (2014) Time-resolved raman spectroscopy for planetary science. 11th International GeoRaman Conference, 5055.pdf

Boyle JF, Chiverrell RC, Schillereff D (2015) Approaches to water content correction and calibration for µXRF core scanning: comparing X-ray scattering with simple regression of elemental concentrations. In: Croudace IW, Rothwell RG (eds) Micro-XRF studies of sediment cores. Springer, Dordrecht

Butz C, Grosjean M, Tylmann W (2013) Hyperspectral imaging of lake sediments. www.specim.fi/files/pdf/Uni_Bern.pdf. Accessed 22 Nov 2014

Butz C, Grosjean M, Enters D, Tylmann W (2014) Exploring the potential of hyper-spectral imaging for the biogeochemical analysis of varved lake sediments. EGU General Assembly 2014, Vienna, Austria, id.7781

Cangemi M, Bellanca A, Borin S, Hopkinson L, Mapelli F, Neri R (2010) The genesis of actively growing siliceous stromatolites: evidence from lake Specchio di Venere, Pantelleria Island, Italy. Chem Geol 318–330

Cremers DA, Radziemsk LJ (2013) Handbook of laser-induced breakdown spectroscopy. Wiley

Croudace IW, Rothwell RG (2010) Micro-XRF sediment core scanners: important new tools for the environmental and earth sciences. Spectrosc Eur 22:6–13

Croudace IW, Rindby A, Rothwell RG (2006) Itrax: description and evaluation of a new sediment core scanner. In: Rothwell RG (ed) New techniques in sediment core analysis, vol 267. Geological Society Special Publication, London, pp 51–63

Croudace IW, Romano E, Ausili A, Bergamin L, Rothwell RG (2015) X-ray core scanners as an environmental forensics tool: a case study of polluted harbour sediment (Augusta Bay, Sicily). In: Croudace IW, Rothwell RG (eds) Micro-XRF studies of sediment cores. Springer, Dordrecht

CSIRO HyLogging Systems (2012) Hyperspectral mineralogical logging and imaging of drill core and chips. http://www.csiro.au/Portals/Publications/Brochures–Fact-Sheets/hylogging.aspx. Accessed 15 Nov 2014

Escárate P, Bailo D, Guesalaga A, Rossi V, Albertini VR (2009) Energy dispersive X-ray diffraction spectroscopy for rapid estimation of calcite in copper ores. Miner Eng 22:566–571

Feng L, Shaul B, Iwanczyk JS, Patt BE, Tull CR (2004) VORTEX: a new high performance silicon multicathode detector for XRD and XRF applications. Proc SPIE 5198:103–110

Grosjean M, Amann B, Butz C, Rein B, Tylmann W (2014) Hyperspectral imaging: a novel, non-destructive method for investigating sub-annual sediment structures and composition. Past Global Changes (PAGES) Magazine 22:10–11

Huntington J (2007) Mineralogical analysis of hylogging data of drill hole BUGD049 bullant gold mine Western Australia CSIRO Exploration and Mining Investigation Report No. P2006/739, January 2007

Huntington JF, Mauger AJ, Skirrow RG, Bastrakov EN, Connor PC, Mason P, Keeling JL, Coward DA, Berman M, Phillips R, Whitbourn LB, Heithersy PS (2004) Automated mineralogical logging of core from the Emmie Bluff, iron oxide copper-gold prospect, South Australia, PACRIM 2004 Congress, Australasian Institute of Mining and Metallurgy Publication Series, 223–230

Izake EL (2010) Forensic and homeland security applications of modern portable Raman spectroscopy. Forensic Sci Int 202:1–8

Kelloway SJ, Ward CR, Marjo CE, Wainwright IE, Cohen DR (2015) Analysis of coal cores using micro-XRF scanning techniques. In: Croudace IW, Rothwell RG (eds) Micro-XRF studies of sediment cores. Springer, Dordrecht

Kristova P, Hopkinson L, Rutt K, Hunter H, Cressey G (2013) Quantitative analyses of powdered multi-minerallic carbonate aggregates using a portable Raman spectrometer. Am Miner 98:401–409

O'Dwyer JN, Tickner JR (2008) Quantitative mineral phase analysis of dry powders using energy-dispersive X-ray diffraction. Appl Radiat Isot 66:1359–1362

Roache TJ, Walshe JL, Huntington JF, Quigley MA, Yang K, Bil BW, Blake KL, Hyvärinen T (2011) Epidote–clinozoisite as a hyperspectral tool in exploration for Archean gold, Australian. J Earth Sci 58:813–822

Rothwell RG, Croudace IW (2015) Micro-XRF studies of sediment cores: a perspective on capability and application in the environmental sciences. In: Croudace IW, Rothwell RG (eds) Micro-XRF studies of sediment cores. Springer, Dordecht

Rothwell RG, Hoogakker B, Thomson J, Croudace IW (2006) Turbidite emplacement on the southern Balearic Abyssal Plain (W. Mediterranean Sea) during marine isotope stages 1–3; an application of XRF scanning of sediment cores in lithostratigraphic analysis. In: Rothwell RG (ed) New techniques in sediment core analysis, vol 267. Geological Society Special Publication, London, pp 51–63

Smith RB (2012) Introduction to hyperspectral imaging, microImages, Inc., www.microimages.com/documentation/Tutorials/hyprspec.pdf. Accessed 15 Nov 2014

Smith GD, Clark RJH (2004) Raman microscopy in archaeological science. J Archaeol Sci 31:1137–1160

Thomson J, Croudace IW, Rothwell RG (2006) A geochemical application of the ITRAX scanner to a sediment core containing eastern Mediterranean sapropel units. In R.G. Rothwell (ed) New techniques in sediment core analysis, vol 267. Geological Society Special Publication, London, pp 51–63

Trachsel M, Grosjean M, Schnyder D, Kamenik C, Rein B (2010) Scanning reflectance spectroscopy (380–730 nm): a novel method for quantitative high-resolution climate reconstructions from minerogenic lake sediments. J Paleolimnol 44:979–994

Weltje GJ, Bloemsma MR, Tjallingii R, Heslop D, Röhl U, Croudace IW (2015) Prediction of geochemical composition from XRF Core Scanner data: a new multivariate approach including automatic selection of calibration samples and quantification of uncertainties. In: Croudace IW, Rothwell RG (eds) Micro-XRF studies of sediment cores. Springer, Dordrecht

# Index





I. W. Croudace, R. G. Rothwell (eds.), *Micro-XRF Studies of Sediment Cores*,
Developments in Paleoenvironmental Research 17, DOI 10.1007/978-94-017-9849-5